Edited by S. David Jackson and Justin S. J. Hargreaves

WILEY-VCH

Metal Oxide Catalysis

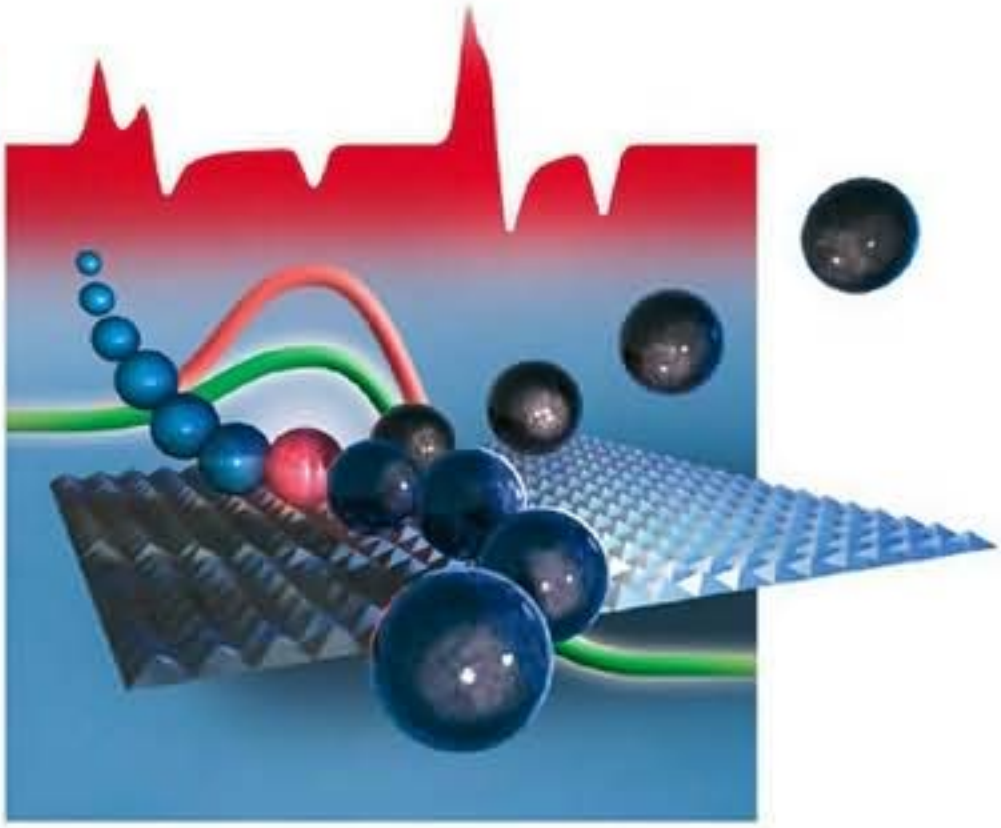

Metal Oxide Catalysis

Edited by
S. David Jackson and
Justin S. J. Hargreaves

Related Titles

C. N. R. Rao, A. Müller,
A. K. Cheetham (eds.)

Nanomaterials Chemistry

Recent Developments and New Directions

2007

ISBN: 978-3-527-31664-9

C. N. R. Rao, A. Müller,
A. K. Cheetham (eds.)

The Chemistry of Nanomaterials

Synthesis, Properties and Applications

2004

ISBN: 978-3-527-30686-2

R. A. van Santen, M. Neurock

Molecular Heterogeneous Catalysis

A Conceptual and Computational Approach

2006

ISBN: 978-3-527-29662-0

H. U. Blaser, E. Schmidt (eds.)

Asymmetric Catalysis on Industrial Scale

Challenges, Approaches and Solutions

2004

ISBN: 978-3-527-30631-2

J. Hagen

Industrial Catalysis

A Practical Approach

2006

ISBN: 978-3-527-31144-6

Metal Oxide Catalysis

Edited by
S. David Jackson and Justin S. J. Hargreaves

WILEY-VCH Verlag GmbH & Co. KGaA

The Editors

Prof. S. David Jackson
University of Glasgow
Department of Chemistry
WestCHEM
Joseph Black Building
Glasgow, G12 8QQ
United Kingdom

Dr. Justin S. J. Hargreaves
University of Glasgow
Department of Chemistry
WestCHEM
Joseph Black Building
Glasgow, G12 8QQ
United Kingdom

Library of Congress Card No.: applied for

British Library Cataloguing-in-Publication Data
A catalogue record for this book is available from the British Library.

Bibliographic information published by the Deutsche Nationalbibliothek
Die Deutsche Nationalbibliothek lists this publication in the Deutsche Nationalbibliografie; detailed bibliographic data are available on the Internet at <http://dnb.d-nb.de>

Cover Design Schulz Grafik-Design, Fußgönheim
Composition SNP Best-set Typesetter Ltd., Hong Kong
Printing Strauss GmbH, Mörlenbach
Bookbinding Litges & Dopf GmbH, Heppenheim

Printed in the Federal Republic of Germany
Printed on acid-free paper

ISBN: 978-3-527-31815-5

Contents to Volume 1

Metal Oxide Catalysis. Edited by S. David Jackson and Justin S. J. Hargreaves

ISBN: 978-3-527-31815-5

Contents to Volume 2

Metal Oxide Catalysis. Edited by S. David Jackson and Justin S. J. Hargreaves

ISBN: 978-3-527-31815-5

Preface

Metal oxide catalysis continues to grow at a rapid rate, reflecting the wide range of chemical reactions that can be enhanced by the use of a metal oxide catalyst. The advances in characterization techniques and their application to the field have improved our understanding of the processes occurring on the surface and in the bulk. This two volume review series is therefore timely.

The first volume comprises a series of in-depth contributions detailing a number of characterization methods frequently applied to metal oxides. The aim of this volume, although not exhaustive, is to provide a basic introduction to each technique and then a general overview of its application in the area of metal oxide catalysis, thereby providing the general background against which many advances in the area of metal oxide catalysis have been made. The second volume is a compilation of review chapters detailing the catalytic applications of oxides and related materials. The contributions to this volume can be subdivided into two general categories – those that detail a specific material, or class of materials, and those that detail a specific reaction, or class of reactions. It was impossible to try to cover all the myriad reactions catalyzed by oxides so we have had to be selective. We hope we have managed to give a flavor of the range of chemistry accessible and would encourage the interested reader to investigate alternative sources for complementary coverage, for example on zeolites, etc.

Taken together, these volumes represent a marker of the high quality research that has been undertaken in the characterization of metal oxides and into the reactions they catalyze. We hope you will find them enjoyable and illuminating.

We would like to take this opportunity to thank all contributors for their chapters. Their cooperation in adhering to the, at times tight, deadlines is much appreciated. Finally, we wish to express our gratitude to the staff at Wiley-VCH, and in particular Manfred Köhl and Stefanie Volk, for their kind assistance in bringing these volumes to fruition.

Glasgow, May 2008

S. D. Jackson
J. S. J. Hargreaves

Metal Oxide Catalysis. Edited by S. David Jackson and Justin S. J. Hargreaves

ISBN: 978-3-527-31815-5

List of Contributors

Khalaf AlGhamdi
University of Glasgow
Department of Chemistry
WestCHEM
Joseph Black Building
Glasgow, G12 8QQ
United Kingdom

Kazushi Arata
Hokkaido University of Education
Department of Science
Hachiman-cho 1-2
Hakodate 040-8567
Japan

Aline Auroux
CNRS-Université Lyon 1
Institut de Recherches sur la Catalyse et l'Environnement de Lyon
UMR 5256
2 avenue Einstein
69626 Villeurbanne
France

Jonathan K. Bartley
Cardiff University
School of Chemistry
Park Place
Cardiff, CF10 3AT
United Kingdom

Simona Bennici
CNRS-Université Lyon 1
Institut de Recherches sur la Catalyse et l'Environnement de Lyon
UMR 5256
2 avenue Einstein
69626 Villeurbanne
France

Guido Busca
Università di Genova
Dipartimento di Ingegneria Chimica e di Processo "G.B. Bonino"
Laboratorio di Chimica delle Superfici e Catalisi Industriale
P.le J.F. Kennedy
16129 Genova
Italy

Fabrizio Cavani
Università di Bologna
Dipartimento di Chimica Industriale e dei Materiali
Viale Risorgimento 4
40136 Bologna
Italy

Metal Oxide Catalysis. Edited by S. David Jackson and Justin S. J. Hargreaves

ISBN: 978-3-527-31815-5

Gabriele Centi
Università di Messina
Dipartimento di Chimica Industriale ed Ingegneria dei Materiali
Salita Sperone 31
98166 Messina
Italy

Lifang Chen
Colorado School of Mines
Department of Chemistry and Geochemistry
304 Coolbaugh Hall
Golden, CO 80401
USA

Mario G. Clerici
Via Europa 34
20097 San Donato Milanese
Italy
and
Enitecnologie S.p.A.
Via Maritano 26
20097 S. Donato Milanese
Italy

Salvatore Coluccia
Università di Torino
Dipartimento di Chimica IFM and Centro di Eccellenza NIS
V. P. Giuria 7
10125 Torino
Italy

Rudy Coquet
Fuel Research Laboratory
Research & Development Division
Nippon Oil Corporation
8, Chidoricho, Naka-ku
Yokohama, 231-0815
Japan

Nicholas F. Dummer
Cardiff University
School of Chemistry
Park Place
Cardiff, CF10 3AT
United Kingdom

Enrica Gianotti
Università di Torino
Dipartimento di Chimica IFM and Centro di Eccellenza NIS
V. P. Giuria 7
10125 Torino
Italy

Lynn F. Gladden
University of Cambridge
Department of Chemical Engineering
Pembroke Street
New Museums Site
Cambridge, CB2 3RA
United Kingdom

Justin S. J. Hargreaves
University of Glasgow
Department of Chemistry
WestCHEM
Joseph Black Building
Glasgow, G12 8QQ
United Kingdom

Kara L. Howard
Cardiff University
School of Chemistry
Main Building
Park Place
Cardiff, CF10 3AT
United Kingdom

Juncheng Hu
South Central University for Nationalities
Key Laboratory of Catalysis and Materials Sciences of the State Ethnic Affairs Commission & Ministry of Education
Wuhan, 430074
China

Graham J. Hutchings
Cardiff University
School of Chemistry
Park Place
Cardiff, CF10 3AT
United Kingdom

S. David Jackson
University of Glasgow
Department of Chemistry
WestCHEM
Joseph Black Building
Glasgow, G12 8QQ
United Kingdom

Hack-Sung Kim
Northwestern University
Department of Chemistry
Center for Catalysis and Surface Science
2145 Sheridan Road
Evanston, IL 60208-3113
USA
and
Argonne National Laboratory
Chemical Sciences and Engineering Division
Argonne, IL 60439
USA

James McGregor
University of Cambridge
Department of Chemical Engineering
Pembroke Street
New Museums Site
Cambridge, CB2 3RA
United Kingdom

Philippe Marion
RHODIA Recherches et Technologie
Pole Grands Procédés Spécialités Industrielles, CRTL
85, Rue des Frères Perret
69190 Saint Fons
France

Gianmario Martra
Università di Torino
Dipartimento di Chimica IFM and Centro di Eccellenza NIS
V. P. Giuria 7
10125 Torino
Italy

Jean-Marc M. Millet
Université Claude Bernard – Lyon 1
Institut de Recherches sur la Catalyse et l'Environnement de Lyon
2 avenue A. Einstein
69626 Villeurbanne
France

Damien M. Murphy
Cardiff University
School of Chemistry
Main Building
Park Place
Cardiff, CF10 3AT
United Kingdom

Ryan Richards
Colorado School of Mines
Department of Chemistry and Geochemistry
304 Coolbaugh Hall
Golden, CO 80401
USA

Robert Schlögl
Fritz-Haber-Institut der Max-Plank-Gesellschaft
Department of Inorganic Chemistry
Faradayweg 4–6
14195 Berlin
Germany

Peter C. Stair
Northwestern University
Department of Chemistry
Center for Catalysis and Surface Science
2145 Sheridan Road
Evanston, IL 60208-3113
USA
and
Argonne National Laboratory
Chemical Sciences and Engineering Division
Argonne, IL 60439
USA

Michael Stockenhuber
University of Newcastle
Chemical Engineering
University Drive
Callaghan Campus, NSW 2308
Australia

Stuart H. Taylor
Cardiff University
School of Chemistry
Cardiff Catalysis Institute
Park Place
Cardiff, CF10 3AT
United Kingdom

Detre Teschner
Fritz-Haber-Institut der Max-Plank-Gesellschaft
Department of Inorganic Chemistry
Faradayweg 4–6
14195 Berlin
Germany

Elaine M. Vass
Fritz-Haber-Institut der Max-Plank-Gesellschaft
Department of Inorganic Chemistry
Faradayweg 4–6
14195 Berlin
Germany

Jacques C. Védrine
Université P. & M. Curie-Paris VI
Laboratoire de Réactivité de Surface
4, place Jussieu
75252 Paris
France

Israel E. Wachs
Lehigh University
Chemical Engineering Department
Operando Molecular Spectroscopy & Catalysis Laboratory
Bethlehem, PA 18015
USA

Richard P.K. Wells
University of Aberdeen
Department of Chemistry
Surface Chemistry and Catalysis Group
Aberdeen, AB24 3UE
United Kingdom

David J. Willock
Cardiff University
School of Chemistry
Main Building
Park Place
Cardiff, CF10 3AT
United Kingdom

Zili Wu
Oak Ridge National Laboratory
Chemical Science Division
Center for Nanophase Materials Sciences
Oak Ridge, TN 37831-6493
USA

Wuzong Zhou
University of St. Andrews
School of Chemistry
Purdie Building, North Haugh
St. Andrews, Fife KY16 9ST
United Kingdom

Contents to Volume 2

Metal Oxide Catalysis. Edited by S. David Jackson and Justin S. J. Hargreaves

ISBN: 978-3-527-31815-5

Contents to Volume 1

Metal Oxide Catalysis. Edited by S. David Jackson and Justin S. J. Hargreaves

ISBN: 978-3-527-31815-5

1
EPR (Electron Paramagnetic Resonance) Spectroscopy of Polycrystalline Oxide Systems

Damien M. Murphy

1.1
Introduction

Electron Paramagnetic Resonance (EPR), sometimes referred to as Electron Spin Resonance (ESR), is a widely used spectroscopic technique to study paramagnetic centers on various oxide surfaces, which are frequently encountered in heterogeneous catalysis. Diamagnetic oxide materials can also be studied using suitable paramagnetic probes, including nitroxides and transition metal ions. These observable paramagnetic centers may include surface defects, inorganic or organic radicals, metal cations or supported metal complexes and clusters. Each of these paramagnetic species will produce a characteristic EPR signature with well defined spin Hamiltonian parameters. However, the magnetic properties, stability and reactivity of these centers may vary dramatically depending on the nature of the support or the measurement conditions. In some case, radicals stable on one surface may be transient on another, while variations in the EPR spectra of these radicals may be observed simply by altering the pre-treatment conditions of the support. Furthermore, the spin Hamiltonian parameters for a particular paramagnetic species may vary greatly from one support to another. A number of "external" perturbations, such as the specific location of the species on a surface, the presence of other interaction species in the catalytic system, the size of the metal particles, and so on, can alter the spin Hamiltonian parameters, resulting in a significantly modified EPR profile. Therefore one must interpret the experimental spectrum with careful consideration of these variables and where possible record the spectra under a variety of conditions to reinforce the assignment. Finally, the accurate analysis of the experimental spectrum can only be achieved by simulation and the resulting spin Hamiltonian parameters can then be compared to values obtained by theoretical treatments. All of the steps are crucial in order to derive a complete description of the electronic structure of the paramagnetic species, and the purpose of this chapter is to explain and illustrate how these analytical steps are performed in the interpretation of EPR spectra.

Metal Oxide Catalysis. Edited by S. David Jackson and Justin S. J. Hargreaves

ISBN: 978-3-527-31815-5

Most of the literature on surface paramagnetic centers since the mid-1990s has originated from studies in heterogeneous catalysis and material science. EPR has long been recognized as a powerful tool for the catalytic chemist, as the high sensitivity of the technique permits the detection of low concentrations of active sites. A number of review articles and monographs have appeared over the years specifically on EPR in catalysis, notably by Lunsford [1], Howe [2], Che [3], Giamello [4], Sojka [5] and Dyrek [6]. The applications of EPR spectroscopy to studies in catalysis and surface chemistry of metal oxides has also been treated in a number of papers [7, 8]. Selected examples illustrate the possibilities offered by EPR techniques towards a deeper understanding of catalyst preparation, the nature of the surface active sites and the types of reaction intermediate as well as details of catalytic reaction mechanisms [9, 10]. Hunger and Weitkamp [11] reviewed the subject of *in situ* spectroscopic methods, including *in situ* EPR to directly follow the evolution of paramagnetic surface intermediates in conditions extremely similar to those occurring in a real catalytic reactor, and so this area will not be covered here.

A complete description of the physics and fundamental concepts behind the EPR technique is beyond the scope of this chapter. Numerous textbooks on the subject of EPR, describing the practicalities of the technique, the fundamental theory and also the primary applications of the technique to different areas of chemistry, physics and biology, are widely available [12–17], in addition to the more specialist textbooks devoted to pulsed methods [18]. It is important to acknowledge that since 1993 there has been extensive development in the areas of pulsed techniques [18] and high-frequency EPR. High-frequency EPR provides several advantages over low-frequency techniques. For example, it offers increased resolution of g values, which is important in systems where spectral lines may not be resolved at lower fields. Additionally, high-frequency EPR has an increased absolute sensitivity making it particularly useful for studying systems where the number of paramagnetic species is inherently low. Pulsed EPR has also provided the experimentalist with additional tools to interrogate the paramagnetic system, particularly in relation to the advanced hyperfine techniques of ENDOR (Electron Nuclear Double Resonance), HYSCORE (Hyperfine Sublevel Correlation), ESEEM (Electron Spin Echo Envelope Modulation) and ELDOR (Electron Electron Double Resonance) detected NMR. In this chapter, only the basic principles of continuous wave (*cw*-) EPR will be presented, since this method is still the most widely used (primarily owing to instrumental availability) in studies of heterogeneous catalysis.

1.2 Basic Principles of EPR

1.2.1 The Electron Zeeman Interaction

The electron is a negatively charged particle which possesses orbital angular momentum as it moves around the nucleus. The electron also possesses spin

angular momentum **S** as it spins about its own axis. The magnitude of **S** is given by

$$\mathbf{S} = (h/2\pi)[S(S+1)]^{1/2} \tag{1.1}$$

where S = the spin quantum number and h = Planck's constant. By restricting the dimension to one specified direction, usually assigned the z direction, then the component of the spin angular momentum can only assume two values:

$$\mathbf{S}_z = M_S h/2\pi \tag{1.2}$$

The term M_S can have $(2S + 1)$ different values: $+S$, $(S - 1)$, $(S - 2)$ and so on. If the possible values of M_S differ by one and range from $-S$ to $+S$ then the only two possible values for M_S are $+1/2$ and $-1/2$ for a single unpaired electron.

The most important physical consequence of the electron spin is the associated magnetic moment, μ_e. This magnetic moment is directly proportional to the spin angular momentum and one may therefore write

$$\mu_e = -g_e \mu_B \mathbf{S} \tag{1.3}$$

The negative sign arises from the fact that the magnetic momentum of the electron is collinear but *antiparallel* to the spin itself. The factor $(g_e\mu_B)$ is referred to as the magnetogyric ratio and is composed of two important factors. The Bohr magneton, μ_B, is the magnetic moment for one unit of quantum mechanical angular momentum:

$$\mu_B = \frac{e\hbar}{2m_e} \tag{1.4}$$

where e is the electron charge, m_e is the electron mass and $\hbar = \frac{h}{2\pi}$. The factor, g_e, is known as the free electron g-factor with a value of 2.002 319 304 386 (one of the most accurately known physical constants). In a simple classical sense, one may view g_e as the proportionality constant between μ_e and $\mu_B S$.

This magnetic moment interacts with the applied magnetic field. In classical terms the energy of the interaction between the magnetic moment (μ) and the field (B) is described by

$$E = -\mu \cdot B \tag{1.5}$$

For a quantum mechanical system one must replace μ by the corresponding operator, giving the following simple spin Hamiltonian for a free electron in a magnetic field:

$$\hat{H} = g_e \mu_B S \cdot B \tag{1.6}$$

If the field is defined along the z direction, then the scalar product simplifies to the following Hamiltonian:

$$\hat{H} = g_e \mu_B S_z \cdot B \tag{1.7}$$

The S_z value in the above equation can then be replaced by M_S (in quantum mechanical terms the only operator in the right hand term above is S_z), giving

$$E = g_e \mu_B B M_S \tag{1.8}$$

Since $M_S = \pm 1/2$ only two energy states are available, which are degenerate in the absence of a magnetic field, but as B increases this degeneracy is lifted linearly as illustrated in Figure 1.1. The separation of the two levels can be matched to a quantum of radiation through the Bohr frequency condition:

$$\Delta E = h\nu = g\mu_B B \tag{1.9}$$

The existence of two Zeeman levels, and the possibility of inducing transitions from the lower energy level to the higher energy level is the very basis of EPR spectroscopy. The resonance experiment can be conducted in two ways; either the magnetic field is kept constant and the applied frequency varied, or the applied frequency is held constant and the magnetic field is varied. In EPR spectroscopy the latter case is usually used since it is far easier to vary the magnetic field over a wide range than to change frequency.

From Equation 1.9 it can be seen that the frequency required for the transition to occur is about 2.8 MHz per Gauss of applied field. This means that for the magnetic field usually employed in the laboratory, the radiation required belongs to the microwave region. For organic radicals the magnetic field used is in the region of 3400 Gauss and the corresponding applied frequency is in the microwave region of the electromagnetic spectrum (ν~9–10 GHz). This corresponds to a wavelength of about 3.4 cm and is known as the X-band frequency. Other commonly used (and commercially available) frequencies include L-band (ν~0.8–

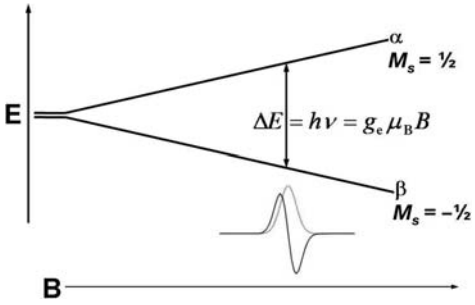

Figure 1.1 Energy levels for an electron spin ($S = \pm 1/2$) in an applied magnetic field B.

1.2 Hz), S-band (ν~3.4–3.8 Hz), K-band (ν~24 GHz), Q-band (ν~34 GHz) and W-band (ν~94 GHz). There are various advantages of going to higher and lower frequencies, depending on the paramagnetic system in question, but X-band offers the best compromise for resolution, intensity and ease of use.

It is worth noting that the SI units of magnetic field strength, or more correctly magnetic flux density, are the Tesla, T, or millitesla, mT. However for historical reasons the older units of Gauss, G, are still commonly used, where 1 mT = 10 G.

There are two fundamental differences between EPR (and NMR) and other spectroscopic techniques. Firstly, the magnetic component of the applied electromagnetic radiation (microwave) interacts with permanent magnetic moments created by the electron (or nucleus in the case of NMR). In many other spectroscopic techniques, permanent or fluctuating electric dipole moments in the sample interact with the electric field component of the electromagnetic radiation. Secondly, a distinguishing feature of EPR is the experimental setup, which is based on a monochromatic radiation source coupled with a variable magnetic field. In other words the EPR spectrum is essentially a plot of microwave absorption (at constant frequency) as a function of applied magnetic field.

At thermal equilibrium and under the influence of the external applied magnetic field, the spin population is split between the two Zeeman levels (Figure 1.1) according to the Maxwell–Boltzmann law:

$$\frac{n_1}{n_2} = e^{\frac{-\Delta E}{kT}} \tag{1.10}$$

where k is the Boltzmann constant, T the absolute temperature and n_1 and n_2 the spin populations characterized by the M_S values of +1/2 and −1/2 respectively. At 298 K in a field of about 3000 G the distribution shows that:

$$\frac{n_1}{n_2} = e^{\frac{-\Delta E}{kT}} = e^{\frac{-g_e \mu_e B}{kT}} \tag{1.11}$$

This gives a value of $n_1/n_2 = 0.9986$. The populations of the two Zeeman levels are therefore almost equal, but the slight excess in the lower level gives rise to a net absorption. However, this would very quickly lead to the disappearance of the EPR signal as the absorption of energy would equalize these two states. Consequently there has to be a mechanism for energy to be lost from the system. Such mechanisms exist and are known as relaxation processes.

1.2.2 Relaxation Processes

If electrons were to be continually promoted from a low energy level to a high level then the populations of the two energy levels would equalize and there would be no net absorption of radiation. In order to maintain a population excess in the

lower level, the odd electrons from the upper level give up the $h\nu$ quantum to return to the lower level and satisfy the Maxwell–Boltzmann law. The release of this energy occurs via a spin relaxation process, of which there are two types, known as spin–lattice relaxation and spin–spin relaxation.

In the first case, the energy is dissipated within the lattice as phonons, that is, vibrational, rotational and translational energy. The mechanism by which this dissipation occurs is known as spin–lattice relaxation. It is characterized by an exponential decay of energy as a function of time. The exponential time constant is denoted T_{1e} and is called the spin–lattice relaxation time. In the second case the initial equilibrium may also be reached by a different process. There could be an energy exchange between the spins without transfer of energy to the lattice. This phenomenon, known as spin–spin relaxation is characterized by a time constant T_{2e} called the spin–spin relaxation time.

When both spin–spin and spin–lattice relaxations contribute to the EPR line, the resonance line width (ΔB) can be written as

$$\Delta B \propto \frac{1}{T_{1e}} + \frac{1}{T_{2e}} \tag{1.12}$$

In general, $T_{1e} > T_{2e}$ and the line width depends mainly on spin–spin interactions. T_{2e} increases on decreasing the spin concentration, that is, the spin–spin distance in the system. On the other hand when T_{1e} becomes very short, below roughly 10^{-7} sec, its effect on the lifetime of a species in a given energy level makes an important contribution to the linewidth. In some cases the EPR lines are broadened beyond detection.

T_{1e} is inversely proportional to the absolute temperature ($T_{1e} \propto T^{-n}$) with n depending on the precise relaxation mechanism. In such a case, cooling the sample increases T_{1e} and usually leads to detectable lines. Thus quite often EPR experiments are performed at liquid nitrogen (77 K) or liquid helium (4 K) temperatures. On the other hand if the spin–lattice relaxation time is too long, electrons do not have time to return to the ground state. The populations of the two levels (n_1 and n_2) tend therefore to equalize and the intensity of the signal decreases, being no longer proportional to the number of spins in the sample itself. This effect, known as saturation, can be avoided by exposing the sample to low incident microwave powers. This is an important consideration, particularly when estimating the number of spins in a paramagnetic system using a reference standard (see Section 1.2.8).

1.2.3
The Nuclear Zeeman Interaction

If the interaction of the electron with an applied external magnetic field were the only effects detectable by EPR, then all spectra would consist of a single line and would be of little interest to chemists. However, the most useful chemical information that can be derived from an EPR spectrum usually results from nuclear

Table 1.1 Nuclear properties and ENDOR frequencies for selected nuclei.

Isotope	Spin (%)	Abundance	Magnetogyric ratio, $\gamma \times 10^{27}$ (J T^{-1})	ENDOR freq. (MHz at 0.350 T)
^{1}H	$\frac{1}{2}$	99.988	28.2105	14.902 18
^{2}H	1	0.011	4.3305	2.2875
^{13}C	$\frac{1}{2}$	1.07	7.0933	3.7479
^{14}N	1	99.636	2.0378	1.077 19
^{15}N	$\frac{1}{2}$	0.364	−2.8585	1.511 04
^{19}F	$\frac{1}{2}$	100	26.5396	14.016 48
^{23}Na	$\frac{3}{2}$	100	7.4620	3.944 33
^{31}P	$\frac{1}{2}$	100	11.4198	6.0380
^{39}K	$\frac{3}{2}$	93.258	1.3165	0.696 33
^{63}Cu	$\frac{3}{2}$	69.15	7.4772	3.961 56
^{65}Cu	$\frac{3}{2}$	30.85	8.010	4.2359

hyperfine structure. The source of this hyperfine structure is the interaction of magnetic nuclei, within the paramagnetic species, with the magnetic moment of the unpaired electron. Many molecules contain nuclei that have a magnetic moment, and these can interact with the electron to give hyperfine structure (Table 1.1).

Some nuclei also possess spin, when the number of neutrons and protons are both uneven, and therefore have spin angular momentum. The spin of a nucleus is described by the spin quantum number, I. The angular momentum of a nucleus with spin I is given by:

$$\text{Nuclear angular momentum } (I) = \hbar[I(I+1)]^{1/2} \tag{1.13}$$

As with electron spin angular momentum (Equation 1.1), the orientation of the vector along an axis is quantized. The magnitude of the angular momentum along the z-axis is given by $M_I h$, where M_I can have the values given by $M_I = +I$, $(I-1)$, $(I-2)$, and so on. Since nuclei possessing nuclear spin give rise to magnetic dipoles, the magnitude of this moment is given by:

$$\mu = \frac{g_n e_p h}{4\pi m_p}\sqrt{I(I+1)} \tag{1.14}$$

where g_n = the nuclear g-factor, e_p = proton charge, m_p = mass of nucleus, and the remaining symbols have their usual meaning. Since many of the terms in

Equation 1.14 are constants, they can all be replaced by another constant called the nuclear magneton μ_N:

$$\mu_N = \frac{e_p \hbar}{2m_p} \tag{1.15}$$

which has a value of $5.050 \times 10^{-29}\,\mathrm{J\,G^{-1}}$. Equation 1.14 may then be rewritten in another form:

$$\mu_N = g_N \mu_N \mathbf{I} \tag{1.16}$$

where the factor $(g_N\mu_N)$ is referred to as the nuclear magnetogyric ratio, γ_N.

Equation 1.16 is analogous to Equation 1.3 for the electron, except now the negative sign is absent since the magnetic moment of the nucleus is collinear and *parallel* to the spin itself. The simple spin Hamiltonian for a nuclear spin can thus be written

$$\hat{H} = -\gamma_N B \cdot I \tag{1.17}$$

and the eigen state values for this are:

$$E = -\gamma B M_I \tag{1.18}$$

Considering the case of a proton, which has $M_I = \pm 1/2$, then there are two spin states. In the absence of an external magnetic field the two spin states are degenerate. However, if an applied external magnetic field is applied the degeneracy is lost and two states of different energy result as shown in Figure 1.2.

In this case, the lower energy state (the α state) has both the magnetic moment and the spin parallel to the applied field. The magnetic moment of an unpaired electron can now not only interact with the external applied field, but also with local nuclear magnetic moments. It is this interaction between electron magnetic moments and nuclear magnetic moments which gives rise to hyperfine structure in the EPR spectrum.

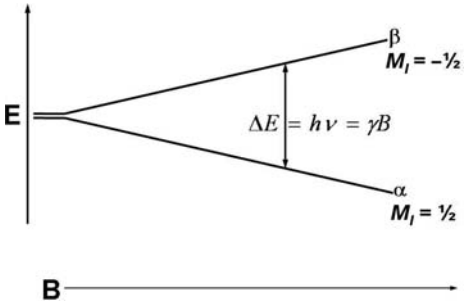

Figure 1.2 Energy levels for a nuclear spin ($I = \pm 1/2$) in an applied magnetic field $\boldsymbol{B}$ (positive γ_N).

1.2.3.1 Isotropic Hyperfine Coupling

The energy of an unpaired electron will now not only depend on the interactions of the unpaired electron (Zeeman level) and the nucleus (Nuclear Zeeman levels) with the applied external magnetic field, but also on the interaction between the unpaired electron and the magnetic nuclei. To explain how one derives the energy terms for such a system, a simple two-spin system ($S = 1/2$, $I = 1/2$) will be considered. The simplified spin Hamiltonian for this two-spin system ($S = 1/2$, $I = 1/2$) in an external applied field **B** is given as:

$$\mathrm{H} = \mathrm{H_{EZ}} - \mathrm{H_{NZ}} - \mathrm{H_{HFS}} \tag{1.19}$$

where EZ = electron Zeeman term, NZ = nuclear Zeeman term, and HFS = hyperfine interaction. This equation takes the form;

$$\hat{H} = g\mu_B B S_Z - g_N \mu_N B I_Z + hSaI \tag{1.20}$$

assuming a = the isotropic hyperfine coupling in Hertz. In the last equation it is also assumed that the g value is isotropic and the external magnetic field is aligned along the z axis. Ignoring second order terms, and in the high field approximation where the electron Zeeman interaction dominates all other interactions, the energy levels for the two-spin system ($S = 1/2$, $I = 1/2$) can be defined as:

$$E(M_S, M_I) = g\mu_B B M_S - g_N \mu_N B M_I + haM_S M_I \tag{1.21}$$

For simplicity, the electron and nuclear Zeeman energy terms can be expressed in frequency units giving:

$$E(M_S, M_I)/h = \nu_e M_S - \nu_N M_I + aM_S M_I \tag{1.22}$$

where $\nu_e = g\mu_B B/h$ and $\nu_N = g_N \mu_N B/h$. The four possible energy levels resulting from this equation (labeled E_a–E_d) can be written as follows:

$$\begin{array}{lcccccccc} & & & & & & M_S & M_I & \\ E_a & = & -\frac{1}{2} g\mu_B B_o & + \frac{1}{2} g_N \mu_N B_o & + \frac{1}{4} ha & & -\frac{1}{2} & +\frac{1}{2} & (1.23a) \\ E_b & = & +\frac{1}{2} g\mu_B B_o & + \frac{1}{2} g_N \mu_N B_o & + \frac{1}{4} ha & & +\frac{1}{2} & +\frac{1}{2} & (1.23b) \\ E_c & = & +\frac{1}{2} g\mu_B B_o & - \frac{1}{2} g_N \mu_N B_o & + \frac{1}{4} ha & & +\frac{1}{2} & -\frac{1}{2} & (1.23c) \\ E_d & = & -\frac{1}{2} g\mu_B B_o & - \frac{1}{2} g_N \mu_N B_o & - \frac{1}{4} ha & & -\frac{1}{2} & -\frac{1}{2} & (1.23d) \end{array}$$

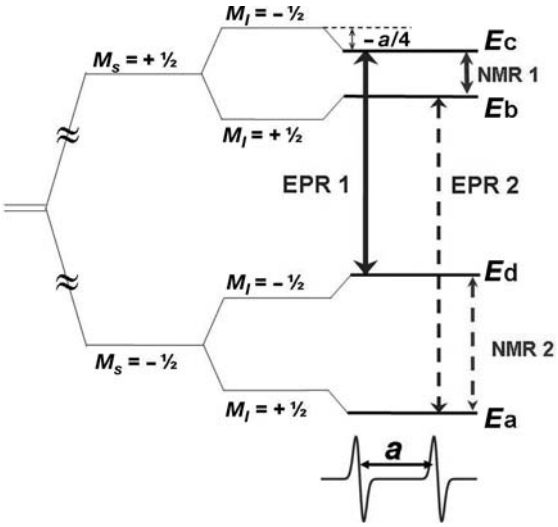

Figure 1.3 Energy level diagram for a two spin system ($S = 1/2$ and $I = 1/2$) in high magnetic field illustrating the electron Zeeman, nuclear Zeeman and hyperfine splittings. a is the isotropic hyperfine coupling with $a > 0$.

By application of the EPR selection rules ($\Delta M_I = 0$ and $\Delta M_S = \pm 1$), it is found that two possible resonance transitions can occur, namely ΔE_{cd} (labelled EPR 1) and ΔE_{ab} (labelled EPR 2), as shown in Figure 1.3:

$$\Delta E_{cd} = E_c - E_d = g\mu_B B + \frac{1}{2}ha_{iso} \tag{1.24a}$$

$$\Delta E_{ab} = E_b - E_a = g\mu_B B - \frac{1}{2}ha_{iso} \tag{1.24b}$$

These two transitions give rise to two absorption peaks at different magnetic field positions and are separated by a, the isotropic hyperfine coupling. It is possible to extract the same value of a by examination of the NMR transitions labeled 1 and 2 in Figure 1.3. These frequencies are accessed in hyperfine techniques such as ENDOR and ESEEM, and are extremely important for measuring very small hyperfine couplings, particularly in cases when a is unresolved in the EPR spectrum.

1.2.3.2 Analysis of Isotropic EPR Spectra

While most paramagnetic species encountered in heterogeneous catalysis will be associated with polycrystalline oxides, it is instructive to first examine the analysis of simple EPR spectra for systems with isotropic symmetry (found in fluid solution). When more than one equivalent nucleus is present in the system, then the energy state described by Equation 1.20 will be split by each equivalent nucleus.

Consider a paramagnet possessing two equivalent hydrogen nuclei; then, the equivalent hydrogen nuclei will split the energy states into a doublet. Since each equivalent nucleus will have the same splitting constant, the splitting by the other equivalent hydrogen will give rise to an overlap of energy levels. The interaction of an unpaired electron with n equivalent nuclei of spin I will produce $2nI + 1$ equally spaced lines. For hydrogen ($I = 1/2$) the relative intensities of the EPR absorptions are given by the binomial expansion of $(1 + x)^n$. The successive sets of coefficients for increasing n are given by Pascal's triangle.

In many cases the unpaired electron can interact with several sets of inequivalent nuclei, usually with different hyperfine couplings. In these cases interpretation of the spectra becomes very complex. Consider the case of an electron interacting with two inequivalent protons. The energy levels are split by the first proton (with coupling of a_1) and then by the second proton (with coupling a_2). Four possible transitions occur, resulting in a spectrum consisting of a "doublet of doublets" (Figure 1.4), each doublet possessing an intensity ratio of 1 : 1.

For a radical consisting of m sets of equivalent nuclei, each counting n number of equivalent nuclei, then the total number of lines is given by

$$N = (2n_1I_1 + 1)(2n_2I_2 + 1)\ldots(2n_nI_n + 1) \tag{1.25}$$

As described earlier, the number of lines in the EPR spectrum is given by the simple equation $2nI + 1$ and this holds true for n equivalent nuclei. For example, for five equivalent protons ($I = 1/2$), then $(2 \times 5 \times 1/2) + 1 = 6$ lines, producing a sextet hyperfine pattern with an intensity ratio of 1 : 5 : 10 : 10 : 5 : 1 (Table 1.2).

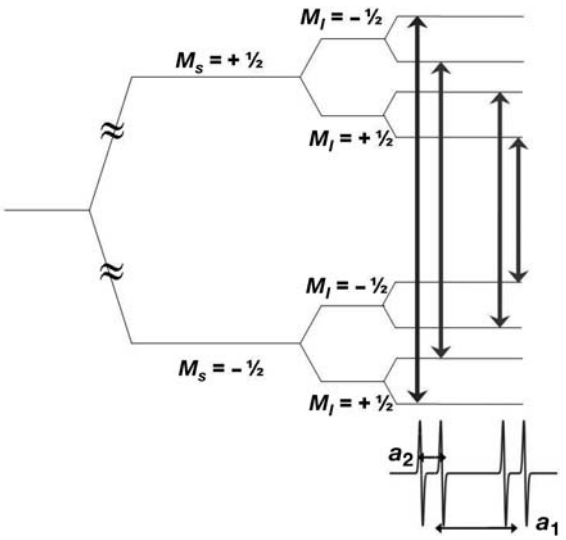

Figure 1.4 Energy level diagram for an unpaired electron ($S = 1/2$) interacting with two inequivalent $I = 1/2$ spin nuclei such that $a_1 > a_2$.

Table 1.2 Coefficients for the binominal expansion $(1 + x)^n$.

n	Pattern	Coefficients
0		1
1	Doublet	1 1
2	Triplet	1 2 1
3	Quartet	1 3 3 1
4	Pentet	1 4 6 4 1
5	Sextet	1 5 10 10 5 1
6	Septet	1 6 15 20 15 6 1
7	Octet	1 7 21 35 35 21 7 1
8	Nonet	1 8 28 56 70 56 28 8 1

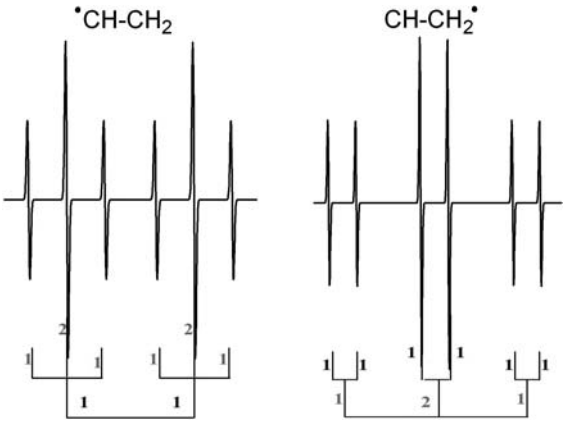

Figure 1.5 Simulated hyperfine patterns and illustrated stick diagrams for the radical fragments $^{\bullet}CHCH_2$ ($a_{CH} > a_{CH2}$) and $CH^{\bullet}CH_2$ ($a_{CH2} > a_{CH}$).

Consider the hypothetical radical fragment $^{\bullet}CH–CH_2$ which is predicted to contain six lines based on a "doublet of triplets", that is, a large doublet arising from the interaction with the CH fragment (producing two lines) and a smaller triplet due to the electron interacting more weakly with the two remote protons of the CH_2 fragment (producing three lines). The resulting stick diagram is shown in Figure 1.5. In the case where the radical is $CH–CH_2^{\bullet}$ the resulting pattern is also predicted to contain six lines, now based on a "triplet of doublets" as shown in Figure 1.5.

As the number of nuclei increases, the complexity of the spectrum rapidly increases since the spectral density depends on the number of inequivalent nuclei according to:

$$\text{Spectral density}_{\text{EPR}} = \frac{\prod_{i=1}^{k}(2N_iI_i+1)}{\sum_{i=1}^{k}2|a_i|N_iI_i} \tag{1.26}$$

This rapid increase in complexity can be illustrated by reference to the radical cation of anthracene shown in Figure 1.6. Two sets of inequivalent proton environments exist, each composed of four protons. Since the number of lines in the spectrum is given by $2nI + 1$, then the total number of predicted lines is $5 \times 5 = 25$ lines. Each group of protons is expected to produce a pentet hyperfine pattern with an intensity ratio of 1:4:6:4:1, and this pattern can indeed be identified in the spectrum (Figure 1.6). The most important point to note in the interpretation of these spectra is that the separation between the first two lines in the wings of the spectrum corresponds to the smallest hyperfine coupling (in this case a_2), regardless of how complex the pattern appears or how many lines are present. By systematically analyzing the spectrum from the outer features in to the middle features, the spectra can be finally assigned. It is common to use simulation programmes to aid in the analysis of such spectra, and, where possible, additional hyperfine techniques such as ENDOR may be used to help deconvolute the pattern. Since the spectral density in ENDOR is given by:

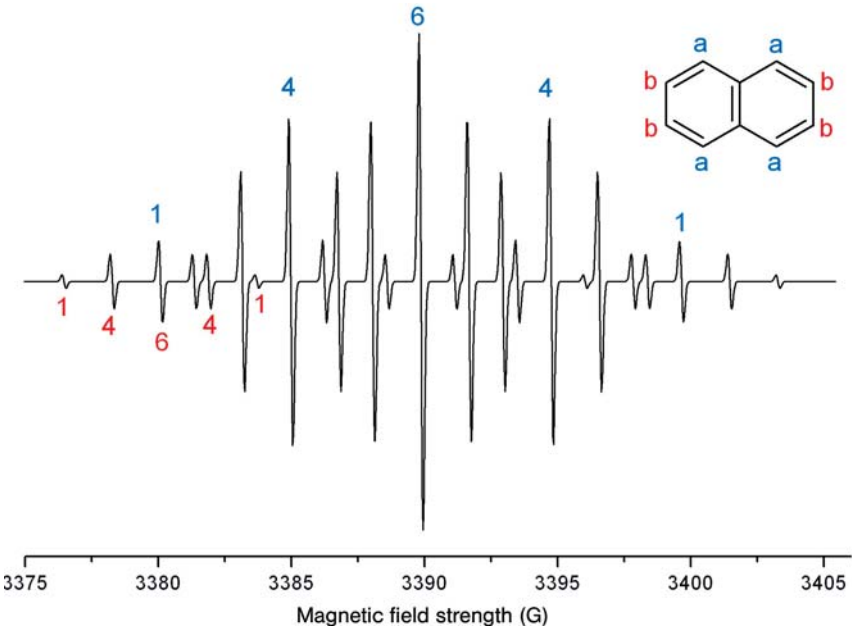

Figure 1.6 Simulated fluid solution EPR spectrum of the radical cation of anthracene. ν = 9.5 GHz, linewidth = 0.15 G, a_1 = 4.89 G, a_2 = 1.81 G.

$$\text{Spectral density}_{\text{ENDOR}} = \frac{2k}{|a_{\max}|} \tag{1.27}$$

where there are k groups of i equivalent nuclei of nuclear spin I_i and $a_{\max}$ denotes the largest hyperfine coupling constant, the resolution enhancement offered by this technique greatly simplifies the analysis.

1.2.4 The g Tensor: Origin and Significance

In Sections 1.2.1– 1.2.3, the basic theory and analysis of EPR spectra in fluid solution phase were examined. However, the theory and analysis of the spectra in the solid state, such as a heterogeneous catalyst, is more complex owing to anisotropies in the simple spin Hamiltonian introduced earlier in Equation 1.20, which only considered isotropic or averaged contributions from g and a. A more appropriate Hamiltonian for the solid state, which takes into account these anisotropies, is given by:

$$\hat{H} = \mu_B \mathbf{S}\cdot\mathbf{g}\cdot\mathbf{B} + \sum_i \left(g_N^i \mu_N^i \mathbf{I}\cdot\mathbf{B} + \mathbf{I}\cdot\mathbf{A}^i\cdot\mathbf{S}\right) \tag{1.28}$$

The isotropic g and a values are now replaced by two 3×3 matrices representing the **g** and **A** tensors and which arise from the anisotropic electron Zeeman and hyperfine interaction. Other energy terms may also be included in the spin Hamiltonian, including the anisotropic fine term **D**, for electron–electron interactions, and the anisotropic nuclear quadrupolar interaction **Q**, depending on the nucleus. Usually the quadrupolar interactions are very small, compared to A and **D**, are generally less than the inherent linewidth of the EPR signal and are therefore invisible by EPR. They are readily detected in hyperfine techniques such as ENDOR and HYSCORE. All these terms (**g, A, D**) are anisotropic in the solid state, and must therefore be defined in terms of a tensor, which will be explained in this section.

According to the basic EPR resonance Equation 1.9, the frequency required for the EPR transition depends only on **B** and μ_B since the g value in this equation is isotropic. However, since the EPR spectrum in the solid state will depend on the relative orientation of the applied field with respect to the paramagnetic species in the powder, Equation 1.9 must be modified to include this angular dependence:

$$h\nu = \mu_B g(\theta, \phi)\mathbf{B} \tag{1.29}$$

where ϕ and θ are the polar angles of the applied field within the molecular g tensor principal axis system (Figure 1.7).

Because g now depends on the angles (θ,ϕ) it should be described using the following electron Zeeman Hamiltonian:

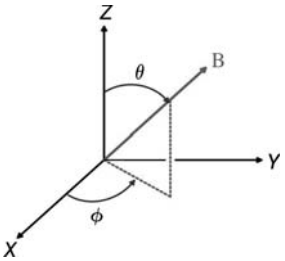

Figure 1.7 Orientation of the magnetic field with respect to the g tensor principal axis system denoted *X, Y, Z*.

$$\hat{H} = \mu_B \cdot \mathbf{S} \cdot \mathbf{g} \cdot \mathbf{B} \tag{1.30}$$

where *g* is now no longer written as a simple scalar quantity. An explicit expression for $g(\phi,\theta)$ can be found by writing the components of the field in the *g* tensor frame via the polar angles defined in Figure 1.7. For example, one must define the *g* value in terms of *B* in all three principal directions, then sum all terms to represent the anisotropic powder profile. This treatment is beyond the scope of this chapter, and can be found in any EPR textbook. However, it is sufficient to note here that the effective *g* value can finally be expressed in a form to encompass the angular terms from Equation 1.29, such that:

$$g(\theta,\phi) = \sqrt{\sin^2\theta\cdot\cos^2\phi\cdot g_1^2 + \sin^2\theta\cdot\sin^2\phi\cdot g_2^2 + \cos^2\phi\cdot g_3^2} \tag{1.31}$$

These angular variations are responsible for the different *g* values found in the EPR spectrum (i.e. qualitatively they depend on the symmetry of the electronic wave function). However these deviations from g_e actually arise from the admixture of orbital angular momentum into the spin ground state via spin orbit coupling. The extent of this admixing depends on which orbital contributes to the spin ground state (p, d or f). The real components of the **g** matrix are then given by:

$$g_{ij} = g_e\delta_{ij} + 2\lambda\sum_{m\neq 0}\frac{\langle m|l_i|n\rangle\langle n|l_j|m\rangle}{E_n - E_m} \tag{1.32}$$

where *ij* are the molecular coordinate axes, λ is the spin orbit coupling constant, E_n is the energy of the SOMO, *m* denotes the filled and empty orbitals with energy E_m, and l_i is the component of the orbital angular momentum operator. The integrals are calculated for an unpaired electron when the molecular orbitals are written as linear combinations of p or d orbitals.

What is important to note here, is the role of orbital angular momentum in the resultant EPR spectrum. For example, spin orbit coupling to empty molecular orbitals produces a negative contribution to g_{ij} while coupling to filled molecular orbitals produces a positive effect on g_{ij}. This is best illustrated with respect to

inorganic radicals, which are sometimes observed directly or indirectly in surface processes. Negative g shifts are found for $11e^{-}\pi^{*}$ diatomic radicals (such as NO, N_2^-, CO^-) compared to the expected positive g shifts for $13e^{-}\pi^{*}$ radicals (such as O_2^-). A similar effect can also be found in transition metal ions since d^1 ions are expected to produce a negative g shift (less than g_e) compared to d^9 metal ions which produce positive g shifts (due to admixture of empty versus filled molecular orbitals). Since l_z does not couple the d_{z^2} orbital to any other orbital, then according to Equation 1.32, a g_z value close to free spin is predicted for a SOMO based primarily on d_{z^2}. Therefore as a first and crude approximation, a g value close to g_e for a TMI complex can be indicative of a d_{z^2} based SOMO.

1.2.5
The A Tensor; Significance and Origin

The isotropic form of the nuclear Zeeman interaction was discussed in detail in Section 1.2.3.1. This interaction is observed in isotropic media, and also in cases where the molecular orbital hosting the unpaired electron has substantial s character. The resulting isotropic hyperfine coupling is related to the finite probability of the unpaired electron being at the nucleus. The spherical symmetry of the s orbital explains the isotropic nature of the interaction which is given by;

$$a_{iso} = \frac{8\pi}{3} g_e g_n \mu_B \mu_n |\Psi_{(0)}|^2 \tag{1.33}$$

where $|\Psi_{(0)}|^2$ is the square of the value of the wavefunction of the unpaired electron. However, for unpaired electrons associated with p, d or f orbitals, no Fermi contact occurs because of the nodes of the corresponding wavefunctions at the nucleus. The electron spin–nuclear spin interaction is therefore due to the non-spherical nature of the orbitals hosting the unpaired electron, and can be described by a classic dipolar interaction between magnetic moments. The interaction is anisotropic since it depends on the orientation of the orbital with respect to the applied field. While the isotropic interaction determines the EPR spectra of species in solution, both isotropic and anisotropic interactions can be visible in the solid state.

The interaction energy between the two magnetic moments (labelled μ_1 and μ_2) is classically given by the equation

$$E = \frac{\mu_1 \cdot \mu_2}{r^3} - \frac{3(\mu_1 \cdot \mathbf{r})(\mu_2 \cdot \mathbf{r})}{r^5} \tag{1.34}$$

where $\mathbf{r}$ is the vector relating the two magnetic moments and r is the distance between the two dipoles. The quantum mechanical analogue of Equation 1.34 is obtained by replacing the dipoles by their corresponding operators:

$$\hat{H} = -g_e \mu_B g_n \mu_n \left(\frac{I \cdot S}{r^3} - \frac{3(I \cdot \mathbf{r})(S \cdot \mathbf{r})}{r^5} \right) \tag{1.35}$$

Since the electron is not localized at one position in space, Equation 1.35 must be averaged over the electron probability distribution function. $\hat{H}$ is averaged to zero when the electron cloud is spherical (as in s orbitals) and comes to a finite value for axially symmetric orbitals. The magnitude of the anisotropic hyperfine interaction then depends on the orientation of the paramagnetic system with respect to the external field.

In the general case, both isotropic and anisotropic hyperfine interactions contribute to the experimental spectrum. The whole interaction is therefore dependent once again on orientation and must be expressed by a tensor. The effective spin Hamiltonian for this more realistic description of a paramagnetic species in the solid state was given earlier in Equation 1.28. Nevertheless the **A** tensor may be split into its component isotropic and anisotropic parts as follows;

$$A^i = \begin{bmatrix} A_1 & 0 & 0 \\ 0 & A_2 & 0 \\ 0 & 0 & A_3 \end{bmatrix} = a_{iso} + \begin{bmatrix} T_1 & 0 & 0 \\ 0 & T_2 & 0 \\ 0 & 0 & T_3 \end{bmatrix} \tag{1.36}$$

where $a_{iso} = (A_1 + A_2 + A_3)/3$. The anisotropic part of the **A** tensor corresponds to the dipolar interaction as expressed by the Hamiltonian in Equation 1.35. In a number of cases, the second term of the matrix in Equation 1.36 is a traceless tensor and has the form $(-T, -T, 2T)$. For this reason, in the case of EPR spectra of paramagnetic species having both isotropic and anisotropic hyperfine couplings and undergoing rapid tumbling in a low viscosity solution, the anisotropic term is averaged to zero and the observed hyperfine coupling corresponds to the isotropic part only. Extremely useful information can be derived from the hyperfine structure of an EPR spectrum including the s and p characters of the orbitals hosting the unpaired electron (or the coefficients of the atomic wavefunctions involved in the SOMO orbital). In simple terms this data can be deduced from the following relations;

$$C_S^2 = \frac{a_{iso}}{A_o} \quad \text{and} \quad C_P^2 = \frac{T}{B} \tag{1.37}$$

where A_o and B are the experimental, or more frequently theoretical, hyperfine couplings assuming pure s and p orbitals for the elements under consideration and coefficient $C_S^2 + C_P^2 = 1$. Appropriate corrections and orbital coefficients must be included to account for the specific orbital hosting the unpaired electron, but Equation 1.37 nevertheless illustrates simply how the spin density can be calculated to first approximation. A series of more detailed examples of these calculations will be presented in Section 1.3.

1.2.6
The D Tensor; Significance and Origin

The spin Hamiltonian described by Equation 1.28 applies to the case where a single electron ($S = 1/2$) interacts with the applied magnetic field and with

surrounding nuclei. However, it is also possible to obtain an EPR spectrum for any system containing more than one unpaired electron. If two or more electrons are present in the system ($S > 1/2$) then a new term must be added to the spin Hamiltonian to account for the interactions between the electrons. For the simplest case with two unpaired electrons the multiplicity of states can result in either a singlet ($S = 0$) or triplet ($S = 1$). Two types of interaction can result between the electrons, namely the electron-exchange interaction (i.e. the separation between the singlet and triplet states) and the electron–electron dipole interaction (i.e. the magnetic interaction between the two electrons). Only the latter interaction will be considered here.

At small distances, the two unpaired electrons will experience a strong dipole–dipole interaction analogous to the interaction between electronic and nuclear magnetic dipoles, and this gives rise to anisotropic hyperfine interactions. The electron-electron interaction is described by the spin–spin Hamiltonian given by:

$$\hat{H}_{SS} = S \cdot D \cdot S \tag{1.38}$$

where **D** is a second rank tensor (the zero field parameter) with a trace of zero. As with the **g** and **A** tensors, the **D** tensor can also be diagonalized so that $D_{xx} + D_{yy} + D_{zz} = 0$. Equation 1.38 can be added to Equation 1.30 to obtain the correct spin Hamiltonian for an $S > 1/2$ system:

$$\hat{H} = \mu_B \cdot \mathbf{S} \cdot \mathbf{g} \cdot \mathbf{B} + S \cdot D \cdot S \tag{1.39}$$

Since the trace of **D** is zero, calculation of the energy state for a system with $S = 1$ requires only two independent parameters, which are designated D and E. The spin coupling is direct in the case of organic molecules in the triplet state and biradicals, but occurs through the orbital angular momentum in the case of transition metal ions. In the latter case, the D and E terms depend on the symmetry of the crystal field acting on the ions:

$$\hat{H} = D\left(S_z^2 - \frac{S^2}{3}\right) + E\left(S_x^2 - S_y^2\right) \tag{1.40}$$

For axially symmetric molecules, the calculated shape of the $\Delta M_S = 1$ lines are given in Figure 1.8. The separation of the outer lines is $2D'$ (where $D' = D/g\mu_B$) while that of the inner lines is D (E is zero in this case). The theoretical line shape for a randomly oriented triplet with $E \neq 0$ is also shown in Figure 1.8. The separation of the outermost lines is again $2D'$ whereas that of the intermediate and inner pairs is $D' + 3E'/2$ and $D' - 3E'/2$ respectively. As the zero-field interactions become comparable to and larger than the microwave energy, the line shape exhibits severe distortions from the simulated case in Figure 1.8.

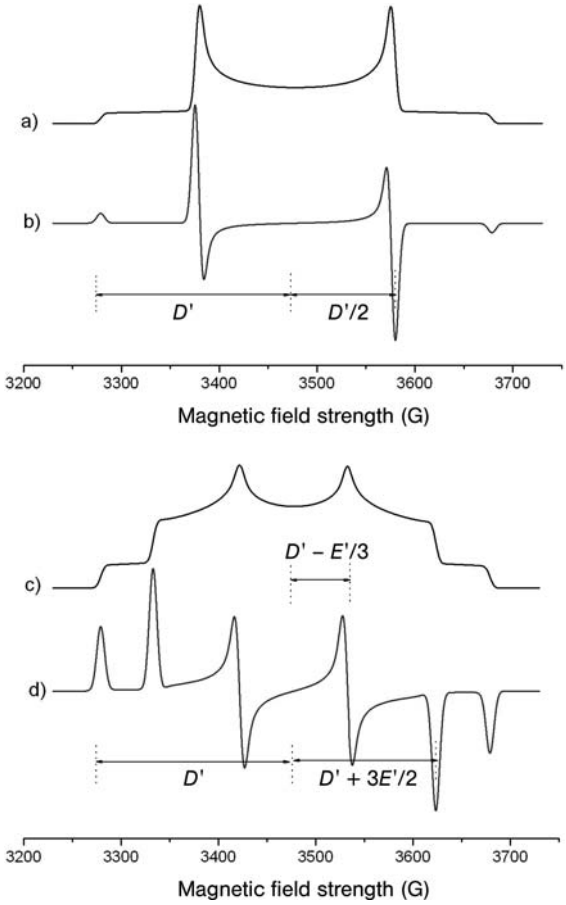

Figure 1.8 Theoretical absorption and first derivative EPR spectra of the $\Delta M_S = 1$ region of a randomly oriented triplet. Top: $S = 1$ for a given value of D ($E = 0$) and isotropic g; bottom: $S = 1$ and $D > E \neq 0$ for an isotropic g.

1.2.7
Powder EPR Spectra

Most heterogeneous catalysts are composed of numerous microcrystallites, randomly oriented in space. Therefore, unlike the more straightforward analysis of fluid solution EPR spectra (or single crystals), the interpretation of powder EPR spectra is more demanding, and often complicated by the presence of different paramagnetic active sites, distribution of **g** and **A** values, loss of spectral resolution and large line-widths. For example, different surface imperfections may create sites with different degrees of micro-heterogeneity, and if a paramagnetic species is associated with such features, then one can expect to observe complicating

features in the spectrum from **g** and **A** strain to distorted and broadened line shape. Various approaches can be adopted to unravel these complexities, and some of them will be mentioned later. However, before presenting these methods for interpreting the spectra of polycrystalline systems, it is first necessary to briefly illustrate how the *g* values of a paramagnet can be extracted from a randomly oriented solid. This analysis of the **g** tensor is generic, since the same angular dependencies also exist for the **A** and **D** tensors.

The powder spectrum of a paramagnetic species dominated by **g** anisotropy is given by the contributions of all molecules in their specific orientations with respect to the external field. The orientation of the external field with respect to the *g* principal axes was shown in Figure 1.7. All orientations will have the same probability in a polycrystalline environment, and this leads to the following equation for computing the line shape of a powder pattern:

$$\int_{-\infty}^{\infty} I(\omega)\cdot d\omega = \int_{0}^{\pi}\int_{0}^{2\pi} \sin\theta\cdot d\theta\cdot d\phi \tag{1.41}$$

According to this equation the total intensity of the EPR spectrum *(I)* is given by the sum of the contributions of each single molecular orientation in a sphere (dependent on θ and ϕ). Powder patterns are therefore usually computed numerically using a simulation program by systematic variation of the angles θ and ϕ between 0 and π and 0 and 2π respectively and weighting the spectral contributions with $\sin\theta$.

While the effective *g* value is expressed in terms of three principal values directed along three axes or directions in a single crystal, only the principal values of *g* can be extracted from the powder spectrum rather than the principal directions of the tensor with respect to the molecular axes. (Therefore it is more correct to label the observed *g* values as g_1, g_2, g_3 rather than g_{xx}, g_{yy}, g_{zz} in a powder sample.) In the simplest case, an isotropic *g* tensor can be observed, such that all three principal axes of the paramagnetic center are identical ($x = y = z$ and therefore $g_1 = g_2 = g_3$). In this case, only a single EPR line would be observed (in the absence of any hyperfine interaction). With the exception of certain point defects in oxides and the presence of signals from conduction electrons, such high symmetry cases are rarely encountered in studies of oxides and surfaces.

More commonly the symmetry of the paramagnetic centers studied in metal oxides will be lower than isotropic, such as axial ($g_{xx} = g_{yy} \neq g_{zz}$ and $A_{xx} = A_{yy} \neq A_{zz}$) rhombic ($g_{xx} \neq g_{yy} \neq g_{zz}$ and $A_{xx} \neq A_{yy} \neq A_{zz}$), monoclinic or triclinic symmetry. For example, consider a simple paramagnetic species ($S = 1/2$) with uniaxial symmetry and no hyperfine interaction. This system can be characterized by two principal axis *g* values called $g_\perp$ and $g_\parallel$. As shown earlier in Equation 1.31 for the general case where $x = y = z$, the variation in the *g* value will depend solely on the angle θ between **B** and the *x*, *y* or *z* axis. For uniaxial symmetry where $x = y \neq z$, then Equation 1.31 simplifies to:

$$B(\theta) = \frac{h\nu}{\mu_B}\left(\sqrt{g_\parallel^2\cos^2\theta + g_\perp^2\sin^2\theta}\right)^{-1} \tag{1.42}$$

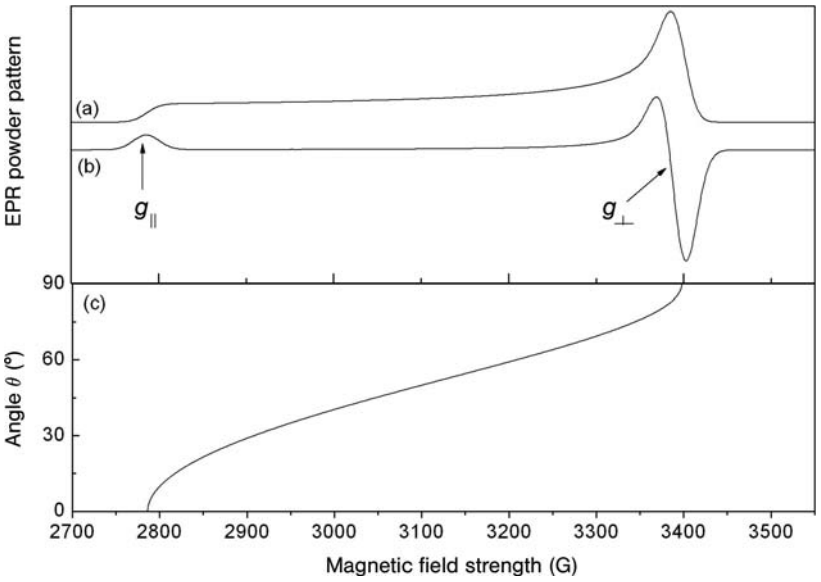

Figure 1.9 (a) Absorption and (b) first derivative EPR lineshape for a randomly oriented $S = 1/2$ spin system with axial symmetry. The angular dependence curve (θ vs field) is shown in (c).

The values of $g_{\perp}$ and $g_{\|}$ therefore set the range of **B** over which absorption occurs, and two singularities will appear at the field positions $B_{\|}$ and $B_{\perp}$. When the field is aligned along the unique axis ($B_{\|}$), absorption occurs for those paramagnets whose field lies along the symmetry axis, corresponding to an angle of $\theta = 0°$. At this orientation only a few spins contribute to the pattern and the spectral intensity has a minimum (edge of the powder pattern) close to 2800 G. As the field moves progressively from $B_{\|}$ to $B_{\perp}$, more spins come into resonance and correspondingly the intensity of the absorption line increases. At $B_{\perp}$, the absorption reaches a maximum since there is now a large plane of orientations with the field perpendicular to the symmetry axis. The *cw*-EPR spectra are always recorded as the first derivative of the absorption (Figure 1.9b), but nevertheless it is still possible to extract the values of $g_{\|}$ and $g_{\perp}$ from the powder spectrum. The variation in the resonance absorption (analogous to the variation in g) as a function of the angle θ can be seen as a smooth curve with two prominent resonances at $B_{\|}(g_{\|})$ and $B_{\perp}(g_{\perp})$, Figure 1.9c. It is important to realize that the entire signal intensity is spread between the field positions $B_{\|}$ to $B_{\perp}$ so in powder spectra with multiple sites or different paramagnetic species, the exact identification of $g_{\|}$ and $g_{\perp}$ can sometimes be difficult.

In the second example, consider the case of a paramagnetic species with rhombic symmetry ($x \neq y \neq z$), characterized by three g values of g_1, g_2 and g_3. The variation in the g values now depends on the two polar angles of θ and ϕ (Equation 1.29) and a typical example of the absorption and first derivative profiles for such a

system with distinct g values is shown in Figure 1.10. Three special cases (called singularities) now occur for the resonant field positions corresponding to (i) $\theta = 0°$, (ii) $\theta = 90° = \phi$ and (iii) $\theta = 90°$, $\phi = 0°$. At $\theta = 0°$ the spins which come into resonance are those for which the applied field lies along the z axis and an absorption edge occurs producing the derivative peak corresponding to g_1. As the field moves away from the z axis, in the zy plane (such that $\phi = 90°$ and only the angle of θ varies) the resonance field position will also vary and a maximum in intensity of the absorption occurs when $\theta = 90° = \phi$ (g_2 in Figure 1.10). A similar situation occurs when the field moves from the z axis but now in the zx plane, such that all intermediate values of θ contribute to the intensity of the absorption line (since $\phi = 0°$ in this plane). The limiting point for this trend is reached when $\theta = 90°$, $\phi = 0°$ (g_3 in Figure 1.10).

The angular dependence plots illustrating the variation in the resonant field positions are thus shown in Figure 1.10c. The most intrinsic feature in the powder pattern of a rhombic $\boldsymbol{g}$ tensor consists of the fact that while only very few orientations contribute to the spectrum at $B||g_1$ and $B||g_3$ (single crystal-like case), several intermediate orientations reveal the same resonance as $B||g_2$ resulting in a maximal absorption at this field.

In the previous examples, only the $\boldsymbol{g}$ anisotropies were considered in the powder profile of the EPR spectra. In the presence of a strong hyperfine interaction (larger than the EPR linewidth), the profile of the spectrum can become even more

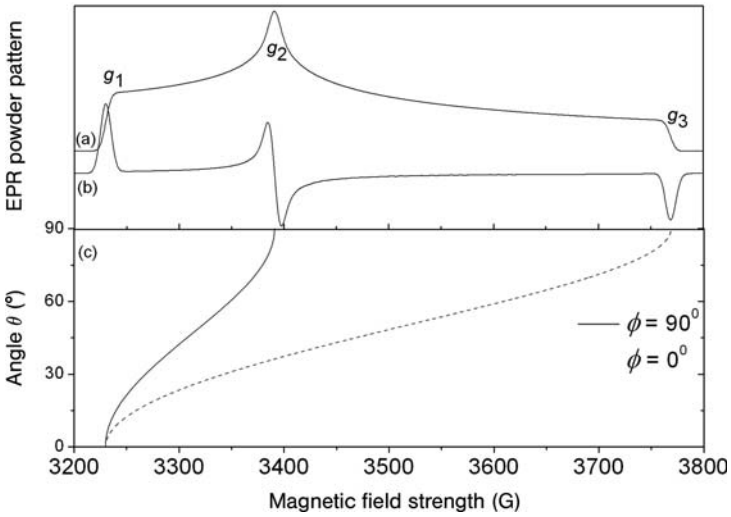

Figure 1.10 (a) Absorption and (b) first derivative EPR lineshape for a randomly oriented $S = 1/2$ spin system with rhombic symmetry ($g_1 = 2.101$, $g_2 = 2.000$, $g_3 = 1.800$, $\nu = 9.5$ GHz). The angular dependence curve (θ vs field) is shown in (c) for two angles of $\phi = 0°$ and $\phi = 90°$.

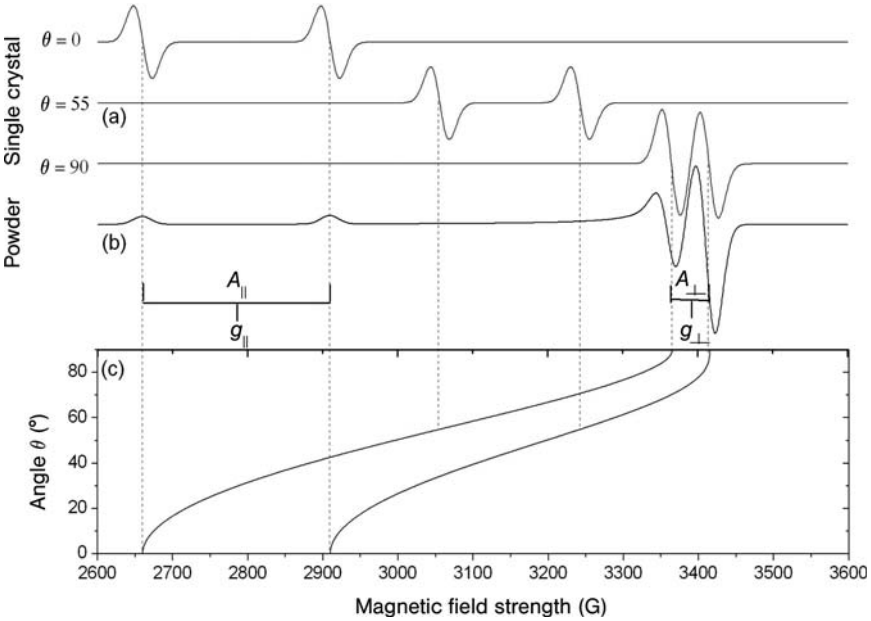

Figure 1.11 (a) Single crystal type (selected orientations of θ = 0°, 55° and 90°) and (b) first derivative powder type EPR lineshapes for a randomly oriented $S = 1/2$, $I = 1/2$ spin system with uniaxial symmetry. The angular dependence curve (θ vs field) for $m_I = \pm 1/2$ is shown in (c).

complex, particularly for large $\boldsymbol{A}$ anisotropies. Consider a simple two-spin system ($S = 1/2$ and $I = 1/2$) in a polycrystalline material, in which the overall symmetry of the paramagnetic center can be described as uniaxial. As before when the field is aligned along the unique z axis ($B_{||}$) so that θ = 0°, absorption occurs for those paramagnets whose field lies along the symmetry axis; this absorption position is defined by $g_{||}$. Owing to the interaction of the electron with the nuclear spin $I = 1/2$, the single $g_{||}$ line will now be split into a pair of lines separated by the hyperfine value $A_{||}$ (see Figure 1.11). As the field moves away from the Z axis, the resonance field position will also change. When the field is parallel to the X and Y directions ($B_{\perp}$) so that θ = 90°, absorption occurs once again as defined by the component $g_{\perp}$. This component is also split into two lines separated by the hyperfine value $A_{\perp}$. In the hypothetical single crystal case, a pair of lines would be observed for every angle of θ (three of these individual orientations are shown as an example in the upper part of Figure 1.11 corresponding to θ = 0°, 55° and 90°). In the powder spectrum, the hyperfine splittings at intermediate orientations of θ are not observed in the envelope; the splittings are only observed at the turning points or singularities corresponding to θ = 0° and 90°. Nevertheless this example demonstrates how the g and A values of $g_{\perp}$, $A_{\perp}$, $g_{||}$ and $A_{||}$ can still be extracted from the powder pattern.

1.2.8 Analysing EPR Powder Spectra; Experimental Considerations

As mentioned earlier, quite often the EPR spectra arising from a heterogeneous polycrystalline system will be complicated by a variety of factors, including the presence of several paramagnetic sites/species, g and A strain, low site symmetry, large linewidths and perhaps loss of resolved hyperfine structure. To resolve these complexities, several steps can be taken during the measurement of the spectra which may either increase spectral resolution or at least separate the components arising from other centers. These steps include measurements at variable powers and temperatures and the use of different isotopes and different frequencies. Some of the important considerations in these variables are discussed below.

1.2.8.1 Quantification of Number of Spins

The intensity of the EPR signal can of course be related to the concentration of the paramagnetic species present in the catalyst. However, although this quantitative analysis is frequently used in the literature to estimate the number of spins, it is inherently difficult to obtain absolute concentrations accurately. The relationship between signal intensity and sample concentration is given by

$$C = \frac{KI}{GP_{ij}} \tag{1.43}$$

where K is a simple proportionality constant, I is the EPR signal intensity, G the spectrometer receiver gain and P_{ij} the EPR transition probability. The proportionality constant K depends on the sample in question, and will be influenced by a variety of factors including (i) the properties of the cavity, with the sample included, (ii) the microwave power incident upon the sample and (iii) the modulation amplitude.

The intensity of the signal must be obtained in the absence of any power saturation. Since the EPR signal consists of a first derivative, rather than an absorbance, this must also be factored into the analysis. Usually double integration of the spectrum is performed over a defined scan range (after careful adjustment to the baseline). Alternatively, for a single symmetric first derivative line, the following simple relation may be used;

$$I = A_{p\text{-}p}w^2 \tag{1.44}$$

where $A_{p\text{-}p}$ is the peak to peak amplitude of the first derivative line and w is the linewidth parameter for the Lorentzian or Gaussian lineshape.

To compare the intensities of two signals (for example, between a known standard and a sample of unknown concentration), one must therefore ensure that K and P_{ij} in Equation 1.43 are identical for both sample and reference standard. In other words, factors (i)–(iii) must be identical. This is surprisingly difficult to achieve in practice, since the sample cell, sample volume, position in the cavity

and dielectric properties of sample and reference standard must be identical if factor (iii) is to be realized. In other words, the standard should ideally have identical EPR properties to that of the unknown, and must be recorded under identical instrumental conditions. Thus, for example, it would be completely inappropriate to use a DPPH reference sample as a standard to determine absolute concentration for a Cu(II)-containing catalyst.

1.2.8.2 Effects of Sample Tumbling and Rotation

In most studies of oxide surfaces, the EPR spectra will be powder-like in origin. However, in some cases, studies may be performed at the liquid–solid interface. In such circumstances, the resulting spectral profile may produce a composite profile containing both isotropic and anisotropic signals. It is rare that the spectra will be completely averaged, and frequently one may only observe distortions to the anisotropic signal (i.e. a broadening of the lines). It is therefore important to consider such effects in some detail.

Rapid tumbling, faster than the EPR timescale, of an anisotropic paramagnetic system will cause an averaging of the **g** and **A** tensors. In the hypothetical case where the tumbling is infinitely rapid compared to the EPR timescale, a fully averaged or isotropic g_{iso} and a_{iso} value will be obtained. This rarely occurs, even under ideal conditions, and in practice evidence of g and A anisotropy can still be manifested in the spectrum; specifically with respect to the linewidths of the individual lines. A good example of this partial averaging effect is shown in Figure 1.12.

This partial averaging of the signals can be easily explained by reference to the dependence of the linewidths on the value of m_I. For an $S = 1/2$ spin system, the peak-to-peak linewidths $\Delta B_{p\text{-}p}$ of the first derivative signal can be expressed as a polynominal in m_I.

$$\Delta B_{p\text{-}p} = A + Bm_I + Cm_I^2 + Dm_I^3 \tag{1.45}$$

where A, B, C and D are constants and all are positive. Usually only the first three terms on the right hand side of Equation 1.45 are considered (since D is usually very small). Clearly the linewidth depends on the value of m_I, and the m_I^2 term causes the outer lines to broaden compared to the inner lines (see Figure 1.12), although the overall shape of the spectrum still remains symmetrical at this point. Variation in the intensity across the spectrum arises from the m_I term, since transitions with the largest negative m_I value will be broadened the least, whilst transitions with the largest positive m_I value will be broadened the most. This is a very useful correlation, since it provides a means of determining the sign of a_{iso} from the spectrum if the term in m_I dominates that in m_I^2. For example, if a_{iso} is positive, the resonance at lowest field must be due to $m_I = +I$ and that at high field due to $m_I = -I$. In Figure 1.12 the reverse situation applies, therefore for ^{51}V, a_{iso} is negative, since the line at lowest field is narrower than the one at higher magnetic field.

A more qualitative way of viewing the changes to the spectra in Figure 1.12, as a function of m_I, is to consider the tumbling process as causing an averaging of

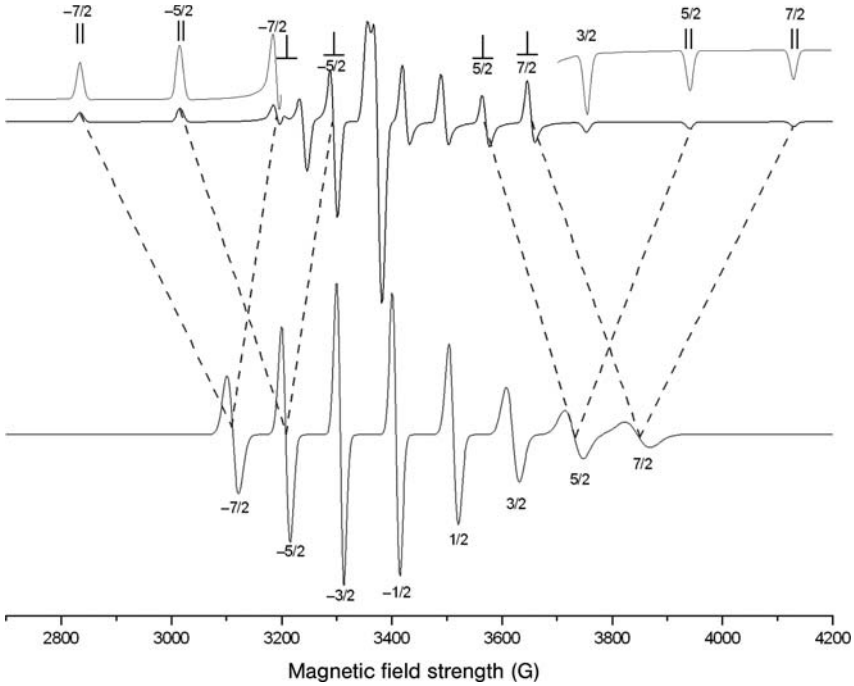

Figure 1.12 Low-temperature (rigid state) and room-temperature (mobile state) spectra of an axial VO species ($I = 7/2$) illustrating the averaging of the parallel and perpendicular hyperfine lines. The hyperfine lines are labeled with the m_I value appropriate to the particular transition.

the resonances attributable to the principal directions of the paramagnetic species. Thus each line due to one particular m_I value is averaged. The greater the difference in the magnetic field between the resonances to be averaged, the more rapidly the paramagnet must tumble in order to completely average. In other words, resonances with a particular m_I value which also have the greatest separation between them are broadened the most. In Figure 1.12, the $m_I = +7/2$ lines (in the parallel and perpendicular direction) are separated by approximately 476 Gauss, compared to the 272 Gauss separation of the two $m_I = -5/2$ lines. In the latter case the resulting line width is therefore narrower. It is therefore vitally important to be aware of partially averaged signals, and their effects on the signal linewidths, when analyzing the spectra.

1.2.8.3 **Physical State of the Sample**

In EPR spectroscopy, it is possible to measure spectra of paramagnetic samples in a variety of forms, including fluid solution, frozen solution, powdered solid or single crystal. Clearly, for heterogeneous polycrystalline systems, such as oxides, the problems of solvent choice, lossy samples, poor quality glass conditions when

frozen, and so on, are all eliminated and this facilitates the analysis of such heterogeneous systems. Polycrystalline samples do not usually present problems with respect to dielectric loss, unless they are of ionic compounds with large ionic charges or if too large a sample is placed into the cavity. With powdered solids it is important to grind the sample sufficiently to avoid any preferential orientation of the crystallites. The occurrence of preferential orientations of paramagnets in either powders or glasses may be examined by re-recording the spectrum after rotating the sample tube to give a different orientation with respect to the magnetic field. If the spectrum changes then there is some preferential orientation of the paramagnet and care must then be exercised in the interpretation of the spectrum.

1.2.8.4 **Multifrequency Measurements**

As mentioned in Section 1.2.1, EPR measurements can be performed at a range of different frequencies, and commercial spectrometers are available covering the range 1–94 GHz. Higher frequencies, including 180, 250 and 360 GHz, are also accessible in several research laboratories around the world. There are several obvious reasons for going to higher frequencies, including improved *g* resolution, improved sensitivity and simplification of spectra (particularly for systems with large zero field splittings) to name a few. Improved resolution of *g* anisotropies and small *g* value differences will undoubtedly be achieved at higher frequencies, but in some cases even moderately higher frequencies (such as K- or Q-band) may provide sufficient resolution compared to X-band, and therefore it is not necessary to make the measurements at higher field.

For example, the simulated powder profiles for a Cu(II) ion (in a square planar environment) at three different frequencies (9.5, 34 and 94 GHz) are shown in Figure 1.13. At 9.5 GHz, the *g* anisotropy is not sufficiently resolved, so that part of the parallel hyperfine component overlaps the perpendicular component. This situation complicates the analysis of the spectrum, particularly with respect to the exact determination of the *g* value, and in some cases deciding whether the spectrum is indeed axial ($g_1 \neq g_2 = g_3$) or slightly rhombic ($g_1 \neq g_2 \approx g_3$). The *g* anisotropy can be easily resolved at higher frequencies (34 or 94 GHz) but, as this example illustrates, Q-band (34 GHz) is already clearly sufficient to provide a clear assignment on exact *g* values. By comparison, the simulated powder profiles for a nitroxide spin probe are shown in Figure 1.13. At X-band frequency (9.5 GHz) the spectrum is dominated by hyperfine anisotropy with three visible lines; the *g* anisotropy is clearly very small and unresolved. At Q-band frequency the spectral resolution is clearly improved, but with a considerable degree of uncertainty in the assignment of g_1 and g_2. At W-band frequency the situation is completely resolved, and the individual *g* components can be extracted from the powder spectrum. Clearly in this particular example, W-band is essential to aid in the analysis of the spectrum. Therefore the choice of frequency largely depends on the nature of the paramagnetic center in question. Generally systems with low *g* anisotropies (small variation in *g* values) will benefit by measurements at W-band and higher frequencies.

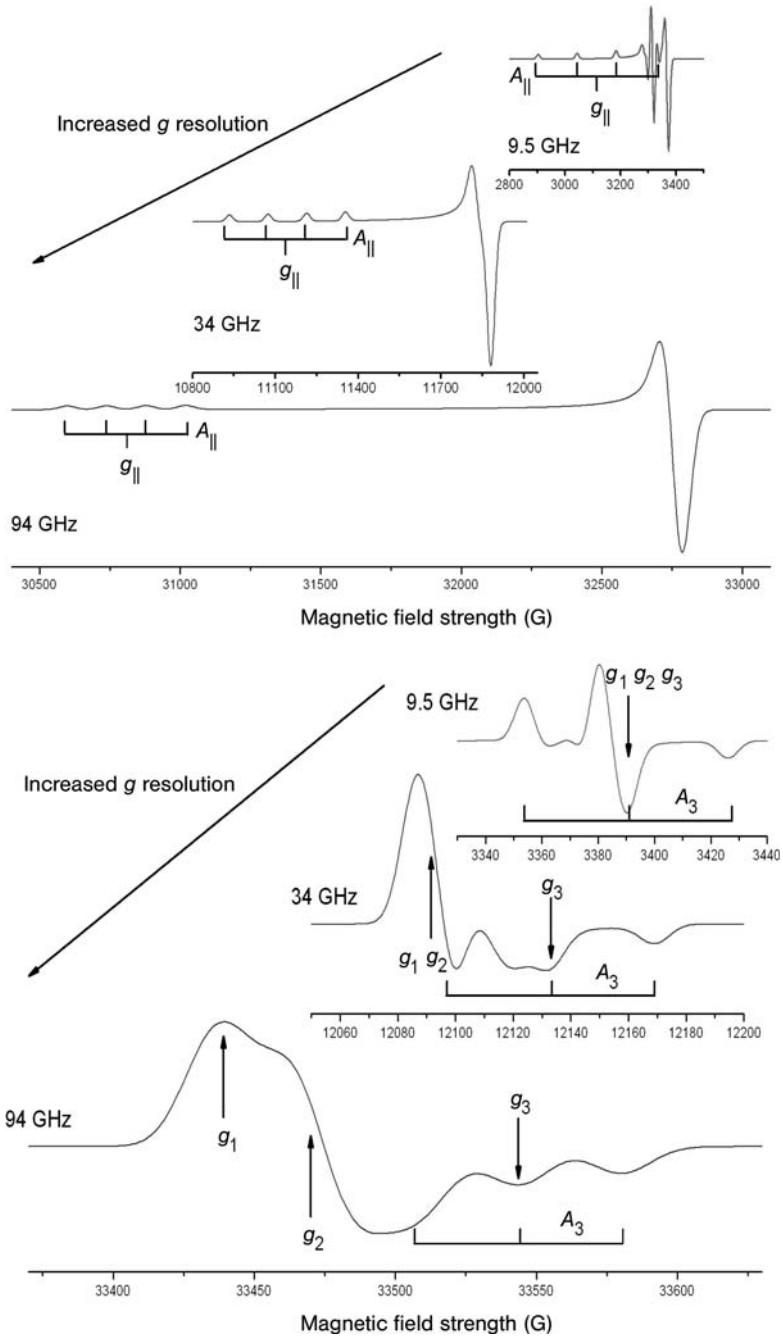

Figure 1.13 Simulated multi-frequency EPR spectra of a Cu(II) ion ($g_{\|} = 2.18$, $g_{\perp} = 2.05$, $A_{\|} = 140\,G$, $A_{\perp} = 15\,G$; upper trace) and nitroxide radical ($g_1 = 2.0084$, $g_2 = 2.006$, $g_3 = 2.002$, $A_1 = 6\,G$, $A_2 = 6\,G$, $A_3 = 36\,G$; lower trace) at X-(9.5 GHz), Q-(34 GHz) and W-(94 GHz) band freq uencies. All field units given in Gauss.

The improved sensitivity at higher field is also a strong motivation for performing high-frequency measurements. For example, depending on the width of the EPR signal, as few as 10^{11} spins can be detected at conventional X-band frequencies, whereas as few as 10^8 spins can be detected at W-band. The downside to this argument is that the sample volume also decreases dramatically at higher frequencies, so the benefits of higher sensitivity may be partially reduced. In some semiconducting oxides, the conduction electrons can produce an EPR signal, but these signals will only be observed with moderate conductivity or with small particles of materials with high conductivity. This arises because the microwave radiation that drives the spin transitions cannot penetrate deeply into highly conductive matter. Owing to the smaller microwave skin depth, high-frequency measurements will clearly benefit studies of the effect of a material's conductivity on the lineshape.

For polycrystalline samples it has also been found that partial orientation of the microcrystallites can occur in the presence of strong magnetic fields. In these circumstances, care must be taken to ensure the samples are immobilized before being brought into the magnetic field, otherwise significant distortion to the lineshape will be observed. For transition metal ion doped zeolite samples, significant g and A strain has also been observed at higher (W-band) frequency. This strain arises from the heterogeneity of the sites for the transition metal ions in the zeolite, so the resultant linewidths are considerably broadened and partially distorted.

1.2.8.5 **Variable Power and Temperature**

The applied microwave power is a very important consideration in EPR. At low values the signal amplitude will increase in direct proportion to the square root of the microwave power received by the sample in the cavity ($I \propto \sqrt{P}$). This relationship only occurs up to a certain level, beyond which the signal amplitude increases less rapidly than required by this equation, and in some cases may even start to decrease. The phenomenon whereby the rate of increase of signal amplitude is less than directly proportional to the square root of the microwave power is known as saturation. If the relationship between signal amplitude and receiver gain is important, as in the quantitative determination of spins, it is essential that non-saturating conditions are used during the measurements. At room temperature, very few transition metal ions will show saturation effects, and lower temperatures such as liquid nitrogen or liquid helium will be required to saturate the signal. By comparison, organic radicals can be easily saturated at room temperature while inorganic radicals can display saturation effects at liquid nitrogen temperatures. The different saturation characteristics for different paramagnetic species is a useful means of deconvoluting overlapping EPR signals for heterogeneous catalysts. Radical intermediates may, for example, be present simultaneously with transition metal ion active centers, but the relative contributions from the two species can be estimated by measuring the spectra at different temperatures and microwave powers.

1.2.9
A Case Study: Surface Adsorbed NO_2

As stated earlier, the amount of information available about a paramagnetic species from a powder EPR pattern is largely determined by the resolution of the spectra. If information on the $\boldsymbol{g}$ and $\boldsymbol{A}$ anisotropy can be extracted from the spectrum, then details on the electronic structure of the paramagnet can be derived. If variable temperature measurements are performed, then information on the dynamics of the species can also be derived. This can be illustrated through an example, based on the EPR spectrum of adsorbed NO_2 on an oxide surface [19].

For NO_2, the unpaired electron is mainly associated with the nonbonding orbital:

$$\psi(4a_1) = c_1N(s) + c_2N(p_z) + c_3O(p_{z1} + p_{z2}) + c_4O(p_{y1} - p_{y2}) \tag{1.46}$$

According to molecular orbital calculations, c_2 is known to be reasonably large, since the electron has substantial nitrogen p_z character. The X-band powder EPR spectrum is shown in Figure 1.14 for $^{14}NO_2$ and $^{15}NO_2$. The spectrum obtained using the ^{14}N isotope is complicated at this frequency, owing to the small $\boldsymbol{g}$ anisotropy (g_1, g_2 and g_3 are very similar to each other) and dominated by the $\boldsymbol{A}$ anisotropy. The analysis is considerably simplified using both higher frequencies (35 GHz) and the ^{15}N isotope ($I = 1/2$).

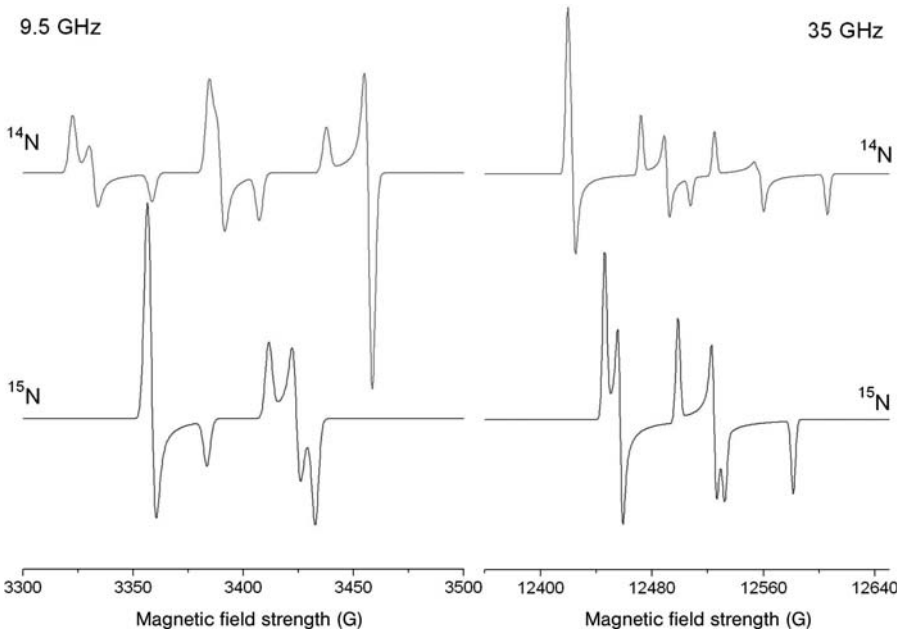

Figure 1.14 EPR spectra at X- and Q-band frequencies of surface adsorbed $^{14}NO_2$ and $^{15}NO_2$ at low temperatures.

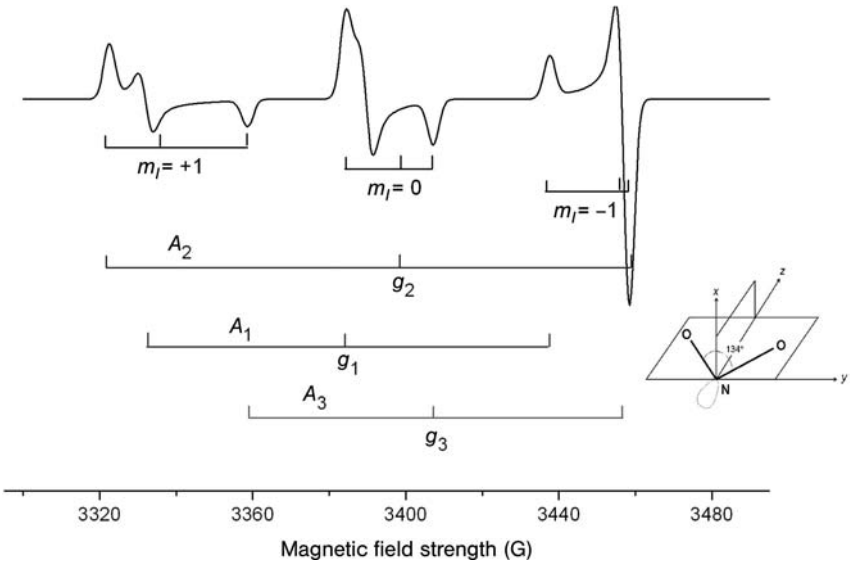

Figure 1.15 Stick diagram of the hyperfine components in the powder EPR spectrum of the randomly oriented $^{14}NO_2$ molecule. The orientation of the molecule is shown in the scheme.

For ^{14}N, the m_I values are +1, 0, −1, and therefore in the non-oriented powder pattern three components of $\boldsymbol{g}$ and $\boldsymbol{A}$ are observed for every m_I state (Figure 1.15). In the single crystal situation only three lines of equal intensity would be observed.

By analysis of the spectra in Figures 1.14 and 1.15, the spin Hamiltonian parameters can be extracted and found to be $g_1 = 2.005$, $g_2 = 2.002$, $g_3 = 1.991$, $A_1 = 52\,\text{G}$, $A_2 = 65\,\text{G}$ and $A_3 = 49\,\text{G}$. The $\boldsymbol{A}$ tensor for the ^{14}N hyperfine may thus be written as

$$A = a_{iso}I + T \tag{1.47}$$

where a_{iso} is the isotropic component (or Fermi contact term) of the hyperfine interaction and **T** is the anisotropic component. Complete analysis of the hyperfine tensor requires detailed information on the sign of the individual couplings. It is not, however, possible to determine the sign of the hyperfine coupling constants from the powder EPR spectrum. By reference to theoretical data, it is possible to determine the signs of the couplings as all positive, since other possible combinations lead to unacceptable results. The isotropic hyperfine coupling constant is also known to be 56 G, therefore only the positive sign values will give the correct value since $a_{iso} = (A_1 + A_2 + A_3)/3$. The tensor can then be broken down into its isotropic and anisotropic components as follows:

$$\begin{bmatrix} 52.7 & & \\ & 49.1 & \\ & & 67.5 \end{bmatrix} = 56.43 + \begin{bmatrix} -3.73 & & \\ & -7.33 & \\ & & 11.07 \end{bmatrix} \tag{1.48}$$

For a pure dipole interaction, the anisotropic term in the above equation should have the form $-a$, $-a$, $2a$. This implies that the unpaired electron is not purely p_z based, but also there must be some occupancy of the orthogonal p orbitals. In other words, the anisotropic tensor is actually the result of two dipolar interactions with two radius vectors, each of which is along a coordinate axis of the molecule. Therefore the anisotropic tensor is the sum of two dipolar coupling tensors and can be decomposed into two traceless components ($-a$, $-a$, $2a$) and ($-b$, $2b$, $-b$) as follows;

$$\begin{bmatrix} 52.7 & & \\ & 49.1 & \\ & & 67.5 \end{bmatrix} = 56.43 + \begin{bmatrix} -6.13 & & \\ & -6.13 & \\ & & 12.26 \end{bmatrix} + \begin{bmatrix} 2.4 & & \\ & -1.2 & \\ & & -1.2 \end{bmatrix} \tag{1.49}$$

Using the reported atomic value of the dipolar ^{14}N constant as $B_0 = \frac{4}{5} g_n \mu_n \langle r^{-3} \rangle_{2p} = 39.62\,G$, one can assess the spin density on the nitrogen 2p orbitals by direct comparison of the experimental $2a$ and $2b$ values to the atomic anisotropic constant of nitrogen using the classic formulas $\rho_{2pz} = c_{2pz^2} = 2a/B_0$ and $\rho_{2px} = c_{2px^2} = 2b/B_0$. The resultant spin densities on the nitrogen $2p_z$ and $2p_x$ orbitals are found to be 0.31 and 0.06 respectively.

The fractional occupancy of the nitrogen s orbital, may be determined from the isotropic coupling constant, which is equal to a_{iso}/A^0_{iso} (where $A^0_{iso} = 8\pi/3 g_n \mu_n \psi|(0)|^2 = 646.2\,G$ is the atomic nitrogen isotropic hyperfine constant). For $^{14}NO_2$, this gives a value of $c_1^2 = 56.43/646.2 = 0.087$. The fraction of the unpaired electron associated with the ^{14}N nucleus is then;

$$c_1^2 + c_2^2 + c_{px}^2 = 0.31 + 0.06 + 0.087 = 0.457 \tag{1.50}$$

The remaining unpaired electron will then be shared with the oxygen p_z orbitals and the surface. Information concerning the geometry of the molecule can be obtained from the hybridization ratio $\lambda^2 = c_p^2/c_s^2$. For planar molecules with C_{2v} symmetry, the dihedral angle of the molecule can be related to the hybridization ratio by $\phi = 2\cos^{-1}(\lambda^2 + 2)^{-1/2}$. Using the values of the p and s orbital occupation given above, the calculated dihedral angle is found to be 132.8°. This can be compared to the known value of 134° for the free molecule.

1.3 Example Applications in Oxide Systems

As discussed earlier, EPR is ideally suited to the study of oxide surfaces, with particular reference to heterogeneous catalysis. This subject area has been reviewed

by the author [20, 21], and the coverage was specifically devoted to paramagnetic centers present exclusively on metal oxide surfaces including S-block oxides, P-block oxides and transition metal oxides, with emphasis on the role of the surface in controlling the properties of the surface-stabilized paramagnetic species. Therefore, rather than providing an exhaustive coverage of the literature in this field, only selective examples will be presented in the following sections. The purpose of these examples is to illustrate how the fundamental concepts and experimental considerations discussed earlier are used in practice and to explore some of the limitations and advantages offered by EPR.

1.3.1 Surface Defects

Surface defects are important sites in heterogeneous catalysis, and these sites can alter the reactivity of the surface or control the anchoring of supported atoms or nanoparticles. However, these defective sites are not easily investigated by many spectroscopic techniques. While modern STM techniques can be used to detect their presence, it is far more difficult to derive useful information about their intrinsic electronic characteristics. Among the many oxides for which surface point defects have been investigated, the group II oxides have received a great deal of attention. These oxides are often used as catalysts or catalytic supports, for example in the oxidative coupling of methane (Li^+ doped MgO), isomerization and alkylation reactions (K doped MgO) or in treatments of automotive exhaust gases (CaO, BaO). Because they are also highly ionic and possess a simple lattice structure, it is no surprise that they are exploited as important model solids for investigations of the structure and reactivity of oxide surfaces in general. They are therefore widely used in surface science (single crystal faces, ultra thin oxide layers), surface chemistry (polycrystalline oxides) and quantum chemical modeling, and EPR spectroscopy has contributed significantly to the elucidation of the surface structure, particularly the surface defects.

In relation to the surface defects on the group II alkaline earth oxides, EPR has been instrumental in unraveling the electronic structure of the defects on both polycrystalline and well defined single crystal surfaces. These trapped electron centers can be formed in a number of different ways. The most convenient means on powders is by exposure of the alkaline earth oxide, such as MgO, to hydrogen atoms [22]. Spontaneous ionization of the H atoms occurs with the subsequent formation of excess electrons on the surface:

$$Mg_n^{2+}O^{2-} + H^{\bullet} \rightarrow Mg_n^{2+}(e^-)(OH^-) \tag{1.51}$$

The singly trapped electron center is paramagnetic and produces a characteristic EPR powder pattern. The electron trapping site, labeled Mg_n^{2+} in Equation 1.51, can either be a single low-coordinated cation ($n = 1$) or a small array of surface cations ($n > 1$), while the proton is stabilized by a single O^{2-} anion as a surface hydroxyl group ($O^{2-} + H^+ \rightarrow OH^-$). A typical X-band *cw*-EPR spectrum for this excess electron center on polycrystalline MgO is shown in Figure 1.16.

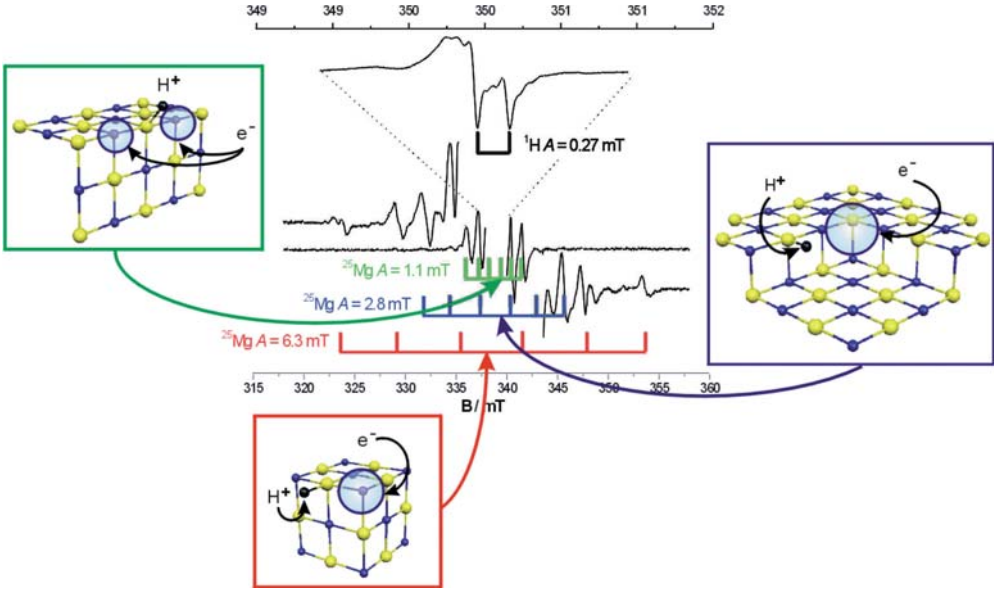

Figure 1.16 EPR spectrum and atomistic models of $(H^+)(e^-)$ centers on MgO. Reproduced from reference [22].

The powder EPR signal is dominated by a hyperfine doublet due to the interaction between the trapped electron and a single proton (^1H, $I = 1/2$). The ^1H hyperfine couplings can be more precisely determined by ENDOR, with values of $A_1 = 2.07$ G, $A_2 = 2.00$ G, $A_3 = 0.31$ G [23]. These hyperfine parameters indicate that the local symmetry of the site is lower than axial; for a purely axial system, the hyperfine parameters should take the form $A_1 = A_2 = A_\perp$ and $A_3 = A_{||}$. Although the difference between A_1 and A_2 is small, the slightly rhombic nature of the parameters is very important and extremely informative. The magnitude of these hyperfine couplings also indicates that the electron–proton interaction is weak.

The overlap of the excess electron wave function with the charge clouds of surface ions creates further hyperfine interactions with the lattice $^{25}Mg^{2+}$ cations ($I = 5/2$ for ^{25}Mg with 10.2% natural abundance). Analysis of these ^{25}Mg hyperfine parameters proved pivotal in deriving a suitable structural model for the defect sites [24]. Three distinct ^{25}Mg hyperfine patterns can be observed (green, blue and red sextet patterns in Figure 1.16) with couplings of 11 G, 30 G and 60 G in the experimental spectrum. The magnitude of the largest hyperfine sextet (60 G) is not consistent with the traditional model of an excess electron center localized in either a bulk or surface anion vacancy, where the interaction is expected to be very weak. This large splitting was explained as arising from a large unpaired electron spin density on a single $^{25}Mg^{2+}$ cation (as opposed to being shared or distributed between an array of cations) [22]. Cluster model DFT calculations confirmed this hypothesis and revealed that the excess electrons could indeed be stabilized by the large electrostatic potential provided by a low coordinated corner or kink Mg_{3c}^{2+}

ion and a nearby proton. Both the experimentally observed EPR parameters and the energetics of the hydrogen ionization reaction, were suitably accounted for theoretically. Based on the EPR results (primarily the ^{H}A and ^{Mg}A hyperfine data) an entirely new model was proposed for the nature of the surface centers based on $(H^+)(e^-)$ electron–proton pairs, bound at morphological surface features such as a corner ion.

The remaining two ^{25}Mg hyperfine patterns (of 30 G and 11 G), could also be interpreted and explained using the new model. Theoretical calculations concluded that the 30 G hyperfine pattern was consistent with a $(H^+)(e^-)$ pair localized at the intersection of two steps. This morphological feature, also known as a reverse corner, is an important defect on polycrystalline MgO and is responsible for a number of interesting reactions, from the heterolytic dissociation of H_2 to the stabilization of alkali metal atoms. The remaining 11 G sextet pattern was more difficult to identify conclusively, since the observed parameters could equally be interpreted as arising from either the classical surface anion vacancy model, $F_s^+(H)$ center, or the $(H^+)(e^-)$ pairs model localized at surface edges and steps [25, 26]. The final assignment was eventually achieved using an MgO surface enriched with ^{17}O ($I = 5/2$). In this case, the unpaired electron produced a superhyperfine interaction with ^{17}O, and two distinct ^{17}O hyperfine sextets were identified [27]. The inequivalencies between the two ^{17}O nuclei, arose from the different spin densities created by the preferential polarization of the trapped electron towards one of the two nuclei. This polarization was created by the nearby surface OH^- group, which has the larger ^{17}O hyperfine coupling while the smaller coupling belongs to the surface O^{2-} lattice anions. This intuitive assignment was confirmed by *ab initio* calculations of the ^{17}O hyperfine tensors, which revealed that only the $(H^+)(e^-)$ pairs model, based at surface steps or edges, is consistent with the experimental data, since the ^{17}O hyperfine couplings for the $F_s^+(H)$ model were far too small.

The above example shows how very detailed information on the electronic structure of surface defect centers can be obtained by EPR even on a heterogeneous polycrystalline oxide, primarily by careful analysis of the hyperfine couplings. However, in many cases the experimental interpretations clearly benefit from complementary theoretical calculations. In this regard, EPR is the ideal partner in such interdisciplinary studies, as the spin Hamiltonian parameters provide a direct means of assessing the theoretical models by providing accurate information on spin densities. At least three different surface sites were comprehensively identified on the MgO surface, and these sites were able to spontaneously ionize H atoms and stabilize the resulting products in the form of $(H^+)(e^-)$ pairs. These $(H^+)(e^-)$ pairs can therefore be regarded as "true" color centers. The *ab initio* calculations show that the $(H^+)(e^-)$ center on MgO (reverse corner) is in fact a deep trap for the electron, which is bound by 3.71 eV and gives rise to two intense electronic transitions in the visible spectrum at 2.07 eV and 2.39 eV [25]. The same is true for corner sites [24]. This finding provides a new framework for future discussions of electron trapping since discrete morphological features, naturally present on surfaces, have been shown to act as potential wells for electron trapping without the exclusive need for surface anion vacancies.

Like the ***A*** tensor, the ***g*** tensor of the surface color centers is also very informative, but the ***g*** anisotropy is so small that it is poorly resolved at traditional X-band frequencies, particularly on a powder sample. Delicate information on the structure of paramagnetic species can however be obtained by analysis of the *g* values, but only if resolved at higher frequencies. For example, information on the point symmetry of the color center can be obtained if accurate *g* values are known. Chiesa and coworkers [28] have performed a unique multifrequency EPR study of trapped electrons on polycrystalline MgO at 9.5, 34, 190 and 285 GHz (Figure 1.17). Owing to the high fields, enhanced resolution of the Zeeman components was achieved confirming the small g anisotropies of $\Delta g_x = -0.002\,94$, $\Delta g_y = -0.002\,86$, $\Delta g_z = -0.001\,01$ with $\Delta g_i = g_i - 2.0023$. This rhombic symmetry, therefore, substantiates the assignment of the dominant surface excess electron species to $(H^+)(e^-)$ pairs (in agreement with the assignment based on analysis of the $^{H}\mathbf{A}$ tensor) bound at the surface steps or edges of the MgO powder and possessing C_{2v} symmetry [28].

Accurate determination of the ***g*** tensors at X-band frequencies can only be achieved provided that a well defined surface is available, as opposed to a polycrystalline powder, and this requires EPR measurements to be performed under ultra high vacuum (UHV) conditions on thin films or single crystals. In this case, the sample can be preferentially aligned with the laboratory magnetic field, so that a given orientation of θ is obtained. The orientational dependence of the *g* tensor can then be systematically probed, and this approach can be far more informative

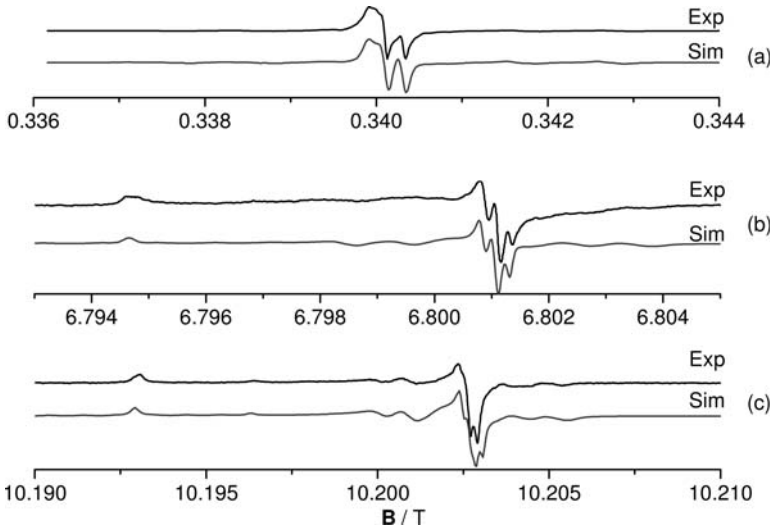

Figure 1.17 Experimental and simulated EPR spectra of $(H^+)(e^-)$ centers recorded at (a) 9.5 GHz, (b) 190 GHz and (c) 285 GHz. The high frequency spectra were obtained with a field modulation of about 0.2 G and a sweep rate of 0.001 G min^{-1}. Reproduced from reference [28].

than the summed powder pattern. Freund is the leading pioneer in the field of UHV-EPR and has shown the potential offered by EPR to the surface science community, through numerous examples ranging from defects [29–31] and adsorbates [32, 33] to model catalysts [34, 35] and supported gold atoms [36, 37]. Freund [29–31] has studied the electronic and geometric properties of trapped electron centers on thin epitaxially grown MgO(001) films on Mo(001) substrates. Idealized point symmetries of the defect sites on MgO were considered, including C_{4v} for the terrace site, C_{2v} for the edge site and C_{3v} for the corner site. For each symmetry, the components of g are dependent on the orientation of the principal g frame with respect to the laboratory reference axis frame; axial g tensors are predicted for the C_{4v} and C_{3v} symmetries whilst a rhombic symmetry is predicted for the edge site possessing C_{2v} symmetry. Rotation of the thin film by an angle θ with respect to **B**, provides information on these symmetry elements, as different components come into resonance for different angles, and these maxima in resonance absorbance will be different for an axial g tensor compared to a rhombic g tensor. The resulting spectra are shown in Figure 1.18.

The spectra were simulated based on the summed contributions from the terrace, edge and corner sites [29]. The results revealed that the g values for the edge sites were $g_{iso} = 2.0001 \pm 0.000\,05$, $\Delta g = 0.000\,40$, $\Delta B = 1.10\,\mathrm{G}$ whereas for the corner site the g values were $g_{iso} = 2.0001 \pm 0.000\,05$, $\Delta g = 0.000\,27$, $\Delta B = 1.06\,\mathrm{G}$. On the basis of the relative contributions of the two signals in the simulations and the angular dependency of the EPR lineshape, it was concluded that electron bombardment on the surface of MgO thin films leads predominantly to trapped electron centers at the edges of the MgO facets [29].

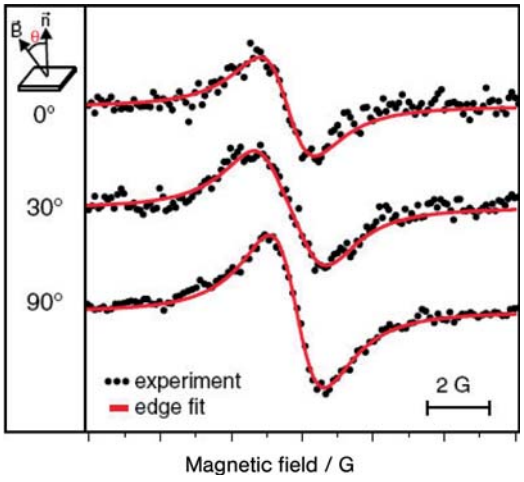

Figure 1.18 Experimental and simulated EPR spectra of color centers on 20 monolayer MgO(001)/Mo(001). Reproduced from reference [29].

1.3.2
Inorganic Radicals

The study of surface-stabilized inorganic radicals by EPR has a long history. This partially arises from their ease of generation and their favorable stability on the ionic oxide surfaces. From a catalysis point of view, such radicals are fundamentally important, since they can act as intermediates or oxidants in the catalytic cycle. If isotopic substitution of the radical is facile, then a very thorough description of the electronic and geometric properties of the species can once again be obtained by analysis of the powder EPR pattern.

In Section 1.2.9, a case study was presented on how EPR was used to identify and characterize the NO_2 radical supported on an oxide surface. To further illustrate the generic nature of this analytical approach in EPR to the investigation of the properties of surface radicals, the case of CO_2^- adsorbed on an MgO surface will be presented. This radical can be easily formed by exposure of CO_2 to MgO containing excess surface electron trapped species (that is the $(H^+)(e^-)$ centers discussed in the previous section). Although it has been studied on different oxides over the years [38, 39], a study by Chiesa and Giamello [40] demonstrates the wealth of information that can be obtained from the powder EPR spectrum. The EPR spectrum for the surface (MgO) supported $^{13}CO_2^-$ species is shown in Figure 1.19.

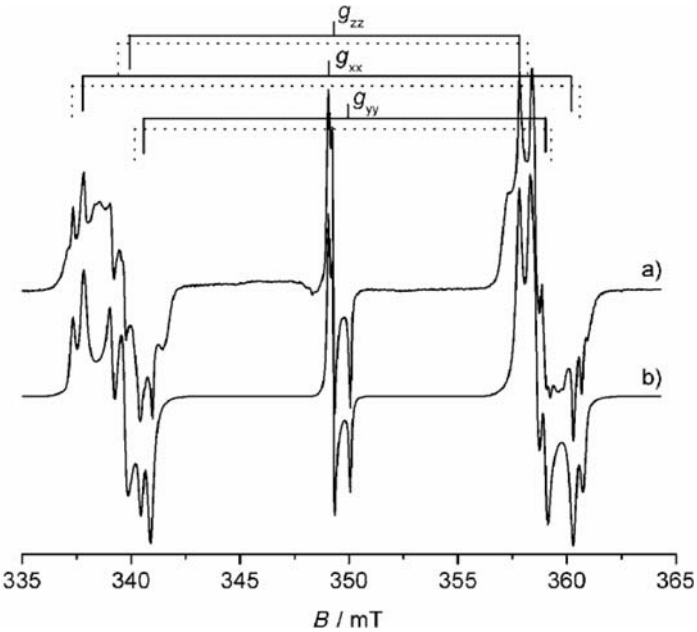

Figure 1.19 Experimental (a) and simulated (b) EPR spectrum of surface adsorbed $^{13}CO_2^-$ radicals. Reproduced from reference [40].

Simulation of the spectrum, revealed that at least two different $^{13}CO_2^-$ radicals are present (i.e. with two different sets of $\boldsymbol{g}$ and $\boldsymbol{A}$ tensors), suggesting that two different surface sites must be available for stabilizing the species. For convenience, only the spectroscopic properties of the most dominant species will be presented here. The experimental $\boldsymbol{g}$ and $\boldsymbol{A}$ tensors were found to be $g_{xx} = 2.0026$, $g_{yy} = 1.9965$, $g_{zz} = 2.0009$, $|A_{xx}| = 507.5$, $|A_{yy}| = 495.2$ and $|A_{zz}| = 629.3$ MHz. The largest deviation of the g value from $g_e = 2.002\,3$, is expected along the y axis (g_y) and is due primarily to admixture of the ground state ($4a_1$) with the first excited state ($2b_1$) while the direction of maximum hyperfine coupling coincides with the principal g value oriented along the z axis. The experimental hyperfine parameters can be decomposed into the isotropic and dipolar parts using Equation 1.47. It is necessary to know the relative signs of the hyperfine coupling for this analysis. However since a_{iso} is too large to be caused by spin polarization, it must be positive. Based on this assumption the experimental matrix can be decomposed as follows:

$$\begin{bmatrix} 507.5 & & \\ & 495.2 & \\ & & 629.3 \end{bmatrix} = 544.0 + \begin{bmatrix} -36.5 & & \\ & -48.8 & \\ & & +85.3 \end{bmatrix} \tag{1.52}$$

The large isotropic component is due to the unpaired electron spin density in the carbon 2s orbital, and this value (544 MHz) can be used to derive an estimate of the carbon 2s orbital contribution to the molecular orbital. Since the theoretical isotropic coupling constant for ^{13}C is 3777 MHz, then $c_{2s}^2 = 544/3777 = 0.144$. The anisotropic dipolar part of the hyperfine arises from unpaired spin density in the $2p_z$ orbital. However because the dipolar contribution in Equation 1.52 cannot be reduced to zero, this implies that a fraction of the spin density is allocated to the 2p orbital perpendicular to the molecular plane. Therefore, the dipolar component of Equation 1.52 must be further decomposed into two symmetrical tensors oriented along the z and x axes:

$$\begin{bmatrix} -36.5 & & \\ & -48.8 & \\ & & +85.3 \end{bmatrix} = \begin{bmatrix} -44.7 & & \\ & -44.7 & \\ & & +89.4 \end{bmatrix} + \begin{bmatrix} +8.2 & & \\ & -4.1 & \\ & & -4.1 \end{bmatrix} \tag{1.53}$$

This information may be interpreted in terms of the unpaired electron being confined to a carbon sp^2 hybrid orbital ($4a_1$) built up by carbon 2s and $2p_z$ and oxygen $2p_z$ atomic orbitals. The $2p_z$ character of the $4a_1$ molecular orbital can be estimated by comparison with the integral:

$$T_0 = 4/5 g_e \mu_B g_n \mu_n \langle 1/r^3 \rangle_{np} \tag{1.54}$$

which is the explicit expression of the dipolar interaction for the external field aligned along the symmetry axis of the $2p_z$ orbital. Since $\langle r\text{-}3 \rangle_{2p} = 5.820$ a.u.$^{-3}$, then

$c^2_{C2p_z}$ is found to be 0.416. Similarly the carbon $2p_x$ character can be determined as $c^2_{C2p_x} = 0.038$. The total electron spin density on the carbon atom is therefore $\rho^{13C} = 0.60$, leaving the remaining spin density to be shared by the oxygen atoms and the surface itself. To estimate the spin densities associated with the two oxygen atoms, one requires isotopic substitution of the radical via $C^{17}O_2^-$. The EPR spectra of $C^{17}O_2^-$ were sufficiently well resolved, that the ^{17O}A hyperfine parameters were easily identified. Analysis of the ^{17O}A tensors was carried out in a similar fashion to that described in Equations 1.47, 1.52 and 1.53 for ^{13}C, and the resultant spin density on oxygen was found to be $\rho^O(2s) = 0.019$, $\rho^O(2p_z) = 0.193$ and $\rho^O(2p_x) = -0.008$. The total spin density on the radical was therefore 1, and this elegant study demonstrates how easily this information can be obtained even from a powder EPR pattern.

Other radical species studied over polycrystalline MgO include O^- [41], O_3^- [42], CO^- [43], O_2^- [44, 45] and N_2^- [46]. For all these radical species, the most detailed information was obtained in cases which used isotopic substitution (^{17}O, ^{13}C, ^{15}N) and where the surface speciation of the radicals was minimized. If several different sites coexist for radical stabilization, then a heterogeneity of g and A values creates uncertainties in the assignments, and it may be more beneficial to sacrifice signal intensity for signal resolution. This was nicely exemplified for the N_2^- radical anion [46]. The latter radical is unusual since it is formed reversibly by low temperature physisorption of N_2 onto MgO containing the $(H^+)(e^-)$ centers [22]. At higher temperatures, the N_2 molecule desorbed from the surface regenerating the original $(H^+)(e^-)$ centers. The species was found to lie parallel to the surface and was unambiguously identified on the basis of the **g** and **A** tensors derived by careful spectral simulation of the $^{14}N_2^-$ and $^{15}N_2^-$ powder EPR patterns. The **g** tensor is typical of an 11 electron π radical with $g_{yy} > g_{xx} >> g_{zz}$ (i.e. $g_{yy} = 2.0042$, $g_{xx} = 2.0018$, $g_{zz} = 1.9719$). The z direction corresponds to the internuclear axis and the x direction is perpendicular to the surface. The hyperfine structure was found to be typical of a species with two equivalent N nuclei with $A_{xx} = 2.90\,G$, $A_{yy} = 21.50\,G$ and $A_{zz} = 4.20\,G$. Analysis of the hyperfine tensor indicated that about 90% of the total electron density is transferred from the surface to the molecule where it is mainly confined to the π^*_y orbital. *Ab initio* theoretical calculations at the DFT level indicated that a small energy barrier separates the unbound $(H^+)(e^-)/N_2$ state from the bound $(H^+)/N_2^-$ state (Figure 1.20). This result agrees with the facile reversibility of the surface-to-molecule electron transfer process. The calculated spin densities were in excellent agreement with those derived from the EPR experiments. The presence of an OH group near the adsorbed radical anion produces a detectable superhyperfine structure on the spectrum and this was also used to establish the correct orientation of the adsorbed radical on the surface [46].

In addition to the study of the $(H^+)(e^-)/N_2^-$ system, a detailed analysis of the analogous $(H^+)(e^-)/O_2^-$ complex was also reported, with particular emphasis on the ^{17}O hyperfine structure of adsorbed O_2^- [44, 45]. The Fermi contact term was evaluated as $a_{iso} = -20.3\,G$ and the resulting dipolar tensor was found to be $B_{xx} = -56\,G$, $B_{yy} = +27.5\,G$, $B_{zz} = +28.6\,G$. These values were later confirmed by

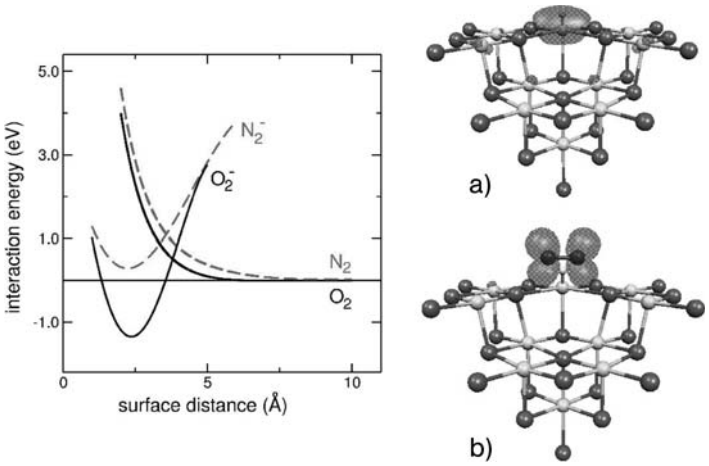

Figure 1.20 Spin density plot for (a) $(H^+)(e^-)$ centers located at a cationic reverse corner and (b) the complex formed by interaction with N_2 or O_2 molecules. On the left hand side the schematic potential energy curves for the interaction of O_2 (solid curve) and N_2 (dotted curve) molecules is shown. Negative values indicate bound states. Reproduced from reference [22].

EPR experiments. The powder spectrum contained a large number of lines and was further complicated by the presence of several off-axis extra features. These features, also known as overshoot lines, are a consequence of the relatively large anisotropy in the principal *g* values compared with substantial values of the hyperfine splitting. These features do not correspond to resonances from principal directions, and have their origins at angles in between the principal axes. They should not therefore be mistakenly interpreted as resonances from principal directions. In the $^{17}O_2^-$ case, the simulation of such a complex pattern of lines gave a_{iso} = 4.8 G and a dipolar tensor (*T*) with a value remarkably close to the theoretically calculated value. This validates the quality of the model but also the capability of modern theoretical approaches in predicting EPR hyperfine parameters. The nonreversibility of the electron transfer process from the oxide surface to the adsorbed molecule was also confirmed by theory (Figure 1.20) [22].

In one sense the radical-forming reactions between O_2 or N_2 with the electron-rich oxide surface are unusual given the low or even negative electron affinities of the two molecules (O_2 = +0.44 eV, N_2 = −2.0 eV). If the driving force for these reactions was exclusively based on the interplay between ionization energy of the surface center and molecular electron affinity, no reaction would occur. However, when electrostatic contributions between the ionic surface and the negative anions are considered, favorable reaction conditions occur. Only low-coordinated sites of the cubic crystals are capable of providing sufficiently strong stabilization energies. This fact exemplifies and highlights the importance of these low-coordinated

surface sites in the chemistry of the MgO surface over and above the rather inert Mg^{2+}_{5c} ions on the planar (100) faces.

1.3.3 Transient Radical Intermediates

Studies of transient radicals in heterogeneous catalysis have been successfully conducted by EPR using various approaches ranging from matrix isolation to spin trapping. In some cases, highly reactive species on oxide surfaces can still be investigated by traditional EPR methods by careful control of the experimental conditions such as temperature. A good example of this approach is the identification of the transient organoperoxy radicals in heterogeneous photocatalysis [47–49]. Photocatalytic oxidation of organic pollutants is frequently carried out using semiconducting polycrystalline powders such as TiO_2. On absorption of a photon, with energy equal to or greater than the band gap of TiO_2, an electron/hole pair is generated in the bulk. These charge carriers migrate towards the catalyst surface where they participate in redox reactions with the adsorbed organic molecules, and ultimately form surface radicals. In many cases, these surface (and desorbed gaseous) radical intermediates have been proposed and implicated in the photo-oxidation mechanism, particularly the oxygen-based radicals since the photocatalytic reactions are performed under aerobic conditions and molecular oxygen is an excellent electron scavenger. Despite the growing evidence for the role of active oxygen species in such reactions, surprisingly few studies have been devoted to exploring the transient intermediates by EPR.

Several EPR studies in heterogeneous photocatalysis have focused on ionic oxygen-centered radicals such as O^-, O_3^- and particularly O_2^-. However, other types of oxygen-based radicals have received far less attention, including the series of thermally unstable peroxyacyl radicals (of general formula $RCO_3^{\bullet}$) [50] and peroxy radicals (of general formula $ROO^{\bullet}$) [47–49]. A representative example of an EPR spectrum for one class of these organoperoxy radicals, is shown in Figure 1.21.

The radical is easily formed by photoirradiation of TiO_2 containing a mixture of a ketone (such as acetone or butanone) and $^{17}O_2$, at 77 K. The measurement temperature is maintained below 200 K, since the radicals are unstable at higher temperatures. After room temperature annealing, only the O_2^- radicals are observed, so it is extremely important to carefully control the experimental temperature if the transient reactive oxygen species are to be detected. The g values for the radical shown in Figure 1.21 were $g_1 = 2.035$, $g_2 = 2.008$, $g_3 = 2.002$, and these are more consistent with a peroxy radical assignment than with a purely ionic assignment (O_2^-). A definitive assignment was obtained via analysis of the ^{17}O hyperfine pattern Figure (1.21) which revealed hyperfine couplings of $^{17O}A_{||}$ (i) = 99.2 G (i.e. for $RO^{17}O^{\bullet}$) and $^{17O}A_{||}$ (ii) = 58.5 G (i.e. for $R^{17}OO^{\bullet}$) centered on the g_3 component at 2.003 [49]. This confirmed the identity of the radical as an $ROO^{\bullet}$ type species rather than $^{17}O_2^-$ for which two equivalent oxygen nuclei are expected. The unpaired spin density in peroxy radicals is known to be localized primarily in the

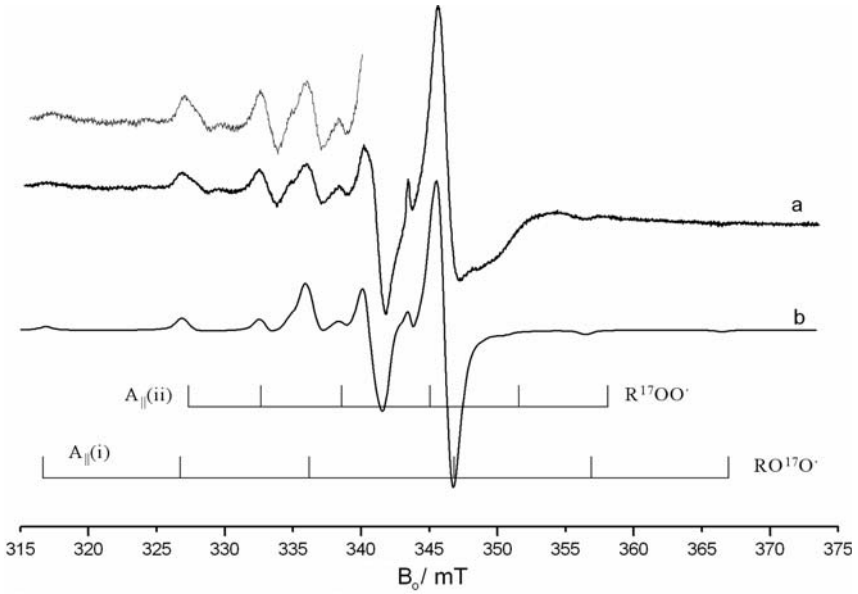

Figure 1.21 Experimental (a) and simulated (b) EPR spectrum of photoirradiated TiO_2 (at 77 K) containing coadsorbed butanone: $^{17}O_2$ in a 5 : 1 ratio (63% isotopic enrichment of ^{17}O). Reproduced from reference [49].

p_z orbitals of the two oxygen atoms, which are aligned parallel to each other, and the anisotropic hyperfine couplings arise from the spin density in the p_z orbitals which is axially symmetric, with $A_{\|} = (a + 2B)\rho$ and $A_{\perp} = (a - B)\rho$ where ρ is the spin density in the p_z orbital. An estimate of the p_z orbital spin density can be calculated using the expression $\rho(i) = |A_{\|}(i)|/\ 154\,G$, where $154\,G = |a + 2B|$. From this expression, and using the simulated hyperfine couplings, the spin density on the terminal oxygen of the butanone-derived peroxy radical was estimated to be 0.64. This falls inside the range of typical spin densities (0.61–0.70) for carbon-based peroxy radicals.

The mechanism of radical generation initially occurs via UV irradiation of the oxide producing surface trapped holes, O^-. Electron transfer from the adsorbed ketone to the surface trapped hole occurs, producing an adsorbed cation radical. This quickly deprotonates by H^+ transfer to the surface oxide, forming an intermediate radical which subsequently reacts with molecular oxygen to form the adsorbed alkylperoxy radical observable by EPR [48].

$$CH_3COCH_{3(a)} + O^-_{(s)} \rightarrow CH_3COCH^{\bullet}_{2(a)} + OH^-_{(s)} \tag{1.55}$$

$$CH_3COCH^{\bullet}_{2(a)} + O_{2(a)} \rightarrow CH_3COCH_2OO^{\bullet}_{(a)} \tag{1.56}$$

Unlike the ionic O_2^- radicals, these neutral peroxy radicals are mobile and can easily diffuse across the TiO_2 surface, undergoing further oxidative and decompo-

sition reactions. The reduced Ti^{3+}_{surf} centers are also involved in the oxidative decomposition pathways of adsorbed ketones, but via a different radical pathway [49]. Ti^{3+} involvement occurs either through the generation of stable inorganic radicals, according to Equation 1.57:

$$O_2 + Ti^{3+} \rightarrow O_2^- + Ti^{4+} \tag{1.57}$$

$$Ti^{3+} + CH_3COCH_3 \rightarrow Ti^{4+} + \{CH_3COCH_3^{\bullet -}\}^* \tag{1.58}$$

$$\{CH_3COCH_3^{\bullet -}\}^* \rightarrow CH_3^{\bullet} + CH_3CO^{\bullet} \tag{1.59}$$

or through the participation of unstable organic intermediates ($\{CH_3COCH_3^{\bullet -}\}^*$) which disproportionates to form methyl ($CH_3^{\bullet}$) and acyl ($CH_3CO^{\bullet}$) radicals (Equations 1.58–1.59). These latter radicals can be indirectly identified through their reactivity with molecular oxygen forming the corresponding organoperoxy radicals ($CH_3OO^{\bullet}$ and $CH_3CO_3^{\bullet}$) or via spin trapping. The O_2^- anions formed according to Equation 1.57 can selectively react with the adsorbed acetone (depending on the temperature) to form an associated $[\text{acetone-}O_2^-]_{(a)}$ surface complex, which can also be classified as an organoperoxy-type species [51]. This reaction can be followed by variable temperature EPR measurements, as shown in Figure 1.22.

At least three sites exist for stabilization of the O_2^- radicals on the polycrystalline TiO_2 powder, as evidenced by three different g_{zz} values of 2.019, 2.023 and 2.026.

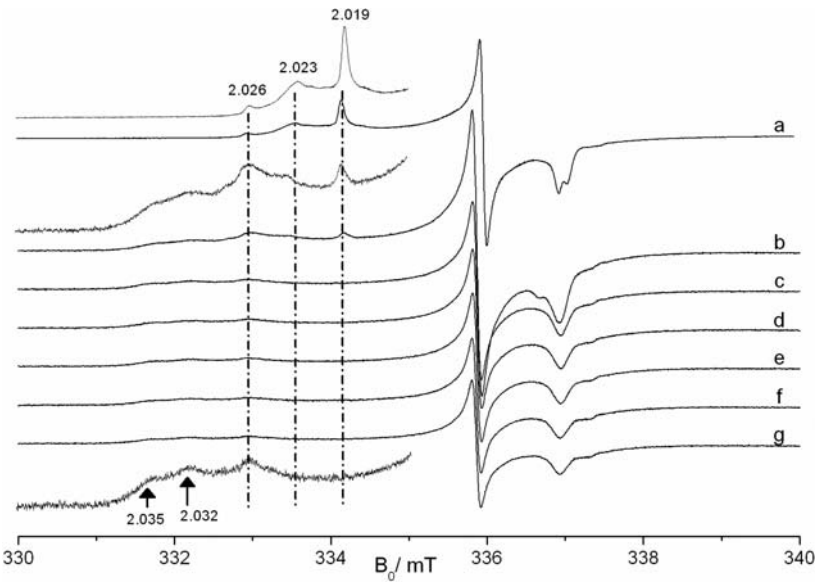

Figure 1.22 (a) EPR spectra of O_2^- radicals formed on thermally reduced TiO_2 at 140 K, and after exposure to acetone at (b) 210, (c) 212, (d) 214, (e) 216, (f) 218 and (g) 220 K. Reproduced from reference [51].

The reactivity of each O_2^- species towards acetone is not, however, the same; the species characterized by g_{zz} = 2.019 reacts first, followed by the second species with g_{zz} = 2.023. Simultaneously new signals emerge at 2.032 and 2.035. These are due to another family of organoperoxy radicals (that is the $[\text{acetone-}O_2^-]_{(a)}$ surface complex), which are thermally unstable. The most reactive O_2^- species with spin Hamiltonian parameters of g_{xx} = 2.005, g_{yy} = 2.011, g_{zz} = 2.019, $^{17O}A_{xx}$ = 7.64 mT and $A_{yy} = A_{zz}$ >1 mT, has been assigned to an oxygen radical stabilized at an anion vacancy (labeled $[\text{Vac}\ldots O_2^-]$). These results illustrate how the same nominal type of radical (O_2^-) can display differences in chemical reactivity depending on the surface site [51].

All of these radical intermediates, classified as organoperoxy species, are thermally unstable, and cannot be observed at temperatures above 250 K. This may partly explain why they have not been widely studied to date by EPR, and at least emphasizes the need to perform the experiments at low temperatures if a complete picture of the oxidative decomposition pathways in heterogeneous photocatalysis is to emerge.

1.3.4
Supported Transition Metal Ions

Transition metal oxides are versatile materials used not only as supports for catalytically active species, but also in diverse applications ranging from pigments to fuel cells to chemical sensors. In most of these applications the redox state of the transition metal ion is instrumental in controlling the final desired chemical, electrical or optical properties of the polycrystalline material or thin film. Various spectroscopic approaches are therefore required to fully characterize the nature of the "active" oxide phase, but few techniques can specifically probe, at the molecular level, the inherent properties responsible for changes in oxidation state, or distinguish the few active surface sites compared to the more abundant inactive sites. EPR is ideally suited to such investigations, primarily because it is very sensitive and also because it probes only the paramagnetic states (the redox changes) [52]. Numerous studies have appeared in recent years at the gas–solid and liquid–solid interface of TiO_2, ZrO_2, CeO_2, ZnO and various oxides of V, Cr, Fe and Cu [20, 21]. Two examples of how EPR has contributed immensely to these fields will be illustrated below.

Pitrzyk and Sojka [53] have investigated the valence and spin states of the active sites in a Co^{2+} exchanged zeolite (β and ZSM-5) during the selective catalytic reduction of nitrogen oxides with propene. Until now no clear evidence of Co^0 formation upon contact with the SCR reagents has been provided, and the existence of an intrazeolite nCo^{2+}/Co^0n couple has not been shown by EPR. Adsorption of CO at low temperature onto the Co^{2+} exchanged zeolite leads to the formation of the paramagnetic $Co^{2+}CO$ adduct characterized by the spin Hamiltonian parameters g_x = 2.234, g_y = 2.179, g_z = 2.016, $|A_x|$ = 44, $|A_y|$ = 34, $|A_z|$ = 76 G (Figure 1.23A). The spectrum was so well resolved that two other sites could be distinguished by computer simulations, illustrating nicely how sensitive the spin Hamiltonian

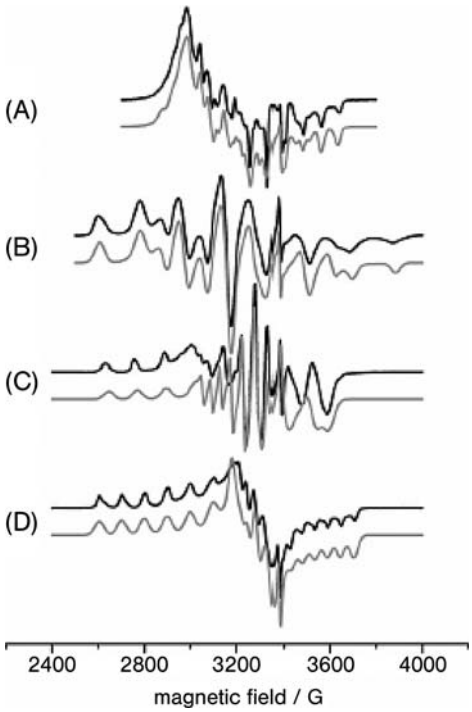

Figure 1.23 X-band experimental (black line) and simulated (grey line) EPR spectra of CoBEA sample after adsorption at 77 K of (A) 10 Torr CO, (B) 6 Torr NO, (C) 10 Torr CO after thermal decomposition (573 K in vacuum) of dinitrosyl species (spectrum B), and (D) 10 Torr propene heated at 443 K after thermal decomposition (573 K in vacuum) of dinitrosyl species (spectrum B). Reproduced from reference [53].

parameters are to their surroundings, and how informative a good simulation can be. After the sample was exposed to NO, the signal changed (Figure 1.23B). The spin Hamiltonian parameters of $g_x = 2.081$, $g_y = 2.195$, $g_z = 2.086$, $|A_x| = 182$, $|A_y| = 102$ and $|A_z| = 31$ G, were consistent with a $Co^{2+}(NO)_2$ dinitrosyl complex. Formation of this cage complex can be rationalized in terms of a spin pairing between the cobalt sites in a spin quartet state $^4Co^{2+}(d^7)$ and two NO ($^2\Pi_{1/2}$) radical ligands: $^4Co^{2+} + 2NO \rightarrow [^2Co(NO)_2]^{2+}$. The resultant spin density is largely located on the metal center ($\rho^{3d} \approx 80\%$). Thus the electronic configuration of cobalt in the dinitrosyl complex corresponds to d^9, which formally is tantamount to the zero-valent state of cobalt [53].

After formation of the dinitrosyl, the sample was evacuated at elevated temperatures and the valence state of cobalt probed again with CO. After such a treatment a new EPR signal was once again observed (Figure 1.23C) with the spin Hamiltonian parameters of $g_x = 2.199$, $g_y = 2.119$, $g_z = 1.973$, $|A_x| = 48$, $|A_y| = 125$, $|A_z| = 35$ G. These parameters are different from those of the initial carbonyl species, $Co^{2+}CO$ in Figure 1.23A, and can in fact be assigned to the Co^0CO species. This led the authors to conclude that the following simplified reaction sequence must be occurring;

$$Co^{2+} \rightarrow Co^{2+}(NO) \rightarrow Co^{0}(NO^{+}) \rightarrow Co^{0}(CO) \tag{1.60}$$

As a result, the reduction of cobalt from the divalent to the zero-valent state changes the chemistry of the system, since Co^0 readily forms complexes with hydrocarbons. This was confirmed by subsequent adsorption of propene, which produced the EPR spectrum shown in Figure 1.23D, with spin Hamiltonian parameters of $g_x = 2.096$, $g_y = 1.924$, $g_z = 2.297$, $|A_x| = 12$, $|A_y| = 52$, $|A_z| = 99$ G. This spectrum was not observed following propene exposure directly to the Co^{2+} sites.

These results highlight for the first time that at SCR temperatures the interaction of NO*x* with co-zeolites, alone or in the co-presence of propene, leads to the reduction of Co^{2+} to Co^0 via dinitrosyl intermediates [53]. The zero-valent cobalt sites generated during decomposition of the dinitrosyl species were found to exhibit enhanced affinity toward coordination of CO and propene, giving rise to the corresponding adducts with characteristic EPR spectra. The same adducts are found during SCR of NO*x* with propene, indicating that the two-electron Co^{2+}/Co^0 redox couple operates in the reaction mechanism. This study demonstrates the power of EPR to detect key intermediates, such as $Co^{2+}(NO)_2$, $Co^0(C_3H_6)_n$, and $Co^0(CO)_n$, in an important catalytic cycle.

Another surface catalytic cycle investigated by EPR has been ethene polymerization using Ziegler–Natta catalysts. Although widely studied, a detailed understanding of the reaction mechanism is far from complete largely owing to the difficulties of characterizing the extremely air-sensitive activated catalysts. Activation with a co-catalyst is usually performed using alkyl aluminum compounds such as trimethylaluminum (TMA) or triethylaluminum (TEA). A major step forward in our understanding of the mechanistic details of this reaction was recently advanced by Freund and coworkers [54, 55] using model systems consisting of an epitaxially grown $MgCl_2$ film onto which $TiCl_4$ was anchored as the active component. During activation it is believed that the Ti ions assume a lower oxidation state and when TMA is used alkyl radicals ($R^{\bullet}$) are generated:

$$TiCl_4 + AlR_3 \rightarrow RTiCl_3 + AlClR_2 \rightarrow TiCl_3 + R^{\bullet} + AlClR_2 \ (R = CH_3) \tag{1.61}$$

but until now no evidence had been presented for the existence of the alkyl radicals. The EPR spectrum of the model $TiCl_4/MgCl_2$ catalyst after activation with TMA is shown in Figure 1.24 [54]. At low $TiCl_4$ coverage the signal shown in Figure 1.24a was observed but, as the $TiCl_4$ content was increased, the intensity of the EPR signal was also found to increase (Figure 1.24b). No evidence was found for the existence of any Ti^{3+} centers, in agreement with the literature where TMA activation leads predominantly to the Ti^{2+} species.

The surface radicals observed in Figure 1.24 do not arise from the expected methyl radicals ($^{\bullet}CH_3$) for which a simple quartet structure of 1 : 3 : 3 : 1 line intensity is expected (as shown in Figure 1.23d). Instead the radical intermediates were assigned to ethyl radicals ($^{\bullet}C_2H_5$), based on comparison with the signals observed for ethyl radicals formed by irradiation of an ethyl chloride matrix at 77 K (Figure 1.24c) [54]. The radicals were shown to originate from the recombination of two methyl radicals according to

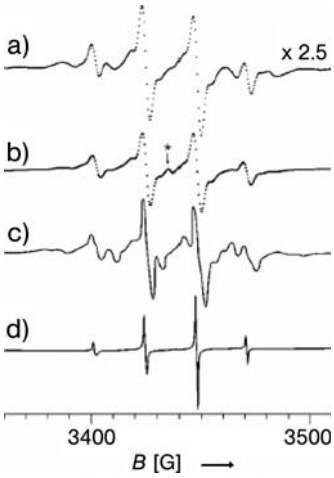

Figure 1.24 EPR spectra of alkyl radicals after (a) $AlMe_3$ adsorption at 40 K on $TiCl_4/MgCl_2$ (small Ti content), (b) $AlMe_3$ adsorption at 40 K on $TiCl_4/MgCl_2$ (higher Ti content), (c) ethyl radicals in an ethyl chloride matrix at 77 K, and (d) methyl radicals on a silica surface at 77 K. Reproduced from reference [54].

$$^{\bullet}CH_3 + Al(CH_3)_3 \rightarrow H_3C{-}^{\bullet}CH_2 + AlH(CH_3)_2 \tag{1.62}$$

The intensity of the $H_3C{-}^{\bullet}CH_2$ signal was attenuated irreversibly above 50 K and decreased below the detection limit above 80 K. This observation was explained by assuming that the ethyl radicals diffuse and recombine at these temperatures, as has been observed for other surface radicals such as $^{\bullet}CH_3$ and NO_2. These results have demonstrated for the first time how free radicals are indeed generated on the surface of an active model Ziegler–Natta catalyst.

1.4 Conclusions

Through the above series of examples, it is clear that EPR offers many advantages for the characterization of paramagnetic species on oxide surfaces. The obvious limitation of the technique is of course that it only detects paramagnetic centers. However, if paramagnetic centers, such as defects, radicals or transition metal ions, are involved in a heterogeneous process, then EPR is the ideal spectroscopic technique. To date most of the studies applied to oxides have used the traditional *cw*-EPR method. Modern pulsed techniques offer far more sensitivity and resolution than *cw*-EPR, and it is certainly hoped that these pulsed techniques will be more widely used as commercial spectrometers become more numerous in research laboratories. Compared to *cw*-EPR, the numerous hyperfine techniques

such as HYSCORE, ENDOR or ELDOR detected NMR can provide far more detailed information on the environment surrounding the local paramagnetic center, enabling a true molecular description of the active site in a heterogeneous system to be achieved. Another major development that will significantly benefit EPR studies on oxide system comes from the interaction between theory and experiment. The quantum theory of EPR parameters is now a very active field and DFT methods have significantly contributed to the interpretation of EPR spectra [56]. As some of the examples here have shown, accurate spin Hamiltonian parameters can be obtained by theory, which can guide the assignments considerably.

Acknowledgments

Dr. Emma Carter for thoroughly proofreading the manuscript and for useful comments and suggestions.

References

1 Lunsford, J.H. (1972) *Advances in Catalysis*, **22**, 265.
2 Howe, R. (1982) *Advances in Colloid and Interface Science*, **18**, 1.
3 Che, M. and Taarit, Y.B. (1985) *Advances in Colloid and Interface Science*, **23**, 235.
4 Che, M. and Giamello, E. (1987) *Studies in Surface Science and Catalysis*, **57**, B265.
5 Sojka, Z. (1995) *Catalysis Reviews–Science and Engineering*, **37**, 461.
6 Dyrek, K. and Che, M. (1997) *Chemical Reviews*, **97**, 305.
7 Sojka, Z. and Che, M. (2001) *Applied Magnetic Resonance*, **20**, 433.
8 Murphy, D.M. and Rowlands, C.C. (2001) *Current Opinion in Solid State and Materials Science*, **5**, 97.
9 Lambert, J.-F. and Che, M. (2000) *Journal of Molecular Catalysis A–Chemical*, **162**, 5.
10 Sojka, Z. (2000) *Applied Magnetic Resonance*, **18**, 71.
11 Hunger, M. and Weitkamp, J. (2001) *Angewandte Chemie–International Edition*, **40**, 2954.
12 Atkins, P.W. and Symons, M.C.R. (1967) *The Structure of Inorganic Radicals*, Elsevier, Amsterdam.
13 Ayscough, P.B. (1967) *Electron Spin Resonance*, Methuen, London.
14 Pilbrow, J.R. (1990) *Transition Ion Electron Paramagnetic Resonance*, Oxford Science Publications, Oxford.
15 Mabbs, F.E. and Collison, D. (1992) *Electron Paramagnetic Resonance of d Transition Metal Compounds (Studies in Inorganic Chemistry)*, Elsevier.
16 Atherton, N.M. (1993) *Principles of Electron Spin Resonance*, Ellis Horwood and Prentice Hall.
17 Weil, J.A., Bolton, J.R. and Wertz, J.E. (1994) *Electron Paramagnetic Resonance: Elementary Theory and Practical Applications*, John Wiley and Sons.
18 Schweiger, A. and Jeschke, G. (2001) *Principles of Pulse Electron Paramagnetic Resonance*, Oxford University Press, Oxford.
19 Lunsford, J.H. (1968) *Journal of Colloid and Interface Science*, **26**, 355.
20 Murphy, D.M. and Giamello, E. (2002) EPR of Paramagnetic Centres on Solid Surfaces, in *Electron Paramagnetic Resonance* (eds B.C. Gilbert, M.J. Davies and D.M. Murphy), Royal Society of Chemistry, Cambridge, **18**, p. 183.
21 Murphy, D.M. and Chiesa, M. (2004) EPR of Paramagnetic Centres on Solid Surfaces, in *Electron Paramagnetic Resonance* (eds. B.C. Gilbert, M.J. Davies and D.M. Murphy), Royal Society of Chemistry, Cambridge, **19**, p. 279.
22 Chiesa, M., Paginini, M.C., Giamello, E., Murphy, D.M., Di Valentin, C. and Pacchioni, G. (2006) *Accounts of Chemical Research*, **39**, 861.

23 Murphy, D.M., Farley, R.D., Purnell, I.J., Rowlands, C.C., Yacob, A.R., Paganini, M.C. and Giamello, E. (1999) *Journal of Physical Chemistry B*, **103**, 1944.

24 Chiesa, M., Paganini, M.C., Giamello, E., Di Valentin, C. and Pacchioni, G. (2003) *Angewandte Chemie–International Edition*, **42**, 1759.

25 Ricci, D., Di Valentin, C., Pacchioni, G., Sushko, P.V., Shluger, A.L. and Giamello, E. (2003) *Journal of the American Chemical Society*, **125**, 738.

26 Chiesa, M., Paganini, M.C., Spoto, G., Giamello, E., Di Valentin, C., Del Vitto, A. and Pacchioni, G. (2005) *Journal of Physical Chemistry B*, **109**, 7314.

27 Chiesa, M., Martino, P., Giamello, E., Di Valentin, C., Del Vitto, A. and Pacchioni, G. (2004) *Journal of Physical Chemistry B*, **108**, 11529.

28 Chiesa, M., Giamello, E., Annino, G., Massa, C.A. and Murphy, D.M. (2007) *Chemical Physics Letters*, **438**, 285.

29 Sterrer, M., Fischbach, E., Risse, T. and Freund, H.-J. (2005) *Physical Review Letters*, **94**, 186101.

30 Di Valentin, C., Neyman, K.M., Risse, T., Sterrer, M., Fischbach, E., Freund, H.-J., Pacchioni, G. and Rosch, N. (2006) *Journal of Chemical Physics*, **124**, 044708.

31 Sterrer, M., Fischbach, E., Heyde, M., Nilius, N., Rust, H-P, Risse, T. and Freund, H.-J. (2006) *Journal of Physical Chemistry B*, **110**, 8665.

32 Katter, U.J., Schlienz, H., Beckendorf, M. and Freund, H.-J. (1993) *Berichte Der Bunsen-Gesellschaft-Physical Chemistry Chemical Physics*, **97**, 340.

33 Katter, U.J., Risse, T., Schlienz, H., Beckendorf, M., Klüner, T., Hamann, H. and Freund, H.-J. (1997) *Journal of Magnetic Resonance*, **126**, 242.

34 Schmidt, J., Risse, T., Hamann, H. and Freund, H.-J. (2002) *Journal of Chemical Physics*, **116**, 10861.

35 Risse, T., Schmidt, J., Hamann, H. and Freund, H.-J. (2002) *Angewandte Chemie–International Edition*, **41**, 1517.

36 Sterrer, M., Yulikov, M., Fischbach, E., Heyde, M., Rust, H.-P., Paccioni, G., Risse, T. and Freund, H.-J. (2006) *Angewandte Chemie–International Edition*, **45**, 2630.

37 Yulikov, M., Sterrer, M., Heyde, M., Rust, H.-P., Risse, T., Freund, H.-J., Pacchioni, G. and Scagnelli, A. (2006) *Physical Review Letters*, **96**, 146804.

38 Lunsford, J.J. and Jayne, J.P. (1965) *Journal of Physical Chemistry*, **69**, 2182.

39 Teramura, K., Tanaka, T., Ishikawa, H., Kohono, Y. and Funabiki, T. (2004) *Journal of Physical Chemistry B*, **108**, 346.

40 Chiesa, M. and Giamello, E. (2007) *Chemistry–A European Journal*, **13**, 1261.

41 Che, M. and Tench, A.J. (1983) *Advances in Catalysis*, **32**, 1.

42 Che, M. and Tench, A.J. (1982) *Advances in Catalysis*, **31**, 77.

43 Giamello, E., Murphy, D.M., Marchese, L., Martra, G. and Zecchina, A. (1993) *Journal of the Chemical Society, Faraday Transactions*, **89**, 3715.

44 Chiesa, M., Giamello, E., Paganini, M.C. and Sojka, Z. (2002) *Journal of Chemical Physics*, **116**, 4266.

45 Ricci, D., Pacchioni, G., Sushko, P.V. and Shluger, A.L. (2003) *Surface Science*, **542**, 293.

46 Chiesa, M., Giamello, E., Murphy, D.M., Pacchioni, G., Paganini, M.C., Soave, R. and Sojka, Z. (2001) *Journal of Physical Chemistry B*, **105**, 497.

47 Gonzalez-Elipe, A.R. and Che, M. (1982) *Journal de Chimie Physique*, **79**, 355.

48 Attwood, A.L., Edwards, J.L., Rowlands, C.C. and Murphy, D.M. (2003) *Journal of Physical Chemistry A*, **107**, 1779.

49 Carter, E., Carley, A.F. and Murphy, D.M. (2007) *Journal of Chemical Physics and Physical Chemistry*, **8**, 113.

50 Jenkins, C.A. and Murphy, D.M. (1999) *Journal of Physical Chemistry B*, **103**, 1019.

51 Carter, E., Carley, A.F. and Murphy, D.M. (2007) *Journal of Physical Chemistry C*, **111**, 10630.

52 Labanowska, M. (2001) *Journal of Chemical Physics and Physical Chemistry*, **2**, 712.

53 Pietrzyk, P. and Sojka, Z. (2007) *Chemical Communications*, **1930**, 1930–1932.

54 Risse, T., Schmidt, J., Hamann, H. and Freund, H.-J. (2002) *Angewandte Chemie–International Edition*, **41**, 1517.

55 Schmidt, J., Risse, T., Hamann, H. and Freund, H.-J. (2002) *Journal of Chemical Physics*, **116**, 10861.

56 Neese, F. (2007) Quantum Chemical Approaches to Spin Hamiltonian Parameters, in *Electron Paramagnetic Resonance* (eds B.C. Gilbert, M.J. Davies and D.M. Murphy), Royal Society of Chemistry, Cambridge, **20**, p. 73.

2
The Application of UV-Visible-NIR Spectroscopy to Oxides

Gianmario Martra, Enrica Gianotti, and Salvatore Coluccia

Dedication

The extension of UV-Vis-NIR spectroscopy to the recognition of the excited states of highly dispersed oxide materials was a step of primary importance in establishing the determining role of the co-ordinative defects in both the optical properties and chemical reactivity of the surface of the "precursors" of presently fashionable nanomaterials. For this, credit goes to Professor Frank Stone, and we personally feel deeply indebted to him for his science and generosity in identifying new directions of true innovation upon which we have based our research work.

2.1 Introduction

UV-Vis-NIR spectroscopy involves the absorption or emission of electromagnetic radiation as a consequence of transitions among the energy states of outer shell electrons. The resulting spectral pattern is then a function of relevant physical-chemical features of the adsorbing/emitting systems, ranging from the oxidation state, local structure and composition of the coordination sphere of transition metal ion complexes to the band structure in solids. Such a dependence rendered this methodology attractive for the study of catalytic materials, since by the end of the 1950s it was becoming apparent that the purely physical description of electrons and holes as agents in heterogeneous catalysis was insufficient. A switch to a more localized model of the interaction between electrons related to surface species and adsorbates was required. Significant examples of the application to relevant problems, are the investigations carried out by Professor F. S. Stone at the beginning of the 1960s on the desorption of O_2 from NiO, monitored through the evolution of the d–d absorption bands due to surface Ni^{II} ions [1], and on the absorption spectra of Cu^{II} ions resulting from the dispersion of CuO in several oxide matrices [2]. As for emission spectra, some years later, Tench and Pott used a phosphorescence spectrometer to measure the photoemission related to surface

Metal Oxide Catalysis. Edited by S. David Jackson and Justin S. J. Hargreaves

ISBN: 978-3-527-31815-5

states in alkaline earth oxides [3]. Since that time, UV-Vis-NIR spectroscopy has been largely employed in the study of heterogeneous catalysts, and a number of reviews devoted to this topic have appeared. Most deal with absorption spectroscopy [4–9], photoluminescence spectroscopy [10–12] being considered less. On this basis, we have decided to detail the application of both aspects of UV-Vis-NIR spectroscopy to the study of oxide catalysts. The first part of the chapter is devoted to a summary of the nature of the different types of electronic transitions producing spectroscopic signals in the three ranges indicated, considering both the discrete energy levels in isolated or slightly clustered centers and the energy bands in systems with larger dimensionality. In all cases, the dependence of the spectral patterns on physical-chemical features of the absorbing/emitting centers has been highlighted. Applications are discussed in the second and third sections, dealing with absorption and emission electronic spectroscopy, respectively. A series of selected examples, representative of the different classes of oxide/oxide-based materials of interest in catalysis and of the structural and functional information that can be derived from their electronic spectra, have been highlighted. Technical and experimental aspects, in particular for absorption measurements, have been extensively treated in previous original work and reviews [13], so only a short summary of their fundamental insights has been presented here, and the interested reader is directed to the quoted literature.

2.2
Types of Electronic Transitions Producing UV-Vis-NIR Bands

The different types of outer shell electronic transitions that occur by absorption or emission of electromagnetic radiation in the UV, Visible and Near IR spectral regions are summarized in Figure 2.1. Since the electronic spectra can be plotted as a function of wavelength (nm), wavenumber (cm^{-1}) or energy (eV), the conversion factors between the various units are reported in Table 2.1.

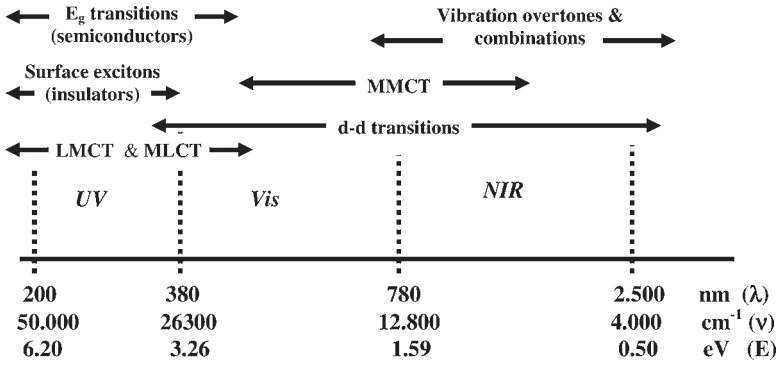

Figure 2.1 Different types of transitions in the UV-Vis-NIR range. Adapted from ref. [4].

Table 2.1 Conversion factors among wavelength λ (nm), wavenumber ν (cm^{-1}), energy E (eV).

	λ (nm)	**$\bar{\nu}$ (cm^{-1})**	**E (eV)**
λ (nm)	1	$(1/\lambda) \cdot 10^{-7}$	$1240/\lambda$
$\bar{\nu}$ (cm^{-1})	$(1/\bar{\nu}) \cdot 10^{7}$	1	$\bar{\nu}/8065.5$
E (eV)	1240/E	E · 8065.5	1

In the following, the main features related to the nature of each type of electronic transition and their dependence on the physical-chemical properties of the absorbing/emitting systems are presented.

2.2.1 Metal-Centered Transitions

d → d transitions occur among the electron energy levels in incompletely filled d^n subshells ($1 \leq n \leq 9$), and so are typical for transition metal ions (TMI). The number and relative position of such levels in TMI complexes (in solution, solid–liquid interfaces [14] or in solid frameworks) results from the splitting of the free ion terms by the ligand field, electron interactions (orbital, spin, spin–orbital angular momentum coupling), configuration interactions and the Jahn–Teller effect [15, 16]. These features in turn are controlled by the oxidation state of the metal ions, the number and kind of ligands and the geometry of their arrangement around the ions. Because all these dependences exist, the correct interpretation of a d–d spectrum can yield relevant information about the nature of metal ions and the composition and structure of the sites where they are hosted. In this respect, effective, quantitative support is provided by the use of Orgel diagrams (from the weak field method) and Tanabe–Sugano diagrams (from the strong field method) [15–18]. Both of these allow the calculation of the crystal field parameter Δ^0, which, for given oxidation states and symmetry of the environment, depends on the nature of the ligands, related to the spectrochemical series [15, 16]. In addition, from Tanabe–Sugano diagrams, the value of the Racah parameter, *B*, for complexed metal ions can be obtained. The ratio between *B* and the corresponding B_0 for free ions (available in the literature) results in the parameter $\beta = B/B_0$, which reflects the covalent character of the metal ion/ligand interaction, which has been arranged in the nephelauxetic series. It may be of interest to note that once the oxidation state and the symmetry are defined, Δ^0 and *B* values can also be derived by combining spectral data and qualitative d term energy levels reported in the literature, such as those depicted in Figure 2.2.

For instance, in the case of d^8 metal ions in a weak ligand environment with an octahedral (or quasi-octahedral, such as C_{2v}) symmetry, Δ^0 and *B* can be easily calculated on the basis of the position (e.g. in cm^{-1}) of ν_1 ($^3A_{2g} \rightarrow {}^3T_{2g}$), ν_2 [$^3A_{2g} \rightarrow {}^3T_{1g}(F)$] and ν_3 [$^3A_{2g} \rightarrow {}^3T_{1g}(P)$] absorption bands,

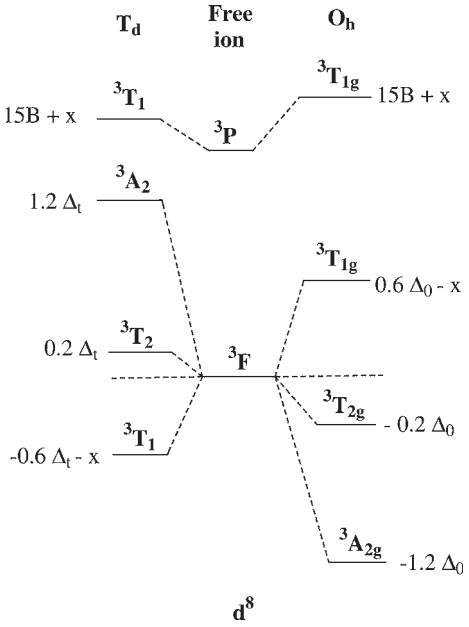

Figure 2.2 Weak field splitting scheme for maximum multiplicity terms of d^8 ions in tetrahedral (left side) and octahedral (right side) complexes. Adapted from ref. [17].

because the energy level scheme (right side) allows the determination of Δ^0 (= ν_1) and B (= $(\nu_2 + \nu_3 - 3\nu_1)/15$).

Normally, d–d transition bands are of weak intensity because they are forbidden by the Laporte (orbital) selection rule (allowed transitions: $\Delta l = \pm 1$; for systems with inversion center: g → u or u → g). However, transitions that are forbidden in octahedral symmetry may be partially allowed in the tetrahedral one, because of d–p mixing in the t_2^a orbital. Moreover, d–d transitions are subject to the spin-selection rule which requires that spin multiplicity of the levels involved be the same ($\Delta S = 0$). However, neither the orbital nor the spin selection rules hold very strictly, because of some relaxation afforded by vibronic coupling, spin–orbit coupling or exchange interaction (in the case of polymetallic systems). Connected with the relaxation of the Laporte rule by vibronic coupling is the phenomenon of "intensity stealing" which can occur when a forbidden and a fully allowed transition involve excited terms close enough in energy to allow a mixing of the electronic wavefunctions, via a vibrational mode of proper symmetry. This is the reason why certain d–d bands which lie close to charge-transfer (see below) bands exhibit abnormally high intensity. Representative values of the intensity of d–d bands in TMI complexes are listed in Table 2.2.

Finally, for the sake of completeness, it must be considered that metal ions of catalytic interest can exhibit absorption bands due to metal centered transitions of other types, as summarized in Table 2.3.

Table 2.2 Representative values for the intensities of d–d transitions in TMI complexes.

Type of d–d transition	Approximate ε
Spin-forbidden, Laporte forbidden	0.1
Spin-allowed, Laporte forbidden	10
Spin-allowed, Laporte forbidden, with d–p mixing (tetrahedral symmetry)	100
Spin-allowed, Laporte forbidden, but with "intensity stealing"	1000

Table 2.3 Types of metal-centered transitions other than d–d.

Type of transition	Comments	Type of ions of catalytic interest
f–f	Laporte forbidden; slightly sensitive to the surroundings; produce weak narrow bands	rare earth ions L^{3+} (e.g. Ce^{3+})
$(n-1)d \rightarrow ns$	Laporte forbidden; often too high in energy to produce bands below 200 nm	Cu^{+}, Ag^{+} (bands in the UV-Vis)
$(n-1)f \rightarrow nd$	Laporte allowed	Ce^{3+}, U^{4+}
$ns \rightarrow np$	Laporte allowed	Sn^{2+}, Sb^{3+}, Bi^{3+}

2.2.2 Charge-Transfer (CT) Transitions

The intense color shown by several inorganic complexes, such as d^0 systems (e.g. MnO_4^-) in which no d–d transitions can occur, is due to transition between electronic states where the electron moves from one group of atoms to another [19]. These charge-transfer (CT) transitions, which are Laporte allowed, produce very intense bands, when the $\Delta S = 0$ selection rule is obeyed, and are sensitive to the nature of both donor and acceptor atoms, to the local and general symmetry of the absorbing centers and to their bonding geometry.

The main features of CT transitions are illustrated in Figure 2.3. If the interaction between the orbitals ϕ_A and ϕ_B (orbitals located on a single atom or groups of atoms) is small, the new orbital ϕ_C is composed mainly of ϕ_B, and ϕ_D is composed mainly of ϕ_A. In the case of MnO_4^-, the lower energy orbital ϕ_B is located on the oxygen ligands and ϕ_A is a metal d orbital. The transition $\phi_C \rightarrow \phi_D$, called a ligand to metal charge-transfer transition (LMCT), produces a decrease by 1 in the metal oxidation state. In other systems, for instance metal carbonyls, where there are high-lying empty ligand orbitals, ϕ_B may be a metal d orbital and ϕ_A a ligand orbital. In this case, a metal to ligand charge-transfer transition (MLCT) occurs and produces an increase by 1 in the metal oxidation state. In fact, the charge transfer is

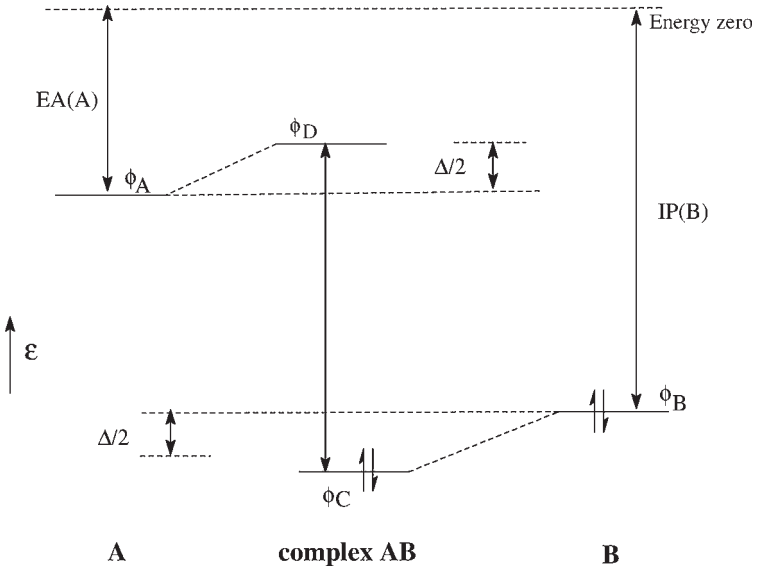

Figure 2.3 Schematic representation of CT transitions. EA(A) = electron affinity of species A; IP(B) = ionization potential of species B; Δ = stabilization energy of AB. Adapted from ref. [19].

never complete and all electronic transitions involve a certain amount of electron redistribution in the excited state compared with the ground state.

LMCT and MLCT transitions depend on the symmetry, on the oxidation state of the metal and on the nature of the ligand or of the other metal atoms. In particular, the energy of CT transitions increases with the optical electronegativity difference between the metal and the ligand [20–22].

Optical electronegativity values (χ_{opt}) are assigned to elements in a given oxidation state and Pauling electronegativity values for halide ions are used as references. The wavenumber of the first CT absorption band is expressed as [23, 24]

$$\chi(\mathrm{cm}^{-1}) = 30000[\chi_{opt}(\text{ligand}) - \chi_{opt}(\text{metal})] \tag{2.1}$$

CT transitions can involve metal ions in all electronic configurations, and then, as in the case of TMIs, are also responsible for optical bands for systems containing d^0 or d^{10} TMIs, that, conversely, do not produce d–d absorption.

Intra-valence, or metal to metal, CT transitions can also occur within systems containing ions of different oxidation state, as $Fe^{2+} \rightarrow Fe^{3+}$ in Fe_3O_4 or $Fe^{2+} \rightarrow Ti^{4+}$ in sapphire [4].

2.2.3
Transitions between Electron Energy Bands in Solids

The assembly of atoms into an array to form a solid leads to the formation of bands of allowed states separated by an energy gap. This results from the fact that when

similar "building blocks" (atoms, unit cells) approach each other the wavefunctions of their electrons start to overlap and, as a consequence of Pauli's exclusion principle, the energy states of all spin-paired electrons shared to form bonds are slightly shifted from the original values when the building blocks are isolated. For instance, by packing N building blocks the $2N$ electrons originally occupying the same orbital must be spread over $2N$ different states, forming a band instead of discrete levels. The distribution of the states so formed depends on the actual distance of the building blocks in the solids, leading to the appearance of a gap in the energy band (E_g). The lower band, which can contain as many states as electrons, and hence be completely filled, is the valence band. The upper band, which may contain no electrons at all or fewer electrons than states, is the conduction band. The extent of the energy gap and the relative electron population determines whether a solid is a metal, a semiconductor or an insulator. This last kind of material has an E_g larger than 3 eV and a negligible concentration of electrons in the upper band (and practically no holes in the lower band). Semiconductors, however, usually exhibit an E_g lower than 3 eV and a density of electrons in the upper band (or holes in the lower band) lower than $10^{20}\,cm^{-3}$. Promotion of electrons from the valence to the conduction band (or to states localized in the gap) can occur by absorption of energy from electromagnetic radiation, thus generating optical transitions. Finally, in metals, the conduction band is populated by electrons, with a concentration of the order of $10^{23}\,cm^{-3}$.

A second fundamental aspect to be considered in relation to optical transitions in solids, is that electron states, other than definite energy assignments, are also characterized by a distribution in the momentum space, related to the movement (i.e. to the kinetic energy) of electrons in the solid. For the sake of pictorial simplicity, bidimensional models of crystals, conceived as a square well potential, are usually employed in this respect, portraying the "parabolic valley" dependence (in one direction) of energy from the "momentum vector" **k**, as schematized in Figure 2.4A. The significance of the downward curvature of the valence band is that if electrons could have a net motion in such a band (i.e. if it were not completely filled), they would be accelerated in the opposite direction with respect to those in the conduction band.

It is important to note that in solids distances between nearest atoms can vary in different directions, and hence the minimum of the valley may not occur at $k_x = k_y = k_z = 0$, but at some point defining a specific direction, as shown in Figure 2.4B for a crystalline solid. In an optical transition, both energy and momentum must be conserved. Because the momentum of a photon, h/λ (λ is the wavelength of light which is typically thousands of ångströms), is very small compared to the crystal momentum h/a (a is the lattice constant, typically a few Ångströms), the photon-absorption process should conserve the electron momentum.

Thus, the absorption coefficient $\alpha(h\nu)$ for a given photon energy $h\nu$ is proportional to the probability, P_{if}, for the transition from the initial state to the final state (governed also by the conservation of momentum), the density of electrons in the initial state, n_i, and also the density of electrons in the final states, n_f. This process must be summed for all possible transitions between states separated by an energy difference equal to $h\nu$:

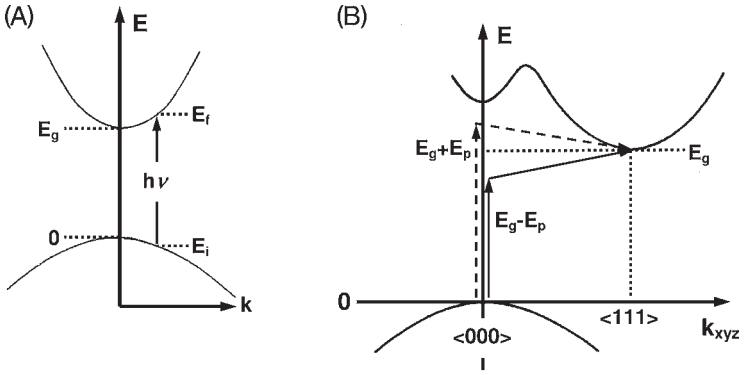

Figure 2.4 Energy versus momentum and possible interband transitions in: (A) a direct-gap two-band system and (B) a solid with conduction band valleys at k = <000> and k = <111>. Adapted from ref. [26].

$$\alpha(h\nu) = A\sum P_{if} n_i n_f \tag{2.2}$$

Depending upon the relationship between the momentum in the initial and final states (which, in turn, depend on the profile of the "parabolic energy valley") direct or indirect transitions can occur, as shown in Figure 2.4, and this affects all the three terms P_{if}, n_i and n_f. It must be noted that in transitions between indirect valleys (Figure 2.4B) momentum is conserved via interaction with a phonon (i.e. a quantum lattice vibration), which can be either emitted or adsorbed. Some additional detail on such transitions will be given in the section dealing with semiconductor oxides.

By using the parabolic valley model, an expression of $\alpha(h\nu)$ for each type of transition (allowed or forbidden in dependence on selection rules) has been obtained [25–27]. As a common feature, for crystalline solids, $\alpha(h\nu)$ appeared expressed in all cases in the form:

$$\alpha(h\nu) = B(h\nu - E_g)^n \tag{2.3}$$

where B contains the dependence on P_{if}, n_i and n_f specific for each type of transition (that essentially rules the transition edge width), E_g is the interband energy gap and n can take values 1/2, 3/2, 2, 3 for direct allowed, direct forbidden, indirect allowed and indirect forbidden transitions, respectively. The value $n = 2$ holds for amorphous materials also, irrespective of the type of transition found in corresponding crystalline materials. Actually, the momentum vector is not conserved in amorphous phases, and to obtain $\alpha(h\nu)$ an integration over the density of states must be made, as in the case of indirect transitions in crystalline systems.

A plot of $[\alpha(h\nu)]^{-n}$ against $E(h\nu)$ (values of the energy range the absorption edge is spread over) should then result in a linear relationship, the intercept with the

$E(h\nu)$ axis being E_g. Examples of the use of this relation will be provided in the section devoted to semiconductor oxides.

As a third point, it must be considered that when an electron is raised to the conduction band, it leaves behind an unoccupied state (a positive hole) in the valence band. Thus the excited electron moves in the field of this positively charged hole, and an e^-/h^+ pair forms which is called an exciton. A detailed discussion of such kinds of states has been the subject of the work of Knox [28]. The binding energy of such a couple slightly decreases the amount of energy required to cause an excitonic transition with respect to a true valence to conduction one, where the excited electron and the corresponding hole are free to move independently in the solids. Hence, excitons generate electron states within the interband energy gap of a solid. The binding energy of excitons depends on the effective e^- and h^+ masses and the dielectric constant of the solid. In semiconductors, such a dependence results in very small binding energy, of the order of 0.01 eV. In solids of such type, excitons exist in principle but will be completely ionized, the corresponding optical transitions vanishing in the edge-shaped E_g absorption. In a typical insulator, on the other hand, effective masses are larger and the dielectric constant is significantly smaller than in semiconductors. Ionized excitons cannot exist at room temperature (or at higher temperatures), generating discrete bands at energy below the E_g edge absorption. Examples will be reported in the section devoted to insulating oxides.

2.3
UV-Vis-NIR Absorption Spectroscopy

2.3.1
Theory of Diffuse Reflectance (DR) Spectroscopy

In the case of powdered catalysts, incident light is almost completely diffused and it is necessary to use Diffuse Reflectance (DR) instead of transmission spectroscopy. Mie theory can be applied to describe a single scattering of light which occurs when light interacts with isotropic and non-interacting small particles. This theory is not suitable for describing the optical properties of powders in which multiple scattering occurs. In this case, it is necessary to use a phenomenological theory that considers the absorbance and scattering coefficients. The Schuster–Kubelka–Munk (SKM) model is widely accepted to describe matt surfaces [29]. The reflectance of a solid includes specular reflectance and diffuse reflectance. This latter, characterized by an angular distribution independent of the incident angle, prevails in the case of powdered solids. Accordingly to the SKM approximation, the diffuse reflectance of a layer of infinite thickness R_∞ is linked to the absorption K and the scattering S coefficients by the expression:

$$K/S = F(R_\infty) = (1 - R_\infty)^2/(2R_\infty) \tag{2.4}$$

$F(R_\infty)$ is the remission, or SKM, function [29].

The reflectance depends upon the K/S ratio and not on the absolute values of K and S. The scattering S coefficient is independent from the wavelength over wide spectral ranges and therefore the SKM function reflects the trend of the absorption K coefficient. Moreover, because SKM is a function of $\alpha(h\nu)$, a plot of $(F(R_\infty)\ h\nu)^{1/n}$ against $h\nu$ can be used to determine E_g in powdered semiconductor oxides.

The SKM theory has some limitations and can be applied only when the following experimental conditions are fulfilled:

i) The incident radiation is monochromatic and completely diffused. The latter condition can be obtained using samples with a high diffusion and low absorption.
ii) The layer is of infinite thickness (generally obtained with a layer depth of 1–2 mm), to avoid loss of radiation by transmission.
iii) The absorption intensity is quite weak [$F(R_\infty) \leq 1$].
iv) Photoluminescence is absent.

Moreover, diffuse reflectance depends on the particle sizes (d). When the particle size decreases, the S coefficient increases since $S \propto 1/d$ (for $d \geq 1\,\mu m$) and this results in an increase of reflectance. It is worth noting that in the case of thin films (layers), the UV absorption spectra are complicated by the superposition of interference effects. The interference oscillations facilitate the semiquantitative determination of the layer thickness (δ), although they prevent the accurate determination of the film absorption spectrum. In addition, a further uncertainty arises from specular and diffuse reflectance by the film. It is possible to solve both problems by measuring the transmittance (T) and reflectance (R) of the light in all directions using the integrating sphere. The fraction of the truly absorbed light is $(1 - R - T)$ and the plot of $-\ln(R + T)$ against λ gives a spectrum in the scale of optical densities. Since the reflected and transmitted beams are phase shifted by $n\delta$ (n is the refractive index), this type of plot is, moreover, smoothed by compensation of the interference effects [30].

Finally, it must be noted that an interesting consequence of the Kubelka–Munk (KM) equation is that DR spectroscopy has excellent properties for the analysis of trace quantities of absorbing centers dispersed in non-absorbing matrices. As shown in the following equation:

$$(1 - R_\infty)^2/(2R_\infty) = K/S = (\ln 10)ac/S \tag{2.5}$$

where c is the concentration of the absorbing species and a is the (base 10) absorptivity, the signal in a DR measurement is given by the difference between the reflectance of the reference and the reflectance of the sample, that is, $(1 - R_\infty)$. For trace amounts of the analyte, the denominator in the KM function ($2R_\infty$) is approximately equal to 2 and does not vary greatly when the concentration of the analyte is changed, provided that ac/S is small. As $(1 - R_\infty)^2$ is proportional to c, the signal $(1 - R_\infty)$ is proportional to $c^{1/2}$. The noise across a reflectance spectrum is approximately constant. Thus, provided that R_∞ is less than about 0.9, the signal-to-noise

ratio (S/N) is proportional to $c^{1/2}$. A reduction in concentration of the absorbing species by a factor of 100, therefore, only leads to a reduction in S/N by a factor of 10. The downside of this effect is that small impurities present in the catalyst (e.g. in the support) can often lead to quite intense bands in the reflectance spectrum.

2.3.2
General Remarks on Methodologies for DR UV-Vis-NIR Measurements

As indicated in the Introduction, considerations related to the instruments, attachments, cells and experimental setup have been extensively reported, so only a few fundamental points will be considered here. In the DR UV-Vis experiments, the light scattered by the solid sample and by the reference is recorded by an integrating sphere coated with a white standard showing a high diffuse reflectance, such as MgO, $BaSO_4$ and more recently polytetrafluoroethylene (PTFE). Experimental details of this attachment and cells that can be used for the measurements have been reported in several articles [4, 9, 13, 31]. By using an appropriate system, *in situ* measurements on catalysts treated following specific protocols and kept in controlled atmosphere are possible; and it may be of interest to report that kinetic aspects of the catalyst activation or of catalyzed reactions can be evaluated (see, for example, refs. [32, 33], respectively). Recently, great effort has been applied to develop *operando* techniques which refer to the spectroscopy of a working catalyst in combination with on-line activity measurements [34–35].

2.3.3
UV Absorption Bands of Insulating Oxides: Excitonic Surface States

Insulators such as alumina, silica and alkaline earth oxides (AEO) employed as catalyst supports or as catalysts have been studied by UV-Vis spectroscopy since the beginning of the application of optical methods to the investigation of finely divided materials. The basic feature to be considered is that the band gap of these oxides is so wide that electron transitions from the valence to the conduction band can be promoted only by electromagnetic radiation in the far/vacuum UV range ($\lambda < 192\,nm$; $\nu > 52\,000\,cm^{-1}$), requiring special equipment. Nevertheless, optical absorptions involving energy states within the main gap produce optical absorption in the near-UV, and these can be observed using conventional spectrophotometers (equipped with an integrating sphere, see above). Among such states are those related the surface, which can be due to the saturation of surface valence states with —OH groups, the presence of supported species (e.g. TMIs) or coordinative unsaturation (typically appearing after dehydration). As for surface hydroxyls, their electronic excitation by laser irradiation at 514.5 nm was found to be responsible for the so called "fluorescence" background of η-Al_2O_3 and MgO, which strongly affects the ability to measure laser Raman spectra of species adsorbed on these oxides [36]. Surface states related to the presence of supported species produce optical absorptions that can be interpreted indepen-

dently of the band state model of the support, and these will be considered in the following sections. Conversely, near-UV-Vis spectroscopy can be considered a useful tool to obtain specific, and in some cases unique, insights on electronic surface states related to unsaturated sites exposed by insulating oxide-based materials. UV bands at 240 and 320 nm were observed for a series of zeolites (faujasite, mordenite, ZSM-5, erionite, offretite). The first band was related to framework Al-O units easily removable by dealumination and dehydroxylation, while the second one was attributed to transitions occurring in an oxoaluminum structure inside the zeolite matrix [37]. Optical absorption of silica materials has been thoroughly investigated by physicists [38], and their results were useful for the assignment of near-UV bands exhibited by silicas (not structured sol–gel derived and mesoporous FMS-16 and MCM-41) outgassed at $T > 673$ K to surface $\equiv SiO^{\cdot}$ and $\equiv Si^{\cdot}$ defects sites, produced by dehydroxylation, responsible for the activity in photometathesis of propene [39]. However, the overwhelming part of the investigation carried out on the electronic surface states of insulating oxides has been focused on AEOs, which is still an area of direct interest in base catalysis [40]. In addition, AEOs are regarded as useful model systems for a number of reasons:

i) Most of them can be obtained in the form of highly dispersed nanocrystalline powders, with specific surface area ranging from ca. 200 to 10 $m^2 g^{-1}$.
ii) They have a simple crystalline structure (rock salt, based upon interpenetrating face centered cubic sub-lattices).
iii) {001} cube faces are predominant in the nanocrystals, as evidenced by transmission electron microscopy, allowing even highly rough AEO surfaces to be described as resulting from the intersection of {001} microfaces [41, 42].

Nelson and Hale [43] published the first DR spectra of AEO powders. They showed that highly dispersed systems have UV optical absorption bands that are not present in the spectra of pure single crystals, which are conversely characterized by an extremely low specific surface area, and hence an almost negligible contribution from surface states. Additional evidence was obtained in the following years [44, 45], and a comprehensive analysis of such bands has been reported by Garrone et al. [46]. The results of this work are an effective example of the wide set of fundamental information which can be derived from the spectroscopic data on the nature of optical transitions, structure and reactivity (and their inter-relationships) of surface sites.

Figure 2.5 summarizes the DR UV spectra of well outgassed samples of MgO, CaO, SrO and BaO powders considered by those authors. Owing to bulk excitonic transitions, the edges are clearly visible in the case of SrO and BaO, while for MgO and CaO they lie beyond the near-UV range (in the dotted part of the spectra). In the spectrum of each oxide some absorptions at frequencies below that edge are present, which are assigned to excitonic transitions involving surface sites (and expected to produce discrete absorptions). Considering SrO first, this latter part of the spectrum is constituted by two absorptions of comparable intensity (I, II)

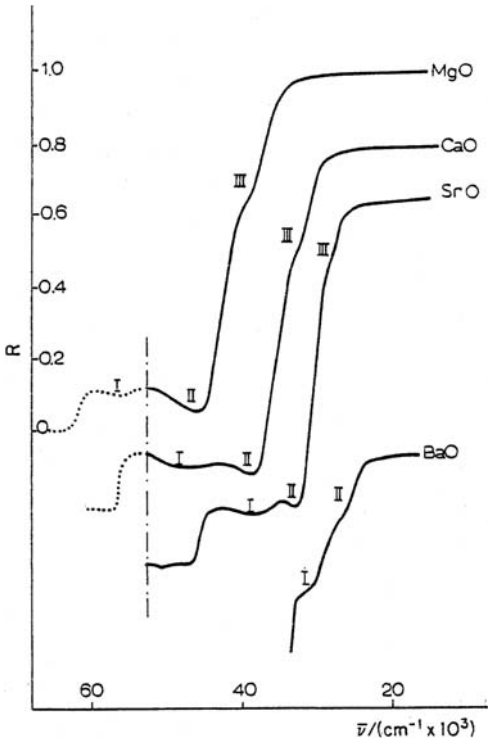

Figure 2.5 Diffuse reflectance spectra of polycrystalline AEO outgassed at 1073 K. Spectra of MgO, CaO and SrO were recorded in the presence of ~10^2 Pa of non-reactive gas (e.g. O_2) to quench possible fluorescence emission. The *R* scale is displaced vertically to avoid overlapping of spectra. The dotted portions of the MgO and CaO spectra at $\nu = 52\,000\,cm^{-1}$ (the vacuum UV) are extrapolations. Reprinted from ref. [46] with permission from Francis & Taylor Ltd.

and a weak shoulder (III), and a similar pattern is exhibited by the spectrum of CaO (edge beyond the instrumental limit). In the case of MgO, where the edge is known to lie at even higher energies, only one band (II) and a weak shoulder (III) are present below $52\,000\,cm^{-1}$, although a spectral inflection near the limit suggests the presence of another band (I) just above that position. The intensity of absorptions labeled as II and III is a function of the specific surface area of the powders used, decreasing in the order MgO ($210\,m^2\,g^{-1}$) > CaO ($110\,m^2\,g^{-1}$) > SrO ($6\,m^2\,g^{-1}$). For such a reason, in the spectrum of BaO ($<1\,m^2\,g^{-1}$) bands due to surface states appear only as shoulders.

Absorptions related to surface states must be affected by interaction with adsorbates, and a typical example of the evolution in such a process of near UV bands of AEO is reported in Figure 2.6, where the spectral patterns obtained by contacting MgO with water vapor are shown. The solid line is the spectrum of the sample

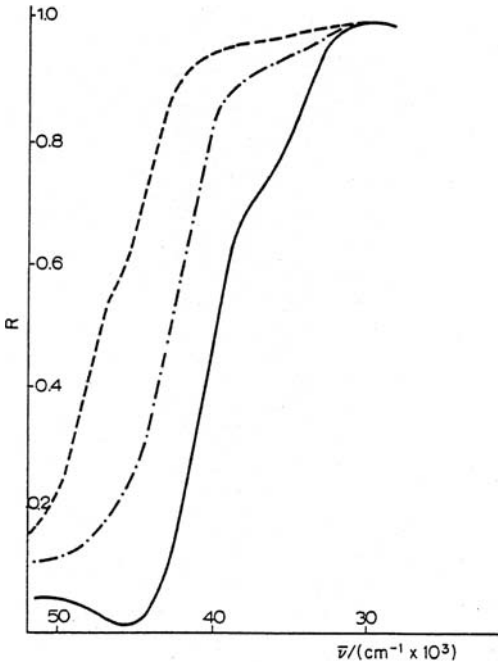

Figure 2.6 The effect of H_2O vapor adsorption at 293 K on the diffuse reflectance spectrum of polycrystalline MgO initially outgassed at 1073 K: (a) original spectrum, (b) after adsorption of a first sub-monolayer dose of H_2O, (c) after adsorption of a second dose. Reprinted from ref. [46] with permission from Francis & Taylor Ltd.

outgassed at 1073 K, while the other two curves are spectra recorded after contact with increasing small doses of H_2O vapor (with coverages lower than monolayer). The main feature to be noticed is that the low-frequency shoulder is eroded preferentially. In addition, as the chemical attack progresses, the band at 46 000 cm^{-1} is depleted and the low-energy tail of another band can be now observed, supporting the hypothesis of the presence of an absorption just above the instrumental limit.

The increase of the sensitivity towards surface reactions along the band series III > II > I (when observed) accounts well for the involvement in such absorptions of surface ions with coordination number decreasing in the same order III < II < I. As indicated above, AEOs have the rock salt structure, with both cations and anions octahedrally six-coordinated in the bulk. Their surface morphology results from the intersection of nano {001} planes, which leads to the exposure of five- (5C), four- (4C) and three- (3C) coordinated ions of facelets, edges and corners respectively. A general consensus has been reached that such sites are responsible for the optical transitions resulting in bands I, II and III, respectively. On this basis, the trend in the intensities of such bands for each AEO (Figure 2.5) can also

be rationalized, with sites in corner positions being definitely less abundant than those on edges, which are in turn much less numerous that those on faces. In addition, this assignment accounts well for the changes in relative intensity of the three bands in dependence on the specific surface area of the material also, the sensitivity of the relative amount of surface sites to this parameter following the scale 3C ≫ 4C ≫ 5C. On such a basis, the relative intensity of near-UV bands in the spectra of a series of powder samples of an AEO differing in surface morphology can be coupled with reactivity data to elucidate the possible structure sensitivity of a catalytic process occurring at its surface [47].

Besides being a probe of the presence of sites in different coordination states and of their different reactivity, near-UV excitonic bands of insulating oxides can be further analyzed to obtain insights into the electronic features of surface sites responsible for such transitions, and the reasons for the peculiar reactivity related to a type of surface site/structure. To achieve this, it must be recalled that the main model for the quantitative prediction of the energies of surface states of highly ionic solids has been developed by Levine and Mark [48], where the exciton gap for surface ions, E_s, is expressed as:

$$E_s = A - I + 2V_s \tag{2.6}$$

where A (the electron affinity of the anion) and I (the ionization energy of the cation) are assumed to be the same as for ions in the bulk, and V_s is the Madelung potential for surface ions, which (neglecting the sign) is given by

$$V_s = z\alpha_s e^2/a \tag{2.7}$$

where z is the charge of the ions, α_s the surface Madelung constant and a the anion–cation distance.

Equivalent relations can be derived for excitonic bulk transitions, by considering the bulk Madelung potential. Independently of the type of material, which determines the values of A, I and a, the dependence of E_s on α_s should be similar, so a plot of E_s against $1/a$ for isostructural ionic materials should be a family of curves with no tendency to intersect. However, this is not the case when the values of the excitonic absorptions of AEO are considered, including those due to bulk excitons (Figure 2.7). The rationalization of such behavior has been provided by assuming that A and I depend not only on the material but also on the co-ordinative state of the ions. In chemical terms, this means that the ionicity of the surface has to vary according to different coordination situations; in particular, ionicity decreases as the ion coordination decreases. Departure from ideal ionicity is then least for sites responsible for excitonic band I, for which a 5C surface configuration is proposed, and greatest for those responsible for excitonic band III, that contains 3C ions.

Ions exposed at the surface in different co-ordinative states are then characterized by different electronic features, which, in the case of oxygen anions of an AEO, result in an increase of their nucleophilic character so relevant to the appearance of the strong basic reactivity typical of these oxides.

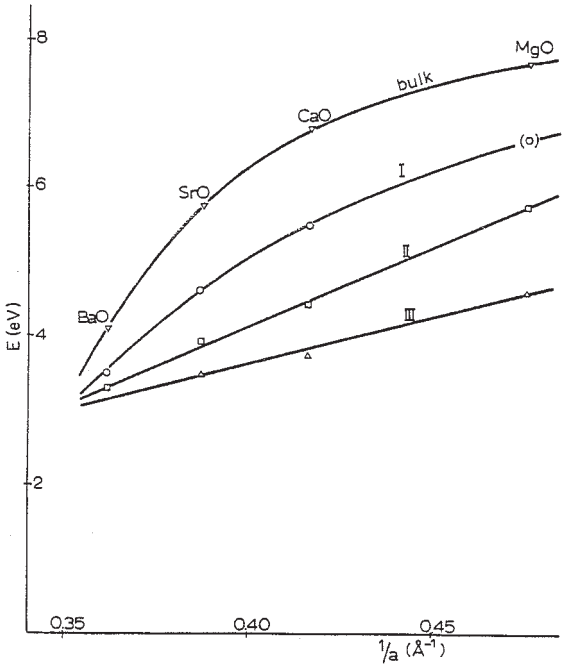

Figure 2.7 Energies and surface transition versus the reciprocal of the anion-cation distance. Reprinted from ref. [46] with permission from Francis & Taylor Ltd.

2.3.4
UV Absorption Bands of Semiconductor Oxides

Many oxides employed as catalysts/photocatalysts, supports for catalysts or, vice versa, supported catalysts, such as SnO, ZnO, Fe_2O_3, TiO_2, ZrO_2, CeO_2, V_2O_5, Nb_2O_5 and WO_3, are semiconductors, and their absorption edge due to the inter-band electron transition fall in the near UV-Vis range. As reported in Section 2.3, in semiconductors excitons undergo ionization, so the optical behavior of these solids is dominated by the fundamental adsorption edge, which, by using the appropriate equation, can be used to determine the E_g of the material.

Among the various possibilities, it is worth noting that in semiconductor oxides where the fundamental absorption edge is due to allowed transitions between indirect valleys (see Figure 2.4B), such as TiO_2 [49, 50], WO_3 [51] and MoO_3 [52], the absorption of photons can occur by coupling with the absorption or emission of a phonon.

Hence, two adsorption coefficients must be considered [53], one (α_a) for the process with phonon absorption:

$$\alpha_a(h\nu) = A(h\nu - E_g + E_p)^2[\exp(E_p/kT) - 1]^{-1} \tag{2.8}$$

and a second one (α_e) for the process with phonon emission:

$$\alpha_e(h\nu) = A(h\nu - E_g - E_p)^2[1 - \exp(-E_p/kT)]^{-1} \quad (2.9)$$

where E_g and E_p are the energy and phonon energy, respectively, and the terms in square brackets contain the dependence on the number of phonons of energy E_p.

Since both phonon and emission absorption are possible when $h\nu > E_g + E_p$, the absorption coefficient is then

$$\alpha(h\nu) = \alpha_a(h\nu) + \alpha_e(h\nu) \quad (2.10)$$

which results in the type of dependence of $\alpha^{1/2}$ on $h\nu$ displayed in Figure 2.8A, from which the value of E_g can be easily obtained. It is worth drawing attention to the fact that that $\alpha_a(h\nu)$ and $\alpha_e(h\nu)$ exhibit a different dependence on the temperature also, as when T is very low (as T_1 in Figure 2.8A), the phonon density is very small (large denominator in Equation 2.11), and therefore $\alpha_a(h\nu)$ is very small. Turning to experimental data, a similar trend in the dependence of α on $h\nu$ has been obtained by Serpone and coworkers [54] in analyzing the spectra of colloidal TiO_2 particles (Figure 2.8B).

For each type/family of semiconductor oxide the value of E_g is related to significant dimensional, structural and/or functional properties, and so the features of the optical absorption edge is a source of relevant insight into such materials.

As for the functional properties directly dependent on the optical absorption edge, a special place is held by the photocatalytic behavior of titania [49, 50]. In this respect, the determination of E_g of TiO_2 materials by electronic spectroscopy data is of great interest. This allows assessment of the effectiveness of treatment/preparation methods intended to decrease the wide E_g (3.2 eV for the anatase form, usually the most active photocatalytically). This is of interest in the quest for visible

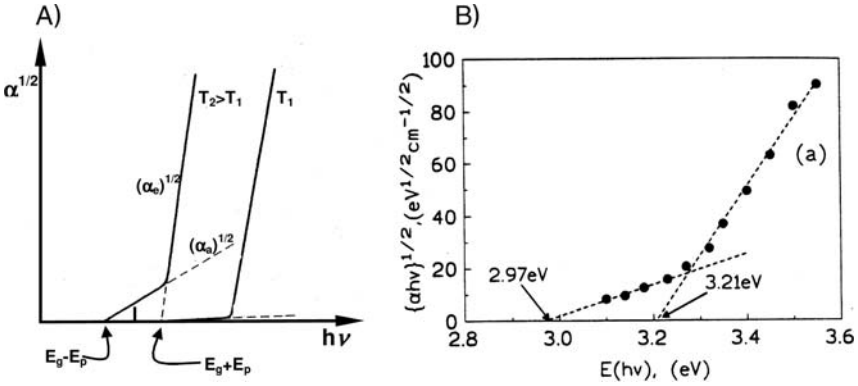

Figure 2.8 Plot of α^{-1} against $E(h\nu)$: panel (A) as from equations and panel (B) for TiO_2 colloidal particles (three samples: 2.1, 13.3 or 26.7 nm) suspended in an aqueous medium (15 g L^{-1}). Panel (A): adapted from ref [26]; panel (B): reprinted with permission from ref. [54]. Copyright 1995 American Chemical Society.

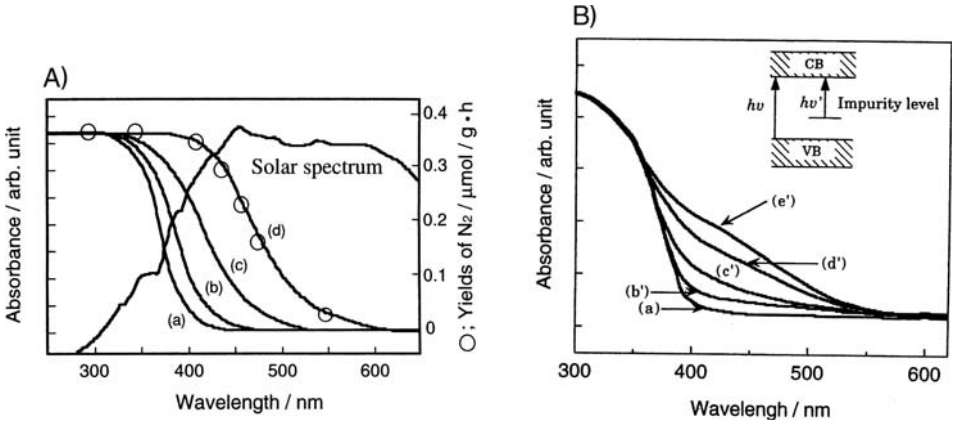

Figure 2.9 DR UV-Vis spectra of TiO_2 doped with Cr ions with different methods. Panel A: (a) unimplanted pure TiO_2, (b)–(d) TiO_2 implanted with increasing amounts of Cr ions: 2.2, 6.6 and 13×10^{-7} mol Cr/g TiO_2 respectively. Open circles are the action spectrum of the material (d) for the photocatalytic decomposition reaction of NO. Panel B: (a) undoped TiO_2, (b′)–(d′) TiO_2 chemically doped with increasing amounts of Cr ions: 1.6, 20, 100, 200×10^{-6} mol Cr/g TiO_2, respectively. Reprinted from ref. [11] with permission from Elsevier.

light-driven photocatalysts, since the UV light required for the parent oxides is only ca. 5% of ground-level solar radiation (the most desirable irradiation source). Significant results have been obtained in the development of the so-called "second generation" TiO_2 photocatalysts [55] obtained by implantation of TMIs, resulting in an actual red-shift of the transition edge (Figure 2.9A), instead of the appearance of new spectral components assignable to transitions involving localized states (Figure 2.9B). Band gap narrowing has been also obtained by using another physical method, radio-frequency magnetron sputtering, to prepare TiO_2 in the form of thin films [55]. Another important possibility for narrowing the TiO_2 band gap is offered by the preparation of TiO_2 materials doped with non-metal impurities, also introduced by using more conventional preparation methods (e.g. sol–gel). In recent years this area has been the object of intense research activity (e.g. N and C doping, see ref. [56]).

Turning to the dependence of E_g on dimensional properties, particle size (<100 nm) can have an effect on the spectral properties of semiconductors when it becomes comparable with the size of the exciton. This gives rise to the so-called Q-size effect (explained in chemical valence terminology in ref. [57]) which, with constant bonding geometry, results in a blue-shift of the absorption edge [58]. Equations relating the band gap shift ΔE_g (measured spectroscopically) to dimensional parameters have been established [57], and a relationship between the particle size estimated in this way and that obtained by other methods, typically TEM, was found (see, for example, ref. [30]). This relationship notwithstanding, in some cases other effects can be responsible for the adsorption edge blue-shift. For instance, the spectroscopic behavior exhibited by TiO_2 particles with decreas-

ing particle size upon anaerobic illumination has been alternatively interpreted on the basis of the Burstein–Moss effect [59], which is a consequence of the fact that the Fermi level of electrons in particles is a function of the irradiation intensity. However, at spectrophotometric light intensities normally used to record absorption spectra, the Burstein–Moss effect should be of little consequence.

In the field of oxide catalysts, besides the case of the optical behavior of nanometric powders of TiO_2 (see ref. [54] and references therein), a typical manifestation of the Q-size effect is the blue-shift of the absorption edge exhibited by very small three-dimensional particles formed by increasing the loading when semiconductor oxides (e.g. V_2O_5, MoO_3, WO_3, Fe_2O_3) dispersed on a support (SiO_2, TiO_2, ZrO_2, Al_2O_3) are prepared.

Higher levels of dispersion (usually obtained at lower loadings) result in the formation of bidimensional patches and monodimensional ribbons of MO_x (M = metal) species, which can be recognized on the basis of a third feature of E_g, that is, its sensitivity to bonding geometry/structure of semiconductor species. A systematic experimental and theoretical study on polyoxometallates [60, 61] demonstrates that the fundamental optical absorption strongly relates to the number of nearest MO_x polyhedral neighbors and the number of bonds between each of those neighbors (corner- or edge-shared polyhedra). For instance, a larger fraction of edge-sharing polyhedra relative to corner-sharing ones should result in a greater molecular orbital overlap between such units, and thus a smaller E_g because of the more extensive sharing of electron density between polyhedra. Conversely, the local symmetry around M^{n+} centers in polymeric structures and the metal–oxygen bond lengths were found to have less influence. On this basis, and by considering appropriate reference materials (another key point in the elucidation of structure/optical feature relationships [60]), the determination of E_g values from the optical absorption edges can trace the evolution of the structure of supported species as a function of loading. Furthermore, the trend obtained can be combined with that exhibited by some functional aspect of interest, to elucidate structure/function relationships, as performed in the case of WO_x/ZrO_2 (Figure 2.10) [62, 63] and VO_x/ox (ox = SiO_2, ZrO_2, Al_2O_3) catalysts [64].

The validity of the approach based on the evaluation of E_g from spectroscopic data disappears as the size of such MO_x decreases towards the limit of isolated species, as bands of energy are turned into discrete energy levels. Hence, the optical behavior can be described in terms of localized charge-transfer transitions involving molecular orbitals. This will be the subject of the next section.

2.3.5
Highly Dispersed Supported Oxo-Species and TMI

2.3.5.1 LMCT Transition Bands as Source of Structural Insight

Highly dispersed surface species, with the limiting form of single-site active centers, play a primary role in a number of catalytic materials because of their peculiar features in terms of activity and selectivity. Both oxo-species and transition metal ions supported on oxides (or in zeotype materials) belonging to these types

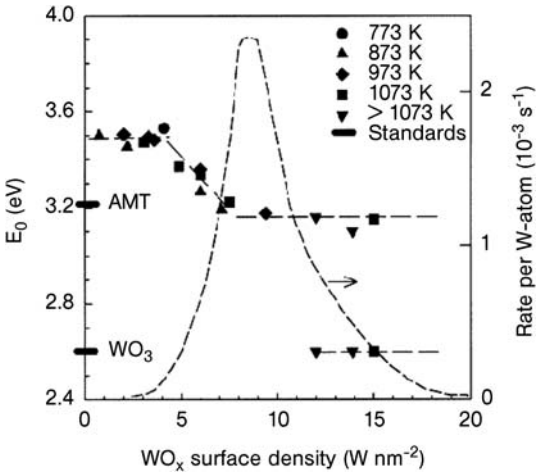

Figure 2.10 Indirect absorption edge energies of WO_x-ZrO_2 samples at several oxidation temperatures and W loadings. Two crystalline W oxide materials (monoclinic WO_3 and ammonium metatungstate) are shown for reference. Dashed curve is a summary of *o*-xylene isomerization rates per W atom (523 K, 0.66 kPa *o*-xylene, 100 kPa H_2). Reprinted with permission from ref. [62]; Copyright 1999 American Chemical Society.

of species can be effectively investigated through their ligand to metal charge-transfer absorptions falling in the UV-Vis range. The main features related to the nature of such transitions have been reported in Section 2.2, while this part will be devoted to examples showing how structural insights into supported species can be provided by the analysis of the features of LMCT bands. Some information arises from the sensitivity of LMCT to the number of ligands surrounding the metal ions, resulting in a decrease of the transition energy as the coordination number increases. A typical example is depicted in Figure 2.11, dealing with the evolution of the local structure of isolated V^{5+} oxo-complexes grafted on the inner walls of a MCM-48 silica support as a function of the hydration level [65].

For each type of coordination number, the position of LMCT bands are sensitive to the presence of M^{n+}—O—M^{n+} linkages. This is found, for example, for species ranging from supported chromates to dichromates and polychromates [66, 67], and for isolated or polymeric VO_4 tetrahedra present in Na_3VO_4 and NH_4VO_3, respectively, which are considered as reference compounds for the interpretation of the spectra of supported V^{5+} species [68].

As a further aspect, it must be considered that in the context of a type of structure, differences in shape and positions of LMCT bands can monitor the occurrence of peculiar local geometries or distortions. Such spectral features can usually be analyzed in more detail, with a consequent higher information output, in the case of catalysts with active centers that are quite homogeneous in structure and with simpler spectra, as more commonly occurs in the case of highly isolated species. These are the conditions for the observation of spectral behavior that can be rationalized in terms of differences in the bond angles connecting the metal

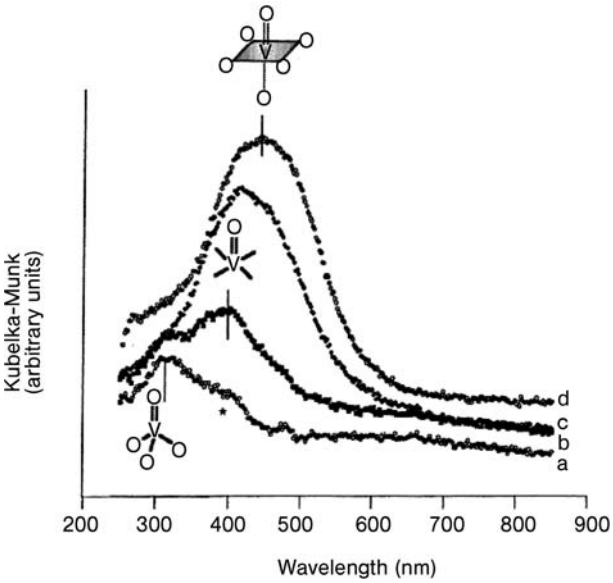

Figure 2.11 Evolution of DR UV-Vis spectra as a function of hydration time (under ambient conditions) for a VO_x/MCM-48 catalyst (V/Si = 0.05): (a) time 0, (b) 10 min, (c) 30 min, (d) 2 h. Reprinted with permission from ref. [65]; Copyright 1996 American Chemical Society.

active sites to a crystalline or amorphous host framework, as in the case of Ti(IV) dispersed in silicalite or at the surface of amorphous silica [69]. Furthermore, it must be noted that changes in the local structure of supported species can occur owing to the adsorption of probe molecules, as in the interaction of NH_3 with Fe^{3+} sites, again in silicalite [70]. As shown in Figure 2.12, in the presence of NH_3, distinct CT absorptions were present (solid line), corresponding to framework Fe^{3+} species in an almost perfect tetrahedral symmetry, as the charge balancing of the negative charge on the zeolite framework can be made by NH_4^+, while after vacuum treatment the CT bands appeared more complex and broader (broken and dotted lines) indicating the formation of Fe^{3+} species with reduced symmetry.

Finally, according to the empirical optical electronegativity theory, CT absorptions are sensitive to factors affecting the electronegativity of the first coordination shell surrounding the metal center, such as the composition of the second shell. Such dependence can be useful in the elucidation of the types of links saturating the coordinative demand of a metal center exposed on a surface, in terms of the possible presence of OH groups, instead of only surface lattice oxygen atoms. This has been the case of tripodal $[(OH)Ti(OSi)_3]$ versus tetrapodal $[Ti(OSi)_4]$ Ti(IV) sites anchored to the inner walls of mesoporous MCM silicas [71]. On the basis of *ab initio* calculations, the presence of OH groups in the coordination sphere was expected to produce a CT sub-band at wavelengths longer than 220 nm, in agreement with the experimental evidence provided by the comparison of the

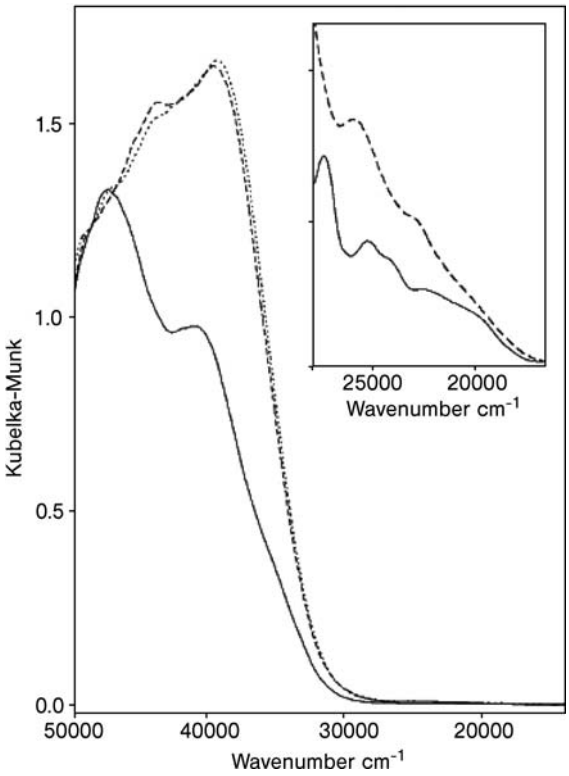

Figure 2.12 Effect of vacuum treatment and NH_3 adsorption on the DR UV-Vis spectra of a Fe-silicalite catalyst (Fe = 1.71 wt%; calcined in air at 773 K): broken line, outgassed at 673 K; full line, after contact with 60 Torr NH_3; dotted line: outgassed at 673 K. Inset: spectral behavior related to d–d transitions; related comments in the original paper. Reprinted from ref. [70], with permission from Elsevier.

experimental DR UV-Vis spectra of original Ti—MCMs with those of the materials after silylation, which converted surface OH groups Ti—OH and Si—OH into Ti—$OSi(CH_3)_3$ and Si—$OSi(CH_3)_3$. The latter actually appears to be characterized by a decrease of adsorption intensity in the 220–240 nm region (Figure 2.13).

2.3.5.2 d–d Transition Bands as a Source of Structural Insight

When oxide catalysts contain TMI in $d^1 \leq d^n \leq d^9$ configuration, additional detailed information on the structure of metal ion sites can be provided by the analysis of the features of their d–d bands. As indicated in Section 2.1, for such an analysis a huge background of literature is available. Selected examples of the different spectral features that can be considered for the derivation of structural and chemical insight for TMI sites in catalysts, or on the evolution of the TMI sites during catalyst preparation, will be presented.

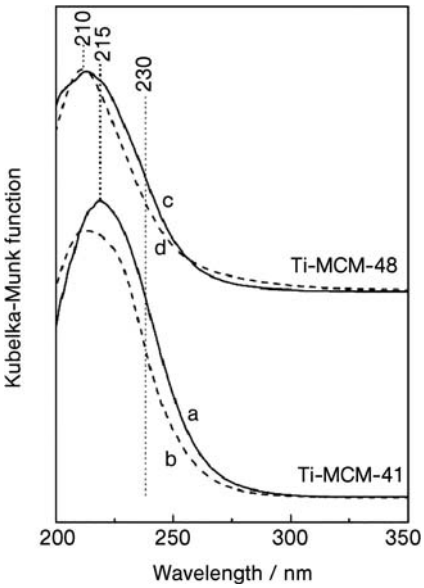

Figure 2.13 DR UV-Vis spectra of (a) calcined Ti-MCM-41, (b) silylated Ti-MCM-41, (c) calcined Ti-MCM-48, silylated Ti-MCM-48. In all cases the Ti loading was of ca 2 wt%; the samples were outgassed at 523 K for 2 h before spectroscopic measurements. Reprinted with permission from ref. [71]. Copyright 2007 American Chemical Society.

In the case of semiconductor systems initially containing TMI in a d^0 state and subsequently reduced, the presence of band-like absorptions assignable to d–d transitions, instead of edge-like features, arises from the formation of localized reduced centers and not the injection of electrons into the conduction band of the support. This has been discussed in the case of the $V_2O_5/WO_3/TiO_2$ EUROCAT SCR catalyst [72].

Focusing on the shape of d–d bands, a profile asymmetry due to the distortion of local structures by the Jahn–Teller effect can be useful in monitoring the isolation of TMI sites with respect to aggregated structures exhibiting a sharp band-gap transition in a similar position. An example is provided by the dependence of the spectral features of CuO/Al_2O_3 catalysts on the copper content (Figure 2.14). It can be observed that Cu^{2+} octahedra are strongly distorted by the Jahn–Teller effect, changing from O_h to D_{4h} symmetry.

Besides asymmetry, band width may be a source of information also. The width of the d–d bands of TMI complexes adsorbed on an oxidic support can be comparable to or even narrower than those observed for the aqueous precursor complexes. This can be related to a high homogeneity of the molecular environment of TMI on the surface, suggesting a possible molecular recognition character of the adsorption process [73].

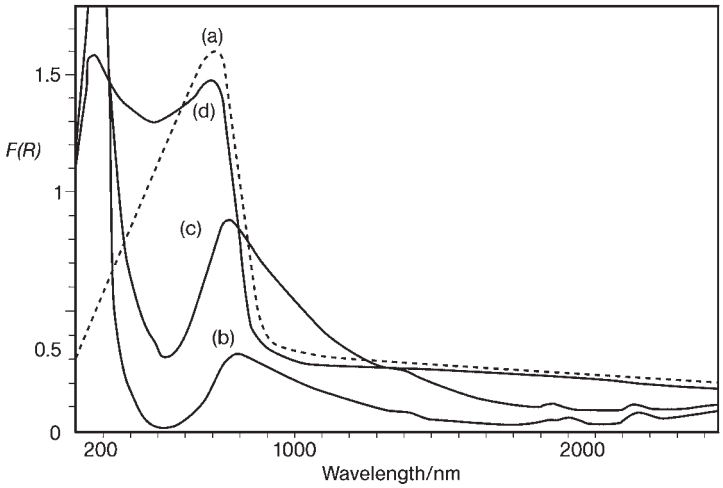

Figure 2.14 DR UV-Vis spectra of copper oxide supported or not on Al_2O_3 in the fresh state: (a) bulk copper oxide diluted into Al_2O_3; (b) 2.1 wt% CuO/Al_2O_3; (c) 4.8 wt% CuO/Al_2O_3; (d) 9.2 wt% CuO/Al_2O_3. Reprinted from ref. [116], with permission from the Royal Society of Chemistry.

Of course, a relevant source of information on the features of a TMI center at the surface of a catalyst, or on its evolution during the catalyst preparation, is the position of d–d bands. These have a dependence upon the composition of the ligand sphere, including oxygen atoms/hydroxy groups at the surface of an oxidic support. If the system can be treated with the model of the cubic ligand field (i.e. octahedral and tetrahedral stereochemistry) and, once known the nature of the ligands, it is possible to analyze the band positions by applying the law of average environment [15]. This states, taking a $[MA_nB_{6-n}]$ complex as an example, that the ligand field will be $\Delta_0^{TOT} = [n\Delta_0^A + (6-n)\Delta_0^B]/6$ (provided that the partial substitution of B with A ligands results in negligible splitting of the octahedral terms). For instance, using this approach, analysis of the progressive shift of d–d bands along a series of preparation steps of Ni/SiO_2 catalysts (Figure 2.15), has allowed evaluation of the Δ_0 related to surface $\equiv SiO^-$ present in the ligand sphere of supported Ni^{2+} ions [74]. Such an approach extended to a larger series of oxidic supports gave rise to a "spectrochemical series of supports" (alumina, zeolite Y and silica) [75]:

$$\Delta_0(AlO) < \Delta_0(ZO) < \Delta_0(SiO)$$

consistent with what was found for square-planar Pd^{2+} complexes [76].

Furthermore, the comparison of the values of the Racah parameter, *B*, obtained from the d–d spectra of a TMI dispersed on a series of supports can give information on the difference in the covalence level of the TMI–support interaction among

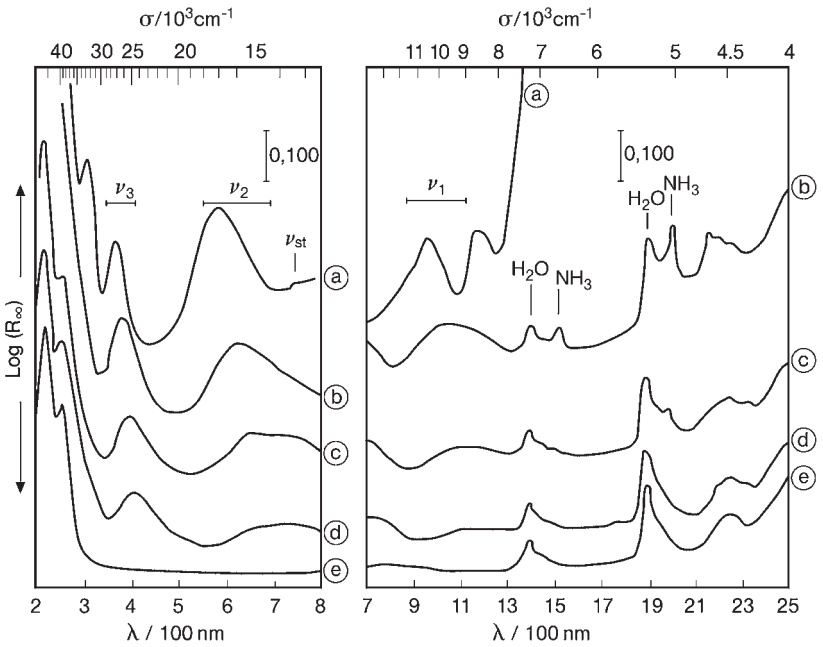

Figure 2.15 DR UV-Vis-NIR spectra of a 1.7 wt% $Ni^{(II)}/SiO_2$ catalyst after different preparation steps: (a) wet after centrifugation; (b) filtered and dried at 293 K in air for 15 h; (c) filtered and dried at 353 K in an oven for 15 h; (d) calcined at 773 K in O_2 and rehydrated for 1 year; (e) unexchanged ammoniated SiO_2 dried in an oven at 353 K for 15 h. Reprinted from ref. [74] with permission from Elsevier.

the various cases. Again in the case of Ni^{2+} ions, the following "nephelauxetic series of supports" was proposed [75]:

$$\beta(\mathrm{AlO}) < \beta(\mathrm{ZO}) < \beta(\mathrm{SiO})$$

indicating that the weaker-field surface ligands have more covalent bonding to the supported ions.

Finally, in deriving structural information from the features of d–d spectra of TMIs, it must be considered that, because of the Laporte selection rule, ion sites with octahedral symmetry can contribute to the spectra only to a very limited extent, and so can escape spectroscopic detection. However, this behavior can be turned into a tool to monitor the distribution of TMIs in sites with different structure as a function of loading, as in the case of CoAPO zeotype materials. In this case, the attainment of a plateau level of the intensity of the d–d bands due to Co^{2+} ions with tetrahedral symmetry that became inserted in the framework indicated the formation of extra-framework species, containing "d–d silent" octahedral Co^{2+} sites with increasing loading (Figure 2.16) [77].

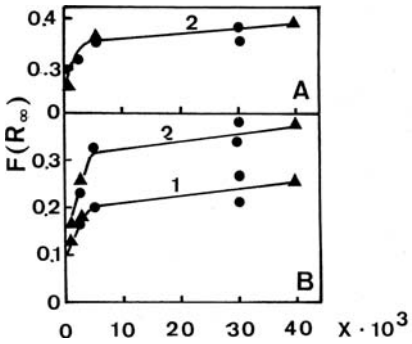

Figure 2.16 Plot of the intensity of the KM function [$F(R_\infty)$] against the Co-content in CoAPO-5 catalysts: (A) as synthesized; (B) after activation in O_2 at 373 K. Curve 1: NIR band; curves 2: Vis bands. Co content is expressed as the value "x" in the formula $(Co_xAl_yP_z)O_2 \cdot n(N/T) \cdot mH_2O$ [$x + y = 0.5$; $z = 0.5$; $n = 0.38$ (triethylamine, T), 0.25 (N,N-diethylethanolamine, N); $m = 8.5$ (with T), 10.3 (with N). Reprinted from ref. [77], with permission from Elsevier.

2.4 UV-Vis-NIR Photoluminescence Spectroscopy

Photoluminescence spectroscopy studies the emission of electromagnetic radiations by a system that returns to its ground electronic state from an excited one previously populated by light absorption. This kind of electronic spectroscopy is a powerful tool in determining the structure, coordination and reactivity of metal centers, especially for metal loadings below 1–2 wt%. In fact, at higher metal loading, a concentration quenching may occur and the photoluminescence becomes less informative.

Photoluminescence (PL) is widely applied to investigate surfaces and surface chemical phenomena with a high degree of sensitivity. The technique provides extremely rich information when applied to the study of photoluminescence sites on bulk oxides with a large surface to volume ratio; on sites located on the surface of a support, for example oxide-supported catalysts; on sites that can be modified by thermal treatments (calcination, reduction, etc.); and when the local environment of the emitting sites is altered by the adsorption of molecular probes. By way of introduction, basic photophysical aspects essential for the rationalization of PL data will be summarized.

2.4.1 Franck–Condon Principle

The Frank–Condon principle is based on the fact that the time of an electronic transition (of the order of 10^{-16} s) is shorter than that of a vibration (of the order of 10^{-14} s). This means that during an electronic transition the nuclei do not change their positions. This phenomenon can be illustrated using the Morse potential energy curves for diatomic molecules (Figure 2.17). The series of horizontal lines

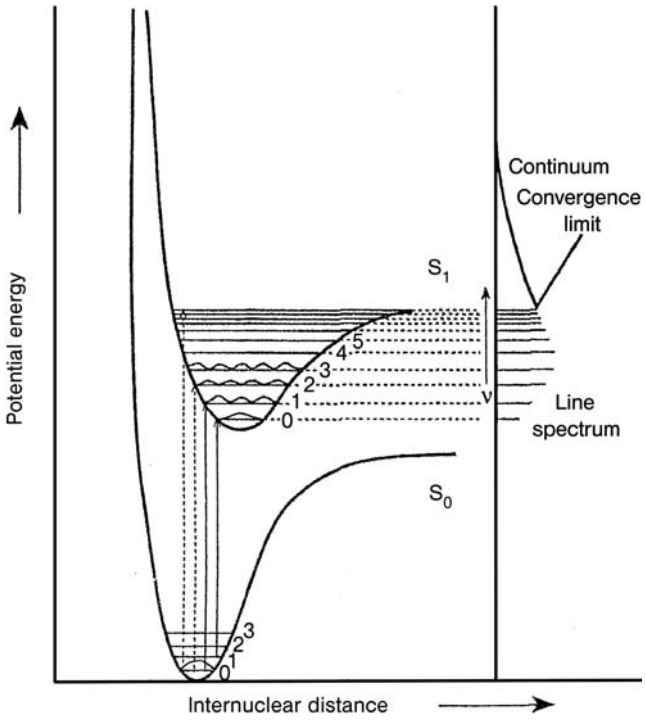

Figure 2.17 Potential energy curves for ground (S_0) and excited (S_1) states. Reprinted from ref. [11], with permission from Elsevier.

represents the vibrational states of the anharmonic oscillator either in the ground singlet state (S_0) in which all electrons are paired or are in the electronic excited singlet state (S_1) in which the unpaired electrons remain with opposite spin. Consequently the electronic transitions, in both absorption and emission processes, occur at constant internuclear distance and should be drawn vertically, as shown in Figure 2.17.

Upon absorption of UV-Vis light, the system moves to an electronic excited state. There are many ways by which the system can return to the ground state involving radiative or non-radiative decays. In the case of radiative decay, the system loses the excitation energy as a photon and two different mechanisms can be involved: fluorescence and phosphorescence. Fluorescence is an emission process between states with the same spin multiplicity (i.e. singlet–singlet transitions), while phosphorescence involves electronic states with different spin multiplicity (i.e. triplet–singlet transitions). Fluorescence lifetimes are normally very short (10^{-9} s for organic molecules). Phosphorescence lifetimes are longer (ranging from 10^{-3} s to minutes) which is because transitions between states of different multiplicity are forbidden by the selection rule $\Delta S = 0$. They thus have very low probability. Frequently, non-radiative decay may also compete.

In the case of solids, the excited ion pair is subject to the influence of its lattice environment, which produces a vibrational relaxation process. The lattice environment, however, is not able to accept the larger energy difference needed to lower the ion pair to the ground electronic state and, therefore, the ion pair may survive long enough to undergo spontaneous emission, releasing the remaining excess of energy as radiation. This electronic transition, denoted as fluorescence, is represented in accordance with the Frank–Condon principle by a vertical line. The fluorescence occurs at a frequency lower than that of the absorption process and the difference between the frequencies is called the Stokes shift.

The light emission normally occurs after some vibrational energy has been dissipated into the surroundings; consequently the fluorescence intensity depends on the ability of the lattice environment (or the surrounding gas-phase molecules) to accept the electronic and vibrational quanta. Thus, it has been observed that molecules with widely spaced vibrational levels, such as molecular oxygen, are able to accept the large quantum of electronic energy and quench the fluorescence. On the other hand, fluorescence emission may be increased by decreasing the temperature, for instance working at liquid nitrogen temperature because, at low temperatures, lattice vibrations are less favored.

When a spin flip occurs for an electron in the S_1 state, an excited triplet state (T_1) is filled. The T_1 state has a lower potential energy than the S_1 state since electron–electron repulsions are lower (Figure 2.18).

Phosphorescence can be observed only by populating the T_1 electronic state, which occurs when the S_1 potential energy curve that has been populated by

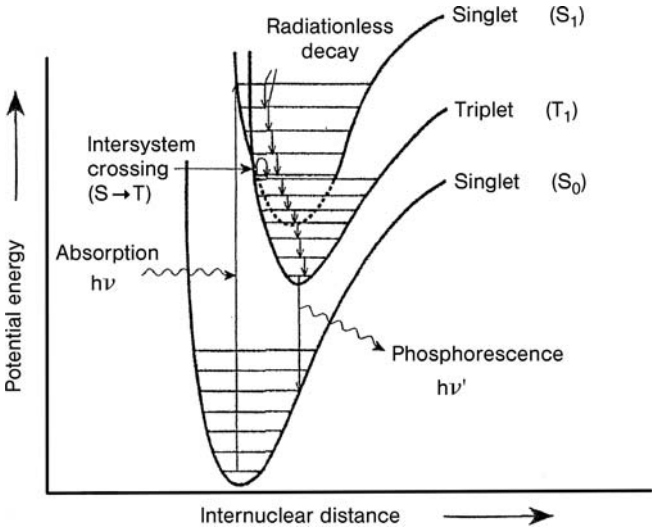

Figure 2.18 Potential energy curves for ground (S_0) and excited singlet (S_1) and triplet (T_1) states. Reprinted from ref. [11], with permission from Elsevier.

absorption phenomena, intersects the T_1 curve sharing a common geometry. The mechanism for changing the spin state of the S_1 is called Intersystem Crossing (ISC). Singlet–triplet transitions may occur by spin–orbit coupling and for this reason the ISC mechanism is expected to take place more efficiently in a molecule with heavy atoms or in an ion pair in a oxidic system since the corresponding spin–orbit coupling constant is large. Upon ISC, the ion pair moves from a vibrational level of S_1 to an iso-energetic vibrational level of the T_1 state, where it continues to release energy into the surroundings, moving down the vibrational levels until it reaches the lowest vibrational state. From this vibrational level, the ion pair may return to the ground state (S_0) by emitting radiation; this phenomenon is called phosphorescence. The T_1–S_0 transition is forbidden by the $\Delta S = 0$ selection rule and consequently the intensity of phosphorescence is normally lower than that of fluorescence. Generally, phosphorescence is enhanced when the material, such as a catalyst, has highly dispersed metal ions or highly localized emitting sites. In these cases, the energy transfer becomes less efficient and there is time for ISC mechanism to take place, as the singlet excited state steps slowly past the intersection point (Figure 2.18).

Finally, we note that radiative decay transitions have the same nature as absorption ones and consequently they obey the same selection rules (see Sections 2.1 and 2.2).

2.4.2
Quantum Efficiency and Lifetime

The quantum efficiency or yield (Φe) and lifetime (τ) are important parameters for identification of the emitting species.

The quantum efficiency, or yield, of photoluminescence (Φe) is defined as the ratio of the numbers of photons emitted from an excited species to the number of photons absorbed. It can be expressed as

$$\Phi_e = k_e/(k_e + k_{IC}) = \Phi^* k_e \tau \tag{2.11}$$

where k_e is the radiative rate constant and k_{IC} is the sum of the unimolecular rate constants of non-radiative processes from the excited states. Φ^* and τ are the concentration of species and the experimental lifetime of the excited state respectively. To achieve a high quantum efficiency it is necessary to minimize k_{IC}, for instance by cooling the sample to low temperature (77 K or 4 K) in order to reduce the contribution of non-radiative processes.

For a single exponential decay, the radiative lifetime (τ_0), obtained from the decay curves of the intensity measured as a function of time, is defined by the mean time the species spends in the excited state prior to return to the ground state. Generally, lifetimes are longer for the upper states reached through a weakly absorbing transition and also as the energy separation between the ground and excited states is larger.

The lifetime is expressed as

$$\tau_0 = 1/(k_e + k_{IC}) \tag{2.12}$$

In the presence of a quenching molecule, the lifetime (τ) is given by

$$\tau = 1/(k_e + k_{IC} + k_q[Q]) \tag{2.13}$$

where k_q is the rate constant of the quenching process and [Q] the concentration of the quencher.

Under conditions of steady and constant illumination, the concentration of the excited state is given by

$$\Phi_0 = I_0/(k_e + k_{IC}) \tag{2.14}$$

but if a quencher molecule is present the concentration becomes

$$\Phi = I/(k_e + k_{IC} + k_q[Q]) \tag{2.15}$$

When the intensity of the excitation light and the concentration of the emitting species are kept constant, the photoluminescence intensity is proportional to the concentration of the excited species.

The presence of a quencher molecule decreases the intensity of photoluminescence since the fluorophore is often returned to the ground state during a diffusive encounter with the quencher. In this process the fluorophore is not chemically modified. For collisional quenching the decrease in intensity is described by the Stern–Volmer equation:

$$(\Phi_0)/(\Phi) = 1 + k_q[Q]/(k_e + k_{IC}) = 1 + \tau_0 k_q[Q] \tag{2.16}$$

A wide variety of molecules can act as quenchers, including oxygen, halogens, amines and electron-deficient molecules.

2.4.3 General Remarks on Methodologies Applied for PL Measurements

A PL spectrum reports the emission intensity as a function of the wavelength of the emitted light when the excitation wavelength and the intensity of the exciting light are fixed at constant values. In some cases, it is possible to observe the vibrational fine structure in the photoluminescence band, especially if the spectra are collected at 77 K. As well as the emission spectrum, the excitation spectrum can also be collected. In this case, the intensity of the emission at a fixed wavelength is plotted as a function of the wavelength of the excitation light, which varies with the extinction coefficient of the absorbing species. Therefore, the excitation spectrum is similar to the absorption one; the advantage of collecting excitation spectra compared to absorption measurements is their greater sensitivity, even for low concentrations of photoluminescent species.

Details on the instruments available for collecting PL spectra are reported in refs. [11, 78]. One of the main points to be stressed is that, because of the high sensitivity of the PL technique, the sample cell has to be made from high-quality fused silica with no impurities, such as Suprasil.

PL is typically collected at 90° to the transmitted light for transparent liquid samples, whilst in the case of pellets or powered samples it is necessary to collect the spectra in front-face geometry, meaning that a swing-away mirror is positioned to allow the collection of the PL of the sample at an angle $45° > \theta > 22°$ (depending on the instrument) with respect to the incident radiation. When oxide catalysts have to be studied it is important to collect the spectra *in vacuo* to remove any gases that might act as a quencher molecules, such as oxygen.

2.4.4 Characterization of Oxide Catalysts by PL

2.4.4.1 Insulating Oxides: the Case of AEO

The possibility of using PL to study insulating oxide catalysts is limited by the position of the absorption bands that can be used for excitation. For this reason, most PL investigations on such types of material were focused on alkaline earth oxides that, as reported above, exhibit excitonic absorptions in the near-UV. In this respect, the background knowledge in this area is based on the series of investigations carried out in the late 1970s and early 1980s on MgO, CaO, SrO and BaO [3, 79–83]. These studies demonstrated that the emission and excitation spectra of AEOs are extremely rich in information, owing to the presence of several bands associated with ions with different local coordination on the surface.

The PL spectra were actually very sensitive to the overall surface structure and this allowed the study of the behavior of each type of luminescence center upon thermal treatment or adsorption of probe molecules. These studies have also shown that, by the way of an energy-transfer process, emission can arise from surface sites that are not necessarily those that absorbed light in the first step of the PL phenomenon. For instance, at 300 K, the energy absorbed by 5- and 4-coordinated sites is transferred to the 3-coordinated ones, whilst at 77 K, the energy-transfer process is largely suppressed and the original emission profiles of 4- and 5-coordinated centers can be observed [41].

From these early studies, the PL technique, which was initially aimed at confirming the observation of surface sites, was gradually extended to explore other related aspects, such as surface structure, decay of the excited states and surface reactivity.

In addition, the adsorption of quencher molecules, such as O_2 and H_2, on AEOs has allowed the clarification of the nature of the luminescence sites present at the surface [81]. In particular, in the case of H_2 adsorption on SrO, a change in the excitation band shape was observed. H_2 may react at different rates with species absorbing in different parts of the excitation band, producing a change in the band shape. No corresponding change in band shape was observed in the emission spectrum. By contrast, O_2 adsorption did not change the shape of either the excitation or the emission bands; only a decrease in intensity was observed. This

spectroscopic evidence suggested (i) that O_2 and H_2 are adsorbed on different sites, (ii) that the absorption and emission processes occur at different, but closely related, sites on the surface and (iii) that energy can be transferred along the surface. In general, O_2 adsorption is associated with regions of the surface that are oxygen-deficient or have a local excess of cations, whilst hydrogen is expected to react with areas that are cation-deficient or have a local excess of oxygen ions. In the case of SrO, most of the intensity loss of the emission was not reversible and H_2 must be strongly held on the surface, probably as hydroxyls. Using analysis of such spectroscopic behavior, it was proposed that the sites on the surface responsible for the light emission are oxygen-deficient or have a local excess of cations, whereas the sites responsible for the light absorption are cation-deficient or have a local excess of oxygen ions [81].

The luminescence band of the AEO, outgassed at 1200 K, was shifted to lower energy as the cation size increased, as reported in Table 2.4 and in Figure 2.19. The excitation spectra were at lower energy than the band gap of the corresponding bulk materials and were similar to the absorption spectra [44, 45]. The excitation processes were, therefore, associated with anions and cations in low coordination located at the surface and led to the formation of excitons (electron-hole pairs):

$$M^{2+}_{LC}O^{2-}_{LC} + h\nu \rightarrow M^{+}_{LC}O^{-}_{LC} \tag{2.17}$$

where LC denotes low coordination.

Surface excitons require less energy in their formation than bulk excitons, owing to the reduced Madelung constant of the coordinatively unsaturated ions at the surface [81].

Furthermore, analysis of the excitation spectra of AEOs has revealed that the excitation bands are characterized by several components, which is evidence that centers with different coordination are present on the surface. The lower the energy, the lower the coordination number. It was established that the three main components identified in the excitation spectra were associated with three surface states with different coordination of the ion involved: O^{2-}_{5C} on extended (001) faces, O^{2-}_{4C} on the edges and O^{2-}_{3C} on the corners. In the bulk lattice of an AEO the ions are octahedrally coordinated.

Table 2.4 Peak positions of the absorption, excitation and emission spectra of the alkaline earth oxides.

Oxide	Absorption (eV)	Excitation (eV)	Emission (eV)
MgO	5.70; 4.58	>5.40; 4.52	3.18
CaO	5.52; 4.40	>5.40; 4.40	3.06
SrO	4.64; 3.96	4.43; 3.94	2.64
BaO	3.60; 3.22	3.70	2.67

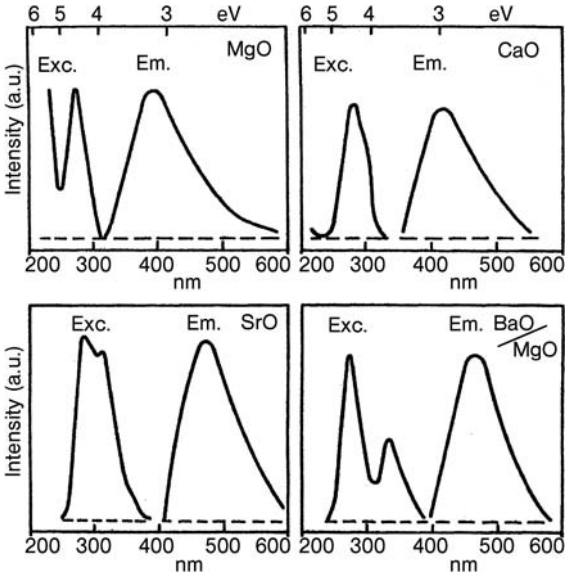

Figure 2.19 Excitation and emission spectra of alkaline earth oxides outgasssed at 1200 K. Dashed lines show quenching by oxygen. Reprinted from ref. [83], with permission from Elsevier.

Among AEOs, MgO is the most studied material and can be considered as a model system. High surface area MgO powders, outgassed at high temperature, exhibit emission bands when excited by UV light at 260–400 nm, with a lower energy than the band gap of MgO single crystals [3, 84]. PL was strongly quenched by the adsorption of oxygen confirming that the emitting sites are located at the surface of the oxide. Moreover, the absorption band of powdered MgO was found at lower frequencies than that observed for bulk MgO single crystals [44, 45]. The photoluminescence of MgO was ascribed to the charge-transfer processes involving surface ions in low coordination present at the MgO surface.

The lifetimes of emitting species are linked to energy transfers, which affect the kinetics of emission processes. In addition, lifetimes also depend on the local environment of the oxide ions involved in PL. Analysis of the lifetimes of the photoluminescent species has revealed two types of emitting sites in MgO oxide. One has a comparatively short lifetime (~10^{-5} s), and is associated with the charge-transfer processes involving low coordinated surface ions, and the other a long lifetime (1–10^{4} s), ascribed to the presence of surface F_s^+ centers [85]. The PL yield was found to change from sample to sample and to depend on the pre-treatment temperature. Moreover, outgassed MgO exhibited a photocatalytic behavior in the cis–trans isomerization of 2-butene [86]. The correlation between the intensity of the short-lifetime PL and the rate of photocatalyzed isomerization indicated that coordinatively unsaturated surface ions play a relevant role in the photocatalytic activity of MgO [86]. More recently, the lifetimes of PL sites of MgO nanocubes

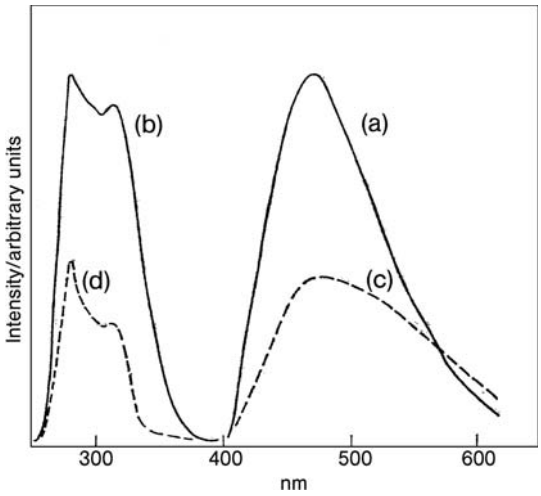

Figure 2.20 Photoluminescence spectra of SrO recorded at 300 K before and after pyridine (Py) adsorption. (a) emission spectrum of SrO; (b) excitation spectrum of SrO; (c) emission spectrum after Py adsorption; (d) excitation spectrum after Py adsorption. Reprinted from ref. [88], with permission from the Royal Society of Chemistry.

have been modeled by means of a kinetic energy-transfer model [87]. This is a complementary approach to the one based on analysis of the position and shape of PL signals, and confirms that the emission and excitation bands are associated with low-coordinated O^{2-}_{LC} oxide ions. Moreover, lifetime measurements also suggested that phosphorescence takes place in the emission process of nanocubic MgO oxide.

PL spectroscopy can also be successfully applied to the characterization and detection of particular molecular structures formed as a result of a reaction on the catalyst surface. This was the case in a PL study of the reaction of pyridine and oxygen with thermally activated SrO [88]. SrO powder is white and the PL spectra at 300 K showed a broad emission band at 475 nm (Figure 2.20 curve a) and an excitation band with at least two maxima at 280 and 315 nm (Figure 2.20 curve b). The sample turned blue-violet upon pyridine adsorption and a very weak PL signal was detected (Figure 2.20 curves c and d). The spectra were not modified by outgassing the excess of pyridine at 300 K and no color change was observed. After admission of oxygen at 300 K, the color changed to yellow-pink and the emission spectrum at 300 K showed a new maximum at 550 nm and a slight increase of the intensity in the 400–450 nm range (Figure 2.21, curves a and b). The emission band recorded at 77 K after addition of O_2 (curve c) is more intense than the one recorded at 300 K (curve a) and showed a fine structure with three main peaks at 429, 457 and 476 nm. The corresponding excitation spectrum has a maximum at 275 nm (Figure 2.21, curve d). The well defined structure is attributed to the emission of bipyridyl species formed on the surface. To identify which isomer of

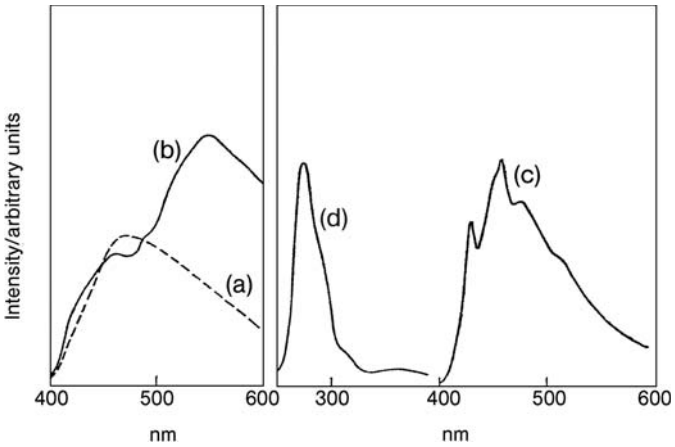

Figure 2.21 Photoluminescence spectra of the SrO + Py + O_2 system. (a) emission spectrum of SrO after Py adsorption at 300 K; (b) emission spectrum of SrO after adsorption of O_2 on preadsorbed Py at 300 K; (c) and (d) emission and excitation spectra of of SrO after adsorption of O_2 on preadsorbed Py at 77 K. Reprinted from ref. [88], with permission from the Royal Society of Chemistry.

bipyridyl (2–2′ or 4–4′-Bpy) is formed on the SrO surface, the emission spectra of the two bipyridyls adsorbed on SrO were recorded after admission of oxygen (Figure 2.22). The spectrum of 4,4′-bipyridyl (curve a) is quite similar to the spectrum obtained after adsorption of pyridine and oxygen on SrO (Figure 2.21, curve c) both in the shape and in the spacing of the vibronic structure. This study has allowed the clarification of the product formed by the interaction of pyridine with oxygen on a SrO surface, namely 4,4′-bipyridyl.

2.4.4.2 Investigations of Highly Dispersed Transition Metal Ions in Oxides or Zeotype-Systems by PL Spectroscopy

PL spectroscopy, combined with lifetime measurements, is a powerful tool for determination of the structure, coordination and oxidation state of TMIs dispersed on different types of support, used as heterogeneous catalysts. This spectroscopic technique is particularly useful for characterizing materials with a very low metal loading (below 1–2 wt%), owing to its high sensitivity. Anpo and coworkers [11] have reviewed the applications of PL to the characterization of catalysts and photocatalysts, covering a wide range of different catalytic systems. Different types of TMI-containing catalysts can be characterized by PL [89]. Systems investigated include vanadium-containing zeolites or mesoporous materials [22, 90–93], molybdenum dispersed on silica [94] or in mesoporous silica [95], chromium oxides anchored on Vycor glass or silica [96, 97], titanium-containing zeolite [98, 99], titanium grafted on mesoporous systems [100, 101] and copper/ZSM-5 catalysts [102–105]. Here, we focus on the PL features of vanadium-containing materials,

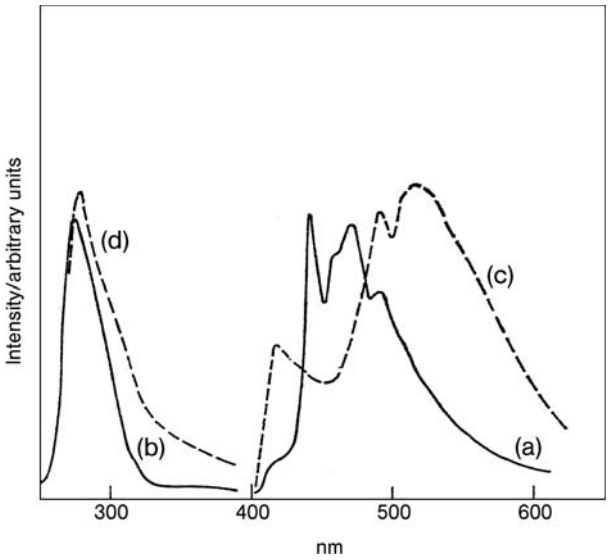

Figure 2.22 Photoluminescence spectra of the SrO + Bpy + O_2 system at 77 K. (a) and (b) emission and excitation spectra of SrO after adsorption of O_2 on preadsorbed 4,4′-Bpy; (c) and (d) emission and excitation spectra of SrO after adsorption of O_2 on preadsorbed 2,2′-Bpy. Reprinted from ref. [88], with permission from the Royal Society of Chemistry.

owing to the richness of information provided by the spectra associated with the vibrational fine structure that can be recorded at low temperature (77 K). This particular application allows the determination of detailed and specific information on the presence of different vanadium species.

In the case of vanadium-containing systems, PL only detects tetrahedral V^V species and, owing to its high sensitivity to the local environment of luminescent centers, allows different types of tetrahedral V^V sites [11, 106–108] to be distinguished.

Vanadium oxides anchored on oxide supports are important heterogeneous catalysts for both the vapor-phase selective oxidation of alkylaromatic hydrocarbons, alkenes and alkanes and the selective reduction of NO [109, 110]. Vanadyl groups (V=O) are considered to be the PL species in vanadium-containing materials. The absorption and emission (phosphorescence) of the UV light arose from the charge-transfer processes on the surface vanadyl groups of the tetrahedrally coordinated VO_4 species involving an electron transfer from O^{2-} to V^{5+} and a reverse radiative decay from the charge-transfer triplet state (Scheme 2.1) [11].

The nature of the oxidic support plays an important role in modulating the nature of vanadium species and the catalytic behavior of the materials. In fact, changes in the electron density of the vanadyl double bond can be produced by the inductive effect through the bonds anchoring the tripodal vanadyl groups to the oxidic support [111]. These electronic effects can be clearly demonstrated using

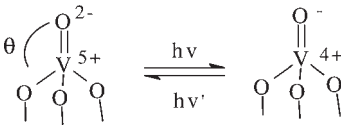

Scheme 2.1 Schematic representation of the CT processes on the surface vanadyl groups of the tetrahedrally coordinated VO_4 species.

PL spectroscopy. A PL study of vanadium oxide supported on different oxides, such as SiO_2, TiO_2, Al_2O_3, K-doped Al_2O_3, ZnO and MgO, was performed by Garcia and coworkers [111]. Excitation in the 250 to 400 nm range led to PL bands in the 550–700 nm range from all solids, and a consistent shift in the emission maximum was evident depending on the acid/base character of the oxide support (Figure 2.23). If the wavelengths of the emission maxima are plotted against the isoelectric point or zero point of charge (PZC) of the oxides (Figure 2.24), a linear correlation is observed. The PZC of the supports can be related to the acid/base character of the oxides [110, 112], meaning that this parameter has a direct influence on the PL, and hence on the molecular orbitals, of the vanadyl groups.

Vanadium loading only modifies the intensity of the emission band and not its position, which depends only on the nature of the support. A significant decrease

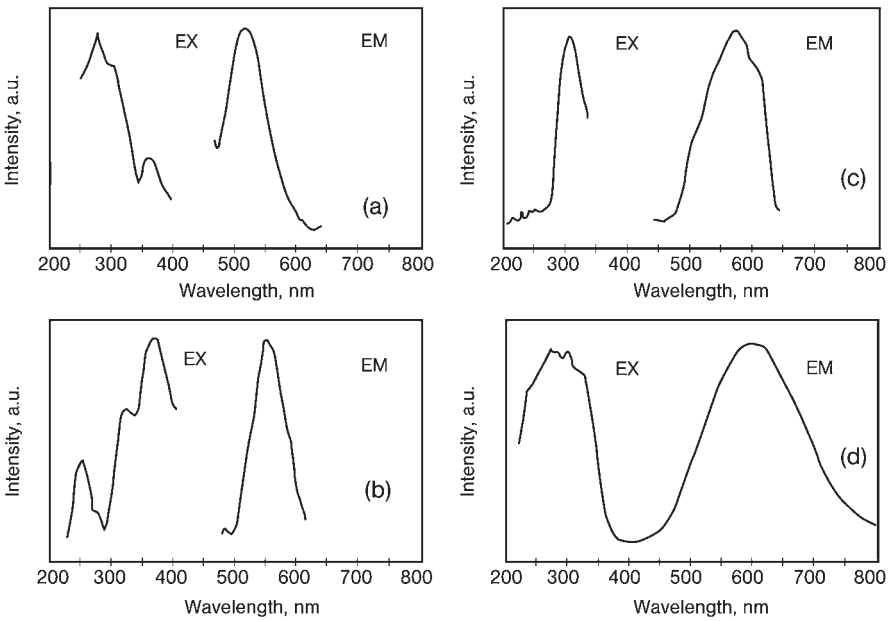

Figure 2.23 Emission and excitation spectra recorded at 300 K of vanadyl group anchored on metal oxide. (a) hydrated 0.8V/SiO_2; (b) 3V/TiO_2; (c) 2V/Al_2O_3; (d) 20V/MgO. Reprinted from ref. [111], with permission from Springer.

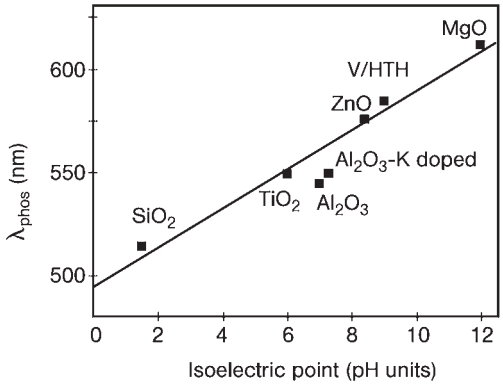

Figure 2.24 Variation of the emission maximum wavelength with the isoelectric point or pcz of the oxide support in supported vanadia catalysts. Reprinted from ref. [111], with permission from Springer.

of the emission intensity is, in fact, observed as the vanadium loading increases, owing to the formation of di-, tri- and polyvanadium aggregates anchored on the support surface instead of isolated vanadyls, which are the most intense emission centers.

PL spectra collected at low temperature (77 K) allow the observation of the vibrational profile of the vanadyl groups. This particular application of PL is extremely useful for distinguishing different kinds of tetracoordinated vanadium sites, as reported by Dzwigaj and coworkers for V^{5+} species incorporated in a β-zeolite framework [93, 113]. The emission spectra collected at 77 K with λ_{ex} = 250 nm of three V-β samples (VSiβ as-synthesized, C-VSiβ calcined and C-Hyd-VSiβ calcined and then hydrated) are reported in Figure 2.25. All the solids exhibit emission

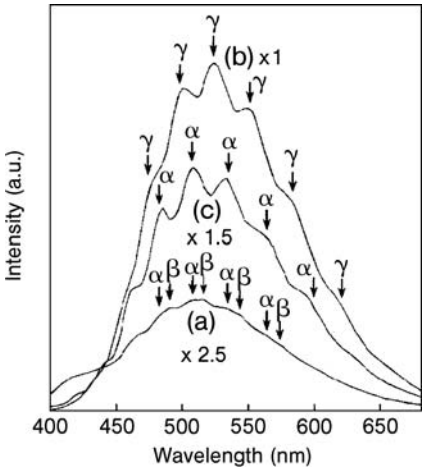

Figure 2.25 Photoluminescence spectra, recorded at 77 K, of (a) VSiβ, evacuated at 353 K for 2 h; (b) C-VSiβ, evacuated at 473 K for 2 h; (c) C-Hyd-VSiβ, evacuated at 473 K for 2 h. Reprinted with permission from ref. [113]; Copyright 1998 American Chemical Society.

maxima at ca. 500 nm together with a vibrational fine structure. The fine structure corresponds to transitions from the lowest vibrational level of the excited triplet state T_1 (V^{IV}—O^-) to the vibrational levels of the ground singlet state S_0 (V^V=O^{2-}) [11, 106–108]. The shapes, positions of maxima and intensities of the components of the vibrational profiles depend on the pre-treatment of the samples. In fact, three vibrational fine structures, ascribed to three different kinds of tetrahedral V^V sites (α, β, γ), can be observed in the emission spectra of the VSiβ samples (Figure 2.25).

Since the separation of the vibrational bands is not well resolved owing to the superposition of different sets of vibrational structure involving tetrahedral V^V sites with different symmetries, analysis of the second derivative of the PL spectra allows the elucidation of the precise structure of the different vanadium sites (Figure 2.26). The second derivative of the VSiβ sample (curve a) shows the presence of two (α and β) main tetrahedral V species. The vibrational energy of the β species is 1054 cm^{-1}, indicating a short V=O bond length (1.54 Å). On the contrary, the γ type species is predominant in the C-VSiβ sample (curve b). The vibrational energy of the γ species is 1036 cm^{-1}, indicating a longer V=O bond length (1.56 Å)

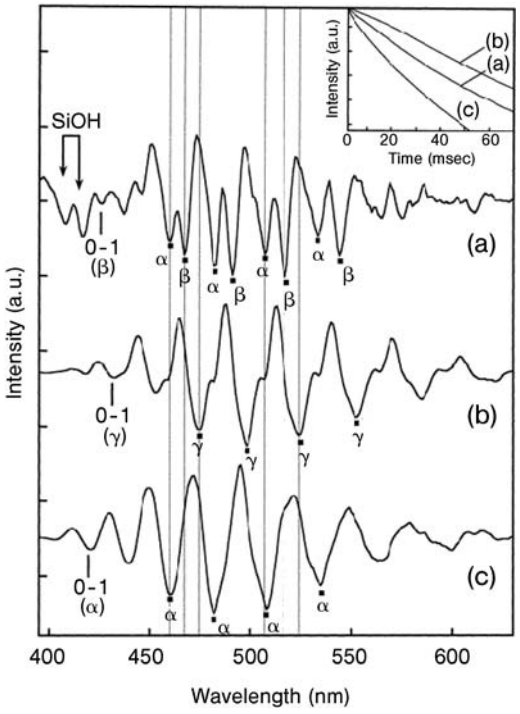

Figure 2.26 Second derivative of the photoluminescence spectra, recorded at 77 K, of (a) VSiβ, evacuated at 353 K for 2 h; (b) C-VSiβ, evacuated at 473 K for 2 h; (c) C-Hyd-VSiβ, evacuated at 473 K for 2 h. The decay curves (insets a, b, and c, logarithmic scale) were monitored at 77 K. Reprinted with permission from ref. [113]; Copyright 1998 American Chemical Society.

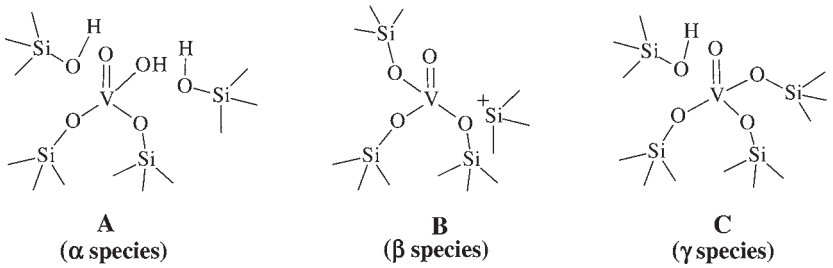

Scheme 2.2 Schematic representation of α, β and γ V sites in VSiβ catalyst. Adapted from ref. [93].

and a higher symmetry than the β one. Finally, in the second derivative spectrum of the C-Hyd-VSiβ sample (curve c), the main contribution of the α-type tetrahedral V species is evident. The vibrational energy of the α-species corresponds to 1018 cm^{-1}, which indicates a longer V=O bond length (1.58 Å) and a higher symmetry compared to γ sites. Both the V=O bond length and the symmetry of V sites decrease in the following order: α > γ > β along with a concomitant increase of the O=V–O(Si, H) bond angle (θ in Scheme 2.1), on the basis of VSEPR arguments which apply for d^0 systems where there is no stabilization effect due to the crystal field [114].

The lifetime of the excited triplet state depends on the degree of distortion of the symmetry of transition metal ions from the ideal tetrahedral one [115]. The decay curves of the PL of the three V samples are reported in the inset of Figure 2.26. The lifetimes are 49 ms for the γ sites, 28 ms for α sites and 88 ms for β sites. The increase in the lifetimes from 28 ms to 88 ms for the sequence α, γ and β species can be attributed to an increasing distortion of the tetracoordinated V sites and to a decrease in the V=O bond length. On the basis of these results, combined also with the DR UV-Vis data, Dzwigaj and coworkers proposed that the three types of tetrahedral V species arise from three different framework sites. In particular, the formation of each type of V site is related to the state of vacant T atom sites (silanol nests). For α species, the authors proposed hydroxylated $(SiO)_2(HO)V{=}O$ sites (structure A Scheme 2.2), for β species, non-hydroxylated $(SiO)_3V{=}O$ sites (structure B in Scheme 2.2) and for γ species non-hydroxylated $(SiO)_3V{=}O$ sites (structure C in Scheme 2.2) [93].

Although based on a selected example, this demonstrates the richness of physical-chemical insights that can be obtained through a deep analysis of PL spectra of catalysts bases on highly dispersed TMI.

2.5 Conclusions

Both fundamental aspects and representative examples of types of investigation and analyses of spectral data for different kinds of oxide-based materials of interest in heterogeneous catalysis and photocatalysis have been reviewed. Hopefully, we

have increased awareness that the use of UV-Vis-NIR spectroscopy, in both absorption and emission modes, could significantly assist in the provision of chemical and structural insight. The development of a detailed description of the nature and properties of surface sites, which is of crucial importance for catalytic materials, may demand some (stimulating and challenging) effort, owing to the multiplicity of factors that can affect the actual features of an electronic spectrum. Of course, it is important to keep in mind that information provided by UV-Vis-NIR spectroscopy is one of the "tesserae" of the complex (but fascinating) mosaic of complementary techniques, both spectroscopic and non-spectroscopic, required to achieve a satisfactory understanding of catalytic materials.

Acknowledgments

The authors acknowledge financial support by Regione Piemonte (Progetto NANOMAT, Docup 2000-2006, Linea 2.4a).

References

1 Haber, J. and Stone, F.S. (1961) *Proceedings of the Chemical Society*, 424.

2 Chapple, F.H. and Stone, F.S. (1964) *Proceedings of the British Ceramic Society*, **1**, 45.

3 Tench, A.J. and Pott, G.T. (1974) *Chemical Physics Letters*, **26**, 5900.

4 Che, M. and Bozon-Verduraz, F. (1997) in *Handbook of Heterogeneous Catalysis* (eds G. Ertl, H. Knözinger and J. Weitkamp), Wiley-VCH Verlag, **2**, p. 641.

5 Delgass, W.N., Haller, G.L., Kellerman, R. and Lunsford, J.H. (1979) Chapters 4 and 6, *Spectroscopy in Heterogeneous Catalysis*, Academic Press, New York.

6 Garbowski, E. and Praliaud, H. (1994) in *Catalyst Characterisation: Physical Techniques for Solid Materials* (eds B. Imelik and J.C. Védrine), Plenum Press, New York, chap. 4.

7 Schoonheydt, R.A. (1984) Chapter 4, *Characterisation of Heterogeneous Catalysts* (ed. F. Delannay), Dekker, New York, p. 125.

8 Stone, F.S. (1983) in *Surface Properties and Catalysis by Non Metals* (eds. J.P. Bonelle, B. Delmon and E.G. Derouane), Reidel, Boston, p. 237.

9 Weckhuysen, B.M. and Schoonheydt, R.A. (1999) *Catalysis Today*, **49**, 441.

10 Anpo, M. (1997) in *Handbook of Heterogeneous Catalysis* (eds G. Ertl, H. Knözinger and J. Weitkamp), Wiley-VCH Verlag, **2**, p. 664.

11 Anpo, M. and Che, M. (2000), *Advances in Catalysis*, **44**, 119.

12 Coluccia, S. (1988) in *Photocatalysis and Environment* (ed. M. Schiavello), Kluwer Academic Press, Dordrecht, p. 191.

13 Weckhuysen, B.M. (2004) Chapter 12, *In-situ Spectroscopy of Catalysts*, Vol. **255**, American Scientific Publishers.

14 Che, M. (1993) in *New frontiers in Catalysis, Proceedings of the 10th International Congress on Catalysis* (eds L. Guczi *et al.*), Elsevier, Amsterdam, p. 31.

15 Figgis, B.N. (1966) *Introduction to Ligand Fields*, Interscience Publishers.

16 Sutton, D. (1968) *Electronic spectra of Transition Metal Complexes*, McGraw-Hill, London.

17 Orgel, L.E. (1955) *Journal of Chemical Physics*, **23**, 1004.

18 Tanabe, Y. and Sugano, S. (1954) *Japanese Journal of Applied Physics*, **9**, 753 and 766.

19 Straughan, B.P. and Walker, S.E. (1976), *Spectroscopy*, Chapman & Hall, p. 144.

20 Gerloch, M. and Constable, E.C. (1994), *Transition Metal Chemistry*, Wiley-VCH Verlag, New York.

21 Jorgensen, C.K. (1962) *Absorption Spectra and Chemical Bonding in Complexes*, Pergamon, New York.

22 Lever, A.B.P. (1984) *Inorganic Electronic Spectroscopy*, 2nd edn, Elsevier, Amsterdam.

23 Jørgensen, C.K. (1970) *Progress in Inorganic Chemistry*, **12**, 101.

24 Duffy, J.A. (1983) *Journal of the Chemical Society, Dalton Transactions*, 1475.

25 Khan, G.A. and Hogarth, C.A. (1991), *Journal of Materials Science*, **26**, 412.

26 Pankove, J.I. (1971) Chapter 3, *Optical Pocesses in Semiconductors*, Dover Publications, New York, p. 34.

27 Tauc, J. (1972) in *Thee Optical Properties of Solids* (ed. F. Abeles), North-Holland Publisher, Amsterdam, p. 277.

28 Konx, R.S. (1963) Theory of excitons, in *Solid State Physics*, (eds F. Seitz and D. Turnbull), Academic Press, Supplement 5.

29 Körtum, G. (1969) *Reflectance Spectroscopy: Principles, Methods and Applications*, Springer-Verlag, New York.

30 Kavan, L., Stoto, T., Graetzel, M., Fitzmaurice, D. and Shlover, V. (1993) *Journal of Physical Chemistry*, **97**, 9493.

31 Weckhuysen, B.M., Verberckmoes, A.A., Debaere, J., Ooms, K., Langhans, I. and Schoonheydt, R.A. (2000) *Journal of Molecular Catalysis A–Chemical*, **151**, 115.

32 Bensalem, A., Weckhuysen, B.M. and Schoonheydt, R.A. (1997) *Journal of Physical Chemistry B*, **101**, 2824.

33 Argyle, M.D., Chen, K., Iglesia, E. and Bell, A.T. (2005) *Journal of Physical Chemistry B*, **109**, 2414.

34 Groothaert, M.H., Lievens, K., Leeman, H., Weckhuysen, B.M. and Schoonheydt, R.A. (2003) *Journal of Catalysis*, **220**, 500.

35 Weckhuysen, B.M. (2002) *Chemical Communications*, 97.

36 Jeziorowski, H. and Knözinger, H. (1977) *Chemical Physics Letters*, **51**, 519.

37 Garbowski, E.D. and Mirodatos, C. (1982) *Journal of Physical Chemistry*, **86**, 97.

38 Skuja, L. (1998) *Journal of Non-Crystalline Solids* and references therein, **239**, 16.

39 Inaki, Y., Yoshida, H., Yoshida, T. and Hattori, T., (2002) *The Journal of Physical Chemistry B*, **106**, 9098.

40 Corma, A. and Iborra, S. (2006) *Advances in Catalysis*, **49**, 239.

41 Coluccia, S., Tench, A.J. and Segall, R.L. (1983) *Journal of the Chemical Society–Faraday Transactions I*, **79**, 1881.

42 Coluccia, S., Baricco, M., Marchese, L., Martra, G. and Zecchina, A. (1993) *Spectrochimica Acta*, **49A**, 1289.

43 Nelson, R.L. and Hale, J.W. (1971) *Discussions of the Faraday Society*, **52**, 77.

44 Zecchina, A., Lofthouse, M.G. and Stone, F.S. (1975) *Journal of the Chemical Society–Faraday Transactions I*, **71**, 1476.

45 Zecchina, A. and Stone, F.S. (1976) *Journal of the Chemical Society–Faraday Transactions I*, **72**, 2364.

46 Garrone, E., Zecchina, A. and Stone, F.S. (1980) *Philosophical Magazine Part B*, **42**, 683.

47 Mellor, I.M., Burrows, A., Coluccia, S., Hargreaves, J.S.J., Joyner, R.W., Kiely, C.J., Martra, G., Stockenhuber, M. and Tang, W.M. (2005) *Journal of Catalysis*, **234**, 14.

48 Levine, J.D. and Mark, P. (1966) *Physical Review*, **144**, 751.

49 Carp, O., Huisman, C.L. and Reller, A. (2004) *Progress in Solid State Chemistry*, **32**, 33.

50 Serpone, N. and Pelizzetti, E. (1989) *Photocatalysis Fundamentals and Applications*, Wiley Interscience, New York.

51 Koffyberg, F.P., Dwight, K. and Wold, A. (1979) *Solid State Communications*, **30**, 433.

52 Carcia, P.F. and McCarron, E.M. (1987) *Thin Solid Films*, **155**, 53.

53 Pankove, J.I. (1975) Chapter 3, *Optical Processes in Semiconductors*, Dover Publications, New York, p. 38.

54 Serpone, N., Lawless, D. and Khairutdinov, R. (1995) *Journal of Physical Chemistry*, **99**, 16654.

55 Anpo, M. and Tackeuchi, M. (2003) *Journal of Catalysis*, **216**, 505.

56 Thompson, T.L. and Yates, T. (2006) *Chemical Reviews*, **106**, 4428.

57 Brus, L. (1986) *Journal of Physical Chemistry*, **90**, 2555.

58 Alivisatos, A.P. (1996) *Science*, **271**, 933.

59 Liu, L. and Bard, A. (1989) *Journal of Physical Chemistry*, **93**, 3232.

60 Fournier, M., Louis, C., Che, M., Chaquin, P. and Masure, D. (1989) *Journal of Catalysis*, **119**, 400.

61 Masure, D., Chaquin, P., Louis, C., Che, M. and Fournier, M. (1989) *Journal of Catalysis*, **119**, 415.

62 Barton, D.G., Shtein, M., Wilson, R.D., Soled, S.L. and Iglesia, E. (1999) *Journal of Physical Chemistry B*, **103**, 630.

63 Wachs, I.E., Kim, T. and Ross, E.I. (2006) *Catalysis Today*, **116**, 162.

64 Tian, H., Ross, E.I. and Wachs, I.E. (2006) *Journal of Physical Chemistry B*, **110**, 9593.

65 Morey, M., Davidson, A., Eckert, H. and Stuckey, G. (1996) *Chemistry of Materials*, **8**, 486.

66 Weckhuysen, B.M., Wachs, I.E. and Schoonheydt, R.A. (1996) *Chemical Reviews*, **96**, 486.

67 Groppo, E., Lamberti, C., Bordiga, S., Spoto, G. and Zecchina, A. (2005) *Chemical Reviews*, **105**, 115.

68 Centi, G., Perathoner, S., Trifirò, F., Aboukais, A., Sissi, C.F. and Guelton, M. (1992) *Journal of Physical Chemistry*, **96**, 2617.

69 Le Noc, N., Trong On, D., Solomykina, S., Echchahed, B., Béland, F., Cartier, C. and Bonneviot, L. (1996) *Studies in Surface Science and Catalysis*, **101**, 611.

70 Bordiga, S., Buzzoni, R., Geobaldo, F., Lamberti, C., Giamello, E., Zecchina, A., Leofanti, G., Petrini, G., Tozzola, G. and Vlaic, G. (1996) *Journal of Catalysis*, **158**, 486.

71 Tabacchi, G., Gianotti, E., Fois, E., Martra, G., Marchese, L., Coluccia, S. and Gamba, A. (2007) *Journal of Physics C–Solid State Physics*, **111**, 4946.

72 Busca, G., Martra, G. and Zecchina, A. (2000) *Catalysis Today*, **56**, 361.

73 Boujday, S., Lambert, J.-F. and Che, M. (2003) *The Journal of Physical Chemistry B*, **107**, 651.

74 Bonneviot, L., Legendre, O., Kermarec, M., Oliver, D. and Che, M. (1990) *Journal of Colloid and Interface Science*, **134**, 534.

75 Lambert, J.-F., Hoogland, M. and Che, M. (1997) *The Journal of Physical Chemistry B*, **101**, 10347.

76 Spielbauer, D., Zeilinger, H. and Knözinger, H. (1993) *Langmuir*, **9**, 460.

77 Schoonheydt, R.A., De Vos, R., Pegrims, J. and Leeman, H. (1989) *Studies in Surface Science and Catalysis*, **49A**, 559.

78 Lakowicz, J.R. (1999) *Principles of Fluorescence Spectroscopy*, 2nd edn, Kluwer Academic/Plenum Publishers.

79 Anpo, M. and Kubokawa, Y. (1980) *Journal of the Chemical Society–Faraday Transactions I*, **76**, 1014.

80 Coluccia, S., Deane, M. and Tench, A.J. (1977) Proceedings of the 6th International Congress on Catalysis, London 1976- Ed. The Chem Soc., London, **1**, 171.

81 Coluccia, S., Deane, M. and Tench, A.J. (1978) *Journal of the Chemical Society–Faraday Transactions I*, **74**, 2913.

82 Coluccia, S. and Borello, E. (1984) Proceedings of the 8th International Congress on Catalysis, Berlin 191984- Ed DECHEMA, **3**, 69.

83 Coluccia S. (1985) *Adsorption and Catalysis on Oxides Surfaces* (eds M. Che and G.C. Bond), Elsevier, Amsterdam, p. 59.

84 Kibblewhite, J.F.J. and Tench, A.J. (1974) *Journal of the Chemical Society–Faraday Transactions I*, **70**, 72.

85 Anpo, M., Yamada, Y., Kubokawa, Y., Coluccia, S., Zecchina, A. and Che, M. (1988) *Journal of the Chemical Society–Faraday Transactions I*, **84**, 751.

86 Anpo, M., Yamada, Y., Coluccia, S., Zecchina, A. and Che, M. (1989) *Journal of the Chemical Society–Faraday Transactions I*, **85**, 609.

87 Chizallet, C., Costentin, G., Krafft, J., Lauron-Pernot, H. and Che, M. (2006) *ChemPhysChem*, **7**, 904.

88 Coluccia, S., Hemidy, J.F. and Tench, A.J. (1978) *Journal of the Chemical Society–Faraday Transactions I*, **74**, 2763.

89 Matsuoka, M. and Anpo, M. (2003) *Journal of Photochemistry and Photobiology A: Chemistry*, **3**, 225.

90 Dzwigaj, S., Matsuoka, M., Anpo, M. and Che, M. (2001) *Catalysis Letters*, **72**, 211.

91 Dzwigaj, S., Matsuoka, M., Anpo, M. and Che, M. (2006) *Microporous and Mesoporous Materials*, **93**, 248.

92 Shiraishi, Y., Morishita, M., Teshima, Y. and Hirai, T. (2006) *The Journal of Physical Chemistry B*, **110**, 6587.

93 Dzwigaj, S., Matsuoka, M., Anpo, M. and Che, M. (2000) *The Journal of Physical Chemistry B*, **104**, 6012.

94 Anpo, M., Kondo, M., Coluccia, S., Louis, C. and Che, M. (1989) *Journal of the American Chemical Society*, **111**, 8791.

95 Higashimoto, S., Tsumura, R., Zhang, S.G., Matsuoka, M., Yamashita, H., Louis, C., Che, M. and Anpo, M. (2000) *Chemistry Letters*, **29**, 408.

96 Anpo, M., Takahashi, I. and Kubokawa, Y. (1982) *Journal of Physical Chemistry*, **86**, 1.

97 Hazenkamp, M.F. and Blasse, G. (1992) *Journal of Physical Chemistry*, **96**, 3442.

98 Zhang, S.G., Ichihashi, Y., Yamashita, H., Tatsumi, T. and Anpo, M. (1996) *Chemistry Letters*, **10**, 895.

99 Lamberti, C., Bordiga, S., Arduino, D., Zecchina, A., Geobaldo, F., Spanò, G., Genoni, F., Petrini, G., Carati, A., Villain, F. and Vlaic, G. (1998) *Journal of Physical Chemistry B*, **102**, 6382.

100 Marchese, L., Maschmeyer, T., Gianotti, E., Coluccia, S. and Thomas, J.M. (1997) *Journal of Physical Chemistry B*, **101**, 8836.

101 Marchese, L., Gianotti, E., Dellarocca, V., Maschmeyer, T., Rey, F., Coluccia, S. and Thomas, J.M. (1999) *Physical Chemistry Chemical Physics*, **1**, 585.

102 Dedecek, J., Sobalik, Z., Tvaruzkova, Z., Kaucky, D. and Wichterlova, B. (1995) *Journal of Physical Chemistry*, **99**, 16327.

103 Dedecek, J. and Wichterlova, B. (1994) *Journal of Physical Chemistry*, **98**, 5721.

104 Barrie, J.D., Dunn, B., Hollingsworth, G. and Zink, J.I. (1989) *Journal of Physical Chemistry*, **93**, 3958.

105 Yamashita, H., Matsuoka, M., Tsuji, K., Shioya, Y., Anpo, M. and Che, M. (1996) *Journal of Physical Chemistry*, **100**, 397.

106 Anpo, M., Sunamoto, M. and Che, M. (1989) *Journal of Physical Chemistry*, **93**, 1187.

107 Patterson, H.H., Cheng, J., Despres, S., Sunamoto, M. and Anpo, M. (1991) *Journal of Physical Chemistry*, **95**, 8813.

108 Iwamoto, M., Furukawa, H., Matsukami, K., Takenaka, T. and Kagawa, S. (1983) *Journal of the American Chemical Society*, **105**, 3719.

109 Centi, G. (1996) *Applied Catalysis A: General*, **147**, 267.

110 Blasco, T. and Lopez Nieto, J.M. (1997) *Applied Catalysis A: General*, **157**, 117.

111 Garcia, H., Lopez Nieto, J.M., Palomares, E. and Solsona, B. (2000) *Catalysis Letters*, **69**, 217.

112 Gil-Llambias, F.J., Escudey-Castro, A.M. and Santos-Blanco, J. (1983) *Journal of Catalysis*, **83**, 225.

113 Dzwigaj, S., Matsuoka, M., Franck, R., Anpo, M. and Che, M. (1998) *Journal of Physical Chemistry B*, **102**, 6309.

114 Gillespie, R.J. (1972) *Molecular Geometry*, Van Nostrand-Reinhold, London.

115 Hazenkamp, M.F., Strijbosch, A.W.P.M. and Blasse, G. (1992) *Journal of Solid State Chemistry*, **97**, 115.

116 Marion, M.C., Garbowski, E. and Primet, M. (1990) *Journal of the Chemical Society–Faraday Transactions*, **86**, 3027.

3
The Use of Infrared Spectroscopic Methods in the Field of Heterogeneous Catalysis by Metal Oxides

Guido Busca

3.1
Introduction

3.1.1
The Evolution of Vibrational Spectroscopies

The fundamentals of transmission/absorption IR spectroscopy were developed in the last decades of the nineteenth century and in the very first years of the twentieth century [1], and, as a consequence, IR spectroscopy rapidly became one of the most widely used techniques for chemical analysis.

Subsequently, it has been recognized that other IR techniques (reflection, emission and photothermal techniques) can also be applied, and that IR spectroscopy only gives partial information on the vibrational structure of most polyatomic species. In fact, selection rules apply to IR light absorption phenomena, so that only vibrational modes that are associated with changes of the molecular dipolar moment can be directly excited.

Another way to obtain part or all the vibrational spectrum of a chemical species is to look at the inelastic scattering of beams other than IR radiation. In other words, when such beams are scattered by a polyatomic species, part of the photons (or particles) lose (or gain) energy by interaction with the vibrational states of the chemical species. The vibrational spectrum is obtained by measuring the difference between the energies of the incident beam and of its small fraction that is inelastically scattered. If the incident radiation is relatively high energy such as UV, visible or near-infrared (NIR) photons we are dealing with Raman spectroscopy, based on the so-called Raman effect, recognized by C.V. Raman in 1928 [2]. Owing to the different selection rules for the Raman effect, the Raman-active modes do not correspond to IR-active modes in centrosymmetric chemical species, and (generally) only partly correspond for non-centrosymmetric species. Thus, Raman spectroscopy is in most cases almost complementary to IR spectroscopy.

Alternatively the entire, or part of the, vibrational spectra of polyatomic chemical species can be obtained by looking at the inelastic scattering of particles other than

Metal Oxide Catalysis. Edited by S. David Jackson and Justin S. J. Hargreaves

ISBN: 978-3-527-31815-5

photons: they can be electrons, and the corresponding techniques are Electron Energy Loss Spectroscopy (EELS) or Inelastic Electron Tunnelling Spectroscopy (IETS), following two different experimental setups. The incident particles can also be neutrons, which gives rise to Inelastic Neutron Scattering Spectroscopy (INS), or atoms, giving rise to Atom Scattering Spectroscopy (ASS). These techniques were developed by physicists, particularly in the 1960s, and have found application mainly in the field of surface chemistry and physics. A further new technique, vibrational Sum Frequency Generation Spectroscopy (SFG) has been recently developed and applied to gas–solid and liquid–solid interfaces on metal catalysts [3] and on oxide surfaces [4].

3.1.2 Application of IR Spectroscopy to the Surface Chemistry of Oxide-Based Materials: a Historical Perspective

It seems that the very first application of IR spectroscopy to the surfaces of oxide materials was reported in 1937 by Buswell and coworkers [5], concerning water adsorbed in montmorillonite. In the 1940s and 1950s, Terenin and coworkers at Leningrad University showed that this technique can be applied widely to molecules adsorbed on solid materials, including metal oxides [6]. In fact most metal oxides only absorb radiation in the low-energy IR region (below 1000 cm^{-1}) while most gaseous or volatile molecules also absorb strongly in the higher energy IR region (4000–1000 cm^{-1}). However, adsorption on solids causes vibrational perturbation of the adsorbate (if adsorbed as such) or can produce a chemical reaction, and the spectroscopic detection and assignment of these phenomena gives information on the adsorption or interaction modes. Ultimately, data are obtained both on the chemical structure of the metal oxide surface and on the perturbation mode of the adsorbate.

The application of IR spectroscopy to catalysis and surface chemistry was later developed in the fifties by Eischens and coworkers at Texaco laboratories (Beacon, New York) in the USA [7] and, almost simultaneously, by Sheppard and Yates at Cambridge University in the UK [8]. Mapes and Eischens published the spectra of ammonia chemisorbed on a silica-alumina cracking catalyst in 1954 [6], showing the presence of Lewis acid sites and also the likely presence of Brønsted acid sites. Eischens, Francis and Pliskin published the IR spectra of carbon monoxide adsorbed on nickel and its oxide in 1956 [9]. Later they presented the results of an IR study of the catalyzed oxidation of CO on nickel at the First International Congress on Catalysis, held in Philadelphia in 1956 [10]. Eischens and Pliskin also published a quite extensive review on the subject of "Infrared spectra of adsorbed molecules" in *Advances in Catalysis* in 1958, where data on hydrocarbons, CO, ammonia and water adsorbed on metals, oxides and minerals were reviewed [11]. These papers evidence clearly the two tendencies observed in subsequent spectroscopic research in the field of catalysis. They are the use of probes to test the surface chemistry of solids and the use of spectroscopy to reveal the mechanism of the surface reactions. They used an *in situ* cell where the catalyst sample was

deposited on a fluorite disk, with fluorite windows and a tungsten-wound quartz furnace, connected to a gas-manipulation apparatus.

The industrial interest in IR spectroscopy in catalysis is demonstrated by the work of Peri and coworkers at Amoco. Peri first published IR studies on the surface properties of alumina in 1960 [12] and performed several studies on alumina, silica and silica-alumina. Peri also published a useful summary of the use of IR spectroscopy in catalysis research in 1984 [13].

In the 1960s and 1970s several different groups investigated the IR spectra of adsorbed probe molecules for the characterization of the surface of metals and oxide catalysts. However, relatively few studies used IR spectra for the study of reaction mechanisms. Among the best results, Kokes and coworkers used IR spectroscopy to investigate the conversion and hydrogenation of olefins on zinc oxide. In particular these authors identified an anti π-allyl species as the intermediate in the double-bond isomerization of 1-butene to 2-butene [14, 15]. In the 1980s, IR techniques underwent a great improvement with the application of Fourier transform instruments [16], first commercialized at the end of the 1970s.

Since the end of the 1970s, IR cells have been developed for *in situ* experiments in flow conditions, with the simultaneous detection of the reaction products and measures of conversion and selectivities [17]. The concept of experiments under *dynamic conditions*, developed by Tamaru [18], has also been very interesting, although it has not found widespread application. More recently this approach has evolved in the concept of *Operando Spectroscopy* [19, 20], with the possibility of applying several spectroscopic techniques simultaneously to the same catalyst sample in working conditions being realized [21]. Among other recent developments, the coupling of IR spectroscopy with different theoretical calculations, the use of IR spectroscopic techniques at liquid helium temperature, or at very low temperature [22], and the development of the reflection technique on oxide layers generated over metal monocrystals [23] have attracted particular interest.

3.2
Experimental Techniques

3.2.1
The Detection of the Vibrational Spectrum of a Polyatomic Chemical Species: IR and Raman Spectroscopies

Any chemical species containing more than one atom, namely polyatomic molecules, molecular ions, molecular radicals and any crystal, can be described in terms of atomic positions, bond lengths and bond angles. However, it was recognized long ago that, in fact, any atom vibrates around its equilibrium position in any condition, giving rise to more or less complex vibrational modes. At absolute zero temperature, all polyatomic chemical species lie at the vibrational ground state. However, they can undergo vibrational excitation and so occupy higher energy vibrational states. The energy difference between nearest vibrational states lie in

the medium and far IR ranges, generally defined by the wavenumber limits 4000–400 cm^{-1} (0.496 > E > 0.0496 eV, medium IR) and 400–10 cm^{-1} (0.0496 > E > 1.24 10^{-3} eV, far-infrared, FIR).

The simplest way to cause vibrational excitation is to allow the chemical species to absorb an energy quantum from an electromagnetic radiation of an appropriate energy, so giving rise to a vibrational transition from the ground state to an excited vibrational state. When electromagnetic radiation with intensity I_0 is incident on a sample, the light may (essentially) be absorbed, reflected or transmitted. From the conservation of energy it follows that

$$I_0 = I_R + I_T + I_A \tag{3.1}$$

where I_0, I_R, I_T and I_A are the intensities of the incident, reflected, transmitted and absorbed radiation, respectively. By dividing Equation 3.1 by I_0, we obtain:

$$R + T + \alpha = 1 \tag{3.2}$$

where $R = I_R / I_0$, $T = I_T / I_0$ and $\alpha = I_A / I_0$ are the apparent reflectance, transmittance and absorptance, respectively, while

$$A = -\log_{10} I_T / I_0 \tag{3.3}$$

is the absorbance. All these units depend, obviously, on the particular radiation used, that is, its energy, E, its frequency, ν, its wavelength, λ, or its wavenumber, $\bar{\nu}$:

$$E = h\nu = hc/\lambda = hc\bar{\nu} \tag{3.4}$$

where h is the Planck constant and c is the velocity of light in a vacuum.

The analysis of the quanta that are actually absorbed by a polyatomic chemical species and those that are not absorbed (so are transmitted) gives information on the vibrational structure of these species and, consequently, on its chemical and geometric structure. This is the transmission/absorption IR technique. However, *selection rules* apply to such a phenomenon. They are simplified as follows:

$$\Delta\nu = \pm 1 \tag{3.5}$$

$$\left(\frac{\partial \mu}{\partial Q}\right)_0 \neq 0 \tag{3.6}$$

On the other hand, the absorbance at a particular wavelength also depends upon the population of the corresponding vibrational states. According to Boltzmann's law:

$$N_i / N_0 = g_i / g_0 \, e^{-\Delta E / kT} \tag{3.7}$$

where N_i is the state population, g_i is the state multiplicity, ΔE is the energy difference between the states 0 and *i*, *T* the absolute temperature and *k* the Boltzmann constant. ΔE values for fundamental vibrational transitions fall in the IR region. The population of the first excited state is very small at room temperature and much lower than the population of the ground state even at 1000 K. This means that only transitions originating from the ground state can be ordinarily excited at ambient, or relatively low, temperature.

Equation 3.5, where ν is the vibrational quantum number, means that only transitions between nearest vibrational states can directly occur in the case of the harmonic oscillator. This means that the IR spectrum is generally mostly constituted by *fundamental transitions*, that is, those associated with excitation from the fundamental state to the first excited state. This condition, however, is relaxed in the case of anharmonic oscillators, so that not only fundamental transitions but also *overtone and combination modes* (also called the *harmonics*, i.e. modes associated with the excitation from the fundamental state to a second or third excited state) can be sometimes observed, although they are usually weak.

Equation 3.6 indicates that only vibrational modes that are associated with a change in the dipole moment μ of the molecule between the extremes of the atomic displacements (*Q* is the normal coordinate) different from zero (i.e. the "polar" modes) can be directly excited.

In the solid state, the polar phonons (those that are IR active) split into two components, the transverse optical mode (TO) and the longitudinal optical mode (LO). This *TO/LO splitting* occurs because the electric field associated with the transverse wave = 0 while that associated with the longitudinal wave is $\neq 0$. The coupling of these modes with the electric fields associated with the vibration gives rise to $\nu_{LO} > \nu_{TO}$. This factor is relevant in relation to the shape and interpretation of the IR spectra of solid materials and will be further considered below.

According to the Beer–Lambert law:

$$A = \varepsilon c l \tag{3.8}$$

the absorbance linearly depends on the molar concentration of the absorbing species *c*, through the molar absorption coefficient ε and the sample pathlength *l*. This relation (rigorously valid only in non-scattering media) is the basis for quantitative analysis performed through IR spectroscopy. The range of the Beer–Lambert law in FTIR spectrometry may be extended [24].

As is well known, the selection rules for Raman spectroscopy may be simplified as follows:

$$\Delta\nu = \pm 1 \tag{3.9}$$

$$\left(\frac{\partial\alpha}{\partial Q}\right)_0 \neq 0 \tag{3.10}$$

which means that in Raman spectroscopy also, only transitions between nearest levels and associated with changes in the *polarizability* α upon motion are allowed for a harmonic oscillator. The first selection rule is relaxed for anharmonic oscillators. Group theory shows that for centrosymmetric chemical species, Raman-active modes are IR inactive, and vice versa. This is the so-called *mutual exclusion rule*. Other modes can be both IR and Raman inactive. For non-centrosymmetric molecular species, modes also occur that are both IR and Raman active. Thus, Raman spectroscopy is in most cases almost complementary to infrared spectroscopy.

Some chemical species are *vibrationally silent*, e.g. monatomic noble gases or *IR inactive*, e.g. homomolecular diatomic molecules (H_2, N_2, O_2, F_2, Cl_2, etc.)

3.2.2 The Transmission/Absorption IR Technique

This technique was originally applied by the pioneers of IR spectroscopy and is still perhaps the most widely used today. However, the application of this technique to solids involves problems of sample form and preparation. This technique can be successfully applied to powdered insulating or semiconducting solids, although problems arise from radiation scattering.

When radiation is incident on a non-absorbing layer consisting of N particles per unit volume, its intensity decreases exponentially with the sample thickness x following the law:

$$I_T = I_0 e^{-\varphi x} = I_0 e^{-N\sigma x} \tag{3.11}$$

so that an apparent absorbance, A', can be defined for an absorbing and scattering medium:

$$A' = -\log_{10} I_T / I_0 = 0.43N\sigma x = 0.43N(\varepsilon' + s)x = A + 0.43Nsx = A + S' \tag{3.12}$$

where φ is the linear attenuation coefficient and σ is the linear attenuation coefficient of one particle. σ contains a component due to absorption, ε', and a component due to scattering, s. So the apparent absorbance is composed of the true absorbance A superimposed upon the component due to the light scattering S'. This simplified approach is similar to that given by Henry [25] who proposed the following expression for the component dependent on scattering:

$$S' = kxd(n-1)^2 / \lambda^2 \tag{3.13}$$

where k is a constant independent of λ but dependent on the particle arrangement, d is the particle diameter and n is the refractive index of the material. On the other hand, according to the Rayleigh theory, S' depends on the third power of the particle diameter (and so linearly on the particle volume) and on the fourth power of the radiation frequency, ν. The effect of scattering on the IR transmission spectra

of powder samples has been studied by Duykaerts [26] who showed that if the particle diameter is sufficiently small (considerably smaller than the IR wavelength), the scattering of the IR radiation is very small. Thus, finally, the apparent absorbance of a layer of a powder depends on its own absorptivity, on the disk thickness and density, on the particle size and on the wavelength.

In practice, to obtain a good spectrum of the fundamental vibrations of an insulating material with the transmission/absorption IR technique, it is necessary to prepare a layer appropriately diluted and sufficiently thin. To do this, the most widely practiced technique involves KBr pressed-discs. KBr is a readily available powdered material which does not absorb in the medium IR region (down to near $400\,cm^{-1}$, but cuts out the FIR). It can be easily mixed homogeneously with the powder to be investigated, and pressed, thus obtaining "diluted" self-supporting disks which are very useful for IR transmission. The spectra so obtained give rise to a baseline due to scattering, that gives very high transmission in the low-frequency region (down to the cut-off near $400\,cm^{-1}$ due to absorption by KBr itself), but generally still sufficient transmission in the higher frequency medium IR region, owing to the wavelength dependence of scattering. Other materials (for example CsI) can be used to produce similar pressed discs, with cut-off limits at even lower frequencies. Alternatively, the powders can be simply deposited in the form of a thin layer on a disk of a transmitting medium.

Because KBr and the other alkali halides absorb in the FIR region, in this region other binding materials must be used. The preparation of disks with polyethylene (which is transparent in most of the FIR region) is the most commonly applied technique. However, in this range the scattering is very low because of the long wavelength involved, so that it is sometimes preferable to simply deposit the powder on a disk of a transmitting material using a solvent that later evaporates.

Another technique, used mostly in the past, is to mull the powder with liquids, such as liquid paraffin (nujol) and perhalogenated organic liquids. The powder is mixed to make a paste from which a layer is formed. Obviously, absorptions from the mulling liquid (e.g. in the C–H stretching and deformation regions for paraffin oils, or C–X modes for halocarbons) also occur and obscure some spectral regions.

3.2.3
The Reflection Techniques

When incident radiation interacts (from the vacuum) with a flat surface, the "reflectance" of the parallel and perpendicular polarized light (with respect to the incidence plane), $R_{\|}$ and $R_{\perp}$, are given by the relations below:

$$R_{\|} = \left| \frac{\varepsilon \cos\theta - \sqrt{\varepsilon - \sin^2\theta}}{\varepsilon \cos\theta + \sqrt{\varepsilon - \sin^2\theta}} \right|^2 \tag{3.14}$$

$$R_{\perp} = \left| \frac{\cos\theta - \sqrt{\varepsilon - \sin^2\theta}}{\cos\theta + \sqrt{\varepsilon - \sin^2\theta}} \right|^2 \tag{3.15}$$

where ε is the complex dielectric constant of the material (assumed to be isotropic) and θ is the incidence angle. From these relations it follows that the reflected light is mainly polarized perpendicular (in fact $R_\perp$ is large while $R_\parallel$ has a minimum for $0 < \theta < 90$). When $\theta = 0$, converting $\varepsilon = (n - ik)^2$, we obtain:

$$R = \frac{(n-1)^2 + k^2}{(n+1)^2 + k^2} \tag{3.16}$$

where n and k are the real and imaginary parts of the absolute index of refraction. For conducting materials, such as metals, the refraction index is totally imaginary, that means that $n = 0$ so that $R = 1$ at any frequency, and the radiation is totally reflected. This is a case of "total" or "specular" reflection.

For insulating or weakly semiconducting materials, like most inorganic compounds, $k = 0$ (i.e. the index of refraction is real) and n varies little in the IR spectrum except between the absorption frequencies, that is, for $\nu > \nu_{LO}$ and $\nu < \nu_{TO}$. This means that outside of the latter skeletal region, monocrystal surfaces of inorganic compounds only weakly reflect the radiation, and the smaller the value of R the greater the value of n. So all light is essentially transmitted, or, better, refracted. However, for $\nu_{LO} > \nu > \nu_{TO}$, the index of refraction is imaginary and $k > 0$ goes through a maximum. This means that near the skeletal absorption region, R again becomes $\cong 1$, that is, the skeletal vibrations of inorganic compounds give rise not only to absorbed radiation in transmission experiments but also to reflected radiation in the reflection experiments (reststrahlen effect). Thus, the specular reflectance for insulating materials, both in the form of monocrystals and in the form of sintered pellets, is frequently the basis for the best determination of the skeletal spectrum, as far as the IR active modes are concerned.

In Figure 3.1, the reflectance spectrum of a MgO monocrystal is reported and is compared with the transmission/ absorption spectrum of a MgO powder. MgO (periclase) has the rock-salt structure: as the other rock-salt type solids, MgO is Raman-silent (as far as the fundamentals are concerned, see below) and only shows one IR-active fundamental mode. The reflection by the MgO monocrystal, is strong between two limits. The upper limit is the so-called LO while the lower limit is the TO.

The TO quoted for MgO at 401 cm^{-1} (see Figure 3.1a) corresponds to the lower frequency limit of the reflectance band while the LO corresponds to the higher energy limit of the reflectance, and is quoted at 718 cm^{-1} for MgO (see Figure 3.1a). For $\nu_{LO} > \nu > \nu_{TO}$ the reflectance is strong and almost constant, while out of these limits the reflectance is very small. The transmission/absorption IR spectrum of the MgO powder is influenced by the TO/LO splitting. In fact it shows the maximum slightly above ν_{TO} (407 cm^{-1} in our spectrum of a polyethylene disk) and a shoulder near ν_{LO}.

Total reflection of IR incident light at any wavelength from a surface can occur in two cases: (i) if the beam arises from a transmitting medium and is incident on the surface of a conducting material; (ii) if the beam arises and is incident within a transmitting medium, but the medium from which the beam arises has

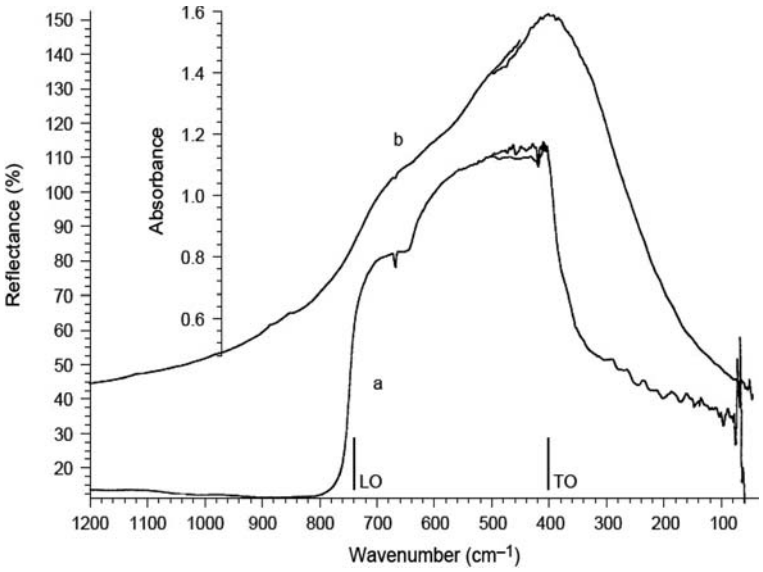

Figure 3.1 (a) FTIR reflectance spectrum of a MgO monocrystal (incidence angle 26.5°, face [001]). (b) FTIR and FTFIR absorption / transmission spectra of MgO powder (reprinted with permission from G. Busca and C. Resini, "Vibrational spectroscopy for the analysis of geological and inorganic materials", in *Encyclopedia of Analytical Chemistry*, Robert A. Meyers ed., Wiley, Chichester, 2000, pp. 10984–11020).

higher refraction index than the other, and the incidence angle is greater than the limit for refraction.

In the first case, it has been recognized that if molecules are adsorbed on the surface of a metal, only part of the grazing incident radiation is reflected, part being absorbed by the adsorbed species. This absorption is greatly increased if the incident radiation is polarized perpendicular to the metal surface. This is the basis of so-called Infrared Reflection Absorption Spectroscopy (IRRAS) [27], which is applied widely to surface studies on metal surfaces. In these conditions, an additional selection rule applies:

$$\left(\frac{\partial \mu_{\perp}}{\partial Q}\right)_0 \neq 0 \tag{3.17}$$

which means that only the adsorbate vibrations associated with a change in the dipole moment perpendicular to the crystal surface are detectable. The total reflection technique can be applied to detect the growth of oxidic layers over metal surfaces (i.e. the skeletal bands of the oxide layers) and this is a widely applied technique in corrosion and electrochemical research, colloid chemistry and coating technology.

The second case refers to the so-called Internal Reflection Spectroscopy, that is used in the so-called Attenuated Multiple Total Internal Reflection technique

(ATR) [28], where an absorbing layer is deposited on one or two external surfaces of a prism. The light penetrates the prism from a free surface and is multiply reflected by the other faces. During the reflection, part of the light penetrates the external layer and is absorbed by it. Thus, in the case of the internal reflection techniques the reflectance is given by the following relation:

$$R = 1 - A = 1 - \varepsilon cd \tag{3.18}$$

where d is the thickness of the layer penetrated by the radiation, c the molar concentration of the absorbing species in that layer and ε the molar absorption coefficient of those species. An interesting variation of this technique is the so-called Cylindrical Internal Reflection technique (CIR), invented by Wilks [29]. In this case, for example, a hydrogel slurry can be analyzed using cylindrical crystals immersed in the medium so that IR radiation is multiply transmitted and reflected at the internal surface. This technique could be successfully applied to heterogeneous catalytic systems at the water–solid interface, or in stages of catalyst preparation (for example zeolite syntheses).

Another interesting variant of the total reflection technique is the so-called Surface Electromagnetic Wave Spectroscopy (SEWS), which consists of the generation of a surface plasmon on a substrate by frustrated total internal reflection in a prism located a few microns from the surface. This plasmon is decoupled by a second prism. Some interesting data relating to surface modes on alumina have been reported with this technique [30].

3.2.4
The Diffuse Reflectance Technique

In recent years, the use of IR spectroscopy of powders in the diffuse reflectance (DR) mode has grown strongly, assisted by the commercialization of appropriate attachments and cells. This technique is particularly attractive because it does not require much effort in sample preparation (the powder is simply deposited in a sample holder). Moreover, this technique, in contrast to the above transmission technique, takes advantage of light scattering, and hence is very useful for studies of surface chemistry.

This technique requires the collection, with appropriate collecting mirrors (such as an integrating sphere), of the radiation scattered by the sample. Obviously, most photons are essentially simply scattered but those corresponding to the energies of vibrational transitions are potentially absorbed. The interpretation of the DR spectra is based on the phenomenological theory of Kubelka and Munk [31, 32] who defined the so-called Kubelka–Munk (KM) function as follows:

$$f(R_\infty) = (1 - R_\infty)^2 / 2R_\infty = k/s \tag{3.19}$$

where R_∞ is the reflectance of an "infinitely thick" layer and may in practice be substituted by $R_\infty - R'_\infty$ (i.e. by the reflectance spectrum from which the reflectance

of a reference transparent material such as KBr has been subtracted). The KM function depends linearly on the absorption coefficient k (which can be expressed as $k = 2.303\varepsilon c$, where ε is the molar absorption coefficient and c is the molar concentration) and inversely on the scattering factor s. Obviously, the greater the absorption coefficient and the smaller the scattering, the higher the KM function. An approximation of the KM function is that k is treated as a variable but s is assumed constant. This is not true in the vicinity of strong absorptions.

More realistic and complex theories consistent with the quite complex nature of the phenomena involved in the DR of light were developed later. Experimental studies have shown that this technique is affected by particle size, granulometric distribution and the refractive index of the particles, which has an important role when the particle size is near the wavelength of the IR radiation. Diffuse reflectance Fourier transform (DRIFT) studies in the FIR region allow detection of the skeletal spectra of materials, such as mixed oxide catalysts, pigments and metal halides.

One important practical problem in DR measurement is the need to cancel the specular reflectance from the front surface of the sample, which generates "negative" bands in the DRIFT spectrum, so causing apparent shifts in the true absorption bands. This is achieved by using appropriate cell designs in commercial DRIFT attachments.

3.2.5 The Emission Technique

According to Kirchoff's law:

$$\varepsilon = I_{em}/I_b = \alpha \tag{3.20}$$

the emittance, ε, (i.e. the ratio of the light emitted by the sample I_{em} with respect to that emitted by a black-body at the same temperature, I_b) is equal to the absorbance, α, of the sample. The emissivity is proportional to the fourth power of the temperature difference between the emitting sample and the detector (Stefan's law). This implies that emissivity is sufficiently strong at relatively high temperatures to give a good signal-to-noise ratio in a large part of the IR spectrum. In fact, the blackbody emission at $T < 1000\,K$ shows its maximum in the medium IR region.

A number of problems arise in connection with the use of emission IR spectroscopy (IRES). One of them arises from the existence of temperature gradients, which can cause self-absorption of the emitted radiation by the colder outer parts of the sample itself; another is concerned with the selective reflection that occurs in the vicinity of strong absorption bands. This reduces the absorptance and hence the emittance. Moreover, perturbations can be created by reflections and emission by the cell elements. These problems, however, can in part be overcome so that IR emission spectra can be successfully recorded and are widely used, for example, in the fields of polymer and corrosion science and mineralogy. Some uses of IRES

of metal oxides and in the field of surface chemistry and catalysis were reviewed some years ago by Sullivan and coworkers [33]. These authors reported several examples of emission spectra of oxide catalysts and of adsorbates on supported metals, and their review cites at least 11 papers concerning metal oxide surfaces. Emission studies on minerals and catalytic materials [34] and on adsorption on metal oxide gas sensors [35] have been published more recently. Some of the advantages of this technique are the very easy sample preparation and its easy applicability at high temperatures (150–400 °C). It can be applied to investigate the temperature-dependence of the radiative properties of materials including, for example, glasses.

3.2.6 Photoacoustic and Photothermal Techniques

When an IR beam is incident on a solid surface it can be absorbed in part, and this leads to its conversion into heat. If the beam is modulated (as in interferometers like those of FTIR instruments) and the solid is in contact with a gas (air, He, Ar, etc.), its conversion to heat gives rise to an acoustic signal. In fact, the periodic temperature rise so obtained causes a periodic modulation of a gas pressure in the cell, and this can be detected by a sensitive microphone. This acoustic signal will be the more intense the stronger is the absorption at a particular wavelength. Reflected and scattered light are not absorbed and hence do not cause a photoacoustic signal. However, light absorbed by the gas over the sample causes signals. This makes necessary the use of monatomic non-absorbing gases (He, Ar, etc.) The photoacoustic effect, discovered as early as in 1880 by Bell [36], could be successfully applied only after the work of Rosencwaig and Gersho [37] in 1976. The main limits of this technique are that (i) it requires a gaseous atmosphere; (ii) the cell needs a microphone close to the sample, so the sample cannot be heated and otherwise activated conveniently; (iii) the technique has an intrinsically low signal-to-noise ratio. On the other hand, the photothermal effect is much more efficient for species in the vapor phase than for bulk and surface species. Photoacoustic spectrometry (PAS) is not exactly a surface spectroscopy, because the penetration of the thermal effect is always significant. The extent of this depends on the modulation frequency, which varies with wavenumber in a FT spectrum. The PAS technique has found successful application in several fields including heterogeneous catalysis, as reviewed in ref. [38].

An alternative technique is the so-called Photothermal Beam Deflection Spectroscopy [PBDS], based on the so-called “mirage” effect first reported by Boccarra and coworkers [39, 40]. In this case, the periodic temperature rise caused by the absorption of the modulated IR radiation (i.e. the photothermal effect) is detected optically because it causes periodic deflections of a laser beam passing close to the surface of the solid sample. The PBDS technique has some advantages over the PAS technique, because of its lower limits of sample dimensions, but it has disadvantages because of the critical geometric setup. Like PAS, PBDS can have advantages with respect to traditional IR technique for the detection of surface

vibrations in very opaque materials. This has resulted in its application to carbons and coals.

3.3
The Vibrational Modes of Molecular Species and of Inorganic Solids

3.3.1
"Isolated" Molecular Species

The total degrees of freedom associated with a chemical species containing N atoms are $3N$. If this chemical species is a molecule in the gaseous state, three of these degrees of freedom are associated with its translations and another three with its rotations, so that, in the most general case, six modes are associated with "external" motions (rotations and translations). The remaining $3N - 6$ degrees of freedom are associated with "internal" vibrational modes. However, if the molecule is a linear one, only two degrees of freedom are associated with rotations, because no rotational freedom exists around the molecular axis. Thus, in this particular case, the degrees of freedom associated to vibrations are $3N - 5$. A complete treatment of the principles of vibrational spectroscopy is beyond the scope of the present chapter. The methods for the determination of the number and the optical activity of the vibrational modes of molecular species can be found in several books [41–43].

The $3N - 6$ (or $3N - 5$) degrees of vibrational freedom give rise to vibrational modes that differ in their symmetry with respect to the symmetry elements of the molecular point group and in their multiplicity. The non-degenerate modes are denoted as A or B in relation to their symmetry or antisymmetry with respect to the rotation about the principal symmetry axis. Doubly degenerate modes and triply degenerate modes are denoted E and F respectively. The subscripts g and u denote modes that are symmetric or antisymmetric, respectively, with respect to the center of symmetry (if any), the superscript symbols ′ and ″ distinguish modes that are symmetric or antisymmetric, respectively, with respect to symmetry planes not containing the principal axis ($\sigma \neq \sigma_v$), while 1,2,3 subscripts are related to the symmetry with respect to other symmetry axes.

Character tables, which can be found in several vibrational spectroscopy books, allow the determination, for any molecular point group, of the species (or irreducible representations) in relation to the symmetry elements typical of that group. As further cited below, the classification in terms of a particular symmetry species determines the activity (IR activity, Raman activity, both IR and Raman activity or inactivity) of any mode.

In the gas phase, the vibrational transitions couple with the rotational ones, giving rise to *rotovibrational spectra*. The different rotovibrational contours depend on the symmetry of the vibration in relation to the symmetry of the molecule, and on the resolution of the rotational components. In some cases, the energy of the "pure" vibrational transition corresponds to the minimum of the absorption band:

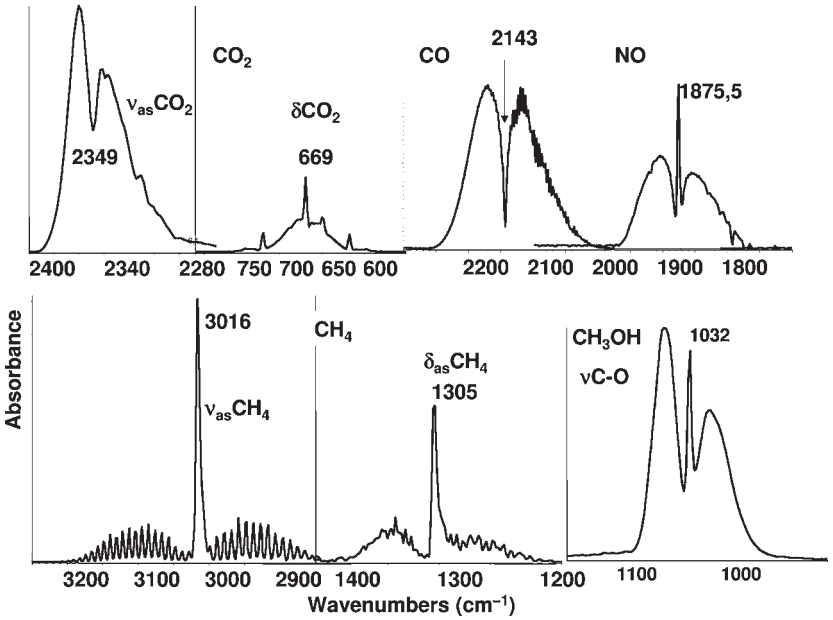

Figure 3.2 FTIR spectra of gaseous CO_2, CO, NO and CH_4 (IR active fundamental modes) and of CH_3OH (C—O stretching mode only).

in fact the "pure" vibrational transition is forbidden because the rotational quantum number does not change. This is the case for gaseous CO_2 and CO, as shown in Figure 3.2. In other cases the energy of the pure vibrational transitions must be determined using the sharp maximum in the middle. In Figure 3.3 the spectrum of gaseous CO is compared with that of CO adsorbed on different solids. The complex structure due to the rotovibrational contour present in the gas phase spectrum is essentially lost upon adsorption. When weakly adsorbed, such as on the OH group of silicalite, some rotational features may still be present (see asterisks in the figure) because the molecule can still rotate around its main axis. The CO stretching frequency for gaseous CO (2143 cm^{-1}) shifts a little down in the liquid phase (2137 cm^{-1}) where the rotational structure has disappeared. Liquid CO is frequently observed upon adsorption on solids at low temperature (such as on silicalite in the figure). Relevant shifts upwards and downwards in the adsorbed state are relative to the different interaction on cationic sites and hydroxyl groups, or on reduced metal centers, on which the use of CO as a probe is based (see below).

3.3.2 Crystalline Solids

When a crystalline solid is considered, the N atoms present in the smallest (primitive) Bravais cell must be taken into consideration to count the fundamental vibrational modes. They give rise to $3N$ total degrees of freedom, three of which

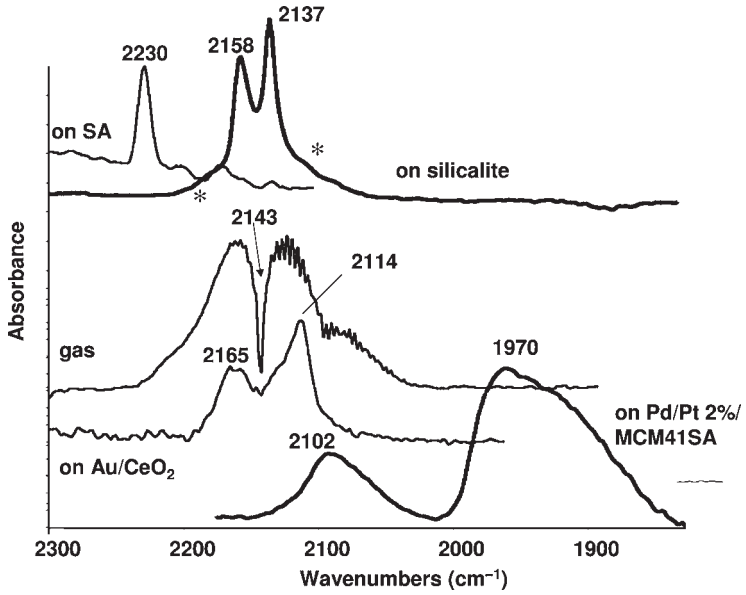

Figure 3.3 FTIR spectra of gaseous CO and of CO adsorbed on silica-alumina, on silicalite (150 K), on Au/CeO_2 and on Pt-Pd alloy nanoparticles on MCM41 mesoporous silica-alumina.

give rise to translational modes of the cell as a whole, which are the acoustic modes. Thus, the vibrational degrees of freedom (optical modes) are, in this case, $3N - 3$.

If the solid is molecular, the molecules (considered to be formed by M atoms, where $M = N/r$ and r is the number of molecules in the smallest Bravais cell) can be treated as for the gas phase, so giving rise to $3M - 6$ (or $3M - 5$ if linear) vibrations for each molecule. The degrees of freedom associated with the "external" modes of every molecular unit ($6r$ for non-linear molecules and $5r$ for linear molecules) give rise to lattice vibrations ("frustrated translations and rotations") and to three acoustic modes. On the other hand, the "internal" vibrations of each molecules should in principle give rise to r-fold splitting, owing to the coupling of the vibrations within its primitive unit cell as a whole.

Analysis of the symmetry of the chemical species under study (i.e. the point group for a "free" molecule, the space and factor groups for a crystal [44]), according to the site symmetry of every atom, allows the determination of the irreducible representation of the total modes and, after the subtraction of the translational and rotational modes (the acoustic modes for the crystals), the irreducible representation of the vibrational (or "optical") modes can be obtained. This means that the number of vibrational modes belonging to the symmetry species associated with the molecular or crystal symmetry can be counted. Consequently, the number of active modes can be counted, according to the symmetry selection rules of the different techniques (in particular IR and Raman).

Every vibrational mode is due to motions of the entire chemical species (the molecule or the primitive unit cell) as a whole. In principle, molecular and crystal dynamics calculations should define rigorously the motions of every atom of the chemical species upon a vibrational mode. This approach gives rise to a very complex picture (at least for large and complex chemical species), so that the results are sometimes not easily interpreted and comparison between the vibrational behavior of similar species is frequently difficult.

However, a *group approximation* can be frequently used. Thus, the vibrational modes can often be approximately attributed to the movements of small groups of atoms. This is possible in particular if very different bonds are present in the molecule, so that the coupling of their movements is negligible. In this way, it is possible to "dissect" the chemical species under study into "pieces" and to consider separately the vibrations of groups of few atoms (like the functional groups in organic compounds). This makes possible a satisfactory, although approximate, interpretation of the vibrational spectra of polyatomic molecules and of some crystals, and allows easy comparison between the vibrational features of related chemical species.

In the case of crystalline solids, more than one equivalent structural unit may be present in the primitive cell. This results in splittings of the fundamental vibrational modes of these units. In the case of many crystalline solid materials "covalent" units (e.g. oxo-anions for oxo-salts) are present, together with other groups bonded by ionic bonds (e.g. the cations in the oxo-salts). According to the above group approximation, the *internal vibrations* of the covalent units can be considered separately from their external vibrations (*hindered rotations and translations* of the group that finally contribute to the *lattice vibrations* and to the acoustic modes of the unit cell) and those of the other units. The presence of a number of covalent structural units in the primitive cell, causes their internal modes to split.

On the other hand, when the unit cell is centrosymmetric the mutual exclusion rule is valid, so that Raman active modes are IR-inactive and vice versa. In practice, for centrosymmetric cells containing N oxo-anions, every internal vibrational mode of the oxo-anion gives rise to $N/2$ IR active modes and $N/2$ Raman active modes.

Additionally, the TO/LO splitting may be relevant and makes more complex the identification of the vibrational modes of crystalline solids.

3.3.3
Amorphous Solids

Amorphous solids differ from crystalline solids because no long-range order occurs. So, variable coupling exists between the vibrational modes of similar or equivalent structural units. Consequently, amorphous solids can be treated in the same way as liquids and gases. The vibrational spectra of amorphous materials can present a smaller number of broader features than those of corresponding crystalline materials, where crystal coupling effects can produce multiple sharp features.

3.4
The Skeletal IR Spectra of Metal Oxides

IR spectroscopy is largely used for the characterization of metal oxide catalysts in relation to their structural features, with additional possible information on their morphology. Several collections of IR, Raman or both IR and Raman spectra of inorganic materials and minerals have been published, and are available electronically. In the following we will briefly review some of the applications of vibrational spectroscopies in the characterization of such materials.

3.4.1
Crystalline Simple Anhydrous Oxides

In network oxide structures the metal–oxygen bonds are all almost equivalent, so that their movements couple extensively. Also stretching and deformation vibrations mix. As a result of this, assignments of the different modes to a particular vibration can be very uncertain. However, the highest frequency vibrational features can be generally associated with stretching modes. The position of these modes can be assumed to be primarily dependent on the coordination of the metal ions involved and on the extent of the condensation of the resulting polyhedra, as shown in Table 3.1. This approach has been proposed by Tarte [45, 46] and is a useful approximation for the interpretation of the IR and Raman skeletal spectra of oxides of unknown structure. On the other hand, and perhaps more correctly, analysis of the spectra suggests that the higher frequency modes are mainly to be assigned to motions of the lighter oxygen atoms, so that they can be assigned to stretchings of oxygen in different coordination states. This alternative approach proposed first by Beattie and Gilson [47], is shown in Table 3.2.

Most simple oxide structures have been the object of extensive studies and complete vibrational analysis. Some examples are summarized in Table 3.3.

Table 3.1 Absorption range (cm–1) of some elements and coordinated compounds.

Atom X	Coordination		
	Tetrahedral XO_4 Isolated	**Octahedral XO_6** Pure oxide	Isolated complex
Ge^{IV}	800–700	700–800	~500
Ti^{IV}	1000–650	600–300	500–400
Al^{III}	850–700	700–300	500–350
Ga^{III}	750–600	600–350	
Cr^{III}		450–300	
Fe^{III}	650–550	650–300	400–300
Mg^{II}	700–550	450–300	
Zn^{II}	650–400	<300	
Fe^{II}		<350	

Table 3.2 Typical oxygen atom vibrational modes for metal oxide structures.

Structure	No. of oxygen atoms	No. of vibrational modes	Stretchings	Frequency region (cm^{-1})	Deformations			
Terminal								
M=O	1	3	1	1500–800	1 degenerate			
MO_2	2	6	asym + sym	1300–700	bending	twisting	Wagging	Rocking
MO_3	3	9	asym(2) + sym	1300–700	2 asym. bendings	sym. bending	2 rockings	Torsion
Bridging								
M—O—M	1	3						
Bent			asym + sym	1200–600	rocking			
Linear			asym		bending degenerate			
Triply bridging								
M_3O	1	3						
Pyramidal			asym(2) + sym	<600				
Planar			asym(2)		out-of-plane			

3.4.1.1 Oxides of Divalent Elements

According to its very high symmetry, the rock-salt structure taken by several divalent metal oxides, (space group $Fm3m \equiv O_h^5$, with $Z = 4$, and with one formula unit only in the smallest Bravais mcell) only gives rise to one triply degenerate IR active mode. The TO quoted for MgO at 401 cm^{-1} (see Figure 3.1a), corresponds to the lower frequency limit of the reflectance band while the LO corresponds to the higher energy limit of the reflectance, and is quoted at 718 cm^{-1} for MgO (see Figure 3.1a). The transmission/absorption IR spectrum of the MgO powder shows the maximum slightly above ν_{TO} (407 cm^{-1} in our spectrum of a polyethylene disk) and a shoulder near ν_{LO}. Other components arise from particles with different morphologies although the microcrystal powder spectrum of MgO is also affected by surface relaxation. ν_{TO} is found near 330 cm^{-1} for MnO (manganosite) and near 405 cm^{-1} for NiO powder, which also have a rock-salt type structure.

Table 3.3 Crystal structures and ion coordinations in solid simple oxides of interest in heterogeneous catalysis.

Cation valence	Structure name	Space group	Z	Coordination			Examples
				Cation	Oxide		
2	Rock salt	$Fm3m$	4	6 (oct)	6 (oct)	F_{1u} (IR)	MgO, CaO, SrO, BaO, MnO, FeO, CoO, NiO, CdO
	Zinc blende	$F\bar{4}3m$	4	4 (tetr)	4 (tetr)	F_2(IR,R)	BeO (H)
	Wurtzite	$P6_3mc$	2	4 (tetr)	4 (tetr)	A_1(IR,R) + $2B_1$(in) + E_1(IR,R) + $2E_2$(R)	BeO (L), ZnO
	Tenorite	$C2/c$	4	4 (sq.pl.)	4	A_g(R) + $2B_g$(R) + $3A_u$(IR) + $3B_u$(IR)	CuO
3		$P3_1$	3	3 (trig.)	1, 2		B_2O_3
	Corundum	$R\bar{3}c$	6	6 (oct)	4	$2A_{1g}$(R) + $2A_{1u}$(in.) + $3A_{2g}$(in.) + $3A_{2u}$(IR) + $5E_g$(R) + $5E_u$(IR)	α-Al_2O_3, α-Cr_2O_3, α-Fe_2O_3, α-Ga_2O_3*
	Tetragonal spinel	$I4_1/amd$	4	4 (tetr), 6 (oct)	3, 4	$2A_{1g}$(R) + $2B_{1g}$(R) + $4B_{2g}$(R) + $6E_g$(R) + $4A_u$(IR) + $6E_u$(IR)	Mn_3O_4 (δ-Al_2O_3)
		$C2/m$	4	4 (tetr), 6 (oct)	3, 4	$10A_g$(R) + $5B_g$(R) + $8B_u$(R) + $4A_u$(R)	θ-Al_2O_3, β-Ga_2O_3
		$P4_132$	8	4 (tetr), 6 (oct)	3, 4	$21F_1$(IR)	γ-Fe_2O_3
	"A"	$P\bar{3}m1$	1	7	6, 4	$2A_{1g}$(R) + $2E_g$(R) + $2A_{2u}$(IR) + $2E_u$(IR)	La_2O_3, Ce_2O_3, Pr_2O_3 (H), Nd_2O_3 (H)
	"C" bixbyite	$Ia\bar{3}$		6 (oct)	4	$4A_g$(R) + $4E_g$(R) + $14F_g$(R) + $5A_u$(in) + $5E_u$(in) + $16F_u$(IR)	Pr_2O_3 (L), Nd_2O_3 (L), α-Mn_2O_3

Table 3.3 *Continued*

Cation valence	Structure name	Space group	Z	Coordination			Examples
				Cation	Oxide		
3, 2,3	(Defective) cubic spinel	*Fd*3*m*	8	4,6	4	$A_{1g}(R) + E_g(R) + F_{1g}(in.) + 3F_{2g}(R) + 2A_{2u}(in) + 2E_u(in) + 4F_{1u}(IR) + 2F_{2u}(in)$	γ-Al_2O_3, η-Al_2O_3, γ-Ga_2O_3, Fe_3O_4, Co_3O_4
4	α-quartz	$P3_221$	3	4 (tetr)	2 (bent)	$4A_1(R) + 4A_2(IR) + 8E(R,IR)$	SiO_2, GeO_2^*
	Rutile	$P4_2/mnm$	2	6 (oct)	3	$A_{1g}(R) + A_{2g}(in) + B_{1g}(R) + B_{2g}(R) + E_g(R) + A_{2u}(IR) + 2B_{1u}(in) + 3E_u(IR)$	TiO_2, MnO_2, GeO_2, SnO_2, β-PbO_2
	Anatase	$I41/amd$	4	6 (oct)	3	$A_{1g}(R) + A_{2u}(IR) + 2B_{1g}(R) + B_{2u}(in) + 3E_g(R) + 2E_u(IR)$	TiO_2^*
	Baddeleyite	$P2_1/c$	4	7	3, 4	$9A_g(R) + 9B_g(R) + 8A_u(IR) + 7B_u(IR)$	ZrO_2 (L)
	Tetragonal zirconia	$P4_2/nmc$	2	8	4	$A_{1g}(R) + 2B_{1g}(R) + 3E_g(R) + A2_u(IR) + B2_u(in) + 2E_u(IR)$	ZrO_2 (M)
	Fluorite	*Fm*3*m*	4	8 (cub.)	4	$F_{1u}(IR) + F_{2g}(R)$	ThO_2, CeO_2, HfO_2, ZrO_2 (H)
5	V_2O_5	*Pmmn*	2	5 (6)	1, 2, 3	$7A_g(R) + 7B_{1g}(R) + 3B_{2g}(R) + 4B_{3g}(R) + 3A_u(in) + 3B_{1u}(IR) + 6B_{2u}(IR) + 6B_{3u}(IR)$	V_2O_5, R-$Nb_2O_5^*$
6	ReO_3	*Pm*3*m*	4	6	2	$2F_{1u}(IR) + F_{2u}(in)$	ReO_3

dist. = distorted; * = metastable phases; L = low temperature form; H = high temperature form; P = high-pressure form.

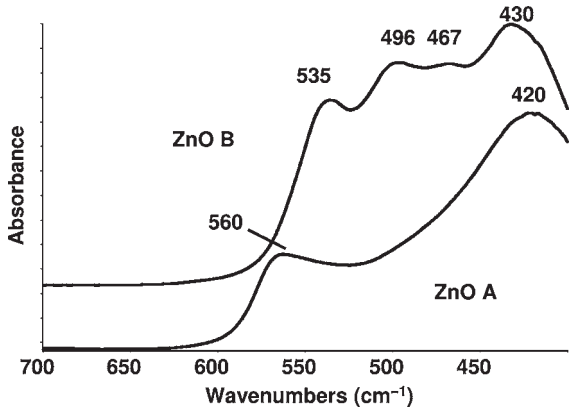

Figure 3.4 FTIR skeletal spectra of two different ZnO samples of ZnO. A: surface area 70 $m^2 g^{-1}$; crystal size 5 μm, porous. B: surface area 4.8 $m^2 g^{-1}$; particle size 0.2 μm.

The effect of morphology is even more evident in the IR spectrum of ZnO (Figure 3.4). This solid belongs to the wurtzite-type structure (wurtzite is the hexagonal polymorph of ZnS), space group $P6_3mc$ with $Z = 2$. As shown in Table 3.3 the irreducible representation for this structure forecasts two IR active modes ($A_1 + E_1$). The two TO fundamental modes are observed, in ZnO monocrystals, at 380 and 407 cm^{-1} [48], the corresponding LO modes baing observed at 574 and 583 cm^{-1}. The resolution of the two vibrational modes is generally not evident in the IR spectra of ZnO powders. According to Andrés Vergés and coworkers [49], thin lamellar ZnO particles show two peaks at 580 cm^{-1} (weak LO) and 406 cm^{-1} (strong, TO). One peak only should be observed for spherical particles, at 494 cm^{-1}. In the spectrum of sample A reported in Figure 3.4, lower spectrum, the particles are lamellar and relatively large and thick, while those of sample B are smaller, highly porous, with two main kinds of morphologies, lamellar (bands at 535 and 438 cm^{-1}) and ellipsoidal (bands at 496, 467 cm^{-1}).

The spectrum of CuO (tenorite) is more complex, characterized by six IR active modes, with at least three sharp peaks in the FIR spectrum (Figure 3.5).

3.4.1.2 Oxides of Trivalent Elements and Spinel-Type Structures

IR spectroscopy can be used to distinguish the different polymorphs of trivalent metal oxides. γ-Al_2O_3, which is the most commonly used form of alumina in catalysis, is mostly obtained by decomposition of the boehmite oxyhydroxide, γ-AlOOH, or of a poorly crystallized hydrous oxyhydroxide called "pseudobohemite" at 600–800 K. It has a cubic structure and is described as a defective spinel, although it can be tetragonally distorted. However, its structure is still under investigation and debate [50, 51]. Calcination at increasing temperatures gives rise to the transformation sequence γ-Al_2O_3 → δ-Al_2O_3 → θ-Al_2O_3 → α-Al_2O_3. δ-Al_2O_3 is a tetragonal spinel superstructure whose unit cell is constituted by three spinel unit blocs with tetragonal deformation, probably with a partial ordering of Al ions

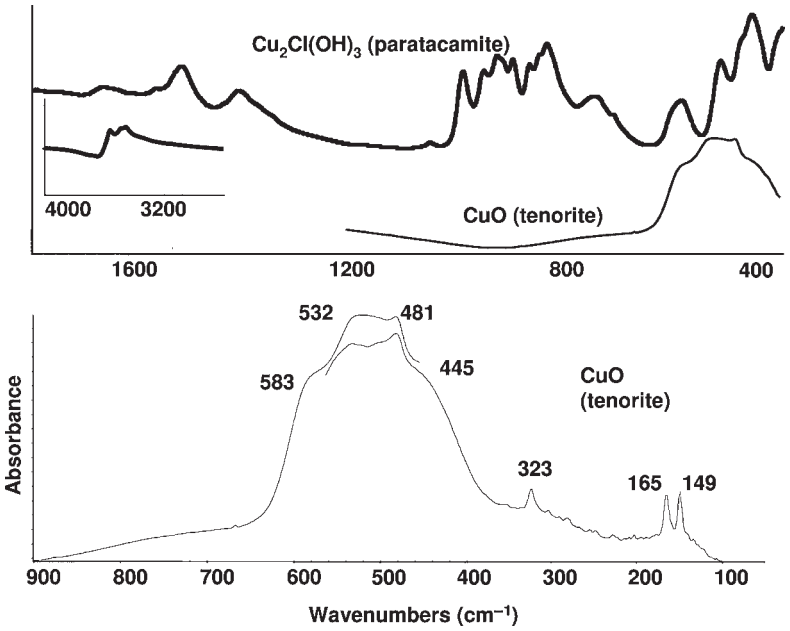

Figure 3.5 FTIR skeletal spectra of paratacamite ($Cu_2Cl(OH)_3$) and its decomposition product tenorite (CuO).

into octahedral sites. It is formed continuously in the temperature range 800–900 K. θ-Al_2O_3 is formed above 900 K with simultaneous decrease of the surface area to near 100 $m^2 g^{-1}$ or less. Its monoclinic structure, which is the same as that of β-gallia, can be derived from that of a spinel, with deformation and some ordering of the defects, with half tetrahedral and half octahedral Al ions. α-Al_2O_3 (corundum) where all Al ions are equivalent in octahedral coordination in a hexagonal close packed oxide array is the thermodynamically stable phase at any temperature and pressure. Alternatively, η-Al_2O_3, also considered to be a spinel structure, is obtained by decomposing Bayerite $Al(OH)_3$. Calcination gives rise to the sequence η-Al_2O_3 → θ-Al_2O_3 → α-Al_2O_3.

Figure 3.6 shows the evolution of the medium IR spectra of a pseudobohemite precipitate with calcination, revealing the formation of different phases. The cubic spinel structure, irrespective of the cation distribution of normal, inverted or random spinels, as well as of defective spinels, belongs to the $O_h^7 = Fd3m$ space group with $Z = 8$. Five Raman active modes and four IR active modes occur. The spectrum of γ-Al_2O_3 is generally mostly characterized by two very broad bands in the medium IR region at 580 and 880 cm^{-1}, respectively, possibly mostly due to vibrations of Al oxide octahedra and tetrahedra, respectively. According to its tetragonal spinel superstructure, 10 IR active modes are expected in the IR spectrum of δ-Al_2O_3 which in fact shows more components. The spectrum of θ-Al_2O_3, a deformed ordered spinel superstructure, presents several sharp maxima, in agreement with the forecast of 12 fundamental vibrations. The six fundamental

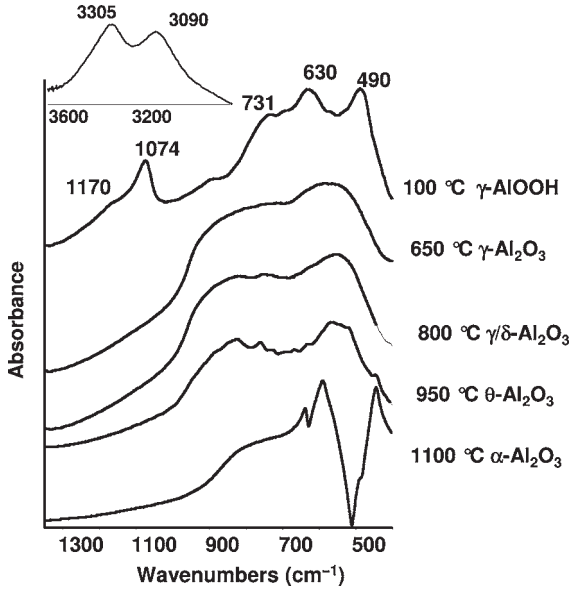

Figure 3.6 FTIR skeletal spectra of the evolution products of calcination of a bohemite (γ-AlOOH) precipitate.

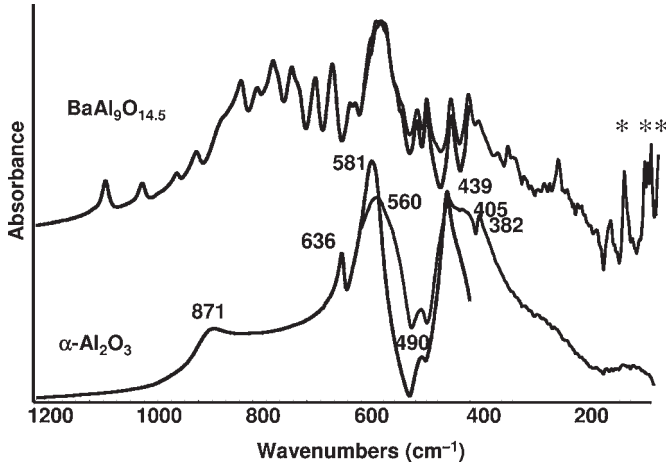

Figure 3.7 FTIR and FTFIR skeletal spectra of α-Al_2O_3 (corundum) and of a β-alumina with composition $BaAl_9O_{14.5}$.

TO modes of α-Al_2O_3 [52] (Figure 3.7, lower part, where both the medium and the far IR regions are shown) correspond to the maxima at 636, 581, 439, 405 and 382 cm^{-1} and to the shoulder at 560 cm^{-1}. No fundamental TO modes are observed above 700 cm^{-1}, in agreement with the six-coordination only for Al in this structure. The bands at 871 and 490 cm^{-1} are due to LO modes [53].

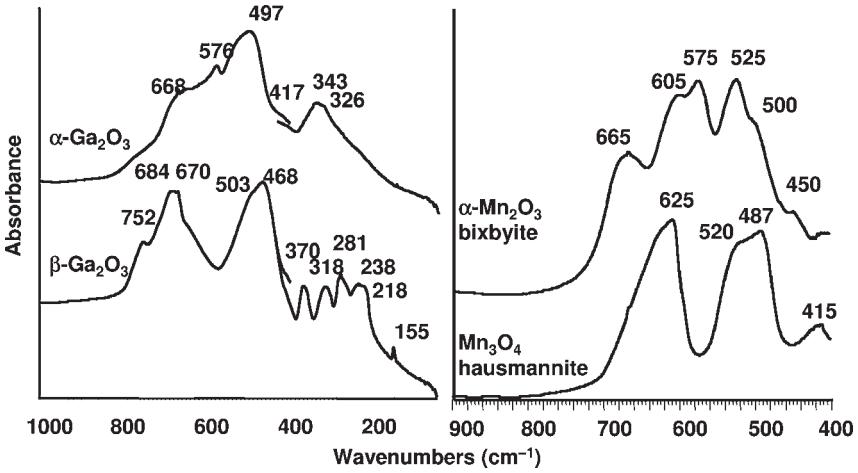

Figure 3.8 FTIR skeletal spectra of β-Ga_2O_3, α-Ga_2O_3, α-Mn_2O_3 and Mn_3O_4.

Similarly, is possible to readily distinguish α-Ga_2O_3, metastable with only octrahedral coordination for Ga ions, from β-Ga_2O_3 which is the thermodynamically stable form with both tetrahedral and octahedral coordination for Ga ions (see Figure 3.8, left). The strong similarity of the spectra of α-Ga_2O_3 and α-Al_2O_3, both corundum structures, is also evident (Figure 3.4, lower left and Figure 3.5, upper part).

Skeletal IR spectroscopy is able to distinguish the polymorphs of ferric oxide (γ-Fe_2O_3, maghemite, which is also a spinel-derived structure, has a much more complex spectrum than the thermodynamically stable polymorph, α-Fe_2O_3, hematite) and both are well distinguished from the spinel mixed valency oxide, magnetite, Fe_3O_4. Similarly, α-Mn_2O_3, bixbyite (type C structure) is easily distinguished from housmannite, the random tetragonal spinel Mn_3O_4 (Figure 3.8, right) and from γ-Mn_2O_3, reported to have a distorted spinel structure [54]. Also the so-called A, B and C rare earth sesquioxides can easily be distinguished by IR spectroscopy [55].

3.4.1.3 Oxides of Tetravalent Elements

IR and Raman spectroscopy can also be applied to distinguish the rutile and anatase TiO_2 polymorphs [56]. Anatase has four IR active skeletal modes while rutile has only three. The skeletal spectra of both are quite sensitive to particle size and morphology. The spectrum of anatase powders is mostly associated with two strong bands at 330 and 480 cm^{-1}, with a broad absorption with some component at higher frequency. The evolution of anatase (metastable) towards rutile (stable) is associated with the appearance of a third strong component in the middle (near 420 cm^{-1}) and the shift of the other maximum upwards to 520 cm^{-1}.

IR spectra clearly distinguish the three zirconia polymorphs [57]. The high-temperature cubic phase has only one IR active skeletal mode, found near 550 cm^{-1} for powders, while tetragonal zirconia (the medium-temperature polymorph) has

three IR active modes, and presents a broad multiple maximum near 500 cm^{-1}, with weaker components near 575 and 160 cm^{-1}. Monoclinic zirconia (baddeleyite) has a much more complex spectrum, with 15 IR active modes. In particular it is well characterized by a strong band evident at 770 cm^{-1}, associated with the movement of oxygen in threefold coordination.

IR spectroscopy allows the analysis of the many polymorphs of manganese dioxide [54] such as α-MnO_2 (hollandite, tetragonal, SG *I*4/*m*), R-MnO_2 (ramsdellite, orthorhombic, *Pbnm*), β-MnO_2 (pyrolusite, tetragonal rutile structure, $P4_2/mnm$), γ-MnO_2 (nsutite, hexagonal), δ-MnO_2 (vernadite, hexagonal) and λ-MnO_2 (spinel-type, cubic, *Fd*3*m*).

α- and β-quartz, α- and β-cristobalite, tridymites, coesite, morganite and silicalite are different polymorphs of silica with tetrahedrally coordinated silicon. So, their vibrational structure, as well as that of amorphous or vitreous silica, in which Si is also tetrahedral, can be discussed in parallel. The IR spectra of all tetrahedral silica polymorphs have bands in three regions: in the region 1300–950 cm^{-1} (very strong, denoted ν_1), 850–600 cm^{-1} (medium strength, ν_2) and near 450 cm^{-1} (very strong, ν_3). Raman spectra show very weak peaks in the 1300–950 cm^{-1} and 850–700 cm^{-1} regions (ν_1 and ν_2 modes), and one or more very strong peaks below 550 cm^{-1}, in a position very sensitive to the overall crystal structure of the solid (ν_4). These features are also present in the spectra of amorphous or vitreous silica; so they represent vibrations of the basic structural units of both crystalline and amorphous silica, that is, SiO_4 tetrahedra and bridging oxygens.

Four main vibrational modes are expected for a tetrahedral silica network. In the C_{2v} symmetry of the Si—O—Si bent units, a symmetric stretching (A_1), an asymmetric stretching (B_1), a bending (A_1) and a rocking mode (B_2) are expected, the modes with A_1, B_1 and B_2 symmetry being both IR and Raman active. The strongest Raman mode, ν_4, is assumed to be a symmetric stretching mode, mainly because Raman peak intensity is generally greater for stretching than for bending modes. However, the coupling of this mode with the Si—O—Si scissoring mode provides an explanation of the low frequency of the strongest Raman peak (550–350 cm^{-1}) in all silica polymorphs. On the other hand, it is clear that in the solid state in order for all Si—O bonds to expand in-phase, most Si—O—Si angles must contract simultaneously. This mode is consequently highly sensitive to the structure of the polymorph, as is indeed observed. The position of the ν_4 peak, in fact, strongly depends on the type of ring present in silicas and silicates. As for the IR spectrum, the strongest complex band is ν_1, observed in the 1300–950 cm^{-1} region and is associated to the asymmetric stretching of the Si—O—Si bridges. However, this mode is split into two components even in the case of vitreous silica, due to either the in-phase (ν_1') or the out-of-phase coupling (ν_1'') of the asymmetric stretching modes of nearest Si—O—Si groups. In other words, this mode couples with the symmetric and asymmetric stretching of the four Si—O bonds of the SiO_4 octahedra. The position of both ν_1' and ν_1'' components is also somewhat sensitive to the size of the rings and/or to the density of the different silica polymorphs. This is particularly true for ν_1', whose shift is stronger, so that it is actually resolved from ν_1'' only in some cases. As discussed above, the ν_2 mode is essentially a

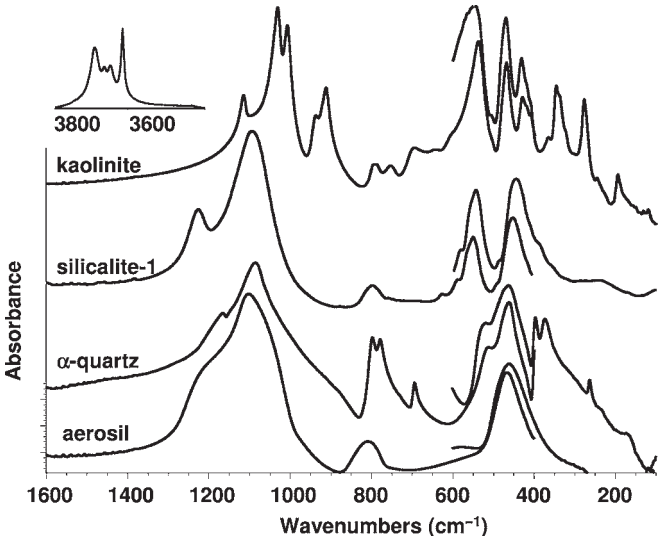

Figure 3.9 FTIR and FTFIR skeletal spectra of amorphous silica (aerosil), α-quartz, silicalite-1 and kaolinite.

bending mode of the Si—O—Si bridges, although mixed with a symmetric stretching mode. Its assignment predominantly to a bending mode is made mainly due to its weakness in the Raman spectra, although its position is more typical of a symmetric stretching mode. This mode appears to be the least sensitive to the structure, although in some cases it splits definitely into more components, as in the case of α-quartz where three well-resolved sharp bands are found. The lowest frequency IR mode, ν_3, is associated with the out-of-plane deformation of the Si—O—Si bridges, that is, a "rocking" mode. This explains why this mode is essentially silent in the Raman spectrum, while being very strong in IR in the region 430–490 cm^{-1} in all silica forms. Besides the four vibrational modes discussed here that are common to all silicas, network silicates and silico-aluminates, other structure-sensitive features are frequently present. They are associated with the splitting of these vibrational modes (bands above 350 cm^{-1}) or to torsional lattice modes (below 400 cm^{-1}).

In Figure 3.9 the FTIR-FTFIR transmission-absorption spectra of an amorphous silica sample (aerosil) and of two crystalline powders (α-quartz and silicalite-1) are compared. The ν_1, ν_2 and ν_3 absorptions (broad) discussed above are evident for amorphous silica. In the case of quartz, sharper components are observable as expected. Ten maxima can be easily observed at 1165, 1086, 798, 779, 694, 519, 463, 397, 373 and 263 cm^{-1}. The irreducible representation for α-quartz (taking the right-handed enantiomorph with space group $P3_221 = D_3^6$, with $Z = 3$) is 4 A1 (R) + 4 A2 (IR) + 8 E (R,IR) so that 12 IR active fundamental modes are expected, each one undergoing TO-LO splittting. Actually, in the ν_1 region (asymmetric Si—O—Si stretching) we expect three fundamental modes, so that in the maximum at 1086 cm^{-1}, which shows shoulders at both sides, certainly more components are

superimposed. Three resolved components are found as expected in the ν_2 region. One fundamental mode is expected to be very weak near 130 cm^{-1}, and this could not be detected.

Silicalite-1 is the totally siliceous form of the zeolite MFI (ZSM-5), another silica polymorph. It belongs to the $P2_1/n = C_{2h}^5$ monoclinic space group (n. 14) with Z = 96. It transforms into an orthorhombic structure, belonging to the $Pnma = D_{2h}^{16}$ space group (n. 62) between 350 and 363 K. Substituted silicalites such as ZSM-5 zeolite (see below) and Ti-silicalite adopt the orthorhombic structure even at room temperature, the transition temperature being strongly shifted to lower temperatures.

Factor group analysis [58] indicates that 429 IR active modes and 432 Raman active modes are expected for the monoclinic structure and 323 IR active modes and 432 Raman active modes are expected for the orthorhombic form. Only 16 components in the IR specrum and 11 components in the Raman spectrum are observed because of the superimposition of many of the expected fundamentals. However, a careful observation of the spectra, with the help of analysis of the perturbations arising from isomorphic substitution and with the aid of derivative spectra, showed the presence of a great number of very weak components (shoulders) in the spectra.

3.4.2 Crystalline Complex or "Mixed" Oxides

3.4.2.1 Solid Solutions

Vibrational spectroscopies give rise to interesting information on the microscopic structure of solid-solution mixed oxides. For example, the state of vanadium in solid solution in TiO_2 anatase catalysts [59], the partial ordering of cations in corundum-type Fe-Cr oxides [60], the real presence of Ti^{4+} in the silicalite framework of TS1 catalysts [58] and the solubility of Al^{3+} ions in the NiO rock-salt structure [61] have been objects of IR spectroscopic studies.

3.4.2.2 Ternary Phases

IR spectroscopy has been largely used to characterize normal, inverse, random and non-stoichiometric AB_2O_4 *spinel-type structures*, such as many divalent aluminates, gallates, ferrites and chromites [62], including superstructures such as those of the defective spinel sesquioxides γ-Fe_2O_3, θ-Al_2O_3 and β-Ga_2O_3. In Figure 3.10 the spectrum of the predominantly inverse spinel $MgFe_2O_4$ is reported, showing three of the four IR active fundamental modes at 563, 402 and 250 cm^{-1}, the fourth one being expected to be at very low frequency.

The so-called *beta-aluminas* are characterized by the existence of layered blocks of a trivalent element (most frequently Al^{3+}, but also Fe^{3+} and Ge^{3+}) with the same spinel structure separated by "mirror planes" where large monovalent (Na or K), divalent (Ba, and sometimes Ca or Sr) and trivalent (La) cations, which do not enter the cubic close packed array of oxide ions of the spinel blocks, are located, together with oxide anions bridging between the blocks. In these planes the cations

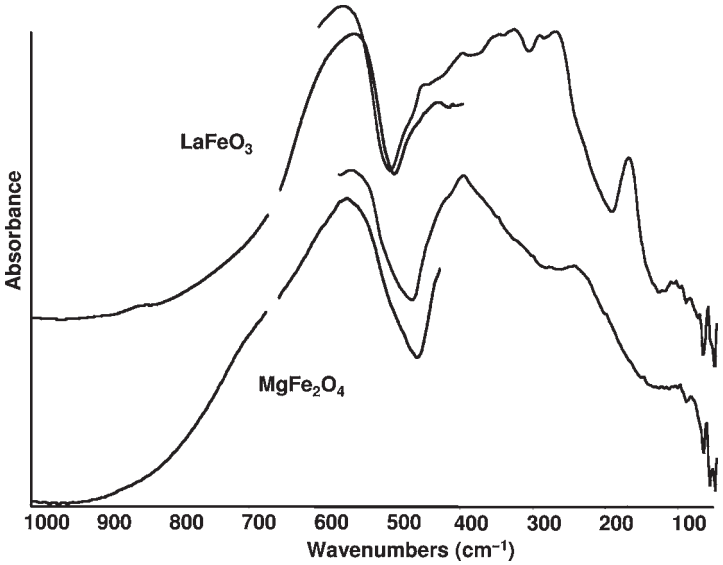

Figure 3.10 FTIR and FTFIR skeletal spectra of $LaFeO_4$ and $MgFe_2O_4$.

are able to diffuse. The metal-to-oxygen stretches involving such ions located in the mirror planes occur in the low-frequency region (FIR). In Figure 3.7, top, the spectrum of a solid with composition $BaAl_9O_{14.5}$, belonging to the beta-alumina family, is reported. At least 34 components may be distinguished, in good agreement with what is expected based on the factor group analysis [63]. The low-frequency bands due to vibrational modes directly involving Ba ions are marked with asterisks in Figure 3.7: those at 73 and 67 cm^{-1} are attributed to Ba ions in the interlayer region, while the peak at 111 cm^{-1} is attributed to interstitial Ba in the spinel blocks in this Ba-rich phase.

IR spectroscopy can be used to distinguish several different phases characterized by the stoichiometry ABO_3 (Table 3.4), such as cubic, tetragonal, orthorombic and rhombohedral *perovskites* (such as $SrTiO_3$, $BaTiO_3$, $LaFeO_3$ and $LaMnO_3$, respectively [56, 64, 65]), from *ilmenites* and *lithium niobate* structures. In Figure 3.10 the spectrum of $LaFeO_3$ is reported. It shows some of the 26 IR active modes expected.

3.4.2.3 **Oxo-Salts**

Oxo-salts involve oxo-anions, which are internally held by covalent bonds between the non-metal atom (or the metal in a very high oxidation state) and oxygen, giving rise to M—O bond orders ranging between 1 and 2. The oxo-anions are further bonded through ionic interactions with the metal cations. So, the vibrational spectra of oxo-salts are dominated, in their high-frequency ranges, by the "internal" vibrations of the oxo-anion. Obviously, splittings of these internal vibrations occur in principle as a result of the couplings of the modes of more than one oxo-anionic units simultaneously present in the smallest Bravais cell.

Table 3.4 Crystal structures of some solid ternary-oxide structures with the stoichiometry ABO_3, and the irreducible representations of the optical modes.

Structure name	Example	Space group		Z	
Ilmenite	$FeTiO_3$	$R\bar{3}$	C_{3i}^2	6	$5A_g$ (R) + $5E_g$(R) + $4A_u$(IR) + $4E_u$(IR)
$LiNbO_3$	$LiNbO_3$	$R3c$	C_{3v}^6	6	$4A_1$ (IR) + $5A_2$ (R) + 9E(IR,R)
Cubic perovskite	$SrTiO_3$	$Pm3m$	O_{h1}	1	$3F_{1u}$(IR) + F_{2u}(in)
Tetragonal perovskite	$BaTiO_3$	$P4mm$	C_{4v}^1	1	$3A_1$(IR,R) + 4E(IR,R) + B_1(R)
Orthorombic perovskite	$LaFeO_3$	$Pnma$	D_{2h}^{16}	4	$7A_g$(R) + $7B_{1g}$(R) + $5B_{2g}$(R) + $5B_{3g}$(R) + $8A_u$(in) + $7B_{1u}$(IR) + $9B_{2u}$(IR) + $9B_{3u}$(IR)
Rhombohedral perovskite	$LaMnO_3$	$R\bar{3}c$	D_{3d}^6	2	A_{1g}(R) + $3A_{2g}$(in) + $4E_g$(R) + $2A_{1u}$(in) + $2A_{2u}$(IR) + $4E_u$(IR)
Calcite	$CaCO_3$	$R\bar{3}c$	D_{3d}^6	2	A_{1g}(R) + $3A_{2g}$(in) + $4E_g$(R)+$2A_{1u}$(in) + $2A_{2u}$(IR) + $4E_u$(IR)
Aragonite	$CaCO_3$	$Pmcn$	D_{2h}^{16}	4	$9A_g$(R) + $6B_{1g}$(R) + $6B_{2g}$(R) + $9B_{3g}$(R) + $6A_u$(in) + $8B_{1u}$(IR) + $8B_{2u}$(IR) + $5B_{3u}$(IR)

The cation-to-anion vibrations (lattice vibrations) are mainly located in the FIR region and their assignments, based on similar considerations to those reported for ionic oxides, are frequently difficult.

Salts with Planar-Trigonal and Pyramidal MO_3^{n-} Oxo-Anions The movements of the four atoms present in the MO_3^{n-} oxo-anions give rise to twelve total modes, of which six are associated with the movements of the anion as a whole (rotations and translations, which contribute to the lattice vibrations and to the acoustic modes of the solid). So, six "internal" vibrations occur. The highest symmetry point group for this ions is D_{3h}, occurring when it is planar trigonal and isolated. This is typical for isolated carbonate, nitrate and orthoborate anions. In this case, as shown in Table 3.5, the symmetric stretching gives rise to a non-degenerate Raman active mode, while the asymmetric stretching is doubly degenerate and both IR and Raman active. Two deformation modes occur, the out-of-plane deformation (δ_{oop}) which is IR active, and the in-plane deformation (δ_{ip}) which is degenerate and both IR and Raman active. By lowering the symmetry, for example to the C_{2v} point group (which occurs when only two of the three oxygen atoms are

Table 3.5 Normal modes of vibrations and their activity for isolated MO_3^{n-} oxo-anions, and typical vibrational frequencies.

Normal modes of vibrations and their activity				
Planar	ν_{sym}	δ_{oop}	ν_{asym}	δ_{ip}
D_{3h}	A_1' (R)	A_1'' (IR)	E′ (IR, R)	E′ (IR, R)
C_{2v}	A_1 (IR,R)	B_2 (IR,R)	A_1 (IR,R)	A_1 (IR,R)
			B_1 (IR,R)	B_1 (IR,R)
Pyramidal	ν_{sym}	δ_{sym}	ν_{asym}	δ_{asym}
C_{3v}	A_1 (IR,R)	A_1 (IR,R)	E (IR, R)	E (IR, R)
C_s	A′ (IR, R)	A′ (IR, R)	A′ (IR, R)	A′ (IR, R)
			A″ (IR, R)	A″ (IR, R)
Typical band positions (cm^{-1})				
BO_3^{3-} planar	1100–900	750–650	1500–1250	600–550
CO_3^{2-} planar	1100–1050	900–850	1480–1380	750–670
NO_3^- planar	1080–1030	840–800	1490–1320	750–690
SO_3^{2-} pyram·	1000–960	670–610	1000–910	520–450
SeO_3^{2-} pyram	850–780	500–400	750–700	400–350
TeO_3^{2-} pyram	800–750	430–330	730–680	350–300

equivalent), the doubly degenerate modes split and all six modes become both IR and Raman active.

The highest symmetry point group for non-planar pyramidal $[MO_3]^{n-}$ oxo-anions (such as sulfite, selenite and tellurite anions) is C_{3v}. In this case too all modes are both IR and Raman active. The symmetric stretching and deformations are non-degenerate while the asymmetric modes are doubly degenerate. Such a degeneracy is broken when symmetry is further lowered. Typical positions for the corresponding modes are reported in Table 3.5. The commonest crystal structures for AMO_3 salts, which have been the object of vibrational studies, are calcite, aragonite, dolomite and nitrates of divalent metals.

Salts with Tetrahedral MO_4^{n-} Oxo-Anions Including High-Aluminum-Zeolites Most of the MO_4^{n-} oxo-anions take a tetrahedral-like coordination. In this case we have nine internal vibrations plus six external vibrations contributing to lattice vibrations and to acoustic modes. When the ion takes its highest symmetry (T_d point group), the symmetric stretching and the symmetric deformation are Raman active, the last being doubly degenerate. The asymmetric stretching and deformation are both IR and Raman active and are triply degenerate. If the symmetry is lowered, the degeneracies are broken and all modes can become IR and Raman active. This is shown in Table 3.6, where the typical positions of such modes are also reported for different oxo-anions. Examples are magnesium orthovanadate $Mg_3(VO_4)_2$ [66] and Scheelite type orthomolybdates such as $CdMoO_4$ [67], whose IR and Raman skeletal spectra have been studied in detail. The presence

Table 3.6 Normal modes of vibrations and their activity for tetrahedral oxo-anions, and typical vibrational frequencies.

Normal modes of vibrations and their activity				
	ν_{sym}	δ_{sym}	ν_{asym}	δ_{asym}
T_d	A_1 (R)	E (R)	F_2 (IR,R)	F_2(IR,R)
C_{3v}	A_1 (IR, R)	E (IR, R)	A_1 (IR, R) E (IR, R)	A_1 (IR, R) E (IR, R)
C_{2v}	A_1 (IR, R)	A_1 (IR, R) A_2 (R)	A_1 (IR, R) B_1 (IR, R) B_2 (IR, R)	A_1 (IR, R) B_1 (IR, R) B_2 (IR, R)
C_1	A (IR, R)	2A (IR, R)	3A (IR, R)	3A (IR, R)
Typical band positions (cm^{-1})				
SiO_4^{4-}	850–800	450–300	1000–850	650–450
GeO_4^{4-}	800–600	350–250	850–650	550–400
PO_4^{3-}	1000–920	420–350	1080–950	600–530
AsO_4^{3-}	900–830	400–320	880–750	500–410
SbO_4^{3-}	800–500	400–300	800–500	400–300
VO_4^{3-}	915–800	500–350	900–730	500–350
NbO_4^{3-}	800–500	400–300	800–500	400–300
SO_4^{2-}	1070–950	520–410	1270–1030	670–570
SeO_4^{2-}	860–810	370–300	940–840	460–390
CrO_4^{2-}	900–830	360–330	960–860	410–330
MoO_4^{2-}	940–860	360–310	910–740	(360–310)
WO_4^{2-}	960–900	355–320	870–830	(355–320)
MnO_4^-	850–820	420–380	940–880	(420–380)
ReO_4^-	1000–950	350–300	950–900	350–300

of a strong complex band with a main maximum at 754 cm^{-1} and the absence of strong bands in the region 1020–900 cm^{-1} provides evidence of the absence of short Mo=O bonds, and the substantial equivalence of the four bonds in the truly tetrahedral molybdate ions in the scheelite structure of $CdWO_4$ (Figure 3.11).

To this family belong high-aluminum zeolites with Si to Al atomic ratio ~1, which are fundamentally Al, alkali orthosilicates, such as the A zeolites (LTA) and some faujasites such as NaX zeolite. In Figure 3.12 the IR spectra are shown of the zeolites NaA (Na-LTA following the IZA international code) and NaX (Na-FAU), as typical cation-containing zeolites whose composition is, in both cases, $Na_{12}Al_{12}Si_{12}O_{48}$. The unit cell of dehydrated NaA zeolite ($Na_{12}(SiO_2)_{12}(AlO_2)_{12}$ formula) belongs to the $Fm3c = O_h^6 \equiv 226$ space group, with $Z = 8$. The number of molecular units in the smallest Bravais cell is 2. Accordingly, 168 atoms are present in the smallest Bravais cell, 144 of which are framework Si, Al and O

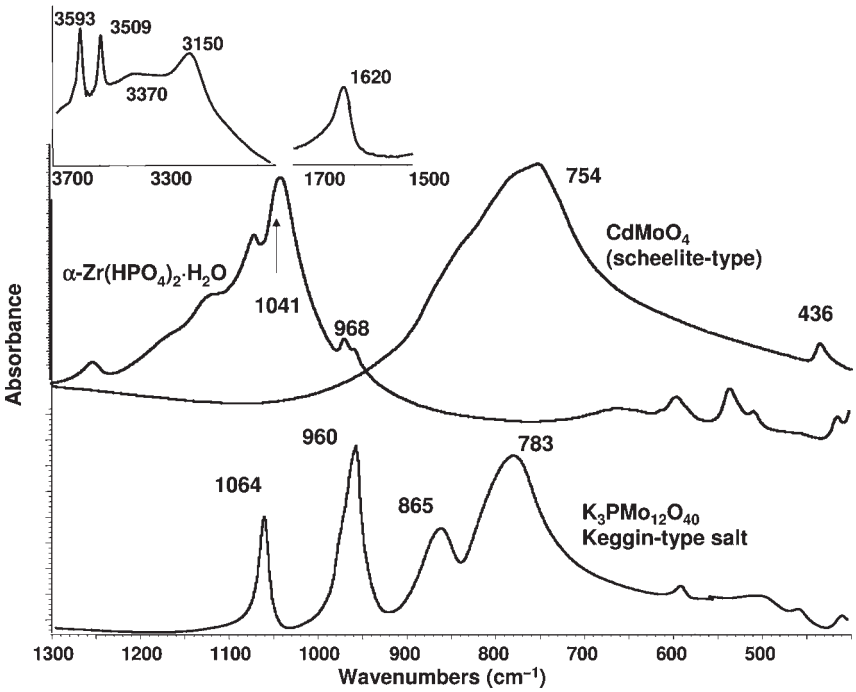

Figure 3.11 FTIR skeletal spectra of α-$Zr(HPO_4)_2{\cdot}H_2O$, CdMoO4 (scheelite type) and the Keggin-type heteropolyacid salt $K_3PMo_{12}O_{40}$.

atoms. Consequently, by applying factor group analysis, 429 optical degrees of freedom are associated with the zeolite LTA framework (Na ions excluded) giving rise to the following irreducible representation:

$$\Gamma_{opt} = 11A_{1g}(R) + 11A_{2g}(ia) + 22E_g(R) + 25F_{1g}(ia) + 25F_{2g}(R) + 7A_{1u}(ia) + 7A_{2u}(ia) + 14E_u(ia) + 28F_{1u}(IR) + 29F_{2u}(ia)$$

Thus 28 IR active modes are expected to fall in the regions of the vibrations of the orthosilicate anions. Of these, we can expect five modes associated with ν_3 (asymmetric stretching) and two modes associated with ν_1 (symmetric stretching), three modes associated with the symmetric deformation (ν_2) and five with the asymmetric deformation ν_4, four hindered rotations, four hindered translations, and, finally, five modes associated with Al—O tetrahedra. We actually observe at least 10 components for framework vibrations. Additionally, the low-frequency modes of Na ions are expected to fall in the FIR region [68], where several bands are indeed observed.

The structure of NaX zeolite also belongs to the $Fm3c = O_h^6 \equiv 226$ space group, with $Z = 8$. Thus, also in this case we expect 28 IR active fundamentals, while we observe at least nine components for the framework spectrum.

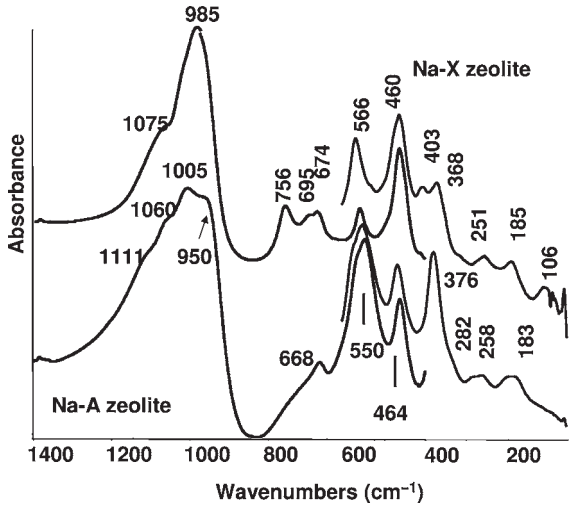

Figure 3.12 FTIR and FTFIR skeletal spectra of zeolites Na-X (Na-FAU) and Na-A (Na-LTA), Si/Al ~ 1 in both cases.

In any case, the spectrum of these high-aluminum zeolites, which can be considered as zeolitic Na,Al-orthosilicates, differ from those of highly siliceous silicates including most zeolites (which are actually framework silicates), and of silica polymorphs (Figure 3.9) in the absence of the typical Si—O—Si symmetric stretching / bending mode occurring near 800 cm^{-1}. They also differ from phyllosilicates such as kaolinite (Figure 3.9, upper spectrum) in the absence of the Si—(OH) stretching modes typically found near 900 cm^{-1}.

The tetrahedral oxo-anions can retain one or two protons in the crystal structure, giving rise to monohydrogen or dihydrogen ortho anions. In this case, at least one of the oxygen atoms is certainly unequivalent to the others, and the vibrations of the O—H group also appear. As an example, several studies have appeared concerning metal monohydrogen orthophosphates and dihydrogen orthophosphates. In Figure 3.11 the spectrum of the interesting compound α-$Zr(HPO_4)_2 \cdot H_2O$ is reported. The band at 968 cm^{-1} is due to the P—O stretching of the POH group while the strong complex band with the maximum at 1040 cm^{-1} is due to PO_3 stretches [69].

Dimeric Condensed Tetrahedral Anions $[X_2O_7]^{n-}$ Salts in which the tetrahedral oxo-anions are condensed through common oxygen atoms are denoted with the prefix pyro- (for dimeric species) or meta- (for polymeric species). The oxo-anions involved have terminal M—O bonds (six in total for dimeric pyro species, two for each atom for polymeric meta anions), and in addition contain M—O—M bridges. Such bridges are generally bent, but they can be sometimes linear, such as in the cases of some pyrosilicates, pyrogermanates, pyrophosphates and pyroarsenates. When the bridge is bent it gives rise (like the Si—O—Si bridges of silica, see above) to an asymmetric stretching mode, a bending/symmetric stretching mode (both

are in-plane modes) and an out-of-plane rocking mode. For silicates, the ν_{as} Si—O—Si and ν_{sym} Si—O—SiO fall in the regions 1050–900 cm^{-1} and near 650 cm^{-1}, respectively. According to Lazarev [70] a linear relationship exists between the bond angle and the parameter $\Delta = (\nu_{as} - \nu_{sym})/(\nu_{as} + \nu_{sym}) \times 100$. When the bridge is linear, (as in thortveitite, $Sc_2Si_2O_7$) the symmetric stretching could become IR inactive (or very weak if the environment is symmetric).

Several studies have been devoted to compounds containing condensed tetrahedral anions $[X_2O_7]^{n-}$ such as pyrovanadates [66], dichromates, pyrosulfates, pyroselenates, pyrophosphates and pyroarsenates, pyroniobates, and so on. Typical of these compounds are the vibrations of the bridging oxygens. Additionally, the spectra show the vibrations of the terminal MO_3. Each terminal MO_3 moiety gives rise to one symmetric and two asymmetric stretchings, one symmetric and two asymmetric bendings, as well as to one twisting and two rocking modes.

In the case of vanadyl pyrophosphate, a very relevant oxidation catalyst, the IR spectra also provide information on the morphology, allowing the distinction of very active catalysts from less active, highly crystalline, materials [71].

Salts with Polymeric Tetrahedral Oxo-Ions: Metasilicates, Layer Silicates and Framework Silicates including Highly Siliceous Zeolites The vibrational spectra of the different kinds of chain and ring silicates are dominated by the vibrations of the Si—O—Si bridges (as already discussed for amorphous silicas and for pyrosilicates, see above) and of Si—O– terminal bonds. The difference between the "network silicate structure" of silica forms and the layer silicate of kaolinite is mainly shown by the presence, in the case of kaolinite, of strong bands with maxima at 940 and 913 cm^{-1}, typically due to Si—(OH) "terminal" stretchings. In this region silicas and network silicates do not absorb. Layer silicates also present the absorptions of Si—O—Si bridges and of terminal silanol groups Si—OH. Both terminal silicate bonds $Si—O^- M^+$ and silanols give rise to strong IR bands in the region 950–1000 cm^{-1} which frequently have significant intensity in the Raman spectra also. Cyclic structures and particular conformations of the chains can give rise to characteristic features, particularly in the lower frequency regions (Si—O—Si rockings and lattice modes). Terminal silanols, such those present in layer silicates, also give rise to OH stretching modes strong in IR, such as those of kaolinite (Figure 3.9).

Highly siliceous zeolites (with Si/Al ratios >>1) are microporous framework alumino-silicate materials. Discussion of the framework skeletal vibrations of highly siliceous zeolites is similar to that reported above for silicas. The addition of aluminum in the framework causes shifts in the positions of the sole band. In particular, the asymmetric Si—O—Si stretching modes of framework silicates, usually observed as a complex very strong absorption in the region 1200–1000 cm^{-1}, tend to shift down a little with Al for Si substitution.

Salts with Condensed Octahedral-Like Oxo-Anions Chains of oxo-anions can "condense" giving rise to octahedral-like chains or multiple chains. This is the case, for example, for several metavanadates forming double chains $[(V_2O_6)^{2-}]_n$ such as

magnesium metavanadate. In this case vibrational features appear due to triply bridging O atoms and to pairs of short divanadyl VO_2 bonds [66]. Similarly, "ortho-tungstate ions", such as those of metal tungstates in the wolframite structure (e.g. $CdWO_4$), condense giving rise to single chains of corner-sharing octahedra. Correspondingly, the spectra can be interpreted in terms of bridging W—O—W oxygens and of pairs of ditungstyl WO_2 terminal groups [67]. Also, the so-called Keggin-type heteropoly-salts such as $K_3[PMo_{12}O_{40}]$ are of this type: the anion, in fact, presents 12 distorted MoO_6 octahedra surrounding a central phosphate tetrahedron. Every molybdenum atom presents one terminal short Mo=O "double bond" which is responsible for the strong stretching band at 960 cm^{-1} (Figure 3.11), with additional Mo—O—Mo bridges (asymmetric stretching at 865 cm^{-1}) and also oxygen atoms triply bridging between one P and two Mo atoms (mainly responsible for the strongest band 783 cm^{-1}. The band at 1064 cm^{-1} is essentially due to P—O asymmetric stretching of the orthophosphate group.

3.4.3
Amorphous versus Crystalline Oxide Materials

In many cases, the skeletal spectra of amorphous oxides are similar to those of the corresponding crystalline materials, with broader and less-resolved features. This is the case, for example, in amorphous versus crystalline V_2O_5 [72]. In a few cases, however, amorphous material may also have relatively unusual features, different from those of the crystalline counterparts. For example, amorphous alumina is characterized by only octahedral cation coordination, in contrast to transitional aluminas which also have tetrahedral Al coordination. The skeletal IR spectrum of amorphous alumina is characterized by a strong band near 550 cm^{-1}, and by the absence of the feature in the region near 800 cm^{-1}, associated with AlO_4 tetrahedra, present in crystalline transitional aluminas [73].

3.5
Skeletal Spectra of Precursors for Metal Oxide Catalysts

Oxide catalysts may be obtained by thermal decomposition of precipitated precursors. These materials, usually easily decomposable solids, may be salts such as carbonates and nitrates, whose skeletal spectroscopic features have been discussed above. Alternatively they may be simple or complex hydroxides.

3.5.1
Metal Hydroxides

The hydroxides in their solid crystalline structures generally form by condensed polyhedra containing the metal element surrounded by oxygen atoms, with hydrogen atoms located externally to their polymeric structures and involved in strong hydrogen bonding. According to this picture, the skeletal spectra of hydroxides

show features typically due to the OH groups, and features to be assigned to the vibrations of MO_x polyhedra. For the latter features, the same considerations already made for oxides are valid.

The vibrations of hydroxyl groups are typically composed of O—H stretches (3800–2000 cm^{-1}, depending upon the extent of H-bonding), in-plane bending (1200–800 cm^{-1}) and out-of-plane deformation (generally below 1000 cm^{-1}). The multiplicity of such modes depends upon the number of hydroxyl groups present in the smallest Bravais cell and in the coupling of their vibrations, and is also dependent on the hydrogen-bonding patterns.

The centrosymmetric structures of LiOH and NaOH, both containing two formula units per unit cell, gives rise to two OH stretching modes, one of which is IR active and the other Raman active. In the case of KOH, whose structure is not centrosymmetric and contains two formula units per unit cell, a split of both IR and Raman active peaks is detectable. The positions of these peaks (in the 3680–3600 cm^{-1} region) shows that no hydrogen bonding occurs in these structures.

The structure of brucite $Mg(OH)_2$ is assumed by most divalent hydroxides. Every layer of $Mg(OH)_2$ contains MgO_6 octahedra with three triply bridging hydroxyl groups pointing up and three pointing down, alternately. The unit cell of the Brucite structure cointains only one $Mg(OH)_2$ unit. So, twelve optical modes should exist. Two OH stretching modes exist, one Raman active (symmetric stretching, A_{1g}, 3655 cm^{-1}) and one IR active (asymmetric OH stretching, A_{2u}, 3700 cm^{-1}). The positions of these modes shows that no hydrogen bonds occur in this structure. Additional two doubly degenerate deformation modes occur, again one is Raman active (E_g) and one is IR active (E_u). Finally, two IR active modes ($A_{2u} + E_u$) and two Raman active modes ($A_{1g} + E_g$) are associated with vibrations of the MgO_6 octahedra. In the Figure 3.13 the spectra of a KBr disk (a) and of a pure powder pressed disk (b) of a commercial "MgO" sample is shown. The spectra show well the band at 3700–3698 cm^{-1} of $Mg(OH)_2$ impurity in the sample. The pure powder spectrum also shows a peak at 3648 cm^{-1}, which probably corresponds to the Raman mode, slightly shifted and activated in IR owing to its location on a surface layer.

The goethite or diaspore structure of α-AlOOH, α-FeOOH, α-CrOOH and α-GaOOH have orthorhombic unit cells, belonging to $Pbnm = D_{2h}^{16} = 62$ space group with $Z = 4$. The overall unit cell and the smallest Bravais cell coincide and contain 16 atoms; thus 45 vibrational modes are expected. All atoms occupy the 4c Wyckoff position in the cell on a reflection plane (C_s site symmetry). The irreducible representation for the IR optical modes of α-MeOOH is as follows, separating the modes due to the hydrogen-bonded OH groups from those of the Me—O skeleton:

$$\Gamma_{Me-O} = 5B_{1u}(IR) + 2B_{2u}(IR) + 5B_{3u}(IR)$$

$$\Gamma_{O-H} = 2B_{1u}(IR) + 1R_{2u}(IR) + 2B_{3u}(IR)$$

Consequently, the IR spectrum is expected to contain 17 fundamental modes, only partly resolved. A typical feature of the spectra of these compounds is the

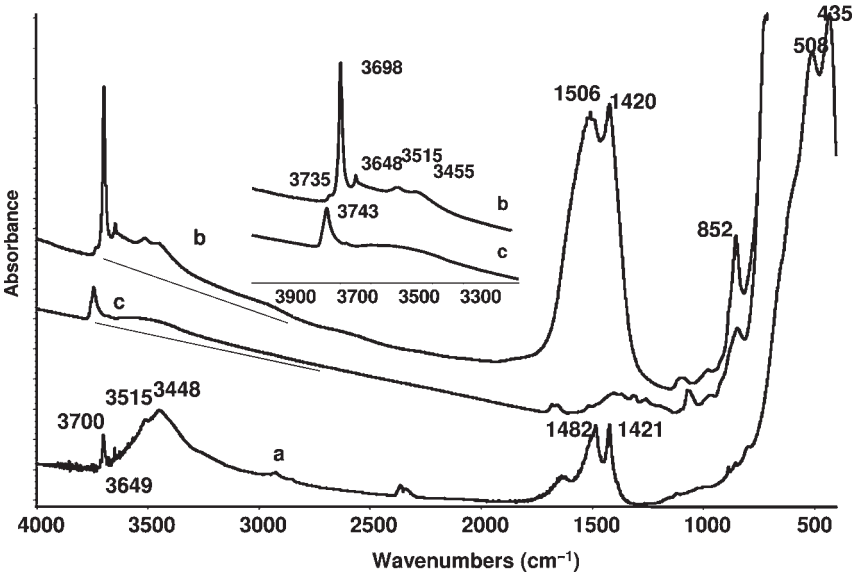

Figure 3.13 FTIR spectra of a "MgO" commercial sample: (a) KBr pressed disk; (b) pure powder pressed disk outgassed at 473 K; (c) pure powder pressed disk outgassed at 873 K.

presence of two IR-active OH stretches, giving rise to a strong band with a shoulder at the higher frequency in the IR spectra (3126, 3050 cm^{-1} for goethite; 3000, 2920 cm^{-1} for diaspore; 2913, 2840 cm^{-1} for α-GaOOH) as well as two strong bending modes (891, 796 cm^{-1} for goethite, 1080, 970 cm^{-1} for diaspore, 1019, 952 cm^{-1} for α-GaOOH), which have been discussed in terms of the geometry of the hydrogen-bonding situations. α-(Cr,Fe)OOH [74] and α-(Fe,Ga)OOH [75], forming goethite-type solid solutions, have been also characterized by IR.

X-ray diffraction analysis indicates that boehmite γ-AlOOH and lepidocrocite γ-FeOOH crystallize in the space group $Cmcm \equiv n.63 \equiv D_{2h}^{17}$, with $Z = 4$. However, such analysis does not reveal the position of the hydrogen atoms. Instead, vibrational spectroscopies can be used to obtain such information. The IR spectra are dominated by two well-split OH stretches (3305, 3090 cm^{-1} for boehmite) and two OH deformations (1170 and 1074 cm^{-1}), see Figure 3.6.

In Figure 3.5 the spectrum of the hydroxy-chloride paratacamite, $Cu_2Cl(OH)_3$, is shown, together with that of its decomposition product CuO. The crystal structure of paratacamite belongs to the $R\,\overline{3}$ space group $\mathrm{n.148} = C_{3i}^{2}$. The number of molecular units in the smallest Bravais cell is 8, so that this cell contains 16 copper atoms, 24 oxygen and hydrogen atoms and 8 chlorine atoms. This gives rise to a very complex vibrational structure, with 213 vibrational freedom degrees, giving rise to 142 vibrational modes of which 72 are Raman active and 70 are IR active. In particular, 24 OH stretching modes are expected (12 IR active and 12 Raman active) together with 24 degenerate OH deformation modes (again 12 IR active and 12 Raman active), 8 Cu—Cl stretching modes (4 IR and 4 R), and also 8 Cu-Cl deformations (4 IR and 4 R), and finally 78 Cu—O modes (40 Raman active and 38 IR active).

It is obvious that most of the modes are superimposed. The IR spectrum clearly shows at least four of the 12 IR active OH stretching modes resolved (see the insert in Figure 3.3) while 12 maxima can be distinguished in the region 1200–700 cm^{-1}, which could correspond to the resolution of all the IR-active OH bending modes. Below 60 cm^{-1} several maxima are also observed, due to Cu—O and Cu—Cl vibrations. The features observed in the region 1700–1300 cm^{-1} are either due to harmonics of lower frequency vibrations or to water and carbonate impurities.

3.5.2
Hydrated Compounds

Gas-phase or isolated water molecules belong to the C_{2v} point group and give rise to three optical modes $2A_1 + B_1$, all both IR and Raman active. The two stretches are at 3756 cm^{-1} (B_1, asymmetric stretch) and at 3657 cm^{-1} (A_1, symmetric stretch) while the bending mode (A_1) is at 1594 cm^{-1}. When water molecules are incorporated into a crystal, their six external modes (arising from frustrated rotations and translations) contribute to lattice modes called "librations" of water molecules (wagging, rocking and twisting modes) and to the acoustic modes. When water is coordinated through oxygen lone pairs to cations (aquo-complexes) the metal–oxygen stretching mode and the corresponding deformation modes appear and couple with the other metal-to-ligand vibrations. The metal–oxygen stretches are most usually located below 600 cm^{-1}. At slightly higher frequencies (900–500 cm^{-1}) the wagging and twisting modes of coordinated water molecules become internal vibrations of the aquo-complex. Coordination *per se* causes relatively weak perturbations on the stretching and bending modes of water. However, coordination is frequently associated with additional hydrogen bonding of water, with other water molecules or with anions present in the crystal structure. This can result in strong shifts down (down to 2000 cm^{-1}) and broadening of the stretching absorptions while the bending modes are not very sensitive and always fall in the region 1700–1550 cm^{-1}. Asymmetric hydrogen bonding (bonding to only one of the two protons of water, gives rise to particular spectra where sharp high-frequency peaks together with broad low-frequency OH stretching modes components are present together. This occurs for α-$Zr(HPO_4)_2 \cdot H_2O$ (Figure 3.11) where two very sharp OH stretching modes at 3593, 3509 cm^{-1}, are due to the free OH groups of the two molecules in the smallest Bravais cell while broader bands at 3370 and 3150 cm^{-1} are due to the H-bonded OH groups of water and the hydrogenphosphate ions [76]. Protonated forms of water such as the oxonium ion H_3O^+ [77] have also been investigated.

3.5.3
Layered Double Hydroxides

Complex precipitates, such as layered double hydroxides, are frequently prepared as precursors of oxide catalysts. Hydrotalcite is a hydrated hydroxy-carbonate mineral with the formula $Mg_6Al_2(OH)_{16}CO_3 \cdot 4H_2O$. It represents the better known and most popular member of a family of layered double metal hydroxide com-

pounds which find a number of applications in several fields. Its thermal decompostion gives rise to a mixed oxide whose virtual composition is $5\,MgO{\cdot}MgAl_2O_4$, although these phases give rise to partial solid solutions depending on decomposition temperature. Such materials find several applications in today's industrial heterogeneous catalysis. Similar materials are obtained using other divalent (Ni, Co, Zn, Cu) and trivalent (Ga, Fe, Cr) elements with different anions (nitrate, chloride, etc.) Hydrotalcite-type solids crystallize in the $R\,\bar{3}m \equiv D_{3d}^5 \equiv \mathrm{n.166}$ space group. The full rhombohedral unit cell contains three cations. However, owing to the presence of three lattice points in the overall rhombohedral unit cell, the smallest Bravais cell only contains one cation, that is, one of the above formula units. Cation distribution in the 3a Wyckoff sites may be considered random. The structure is formed by brucite-type layers with the formula $M(OH)_2$ with carbonate ions in the interlayer region to balance the charge excess due to the substitution of the trivalent cation for the divalent one. Obviously, there are two trivalent cations per carbonate ion. The water content is also related to the proportion of trivalent cations. For $x = 0.33$ (for every three cations, one is trivalent) there is half a water molecule and one sixth of a carbonate ion per smallest Bravais cell. The brucite-type layers are made of flattened octahedral MO_6 and triply bridging hydroxyl groups. Both water molecules and carbonate ions stay planar centrally between the layers and parallel with respect to them. The distance between the protons of both hydroxyls and water and the oxygen atoms of the carbonate ions and water are such that hydrogen bonding should be considered to be negligible. The IR spectra show the features of hydroxyl groups and of the anions [78].

3.5.4
Impure Metal Oxides

Commercial metal oxide powders may be contaminated by molecules from the atmosphere as well as those arising from the preparation procedure. Among typical contaminants, water may produce hydroxides while carbon dioxide can produce surface or bulk carbonates. This is the case of the "MgO" sample whose spectrum is reported in Figure 3.13a, which shows the OH stretching band near $3700\,cm^{-1}$ of $Mg(OH)_2$ and the strong bands in the region $1500–1400\,cm^{-1}$ due to the C=O stretching of carbonate species. Both features disappear on heating under vacuum, owing to decomposition to MgO. Other frequent contaminants are sulfates and hydrocarbon species.

3.6
The IR Spectroscopy of Adsorbed Probe Molecules for Surface Chemistry Characterization

IR spectroscopy of adsorbed probe molecules is mostly performed with either the transmission/absorption technique or with the DRIFT technique. In the transmission/absorption technique, self-supporting pressed disks of the pure oxide powders

are prepared and put into the IR beam, in an appropriate cell that allows heating, cooling and gas/vapor manipulation. Activation is mostly performed by outgassing at relatively high temperature. In the case of DRIFT experiments the catalyst is deposited on the sample holder, with gentle pressure, and activation is mostly performed by flowing in inert dry gas.

The transmission/absorption IR spectrum of the oxide disk has a baseline slope increasing towards higher frequency, reflecting the scattering of the beam, which increases with increasing frequency (wavenumber), as shown in Figure 3.13b and c, where the spectra of pressed discs of a "MgO" commercial powder are reported. The slope depends on the particle size and may be very steep for powders that are constituted by quite large particles (near 1 μm). Thus, transmission for large particle size oxides may be zero at 4000 cm^{-1} or even lower frequencies. In the case of DRIFT, the reflectance actually increases by increasing scattering, so that the baseline is flat or even decreasing. The absorptions due to the surface hydroxyl groups are superimposed on this line, in the region 3800–3000 cm^{-1}. In some cases, absorptions due to overtones of bulk or surface metal oxide stretching vibrations are also superimposed on the scattering line. On the low-frequency side, below 1300–600 cm^{-1} depending on the skeletal spectrum of the solid, the absorptions due to bulk skeletal fundamental vibrations cut off the spectra of the pure powder disks.

The advantages of the DR technique over the transmission/absorption technique in the field of the surface chemistry of oxides are:

1) easier sampling;
2) applicability to powders that scatter too much for the transmission/absorption technique, assuming the surface area is sufficiently high to detect surface vibrations with a sufficiently high signal-to-noise ratio;
3) slightly lower sensitivity to bulk conduction phenomena, because of a higher surface-to-bulk sensitivity ratio.

In effect, for general purposes (adsorption studies on relatively small-crystal-size powders) the main advantage of the DR technique is the first one, with the disadvantages of: (i) less easy optical setting up; (ii) the requirement to work in flow rather than in vacuum (mainly because the sample is not pressed and powders are highly mobile in vacuum, and because of a more difficult evacuation of the cell, due to their design and size) with a consequently more difficult sample activation.

The spectra of adsorbed and surface species obtained using transmission and DR techniques are very similar in quality, in regard to resolution, signal-to-noise ratio and sensitivity.

3.6.1 Infrared Characterization of Surface Element–Oxygen Bonds

3.6.1.1 Surface M–O–M Bridges

The adsorption of probe molecules may provide evidence of the existence of metal–oxygen bonds at the surface of a metal oxide. In Figure 3.14, the subtraction

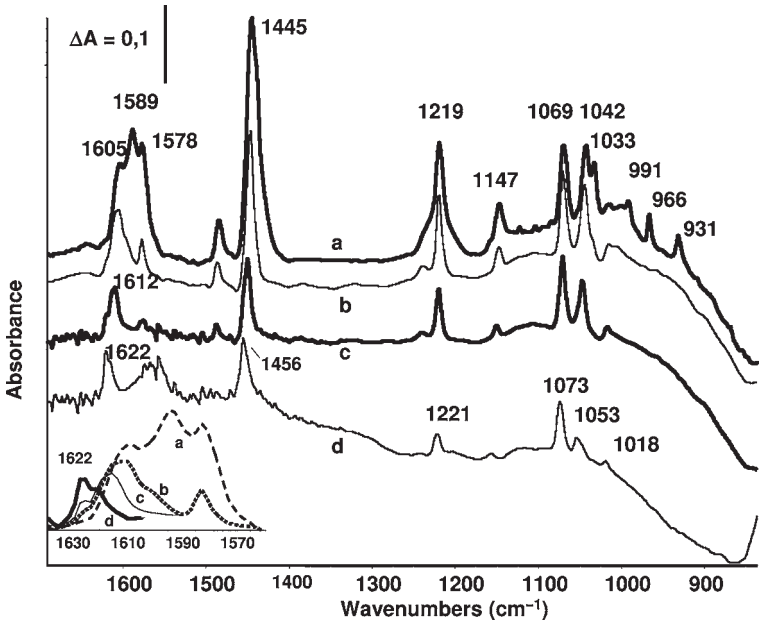

Figure 3.14 FTIR spectra of the surface species produced by adsorption of pyridine on β-Ga_2O_3 activated at 673 K: (a) in the presence of 1 Torr of the vapor and after outgassing at (b) room temperature, (c) 373 K, (d) 523 K. The spectrum of the activated sample has been subtracted from those recorded after adsorption.

spectra relative to the adsorption of pyridine on β-Ga_2O_3 are reported. Besides the sharp "positive" peaks due to adsorbed pyridine, a broad "negative" band is observed in the range 850–880 cm^{-1}, with a tail towards higher frequencies. A similar absorption is found in several other cases, such as on aluminas [79] and aluminates [80] just above the cut-off due to the skeletal modes, and is attributed to the relaxation of surface metal–oxygen bonds by adsorption of molecular probes.

The existence of surface metal–oxygen bonds can also be indirectly deduced by the reactivity of these bonds with molecules from the gas phase, such as the surface hydration producing new hydroxyls, the surface carbonation producing carbonates, and also some more complex reactivity, such as the reactivity with alkoxysilanes producing surface alkoxides that may later be converted to surface hydroxides by elimination [81].

3.6.1.2 Surface M=O "Double" Bonds on Binary Oxides

Metals and other elements in very high oxidation states can give rise to element–oxygen double bonds in their oxides. This is the case for vanadyl, niobyl, molybdenyl, chromyl and tungstyl groups, as well as of P=O bonds present in oxo-compounds of the corresponding elements. The location at the surface of

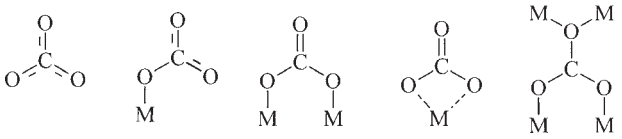

Scheme 3.1 Posible coordinations of carbonate ions and other trigonal anions (nitrates, borates): I: trigonal symmetric; II: monodentate; III bidentate (bridging); IV chelating; V: polydentate.

such bonds has been observed in the cases of V=O bonds (1038 cm^{-1}) at the surface of V_2O_5 [82], Nb=O bonds at the surface of niobic acid ($Nb_2O_5 \cdot nH_2O$) [83] and W=O bonds at the surface of WO_3 (950 or 1040 cm^{-1}) [84]. These features are more clearly observed as negative bands in the subtraction spectra after adsorption of probe molecules (spectrum recorded after adsorption from which the spectrum of the "clean" sample has been subtracted), showing that such surface species are perturbed upon adsorption. Note that double bonds also exist in the bulk but adsorb at lower frequencies in vanadia and niobia, while they do not exist in the bulk of tungsta (a distorted ReO_3 structure with octahedral coordination for the cations) but are formed at the surface as in the structure of several tungstate species.

3.6.1.3 Surface Oxo-Anions

Surface Carbonate, Nitrate and Borate Species As already reported (Table 3.5), free carbonate, nitrate and borate ions, as a result of their trigonal D_{3h} symmetry, have one characteristic strong IR vibration (ν_3; asymmetric XO stretch) found near 1480 cm^{-1} for borates, 1415 cm^{-1} for carbonates and near 1380 cm^{-1} for nitrates, together with two lower frequency IR-active deformation modes.

The lowering of the symmetry connected with coordination causes the splitting of the doubly degenerate ν_3 vibration, as well as the IR activation of ν_1, the Raman-active symmetric deformation mode. Four different types of carbonate ions are usually considered as possible surface species. They can be represented by the simplified models I–IV (Scheme 3.1). Type I (symmetrical) refers to a surface species whose spectroscopic features correspond to those of a non-coordinated ion. Monodentate, bridging, chelating and polydentate structures may also be formed. The structures may be distinguished considering in parallel the stability (polydentate > bidentate > chelating > monodentate) and the extent of the splitting of $\Delta\nu_3$ (bidentate ≥ chelating > monodentate ≥ polydentate) [85]. Some carbonate species, characterized by very large $\Delta\nu_3$ and very weak stability have been denoted as "covalent" or "organic-like", but are most likely due to bent very strongly perturbed CO_2 molecules [86]. Bicarbonate ions $[HCO_3]^-$ can also be formed by adsorption of or contamination by CO_2. These species are characterized by νOH modes near 3620 cm^{-1}, δOH modes near 1300–1200 cm^{-1}, as well as by two νC=O modes (~1600 and ~1450 cm^{-1}).

Surface Silicate and Hydrogen-Silicate Species The addition of silica to oxides such as alumina and titania is sometimes due to the need to enhance surface area and thermal

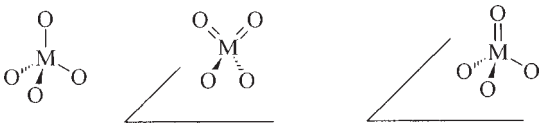

Scheme 3.2 Left: isolated truly tetrahedral metallate species: the four M—O bonds are equally long and the O—M—O angle is near 109°28′; the point group is T_d; middle, "deformed" fourfold coordinated metallate species, i.e. di-oxo species, the point group is C_{2v}; right, "deformed" fourfold coordinated metallate species, i.e. mono-oxo species, the point group is C_{3v}.

stability and retard phase transitions [87]. Surface silication using silicon alkoxides is also sometimes performed in order to modify the surface acidity [88, 89]. These treatments generally give rise mostly to surface hydrogen-silicate species $[HOSiO_3]^{3-}$, well characterized by the characteristic OH stretching of surface silanol groups near 3735 cm^{-1}, and strong Si—O stretching modes in the region around 1000 cm^{-1}. In the case of basic oxides, such as MgO and CaO, bulk orthosilicate species form easily [90]. This also occurs by the reactive adsorption of methylsiloxanes [91].

Surface Sulfates Tetrahedral oxo-anions give rise to nine internal vibrations plus six external vibrations contributing to lattice vibrations and to acoustic modes of the solid. When the ion takes its highest symmetry (T_d point group) the symmetric stretching and the symmetric deformation are Raman active, the last being doubly degenerate. The asymmetric stretching and deformation are both IR and Raman active and are triply degenerate. By lowering of the symmetry, as occurs on surfaces (Scheme 3.2), the degeneracies are broken and all modes can become IR and Raman active. Scheme 3.2 shows possible geometries of these species, when they are located on surfaces.

Spectroscopic studies showed that the sulfate ions [92] on ionic oxides in dry conditions at low coverage, are tetracoordinated with one short S=O bond (mono-oxo structure), characterized by very strong S=O bands in the range 1420–1350 cm^{-1}. In Figure 3.15 the spectrum of a sulfated ceria-alumina is presented; the band at 1380 cm^{-1} is in fact due to this S=O stretching mode. S—O single-bond stretching modes are observed below 1250 cm^{-1}, with the corresponding overtone modes in the region 2500–1900 cm^{-1}. At higher coverage, disulfate species are assumed to exist [93, 94], although real proof of this probably does not exist. However, surface sulfate species are strongly sensitive to hydration. The spectrum changes extensively and the species probably convert into dioxo species.

Surface Vanadate, Molybdate and Tungstate Species The pure and mixed oxides and the salts of vanadium, molybdenum and tungsten in their higher oxidation states are used widely as heterogeneous catalysts, for selective oxidation as well as for acid catalysis. Similarly, supported chromia and rhenium oxides find wide application in different catalytic processes.

For most of the oxide-supported "monolayer" oxides (e.g. vanadia, molybdena and tungsta supported on alumina), titania, zirconia and silica surface species are

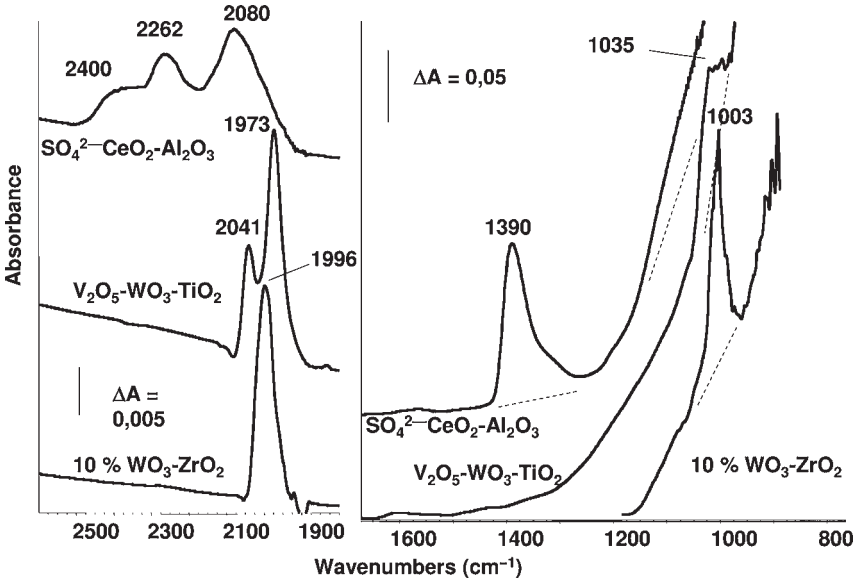

Figure 3.15 FTIR spectra of pure powder pressed disks of sulfated ceria-alumina, V_2O_5-WO_3-TiO_2 catalyst and WO_3-ZrO_2 catalyst.

observed (at least at low loadings, i.e. well below the loading corresponding to the "theoretical geometric monolayer") which are spectroscopically characterized after treatments which allow the desorption of water [42, 47]. Features include:

(i) a very high position of the very intense band observed in IR and Raman activity, similar to that of gaseous mono-oxo species;
(ii) the coincidence of the position of the band detected in Raman and IR spectra and its non-complexity in both cases;
(iii) the detection in the IR spectrum of a single overtone band.

Partial $^{18}O/^{16}O$ exchange experiments showed a simple splitting like that found, for example, in the cases of WO_3/Al_2O_3 [95] and V_2O_5/TiO_2 catalysts [96].

These data are a strong demonstration that the species are isolated and mono-oxo. In Figure 3.15, the fundamental (right) and first overtone region (left) for a WO_3/ZrO_2 acid catalyst and of a V_2O_5-WO_3/TiO_2 SCR. DeNOx catalyst are shown. The strong band at 1003 cm^{-1} and the weaker one at 1996 cm^{-1} are due to the stretching mode (fundamental and first overtone, respectively) of W=O "double bonds" of mono-oxo tungstyl species of the WO_3/ZrO_2 catalyst. The same modes are found at ~990 and 1973 cm^{-1} for the V_2O_5-WO_3/TiO_2 catalyst where the bands at 1035 and 2041 cm^{-1} are due to the fundamental and the first overtone, respectively, of the V=O double bonds.

On the other hand, a further demonstration of the "isolated" nature of these species is expected from the absence of modes assignable to M—O—M asymmetric

stretchings. These modes are expected to be very strong in the IR spectra, but unfortunately the region of these modes is not available for alumina and titania supported catalysts because of the opacity of the pressed disks in this region. In the case of zirconia supported catalysts, where this region is in part available, this band is not present, at least for low loaded molybdena [97] and tungsta [98] samples. This topic has been discussed in detail previously [99]. At high loadings, most authors agree that polymeric anions form.

3.6.2
Spectroscopic Detection of Surface Brønsted Acid Sites

The fragments arising from the dissociative adsorption of water on the surface of metal oxides give rise to hydroxyl groups that are potentially active Brønsted acid sites [100] or basic sites. Such surface hydroxyl groups can be detected directly, recording the IR spectra of the oxide catalyst powders after treatments that allow the desorption of molecularly adsorbed water, in the region 3800–3000 cm^{-1}, where the O—H stretching modes (νOH_s) fall. The position and shape of the νOH bands of the surface hydroxyl groups is informative on their coordination. Covalent oxide components [101, 102] usually give rise to very typical strong sharp peaks due to covalently bonded terminal OH groups. For example, silica-containing oxides (e.g. any silicas and silicated oxides, see Figure 3.16) almost invariably show a peak in the range 3750–3730 cm^{-1} while P_2O_5-containing samples contain a sharp band at 3670–3650 cm^{-1} observed in supported phosphoric acid samples [103–105] and in several bulk phosphates [69, 83, 106–108]. Similarly, B—OH bonds give a sharp band at 3710–3690 cm^{-1} [109, 110], Ge—OH bonds at 3685–3670 cm^{-1}.

Conversely, in ionic oxides bridging and triply bridging hydroxyl groups are also formed at the surface. Thus, the OH spectrum is frequently more complex (see, for example, Figure 3.17 for alumina and Figure 3.18 for gallias, zirconias and ceria). It is usually agreed that the OH stretching is highest for terminal OH

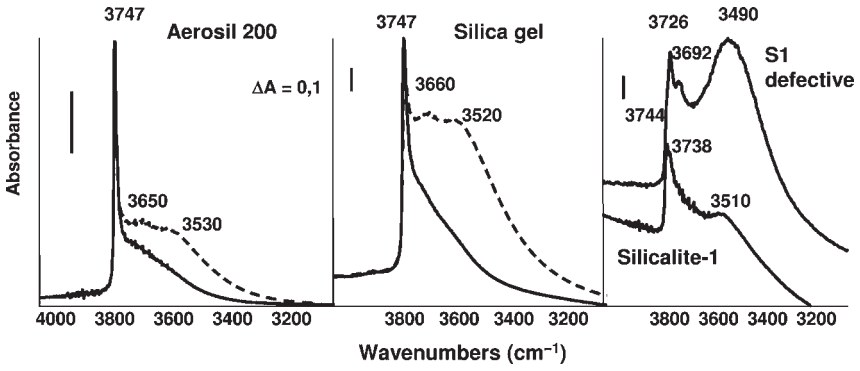

Figure 3.16 FTIR spectra of the surface hydroxyl groups of SiO_2 samples after outgassing at 473 K (broken lines) and 673 K (full lines).

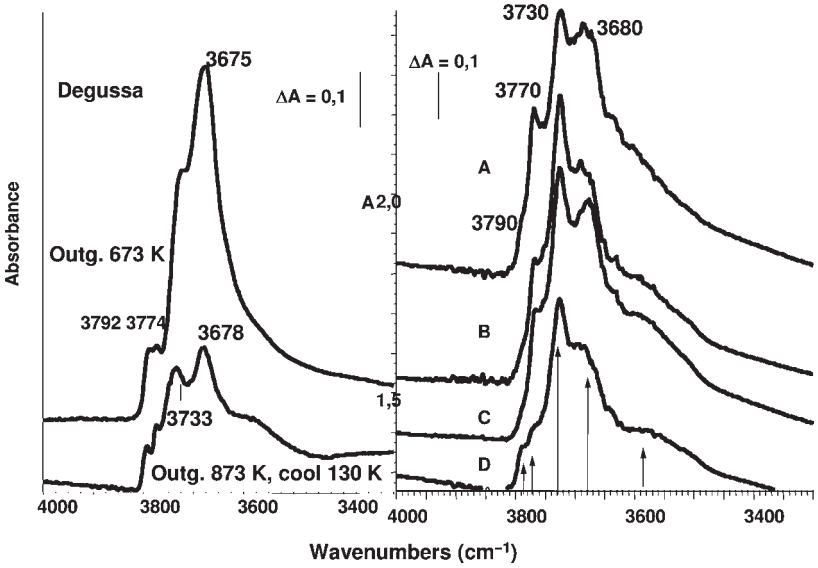

Figure 3.17 FTIR spectra of the surface hydroxyl groups of γ-Al_2O_3 samples: left aluminum oxide C from Degussa after outgassing at 673 K and 873 K; right, samples from Akzo (A), Sud Chemie (B), Engelhardt (C) and Condea (D), all having surface area in the range 180–200 $m^2 g^{-1}$.

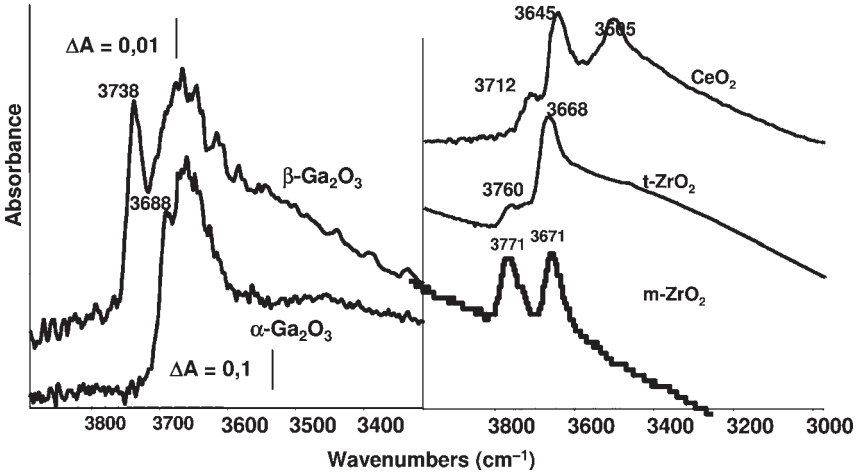

Figure 3.18 FTIR spectra of the surface hydroxyl groups of α-Ga_2O_3, β-Ga_2O_3, monoclinic ZrO_2, tetragonal ZrO_2 and CeO_2, all after outgassing at 773 K.

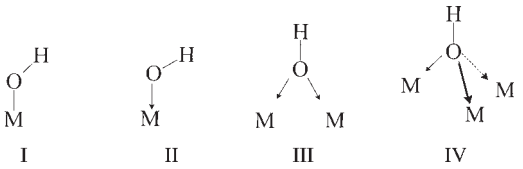

Scheme 3.3 Structure of hydroxyl groups on metal oxides: I: covalent, terminal; II: ionic, terminal, III: ionic, bridging; IV: ionic, triply bridging.

groups, intermediate for bridging and lowest for triply bridging OH groups (see Scheme 3.3) This approach was first systematically proposed by Tsyganenko and Filimonov [111]. Interesting support for this approach was given more recently by the group of Lavalley [112] who showed a relationship between the OH stretching bands of the surface hydroxyl groups and the C—O stretching bands of the surface methoxy groups of methoxylated oxides, namely zirconia, ceria and thoria.

3.6.2.1 Hydroxyl Groups in Silica

Structurally, amorphous silica is quite a covalent material [101, 102] whose surface behavior is dominated by the chemistry of the terminal silanol groups, characterized by a sharp and strong IR OH stretching band at 3748–3730 cm^{-1} (Figure 3.16). The IR band of silanol groups always presents a tail to lower frequencies, which has been in part attributed to geminal silanols. Near-lying terminal silanol groups also make hydrogen bonds with each other, giving rise to chain-bonded hydroxyls. These groups, responsible for broad OH stretching bands near 3650 and 3530 cm^{-1}, condense upon outgassing at high temperature, to produce gas-phase water and surface siloxane bridges. The relative amount of isolated and H-bonded silanols depends on porosity [113], as shown in Figure 3.16 where the spectra of a highly porous silica gel are compared with those of an almost non-porous material (Aerosil). The silanols make the surface of highly hydroxylated silicas strongly hydrophilic, and their wet surfaces are even more active in adsorption. It is well known that hydrogen bonds also occur between the silanol groups and non-polar molecules such as hydrocarbons, allowing the use of silicas for adsorption of these compounds.

Silicalite-1 is a fully siliceous zeolite, with the MFI structure. Its crystalline framework, composed of SiO_4 tetrahedra, has an essentially covalent and hydrophobic character. When well crystalline, hydrophilic silanols, whose acidity is comparable with that of silica [113, 114], are present essentially at the external surface (Figure 3.16). However, when prepared in a "defective" form, nests of H-bonded silanol exist, giving rise to a quite complex IR spectrum in the OH stretching region with a prominent band at 3500 cm^{-1} and several sharp maxima in the range 3745–3650 cm^{-1}; they are at least in part located in the channels [115] and make the structure more hydrophilic.

3.6.2.2 Hydroxyl Groups in Alumina

Many studies have been devoted to the multiplicity of the surface hydroxyl groups of aluminas. After the work of Peri [116], and of Tsyganenko and Filimonov [111],

Table 3.7 Surface OH groups on sesquioxides.

	γ-Al_2O_3	α-Al_2O_3	γ-Fe_2O_3	α-Fe_2O_3	β-Ga_2O_3	α-Ga_2O_3
$_{IV}M^{3+}$ I	3790	–	3740	–	3745	
$_{IV}M^{3+}$ II	3770	–	3725	–	3738	
$_{VI}M^{3+}$ I	3730	3730	3675	3680, 3660	3685	3688
Bridging	3680	3690	3640	3640	3670	3660
Triply bridging	3580	3550	3450	3480, 3440	3550	

Knözinger and Ratnasamy reported a very popular model of the different exposed planes of spinel type aluminas [117]. This model has been later modified by Busca and coworkers [80, 118] and reviewed by Morterra and Magnacca [119]. More recently, additional investigations have been published by Tsyganenko and Mardilovich [120] and, on the basis of theoretical calculations by Fripiat and coworkers [121], by Digne and coworkers [122], who also attempted to model the interaction of probe molecules. Lambert and Che [123] further reviewed these models and demonstrated that the problem is still not solved. At least five components are usually present in the IR spectrum of the hydroxyl groups of aluminas (Figure 3.17), at about 3790, 3770, 3740–3720, 3700–3670 and 3580 cm^{-1}, although in many cases the observed peaks are multiple. The available data show that the hydroxyl groups absorbing at higher frequency (above 3700 cm^{-1}) are available for interaction with molecular probes, while those absorbing below 3700 cm^{-1} appear to be substantially inactive [124, 125]. Liu and Truitt [126] emphasized the close proximity of surface OH groups of aluminas to Lewis acid sites. The bands below 3700 cm^{-1} are more sensitive to outgassing than those above 3700 cm^{-1} (Figure 3.13, left) suggesting that they can be hydrogen bonded. To our knowledge, a complete investigation of the accessibility of these sites has not yet been published.

3.6.2.3 Surface Hydroxyl Groups of Other Sesquioxides and of Spinel-Type Mixed Oxides

The spectra of the surface hydroxyl groups of oxides with similar structures show some parallelism [118, 119]. In Figure 3.18, left, the spectra of the surface hydroxyl groups of gallia polymorphs α-Ga_2O_3 and β-Ga_2O_3 are shown. In Table 3.7 the observed bands for these solids are compared with those observed for the corresponding alumina polymorphs α-Al_2O_3 and θ- and γ-Al_2O_3, as well as for the polymorphs of ferric oxide α-Fe_2O_3 and γ-Fe_2O_3. α-Al_2O_3, α-Fe_2O_3 and α-Ga_2O_3 are isostructural as is α-Cr_2O_3 (corundum–haematite structure) with only octahedral coordination for the cations, while β-Ga_2O_3, θ- and γ-Al_2O_3 and γ-Fe_2O_3 are all structures derived from non-stoichiometric spinels with both tetrahedral and octahedral coordination for the cations. The IR spectra of the surface hydroxyl groups show some similarity, supporting the assignments of the higher frequency band to terminal OH groups on cations in a tetrahedral-like environment. These bands are always split, and are present in the spectra of the spinel-type sequioxides, but

absent from those of corundum sesquioxides. The spectra of the surface OH groups of stoichiometric spinels, such as magnesium, zinc, cobalt and nickel aluminates and ferrites [118, 119], show these bands, but unsplit, confirming the above assigment with the additional information that the presence of cation vacancies in the spinel structure is associated with this splitting.

3.6.2.4 Surface Hydroxyl Groups of Rock-Salt-Type Metal Oxides

Rock-salt-type oxides generally show only one predominant band: 3745 cm^{-1} for MgO (see Figure 3.13c), 3682 cm^{-1} for MnO [101], 3680 cm^{-1} for CoO [127] and NiO [128]. These bands are due to OH groups located above cations in overall octahedral coordination.

3.6.2.5 Surface Hydroxyl Groups of the Oxides of Tetravalent Metals

The surface hydroxyl groups of the TiO_2 polymorphs anatase and rutile have been the subject of several IR studies. Anatase shows a more complex spectrum, with a complex OH stretching band above 3700 cm^{-1} not found for rutile [129]. The surface hydroxyl groups of ZrO_2 polymorphs, tetragonal and monoclinic, have also been the object of several studies. A doublet near 3770 and 3670 cm^{-1} is typically found at the surface of monoclinic zirconia [130]. For tetragonal zirconia, a main band is usually found between 3690 and 3660 cm^{-1}, with additional weaker components (see Figure 3.18, right) [131]. Ceria, CeO_2, presents a main band near 3640 cm^{-1} and a weaker one near 3710 cm^{-1}, together with a third broader feature at 3505 cm^{-1} (see Figure 3.18).

3.6.2.6 The Surface Hydroxyl Groups of Sulfated and Tungstated Oxides

Much interest has been devoted recently to tungstated oxides mainly in relation to their use as active components of vanadia catalysts for the selective catalytic reduction of NO_x by ammonia and to their activity in the paraffin skeletal isomerization reaction. Anatase and tetragonal zirconia give rise to better catalysts than rutile and monoclinic zirconia.

A particular feature of tungsta-based catalysts concerns the possible reduction of tungsten oxide to lower oxidation states. Residual surface OH groups of such materials do not present well defined sharp bands, but quite broad features [132]. They have been attributed to the hydrated form of surface tungstyl species, see Scheme 3.4. It has been suggested that stronger Brønsted acid sites are generated when tungsten is reduced to lower valency [133, 134]

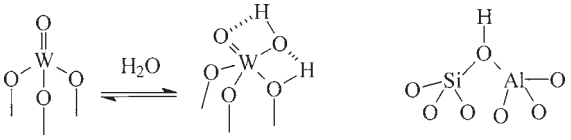

Scheme 3.4 Proposed structures for anhydrous and hydrated forms of surface tungstyl species (left) and of the bridging OH groups of zeolites.

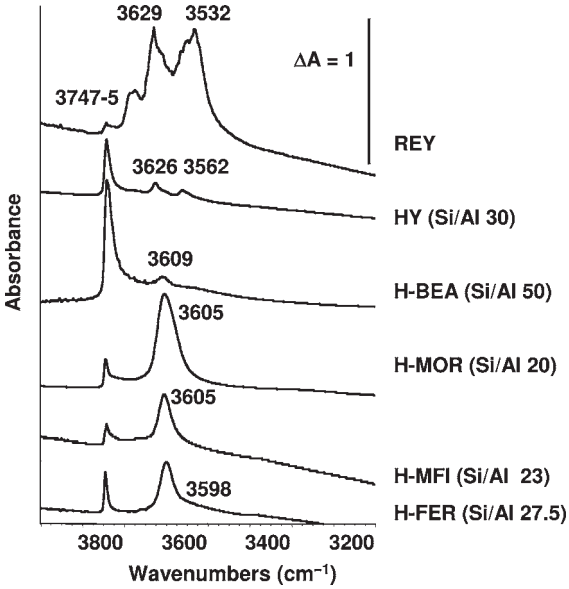

Figure 3.19 FTIR spectra of zeolite samples, all activated at 723 K.

Also sulfation of metal oxides introduces quite strong Brønsted acidity and, in general, enhances the catalytic activity in acid-catalyzed reactions. Zirconia (tetragonal more than monoclinic), when sulfated becomes very active for some hydrocarbon conversion reactions. IR spectra show a band in the range 3645–3630 cm^{-1}, to which the catalytic activity is attributed.[93, 135]. In sulfated titania, the strong Brønsted acidity is associated to an OH stretching band at 3695 cm^{-1} [129]. Sulfation of silica gives rise to an unstable material, which apparently does not present characteristic OH groups.

3.6.2.7 The Surface Hydroxyl Groups of Protonic Zeolites

Protonic zeolites find industrial applications as acid catalysts in several hydrocarbon conversion reactions. The excellent activity of these materials is due to two main properties: a strong Brønsted acidity of bridging Si—(OH)–Al sites (Scheme 3.4, right) generated by the presence of aluminum inside the silicate framework and shape selectivity effects due to the molecular sieving properties associated with the well defined crystal pore sizes, where at least some of the catalytically active sites are located.

The spectra of protonic zeolites (Figure 3.19) show, in addition to a band of weakly acidic external terminal silanol groups at 3745–8 cm^{-1}, well defined and strong bands in the region between 3650 and 3500 cm^{-1}, due to the bridging hydroxyl groups. The position of this band is dependent on the size of the zeolite cavities, νOH being generally the lower the smaller the cavity. The OH stretching band position and width can be influenced by H-bonding within the cavity. In the case of zeolites with more than one type of quite different cavities, splitting of the

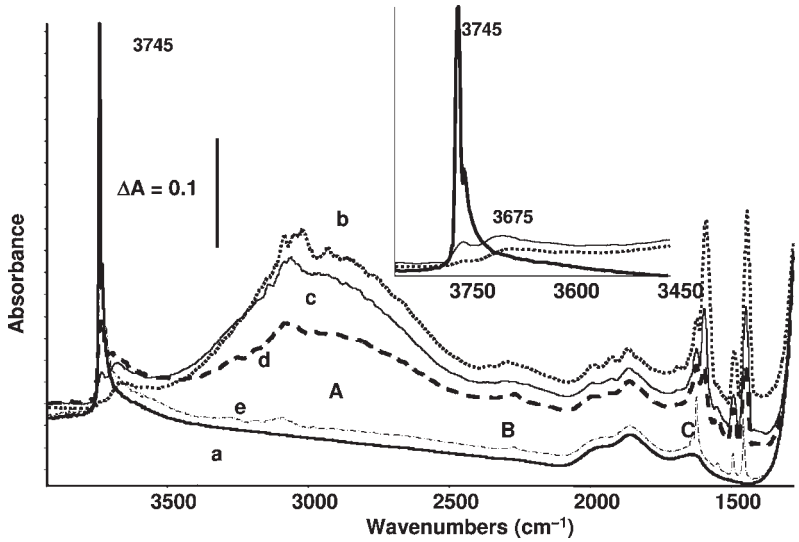

Figure 3.20 FTIR spectra of a MCM-41 type mesoporous silica-alumina (a) after activation by outgassing at 773 K; (b) in contact with 1 Torr pyridine vapour; after outgassing at room temperature for (c) 10 min; (d) 1 h (d) and (e) after outgassing at 523 K for 10 min.

band of the bridging hydroxyl groups can be observed. For the same zeolite structure, the intensity of νOH strongly depends on the Al content, its position being also slightly affected by composition. Data concerning protonic zeolites that find practical applications in the industry, such as H-FER, H-MFI, H-MOR, H-BEA, H-MWW, H-MAZ and H-FAU, have been reviewed [100].

3.6.2.8 The Surface Hydroxyl Groups of Microporous and Mesoporous Silica-Aluminas (SAs)

The IR spectra of silica-aluminas (SAs), both microporous and mesoporous, always present a very sharp band near 3747 cm^{-1}, as shown in Figure 3.20 for a mesoporous MCM-41 type SA sample with Si/Al atomic ratio 20. This band is certainly due to terminal silanols, spectroscopically very similar to those of pure silicas and of any silica-containing material. A tail towards lower frequencies is likely due (as for pure silica) to H-bonded and geminal silanols. Several papers reported the complete absence of bands assignable to bridging OH groups. Gora-Marek and coworkers [136, 137] re-proposed recently the existence of bridging OH groups in mesoporous SAs, reported in a few previous investigations. In contrast, Crépeau and coworkers [138] did not find any other species except terminal silanols on their strongly Brønsted acidic SA samples. Garrone and coworkers [139] found that a weak band at 3611 cm^{-1} is associated with molecular water adsorbed on mesoporous SA, and found a significant acidity for adsorbed H_2O.

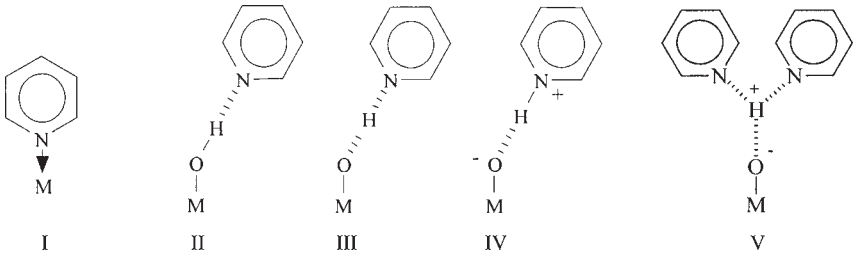

Scheme 3.5 Adsorption modes of a base (in this case pyridine) on the surface Lewis (I) and Brønsted sites (in this case terminal) on a solid oxide surface.

Bevilacqua and coworkers [113] re-investigated the surface hydroxyl groups and the surface acidity of silica, silicalite, mesoporous and microporous SAs, silicated aluminas, aluminated silicas and silicalite, and of some zeolites, by IR spectroscopy. Extremely small bands near 3610 cm^{-1} may be found on some SA samples (mostly prepared in organic media) and on aluminated silicas after activation, thus not being associated to adsorbed water. These bands certainly correspond to very few OH groups, and impurities (such as bicarbonates) might contribute to their formation. Bevilacqua and coworkers [113] suggested that, in disordered mesoporous or microporous amorphous materials, zeolite-like pores may accidentally form and host zeolite-like bridging hydroxyl groups.

3.6.3 Spectroscopic Characterization of the Strength of the Surface Brønsted Acid Sites

Different methods have been proposed to characterize the acid strength of the surface hydroxyl groups on solid oxides. Basic probes allow detection of several different interactions with acidic sites, as shown in Scheme 3.5. Species I depicts a typical Lewis interaction, where the base coordinates as such on Lewis acid sites located at the solid's surface. Species II to IV depict interactions of bases at surface Brønsted-type acid sites. Species II occurs when the acid–base interaction is very weak, and only results in a hydrogen bonding. Strictly speaking, this phenomenon does not enter into the Lowry–Bronsted definition of acidity. However, it can be demonstrated that this is what occurs when a true base (which can be protonated by an acid) interacts with a too weak acid or, alternatively when a true Brønsted acid interacts with a too weak base. Species IV depicts the true Brønsted acid–base interaction, with a total transfer of the proton from the Brønsted acidic OH to the base, resulting in its protonation and in the formation of its conjugated acid. Species III is an intermediate case that gives rise to a partial proton transfer and the formation of a "symmetric hydrogen bond" with the proton nearly halfway between the base and the acid's conjugated base. Species similar to V (protonated dimeric species of the base) are well known in homogeneous inorganic chemistry.

Reasons for the choice of one or other probe have been discussed previously [101, 102]. In Table 3.8 data are reported concerning the basicity of some probe molecules

Table 3.8 Molecular probes applied for surface acidity characterization.

Base			Conjugated acid	Base strength	
Family	**Example**			**pK_a**	**PA**
Cyclic amines	piperidine	$C_5H_{10}NH$	$C_5H_{10}NH_2^+$	11.1	933
Alkyl amines	*n*-butylamine	n–C_4H_9–NH_2	n–C_4H_9–NH_3^+	10.9	916
Ammonia		NH_3	NH_4^+	9.2	857
Phosphines	trimethyl-phosphine	$(CH_3)_3P$	$(CH_3)_3PH^+$	8.65	957
Phosphine oxides	trimethyl-phosphine oxide	$(CH_3)_3P{=}O$	$(CH_3)_3P{=}OH^+$		907
Heterocyclic amines	pyridine	C_5H_5N	$C_5H_5NH^+$	5.2	928
Ketones	acetone	$(CH_3)_2C{=}O$	$(CH_3)_2C{=}OH^+$	–7.2	824
Ethers	dimethylether	$(CH_3)_2O$	$(CH_3)_2OH^+$	~–3	792
Nitriles	acetonitrile	CH_3–C≡N	CH_3–C≡NH^+	–10.4	783
Hydrocarbons	benzene	C_6H_6	$C_6H_7^+$		750
	ethylene	$H_2C{=}CH_2$	CH_3-CH_2^+		680
Carbon monoxide		CO	$[HCO]^+$		598
Nitrogen		N_2			477
Hydrogen		H_2			422
Argon		Ar			369

expressed as pK_a of the conjugated acid and as proton affinity (PA). The former parameter, pK_a, is relevant with respect to acid–base interactions occurring in water solution, which, consequently, also implies solvation with water of both the base and its conjugated acid. The latter parameter, PA, is more appropriate for gas-phase interactions. Interestingly, the two scales are not coincident, for example ammonia is associated with a higher pK_a and lower PA than pyridine. This means that ammonia is more basic than pyridine in water, but is expected to be less basic than pyridine in the gas phase. The greater solvation of the ammonium ion in water (with the formation of four H-bonds) compared with the pyridinium ion could be the reason for this invertion of their relative acidity in water with respect to the gas phase. Some kind of solvation also occurs on oxide surfaces and, in particular, in the micropores of zeolites. Our own data indicate that on metal oxide surfaces ammonia is at least sometimes more easily protonated than pyridine.

The results of these studies for some solid oxide materials have been summarized in Table 3.9.

3.6.3.1 Techniques for the Evaluation of the Strength of Surface Brønsted Acid Sites

The Hydrogen-Bonding Method The strength of the acid–base interaction depends on the acid strength of the acid as well as on the basic strength of the base. When the acid or the base is too weak to allow proton transfer, the interaction results in hydrogen bonding. In intermediate cases, the proton transfer may be only partial

Table 3.9 Evaluation of the Brønsted acid strength of surface hydroxy-groups on catalytic materials by different IR techniques. The Brønsted acid strengths roughly decrease from top to bottom.

Catalysts		ΔνOH	ΔνOH cm^{-1}	Behavior with	Polymerization of				Protonation of				
↓	νOH cm^{-1}	CO	Aceto nitrile	*n*-C_4H_8	C_2H_4	C_3H_6	*i*-C_4H_8	C_4H_6	Acetonitrile	Pyridine	NH_3	*n*-Butyl amine	Piperidine
PA→		594	783	~750	680	752	802	783	783	912	846		933
H-zeolites	3650–3500	~300–340	ABC	polym + isom	yes	yes	yes	yes	yes[a)]	yes	yes	yes	yes
SO_4^{2-}/oxide	3650–3630	~140	ABC	polym	yes	yes	yes	yes	no	yes	yes	yes	yes
WO_3/oxide	Broad		ABC	polym	tr	yes	yes	yes	no	yes	yes	yes	yes
SiO_2–Al_2O_3	~3745	~70–150 ~300	ABC	polym	no	yes	yes	yes	no	yes	yes	yes	yes
H_3PO_4/SiO_2	~3660	~180–200	ABC	polym	no	no	yes	yes	no	yes	yes	yes	yes
$Nb_2O_5 \cdot H_2O$	3740–3705		~500						no	yes	yes		

AlF_3	3730 3655	~150	>500				yes	yes	no	tr	yes	yes	yes
SiO_2–TiO_2	~3740	~70–150	~450	polym tr	no	no	tr		no	no	yes	yes	yes
Al_2O_3–B_2O_3	3800–3650	~70–150	480–420 330–280	butoxide tr	no	no		yes	no	no	yes[b)]	yes	yes
Silicated γ-Al_2O_3	~3740	~70–150	480–420 330–280	ΔνOH 200–300	no	no	no		no	no	yes[b)]	yes	yes
γ-Al_2O_3	3800–3650	~70–100	450–400 330–280	ΔνOH 200–300	no	no	no	yes	no	no	yes[b)]	yes	yes
TiO_2-anatase	3750–3650	~110–150	<300		no	no	no	no	no	no	tr	tr	yes
am-SiO_2	~3745	~70–150	400	Δ νOH 150–200	no	no	no	no	no	no	no	no	no

a Likely formation of protonated bridging species $[CH_3CN \ldots H \ldots NCCH_3]^+$.
b Likely disproportionation $2NH_3 \rightarrow NH_2^- + NH_4^+$; isom = isomerization; polym = polymerization; tr = traces.

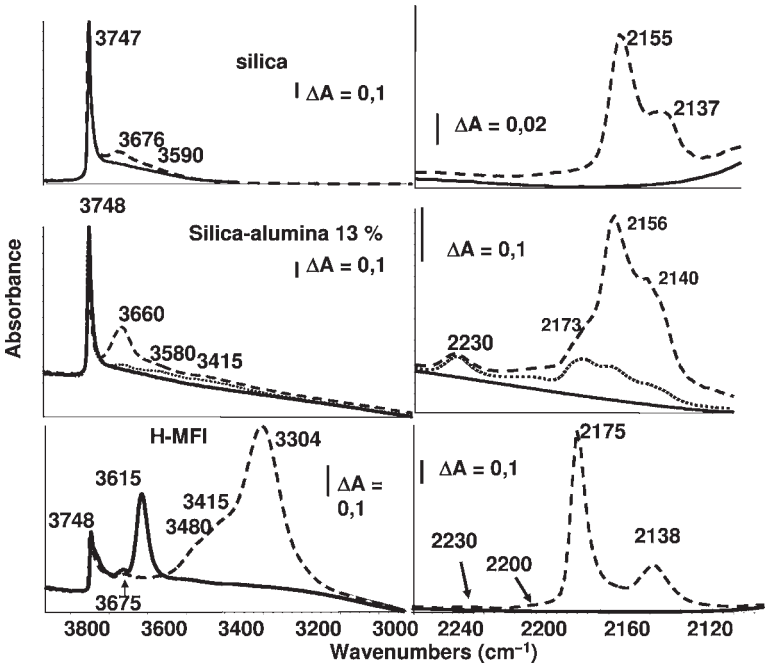

Figure 3.21 FTIR spectra of amorphous silica (Aerosil from Degussa), silica-alumina (Strem, Al_2O_3 13%), and H-MFI zeolite (Zeolyst, Si/Al = 25) after activation (full lines) and after contact with CO gas at 140 K (broken lines).

so that *symmetrical strong hydrogen bonding* occurs. These two situations can be detected and distinguished spectroscopically from protonation and interaction with Lewis sites.

In both these cases, the spectrum of the adsorbed base is only weakly perturbed with respect to the liquid. However, hydrogen bonding causes the shift down and the broadening of the OH stretching bands of the surface hydroxyl groups. Simple hydrogen bonding gives rise to the formation of well defined although broad OH stretching bands, and the shift of the maximum of the νOH band upon interaction can be taken as a measure of the H-bonding interaction. If the same base is used on different surfaces, the shifts measure the acid strengths of the corresponding protonic centres, according to the Bellamy–Hallam–Williams relation [140]. Very weak bases that can be protonated only with difficulty, such as nitriles or hydrocarbons (e.g. ethylene or benzene), can be used for this purpose. Low-temperature adsorption of even weaker "bases", such as hydrogen or CO, is also useful experimentally in this respect. In particular, the low-temperature adsorption of CO has been particularly widely used in recent years.

In Figure 3.21 the effect of low-temperature adsorption of CO on the spectrum of the surface OH groups of silica, silica-alumina and a zeolites (H-MFI) is shown. The adsorption of CO on the silanol groups present on silica results in the forma-

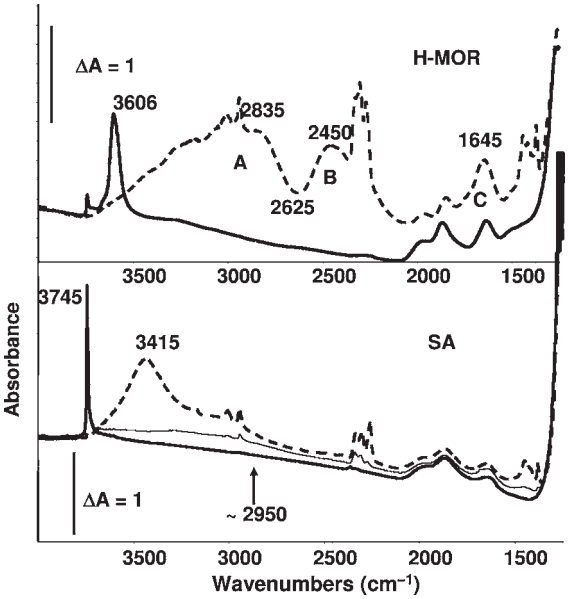

Figure 3.22 FTIR spectra of H-MOR (Zeolyst, Si/Al = 10), up, and of an amorphous silica alumina (Strem, Al_2O_3 13%), after activation (full lines) and in contact with 5 Torr acetonitrile vapour (broken lines) and after outgassing at room temperature 30 min (point line). A, B, C denote the components associated to quasi-symmetrical hydrogen bonding.

tion of H-bonded Si—OH · · · CO complexes with νCO at 2155 cm^{-1} (i.e. shifted up around 18 cm^{-1} with respect to liquid CO), and νOH at 3676 and 3590 cm^{-1}, that is,with downshifts of ΔνOH ~ 70 cm^{-1} and ~155 cm^{-1}. In the case of SA, additional components are found at νOH 3415 cm^{-1} (ΔνOH > 300 cm^{-1}) and at νCO 2173 cm^{-1}, showing the existence of a fraction of silanol groups with stronger acidity. In the case of the H-MFI zeolite the hydroxyl group 3615 cm^{-1} is shifted down to 3304 cm^{-1} (ΔνOH ~ 310 cm^{-1}), and νCO is at 2175 cm^{-1}, again showing very strong acidity.

In Figure 3.22, the spectra relative to the interaction of acetonitrile with a commercial microporous SA are shown. Two kinds of H-bonded complexes are formed, one of which is characterized by νOH at 3415 cm^{-1} (ΔνOH ~330 cm^{-1}), which, as in silica, is due to normal silanols, and the other by νOH ~2950 cm^{-1} (ΔνOH ~800 cm^{-1}), confirming that a fraction of silanol groups of SAs have strong acidity.

With stronger bases, the formation of even stronger "symmetrical" hydrogen bonding causes the appearance of an almost continuous absorption in the overall spectrum, with three maxima and two minima, the so-called ABC contour. The minima correspond to the first overtones of the MOH deformation modes, the in-plane deformation δOH, and the out-of-plane deformation, γOH. The overall ABC contour is due to the Fermi resonance of the νOH mode (strongly shifted downwards and broadened) with these overtones, both strongly shifted upwards

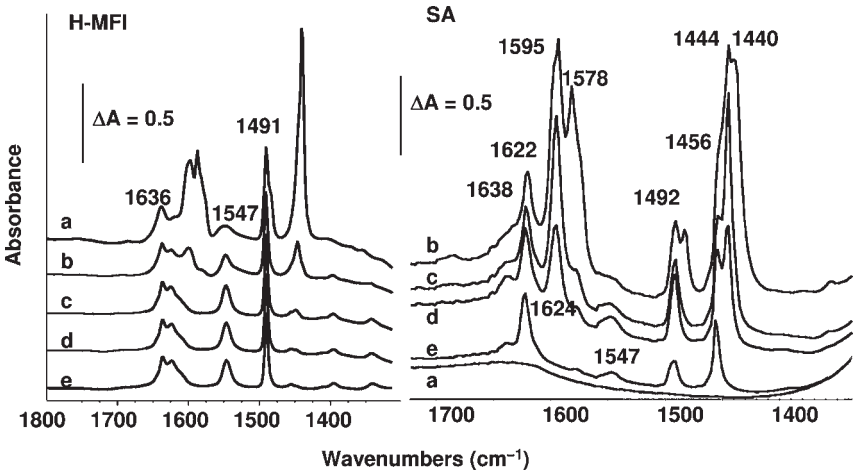

Figure 3.23 FTIR spectra of: left, pyridine adsorbed on H-MFI zeolite (a) in contact with 1 Torr pyridine vapour and after outgassing (b) at room temperature for 10 min, (c) at 373 K for 10 min, (d) at 473 K for 10 min, (e) at 573 K for 10 min; right, an MCM-41 type mesoporous silica-alumina (a) after activation by outgassing at 773 K; (b) in contact with 1 Torr pyridine vapour; after outgassing at room temperature for (c) 10 min, (d) 1 h; (e) after outgassing at 523 K for 10 min, see Figure 3.16.

like the corresponding fundamentals. This occurs, for example, when acetonitrile adsorbs on H-MOR zeolite (Figure 3.22, upper spectra), but also when pyridine adsorbs on mesoporous SA (Figure 3.20) where there is a complex distribution of OH groups having different Bronsted acidity, some of which form "quasi symmetrical" H-bonds with pyridine.

The Basic Strength Method The presence of Brønsted acid sites can be detected "indirectly" by studying the interaction of bases of appropriate strength and by monitoring the formation of the corresponding protonated species. This is performed easily with quite strong bases, when the spectroscopic features of the base are readily distinguishable from those of its protonated conjugate acid. This occurs in particular with ammonia and pyridine, which are in fact generally used, as well as with other amines such as, for example, *n*-butylamine, piperidine, lutidine, quinoline, and so on. In Figure 3.23 the spectra of pyridine adsorbed on H-MFI zeolite (left) and on mesoporous SA (right) are compared. The spectrum recorded on H-MFI after outgassing, with bands at 1636, 1625, 1547, 1491 cm^{-1} is due to pyridinium ions (8a, 8b, 19a and 19b modes), formed by pyridine protonation. In contrast, on SA the predominant features after outgassing (1622, 1578, 1492, 1456 cm^{-1}), are due to molecular pyridine coordinated over Lewis sites (again 8a, 8b, 19a and 19b modes), with small amounts of pyridinium ions (1638, 1547 cm^{-1}). The bands observed at higher coverages (1595, 1578, 1480, 1440 cm^{-1}) are due, in both cases, to molecular pyridine involved in H-bonding.

The Olefin Polymerization Method Olefins are very reactive towards the electrophilic attack of a Brønsted acid, and can undergo proton-catalyzed cationic polymerization at low temperature. The faster this phenomenon occurs, the stronger the Brønsted acid and the more electron-rich is the olefinic double bond. The experiment must be performed in a medium–low temperature range (e.g. room temperature) with olefin pressures of the order of 20–200 Torr in order to favor the oligomerization from the point of view of thermodynamics. The observed polymerization rate in our experimental conditions follows the order: 1,3-butadiene > isobutene > propene > ethylene [140–142]. Actually, ethylene polymerization is (in the conditions used to evaluate the surface acidity of oxide catalysts) only observed with very strong Brønsted acids, while some weak Brønsted acids only allow the polymerization of butadiene. Additionally, it can be observed that very strong Brønsted acids cause the formation of branched polymeric chains from linear olefins, for example polyisobutene formation from both isobutene and from 1-butene and likely also from ethylene [143]. Alumina OH groups, although unable to cause polymerization of the four butene isomers, cause the polymerization of 1,3-butadiene.

3.6.3.2 The Brønsted Acidity of Simple Metal Oxides

It is evident that the ability to protonate a base depends upon the strength of the base. The ability to protonate pyridine can be taken as the discriminatory behavior to define an oxide catalyst as a Brønsted acid. Typical ionic oxides, such as alkaline earth oxides, cupric oxide, zinc oxide, aluminas, gallias, ferric oxides, chromic oxide (Cr_2O_3), titanias, zirconias, ceria and thoria, even when highly hydroxylated, are not able to protonate pyridine. Also, low-valency typical covalent oxides, such as silicas (including silicated oxides), germania and boria-containing catalysts, do not protonate pyridine. Consequently, such oxides are either weakly or non-Brønsted acidic. On the contrary, pyridine is protonated on higher oxidation state oxides such as vanadia, niobia, molybdena and tungsta, either in bulk form or when supported. Also, materials containing surface chromic anhydride (CrO_3), bulk or supported phosphates and sulfated oxides protonate pyridine. This is associated with the presence of M=O double bonds and the possibility of delocalizing the anionic charge after dissociation [101]. Olefin oligomerization tests agree with studies performed using protonable bases, showing that surfaces that are able to protonate pyridine also cause propene oligomerization, while surfaces that protonate piperidine only, such as alumina, are not able to oligomerize propene but may cause 1,3-butadiene oligomerization (Table 3.9).

3.6.3.3 The Brønsted Acidity of Protonic Zeolites

The strong Brønsted acid strength of the bridging OH groups of zeolites is confirmed by adsorption of basic probes followed by different techniques. Quite strong bases such as pyridine are easily protonated, as shown in the spectra on the left hand side of Figure 3.23, where the bands of pyridinium ions (1636, 1625, 1547, 1491 cm^{-1}) are strongly predominant after pyridine adsorption on H-MFI. Weak bases such as nitriles and CO hydrogen bond with these OH

groups with a strong shift down of the νOH mode. In Figure 3.21, the spectra of H-MFI before and after low-temperature adsorption of CO are reported. The band at 3615 cm^{-1}, due to bridging OH groups, shifts down to near 3300 cm^{-1}, with a $\Delta\nu$ ~315 cm^{-1}, evidencing the strong acidity of these groups. In parallel, the CO triple-bond stretching shifts up from 2138 cm^{-1} for the liquid like species to > 2175 cm^{-1}.

Most data agree that when the Al content is relatively low, the amount of Brønsted sites in zeolites actually strictly depends on Al concentration, according to theory. The ratio between catalytically active sites and Al ions ranges apparently from 80 to 100% for highly siliceous extraframework-species-free zeolites.

Many investigations, also using IR spectroscopic methods, have been performed with the aim of revealing the degree of acid strength of different zeolites. Experimental as well as theoretical data [77] show that besides the interactions of the functional groups of the probe molecules with the zeolite's Brønsted sites, the van der Waals interactions of other unreactive groups of atoms with the zeolite cavity walls may be very relevant, and participate in the stabilization of the adsorbed species [100]. These interactions may vary significantly as a function of the type of zeolite and the dimension and shape of the cavities as well as the Al and proton content and the presence of extra-framework species. Also, they depend on the size and shape of the probe molecule. These "confinement effects" make the cavities of the single zeolite structures unique solvation and reactivity environments and play an important role in catalysis by zeolites. They also account for the discrepancies among the acid strengths measured using different probes and different techniques.

In the case of zeolites, studies have also been performed to distinguish sites located at the external surface from those present in the cavities, and also to distinguish the position in different cavities for zeolites with a complex pore structure. This can be performed using molecules having different molecular sizes but similar chemical behavior. Some of the useful molecules are shown in Scheme 3.6.

Internal versus External and Extraframework Sites in Zeolite Acid Catalysis: the Use of Hindered Basic Probes Catalytically active sites also exist on the external surface and at the pore mouth of zeolite crystals. These sites are considered to be responsible for unwanted non-selective catalysis. On the other hand, H-zeolites also catalyze reactions of molecules that do not enter the cavities because of their larger size. So, the external surface of zeolites is certainly active in acid catalysis. Additionally, the bulk and surface Si/Al compositions of a zeolite could be different and different preparation procedures can be chosen to modify this ratio.

The external surfaces of H-FER [143–145], H-MFI [146, 147] and H-MOR [147, 148] have been studied by IR spectroscopy of adsorbed hindered aliphatic nitriles, pyridine [145, 146], lutidine and aromatic hydrocarbons [149]. Terminal silanols and Lewis acid sites exist at the external surface of H-FER, H-MFI and H-MOR. Interestingly, the acidity of the external silanol OH groups of zeolites can be enhanced with respect to those of silica, appearing similar to those of SA. The very

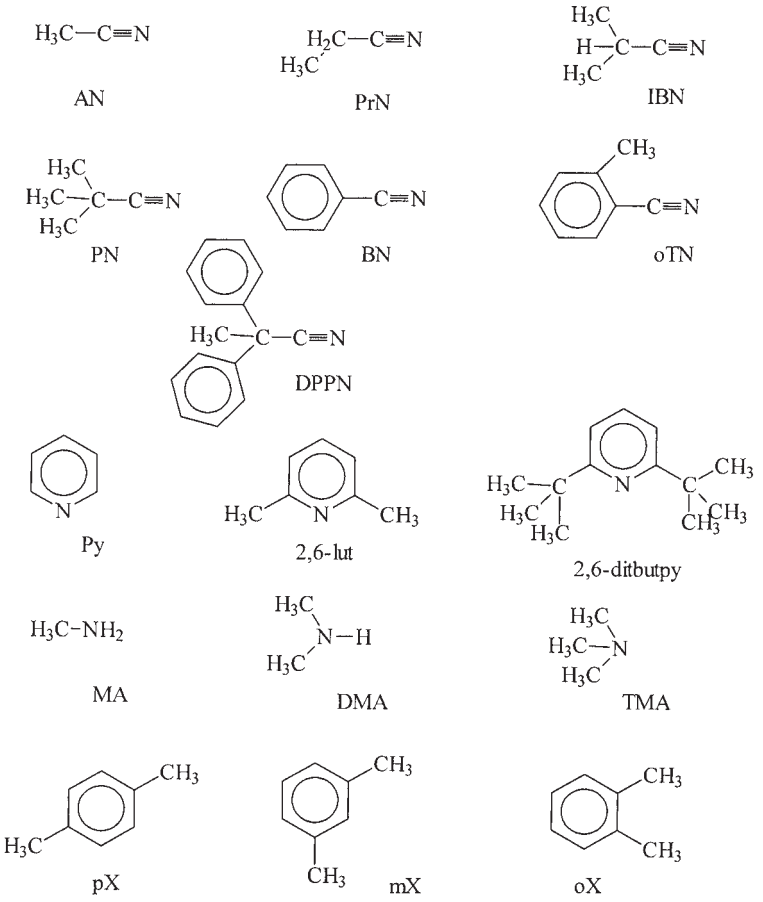

Scheme 3.6 Probe molecules for the study of localization of active sites in microporous materials: AN = acetonitrile; PrN = propionitrile; IBN = isobutyronitrile; PN = pivalonitrile (2,2-dimethyl-propionitrile); BN = benzonitrile; oTN = *ortho*-toluonitrile; DPPN = 2,2-diphenylpropionitrile; py = pyridine; 2,6-lut = 2,6-dimethylpyridine, 2,6-lutidine; 2,6,ditbpy = 2,6, di-*tert*-butyl-pyridine; MA = methylamine; DMA = dimethyl amine; TMA = trimethylamine; pX, mX, oX = *para*-, *meta*- and *ortho*-xylene.

strong bridging Brønsted acid sites, however, do not apparently exist at the external surface, being totally confined to the internal surface.

Zeolite catalysts are frequently applied after treatments that tend to increase their stability and also to further enhance surface acidity and shape selectivity effects. These treatments, such as steam dealumination, can cause a decrease in the framework Al content and the release of aluminum-containing species from the framework. This can contribute to the stability of the framework, but extra-framework species can also contain additional catalytically active acid sites. These particles can also narrow the size of the zeolite channels or of their mouths, so improving the shape selectivity effects. Extra-framework material (EF) can also

arise from the preparation or the activation procedure or by addition of other components by impregnation or ion exchange. The presence of EF material gives rise to the presence of strong additional bands in the IR OH-stretching spectrum. In general, IR bands above 3750 cm^{-1}, and in the region 3730–3650 cm^{-1} in protonic zeolites, is attributed to OH groups on EF materials.

Some authors believe that EF material is released at the external surface of zeolites. The use of hindered nitriles, however, demonstrated that the EF material produced by thermal treatment in H-MOR is in the interior of the side pockets [150]. Similarly in a sample of H-MFI, EF material was found to be located in the interior of the channels [150].

IR Determination of the Location of Acid Sites and of the Diffusivity of Large Molecules in Protonic Zeolites with Complex Pore Structure The use of hindered nitriles as probe molecules can be used to to distinguish Brønsted sites located in different cavities in complex pore zeolites. The framework of the FER zeolite gives rise to two kinds of channels, one of which is a 10-membered ring, and the other a smaller 8-membered ring. H-FER sample shows a single band due to bridging OH groups centered at 3595 cm^{-1}. Acetonitrile (AN) perturbs this band strongly, while propionitrile (PN) does not perturb it at all, being unable to enter either type of cavity. Consequently, we attempted to distinguish the sites in the two channels by using isobutyronitrile (IBN) as a probe (Figure 3.24). Upon IBN adsorption, the band of

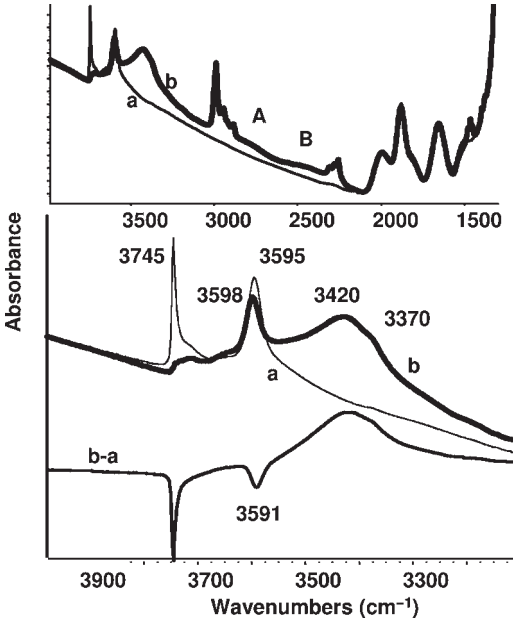

Figure 3.24 FTIR spectra of H-FER zeolite (Zeolyst, Si/Al = 27.5) (a) after activation; (b) after contact with IBN vapour. b–a: subtraction spectrum.

the external terminal silanols is fully perturbed and shifted to 3420 cm^{-1} with a component near 3370 cm^{-1}. IBN interacts also with part of the bridging OH groups of H-FER. Upon adsorption of IBN in fact, the band of bridging OH groups decreases only slightly in intensity. Part of it is unperturbed and does not change its shape and breadth. Accordingly, a weak A,B,C pattern appears, due to the strong interaction of part of the H-FER bridging OH groups with IBN. The maximum of the unperturbed band of the bridging OH groups is at 3598 cm^{-1}, while the maximum of the band of the OH groups which are perturbed by IBN (read as a minimum in the subtraction spectrum) is at 3591 cm^{-1}. We consequently assign the band at 3591 cm^{-1} to the OH groups located in the 10-membered ring channel (accessible to IBN) and that at 3598 cm^{-1} (inaccessible to IBN) to the OH groups located in the 8-membered ring channels. Analysis of the intensities of the two bands indicates that they are not far from the ratio 1 : 1.

Similar studies have been performed on H-BEA [151], allowing the distinction of the sites in the two channels of this structure, and on H-MOR [149, 150] where three different types of OH group have been distinguished, located in the main channels, in the intersection between main channels and side pockets and in the side pockets. In the case of H-Y faujasite, the sites located in the supercages and in the sodalite cages are easily distinguished. Using trimethylamine as a probe, a third component, which is not perturbed at all by the probe, at 3501 cm^{-1}, assigned to OH groups in the hexagonal prisms, is also observed [152].

These studies also allowed the determination of the diffusivity of molecules having different steric hindrance in the cavities of these zeolites, as summarized in Table 3.10.

3.6.4
Spectroscopic Detection and Characterization of the Surface Lewis Acid Sites

As already mentioned, coordinatively unsaturated cations exposed at the surface of ionic oxides give rise to surface Lewis acid sites. Basic molecules can, consequently, interact with these sites by forming a new coordination bond, so completing or increasing the overall coordination at the surface cation, as shown in structure I of Scheme 3.5. Upon this interaction, electrons transfer from the basic molecules towards the catalyst surface. This electronic perturbation (and sometimes the molecular symmetry lowering) arising from this contact are the causes of a vibrational perturbation of the adsorbate. In most cases, the vibrational perturbation only consists in shifts of some vibrational frequencies, the more pronounced the stronger the interaction, that is, the greater the Lewis strength of the surface site. Consequently, the shift of the position of some very sensitive bands of the adsorbate upon adsorption can be taken as a measure of the Lewis acid strength of the surface sites.

As an example, in Figure 3.14 the spectra of pyridine molecularly adsorbed on β-Ga_2O_3 are shown. The spectra are due to molecular Lewis-bonded pyridine, without any absorption assignable to pyridinium ions. It is evident that the 8a and 19b pyridine bands (1580 and 1438 cm^{-1} in the liquid) are shifted significantly

Table 3.10 Summary of the characteristics of protonic zeolites and on the diffusion of molecular probes in their cavities as measured by IR spectroscopy at room temperature.

Code	Channels/cages	Channel size (Å)	IR νOH (cm^{-1})	—CN				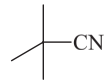	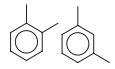
FER	8-ring channel [010]	3.5 × 4.8	3598	E	E	D	D	D	D
	10-ring channel [001]	4.2 × 5.4	3591	E	E	E	D	D	D
MFI	10-ring channel [100] (sinusoidal)	5.1 × 5.5	~3610 channel	E	E	E	E	D	D
	10-ring channel [010] (straight)	5.3 × 5.6	~3620 intersect	E	E	E	E	D	D
BEA	12-ring channels [001]	5.6 × 5.6	3609	E	E	E	E	D	D
	12-ring channels [100]	6.6 × 6.7	3628, 3608, 3590	E	E	E	E	E	D
MOR	8-ring compressed channels [001]	2.6 × 5.7	3588 side-pocket	E	D	D	D	D	D
	8-ring side pockets [010]	3.4 × 4.8	3609 intersect	E	D	D	D	D	D
	12-ring main channels [001]	6.5 × 7.0	3605 main chann	E	E	E	E	E	D
FAU	Hexagonal prisms accessed through 6-ring channels	ca 2.7 × 2.7	3501	D	D	D	D	D	D
	Sodalite cages accessed through 6-ring channels	ca 2.7 × 2.7	3553	D	D	D	D	D	D
	Supercages accessed through 12-ring main channels [111]	7.4 × 7.4	3625	E	E	E	E	E	E

E = easy; D = difficult

upwards upon adsorption. The 8a mode is clearly multiple (three components can be distinguished, at 1622, 1615–1605 and ~1590 cm^{-1}, due to multiple adsorption sites. The behavior observed with β-Ga_2O_3 is very similar to that observed on transitional aluminas (see below).

Similar experiments can be performed using nitriles as probe molecules. These molecules are weaker as bases and this sometimes allows a better resolution in the detection of the Lewis sites. Analysis is based on the study of the C≡N stretching region. In this region liquid acetonitrile shows a strong doublet at 2294, 2254 cm^{-1}, where the latter band is definitely stronger than the former. This doublet is due to the Fermi resonance between the C≡N stretching and a δCH_3 + νC—C combination. The virtual position of the CN stretching fundamental shifts upwards by increasing electron withdrawal from the N lone pair upon adsorption, and this causes the experimental position of both components of the doublet to shift up. Simultaneously, however, the relative intensities of the two components progressively inverts. Deuteroacetonitrile CD_3CN and other nitriles have single CN stretchings. They can also be used to determine the location of Lewis sites in pores and cavities.

Low-temperature adsorption of CO is widely used as an acid site probe. In Figure 3.3 the spectra of CO over different solids are compared. The CO stretching band may shift strongly up when it bonds as terminal carbonyl species on highly acidic cationic centers, and can shift down significantly when it bridges over two or three metal atoms over an extended metal surface. In Table 3.11 the position of some sensitive bands over oxide surfaces is reported, allowing the measurement of their Lewis acidity.

3.6.4.1 The Lewis Acid Sites of Aluminas and SAs

The catalytic activity of transitional aluminas (γ–, η–, δ–, θ–Al_2O_3) are undoubtedly mostly related to the Lewis acidity of a small number of low coordination surface aluminum ions, as well as to the high ionicity of the surface Al—O bond [101]. Alumina's Lewis sites have been well characterized by adsorption of several probes. They are the strongest among metal oxides. The number of such very strong Lewis sites present on transitional alumina surfaces depend on the dehydroxylation degree (depending on the activation temperature) and on the particular phase and preparation.

It seems that, although the different alumina spinel-type phases react a little differently to outgassing, the density of the strongest Lewis acid sites tends to decrease a little as the calcination temperature of the alumina increases (i.e. upon the sequence $\gamma \rightarrow \delta \rightarrow \theta$, which is also a sequence of decreasing surface area). As a result of this the number of strongest acid sites per gram significantly decreases in this sequence, although catalyst stability increases.

Although it is clear that surface Lewis acid sites on alumina are due to coordinatively unsaturated Al^{3+} ions, it is not fully clear what is the coordination of such surface ions. Most authors agree that at least three different types of Lewis acid sites (weak, medium, strong) exist on transitional aluminas, arising in some way from the two or three coordinations of the ions in the bulk spinel-type structure,

Table 3.11 Position (cm^{-1}) of the sensitive IR bands of adsorbed basic probe molecules on different catalyst surfaces. The Lewis acid strength roughly decreases from top to bottom.

Adsorbate	CO	Pivalonitrile	Pyridine	Ammonia	Adsorbing site type
IR mode	νCO	νCN	8a	δ_{sym} NH_3	
AlF_3		2309, 2305	1627		$_{IV}Al^{3+}$
Zeolites (external surface)	2230	2300	1625	Masked	$_{IV}Al^{3+}$
Silica-alumina	2235	2296	1625	Masked	$_{IV}Al^{3+}$
γ-Al_2O_3	2235	2296	1625	1295	$_{IV}Al^{3+}$
	2210–2190		1615	1265	$_{IV}Al^{3+}$
	2170		1595	1220	$_{VI}Al^{3+}$
Alumina-pillared montmorillonite		2290	1625	Masked	$_{IV}Al^{3+}$
Acid-treated montmorillonite		2295	1625	Masked	$_{IV}Al^{3+}$
SiO_2–TiO_2	2226 w	2308 w		Masked	Ti^{4+}
	2208	2285	1610		
WO_3, unsupported	=	2290	1613	1275, 1222	$_{VI}WO^{4+}$
ZrO_2	2195		1606	1210, 1160	Zr^{4+}
	2170				
Sulfated zirconia	2160		1606	1210, 1150	Zr^{4+}
TiO_2 anatase	2208	2285	1610	1225	$_{V}Ti^{4+}$
	2182	2260		1185	$_{VI}Ti^{4+}$
Liquids	2143	2236	1583	1054	

namely octahedral and tetrahedral (normal spinel positions) and trigonal. Pyridine adsorption produces three components for the 8a vibrations at 1624, 1618 and 1597 cm^{-1}, attributed to three diffent Lewis bonded species. Liu and Truitt [126] emphasized the close proximity of Lewis acid sites to surface OH groups while in their study Lundie and coworkers [153] identified four different Lewis acid sites arising from coordinatively unsaturated octahedral (the weakest) and tetrahedral sites (the three strongest), three of which are considered to be associated with three different types of hydroxyl groups.

Very strong Lewis acid sites can be detected on the surface of SA, characterized by νCO of adsorbed carbon monoxide at 2230 cm^{-1} (Figure 3.21), as well as by the 8a mode of adsorbed pyridine at 1625 cm^{-1} (Figure 3.23) They are certainly due to highly uncoordinated Al ions and correspond to the strongest Lewis sites of transitional alumina or perhaps are even stronger, owing to the induction effect of the covalent silica matrix. This makes SA also a very strong catalyst for Lewis acid catalyzed reactions.

3.6.4.2 Lewis Acidity of Other Ionic Oxides

The strongest Lewis acidic oxides in normal circumstances are alumina and gallia, that is, oxides of elements at the limit of the metallic character. The same elements also give rise to halides characterized by even stronger Lewis acidity. Medium to

medium-strong Lewis acidity is found for other ionic oxides such as zirconias, titanias, iron oxides, and so on.

3.6.4.3 Lewis Acidity of Highly Covalent Oxides

Lewis acidity is not usually observed for the covalent oxides of non-metal elements. Interestingly in the case of silica, Lewis acidity is generally not found but it can appear after very harsh pretreatment under outgassing [154]. The polarizing power of the "cations" in the covalent oxide, is higher than 8. This shows that the reason for the absence of Lewis acidity on the surface of these oxides is the difficulty of breaking the M—(OH) bonds, which are so covalent owing to the strong polarizing power of the cation that would result by dissociation, with water desorption. Additionally, when Si(OH) groups actually break, couples of them tend to give rise to "strained" Si—O—Si bridges, becuase of the strength of Si—O bonds, neutralizing Lewis acidic coordinatively unsaturated Si ions. On the contrary, dehydroxylation of ionic oxides is easier, and results in the generation of Lewis acid sites that are sufficiently stable to stay as such under relatively mild conditions.

On germania, Lewis acidity is generally not found. Oxides of transition metals in very high oxidation states, such as vanadia, niobia, tungsta and molybdena, show strong Lewis acidity, attributed to the coordinative unsaturation of vanadyl [82], niobyl [83], tungstyl [84] and molybdenyl ions at the surface. The supported oxides of pentavalent vanadium and niobium and of hexavalent tungsten and molybdenum also display strong Lewis acidity [99].

3.6.4.4 Lewis Acidity of Protonic Zeolites

Studies of adsorbed hindered molecules demonstrate that in non-defective zeolites quite strong Lewis acidity is usually present at the external surface [149–152]. Additional Lewis acidity occurs due to extra-framework aluminum oxide species [100, 153].

3.6.5 Determination of the Oxidation State of Cationic Centers

Carbon monoxide is a very weak base, widely used for the surface characterization of cationic centers on metal oxide surfaces [155]. The electronic structure of CO implies a triple bond between C and O, according to the stretching frequency measured at 2143 cm^{-1} for the free molecule in the gas. In principle, the 14 electrons are distributed symmetrically between C and O atoms, so that the lower positive charge of the C nucleus with respect to O implies the formation of a dipole with the negative charge at the C atom, in spite of the lower electronegativity of C with respect to O. For this reason, the CO molecule tends to interact through the C end with cationic centers. This interaction is rather weak, usually completely reversible by outgassing at ambient temperature and should be studied at room or lower temperature (e.g. at liquid nitrogen temperature, 77 K). According to theoretical calculations, this interaction is a simple polarization, with no formation of a true coordinative σ bond with the cationic center. This interaction tends to

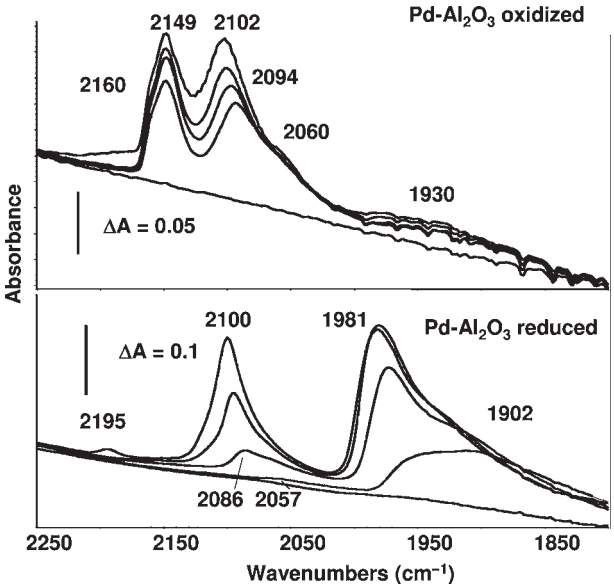

Figure 3.25 FTIR spectra of carbon monoxide adsorbed on PdO_x /γ-Al_2O_3 catalyst, after previous calcination in air at 673 K (upper spectra) and after reduction in hydrogen (1 atm) at 673 K (lower spectra). The first spectra in each series has been obtained in contact with 10 Torr CO at 130 K for 5 min. The other spectra were recorded upon outgassing (10^{-3} Torr) on warming to 270 K.

increase the CO bond order, so that the CO stretching frequency tends to increase. Accordingly, the experimental measure of the CO stretching frequency for CO interacting with surface cations can be taken as a measure of the polarizing power of the cation or, in other terms, of its Lewis acidity (see Table 3.11).

However, when the cation or the metal atom contains, besides empty orbitals, full or partly filled d-type orbitals, they can interact with the empty π^*-type orbitals of CO, via a π-type electron backdonation from the metal to CO. This implies that these antibonding orbitals become partly filled, so that the bond order and the CO stretching frequency is decreased by this last interaction. In this case, the interaction can become very strong and very stable metal–carbonyl complexes can be formed. The experimental CO stretching frequency in this case is a complex function of the electron accepting power of the cation (Lewis acidity) and of its π-type electron donating power. Accordingly, the CO stretching frequency of CO adsorbed on several transition metal cations is very informative concerning the oxidation state of the adsorbing ion.

In Figure 3.25 the IR spectra of CO adsorbed at low temperature over a Pd/γ-Al_2O_3 catalyst after oxidizing (upper spectra) and reducing pre-treatments (lower spectra) are reported. In the oxidized catalysts a strong band composed of a main maximum at 2149 cm^{-1} and a pronounced shoulder at 2160 cm^{-1} is evident. This

band is no longer observed in the case of the reduced catalyst. This band is certainly due to carbonyl species adsorbed over oxidized Pd centers, which are reduced by the treatment in hydrogen. The position of this band allows its assignment to carbonyls bound to Pd^{2+} sites.

For both oxidized and reduced surfaces, a strong band is found centered very near 2100 cm^{-1} with an additional component envisaged as a shoulder in the region near 2060 cm^{-1}. The maximum tends to shift in both cases to lower frequencies by outgassing and decreasing CO coverage, down to 2085 cm^{-1}. These features can be quite confidently assigned to terminal carbonyls adsorbed on zero valent Pd atoms. In agreement with this, CO adsorption on Pd monocrystals show that terminal carbonyls are found near 2095 cm^{-1} on both the (111) and (100) planes.

At lower frequencies only a very weak and broad absorption centered at 1930 cm^{-1} is found in the case of the oxidized catalyst. On the contrary, a very strong band is observed in the case of the reduced catalyst with a main maximum centered at 1981 cm^{-1}, and a pronounced shoulder near 1900 cm^{-1}. By outgassing the main compomnent decreases quickly in intensity and its maximum tends to shift down to 1940 cm^{-1}, while the lower frequency shoulder does not decrease in intensity and becomes predominant at lower CO coverages. The vibrational range of these absorptions allows their assignment to bridging carbonyls over Pd metal particles. According to Binet and coworkers [156], the sharper band in the region 1980–1940 cm^{-1} should be assigned to CO on Pd particles exposing a (100) type face while the broader and more strongly bonded band in the 1930–1850 cm^{-1} region should be assigned to species adsorbed on Pd particles exposing a (111) type face. Analysis of the intensity of the bands shows that the reduction treatment causes the complete disappearance of the bands of oxidized Pd centers and the simultanous strong growth of the bands of bridging carbonyls on zero valent Pd. However, also, the bands due to terminal carbonyls on zero valent Pd grow by a factor of 2 during reduction. This suggests that zero valent Pd particles are already present in the oxidized sample but grow in size and number upon reduction.

In Figure 3.26 the IR spectra of CO adsorbed at low temperature (130–230 K on an uncompletely reduced Cu-ZnO-Al_2O_3 catalyst are shown. The main maximum is found at 2150 cm^{-1}, with smaller maxima at 2176 and 2120 cm^{-1}, with an evident tail towards lower and higher frequencies. Upon outgassing during warming, the band at 2150 cm^{-1} tends to disappear rapidly (see arrow in Figure 3.26, right), showing that it is due, at least in part, to a very weakly adsorbed species, possibly physisorbed on the surface hydroxyl groups. However, a component now at 2161 cm^{-1} persists during low-temperature outgassing. This feature can be assigned to CO adsorbed either on Zn^{2+} or on Cu^{2+} ions, although the assignment of at least part of this band to the lower frequency component of Cu^{+} dicarbonyls is also possible. The higher frequency component decreases less in intensity and shifts from 2176 to 2204 cm^{-1} with decreasing coverage. Its position and behavior agrees with an assignment to CO adsorbed on Al^{3+} cations. The lower frequency band is found at 2120 cm^{-1} at the highest coverages but has a complex behavior. Its maximum shifts to higher frequencies towards 2130 cm^{-1} by outgassing and decreases in intensity, but at higher temperatures 200–230 K) the band broadens

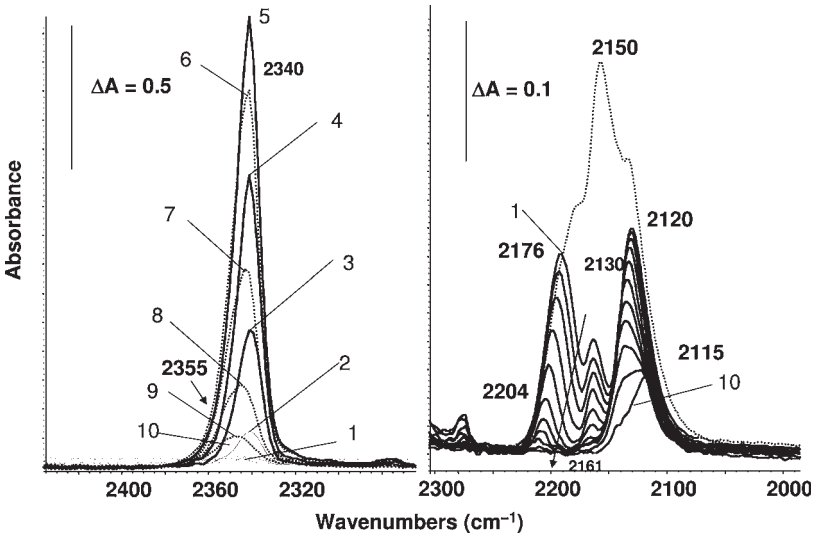

Figure 3.26 FTIR spectra of CO adsorbed at 140 K (increasing admissions, left) over a Cu-ZnO-Al_2O_3 catalyst (5 : 52 : 43 Cu : Zn : Al atomic ratios) calcined at 450 °C. Right: under desorption at increasing temperatures (1 to 10 correspond to increasing temperature in the range130–230 K).

and moves to lower frequency again (2115 cm^{-1}). The position and stability of this band strongly suggests that it is mainly due to the carbonyls of Cu^+ ions or of small clusters of zerovalent copper. It is in fact well known that carbonyls on bulk Cu metal are very weakly adsorbed and usually responsible for absorptions below 2100–2070 cm^{-1}. It cannot be excluded that such species are present at the lowest temperatures and are responsible for the tail at lower frequency of this band. On the other hand, to assign the bands due to adsorbed CO, we have also to take into account that during CO desorption at 140–170 K a strong absorption is formed and grows at 2340 cm^{-1} which is certainly due to adsorbed CO_2 (Figure 3.26). By further warming and outgassing the band decreases in intensity and disappears at 230 K. Under these conditions, however, a shoulder at 2355 cm^{-1} forms and disappears. The latter components can be confidently assigned to CO_2 adsorbed on Al^{3+} ions. The formation, at so low a temperature, of adsorbed CO_2 is certainly due to the existence of very active oxidizing sites, in spite of the reduction pre-treatments. According to previous studies [157, 158], Cu^{2+} is very active for the low-temperature oxidation of CO. Consequently we conclude that at least part of the band at 2160 cm^{-1} is due to Cu^{2+} carbonyls that convert into CO_2 complexes of Cu^+ or Cu^0. Some of the adsorbed CO relocates to the new reduced centers and this may be at the origin of the sudden downwards shift of the band of adsorbed CO observed after the desorption of CO_2. During desorption, part of the CO_2 readsorbs on the stronger Lewis acidic Al^{3+} ions.

Nitrogen monoxide has one electron more than CO, so that the same electron configuration could apply with the additional electron in an antibonding π^*-type orbital. The bond order is decreased to 2.5 and this is reflected in the lower stretching frequency (1875 cm^{-1} for NO gas, see Figure 3.2, upper right hand side). Thus, the NO molecule is a radical and this makes its reactivity far higher. It easily dimerizes to N_2O_2, is easily oxidized to NO^+, to nitrites NO_2- or to NO_2, and is easily reduced to NO^- and to N_2O. NO can also easily disproportionate and is thermodynamically unstable towards decomposition to $N_2 + O_2$. This makes this molecule very reactive, so its successful use as a probe for cationic centers is limited.

However, NO can also interact with surface metal centres on metal oxides, giving rise to surface mononitrosyl, *gem*-dinitrosyl and trinitrosyl species. When the cation or the metal atom contains, besides empty orbitals, full or partly filled d-type orbitals, they can interact with the π^*-type orbitals of NO molecules, via a π-type electron back-donation. This gives rise to bent nitrosyls, where N is likely sp^2 hybrid and the NO stretching frequency is decreased.

Adsorbed NO can be even more sensitive than adsorbed CO to the oxidation state of the cations. The use of NO as a probe allows, for example, the determination of the oxidation state of Co ions in zeolites better than CO [159], showing the existence of both Co^{3+} and Co^{2+} species. In fact, the bands observed at 1901, 1817 cm^{-1} are due to $[Co(NO)_2]^{2+}$ *gem*-dinitrosyl species, while that at 1945 cm^{-1} is assigned to $[Co\text{-}NO]^{3+}$ mononitrosyl. The three bands due to adsorbed CO at 2204, 2198 and 2188 cm^{-1} arise from cobalt carbonyls, but assignment of the oxidation state is difficult.

3.6.6
External versus Internal Cationic Sites and Complex Interactions in Cation Exchanged Zeolites

The external versus internal surface has also been investigated in the case of Co-H-zeolites active in the selective catalytic reduction of NO by methane [20]. The highly hindered nitrile, ortho-toluonitrile (oTN) has been used, co-adsorbed with CO and NO. The pre-adsorption of oTN poisons the external cationic sites of Co-H-ZSM5. Successive adsorption of CO shows that some of the Co ions are on the inner surface and some on the outer surface. The coadsorption of oTN and NO shows that trivalent Co ions are actually located in the internal cavity surface of Co-H-ZSM-5 while divalent Co ions distribute almost equally in the internal and external surface.

Similarly, Co ions at the external surface of Co-H-FER and Co-H-MOR have been detected. Similar experiments with hindered nitriles show the location of alkali ions at the external surface of alkali-MOR zeolites [160]. CO mainly adsorbs at the external surface of the small pore zeolite 3A (K-LTA) while it enters the cavities of zeolite 4A (Na-LTA) [161].

The use of CO and nitriles as probes also reveal the possibility of interactions of adsorbed molecules with other cations in zeolite channels [162, 163].

Table 3.12 Molecular probes applied for surface basicity characterization.

Compound	Formula	Reactivity
Carbon dioxide	CO_2	Carbonates, bicarbonates, linear coordination on Lewis sites
Carbon monoxide	CO	Formates, carbonite, polymeric anionic species, dioxycarbene
Carbon disulfide	CS_2	S_2CO^-, CO_3^{2-}, other species
Sulfur dioxide	SO_2	Sulphites, disulphites, hydrogensulphite
Pyrrole	H_4C_4NH	H-bonding, pyrrolate anions
Chloroform	$H{-}CCl_3$	H-bonding, coordination by chlorine on Lewis acid sites, hydrolysis
Acetonitrile	$CH_3{-}CN$	$^-CH_2{-}CN$ anions, previous coordination by nitrogen on Lewis acid sites
Alcohols	R—OH	$R{-}O^-$ anions, undissociative coordination, different H-bondings
Thiols	R—SH	$R{-}S^-$ anions, undissociative coordination, different H-bondings
Trimethylborate	$(CH_3O)_3B$	Tetrahedral borate, dissociation
Borontrifluoride	BF_3	$F_3B{\leftarrow}O^{2-}$, dissociation
Ammonia	NH_3	H-bonding, $^-NH_2$ anions, coordination by nitrogen on Lewis acid sites
Pyridine	H_5C_5N	$H_5C_4N^-$ anions, coordination by nitrogen on Lewis acid sites, dimerization
Nitromethane	CH_3NO_2	$H_2CNO_2^-$, CNO^- formed by decomposition

3.6.7 Characterization of Surface Basicity

In contrast to acidity characterization with basic probes, the use of "acidic" molecules to probe surface basicity is far less satisfactory. In fact, all acidic (or electrophilic) molecules (Table 3.12) also contain accessible nucleophilic (basic) atoms. It seems impossible to find a molecule that actually only interacts specifically with basic sites. On the other hand, metal oxides that display significant surface basicity

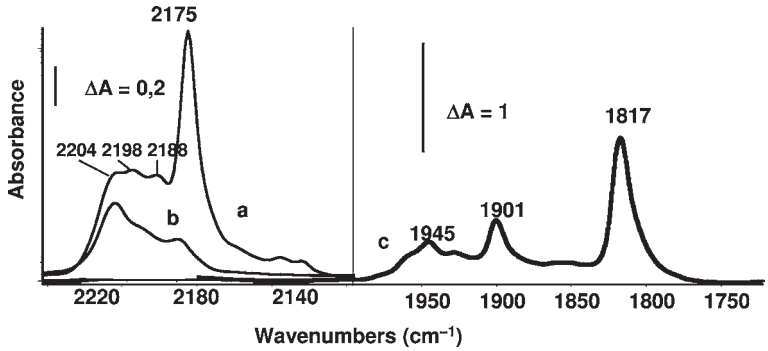

Figure 3.27 FTIR spectra of CO adsorbed at 140 K (a) and after outgassing at 120 K (b), and of NO adsorbed at 300 K (c) on Co-H-MFI zeolite.

are always very ionic and also carry Lewis acidity, although weak [101, 102]. So, in this case the *acido-basicity* more than *pure basicity* properties are relevant.

The oxides of alkaline earth metals are the strongest solid bases among stable metal oxides. They present very high reactivity when treated in vacuum at very high temperatures. These treatments generate highly exposed cations and anions that induce very complex radical-type chemistry, such as that producing polymeric CO species from carbon monoxide. In their normal use, however, alkaline earth oxides are partly hydroxylated and carbonated, but still present high surface basicity. Lanthanide oxides such as La_2O_3 and Nd_2O_3 are also strong bases as well as lanthanum, or other rare earth, containing perovskites. This is essentially due to the very low polarizing power of the corresponding cations, which have large size and relatively low charge. Oxides of alkali metals should be even stronger bases. Their basic reactivity is so high that they are essentially non-stable under normal conditions, that is, in the presence of water vapor, which is sufficient to convert them into the corresponding hydroxides. On the other hand, similar stability problems occur also with pure alkaline earth oxides. For this reason, basic solid oxide catalysts mostly contain alkali and/or alkaline earth cations in thermally stable mixed oxide phases. Basic zeolites and systems based on oxides (mainly alumina) containing alkali or alkaline earth ions are apparently the most used both for industrial applications and in academic research [163, 164]. Even stronger bases are the "superbases" where alkali metallic phases are produced, but these will be not considered here.

EF material free, alkali exchanged zeolites are used as quite mild basic catalysts. Light alkali and alkaline earth metal zeolites, such as Na-X, Na-Y [165], alkali-MOR, Na-A and Ca-A [166], have a mild Lewis acid behavior and do not appear to have strong basic character. The same occurs for Na-silica-alumina [167]. However, heavy alkali metal zeolites such as Cs-Y actually act as base catalysts, or rather as acid–base catalysts, for example for toluene side-chain alkylation. Stronger basic character arises from impregnation of alkali zeolites with alkali salts, later

decomposed to occluded alkali oxide, as evidenced by CO_2 adsorption microcalorimetry. The characterization of such materials is still quite poor.

Several studies have been devoted to the characterization of metal oxide carriers impregnated by alkali and alkaline earth metal ions. Doping of most metal oxides with large-size cations results in their accumulation at the surface. In fact, due to their size, such cations cannot penetrate into the vacancy sites of the close packing oxide arrays of most oxide carriers, such as alumina and titania. Alkali metal cations remain exposed at the surface where their weak Lewis acidity (corresponding to the strong acidity of the oxide anions) is easily detectable by conventional probes. This has been shown using IR spectroscopy of adsorbed ammonia and pyridine, for example, for the systems K_2O-TiO_2 [168], SrO-TiO_2 [169] and CaO-Al_2O_3 [170]. Such surface layers adsorb carbon dioxide very strongly so that bulk carbonate particles can form, as in the case of the BaO-Al_2O_3 system [171].

In the case of Ba-β-alumina [172] and La-β-alumina, the surface apparently only exposes the large low valency cations, detectable by adsorbing bases, and very basic oxygen species that adsorb CO_2 in the form of carbonates. The decomposition temperature of surface carbonates on Ba-β-alumina ($BaAl_{12}O_{19}$) has been followed by IR under outgassing, and compared with the same experiment using MgO. $BaAl_{12}O_{19}$ appears to be far more basic than pure alumina and most pure oxides but less basic than pure alkaline earth oxides.

Perovskite-type phases can form when small cations and large cations combine in a mixed oxide. The surface, however, appears to be largely dominated by the large cations and basic oxide anions, as in the cases of $BaTiO_3$ [173], $SrTiO_3$ [171] and several lanthanum perovskites [174].

Magnesium aluminates produced by decomposition of hydrotalcites (the layered double hydroxides with formula $Mg_6Al_2(OH)_{16}CO_3 \cdot 4H_2O$) are currently very popular base catalysts. Their thermal decompostion gives rise to a mixed oxide whose virtual composition is $5\,MgO \cdot MgAl_2O_4$, although these phases give rise to partial solid solutions depending on the decomposition temperature. Stoichiometric $MgAl_2O_4$, is essentially a normal spinel phase with tetrahedrally coordinated magnesium and octahedrally coordinated Al. Actually, due to partial inversion of the spinel structure, low coordination Al cations typical of spinel-type aluminas can be detected at the surface and produce a small density of very strong Lewis acid sites [175]. Excess magnesium ions result in the segregation of large amounts of MgO, causing the predominance of basic character. CO_2 adsorption forms surface carbonates, which are stable up to near 773 K.

3.6.8
Use of Isotopically Labeled Molecules

The energy and the frequency of the molecular vibrational modes depend on the mass of the atoms directly involved as well as on the bond energy. Consequently, the position of the absorption peaks are shifted when isotopically labeled molecules are used. This is a useful property for the confirmation of the assignment of vibrational modes when needed. The adsorption of heavy water allows investiga-

tion of the surface hydroxyls, converted into deuteroxyls. Similarly, the use of deuterated organics facilitates the distinction of CH deformation modes (which are shifted when deuterated organics are used) from CO stretching modes that can occur in similar positions. This has been used, for example, to provide a more precise characterization of the adsorption modes of methanol on alumina, using deuterated methanols [176]. Similarly, $^{16}O/^{18}O$ exchange at the surface of oxides can be performed with $^{18}O_2$ or with $H_2{}^{18}O$ and this allows confirmation of the state of surface metal–oxygen bonds [92, 95, 96]. Also the use of ^{13}C and ^{15}N labeled molecules, for example ^{13}CO, $^{13}CO_2$ and ^{15}NO, provide clarification of the structure of surface species.

3.7 Infrared Studies of the Mechanisms of Heterogeneously Catalysed Reactions

After reviewing the successful application of this technique for the characterization of solid surfaces in 1984, Peri [13], one of the pioneers of IR spectroscopy in catalysis, stated that "rather limited real success has been achieved to date in the search for active intermediates on catalyst surfaces by IR methods." However, the previously described work of Kokes [14, 15] and Tamaru [18] were cited as successful examples. In an interesting book, Davydov summarized several examples of the application of IR spectroscopy to determine the mechanisms of oxide-catalyzed processes [177]. In a more recent review, published in 1996, the present author reported several examples of studies of the surface reactivity of organic molecules on metal oxides, providing information on the mechanisms of heterogeneously catalyzed partial and total oxidation [178]. IR spectroscopy can be applied in static conditions, looking at the evolution of adsorbed species at the surface. This approach frequently allows the detection of the different steps of the catalytic reaction, such as the adsorption of reactants, the step-by-step evolution to products and, finally, the desorption of the products. This provides information on the pathways of several reactions such as, among recent work performed in our laboratory, the conversion of synthesis gas to methanol, methane and higher hydrocarbons [179], the steam reforming of methanol [180], the skeletal and double-bond isomerization of olefins [181, 182] and the reactions for the catalytic abatement of NO_x [183, 184]. These studies allow the development of understanding of the basic chemistry of the catalytic phenomena.

In situ and *operando* studies [19–21] refer to investigations performed under flow conditions with the simultaneous detection of the reaction products (usually by gas chromatography) and the measure of conversion/selectivity as a function of the reaction parameters. These studies have the strong advantage of looking at the state of the catalyst during reaction, but the simultaneous disadvantage of not allowing the trapping of the active species, which may be present in very low concentration (if at all) during real catalysis, with inactive spectator species being possibly much more evident. As discussed previously [179], the most informative approach, in the opinion of the present author, is the combination of *operando*

studies with surface science studies performed in static conditions or flushing inert gas [185], following the evolution of the adsorbed species with the variation of the temperature, and also in conditions where conversion does not occur at all and the products are still not formed, that is, in conditions that are not *operando*.

Lamberti and coworkers [186] have reviewed some successful application on the use of IR spectroscopy on reaction mechanism studies performed in their laboratory.

References

1 Jones, R.N. (1985) in *Chemical, Biological and Industrial Applications of Infrared Spectroscopy* (ed. J.R. Durig), John Wiley & Sons, Inc., NewYork, pp. 1–50.

2 Raman, C.V. (1928) *Journal of Physical Chemistry*, **2**, 387–98.

3 Somorjai, G.A. and McCrea, K.R. (2000) *Advanced Catalysis*, **45**, 385–438.

4 Liuy, W., Zhang, L. and Shen, Y.R. (2005) *Chemical Physics Letters*, **412**, 206–9.

5 Krebs, A.M., Buswell, K. and Rodebush, W.H. (1937) *Journal of the American Chemical Society*, **59**, 2603–5.

6 (a) Terenin, A. (1940) *Zhurnal Fizicheskoi Khimii*, **14**, 1362; (b) Terenin, A. and Roev, L. (1959) *Spectrochimica Acta*, **11**, 946–57.

7 Mapes, J.E. and Eischens, R.P. (1954) *Journal of Physical Chemistry*, **58**, 1059–62.

8 (a) Sheppard, N. and Yates, D.J.C. (1956) *Proceedings of the Royal Society*, **A238**, 69; (b) Sheppard, N. (1994) *Spectroscopy Europe*, **6**, 20.

9 Eischens, R.P., Francis, S.A. and Pliskin, W.A. (1956) *Journal of Physical Chemistry*, **60**, 194–201.

10 Eischens, R.P. and Pliskin, W.A. (1957) *Advances in Catalysis and Related Subjects*, **9**, 662–8.

11 Eischens, R.P. and Pliskin, W.A. (1958) *Advances in Catalysis and Related Subjects*, **10**, 1–56.

12 Peri, J.B. and Hannan, R.B. (1960) *Journal of Physical Chemistry*, **64**, 1526–30.

13 Peri, J.B. (1984) in *Catalysis, Science and Technology*, (eds J.R. Anderson and M. Boudart) Vol. **5**, Springer, Berlin, pp. 171–220.

14 Chang, C.C., Conner, W.C. and Kokes, R.J. (1973) *Journal of Physical Chemistry*, **77**, 1957–64.

15 Kokes, R.J. (1973) *Accounts of Chemical Research*, **6**, 226–33.

16 Moffatt, D.J., Kauppinen, J.K. and Mantsch, H.H. (1991) *Canadian Journal of Chemistry/Revenue Canadienne de Chimie*, **69**, 1781–5.

17 Joly, J.F., Zanier-Szydlowsky, N., Colin, S., Raatz, F., Saussey, J. and Lavalley, J.C. (1991) *Catalysis Today*, **9**, 31–8.

18 Tamaru, K. (1978) Dynamic Heterogeneous Catalysis, Academic Press, New York.

19 Bañares, M.A. (2005) *Catalysis Today*, **100**, 71–7.

20 Montanari, T., Marie, O., Daturi, M. and Busca, G. (2007) *Catalysis Today*, **7**, 216–22.

21 Brückner, A. and Kondratenko, E. (2006) *Catalysis Today*, **113**, 16–24.

22 Spoto, G., Bordiga, S., Zecchina, A., Cocina, D., Gribov, E.N., Regli, L., Groppo, E. and Lamberti, C. (2006) *Catalysis Today*, **113**, 65–80.

23 Freund, H.J. (2005) *Catalysis Today*, **100**, 3–9.

24 Zhu, C. and Griffiths, P.R. (1998) *Applied Spectroscopy*, **52**, 1403–8 and 1409–13.

25 Henry, R.L. (1948) *Journal of the Optical Society of America*, **38**, 775–89.

26 (a) Lejeune, R. and Duykaerts, G. (1954) *Spectrochimica Acta*, **6**, 194–7; (b) Duykaerts, G. (1959), *Analyst*, **84**, 201.

27 Pritchard, J. (1978) in Chemical Physics of Solids and Their Surfaces, vol. **7**, RSC, London, pp. 157–79.

28 Harrick, N.J. (1967) Internal Reflection Spectroscopy, Interscience, New York.

29 Wilks, P. (1984) *European Spectroscopy News*, **55**, 26.

30 Safranovsky, P.A., Kuzik, L.A. and Zhinzhin, G.H. (1990) *Journal of Electron Spectroscopy and Related Phenomena*, **54/55**, 457–68.

31 Kubelka, P. and Munk, F. (1931) *Zeitschrift fur Technische Physik*, **12**, 593.

32 (a) Brimmer, P.J. and Griffiths, P.R. (1987) *Applied Spectroscopy*, **41**, 791–7; (b) Brimmer, P.J. and Griffiths, P.R. (1988) *Applied Spectroscopy*, **42**, 242–7.

33 Sullivan, D.H., Conner, W.C. and Harold, M.P. (1992) *Applied Spectroscopy*, **46**, 811–18.

34 Frost, R.L. and Kloprogge, J.T. (1999) *Applied Clay Science*, **15**, 431–45.

35 Pohle, R., Fleischer, M. and Meixner, H. (2001) *Sensors and Actuators*, **78**, 133–7.

36 Bell, A.G. (1980) *American Journal of Science*, **29**, 305.

37 Rosencwaig, C.A. (1980) Photoacoustics and Photoacoustic Spectroscopy, John Wiley & Sons, Inc., New York.

38 Ryczkovski, J. (2007) *Catalysis Today*, **124**, 11–20.

39 Boccara, A.C., Fournier, D. and Badoz, J. (1980) *Applied Physics Letters*, **36**, 130–2.

40 Low, M.J.D., Morterra, C., Severdia, A.G. and Tascon, J.M.D. (1984) in Catalytic Materials, Relationship between Structure and Reactivity, ACS, (eds T.E. Whyte, R.A. Dalla Betta, E.G. Derogane and R.T.K. Baker), Washington, pp. 411–25.

41 Turrell, G. (1972) Infrared and Raman Spectra of Crystals, Academic Press, London.

42 Decius, J.C. and Hexter, R.M. (1977) Molecular Vibrations in Crystals, McGraw-Hill (USA).

43 Nakamoto, K. (1986) Infrared and Raman Spectra of Inorganic and Coordination compounds, John Wiley & Sons, Inc., New York.

44 Fateley, W.G., Dollish, F.R., McDevitt, N.T. and Bentley, F.F. (1972) Infararead and Raman Selection Rules for Molecular and Lattice Vibrations, John Wiley & Sons, Inc., New York.

45 Tarte, P. (1962) *Spectrochimica Acta*, **18**, 467–83.

46 Tarte, P. (1967) *Spectrochimica Acta*, **23A**, 2127–43.

47 Beattie, I.R. and Gilson, T.R. (1969) *Journal of the Chemical Society A*, 2322–7.

48 Calleja, J.M. and Cardona, M. (1977) *Physical Review*, **B16**, 3753.

49 Andrés Vergés, M., Mifsud, A. and Serna, C.J. (1990) *Journal of the Chemical Society–Faraday Transactions*, **86**, 959–63.

50 Zhou, R.S. and Snyder, R.L. (1991) *Acta Crystallographica Section B*, **47**, 617–30.

51 Krokidis, X., Raybaud, P., Gobichon, A.-E., Rebours, B., Euzen, P. and Toulhoat, H. (2001) *Journal of Physical Chemistry B*, **105**, 5121–30.

52 Barker, A.S. (1973) *Physical Review*, **132**, 1474.

53 Sanchez Escribano, V., Gallardo Amores, J.M., Finocchio, E., Daturi, M. and Busca, G. (1995) *Journal of Materials Chemistry*, **5**, 1943–51.

54 Julien, C.M., Massot, M. and Poinsignon, C. (2004) *Spectrochimica Acta Part A*, **60**, 689–700.

55 Bloor, D. and Dean, J.R. (1972) *Journal of Physics C-Solid State Physics*, **5**, 1237–52.

56 Busca, G., Ramis, G., Gallardo Amores, J.M., Sanchez Escribano, V. and Piaggio, P. (1994) *Journal of the Chemical Society–Faraday Transactions*, **90**, 3181–90.

57 Fernandez Lopez, E., Sanchez Escribano, V., Panizza, M., Carnasciali, M.M. and Busca, G. (2001) *Journal of Materials Chemistry*, **11**, 1891–7.

58 Astorino, E., Peri, J., Willey, R.J. and Busca, G. (1995) *Journal of Catalysis*, **157**, 482–500.

59 Busca, G., Tittarelli, P., Forzatti, P. and Tronconi, E. (1987) *Journal of Solid State Chemistry*, **67**, 91–7.

60 Baraton, M.I., Busca, G., Prieto, M.C., Ricchiardi, G. and Sanchez Escribano, V. (1994) *Journal of Solid State Chemistry*, **112**, 9–14.

61 Busca, G., Lorenzelli, V. and Sanchez Escribano, V. (1992) *Chemistry of Materials*, **4**, 595–605.

62 Busca, G., Daturi, M., Kotur, E., Oliveti, G. and Willey, R.J. (1995) in Preparation

of Catalysts VI (eds G. Poncelet, *et al.*), Elsevier Science, pp. 667–76.
63 Bellotto, M., Busca, G., Cristiani, C. and Groppi, G. (1995) *Journal of Solid State Chemistry*, **117**, 8–15.
64 Busca, G., Buscaglia, V., Leoni, M. and Nanni, P. (1994) *Chemistry of Materials*, **6**, 955–61.
65 Daturi, M., Busca, G. and Willey, R.J. (1995) *Chemistry of Materials*, **7**, 2115–26.
66 Busca, G., Ricchiardi, G., Siew Hew Sam, D. and Volta, J.C. (1994) *Journal of the Chemical Society–Faraday Transactions*, **90**, 1161–70.
67 Daturi, M., Busca, G., Borel, M.M., Leclaire, A. and Piaggio, P. (1997) *Journal of Physical Chemistry*, **101B**, 4358–69.
68 Butler, W.M., Angell, C.L., Mc Allister, W. and Risen, W.M. (1977) *Journal of Physical Chemistry*, **81**, 2061–8.
69 Busca, G., Lorenzelli, V., Galli, P., La Ginestra, A. and Patrono, P. (1987) *Journal of the Chemical Society–Faraday Transactions I*, **83**, 853–65.
70 Lazarev, A.N. (1972) Vibrational Spectra and Structure of Silicates, Consultants Bureau, New York.
71 Busca, G., Cavani, F., Centi, G. and Trifirò, F. (1986) *Journal of Catalysis*, **99**, 400–14.
72 Sanchez, C., Livage, J. and Lucazeau, G. (1982) *Journal of Raman Spectroscopy*, **12**, 68.
73 Abbattista, F., Delmastro, S., Gozzelino, G., Mazza, D., Vallino, M., Busca, G., Lorenzelli, V. and Ramis, G. (1989) *Journal of Catalysis*, **117**, 42–51.
74 Busca, G., Ramis, G., Prieto, M.C. and Sanchez Escribano, V. (1993) *Journal of Materials Chemistry*, **3**, 665–73.
75 Gallardo-Amores, J.M., Sanchez Escribano, V. and Busca, G. (1999) *Journal of Materials Chemistry*, **9**, 1161–6.
76 Horsley, S.E., Nowell, D.V. and Stewart, D.T. (1974) *Spectrochimica Acta*, **30A**, 535–41.
77 Stoyanov, E.S., Kim, K.C. and Reed, C.A. (2006) *Journal of the American Chemical Society*, **128**, 1948–58.
78 Frost, R.L., Weier, M.L., Clissold, M.E. and Williams, P.A. (2003) *Spectrochimica Acta Part A–Molecular and Biomolecular Spectroscopy*, **59**, 3313–19.
79 Lavalley, J.C. and Benaissa, M. (1984) *Journal of the Chemical Society D–Chemical Communications*, 908–9.
80 Busca, G., Lorenzelli, V., Sanchez Escribano, V. and Guidetti, R. (1991) *Journal of Catalysis*, **131**, 167–77.
81 Marrone, M., Montanari, T., Busca, G., Conzatti, L., Costa, G., Castellano, M. and Turturro, A. (2004) *Journal of Physical Chemistry B*, **108**, 3563–72.
82 Busca, G., Ramis, G. and Lorenzelli, V. (1989) *Journal of Molecular Catalysis*, **50**, 231–40.
83 Armaroli, T., Busca, G., Carlini, C., Giuttari, M., Raspolli Galletti, A.M. and Sbrana, G. (2000) *Journal of Molecular Catalysis*, **151**, 233–43.
84 Ramis, G., Cristiani, C., Elmi, A.S., Villa, P.L. and Busca, G. (1990) *Journal of Molecular Catalysis*, **61**, 319–31.
85 Busca, G. and Lorenzelli, V. (1982) *Journal of Materials Chemistry*, **7**, 89–126.
86 Ramis, G., Busca, G. and Lorenzelli, V. (1991) *Materials Chemistry and Physics*, **29**, 425–35.
87 Odenbrand, C.U.I., Andersson, S.L.T., Andersson, L.A.H., Brandin, J.G.M. and Busca, G. (1990) *Journal of Catalysis*, **125**, 541–53.
88 Yi, L., Ramis, G., Busca, G. and Lorenzelli, V. (1994) *Journal of Materials Chemistry*, **4**, 1755–61.
89 Finocchio, E., Busca, G., Rossini, S., Cornaro, U., Piccoli, V. and Miglio, R. (1997) *Catalysis Today*, **33**, 335–52.
90 Riccio, M., Montanari, T., Castellano, M., Turturro, A., Negroni, F.M. and Busca, G. (2007) *Colloids and Surfaces A–Physicochemical and Engineering Aspects*, **294**, 181–90.
91 Finocchio, E., Garuti, G., Baldi, M. and Busca, G. (2008) in press.
92 Saur, O., Bensitel, M., Mohammed Saad, A.B., Lavalley, J.C., Tripp, C.P. and Morrow, B.A. (1986) *Journal of Catalysis*, **99**, 104–10.
93 Klose, B.S., Jentoft, F.C., Joshi, P., Trunschke, A., Schlögl, R., Subbotina, I. R. and Kazansky, V.B. (2006) *Catalysis Today*, **116**, 121–31.

94 Manoilova, O., Olindo, R., Otero Areán, C., and Lercher, J.A. (2007) *Catalysis Communications*, **8**, 865–70.

95 Stencel, J.M., Makovsky, L.E., Diehl, J.R. and Sarkus, T.A. (1984) *Journal of Raman Spectroscopy*, **15**, 283.

96 Ramis, G., Cristiani, C., Forzatti, P. and Busca, G. (1990) *Journal of Catalysis*, **124**, 574–5.

97 Payen, E., Gengembre, L., Maugé, F., Duchet, J.C. and Lavalley, J.C. (1991) *Catalysis Today*, **10**, 521–39.

98 Gutierrez-Alejandre, A., Castello, P., Ramirez, J., Ramis, G. and Busca, G. (2001) *Applied Catalysis A: General*, **216**, 181–94.

99 Busca, G. (2002) *Journal of Raman Spectroscopy*, **33**, 348–58.

100 Busca, G. (2008) *Chemical Reviews*, **107**, 5366–71.

101 Busca, G. (1999) *Physical Chemistry Chemical Physics*, **1**, 723–36.

102 Busca, G. (2005) in Metal Oxides: Chemistry and Applications (ed. J.L.G. Fierro), CRC Press, Boca Raton, Fl, pp. 247–318.

103 Busca, G., Ramis, G., Lorenzelli, V., Rossi, P.F., La Ginestra, A. and Patrono, P. (1989) *Langmuir*, **5**, 911–16.

104 Ramis, G., Busca, G., Lorenzelli, V., Rossi, P.F., Bensitel, M., Saur, O. and Lavalley, J.C. (1988) *Proceedings of the 9th International Congress on Catalysis, Calgary, Canada*, Vol. IV, pp. 1874–81.

105 Ramis, G., Yi, L., Busca, G., del Martín, M., Arco, C., Rives, V. and Sanchez Escribano, V. (1998) *Materials Chemistry and Physics*, **55**, 173–87.

106 Busca, G., Cavani, F., Centi, G. and Trifirò, F. (1986) *Journal of Catalysis*, **99**, 400–14.

107 Abbattista, F., Delmastro, S., Gozzelino, G., Mazza, D., Vallino, M., Busca, G. and Lorenzelli, V. (1990) *Journal of the Chemical Society–Faraday Transactions. I*, **86**, 3653–8.

108 Ramis, G., Busca, G., Lorenzelli, V., La Ginestra, A., Galli, P. and Massucci, M.A. (1988) *Journal of the Chemical Society–Dalton Transactions*, 881–6.

109 DelMastro, S., Gozzellino, G., Mazza, D., Vallino, M., Busca, G. and Lorenzelli, V. (1992) *Journal of the Chemical Society–Faraday Transactions I*, **88**, 2065–70.

110 Armaroli, T., Bevilacqua, M., Trombetta, M., Milella, F., Gutièrrez Alejandre, A., Ramirez Solis, J., Notari, B., Willey, R.J. and Busca, G. (2001) *Applied Catalysis A: General*, **216**, 59–71.

111 Tsyganenko, A. and Filimonov, V.N. (1972) *Spectroscopy Letters*, **5**, 477–87.

112 Montagne, X., Lynch, J., Freund, E., Lamotte, J. and Lavalley, J.C. (1987) *Journal of the Chemical Society–Faraday Transactions I*, **83**, 1417–25.

113 Bevilacqua, M., Montanari, T., Finocchio, E. and Busca, G. (2006) *Catalysis Today*, **116**, 132–42.

114 Astorino, E., Peri, J., Willey, R.J. and Busca, G. (1995) *Journal of Catalysis*, **157**, 482–500.

115 Zecchina, A., Bordiga, S., Spoto, G., Marchese, L., Petrini, G., Leofanti, G. and Padovan, M. (1992) *Journal of Physical Chemistry*, **96**, 4991–7.

116 Peri, J.B. (1965) *Journal of Physical Chemistry*, **69**, 211–20.

117 Knözinger, H. and Ratnasamy, P. (1978) *Catalysis Reviews–Science and Engineering*, **17**, 31–70.

118 Busca, G., Lorenzelli, V., Ramis, G. and Willey, R.J. (1993) *Langmuir*, **9**, 1492–9.

119 Morterra, C. and Magnacca, G. (1996) *Catalysis Today*, **27**, 497–532.

120 Mardilovich, A.A. and Tsyganenko, P.P. (1996) *Journal of the Chemical Society–Faraday Transactions*, **92**, 4843–52.

121 Fripiat, J., Alvarez, L., Sanchez Sanchez, S., Martinez, E., Morades, E., Saniger, J. and Sanchez, N. (2001) *Applied Catalysis A: General* **215**, 91–100.

122 Digne, M., Sautet, P., Raybaud, P., Euzen, P. and Toulhoat, H. (2002) *Journal of Catalysis.*, **211**, 1–5.

123 Lambert, J.F. and Che, M. (2000) *Journal of Molecular Catalysis. A–Chemical*, **162**, 5–18.

124 Malpartida, I., Larrubia Vargas, M.A., Alemany, L.J. and Busca, G. (2007) *Applied Catalysis B: Environmental*, **80**, 214–25.

125 Bevilacqua, M. and Busca, G. (2008) in press.

126 Liu, X. and Truitt, R.E. (1997) *Journal of the American Chemical Society*, **119**, 9856–60.

127 Busca, G., Guidetti, R. and Lorenzelli, V. (1990) *Journal of the Chemical Society–Faraday Transactions I*, **86**, 989–94.
128 Busca, G., Lorenzelli, V. and Sanchez Escribano, V. (1992) *Chemistry of Materials*, **4**, 595–605.
129 Busca, G., Saussey, H., Saur, O., Lavalley, J.C. and Lorenzelli, V. (1985) *Applied Catalysis*, **14**, 245–60.
130 Bensitel, M., Saur, O., Lavalley, J.C. and Morrow, B.A. (1987) *Materials Chemistry and Physics*, **17**, 249–58.
131 Jacob, K.-H., Knözinger, E. and Benier, S. (1993) *Journal of Materials Chemistry*, **3**, 651–7.
132 Gutierrez-Alejandre, A., Castillo, P., Ramirez, J., Ramis, G. and Busca, G. (2001) *Applied Catalysis A: General*, **216**, 181–94.
133 Baertsch, C.D., Komala, K.T., Chua, Y.-H. and Iglesia, E. (2002) *Journal of Catalysis*, **205**, 44–57.
134 Kuba, S., Che, M., Grasselli, R.K. and Knözinger, H. (2003) *Journal of Physical Chemistry B*, **107**, 3459–63.
135 Manoilova, O., Olindo, R., Otero Areán, C. and Lercher, J.A. (2007) *Catalysis Communications*, **8**, 865–70.
136 Góra-Marek, K., Derewinski, M., Sarv, P. and Datka, J. (2005) *Catalysis Today*, **101**, 131–8.
137 Góra-Marek, K. and Datka, J. (2006) *Applied Catalysis A: General*, **302**, 104–9.
138 Cseri, G., Crépau, V., Montouillout, A., Vimont, L., Mariey, T. and Maugé, F. (2006) *Journal of Physical Chemistry. B*, **110**, 15172–85.
139 Garrone, E., Onida, B., Bonelli, B., Busco, C. and Ugliengo, P. (2006) *Journal of Physical Chemistry. B*, **110**, 19087–92.
140 Ramis, G., Busca, G. and Lorenzelli, V. (1989) in Structure and Reactivity of Surfaces (eds A. Zecchina, G. Costa and C. Morterra), Elsevier, pp. 777–86.
141 Busca, G. (1998) *Catalysis Today*, **41**, 191–206.
142 Trombetta, M., Busca, G., Rossini, S.A., Piccoli, V. and Cornaro, U. (1997) *Journal of Catalysis*, **168**, 349–63.
143 Trombetta, M. and Busca, G. (1999) *Journal of Catalysis*, **187**, 521–3.
144 Trombetta, M., Busca, G., Lenarda, M., Storaro, L. and Pavan, M. (1999) *Applied Catalysis A: General*, **182**, 225–35.
145 Montanari, T., Bevilacqua, M., Resini, C. and Busca, G. (2004) *Journal of Physical Chemistry. B*, **108**, 2120–7.
146 Trombetta, M., Armaroli, T., Gutiérrez-Alejandre, A., Ramírez, J. and Busca, G. (2000) *Applied Catalysis A: General*, **192**, 125–36.
147 Montanari, T., Bevilacqua, M. and Busca, G. (2006) *Applied Catalysis A: General*, **307**, 21–9.
148 Bevilacqua, M. and Busca, G. (2002) *Catalysis Communications*, **3**, 497–502.
149 Armaroli, A., Bevilacqua, M., Trombetta, M., Gutièrrez Alejandre, A., Ramirez, J. and Busca, G. (2001) *Applied Catalysis A: General*, **220**, 181–90.
150 Trombetta, M., Armaroli, T., Gutièrrez Alejandre, A., Gonzalez, H., Ramirez Solis, J. and Busca, G. (2001) *Catalysis Today*, **65**, 285–92.
151 Trombetta, M., Busca, G., Storaro, L., Lenarda, M., Casagrande, M. and Lucchini, V. (2000) *Physical Chemistry Chemical Physics*, **2**, 3529–37.
152 Romero Sarria, F., Blasin-Aube, V., Saussey, J., Marie, O. and Daturi, M. (2006) *Journal of Physical Chemistry B*, **110**, 13130–7.
153 Lundie, D.T., McInroy, A.R., Marshall, R., Winfield, J.M., Jones, P., Dudman, C.C., Parker, S.F., Mitchell, C. and Lennon, D. (2005) *Journal of Physical Chemistry B*, **109**, 11592–601.
154 Morrow, B.A. and Cody, I.A. (1976) *Journal of Physical Chemistry*, **80**, 1995–8.
155 Hadjiivanov, K.I. and Vayssilov, G.N. (2002) *Advances in Catalysis*, **47**, 307–511.
156 Binet, C., Jadi, A. and Lavalley, J.C. (1989) *Journal De Chimie Physique*, **86**, 451–70.
157 Busca, G. (1987) *Journal of Molecular Catalysis*, **43**, 225–36.
158 Gallardo Amores, J.M., Sanchez Escribano, V., Busca, G. and Lorenzelli, V. (1994) *Journal of Materials Chemistry*, **4**, 965–71.
159 Montanari, T., Marie, O., Daturi, M. and Busca, G. (2005) *Catalysis Today*, **110**, 339–44.
160 Salla, I., Montanari, T., Salagre, P., Cesteros, Y. and Busca, G. (2005) *Physical Chemistry Chemical Physics*, **7**, 2526–33.
161 Montanari, T., Salla, I. and Busca, G. (2008) *Microporous and Mesoporous Materials*, **109**, 216–22.

162 Salla, I., Montanari, T., Salagre, P., Cesteros, Y. and Busca, G. (2005) *Journal of Physical Chemistry B*, **109**, 915–22.

163 Weitkamp, J., Hunger, M. and Rymsa, U. (2001) *Microporous and Mesoporous Materials*, **48**, 255–70.

164 Davis, R.J. (2003) *Journal of Catalysis*, **216**, 396–405.

165 Kozyra, P., Salla, I., Montanari, T., Datka, J., Salare, P. and Busca, G. (2006) *Catalysis Today*, **114**, 188–96.

166 Montanari, T. and Busca, G. (2008) *Vibration Spectroscopy*, **46**, 45–51.

167 Montanari, T., Kozyra, P., Salla, I., Datka, J., Salare, P. and Busca, G. (2006) *Journal of Materials Chemistry*, **16**, 995–1000.

168 Busca, G. and Ramis, G. (1986) *Applied Surface Science*, **27**, 114–26.

169 Gallardo Amores, J.M., Sanchez Escribano, V., Daturi, M. and Busca, G. (1996) *Journal of Materials Chemistry*, **6**, 879–86.

170 Morterra, C., Magnacca, G., Cerrato, G., Del Favero, N., Filippi, F. and Folonari, C.V. (1993) *Journal of the Chemical Society–Faraday Transactions*, **89**, 135–50.

171 Prinetto, F., Ghiotti, G., Nova, I., Lietti, L., Tronconi, E. and Forzatti, P. (2001) *Journal of Physical Chemistry B*, **105**, 12732–5.

172 Busca, G., Cristiani, C., Forzatti, P. and Groppi, G. (1995) *Catalysis Letters*, **31**, 65–74.

173 Busca, G., Buscaglia, V., Leoni, M. and Nanni, P. (1994) *Chemistry of Materials*, **6**, 955–61.

174 Daturi, M., Busca, G. and Willey, R.J. (1995) *Chemistry of Materials*, **7**, 2115–26.

175 Rossi, P.F., Busca, G., Lorenzelli, V., Waquif, M., Saur, O. and Lavalley, J.C. (1991) *Langmuir*, **7**, 2677–81.

176 Busca, G., Rossi, P.F., Lorenzelli, V., Benaissa, M., Travert, J. and Lavalley, J.C. (1985) *Journal of Physical Chemistry*, **89**, 5433–9.

177 Davydov, A.A. (1990) Infrared Spectroscopy of Adsorbed Species on the Surface of Transition Metal Oxide, John Wiley & Sons, Inc.

178 Busca, G. (1996) *Catalysis Today*, **27**, 457–96.

179 Sanchez Escribano, V., Larrubia Vargas, M.A., Finocchio, E. and Busca, G. (2007) *Journal of Materials Chemistry*, **316**, 68–74.

180 Larrubia Vargas, M.A., Busca, G., Costantino, U., Marmottini, F., Montanari, T., Patrono, P., Pinzari, F. and Ramis, G. (2007) *Journal of Molecular Catalysis. A: Chemical*, **266**, 188–97.

181 Busca, G., Finocchio, E., Lorenzelli, V., Trombetta, M. and Rossini, S.A. (1996) *Journal of the Chemical Society–Faraday Transactions I*, **92**, 4687–93.

182 Trombetta, M., Busca, G., Rossini, S.A., Piccoli, V. and Cornaro, U. (1997) *Journal of Catalysis*, **168**, 334–48.

183 Busca, G., Lietti, L., Ramis, G. and Berti, F. (1998) *Applied Catalysis B–Environmental*, **18**, 1–36.

184 Busca, G., Larrubia, M.A., Arrighi, L. and Ramis, G. (2005) *Catalysis Today*, **107–108**, 139–48.

185 Tibiletti, D., Goguet, A., Reid, D., Munier, F.C. and Burch, R. (2006) *Catalysis Today*, **113**, 94–101.

186 Lamberti, C., Groppo, E., Spoto, G. Bordiga, S. and Zecchina, A. (2007) *Advances in Catalysis*, **51**, 1–74.

4
Resonance Raman Spectroscopy – Θ-Al_2O_3-Supported Vanadium Oxide Catalysts as an Illustrative Example

Zili Wu, Hack-Sung Kim, and Peter C. Stair

4.1
Introduction

Raman spectroscopy is a powerful tool for characterizing the molecular structure of catalytic materials under *in situ* conditions. In recent years, resonance Raman studies of heterogeneous catalysts have added additional dimensions to this technique by providing the capability of probing the heterogeneity of surface catalytic sites. Specifically, the heterogeneously distributed catalytic phases (sites) with different electron absorptions can be selectively resonance enhanced in Raman spectroscopy by using appropriate laser excitation. Thus different catalytic sites can be individually probed via varying laser excitations (multi-wavelength excitation). In this chapter, we present an example of applying the resonance Raman spectroscopy technique for investigating the structure of V/Al_2O_3 catalysts under various oxidation and reduction conditions as an illustrative example of the power of the technique. The example shows that multi-wavelength-excited Raman spectroscopy is able to provide not only qualitative information on the structure of different surface VO_x species but also quantitative information on the distribution of these VO_x species as a function of vanadium loading. The reduction behaviors of the different VO_x species (monovanadate, polyvanadate and V_2O_5) have been distinguished by this method. Raman spectroscopy application to butane dehydrogenation catalyzed by VO_x species is given in Volume 2 of this series. It is expected that multi-wavelength-excited Raman spectroscopy will be employed for more applications in catalysis and material science studies.

Metal Oxide Catalysis. Edited by S. David Jackson and Justin S. J. Hargreaves

ISBN: 978-3-527-31815-5

4.2
Structure of Al_2O_3-Supported Vanadia Catalysts

4.2.1
Introduction

Supported vanadia catalysts have attracted significant interest in recent decades because of their favorable catalytic performance in many redox reactions [1–6], such as dehydrogenation and oxidative dehydrogenation of alkanes to olefins, oxidation of methanol to formaldehyde, ammoxidation of aromatic hydrocarbons and selective reduction of NO_x. A better understanding of the catalytic properties of supported vanadium oxides requires determination of the structure–reactivity relationships of the supported VO_x catalysts. Raman spectroscopy has been successfully, and frequently, employed by many research groups for characterization of the molecular structure of supported vanadium oxides [2, 4–18]. For vanadia supported on most oxide supports, for example SiO_2, Al_2O_3, TiO_2, ZrO_2 and MgO, three types of surface vanadia species have been identified: isolated vanadia, polymerized vanadia and crystalline V_2O_5. The presence of these species is a function of the method of preparation, the VO_x loading, the nature of the support and the ambient environment [2, 4–11, 15]. For dehydrated, supported VO_x, three kinds of bonds between vanadium and oxygen are present in these VO_x species: V=O, V—O—V and V—O—S (where S refers to the support). It is generally accepted that the bridging V—O—S bond is critical for redox reactions catalyzed by supported VO_x [4–6, 13, 18]. The discrimination of different surface VO_x species has usually been based on their characteristic Raman features. Isolated and polymerized VO_x species have been characterized by sharp V=O stretching bands in the range 990–1050 cm^{-1}, broad Raman features in the range 500–950 cm^{-1} have been attributed to V—O—V stretching in polymerized VO_x and the presence of V_2O_5 is indicated by an intense V=O stretching band at 995 cm^{-1}. The catalytic properties of supported VO_x catalysts have been shown to be sensitive to the distribution of these surface VO_x species [4–6, 10, 13, 15].

In addition to the structure in the dehydrated state, the structure of supported vanadia catalysts under redox reaction conditions is directly related to the catalytic performance. Vanadia catalysts are usually reduced to some extent during a redox reaction, and the reduced vanadia species have been proposed as the active sites [4, 19–24]. Therefore, information on the valence state and molecular structure of the reduced vanadia catalysts is of great interest. A number of techniques have been applied to investigate the reduction of supported vanadia catalysts, such as temperature programmed reduction (TPR) [25–27], X-ray photoelectron spectroscopy (XPS) [21], electron spin resonance (ESR) [22], UV-Vis diffuse reflectance spectroscopy (UV-Vis DRS) [18, 28–32], X-ray absorption fine structure spectroscopy (XAFS) [11] and Raman spectroscopy [5, 26, 33–41]. Most of these techniques give information only on the oxidation state of vanadium species. Although Raman spectroscopy is a powerful tool for characterization of the molecular structure of supported vanadia [4, 29, 42], it has been very difficult to detect reduced supported

vanadia species with conventional (visible) Raman measurements [26, 33–39]. A widely accepted explanation for this phenomenon is that the Raman cross-section of reduced vanadium oxide species is very small or even near zero [43]. Thus, it remains challenging to employ Raman spectroscopy for the determination of information on the molecular state of reduced vanadia species.

It is notable that most Raman studies of supported VO_x catalysts have been carried out using a single excitation wavelength in the visible region (488, 514 or 532 nm) [3–15]. However, several investigations on supported transition metal oxides [16, 17, 44, 45], including vanadium oxides [16, 17] under ambient conditions, using both UV and visible wavelength Raman excitations suggest that more complete, and sometimes new, structural information on supported metal oxides may be achieved by using multiple excitation wavelengths. The reason for this lies in the strong electronic absorption in the UV and visible wavelength regions exhibited by most transition metal oxides, which make it possible to measure resonance-enhanced Raman spectra. Under circumstances where supported VO_x species are present in a distribution of cluster sizes or coordination geometries, it is likely that these species also possess a corresponding distribution of electronic absorption wavelengths. Excitation of Raman spectra within the absorption region will produce resonance-enhanced spectra from the subset of VO_x species with absorptions at the excitation wavelength. By measuring the Raman spectra at several wavelengths, more information can be obtained about the various VO_x species in the distribution. Moreover, when UV excitation is employed, Raman spectra can even be obtained from supported VO_x at low loadings (<1% wt) on oxides with strong fluorescence because of the avoidance of fluorescence and enhanced sensitivity [38, 46]. In addition, the decreased self-absorption effects in the UV region indicated by *in situ* UV-Vis DRS studies of reduced VO_x and CrO_x [18, 28–31, 47, 48] suggests UV Raman spectroscopy may be capable of detecting reduced supported metal oxides.

In this case study, we have carried out further investigation into the structure of VO_x supported on alumina under both oxidized (dehydrated) and reduced environments using both UV- (244 nm) and visible- (488 nm) excited Raman spectroscopy. Special attention has been directed towards the structure of supported VO_x at extremely low surface density (down to 0.01 V nm^{-2}).

4.2.1.1 Dehydrated State

The visible and UV Raman spectra of dehydrated V/θ-Al_2O_3 are shown in Figure 4.1. The visible Raman spectra (Figure 4.1a) of V/θ-Al_2O_3 with a surface VO_x density lower than 0.16 V nm^{-2} are dominated by fluorescence from the θ-Al_2O_3 support. Samples with surface VO_x densities above 0.16 V nm^{-2} start to show Raman bands from VO_x species: a weak broad band centered at 915 cm^{-1}, a V=O vibration at 1023 cm^{-1} for 0.16 V, 1030 cm^{-1} for 1.2 V and 1035 cm^{-1} for 4.4 V and 8.8 V samples, and an intense band at 994 cm^{-1} characteristic of V_2O_5 for 4.4 V and above. The broad band at ~915 cm^{-1} has previously been ascribed to V—O—V stretching modes and has been used as a proof for the presence of polymerized VO_x species [5]. Here we assign it to the interface mode, V—O—Al, based on recent

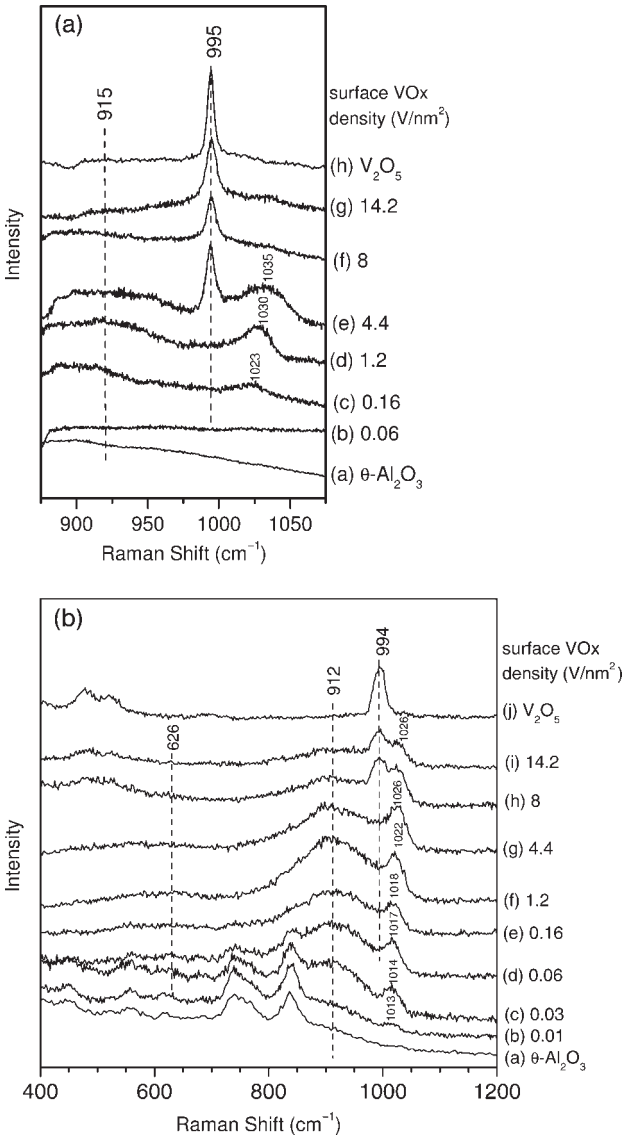

Figure 4.1 Raman spectra of dehydrated V/θ-Al_2O_3 as a function of surface VO_x density (V nm^{-2}): (a) visible ($\lambda_{excitation}$ = 488 nm); (b) UV ($\lambda_{excitation}$ = 244 nm).

density functional theory calculations of the VO_x—Al_2O_3 system [6]. This assignment is confirmed by the following UV Raman results.

UV Raman spectra of dehydrated V/θ-Al_2O_3 are shown in Figure 4.1b. It is striking to note that some Raman features due to surface VO_x species can be distinguished for V/θ-Al_2O_3 samples at extremely low surface densities, even down to

0.01 V nm^{-2}, namely a weak Raman band at 1013 cm^{-1} and a broad shoulder at around 912 cm^{-1}. Detection of these Raman features, not seen in the visible Raman spectra, result from the avoidance of fluorescence and possible enhancement by the resonance Raman effect. The broad feature centered at 912 cm^{-1} is present with medium intensity at all loadings, suggesting that this broad Raman feature cannot be exclusively assigned to V—O—V stretching and it is consistent with the theoretical assignment to V—O—Al bonds [6]. The 1013 cm^{-1} band, assigned to the V=O stretching mode of surface VO_x species, shifts gradually to higher wavenumber as the surface VO_x density increases. This band remains observable at ca 1026 cm^{-1} for a surface VO_x density of 14.2 V nm^{-2}, a result which is clearly different from the visible Raman spectra (Figure 4.1a) where the V=O band is above 1030 cm^{-1} for surface VO_x densities greater than 1.2 V nm^{-2} and disappears above monolayer loading (8 V nm^{-2}). The differences in Raman shift and in intensity versus VO_x density between visible- and UV-excited Raman spectra suggest the presence of different types of surface VO_x species on the Al_2O_3 support. At medium surface VO_x densities (0.16–4.4 V nm^{-2}), a weak broad feature appears near 625 cm^{-1}, indicating the formation of polymerized VO_x species on the surface. When the surface VO_x density is above 8 V nm^{-2}, the formation of crystalline V_2O_5 is evident from the characteristic band at 994 cm^{-1} and additional bands in the range 400–600 cm^{-1}.

The results from both UV and visible Raman measurements suggest an evolving picture of surface VO_x species on θ-Al_2O_3: V/Al_2O_3 with a surface density lower than 1.2 V nm^{-2} possesses mainly isolated VO_x in tetrahedral coordination. At surface densities higher than 1.2 V nm^{-2}, polymerized VO_x participate to a larger extent on the surface, and V_2O_5 forms at a surface VO_x density above 4.4 V nm^{-2}. This picture is further supported by our UV-Vis DRS and TPR measurements (not shown here) of V/θ-Al_2O_3 samples [49].

Comparing the UV and visible Raman spectra of V/θ-Al_2O_3 samples, two kinds of V=O band shifts can be distinguished: a shift as a function of excitation wavelength for the same sample and a shift as a function of surface VO_x density for a series of samples. The latter shift, from 1012 to 1027 cm^{-1} as the surface VO_x density increases from 0.01 to 14.2 V nm^{-2} in the case of UV-excited Raman spectra, can be ascribed to structural changes of the surface VO_x and possibly vibrational coupling between V=O oscillators. The former shift, the same sample showing V=O stretching bands at different frequencies, 8–10 cm^{-1}, in UV Raman and visible Raman spectra, indicates that UV and visible excitation detect different VO_x species present on the support. This kind of band shift can be explained in terms of the resonance enhancement effect. The UV-Vis absorption spectra of V/θ-Al_2O_3 (Figure 4.2) show significant absorption bands at both 244 and 488 nm laser wavelengths for samples with surface densities above 1.2 V nm^{-2}. This implies that the Raman spectra at both wavelengths are resonance enhanced. The longer wavelength absorption increases in intensity with vanadia loading, relative to the short wavelength absorption. This demonstrates that a mixture of surface vanadia species is present and is consistent with a picture where polymerized VO_x species are resonance enhanced under visible laser excitation while isolated and less

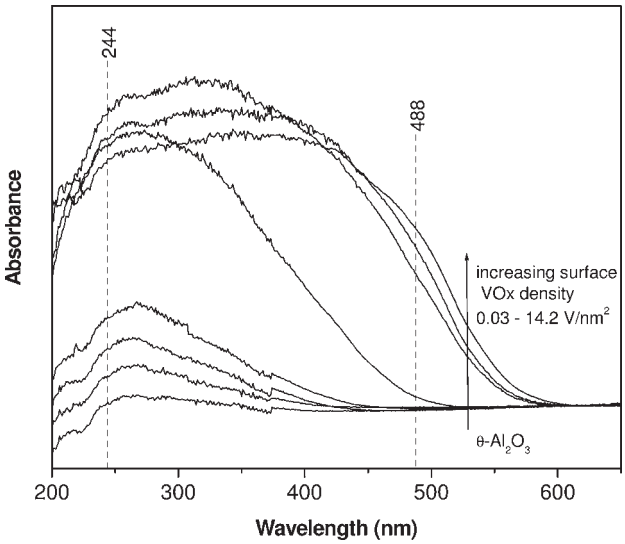

Figure 4.2 UV-Vis DRS spectra of dehydrated V/θ-Al_2O_3 as a function of surface VO_x density (V nm^{-2}).

polymerized VO_x are resonance enhanced under UV laser excitation. The selective enhancement of VO_x species with different cluster sizes is similar to the case of resonance Raman spectroscopic characterization of conjugated polyene sequences where different excitation wavelengths give different C=C stretching frequencies, thus allowing conjugated polyenes with different sequence lengths to be detected [50]. Interestingly, the higher V=O Raman shift measured under visible compared to UV excitation is consistent with this picture by reference to the measurements on single crystal model catalysts since the V=O infrared frequencies are found to increase with increasing V=O surface density [51]. Thus, it would appear that visible-excited Raman spectra are more sensitive to polymeric or cluster VO_x and UV-excited Raman spectra are more sensitive to isolated and less polymerized VO_x species.

UV and visible Raman measurements of CrO_x/θ-Al_2O_3 were also conducted to see if the selective resonance Raman detection of different surface metal oxide species is a general phenomenon (Figure 4.3). For simplicity, the comparison of the spectra features focuses on the Raman band due to Cr=O stretching at 1015 cm^{-1}. In contrast to the case of VO_x/θ-Al_2O_3, the Cr=O stretching vibration is observed at the same Raman shift in both UV and visible Raman spectra and for all the CrO_x/θ-Al_2O_3 samples. The absence of both excitation-energy-dependent shifts and coverage-dependent shifts of ν(Cr=O) leads to the assumption that the CrO_x species are homogeneously distributed, that is only one type of CrO_x species is formed on the support surface, either monochromate, dichromate or polychromate. However, the results in Figure 4.3 cannot rule out inhomogeneity in the surface CrO_x species. However, excitation-dependent shifts in the Raman band

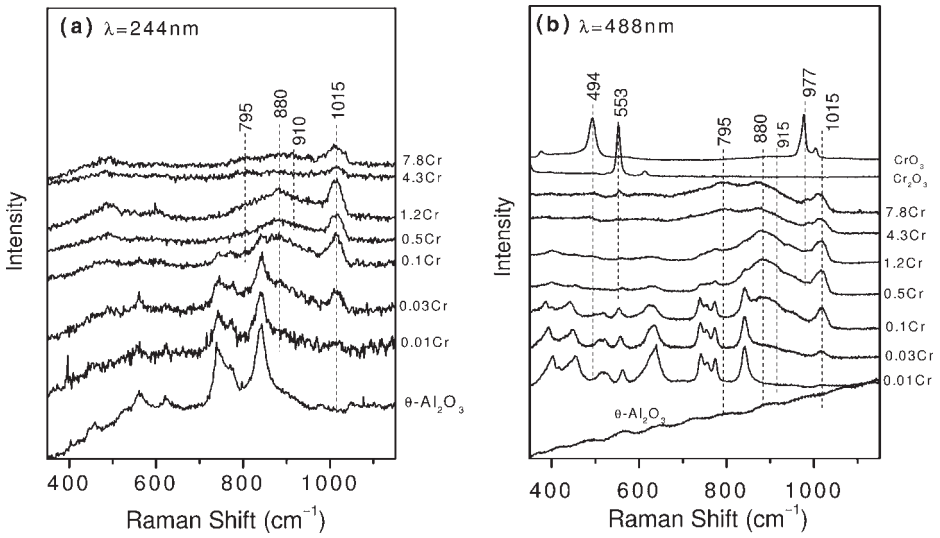

Figure 4.3 Raman spectra of dehydrated $Cr/\theta\text{-}Al_2O_3$ as a function of surface CrO_x density ($V\,nm^{-2}$): (a) UV ($\lambda_{excitation}$ = 244 nm); (b) visible ($\lambda_{excitation}$ = 488 nm).

positions from inhomogeneously distributed systems are rarely observed for any of a number of reasons, as detailed elsewhere [52]. The most important reason for most systems [52], and the likely one for $CrO_x/\theta\text{-}Al_2O_3$, is that the changes in the environment of species which lead to inhomogeneous broadening of the electronic absorption are not correlated with corresponding changes in the Cr=O vibrational frequency. If, for example, multiple CrO_x species have overlapping electronic absorptions, then the observed Raman shift will be an average over the species. Additional Raman measurements of the $CrO_x/\theta\text{-}Al_2O_3$ system using a series of excitation wavelengths could resolve this issue.

4.2.1.2 **Reduced State**

UV Raman spectra of $VO_x/\theta\text{-}Al_2O_3$ with low surface VO_x density (0.06 and 0.16 $V\,nm^{-2}$) show that the bands due to $\theta\text{-}Al_2O_3$ at 746 and 841 cm^{-1} increase relative to those of surface VO_x species with Raman bands at ca 915 and 1018 cm^{-1} after hydrogen treatment at temperatures of 673 K and above, which is an indication of the reduction of surface VO_x species. This is consistent with *in situ* UV-Vis DRS measurements from $V/\theta\text{-}Al_2O_3$, which show decreasing absorbance in the UV region upon hydrogen reduction. This results in reduced self-absorption and increased Raman intensity from $\theta\text{-}Al_2O_3$ upon hydrogen reduction of $VO_x/\theta\text{-}Al_2O_3$. A new Raman feature is observed near 880 cm^{-1} when the samples are reduced at 873 K, while the intensities of the bands due to oxidized VO_x species decrease greatly. The relative intensity change of the bands due to V=O (~1018 cm^{-1}) and V—O—Al (~915 cm^{-1}) as a function of reduction temperature shows that the intensity of the band due to V—O—Al bond decreases more rapidly than that due to

V=O. This is an indication that the V–O–Al interface bond is much easier to reduce than the V=O bond.

The hydrogen-reduction of VO_x/θ-Al_2O_3 samples with intermediate VO_x density (1.2 and 4.4 V nm^{-2}) was studied by both UV and visible Raman spectroscopy. As an example, the Raman spectra of 1.2 V samples reduced by hydrogen at different temperatures are shown in Figure 4.4. For the oxidized sample, the V=O stretching band is observed at different Raman shifts in the UV (1021 cm^{-1}) and visible (1034 cm^{-1}) excited Raman spectra. This is explained in the previous section in terms of selective resonance enhancement, monovanadate and polyvanadate species being resonance enhanced in UV Raman and visible Raman, respectively. When the 1.2 V sample was treated in hydrogen, the Raman intensity from surface VO_x species decreased at both excitation wavelengths. There is a slight and gradual red shift of the band due to V=O in the visible Raman spectra as a function of reduction temperature, from 1034 to 1023 cm^{-1}. The bands due to VO_x species totally disappear in the visible Raman spectra after hydrogen reduction at 873 K, consistent with previous visible Raman studies [26, 33–39]. However, Raman bands are still observable at 870, 910 (shoulder) and 1021 cm^{-1} in the UV Raman spectra, even after hydrogen treatment at 973 K. This apparent difference between the two excitation wavelengths suggests that the VO_x species detected by visible Raman are much easier to reduce than those detected by UV Raman, that is, polyvanadate is more easily reduced than monovanadate. Considering the structural differences between monovanadate and polyvanadate species, it is reasonable to deduce that the V–O–Al bond is more difficult to reduce than the V–O–V bond.

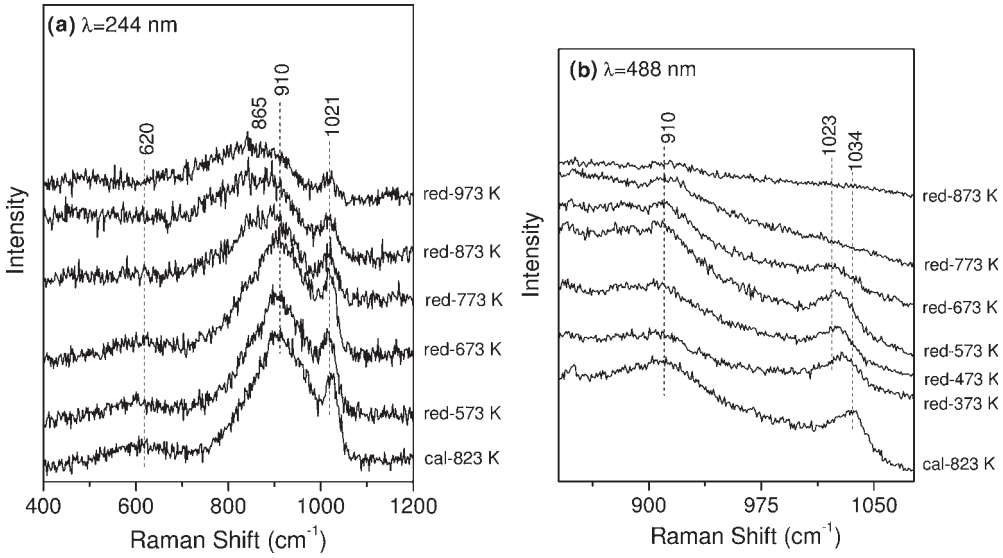

Figure 4.4 Raman spectra of 1.2 V sample reduced by hydrogen at different temperatures: (a) UV ($\lambda_{excitation}$ = 244 nm; (b) visible ($\lambda_{excitation}$ = 488 nm).

The new UV Raman band centered at 870 cm^{-1}, similar to the band observed on samples with lower vanadia loadings after high temperature hydrogen treatment, may be attributed to reduced VO_x species. This broad feature is also observed on VO_x/θ-Al_2O_3 samples with higher VO_x density (4.4, 8 and 14.2 V nm^{-2}) after hydrogen-reduction at high temperatures. However, as the size and proximity of polyvanadate species increases with loading, the VO_x/θ-Al_2O_3 samples become more easily reduced as evidenced by a more pronounced weakening of the Raman bands due to surface oxide vanadia species in both UV and visible Raman spectra after hydrogen-reduction at high temperatures. This model is also consistent with the quantitative results from H_2-TPR (not shown here) where the vanadium average oxidation state decreases with increasing surface VO_x density.

To aid the interpretation of the Raman spectra from V/θ-Al_2O_3 samples reduced by hydrogen at high temperatures, both UV and visible Raman spectra of different bulk VO_x compounds, V_2O_5, V_6O_{13}, VO_2 and V_2O_3, were measured in flowing helium at room temperature. In the UV Raman spectra, all the bulk VO_x samples produce a broad band in the range 400–600 cm^{-1}, due to V_2—O and V_3—O bridging modes. A band at 875 cm^{-1}, which can be assigned to V—O—V stretching, is observed in the spectra of all bulk VO_x except for V_2O_5. This band becomes broader following the sequence V_6O_{13}, VO_2 and V_2O_3, resulting in a feature similar to the 870 cm^{-1} band observed on V/θ-Al_2O_3 samples reduced by hydrogen at high temperatures. In the Raman shift range near 1000 cm^{-1}, where V=O stretching usually appears, the four VO_x compounds exhibit Raman bands at different wavenumbers. In the visible Raman spectral region (830–1080 cm^{-1}), Raman bands are detectable only for V_2O_5 and V_6O_{13}. Since H_2-TPR and *in situ* UV-Vis DRS of VO_x/θ-Al_2O_3 samples reduced in hydrogen indicate the presence of V^{3+}/V^{4+} species after high-temperature reduction [53], we suggest that the new UV Raman band observed from V/θ-Al_2O_3 samples centered at ca 870 cm^{-1} after high-temperature hydrogen treatment is due to reduced VO_x species, similar to V_2O_3.

UV Raman spectra after re-oxidation of reduced V/θ-Al_2O_3 samples show very similar features to those of freshly calcined samples, indicating that the reduction of V/θ-Al_2O_3 samples is reversible. However, additional visible Raman spectra of the re-oxidation process are highly desirable, as they may provide information on the redox behavior of polyvanadate species.

4.2.2 Summary

The structures of VO_x species on θ-Al_2O_3 under both oxidizing and reducing atmospheres have been investigated by multi-wavelength Raman spectroscopy together with H_2-TPR and *in situ* UV-Vis DRS techniques. The multi-wavelength Raman method enables selective identification of three different vanadia species: isolated VO_x species are resonance enhanced by UV excitation while polymerized VO_x and V_2O_5 by visible excitation. The study of reduced V/θ-Al_2O_3 samples suggests that UV Raman is more powerful than conventional visible Raman for studies of reduced metal oxide catalysts. This is mainly due to a combination of

decreased self-absorption and resonance enhancement in UV Raman. These results suggest that a complete structural characterization of supported metal oxide catalysts requires a multi-wavelength excitation approach in Raman spectroscopy.

4.3 Quantification of Surface VO_x Species on Supported Vanadia Catalysts

For supported vanadia catalysts, the distribution of different vanadia species, i.e. monovanadate, polyvanadate and V_2O_5, on the support depends upon vanadia coverage and the method of preparation. This distribution presents difficulties in the identification of the active and selective sites for catalytic reactions. Quantitative information on the speciation of surface vanadia is an important tool for understanding structure/function relationships for these catalysts. Qualitative determination of the three vanadia species is accessible by several techniques such as Raman, UV-Vis, NMR spectroscopies and others [4]. However, quantification of the individual vanadia species is more difficult because these techniques only provide information about the mixture as a whole. The previous sections on multi-wavelength Raman spectroscopic studies of V/Al_2O_3 catalysts show the possibility of selectively detecting different vanadia species via different laser excitations, which makes the quantification of the individual VO_x species possible using multi-wavelength Raman spectroscopy. Because supported vanadia has high absorbance in the UV region and sometimes in the visible region, the self-absorption effect [54] greatly affects the measured Raman intensity. Consequently, quantification of surface vanadia species requires a correction to the measured intensities to account for self-absorption. Either internal or external standards can be employed for this purpose [54–56]. The external standardization method for solid samples which absorb radiation makes use of the diffuse reflectance of the samples to correct the measured Raman intensity [54–56]. Thus, the combination of multi-wavelength Raman spectroscopy and UV-visible diffuse reflectance spectroscopy of V/Al_2O_3 samples can be applied for quantification of different vanadia species.

The measured Raman intensity ψ_∞ can be corrected using the equation [54]

$$I_c = \psi_\infty \frac{1 - R_\infty}{[R_\infty(1 + R_\infty)]} \tag{4.1}$$

where I_c is the corrected Raman intensity and R_∞ is the diffuse reflectance at the wavelength of the Raman scattered radiation. Several restrictions apply when using Equation 4.1 as outlined elsewhere [54]. Briefly, the scattering coefficient of the sample must not change among a series of sample measurements; the sample must not be too strongly absorbing; and the diffuse reflectance R_∞ must be identical at the excitation wavelength and the wavelength of the Raman bands.

Since only the UV Raman spectra (Figure 4.1) give measurable information for all V/θ-Al_2O_3 samples (0.01–14.2 V nm^{-2}), the diffuse reflectance spectra (Figure

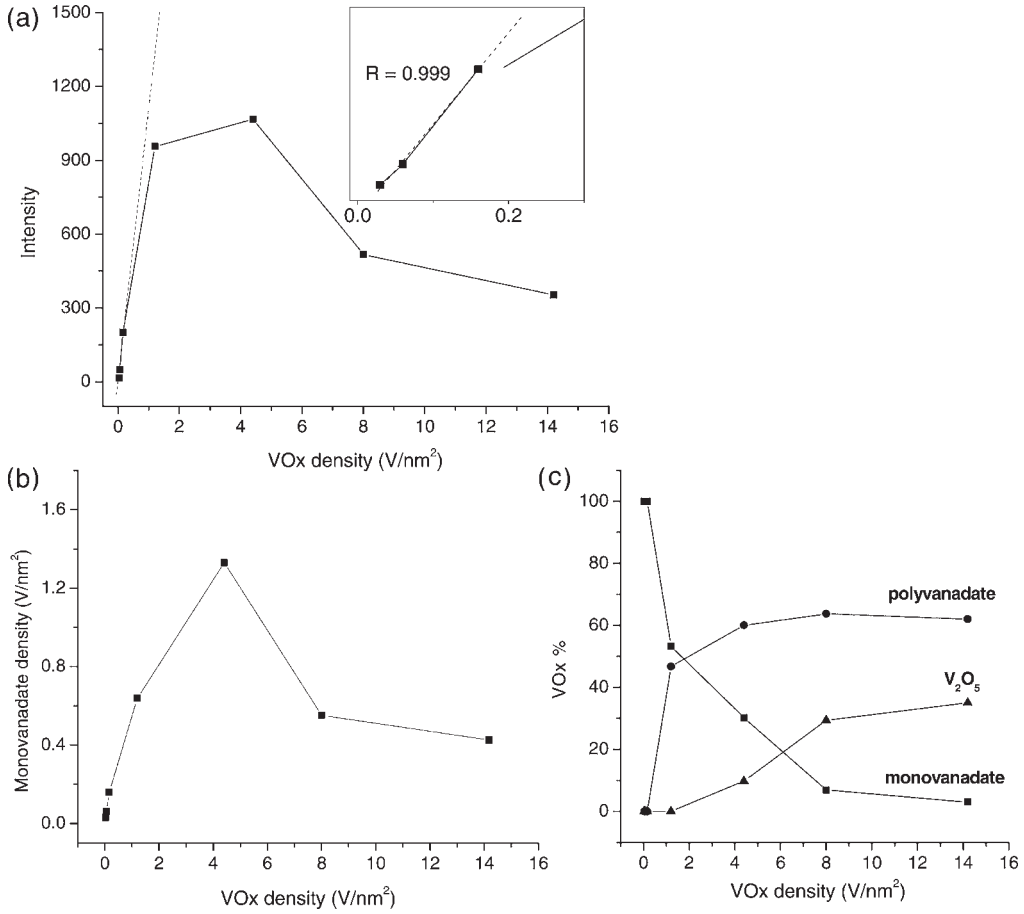

Figure 4.5 (a) Uncorrected and UV-Vis diffuse reflectance-corrected Raman band intensity of surface vanadia species (band at ~1015 cm^{-1}) as a function of surface VO_x concentration in V/θ-Al_2O_3 system. (b) Amount of monovanadate as a function of surface VO_x density. (c) Distribution of monovanadate, polyvanadate and crystalline V_2O_5 as a function of surface VO_x density.

4.2) are combined with UV Raman spectra for the correction of self-absorption. Figure 4.5a presents the corrected and uncorrected Raman intensities of VO_x (band at ca 1015 ~ 1026 cm^{-1}) as a function of surface VO_x concentration. At VO_x concentrations <1 mol% (1.2 V nm^{-2}) (see inset in Figure 4.5a), the corrected intensity is linearly proportional to the surface VO_x concentration, in agreement with the results from the internal standardization using θ-Al_2O_3 [54]. The corrected intensity versus VO_x concentration is no longer linear as the VO_x concentration increases to 1 mol% and above. This non-linearity is not due to the breakdown of the three requirements for using Equation 4.1.

The linear relationship between corrected Raman intensity and VO_x concentration in the concentration range 0.01–0.14 mol% with both internal and external standards suggests the presence of one type of surface VO_x species, namely monovanadate. This is consistent with the selective detection of monovanadate by UV Raman [25]. The linearity also suggests that the Raman cross-section of monovanadate is essentially constant as the monovanadate concentration changes more than 10-fold. Thus, the non-linear behavior at VO_x concentrations higher than 0.14 mol% is unlikely to be due to a change in the Raman cross-section of monovanadate. At VO_x concentrations of 1 mol% and above, a mixture of different VO_x species exists on the Al_2O_3 support and only a fraction of the vanadia species (monovanadate) are detected by UV Raman spectroscopy. Therefore the plot in Figure 4.5a is not expected to be linear. Under these circumstances, the plot in Figure 4.5a would be indicative only of the concentration of monovanadate species detected by UV resonance Raman spectroscopy. The amount of this species increases at low surface VO_x concentration and decreases at high VO_x concentrations as shown in Figure 4.5b.

The amounts of polyvanadate and crystalline V_2O_5 can now be obtained since the amounts of total vanadium and monovanadate are known. It is also known that the relative Raman cross-section of V_2O_5 and dispersed VO_x is about 10 for visible Raman measurements [56]. With this knowledge, the individual amounts of polyvanadate and V_2O_5 can be calculated based upon fitting visible Raman peaks from V/θ-Al_2O_3 samples [25] (assuming the amount of V_2O_5 and polyvanadate can be represented by the peak areas at 995 and ~1030 cm^{-1}, respectively). The distribution of the three VO_x species is plotted as a function of surface VO_x density as shown in Figure 4.5c. It is seen that (a) monovanadate species predominate on the surface at low vanadia loadings, (b) polyvanadate species predominate at intermediate vanadia loadings and (c) there is a mixture of monovanadate, polyvanadate and V_2O_5 on the support surface at intermediate and high vanadia loadings.

Quantification greatly aids the understanding of the catalytic contributions of different vanadia species during catalytic reactions. For example, our preliminary activity test over these supported VO_x catalysts showed that the 1.2 V/θ-Al_2O_3 sample exhibits better stability than higher loading catalysts for butane dehydrogenation in dilute feed [57]. The explanation is that the monovanadate species (ca 50% on the surface) dilute the polyvanadate species so that the two-dimensional coke species responsible for catalyst deactivation are less likely to form [40, 57].

Our quantification result clearly supports the general assumption that for supported VO_x catalysts, polyvanadates and V_2O_5 predominate on the support surface with increasing VO_x loading. However, we should point out that this method has limitations. Figure 4.6 shows two distinct UV Raman bands centered at 997 cm^{-1} and 1015 cm^{-1} for the 0.16 V/θ-Al_2O_3 sample. They are attributed to V=O stretching vibrations from two distinct vanadyl species. The relative intensities of the two bands changes as a function of excitation wavelength, indicating that there are at least two different types of isolated monovanadate species in the 0.16 V sample. This is likely due to the fact that isolated vanadate species are bonded to distinct sites on the alumina surface, and these species would be expected to possess

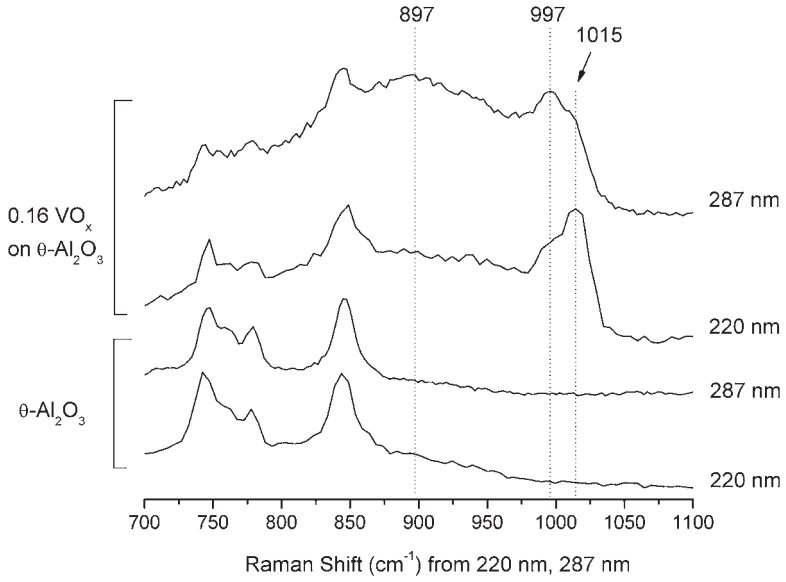

Figure 4.6 UV Raman spectra ($\lambda_{excitation}$ = 220 nm, 287 nm) of dehydrated 0.16 V sample and θ-alumina. Two distinct Raman bands at 997 cm^{-1} and 1015 cm^{-1} for the 0.16 V sample are attributed to V=O stretching vibrations from two distinct vanadyl species. A broad band at ~897 cm^{-1} can be assigned to V–O–Al stretching vibrations.

correspondingly distinct electronic absorption wavelengths. Thus, selective resonance-enhanced Raman measurements will be able to distinguish different subsets of monovanadate species using suitable excitation wavelengths. This will also be true for $V/\theta\text{-}Al_2O_3$ samples with a mixture of different VO_x structures (monovanadates, polyvanadates and V_2O_5). Therefore, it may be possible to map out VO_x species with a distribution of sizes and coordination geometries by employing as many excitation wavelengths as possible in a Raman study. Currently, it appears that the Raman measurements using 244 and 488 nm excitation represent only a subset of monovanadates and polyvanadates, respectively, and the quantification of VO_x species obtained from these two excitations is a simplified model. This two-excitation-wavelength-based quantification can be considered as the first step in the approach to a complete quantification of VO_x.

4.3.1 Summary

A combination of UV-Vis DRS and UV and visible Raman spectroscopy allow quantification of surface VO_x species in $V/\theta\text{-}Al_2O_3$ samples with different VO_x densities. It is shown that monovanadate species are the predominant species on the surface at low surface VO_x density but they decrease in fraction and quantity

as the surface VO_x density increases. Polyvanadate and crystalline V_2O_5 dominate at intermediate and high surface VO_x density. The three vanadia species co-exist on the sample even at the highest VO_x density (which is almost two monolayers in coverage). The quantitative information gained assists the determination of the specific catalytic contributions by these different vanadia species. It is also apparent that a complete quantification of surface VO_x species in a heterogeneous supported VO_x catalyst by Raman spectroscopy requires measurements using as many laser excitation wavelengths as possible.

4.4 Conclusion

This short chapter has illustrated the application of Raman spectroscopic techniques to the elucidation of structure–activity relationships in the V//θ-Al_2O_3 system. This system, in which a number of different VO_x species with differing catalytic activity exist, provides a useful case study to illustrate the power of Raman spectroscopy. Examples have been chosen that demonstrate the utility of application of the multi-wavelength method to the determination of the simultaneous presence of isolated, polymerized and V_2O_5 species. Furthermore, combination of UV-Vis DRS and UV-Vis Raman spectroscopy has been demonstrated to be very powerful in the quantification of such species, which is a key requirement in the elucidation of their respective catalytic activity. In summary, the power of multiple Raman techniques can be seen from the examples given, which go a long way towards the development of a detailed understanding of the catalytic activity of these systems. Further exciting developments in the application of Raman spectroscopy can be anticipated.

Acknowledgements

This work was financially supported by ATHENA and the Chemical Sciences, Geosciences and Biosciences Division, Office of Basic Energy Sciences, Office of Science, US Department of Energy under Grant No. DE-FG02-97ER14789. The Athena project is funded by the Engineering & Physical Sciences Research Council (EPSRC) of the UK and Johnson Matthey plc.

References

1 Bond, G.C. and Tahir, S.F. (1991) Vanadium oxide monolayer catalysts: preparation, characterization and catalytic activity. *Applied Catalysis*, **71** (1), 1–31.

2 Reddy, B.N., Reddy, B.M. and Subrahmanyam, M. (1991) Dispersion and 3-picoline ammoxidation investigation of vanadium oxide/aluminum oxide (V2O5/a-Al2O3) catalysts. *Journal of the Chemical Society, Faraday Transactions*, **87** (10), 1649–55.

3 Deo, G., Wachs, I.E. and Haber, J. (1994) Supported vanadium oxide catalysts. Molecular structural characterization and reactivity properties. *Critical Reviews in Surface Chemistry*, **4** (3 & 4), 141–87.

4 Wachs, I.E. and Weckhuysen, B.M. (1997) Structure and reactivity of surface vanadium oxide species on oxide supports. *Applied Catalysis A: General*, **157** (1–2), 67–90.

5 Banares, M.A. and Wachs, I.E. (2002) Molecular structures of supported metal oxide catalysts under different environments. *Journal of Raman Spectroscopy*, **33** (5), 359–80.

6 Weckhuysen, B.M. and Keller, D.E. (2003) Chemistry, spectroscopy and the role of supported vanadium oxides in heterogeneous catalysis. *Catalysis Today*, **78** (1–4), 25–46.

7 Went, G.T., Oyama, S.T. and Bell, A.T. (1990) Laser Raman spectroscopy of supported vanadium oxide catalysts. *Journal of Physical Chemistry*, **94** (10), 4240–6.

8 Deo, G. and Wachs, I.E. (1991) Predicting molecular structures of surface metal oxide species on oxide supports under ambient conditions. *Journal of Physical Chemistry*, **95** (15), 5889–95.

9 Vuurman, M.A. and Wachs, I.E. (1992) In situ Raman spectroscopy of alumina-supported metal oxide catalysts. *Journal of Physical Chemistry*, **96** (12), 5008–16.

10 Wachs, I.E. (1996) Raman and IR studies of surface metal oxide species on oxide supports: supported metal oxide catalysts. *Catalysis Today*, **27** (3–4), 437–55.

11 Olthof, B., Khodakov, A., Bell, A.T. and Iglesia, E. (2000) Effects of Support Composition and Pretreatment Conditions on the Structure of Vanadia Dispersed on SiO_2, Al_2O_3, TiO_2, ZrO_2, and HfO_2. *Journal of Physical Chemistry B*, **104** (7), 1516–28.

12 Argyle, M.D., Chen, K.D., Bell, A.T. and Iglesia, E. (2002) Effect of catalyst structure on oxidative dehydrogenation of ethane and propane on alumina-supported vanadia. *Journal of Catalysis*, **208** (1), 139–49.

13 Cortez, G.G. and Banares, M.A. (2002) A Raman Spectroscopy Study of Alumina-Supported Vanadium Oxide Catalyst during Propane Oxidative Dehydrogenation with Online Activity Measurement. *Journal of Catalysis*, **209** (1), 197–201.

14 Khodakov, A., Olthof, B., Bell, A.T. and Iglesia, E. (1999) Structure and catalytic properties of supported vanadium oxides: support effects on oxidative dehydrogenation reactions. *Journal of Catalysis*, **181** (2), 205–16.

15 Christodoulakis, A., Machli, M., Lemonidou, A.A. and Boghosian, S. (2004) Molecular structure and reactivity of vanadia-based catalysts for propane oxidative dehydrogenation studied by in situ Raman spectroscopy and catalytic activity measurments. *Journal of Catalysis*, **222** (2), 293–306.

16 Xiong, G., Li, C., Li, H.Y., Xin, Q. and Feng, Z.C. (2000) Direct spectroscopic evidence for vanadium species in V-MCM-41 molecular sieve characterized by UV resonance Raman spectroscopy. *Chemical Communications (Cambridge, United Kingdom)*, **8**, 677–8.

17 Chua, Y.T., Stair, P.C. and Wachs, I.E. (2001) A comparison of ultraviolet and visible raman spectra of supported metal oxide catalysts. *Journal of Physical Chemistry B*, **105** (36), 8600–6.

18 Wachs, I.E., Jehng, J.-M., Deo, G., Weckhuysen, B.M., Guliants, V.V., Benziger, J.B. and Sundaresan, S. (1997) Fundamental studies of butane oxidation over model-supported vanadium oxide

catalysts: molecular structure-reactivity relationships. *Journal of Catalysis*, **170** (1), 75–88.

19 Kanervo, J.M., Harlin, M.E., Krause, A.O.I. and Banares, M.A. (2003) Characterization of alumina-supported vanadium oxide catalysts by kinetic analysis of H2-TPR data. *Catalysis Today*, **78** (1–4) 171–80.

20 Koranne, M.M., Goodwin, J.G.Jr and Marcelin, G. (1994) Characterization of silica- and alumina-supported vanadia catalysts using temperature programmed reduction. *Journal of Catalysis*, **148** (1), 369–77.

21 Harlin, M.E., Niemi, V.M. and Krause, A.O.I. (2000) Alumina-supported vanadium oxide in the dehydrogenation of butanes. *Journal of Catalysis*, **195** (1), 67–78.

22 Harlin, M.E., Niemi, V.M., Krause, A.O.I. and Weckhuysen, B.M. (2001) Effect of Mg and Zr Modification on the activity of VOx/Al_2O_3 catalysts in the dehydrogenation of Butanes. *Journal of Catalysis*, **203** (1), 242–52.

23 Gao, X., Jehng, J.-M. and Wachs, I.E. (2002) In situ UV-vis-NIR diffuse reflectance and raman spectroscopic studies of propane oxidation over ZrO_2-supported vanadium oxide catalysts. *Journal of Catalysis*, **209** (1), 43–50.

24 Wachs, I.E., Chen, Y., Jehng, J.-M., Briand, L.E. and Tanaka, T. (2003) Molecular structure and reactivity of the Group V metal oxides. *Catalysis Today*, **78** (1–4) 13–24.

25 Gao, X., Banares, M.A. and Wachs, I.E. (1999) Ethane and n-butane oxidation over supported vanadium oxide catalysts: an in situ UV-visible diffuse reflectance spectroscopic investigation. *Journal of Catalysis*, **188** (2), 325–31.

26 Ruitenbeek, M., Van Dillen, A.J., de Groot, F.M.F., Wachs, I.E., Geus, J.W. and Koningsberger, D.C. (2000) The structure of vanadium oxide species on . gamma-alumina; an in situ X-ray absorption study during catalytic oxidation. *Topics in Catalysis*, **10** (3–4) 241–54.

27 Wachs, I.E. and Chan, S.S. (1984) In situ characterization of small vanadium oxide (V_2O_5) crystallites supported on titanium dioxide (anatase). *Applied Surface Science*, **20** (1–2), 181–5.

28 Wachs, I.E., Jehng, J.-M., Deo, G., Weckhuysen, B.M., Guliants, V.V. and Benziger, J.B. (1996) In situ Raman spectroscopy studies of bulk and surface metal oxide phases during oxidation reactions. *Catalysis Today*, **32** (1–4, Proceedings of the 5th European Workshop Meeting on Selective Oxidation by Heterogeneous Catalysis, 1995), 47–55.

29 Sun, Q., Jehng, J.-M., Hu, H. Herman, R.G., Wachs, I.E. and Klier, K. (1997) In situ Raman spectroscopy during the partial oxidation of methane to formaldehyde over supported vanadium oxide catalysts. *Journal of Catalysis*, **165** (1), 91–101.

30 Mul, G., Banares, M.A., Cortez, G. Garcia, van der Linden, B., Khatib, S.J. and Moulijn, J.A. (2003) MultiTRACK and operando Raman-GC study of oxidative dehydrogenation of propane over alumina-supported vanadium oxide catalysts. *Physical Chemistry Chemical Physics*, **5** (20), 4378–83.

31 Banares, M.A., Cardoso, J.H., Agullo-Rueda, F., Correa-Bueno, J.M. and Fierro, J.L.G. (2000) Dynamic states of V-oxide species: reducibility and performance for methane oxidation on V2O5/SiO2 catalysts as a function of coverage. *Catalysis Letters*, **64** (2–4) 191–6.

32 Christodoulakis, A., Machli, M., Lemonidou, A.A. and Boghosian, S. (2004) Molecular structure and reactivity of vanadia-based catalysts for propane oxidative dehydrogenation studied by in situ Raman spectroscopy and catalytic activity measurements. *Journal of Catalysis*, **222** (2), 293–306.

33 Argyle, M.D., Chen, K.D., Iglesia, E. and Bell, A.T. (2005) In situ UV-visible spectroscopic measurements of kinetic parameters and active sites for catalytic oxidation of alkanes on vanadium oxides. *Journal of Physical Chemistry B*, **109** (6), 2414–20.

34 Sullivan, V.S., Jackson, S.D. and Stair, P.C. (2005) In situ ultraviolet Raman spectroscopy of the reduction of chromia on alumina catalysts. *Journal of Physical Chemistry B*, **109** (1), 352–6.

35 Li, C. (2003) Identifying the isolated transition metal ions/oxides in molecular sieves and on oxide supports by UV

resonance Raman spectroscopy. *Journal of Catalysis*, **216** (1–2), 203–12.
36 Gao, X. and Wachs, I.E. (2000) Investigation of surface structures of supported vanadium oxide catalysts by UV-vis-NIR diffuse reflectance spectroscopy. *Journal of Physical Chemistry B*, **104** (6), 1261–8.
37 Weckhuysen, B.M., De Ridder, L.M. and Schoonheydt, R.A. (1993) A quantitative diffuse reflectance spectroscopy study of supported chromium catalysts. *Journal of Physical Chemistry*, **97** (18), 4756–63.
38 Li, C. and Stair, P.C. (1996) An advance in Raman studies of catalysts: ultraviolet resonance Raman spectroscopy. *Studies in Surface Science and Catalysis*, **101** (11th International Congress on Catalysis – 40th Anniversary, 1996, Pt B), 881–90.
39 Li, C. and Stair, P.C. (1997) Ultraviolet Raman spectroscopy characterization of coke formation in zeolites. *Catalysis Today*, **33** (1–3), 353–60.
40 Chua, Y.T. and Stair, P.C. (2000) A novel fluidized bed technique for measuring UV Raman spectra of catalysts and adsorbates. *Journal of Catalysis*, **196** (1), 66–72.
41 Xie, S., Iglesia, E. and Bell, A.T. (2000) Effects of hydration and dehydration on the structure of silica-supported vanadia species. *Langmuir*, **16** (18), 7162–7.
42 Xie, S., Iglesia, E. and Bell, A.T. (2001) Effects of temperature on the Raman spectra and dispersed oxides. *Journal of Physical Chemistry B*, **105** (22), 5144–52.
43 Dupuis, A.C., Haija, M. Abu, Richter, B., Kuhlenbeck, H. and Freund, H.J. (2003) V_2O_3(0 0 0 1) on Au(1 1 1) and W(1 1 0): growth, termination and electronic structure. *Surface Science*, **539** (1–3), 99–112.
44 Xiong, G., Li, C., Feng, Z.C., Ying, P.L., Xin, Q. and Liu, J.K. (1999) Surface coordination structure of molybdate with extremely low loading on gamma-alumina characterized by UV resonance Raman spectroscopy. *Journal of Catalysis*, **186** (1), 234–7.
45 Xiong, G., Feng, Z., Li, J., Yang, Q., Ying, P., Xin, Q. and Li, C. (2000) UV resonance Raman spectroscopic studies on the genesis of highly dispersed surface molybdate species on .gamma.-alumina. *The Journal of Physical Chemistry B*, **104** (15), 3581–8.
46 Stair, P.C. and Li, C. (1997) Ultraviolet Raman spectroscopy of catalysts and other solids. *Journal of Vacuum Science and Technology. A, Vacuum, Surfaces, and Films*, **15** (3, Pt 2), 1679–84.
47 Tian, H., Ross, E.I. and Wachs, I.E. (2006) Quantitative determination of the speciation of surface vanadium oxides and their catalytic activity. *Journal of Physical Chemistry B*, **110** (19), 9593–600.
48 Catana, G., Rao, R.R., Weckhuysen, B.M., Van Der Voort, P., Vansant, E. and Schoonheydt, R.A. (1998) Supported vanadium oxide catalysts: quantitative spectroscopy, preferential adsorption of V4+/5+;, and Al_2O_3 coating of zeolite Y. *Journal of Physical Chemistry B*, **102** (41), 8005–12.
49 Wu, Z., Kim, H.-S., Stair, P.C., Rugumini, S. and Jackson, S.D. (2005) On the structure of vanadium oxide supported on aluminas: UV and visible Raman spectroscopy, UV-visible diffuse reflectance spectroscopy, and temperature-programmed reduction studies. *Journal of Physical Chemistry*, **109**, 2793–800.
50 Gerrard, D.L. and Maddams, W.F. (1981) Resonance Raman spectrum of degraded poly(vinyl chloride). 3. Background studies. *Macromolecules*, **14** (5), 1356–62.
51 Magg, N., Giorgi, J.B., Schroeder, T., Baeumer, M. and Freund, H.-J. (2002) Model catalyst studies on vanadia particles deposited onto a thin-film alumina support. 1. structural characterization. *Journal of Physical Chemistry B*, **106** (34), 8756–61.
52 Yamaguchi, T., Kimura, Y. and Hirota, N. (1998) Solvation state selective excitation in resonance Raman spectroscopy. II. Theoretical calculation. *Journal of Chemical Physics*, **109** (20), 9084–95.
53 Wu, Z., Stair, P.C., Rugmini, S. and Jackson, S.D. (2007) Raman spectroscopic study of V/θ-Al_2O_3 catalysts: quantification of surface vanadia species and their structure reduced by hydrogen. *Journal of Physical Chemistry C*, (in press).
54 Cavani, F., Cortelli, C., Frattini, A., Panzacchi, B., Ravaglia, V., Trifiro, F., Fumagalli, C., Leanza, R. and Mazzoni, G. (2005) A new approach to the charac-

terization of V species in doped-V/Ti/O catalysts by means of TPR and TPO measurements: a study of the effect of promoters in the oxidation of o-xylene. *Studies in Surface Science and Catalysis*, **155**, 153–65.

55 Magg, N., Immaraporn, B., Giorgi, J.B., Schroeder, T., Baumer, M., Dobler, J., Wu, Z., Kondratenko, E., Cherian, M., Baerns, M., Stair, P.C., Sauer, J. and Freund, H.-J. (2004) Vibrational spectra of alumina- and silica-supported vanadia revisited: An experimental and theoretical model catalyst study. *Journal of Catalysis*, **226** (1), 88–100.

56 Weckhuysen, B.M., Verberckmoes, A.A., Debaere, J., Ooms, K., Langhans, I. and Schoonheydt, R.A. (2000) In situ UV-Vis diffuse reflectance spectroscopy–on line activity measurements of supported chromium oxide catalysts: relating isobutane dehydrogenation activity with Cr-speciation via experimental design. *Journal of Molecular Catalysis A: Chemical*, **151** (1–2), 115–31.

57 Wu, Z. and Stair, P.C. (2006) UV Raman spectroscopic studies of V/θ-Al_2O_3 catalysts in butane dehydrogenation. *Journal of Catalysis*, **237** (2), 220–9.

5
Solid-State NMR of Oxidation Catalysts

James McGregor

5.1
Introduction

5.1.1
Oxides in Catalysis

Metal oxide materials are employed extensively both as catalysts and catalyst supports for a wide variety of reactions [1–4]. Industrially relevant processes in which bulk oxides act as the catalyst include the production of sulfuric acid from SO_2 over mixed potassium/vanadium oxides, the oxidation of butane to maleic anhydride over vanadium-phosphorus oxides and the production of synthesis gas from methane and steam over rare earth pyrochlores. Such reactions exploit the redox properties of oxides, while their acid–base character is employed in transformations such as alkane isomerization and catalytic cracking. Aluminum oxide (alumina) is an effective catalyst for double-bond isomerization, although it is perhaps more widely employed as a catalyst support. A wide variety of metal oxides, including Al_2O_3, SiO_2, TiO_2, Ga_2O_3, SnO_2 and ZrO_2 are employed to support and disperse the active metal phase in a huge number of catalysts. Such materials have applications in many areas including hydrogenation, dehydrogenation and oxidation reactions. Frequently, the benefits provided by supported catalysts are combined with the activity of metal oxides. For instance, vanadium oxide supported on alumina is widely employed as a catalyst in the oxidative dehydrogenation of light alkanes [5–7].

5.1.2
Studying Metal Oxide Catalysts

Owing to the importance of metal oxides in catalysis their structure is widely studied. The aim of such work is to establish structure–activity relationships, whereby the structural parameters of the materials responsible for their activity, and their mode of action, are identified. Industrial catalysts, however, are often highly complex materials and identifying such relationships is not a simple task.

Metal Oxide Catalysis. Edited by S. David Jackson and Justin S. J. Hargreaves

ISBN: 978-3-527-31815-5

Furthermore, both bulk and surface properties of the materials can play important roles. For instance the oxidation of alkanes over vanadium-based oxides is believed to proceed via a Mars–van Krevelen mechanism [8, 9] with lattice (bulk) oxygen being the active oxygen species. In metal oxide-based cracking catalysts, however, activity is directed by the surface acidity of the material.

There are, therefore, a number of distinct structural characteristics which must be identified in order to fully understand the action of oxide catalysts. Bulk properties of interest include the identification of distinct crystallographic phases present in the catalyst; the local environment of the nuclei in either crystalline phases or amorphous materials; and the redox properties of the catalyst. Surface properties impacting on catalytic activity include the local environment of nuclei at the surface; acid–base behavior; the number and concentration of acid sites, including hydroxyl groups and the nature of these acid sites.

Solid-state NMR is perhaps unique in its ability to probe each of these characteristics. In particular, its sensitivity to local geometry and coordination environments provides advantages over many more traditional characterization methods. However, no single NMR experiment can furnish the investigator with data in each and all of these areas. A number of distinct, innovative, approaches have been developed to probe different structural features. A number of these are outlined below.

In addition to providing information on the structural characteristics of catalysts, NMR is also widely employed in the study of catalytic processes. Through studying the interaction of reactant and product molecules with the catalyst surface, insights can be gained into the mechanism of the reactions occurring. Both *in situ* and *ex situ* methods have been used to great effect in this area. Such studies are outside the scope of this chapter. However, excellent reviews in this area have been prepared by a number of authors [10–15], while the application of NMR imaging to catalysts and catalytic processes is discussed by Gladden and coworkers [16].

This chapter focuses on the application of solid-state NMR techniques for the characterization of oxidation catalysts. Initially, a brief introduction to these techniques is provided (Section 5.2), within which methods suitable for the study of both bulk structure (Section 5.2.1) and surface characteristics (Section 5.2.2), are described. Examples of the application of these techniques are then provided in Section 5.3, for bulk oxides, and Section 5.4, for surface properties. Finally, Section 5.5 provides an outlook as to future directions in this area.

5.2 NMR Techniques

Solid-state NMR has become a fundamental part of the toolkit to characterize catalysts and other solid materials. It is now routine to employ one of the many NMR techniques available to extract information about both the surface properties and the bulk properties of catalysts. Additional information on redox properties and

metal oxidation states – key properties for metal oxides and oxidation catalysts – can also be elucidated.

The principal difference between the NMR spectra of liquid samples and those acquired in the solid state is that linewidths of solid samples are very much broader than those for liquids. This difference arises because, in liquids, molecular tumbling averages anisotropic interactions and therefore removes them from the spectrum. To be in a position to overcome this problem it is necessary to understand the properties that give rise to an NMR spectrum.

The key properties of nuclei that allow them to be probed by NMR are nuclear magnetism and nuclear spin. Quantum mechanics dictates that the angular momentum of any system is quantized and can take only the values:

$$\frac{h}{2\pi}\sqrt{S(S+1)} \tag{5.1}$$

As the spin quantum number, S, can take only integer or half-integer values, nuclear spin can only take either integer, or half-integer values. Only when nuclear spin is greater than zero does a nucleus have a magnetic moment (μ). It is the magnetic moment which is manipulated in NMR spectroscopy, and hence only nuclei with a spin >0 can be investigated by NMR. Table 5.1 shows the nuclear spin of a number of nuclei commonly probed in solid-state NMR spectroscopy.

The relationship between the magnetic moment and angular momentum, **P**, is given by:

$$\mu = \gamma \times \mathbf{P} \tag{5.2}$$

where γ is the gyromagnetic ratio. ^{1}H has a nuclear spin $I = 1/2$. Quadrupolar nuclei, that is, those with $I > 1/2$, such as ^{51}V ($I = 7/2$) or ^{27}Al ($I = 5/2$), possess a non-spherical charge distribution that can couple to electric-field gradients present in most solid-state materials. This can have a large effect on the observed spectrum and leads to, for example, quadrupolar broadening of peaks, hindering spectral interpretation.

In the presence of a magnetic field a nucleus with $I > 0$ experiences a number of interactions. These interactions may each be expressed as a Hamiltonian with the overall effect being expressed as:

$$H = H_Z + H_D + H_{CS} + H_J + H_Q \tag{5.3}$$

where H_Z, H_D, H_{CS}, H_J and H_Q correspond to the Zeeman, dipolar, chemical shift, indirect (J-) coupled and quadrupolar interactions.

The Zeeman interaction is the lifting of the degeneracy of the energy levels in a nucleus by the application of a magnetic field, B_0. This results in the development of $2I + 1$ energy levels as shown in Figure 5.1. Nuclear spins exhibit a dipole moment which interacts with that of other nuclei, known as dipolar coupling, D.

Table 5.1 Nuclear spin and other properties of NMR active nuclei commonly found in oxidation catalysts.

Nucleus	Spin	Resonant frequency (MHz)	Natural abundance (%)	Sensitivity wrt ^{1}H	Quadrupole moment (10^{-28} m^2 A)
^{1}H	$\frac{1}{2}$	200.106 73	100	1	0
^{2}H	1	30.7176	<0.1	<0.000 01	0.0028
^{11}B	$\frac{3}{2}$	64.2020	80.3	0.133	0.04
^{13}C	$\frac{1}{2}$	50.331 538	1.1	0.000 18	0
^{14}N	1	14.455 32	99.6	0.001	0.01
^{15}N	$\frac{1}{2}$	20.276 74	0.3	<0.000 01	0
^{17}O	$\frac{5}{2}$	27.1284	<0.1	0.000 01	−0.026
^{19}F	$\frac{1}{2}$	188.2543	100	0.0834	0
^{23}Na	$\frac{3}{2}$	52.9314	100	0.092	0.14
^{27}Al	$\frac{5}{2}$	52.1418	100	0.210	0.15
^{29}Si	$\frac{1}{2}$	39.7342	4.7	0.0004	0
^{31}P	$\frac{1}{2}$	81.0045	100	0.066	0
^{43}Ca	$\frac{7}{2}$	13.463 62	0.15	0.000 01	−0.049
^{50}V	6	19.951 50	0.3	0.017	0.209
^{51}V	$\frac{7}{2}$	52.593	99.7	0.381	−0.05
^{69}Ga	$\frac{3}{2}$	48.034	60.4	0.042	0.19
^{71}Ga	$\frac{3}{2}$	61.0248	39.6	0.056	0.12
^{85}Rb	$\frac{5}{2}$	19.320 76	72.2	0.0073	0.26
^{87}Rb	$\frac{3}{2}$	65.4757	27.9	0.049	0.12
^{89}Y	$\frac{1}{2}$	9.803 73	100	0.000 12	0
^{95}Mo	$\frac{5}{2}$	13.0378	15.7	0.0005	0.011
^{97}Mo	$\frac{5}{2}$	1.3104	9.46	0.0003	0.013
^{115}Sn	$\frac{1}{2}$	65.7624	0.4	0.000 12	0
^{117}Sn	$\frac{1}{2}$	71.2896	7.6	0.0034	0
^{129}Xe	$\frac{1}{2}$	55.3519	26.4	0.0056	0
^{131}Xe	$\frac{3}{2}$	16.408 17	21.2	0.0006	−0.12
^{133}Cs	$\frac{7}{2}$	26.248 04	100	0.047	−0.003
^{138}La	5	26.400 37	<0.1	<0.000 01	0.51
^{139}La	$\frac{7}{2}$	28.267 68	99.9	0.059	0.22

The extent of this is dependent upon factors including the species involved and the internuclear distance between them. In a strong magnetic field, the dipolar coupling is dependent upon the orientation of the internuclear vector with the external magnetic field such that:

$$D \propto 3\cos^2\theta - 1 \tag{5.4}$$

The chemical shift interaction results in a shift in the basic resonance frequency of the nucleus being examined and arises from the concurrent interaction of

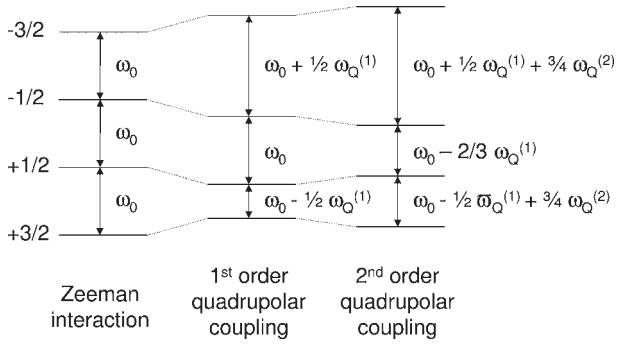

Figure 5.1 The effect of quadrupole interactions on an $I = 3/2$ nucleus in a magnetic field. The Zeeman interaction splits the levels by an equal amount, ω_0 (the Larmor frequency in frequency units). The central +1/2 to −1/2 transition is unaffected by first order coupling $\omega_Q^{(1)}$; however, second order coupling, $\omega_Q^{(2)}$, affects all transitions.

the nucleus with the orbital moment of the surrounding electrons, and of these electrons with B_0, the static field. Nuclei rarely possess spherically symmetric electron distributions and as a result there is a dependence of the chemical shift on molecular orientation, referred to as chemical shift anisotropy (CSA). Powder samples exhibit a broad (static) NMR signal, the boundaries of which represent the molecular orientations with the smallest and largest effect on chemical shift.

Indirect (or J-) coupling is the coupling of spins to each other through chemical bonds. For a pair of spins, *i* and *j*, the Hamiltonian of the spin-spin coupling is:

$$H_J = \pi \times J \times 2\mathbf{I}_i \cdot \mathbf{I}_j \tag{5.5}$$

where J is the coupling constant.

The final nuclear spin interaction is quadrupolar coupling. Quadrupolar nuclei are those with $I > 1/2$. For $I > 1$ only ^{10}B ($I = 3$), ^{50}V ($I = 6$) and ^{177}Lu ($I = 7$) have integral spin. All remaining nuclei, including catalytically relevant nuclei such as ^{51}V ($I = 7/2$) and ^{27}Al ($I = 5/2$), have half-integer spins. As stated above, the non-spherical charge distribution of quadrupolar nuclei leads to coupling with electric field gradients in solid-state materials. This interaction is described by:

$$H_Q = \mathbf{I}_i \cdot \mathbf{Q} \cdot \mathbf{I}_i \tag{5.6}$$

where $\mathbf{Q}$ is the quadrupole moment of spin *i*. Figure 5.1 shows the effect of quadrupolar interactions on a quadrupolar nucleus. For simplicity a nucleus of spin = 3/2 has been shown although this can be extended to higher spin nuclei.

The resonance frequency of the central transition (+1/2 → −1/2) is unchanged by the first-order quadrupolar Hamiltonian. Other (satellite) transitions are, however, shifted by an amount proportional to the first-order quadrupolar coupling constant $\omega_Q^{(1)}$. The result of this is to substantially broaden resonances from

the satellite transitions. Second-order quadrupolar coupling does have an effect on the central transition, broadening it and thus causing the linewidth to increase. As a result, linewidths from quadrupolar nuclei are greater than those from $I = 1/2$ nuclei such as ^{1}H. One of the effects of second-order quadrupolar coupling is to produce an irremovable isotropic quadrupolar shift. In liquids, rapid molecular orientation eliminates the effects of this shift.

There are therefore a wide number of interactions that influence NMR-active nuclei, giving rise to potentially very complex spectra from which it can be difficult to extract the parameters of interest, particularly in the case of complex materials such as catalysts. The ever increasing development of instrumentation, however, making, for instance, higher magnetic fields or higher spinning speeds (where appropriate) accessible, has made possible the development of many advanced NMR techniques. These techniques, applied correctly, allow a wealth of information to be extracted from NMR spectra. The approach taken can be to remove interactions which complicate spectra, such as line broadening in the case of magic angle spinning (MAS) (Section 5.2.1.1). Alternatively, it may be desirable to selectively probe otherwise unwanted interactions. Off-resonance nutation NMR (Section 5.2.1.4), for instance, reveals the structural information present in the quadrupole interaction, while double resonance techniques (Section 5.2.2.1) re-introduce dipolar couplings, removed under magic angle spinning. Through such approaches it is possible to extract a wide variety of information, even from structurally complex oxidation catalysts. The following sections outline techniques that are relevant in this area.

5.2.1 Bulk Structure of Catalysts

Spectroscopic approaches to the study of oxidation catalysts focus on two main areas – the characterization of the bulk structure of the material and the identification of distinct surface environments. The bulk structure and, where appropriate, phase of catalytic materials is of key importance in dictating their activity, particularly in processes involving redox mechanisms. Solid-state NMR techniques can prove particularly advantageous in this area. For instance, unlike X-ray diffraction, NMR can probe both crystalline and amorphous structures. However, as discussed above, achieving high-resolution spectra in the solid-state is complicated by the numerous interactions giving rise to line broadening effects, complicating spectral interpretation. The following sections outline experimental approaches to overcome these challenges, with a focus on those techniques that can be applied to metal oxide catalysts.

5.2.1.1 Magic Angle Spinning

MAS is the most common technique employed in solid-state NMR to remove line broadening. It involves fast mechanical sample rotation about an axis inclined at 54°44′ (the value where $3\cos^2\theta - 1 = 0$, Equation 5.4) to the direction of the external magnetic field. It can remove line broadening from dipolar interactions (averaged

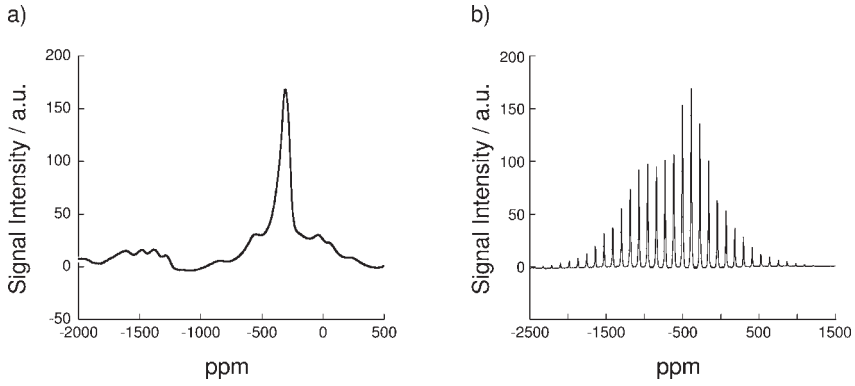

Figure 5.2 (a) Static and (b) MAS NMR spectra of V_2O_5. Spinning rate (for MAS) = 14 kHz. B_0 = 9.40 T.

to zero), chemical shift anisotropy (averaged to a non-zero value) and quadrupolar interaction to first order, and reduce quadrupolar interaction to second order by a factor of four.

MAS NMR mimics the rapid time-averaged tumbling molecular motion that occurs in liquid samples. The overall result is that the signal becomes much narrower and the isotropic peaks can be individually observed. In practice, MAS is achieved by loading the sample into a rotor that is axially symmetric about its axis of rotation. The sample is then spun, via an air turbine mechanism, at the magic angle to the applied magnetic field. MAS NMR is discussed in detail in a number of references, for example [17, 18].

Applications of solid-state MAS NMR, discussed in the forthcoming sections, include the measurement of ^{1}H chemical shifts, allowing distinct Brønsted acid sites to be identified and differentiated; the study of different Al coordination environments in aluminas by ^{27}Al MAS NMR; and the characterization of vanadium sites in vanadium oxide catalysts by ^{51}V MAS NMR. An example of the effect of MAS, as compared to static NMR measurements, is shown in Figure 5.2 for V_2O_5. Both ^{51}V and ^{27}Al are quadrupolar nuclei, hence anisotropic effects are not removed through MAS alone. Other techniques may therefore be necessary to achieve high-resolution spectra, particularly for non-crystalline samples.

5.2.1.2 **Multiple Quantum Magic Angle Spinning**

In order to remove the anisotropic effects of quadrupolar interactions which can obscure MAS spectra other techniques such as Double Rotation (DOR) [18, 19], Dynamic Angle Spinning (DAS) [18] or Multiple Quantum Magic Angle Spinning (MQMAS) have to be employed. Of these the most simple to apply practically is MQMAS, which can be conducted on a standard MAS-equipped NMR spectrometer. A number of texts and review papers discuss MQMAS in significant technical detail [20, 21].

MQMAS was first proposed in 1995 by Harwood and Frydman [22, 23]. The aim of the technique is to refocus the second-order quadrupole effects, which otherwise

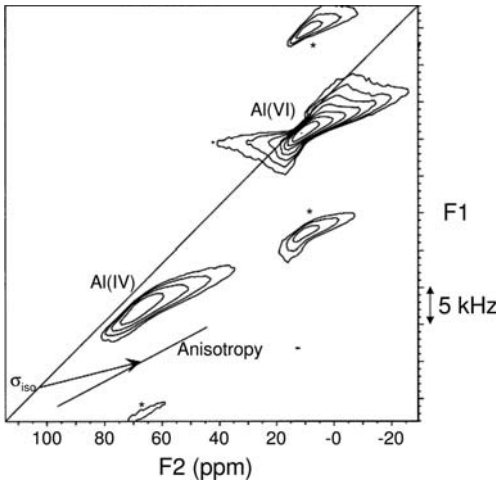

Figure 5.3 ^{27}Al 3Q-MAS spectrum of γ-Al_2O_3. Both tetrahedral, Al(IV), and octahedral, Al(VI), environments are detected. Spinning sidebands are marked with an asterisk. Adapted from ref. [24]; reprinted with permission from the American Chemical Society.

broaden the observed resonance [22]. This involves the correlation of single and odd-integer multiple quantum coherences in a two-dimensional NMR experiment while spinning at the magic angle. To observe this, it is necessary to convert the multiple quantum coherence to a single quantum coherence by inserting pulses or delays into the applied pulse sequence.

The result of the MQMAS experiment is to generate a two-dimensional spectrum consisting of a number of distinct features, as illustrated in Figure 5.3. Along one axis the isotropic chemical shifts, and hence the crystallographic inequivalent nuclei, are mapped out, while along the other quadrupole-induced shifts are mapped out. Figure 5.3 shows a triple quantum spectrum of γ-Al_2O_3 acquired by Kraus and coworkers [24]. Aluminum in tetrahedral coordination environments is denoted Al(IV), while those nuclei that are octahedrally coordinated are denoted Al(VI). That the signals curve away from the isotropic chemical shift axis at low parts per million (ppm) values indicates that the resonances experience a distribution in both quadrupolar and chemical shift interactions.

5.2.1.3 **Satellite Transition Magic Angle Spinning**

Satellite Transition MAS (SATRAS or STMAS), developed by Gan in 2000 [25], is an alternative approach to MQMAS for the acquisition of high-resolution NMR spectra of quadrupolar nuclei. The principal advantage of SATRAS over MQMAS is that it is not dependent upon an efficient transfer of multiple-quantum coherences. Like MQMAS, SATRAS is a 2D experiment performed under MAS conditions. The technique involves exciting the satellite transitions in the spin manifold of quadrupolar nuclei using short radio frequency (rf) pulses. The second-order

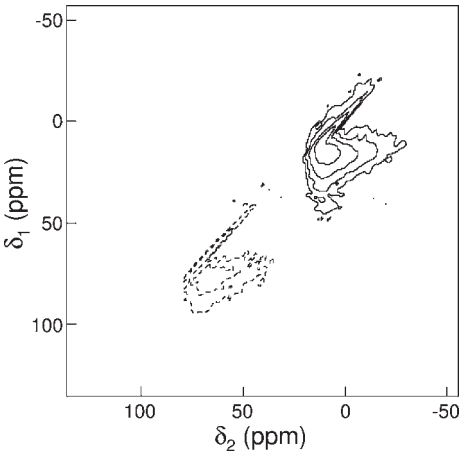

Figure 5.4 ^{27}Al 2D-SATRAS NMR of γ-Al_2O_3. The MAS rate was 30 kHz. Contour levels are shown at 8, 16, 32, and 64% of the maximum intensity. Adapted from ref. [26]; reprinted with permission from Elsevier.

quadrupolar broadenings of these satellite and the central transitions differ only by a scaling factor. As a result, a high-resolution spectrum can be obtained through a correlation of the single-quantum satellite and central transitions. This is achieved through a two-pulse sequence where the first pulse excites satellite transitions and the second pulse transfers coherence to the central transition. Since its development, SATRAS has been applied to a range of catalytically relevant systems [26–29]. Figure 5.4 shows a SATRAS spectrum of γ-Al_2O_3 acquired by Ashbrook and Wimperis [26]. Signals at ~8 and 65 ppm correspond to aluminum in octahedral and tetrahedral coordination environments respectively. The broadening of the resonances is due to both quadrupolar and isotropic parameters, indicating the amorphous nature of the material.

5.2.1.4 **Off-Resonance Nutation NMR**

Techniques such as MQMAS aim to enhance spectral resolution through averaging quadrupolar contributions to spectra. However, the quadrupole interaction itself can be a source of valuable information. This information is, however, often difficult to extract from static or MAS spectra, owing to the poor spectral resolution resulting from a distribution of chemical shifts, residual dipolar broadening or quadrupolar interactions. Off-resonance nutation NMR, a technique developed by Samosan and Lippmaa [30, 31], aims to overcome these problems. Nutation NMR describes the behavior of the spin system in the rotating frame during rf irradiation whereby the influence of the chemical shifts is dramatically reduced. Off-resonance nutation is a variant on this where the behavior of the spin system is instead monitored in the effective field, thereby increasing the upper limit of accessible quadrupolar coupling values. A comprehensive review of both theoretical and practical aspects of off-resonance nutation NMR is provided by Kentgens [32].

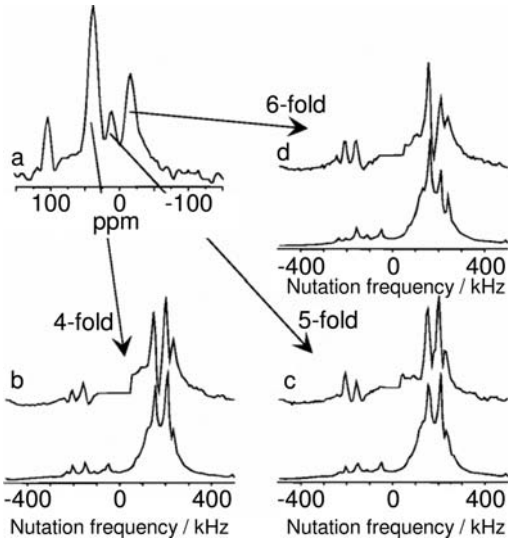

Figure 5.5 (a) ^{27}Al MAS spectrum of amorphous $AlPO_4$. Resonances are Al(IV) (42 ppm), Al(V) (12 ppm), and Al(VI) (−11 ppm). The peak at 105 ppm is due to an Al impurity in the Si_3N_4 rotor. For every coordination the experimental (top) and simulated (bottom trace) off-resonance nutation spectrum is given: (b) fourfold coordination, (c) fivefold coordination, (d) sixfold coordination. Adapted from ref. [24]; reprinted with permission from the American Chemical Society.

Catalytically relevant applications of this technique are focused around the study of ^{27}Al-containing systems [24, 32]. Figure 5.5 shows a single-pulse MAS ^{27}Al spectrum and the experimental and simulated off-resonance nutation spectra for each individual coordination environment in $AlPO_4$, a widely used catalyst support [24]. From these spectra the quadrupolar coupling constants were determined to be 3.4, 3.1 and 2.7 MHz for 4-, 5- and 6-coordinated Al sites respectively. While off-resonance nutation NMR lacks the resolution of MQMAS in discriminating overlapping sites, it has proved itself more reliable in detecting all of the distinct coordination environments present in a sample [32].

5.2.1.5 **Spin-Echo Mapping**

While the techniques described above are widely applied in the study of metal oxide catalysts, they are not necessary suitable for systems that contain paramagnetic nuclei. Paramagnetic nuclei, as discussed in Section 5.3.1.2, are not observable by conventional NMR techniques and furthermore can increase the linewidths, sometimes to beyond observable limits, of neighboring nuclei. This poses a problem when studying catalytic metal oxides that contain paramagnetic centers. Vanadium phosphorus oxides (VPO), for instance, contain paramagnetic V^{4+}.

Spin-echo mapping allows the indirect observation of paramagnetic centers by discerning their effect on neighboring nuclei. The technique was developed

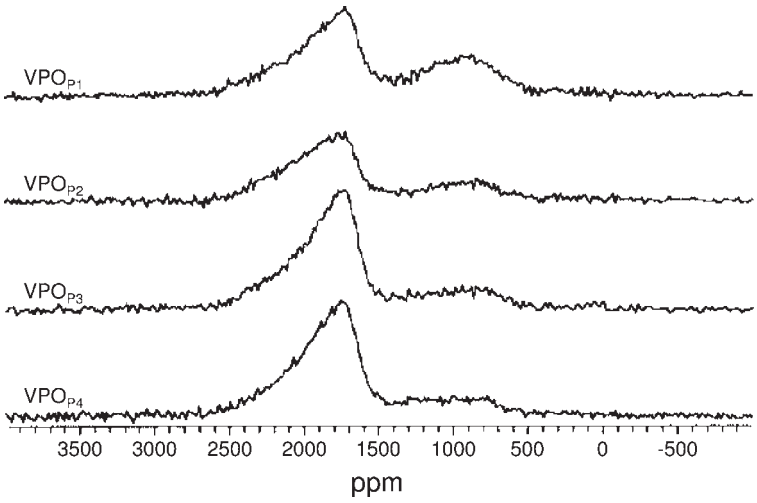

Figure 5.6 ^{31}P NMR spin-echo mapping spectra of VPO$_{P1}$, VPO$_{P2}$, VPO$_{P3}$ and VPO$_{P4}$ catalyst precursors. V^{4+} species appear at 1725–1770 ppm and V^{4+}–V^{5+} dimers at ~900 ppm. Adapted from ref. [35]; reprinted with permission from the Royal Society of Chemistry.

through the work of Li and coworkers [33], and its early application to VPO catalysts has been reviewed by Tuel and coworkers [34]. In such systems, information on the oxidation state of vanadium can be investigated through observing the influence of vanadium on the ^{31}P spectrum. For instance, ^{31}P nuclei bonded to V^{5+} nuclei are observed at 0 ppm, while those bonded to V^{4+} appear at ~2500 ppm. Figure 5.6 shows ^{31}P spin-echo mapping spectra of four distinct VPO catalyst precursors VPO$_{P1}$, VPO$_{P2}$, VPO$_{P3}$ and VPO$_{P4}$ prepared by two different methods [35]. VPO$_{P1}$ and VPO$_{P2}$ are prepared from orthophosphoric acid and correspond to samples before and after water reflux. VPO$_{P3}$ and VPO$_{P4}$ correspond to materials synthesized from pyrophosphoric acid, again before and after water reflux. Two different V environments are observed, V^{4+} in the $VOHPO_4 \cdot 0.5H_2O$ structure with a signal at 1725–1770 ppm and V^{4+}–V^{5+} dimers with a signal at around 900 ppm. The results show that the dimers formed by the latter route have a higher stability in water. In addition to characterizing vanadium sites, spin-echo mapping has also been used to provide similar information on paramagnetic cobalt centers [36].

Applied to VPO catalysts, spin-echo mapping not only provides information on the oxidation state of different vanadium nuclei, but can also differentiate different phases with the same oxidation state. The development of a NMR technique to probe such materials has been extremely valuable, as their often poorly crystalline nature prevents characterization through X-ray diffraction. Additionally, variable-temperature spin-echo mapping has been shown capable of determining magnetic characteristics of materials, such as their Weiss temperature [34, 37].

5.2.2 Surface Structure of Catalysts

While understanding the bulk structure of a catalyst is of obvious importance it is often desirable to acquire information selectively about the nature of the catalyst surface. Such information may include the nature of any acid sites present, or differences in the coordination of atoms at the surface as compared to those in the bulk. NMR is ideally suited to such studies owing to its inherent sensitivity to the local environment of the nuclei under observation.

5.2.2.1 Double-Resonance Techniques

It is often the case that nuclei present at the surface of catalysts are also present in the bulk, such as oxygen atoms in metal oxides. Therefore, a number of innovative techniques have been developed in order to selectively probe surface species. Frequently this entails the use of double-resonance methods, involving, for example, polarization transfer between two nuclei.

Cross Polarization Cross-polarization (CP) NMR, normally combined with MAS (CP-MAS NMR), provides selective information about nuclei at the surface of a material. This technique is used to enhance the signal of surface nuclei (often the metal nuclei, for example ^{71}Ga or ^{27}Al in the case of metal oxides such as Ga_2O_3 or Al_2O_3) by magnetization transfer from the nuclei of a species present in, or adsorbed onto, the surface. These nuclei are most commonly ^{1}H from surface hydroxyls or adsorbed probe molecules, although examples of transferring magnetization from the metal nuclei in order to study the surface oxygen species also exist [38]. In order to establish magnetization transfer, the rf pulses applied on the two frequency channels must fulfill the Hartmann–Hahn condition [39]. The surface-selective nature of this experiment arises from the fact that the cross-polarization rate is dependent upon the magnitude of the dipolar interaction between the two nuclei involved and hence on their internuclear distance. In cases where the nucleus of interest is quadrupolar, for instance in ^{1}H-^{27}Al CP-MAS NMR, the central 1/2–1/2 transition is spin-locked and a modified Hartman–Hahn condition applies [39].

Figure 5.7 shows both ^{29}Si MAS NMR and ^{1}H $\rightarrow$ ^{29}Si CP-MAS NMR spectra of (a) a silica-alumina support (ASA) and (b) a NiMo/ASA catalyst [40]. As can be seen, the CP experiment selectively enhances the signals at –100 and –86 ppm. These signals correspond to silicon atoms coupled to ^{1}H nuclei of OH groups. Comparing the spectra of the supported catalyst with that of the pure support, a strong decrease in intensity is observed at –86 ppm and a slight decrease at –100 ppm. This indicates that Mo and Ni species interact with the silanol groups and are adsorbed more easily on the geminal silanols present on the support.

Other Double Resonance Techniques Despite the fact that dipolar couplings add to line broadening and are removed through techniques such as MAS, it is often desirable to re-introduce them. This is because dipolar couplings contain informa-

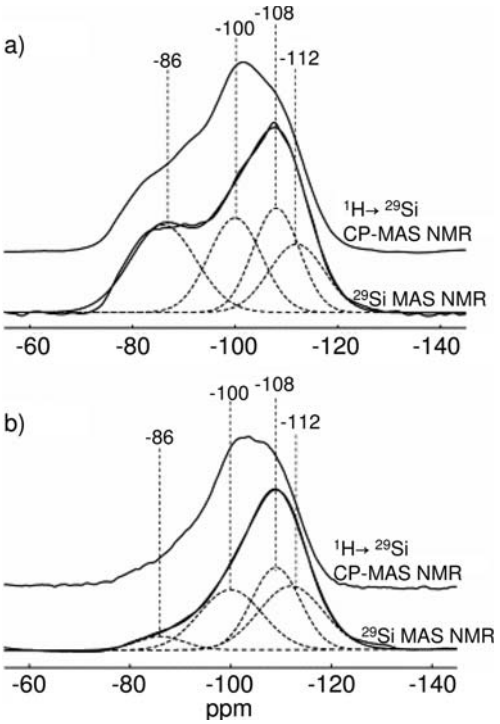

Figure 5.7 ^{29}Si MAS NMR and 1H → ^{29}Si CP/MAS NMR spectra of (a) a silica-alumina support (ASA) and (b) NiMo/ASA catalyst. Adapted from ref. [40]; reprinted with permission from Elsevier.

tion about the environment of the nuclei, including interatomic distances. DOR experiments are therefore often used to determine dipolar couplings between different nuclei. Examples of such techniques include Rotational Echo Double Resonance (REDOR) [41, 42], Rotational Echo Adiabatic Passage Double Resonance (REAPDOR) [43, 44], Spin-Echo Double Resonance (SEDOR) [45], Transferred-Echo Double Resonance (TEDOR) [41, 46] and Transfer of Population in Double Resonance (TRAPDOR) [47, 48]. TRAPDOR was developed by Grey and coworkers [47, 48] and exploits the heteronuclear dipole coupling between quadrupolar and spin-1/2 nuclei, thus revealing connectivity and spatial interactions. It facilitates the recoupling of quadrupole spins in Zeeman states other than ±1/2. DOR experiments have been employed by a number of workers in order to determine the location of Brønsted acid sites on catalyst surfaces. For instance, Yang and coworkers have used TRAPDOR to study the acid sites on a sulfated aluminum oxide catalyst [49]. Figure 5.8 shows ^{1}H spin-echo spectra of (a) γ-Al_2O_3, (b) SO_3/γ-Al_2O_3, (c) SO_3/γ-Al_2O_3 (under TRAPDOR conditions) and (d) difference spectrum of (b) and (c). The ^{1}H source is surface hydroxyl groups. Under TRAPDOR conditions the ^{1}H signals at 0.3, 2.4 and 4.3 ppm are significantly suppressed, while the intensity of the 11.2 ppm signal remains almost unchanged. This indicates that

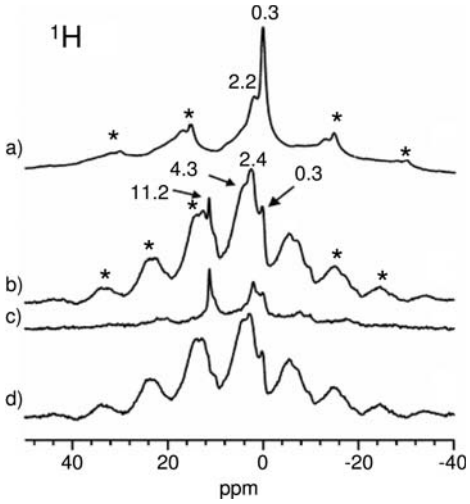

Figure 5.8 ^{1}H spin-echo spectra of (a) γ-Al_2O_3(without Al irradiation), (b) SO_3/γ-Al_2O_3(without Al irradiation), (c) SO_3/γ-Al_2O_3(with Al irradiation), (d) difference spectrum of (b) and (c). Asterisks denote spinning sidebands. Adapted from ref. [49]; reprinted with permission from the Royal Society of Chemistry.

the ^{1}H species giving rise to the peak at 11.2 ppm are not in close proximity to an Al nucleus and may instead be bound to a sulfur atom.

5.2.2.2 Spin-Echo Techniques

As discussed above, one of the key requirements in obtaining high-resolution NMR spectra in the solid state is to overcome the various line-broadening mechanisms that exist. Inhomogeneous broadening occurs because of the variation of the macroscopic magnetic field over the sample, during the NMR experiment. This may be caused by susceptibility effects or by imperfections in the instrumentation. Spin-echo methods reverse the inhomogeneous part of the signal decay through the application of a second rf pulse during the experiment. A spectrum is then generated through the Fourier transformation of the echo-train, yielding information on, for example, coupling constants. Such processes are discussed in detail in a number of texts [50, 51].

Spikelet-Echo The spikelet-echo experiment involves the digitization of an entire train of spin-echoes [52]. The spectra produced by this method consist a series of sharp "spikelets" (see Figure 5.9) which reveal the presence of more than one species through inconsistencies in the spikelet spacings and linewidths, as these are dependent upon the spin–spin relaxation time, T_2, and hence species sensitive. Figure 5.9 shows a ^{17}O MAS NMR spikelet spectrum of a partially metamict zircon ($ZrSiO_4$) as measured by Ashbrook and Farnan [53]. Two peaks are observed in the spectrum. The peak at ~150 ppm is typical of oxygen in a non-bridging environ-

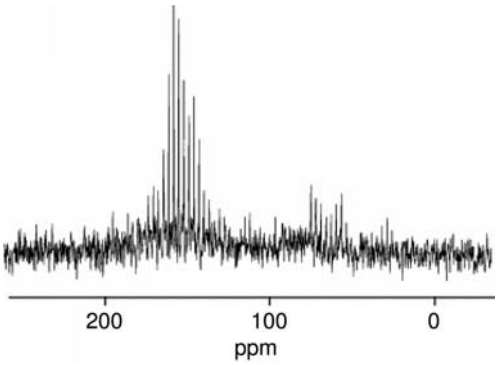

Figure 5.9 ^{17}O spikelet-echo MAS NMR spectra of a partially metamict $ZrSiO_4$. Adapted from ref. [53]; reprinted with permission from Elsevier.

ment such as those found in the isolated SiO_4 tetrahedra, while that at ~65 ppm is typical of oxygen species that bridge SiO_4 tetrahedral units.

5.2.2.3 **CRAMPS**

Combined Rotation and Multiple Pulse Spectroscopy (CRAMPS) is a technique in which the dipolar interaction is averaged through a multiple-pulse sequence [54, 55]. The simultaneous spinning around the magic angle, as in MAS NMR, averages the chemical shift anisotropy. Under appropriate conditions, CRAMP spectra can be of greater resolution than MAS NMR spectra. While CRAMPS is not exclusively a surface-sensitive technique, the majority of catalytic applications have focused on the study of adsorbed species, and the information on surface structure that can be extracted from their spectra.

Fitzgerald and coworkers have employed CRAMPS to identify and monitor the ^1H species of surface Al—OH groups and physisorbed water associated with a high surface area alumina [56]. Figure 5.10 shows the ^1H CRAMPS spectra of four alumina samples dehydrated under a variety of conditions. The data show that heating at 25 °C and 110 °C at ambient pressure results in the partial removal of physisorbed water (4.0 ppm). The other peaks in the spectra correspond to octahedral AlOH (3.0 ppm) and Al_2OH (8.2 ppm) sites.

5.3
Structure of Bulk Oxides

Metal oxide-based materials are widely employed as catalysts for a wide number of applications, particularly in processes such as dehydrogenation and oxidation, where redox chemistry is important. The structure of metal oxides facilitates these reactions through the transfer of oxygen, or the removal of hydrogen. In order to fully understand the structural dependence of these processes, and hence to refine existing catalysts and catalytic processes and to develop new active materials, it is

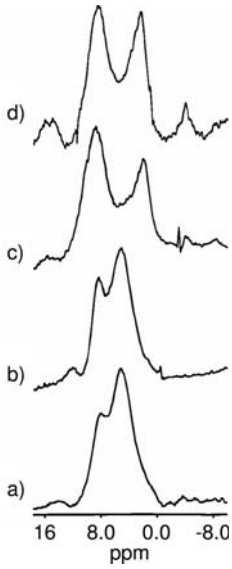

Figure 5.10 ^{1}H CRAMP spectra (360 MHz) of $Al_2O_3 \cdot 2.05H_2O$ materials prepared following various dehydration procedures: (a) desiccation over Drierite at ambient pressure (725 Torr) for 72 h, (b) heating at 110 °C (in ambient pressure) for 5 h, (c) heating at 110 °C (in ambient pressure) for 5 h, followed by evacuation at 6.5 mTorr for 24 h, and (d) heating at 110 °C under vacuum (8 mTorr) for 24 h. Adapted from ref. [56]; reprinted with permission from the American Chemical Society.

necessary to understand the structure of the oxides themselves and the active sites within them. Solid-state NMR techniques have proven to be an invaluable tool in this area. Such techniques and their applications are outlined in the coming sections.

5.3.1 Vanadium Oxide Catalysts

Vanadium catalysts are among the most significant metal oxide catalysts. For instance, considering only supported catalysts, between 1967 and 2000, 28% of all published papers were concerned with vanadium oxide-based materials [57]. This represents a greater fraction than for any other metal or metal oxide. One reason for this is the wide range of applications in which vanadium oxide catalysts may be employed, examples of which are outlined below.

5.3.1.1 Supported Vanadium Oxide Catalysts

Supported vanadium catalysts, whereby vanadium oxide is dispersed on a support such as alumina or titania are of particular importance in, for instance, the oxidative dehydrogenation of alkanes [58–64]. Such materials have attracted considerable interest in the direct dehydrogenation of butane, where a key driver is to identify the relationship between catalytic activity and structural properties [5, 6, 65–68]. In the pure (solid) metal oxides the coordination of vanadium is well defined. However, this is not necessarily true in the case of supported catalysts. Vanadium may be present on the support surface as: isolated vanadium ions; dimeric or polymeric species; one- and two-dimensional chains of vanadium ions;

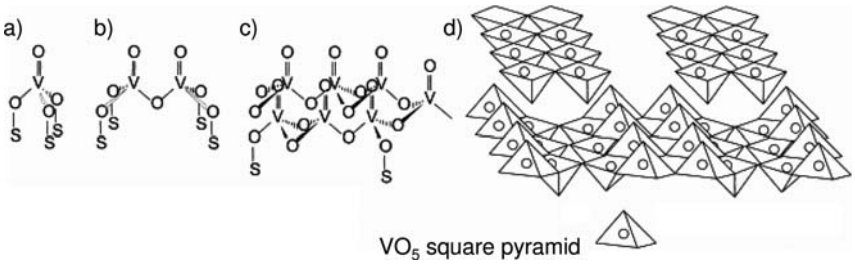

Figure 5.11 Possible molecular configurations for supported vanadium oxides (S represents the support): (a) isolated vanadium oxide species; (b) dimeric vanadium oxide species; (c) two-dimensional vanadium oxide chains; (d) V_2O_5 crystals. Adapted from ref. [69]; reprinted with permission from Elsevier.

amorphous or crystalline oxides such as V_2O_5; or as a mixed metal oxide phase with the support, such as $AlVO_4$ in the case of an alumina support [69]. Examples of these are shown in Figure 5.11. A ^{51}V MAS NMR spectrum of pure V_2O_5 is shown in Figure 5.2.

The complex nature of vanadium species in catalytic materials means that no single technique is ideally suited to their study. ^{51}V NMR techniques can, however, provide information on the local environment of vanadium nuclei, including the geometry and coordination number of V^{5+} species, the number of non-equivalent

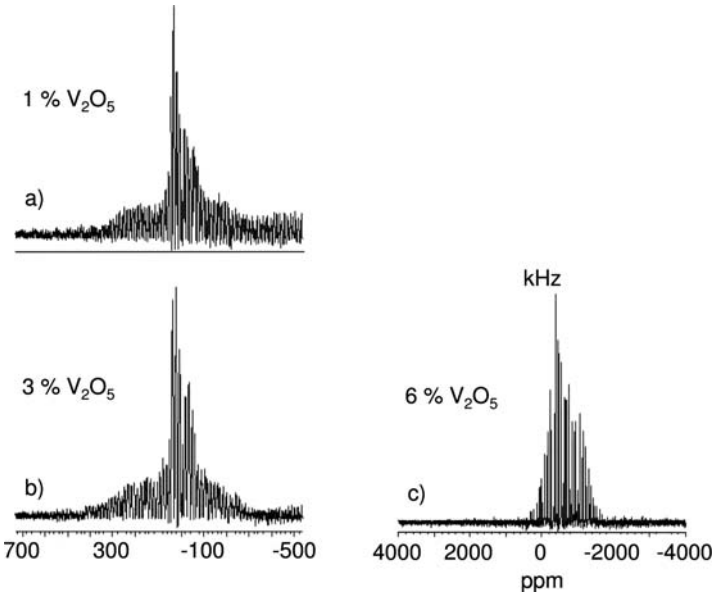

Figure 5.12 ^{51}V MAS NMR spectra of three different VO_x/TiO_2 catalysts. Vanadia loadings are: (a) 1 wt% V_2O_5 (b) 3 wt% V_2O_5 and (c) 6 wt% V_2O_5. Adapted from ref. [89]; reprinted with permission from the American Chemical Society.

V^{5+} sites, the nature of atoms in the first coordination sphere and the distortion of this sphere. The quadrupolar (spin = 7/2) ^{51}V isotope has a natural abundance of 99.76%, and a relative NMR intensity, with respect to ^{1}H, of 0.38. These characteristics make vanadium in the 5+ oxidation state an attractive nucleus to study by NMR techniques.

Much of the pioneering work in this area was conducted by Mastikhin and coworkers employing both static and MAS techniques [27, 70–87]. These studies probed the development of different vanadate sites on the catalyst surface as a function of vanadium loading. For instance, for Al_2O_3-supported vanadium it was observed that at low loadings (~1 wt% V) isolated VO_4 tetrahedra were present as indicated by a species with a chemical shift of –750 ppm [73]. On increasing the catalyst loading, a second species, assigned to polymeric vanadate species in which vanadium exists in a distorted octahedral environment (–350 ppm), is evident in the spectra. At higher loadings, evidence of vanadium in a V_2O_5-like environment is observed. V_2O_5 has an isotropic chemical shift of –612 ppm. When high loadings are coupled with high calcination temperature the formation of $AlVO_4$ is observed. The spectrum of $AlVO_4$ is discussed in Section 5.3.1.3. In addition to Al_2O_3 supports [70, 71, 73, 74, 77, 79, 86] this group have also studied vanadium supported on SiO_2 [70, 74, 79], SnO_2 [72, 74, 75, 79, 86], TiO_2 [74, 79, 81, 86, 87], ZrO_2 [74], Sb_2O_5 [75], $AlPO_4$ [74, 79, 82], MgO [79] and a number of promoted or mixed-oxide supports [27, 74, 76, 78–80, 82, 85–87].

Similar studies on other supported vanadium oxide catalysts have been carried out by other workers with similar results [88–93]. Among the materials studied are VO_x/Ga_2O_3 and $VO_x/MgAl_2O_4$ catalysts for the oxidative dehydrogenation of propane [94, 95] and VO_x/TiO_2 catalysts for the selective catalytic reduction of NO_x. Figure 5.12 shows ^{51}V MAS NMR spectra of three VO_x/TiO_2 catalysts differentiated only by their loading [89]. The changes occurring in the spectra as a function of loading are indicative of the development of new surface vanadate species, with domains of V_2O_5 dominating at 6 wt% V_2O_5. A feature of these studies is that crystalline V_2O_5 is typically only observed in ^{51}V NMR spectra of supported catalysts above the theoretical monolayer coverage. This is the loading at which the support surface is entirely covered by a two-dimensional vanadate network. The value at which this occurs varies with the nature of the support surface and the geometry of the vanadate species present. For γ-Al_2O_3, TiO_2 and ZrO_2 monolayer coverage is typically achieved at vanadium loadings of ~3.5 to 7 wt% [57].

The nature of vanadium species on different supports can vary significantly. For instance, the polymeric vanadate species shown in Figure 5.11 and observed on alumina supports, does not form on silica-supported catalysts [62, 96]. Sasikala and coworkers have added metal ion modifiers in an attempt to increase the dispersion of vanadate species in VO_x/SiO_2 catalysts and thereby improve catalytic activity [97]. Figure 5.13 shows that, unlike that for VO_x/SiO_2, the ^{51}V MAS NMR spectrum of aluminum-modified VO_x/SiO_2 exhibits a side band pattern similar to that of bulk-like V_2O_5 superimposed over a broad peak characteristic of tetrahedral V^{5+} species. From these results it can be inferred that the dispersion of vanadia is indeed better on the modified support.

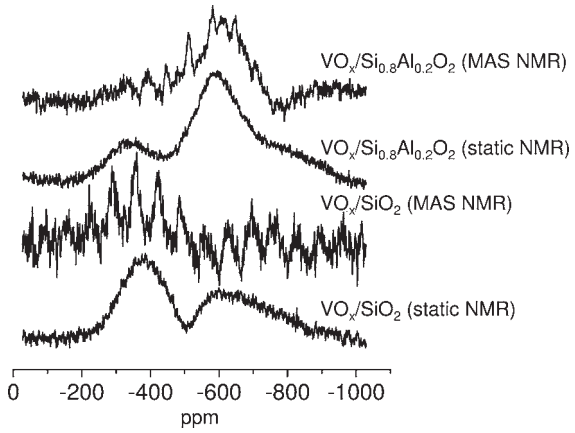

Figure 5.13 ^{51}V static and MAS NMR spectra of V_2O_5, VO_x/SiO_2 and VO_x supported on aluminum-modified SiO_2 ($Si_{0.8}Al_{0.2}O_2$). Adapted from ref. [97].

A knowledge of the nature of the vanadium species on the catalyst surface allows links to be made between catalyst structure and catalytic action [98]. Steinfeldt and coworkers have investigated the effect of both catalyst loading and calcination temperature for VO_x/Al_2O_3 catalysts [99]. The effect of loading is similar to that seen by other workers and discussed above. The effect of calcination temperature is dependent upon loading. At high (up to 700 °C) calcination temperatures $AlVO_4$ forms, but only at loadings of greater than 4.5 wt% V. At lower loadings the dispersion of more crystalline vanadium into polymeric, tetrahedrally coordinated vanadium species is observed. The link between speciation and activity was established by testing the catalysts for the oxidative dehydrogenation of propane (ODP). Correlating NMR and activity measurements it was concluded that isolated and polymerized tetrahedrally coordinated V^{5+} species are active in propane dehydrogenation while $AlVO_4$ and bulk-like V_2O_5 have only a low catalytic activity. In a similar study we have investigated the direct dehydrogenation of butane over VO_x/Al_2O_3 catalysts. Calcination of a catalyst with a vanadium loading of 3.5 wt% at 973 K resulted in reduction in the intensity of the V_2O_5 peak in the MAS NMR spectrum of 71%. Simultaneously a broad peak, assigned to more dispersed vanadium in tetrahedral environments, appears (Figure 5.14). Similarly to Steinfeldt's observation, when the catalyst loading was increased to 8 wt% V the formation of $AlVO_4$ was observed after calcination at 700 °C. Catalytic studies on the same catalysts have related dehydrogenation activity to the presence of polymeric vanadate species [5].

Recent developments have allowed for an improved understanding of the local environment of vanadium in supported catalysts. Lapina and coworkers [27] have studied phosphorus-modified VO_x/TiO_2 catalysts by SATRAS and MQMAS techniques. A key question in such materials is what influence the phosphorus has on the structure of the catalyst. This is not directly answerable by conventional

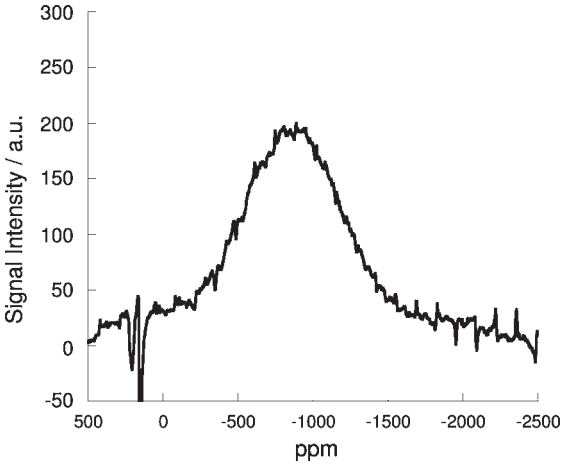

Figure 5.14 ^{51}V MAS NMR of 3.5 wt% vanadium VO_x/Al_2O_3 catalyst after calcination at 700 °C. Spinning rate = 14 kHz. B_0 = 9.40 T.

NMR techniques as a detailed knowledge of all the NMR parameters, such as chemical shielding anisotropy and quadrupole tensor parameters, as well as their distributions, is necessary to draw detailed conclusions on the local environment and long-range order of V atoms. However, the SATRAS analysis of ^{51}V MAS spectra coupled with the results of ^{51}V 3Q–MAS and 5Q–MAS studies (Figure 5.15) can provide this information and demonstrate the formation of a V—P—Ti compound, in contrast to previous hypotheses for such systems.

^{51}V MQMAS studies are at present relatively rare. However, MQMAS techniques have been applied in studies of other nuclei such as ^{27}Al and ^{95}Mo (see Section 5.3.2). The success of these studies suggests that ^{51}V MQMAS NMR may play a role in future investigations of vanadium oxide catalysts.

It is relatively straightforward to characterize V^{5+}-containing systems by techniques such as MAS and MQMAS NMR. This is not true, however, for materials in which vanadium is in a lower oxidation state. Only diamagnetic species can be detected by NMR and, under ambient and reaction conditions, only V^{5+} is diamagnetic. Both V^{3+} and V^{4+} are paramagnetic and as such are themselves unobservable and may, under certain structural conditions, prevent the observation of V^{5+}. This is due to the dipole interaction between the magnetic moments of the V^{5+} nuclei and the paramagnetic nuclei, causing the spectral lines to be broadened, often beyond detection [100]. This may be the result of a direct linkage between the para- and diamagnetic ions [84] or an interaction based on spatial proximity. Shubin and coworkers [101] calculated that, in V_2O_5, no NMR signal would be detected from a V^{5+} ion within a ~10 Å spherical radius of a V^{3+} ion.

This problem is highlighted in the case of an alumina-supported vanadium catalyst employed for the dehydrogenation of *n*-butane. The hydrocarbon creates a reducing environment, which results in a reduction in the oxidation state of

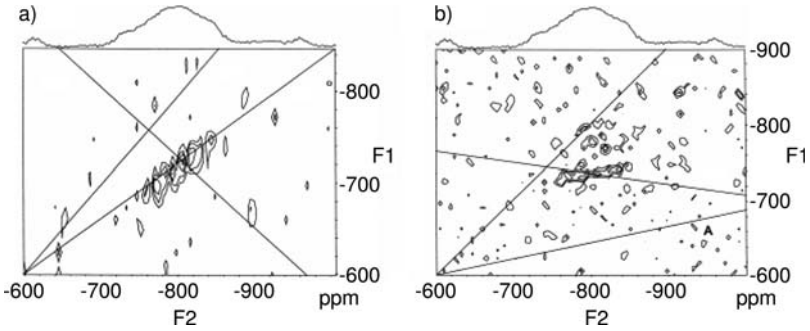

Figure 5.15 (a) ^{51}V 3Q-MAS and (b) 5Q-MAS spectra of VO_x/TiO_2 catalyst containing 10 wt% P_2O_5. Adapted from ref. [27]; reprinted with permission from Elsevier.

vanadium in the catalyst. Figure 5.16 shows ^{51}V NMR spectra for the fresh catalyst and for the sample after reaction. In contrast to the fresh catalyst the reacted catalyst shows no observable NMR spectrum. It is not possible to quantify the degree of reduction of the catalyst samples based on ^{51}V NMR measurements alone. In V_2O_5 a V^{3+} content of only 2% has been observed to result in a decrease in signal intensity from V^{5+} of 70% [84].

The decrease in signal intensity caused by the presence of paramagnetic nuclei presents a challenge in NMR spectroscopy. However, a variety of NMR techniques have been developed to overcome this difficulty. Specifically, information concerning the nature, location and oxidation state of vanadium nuclei can be obtained from the NMR spectra of neighboring nuclei. Examples of such techniques will be described in the following section, focusing on VPO catalysts.

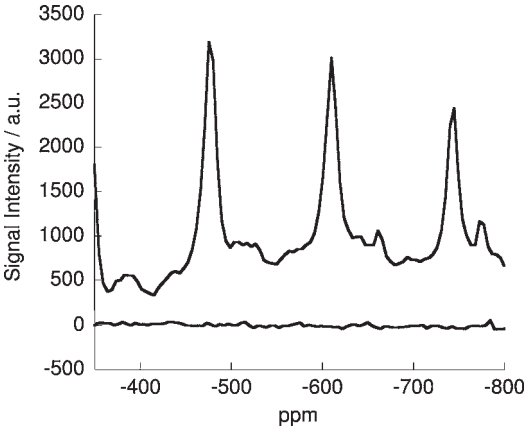

Figure 5.16 ^{51}V MAS NMR of 8 wt% vanadium VO_x/Al_2O_3 catalyst prior to reaction (top) and after reaction with butane at 600 °C (bottom). Spinning rate = 14 kHz. B_0 = 9.40 T.

5.3.1.2 VPO Catalysts

VPO catalysts are widely employed for the oxidation of butane to maleic anhydride [1, 102–104]. As such, a large number of studies have focused on developing an improved understanding of their structure. This task is complicated by the fact that numerous different VPO phases exist, each with a different structure. In particular, the relative distribution of V^{4+} and V^{5+} is crucial in determining catalytic activity [105]. As these materials contain V^{4+}, conventional NMR measurements on either ^{51}V or ^{31}P can result in signals that are very much broadened under the influence of the unpaired electrons in the paramagnetic nuclei. ^{31}P spin-echo mapping is, however, ideally suited to the study of such catalysts. This technique allows paramagnetic nuclei to be indirectly observed through the observation of a large ^{31}P spectral region. VPO catalyst systems represent the main area of application for this approach. The use of NMR spectroscopy has benefits over techniques such as X-ray diffraction (XRD), which cannot be applied to poorly crystalline materials, and over X-ray photoelectron spectroscopy, which provides information only on the surface species.

Li and coworkers were the first group to apply a spin-echo mapping technique to vanadium–phosphorus materials [33]. Studying $VOPO_4$ treated in *n*-butane, both V^{4+} and V^{5+} phases could be distinguished, and their evolution monitored over the course of reaction. In this manner it is possible to make inferences as to the active phase of the catalyst. For instance, when treated with butane or butene, the spectra of β-$VOPO_4$ indicate that, as expected, the proportion of V^{4+} relative to V^{5+} increases. $(VO)_2P_2O_7$ is, however, relatively unaffected by exposure to such compounds. This indicates that the reducing hydrocarbons interact with the former phase but not the latter, implying that it is the β-$VOPO_4$ that is catalytically active.

The most common application of spin-echo mapping is to identify different phases and their oxidation states in VPO catalysts [33, 105–111]. Tuel has reviewed much of the early literature in this area [110]. More recently Siegel has applied ^{31}P spin-echo mapping, and ^{31}P MAS NMR, to the study of catalysts prepared from VPO-NbPO precursors [112]. NMR results show that the chemical shift of ^{31}P in the $VOHPO_4 \cdot 0.5H_2O$ precursor is ~100 ppm higher than the value of ~1625 ppm observed in the absence of Nb. The physical proximity of Nb to P indicated by this change suggests that Nb acts as a dopant to the VPO catalyst altering the V^{4+}/V^{5+} ratio. The new catalyst has both improved catalytic performance and a shorter activation period than the undoped material.

Spin-echo mapping therefore provides valuable structural information on VPO catalysts, and can also be used, for example, to determine magnetic characteristics such as the Weiss temperature of pure phases. Additionally, standard MAS NMR techniques have successfully been employed to yield important information on VPO catalysts, in a similar manner as for supported catalysts discussed above [105, 106, 108, 112, 113].

5.3.1.3 Other Vanadates

Other vanadate materials are also widely employed as catalysts, notably K-V-O materials in the oxidation of SO_2 to sulfuric acid. Such catalysts typically contain

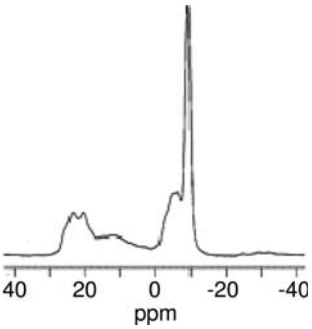

Figure 5.17 ^{27}Al MAS NMR spectra of $AlVO_4$ recorded at B_0 = 21.15 T (234.5 MHz). Adapted from ref. [120]; reprinted with permission from the Royal Society of Chemistry.

vanadium in a 5+ oxidation state. Lapina and coworkers [74] have provided a thorough review of ^{51}V NMR assignments (both MAS and static) for these materials and a large number of other vanadates containing V atoms in a range of different environments. As an example of the role ^{51}V solid-state NMR can play in the study of such systems, Lapina and coworkers consider the nature of active complex in SO_2 oxidation over K-V-O catalysts. Through a comparison of the spectra of catalysts with those of model compounds it is proposed that the active phase contains vanadium atoms in a square-pyramidal coordination in a $K_3VO_2SO_4S_2O_7$ phase which forms during reaction.

In addition to K-V-O catalysts [114, 115], other vanadates which have been the subject of NMR study include V-Mg-O materials [116], bismuth vanadates [117], $LaVO_4$ [118] and aluminum orthovanadate ($AlVO_4$) [77, 86, 119–121], which as discussed above also has relevance to VO_x/Al_2O_3 catalysts. In a study of $AlVO_4$, Neilsen has applied both ^{51}V MAS NMR and ^{51}V and ^{27}Al MQMAS techniques in order to elucidate the structural environment of aluminum and vanadium nuclei [120, 121]. Figure 5.17 shows ^{27}Al MAS spectra acquired at 21.15 T which indicate the presence of three distinct Al sites confirming that $AlVO_4$ is isostructural with $FeVO_4$, that is, that it contains one pentacoordinated Al site and two AlO_6 octahedra. ^{51}V 3Q-MAS spectra have also been acquired at 14.1 T. These indicate the presence of three isolated VO_4 tetrahedra as shown in Figure 5.18. In addition to being significant in their own right, studies on $AlVO_4$ are also valuable for the identification of such species in VO_x/Al_2O_3 catalysts. Figure 5.19 shows a ^{27}Al MAS NMR spectrum of 8 wt% vanadium VO_x/Al_2O_3 after calcination at 700 °C. Comparison with Figure 5.17 allows the formation of $AlVO_4$ to be confirmed.

MQMAS NMR has also proven to be a useful for structural characterization of other vanadates, such as $LaVO_4$ [118] and will likely become widely applied in such studies in the coming years.

5.3.2
Other Metal Oxide Catalysts

All of the above studies have focused on oxides containing vanadium. While vanadium catalysts are very widely used, and studied, the use of solid-state NMR is not

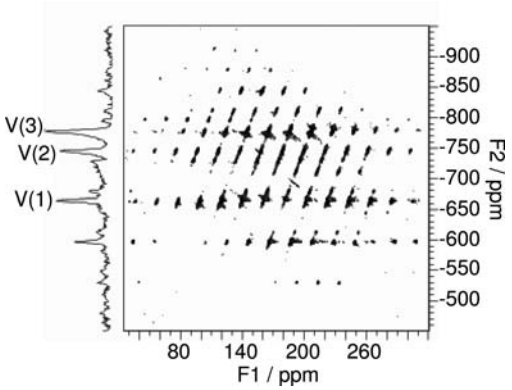

Figure 5.18 ^{51}V 3Q-MAS NMR spectrum of $AlVO_4$. Spinning rate = 10.5 kHz. B_0 = 14.1 T. The projection onto the anisotropic dimension (F2) is a summation. V(1), V(2), and V(3) indicate the isotropic peaks in this dimension for the three ^{51}V sites. Adapted from ref. [121]; reprinted with permission from the American Chemical Society.

restricted to such materials. Indeed ^{95}Mo, ^{89}Y, ^{119}Sn, ^{71}Ga and ^{43}Ca solid-state NMR techniques have been applied to the study of metal oxide catalysts. Additionally, ^{27}Al and ^{29}Si may be applied not only to alumina and silica supports but also to mixed-metal oxides. ^{17}O NMR has also been employed to study the environment of oxygen atoms in oxide materials [38, 79, 122–124].

Molybdenum oxide catalysts are widely employed in oxidation, hydrodesulfurization and hydrodenitrogenation reactions. The active phase is most commonly supported on alumina, although mixed-metal oxides are also used. As for supported vanadium catalysts, both static and MAS NMR techniques were widely employed in early studies of such systems [125–129]. Like ^{51}V and ^{27}Al, ^{95}Mo is a

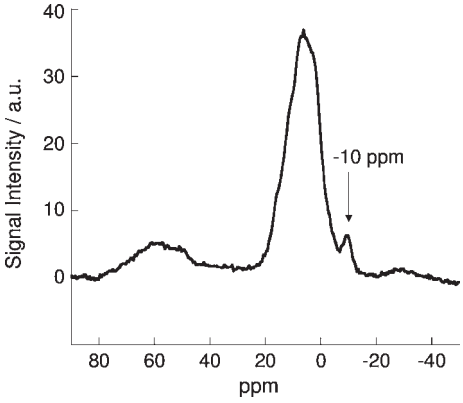

Figure 5.19 ^{27}Al MAS NMR spectrum of 8 wt% vanadium VO_x/Al_2O_3 calcined at 700 °C The peak at –10 ppm corresponds to $AlVO_4$. Spinning rate = 14 kHz. B_0 = 9.40 T.

quadrupolar nucleus (spin = 5/2), with a natural abundance of 15.8%. Its relatively small quadrupole moment ($0.011 \times 10^{-28}\,m^2\,A$) means that problems associated with line broadening are minimal.

In addition to conventional static and MAS measurements on molybdenum oxide catalysts, static-echo techniques have also been applied [125, 127, 129]. Spin-echo spikelet experiments allow the presence of dynamically active surface-interactive molybdenum oxide species to be resolved. Figure 5.20 compares the spikelet-echo spectra of MoO_x/Al_2O_3 of different loadings before and after calcination. The existence of the broad resonance on which the observed spikelets are superimposed indicates that the surface is dynamically inhomogeneous. As discussed in Section 5.2.2.2 the basis of the spikelet-echo experiment is that surface species with high mobility will have short spin–spin relaxation times (T_2) in comparison with species immobilized on the surface. The spikelet-echo experiment is designed to distinguish species on the basis of their T_2 values.

More recently ^{95}Mo MQMAS spectroscopy has been applied to the study of molybdates [130]. Figure 5.21 shows the ^{95}Mo 3Q-MAS spectra of $[(NH_4)_6Mo_7O_{24}]\cdot 4H_2O$ powder obtained at 19.6 T. This spectrum demonstrated that the peak observed in the one-pulse MAS spectrum (also shown in Figure 5.21) at ~30 ppm was in fact a convolution of signals from two distinct ^{95}Mo sites.

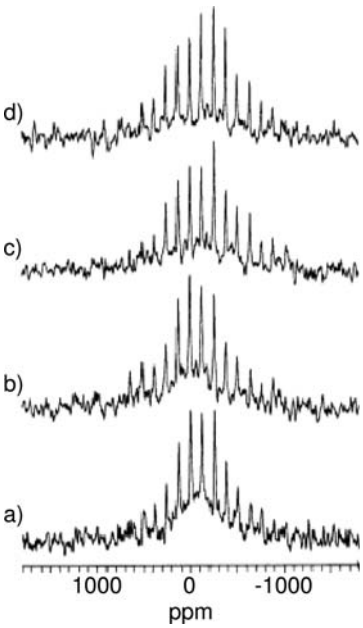

Figure 5.20 Spikelet echo spectra of the central transition obtained for uncalcined and calcined MoO_x/Al_2O_3 catalysts with 16 wt% and 24 wt% loadings. (a) 16% uncalcined, (b) 24% uncalcined, (c) 16% calcined, and (d) 24% calcined. Adapted from ref. [125]; reprinted with permission from the American Chemical Society.

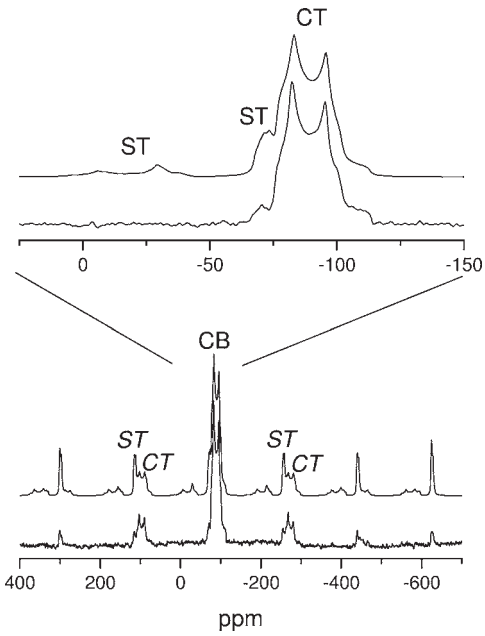

Figure 5.21 ^{95}Mo MAS NMR of $[(NH_4)_6Mo_7O_{24}]\cdot 4H_2O$. The lower trace is the one-pulse spectrum obtained at 54 MHz (B_0 = 19.6 T). The upper trace was generated by SIMPSON. Adapted from ref. [130]; reprinted with permission from the American Chemical Society.

These sites have similar chemical shifts, hence are difficult to resolve by MAS NMR, but have different $C_{Q\eta}$ allowing them to be distinguished by MQMAS NMR.

^{95}Mo NMR spectroscopy is becoming increasingly applied to the study of molybdenum oxide catalysts [131–134], while a number of more exotic nuclei have also been the subject of study in catalytically relevant systems. These include ^{89}Y [135], ^{71}Ga [136] and ^{43}Ca [137]. Trokiner and coworkers have acquired one-pulse and spin-echo ^{43}Ca spectra of calcium peroxide and its precursors [137]. These studies aimed to gain insight into the mechanism of hydrogen peroxide disproportionation as catalyzed by calcium hydroxide. ^{43}Ca NMR spectra of CaO, $Ca(OH)_2$, $CaO_2\cdot 8H_2O$ and $CaO_2\cdot 2H_2O_2$ have all been acquired, characterizing the species involved in the generation of singlet oxygen that is key to the reaction mechanism. The value of the isotropic chemical shift in these compounds decreases through the series 136 ± 1, 71 ± 3, 2 ± 2, –40 ± 3 ppm. This change is indicative of progressively increased shielding as the number of peroxo groups in the two first coordination shells of the Ca^{2+} ion increases. ^{71}Ga and ^{69}Ga solid-state NMR techniques are also increasingly widely applied to gallium-containing catalysts [136, 138–140]. Ga NMR, and the challenges involved in acquiring spectra from such systems, is discussed in detail in Section 5.3.3.2.

5.3.3 Metal Oxide Supports

Metal oxides are widely used as catalyst supports. For instance, α-Al_2O_3 is employed as a support for catalysts in the partial oxidation of ethylene to ethylene oxide, because a non-reactive material is essential for such applications [141]. However, aluminas are also important catalysts in their own right. Transition aluminas are known to catalyze the isomerization of alkenes, the dehydration of alcohols, H/D exchange reactions and C—H bond activation [142]. Consequently, the development of an understanding of both their bulk and their surface structure has been a key goal in catalysis, with solid-state NMR being widely employed to this end.

In addition to aluminas, other oxides such as SiO_2, SnO_2 and Ga_2O_3 are also employed as catalyst supports. As these materials also contain NMR-active nuclei, such as ^{119}Sn or ^{71}Ga, it is also possible to apply solid-state NMR to their characterization. In general the study of such oxides is not as well developed as that of ^{27}Al NMR. However, recent technical and theoretical advances have led to an increasing interest in these materials.

5.3.3.1 Aluminum Oxides

Solid-state ^{27}Al NMR has been applied to the study of aluminas and catalytic materials since the 1950s [143]. In 1960 O'Reilly reported the use of ^{27}Al NMR spectroscopy to identify different structural environments – tetrahedral and octahedral Al atoms – in α- and γ-Al_2O_3 [144]. The characterization of the structural environment of Al atoms remains the main application of ^{27}Al NMR in catalysis. Al atoms in alumina can occupy different geometries, principally octahedral (AlO_6), pentahedral (AlO_5) and tetrahedral (AlO_4). In MAS NMR these species show signals at distinct frequencies corresponding to –10 to 20 ppm (AlO_6), 30–40 ppm (AlO_5) and 50–85 ppm (AlO_4) [145, 146]. A ^{27}Al MAS NMR spectrum (acquired at 9.40 T with a spinning rate of 14 kHz) of a VO_x/Al_2O_3 catalyst, with a vanadium loading of 8 wt%, showing alumina containing aluminum in all three environments, is shown in Figure 5.22. The proximity of these peaks to one another can make resolution of individual peaks quite complex. Better resolution can be obtained through other NMR techniques such as MQMAS NMR; however, the approach often employed is to computationally simulate the experimental spectrum, optimizing various NMR parameters such as chemical shift, chemical shift anisotropy, asymmetry parameter and line broadening. Various packages are available for such work including SIMPSON, a general purpose solid-state NMR simulation software, developed by Bak and coworkers [147]. SIMPSON has previously been employed to simulate ^{27}Al NMR spectra by Goldbourt and Madhu [148]. This approach has been successfully employed by a number of workers on a variety of systems [149–151].

The change in the structure of aluminas through the dehydration sequence from either gibbsite or boehmite to, ultimately, α-Al_2O_3, is perhaps where ^{27}Al NMR spectroscopy has been most frequently applied. The results of a selection these

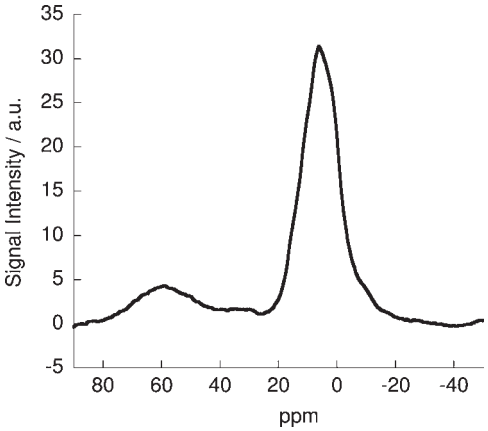

Figure 5.22 ^{27}Al MAS of 8 wt% vanadium VO_x/Al_2O_3. Spinning rate = 14 kHz. B_0 = 9.40 T.

studies, in terms of the distribution of aluminum coordinations are summarized in Table 5.2.

Solid-state NMR has a number of advantages over other techniques for characterizing the structure of alumina. For instance, if the phase is determined by XRD it is possible that crystallites of other phases, too small to be detected by XRD, are also present. The influence of such small crystallites will, however, be apparent in the ratio of aluminum in different coordination environments. Furthermore, examples of alumina phases being incorrectly assigned because of a reliance on X-ray diffractograms are present in the literature. Pecharroman and coworkers [155] studied an alumina previously assigned as δ-Al_2O_3 through inspection of XRD data. Through a combination of infrared measurements and ^{27}Al MAS NMR

Table 5.2 The distribution of Al(VI) (octahedral), Al(IV) (tetrahedral) and Al(V) (pentacoordinate) aluminum in alumina polymorphs and precursors as determined by literature ^{27}Al NMR studies.

	% Al(VI)	% Al(IV)	% Al(V)	References
Gibbsite	100	0	0	[146], [152], [153], [154], [155], [225]
Boehmite	100	0	0	[146]
ρ	55	25	20	[152], [150], [154]
η	71 ± 1	21 ± 1	0	[152], [154]
χ	73	20	7	[150], [154]
κ	75	25	0	[156]
γ	72 ± 4	29.5 ± 4	1.5 ± 4	[24], [151], [152], [153], [154], [155], [226]
γ′	69	31	0	[153]
δ	57	43	0	[152]
θ	57.5 ± 4.5	42.5 ± 4.5	0	[152], [154]
α	100	0	0	[146], [151], [155], [226]

data revealing the distribution of Al sites, the sample was shown to in fact be a mixed-phase γ/θ/α-alumina.

Additionally, Paglia and coworkers [158] have recently identified a new alumina phase, denoted γ′-Al_2O_3 through the use of ^{27}Al MAS NMR. γ′-Al_2O_3 occurs in the dehydration sequence of boehmite after γ-Al_2O_3 where δ-Al_2O_3 might be expected. θ-Al_2O_3 and α-Al_2O_3 formed as normal at higher temperatures.

There are a number of technical considerations to take into account when dealing with ^{27}Al MAS NMR. Notably, the spinning speed, that is the rate at which the sample is spun about the magic angle, has a significant influence on ^{27}Al MAS NMR spectra. This is most apparent when considering the peak corresponding to AlO_5 at ~30 ppm. For instance, Meinhold and coworkers observed that the intensity of this peak increased as the spinning speed was raised from 8 kHz to 15 kHz [152]. This is evident when comparing the results of different workers investigating the same alumina polymorphs. In studies of AlO_5 containing ρ- and χ-aluminas, Meinhold and coworkers [152] and Kunath-Fandrei and coworkers [150] report AlO_6 : AlO_5 : AlO_4 ratios of 55 : 20 : 25 and 73 : 7 : 20 for ρ- and χ-Al_2O_3 respectively. MacKenzie and coworkers [154], however, report ratios of 69 : 9 : 22 and 79.5 : 0.5 : 20. Meinhold and coworkers employed spinning rates up to 15 kHz and Kunath-Fandrei and coworkers used 14 kHz but MacKenzie and coworkers employed a rate of only 12 kHz thereby explaining the discrepancy between the datasets. While the AlO_5 peak is most affected by this phenomenon the AlO_6 and AlO_4 peaks are also slightly affected, with AlO_4 showing less change than AlO_6 [152]. An additional effect of spinning speed is on the NMR linewidths obtained. For instance, high spinning speeds decrease the linewidth of the octahedral peak [152].

In addition to conventional MAS NMR, MQMAS NMR has also been employed in the study of aluminas [24, 156, 159–162]. Figure 5.23 shows a MQMAS spec-

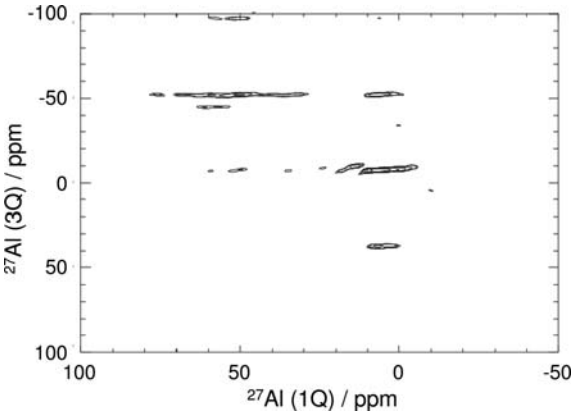

Figure 5.23 ^{27}Al MQMAS spectrum of 8 wt% vanadium VO_x/Al_2O_3. In contrast with the ^{27}Al MAS spectrum (Figure 5.22), different Al coordination environments are more readily distinguishable. Spinning rate = 10 kHz. B_0 = 9.40 T. Shifted-echo spectra were acquired using the pulse sequence of Brown and Wimperis [163].

trum of the same VO_x/Al_2O_3 catalyst shown in Figure 5.22. The advantages of MQMAS in identifying different sites are evident with Al in tetra-, penta- and octahedral environments being clearly distinguished.

Quartararo has employed ^{27}Al MQMAS NMR to the study of phosphorus-modified aluminas [160–162]. 3Q-MAS NMR spectra reveal that the influence of the phosphorus modifier on Al_2O_3 is critically dependent on the synthesis method employed, with two new aluminum phosphate phases forming if P is added at a later stage in the synthesis [160]. MQMAS NMR has also been applied to aluminophosphate materials by Antonijevic and coworkers [28]. ^{27}Al 3Q-MAS NMR spectra were used in conjunction SATRAS NMR under MAS conditions in order to probe molecular-scale dynamics. Figure 5.24 shows ^{27}Al MQMAS and SATRAS spectra for both a calcined and dehydrated aluminophosphate (AlPO-14) and for an isopropylamine-templated aluminophosphate (ipa-AlPO-14). The broadening

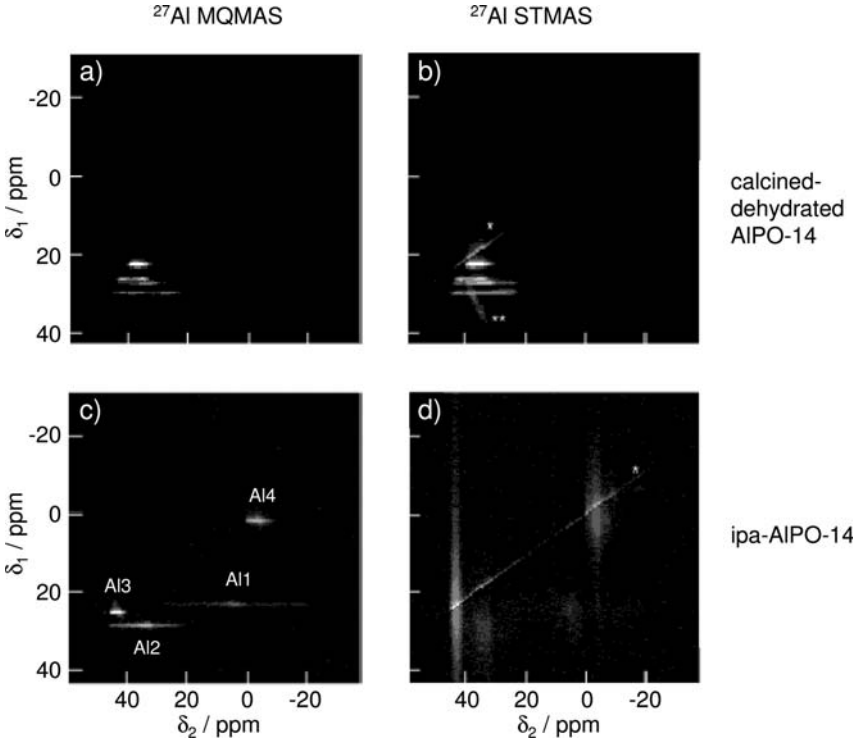

Figure 5.24 (a)–(d) ^{27}Al MQMAS (triple-quantum) and SATRAS NMR spectra of calcined-dehydrated AlPO-14 and ipa-AlPO-14. The MAS rate was 20 kHz. In the STMAS spectra, the central-transition autocorrelation peak and its contribution to the isotropic projection is indicated by *, while an outer satellite-transition correlation peak is indicated by **. Adapted from ref. [28]; reprinted with permission from the American Chemical Society.

observed in the SATRA spectrum of ipa-AlPO-14 relative to the AlPO-14 spectrum can be assigned to dynamics-driven modulation of the ^{27}Al quadrupolar interaction on the microsecond timescale.

In addition to MAS and MQMAS NMR, other techniques have also been applied to the study of aluminum oxides to provide further information. Off-resonance nutation NMR can assist in the interpretation on MAS and MQMAS spectra by providing information on the average quadrupolar interaction in a sample. Kraus and co-workers have applied this technique to γ-Al_2O_3 supports and to γ-Al_2O_3-supported hydrotreating catalysts [24]. Using this method quadrupolar coupling constants were calculated for Al atoms in tetrahedral (>5.0 MHz) and octahedral sites (4.5 MHz). These were then used in conjunction with results from MAS and MQMAS experiments to develop a model of both the bulk and the surface structure of the alumina under study.

5.3.3.2 Other Oxide Supports

It is not only alumina supports which may be investigated through NMR spectroscopy. Any support material containing NMR-active nuclei is suitable for study. MAS has been applied to silica [164], aluminum phosphate [131, 165] and SnO_2 supports [166, 167]. The nuclei of interest in studies of SnO_2 is ^{119}Sn. ^{119}Sn NMR studies have also been conducted on pyrochlores ($Ln_2Sn_2O_7$ where Ln is a lanthanide) which are catalysts for the oxidative coupling of methane [168–170]. In such investigations, analyses of the NMR lineshape, in addition to information gained from the chemical shift value, have proved informative in extracting structural information, notably on the ionic radius of Sn atoms in such compounds.

Gallium oxide (Ga_2O_3) is also used as a support material for metal catalysts in addition to being a photocatalyst in its own right [94, 171–175]. As with Al_2O_3, different polymorphs of Ga_2O_3 exist, with the distribution of gallium coordination environments differing between polymorphs. For instance, in β-Ga_2O_3 50% of Ga atoms are located in tetrahedral sites and 50% in octahedral sites. α-Ga_2O_3 contains only octahedral Ga sites.

There are two NMR active isotopes of gallium, both of which, like ^{27}Al, are quadrupolar. These are ^{71}Ga (40% natural abundance, spin = 3/2) and ^{69}Ga (60% natural abundance, spin = 3/2). Solid-state NMR studies of Ga_2O_3, however, present a much greater technical challenge than the study of Al_2O_3. As discussed above, in ^{27}Al NMR spectra the second-order quadrupolar broadening can be reduced through the application of high magnetic fields and, in MAS experiments, high spinning rates. This allows for the resolution of different sites without interference from overlapping spinning side-bands. For ^{71}Ga, however, the second-order quadrupolar broadening is so large that even at high magnetic fields and MAS spinning rates spectra can remain unresolved. As a result the resolution of static spectra is greater than that of those acquired under MAS conditions. The quadrupolar moment of ^{69}Ga is 70% larger than that of ^{71}Ga, accentuating the difficulties encountered with ^{71}Ga. As a result the majority of studies have focused on ^{71}Ga NMR, despite the lower natural abundance of this nucleus. These problems have been discussed in detail by a number of workers [28, 136, 176, 177].

Significant progress in overcoming these challenges was made through the work of Massiot and coworkers on the Quadrupolar Phase Adjusted Spinning Sideband (QPASS) technique [136, 176–180]. QPASS is a two-dimensional NMR technique that separates spinning sidebands (ssbs) before summing them to reconstruct an infinite spinning rate spectrum. This removes the problem of overlapping ssbs; however, it comes at the expense of significantly greater acquisition times. Figure 5.25 shows a comparison of static, MAS and the projected QPASS spectra for β-Ga_2O_3. Two different sites, corresponding to tetrahedral and octahedrally coordinated Ga nuclei, are observed. As for Al_2O_3 chemical shifts of Ga are indicative of the coordination environment. Tetrahedrally coordinated Ga typically has a chemical shift around 200 ppm, 5-coordinate Ga is ~75 ppm and 6-coordinate Ga ~0 ppm. As with Al NMR, peak asymmetry, with an upfield tail, indicates a distortion from ideal geometry.

Ash and coworkers have studied a wide variety of model compounds containing Ga in different coordination environments [29]. Employing a range of solid-state NMR techniques including Variable Offset Cumulative Spectra (VOCS), Rotor-Assisted Population Transfer (RAPT), SATRAS and MQMAS NMR to overcome the difficulties associated with gallium nuclei, and probing both ^{69}Ga and ^{71}Ga, the dependence of chemical shift on coordination environment has been clearly shown. Furthermore, through consideration of the magnitude of the electric field gradient, the influence of the second coordination sphere can be observed, and charged environments (e.g. GaO_4^-) can be easily distinguished from neutral ones (e.g. GaO_4). Solid-state NMR is therefore, in the case of Ga, more sensitive to such properties than solution NMR.

The relationship of gallium oxide structure, as revealed by NMR, to catalytic activity in the conversion of methanol to diethyl ether has been investigated by

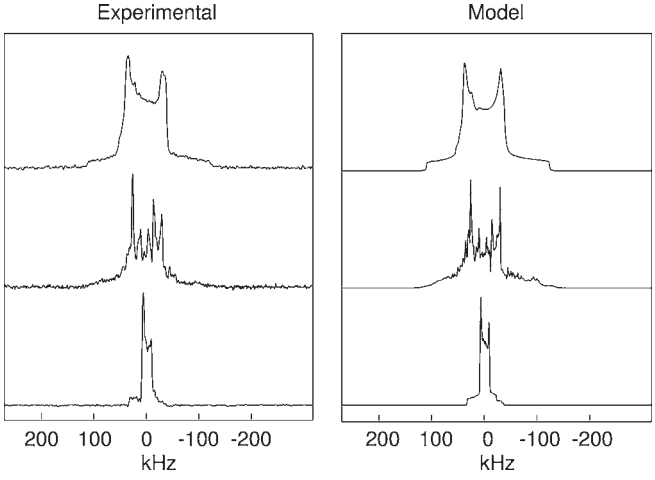

Figure 5.25 Static, MAS and QPASS spectra of β-Ga_2O_3. Adapted from ref. [177]; reprinted with permission from EDP Sciences.

Lavalley [181], revealing that both α- and β-Ga_2O_3 showed the same apparent rate despite the differences in their bulk structure. This surprising result was explained through the proposed similarity of the surface properties of the materials under reaction conditions. Other Ga-containing catalyst systems have been investigated through the efforts of a number of research groups [136, 138–140].

5.4 Surface Properties of Metal Oxides

Section 5.3 considered NMR spectroscopic approaches to the bulk characterization of oxides and oxidation catalysts. Catalytic activity is, however, intrinsically linked with the nature of the catalyst surface and hence a number of techniques have been developed in order to probe this. As discussed in Section 5.1, two of the most significant parameters impacting on catalyst activity are the acid–base characteristics of a surface and the redox properties of the material, and NMR techniques exist to probe both of these characteristics. One of the most common techniques to probe surface structure is CP-MAS NMR, in particular CP from hydrogen to the nucleus of interest – either the metal or the oxygen of the metal oxide. Historically, the source of surface ^1H species has often been those naturally present on the catalyst surface, as chemisorbed hydroxyls or physisorbed water. As such, much of the work in this area involves the study of supports such as SiO_2. Applications of CP-MAS and other spectroscopic approaches to the study of oxide surfaces are outlined in the following sections.

5.4.1 Surface Structure

The most widely employed tool to probe the surface structure of oxide catalysts is CP-MAS NMR. Sindorf and Maciel first demonstrated $^1H \rightarrow {}^{29}Si$ CP in 1980 [182], in a study of the surface of silica gels. A discussion of the development of CP and other surface characterization techniques is provided by Maciel and Ellis [183]. More recently Aramendia and coworkers have applied CP-MAS NMR to the study of the silica support of a Pd/SiO_2 catalyst [184]. Figure 5.26 shows the CP-MAS NMR spectrum of a silica support showing three distinct signals at –110, –101 and –92 ppm, which are assigned to Si atoms in Si—O tetrahedra of the SiO_2 structure, silanol groups and silanodiol groups respectively.

Sasikala and coworkers have employed ^1H-^{29}Si CP-MAS NMR in the study of VO_x/SiO_2 catalysts [97]. They have acquired spectra of SiO_2, modified silica samples and vanadia-impregnated samples and have compared them to ^{29}Si single-pulse and CP-MAS NMR spectra. Surface hydroxyl groups provide the ^1H source in these experiments. The CP-MAS technique is inherently sensitive to the structure of the surface silica units. This allows a number of distinct silica units on the surface to be identified, something that is impossible through conventional single-pulse MAS NMR. The effect of vanadium impregnation is to reduce the intensity of the

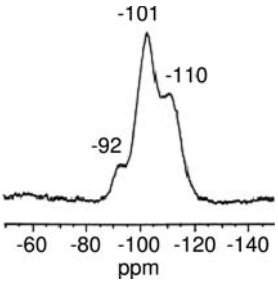

Figure 5.26 ^{29}Si CP-MAS NMR spectrum of an SiO_2 catalyst support. Adapted from ref. [184]; reprinted with permission from Elsevier.

peak corresponding to silica units comprising two SiO_4 tetrahedra attached to Si^{4+} (manifested as the shoulder on the downfield side of the peak at ~−100 ppm). This is due to the breakage of Si—O—Si units in larger structural units.

In addition to studies of silica supports work has also been carried out focusing on aluminas. However, the application of $^1H \rightarrow {}^{27}Al$ CP-MAS NMR is complicated as compared to $^1H \rightarrow {}^{29}Si$ CP, as this involves transfer between a half-integer nucleus (^1H) and a quadrupolar nucleus (^{27}Al). The issues surrounding this have, however, been discussed in depth by a number of workers [183, 185–190]. Despite these challenges, the application of $^1H \rightarrow {}^{27}Al$ CP-MAS NMR to catalytic systems has been successfully demonstrated. The first such study was carried out by Morris and Ellis in 1989 [186] for hydrated γ-Al_2O_3. However, this was only partially successful as it failed to observe any tetrahedrally coordinated surface aluminum as result of processes which are unfavorable to CP, including fast spin–lattice relaxation [186].

Some of the problems with CP from adsorbed hydroxyls or water molecules can be overcome through adsorbing a hydrogen-containing base molecule, such as pyridine, and using this as the source of ^1H species [186]. This allows the surface to be dehydroxylated, eliminating the possibility of dynamic surface processes providing highly efficient quadrupolar relaxation pathways broadening signals beyond detection. Furthermore, as demonstrated by Coster and coworkers [191], chemisorbed water induces surface reconstruction of aluminas. Therefore, CP-MAS NMR spectra acquired from hydrated alumina surfaces do not represent the true nature of the surface during catalytic operation. Ammonia may used in the same manner as pyridine to provide a ^1H source for $^1H \rightarrow {}^{27}Al$ CP-MAS NMR experiments. This has been exploited by Alvarez and coworkers [192], who compared the distribution of 4-, 5- and 6- coordinate Al atoms at the surface, as indicated by CP-MAS, with molecular dynamics simulations. Good agreement was achieved between theory and experiment.

In addition to CP to the metal nuclei in metal oxides, $^1H \rightarrow {}^{17}O$ or $M \rightarrow {}^{17}O$ (where M is a metal nucleus) CP-MAS NMR is also possible. The pioneering work in this area was conducted by Oldfield and coworkers [38, 124, 149, 193]. In a study of SiO_2, a previously unobserved resonance for amorphous silica, assigned to silanol (Si—O—H) sites present on the surface, was identified through the use of

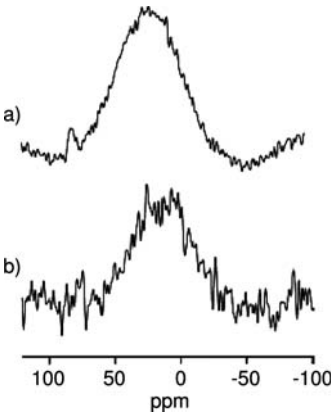

Figure 5.27 ^{17}O cross-polarized MAS NMR spectra of (a) 35% ^{17}O-enriched and (b) natural abundance boehmite. In both cases, the MAS rate was 7 kHz. Adapted from ref. [53]; reprinted with permission from Elsevier.

$^{17}O \rightarrow {}^{1}H$ CP. Ashbrook and Smith have reviewed the application of ^{17}O NMR techniques, including $^{1}H \rightarrow {}^{17}O$ CP-MAS NMR, to oxygen-containing materials [194]. Ashbrook and coworkers had previously performed $^{1}H \rightarrow {}^{17}O$ CP-MAS NMR to boehmite, an aluminum hydroxide precursor to catalytic aluminas [53]. This allowed the observation of the hydroxyl oxygen species at natural abundance levels, providing significant sensitivity gains over conventional NMR methods. Spectra were also acquired of ^{17}O-enriched boehmite which, as Figure 5.27 shows, provides a significant signal enhancement.

5.4.2 Surface Acidity

In addition to understanding the bulk structure of catalysts and the distribution of bulk nuclei at the surface, an appreciation of the number and nature of acid sites is also of key importance. A number of NMR techniques have been developed in order to probe both Lewis and Brønsted acidity at surfaces, and extensive reviews on many of them have been produced by various authors [183, 195, 196].

5.4.2.1 Brønsted Acid Sites

Brønsted acid sites can be directly probed through solid-state ^{1}H NMR spectroscopy, as chemical shifts can be correlated with acid strength [195, 197, 198]. The precise chemical shift observed for any given Brønsted acid site is dependent on the material upon which it is located. For instance, on silica values of ~1.6 ppm are typically observed; zirconia has two distinct OH sites, at 2.4 and 4.8 ppm; while on alumina a typical range may be –0.2 to 4.3 ppm. Early studies employing ^{1}H NMR to study Brønsted acid sites focused on the characterization of the surface of amorphous silica–alumina materials [165, 199–201]. Extensive work, however,

has also been conducted on supported catalysts and catalyst supports, including alumina-supported catalysts.

The possible coordination environments of OH groups on Al_2O_3 is dictated by the surface termination of the alumina; thus a wider variety of OH sites is possible on γ-Al_2O_3, which contains both octahedrally and tetrahedrally coordinated Al nuclei, than on α-Al_2O_3 in which only octahedral sites are present. The interaction between OH groups and the surface of a transition alumina, and alumina-supported vanadia and molybdenum catalysts, has been probed by ^{1}H MAS NMR spectroscopy [202]. In all cases a number of distinct OH sites are clearly identified. The effect of vanadia deposition on Al_2O_3 is to titrate the surface hydroxyl groups, with the most basic groups being titrated preferentially (Figure 5.28). ^{1}H MAS NMR also reveals unreacted alumina hydroxyls present in the catalysts, which are located in closed pores of the alumina support. These were not directly detectable by IR spectroscopy. In the same work, deuteration experiments indicate the presence of some accessible ^{1}H nuclei present only at high vanadia loadings. These ^{1}H species, also not revealed by IR studies, are suspected to be Brønsted sites. These sites are not removed, even at monolayer coverages of vanadium oxide. In addition to alumina-supported catalysts, Mastikhin and coworkers have also, through ^{1}H MAS NMR, investigated Brønsted acid sites on V/SnO_2, V/Sb_2O_4 [75], V/TiO_2-ZrO_2, [76], V/TiO_2 [81], $V/AlPO_4$ [203], V/TiO_2-SiO_2 [83] and (VO_x/WO_y)/(TiO_2-Al_2O_3) [85] catalysts.

Wang and coworkers have studied the strength and concentration of acid sites on a MoO_x/SnO_2 catalyst [167]. As shown in Figure 5.29, at least two ^{1}H signals

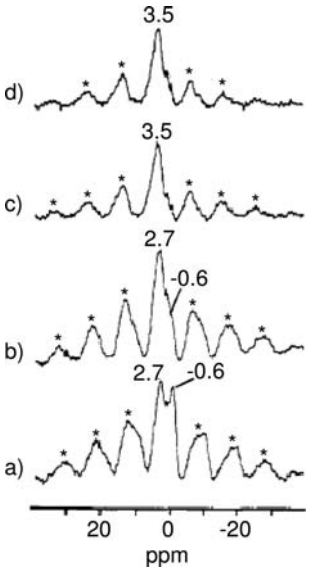

Figure 5.28 ^{1}H MAS NMR spectra of VO_x/Al_2O_3 catalysts as a function of vanadium oxide content: (a) 0%, (b) 5%, (c) 17%, and (d) 19%. Asterisks denote spinning sidebands. Adapted from ref. [202]; reprinted with permission from Elsevier.

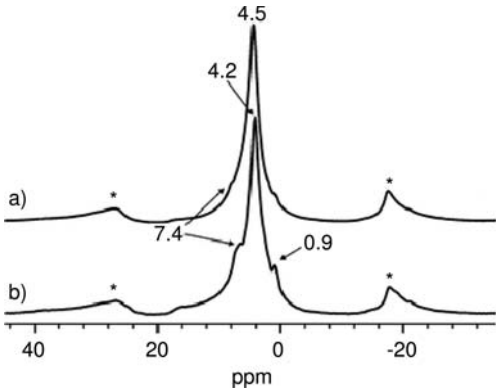

Figure 5.29 ^{1}H MAS spectra of SnO_2 support (a) and MoO_3/SnO_2 catalyst (b). The asterisk denotes spinning sidebands. Adapted from ref. [167]; reprinted with permission from the Royal Society of Chemistry.

(0.9 and 4.2 ppm) corresponding to OH groups are observed over the pure support. Deposition of molybdenum species onto the support results in a shift of the downfield peak to 4.5 ppm, and the intensity of the signal at 0.9 ppm is reduced, most probably indicating the interaction of Mo with the surface Sn—OH groups. Elsewhere ^{1}H MAS NMR has been applied to the study of the coordination of OH groups on MgO [204] and to SiO_2, $AlPO_4$ and $Mg_3(PO_4)_2$, which are used as supports for palladium hydrogen-transfer hydrogenation catalysts [184]. Figure 5.30

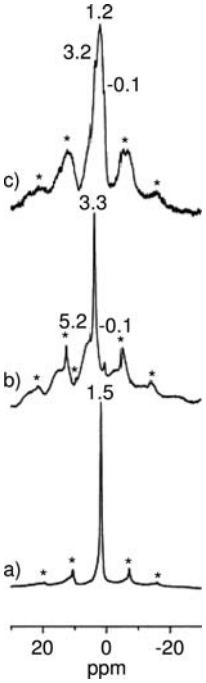

Figure 5.30 ^{1}H MAS NMR spectra for (a) SiO_2, (b), $AlPO_4$ and (c) $Mg_3(PO_4)_2$ supports. Sidebands are marked with an asterisk. Adapted from ref. [184]; reprinted with permission from Elsevier.

compares the ^{1}H MAS NMR spectra for these three materials. The SiO_2 spectrum contains only one peak, at 1.8 ppm, corresponding to isolated Si—OH groups; $AlPO_4$ contains two distinct OH groups as shown by signals at –0.1 and 3.3 ppm; while the spectrum of $Mg_3(PO_4)_2$ contains three distinct hydroxyl peaks (3.1, 1.2 and –0.1 ppm) that have been assigned to P—OH, Mg—OH and basic Mg—OH groups, respectively.

In addition to conventional ^{1}H MAS NMR measurements, more sophisticated techniques such as CRAMPS [201] and spin-echo double resonance [205] can be applied to the study of surface hydroxyl groups. Deng and coworkers [205] have applied ^{1}H{^{23}Na} double resonance to the study of Na_2CO_3–γ-Al_2O_3 catalysts. Through this it can be deduced with which surface nuclei different OH groups are associated. In particular, under the strong irradiation of sodium during the spin-echo experiment the ^{1}H signals corresponding to hydroxyl groups strongly associated with sodium atoms will be suppressed, while those associated with other surface species will remain unaffected. In this example three distinct surface OH groups were identified, manifested in signals at 0 ppm (more basic Al—OH), 2 ppm (more acidic Al—OH) and 4.5 ppm (OH associated with Na).

Taking a similar approach, Crepeau and coworkers have conducted ^{1}H{^{27}Al} TRAPDOR experiments on silica–alumina catalysts in order to distinguish ^{1}H nuclei on sites adjacent to Al nuclei from other OH groups [206]. Two types of ^{1}H species are observed in conventional ^{1}H MAS spectra – at 1.8 and 2.8 ppm. During the TRAPDOR experiment the use of ^{27}Al irradiation during ^{1}H signal acquisition suppresses the signal from hydrogen nuclei in close proximity to aluminum atoms. As Figure 5.31 shows, this results in the suppression of the ^{1}H signal at 2.8 ppm. These nuclei, representing a relatively small fraction of the

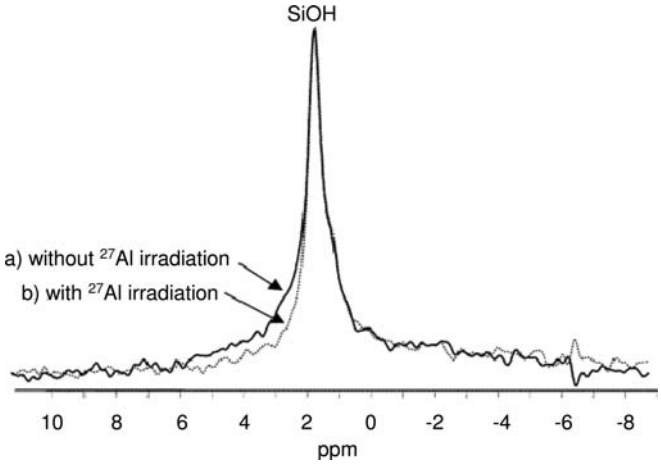

Figure 5.31 ^{1}H {^{27}Al} TRAPDOR experiment of Si_4OAl_6O (Spinning rate = 10 kHz. B_0 = 9.4 T). The full and the dotted lines correspond, respectively, to ^{1}H MAS spectrum acquired without and with ^{27}Al irradiation. Adapted from ref. [206]; reprinted with permission from the American Chemical Society.

total ^{1}H density, are therefore located close to Al sites. The majority of hydrogen nuclei are therefore located further from Al sites and are therefore likely to exist as silanol groups.

In addition to directly probing Brønsted acid sites through ^{1}H NMR, characterization can also be carried out through observing the resonance of an appropriate probe molecule. The ^{31}P-resonance of organic phosphine and phosphine oxides bound to Brønsted acid sites is distinct from that of the same materials bound to Lewis acid sites [207–209]. Again the chemical shift can be correlated with acid strength, with higher chemical shifts corresponding to more acidic sites. Such a method has been employed by Wang and coworkers to characterize acid sites on MoO_x/SnO_2 catalysts using trimethylphosphine as the probe molecule [167].

Chen and coworkers employed trimethylphosphine oxide (TMPO) as the probe molecule to characterize pure and sulfated zirconia both with and without a metal promoter [210]. On pure ZrO_2 resonances were detected at 62, 53, 41 and 34 ppm. The peaks at 53 and 62 ppm correspond to physisorbed TMPO while the peaks at 62 and 53 ppm can be assigned to TMPO adsorbed on Brønsted (B) and/or Lewis (L) acid sites. Upon hydration the intensity of both these signals diminished, indicating that they in fact correspond to Lewis acid sites. Had they been Brønsted sites the interaction between TMPO and the catalyst would have been too strong to be influenced by hydration. Upon addition of a metal promoter additional resonances are observed at 87, 76, 68 and 65 ppm. Hydration experiments confirm that these new sites are Brønsted acid sites. Furthermore, quantification of the distinct acid sites identified on the catalyst has been carried out, based on the assumption that each TMPO molecule can only be adsorbed on one acid site.

In addition to organic phosphines and phosphine oxides, other probe molecules which have been successfully employed in the study of Brønsted sites include alkanenitriles [211–213] (^{13}C and ^{15}N NMR), acetone [167] and CO [214] (^{13}C NMR).

5.4.2.2 Lewis Acid Sites

As alluded to above, probe molecules such as organic phosphates can also be used to probe Lewis acid sites. However, the most common probe molecules employed are nitrogen-containing species, in particular ammonia, alkylamines and pyridine. For the latter two either ^{13}C or ^{15}N NMR techniques may be applied; however, ^{15}N NMR is generally preferred as the resultant spectra appear less complex and, as adsorption to the surface occurs via the nitrogen atom, the observed resonance shifts are larger than they would be for ^{13}C spectra. The development of this method to investigate Lewis acidity of aluminas and silica–aluminas has previously been discussed in detail by Eckert [196] and by Maciel and Ellis [183] and will only briefly be recapped here.

The initial studies demonstrating the feasibility of using probe molecules to study acid sites were conducted by Gay and coworkers from 1977 onwards [215, 216]. This approach was further developed by Dawson and coworkers who employed ^{13}C CP-MAS NMR to investigate the number and nature of acid sites on γ-Al_2O_3 through the adsorption of *n*-butylamine and pyridine [217, 218]. In the case of

n-butylamine adsorption, four distinct resonances, at ~49, 40, 33 and 30 ppm, were identified in the region expected for the two α and β carbons of the butyl group. By comparison with spectra of solid HCl and BCl_3 adducts of *n*-butylamine, a Lewis acid adsorption site (where the alkylamine is bonded directly to a surface Al) is clearly identified. The fact that the chemical shift of these peaks is higher than the corresponding peaks for the BCl_3 adduct shows that the γ-Al_2O_3 surface Lewis acid site is stronger than BCl_3.

This field, including the shift of focus to ^{15}N MAS and CP-MAS NMR of ^{15}N-enriched adsorbates, was subsequently developed by a number studies on materials such as γ-alumina and amorphous silica–aluminas [211–213, 219–222]. Similarly, solid-state ^{15}N NMR studies employing N_2O as the adsorbate have also yielded success [83, 85, 223].

The use of ^{15}N spectroscopy fell out of favor as a means of characterizing acid sites, as probe molecules such as pyridine can undergo fast chemical exchange on some catalysts at room temperature [224]. However, Haw and coworkers [225] addressed this problem by conducting experiments at a sufficiently low temperature to ensure slow-exchange spectra. This approach also resulted in higher sensitivity through improved CP efficiency, the Boltzmann factor and reduced coil noise. Figure 5.32 shows a pyridine-^{15}N NMR titration of sulfated zirconia. Peaks

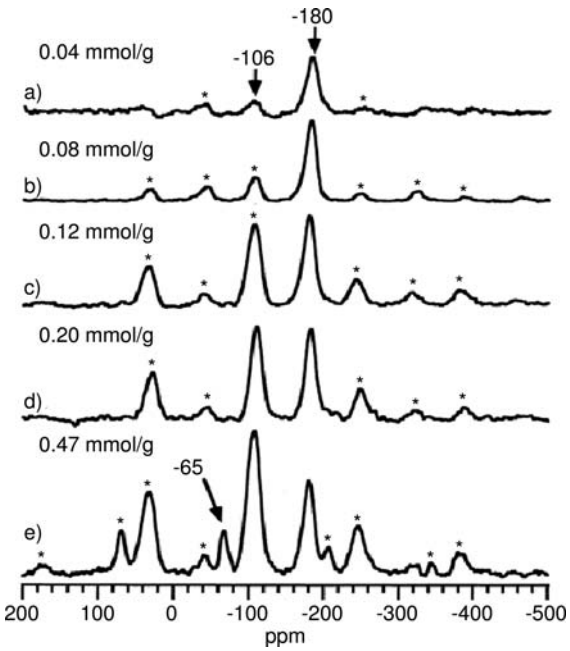

Figure 5.32 ^{15}N CP-MAS spectra of pyridine-^{15}N titrating sulfated zirconia (4.57 wt% S): (a) 0.04 mmol/g, (b) 0.08 mmol/g, (c) 0.12 mmol/g, (d) 0.20 mmol/g, and (e) 0.47 mmol/g. Adapted from ref. [225]; reprinted with permission from the American Chemical Society.

at –180 ppm and –106 ppm, are assigned to Brønsted and Lewis acid sites respectively. The peak at –65 ppm corresponds to excess titrant.

Shimizu and coworkers have also studied pyridine adsorption over zirconia-based catalysts – in this case tungstated zirconia [226]. In this work ^{15}N MAS NMR experiments (spinning speed 5–7 kHz) were carried out at 140 K, providing the advantages of low-temperature studies described above. Reduced zirconia, with no tungsten, yields a ^{15}N NMR spectrum with only one peak at –96 ppm. This can be assigned to pyridine bound to Lewis acid sites. Upon the addition of tungsten three peaks were observed, at –72 ppm, –108 ppm and –181 to –173 ppm. These were assigned to physisorbed pyridine, Lewis complexes and Brønsted complexes respectively. Brønsted acid sites were stronger after reduction of the tungstated catalyst, an effect which was deemed to result in enhanced activity of the catalysts for *o*-xylene isomerization.

5.5 Outlook

The development of new and improved NMR techniques is continual and fast-paced, with the range of systems that are suitable for study and the information that can be elucidated from them increasing all the time. Recent years have seen a shift away from one-dimensional NMR techniques towards two-dimensional techniques, such as MQMAS, which are often capable of providing higher resolution. In particular, the recent development of the SATRAS technique opens up new possibilities. In addition to the applications outlined above, Antonijevic and coworkers [28] have reported on the use of SATRAS to study host–guest interactions and guest dynamics in framework solids. Nuclei that could be studied by this method include ^{17}O, ^{23}Na, ^{27}Al and ^{71}Ga.

Existing techniques are also likely to be applied to a wider range of nuclei as they become increasingly established. For instance, MQMAS has, to date, been applied to a relatively small number of nuclei but recent studies have begun to expand this number, for example to ^{51}V [27]. Advances in technical capabilities may also prove significant, as higher field strengths and, in the case of MAS, spinning rates become accessible. This will lead to increased information being extracted from existing techniques as spectral resolution improves.

NMR is a valuable tool for acquiring important information that provides real insights into catalyst structure and catalytic behavior. In the coming years, however, improvements in hardware are likely to result in NMR becoming even more significant as experiments reveal ever more information and developments within other fields become adopted for the study of catalysts.

Acknowledgments

The ATHENA project, supported by EPSRC of the UK and Johnson Matthey plc. is gratefully acknowledged for funding aspects of the research reported herein.

Additionally, Drs Melinda J. Duer and Robin Stein of the University of Cambridge, Department of Chemistry, are thanked for conducting the experiment described in Figure 5.23. Finally, Prof. Lynn F. Gladden of the University of Cambridge, Department of Chemical Engineering, is thanked for her valuable input and guidance in the preparation of this chapter.

References

1 Madeira, L.M. and Portela, M.F. (2002) *Catalysis Reviews–Science and Engineering*, **44**, 247.
2 Grzybowska-Swierkosz, B. (2000) *Topics in Catalysis*, **11**, 23.
3 Dunn, J.P., Stenger, H.G. and Wachs, I.E. (1999) *Catalysis Today*, **51**, 301.
4 Hucknall, D.J. (1974) *Selective Oxidation of Hydrocarbons*, Academic Press, New York.
5 Jackson, S.D., Rugmini, S., Stair, P.C. and Wu, Z.L. (2006) *Chemical Engineering Journal*, **120**, 127.
6 Wu, Z.L. and Stair, P.C. (2006) *Journal of Catalysis*, **237**, 220.
7 Jackson, S.D. and Rugmini, S. (2007) *Journal of Catalysis*, **251**, 59.
8 Sloczynski, J., Grabowski, R., Kozlowska, A., Tokarz-Sobieraj, R. and Witko, M. (2007) *Journal of Molecular Catalysis A: Chemical*, **277**, 27.
9 Mars, P. and van Krevelen, D.W. (1954) *Chemical Engineering Science*, **3**, 41.
10 Hunger, M. and Wang, W. (2006) Characterization of solid catalysts in the functioning state by nuclear magnetic resonance spectroscopy. *Advances in Catalysis*, **50**, 149.
11 Hunger, M. and Weitkamp, J. (2001) *Angewandte Chemie–International Edition*, **40**, 2954.
12 Roe, D.C., Kating, P.M., Krusic, P.J. and Smart, B.E. (1998) *Topics in Catalysis*, **5**, 133.
13 Bonardet, J.L., Barrage, M.C. and Fraissard, J. (1996) NMR techniques for studying the coking of zeolite-based catalysts, in *Deactivation and Testing of Hydrocarbon-Processing Catalysts* (eds P. O'Connor, T. Takatsuka and G.L. Woolery), American Chemical Society, Washington DC, 1996, 99.
14 Derouane, E.G., Fraissar, J., Fripiat, J.J. and Stone, W.E.E. (1972) *Catalysis Reviews–Science and Engineering*, **7**, 121.
15 Haw, J.F. (1994) In Situ NMR, in *NMR Techniques in Catalysis* (eds A.T. Bell and A. Pines), Marcel Dekker. Inc., New York, p. 195.
16 Gladden, L.F., Mantle, M.D. and Sederman, A.J. (2006) Magnetic resonance imaging of catalysts and catalytic processes. *Advances in Catalysis*, **50**, 1.
17 Callaghan, P.T. (1991) *Principles of Nuclear Magnetic Resonance Microscopy*, Clarendon Press, Oxford.
18 Laws, D.D., Bitter, H.-M.L. and Jerschow, A. (2002) *Angewandte Chemie–International Edition*, **41**, 3096.
19 Llor, A. and Virlet, J. (1988) *Chemical Physics Letters*, **152**, 248.
20 Duer, M.J. (2004) *Introduction to Solid-State NMR Spectroscopy*, Blackwell, Oxford.
21 Kentgens, A.P.M. (1997) *Geoderma*, **80**, 271.
22 Frydman, L. and Harwood, J.S. (1995) *Journal of the American Chemical Society*, **117**, 5367.
23 Medek, A., Harwood, J.S. and Frydman, L. (1995) *Journal of the American Chemical Society*, **117**, 12779.
24 Kraus, H., Prins, R. and Kentgens, A.P.M. (1996) *Journal of Physical Chemistry*, **100**, 16336.
25 Gan, Z. (2000) *Journal of the American Chemical Society*, **122**, 3242.
26 Ashbrook, S.E. and Wimperis, S. (2002) *Journal of Magnetic Resonance*, **156**, 269.
27 Lapina, O.B., Khabibulin, D.F., Shubin, A.A. and Bondareva, V.M. (2000) *Journal of Molecular Catalysis A: Chemical*, **162**, 373.
28 Antonijevic, S., Ashbrook, S.E., Biedasek, S., Walton, R.I., Wimperis, S. and Yang, H.X. (2006) *Journal of the American Chemical Society*, **128**, 8054.

29 Ash, J.T. and Grandinetti, P.J. (2006) *Magnetic Resonance in Chemistry*, **44**, 823.

30 Samoson, A. and Lippmaa, E. (1983) *Physical Review B*, **28**, 6567.

31 Samoson, A. and Lippmaa, E. (1983) *Chemical Physics Letters*, **100**, 205.

32 Kentgens, A.P.M. (1998) *Progress in Nuclear Magnetic Resonance Spectroscopy*, **32**, 141.

33 Li, J., Lashier, M.E., Schrader, G.L. and Gerstein, B.C. (1991) *Applied Catalysis*, **73**, 83.

34 Tuel, A., SananesSchulz, M.T. and Volta, J.C. (1997) *Catalysis Today*, **37**, 59.

35 Lopez-Sanchez, J.A., Griesel, L., Bartley, J.K., Wells, R.P.K., Liskowski, A., Su, D.S., Schlogl, R., Volta, J.C. and Hutchings, G.J. (2003) *Physical Chemistry Chemical Physics*, **5**, 3525.

36 Simon-Masseron, A., Josien, L., Delmotte, L. and Patarin, J. (2004) *Microporous and Mesoporous Materials*, **71**, 143.

37 Sananes, M.T. and Tuel, A. (1996) *Solid State Nuclear Magnetic Resonance*, **6**, 157.

38 Haase, J. and Oldfield, E. (1994) *Solid State Nuclear Magnetic Resonance*, **3**, 171.

39 Hartmann, S.R. and Hahn, E.L. (1962) *Physical Review*, **128**, 2042.

40 Qu, L.L., Zhang, W.P., Kooyman, P.J. and Prins, R. (2003) *Journal of Catalysis*, **215**, 7.

41 Vaneck, E.R.H. and Veeman, W.S. (1993) *Solid State Nuclear Magnetic Resonance*, **2**, 307.

42 Gullion, T. and Schaefer, J. (1989) *Journal of Magnetic Resonance*, **81**, 196.

43 Gullion, T. (1995) *Journal of Magnetic Resonance Series A*, **117**, 326.

44 Gullion, T. (1995) *Chemical Physics Letters*, **246**, 325.

45 Wang, P.K., Slichter, C.P. and Sinfelt, J.H. (1984) *Physical Review Letters*, **53**, 82.

46 Hing, A.W., Vega, S. and Schaefer, J. (1992) *Journal of Magnetic Resonance*, **96**, 205.

47 Gray, C.P., Veeman, W.S. and Vega, A.J. (1993) *Journal of Chemical Physics*, **98**, 7711.

48 Gray, C.P. and Veeman, W.S.G (1992) *Chemical Physics Letters*, **192**, 379.

49 Yang, J., Zhang, M.J., Deng, F., Luo, Q., Yi, D.L. and Ye, C.H. (2003) *Chemical Communications*, 884.

50 Levitt, M.H. (2005) *Spin Dynamics: Basics of Nuclear Magnetic Resonance*, John Wiley & Sons, Ltd, Chichester.

51 Callaghan, P.T. (1993) *Principles of Nuclear Magnetic Resonance Microscopy*, Oxford University Press, Oxford, p. 516.

52 Cheng, J.T. and Ellis, P.D. (1989) *Journal of Physical Chemistry*, **93**, 2549.

53 Ashbrook, S.E. and Farnan, I. (2004) *Solid State Nuclear Magnetic Resonance*, **26**, 105.

54 Waugh, J.S., Huber, L.M. and Haeberlen, V. (1986) *Physical Review Letters*, **20**, 180.

55 Burum, D.P. and Rhim, W.K. (1979) *Journal of Chemical Physics*, **71**, 944.

56 Fitzgerald, J.J., Piedra, G., Dec, S.F., Seger, M. and Maciel, G.E. (1997) *Journal of the American Chemical Society*, **119**, 7832.

57 Weckhuysen, B.M., van der Voort, P. and Catana, G. (2000) *Spectroscopy of Transition Metal Ions on Surfaces*, Leuven University Press, Leuven.

58 Harding, W.D., Birkeland, K.E. and Kung, H.H. (1994) *Catalysis Letters*, **28**, 1.

59 Michalakos, P.M., Birkeland, K. and Kung, H.H. (1996) *Journal of Catalysis*, **158**, 349.

60 Nieto, J.M.L., Concepcion, P., Dejoz, A., Knozinger, H., Melo, F. and Vazquez, M.I. (2000) *Journal of Catalysis*, **189**, 147.

61 Nieto, J.M.L., Concepcion, P., Dejoz, A., Melo, F., Knozinger, H. and Vazquez, M.I. (2000) *Catalysis Today*, **61**, 361.

62 Owens, L. and Kung, H.H. (1993) *Journal of Catalysis*, **144**, 202.

63 Owens, L. and Kung, H.H. (1994) *Journal of Catalysis*, **148**, 587.

64 Wada, K., Yamada, H., Watanabe, E. and Mitsudo, T. (1998) *Journal of the Chemical Society–Faraday Transactions*, **94**, 1771.

65 Wu, Z.L., Kim, H.S., Rugmini, S., Jackson, S.D. and Stair, P.C. (2005) *Abstracts of Papers of the American Chemical Society*, **229**, U863.

66 Wu, Z.L., Kim, H.S., Stair, P.C., Rugmini, S. and Jackson, S.D. (2005) *Journal of Physical Chemistry B*, **109**, 2793.

67 Magg, N., Immaraporn, B., Giorgi, J.B., Schroeder, T., Baumer, M., Dobler, J., Wu, Z.L., Kondratenko, E., Cherian, M., Baerns, M., Stair, P.C., Sauer, J. and Freund, H.J. (2004) *Journal of Catalysis*, **226**, 88.

68 Jackson, S.D., Lennon, D., Webb, G. and Willis, J. (2001) Processes occurring during deactivation/regeneration of a vanadia/alumina catalyst under propane dehydrogenation conditions. Paper presented at Catalyst Deactivation 2001: Proceedings of the 9th International Symposium, Lexington, KY, USA, October 2001, p. 271.

69 Weckhuysen, B.M. and Keller, D.E. (2003) *Catalysis Today*, **78**, 25.

70 Mastikhin, V.M., Lapina, O.B. and Simonova, L.G. (1984) *Reaction Kinetics and Catalysis Letters*, **24**, 127.

71 Chary, K.V.R., Rao, V.V. and Mastikhin, V.M. (1989) *Journal of the Chemical Society–Chemical Communications*, 202.

72 Narsimha, K., Reddy, B.M., Rao, P.K. and Mastikhin, V.M. (1990) *Journal of Physical Chemistry*, **94**, 7336.

73 Lapina, O.B., Mastikhin, V.M., Simonova, L.G. and Bulgakova, Y.O. (1991) *Journal of Molecular Catalysis*, **69**, 61.

74 Lapina, O.B., Mastikhin, V.M., Shubin, A.A., Krasilnikov, V.N. and Zamaraev, K.I. (1992) *Progress in Nuclear Magnetic Resonance Spectroscopy*, **24**, 457.

75 Reddy, B.M. and Mastikhin, V.M. (1992) *Solid State Nuclear Magnetic Resonance*, **1**, 245.

76 Reddy, B.M., Reddy, E.P., Srinivas, S.T., Mastikhin, V.M., Nosov, A.V. and Lapina, O.B. (1992) *Journal of Physical Chemistry*, **96**, 7076.

77 Sobalik, Z., Markvart, M., Stopka, P., Lapina, O.B. and Mastikhin, V.M. (1992) *Journal of Molecular Catalysis*, **71**, 69.

78 Lapina, O.B., Mastikhin, V.M., Nosov, A.V., Beutel, T. and Knozinger, H. (1992) *Catalysis Letters*, **13**, 203.

79 Zamaraev, K. (1993) *Journal of Molecular Catalysis*, **82**, 275.

80 Lapina, O.B., Nosov, A.V., Mastikhin, V.M., Dubkov, K.A. and Mokrinski, V.V. (1994) *Journal of Molecular Catalysis*, **87**, 57.

81 Pinaeva, L.G., Lapina, O.B., Mastikhin, V.M., Nosov, A.V. and Balzhinimaev, B.S. (1994) *Journal of Molecular Catalysis*, **88**, 311.

82 Lakshmi, L.J., Srinivas, S.T., Rao, P.K., Nosov, A.V., Lapina, O.B. and Mastikhin, V.M. (1995) *Solid State Nuclear Magnetic Resonance*, **4**, 59.

83 Mastikhin, V.M., Terskikh, V.V., Lapina, O.B., Filimonova, S.V., Seidl, M. and Knozinger, H. (1995) *Solid State Nuclear Magnetic Resonance*, **4**, 369.

84 Lapina, O.B., Shubin, A.A., Nosov, A.V., Bosch, E., Spengler, J. and Knozinger, H. (1999) *Journal of Physical Chemistry B*, **103**, 7599.

85 Mastikhin, V.M., Terskikh, V.V., Lapina, O.B., Filimonova, S.V., Seidl, M. and Knozinger, H. (1995) *Journal of Catalysis*, **156**, 1.

86 Kalinkin, P., Kovalenko, O., Lapina, O., Khabibulin, D. and Kundo, N. (2002) *Journal of Molecular Catalysis A: Chemical*, **178**, 173.

87 Lapina, O.B., Shubin, A.A., Khabibulin, D.F., Terskikh, V.V., Bodart, P.R. and Amoureux, J.P. (2003) *Catalysis Today*, **78**, 91.

88 Sohn, J.R., Han, J.S. and Lim, J.S. (2005) *Materials Chemistry and Physics*, **91**, 558.

89 Nielsen, U.G., Topsoe, N.Y., Brorson, M., Skibsted, J. and Jakobsen, H.J. (2004) *Journal of the American Chemical Society*, **126**, 4926.

90 Grasser, S., Haessner, C., Kohler, K., Lefebvre, F. and Basset, J.M. (2003) *Physical Chemistry Chemical Physics*, **5**, 1906.

91 Sohn, J.R., Seo, K.C. and Pae, Y.I. (2003) *Bulletin of the Korean Chemical Society*, **24**, 311.

92 Sohn, J.R., Han, J.S. and Lim, J.S. (2004) *Journal of Industrial and Engineering Chemistry*, **10**, 1003.

93 Radhika, T. and Sugunan, S. (2006) *Journal of Molecular Catalysis A: Chemical*, **250**, 169.

94 Pujol, A.P., Valenzuela, R., Fuerte, A., Wloch, E., Kubacka, A., Olejniczak, Z., Sulikowski, B. and Corberan, V.C. (2003) *Catalysis Today*, **78**, 247.

95 Evans, O.R., Bell, A.T. and Tilley, T.D. (2004) *Journal of Catalysis*, **226**, 292.

96 Wachs, I.E. and Weckhuysen, B.M. (1997) *Applied Catalysis A: General*, **157**, 67.

97 Sasikala, R., Sudarsan, V. and Kulshreshtha, S.K. (2006) *European Journal of Inorganic Chemistry*, 4151.

98 Banares, M.A. and Khatib, S.J. (2004) *Catalysis Today*, **96**, 251.

99 Steinfeldt, N., Muller, D. and Berndt, H. (2004) *Applied Catalysis A: General*, **272**, 201.

100 Shubin, A.A., Lapina, O.B. and Bondareva, V.M. (1999) *Chemical Physics Letters*, **302**, 341.

101 Shubin, A.A., Lapina, O.B., Bosch, E., Spengler, J. and Knozinger, H. (1999) *Journal of Physical Chemistry B*, **103**, 3138.

102 Hutchings, G.J. (1991) *Applied Catalysis*, **72**, 1.

103 Bruckner, A. (2003) *Catalysis Reviews–Science and Engineering*, **45**, 97.

104 Kung, H.H. (1994) Oxidative dehydrogenation of light (C-2 to C-4) alkanes. *Advances in Catalysis*, **40**, 1.

105 Abon, M., Bere, K.E., Tuel, A. and Delichere, P. (1995) *Journal of Catalysis*, **156**, 28.

106 Ben Abdelouahab, F., Olier, R., Guilhaume, N., Lefebvre, F. and Volta, J.C. (1992) *Journal of Catalysis*, **134**, 151.

107 Sananes, M.T., Tuel, A. and Volta, J.C. (1994) *Journal of Catalysis*, **145**, 251.

108 Guliants, V.V., Benziger, J.B., Sundaresan, S., Wachs, I.E., Jehng, J.M. and Roberts, J.E. (1996) *Catalysis Today*, **28**, 275.

109 Sananes, M.T. and Tuel, A. (1996) *Solid State Nuclear Magnetic Resonance*, **6**, 157.

110 Tuel, A., Sananes-Schulz, M.T. and Volta, J.C. (1997) *Catalysis Today*, **37**, 59.

111 Kiely, C.J., Burrows, A., Sajip, S., Hutchings, G.J., Sananes, M.T., Tuel, A. and Volta, J.-C. (1996) *Journal of Catalysis*, **162**, 31.

112 Siegel, R., Dupre, N., Quarton, M. and Hirschinger, J. (2004) *Magnetic Resonance in Chemistry*, **42**, 1022.

113 Vedrine, J.C., Millet, J.M.M. and Volta, J.C. (1989) *Faraday Discussions*, **87**, 207.

114 Mastikhin, V.M., Lapina, O.B. and Lyakhova, V.F. (1980) *Reaction Kinetics and Catalysis Letters*, **14**, 317.

115 Mastikhin, V.M., Lapina, O.B., Lyakhova, V.F. and Simonova, L.G. (1981) *Reaction Kinetics and Catalysis Letters*, **17**, 109.

116 Lapina, O.B., Simakov, A.V., Mastikhin, V.M., Veniaminov, S.A. and Shubin, A.A. (1989) *Journal of Molecular Catalysis*, **50**, 55.

117 Hardcastle, F.D., Wachs, I.E., Eckert, H. and Jefferson, D.A. (1991) *Journal of Solid State Chemistry*, **90**, 194.

118 Nielsen, U.G., Jakobsen, H.J. and Skibsted, J. (2003) *Solid State Nuclear Magnetic Resonance*, **23**, 107.

119 Ekambaram, S. and Patil, K.C. (1995) *Journal of Alloys and Compounds*, **217**, 104.

120 Nielsen, U.G., Skibsted, J. and Jakobsen, H.J. (2001) *Chemical Communications*, **29**, 2690.

121 Nielsen, U.G., Boisen, A., Brorson, M., Jacobsen, C.J.H., Jakobsen, H.J. and Skibsted, J. (2002) *Inorganic Chemistry*, **41**, 6432.

122 Xu, Z. and Stebbins, J.F. (1998) *Geochimica Et Cosmochimica Acta*, **62**, 1803.

123 Mastikhin, V.M., Lapina, O.B. and Simonova, L.G. (1984) *Reaction Kinetics and Catalysis Letters*, **26**, 431.

124 Oldfield, E. (1994) *Abstracts of Papers of the American Chemical Society*, **208**, 188.

125 Edwards, J.C., Adams, R.D. and Ellis, P.D. (1990) *Journal of the American Chemical Society*, **112**, 8349.

126 Edwards, J.C., Zubieta, J., Shaikh, S.N., Chen, Q., Bank, S. and Ellis, P.D. (1990) *Inorganic Chemistry*, **29**, 3381.

127 Edwards, J.C. and Ellis, P.D. (1991) *Langmuir*, **7**, 2117.

128 Segawa, K., Soeya, T. and Kim, D.S. (1991) *Research on Chemical Intermediates*, **15**, 129.

129 Han, O.H., Lin, C.Y., Sustache, N., McMillan, M., Carruthers, J.D., Zilm, K.W. and Haller, G.L. (1993) *Applied Catalysis A: General*, **98**, 195.

130 de Lacaillerie, J.B.D., Barberon, F., Romanenko, K.V., Lapina, O.B., Le Polles, L., Gautier, R. and Gan, Z.H. (2005) *Journal of Physical Chemistry B*, **109**, 14033.

131 Kraus, H. and Prins, R. (1996) *Journal of Catalysis*, **164**, 251.

132 Serebrennikova, Y.M., Fedotov, M.A., Nikitenko, S.G., Kochubei, D.I. and Startsev, A.N. (2002) *Kinetics and Catalysis*, **43**, 585.

133 Knobl, S., Zenkovets, G.A., Kryukova, G.N., Maksimovskaya, R.I., Larina, T.V., Vasenin, N.T., Anufrienko, V.F., Niemeyer, D. and Schlogl, R. (2003) *Physical Chemistry Chemical Physics*, **5**, 5343.

134 Hove, A.R., Bildsoe, H., Skibsted, J., Brorson, M. and Jakobsen, H.J. (2006) *Inorganic Chemistry*, **45**, 10873.

135 Gray, C.P., Smith, M.E., Cheetham, A.K., Dobson, C.M. and Dupree, R. (1990) *Journal of the American Chemical Society*, **112**, 4670.

136 Massiot, D., Revel, R., Magnenet, C. and Bazin, D. (2000) *Solid State Nuclear Magnetic Resonance*, **16**, 103.

137 Trokiner, A., Bessiere, A., Thouvenot, R., Hau, D., Marko, J., Nardello, V., Pierlot, C. and Aubry, J.-M. (2004) *Solid State Nuclear Magnetic Resonance*, **25**, 209.

138 Garcia-Sanchez, M., Magusin, P., Hensen, E.J.M., Thune, P.C., Rozanska, X. and van Santen, R.A. (2003) *Journal of Catalysis*, **219**, 352.

139 Jarry, B., Launay, F., Nogier, J.P., Montouillout, V., Gengembre, L. and Bonardet, J.L. (2006) *Applied Catalysis A: General*, **309**, 177.

140 Pal, P., Quartararo, J., Abd Hamid, S., Derouane, E., Vedrine, J., Magusin, P. and Anderson, B. (2005) *Canadian Journal of Chemistry-Revue Canadienne De Chimie*, **83**, 574.

141 Brengle, A.S., Sobrante, E. and Stewart, H.R. (1955) United States Patent 2,709,173.

142 Knozinger, H. and Ratnasamy, P. (1978) *Catalysis Reviews–Science and Engineering*, **17**, 31.

143 O'Reilly, D.E. (1958) *Journal of Chemical Physics*, **28**, 1262.

144 O'Reilly, D.E. (1960) *Advances in Catalysis*, **12**, 31.

145 Engelhardt, G. and Michel, D. (1987) *High-Resolution Solid-State NMR of Silicates and Zeolites*, John Wiley and Sons, Chichester.

146 Slade, R.C.T., Southern, J.C. and Thompson, I.M. (1991) *Journal of Materials Chemistry*, **1**, 563.

147 Bak, M., Rasmussen, J.T. and Nielsen, N.C. (2000) *Journal of Magnetic Resonance*, **147**, 296.

148 Goldbourt, A. and Madhu, P.K. (2005) Multiple-quantum magic-angle spinning: high-resolution solid-state NMR of half-integer spin quadrupolar nuclei. *Annual Reports on NMR Spectroscopy*, **54**, 81.

149 Walter, T.H. and Oldfield, E. (1989) *Journal of Physical Chemistry*, **93**, 6744.

150 Kunathfandrei, G., Bastow, T.J., Hall, J.S., Jager, C. and Smith, M.E. (1995) *Journal of Physical Chemistry*, **99**, 15138.

151 Lee, M.H., Cheng, C.F., Heine, V. and Klinowski, J. (1997) *Chemical Physics Letters*, **265**, 673.

152 Meinhold, R.H., Slade, R.C.T. and Newman, R.H. (1993) *Applied Magnetic Resonance*, **4**, 121.

153 Chen, F.R., Sheng, S.S., Zhang, W.M., Guo, X.X. and Fripiat, J.J. (1992) *Journal of the Chemical Society–Faraday Transactions*, **88**, 887.

154 MacKenzie, K.J.D., Temuujin, J. and Okada, K. (1999) *Thermochimica Acta*, **327**, 103.

155 Pecharroman, C., Sobrados, I., Iglesias, J.E., Gonzalez-Carreno, T. and Sanz, J. (1999) *Journal of Physical Chemistry B*, **103**, 6160.

156 Ollivier, B., Retoux, R., Lacorre, P., Massiot, D. and Ferey, G. (1997) *Journal of Materials Chemistry*, **7**, 1049.

157 Slade, R.C.T., Southern, J.C. and Thompson, I.M. (1991) *Journal of Materials Chemistry*, **1**, 875.

158 Paglia, G., Buckley, C.E., Rohl, A.L., Hart, R.D., Winter, K., Studer, A.J., Hunter, B.A. and Hanna, J.V. (2004) *Chemistry of Materials*, **16**, 220.

159 Iwamoto, R., Fernandez, C., Amoureux, J.P. and Grimblot, J. (1998) *Journal of Physical Chemistry B*, **102**, 4342.

160 Quartararo, J., Guelton, M., Rigole, M., Amoureux, J.P., Fernandez, C. and Grimblot, J. (1999) *Journal of Materials Chemistry*, **9**, 2637.

161 Quartararo, J., Rigole, M., Guelton, M., Amoureux, J.P. and Grimblot, J. (1999) *Journal De Chimie Physique Et De Physico-Chimie Biologique*, **96**, 1536.

162 Quartararo, J., Amoureux, J.P. and Grimblot, J. (2000) *Journal of Molecular Catalysis A: Chemical*, **162**, 353.

163 Brown, S.P. and Wimperis, S. (1997) *Journal of Magnetic Resonance*, **124**, 279.

164 Polarz, S., Neues, F., Berg, M.W.E., Grunert, W. and Khodeir, L. (2005) *Journal of the American Chemical Society*, **127**, 12028.

165 Cheung, T.T.P., Willcox, K.W., McDaniel, M.P., Johnson, M.M., Bronnimann, C. and Frye, J. (1986) *Journal of Catalysis*, **102**, 10.

166 Pilkenton, S. and Raftery, D. (2003) *Solid State Nuclear Magnetic Resonance*, **24**, 236.

167 Wang, J.Q., Su, Y.C., Xu, J., Ye, C.H. and Deng, F. (2006) *Physical Chemistry. Chemical Physics*, **8**, 2378.

168 Berry, F.J. (1981) *Advances in Catalysis*, **30**, 97.

169 Clayden, N.J., Dobson, C.M. and Fern, A. (1989) *Journal of the Chemical Society – Dalton Transactions*, 843.

170 Gray, C.P., Dobson, C.M., Cheetham, A.K. and Jakeman, R.J.B. (1989) *Journal of the American Chemical Society*, **111**, 505.

171 Hou, Y.D., Wang, W.C., Wu, L., Ding, Z.X. and Fu, X.Z. (2006) *Environmental Science and Technology*, **40**, 5799.

172 Choudhary, V.R., Samanta, C. and Choudhary, T.V. (2006) *Applied Catalysis A: General*, **308**, 128.

173 Michorczyk, P., Gora-Marek, K. and Ogonowski, J. (2006) *Catalysis Letters*, **109**, 195.

174 Collins, S.E., Baltanas, M.A. and Bonivardi, A.L. (2005) *Applied Catalysis A: General*, **295**, 126.

175 Fujitani, T., Saito, M., Kanai, Y., Watanabe, T., Nakamura, J. and Uchijima, T. (1995) *Applied Catalysis A: General*, **125**, L199.

176 Massiot, D., Farnan, I., Gautier, N., Trumeau, D., Trokiner, A. and Coutures, J.P. (1995) *Solid State Nuclear Magnetic Resonance*, **4**, 241.

177 Massiot, D., Montouillout, V., Fayon, F., Florian, P. and Bessada, C. (1998) *Journal De Chimie Physique Et De Physico-Chimie Biologique*, **95**, 270.

178 Massiot, D., Vosegaard, T., Magneron, N., Trumeau, D., Montouillout, V., Berthet, P., Loiseau, T. and Bujoli, B. (1999) *Solid State Nuclear Magnetic Resonance*, **15**, 159.

179 Massiot, D., Montouillout, V., Magnenet, C., Bessada, C., Coutures, J.P., Forster, H., Steuernagel, S. and Mueller, D. (1998) *Comptes Rendus De L Academie Des Sciences Serie Ii Fascicule C-Chimie*, **1**, 157.

180 Massiot, D., Montouillout, V., Fayon, F., Florian, P. and Bessada, C. (1997) *Chemical Physics Letters*, **272**, 295.

181 Lavalley, J.C., Daturi, M., Montouillout, V., Clet, G., Arean, C.O., Delgado, M.R. and Sahibed-dine, A. (2003) *Physical Chemistry Chemical Physics*, **5**, 1301.

182 Maciel, G.E. and Sindorf, D.W. (1980) *Journal of the American Chemical Society*, **102**, 7606.

183 Maciel, G.E. and Ellis, P.D. (1994) NMR characterization of silica and alumina surfaces, in *NMR Techniques in Catalysis* (eds A.T. Bell and A. Pines), Marcel Dekker, New York, p. 231.

184 Aramendia, M.A., Borau, V., Jimenez, C., Marinas, J.M., Ruiz, J.R. and Urbano, F.J. (2000) *Solid State Nuclear Magnetic Resonance*, **16**, 217.

185 Morris, H.D., Bank, S. and Ellis, P.D. (1990) *Journal of Physical Chemistry*, **94**, 3121.

186 Morris, H.D. and Ellis, P.D. (1989) *Journal of the American Chemical Society*, **111**, 6045.

187 Harris, R.K. and Nesbitt, G.J. (1988) *Journal of Magnetic Resonance*, **78**, 245.

188 Walter, T.H., Turner, G.L. and Oldfield, E. (1988) *Journal of Magnetic Resonance*, **76**, 106.

189 Woessner, D.E. (1987) *Zeitschrift Fur Physikalische Chemie Neue Folge*, **152**, 51.

190 Vega, S. (1981) *Physical Review A*, **23**, 3152.

191 Coster, D., Blumenfeld, A.L. and Fripiat, J.J. (1994) *Journal of Physical Chemistry*, **98**, 6201.

192 Alvarez, L.J., Blumenfeld, A.L. and Fripiat, J.J. (1998) *Journal of Chemical Physics*, **108**, 1724.

193 Oldfield, E. and Kirkpatrick, R.J. (1985) *Science*, **227**, 1537.

194 Ashbrook, S.E. and Smith, M.E. (2006) *Chemical Society Reviews*, **35**, 718.

195 Mastikhin, V.M., Mudrakovsky, I.L. and Nosov, A.V. (1991) *Progress in Nuclear Magnetic Resonance Spectroscopy*, **23**, 259.

196 Eckert, H. (1994) NMR spectroscopy of bulk oxide catalysts, in *NMR Techniques in Catalysis* (eds A.T. Bell and A. Pines), Marcel Dekker, New York, p. 195.

197 Datka, J., Geerlings, P., Mortier, W. and Jacobs, P. (1985) *Journal of Physical Chemistry*, **89**, 3488.

198 Pfeifer, H., Freude, D. and Hunger, M. (1985) *Zeolites*, **5**, 274.

199 Schreiber, L.B. and Vaughan, R.W. (1975) *Journal of Catalysis*, **40**, 226.

200 Hunger, M., Freude, D., Pfeifer, H., Bremer, H., Jank, M. and Wendlandt, K.P. (1983) *Chemical Physics Letters*, **100**, 29.

201 Bronnimann, C.E., Chuang, I.S., Hawkins, B.L. and Maciel, G.E. (1987) *Journal of the American Chemical Society*, **109**, 1562.

202 Mastikhin, V.M., Nosov, A.V., Terskikh, V.V., Zamaraev, K.I. and Wachs, I.E. (1994) *Journal of Physical Chemistry*, **98**, 13621.

203 Lakshmi, L.J., Srinivas, S.T., Rao, P.K., Nosov, A.V., Lapina, O.B. and Mastikhin, V.M. (1995) *Solid State Nuclear Magnetic Resonance*, **4**, 59.

204 Chizallet, C., Costentin, G., Lauron-Pernot, H., Maquet, J. and Che, M. (2006) *Applied Catalysis A: General*, **307**, 239.

205 Deng, F., Wang, G., Du, Y., Ye, C., Kong, Y. and Li, X. (1997) *Solid State Nuclear Magnetic Resonance*, **7**, 281.

206 Crepeau, G., Montouillout, V., Vimont, A., Mariey, L., Cseri, T. and Mauge, F. (2006) *Journal of Physical Chemistry B*, **110**, 15172.

207 Lunsford, J.H., Rothwell, W.P. and Shen, W. (1985) *Journal of the American Chemical Society*, **107**, 1540.

208 Baltusis, L., Frye, J.S. and Maciel, G.E. (1986) *Journal of the American Chemical Society*, **108**, 7119.

209 Baltusis, L., Frye, J.S. and Maciel, G.E. (1987) *Journal of the American Chemical Society*, **109**, 40.

210 Chen, W.H., Ko, H.H., Sakthivel, A., Huang, S.J., Liu, S.H., Lo, A.Y., Tsai, T.C. and Liu, S.B. (2006) *Catalysis Today*, **116**, 111.

211 Junger, I., Meiler, W. and Pfeifer, H. (1982) *Zeolites*, **2**, 310.

212 Michel, D., Germanus, A. and Pfeifer, H. (1982) *Journal of the Chemical Society – Faraday Transactions I*, **78**, 237.

213 Haw, J.F., Chuang, I.S., Hawkins, B.L. and Maciel, G.E. (1983) *Journal of the American Chemical Society*, **105**, 7206.

214 Michael, A., Meiler, W., Michel, D., Pfeifer, H., Hoppach, D. and Delmau, J. (1986) *Journal of the Chemical Society – Faraday Transactions I*, **82**, 3053.

215 Gay, I.D. (1977) *Journal of Catalysis*, **48**, 430.

216 Liang, S.H.C. and Gay, I.D. (1980) *Journal of Catalysis*, **66**, 294.

217 Dawson, W.H., Kaiser, S.W., Ellis, P.D. and Inners, R.R. (1981) *Journal of the American Chemical Society*, **103**, 6780.

218 Dawson, W.H., Kaiser, S.W., Ellis, P.D. and Inners, R.R. (1982) *Journal of Physical Chemistry*, **86**, 867.

219 Maciel, G.E., Haw, J.F., Chuang, I.S., Hawkins, B.L., Early, T.A., McKay, D.R. and Petrakis, L. (1983) *Journal of the American Chemical Society*, **105**, 5529.

220 Ripmeester, J.A. (1983) *Journal of the American Chemical Society*, **105**, 2925.

221 Majors, P.D., Raidy, T.E. and Ellis, P.D. (1986) *Journal of the American Chemical Society*, **108**, 8123.

222 Majors, P.D. and Ellis, P.D. (1987) *Journal of the American Chemical Society*, **109**, 1648.

223 Mastikhin, V.M., Mudrakovsky, I.L. and Filimonova, S.V. (1988) *Chemical Physics Letters*, **149**, 175.

224 Haw, J.F., Chuang, I.S., Hawkins, B.L. and Maciel, G.E. (1983) *Journal of the American Chemical Society*, **105**, 7206.

225 Haw, J.F., Zhang, J.H., Shimizu, K., Venkatraman, T.N., Luigi, D.P., Song, W.G., Barich, D.H. and Nicholas, J.B. (2000) *Journal of the American Chemical Society*, **122**, 12561.

226 Shimizu, K., Venkatraman, T.N. and Song, W.G. (2002) *Applied Catalysis A: General*, **225**, 33.

6
Photoelectron Spectroscopy of Catalytic Oxide Materials

Detre Teschner, Elaine M. Vass, and Robert Schlögl

6.1
Introduction

Heterogeneous catalysis is one of the most important tools for industrial chemical processes, making them economically feasible and also environmentally friendlier. Although heterogeneous catalysis has long been established in the chemical industry, and our understanding of how catalysts function has greatly improved since the 1980s, the lack of a widely accepted, universal theory of heterogeneous catalytic reactions makes this field of physical chemistry still an "undiscovered land". Since most of the catalysts are solid materials, their surface geometric and electronic structure should hold the key to the desired understanding of their working principles. Among the various experimental techniques employed to study surface properties, Photoelectron Spectroscopy (PES) plays an important role. Owing to the short mean free path of photoelectrons in the solid, PES is strongly biased towards the top few atomic layers of the solid, depending on the kinetic energy of the detected electrons. The technique thus probes surface and near-surface electronic properties of the solid sample, starting from the chemical (oxidation) state of its constituents to the more complex valence-band electronic structure. The latter, in combination with quantum chemical calculations, proved to be essential in understanding the main bulk electronic structure of solid materials between 1970 and 1990, and the combination is expected to experience a revival, thus rejuvenating surface chemistry. Furthermore, X-ray Photoelectron Spectroscopy (XPS) can provide information regarding the elemental stoichiometry of the near-surface region, which is often different from the bulk composition. The catalytic function is acknowledged to be essentially dependent on the surface composition and electronic properties, which make PES (and especially XPS) a popular surface analytical tool.

Metal oxides currently find widespread application in many fields of industry from IT to chemical technologies, as in catalysis. In this chapter, after briefly reviewing the basic principles and elements of PES and introducing how *in situ* experimentation can provide an additional playing field to catalysis, we will

Metal Oxide Catalysis. Edited by S. David Jackson and Justin S. J. Hargreaves

ISBN: 978-3-527-31815-5

critically review a couple of areas of metal oxide catalysis in relation to the application of PES.

6.2
XPS as a Surface-Sensitive Technique

6.2.1
Basic Principles

(X-ray) PES is based on the observation of the photoelectric effect, in which a photon reaching a sample can liberate an electron, which subsequently escapes into the vacuum. As a result of energy conservation, such a transition occurs only if the energy of the impinging photon ($h\nu$) is higher than the energy required to remove the electron from the system. This latter is expressed as a sum of two terms: firstly, the binding energy (E_B) describing the energy needed to remove an electron from a certain orbital, and secondly the work function (ϕ), which is the energy required to take an electron from inside the solid to the vacuum level. Therefore in the simplest view, the binding energy of an electron can be calculated by measuring the energy-dependent photocurrent and using the equation

$$E_B = h\nu - E_K - \phi \tag{6.1}$$

where E_K is the measured kinetic energy of the emitted electron.

The photoemission process creates a final state that has a positive hole, that is, it is lacking one electron with respect to the initial state. Hence, in a more fundamental treatment, the binding energy of an orbital x will be the difference between the total energies of the final hole state (with $N - 1$ electrons) and of the initial state (with N electrons):

$$E_B(x) = E_{tot}(N-1) - E_{tot}(N). \tag{6.2}$$

Since solving the Schrödinger equation for systems investigated in XPS is not possible, several approximations have been applied to theoretically describe the photoelectric process and to calculate binding energies. It is far beyond the scope of this chapter to present these models; instead the reader is referred to the corresponding literature [1, 2].

The fact that binding energies of a particular core level in the same atom but in different chemical environments are different has made XPS a popular technique for characterizing solid materials. The energy difference observed in binding energies is called the chemical shift. In a simplified model, chemical shift occurs owing to different screening of the Coulomb interaction between the nucleus and the probed orbital through valence electrons. Therefore, binding energies are readily correlated with the partial charge on an atom. With increasing positive charge (i.e. lower screening through valence electrons) on an atom/ion in a molecule, the

binding energy increases and vice versa. In fact in this very effective view, binding energy is a function of initial state effects. Equation 6.2 indicates clearly, however, the often neglected fact that the measured binding energy of the investigated system is not only affected by its initial state but also by its final state. Such final state effects, for example inter- or extra-atomic relaxations and core polarization, are necessary to account for secondary structures observed in photoelectron spectra.

6.2.2 Instrumentation

6.2.2.1 The Conventional Setup

XPS instruments have been commercially available for several decades. Obviously, significant developments have been made to the instrumentation since the technique was introduced, and we will only briefly describe the currently available standard equipment. Major manufacturers in this area include: JEOL, Kratos, Omicron, PHI, Scienta, SPECS and Thermo VG.

Photons provided by the X-ray source illuminate the sample, giving rise to the processes described in the previous section. Typically, two methods are used to produce X-rays: laboratory experiments use the bombardment of a metallic target with high-energy electrons (dual anode source: Al Kα, Mg Kα), whereas setups connected to a synchrotron beamline can make use of the highly intense synchrotron light. The electron lens system is placed between the sample and analyzer and transmits electrons into the analyzer. Electrons passing through the lenses are focused onto the input slit of the analyzer and are retarded to the pass energy (E_{pass}) for subsequent energy analysis. The lens systems can usually be operated in several different modes for spatial and angularly resolved studies and for different spot sizes to fulfill the requirements of different users. Commercial XPS instruments use electrostatic analyzers, of which the hemispherical analyzer (HSA) is the most commonly used. Electrons entering the HSA through the entrance slit are deflected into elliptical trajectories by the radial electrical field between the inner and outer hemispheres. Only electrons with kinetic energies in a certain energy interval are able to pass through the full deflection angle from the entrance to the exit slit. Electrons selected by the analyzer are multiplied and counted by the electron detector. These main components of an XPS setup are contained within an ultra-high vacuum (UHV) system to (i) maintain low pressure for the electron detector and the X-ray source, (ii) avoid discharge in the lens system, (iii) increase spectrum intensity (signal/noise ratio), and (iv) maintain surface cleanliness if required. UHV conditions are achieved with turbo pumps, ion pumps or sublimation pumps. All of these components use electronics as their power supply and control unit.

6.2.2.2 *In situ* (High-Pressure) Setup

The conventional (UHV) XPS technique is a powerful tool to study surface composition and electronic states. However, these properties are strongly dependent

on the experimental conditions, such as the temperature and the gas phase above the investigated sample. It is increasingly realized that catalysts are dynamic materials whose active centers are formed or transformed under reaction conditions. Therefore direct *in situ* (i.e. not "pre-treat and transfer") experimentation is highly beneficial in many fields of material science, particularly in catalysis. Since any photon source and detector require UHV conditions, the minimum requirement for *in situ* operation is the separation of these units from the gas atmosphere.

A schematic of a high-pressure XPS setup is shown in Figure 6.1. Independently of the source applied, a thin X-ray window separates the X-ray source from the experimental cell. As with conventional XPS instrumentation, X-rays from the source hit the sample and induce the photoelectric effect. After traveling in the sample cell, some of the photoelectrons reach the entrance aperture of the differential pumping stages and pass through to the electron energy analyzer. Application of differential pumping thus allows minimization of the travel path of photoelectrons in the gas phase. A major advantage of the system is that a gas atmosphere can be introduced into the sample cell instead of the UHV conditions that are obligatory for conventional XPS. The pressure of gas that can be applied in the sample cell is limited by scattering of photoelectrons by gas-phase molecules, which leads to a decrease in photoelectron signal. The maximum pressure depends on several factors, such as the distance between the sample and the first aperture, the aperture diameter, the intensity of the X-ray source, photoelectron collection and detection efficiencies, the kinetic energy of photoelectrons and the type of gas. Electrostatic lenses placed in the differential pumping stages can significantly increase the collection of photoelectrons.

Differential pumping in XPS was first used by Siegbahn and coworkers to study free molecules [3]. Ten years later, by using one differential pumping stage around a high-pressure cell, the first experiments were carried out on solids in a gaseous atmosphere [4]. Later designs applied additional pumping stages and/or electro-

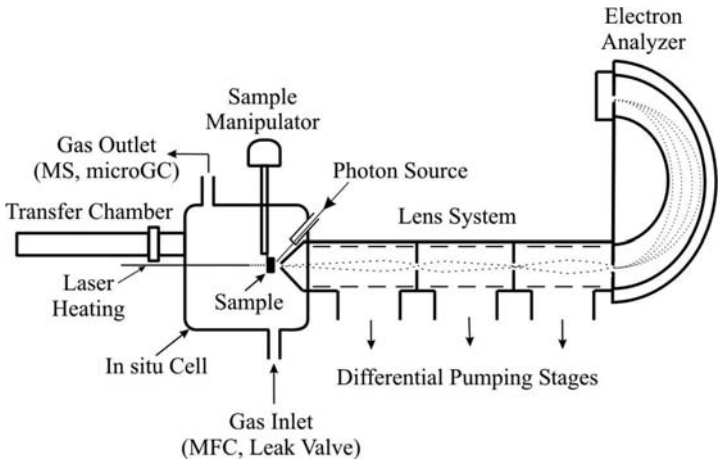

Figure 6.1 Schematic representation of an *in situ* XPS setup.

static lenses accepting electrons from a higher solid angle [5, 6]. By using a molecular beam directed towards a surface, relatively high local pressures (up to 10^{-2} mbar) can be achieved in front of a sample, while the base pressure of the analyzer chamber is still in the 10^{-6}–10^{-7} mbar range. Such experiments are carried out, for example, in Steinrück's group [7].

Our survey of the recent literature on high-pressure XPS in the (0.1–5) mbar range indicates that mainly two groups (Salmeron at Berkeley and that of the authors) contribute to this field. These instruments were developed as a result of close cooperation between the two groups, and their operation principle is nearly identical. Both setups operate at their local synchrotron source. The samples are usually transferred from a pre-chamber and can be mounted inside the reaction cell, 1–2 mm away from an aperture, which is the entrance to the differentially pumped stages of the lens system of the hemispherical analyzer. The sample can be heated from behind using an infrared laser system. Gas flows into the reaction cell are regulated by leak valves and mass-flow controllers. The gas-phase composition, to monitor ambient cleanness or catalytic activity, is recorded on-line by mass spectrometers located either in the first differentially pumped lens stage or connected directly to the reaction chamber. The surface of the sample can optionally be cleaned by Ar^+ sputtering.

The high-pressure setup can be easily adapted for use in near-edge X-ray Absorption Spectroscopy (XAS). In this process the incoming excitation energy is scanned across a range (dependent on the synchrotron light available and the absorption edge of interest). All electrons emitted by the sample are collected and amplified to produce a current. This form of XAS is called Total Electron Yield (TEY). (The reader is referred to Stoehr [8] for an in-depth discussion of XAS.) The possibilities of this technique will be briefly highlighted in Section 6.3.2.

6.2.3 Quantification of XPS Spectra

The intensity of an XPS peak (I_A) is a strong function of (i) the incoming photon flux, (ii) the concentration of the given element, (iii) its photoionization cross-section (which is excitation-energy dependent), (iv) the mean free path of the emitted photoelectron, and (v) further instrumental parameters (such as photoelectron collection and detection efficiency). By defining atomic sensitivity factors (S, as an overall factor summing up the effects of iii–v), the atom fraction of any element in a sample can be calculated as:

$$X_A = (I_A/S_A) \Big/ \sum (I_i/S_i) \tag{6.3}$$

assuming constant photon flux, as in the typical XPS setup using Mg or Al Kα excitation, and homogeneous distribution of the constituent elements. Such sensitivity factors are known and commonly used; however, the accuracy of the calculation relies on the rare situation of an atomically homogeneous distribution of elements in the sampling depth. For example, overlayer-type contamination has a

strong effect of decreasing the intensity of low E_K (high E_B) peaks, affecting the calculation. If a synchrotron source is used (with a known photon flux versus energy function), this effect can be circumvented by tuning the photon energy of each investigated core level to record continuously electrons with similar kinetic energy. As an additional benefit, the sampling depth for all elements will be similar. This approach opens up the possibility to perform non-destructive depth profiling experiments via intentional variation of photoelectron E_K.

Based on the Lambert–Beer-type law of exponential attenuation of peak intensity (I) with excitation depth (z),

$$I(z) = I_0 \, e^{-(z/\lambda \cos\theta)} \tag{6.4}$$

where λ is the attenuation length and θ is the angle of emission with respect to the surface normal, known depth distributions of constituents can be modeled and the thickness of layers can be calculated [9, 10].

6.2.4 The XPS Spectrum (a Qualitative Picture)

An X-ray photoelectron spectrum is an electron-intensity (e.g. counts per second) plot as a function of binding energy. It is either a wide scan showing different types of transitions (core levels, Auger lines, valence levels, secondary structures) or plotted in a narrow E_B range displaying only one particular feature. The baseline going through an elastic transition increases with increasing binding energy, owing to electrons that have suffered some energy loss during their escape.

6.2.4.1 X-ray Transitions

Core-level excitation from a closed sub-shell results in the most intense and typically narrow photoelectron lines. The width of a core level measured at half its maximum height, full width at half maximum (FWHM), is usually defined as the convolution of the width of the photon source, the natural line-width and the analyzer resolution. All transitions (except from s levels) give rise to doublets due to spin–orbit coupling, in which the spin of the unpaired electron left in the orbital can couple in a parallel or an anti-parallel manner with its orbital angular momentum. As all the relevant elements (except H) show at least one transition detectable by this technique, and the core levels of different elements are usually readily distinguishable, XPS is widely used for elemental analysis in the sampling depth of the topmost atomic layers.

Following the formation of an initial core level vacancy (E_{B1}), an electron from a higher lying level (E_{B2}) drops down to fill this vacancy. If the energy difference between these two orbitals is high enough to remove a third electron from its orbital (E_{B3}), then this electron can leave the sample with kinetic energy

$$E_K(123) \approx E_{B1} - E_{B2} - E_{B3} \tag{6.5}$$

This process is called Auger transition and as a result Auger lines will show up in the XPS spectra. They appear as a group of lines, as several Auger transitions can occur. Because Auger electrons have kinetic energies independent of the initial photon radiation, they appear in the binding energy plot at different energy positions when different photon excitation is applied.

The energy levels approximately 5–20 eV below the vacuum level (i.e. low E_B) correspond to bonding or delocalized orbitals. In a typical solid sample these closely spaced orbitals overlap and form a valence (electronic) band. The Fermi level, E_F, designates the energy separation between filled and empty states at zero Kelvin and represents a reference position of zero on the binding-energy scale of solid samples. The structure of the valence (and conduction) band determines optical and electrical transport properties, chemical reactivity and catalytic properties. As, however, all the components of the investigated sample contribute to the valence band spectrum, its interpretation generally requires theoretical (density of states) calculations with high predictive ability.

Core polarization will give rise to multiplet splitting of the investigated core level if the system has an unpaired open valence configuration. The coupling of the remaining core electron with the unpaired valence electrons can create several final states with different energies.

After core hole formation, relaxation in the valence orbitals can give rise to promotion of valence electrons into unoccupied levels. If this reorganization is fast, and the energy required for this transition is not available to the primary photoelectron, shake-up satellites can show up on the low kinetic energy (high E_B) side of the main peak. Further loss lines can be created if the photoelectron passing the solid excites group oscillation of the conduction electrons (plasmon loss).

Additional secondary features, X-ray satellites, can appear in the spectra if a non-monochromatic source is used; moreover X-ray ghost lines show up when the exciting photon originates from impurity elements in the X-ray source.

6.2.4.2 **Binding Energy in Practice; An Issue?**

A substantial part of the information obtainable from a photoemission experiment concerns the qualitative data derived from line positions and line profiles for unresolved contributions to a given excitation line. This information, dealing with binding energies of core and to a lesser extent of valence lines, is used to deduce qualitative chemical information about the bonding and reactivity of species under consideration. The acronym "ESCA" (electron spectroscopy for chemical analysis) expresses this application of PES and was historically the major driver for the popularization of the method before it became apparent that it is a surface-sensitive technique requiring detailed information about surface structure and purity of a sample in order to derive meaningful average information about the bulk chemical bonding.

For the purpose of catalyst analysis, the weaknesses of ESCA turn into strengths as it is the chemical bonding of the outer surface of a solid that is of interest and only to a lesser extent its bulk chemical structure. Most of our theoretical understanding of chemical bonding refers, however, to the bulk state (crystal structures)

and cannot directly be applied for the interpretation of PES result. As outlined elsewhere in the chapter, the surface sensitivity of PES is a function of its excitation energy and is thus to a certain degree variable. Under no conditions can pure surface sensitivity be realized; the information must always be divided into a bulk and a surface contribution.

The fact that PES strongly perturbs the electronic structure of an atom [11–13] (also the preceding section) renders it difficult to compare the binding energy of an energy level obtained from the position of an experimental spectrum to a calculated value of the inverse dissociation energy of the respective state obtained by theoretical treatment. Moreover, there are serious experimental issues with defining the energy scale of the method in an absolute way. Today, it is customary to use the following conventions for an experimental binding-energy scale and to discuss the positional information in PES in terms of "chemical shift", which is given for each element and each energy level with the convention that the elemental state of the atom serves as zero for the chemical-shift scale. For a few elements of relevance in the present context this definition is not easy, as the elemental state is not solid, which causes additional problems with the shift scales. In these cases (notably for oxygen) experimental binding-energy positions frequently observed are used as zero for the shift scale (e.g. 530.0 eV for oxygen 1s).

The quantities contributing to the position of a photoelectron (PE) line in solids can be summarized by the following equation:

$$E_B = E_{hv} - E_K - E_{rel} - E_{exp} - E_{ch} \tag{6.6}$$

Detailed treatments of this issue can be found in the literature [3, 14, 15]. Here we only briefly review the contributions under practical considerations and without discussing the deep quantum chemical implications involved.

The binding energy (E_B) should be given as the position of the center of gravity of a fit of the experimental line profile obtained after satellite subtraction (for laboratory experiments) and non-linear background correction [16]. The profile function used to approximate the lines must be calibrated for a given analyzer and must not be changed during the fitting of different spectra.

The excitation energy (E_{hv}) should be as monochromatic as possible to maximize the resolution of the experiment. The kinetic energy (E_K) is the direct experimental result of the PE experiment. It is used as energy scale in Auger spectroscopy but today no longer in PE spectra. Note that this is not the case in older literature where often the kinetic energy was plotted.

The kinetic energy contains the original chemical information of the PE experiment. If the kinetic energy of the emission from the same energy level is compared for samples with a different chemical bonding (different ground state electronic structure) then one observes a shift between the positions of the emission maxima that is considered as being proportional to the difference in ground state electron density in the valence band. This effect is the origin of chemical shift scales that exist as empirical correlations for many elements. As a rule of thumb, it is assumed that a difference of one formal oxidation state unit will lead to a ground state

chemical shift of about 1 eV for d-block elements. In main group elements this shift increment can be larger. It needs to be pointed out that these rules are not supported by quantum chemical considerations and that many exceptions exist. Nevertheless, they are very popular and give rise to frequent and extensive debates in the literature about the nature of chemical bonding in a particular system. In light of the lack of theoretical justification for such shift scales, it is not recommended to use such shift arguments in attempts to derive a description of the chemical bonding. Other properties of the experimental spectrum, such as the satellite features [11, 14, 17, 18] or the valence band, should be used instead. Despite these caveats, the use of these correlations is frequent in catalysis science and several examples of their application in vanadium-based systems will be discussed below. It is, however, no surprise that substantial differences and debates exist in the literature about the nature of the chemical bonding as derived from such empirical correlations. It is only considered useful to consider empirical shift arguments as ordering criteria for systems with different chemical bonding, being related, for example, to functional performance. The jump to the conclusion that ground state electronic differences may be responsible for observed functional differences (activities or selectivity in catalysis) is unjustified on the basis of chemical shift arguments. A prominent example of this debate is the role of putative pentavalent vanadium compounds in selective oxidation catalysis, which will be elaborated in detail below. An exception would be the comparison of spectra of different samples of the same general chemical compound of a given element, for example the analysis of a series of defect species of an oxide of a given transition metal. Also in a series of compounds with large electrostatic contributions to the chemical bonding (salts) [19–22], the assumption of a large contribution of ground state electron density to the chemical shift may be valid.

The relaxation energy (E_{rel}) is a sum of contributions describing the response of the electronic structure to the creation of the core hole on the femtosecond timescale. This response is detected by the photoelectron leaving as an exit wave from the excited atom and modifies its energy to a considerable extent. The effect is larger the deeper the core hole in energy, and can reach values of about 10% of the total energy. For deep core holes the relaxation is only weakly dependent on the chemical nature of the sample, but this is not the case [15, 23, 24] for high-lying core levels. The relaxation phenomena are caused by the partial or complete screening of the initial core hole by the surrounding electrons. The effectiveness of the screening depends on the extent of overlap between the wave functions of the parent state and the state that contributes to the screening. The screening is largely dominated quantitatively by weakly localized valence states, for example "free electrons" from metals are very effective. Also valence electrons from surrounding atoms can effectively contribute to the core hole relaxation (extra-atomic contribution). These two contributions mean that the chemical structure can have a substantial effect on the extent of core hole relaxation when comparing chemical compounds with insulating properties and high oxidation states to matrices with metallic properties and low oxidation states. As the total contribution of relaxation to the experimental binding energy is large (easily a few tens of electron volts) it

is quite likely that small changes in the relaxation pathways created by a difference in chemical bonding of an atom will cause substantial changes in the binding-energy scale (a few electron volts) that are not caused by the difference in ground state valence electron density. A common example of such a relaxation shift is the change in PES spectra of nanoparticles as a function of their particle size [23, 25, 26]. Nanostructures change lattice constant or long-range structural ordering at much larger sizes than the transition that occurs from collective to atomic electronic structure (at cluster sizes below 100 atoms). The subtle changes in long-range ordering exert a sizeable effect on relaxation (up to about 1 eV) whereas the local ground state electronic structure stays largely unperturbed (e.g. metallic). At the limit of nanoparticles PES can become, by the action of relaxation phenomena, a structure-sensitive method, although the basic physical information is massively dominated by the inner-atomic contributions [27, 28].

The term E_{exp} summarizes all contributions arising from the experimental setup. In PES it is necessary that electrons first leave the sample where they have to overcome, besides the local binding energy, the collective attraction of the work function. At the surface of the electron detector, the photoelectron has to penetrate back into a solid where the inverse of the work function becomes liberated as energy gain. As these two quantities, with absolute values between 3 and 6 eV, are largely unknown and vary strongly with geometric surface state and with the presence of adsorbate in the spectrometer and at the sample, it became customary to lump these contributions into a correction voltage that is applied to the analyzer and set by calibration using a series of polycrystalline clean metal samples [29] (copper, silver and gold) that can also be used to determine the linearity of the binding-energy scale. The term thus does not occur in evaluations of correctly calibrated instruments as long as solids are being measured. In the present context of *in situ* catalytic studies, the data are often compared to gas-phase spectra. Such samples do not exhibit a work function and thus the work function correction applied to the spectrometer gives rise to an incorrect calibration of the binding-energy scale for gases. The convention for gases is to use the lone pair emission lines for Ar and di-nitrogen as calibration standards [3], and these show different values in solid-state spectrometers and in dedicated gas-phase instruments. Care must thus be taken when comparing binding energies between adsorbates and free molecules, where not only strong relaxation effects but also substantial experimental peculiarities of the instruments used may lead to hard-to-interpret "chemical shifts." In unfortunate cases the effects may cancel out, as relaxation shift and unintentionally applied work function correction are of the same order of magnitude (5 eV).

The term E_{ch} stands for charging contributions. This term is absent in spectra of samples exhibiting a finite density of states at the Fermi level. For all practical purposes this is correct for all true metals and for many semiconductors with intrinsic states near zero binding energy. Many systems relevant in catalysis do, however, not fulfill this condition (all non-black samples, glasses, porous materials, supports) or even worse, are composites of metallic and non-metallic systems, giving rise to mixed metallic–insulating behavior of their surface under PES. Such

systems are mostly supported catalysts [30] but also working catalysts with a metallic bulk covered with non-metallic deposits or with a water film. Partly reduced semiconducting solids, or strongly defective semiconductors exhibiting extrinsic states from defects within their band gap, also belong to the class of systems which exhibit no defined zero point of binding energy. Three phenomena will result from this situation, all affecting individually or in concert the binding-energy scale.

In the simplest case of extrinsic semiconductors, the temperature and all chemical processes modifying the abundance and nature of the defect states will modify the zero of the binding-energy scale and so cause "shifts" that are solely due to calibration and not at all to local electronic structure modification (e.g. most oxidation states in an oxide are not affected if a fraction of the extrinsic defects are created or healed by diffusion of oxygen species, yet shifts up to 2 eV can result from this process).

The second most frequent state is an apparent shift of the binding-energy scale due to insufficient flow of electrons between sample and spectrometer (insulation) causing a stable electric field gradient [31, 32] to occur between sample surface and spectrometer. This field can be very substantial, causing charging shifts that range between a few electron volts in laboratory instruments to a few hundreds of electron volts in synchrotron-based experiments, as the magnitude of the field depends on the photoelectron flux. Typical measures for avoiding the adverse consequences are (i)"calibration" with an assumed position of a photoelectron line (carbon at 285 eV or oxygen at 530 eV are frequent examples) (ii) charge injection into the surface by shining electrons or low-energy photons on it with the strong risk of modifying the chemical state of the native surface (chemical reduction) and (iii) increasing the electron carrier density (electrons or protons) by heating the sample or by performing a chemical reaction *in situ*.

The most difficult case of a poorly defined binding-energy scale is the occurrence of differential charging. This very frequent case occurs with chemically inhomogeneous systems (supported catalysts, metals with hydrocarbon deposits, oxide patches on metals, partly reduced oxides). In these cases, a distribution of binding-energy scales exist giving rise to a distribution of emission line positions. Neither common referencing nor the application of charge neutralization will remove this distribution. In fortunate cases, a series of discernible peak structures will occur. In many cases, however, an unresolved distribution will cause line broadening of unknown shape. A clear indication of the presence of differential charging is the modification of emission lines in shape and/or position with a variation in X-ray excitation conditions (intensity or angle of incidence). If this occurs the data are basically not interpretable and the experiment cannot be continued in any meaningful way.

For the purpose of the present chapter, a comment on the interpretation of oxygen 1s binding energies in oxides seems appropriate. The contribution of the surface terminating layer and of a possible adsorbate to the total O 1s spectrum of an oxide catalyst is low (an estimated 15% for laboratory XPS) as in oxides the depth of information [33] is commonly larger than estimated from the universal relation between kinetic energy and escape depth, which is valid for metals only.

The chemical shift of the bulk contribution to the oxygen 1s spectrum is dominated by the valence state mixing between oxygen and metal centers. The electronegative oxygen tends to abstract electron density from the metal centers, with resulting high local ground state electron densities at oxygen and low binding energies of about 528.5 eV for later transition metal systems. In early transition metal systems, the charge redistribution is less effective, shifting the binding energy up to 531.5 eV with a large family of binding-energy values at about 530.5 eV. Main group elements are even less effective charge-donating partners, giving rise to positions of up to 533 eV for water and silicon oxides. In this latter group, the geometry of the bonding has a substantial influence on the binding energy, making XPS a structure-sensitive tool. In d-block metal oxides, only major changes in the d–p rehybridization (for example in copper oxides with 529.5 eV for CuO and 530.5 eV for Cu_2O) exert a significant influence, otherwise the position is rather insensitive to, for example, the formal oxidation state of metal center. Compilations of such data with a chemically broad span of samples are available [17, 34, 35].

The interpretation of the oxygen contribution of the terminating layer to the O 1s spectrum should follow different considerations. It is known that oxides terminate by very strong structural relaxations [36–41], making the bulk chemical bonding of oxygen a very poor approximation of their surface. In brief, oxides terminate in their most stable form by creating formal oxygen–metal double bond groups ("-yl structures") also for metals where such -yl structures are not known in the form of bulk compounds. Such terminations are stable and non-reactive, requiring defect sites for adsorption and catalysis. The nature of defects can be the incorporation of hydroxyl groups originally thought to be the main terminating species [42], but many other configurations of weakly held atomic or molecular oxygen [40, 43–47] are also under debate. For the present consideration it follows that all oxides should exhibit a low-energy contribution, situated below 530 eV for stable terminations, and further contributions above 531 eV characterizing the defect oxygen species, from which a discrimination between atomic species and hydroxyl groups may be very difficult in the absence of valence band spectra, where they yield single peak and dual peak structures that allow discrimination.

In practice, asymmetric O 1s peaks are often found for oxide systems, and these find their explanation in the coexistence of a surface spectrum and a bulk spectrum. The contribution of the surface spectrum for polar systems and in the presence of water strongly bound via hydrogen bridges (and thus not pumped away in a normal XPS system without thermal desorption) may then be larger than the estimated 15% and could amount to a clearly visible structure. The contribution of the -yl species, however, is frequently not easily detectable, as its abundance is strictly limited to a maximum of one monolayer, being sub-stoichiometric with respect to a close packed metal layer as it saturates two dangling coordinations per oxygen atom.

Efforts to separate the oxygen 1s spectrum into bulk and surface components are desirable, as the description of chemical reactivity requires a description of the terminating oxide structure. In cases where well characterized surface-science

model compounds are available [36, 37, 48–54] one can justify the fitting of a broad spectrum to different dominating and minor components, using the spectral parameters of the model systems to account for the bulk and the -yl contributions and assigning the unexplained part of the spectral weight to defects and adsorbate features. In the majority of the other cases, one may use *in situ* thermal desorption and/or re-oxidation as means to justify the splitting of the convoluted oxygen PES into bulk and surface contributions. Care must be taken not to choose such severe conditions of surface modification that the bulk becomes affected. This can become a matter of considerable experimental effort, as many oxides (in particular early transition metal oxides) do exhibit pronounced tendencies to form complex sub-oxides [55–59]. It is, however, almost never right to assume one type of oxygen species to be sufficient to describe the bulk and the surface of an oxide system.

If the separation of the spectrum into bulk and surface contributions was successful, then an estimation of the chemical reactivity can be given using the rationale as a basis that the reactivity will be nucleophilic for low binding-energy species and electrophilic for species with high binding energies (above 531 eV). This assignment of nomenclature [60] refers to the reactivity of oxygen with respect to C—H bonds, representing a very common case of the reactivity required in hydrocarbon transformation (partial and deep oxidation). The suggestions given here should serve as guidelines rather than as strict rules for assigning spectra. A large number of peculiarities, such as those mentioned above, of the system under study need to be considered, as well as the strict and conclusive elimination of binding-energy scale artefacts already described. Only then can peak deconvolution be made with the degree of chemical resolution required for reactivity assignments without simply converting wishful thoughts into unresolved lines.

6.3 Case Studies

6.3.1 Applications of XPS to Vanadium Oxides

Metal oxides play an important role in many fields of our society, one of which is heterogeneous catalysis. These materials can be applied as carriers of an active component, and also as the active material itself. We have selected vanadium – and vanadium-containing – oxides as our topic, because they are involved in many catalytic processes, most likely due to their versatile electronic structure. Vanadium, with its valence atomic electron configuration of $3d^3 4s^2$, forms different types of oxides ranging from insulators to metal, depending on the valence shell configuration and temperature. Their electronic structure was comprehensively studied by several research groups [50, 61–67]. Zimmermann and coworkers [63] demonstrated a strong hybridization between the V 3d and O 2p orbitals, and owing to the covalency in bonding, such early transition metal oxides (e.g. V_xO_y) cannot be considered as simple Mott–Hubbard compounds. Density-functional theory(DTF)

calculations [64, 67] confirmed the strong hybridization of the valence oxygen and vanadium orbitals in V_2O_5, and related the distortion of the VO_6 octahedra to the unique electronic structure of the conduction band. A recent DFT cluster study [50] mimicking V_2O_5 has clearly indicated that the local charges (Mulliken) of the different cluster atoms are much smaller than formal valence charges ($V^{+1.4}$; $O^{-0.26}$, $O^{-0.58}$, $O^{-0.78}$ for the three different lattice O positions), in line with the suggested covalent bonding contribution. DFT calculations on other oxides reported similar discrepancies between partial and formal charges [68–71]. It is well known among quantum chemists, and we would also stress, that although Mulliken charges and formal valence charges may yield the same qualitative picture, they cannot be compared on a quantitative basis. Formal valence charges may be useful in certain cases, but if considered as a universal tool, they can easily lead to erroneous conclusions and reaction models, as often observed in the heterogeneous catalysis community. In what follows, we will use integer valence charges (e.g. V^{5+}) to represent formal oxidation states, while fractional numbers (e.g. $V^{+1.4}$) will indicate local charges calculated by DFT methods.

The electronic structure of vanadium oxides is crucial to their reactivity. Determination of even the formal oxidation state of vanadium from XPS can, however, be non-trivial, owing to a variety of factors. Firstly, examination of binary vanadium oxides has highlighted that there appear to be differences in binding-energy positions and FWHM for single crystal and powder samples (see Table 6.1). In general, the binding energy quoted for V_2O_5 is quite consistent, ranging from 516.9 to 517.2 eV. However, Table 6.1 shows that the ranges of energies given for V^{4+} and V^{3+} in the literature are considerably wider, and in some cases overlap. This can be for a number of reasons, including variations in equipment/analyzer, surface cleaning method, background and satellite subtraction and subsequent calibration of the binding-energy scale. A relatively reliable binding-energy calibration method, at least in the case of reduced oxides, may be to use the band gap transition of the V 3d peak in the valence band [63]. Additionally, the widths of V 2p core levels increase from V_2O_5 to open valence VO_2 and to V_2O_3. This behavior is due to the increasing number of available multiplet configurations in the corresponding photoelectron final states, that is, non-resolved multiplet splitting occurs in V 2p core levels of lower valence vanadium oxides. This effect is also observed in the mixed valence vanadium oxides such as V_6O_{13} ($V_{2n}O_{5n-2}$, Wadsley phase) or V_4O_7 and V_3O_5 (V_nO_{2n-1}, Magnéli phase). An XPS study of these phases [74] has shown similarities to the studies of V_2O_5, VO_2 and V_2O_3, where strong hybridization between the O 2p and V 3d states is observed. The broad nature of the V 2p peak of the mixed oxide phases was attributed to the mixture of oxidation states present as well as to surface defects.

Further difficulties in measuring vanadium oxides arise from reliable preparation of reference compounds and reduction of vanadium caused by UHV conditions and beam damage [78, 79]. Hence, it is advantageous to confirm the phases present by additional analytical techniques.

As expected, the difficulties in relating binding energies to formal oxidation states of vanadium becomes more complex in the case of supported vanadium

Table 6.1 XPS binding energy positions of a selection of V_xO_y materials from literature.

Sample	Binding Energy of V2p$_{3/2}$ and O1s/eV (FWHM)[a]					E_B Calibration	Reference
	V^{5+}	V^{4+}	V^{3+}	V^0	O1s		
V_xO_y on V foil	516.9	515.8	–	–	–	Au 4f$_{7/2}$	[72]
V_2O_3(001) on W(100) and Au(111)	517.15	–	515.15	–	~530	W 4f$_{7/2}$	[52]
V_xO_y on V	517.2	515.8	515.2	512.4	–	Au 4f$_{7/2}$ 84.0 eV	[73]
Single crystals V_2O_5, VO_2, V_2O_3, V (foil)	516.9 (1.6)	516.2 (3.2)	515.7 (4.2)	512.4 (2.0)	529.8–530.1	F.E.	[61]
V_2O_5, VO_2, V_2O_3, V_6O_{13}, V_4O_7, V_3O_5	517.2 (1.2)	516 (1.95)	515.85	512.2	–	C 1s 285 eV	[74]
Powders V_2O_5, VO_2, V (foil)	516.4 (3.0)	516.1 (3.4)	–	512.7	529.8–530.0	C 1s 284.6 eV	[75]
V_2O_5 (s.c.), V_6O_{13}, VO_2, V_2O_3	517.0 (1.3)	515.65 (4.0)	515.1 (4.8)	–	529.8–530.0	O 1s 529.8/530 eV	[76]
V_2O_5, VO_2, V_2O_3	517.2	516.0	514.0	–	–	C 1s 284.8 eV	[77]

a FWHM in brackets if given in text.

oxide catalysts (see Table 6.2). Again, accurate calibration of the binding-energy scale is essential as, in the case of the catalysts shown, there is a difference of ~0.5 eV in the calibration energy chosen for the C 1s peak alone. As the catalyst support is normally an insulating material, charge compensation is made by calibrating the binding-energy scale to a known value. In many cases the choice of value (support peak or carbon) can cause discrepancies between quoted binding energy values. Achieving an accurate peak fit of the V 2p$_{3/2}$ region ideally requires prior knowledge of the position and FWHM of each oxidation state, as determined from reference compounds. However, Tables 6.1 and 6.2 highlight the difficulties surrounding this simple strategy.

Perhaps the starting place for investigations of supported metal oxide catalysts by XPS should be the examination of well characterized model systems. Several authors have investigated V_xO_y films supported on a number of metal substrates

Table 6.2 XPS binding energy positions of deconvoluted V $2p_{3/2}$ peaks of V_xO_y/support catalysts from literature

Sample	Binding energy of V2$p_{3/2}$ and O1s (eV) (FWHM)[a]					E_B Calibration	Reference
	V^{5+}	V^{4+}	V^{3+}	V?	O1s		
V_xO_y/γ-Al_2O_3	517.2–517.3	–	515.5–515.8			Al 2p 74.5 eV	[80][b]
V_2O_5, V-Al-O catalyst	517.0	515.75	515.2		~531	C 1s 285 eV	[81]
VPO, V_xO_y/γ-Al_2O_3	518.0	516.9	–	$V^{<3+}$ 515.1		C 1s 284.5 eV, Al 2p 74.5 eV	[79]
V_xO_y/γ-Al_2O_3	518.0	516.9	–			V 2p of $VOPO_4$ at 518 eV	[82]
V_xO_y/Al_2O_3	517.4–517.6	516.4–516.5	515.8–515.9			Al 2p 74.5 eV	[83]
V_xO_y/Al_2O_3-ZrO_2	518.1–2 (1.8–2.0)	–	–		531.8–532	C 1s 284.6 eV	[84]
V_xO_y/SBA-15	517.3 (2.1)	–	515.9 (2.1)	518.7[c] (2.1)	–	Si 2p 103.6 eV	[85, 86]
V_xO_y/SBA-15	517.1	516.1	–		532.8–533.0	C 1s 284.6	[87]

a FWHM in brackets if given in text.
b Eberhardt and coworkers used principal component analysis and iterative transformation factor analysis to determine number of components and position.
c High E_B caused by final state effects; due to presence of small conducting particles on insulating substrate (see references for further details).

[36, 52, 72, 73, 88, 89]. The benefits of such studies are that in the case of insulating oxides, charging is reduced owing to the enhanced conductivity of the thin film in contact with a metal substrate. Nevertheless, even XPS spectra from model systems can prove challenging to interpret. It has been reported that satellite peaks from V 2p may have to be taken into account when fitting peaks to the V 2p envelope [52, 63]. Dupuis and coworkers [52] investigated V_2O_3 on W(110) and used two peaks in their description of the V $2p_{3/2}$ curve (Figure 6.2). They attributed the higher energy feature (517.5 eV) to vanadyl groups with a formal oxidation state of 5+ and the lower peak (515.15 eV) to bulk V_2O_3. This assignment was aided by angle-resolved depth profiling, which showed an enhancement of the peak attributed to vanadyl groups closer to the surface. Although the peak position is in good agreement with that of V^{5+}, the FWHM is considerably broader than that of the V_2O_5 crystal shown for comparison [52]. Additionally, broadening of the O 1s peak

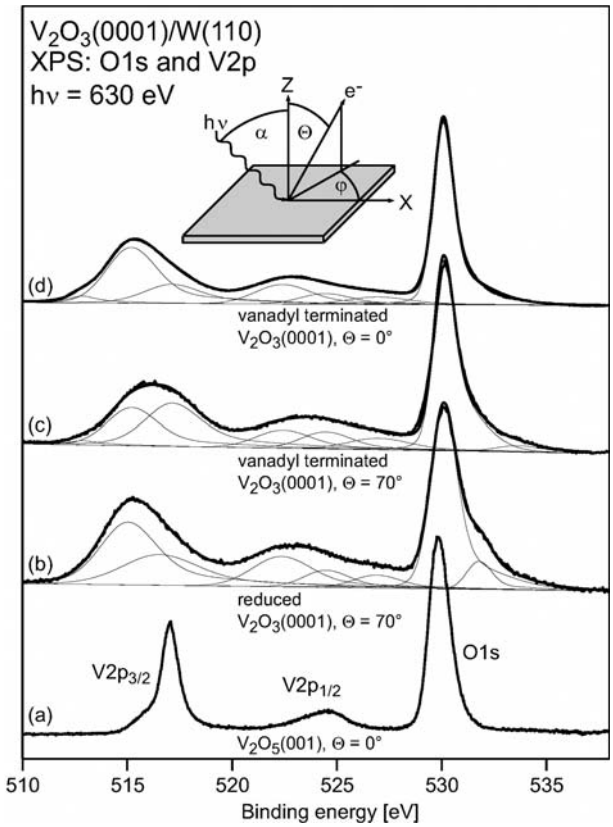

Figure 6.2 V 2p and O 1s region of V_2O_3 (0001) on W(110) in comparison with V_2O_5 according to Dupuis and coworkers [52]. The spectra indicate that the V_2O_3 (0001) surface is terminated with vanadyl groups.

was observed, which may be due to the formation of hydroxyl groups. Dupuis and colleagues suggested that in addition to oxidation state, screening effects can have an influence on the observed binding energy, the effect of which is greater for bulk atoms. The same group reports a correlation between intensity of the V 3d contribution and increasing vanadium reduction [36, 52]. Studies of similar systems [36, 88, 89] under various conditions – hydrated, reduced, oxidized – confirm that combined analysis of the core level and valence band XPS provides greater information about changes in the vanadium oxide's surface. The presence of a more oxidized surface of vanadium oxide films compared with deeper layers was confirmed by Alov and coworkers [73]. They used XPS and detected a higher ratio of V^{5+} and V^{4+} on the outer part of the film, whereas lower oxidation states were concentrated at greater depths.

Fresh and post-reaction supported vanadium oxide catalysts have been examined by several authors (references and E_B values of some examples are given in

Table 6.2). In general, XPS of "fresh" catalysts shows mainly oxidized vanadium (V^{5+}). After reduction treatments, a decrease in oxidation state is observed. However, the extent of reduction depends on a number of factors, such as reduction temperature, reducing agent and partial pressure of the reducing gas, as well as the method used to transfer the reduced sample to the measurement chamber. Ideally, contact with air should be minimized, or excluded if possible, to prevent re-oxidation of the catalyst when the sample is transferred from a reactor to the UHV measurement chamber. This problem can be circumvented by *in situ* instrumentation as discussed later.

In the following sections, we present a critical overview of the application of X-ray photoelectron spectroscopy in vanadium-oxide related catalytic literature (including dehydrogenation, oxidative dehydrogenation and selective oxidation processes). Our focus will concentrate on the strengths and weaknesses of the method and will explore what *in situ* experimentation can contribute to this field.

6.3.2 Direct and Oxidative Dehydrogenation

Removal of hydrogen from a hydrocarbon to form its unsaturated derivative is an important step towards the formation of chemical feedstocks. Unsaturated hydrocarbons are often more reactive and in high demand, hence the process is of great value within industry. An additional benefit is the formation of hydrogen, which if separated from the products would prove to be highly valuable. Dehydrogenation is usually an endothermic reaction, requiring high temperature and low pressure to ensure a sufficient yield of product. The exception is for dehydrogenation of compounds such as cyclohexane where the formation of more stable aromatic derivatives creates more favorable thermodynamics. Fortunately, the thermodynamics of the reaction can be enhanced by addition of oxygen (oxidative dehydrogenation). In this case water is formed as a product, resulting in a thermodynamically favorable reaction. The major goal within the dehydrogenation reaction is to find catalysts that are highly selective to the required product while limiting carbon deposition, which can lead to catalyst poisoning. The majority of processes for the dehydrogenation of light alkanes use catalysts containing chromia or platinum supported on alumina [90–92]. However supported vanadium oxides have also shown applicability for the catalysis of oxidative dehydrogenation [93–96] and dehydrogenation [83, 97–99] of light alkanes.

6.3.2.1 Selective Dehydrogenation of *n*-Butane over V_xO_y/Alumina

In each of the studies described so far, XPS was measured under UHV conditions. However, previous studies of oxide catalysts [100] have shown that by using a specially designed high-pressure *in situ* XPS apparatus, XP spectra can be measured under reaction conditions in the millibar pressure range. This technique was applied to a selection of V_xO_y/δ-alumina catalysts (1–8 wt% V) to determine their electronic structure under oxidative and reaction (*n*-butane) atmospheres

[101]. Initially the "fresh" catalysts were examined, in an atmosphere of 0.5 mbar of oxygen at elevated temperature (623 K). From XPS, the predominant vanadium species was V^{5+}, independently of the vanadium loading (1, 3.5 and 8 wt% V on alumina). Typically less than 4% of reduced species was observed under these conditions. This is in agreement with other measurements of "fresh" catalysts as, for example, Harlin and coworkers [83] reported that their calcined catalyst contained 100% V^{5+}, according to conventional XPS. In contrast, several authors [82] suggest a higher ratio of reduced vanadium in fresh catalysts, but this may be due to the absence of any oxidative pre-treatment or to damage caused by beam or UHV conditions. By measuring XPS in an oxygen atmosphere and at elevated temperature, as in the work of the present authors, both reduction and charging of insulating samples are reduced compared with conventional XPS systems.

Although in our case the oxidation state remains unchanged with loading, it is likely according to the literature [102, 103] that the structures of vanadium oxide on the alumina surface vary greatly. By using the complementary technique of XAS (Section 6.2.2.2), information about not only the oxidation state but also the local environment of the element under investigation can be determined. The vanadium L_3 edge was measured for each of the three catalysts, under the same conditions as for XPS, as shown in Figure 6.3. This edge is due to electronic transitions from vanadium $2p_{3/2}$ to 3d. The results were compared with a series of

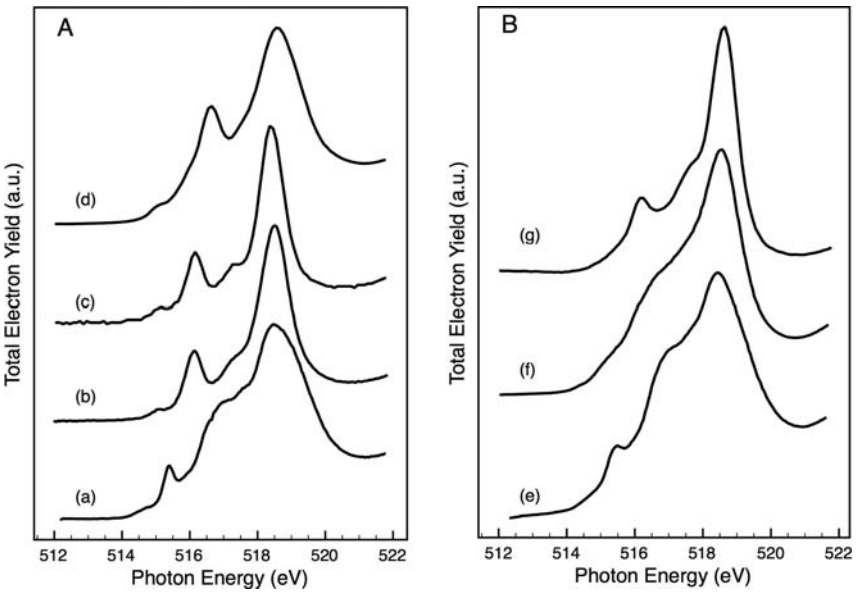

Figure 6.3 V L_3 NEXAFS edge of (A) reference materials: (a) V_2O_5 single crystal, (b) $Mg_2V_2O_7$ (c) $Mg_3V_2O_8$ (d) MgV_2O_6 and (B) fresh catalysts: (e) 8% V/alumina, (f) 3.5% V/alumina and (g) 1% V/alumina. All spectra were measured in an oxygen atmosphere (0.5 mbar) at 623 K and an angle of 55°.

reference compounds as shown in Figure 6.3A. The spectra shown in the figure represent a selection of possible vanadium-oxygen linkages. Comparison of the spectra indicate that 8% V/alumina corresponds well with the spectrum of crystalline V_2O_5. The low-loading catalyst (1% V/alumina) corresponds well with the $Mg_3V_2O_8$ (monomeric) and the $Mg_2V_2O_7$ (dimeric) compounds, whereas the 3.5% V/alumina catalyst did not appear to match any specific reference compound. Although a stable reference material for the polyvanadate structure was not available, from the appearance of the vanadium L_3 edge of the 3.5% V/alumina catalyst, it is likely that a mixture of species was present, possibly including V_2O_5 crystallites and polyvanadates as suggested from (UV-)Raman spectroscopy of the same catalysts [103]. Owing to a high degree of complexity, theoretical calculations to define the origin of the features of the vanadium $L_{2,3}$ edge are limited. De Fransco and coworkers [104] have presented a density-functional investigation of V_2O_5. Although able to calculate theoretical absorption K edges that are similar to experimental results, vanadium L-edge calculations still contained discrepancies from experiment. In different studies [105, 106], first principles multi-electron calculations of VO_2 and V_2O_3 were found to fit well to experimental findings, although there was still some disagreement with the V_2O_5 system. Therefore, detailed calculations of the vanadium L edge of magnesium vanadate compounds would be necessary to relate the fine structure of the electronic transitions to the structure of the compounds.

Additionally, the catalysts were examined under reaction conditions. The results of XPS analysis of an 8% V/alumina catalyst under *n*-butane dehydrogenation conditions can be seen in Figure 6.4. During the dehydrogenation reaction in *n*-butane (0.4 mbar) and at a reaction temperature of 723 K, the formal oxidation state of vanadium was greatly reduced from the initial mixed oxidation state of 5+/4+ after O_2/H_2 pre-treatment. The broadening of the V $2p_{3/2}$ peak and the position of the lower binding energy component is in agreement with the findings of Dupuis and coworkers [52] for V^{3+}. One group reports the presence of only V^{5+} and V^{3+} on a vanadium/alumina catalyst as determined by statistical methods [80]. In that study, both the number of major components and their peak position were determined by principal component analysis and iterative transformation factor analysis. However, as shown in Tables 6.1 and 6.2, various authors report a value in between that of V^{5+} and V^{3+}, which they assign to VO_2 or a V^{4+} species. In our case it is reasonable to fit the V 2p envelope with three peaks representing V^{5+}, V^{4+} and V^{3+} (see Figure 6.4A). Adsorption studies of probe molecules (e.g. NO or CO) also suggest the presence of vanadium species with formal oxidation states of 3, 4 and 5+ [107, 108]. This is in agreement with the work of Harlin and coworkers [83], who proposed that the active center for the dehydrogenation reaction (of *n*-butane and *i*-butane at 853 K) is as a result of surface vacancies due to V^{3+} and V^{4+} at the catalyst surface. They also suggest that reduction of vanadium is due to reaction not only with the feedstock but also with the reaction products (butenes, butadiene and with small amounts of cracked products). In addition to surface reduction, these lines broaden with lower oxidation state, owing to multiplet splitting. However, it can also be seen that the FWHM of the 5+ component increases. This

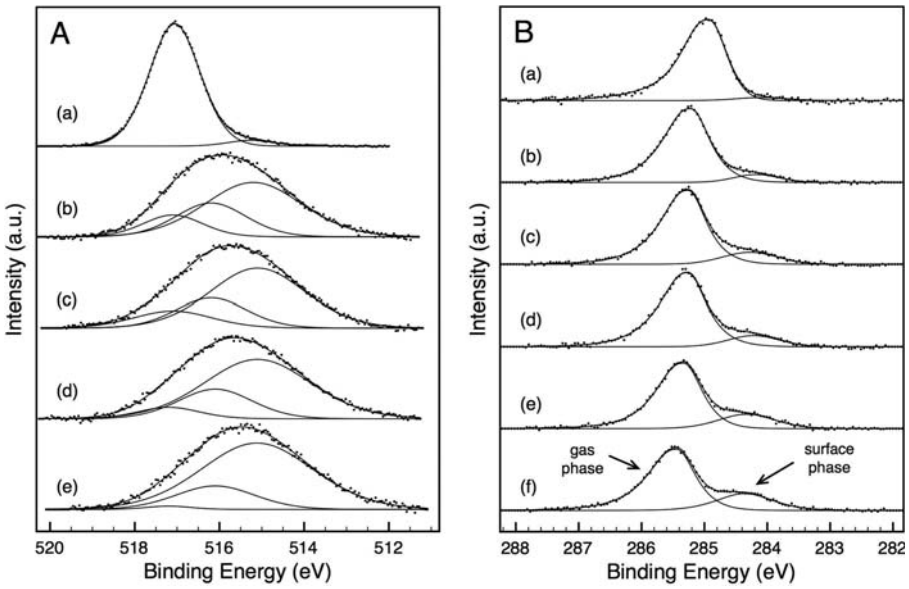

Figure 6.4 (A) XP spectra of V $2p_{3/2}$ region of 8% V/alumina in (a) 0.5 mbar oxygen and 0.4 mbar *n*-butane (723 K), after (b) 53 min, (c) 87 min, (d) 129 min and (e) 186 min. (B) XPS of C1s region during reaction in *n*-butane (0.4 mbar, 723 K) after (a) 60 min, (b) 96 min, (c) 114 min, (d) 118 min, (e) 134 min and (f) 174 min in the reaction mixture.

effect can be seen in the V 2p fittings of Dupuis and coworkers [52], hence it is not an effect restricted to powder samples. Hess and coworkers [85, 86] observed an additional feature in their XPS of V_xO_y/SBA-15 samples, at even higher binding energy than expected for V^{5+}. This was attributed to charging in the final state by the presence of small particles on an insulating support. Hence, the broadening of the V^{5+} contribution may have a final state origin or it could be due to the presence of neighboring reduced atoms.

Concomitantly to the XPS measurements, on-line mass spectrometry shows the main products as butenes, butadiene and, to a lesser extent, benzene. Although this study was performed at reduced pressure, reaction products were similar to those found in high-pressure (1 bar) studies [83, 97]. (Previous studies of *n*-butane dehydrogenation have also detected benzene in the product stream [83].) The combination of low partial pressure of feed with parallel surface monitoring provides a unique tool to follow the processes occurring during the initial period of reaction/deactivation in "slow-motion." Indeed, even under our low-pressure conditions, deactivation of the catalyst and deposition of carbon were observed. Owing to these processes, regeneration cycles were performed by treating the catalyst first in oxygen then in hydrogen at 723 K. After each regeneration, the activity of the

catalysts towards butene and butadiene increased slightly, in agreement with the findings of Jackson and coworkers [109] with 1 bar *n*-butane dehydrogenation at 873 K over the 3.5% V/alumina catalyst. Furthermore, the same group found that V_xO_y/alumina catalysts containing polyvanadates were more effective at dehydrogenation than isolated species [97].

An additional feature of the XPS analysis was the formation of surface carbon during the reaction. Figure 6.4B shows that during the reaction the gas-phase peak shifts to higher binding energy, revealing a surface carbon species which increases as the reaction time increases. The binding energy of the surface carbon species (~284.2 eV) is typical of graphene or aromatic carbon [110]. The formation of a surface carbon species correlates with the mass spectra; surface carbon appears at the point of maximum in benzene formation. It then increases as benzene formation decreases. Hence, it appears that the deposition of carbon on the surface is linked to the retention of benzene. The percentage of surface carbon did not reach more than 3% of the total surface (XPS measured at a kinetic energy of 290 eV, which corresponds to an escape depth of ~1 nm owing to the "universal curve" [111]), during the sub-millibar *in situ* reaction.

Links between changes in activity and surface structure can be clearly observed in Figure 6.5. The oxidation state of vanadium first decreases before carbon begins to form on the surface. The figure shows that deactivation only becomes more significant after formation of carbon, and the vanadium continues to be reduced.

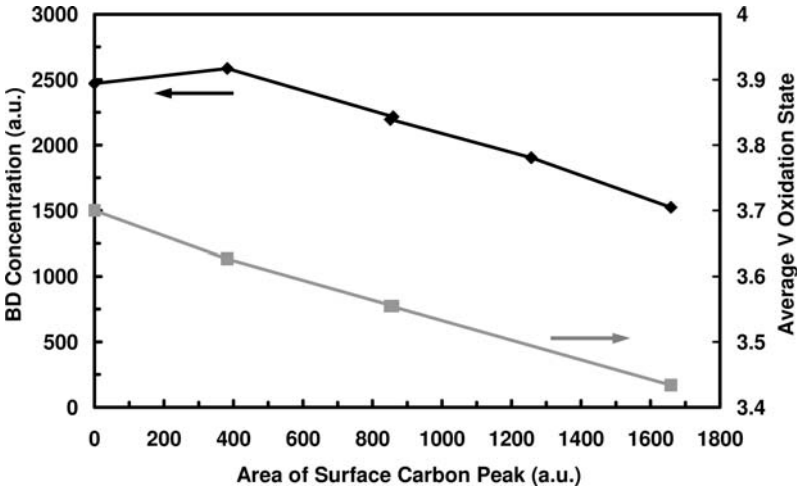

Figure 6.5 Structure-activity link between growth of surface carbon, formation of butadiene (BD) and formal oxidation state of vanadium (reaction conditions: 0.4 mbar *n*-butane and 723 K).

Therefore, it can be postulated that by increasing the number of reduced vanadium sites (as observed by XPS), the number of adjacent sites available for strong hydrocarbon chemisorption increase. Thus XPS indicates that multiple reduced sites may be required for coke formation. Although reduced sites may be active for dehydrogenation, the benefit of maintaining mixed oxidation states may be to separate reduced vanadium sites. Literature suggests that the loading and the type of site (e.g. isolated VO_4 units) influences the reducibility of supported vanadium catalysts [96, 103]. *In situ* Auger electron yield XAS at the carbon K-edge (not shown) have a strong feature at ~285 eV during the dehydrogenation reaction, due to a π^* resonance from unsaturated hydrocarbon(s), which agrees well with the C 1s binding energy. In the mechanism of dehydrogenation, hydrogen is initially removed to form an alkene; if the reaction is selective it may stop here. In the case that the catalyst is unselective, the alkene can be dehydrogenated further to form multiple unsaturation and coke precursors. Studies of coke formation suggest that the dehydrogenation process is followed first by polymerization, then by aromatization of surface species. The formation of benzene can be explained by hydrogenolysis of the secondary–secondary C—C bond of butane followed by oligomerization to benzene.

In addition to our *in situ* study, catalysts deactivated at 100 mbar pressure were examined after treatment in an adjoining high-pressure reaction cell (*n*-butane, 723 K). The samples were transferred without exposure to air and, as expected, the concentration of surface carbon was much greater (~45%). Reduction of the V/Al ratio suggests that either particle agglomeration or preferential deposition of carbon on vanadium occurs, resulting in a reduction of the vanadium signal. It appears that this process is irreversible, as *in situ* reactivation measurement in oxygen (after two activation/reaction cycles) does not show the same composition as the "fresh" sample.

Although carbon XAS is rarely applied in catalysis, several studies have looked at the carbon K-edge of post-reaction carbonaceous species using electron energy loss spectroscopy [91, 112]. This can contain valuable information about the nature of carbon deposited on the catalyst during deactivation. A range of catalysts (1–8% V/alumina) were examined after deactivation in 1 bar of *n*-butane at 873 K. The main feature for all of the catalysts was a strong π^* (~285 eV) resonance, which is due to the presence of unsaturated hydrocarbons. At higher energies in the region associated with σ-related features, the spectra were relatively featureless and suggested the presence of disordered carbon [113]. Although the higher loading catalysts were similar, the 1% V/alumina catalyst showed a shoulder on the low-energy side of the main feature which suggested the formation of a styrene-like compound, in agreement with findings of Wu and coworkers [99].

By combining the techniques of XPS and XAS, insights into the electronic structure of the dehydrogenation catalysts V_xO_y/alumina have been observed, and, by correlation with activity data, a greater understanding of the dehydrogenation mechanism and subsequent coke formation, was possible.

6.3.2.2 Oxidative Dehydrogenation of *n*-Butane

As mentioned previously, the main advantages of oxidative dehydrogenation are enhanced thermodynamics together with a reduction in coking. Oxidative dehydrogenation of alkanes has been investigated by a number of authors [93–96, 114, 115]. Oxidative dehydrogenation catalysts are normally based on mixed-metal oxides, and vanadium oxide-based catalysts are among the most successful of those considered. Thus, the V_xO_y/alumina catalysts used for *in situ* butane dehydrogenation (Section 6.3.2.1) were also examined under the conditions of *in situ* oxidative dehydrogenation.

The addition of oxygen (1–2 vol%) to an *n*-butane feed resulted in strong changes in the vanadium $2p_{3/2}$ spectra and to a lesser extent in the vanadium L_3 edge (not shown). Figure 6.6 indicates that on addition of oxygen, a significant amount of V^{5+} species were maintained, compared with direct dehydrogenation conditions. This is not completely unexpected, as in the absence of oxygen in the reaction feed any oxygen removed from the catalyst during reaction is not replenished. Unfortunately, keeping V^{5+} as the main species was accompanied by an increase in the formation of oxygenated side-products such as furan, dihydrofuran and CO_x, which have been observed during *n*-butane oxidation and to a lesser extent in the initial stage of dehydrogenation [83]. However, surface carbon was not detected and only the gas-phase peak from butane was observed in the C 1s region. This is likely due to the automatic removal of surface carbon species by the oxygen in the feed (or prevention of irreversible adsorption), thus reducing

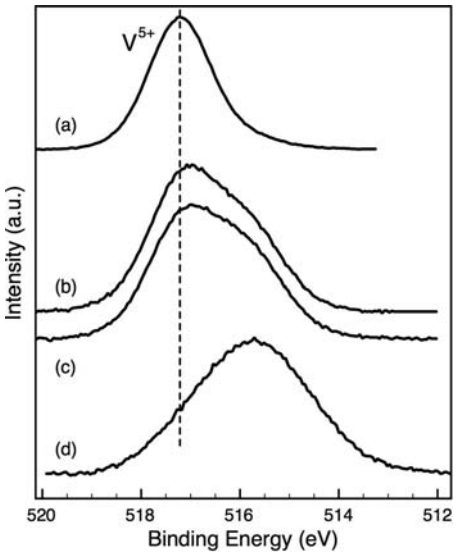

Figure 6.6 Comparison of V $2p_{3/2}$ XPS of 3.5% V/alumina at 723 K in (a) 0.5 mbar oxygen, (b) 0.4 mbar 2% O_2 in *n*-butane, (c) 0.4 mbar 1% O_2 in *n*-butane and (d) 0.4 mbar *n*-butane.

the need for catalyst regeneration; however, this is at the expense of reduced selectivity.

Lopez-Nieto and coworkers [93, 95] proposed that tetrahedral V^{5+} is the active and selective site for oxidative dehydrogenation of short chain alkanes (C_2—C_4) and isolated sites prevent the occurrence of consecutive reactions, that is, to total oxidation products. Others suggested that neither terminal V=O nor bridging V—O—V bonds are essential to the catalytic activity of alumina supported vanadium oxide catalysts, but rather that V—O—Al bonds play a crucial role [96]. On the other hand, Iglesia and coworkers [116] measured the extent of reduction of active VO_x surface on γ-Al_2O_3 during oxidative dehydrogenation (ODH) of propane by *in situ* UV-Vis spectroscopy, and observed a positive correlation with the reaction rate. Transient observations during changes in C_3H_8 and O_2 concentrations clearly indicated that only a fraction of the prevalent reduced centers (~30–40%) are responsible for the catalytic turnover. Blasco and coworkers [117] identified V^{4+} species in post-reaction (ODH of ethane and *n*-butane) catalysts, the contribution of which increased with increased conversion of reactants. Additionally, the highest formaldehyde signal was observed in temperature programmed desorption experiment from adsorbed methanol when the vanadyls were partially removed from the V_2O_5 surface [118]. Furthermore no formaldehyde formed from perfectly vanadyl-terminated surface. Our results are in line with these latter findings, and suggest that careful control of the surface oxidation state by addition of oxidizing agents can be useful in stabilizing the active catalytic site as well as in preventing coke deposition. Steps taken to reduce coke formation include control of feed gas composition (for example inclusion of hydrogen, steam, carbon dioxide or oxygen to prevent chemisorption of hydrocarbons [119]) and addition of promoters to modify the surface properties [119–123]. However, addition of oxidizing gases should be minimized to prevent reduction in selectivity through formation of side-products.

6.3.3 Selective Oxidation

Selective oxidation of hydrocarbons is of key importance in functionalization of hydrocarbon molecules. It is always a multi-step process with consecutive abstraction of hydrogen and addition of oxygen atoms. The difficulty of this reaction is, undoubtedly, that the process should go through these many steps, but also should stop at the desired product. Such requirements can be met by complex mixed-metal oxides, and the XPS characterization of two selected examples is briefly reviewed here.

6.3.3.1 *n*-Butane Selective Oxidation to Maleic Anhydride Over VPO

Maleic anhydride (MA) is an important intermediate in the production of chemicals such as unsaturated polyester resins, lube oil additives, maleic copolymers and others [124]. Currently, MA is predominantly produced by the oxidation of butane, and all industrial catalysts for this reaction are based on vanadium phos-

phorus oxides (VPO). Different types of technology were developed (fixed, fluidized or transported bed reactors), and an important aspect of the following discussion is that the catalyst is able to operate in both oxidizing and reducing environments.

Several review papers have been published on VPO materials, covering various aspects, from preparation and characterization to the catalytic properties, with focus on the reaction mechanism [125–129]. In brief, VPO as a complex catalytic system can comprise many distinct and known phases (α-, β-, γ-, δ-$VOPO_4$, $(VO)_2P_2O_7$, $VO(PO_3)_2$, VPO_4, etc.) but also less well characterized amorphous material. It is prepared by different (e.g. aqueous, alcoholic) routes with the intermediate formation of $VO(HPO_4)\cdot 0.5H_2O$, the hemihydrate, which is the precursor of the active catalyst. Depending on the P : V ratio in the precipitation and the conditions of the heat treatment of the precursor material, the prepared "non-equilibrated" catalyst can comprise different phases with various degrees of crystallinity and defect structure. However, after long-term operation the catalysts prepared in the conventional VPD route exhibited high crystallinity and the only phase identified by XRD was $(VO)_2P_2O_7$ (VPP) [128, 130–134]. This led several research groups to conclude that $(VO)_2P_2O_7$ (i.e. V^{4+}) is the active material and that its (100) crystal plane (which is supposed to be the most exposed) contains the active sites. Different preparation routes, however, resulted in materials with non-uniform bulk structure and different Brunauer–Emmett–Teller surface area, but comparable intrinsic activity [129, 135]. This led Hutchings to conclude that the surfaces exposed on these different materials must all be the same, even though their bulk structures are completely different. Furthermore, the necessity of crystallinity becomes dubious considering that the amorphous vanadium phosphate catalyst prepared by the same group (Hutchings and coworkers) [136] in supercritical CO_2 conditions was more active (MA formation rate per surface unit) than the comparable crystalline VPO catalysts, although with worse selectivity. Previously, combined XRD, ^{31}P NMR and Raman studies [137–139] indicated that XRD alone is not sufficient for identifying the presence of minority phases, and that not only V^{4+} but some V^{5+} species exist in almost all materials. Many studies [137, 140–144] provided indirect evidence that vanadium in both oxidation states is needed for the whole catalytic process. Furthermore, Coulston and coworkers [145] argued about the central role of V^{5+}, as its reduction showed a good quantitative correlation with the MA formation on supported VPO. Thus there is no clear agreement in the literature about the active sites of the reaction. Even the reaction mechanism, the participation of lattice or various types of surface oxygen species (O_2^-, O_2^{2-}, O^-) and the role of phosphorus enrichment remain under discussion [126, 128, 146–150].

Being relatively surface sensitive, XPS can contribute to an understanding of this catalytic system, and has already done so. It gives valuable information on the formal oxidation state and the stoichiometry of the constituents in the sampling depth of the technique. However, XPS investigations reported in the literature are

not without problems. VPOs are insulators at room temperature and *in vacuo* (under conventional XPS conditions); hence the emission of electrons from the samples leaves the surface charged making the exact binding energy identification difficult. Charge compensation using an electron flood gun reduces charging effects, and referencing the binding-energy scale to "adventitious" carbon contamination is widely applied. In fact, in the reviewed research papers on VPO-related materials, the vast majority calibrate the binding-energy scale according to the observed C 1s energy. A few others use arbitrarily taken P 2p energies. As not the same C 1s binding energy is used as reference (C 1s: 284.5–285 eV), and because this peak can be relatively broad (because of charging or overlapping components), the uncertainty of position will be high, and the reported E_Bs of V/P/O core levels, even in very similar materials, strongly diverge (Table 6.3). A further complication arises if the main VPO material is differentially charged compared to the carbon taken as reference. This can frequently happen considering the different conductivity of carbon and the oxide material. Most VPOs have open valence orbitals with V 3d electrons at ~1 ± 0.2 eV E_B (Figure 6.7), similar to binary vanadium oxides in non-V^{5+} states [63]. Since, except for charging, no significant spectral difference between the insulating and metallic phases of VO_2 has been observed, a more appropriate referencing of VPOs can be achieved, circumventing differential charging, by means of the V 3d transition. In the reviewers' opinion, differential charging is the main reason that most of the reported core level binding energies in the VPO-related literature are markedly higher than for example, in the V_xO_y system. For example, the V 2p energy of binary oxides is found at 517.1 ± 0.1 eV for V_2O_5 and 516.0 ± 0.2 eV for VO_2. On the contrary, most of the E_B values of V 2p in VPOs corresponding to the V^{4+} state are reported in the range 516.8–518.2 eV, which is 1–2 eV higher than in the binary VO_2. This binding-energy offset is usually conserved in O 1s and P 2p core levels, as well. Fortunately, Garbassi and coworkers [160] noticed that the binding-energy difference (O 1s–V 2p) can be related to the oxidation state of vanadium. Later, Coulston [158] proposed a quantitative correlation between the average oxidation state of vanadium and the previously mentioned splitting of the transition centroids, according to the following equation:

$$V_{ox} = 13.82 - 0.68[\text{O 1s} - \text{V 2p}(3/2)] \tag{6.7}$$

This equation has been extensively accepted and applied, and thus comparison of various VPO materials in different publications has been possible (see Table 6.3). Although calculating the mean oxidation state of vanadium is exceptionally valuable (especially with spectra lacking resolution), it allows determination of the fraction of different contributions if only two oxidation states are present in the sample (i.e. it is not useful if V^{5+}/ V^{4+}/ V^{3+} are simultaneously present). Furthermore, with a significantly high E_B contribution in the O 1s line (from adsorbed water, OH groups and carbon-related O) the equation will overestimate the degree of reduction of the formal vanadium valence.

Table 6.3 XPS binding energies of VPO and related materials according to the literature survey.

Reference	E_B V2p (3/2)	E_B O1s	ΔE_B (O1s-V2p 3/2)	E_B P2p	E_B reference	V^{5+}/V^{4+}	P/V	Note
[137]	518 and 516.9	530.5	12.5 and 13.6	131.7	C1s: 284.5	0.21 Co:0.3; Fe:0.14	~2%	VPO Co-VPO Fe-VPO
[151]	518 and 516.9				C1s: 284.5	15% V^{5+}		VPO
[138]	518 and 516.9				C1s: 284.5	V5+: 47↓ to 37%		VPOs with different activation time on stream
[134]	518.2 and 516.9 518.2 and 516.9 517	531.3 (532.6) 531.3 (532.6) 531.3 (532.5)	13.1 and 14.4 13.1 and 14.4 14.3	133.6 133.7 133.7	C1s: 284.9	50:50? 50:50? Only V^{4+}		Calcined sample Non-equilibrated VPO Equilibrated VPO
[152]		532.35		135	P2p: 135			$Na_4P_2O_7 \cdot 10H_2O$
[153]	517.7	(~532.0) 533.51	~14.3	135	P2p: 135	(V^{4+})		$VO(H_2PO_4)_2$ V3d: ~3 eV!
[154]	518.25	532.62	14.37	135	P2p: 135	(V^{4+})		$VOHPO_4$*$0.5H_2O$ V3d: ~3.5 eV! C1s:285 eV diff. charging
[155]	519.84	533.07	13.23	135	P2p: 135	(V^{5+})		$VOPO_4 \cdot 2H_2O$ C1s:286.1 eV!
[156]	517.7–517.9	532.2	14.3–14.5		C1s: 284.6		2.8 2.6	Eq.VPO Addition of Co(2+)

[140]	517.9	532.3	14.4	134.3	C1s: 284.6		1.8 (up to 7.8)	(Ref compounds) and VPOs After H_2 or inert: P/V↑↑↑[a)]
[157]	517.7–517.9	532.2	14.3–14.5		C1s: 284.6		2.8 2.6–3.5	Un-promoted VPO Co-promoted VPO Surface enrichment of Co
[158]							~stoichiometry	ΔE_B (O1s-V2p 3/2) Formula
[141]	518 516.9				C1s: 284.5	30%–70% 50%–50%	1.6 1.55	VPO Nb^{5+} doped VPO
[142]	517.5–517.2 Fit: 518,516.9	~531.4	13.9–14.2		C1s: 284.5	47%–53% 37%–63%	1.6	VPO (0.1 h TOS) VPO (132 h TOS)
[159]	517.0 517.1	531.3 531.5	14.3 14.4	134.0 134.1	C1s: 284.6		1.4 2.4	Bulk VPO $VPO/ZrO_2(H_3PO_4)$
[160]	516.0 and 517.2	530.2	13.0 and14.2	~133.3 as overall max.	C1s: 284.6		1.2-2.3	Depending on the nominal P/V, but surface P enrichment
[161]	517.7/517.6 517.5/517.5	532.2/532.4 531.9/532.1	14.5/14.8 14.4/14.6	133.9/134.1 134/134	C1s: 284.8		1.23/1.54 1.6/1.82	VPO1/VPO2 VPBiO1/VPBiO2
[162]	518	532.3	14.3	133.9–134.3	C1s: 284.6		2.5-2.9 Refs: 1.2!![b)]	VPO, Mo-VPO β-$VOPO_4$ and $(VO)_2P_2O_7$

a After treatment with H_2 or inert, the P/V ratio strongly increased (up to 7.8).
b Reference VPO phases gave P/V ratio 1.2, while catalysts up to 2.9.

Table 6.3 *Continued*

Reference	E_B V2p (3/2)	E_B O1s	ΔE_B (O1s-V2p 3/2)	E_B P2p	E_B reference	V^{5+}/V^{4+}	P/V	Note
[163]	517.3–517.1 517.1–517.4	531.4–531.6 532.6–9 (SiO2)	14.1–14.5	133.6–7 133.7–134	C1s: 284.6			VPO bulk VPO/SBA-15
[143]	518 and 516				C1s: 284.5	28/72		In fuel rich (O2/C4:0.6)
[164]	516.8 517				C1s: 284.6		1.5 After r: 1.3[c]	5% VPO/MCM-41 5% VPO after reaction
[165]	517.5			134.1	C1s: 285			VPO glasses for cross section
[166]	516.6	531.2	14.6		C1s: 284.8			$VOHPO_4 \cdot 0.5H_2O$
[167]	518, 516.9	~532	~14, 15.1		C1s: 284.5?	82/18		fresh VPO.
[79]	~517.2	~531.3	14.1 14.4		C1s: 284.5			VPO UHV effect on V^{5+}
[149]	517.4–517.1	531.6–531.2	14.5–13.9	133.6–133.9	C1s: 285		1.37–1.68	(Bi)-VPOs
[150]	517.6–517.8	532–532.6		133.7–134.1	C1s: 285		1.32–2.05	(Co)-VPOs
[168]	~517.2	531.2			C1s: 284.6		1.3–1.4	(Cs)-VPOs (Ref. VPO glasses)
[20]		530.3–531.7 530.4–531.9		132.3–133.8 132.8–134.5	C1s: 285			Alkali phosphate, Pyrophosphate ΔE_B O-P ~const.

c The P/V ratio decreased after reaction to 1.3.

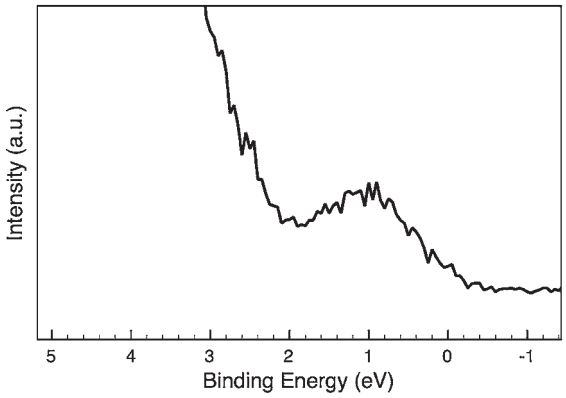

Figure 6.7 Top of the valence band of a VPO catalyst showing the band gap transition of V 3d.

In addition, the existence of different oxidation states can be determined by curve fitting of the recorded spectrum. In the case of vanadium, however, the situation is a bit more complex, as final state effects can complicate the spectral interpretation. As all the lower valence vanadium cations have open valence shells, multiple splitting, which is typically not resolved in the V 2p region, will significantly broaden (sometimes asymmetrically) the lower valence components. Therefore one has to use known, but widely different, FWHM values to fit the individual components. Spectral resolution depends strongly on the instrumentation; hence adequate fitting results can be obtained after carrying out XPS experiments on known reference compounds, and applying the observed (or at least similar) spectral function in the fitting procedure of VPOs. Unfortunately such data treatment has almost never been carried out, and only arbitrarily taken reference positions were fixed in fitting VPO spectra and forcing the algorithm to observe different valences in an unresolved spectral envelope. Considering the strong scattering and shift of the core level E_Bs (Table 6.3), the reliability of such data treatment is highly questionable.

Another widely neglected fact in the VPO literature when interpreting XPS data is that information arises from a certain depth. This, using Mg or Al Kα excitation, is as high as ~3 nm, the technique being thus *a priori* not sensitive to the top surface layer on which the catalytic reaction proceeds. Furthermore, the sample can be inhomogeneous in the top few layers, allowing no conclusions to be drawn as to whether a certain state coexists on the surface or not. This problem can be circumvented by carrying out XPS investigations with a tunable X-ray source at a synchrotron as detailed below. Figure 6.8 compares the *in situ* V 2p core levels of two, approximately equally active, VPO materials (VPO_{P4}, VPO_{P9}: prepared in Hutchings' laboratory [169]), under fuel-lean *n*-butane oxidation conditions, at two different excitation energies. The spectra were published in a preliminary form [100]. Note that referencing the binding-energy scale to the V 3d valence transition

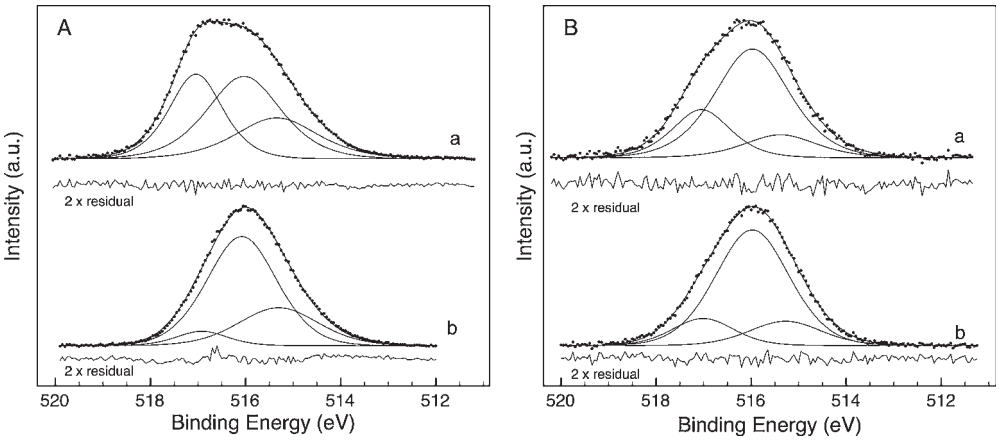

Figure 6.8 Vanadium $2p_{3/2}$ region of two VPO catalysts (a: VPO_{P9}, b: VPO_{P4}) *in situ* under butane selective oxidation conditions (T: 673 K) at two excitation energies. (A) 1254 eV ("bulk" sensitive), as typically applied in laboratory XPS experiments. (B) 730 eV ("surface" sensitive). As the spectral function of V^{4+} in VPO is not known, formally three Gauss-Lorenz curves were used to approximate the obviously visible V^{5+} contribution in VPO_{P9} and to account for the asymmetry seen on the low E_B side of the peaks. Although this latter peak, according to its E_B, might be assigned to V^{3+}, its identification purely on this basis is not straightforward. Its location however seems to be more sub-surface than directly on the surface.

(Figure 6.7) makes the V 2p core levels of VPOs analogous to binary oxides! Furthermore, applying Coulston's equation (Equation 6.7), calculated average valences nicely agree with the result of the curve fitting. According to the electron attenuation in the solid, the applied excitation energies correspond to approximately 1 and 3 nm information depth, respectively the notification "surface" and "bulk". At 1254 eV excitation energy (which is typically also applied in laboratory experiments with Mg Kα excitation) the two samples are clearly different, mainly because of the relatively high V^{5+} contribution in VPO_{P9}. However, surface-sensitive spectra indicate many more similarities. Undoubtedly, VPO_{P9} is inhomogeneous in the top 1–3 nm: some V^{5+} species (phase?) sit in sub-surface positions, while mainly V^{4+} occupies the top surface position. As opposed to VPO_{P9}, VPO_{P4} is fairly homogeneous in XPS sampling depth. However, in line with the fitting results, the opposite asymmetry of the peaks for surface- and bulk-sensitive modes clearly indicates a small V^{5+} contribution at the surface. Whether or not VPO_{P9} also contains V^{5+} in the top layer is not easily concluded simply on the basis of the spectra. (Note that, theoretically, it is possible to answer this question, if a precise geometrical model of the terminating few layers of VPO material is available. However, the characteristics of the top few layers are widely disputed in the VPO community, and furthermore the V^{5+} phase in the sub-surface position is not compatible with the $(VO)_2P_2O_7$ structure. We thus decided not to model our depth distribution.) Based on similar catalytic performance, however, it is likely that both materials

contain small V^{5+} centers in a V^{4+} matrix at the surface. This result is in line with numerous literature reports [79, 137, 140–143, 149, 157, 167] derived from conventional XPS experiments, in which, however, precaution is necessary. It is important to note that different conclusions would have been drawn on the sole basis of the spectra at typical laboratory XPS excitation! The similarity of the two VPO materials is further manifested in the surface-sensitive O 1s spectra (Figure 6.9A), indicating nearly identical oxygen species. The main line at ~530 eV is in accordance with the lattice oxygen in binary vanadium oxide systems, while the higher E_B components might, as a first approximation, correspond to more electrophilic surface oxygen species, for example OH groups or various oxygen species bonded to phosphorus or carbon [149, 152, 166, 170]. (It is assumed in the literature that phosphate and pyrophosphate oxygen is more electrophilic and should appear at significantly higher binding energy than oxygen bonding to vanadium.) Comparison of these spectra with binary vanadium oxides has serious consequences in data interpretation: in both cases the main line is found at the same E_B. Therefore, either (i) the surface consists mainly of VO_x in VPO, and there is a considerable excess of vanadium on the surface or (ii) phosphorus linkage does not modify the binding energy of lattice oxygen (at least within the resolution of our and previous XPS studies). In either case, most XPS interpretations and their consequences related to mechanistic considerations in the literature would need substantial revision! To be able to further comment on this issue, the surface P/V ratio has to be taken into consideration.

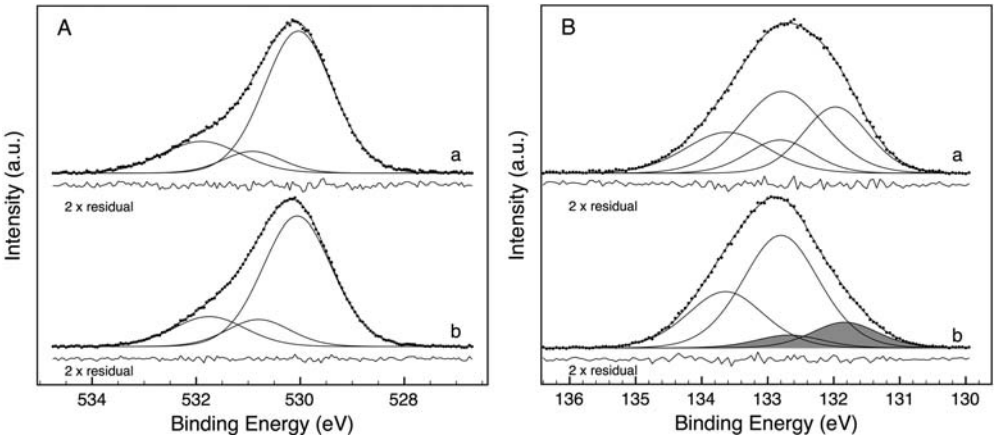

Figure 6.9 (A) Oxygen 1s region of two VPO catalysts (a: VPO_{P9}, b: VPO_{P4}) *in situ* under butane selective oxidation condition (T: 673 K) recorded at 730 eV ("surface" sensitive) excitation energy. (B) Phosphorus 2p region of two VPO catalysts (a: VPO_{P9}, b: VPO_{P4}) *in situ* under butane selective oxidation conditions (T: 400 °C) recorded at 854 eV ("bulk" sensitive) excitation energy.

The second motivation for doing an XPS analysis of materials is to learn about the elemental stoichiometry of the near-surface region, which brings us to the widely disputed issue of the P/V ratio of VPOs. The P/V ratio is often considered to be an important factor in the catalytic properties of VPO [126, 128, 140, 171, 172]. This is mainly based on conventional XPS experiments, in which phosphorus enrichment in the top few nanometers was found [140–142, 150, 156, 157, 159–162, 164, 168, 172, 173]. According to a literature survey, the P/V ratio varied mainly in the range of 0.8–3 (Table 6.3). Owing to the different sampling depth of V 2p and P 2p in typical ESCA experiments (as a result of the different kinetic energies of the photoelectrons), surface impurities (e.g. carbon deposits) will attenuate the lower KE electrons from vanadium more strongly and hence slightly overestimate the P/V ratios. Furthermore, the calculation relies on the often-questioned accuracy of photoemission cross-sections or sensitivity factors. To circumvent this problem, several attempts were made to apply reference substances in recalibrating possible incorrect sensitivity factors [158, 165, 168, 174]. Okuhara and coworkers [165, 174] prepared VPO glasses with different stoichiometry, and found that the Scofield [175] sensitivity factors overestimate the P/V ratio by a factor of 4.1/2.75 (i.e. by approximately +50%), decreasing the P/V ratio of their VPO samples to values close to the nominal bulk composition. In the same vein, using VPO glass Richter and coworkers [168] found a much smaller discrepancy of only ~14%, and their estimation gave a surface P/V ratio of 1.3–1.5. Considering the sampling depth as 3 nm and assuming a profile of P segregation, the phosphorus concentration in the top layer was assumed to be even higher. Ion-scattering spectroscopy experiments, showing a P/V ratio of 2–3, confirmed this hypothesis. Coulston and coworkers [158] used organometallic complexes containing vanadium and phosphorus for XPS calibration. The observed deviation was as high as ~+75%, overestimating the theoretically calculated composition of the phosphorus content. In this way, the surface composition of different VPO phases nicely approached the nominal bulk values. Interestingly, the Scofield sensitivity factors gave a fairly reasonable $V_2O_{5.18}$ stoichiometry for vanadium pentoxide, indicating that the problem of high P/V ratios is manifested in the phosphorus calculation. As Richter [168] pointed out, the VPOs (even VPO glasses) are sensitive to water/moisture, giving rise to hydrolysis of V—O—P bonds and hydration of phosphate groups (see below). Therefore, if moisture-driven segregation of P occurs in both VPOs and VPO glasses, the recalibration of cross-sections will simply cancel out the P segregation, resulting in a stoichiometry resembling that of the bulk. Unfortunately, even for organometallic complexes it has not been proven that the ligands do not undergo X-ray-induced damage and are stable under UHV conditions, which may hamper determination of the real P/V ratio. Hence the calculated P/V ratios (whether recalibrated or not), should be approached, in most cases, with caution.

There might, however, be some exceptions. Once the calculated ratios exceed 2, even using Coulston's recalibration, the P/V ratio (2/1.75) will be high enough to account for a surface terminated by pyrophosphate groups. Sometimes, values even higher than 2 were reported (see Table 6.3), which would clearly indicate

phosphorus segregation to the surface. In other cases, P enrichment is strongly indicated when, using the same calculations, a series of samples shows a clear variation/tendency in the P/V ratio. Such a situation was described in [150, 160, 162, 164]. Phosphorus enrichment was further supported by low-energy ion scattering (LEIS) experiments by two independent research groups [142, 176]. This technique, as opposed to XPS, is sensitive to the topmost surface layer. Delichère and coworkers [142] observed an initial P/V ratio of 2.35, which slowly decreased to below 1.2 by the end of the measurement owing to the sputtering nature of the experiment. From the sputtering profile of the individual elements, they concluded that, in fact, it is not an enrichment of phosphorus, but rather a deficiency of vanadium, that is responsible for the observations. Jansen and coworkers [176] detected a P/V ratio of 2 ± 0.2 and they argued that VPO catalysts could be terminated by a distorted vanadyl pyrophosphate structure, where the excess phosphorus is positioned between the vanadyl units and the phosphate groups. To sum up, there are many cases in which no conclusion on surface enrichment can be drawn; however, in many others phosphorus does indeed seem to segregate to the surface.

Phosphorus spectra were collected during *in situ* experiments as well; hence the P/V ratios could be calculated. Applying theoretical cross-sections by Yeh and Lindau [177], the P/V ratios were as high as 2.5. When using measurements on reference $VOPO_4$ phases, the ratio drops to ~1.2–1.3, as calculated by Kleimenov [100]. Repeated experiments on VPO_{P4} confirmed the small phosphorus excess in the topmost layers (~1.2) while with higher (~3 nm) sampling depth the ratio approached the nominal stoichiometry of 1. Note, however, that possible phosphate segregation in the reference material might give rise to underestimation of the P/V ratio of our VPOs.

As opposed to the P/V ratios, the phosphorus core levels are rarely depicted in the literature. *In situ* P 2p spectra are show in Figure 6.9B. In general, phosphorus in the non-elemental form is represented by an unresolved doublet with energy separation of ~0.85 eV and area ratio of 2 : 1. The shape of our P 2p spectra can be best described by the presence of at least two doublets, indicating a minimum number of two distinct phosphorus species. Two doublets were used in the curve fitting procedure. The 3/2 spin orbit component of the more abundant species is close to the maximum of the 2p envelope at 132.8 eV, which is again lower than most of the reported energies. Morgan and coworkers [20] investigated alkali phosphates and pyrophosphates, and cesium and potassium pyrophosphate would match perfectly to this energy. All the other (Rb, Na, Li) pyrophosphates would also fit, assuming small differential charging in Morgan's work, relative to the reference C1s line, as the separation of O 1s–P 2p was mainly independent of the type of cation. Morgan observed the corresponding phosphate 2p values at 0.5–0.7 eV lower energy, which is not far away from the 0.8–0.9 eV in our case. Therefore, we suppose the presence of mixed pyrophosphate/phosphate species in the surface-near region. Recalling the V 2p spectra, VPO_{P9} contained significant amounts of V^{5+}, which is most likely one of the phosphate phases/species, while the other sample contained much less. The relative concentration of

V^{5+}/V^{4+} in both samples fits quite well to the phosphate/pyrophosphate ratio, indicating the correspondence of the two core levels. Obviously, owing to lack of resolution in the 2p core level, the presence of additional P species cannot be excluded.

The entirely neglected, but extremely important, region of XPS investigations of VPO material is the valence band. The high-lying levels correspond to bonding, anti-bonding and delocalized orbitals, which hold essential information about the catalytic properties of the material. As the valence region is more sensitive to the chemical environment (temperature, presence of reactive gases; i.e. reaction conditions) than the core levels, *in situ* instrumentation is highly beneficial, and is expected to unravel important pieces in the puzzle of VPO chemistry. Fortunately, recent advances in theoretical calculations can facilitate the interpretation of the complex overlapping structures observed in the valence band. Considering first a naive ionic view, VPOs with fully oxidized vanadium and phosphorus (V^{5+}, P^{5+}) will show only an O 2p contribution in the valence band. From the more simple V_2O_5 system, it can be easily concluded that it is most likely incorrect, as all-electron DFT calculations by Eyert and Höck [64] have clearly shown strong hybridization of the crystal field split V 3d and O 2p states. Therefore in the valence band of VPOs a strong mixing of V 3d, O 2p and P 3p/3s orbitals is expected. Using cluster and DFT calculations, Hermann, Witko and coworkers [69, 70] investigated the electronic structure of the perfect VPP surface and model clusters. The calculations show that vanadyl pyrophosphate forms a material with mixed ionic–covalent character. According to DFT results, the vanadium atoms are described by atomic charges ~+1.0 and phosphorus atoms by ~+1.3 [69]. Major covalent contributions participate in the V—O as well as in the P—O bonding. Triply coordinated oxygen sites are found to be the most negatively charged (–0.74). Furthermore, the calculations indicated that doubly coordinated oxygen sites and oxygen atoms singly coordinated to phosphorus are characterized by a similar local susceptibility with respect to electrophilic attack. Figure 6.10 depicts the valence band region of VPO_{P9} *in situ* (as shown previously for the low-lying core levels). Since vanadium is mainly in the reduced formal V^{4+} state, its 3d orbital contribution at ~1 eV represents the highest occupied molecular orbital (HOMO) state of VPO. The 2–7 eV region is typically occupied by non-bonding O 2p and mixed bonding orbitals in vanadium oxides, while the features between 8 and 12 eV are characteristic of P—O mixed orbitals [170]. XPS analysis by Sherwood and coworkers [152–155] of different (pyro)phosphate materials indicate a non-negligible contribution of the (pyro)phosphate orbitals in the higher lying 3–8 eV region, as well. Thompson and coworkers [178, 179] calculated local and total density of states (DOS) of vanadyl pyrophosphate. Their calculation included DOS of bulk, relaxed and non-relaxed (100) surface, pyrophosphate termination and the hydrated surface. Our data adequately reproduced the hydrated surface (the calculation is included in Figure 6.10), while it did not match the other DOS curves. Some of the intensity marked by "○" might be described by additional contributions from phosphate orbitals [170], and the arrow indicates a tiny contribution

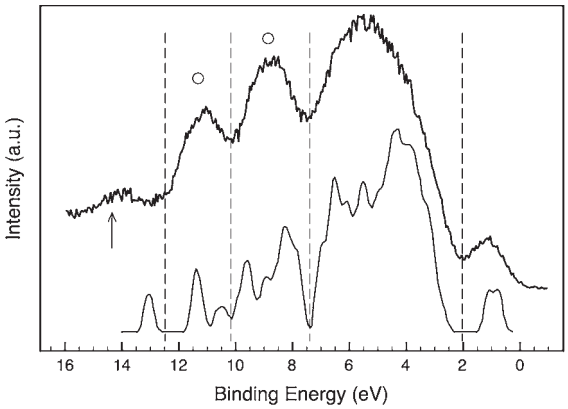

Figure 6.10 Synchrotron based valence band spectrum of VPO_{P9} *in situ* under butane selective oxidation conditions (T: 673 K). In comparison, the total density of states according to DFT cluster calculation [178] of hydrated VPP is shown. The DFT result is reproduced with kind permission of D. Thompson. The theoretical curve is aligned with the experiment to coincide with the band gap transition at ~1 eV. (The peak marked by the arrow corresponds to gas phase signal, while intensity in the position labeled with a circle "○" is partly due to phosphate orbitals.)

from gas-phase O_2. (Some tiny contribution of O_2 is blurred at ~6.5, 11 and 12.5 eV, as well.) Recalling the problem with the O 1s spectra, they seem to be the most compatible with the interpretation of O 1s being composed of a main unresolved peak of lattice oxygen of all types (V—O, P—O, V—O—PV, V—O—P; remember the relatively small difference in their electron population [69]) and a higher binding energy hydroxyl peak (P—OH, V—OH). As most of the VPO material contains a significant amount of carbon from the preparation steps, it will also give a small contribution to the O 1s envelope. The weak photon energy dependence of the O 1s envelopes (not shown) and the relatively high information depth of the valence band (1–2 nm) indicate that not only the top, but likely more layers (2–3) are hydrolyzed and hydrated. The enrichment of phosphorus at the surface was clearly linked to this process [168]. Nevertheless, the mismatch of the hydrated and all the other surfaces calculated by Thompson clearly indicates that mechanistic considerations have to start with a highly hydrated (and likely defect-rich [180, 181]) surface, which will obviously modify the acid–base character of the material. Further, the DOS calculations have shown that the lowest unoccupied molecular orbital (LUMO) of VPP was composed of V 3d unoccupied orbitals, strongly suggesting that both Lewis acid and base character reside in reduced vanadium centers.

Armed with these results, in what follows we attempt to construct a model best describing the observations and the essential literature knowledge on VPO chemistry. Vanadium phosphates are fascinating materials, capable of abstracting hydrogen and transferring many electrons and oxygen during the selective oxida-

tion of butane. In spite of the proposed correlation between the unique bulk structure of VPP and the oxidation process, the overwhelming evidence (effectiveness of different bulk structures, amorphous VPO, significant P excess at the surface) suggest that the active site of the reaction cannot be represented as a simplified termination of the VPP phase. However, the surface seems to have some similarities with VPP: it is a strongly hydrolyzed and hydrated VPP [182], and likely containing additional minority of V^{5+} (and possibly V^{3+} sub-surface) sites, as well. The high P/V ratio is apparently the consequence of the local structure decomposing, slowly releasing phosphoric acid [168], which segregates to the surface. This process is in line with the regenerative treatment of VPO catalysts using phosphorus compounds and/or steam, according to patent literature (for example refs [183, 184]). The destruction of the top few layers is compatible with the 1 nm non-crystalline adlayer found on equilibrated catalysts after back extrapolation to zero time (to remove beam damage) in high-resolution transmission electron microscopy (TEM) experiments [185]. The local nucleophilicity in the surface is manifested through occupied vanadium 3d orbitals (see valence band), but empty vanadium 3d levels predominate in low-lying conduction band regions, indicating that vanadium is also the surface acid site [178, 186]. The kinetic isotope effect in butane oxidation indicated that the rate-determining step is the activation of a methylene C—H bond [146]. Nucleophilic activation of the methylene position was deduced by comparing the HOMO–LUMO structure of butane [185]. Quantum chemical calculations [186] of butane adsorption on VPP clusters have shown that butane is adsorbed via nucleophilic attack of methylene carbon on vanadium, donating electron density toward it. Concomitantly, transfer of electron density from vanadium to methylene hydrogen occurs, with rupture of the C—H bond. Since the vanadium sites, being the most nucleophilic centers, are not modified upon hydration, the calculation gives a highly likely scenario on the decomposed VPP surface as well. Furthermore, in the post-activation steps the participation of mono-coordinated terminal P—O oxygen (as the most basic O) was suggested by the calculations. However, hydration clearly changed that part of the surface DOS [178] thus eliminating the possibility of this scenario. It was shown that butadiene, and to a lesser extent furan, can be produced on reduced VPP and the formation of MA was strongly hindered [144]. Lattice oxygen ions located in the top surface (and to a lesser extent in the sub-surface) layer are suggested to be responsible for the oxidation of butane [146]. Hence it is reasonable to assume, as suggested in many publications [137, 140–145, 187], that V^{5+} sites are necessary in the last oxygen insertion steps. This is compatible with the XPS observations. Although, up to now VPO is the only relevant material for this process, MA can be formed on supported binary V_xO_y, but with lower selectivity [188–190]. That said, the role of phosphorus in VPO seems to increase MA selectivity by isolating individual V_xO_y active ensembles in two dimensions, controlling the over-oxidation of the vanadium ensemble [128, 191] (i.e. hampering the formation of V_2O_5). Consequently, the total oxidation is rendered a minority path. A similar model was constructed and proposed recently by Schlögl [185].

6.3.3.2 Direct Oxidation of Propane to Acrylic Acid Over MoV-Based Mixed Metal Oxides

In recent years, the direct (amm)oxidation of propane into acrylic acid (or to acrylonitrile) has received considerable interest from both an industrial [192–194] and an academic point of view [127, 195, 196], owing to its possible high economic benefit in future technology. Although many different types of materials were investigated for this process, by far the most promising is the orthorhombic phase of a mixed Mo/V/(Te or Sb)/Nb oxide, called M1 [197]. Its structure, shown in Figure 6.11, was refined by DeSanto and coworkers [198] and Murayama and coworkers [199], and consists of five-, six- and seven-membered rings of corner-linking octahedra. The octahedra are proposed to be occupied by molybdenum and vanadium, the pentagonal ring (pentagonal bipyramid) by niobium, and the larger channels with tellurium (or antimony). Another phase often found in MoVTeNb mixed oxides is the so-called M2 phase, which, however, was shown to be inactive for propane activation, but revealed good activity and selectivity in the subsequent reaction steps [197, 200, 201]. M1 crystallizes in the form of needles, and its basal (001) plane, exposing the multi-membered rings, was suggested to contain the active sites of the selective oxidation reaction [202–204]. In numerous communications, Grasselli and coworkers [204–206] proposed a detailed reaction mechanism at the molecular level assuming perfect termination of the basal plane on the basis of "chemical reasoning". The few XPS investigations (Table 6.4) on the M1 phase, however, indicated that the surface is typically enriched by Te (or Sb) and is deficient in V [202, 208–212]. The enrichment of Te was as high as +233%, compared to the bulk composition. Phase-pure M1 samples prepared by Celaya [218] were investigated by *in situ* XPS under propane oxidation conditions in the sub-millibar pressure range. In line with the *ex situ* XPS experiments, the top few layers were significantly different from the bulk (Figure 6.12), that is, Te was strongly enriched while V and Nb were depleted. Even more importantly, the surface seems to possess a certain flexibility, since the addition of water to the feed

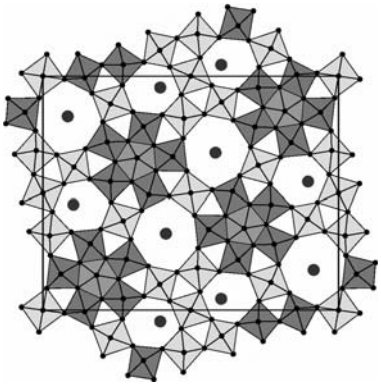

Figure 6.11 Schematic representation of the structure of M1 phase along the (001) direction as determined in [198].

Table 6.4 XPS characteristics of the MoVTeNb related materials according to the literature survey.

Ref.	V2p (3/2)		Mo 3d (5/2)		Nb 3d (5/2)		Te 3d (5/2) [Sb 3d 5/2]		Note
	E_B (eV) [identified as]	Relative change to the bulk (%)	E_B (eV) [identified as]	Relative change to the bulk (%)	E_B (eV) [identified as]	Relative change to the bulk (%)	E_B (eV) [identified as]	Relative change to the bulk (%)	
[207]	516.7–516.5 [5+ and 4+]		232.5–232.8 [6+ and 5+]		206.3–206.6 [mainly 5+]		576.2–576.3 [4+]		MoVTeNb
[208]	516.7 [4+]	–39%	235.7/234.6 (3/2!) [6+/5+]	norm. to Mo[a)]	206.8 [5+]	–7%	576.7 [4+ and 6+]	+233%	M1 (Te) before ammoxidation
[208]	516.7 [4+]	–50%	235.5 (3/2!) [6+]	norm. to Mo	206.7	+33%	576.7 [4+ and 6+]	+167%	M1 (Te) after ammoxidation
[208]	516.3 [4+]	–50%	235.9/234.8 (3/2!) [6+/5+]	norm. to Mo	206.3 [5+]	+33%	*540.1 [4+ and 6+]*	*+123%*	M1 (Sb) before ammoxidation
[208]	516.1 [4+]	–43%	235.9/234.8 (3/2!) [6+/5+]	norm. to Mo	206.3 [5+]	+27%	*540.1 [4+ and 6+]*	*+92%*	M1 (Sb) after ammoxidation
[209]	516.2/517.3 [82% 4+]	0%	232.7/231.7 [56% 6+]	norm. to Mo	?[b)] [5+]	+46%	576.2 [4+]	+32%	T6-2 sample (M1)
[210]	516.2/517.3 [84% 4+]	0%	232.7/231.7 [57% 6+]	norm. to Mo	? [5+]	–9%	576.2 [4+]	+91%	NC-5 (M1)

[211]	516.7	–45%	232.8/231.9 [81% 6+]	norm. to Mo	207.2 [5+]	+27%	576.7 [6+]	+64%	M1 before ammoxidation
[211]	516.3	–55%	232.8/231.9 [72% 6+]	norm. to Mo	207.2 [5+]	+18%	576.4 [6+]	+73%	M1 after ammoxidation
[202]	516.1 [4+]	–49%	232.4 [6+]	+22%	–	–	575.9 [4+]	+13%	$Mo_6V_3Te_1O_x$ (M1) (Air/N2 grinding)
[212]	? [4+]	–28%	? [93% 6+]	norm. to Mo	? [5+]	+42%		+73%	M1
[213]	?	–21%	?	norm. to Mo	?	–41%	?	0%	HT-5 (MoVTeNb)
[214]	516.4/517.5 [85% 4+]	–14	232.8/231.8 [57% 6+]	norm. to Mo	206.5 [5+]	+12	576.3 [4+]	+12	MoVTeNb-5
[215]	517.0 [5+]	+130	232.0 [6+]		–	–	576.5 [4+]	–20	$MoV_{0.2}Te_{0.1}/SiO_2$(I) (Not M1)
[216]	516.7-517.1 [5+]	–48%	232.8/231.5 [mainly 6+]	–6%	207.3 [5+]	–14%	576.3-576.8 [4+ and 6+]	+57%	MN-30: after ammoxidation (M2 phase)
[205]	516.9-515.6 [5+ and 4+]		232.7/231.6 [6+ and 5+]		207.1 [5+]		576.1/572.9 [4+ and 0]		M1
[217]	516.3/517.3 [mainly 4+]	–20%	~232.6 [mainly 6+]	norm. to Mo	?	–12%	?	+83%	#678 (M1andM2)

a Changes in surface concentration relative to bulk were normalized to Mo concentration.
b Binding energy is not given in the publication.

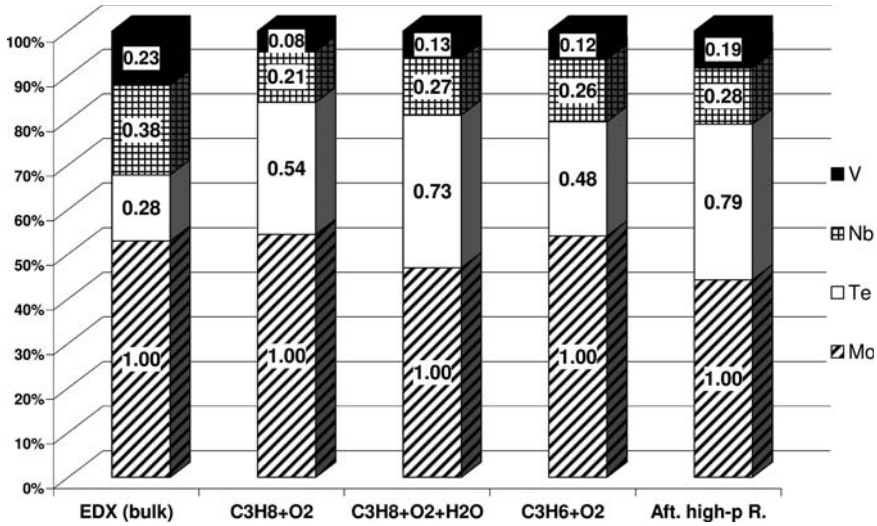

Figure 6.12 Bulk sensitive Elemental composition of an M1 material (M1#1), (according to EDX) in comparison with its surface composition at different conditions as measured by XPS. XPS experiments were carried out *in situ*. Conditions were from left to right: 0.25 mbar $C_3H_8 + O_2$ mixture at 623 K; 0.25 mbar $C_3H_8 + O_2 + H_2O$ at 623 K; 0.25 mbar $C_3H_6 + O_2$ at 623 K; 0.3 mbar O_2 at room temperature after catalytic reaction at 1 bar ($C_3H_8 + O_2 + H_2O + N_2$).

further increased the Te concentration (and possibly increased V and Nb as well), while in the follow-up experiment in propene oxidation without water, Te partly segregated back into the bulk. A post-reaction sample, after quenching the reaction, taken from an atmospheric reactor with typical feed composition gave approximately similar results to *in situ* experiments with water. The characteristic enrichment/depletion profiles of M1 was further validated by LEIS experiments [219, 220]. The surface composition thus cast doubts on the validity of the naive view that the surface could be terminated by an ideal basal plane. On the contrary, high-resolution TEM indicated that the crystals were encapsulated by a 1 nm thick layer without long-range ordering [217]. It was concluded that the short-range ordered terminating layer was necessary to accommodate the essential transport of lattice oxygen and electrons for the selective catalytic function.

Table 6.4 shows some variation in the actual binding energies, which can be partly related to different materials and partly to the lack of universality applied to aligning the E_B scale. The reference point is typically the C 1s line at somewhat arbitrary energies (284.4–285 eV) and some publications do not indicate their referencing procedure at all. However, there are clearly some obvious tendencies to observe in Table 6.4. For example, most materials contain vanadium in mainly the 4+ formal oxidation state; molybdenum is usually fitted to obtain two (6+ and 5+) components, that is, its peak maximum is observed between the position of these two oxidation states; the E_B values of niobium are somewhat lower, and those of

tellurium higher, than the corresponding binary (Nb_2O_5, TeO_2) materials. These observations become even clearer in Table 6.5, in which the binding energies for two M1 materials recorded *in situ* during propane oxidation are listed in comparison to reference materials measured, also *in situ*, under oxygen at elevated temperature. This procedure of investigating the reference materials under *in situ* conditions ensures that only clean materials are compared, which becomes important owing to the small sampling depth probed by the low-KE electrons. The insignificant difference in O 1s binding energy clearly indicates that the "ionicity" of lattice oxygen of the reference binary systems is very similar, and that O 1s will be an insensitive tool for obtaining information on oxygen species. On the other hand, the more sensitive valence band might contain information that could facilitate the understanding of the electronic structure of binary and complex mixed-metal oxides. Since the M1 phase contains mainly molybdenum (6+) oxide, we shall first examine the valence band of MoO_3. Figure 6.13 depicts the measured valence band using synchrotron radiation with different photon energies compared with DFT cluster calculation. As stated previously, the formal oxidation states would dictate an ionic picture with filled O 2p and empty Mo 4d orbitals. From this picture, no significant modification of the valence band envelope is expected, since the various symmetry components of oxygen 2p orbitals would not be preferentially enhanced or weakened. The observed results are, however, truly different. Intensity in the low-lying region of 6–9.5 eV is strongly attenuated at lower excitation energies, that is, for lower KE electrons. Conversely, orbitals

Table 6.5 XPS binding energies of the M1 phase MoVTeNb materials under reaction conditions (see Figure 6.12) in comparison with reference binary oxides measured under oxygen at elevated temperature (623–673 K). At these conditions charging was practically not observed. Experiments used low kinetic energy electrons, and hence were sensitive to the topmost layers.

Sample	O1s (eV)	V2p (3/2) (eV)	Mo3d (5/2) (eV)	Nb3d (5/2) (eV)	Te3d (5/2) (eV)
V_2O_5	530.1	517.2			
MoO_3	530.5		232.6		
Nb_2O_5	530.1[a)]			207.2[a)]	
TeO_2	530.1–530.4[b)]				575.9[b)]
M1#1 $C_3H_8 + O_2$	530.1	516	232.3 (~231)	206.4	576.1
M1#1 $C_3H_8 + O_2 + H_2O$	530.1–530.2	516	232.2 (~231)	206.4	576.2
M1#2 $C_3H_8 + O_2 + H_2O$	530.2	516.1	232.3[c)]	206.6	576.2

a XPS Handbook: 530.6 eV; 207.5 eV.
b XPS Handbook: 530.2 eV; 575.7 eV.
c Measured in $C_3H_8 + O_2$ (without addition of water).

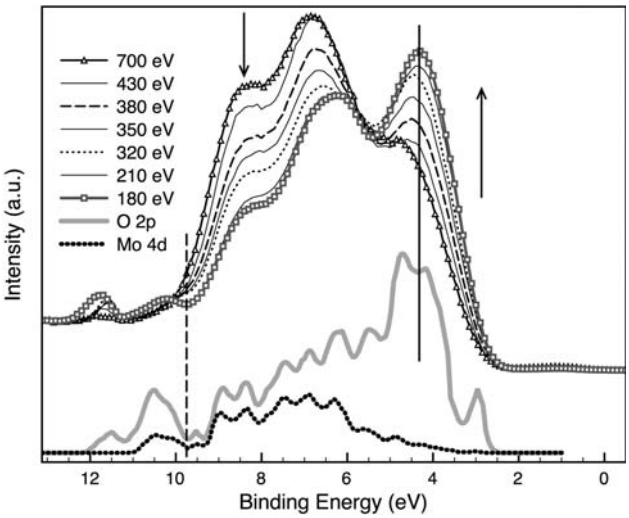

Figure 6.13 Synchrotron based valence band spectra of MoO_3 at different excitation energies. MoO_3 was measured at 623 K in 0.5 mbar O_2 to remove carbon contamination and minimize reduced molybdenum sites. As comparison, the partial density of states according to DFT cluster calculation [68] of O 2p and Mo 4d is shown. DFT result is reproduced with kind permission of K. Hermann. The theoretical curves are aligned to the experiment to coincide with the onset of high-lying valence orbitals at ~2.5 eV. (The peaks above 10 eV in experiments correspond to gas-phase O_2 signal, while those of the calculation are due to bond saturation of peripheral oxygen by hydrogen. Therefore this latter has to be considered as a cluster artefact).

around 4.3 eV are strongly enhanced. The changes can be easily understood considering the variations in the cross-section (CS) of corresponding orbitals. Typically all CS values increase towards lower energies, but their slope can vary. The ratio of O-2p/Mo-4d CS strongly increases from 0.07 at 1041 eV to almost 1.6 at 151.4 eV (Table 6.6). Therefore the spectrum at low-energy excitation corresponds mainly to the various oxygen orbitals, while the enhanced intensities at higher energy are due to molybdenum 4d orbitals. All this is in perfect agreement with the DFT calculations [68] shown for comparison. As a consequence, MoO_3 is not fully ionic and there are appreciable covalent contributions. The calculated Mulliken populations show that the molybdenum centers can be described as $Mo^{2.2+}$ and the negative oxygen charges scale with coordination (from –0.5 to –1) [68, 221]. Therefore the bridging oxygens exhibit more ionic character and are more prone to vacancy formation than the terminal oxygens, which are more covalent.

Moving to further reference materials listed in Table 6.5, all of them, except V_2O_5, exhibit similar CS variations (Table 6.6) giving the opportunity to investigate their possible covalency by XPS. The excitation-energy-dependent valence bands of Nb_2O_5 and TeO_2 (not shown) indicate a qualitatively similar picture to that detailed for MoO_3, suggesting a similar mixed covalent/ionic structure. Although the ratio of O 2p/V 3d CS values remains unchanged in the 150–1040 eV region,

Table 6.6 Theoretical atomic subshell photoionization cross-sections for MoVTeNb-related valence band orbitals at different photon energies, according to the calculations of Yeh and Lindau [177].

	151.4 eV	200 eV	600 eV	1041 eV
O 2p	0.404	0.184	0.0061	0.000 89
V 3d; 4s	0.645; 0.028	0.311; 0.019	0.01; 0.0032	0.0015; 0.001
Mo 4d; 5s	0.254; 0.009	0.257; 0.0054	0.047; 0.0011	0.012; 0.0004
Nb 4d; 5s	0.191; 0.0086	0.184; 0.0052	0.03; 0.0011	0.0079; 0.0004
Te 5s; 5p	0.064; 0.06	0.044; 0.047	0.0083; 0.011	0.0033; 0.0049
O2p/V3d	0.63	0.59	0.61	0.59
O2p/Mo4d	1.59	0.72	0.13	0.07
O2p/Nb4d	2.12	1	0.2	0.11
O2p/Te5p	6.31	4.18	0.73	0.27

DFT calculations, as discussed in Section 6.3.1, yield a similar picture. Furthermore, modification of the valence band envelope as a function of $h\nu$ was characteristic for all M1 and reference catalysts. Therefore it should be stressed that although we adopt the formalism of oxidation states it is essentially always only a formal oxidation state, which is just a chemical tool but does not represent any serious physical meaning, since the electron occupations are considerably different.

Now, by comparing the valence-band region of catalytic materials with the reference oxides (Figure 6.14) we may hope to get a better understanding of the surface electronic structure of our M1 phase. The comparison is made at 180 eV excitation that probes mainly oxygen orbitals (see above). Oxygen 2p in the binary oxides is clearly distinguishable by its unique features. Without going into detail we would like to stress just two points. First, the valence bands of the reference oxides do not show any intensity in the band gap (~1 eV) that would be an indication of a considerable number of oxygen vacancies reducing the corresponding metal cations. Second, tellurium dioxide, because of its tellurium 5p electrons, shows a measurable intensity at 2 eV, which is typically lower than the HOMO of the other oxides. The valence-band spectra of the catalytic materials recorded under reaction conditions are unexpectedly very similar, indicating that they are likely to share the same structural unit at the surface. This becomes important considering the widely different selectivity of the samples: MoV is unable to produce acrylic acid (AA) while the two samples with M1 phase reach a selectivity to AA of 70% or more. All samples show spectral intensity in the band gap (E_B: 1 eV), which fits well with the vanadium state being in its formal 4+ oxidation state. That the intensity in the band gap is small should be no surprise considering the low vanadium content at the top layers (Table 6.4, Figure 6.14). Moreover, it shows clearly that molybdenum cannot be reduced in significant amounts, otherwise the band-gap feature would be more intense [68]. It is also obvious that no V_2O_5-like

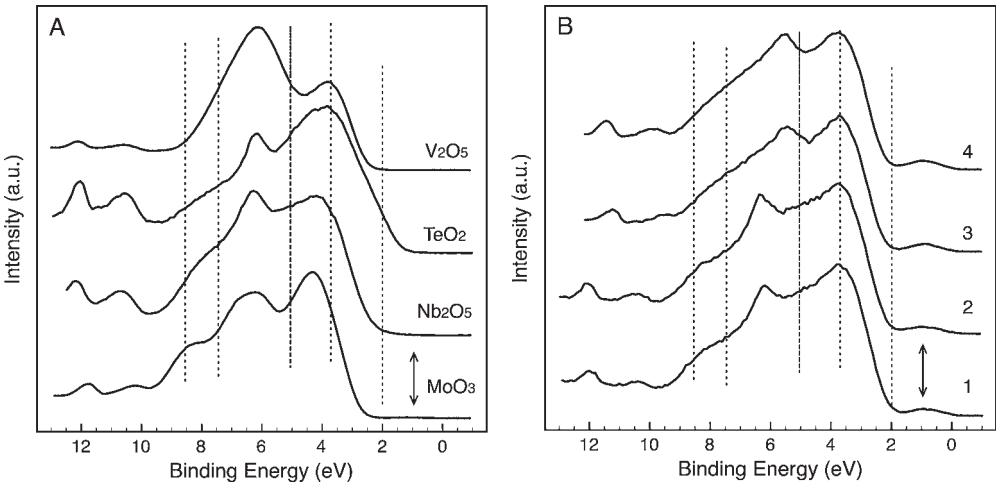

Figure 6.14 Synchrotron based valence band spectra (hν = 180 eV) of clean reference binary oxides (A) and catalytic materials under reaction conditions (B). The reference oxides were recorded at elevated temperature (623–673 K) in 0.2–1 mbar oxygen to remove carbon contamination and minimize reduction. The M1 catalysts (1: M1#1, 2: M1#2) are under propane oxidation conditions with addition of steam to the feed. 3: Mo_5O_{14}-type MoVW-oxide under propene oxidation with addition of steam. 4: Mo_5O_{14}-type MoV-oxide under propene oxidation. Reaction pressure: 0.25–0.6 mbar; temperature 623 K. (The small peaks above 10 eV and around 6 eV correspond to gas phase signals. Their positions relative to the surface signal depend on the potential field in front of the sample and are thus not constant on the conventional E_B scale referenced to the work function).

micro-domain could exist in any of the catalysts. Further, the lack of intensity at 2 eV demonstrates that the high excess of tellurium cannot be in the form of binary TeO_2 at the surface. Hence tellurium should be either in a local environment as for the other cations, or in a formal oxidation state of 6+. The final observation we emphasize is the shift of both the O 2p maximum (3.7 eV) and the onset of 2p at the top of valence band (2 eV) relative to the main constituent MoO_3. This is in line with the slight shift of the O1s peak shown in Table 6.5.

Since Mo 3d is the most often reported and depicted core level in the MoVTeNb literature, it is worth considering it here as well. In many publications, partially reduced molybdenum (Mo^{5+}) was reported (see Table 6.4) and its importance for catalysis was considered. Unfortunately, *in situ* experiments (Figure 6.15A) cannot validate the sometimes relatively high concentration of reduced Mo species. Apart from a 0.4 eV binding-energy shift of the main Mo 3d peak relative to the position of MoO_3, the concentration of Mo^{5+} (~231 eV) in M1 is below 5% under propane oxidation condition. This is in good agreement with the *in situ* XAS experiments by Safanova and coworkers [222], although the Mo K-edge is intrinsically bulk sensitive. The main component of Mo 3d can be well represented by one relatively narrow and symmetric Gauss–Lorenz function, indicating the presence of only

one species. That the situation may be rather more complex is illustrated in Figure 6.15B showing *in situ* Mo 3d spectra of the MoV oxide. The bottom curve obtained at room temperature obviously contains reduced Mo sites. In parallel, a significant amount of carbon was observed on the surface. However, as the sample was heated up in the reaction mixture (here propene + O_2), carbon and Mo^{5+} disappeared (or decreased strongly) thus underlining the correlation of the two species. During reaction, no surface carbon could be distinguished and only the gas-phase signal of the feed was observed. The Mo 3d signal became essentially symmetric and could have been approximated by one broad symmetric function. The reason we did not do this is shown in relation to the top curve observed after introduction of water into the reaction feed. The peak is now clearly asymmetric and can be well fitted with two narrower functions. The position of the higher energy component is close to the position of "classical 6+" in the binary system and the low E_B component is situated at ~232.0 eV. This latter peak can clearly not be interpreted within the initial state approximation with a formal ionic picture (Mo^{5+}: ~231 eV). If we disregard the ionic formalism, however, the binding-energy shift could represent a small partial reduction of the localized positive charge of the cation. This can be the case if removal of an insignificant amount of lattice oxygen is accompanied by reorganization of the lattice metal polyhedra (from corner to edge sharing) and the corresponding reduction could be delocalized throughout a whole micro-domain. Another explanation could be that the E_B is also a function of the

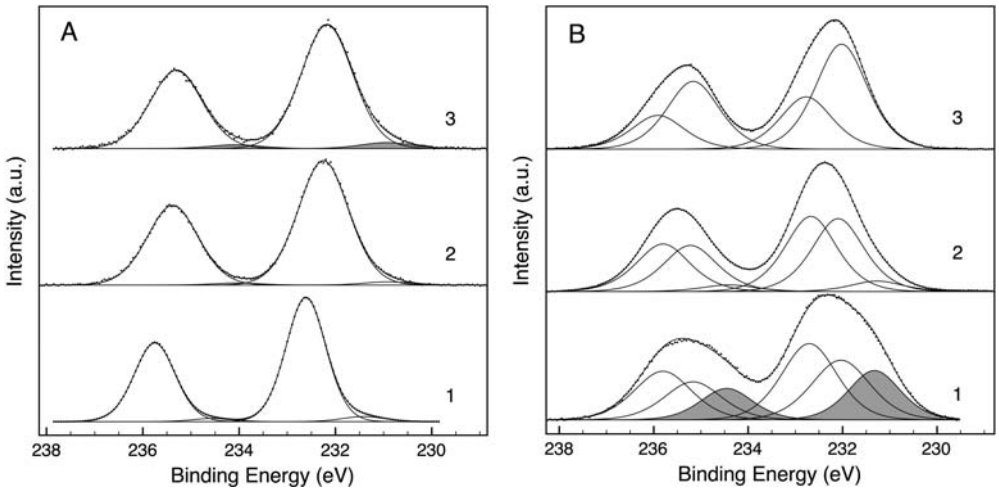

Figure 6.15 Synchrotron based Mo 3d spectra of (A), 1: clean, insignificantly reduced MoO_3, 2: M1#1, 3: M1#2. The spectra of M1 catalysts (2, 3) were recorded during propane oxidation with steam (as shown previously). Spectra in (A) were collected with high surface sensitivity (hv: 410 eV). (B) shows Mo 3d of Mo_5O_{14}-type MoV-oxide in 1: propene oxidation feed at RT, 2 (and 3): propene oxidation feed at 623 K without (with steam). Spectra in (B) were recorded with 710 eV excitation energy. The shaded component corresponds to Mo^{5+}.

final excited state. If the screening of the core hole can be modified, this could give rise to non-uniform binding energies. As pointed out by Wertheim [223], this can indeed happen with Mo 3d of, for example, $K_{0.3}MoO_3$, in which he identified two alternative screening channels, owing to the appearance of a conduction band of Mo 4d character below the Fermi level. Since M1 is an n-type semiconductor under reaction conditions, with high-lying electrons as the main charge carriers (Figure 6.14B), there is a possibility of substituting the classical (O 2p–Mo 3d) charge-transfer screening process by a d–d transition. Owing to the low concentration of Mo^{5+} species this would, however, indicate an "interatomic" V 3d–Mo 3d screening process.

The somewhat low E_B of Nb 3d in M1 as compared to Nb_2O_5 and the asymmetry in its envelope observed at each and every condition (not shown, but also noted in ref. [207]), would indicate similar final-state effects being operative in defining the niobium binding energy. It is interesting in this context that tellurium 3d has negligible asymmetry in its peak form. The slightly higher E_B, relative to TeO_2, may suggest a partially more ionic cation, as suggested by the lack of TeO_2-related intensity at 2 eV in the valence band, which could make oxygen insertion facile from TeO_x.

Turning now to the reaction side, it is generally accepted that the rate-limiting step of propane selective (amm)oxidation is activation of the first C—H bond. Vanadium 5+ was proposed by several authors as being responsible for this elementary step [148, 204–206]. However, XPS does not seem to support this proposal, since vanadium was observed in its formal 4+ oxidation state on the surface of M1 (Tables 6.4 and 6.5). The deficiency of the surface in vanadium and the minority of its V^{5+} fraction (if any) relative to V^{4+} cast serious doubts that vanadium in it highest oxidation state is responsible for the most demanding elementary step of C—H bond activation of propane. Ueda and coworkers [212, 224] have shown that the Te- and Nb-free MoV with M1 structure can activate propane as effectively as MoVTeNb, although with poor selectivity towards AA. Taking into account the mechanism proposed for butane activation on VPOs (Section 6.3.3.1), it is more reasonable to consider the importance of Lewis basic V^{4+} sites for the first C—H activation step. The suspiciously high tellurium content at the M1 surface indicates that Te is an essential catalytic component, promoting the formation of AA, possibly by the oxidation of a propene-like surface intermediate. As Te is effective in allylic oxidation of olefins, the higher activity of Te-containing catalysts for propene conversion over the Te-free M1 catalysts caused Ueda and coworkers [212, 224] to conclude that the rapid allylic-hydrogen abstraction from propene on the Te site to produce acrolein is the origin of the effective nature of M1-(Te). It is also well known [225–228] that MoV-based mixed oxides can convert acrolein to AA with very high selectivity at almost full conversion, but at much lower temperature. By using *in situ* diffuse reflectance Fourier transform spectroscopy, Vogel and coworkers [229] concluded that this reaction was facilitated by Lewis acid sites on which acrolein adsorbs with its carbonyl group. On the other hand, Tichy [226] stressed the importance of vanadium 4+ sites and the presence

of a high steam concentration, which will block Lewis acid sites and increase Brønsted acidity, enabling desorption of acids from the surface. The high surface Te concentration might be further beneficial by diluting possible neighboring acrolein oxidation sites, thus decreasing the temperature margin between acrolein oxidation (500 K for M1-phase MoV-oxide) and propane oxidation to avoid over-oxidation. To conclude, the uniqueness of the MoVTeNb M1 phase materials seems to be related to their ability to host a surface structure that facilitates the elementary steps of propane (amm)oxidation and is able to supply oxygen from the sub-surface hexagonal/heptagonal channel [208, 222] and transfer electrons through its subsurface interlayer [217]. The dynamic character of the surface (reversible modification of surface composition) with the high similarity of the O 2p-related valence bands of M1 and model MoV oxide catalysts indicate that the top few layers, although being high-resolution TEM amorphous, should posses a certain structural motif that allows high specificity during catalytic turnover if the correct cationic centers are placed next to each other. The combination of the right surface structures, diluted Lewis basicity and a large excess of stable TeO_x (or analogous) sites seems to hold the key to successful propane oxidation chemistry.

6.4 Summary

The rational design of heterogeneous catalysts requires an understanding of surface processes on a molecular level that inherently involves knowledge of the active state of the solid surface. Since catalysis is a dynamic event, requiring a flexible and metastable site for catalytic turnover, the only plausible choice for spectroscopic experiments is the application of a reaction-like environment during observation. For experimentalists, PES provides a tool to investigate the surface electronic structure of catalytically relevant materials. Recent developments in *in situ* experimentation have now made it possible to investigate the active surface state during catalytic turnover. The examples detailed in this chapter clearly indicate the need for rapidly expanding the number of *in situ* studies in many catalytic systems, as these will contribute to a greater and deeper understanding of the working principles of heterogeneous catalysis. Further experimental development (photon sources with higher brilliance, smaller aperture sizes, more efficient lens systems and better electron detection) will allow us to reach even more realistic pressure conditions, which will broaden the spectrum of those catalytic reactions that will be successfully implemented in *in situ* XPS investigations. Since the valence and conduction band of the solid defines the "playground" of the surface processes, it is very desirable that *in situ* studies progressively concentrate on these spectral regions. However, as their interpretation requires massive support from theoreticians, the new age of exploration of surface reactions requires substantial joint efforts from experimentalists and theoreticians.

Acknowledgments

The authors would like to thank their immediate coworkers who participated in the BESSY experiments: M. Hävecker, A. Knop-Gericke, P. Schnörch, S. Zafeiratos and E. Kleimenov for their invaluable contribution to the experiments detailed in this text. Support from the BESSY synchrotron in Berlin is gratefully acknowledged. Finally thanks to the SfB Germany and Athena Project (jointly funded by Johnson Matthey Catalysts and EPSRC of the UK) for financial support.

References

1 Fadley, C.S. (1978) Basic Concept of X-ray Photoelectron Spectroscopy, in *Electron Spectroscopy: Theory, Techniques and Applications II* (eds C.R. Brundle and A.D. Baker), Academic, New York, p. 2.

2 Hüfner, S. (2003) *Photoelectron Spectroscopy; Principles and Applications*, Springer, Berlin Heidelberg New York.

3 Siegbahn, K., Nordling, C., Johansson, G., Hedman, J., Heden, P.F., Hamrin, K., Gelius, U., Bergmark, T., Werme, L.O., Manne, R. and Baer, Y. (1969) *ESCA Applied to Free Molecules*, North-Holland Publishing Company.

4 Joyner, R.W., Roberts, M.W. and Yates, K. (1979) *Surface Science*, **87**, 501.

5 Ruppender, H.J., Grunze, M., Kong, C.W. and Wilmers, M. (1990) *Surface and Interface Analysis*, **15**, 245.

6 Ogletree, D.F., Bluhm, H., Lebedev, G., Fadley, C.S., Hussain, Z. and Salmeron, M. (2002) *Review of Scientific Instruments*, **73**, 3872.

7 Zhu, J.F., Kinne, M., Fuhrmann, T., Denecke, R. and Steinrück, H.-P. (2003) *Surface Science*, **529**, 384.

8 Stöhr, J. (1992) *NEXAFS Spectroscopy*, Springer-Verlag, Berlin-Heidelberg, New York.

9 Grant, J.T. (2003) *Software for Processing AES and XPS Data*, IM Publications and SurfaceSpectra Limited, Charton Manchester.

10 Tougaard, S. (2003) *Quantification of Nano-structures by Electron Spectroscopy*, IM Publications and SurfaceSpectra Limited, Charton Manchester.

11 Clark, D.T. and Dilks, A. (1976) *Journal of Polymer Science Part A – Polymer Chemistry*, **14**, 533.

12 Bancroft, G.M. (1975) *Chemical Physics Letters*, **32**, 173.

13 Birkenstock, U., Holm, R., Reinfandt, B. and Storp, S. (1985) *Journal of Catalysis*, **93**, 55.

14 Fuggle, J.C. and Martensson, N. (1980) *Journal of Electron Spectroscopy and Related Phenomena*, **21**, 275.

15 Gelius, U. (1974) *Physica Scripta*, **9**, 133.

16 Wertheim, G.K. (1975) *Journal of Electron Spectroscopy and Related Phenomena*, **6**, 239.

17 Ivanovsky, A.L., Gubanov, V.A., Shveikin, G.P. and Kurmaev, E.Z. (1981) *Journal of the Less-Common Metals*, **78**, 1.

18 Larsson, S. (1976) *Journal of Electron Spectroscopy and Related Phenomena*, **8**, 171.

19 Jadoul, M.A. (1978) *Etude des Spectres E.S.C.A. des Halogenures de Fer(II) et (III)*, Ms Thesis, Facultes Universitaires Notre-Dame de la Paix, Namur.

20 Morgan, W.E., Van Wazer, J.R. and Stec, W. (1973) *Journal of American Chemical Society*, **95**, 751.

21 van der Laan, G., Westra, C., Haas, C. and Sawatzky, G.A. (1981) *Physical Review B*, **23**, 4369.

22 Scrocco, M. (1981) *Physical Review B*, **23**, 4381.

23 Richter, B., Kuhlenbeck, H., Freund, H.J. and Bagus, P.S. (2004) *Physical Review Letters*, **93**, 26805.

24 Wertheim, G.K., DiCenzo, S.B., Buchanan, D.N. and Bennett, P.A. (1985) *Solid State Communications*, **53**, 377.

25 Mavrikakis, M., Stoltze, P. and Norskov, J.K. (1999) *Catalysis Letters*, **64**, 101.

26 Joseph, Y., Besnard, I., Rosenberger, M., Guse, B., Nothofer, H.G., Wessels, J.M., Wild, U., Knop-Gericke, A., Su, D.S., Schlögl, R., Yasuda, A. and Vossmeyer, T. (2003) *Journal of Physical Chemistry B*, **107**, 7406.

27 Martensson, N., Berndtsson, A. and Nyholm, R. (1980) *Journal of Electron Spectroscopy and Related Phenomena*, **19**, 299.

28 Martensson, N. and Johansson, B. (1979) *Solid State Communications*, **32**, 791.

29 Johansson, G., Hedman, J., Berndtsson, A., Klasson, M. and Nilsson, R. (1973) *Journal of Electron Spectroscopy and Related Phenomena*, **2**, 295.

30 Jentoft, F.C., Weinberg, G., Wild, U., Schlögl, R. and Wakai, F. (1999) *Photoelectron Spectroscopy as a Tool for Studying Ceramic Interfaces: A Tutorial*, Wiley-VCH Verlag GmbH, Weinheim.

31 Barr, T.L. (1989) *Journal of Vacuum Science and Technology A*, **7**, 1677.

32 Wark, M., Koch, M., Bruckner, A. and Grünert, W. (1998) *Journal of the Chemical Society–Faraday Transactions*, **2033**, 94.

33 Hupfer, B., Schupp, H., Andrade, J.D. and Ringsdorf, H. (1981) *Journal of Electron Spectroscopy and Related Phenomena*, **23**, 103.

34 Storp, S. and Holm, R. (1977) *Surface Science*, **68**, 10.

35 Holm, R. and Storp, S. (1976) *Applied Physics*, **9**, 217.

36 Abu Haija, M., Guimond, S., Romanyshyn, Y., Uhl, A., Kuhlenbeck, H., Todorova, T.K., Ganduglia-Pirovano, M.V., Döbler, J., Sauer, J. and Freund, H.-J. (2006) *Surface Science*, **600**, 1497.

37 Freund, H.J. (1995) *Physica Status Solidi B*, **192**, 407.

38 Freund, H.H., Kuhlenbeck, H., Staemmler, V., Twerenbold, D. and Webb, R.H. (1996) *Reports on Progress in Physics*, **59**, 283.

39 Shaikhutdinov, S. and Weiss, W. (2000) *Journal of Molecular Catalysis A: Chemical*, **158**, 129.

40 Che, M. and Bond, G.C. (1985) *Adsorption and Catalysis on Oxide Surfaces*, Elsevier Science Publishers, Amsterdam.

41 Ketteler, G., Weiss, W., Ranke, W. and Schlögl, R. (2001) *Physical Chemistry Chemical Physics*, **3**, 1114.

42 Boehm, H.P. (1966) *Angewandte Chemie*, **78**, 617.

43 Heber, M. and Grünert, W. (2000) *Journal of Physical Chemistry B*, **104**, 5288.

44 Chen, J.G., Crowell, J.E. and Yates, J.T. (1986) *Journal of Chemical Physics*, **84**, 5906.

45 Bukhtiyarov, V.I., Hävecker, M., Kaichev, V.V., Knop-Gericke, A., Mayer, R.W. and Schlögl, R. (2003) *Physical Review B*, **6723**, 5422.

46 Knop-Gericke, A., Hävecker, M., Schedel-Niedrig, T. and Schlögl, R. (2001) *Topics in Catalysis*, **15**, 27.

47 Che, M. and Tench, A.J. (1983) *Advances in Catalysis*, **32**, 1.

48 Xu, C., Hassel, M., Kuhlenbeck, H. and Freund, H.J. (1991) *Surface Science*, **258**, 23.

49 Freund, H.J., Dillmann, B., Seiferth, O., Klivenyi, G., Bender, M., Ehrlich, D., Hemmerich, I. and Cappus, D. (1996) *Catalysis Today*, **32**, 1.

50 Hermann, K., Witko, M., Druzinic, R., Chakrabarti, A., Tepper, B., Elsner, M., Gorschlüter, A., Kuhlenbeck, H. and Freund, H.J. (1999) *Journal of Electron Spectroscopy and Related Phenomena*, **98**–*9*, 245.

51 Weiss, W., Boffa, A.B., Dunphy, J.C., Galloway, H.C., Salmeron, M.B., Somorjai, G.A., Freund, J. and Umbach, E. (1993) *The Structure and Reactivity of Oxide Thin Films Grown on Transition Metal Surfaces*, Springer Verlag.

52 Dupuis, A.-C., Haija, M.A., Richter, B., Kuhlenbeck, H. and Freund, H.-J. (2003) *Surface Science*, **539**, 99.

53 Rainer, D.R. and Goodman, D.W. (1998) *Journal of Molecular Catalysis A: Chemical*, **131**, 259.

54 Corneille, J.S., He, J.W. and Goodmann, D.W. (1995) *Surface Science*, **338**, 221.

55 Tessier, L., Bordes, E. and Gubelmann-Bonneau, M. (1995) *Catalysis Today*, **24**, 335.

56 Engeser, M., Schlangen, M., Schröder, D., Schwarz, H., Yumura, T. and Yoshizawa, K. (2003) *Organometallics*, **22**, 3933.

57 Su, D.S., Hebert, C., Willinger, M. and Schlögl, R. (2003) *Micron*, **34**, 227.

58 Hermann, K., Michalak, A. and Witko, M. (1996) *Catalysis Today*, **32**, 321.

59 Wang, D., Su, D.S. and Schlögl, R. (2003) *Crystal Research and Technology*, **38**, 153.

60 Haber, J. (1997) Oxidation of Hydrocarbons, in *Handbook of Heterogeneous Catalysis* (eds G. Ertl, H. Knözinger and J. Weitkamp), John Wiley & Sons, Weinheim, Vol. **5**, p. 2253.

61 Sawatzky, G.A. and Post, D. (1979) *Physical Review B*, **20**, 1546.

62 Shin, S., Suga, S., Taniguchi, M., Fujisawa, M. and Kanzaki, H. (1990) *Physical Review B*, **41**, 4993.

63 Zimmermann, R., Claessen, R., Reinert, F., Steiner, P. and Hüfner, S. (1998) *Journal of Physics: Condensed Matter*, **10**, 5697.

64 Eyert, V. and Höck, K.-H. (1998) *Physical Review B*, **57**, 12727.

65 Hébert, C., Willinger, M., Su, D.S., Pongratz, P., Schattschneider, P. and Schlögl, R. (2002) *The European Physical Journal B*, **28**, 407.

66 Laubach, S., Schmidt, P.C., Thißen, A., Fernandez-Madrigal, F.J., Jaegermann, W., Wu, Q.-H., Klemm, M. and Horn, S. (2007) *Physical Chemistry Chemical Physics*, **9**, 2564S.

67 Willinger, M., Pinna, N., Su, D.S. and Schlögl, R. (2004) *Physical Review B*, **69**, 155114.

68 Tokarz-Sobieraj, R., Hermann, K., Witko, M., Blume, A., Mestl, G. and Schlögl, R. (2001) *Surface Science*, **489**, 107.

69 Witko, M., Tokarz, R., Haber, J. and Hermann, K. (2001) *Journal of Molecular Catalysis A: Chemical*, **166**, 59.

70 Witko, M. and Tokarz-Sobieraj, R. (2004) *Catalysis Today*, **91–2**, 171.

71 Sayede, A.D., Amriou, T., Pernisek, M., Khelifa, B. and Mathieu, C. (2005) *Chemical Physics*, **316**, 72.

72 Romanyuk, A. and Oelhafen, P. (2007) *Thin Solid Films*, **515**, 6544.

73 Alov, N., Kutsko, D., Spirovova, I. and Bastl, Z. (2006) *Surface Science*, **600**, 1628.

74 Demeter, M., Neumann, N. and Reichelt, W. (2000) *Surface Science*, **454**, 41.

75 Kasperkiewicz, J., Kovacich, J.A. and Lichtman, D. (1983) *Journal of Electron Spectroscopy and Related Phenomena*, **32**, 123.

76 Mendialdua, J., Casanova, R. and Barbaux, Y. (1995) *Journal of Electron Spectroscopy and Related Phenomena*, **71**, 249.

77 Kondratenko, E.V., Ovsitser, O., Radnik, J., Schneider, M., Kraehnert, R. and Dingerdissen, U. (2006) *Applied Catalysis A: General*, **319**, 98.

78 Su, D.S. (2002) *Analytical and Bioanalytical Chemistry*, **374**, 732.

79 Suchorski, Y., Rihko-Struckmann, L., Klose, F., Ye, Y., Sundmacher, M., Alandjiyska, K., and Weiss, H. (2005) *Applied Surface Science*, **249**, 231.

80 Eberhardt, M.A., Proctor, A., Houalla, M. and Hercules, D.M. (1996) *Journal of Catalysis*, **160**, 27.

81 Chenakin, S.P. and Prada Silvy, R. (2005) *Journal of Physical Chemistry B*, **109**, 14611.

82 Klose, F., Wolff, T., Lorenz, H., Seidel-Morgenstern, A., Suchorski, Y., Piórkowska, M. and Weiss, H. (2007) *Journal of Catalysis*, **247**, 176.

83 Harlin, M.E., Niemi, V.M. and Krause, A.O.I. (2000) *Journal of Catalysis*, **195**, 67.

84 Chary, K.V.R., Kumar, C.P., Rajiah, T. and Srikanth, C.S. (2005) *Journal of Molecular Catalysis A*, **243**, 149.

85 Hess, C. (2007) *Journal of Catalysis*, **248**, 120.

86 Hess, C., Wild, U. and Schlögl, R. (2006) *Microporous and Mesoporous Materials*, **95**, 339.

87 Liu, W., Lai, S.Y., Dai, H., Wang, S., Sun, H. and Au, C.T. (2007) *Catalysis Letters*, **113**, 147.

88 Abu Haija, M., Guimond, S., Uhl, A., Kuhlenbeck, H. and Freund, H.-J. (2006) *Surface Science*, **600**, 1040.

89 Guimond, S., Abu Haija, M., Kaya, S., Lu, J., Weissenrieder, J., Shaikhutdinov, S., Kuhlenbeck, H., Freund, H.-J., Döbler, J. and Sauer, J. (2006) *Topics in Catalysis*, **38**, 117.

90 Larese, C., Campos-Martin, J.M. and Fierro, J.L.G. (2000) *Langmuir*, **16**, 10294.

91 Weckhuysen, B.M. and Schoonheydt, R.A. (1999) *Catalysis Today*, **51**, 223.

92 Johnson Matthey PLC, *Alkane Dehydrogenation Catalyst*, EP patent **937**, 687A.

93 Blasco, T. and Nieto López, J.M. (1997) *Applied Catalysis A: General*, **157**, 117.

94 Chen, K., Bell, A.T. and Iglesia, E. (2000) *Journal of Physical Chemistry B*, **104**, 1292.

95 Nieto López, J. M. (2006) *Topics in Catalysis*, **41**, 3.

96 Martínez-Huerta, M.V., Gao, X., Tian, H., Wachs, I.E., Fierro, J.L.G. and Bañares, M.A. (2006) *Catalysis Today*, **118**, 279.

97 Jackson, S.D., Rugmini, S., Stair, P.C. and Wu, Z. (2006) *Chemical Engineering Journal*, **120**, 127.

98 Volpe, M., Tonetto, G. and de Lasa, H. (2004) *Applied Catalysis A: General*, **272**, 69.

99 Wu, Z. and Stair, P.C. (2006) *Journal of Catalysis*, **237**, 220.

100 Kleimenov, E., Bluhm, H., Hävecker, M., Knop-Gericke, A., Pestryakov, A., Teschner, D., Lopez-Sanchez, J.A., Bartley, J.K., Hutchings, G.J. and Schlögl, R. (2005) *Surface Science*, **575**, 181.

101 Vass, E.M., Hävecker, M., Zafeiratos, S., Teschner, D., Knop-Gericke, A. and Schlögl, R. (2008) *Journal of Physics Condensed Matter*, **20**, 184016.

102 Burcham, L.J., Deo, G., Gao, X. and Wachs, I.E. (2000) *Topics in Catalysis*, **11**/*12*, 85.

103 Wu, Z., Kim, H.-S., Stair, P.C., Rugmini, S. and Jackson, S.D. (2005) *Journal of Physical Chemistry B*, **109**, 2793.

104 De Francesco, R., Stener, M., Causà, M., Toffoli, D. and Fronzoni, G. (2006) *Physical Chemistry Chemical Physics*, **8**, 4300.

105 Brik, M.G., Ogasawara, K., Ishii, T., Ikeno, H. and Tanaka, I. (2006) *Radiation Physics and Chemistry*, **75**, 1564.

106 Brik, M.G., Ogasawara, K., Ikeno, H. and Tanaka, I. (2006) *The European Physical Journal B*, **51**, 345.

107 Concepción, P., Reddy, B.M. and Knözinger, H. (1999) *Physical Chemistry Chemical Physics*, **1**, 3031.

108 Hadjiivanov, K., Concepción, P. and Knözinger, H. (2000) *Topics in Catalysis*, **11**, 123.

109 Jackson, S.D. and Rugmini, S. (2007) *Journal of Catalysis*, **251**, 59.

110 Rodriguez, N.M., Anderson, P.E., Wootsch, A., Wild, U., Schlögl, R. and Paál, Z. (2001) *Journal of Catalysis*, **197**, 365.

111 Seah, M.P. and Dench, W.A. (1979) *Surface and Interface Analysis*, **1**, 2.

112 Shimada, H., Imamura, M., Matsubayashi, N., Saito, T., Tanaka, T., Hayakawa, T. and Kure, S. (2000) *Topics in Catalysis*, **10**, 265.

113 Fayette, L., Marcus, B. and Mermoux, M. (1998) *Physical Review B*, **57**, 14123.

114 Guliants, V.V. (1999) *Catalysis Today*, **51**, 255.

115 Mamedov, E.A. and Cortés Corberán, V. (1995) *Applied Catalysis A: General*, **127**, 1.

116 Argyle, M.D., Chen, K., Resini, C., Krebs, C., Bell, A.T. and Iglesia, E. (2004) *Journal of Physical Chemistry B*, **108**, 2345.

117 Blasco, T., Galli, A., Nieto, J.M.L. and Trifirò, F. (1997) *Journal of Catalysis*, **169**, 203.

118 Kuhlenbeck, H. (2007) personal communication.

119 Bartholomew, C.H. (2001) *Applied Catalysis A: General*, **212**, 17.

120 Bañares, M.A. (1999) *Catalysis Today*, **51**, 319.

121 Cortez, G.G., Fierro, J.L.G. and Bañares, M.A. (2003) *Catalysis Today*, **78**, 219.

122 Harlin, M.E., Niemi, V.M., Krause, A.O.I. and Weckhuysen, B.M. (2001) *Journal of Catalysis*, **203**, 242.

123 Lemonidou, A.A., Nalbandian, L. and Vasalos, I.A. (2000) *Catalysis Today*, **61**, 333.

124 Felthouse, T.R., Burnett, J.C., Horrell, B., Mummey, M.J. and Kuo, Y.-J. (2001) *Maleic Anhydride, Maleic Acid, and Fumaric Acid*, John Wiley & Sons, Ltd.

125 Ballarini, N., Cavani, F., Cortelli, C., Ligi, S., Pierelli, F., Trifirò, F., Fumagalli, C., Mazzoni, G. and Monti, T. (2006) *Topics in Catalysis*, **38**, 147.

126 Centi, G. (1993) *Catalysis Today*, **16**, 5.

127 Centi, G., Cavani, F. and Trifirò, F. (2001) *Selective Oxidation by Heterogeneous Catalysis*, Kluwer Academic/Plenum Publishers, New York.

128 Centi, G., Trifirò, F., Ebner, J.R. and Franchetti, V.M. (1988) *Chemical Reviews*, **88**, 55.

129 Hutchings, G.J. (2004) *Journal of Materials Chemistry*, **14**, 3385.

130 Thompson, M.R. and Ebner, J.R. (1992) in *New Developments in Selective Oxidation by Heterogeneous Catalysis* (eds P. Ruiz and B. Delmon), Elsevier, Amsterdam, p. 352.

131 Stefani, G., Budi, F., Fumagalli, C. and Suciu, G.D. (1990) *Feuidized bed oxydation of n-butane: A new commercial process for maleic anhydride*. In: *New Developments in Selective Oxidation* (eds G. Centi and F. Trifirò), Elsevier, Amsterdam, p. 537.

132 Guliants, V.V., Benziger, J.B., Sundaresan, S., Wachs, I.E., Jehng, J.-M. and Roberts, J.E. (1996) *Catalysis Today*, **28**, 275.

133 Guliants, V.V., Benziger, J.B., Sundaresan, S., Yao, N. and Wachs, I.E. (1995) *Catalysis Letters*, **32**, 379.

134 Albonetti, S., Cavani, F., Trifirò, F., Venturoli, P., Calestani, G., López Granados, M. and Fierro, J.L.G. (1996) *Journal of Catalysis*, **160**, 52.

135 Hutchings, G.J., Kiely, C.J., Sananes-Schulz, M.T., Burrows, A. and Volta, J.-C. (1998) *Catalysis Today*, **40**, 273.

136 Hutchings, G.J., Lopez-Sanchez, J.A., Bartley, J.K., Webster, J.M., Burrows, A., Kiely, C.J., Carley, A.F., Rhodes, C., Hävecker, M., Knop-Gericke, A., Mayer, R.W., Schlögl, R., Volta, J.-C. and Poliakoff, M. (2002) *Journal of Catalysis*, **208**, 197.

137 Ben Abdelouahab, F., Olier, R., Ziyad, M. and Volta, J.-C. (1995) *Journal of Catalysis*, **157**, 687.

138 Abon, M., Béré, K.E., Tuel, A. and Delichère, P. (1995) *Journal of Catalysis*, **156**, 28.

139 Volta, J.-C. (1996) *Catalysis Today*, **32**, 29.

140 Cornaglia, L.M. and Lombardo, E.A. (1995) *Applied Catalysis A: General*, **127**, 125.

141 Duarte de Farias, A.M., Gonzalez, W.A., Pries de Oliveira, P.G., Eon, J.-G., Herrmann, J.-M., Aouine, M., Loridant, S. and Volta, J.-C. (2002) *Journal of Catalysis*, **208**, 238

142 Delichère, P., Béré, K.E. and Abon, M. (1998) *Applied Catalysis A: General*, **172**, 295.

143 Mota, S., Abon, M., Volta, J.-C. and Dalmon, J.A. (2000) *Journal of Catalysis*, **193**, 308.

144 Rodemerck, U., Kubias, B., Zanthoff, H.-W., Wolf, G.-U. and Baerns, M. (1997) *Applied Catalysis A: General*, **153**, 217.

145 Coulston, G.W., Bare, S.R., Kung, H., Birkeland, K., Bethke, G.K., Harlow, R., Herron, N. and Lee, P.L. (1997) *Science*, **275**, 191.

146 Pepera, M.A., Callahan, J.L., Desmond, M.J., Milberger, E.C., Blum, P.R. and Bremer, N.J. (1985) *Journal of American Chemical Society*, **107**, 4883.

147 Wang, D. and Barteau, M.A. (2003) *Catalysis Letters*, **90**, 7.

148 Millet, J.-M.M. (2006) *Topics in Catalysis*, **38**, 83.

149 Zazhigalov, V.A. (2002) *Kinetics and Catalysis*, **43**, 514.

150 Zazhigalov, V.A., Haber, J., Stoch, J., Pyatnitzkaya, A.I., Komashko, G.A. and Belousov, V.M. (1993) *Applied Catalysis A: General*, **96**, 135.

151 Abon, M., Béré, K.E. and Delichère, P. (1997) *Catalysis Today*, **33**, 15.

152 Gaskell, K.J., Asunskis, A.L. and Sherwood, P.M.A. (2002) *Surface Science Spectra*, **9**, 135.

153 Asunskis, D.J. and Sherwood, P.M.A. (2002) *Surface Science Spectra*, **9**, 128.

154 Asunskis, D.J. and Sherwood, P.M.A. (2002) *Surface Science Spectra*, **9**, 121.

155 Asunskis, D.J. and Sherwood, P.M.A. (2002) *Surface Science Spectra*, **9**, 114.

156 Carrara, C., Irusta, S., Lombardo, E. and Cornaglia, L. (2001) *Applied Catalysis A: General*, **217**, 275.

157 Cornaglia, L.M., Carrara, C.R., Petunchi, J.O. and Lombardo, E.A. (2000) *Catalysis Today*, **57**, 313.

158 Coulston, G.W., Thompson, E.A. and Herron, N. (1996) *Journal of Catalysis*, **163**, 122.

159 Feng, R.-M., Yang, X.-J., Chen, Y., Ji, W.-J., and Au, C.-T. (2007) *Journal of Catalysis*, **246**, 166.

160 Garbassi, F., Bart, J.C.J., Tassinari, R., Vlaic, G. and Lagarde, P. (1986) *Journal of Catalysis*, **98**, 317.

161 Haber, J., Zazhigalov, V.A., Stoch, J., Bogutskaya, L.V. and Batcherikova, I.V. (1997) *Catalysis Today*, **33**, 39.

162 Irusta, S., Boix, A., Pierini, B., Caspani, C. and Petunchi, J. (1999) *Journal of Catalysis*, **187**, 298.

163 Li, X.-K., Ji, W.-J., Zhao, J., Zhang, Z.-B. and Au, C.-T. (2006) *Journal of Catalysis*, **238**, 232.

164 Nie, W., Wang, X., Ji, W.-J., Yan, Q., Chen, Y. and Au, C.-T. (2001) *Catalysis Letters*, **76**, 201.

165 Okuhara, T., Nakama, T. and Misono, M. (1990) *Chemistry Letters*, **10**, 1941.

166 O'Mahony, L., Curtin, T., Zemlyanov, D., Mihov, M. and Hodnett, B.K. (2004) *Journal of Catalysis*, **227**, 270.

167 Rihko-Struckmann, L.K., Ye, Y., Chalakov, L., Suchorski, Y., Weiss, H. and Sundmacher, K. (2006) *Catalysis Letters*, **109**, 89.

168 Richter, F., Papp, H., Götze, T., Wolf, G.-U. and Kubias, B. (1998) *Surface and Interface Analysis*, **26**, 736.

169 Lopez-Sanchez, J.A., Griesel, L., Bartley, J.K., Wells, R.P.K., Liskowski, A., Su, D.S., Schlögl, R., Volta, J.-C. and Hutchings, G.J. (2003) *Physical Chemistry Chemical Physics*, **5**, 3525.

170 Sherwood, P.M.A. (2002) *Surface Science Spectra*, **9**, 62.

171 Trifirò, F. (1993) *Catalysis Today*, **16**, 91.

172 Ebner, J.R. and Thompson, M.R. (1993) *Catalysis Today*, **16**, 51.

173 Hodnett, B.K., Permanne, P. and Delmon, B. (1983) *Applied Catalysis*, **6**, 231.

174 Okuhara, T. and Misono, M. (1993) *Catalysis Today*, **16**, 61.

175 Scofield, J.H. (1976) *Journal of Electron Spectroscopy and Related Phenomena*, **8**, 129.

176 Jansen, W.P.A., Ruitenbeek, M., Denier v.d. Gon, A.W., Geus, J.W. and Brongersma, H.H. (2000) *Journal of Catalysis*, **196**, 379.

177 Yeh, J.J. and Lindau, I. (1985) *Atomic Data and Nuclear Data Tables*, **32**, 1.

178 Thompson, D.J., Ciobîcă, I.M., Hodnett, B.K., van Santen, R.A. and Fanning, M.O. (2003) *Surface Science*, **547**, 438.

179 Thompson, D.J., Ciobîcă, I.M., Hodnett, B.K., van Santen, R.A. and Fanning, M.O. (2004) *Catalysis Today*, **91–2**, 177.

180 Gai, P.L. and Kourtakis, K. (1995) *Science*, **267**, 661.

181 Haras, A., Duarte, H.A., Salahub, D.R. and Witko, M. (2002) *Surface Science*, **513**, 367.

182 Zanthoff, H.-W., Sananes-Schulz, M., Buchholz, S.A., Rodemerck, U., Kubias, B. and Baerns, M. (1998) *Applied Catalysis A: General*, **172**, 49.

183 Click, G.T. and Barone, B.J. (1986) US Patent 4,596,878.

184 Hamashima, N., Asami, M., Suzuki, S., Ichiki, T., Ueno, H. and Arnold, S.C. (1996) PCT/US96/04635.

185 Bluhm, H., Hävecker, M., Kleimenov, E., Knop-Gericke, A., Liskowski, A., Schlögl, R. and Su, D.S. (2003) *Topics in Catalysis*, **23**, 99.

186 Thompson, D.J., Fanning, M.O. and Hodnett, B.K. (2003) *Journal of Molecular Catalysis A: Chemical*, **198**, 125.

187 Volta, J.-C. (2000) *Chimie*, **3**, 717.

188 Chen, X.-W., Zhu, Z., Hävecker, M., Su, D.S. and Schlögl, R. (2007) *Materials Research Bulletin*, **42**, 354.

189 Wachs, I.E., Jehng, J.-M., Deo, G., Weckhuysen, B.M., Guliants, V.V., Benziger, J.B. and Sundaresan, S. (1997) *Journal of Catalysis*, **170**, 75.

190 Hävecker, M., Pinna, N., Weiß, K., Sack-Kongehl, H., Jentoft, R.E., Wang, D., Swoboda, M., Wild, U., Niederberger, M., Urban, J., Su, D.S. and Schlögl, R. (2005) *Journal of Catalysis*, **236**, 221.

191 O'Connor, M., Dason, F. and Hodnett, B.K. (1990) *Applied Catalysis*, **64**, 161.

192 Ushikubo, T., Nakamura, H., Koyasu, Y. and Wajiki, S. (1995) U.S. Patent 5,380,933.

193 Lin, M. and Linsen, M. (1999) EP patent 962,253 A2.

194 Hatano, M. and Kayo, A. (1992) EP patent 0,318,295 B1.

195 Lin, M.M. (2001) *Applied Catalysis A: General*, **207**, 1.

196 Novakova, E.K. and Védrine, V.C. (2006) *Propane Selective Oxidation to Propene and Oxygenates on Metal Oxides*. In: *Metal Oxides, Chemistry and Applications* (ed. J.L.G. Fierro), CRC Press, Boca Raton, p. 414.

197 Ushikubo, T., Oshihara, K., Kayo, A. and Hatano, M. (1997) *Ammoxidation of Propane Over Mo-V-Nb-Te Mixed Oxide Catalysts*. In: *Studies in Surface Science and Catalysis* (eds C. Li and Q. Xin), Elsevier, Amsterdam, Vol. **112**, p. 473.

198 DeSanto, P. Jr, Buttrey, D.J., Grasselli, R.K., Lugmair, C.G., Volpe, A.F. Jr, Toby, B.H. and Vogt, T. (2004) *Zeitschrift für Kristallographie*, **219**, 152.
199 Murayama, H., Vitry, D., Ueda, W., Fuchs, G., Anne, M. and Dubois, J.L. (2007) *Applied Catalysis A: General*, **318**, 137.
200 Baca, M., Pigamo, A., Dubois, J.L. and Millet, J.-M.M. (2003) *Topics in Catalysis*, **23**, 39.
201 Botella, P., López Nieto, J.M. and Solsona, B. (2002) *Catalysis Letters*, **78**, 383.
202 Oshihara, K., Hisano, T. and Ueda, W. (2001) *Topics in Catalysis*, **15**, 153.
203 Guliants, V.V., Bhandara, R., Al-Saeedi, J.N., Vasudevan, V.K., Soman, R.S., Guerrero-Pérez, O. and Banares, M.A. (2004) *Applied Catalysis A: General*, **274**, 123.
204 Grasselli, R.K., Buttrey, D.J., DeSanto, P. Jr, Burrington, J.D., Lugmair, C.G., Volpe, A.F. Jr and Weingand, T., (2004) *Catalysis Today*, **91–2**, 251.
205 DeSanto, P. Jr, Buttrey, D.J., Grasselli, R.K., Pyrz, W.D., Lugmair, C.G., Volpe, A.F. Jr, vogt, T. and Toby, B.H. (2006) *Topics in Catalysis*, **38**, 31.
206 Grasselli, R.K., Buttrey, D.J., Burrington, J.D., Andersson, A., Holmberg, J., Ueda, W., Kubo, J., Lugmair, C.G. and Volpe, A.F. Jr (2006) *Topics in Catalysis*, **38**, 7.
207 Asakura, K., Nakatani, K., Kubota, T. and Iwasawa, Y. (2000) *Journal of Catalysis*, **194**, 309.
208 Baca, M. and Millet, J.-M.M. (2005) *Applied Catalysis A: General*, **279**, 67.
209 Botella, P., Concepción, P., López Nieto, J.M. and Moreno, Y. (2005) *Catalysis Today*, **99**, 51.
210 Ivars, F., Botella, P., Dejoz, A., López Nieto, J.M., Concepción, P. and Vázquez, M.I. (2006) *Topics in Catalysis*, **38**, 59.
211 Millet, J.-M.M., Roussel, H., Pigamo, A., Dubois, J.L. and Jumas, J.C. (2002) *Applied Catalysis A: General*, **232**, 77.
212 Ueda, W., Vitry, D. and Katou, T. (2004) *Catalysis Today*, **96**, 235.
213 Botella, P., García-González, E., Dejoz, A., López Nieto, J.M., Vázquez, M.I. and González-Calbet, J. (2004) *Journal of Catalysis*, **225**, 428.
214 Concepción, P., Botella, P. and López Nieto, J.M. (2004) *Applied Catalysis A.: General*, **278**, 45.
215 Huang, C., Guo, W., Yi, X., Weng, W. and Wan, H. (2007) *Catalysis Communication*, **8**, 162.
216 Holmberg, J., Hansen, S., Grasselli, R.K. and Andersson, A. (2006) *Topics in Catalysis*, **38**, 17.
217 Wagner, J.B., Timpe, O., Hamid, F.A., Trunschke, A., Wild, U., Su, D.S., Widi, R.K., Abd Hamid, S.B. and Schlögl, R. (2006) *Topics in Catalysis*, **38**, 51.
218 Celaya Sanfiz, A., Hansen, T.W., Girgsdies, F., Schnörch, P., Teschner, D., Looi, M.H., Hamid, S.B.A., Trunschke, A. and Schlögl, R., to be submitted.
219 Guliants, V.V., Bhandara, R., Brongersma, H.H., Knoester, A., Gaffney, A.M. and Han, S. (2005) *Journal of Physical Chemistry B*, **109**, 10234.
220 Guliants, V.V., Bhandara, R., Hughett, A.R., Bhatt, S., Schuler, B.D., Brongersma, H.H., Knoester, A., Gaffney, A.M. and Han, S. (2006) *Journal of Physical Chemistry B*, **110**, 6129.
221 Hermann, K. and Witko, M. (2001) in *The Chemical Physics of Surfaces: Oxide Surfaces* (ed D.P. Woodruff), Elsevier, New York, Vol. **9**, p. 136.
222 Safanova, O.V., Deniau, B. and Millet, J.-M.M. (2006) *Journal of Physical Chemistry B*, **110**, 23962.
223 Wertheim, G.K., Schneemeyer, L.F. and Buchanan, D.N.E. (1985) *Physical Review B*, **32**, 3568.
224 Ueda, W., Vitry, D. and Katou, T. (2005) *Catalysis Today*, **99**, 43.
225 Ogawa, M. (1987) JP patent 62–34742B.
226 Tichý, J. (1997) *Applied Catalysis A: General*, **157**, 363.
227 Wada, M., Ninomiya, M., Yanagisawa, I. and Ohara, T. (1978) JP patent 53–6127B.
228 Cavani, F., Trifirò, F. (1992) *Applied Catalysis A: General*, **88**, 115.
229 Krauß, K., Drochner, A., Fehlings, M., Kunert, J. and Vogel, H. (2000) *Journal of Molecular Catalysis A: Chemical*, **162**, 413.

7
X-ray Absorption Spectroscopy of Oxides and Oxidation Catalysts

Michael Stockenhuber

7.1
Principles of EXAFS

A number of modern physical techniques are used to characterize heterogeneous catalysts. These methods range from techniques probing the interaction of catalysts with probe molecules, to *in situ* surface characterization techniques as well as structural elucidation under both *in situ* and *ex situ* conditions. In general, interaction of catalysts with probe molecules is followed using some spectroscopic property of the probe molecule itself and/or the changes induced by the heterogeneous catalyst. The spectroscopic techniques used include vibrational spectroscopies, NMR spectroscopy, UV-Vis spectroscopy and mass spectrometry to name a few examples. Similarly, *in situ* techniques tend to use properties of probe molecules but also combined with structural techniques such as X-ray diffraction (XRD) and X-ray absorption spectroscopy (XAS). In recent years XAS has been widely used in the characterization of catalysts and catalyst surfaces.

XAS is clearly going beyond the capabilities of a number of structural techniques, including XRD, transmission electron microscopy (TEM), scanning electron microscopy (SEM), secondary-ion mass spectrometry (SIMS) and ion scattering. The issues with any of the UHV techniques is their apparent incapability to operate under real conditions as well as the inherent difficulty in applying them to highly disordered and/or sub-nanoscale materials. Diffraction techniques on the other hand are not applicable to very small clusters or materials without long-range order. XAS is unique in that it can be operated under more or less any environmental conditions, owing to the very limited experimental complexity of the spectroscopic technique itself.

Sample environments for X-ray absorption spectroscopy include liquid-phase reactions, high temperatures and high pressures.

Characterization of oxides and some *in situ* applications of XAS will be introduced and discussed. Although XAS is relatively widespread in its application, it is the intention of this short chapter to set out the fundamentals of the technique as it is important for the practitioner to understand the basic principles. While it is not necessary to completely understand the quantum chemical background of

Metal Oxide Catalysis. Edited by S. David Jackson and Justin S. J. Hargreaves

ISBN: 978-3-527-31815-5

extended X-ray absorption fine structure (EXAFS), a brief introduction to the physical processes is given. Some details of the theory can be found in a few older textbooks [1, 2].

7.1.1 Basic Principles of X-ray Absorption Spectroscopy (XAS)

Photons are absorbed by any form of matter, the degree of absorption being dependent on the photon energy (which can be calculated from its frequency by $E = h\nu$). X-rays are rather high-energy photons, thus the interaction with matter happens with a "high-energy part" of the matter, in this case the inner electrons. If X-rays interact with atoms, and they are of sufficient energy, they can eject a core electron. Scanning a large energy range of X-rays, one observes that the absorption of the X-rays occurs in a stepwise manner, that is, absorption is quantized.

For XAS, the main edges of interest are the K- and L-edges. K-edge absorption means that the energy of the X-rays corresponds to the energy of the s electrons, whereas L-edge absorption corresponds to a p core level. At the absorption edge, it is found that there is a fine structure which is only present for atoms that have got nearest neighbors. For an isolated atom, the absorption edge would essentially be featureless.

Figure 7.1 shows a typical absorption edge of a metal oxide. The oscillations above the edge are due to the backscattering from neighboring atoms.

Physically, the core electron (the s electron for a K-edge) is ejected by the X-ray photon. This core electron then has a kinetic energy, E_k which is equal to: $E_k = h\nu - E_b$ where E_b = the binding energy.

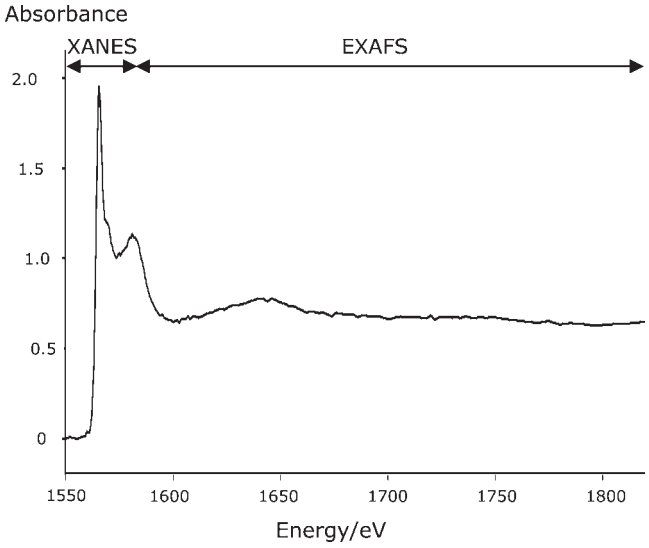

Figure 7.1 A full XAS spectrum of aluminum in zeolite H-FER at 423K at $P_{total} < 10^{-6}$ mbar.

The binding energy is the core-level energy of the electron, and thus it is constant for a given element. This electron (with low kinetic energy) can then interact with valence electrons of the atoms present. This interaction with valence electrons is called X-ray Absorption Near-Edge Structure (XANES) or Near-Edge X-ray Absorption Fine Structure (NEXAFS). XANES thus probes the transition of core electrons into unoccupied electronic states (such as s→p, p→d). The interest in XANES stems from the fact that the final states may be mixed with other orbitals. XANES has a very high level of complex multiple scattering paths, which includes electronic and structural components. In transition metals, pre-edges can be found that essentially probe transitions from s to d orbitals. Quite often these are indicative of the coordination environment, because the transition is forbidden in octahedral symmetry. Thus, the intensity of the pre-edge is extremely enhanced for metal compounds with tetrahedral symmetry.

EXAFS is the interaction of higher kinetic energy photoelectrons, which do not tend to interact with the valence electrons. In this case the process is simply a scattering process, which results in the variation of the absorption coefficient at higher photon energies. In Figure 7.2 a pictorial representation of the process involving backscattering is shown.

The X-rays generated remove a core electron, which can act as a spherical wave which moves away from the backscattering atom. As mentioned, this photoelectron has higher kinetic energy than the photoelectron that results in XANES. The outgoing wave can now be backscattered by any next nearest neighbor atom, which is in itself the source of a "returning" backscattered electron wave. This backscattered electron wave is in phase with the outgoing wave and can show an interference pattern. The position of the maxima and minima depend on the energy of the photoelectron as well as the distance and number of neighbors. The interference pattern is the variation of the total mass absorption coefficient of the energy of the incoming photon. This can be observed as EXAFS.

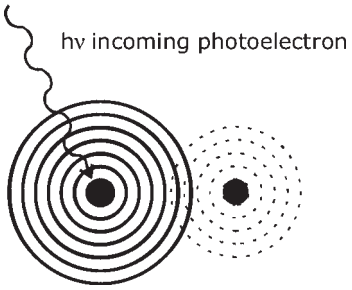

Figure 7.2 A pictorial representation of the processes involved in EXAFS spectroscopy. The incoming X-ray photon generates a photoelectron from the core level with higher energy. The electron wave of the photoelectron (solid line circles) is backscattered by the next nearest neighbor. This backscattering (dashed line circles) generates an outgoing electron wave that gives an interference pattern with the photoelectron wave.

The intensity of the EXAFS oscillation is dependent on a number of factors. First, the number and nature of backscattering atoms is a major contributor to the intensity of the oscillations. Different absorbers have different backscattering powers so the amplitude is dependent on the element which is the next nearest neighbor to the absorber atom. Depending on the absorber and the system, not all ejected electrons take part in the scattering process – up to 30% of the photoelectrons go into shake-up/down processes and are not available for EXAFS or XANES spectroscopy (see below).

If there is a spread in the distances (statically) of the next nearest neighbors this results in a reduction in intensity, which can be observed as an increase of the Debye–Waller factor. Dynamic changes, such as those induced by changing temperature, result in a reduced amplitude and increased Debye–Waller factor. The change in the amplitude is also a function of the energy; at higher electron energies the reduction of the amplitude is more significant than at lower energies.

A simplified form of the EXAFS equation can be written as follows:

$$\chi(k) = \sum_j \frac{N_j f_j(k) e^{-2k2\sigma_j^2}}{kR_j^2} \sin[2kR_j + \delta_j(k)] \tag{7.1}$$

The main parameters in this equation are:

$\chi(k)$ = EXAFS interference function
k = photoelectron wavevector $k = \sqrt{\frac{2m(E-E_0)}{\hbar^2}}$
N = coordination number of neighboring atom
R = distance to neighboring atom
σ^2 = square disorder of neighboring distance (Debye–Waller factor)
f_j = scattering amplitude
δ_j = phase-shift

Equation 7.1 represents a version of the EXAFS function that uses a spherical wave without any inelastic scattering. However, in a real system inelastic scattering occurs and the finite lifetime of the core level may result in the photoelectron not being scattered.

A damped wave function can be used in the calculation which leads to the following equation:

$$\chi(k) = \sum_j \frac{N_j f_j(k) e^{-2R_j/\lambda(k)} e^{-2k2\sigma_j^2}}{kR_j^2} \sin[2kR_j + \delta_j(k)] \tag{7.2}$$

λ represents the photoelectron mean free path.

Another correction that has to be made is the Amplitude Reduction Factor (AFAC) (sometimes called s_0^2) This accounts for the relaxation of the other electrons in the absorbing atom to the core hole. It normally has a size of $0.7 < \text{AFAC} < 1$. It is directly correlated to the amplitude of the EXAFS, and thus has strong correlation with the coordination number, as shown in Equation 7.3:

$$\chi(k) = \sum_j \frac{N_j \mathrm{AFAC} f_j(k) \mathrm{e}^{-2R_j/\lambda(k)} \mathrm{e}^{-2k2\sigma_j^2}}{kR_j^2} \sin[2kR_j + \delta_j(k)] \tag{7.3}$$

The need to take AFAC and inelastic scattering in to account results in a generally reduced accuracy of the coordination number determination in EXAFS. This can in part be overcome by using appropriate standards and a procedure outlined in ref. [3]. The process is described in detail in Section 7.1.4.

So far we only have included single scattering pathways. Especially for extended solids, multiple scattering becomes much more important. Figure 7.3 shows potential pathways for scattering.

In the EXAFS equation, all scattering from all neighbors is added to form the total function. In principle it also includes all possible multiple scattering pathways. The contribution of the different pathways depends on the angle between say three different atoms, as indicated in Figure 7.3. The triangular scattering path shown has the smallest amplitude, whereas the amplitude of the focused pathways as illustrated in Figure 7.3 exhibit important and significant contributions. In general multiple scattering contributions of structures with any angles larger than 150° need to be considered as important. Triangular pathways can also become relevant if there are many of these multiple pathways. Especially for extended solids such as oxides, multiple scattering has been shown to become crucial for the calculation of the structure [4]. If there is only one shell considered, the general rule is that multiple scattering is of limited importance.

7.1.2
Experimental Setup

XAS experiments are in general very simple to perform. For hard X-rays there is no necessity to provide any special atmosphere. However, quite often the light

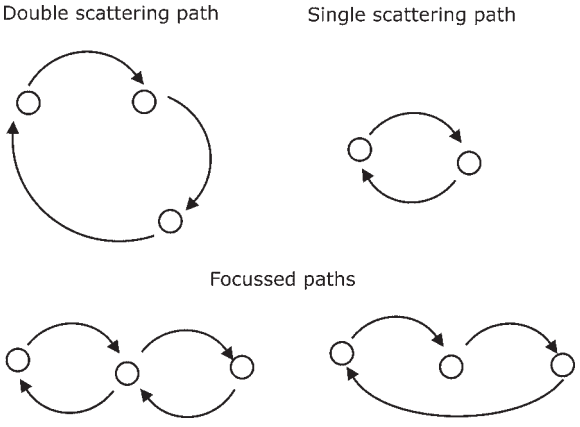

Figure 7.3 An illustration of multiple scattering pathways.

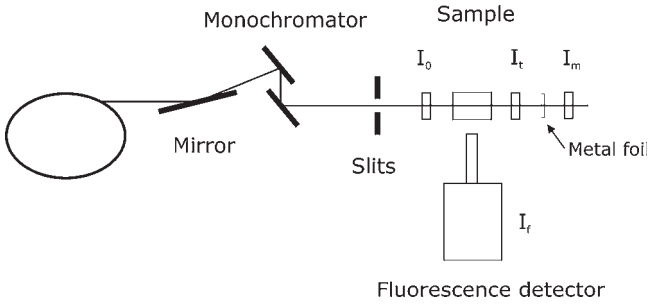

Figure 7.4 A typical XAS experimental set-up.

goes through pathways that are either evacuated or filled with He to reduce absorption of the less hard X-rays. For softer X-rays, such as the transition metal L-edges, Al, Si, S, P or As, a vacuum system has to be used to reduce the non-specific absorption of the X-rays. However, even in these cases gas atmospheres can be used as long as pathlengths are kept short. One of the major advantages of X-ray absorption spectroscopy is the comparably undemanding experimental setup. It has been used for *in situ* measurements of heterogeneous catalytic reactions, electrochemistry and fast reaction kinetics.

Figure 7.4 shows the experimental set-up of a typical XAS experiment. For most EXAFS experiments the source is a synchrotron. Laboratory sources are rare and usually do not exhibit enough intensity to get usable EXAFS spectra.

The photon sources from synchrotrons range from bending magnets, to wigglers and undulators. The specific device used depends on the frequency range and brightness required for the specific application.

Often the white beam is reflected by a mirror, which can be used for harmonic rejection and focusing on the sample.

The mirrors normally have to be cooled (often using gallium) since they are exposed to more or less the full intensity of the white beam. The monochromators for harder X-rays are often silicon single crystals exposing (220) or (111) planes. For lower energy photons such as the Mg, Si and Al edges, Y66B single crystals can be used. Below 1000 eV (e.g. first row transition metal L-edges, the O K-edge and the C K-edge) the technology changes significantly and gratings are used.

In transmission methods, after the monochromator, the optical path traverses through the I_0 detector, the sample chamber, the I_t detector and, for energy calibration, through a foil and the I_m detector.

7.1.3
Detection Methods

Absorption is the simplest method for measuring an X-ray spectrum. The incoming radiation, I_0 is measured and related it to the transmitted radiation (I_t).

Absorption is then given by:

$$\mu t = \ln\left(\frac{I_0}{I_t}\right) \tag{7.4}$$

where t is the sample thickness. and μ is the linear mass absorption coefficient.

This method makes use of all the photons that are incident on the sample.

To measure the absorption signal, a monochromator is stepped through the energy range and the variation of the mass absorption coefficient measured as a function of the Bragg angles (i.e. energy.) For significantly faster scanning, the full EXAFS energy range of radiation is shone on the sample and the emitted radiation is detected spatially using X-ray detector plates [5–9]. The detectors most commonly used for absorption are ion chambers, which are filled with gases with compositions dependent on the X-ray energy. The absorption of the gas should be in the range of 20% for the I_0 detector and 80% for the I_t detector.

Sometimes it is of advantage to measure absorption not directly, but by associated processes. This is mainly used when the X-ray absorption is only a small fraction of the total absorption process. Problems with absorption are often observed with highly diluted samples and also for low-energy EXAFS. In these cases the transmission results from the difference of either two nearly identical signals or two vastly different signals, both needing very accurate data.

Two of the techniques applied in this category are Auger electron process and X-ray fluorescence process. A schematic in Figure 7.5 shows the processes for these two techniques. These two processes compete with one another, and their relative abundance is dependent on the atomic number of the absorber. In general fluorescence is more pronounced for heavier elements, whereas the Auger process is more prominent for lighter elements.

In addition to the removal of one core electron by the incident X-rays (photoelectron process), the Auger process is taking place approximately 10^{-14} seconds after the photoelectron event. In this process an outer electron falls into the inner orbital vacancy from the photoelectron process and a second electron is emitted

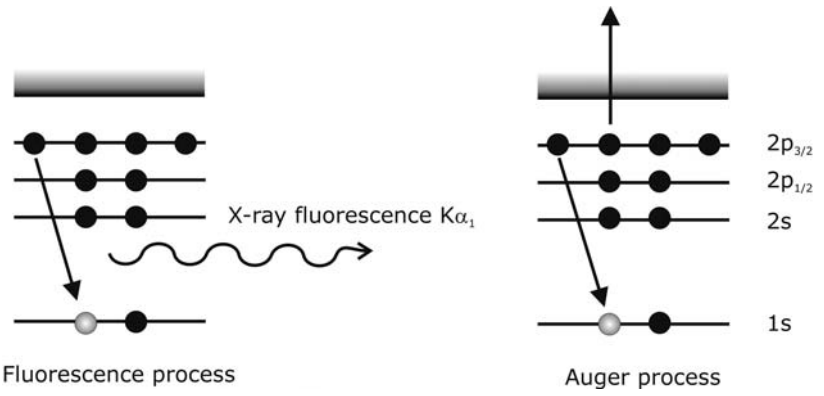

Figure 7.5 Processes resulting from the removal of a photoelectron by X-rays.

carrying the excess energy. The Auger electron carries and energy equal to the difference between the energy of the initial ion and the double charged final state. The Auger process is competing with the fluorescence process.

Fluorescence radiation is a result of the filling of a core hole (created by the absorption process) by outer electrons. For K-edges $K_{\alpha 1}$ radiation is emitted, which is characteristic of the absorbing element. There is significant background created by Compton radiation and elastic scattering. This radiation is at higher energy than the fluorescence line. Thus, detectors need to be energy discriminative. The scattering contributions can be removed using as a filter a metal foil with an atomic number (Z) one lower than the element of interest. Compton and elastic scattering frequencies are often above the absorption edge of the $Z - 1$ element and so they are removed.

Modern solid-state detectors have windowing functions that can filter the fluorescence radiation.

7.1.4 Data Reduction

As mentioned, EXAFS is defined by the variation of the mass absorption coefficient:

$$\chi(k) = \frac{\mu(E) - \mu_0(E)}{\mu_0(E_0)} \tag{7.5}$$

Equation 7.5 describes the energy-dependent EXAFS oscillations that can be interpreted using the EXAFS equation (as given in Equation 7.1 or Equation 7.2). $\chi(k)$ EXAFS as a function of electron wave vector.

The mass absorption coefficient is determined experimentally from the curves as illustrated in Figure 7.2 $\mu_0(E)$ is the smooth atomic background, whereas $\mu_0(E_0)$ is the edge step. The edge step is the mass absorption coefficient at the edge position. This can be determined by extrapolating the post-edge baseline or from the edge position. The edge position can be defined as the first point of inflection at the absorption edge.

EXAFS analysis is performed by a number of data treatment steps:

1. Deglitch the individual spectra.
2. Add the experimental spectra and individual contributions of the detectors (for, e.g., fluorescence).
3. Convert intensities to μ.
4. Subtract a background function pre-edge.
5. Normalize the spectra to an absorption of 1.
6. Subtract a background function post-edge to obtain $\chi(E)$.
7. Obtain E_0 and convert to $\chi(k)$, that is, convert from energy to k-space.
8. Define a model and calculate the sum of the model function from the EXAFS equation as, for example, from Equation 7.3.
9. Compare the calculated function with experimental $\chi(k)$ and minimize the differences.

Steps 8 and 9 are specific to the SRS Daresbury Laboratory suite of programs, which will be the focus of this discussion. Other programs use Fourier filtering techniques to isolate the contribution of the various shells. A number of other software programs use this technique. Fourier filtering can be problematic as outlined in refs [10, 11].

Deglitching is often necessary depending on the type and spectral region of the monochromator. The easiest way of deglitching is removal of the datapoints. A more detailed guide to deglitching can be found on: http://srs.dl.ac.uk/xrs/index.html

The Daresbury suite of programs used to add and convert data are Excalib and Exspline, and the EXAFS fitting is called Excurv98.

There are a number of other programs available (often free of charge or with nominal costs) such as FEFF and viper (which uses FEFF code).

Exspline is an X-window-based program that uses spline first for pre- and post-edge fitting baselines. It has the advantage that the Fourier transform, the EXAFS and the pre- and post- baseline fit can be observed interactively. This is a great improvement on Exback, which used non-interactive baseline correction.

Owing to the various processes detailed above, the EXAFS oscillations decay quickly with the photoelectron wavevector (k). The EXAFS is often weighed as k, k^2 or k^3 to increase the intensity of the oscillations at higher k values.

Figure 7.6 shows the EXAFS oscillation together with the amplitude of the Fourier transform of the Al K-edge of the zeolite Na-FAU. The spectrum and its Fourier transform (FT) are shown together with fitted data. The first peak in the Fourier transform can be found at 1.67 Å. However the real position of the peak is at 1.74 Å.

The discrepancy between the two values is a result of the phase-shift function, which is included in Equation 7.3. Phase shifts are dependent on the absorber atom and can be calculated by *ab initio* methods. The model building for phase-shift files include a model of the most abundant atomic neighbor for a specific atom.

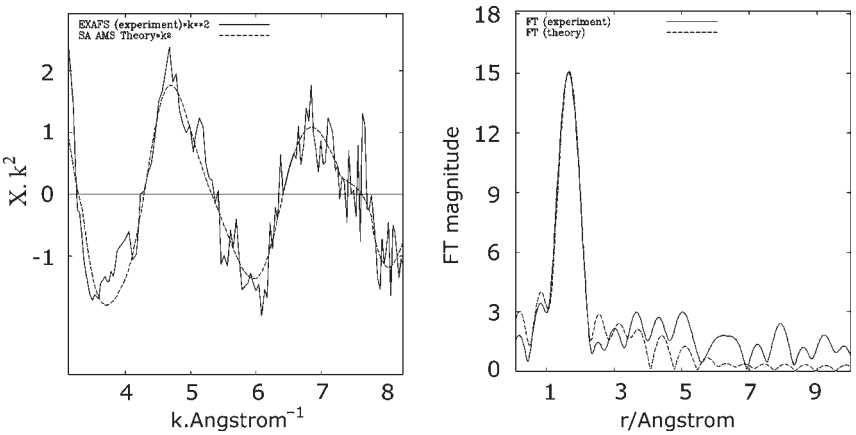

Figure 7.6 EXAFS and FT transformed spectra of Na-FAU. The dashed line represents fitted and the solid line experimental data.

Fourier transformation of EXAFS makes $\chi(k)$ a complex number, but often the FT is only represented by its amplitude, as shown in Figure 7.6.

Often the FT (as seen in Figure 7.6) shows well separated peaks and is then used to perform the fitting procedure in Fourier space or to filter the data. Of course, in this case a windowing function has to be applied with all its associated problems. The filtering is often performed at higher r values to remove some of the noise.

The filtering process itself introduces an arbitrary function, which can cause artifacts. For instance, the statistical significance of shells is altered [10]. Unless Eigen functions are used for the Fourier filtering [11] the introduction of the arbitrary function to perform Fourier filtering should be omitted. If absolutely necessary (for example if there are problems with baseline correction) very wide filtering functions can help in reducing the problem.

The fitting procedure is normally carried out consecutively, that is, shells are added to the fitting process as seems appropriate. Every shell should be checked for statistical significance, that is, if the addition of, normally, three parameters (σ, R,N) is statistically viable. The check can be made by comparison of the change in the Fit index with F-test values, as outlined in ref. [12]. The oscillations are often very broad and with few features for oxides. In this case good statistical parameters are especially important.

Interpretation of XANES is significantly more difficult than for EXAFS. The EXAFS equation breaks down in the low-k XANES region and the mean free path goes up. The XANES region is even more complicated by the significant multiple scattering than EXAFS. However, the electronic transitions can be handled as a fingerprint and the XANES, the white line intensity and edge position are a measure of the electron density. XANES can provide us with important information of the chemistry of the probed solid. For instance for transition metals the pre-edge peak can distinguish between octahedral, square planar, tetrahedral or distorted tetrahedral coordination. The oxidation state of transition metal species can also be determined from the XANES.

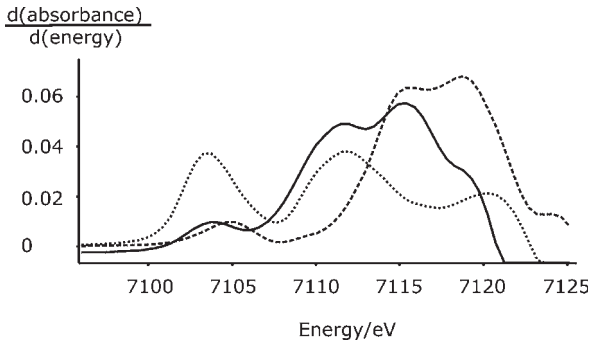

Figure 7.7 Differential XANES spectra of iron containing compounds. Dotted line Fe metal, full line FeO dashed line Fe_2O_3. Adapted from ref. [13].

Figure 7.7 shows typical derivative XANES spectra of some iron oxides and iron metal. The edge position is in the maximum of the second peak for the oxides. It can be seen that the edge position changes significantly depending on the oxidation state. It also shows that the variation of the XANES is significant, and can be used as a fingerprint to determine the species present in the oxide.

Pre-edges as observed in Figure 7.7, which are found in transition metals with partially filled d-shells, can be indicative of the coordination environment of the transition metal. The pre-edge can be interpreted as an s–d transition, which is forbidden in octahedral symmetry. Only small pre-edges are found for transition metal compounds having octahedral or distorted tetrahedral symmetry. On the other hand, tetrahedral compounds can have big pre-edges which can be used as an indicator for the coordination chemistry. For example tetrahedral $FePO_4$ and Fe-MFI zeolites exhibit significant pre-edges, whereas most transition metal exchanged zeolites, the iron oxides and iron salts only show smallish s–d transitions.

It is interesting to note that oxygen XANES exhibits pre-edges if bound to a transition metal (e.g. Co), as well.

XANES probes the transition of core electrons into unoccupied electronic states. The final states may be mixed with other orbitals and can be used to determine the coordination environment of an element in a compound, its electron density and oxidation state. The intensity can be used to accurately determine relative oxidation state ratios. Furthermore, XANES can be used to determine relative amounts of species by linear combination of individual compounds. In recent years, the codes for XANES calculation (especially John Rehr's FEFF code), have significantly improved and it can be expected that theoretical models of compounds will be accurately determined by XANES measurement and calculation in the future.

XANES and EXAFS complement each other very well and are ideal to determine the site structure of even mixtures of catalysts or oxides.

7.2 Applications of EXAFS

XAS is in general less accurate than XRD techniques. The accuracy depends on the edge energy, the resolution of the monochromator and, last but not least, the quality of model building. As a general rule distances can be determined up to 5×10^{-3} Å and coordination numbers at maximum to 10%. This is clearly inferior to XRD.

However, as mentioned in the introduction, the main advantage of XAS compared to other structural techniques is its element specificity, its potential operation under more or less any experimental conditions, its applicability for amorphous and X-ray amorphous materials and its straightforward sample preparation. In the following, some applications of XAS in catalytic systems will be discussed.

XAS was originally used mainly for supported metal catalysts. XRD, despite being applicable under reaction conditions of high temperatures and pressures, is not normally able to detect small clusters of noble and other metals in supported catalysts. A significant number of systems are too small to be detected by conventional XRD techniques because they become X-ray amorphous due to line broadening. Group VIII noble metals were among the first catalysts investigated and the work by Lytle and also Sinfelt is of particular note in this area [14, 15]. These classic investigations, and especially *in situ* investigation [16], paved the way for modern XAS in catalysis.

7.2.1 Acid Zeolites

Zeolites are crystalline alumosilicates with a regular pore structure. These materials have been used in major catalytic processes for a number of years. A significant number of processes use zeolites as catalysts either as supports or as catalysts themselves. The application using the largest quantities of zeolites is Fluid Catalytic Cracking (FCC). The first zeolites used as catalysts for FCC were reported in a 1961 patent by Exxon [17] and very quickly replaced many of the amorphous silica alumina catalysts which dominated the process up to that time. The zeolites with significant cracking activity are ultrastable Faujasite (USY), ZSM-5 (alternatively known as MFI), mordenite, offretite and erionite. By far the highest volume of zeolite type used for this application are USY zeolites.

The catalytic activity of zeolites has its origin in the fact that some of the silicon atoms in the crystalline framework of the solids are replaced by an aluminum atom. Since aluminum is trivalent, the replacement of the tetravalent silicon results in the introduction of a negative charge into the zeolite lattice. This negative charge has to be compensated by a cation. When synthesized, most zeolite materials have sodium as a counter-cation, resulting in very little catalytic activity for acid-catalyzed reactions. Therefore zeolites are normally exchanged by rare earth or ammonium cations to create catalytically active acidic sites. The ammonium cations are normally decomposed at higher temperatures leaving residual H^+ species, forming the Brønsted acidic site. Mixed rare earth and ammonium zeolites are among the most widely used zeolite formulations for FCC.

Despite the enormous commercial success and widespread use of acidic zeolite catalysts, important questions on the local structure of zeolitic materials remain unanswered. The local structure of aluminum in the zeolites has proven rather elusive to investigation.

It has proved difficult to establish the local structure surrounding these aluminum sites by diffraction methods because the similarity of the backscattering powers of aluminum and silicon result in the elements being virtually indistinguishable using these methods. Although aluminum is slightly larger than silicon, most crystallographic data on zeolites does not report any distinction between silicon and aluminum atoms in the lattice. Neutron diffraction [18] is one of the few techniques able to provide direct structural data on the position of the

zeolitic proton. Neutron diffraction has been used both to characterize the average proton site structure and to investigate the interaction of the sites with reactant molecules.

Magic Angle Spinning (MAS) Nuclear Magnetic Resonance (NMR) also had some success in determining proton positions. Side-band analysis from solid-state ^{1}H NMR was used to determine proton positions [19, 20] in ZSM-5 type zeolites.

In addition to the limited experimental techniques, some theoretical studies on the local structure of aluminum sites in the zeolites were published in the early 1990s [21]. More recently, some systematic studies of the acid–base properties of zeolites were determined using theoretical approaches. It was suggested that the local structure of the zeolites has some influence on the acid strength of the individual sites [22, 23]. It has long been recognized, for example, that the concentration of aluminum has significant influence on the acid strength of individual sites. Variations in the acid strength were suggested to depend on the structure type and concentration of lattice aluminum, which result in a variation of the local site structure. In contrast to earlier studies [24], the authors suggested no direct correlation of acid strength with bond angles. The authors also reported that the Al—O bond that carries the acidic proton is longer than the other Al—O bonds [22, 25, 26].

The first EXAFS study of aluminum in zeolites was a study of Na- and H-FAU (Faujasite) by Koningsberger and coworkers [27]. The authors observed slight variations in the Al—O bond lengths when comparing Na-, H- and NH_4-form zeolites. However, they did not find any significant variations between the four different aluminum–oxygen bond distances. This is in contrast to the theoretical calculations, which suggested an increased Al—O distance for one of the Al—O bonds. Similarly, more recently Bell and coworkers [28] did not find an increased distance Al—O distance for acidic and Cu-exchanged ZSM-5 . Bell suggested that his data does not support a distinction between Al—O bonds but did not give any statistical support for this conclusion.

In line with the theoretical predictions [4, 29] an increased Al—O distance was observed by some workers. Furthermore multiple scattering calculations enabled calculation of the detailed local structure, including bond angles. The group that initially reported very similar Al—O distances [27, 30] later observed a variation under *in situ* conditions [31]. This is not too surprising, since other cations were found to relax the zeolite local structure to a more regular tetrahedron [32] (Figure 7.8). Sorption of water and the presence of alkali metal or ammonium countercations result in the more regular tetrahedral structure that had been reported in the earlier papers [27, 30].

Weaker bases such as toluene or isopropanol induced some relaxation of the aluminum in acidic zeolites. Water also exhibited a similar effect [32], R.W. Joyner, A.D. Smith, and M. Stockenhuber 2007, unpublished].

One of the disadvantages of EXAFS in general is that it is an averaging technique. Thus it is very important to make sure the zeolites are very well defined. Other techniques such as ^{27}Al MAS NMR spectroscopy and *in situ* infrared spectroscopy are needed to ensure single aluminum sites. Depending on the data quality it is also possible to define more than one type of site; however, in this case

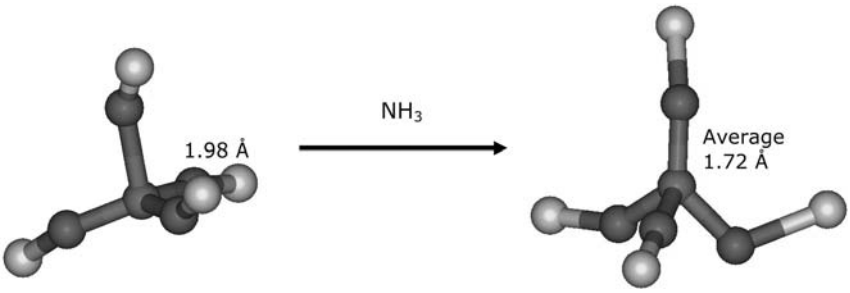

Figure 7.8 The relaxation of the aluminum tetrahedron upon adsorption of ammonia on H-ZSM-5. Adapted from ref. [33].

statistical analysis is absolutely crucial for the determination of the number of statistically relevant shells [12]. XAS can also be used to characterize site variations. It has been suggested that XANES can be used to distinguish between tetrahedral, octahedral, distorted octahedral and square planar geometry [30, 33].

However, the accuracy of the *ab initio* calculations for the large number of multiple scattering pathways present in the XANES region is limited and thus difficulties arise in the interpretation of the data (see above).

XANES, particularly the edge position and white line intensity, can, however, give a good indication of the electron density of the aluminum. The electron density on the aluminum atom then in turn influences the electron density on the oxygen, which can have an influence on acid strength of the solid.

A more direct approach to assess this has been made very recently [R.W. Joyner, J.A. Purten, C. France and M. Stockenhuber, 2007, unpublished]. Oxygen EXAFS was recorded for the first time in zeolites and it was possible to get accurate data for Co—O and K—O structures from oxygen K-edge data. The XANES for oxygen also exhibited very rich features which can easily distinguish between the various counter-cations. It was also possible to separate oxygen interacting with cations from "spectator oxygen" atoms. Oxygen X-ray absorption is relatively difficult experimentally because a good vacuum has to be achieved. Furthermore, detector technology is difficult for the low energies involved. This initial study used electron yield detection, which is rather noisy and needs mixing of the zeolite with graphite to get better conductivity. However, solid-state and gas microstrip detectors exist that can be used for oxygen K-edge detection at 530 eV.

7.2.2 Transition Metal Exchanged Zeolites

Exchanging the proton forms of zeolites with transition metals leads to redox active catalysts. Great interest in this technology was triggered at the beginning of the 1990s, when Iwamoto [34–36] reported the use of copper exchanged ZSM-5 material for the selective catalytic reduction of NO_x. The incentive for this reaction came from the potential use of the NO reduction process in diesel and lean-burn engines.

EXAFS of transition metal exchanged zeolites is the best technique for direct structure analysis of these materials. Under ideal conditions, the transition metal forms single atoms or very small clusters, which are X-ray amorphous. EXAFS, on the other hand, in particular for the harder edges, can determine the local structure of exchanged zeolites very well. It is not surprising that EXAFS spectroscopy has been widely used to characterize Cu-ZSM-5 materials. Among the first to characterize copper species in zeolites was Hamada as early as 1990 [37]. It was suggested that there are significant differences in the copper species present in the ZSM-5 zeolite as compared to bulk copper oxides, and a number of authors proposed that the copper species present in zeolites depend on the loading. At lower loadings single copper ions were thought to be present in cationic zeolite positions, whereas at higher loadings small copper clusters were thought to be the active species in the NO_x reduction process [37, 38]. The nuclearity of the clusters can be determined from fitting the coordination numbers and should generally be treated with some caution. However, a combination of the use of good standards and cautious data treatment generally allows determination of the cluster sizes involved, even for oxidic materials, which are more difficult to analyze than metal clusters. The advantage of *in situ* determination of EXAFS and XANES is very well demonstrated in a number of studies, both of variation of the local structure and of the oxidation state under reactive conditions [38, 39]. Deactivation of the catalyst under reaction conditions is one of the biggest problems of Cu-zeolite catalysts. It is therefore not surprising that a number of studies have attempted to understand the origin of the problem using XAS. Sulfur and water tolerance have been investigated in detail [40, 41].

It was suggested by a number of authors that sintering similar to metal catalysts leads to deactivation of copper-modified zeolites.

Sulfate formation and coke deposition were often excluded as reasons for deactivation, using EXAFS spectroscopy. The formation of larger clusters in the zeolite, which can also lead to destruction of the host structure, can be observed by an increase in the coordination number of the Cu—Cu scattering contribution to the EXAFS.

The formation of extended oxidic species was deemed detrimental to the catalytic performance by most authors. XAS has been instrumental in the detection of these species.

Deactivation of the copper zeolites under de-NO_x conditions was one of the major reasons why the catalyst was never used in a commercial application. Recent environmental legislation intensified the hunt for a water- and sulfur-stable active catalyst. One of the most successful preparative methods was reported by Hall and Feng [42, 43]. They reported excellent de-NO_x performance based on an iron exchanged ZSM-5 zeolite. The activity was reported to remain constant for extended times, even under high water and sulfur content conditions. The initial catalytic study initiated a whole raft of characterization studies by a number of groups. The interest was significantly increased when it became obvious that there are issues with catalyst preparation reproducibility [44, 45]. XAS was crucial in the discussion of the structure of active sites for de-NO_x and the site responsible for the high

activity of iron-containing zeolite catalysts in the benzene to phenol [46] and methane to methanol [47] reactions.

Discussion of the active site structure remains current. The catalytic process and activity of these materials is so unique that much effort is being put into their structural elucidation.

Iron-modified zeolites were first prepared in the late 1960s. The major understanding of the structure in these materials came from NO adsorption on the zeolites, which was followed by infrared spectroscopy and by electron spin resonance (ESR), and to a limited extent Mössbauer, spectroscopy. The limitations using these spectroscopic techniques were that for ESR spectroscopy most of the iron in the zeolite does not show a signal, whereas Mössbauer spectroscopy is probing the average of all the iron species present, which makes distinction of sites difficult. A combination study using XAS and infared spectroscopy was most valuable in the early determination of the structure of sites in iron exchanged ZSM-5 zeolites [13].

Aqueous exchange with iron (which is very different to other techniques) led to the formation of iron nanoclusters, which were shown to be highly active in the selective catalytic reduction of NO_x. Figure 7.9 shows the suggested structures taken from ref. [13].

The structure observed depended on the preparation procedures. It was found that the relative amounts of the various species strongly depends on the initial preparation procedure of the catalyst. In the absence of oxygen, more active species and more Fe_4O_4 were found. If catalysts were prepared initially in the presence of oxygen, more isolated species and smaller clusters were formed.

The most interesting feature in these materials was the presence of an iron–iron distance slightly above 2.5 Å. Fe—Fe distances in transition metal oxides would be expected to be about 3.0 Å. The structure is very similar to the Fe—S clusters observed in some life-forms, and have also been synthesized as biomimics.

The cluster size of the transition metal in zeolites was determined for a number of different preparations. In the mesoporous MCM-41 materials [48, 49] isolated clusters were observed, whereas for some solid-state exchanged and chemical vapor deposition samples dimeric species similar to methane monooxygenase were suggested [50, 51]. To date the discussion centers on clustered versus isolated species present in the various zeolites.

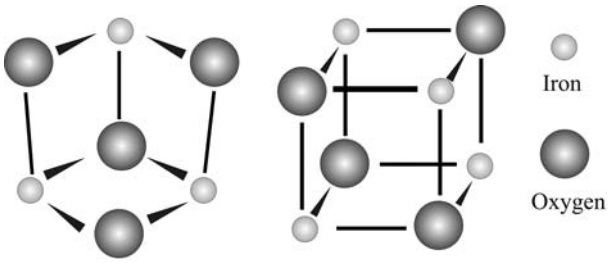

Figure 7.9 The Fe-O nanoclusters as inferred from X-ray absorption spectroscopic studies. Adapted from ref. [13].

The combination of infrared spectroscopy and XAS has been extremely useful in the understanding of site structure. Infrared spectra [13, 50, 52] of adsorbed probe molecules can help to differentiate between different types of site. They are discriminative in the sense that the probe molecules will adsorb with different thermodynamic parameters on the different sites. XAS on the other hand will average over all the different sites present in the zeolite. This can of course be an advantage, but is also a disadvantage in the sense that the active site can be lost in the signal of the other species. Some combined X-ray absorption infrared instrumentation is currently being developed and tested for metal catalysts [53, 54]. The data quality of oxides tend not to be as good as for the metal catalysts, but similar instrumentation could be used for a number of applications for oxidic catalysts.

One of the major current challenges is the structural investigation of the benzene to phenol oxidation catalyst. The Fe-MFI material used for this application was suggested to work only after activation by steaming or high-temperature treatment.

A zeolite treated with steam at about 800 °C was found to exhibit large quantities of α-sites, which were suggested to be responsible for the oxidation reaction [55]. Once loaded with α-oxygen, the α-sites can oxidize benzene to phenol and methane to methanol at room temperature. The catalysts have to be loaded at a higher temperature with N_2O and can then perform the selective oxidation. The structural properties responsible for this chemistry are under intense debate. A number of authors suggest, as already mentioned, that dimeric species are responsible for the formation of the α-oxygen, while others suggest isolated cations. Fe(IV) species have been suggested by a few authors, but disputed by others [56]. Until 2006, iron in zeolites was the only catalyst for this rather unusual reaction. Only since then have other systems been found that can perform this selective oxidation [57, 58]. The iron system was shown to contain coordinatively unsaturated iron which can perform the selective oxidation of benzene to phenol.

7.2.3
Selective Oxidation Catalysts

Selective oxidation of hydrocarbons is a very demanding process for any catalytic system. The main problem of selective oxidation is the prevention of total oxidation.

The total oxidation products (water and CO_2) are of no significant value apart from the heat that is generated, which means that any system developed needs very good selectivity if it is to be applied industrially. In recent years, titanium silicalite 1 (TS-1) has been shown to be a very effective oxidation catalyst. It can be used in a number of oxidations as outlined in Table 7.1. The table shows that a vast number of different reactions can be catalyzed by hydrogen peroxide over TS-1, which was a major breakthrough in oxidation catalysis in the 1980s. The problem is, of course, the use of H_2O_2 which preferably should be replaced by oxygen.

Table 7.1 Reactions catalyzed by TS-1 using H_2O_2 as oxidant.

Reactant	Product
Alkenes	Epoxides
Phenol	Diphenols
Amines	Hydroxylamines
Alkanes	Alcohols, ketones, aldehydes
Sulfides	Sulfoxides
Alcohols	Ketones, aldehydes
Amines, ketone + NH_3	Oximes

TS-1 is a silicalite (SiO_2 with the ZSM-5 structure) analog (Figure 7.10) in which some of the Si atoms are replaced by Ti atoms.

Unlike aluminum, titanium is tetravalent and can exhibit different oxidation states. Thus TS-1 is non-acidic if isomorphously substituted. TS-1 is relatively difficult to synthesize, which is probably one of the reasons the site structure was under debate for quite some time. TS-1 can only be synthesized with a maximum of 3 wt% Ti; if more Ti is added extra-framework titanium is formed. Initially, it was suggested from XAS that octahedral sites are formed in the silicalite framework [60]. However, later more and more groups suggested tetrahedral isomorphous substitution of the titanium sites in the MFI framework [61–63]. It is now more or less generally accepted that the Ti is four-coordinate and has a Ti—O distance of 1.79–1.81 Å. This is a significantly increased distance compared to the Si—O distance 1.605 Å, which is constant for a vast number of oxides [4]. The increase in

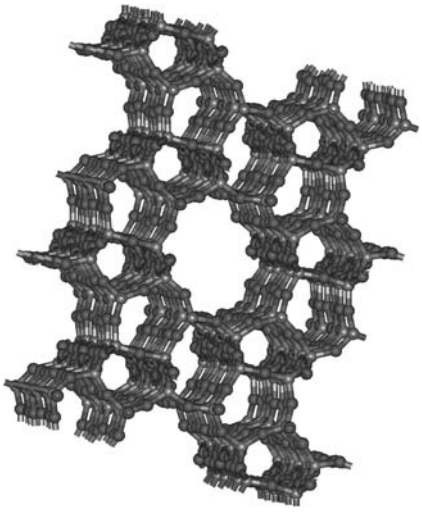

Figure 7.10 The silicalite structure looking along the straight channels [59].

the distance is not surprising, taking into account the ionic radius change from 40 pm to 60 pm. The increase in the Ti—O distance can also be observed in the unit cell parameters, which can be determined by diffraction methods.

XAS has been shown to be one of the few techniques able to determine the site structure for TS-1. In an ideal TS-1 the sites are isolated and are X-ray amorphous to diffraction techniques. The increase in the unit cell parameters is the only strong indication of a change in the TS-1 structure due to isomorphic substitution. Again, similarly to aluminum, the backscattering amplitudes of titanium are similar to silicon, making detection difficult. Not only was the full multiple scattering approach, used by Sankar and coworkers [62], important for detailed structural analysis but XANES was also crucial in these investigations. There is hardly any pre-edge p–d transition at 4967 eV in TS-1 with less than perfect tetrahedral coordination. The pre-edge mentioned stems from a p–d transition that is only allowed from the selection rules for tetrahedral coordination symmetry. It is a good fingerprint for this coordination and can be used as an analytical tool to observe distortions of the local structure *in situ*.

The pre-edge intensity very often increases only upon removal of any adsorbed water vapor [64]. The water vapor acts as a ligand, which changes the intensity of the pre-edge peak. This is crucial for the understanding of how the oxidation catalysis works, since TS-1 is mostly used in aqueous solutions with hydrogen peroxide. It has been suggested that EXAFS can show the presence of titanium peroxo species on TS-1 [65].

The use of zeolites and zeotypes for selective oxidation reactions is a relatively new development. Classic selective oxidation catalysts are mixed-metal oxides with relatively low surface areas and good dispersion of the various active components. The classical selective oxidation catalysts for propene to acrolein synthesis are mixed oxide catalysts such as bismuth molybdate. Despite most of these catalysts being crystalline and exhibiting long-range order, XAS has the advantage of being element specific. It can determine oxidation states and can also directly probe very low concentrations of one metal component in a matrix.

The selective oxidation of propylene to acrolein was suggested to occur via a Mars–van Krevelen mechanism (i.e. reaction of the hydrocarbon with lattice oxygen), where in the first step bismuth dehydrogenates propene to form an allylic species. This has mainly been concluded from isotopic scrambling studies. The oxidation step itself is believed to occur via the mechanism shown in Figure 7.11. The hydroxyl groups on the surface are believed to be mobile and can form water, which desorbs. The final step is the re-oxidation of molybdate species, which is still not understood in full detail.

Despite the fact that most industrial catalysts are multi-component mixed oxides, the active phases for the selective oxidation are thought to be the α- , β- and γ-bismuth molybdates ($Bi_2O_3 \cdot 3MoO_3$, $Bi_2O_3 \cdot 2MoO_3$, $Bi_2O_3 \cdot MoO_3$, respectively) [66]. Using a combination of time- and temperature-resolved Mo K-edge XANES/XRD experiments, Sankar and coworkers [67] studied the formation of the various phases of the oxidation catalyst in great detail. Principal component analysis was used to determine the formation of various amorphous phases, whereas XRD was

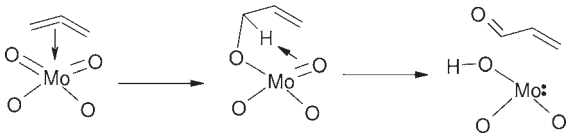

Figure 7.11 The reaction mechanism of propylene oxidation on molybdate species.

used to observe the formation of crystalline phases. In addition, the authors used infrared studies to complement the structural investigation. For α-bismuth molybdate the authors were able to conclude that the formation of the α-phase started at temperatures as low as 200 °C and the final crystalline phase was entirely finished at 400 °C. No intermediate phases were formed. In contrast, the formation of the β-phase is much more complex and was suggested to start from dehydrated and hydrated precursors. All three components were observed during the formation of the β-phase by XANES, despite X-ray diffraction patterns not showing any changes. During calcination even above 500 °C some 5% of γ-phase was observed by principal component analysis. It was suggested that heating at 600 °C for at least 1 h is necessary to obtain a phase-pure product.

For the γ-phase, an intermediate phase in addition to the β-phase was suggested to be formed above 140 °C and the β product is an intermediate for the formation of γ-bismuth molybdate.

To understand the mechanism in terms of the structures and oxygen sites involved, O K-edge XANES was used to probe oxygen sites on (010) single-plane MoO_3 species. Using a combination of angle-resolved XANES and density functional theory cluster calculations the authors were able probe the final-state orbitals of the different coordinated oxygen sites in MoO_3 as well as those from vacant sites [68]. This has only been demonstrated for very well defined surfaces but it can be envisaged that O K-edge EXAFS will provide direct information on oxygen vacancies, structure and bonding in real catalysts.

XAS on molybdenum oxides was carried out at the Mo K-edge at 19.999 keV [69] under *in situ* conditions during reduction and oxidation using propene and oxygen. On propene reduction, the authors did not observe any phase changes using XRD [70]. On the other hand significant molybdenum reduction was observed using XRD. Principal component analysis of the XANES revealed that $Mo_{18}O_{52}$ was an intermediate during the partial reduction of MoO_3. In line with the reduction by propene, the authors found the same $Mo_{18}O_{52}$ phase when oxidizing MoO_2 with oxygen.

The $Mo_{18}O_{52}$ phase found is non-crystalline, as the authors point out. No additional diffraction peaks were found. In addition to the multi-component analysis of the XANES spectra the authors observed a significant change in the Mo—O and Mo—Mo distances at 573 K, where XANES suggested the formation of a $Mo_{18}O_{52}$ phase.

The authors suggested that the $Mo_{18}O_{52}$ phase consists of crystallographic shear planes similar to crystalline $Mo_{18}O_{52}$, which would be similar in their XANES signature. The shear planes were also suggested by electron microscopy studies

[71]. At higher temperature the authors suggested the formation of Mo_4O_{11} species.

From the EXFAS and XANES as well as XRD studies the authors concluded that below 600 K propene reacts with oxygen on the surface and no involvement of bulk oxygen can be found, whereas between 600 and 700 K selective oxidation involving the $Mo_{18}O_{52}$ phase is taking place. Similarly, partial oxidation involving lattice oxygen (Mars–van Krevelen mechanism) was suggested at temperatures above 700 K, involving a Mo_4O_{11}-type phase.

A multi-edge study on MoVSbNb oxide catalyst for selective oxidation has been published [72], in which the Sb L1-edge, the Mo-K edge and the V K-edge were studied. Under the operating conditions the authors found varying oxidation states of antimony and vanadium depending on the propane/oxygen ratio, but the molybdenum oxidations state was more or less constant. They also found that even the annealing of the phase resulted in reduction of antimony.

7.3 Conclusion

In this short review, the background to the EXAFS technique and its application to catalytic oxidation and oxide-based systems have been described. It is clear that in certain situations, EXAFS possess significant advantages compared to standard diffraction techniques. Furthermore, the ease of its application as an *in situ* or *operando* technique and the general simplicity of its experimental setup make it extremely versatile. Although there are potential limitations in its application to systems where a range of local element environments are present, these can, to an extent, be alleviated by the use of complementary FTIR techniques and the combination of XAS and FTIR spectroscopies is extremely powerful. Coupled with the increasing number of studies investigating soft edges (e.g. Al and O K-edges), and the improvements in XANES analyses progressing beyond the simple fingerprint type analyses generally practiced, it is clear that future exciting developments with this technique can be anticipated.

References

1 Teo, B.K. and Joy, D.C. (eds) (1981) *EXAFS Spectroscopy, Techniques and Applications*, Plenum Press, New York.

2 Koningsberger, D.C. and Prins, R. (eds) (1988) *X-ray Absorption: Principles, Applications, Techniques of EXAFS, SEXAFS and XANES*, Wiley-Interscience.

3 Moen, A. (1995) Synthetic and X-ray absorption spectroscopic studies on some metal-containing zeotypic silicoaluminum phosphates. PhD Thesis University of Trondheim.

4 Joyner, R.W., Smith, A.D., Stockenhuber, M. and van den Berg, M.W.E. (2004) *Physical Chemistry Chemical Physics*, **6**, 5435–9.

5 Salvini, G., Headspith, J., Thomas, S.L., Derbyshire, G., Dent, A., Rayment, T., Evans, J., Farrow, R., Diaz-Moreno, S. and Ponchut, C. (2005) Nuclear instruments &

methods. *Physics Research Section A: Accelerators, Spectrometers, Detectors and Associated Equipment*, **551**, 27–34.
6 Newton, M.A., Jyoti, B., Dent, A.J., Fiddy, S.G. and Evans, J. (2004) *Journal of the Chemical Society, Chemical Communications*, 2382–3.
7 Dent, A.J. (2002) *Topics in Catalysis*, **18**, 27–35.
8 Mallozzi, P.J., Schwerzel, R.E., Epstein, H.M. and Campbell, B.E. (1981) *Physical Review*, **A23**, 824–8.
9 Mallozzi, P.J., Schwerzel, R.E., Epstein, H.M. and Campbell, B.E. (1979) *Science*, **206**, 353–5.
10 Joyner, R.W. and van Santen, R.A. (1993) NATO ASI Series, *Series C: Mathematical and Physical Sciences*, **398**, 1–2.
11 Krylov, A.S., Poliakoff, J.F. and Stockenhuber, M. (2000) *Physical Chemistry Chemical Physics*, **2**, 5743–9.
12 Joyner, R.W., Martin, K.J. and Meehan, P. (1987) *Journal of Physics C – Solid State Physics 20*, 4005–12.
13 Joyner, R. and Stockenhuber, M. (1999) *Journal of Physical Chemistry*, **B 103**, 5963–76.
14 Lytle, F.W., Via, G.H. and Sinfelt, J.H. (1977) *Journal of Chemical Physics*, **67**, 3831–2.
15 Lytle, F.W., Sayers, D.E. and Moore, E.B. (1974) *Applied Physics Letters*, **24**, 45–7.
16 Lytle, F.W., Greegor, R.B., Marques, E.C., Biebesheimer, V.A., Sandstrom, D.R., Horsley, J.A., Via, G.H. and Sinfelt, J.H. (1985) ACS Symposium Series 288, 280–93.
17 Kimberlin, C.N.Jr and Gladrow, E.M. (1961) US Patent 2971903, to (Esso Research and Engineering Co.).
18 Olson, D.H., Toby, B.H. and Reisner, B.A. (2001) *Studies in Surface Science and Catalysis*, **135**, 1431–8.
19 Freude, D. and Klinowski, J. (1988) *Journal of the Chemical Society, Chemical Communications*, 1411–13.
20 Hunger, M., Freude, D. and Pfeifer, H. (1988) *Catalysis Today*, **3**, 507–12.
21 Schroder, K.P., Sauer, J., Leslie, M., Catlow, C.R.A. and Thomas, J.M. (1992) *Chemical Physics Letters*, **188**, 320–5.
22 Brandle, M., Sauer, J., Dovesi, R. and Harrison, N.M. (1998) *Journal of Chemical Physics*, **109**, 10379–89.
23 Brandle, M. and Sauer, J. (1997) *Journal of Molecular Catalysis A – Chemical*, **119**, 19–33.
24 Lin, C.Y. and Haller, G.L. (1995) *Science and Technology in Catalysis*, **1994** (92), 173–8.
25 Eichler, U., Brandle, M. and Sauer, J. (1997) *Journal of Physical Chemistry*, **B 101**, 10035–50.
26 Brandle, M. and Sauer, J. (1998) *Journal of the American Chemical Society*, **120**, 1556–70.
27 Koningsberger, D.C. and Miller, J.T. (1994) *Catalysis Letters*, **29**, 77–90.
28 Drake, I.J., Zhang, Y.H., Gilles, M.K., Liu, C.N.T., Nachimuthu, P., Perera, R.C.C., Wakita, H. and Bell, A.T. (2006) *Journal of Physical Chemistry*, **B 110**, 11665–76.
29 Joyner, R.W., Smith, A.D., Stockenhuber, M. and Van den Berg, M.W.E. (2004) *Studies in Surface Science and Catalysis*, **154B**, 1406–10.
30 van Bokhoven, J.A., Sambe, H., Ramaker, D.E. and Koningsberger, D.C. (1999) *Journal of Physical Chemistry B*, **103**, 7557–64.
31 van Bokhoven, J.A., Van der Eerden, A.M.J. and Prins, R. (2004) *Journal of the American Chemical Society*, **126**, 4506–7.
32 Joyner, R.W., Sonntag, O., Smith, A.D. and Stockenhuber, M. (2007) *Studies in Surface Science and Catalysis*, **170**, 756–61.
33 van Bokhoven, J.A., Sambe, H., Koningsberger, D.C. and Ramaker, D.E. (1997) *Journal of Physics*, **IV7**, 835–40.
34 Iwamoto, M., Yahiro, H., Tanda, K., Mizuno, N., Mine, Y. and Kagawa, S. (1991) *Journal of Physical Chemistry*, **95**, 3727–30.
35 Sato, S., Yoshihiro, Y., Yahiro, H., Mizuno, N. and Iwamoto, M. (1991) *Applied Catalysis*, **70**, L1–L5.
36 Iwamoto, M., Yahiro, H., Shundo, S., Yoshihiro, Y. and Mizuno, N. (1991) *Applied Catalysis*, **69**, L15–L19.
37 Hamada, H., Matsubayashi, N., Shimada, H., Kintaichi, Y., Ito, T. and Nishijima, A. (1990) *Catalysis Letters*, **5**, 189–96.
38 Gruenert, W., Hayes, N.W., Joyner, R.W., Shpiro, E.S., Siddiqui, M.R.H. and Baeva, G.N. (1994) *Journal of Physical Chemistry*, **98**, 10832–46.
39 Thomas, J.M. and Greaves, G.N. (1993) *Catalysis Letters*, **20**, 337–43.

40 Kim, M.H., Nam, I.S. and Kim, Y.G. (1997) *Applied Catalysis B – Environmental*, **12**, 125–45.

41 Kharas, K.C.C., Robota, H.J. and Liu, D.J. (1993) *Applied Catalysis B – Environmental*, **2**, 225–37.

42 Feng, X.B. and Hall, W.K. (1997) *Journal of Catalysis*, **166**, 368–76.

43 Feng, X.B. and Hall, W.K. (1996) *Catalysis Letters*, **41**, 45–6.

44 Hall, W.K., Feng, X.B., Dumesic, J. and Watwe, R. (1998) *Catalysis Letters*, **52**, 13–19.

45 Marturano, P., Kogelbauer, A. and Prins, R. (2000) *Journal of Catalysis*, **190**, 460–8.

46 Kharitonov, A.S., Sheveleva, G.A., Panov, G.I., Sobolev, V.I., Paukshtis, Y.A. and Romannikov, V.N. (1993) *Applied Catalysis A: General*, **98**, 33–43.

47 Dubkov, K.A., Sobolev, V.I. and Panov, G.I. (1998) *Kinetics Catalysis*, **39**, 72–9.

48 Stockenhuber, M., Joyner, R.W., Dixon, J.M., Hudson, M.J. and Grubert, G. (2001) *Microporous and Mesoporous Materials*. **44**–45, 367–75.

49 Stockenhuber, M., Hudson, M.J. and Joyner, R.W. (2000) *Journal of Physical Chemistry*, **B 104**, 3370–4.

50 Marturano, P., Drozdova, L., Kogelbauer, A. and Prins, R. (2000) *Journal of Catalysis*, **192**, 236–47.

51 Marturano, P., Drozdova, L., Pirngruber, G.D., Kogelbauer, A. and Prins, R. (2001) *Physical Chemistry Chemical Physics*, **3**, 5585–95.

52 Berlier, G., Spoto, G., Bordiga, S., Ricchiardi, G., Fisicaro, P., Zecchina, A., Rossetti, I., Selli, E., Forni, L., Giamello, E. and Lamberti, C. (2002) *Journal of Catalysis*, **208**, 64–82.

53 Newton, M.A., Dent, A.J., Fiddy, S.G., Jyoti, B. and Evans, J. (2007) *Catalysis Today*, **126**, 64–72.

54 Newton, M.A., Dent, A.J., Fiddy, S.G., Jyoti, B. and Evans, J. (2007) *Physical Chemistry Chemical Physics*, **9**, 246–9.

55 Sobolev, V.I., Kharitonov, A.S., Paukshtis, Y.A. and Panov, G.I. (1993) *Journal of Molecular Catalysis*, **84**, 117–24.

56 Pirngruber, G.D., Grunwaldt, J.D., van Bokhoven, J.A., Kalytta, A., Reller, A., Safonova, O.V. and Glatzel, P. (2006) *Journal of Physical Chemistry*, **B 110**, 18104–7.

57 Kubacka, A., Wang, Z.L., Sulikowski, B. and Corberan, V.C. (2007) *Journal of Catalysis*, **250**, 184–9.

58 Shiju, N.R., Fiddy, S., Sonntag, O., Stockenhuber, M. and Sankar, G. (2006) *Journal of the Chemical Society, Chemical Communications*, 4955–7.

59 Bando, K.K., Saito, T., Sato, K., Tanaka, T., Dumeignil, F., Imamura, M., Matsubayashi, N. and Shimada, H. (2002) *Topics in Catalysis*, **18**, 59–65.

60 Behrens, P., Felsche, J., Vetter, S., Schulzekloff, G., Jaeger, N.I. and Niemann, W. (1991) *Journal of the Chemical Society, Chemical Communications*, 678–80.

61 Schultz, E., Ferrini, C. and Prins, R. (1992) *Catalysis Letters*, **14**, 221–31.

62 Gleeson, D., Sankar, G., Catlow, C.R.A., Thomas, J.M., Spano, G., Bordiga, S., Zecchina, A. and Lamberti, C. (2000) *Physical Chemistry Chemical Physics*, **2**, 4812–17.

63 Pei, S., Zajac, G.W., Kaduk, J.A., Faber, J., Boyanov, B.I., Duck, D., Fazzini, D., Morrison, T.I. and Yang, D.S. (1993) *Catalysis Letters*, **21**, 333–44.

64 Rey, F., Sankar, G., Maschmeyer, T., Thomas, J.M. and Bell, R.G. (1996) *Topics in Catalysis*, **3**, 121–34.

65 Bonino, F., Damin, A., Ricchiardi, G., Ricci, M., Spano, G., D'Aloisio, R., Zecchina, A., Lamberti, C., Prestipino, C. and Bordiga, S. (2004) *Journal of Physical Chemistry*, **B 108**, 3573–83.

66 Grasselli, R.K. (2001) *Topics in Catalysis*, **15**, 93–101.

67 Beale, A.M., Le, M.T., Hoste, S. and Sankar, G. (2005) *Solid State Sciences*, **7**, 1141–8.

68 Cavalleri, M., Hermann, K., Guimond, S., Romanyshyn, Y., Kuhlenbeck, H. and Freund, H.J. (2007) *Catalysis Today*, **124**, 21–7.

69 Ressler, T., Wienold, J., Jentoft, R.E. and Neisius, T. (2002) *Journal of Catalysis*, **210**, 67–83.

70 Ressler, T., Wienold, J., Jentoft, R.E. and Girgsdies, F. (2003) *European Journal of Inorganic Chemistry*, **2**, 301–12.

71 Gai Boyes, P.L. (1992) *Catalysis Reviews – Science and Engineering*, **34**, 1–54.

72 Safonova, O.V., Deniau, B. and Millet, J.M.M. (2006) *Journal of Physical Chemistry*, **B110**, 23962–23967.

8
Theory: Periodic Electronic Structure Calculations

Rudy Coquet, Kara L. Howard, and David J. Willock

8.1
Introduction

This chapter considers how periodic electronic structure calculations can be used to understand the chemical properties of oxides. It begins with a brief overview of the methods used in the simulation of oxides with periodic quantum chemistry, highlighting the treatment of the electron–electron interaction, which is the most challenging part of any approach. The basic treatment of the exchange energy using the Hartree–Fock (HF) approximation and of exchange and correlation in Density functional theory (DFT) are given. The simulation of bulk oxide structures and surfaces, including some practical aspects of checking the accuracy of calculations, are then discussed. This is followed by a section on systems with strong electron localization such as transition metal oxides and in particular anion defects on their surfaces. Throughout the chapter results are drawn from the literature to compare the various approaches and highlight the strengths and weaknesses of each.

We finish with a brief look at surface adsorption on oxides of catalytic importance. Among the most challenging problems are those in which redox activity of an oxide is required.

The periodic approach is not the only one available for atomistic simulations of these materials and we should first mention that much progress has been made in the application of molecular quantum chemical methods using cluster representations of the local structure of oxide materials [1, 2]. More recently, this has given way to mixed quantum mechanics/molecular mechanics (QM/MM) calculations. In QM/MM simulations the important region, the active site for catalysis, is represented at a quantum chemical level while the influence of its environment, the extended solid, is represented using the computationally less-demanding atomistic force field approach. This allows complex structures such as metal particles supported on oxides to be tackled [3].

However, in this contribution we will concentrate on quantum chemistry calculations in which the whole simulation is carried out at the quantum chemical level.

Metal Oxide Catalysis. Edited by S. David Jackson and Justin S. J. Hargreaves

ISBN: 978-3-527-31815-5

The nature of materials such as oxides is then captured by using periodic boundaries with which the idea of a band structure can be brought to bear.

8.2
Electronic Structure Methods

The details of practical approaches to electronic structure calculations are available in a number of text books [4] and here we will just cover the main points of each as required for application in the study of oxides. The ultimate goal of these methods is to provide a solution to the time-independent Schrödinger equation for multi-electron systems. We begin with the two main approaches used in molecular quantum chemistry, HF and DFT, and will concentrate on their treatment of the exchange and correlation contributions to the electron–electron interaction. This background will aid in the understanding of the range of results published on the properties of oxides from the various theoretical approaches applied. There then follows a section on band theory, illustrating the adaptations required when periodic boundary conditions are introduced.

8.2.1
Hartree–Fock

HF theory allows a set of molecular orbitals, ϕ_i, to be constructed which are solutions to the Fock equations:

$$F_i\phi_i = E_i\phi_i \tag{8.1}$$

where E_i is the energy of the i^{th} one-electron energy level and F_i is the Fock operator:

$$F_i = h_i + \sum_{j\neq i}^{N}(J_{ij} - K_{ij}) \quad \text{with} \quad h_i = -\frac{1}{2}\nabla_i^2 - \sum_a \frac{Z_a}{|R_a - r_i|} \tag{8.2}$$

Throughout this chapter, when discussing electronic structure we will use atomic units in which the charge on the electron and its mass are unity; this simplifies the form of equations such as Equation 8.2. In Equation 8.2, h_i contains the kinetic energy of an electron (first term) and the external potential of the nuclear centers in the system, which have charge Z_a and co-ordinates R_a, the electron co-ordinate being r_i. The second term in F_i is a sum over all occupied states, other than i, to give the electron–electron interaction energy. This is expressed in terms of the Coulomb, J_{ij}, and exchange, K_{ij}, operators which are discussed more fully in the next section. These electron–electron interactions in the Fock operator mean that each one-electron molecular orbital is influenced by the rest of the set of occupied molecular orbitals. The set of equations for the molecular orbitals can

be solved by making an initial guess for the form of the molecular orbitals. These are used to calculate F_i, but are likely to alter when Equation 8.1 is solved so that the contributions of J_{ij} and K_{ij} to F_i will also be changed. A new estimate of the Fock operator can then be made from the new solutions and used in turn to generate a new set of molecular orbitals. This process is repeated until the molecular wavefunctions no longer alter from one cycle to the next, that is, a self-consistent set of molecular orbitals is obtained.

In practical problems, the molecular orbitals themselves are constructed using the idea of a linear combination of atomic orbitals or, more generally, a linear combination of basis functions, χ_j:

$$\phi_i = \sum_j c_{ij}\chi_j \tag{8.3}$$

where the coefficient, c_{ij}, sets how much of basis function, χ_j, to include in the i^{th} molecular orbital. It is these coefficients that are obtained via the self-consistent solution of Equation 8.1. Usually the number of atomic functions used in the basis set of a calculation is more than the total number of occupied atomic orbitals in the free atoms. The extra flexibility this introduces into the basis set allows features such as polarized bonds and weak intermolecular interactions, such as hydrogen bonding, to be better represented.

8.2.1.1 Exchange Energy

When discussing the electronic structure of molecules and solids, one-electron descriptions, such as the molecular orbitals of Equation 8.1, are quite intuitive. It is common to talk about individual electrons occupying particular states. For example, reactions often occur by the mixing of the highest occupied molecular orbital (HOMO) of one species and the lowest unoccupied molecular orbital (LUMO) of another. In such a reaction the electrons in the HOMO state move into the new mixed orbital, lowering their energy. The HOMO and LUMO states are each pairs of one-electron molecular orbitals, since in the simplest case an orbital giving the spatial distribution for a spin up electron has an identical partner for spin down. Multi-electron wavefunctions that describe the whole electronic structure in this picture are constructed from the one-electron states. So, for example, in a four-electron system in which all the electronic states are doubly occupied (spin up and spin down), based on Hartree–Fock theory we can write:

$$\begin{aligned}\Psi(r_1 \ldots r_4) = \frac{1}{\sqrt{4!}}\big(&\phi_1^{\alpha}(r_1)\phi_2^{\alpha}(r_2)\phi_3^{\beta}(r_3)\phi_4^{\beta}(r_4) - \phi_1^{\alpha}(r_2)\phi_2^{\alpha}(r_1)\phi_3^{\beta}(r_3)\phi_4^{\beta}(r_4) + \\ &\phi_1^{\alpha}(r_2)\phi_2^{\alpha}(r_3)\phi_3^{\beta}(r_1)\phi_4^{\beta}(r_4)\ldots\big)\end{aligned} \tag{8.4}$$

That is, the multi-electron wavefunction is formed from products of molecular spin orbitals. Here, $\phi_i^{\beta}(r_j)$ means the j^{th} electron with co-ordinate r_j is in the i^{th} molecular orbital with β spin. The spin should be thought of as an additional

co-ordinate that takes on one of two values for each electron (α spin up and β spin down, say). Having the spin states explicitly separated in this way allows the energy levels for α and β spins to differ and is referred to as unrestricted Hartree–Fock (UHF). In many cases the spatial part of the orbitals are the same for α and β spin and so it is computationally cheaper to calculate only a single set of spatial functions and assign pairs of spin up and spin down electrons. However, this is a constraint on the orbital energies and so is referred to as restricted Hartree–Fock (RHF). The dotted line in Equation 8.4 means that additional terms are actually included but not written here for clarity. The multiple terms must be included so that the electrons remain indistinguishable from one another. In fact there will be 24 terms in all, with every permutation of electrons in molecular spin orbitals included, hence the normalization factor of $1/\sqrt{4!}$. The terms in Equation 8.4 are generated following the rule that if any two electrons are swapped the sign of the multi-electron wavefunction should change. These anti-symmetrized wavefunctions are often written in the more compact form of Slater determinants [5]. To calculate the electron–electron interaction energy in this system we form integrals of the type:

$$E_{ee}^{12} = \frac{1}{4!}\int_{-\infty}^{\infty} \Psi^*(r_1 \ldots r_4)\frac{1}{r_{12}}\Psi(r_1 \ldots r_4)\,\mathrm{d}r_1 \ldots \mathrm{d}r_4 \tag{8.5}$$

where the superscript "*" is used to indicate the complex conjugate of the wavefunction and $1/r_{ij}$ is the Coulomb operator for the interaction between electrons i and j which are a distance r_{ij} apart. The integration is over all electron co-ordinates and over all space and can be carried out by substituting from Equation 8.4 into Equation 8.5. At first sight, even for our four-electron example, this should give a set of 576 integrals over the molecular spin orbital products to evaluate. This is quickly reduced to 275 since electron i with j is duplicated by j with i and electron self-interactions can be ignored. In addition only certain types of these integrals are non-zero. Each integral contains all four electron co-ordinates, but the operator in Equation 8.5 only affects electrons 1 and 2, so that the other electrons can be treated separately. Through the normalization conditions required of molecular orbitals, electrons 3 and 4 will simply give factors of 1 in integrals of products for which they are in the same molecular spin orbital on either side of the operator. When they are in different orbitals to left and right their orthogonality gives 0. This leaves only 12 terms in which electrons 1 and 2 are in the same spin orbitals on either side of the operator, such as:

$$J_{12} = \frac{2}{4!}\int_{-\infty}^{\infty} \phi_1^{*\alpha}(r_1)\phi_2^{*\alpha}(r_2)\frac{1}{r_{12}}\phi_1^{\alpha}(r_1)\phi_2^{\alpha}(r_2)\,\mathrm{d}r_1\mathrm{d}r_2 \tag{8.6}$$

which is the Coulomb integral giving the electrostatic repulsion between the electron density of electron 1 in molecular orbital 1 with that of electron 2 in molecular

orbital 2. A factor of 2 occurs here because electrons 3 and 4 can be either way round in orbitals 3 and 4. We say "terms such as" because the form of $\Psi(r_1 \ldots r_4)$ means we will also obtain Coulomb integrals for electron 1 in orbital 2 and electron 2 in orbital 3 and so on. There are actually 12 terms in total and the role of the normalizing factor in ensuring no over-counting takes place can now be seen. Expressions such as Equation 8.6 are Coulomb integrals because each electron is in the same molecular orbital to the left and to the right of the operator in J. However, there is another type of term that arises from Equation 8.5:

$$K_{12} = -\frac{2}{4!}\int_{-\infty}^{\infty} \phi_1^{*\alpha}(r_2)\phi_2^{*\alpha}(r_1)\frac{1}{r_{12}}\phi_1^{\alpha}(r_1)\phi_2^{\alpha}(r_2)\mathrm{d}r_1\mathrm{d}r_2 \tag{8.7}$$

The exchange integral is a consequence of the condition that electrons are indistinguishable, which leads to Equation 8.4 for the multi-electron wavefunction. It has the opposite sign to the Coulomb integral because of the anti-symmetry property of multi-electron wavefunctions; we still require electrons 3 and 4 to remain in the same molecular orbitals to the left and right of the operator, that is, there has only been one exchange.

For electrons of different spin the Coulomb integral will work in the same way, but the exchange integral becomes:

$$-\frac{2}{4!}\int_{-\infty}^{\infty} \phi_1^{*\alpha}(r_2)\phi_4^{*\beta}(r_1)\frac{1}{r_{12}}\phi_1^{\alpha}(r_1)\phi_4^{\beta}(r_2)\mathrm{d}r_1\mathrm{d}r_2 = 0 \tag{8.8}$$

This result occurs because the electron spins have changed from left to right of the operator and so integration over the spin degrees of freedom gives zero. This important result means that the exchange energy is only relevant to electrons with the same spin.

HF theory is built on the idea of one-electron states and makes the integrals tractable by assuming that each electron experiences the average or mean field of all the others in the system. Then it is possible to solve for the one-electron states by taking the potential of each electron including a contribution from the Coulomb and exchange integrals following Equation 8.2. All other electrons in the system are averaged out using their one-electron wavefunctions in the J and K integrals. As mentioned earlier, altering the wavefunction of an electron in response to this potential changes the energy of all the other one-electron states and so the electronic structure has to be solved iteratively until a self consistent condition is reached.

8.2.1.2 **Correlation**

The HF approach gives an exact treatment of the exchange interaction between electrons. However, because it uses the mean field approximation, it ignores the effect of the Coulomb interaction on the relative positions of the electrons at

any instant. Electron motion is correlated, as can easily be seen from the form of the anti-symmetrized wavefunctions, Equation 8.4. Imagine that electron 1 and electron 2 move to exactly the same co-ordinate in space, that is, $r_1 = r_2$. If this were to happen, all pairs of terms with electron 1 and electron 2 exchanged in $\Psi(r_1 \ldots r_4)$ would cancel out and the wavefunction collapse to zero. This means that the probability of two electrons occupying the same point is zero and the electron motion must be correlated to ensure that no two electrons with the same spin arrive at the same coordinate. This correlation leads to the so-called Fermi hole. If we plot the wavefunction as a function of the electron–electron separation it must go to zero at $r_{12} = 0$. At larger distances the Coulomb repulsion between the electrons will also affect their correlated motion. In HF theory, this correlation caused by Coloumb repulsion is ignored through use of the mean field approximation implicit in the J and K integrals. Correlation will tend to result in electrons avoiding one another more than would be expected from the mean field approximation and so HF over-emphasizes the electron–electron repulsion.

Correlation can be re-introduced into wavefunction-based theories through perturbation methods (such as Møller–Plesset [6] MP2 or MP4) or the mixing in of excited-state multi-electron wavefunctions (the configuration interaction (CI) methods [7]). However, currently the computational cost of these calculations in periodic simulations is too great for their widespread use. In molecular simulation, MP2 has been used for some time and its importance in describing the long-range correlation required for van der Waals interactions of alkanes with zeolites has recently been pointed out [8].

8.2.2
Density Functional Theory (DFT)

DFT is based on the notion that the electron density is uniquely defined by the external potential, which for a molecule or condensed solid is simply the interaction potential with the constituent nuclei. This was put forward as the Hohenberg–Kohn theorem [9] which states that the ground-state electron density $\rho_0(r)$ minimizes the energy functional, $E[\rho(r)]$, which for a system of electrons interacting with nuclei is given by:

$$E[\rho(r)] = F[\rho(r)] - \sum_a \int_{-\infty}^{\infty} \frac{Z_a \rho(r)}{|R_a - r|} \mathrm{d}^3 r \tag{8.9}$$

where $F[\rho(r)]$ is a universal functional that has to account for the kinetic energy of the electron density and the electron–electron interaction. These terms are "functionals" because the energies depend on the entire function $\rho(r)$ rather than its particular value at a particular point in space. In principle, the ground-state energy and electron density may be found using a variational minimization of the electron density $\rho(r)$, a process which scales linearly with the system size. This is much more attractive than HF theory because the number of

Coulomb and exchange integrals increases rapidly with the number of electrons considered.

The form of $F[\rho(r)]$ is crucial for any successful application of DFT. Kohn and Sham postulated [10] that $F[\rho(r)]$ can be written:

$$F[\rho(r)] = T_S[\rho(r)] + \frac{1}{2}\int_{-\infty}^{\infty}\int_{-\infty}^{\infty}\frac{\rho(r)\rho(r')}{|r-r'|}\mathrm{d}^3r'\mathrm{d}^3r + E_{XC}[\rho(r)] \tag{8.10}$$

where the first term $T_S[\rho(r)]$ is the kinetic energy of a system of non-interacting electrons with density $\rho(r)$ and the second is the classical electron–electron Coulomb interaction, playing the role of the J integrals discussed for HF theory. However, instead of multiple integrals over electron co-ordinates, we now have a simpler double integral over the electron density. The final term, $E_{XC}[\rho(r)]$, is the exchange-correlation energy, which has the simple definition in DFT that it must compensate for the use of non-interacting electron states in the kinetic energy and include the exchange and correlation factors discussed above.

Progress is usually made by writing the electron density in terms of a set of one-electron wavefunctions, ψ_i, such that;

$$\rho(r)\mathrm{d}^3r = \sum_i \psi_i^*(r)\psi_i(r)\mathrm{d}^3r \tag{8.11}$$

The sum is over all occupied orbitals and d^3r is an infinitesimal volume. As in the HF case these spatial orbitals will have an associated spin component for each electron. These one-electron wavefunctions are just a convenient way to represent the density during the calculation and so we have used a new symbol to distinguish them from the one-electron HF molecular orbitals. They are actually for a fictitious system of non-interacting electrons that is made to have the same density as the interacting electron system we are interested in. This gives a straightforward method to obtain the kinetic energy term and allows $E[\rho(r)]$ to be minimized with respect to $\rho(r)$ using a basis set representation of the one-electron wavefunctions, via the set of equations,

$$\left(-\nabla_i^2 + V_{\mathrm{eff}}(r)\right)\psi_i(r) = \varepsilon_i\psi_i(r) \tag{8.12}$$

for each state i, where V_{eff} is an "effective potential";

$$V_{\mathrm{eff}}(r) = V_{\mathrm{ext}}(r) + \int_{-\infty}^{\infty}\frac{\rho(r')}{|r-r'|}\mathrm{d}^3r + V_{XC}(r) \tag{8.13}$$

and $V_{XC}(r)$ is the exchange-correlation potential obtained from $\dfrac{\partial E_{XC}}{\partial\rho(r)}$. The only constraint on this process is that the integral of $\rho(r)$ over all space is constant since this is fixed by the number of electrons in the system.

These equations map the problem of a system of interacting electrons onto a system of non-interacting electrons moving in an effective potential. The behavior of the exchange-correlation potential as a function of the electron density is a complex problem. The interactions it represents can be long-range in nature, so even if the "correct" form of E_{XC} were known, its calculation would be as complex as the post-HF methods mentioned at the end of the previous section. To make DFT practical and efficient, approximations for E_{XC} are introduced.

The simplest approach, known as the Local Density Approximation (LDA), defines E_{XC} as:

$$E_{XC}[\rho(r)] = \int_{-\infty}^{\infty} \rho(r)\varepsilon_{XC}^{hom}[\rho(r)]d^3r \tag{8.14}$$

where $\varepsilon_{XC}^{hom}[\rho(r)]$ is the exchange-correlation energy per unit volume of a homogeneous electron gas of density $\rho(r)$. The exchange contribution for $\varepsilon_{XC}^{hom}[\rho(r)]$ can be calculated exactly but the correlation requires a reference calculation using a high-level method. The use of the homogeneous electron gas (external potential zero everywhere) allowed a very accurate calculation to be carried out by Ceperley and Alder using quantum Monte Carlo techniques [11]. The resulting data has been parameterized to analytical functions by Vosko, Wilk and Nusair [12] and by Perdew and Wang [13]. Computer implementation of the LDA and its extension to a spin unrestricted form LSDA (in which the densities for spin up and spin down electrons are allowed to differ) depend on these parameterized forms of $\varepsilon_{XC}^{hom}[\rho(r)]$.

In the LSDA approach, the exchange and correlation are calculated purely based on the density at each point in the system, assuming that these quantities will be the same as in a uniform gas of electrons with the same density. This is only really the case when the electron density is a slowly varying function of position, such as in the valence states of the alkali metals [14]. Despite this, LSDA has been found to give useful insights in a wide range of solid-state systems, including metal oxides.

Ideally we would like to also include the longer range correlation effects, and a first step toward this is using functionals that depend not only on the local density but also on the gradient of the density. The gradient of the density is also a local property but gives information on how the density is varying in the immediate vicinity of a given point. Functionals of this type fall under the generalized gradient approximation (GGA) and simply add terms depending on the gradient of the electron density to the parameterization of E_{XC}. Although GGAs do not offer a consistent improvement over LDA in all types of system, they have been shown to improve on the LDA for calculations of molecular structures and bond energies [15]. There are many different approaches to the form and parameterization of a GGA and these are given acronyms based on the names of the people who derived them. Among the most widely used are PBE (Perdew, Burke and Ernzerhof) [16], and its revision based on surface calculations revised PBE,

RPBE [17], PW91 (Perdew and Wang 1991) [18, 19] and BLYP (the exchange functional of Becke [20] with correlation functional from by Lee, Yang and Parr) [21]. In the remainder of the text we shall use these acronyms without further referencing.

In the LSDA and GGA approaches, the Coulomb integrals are calculated on the same footing as in HF theory, but using the Kohn–Sham orbitals. However, the exchange contribution is taken from a functional of the density and so the interplay of the Coulomb and exchange energies, which is clear under the HF approach, is not so well balanced in DFT. In particular, using V_{XC} based on the density in Equation 8.12 implies that each electron contributes to its own potential, the so called self interaction problem.

To look into this, hybrids between DFT and HF have been introduced. In this approach, the HF exchange expression is used with the Kohn–Sham orbitals, mixing "exact-exchange", E_X^{exact}, with conventional GGAs, in the general form;

$$E_{XC}^{hybrid} = E_{XC}^{LSDA} + a_0\left(E_X^{exact} - E_X^{LSDA}\right) + a_X \Delta E_X^{B88} + a_C \Delta E_C^{GGA} \tag{8.15}$$

where E_{XC}^{LSDA} is the exchange and correlation energy according to the LSDA, the bracketed term is a correction to the exchange energy from the difference between exact and local density exchange and the final two terms are gradient corrections along the lines of the GGA. The three parameters a_0, a_X and a_C can be set against experimental reference data for small molecules. In Becke's original paper [22], PW91 was used for the GGA correlation part of Equation 8.15 and a fit to 56 atomization energies, 42 ionization potentials, 8 proton affinities and 10 total atomic energies gave parameter values of $a_0 = 0.20$, $a_X = 0.72$ and $a_C = 0.81$. One of the most ubiquitous hybrid functions, also based on this approach, is named B3LYP, with the "3" referring to the number of parameters. This replaces the GGA correlation in Becke's scheme with the functional of Lee, Yang and Parr mentioned above.

Hybrids give significant improvement over GGAs for many molecular properties and are widely used in studies of metal complexes and homogeneous catalysis [23]. They have been more slowly adopted in solid-state chemistry than in the molecular area because of the difficulty of computing the exact-exchange part within the plane-wave basis set approach discussed below. However, as we will see, in the simulation of oxides they give an improvement in the relative energies of filled and empty states and have advantages in problems for which electron localization has to be described.

It should be remembered that DFT is designed to reproduce the ground-state density of the system under consideration. It is not concerned with excited states and so the relative energy of filled and empty orbitals is not as well defined as in the HF approach. We will see that, in solid-state calculations, this results in a poor estimation of the band gap for insulators when using LSDA or GGA functionals. To tackle excitations directly, the more computationally demanding time-dependent DFT methodology has been developed and this does allow spectroscopic excitation energies to be calculated [24].

8.2.3 Periodic Quantum Chemistry

8.2.3.1 Band Theory

In a crystal, the wavefunctions and density are formally of infinite extent and so to represent the wavefunctions using the linear combination of atomic orbitals familiar from molecular quantum mechanics would require an infinite basis set. Such an approach is clearly impractical; however, the periodicity of the system suggests that only the unit cell of the lattice is really required. This, with some provisos outlined below, is indeed the case. A very comprehensive discussion of band theory and the implementation of periodic DFT has been published by Payne and coworkers [25], and more recently Hill and coworkers have produced a book covering background theory and applications in materials science [26]. In this section we give an overview of the methodology that takes the molecular orbitals of isolated species into the band states of solids.

Firstly, note that it is the electron density that is observed experimentally in X-ray diffraction (XRD) experiments and so is used to define the unit cells of crystalline solids. In a periodic system, this means that the electron density has to have the same repeat distance as the lattice in all directions. Bloch's theorem points out that the restriction this imposes on the underlying wavefunctions is actually less rigorous since the relationship between electron density, $\rho(r)$, at an arbitrary point, r, and the one-electron wavefunctions obtained from calculations (HF or DFT) is:

$$\rho(r)\mathrm{d}^3r = 2\sum_{j=1}^{N/2}\psi_j^*(r)\psi_j(r)\mathrm{d}^3r \tag{8.16}$$

for an N electron system. This is similar to Equation 8.11 except that we have assumed that spin up and spin down states have the same spatial distribution and are occupied pairwise. A correctly periodic density can be achieved by writing the wavefunctions as the product of a function with the same periodicity as the lattice, $\chi_j(r)$, and a function which varies on a longer length scale:

$$\psi_{j,k} = \chi_j(r)\exp(i\boldsymbol{k}\cdot\boldsymbol{r}) \tag{8.17}$$

where i is the square root of -1 and $\boldsymbol{k}$ defines a reciprocal space vector:

$$\boldsymbol{k} = \frac{1}{N_a}\boldsymbol{a}^* + \frac{m}{N_b}\boldsymbol{b}^* + \frac{n}{N_c}\boldsymbol{c}^* \tag{8.18}$$

N_a is the number of cells in the sample along the **a**-direction with N_b and N_c the number along **b** and **c** respectively, l, m and n are integers with ranges set by the corresponding N value, $-N_a/2 \le l < N_a/2$ and so on. In Expression 8.18 reciprocal

space vectors are indicated by a superscript "*". These are related to the real space lattice vectors via:

$$\boldsymbol{a}^* = \frac{2\pi}{V_c}\boldsymbol{b}\times\boldsymbol{c}$$

$$\boldsymbol{b}^* = \frac{2\pi}{V_c}\boldsymbol{c}\times\boldsymbol{a}$$

$$\boldsymbol{c}^* = \frac{2\pi}{V_c}\boldsymbol{a}\times\boldsymbol{b} \tag{8.19}$$

The function $\chi_j(r)$ in Equation 8.17 can be thought of as the periodic extension of the basis functions used in molecular orbital problems. For example, in an oxide in which there is a single oxygen ion in the unit cell the set of O(2s) functions repeated throughout the lattice would form a suitable $\chi_j(r)$. One possible Bloch state is simply to set $\boldsymbol{k}$ = (0, 0, 0) which would give neighboring O(2s) orbitals in phase with one another and so there would be a bonding interaction for this orbital across the unit cell boundary. Another possible solution is that O(2s) orbitals in adjacent cells have an anti-bonding interaction. This is obtained along the **a** lattice vector direction for $\boldsymbol{k}$ = ($\boldsymbol{a}^*$/2, 0, 0), which for the O(2s) orbitals must give a higher energy solution than $\boldsymbol{k}$ = (0, 0, 0). The N_a, N_b and N_c values in (18) tend to be large, tending to infinity, so that the variable $\boldsymbol{k}$ is virtually continuous. This means that the energy of the Bloch states between these extremes, of $\boldsymbol{k}$ = (0, 0, 0) (all bonding along **a**) and $\boldsymbol{k}$ = ($\boldsymbol{a}^*$/2, 0, 0) (all anti-bonding along **a**), will vary smoothly.

The plot of energy against $\boldsymbol{k}$ is the dispersion for the band and gives the variation in energy for each local cell orbital. An example plot for ZnO in the zinc blende structure is shown in Figure 8.1a. This band structure was produced using a HF calculation with correlation corrections introduced from separate cluster calculations [27]. Although ZnO occurs naturally in the hexagonal wurtzite structure, the cubic cell of zinc blende (Figure 8.1b) was used in this study of the effect of the local environment of the Zn^{2+} cation on the band structure and provides a simple illustration of the features of a dispersion plot. The three-dimensional nature of reciprocal space means that the values of $\boldsymbol{k}$ that are plotted in band-structure dispersion plots can only give a representative variation of the band energies along particular paths. These paths are usually chosen to include the maxima and minima that occur at special points where the $\boldsymbol{k}$ vector has a simple relation to the reciprocal space vectors. The special point $\boldsymbol{k}$ = (0, 0, 0) is always labeled $\tilde{A}$. In Figure 8.1a, moving to the right of the $\tilde{A}$ point ends at the special position $\boldsymbol{k}$ = (1, 0, 0), labeled *X*. Along this path only *h* has been varied in Equation 8.18. The zinc blende structure is based on the cubic unit cell shown in Figure 8.1b and so the reciprocal space cell is also cubic and the three directions [1 0 0], [0 1 0] and [0 0 1] are equivalent. Hence, there is no need to show the dispersion along paths directly to *Y* or *Z*. To the left of the $\tilde{A}$ point in Figure 8.1a the plot ends at $\boldsymbol{k}$ = (1/2, 1/2, 1/2),

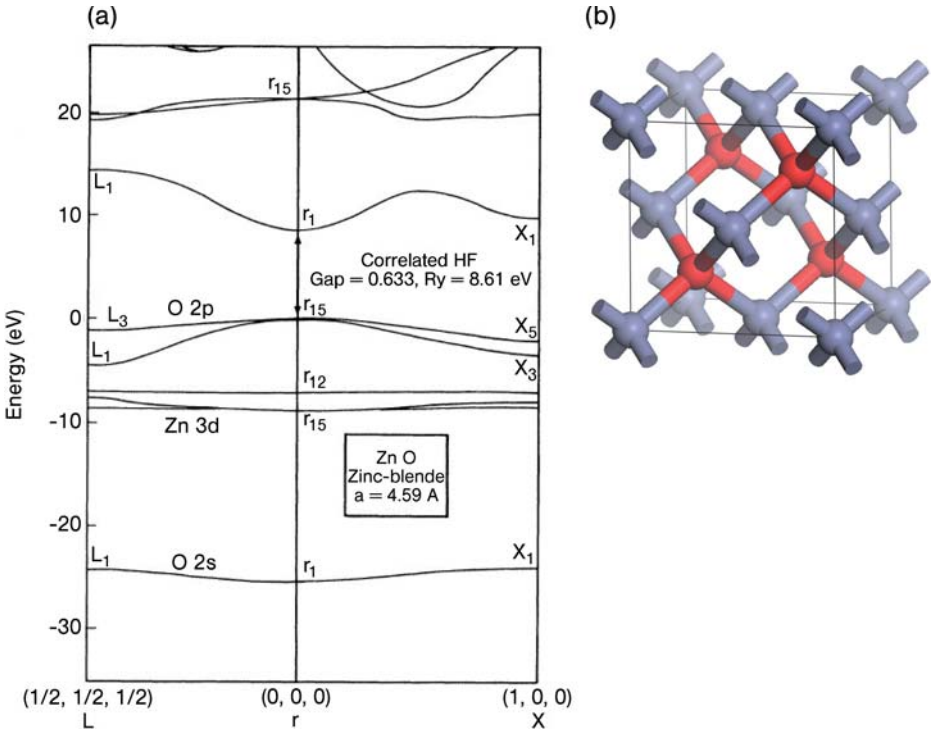

Figure 8.1 (a) The calculated dispersion curves for ZnO in the zinc blende structure. From ref. [27]. (b) The zinc blende unit cell. Zinc, blue; oxygen, red.

labeled *L*, so the path taken involves increasing each of *l*, *m* and *n* in Equation 8.18 by the same amount.

Figure 8.1 also illustrates that the band width depends on the $\chi_j(r)$ function being used in the Bloch states (17). The O(2s) orbital is the lowest energy atomic orbital and forms a low-lying band with little dispersion, that is, the band width is small. This orbital is relatively tightly bound to the atomic core and the overlap between O(2s) orbitals in neighboring unit cells will be small. The O(2p) orbital on the other hand is more diffuse and so the overlap between neighboring cells leads to a calculated band width of around 5 eV.

The smooth variation of energy with $\boldsymbol{k}$ means that the whole band structure can be interpolated from a finite number of $\boldsymbol{k}$-points. The total energy of the system can then be estimated by integrating over the occupied portion of the band structure. To this end, computationally efficient methods for sampling $\boldsymbol{k}$ in three dimensions taking advantage of lattice symmetry have been proposed and are widely used [28]. The convergence of calculations with the number of $\boldsymbol{k}$-points is an important check that should be made at the start of a simulation project. As an example, Table 8.1 shows the variation in the calculated total energy for MoO_3 as a function of the *k*-point sampling grid. Here the total energy per unit cell is

Table 8.1 Convergence of the bulk energy for MoO_3, with respect to the *k*-point grid using a planewave basis (E_{cut} = 520 eV) and PBE functional within the VASP code.

***k*-point grid**[a)]	**MoO_3 bulk energy (eV)**	**ΔE**[b)] **(eV)**
$3 \times 1 \times 3$	−130.168 980	–
$3 \times 3 \times 3$	−130.171 210	0.002 230
$5 \times 3 \times 5$	−130.271 510	0.100 300
$7 \times 3 \times 7$	−130.272 620	0.001 110
$9 \times 3 \times 9$	−130.272 710	0.000 090
$11 \times 3 \times 11$	−130.272 680	0.000 030
$15 \times 5 \times 15$	−130.272 680	0.000 000

a Grid quoted as number of points sampled in the $\boldsymbol{a}^* \times \boldsymbol{b}^* \times \boldsymbol{c}^*$ reciprocal lattice directions.

b ΔE is the difference in energy between two consecutive *k*-point grids.

calculated using a gradient-corrected DFT technique so that the energy quoted corresponds to the total energy of the valence electrons per unit cell. The bulk MoO_3 lattice parameters are a = 3.963 Å, b = 13.855 Å and c = 3.696 Å [29], so that the $\boldsymbol{b}$ lattice vector is significantly longer than $\boldsymbol{a}$ or $\boldsymbol{c}$. This means that orbital overlap is expected to be weaker in the **b** direction than in **a** or **c** and correspondingly the dispersion in the band moving along $\boldsymbol{b}^*$ is less. Hence the number of grid points required in the $\boldsymbol{b}^*$ direction is fewer than in $\boldsymbol{a}^*$ or $\boldsymbol{c}^*$. From Table 8.1 we can see that the energy of the bulk is converged to a precision of 10^{-3} eV (or 0.1 kJ mol^{-1}) for a $\boldsymbol{k}$-point grid of $5 \times 3 \times 5$.

This idea that large unit cell dimensions in real space require fewer samples to be taken in reciprocal space can also be useful when working with supercells. A supercell calculation uses multiple crystallographic cells as the repeated simulation unit. For example, in calculations on surfaces this allows reconstruction on a length scale longer than is allowed by the minimal unit cell. The sampling of reciprocal space in supercell calculations can be reduced because multiple $\boldsymbol{k}$-points of the normal unit cell can be represented in real space. This idea is illustrated in Figure 8.2 using a one-dimensional example with a single s-orbital per site. In the minimal unit cell sampling at $k = \pm\pi/a$ corresponds to a wavefunction with phase alternation between neighboring sites (in one dimension $a^* = 2\pi/a$), which is at the top of the band. If we use a supercell with a length of $2a$ this wavefunction can be represented with $k = 0$ because there are now two possible cell orbitals. The total number of orbitals has not changed, but in the new cell one band would be formed from the state with neighbors in the same phase and a different band would be formed with neighboring states out of phase. The third state shown at the top of the diagram would still require a reciprocal space point away from k = 0, as its repeat length is longer than $2a$. Doubling the cell once more allows all three states to be represented in real space.

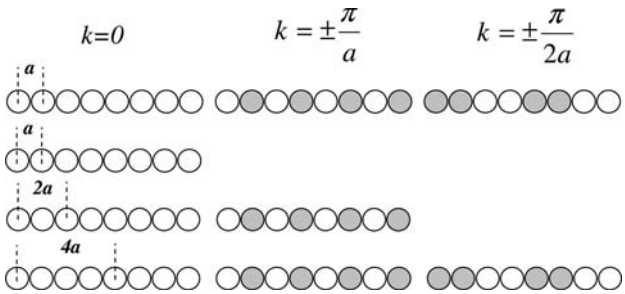

Figure 8.2 One-dimensional example of using supercells to reduce *k*-point sampling. With a minimal unit cell of dimension *a*, the states shown on the top line require 3 *k*-points to be sampled. Doubling the unit cell allows the first two states to be generated at $k = 0$; with a unit cell dimension of 4*a* all three states are contained within the local cell wavefunctions.

Table 8.2 The affect of unit cell size on calculated binding energy for α-alumina.

Multipliers for *a*, *b* (Å)	Formula of repeating unit	Cell volume relative to Rhomb. cell	Binding energy[c)] per unit volume (eV Å^{-3})
Rhomb.[a)]	Al_4O_6	1	–0.6951
1,1[b)]	$Al_{12}O_{18}$	3	–0.7175
2,1[b)]	$Al_{24}O_{36}$	6	–0.7151
3,1[b)]	$Al_{36}O_{54}$	9	–0.7173
4,1[b)]	$Al_{48}O_{72}$	12	–0.7173

a The rhombohedral unit cell is the primitive cell; all other calculations employ the more usual hexagonal unit cell.

b These structures were based on the experimental hexagonal unit cell with $a = b = 4.759$ Å, $c = 12.991$ Å and $\gamma = 120°$.

c Binding energy is defined as the difference between the total energy of the unit cell and the sum of total energies for the same neutral atoms in isolation. This is quoted per unit volume to allow comparison of the differently sized cells.

This effect can be seen in calculations on real materials; Table 8.2 shows the convergence of the binding energy per unit volume of α-Al_2O_3 with cell size calculated using gradient-corrected DFT with a localized basis set in the DSOLID package [30]. The binding energy is with respect to DFT calculations on the neutral atomic species and so the values quoted are considerably smaller in magnitude than for the earlier MoO_3 example.

8.2.3.2 **Basis Sets**

A basis set is required to describe the cell periodic part of the Bloch function in Equation 8.17. It is possible to use localized functions based around the atomic

orbital like the basis sets found in molecular quantum chemistry. This is the approach used in the CRYSTAL [31, 32] code which employs Gaussian functions for the radial part of the atomic orbitals. The codes SIESTA [33], DMOL^3 (and its predecessor DSOLID) [34] also use localized basis sets but store the radial decay of the basis functions on a numerical grid. For the localized basis set, work has also to be undertaken to optimize the functions used for the solid state, as the radial decay profiles used in molecular problems are usually not appropriate [35]. For example, the O^{2-} ion is more diffuse than an oxygen atom in a molecule and so the basis sets used for molecular quantum chemistry will not perform well. An alternative approach is to use the periodic nature of the system to build the electronic wavefunctions as sets of plane-waves. Codes that take this avenue include VASP [36], DACAPO [37] and CASTEP [38]. The Carr Parinello molecular dynamics code (CPMD) [39] is also a plane-wave code with the added feature that the electronic degrees of freedom are included in the evolution of the system based on Newton's laws. The plane-wave basis is specific to the solid state and so some background is given in the following text.

Any function used as the local part of the wavefunction description must be periodic in the cell dimensions. In a plane-wave basis this is ensured by choosing a linear combination of plane-waves with particular reciprocal space vectors:

$$\chi_j(\boldsymbol{r}) = \sum_G c_{j,G} \exp(i\boldsymbol{G}\cdot\boldsymbol{r}) \tag{8.20}$$

in which the coefficient c_{jG} is the amount of the plane-wave with reciprocal wave vector $\boldsymbol{G}$ to include in local function j. Each $\boldsymbol{G}$ vector is described by the equations

$$\boldsymbol{G}\cdot\boldsymbol{T} = 2\pi m \quad \boldsymbol{T} = u\boldsymbol{a} + v\boldsymbol{b} + w\boldsymbol{c} \tag{8.21}$$

that is, the vector dot product between an acceptable $\boldsymbol{G}$ vector and any real space vector, $\boldsymbol{T}$, which is a combination of real space lattice vectors (u,v,w are integers), gives an integral number of 2π radians. Under this condition any two points in the lattice that are separated by a vector such as $\boldsymbol{T}$ must have the same value of $\chi_j(\boldsymbol{r})$. Note that the $\boldsymbol{G}$ vectors have a repeat which is contained within the unit cell while the $\boldsymbol{k}$-vectors used in the Bloch states of Equation 8.17 have periods on a larger scale.

The use of plane-waves as a basis in this way is just like taking the Fourier transform of a known function. A simple one-dimensional illustration of this is shown in Figure 8.3. Three waves which obey the periodic boundary condition set by a unit cell of length 2 units (m = 1–3 in Equation 8.21) are shown in Figure 8.3a. The target function is a periodic set of Gaussians shown at the top of Figure 8.3b. Since the target function is known, the coefficients, $c_{j,G}$, can be calculated analytically and the basis summed following Equation 8.20. Figure 8.3b shows

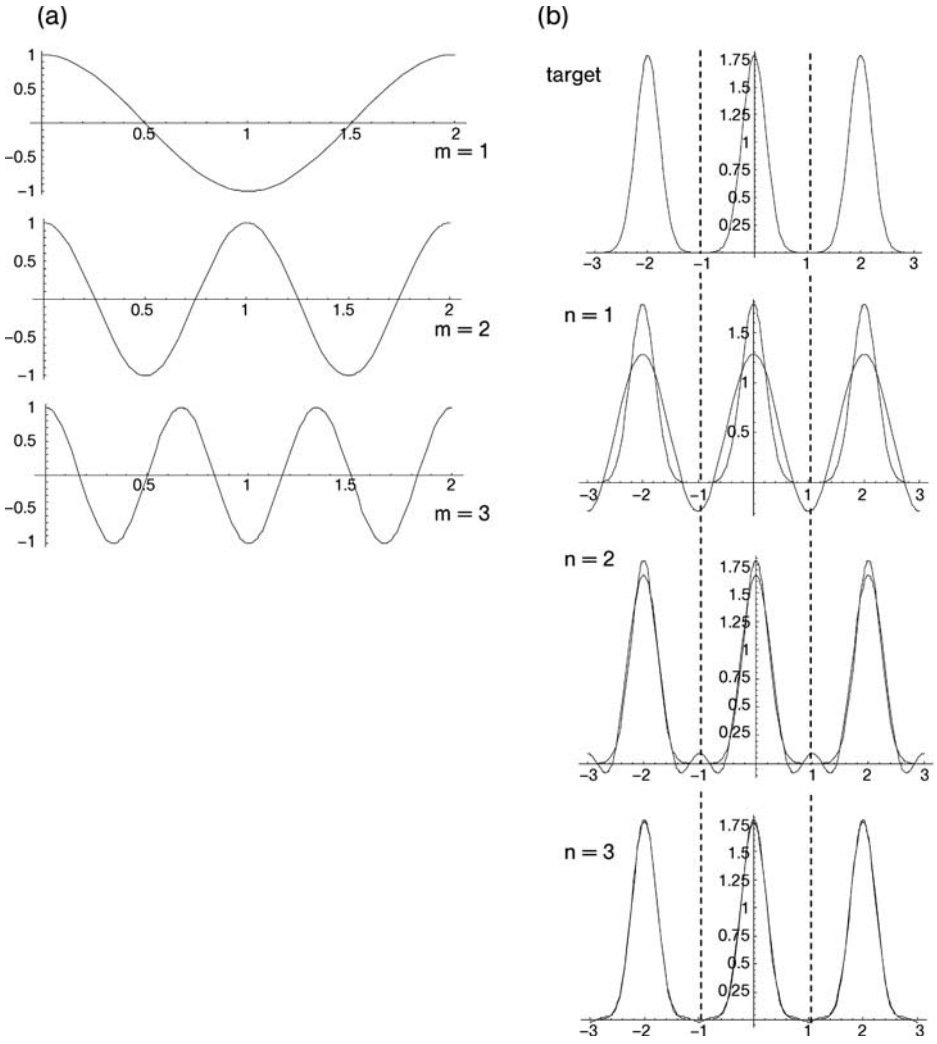

Figure 8.3 (a) One-dimensional example of a plane wave basis set for a unit cell of length 2 consisting of 3 functions. (b) Application of the basis to generate a target function which is a periodic set of Gaussians.

how the agreement between the target function and that constructed from the plane-wave basis becomes better as the number of plane-waves used, n, is increased. This Gaussian example is a particularly simple one because the function varies quite smoothly with position, as do the plane-waves, and so after three basis functions are included the match with the target is already very good. In a DFT calculation the target functions are not known and so the coefficients, $c_{j,G}$, are solved for as part of the self-consistent solution of the Kohn–Sham equations.

The plane-wave basis has the advantage that it can be systematically improved by simply increasing the number of plane-waves used. The basis set is usually truncated, based on an energy cut off, E_{cut}, which defines the kinetic energy limit for the plane-waves. The corresponding maximum $\boldsymbol{G}$ vector is related to the energy cut off via,

$$|\boldsymbol{G}|_{max} = \frac{2\pi}{h}\sqrt{2m_e E_{cut}} \tag{8.22}$$

Here we have reverted to SI units so that m_e (the electron mass) and h (the Planck constant) appear in the formula. In most programs this $|\boldsymbol{G}|_{max}$ value is used along with Equation 8.21 to determine the number of plane-waves in the basis set for the entire calculation by setting the maximum value of the integer, m. It has been pointed out by Pulay that Equation 8.21 implies that the basis set is actually dependent on the size of the unit cell, since $\boldsymbol{T}$ depends on the lattice vectors. This can lead to additional stresses in calculations in which the cell volume is allowed to vary. These appear because the quality of the basis set changes with cell dimensions. In particular, when the volume of a unit cell is estimated using a plane-wave basis, separate optimizations of the ions within a series of fixed volume cells is more reliable than allowing the cell volume to be optimized during a single run.

The goal of periodic calculations is to generate a reliable estimate for the electron density of the unit cell. However, many chemical concepts of bonding rely on ideas that are not so easily defined, such as atomic charges with which to quantify the ionicity of the system. The expression for the electron density in terms of molecular orbitals Equation 8.16 does allow a partitioning of the charge density to be undertaken to access such quantities. In terms of the basis set the density can be re-written:

$$\rho(r)\mathrm{d}^3r = 2\sum_{j=1}^{N/2}\sum_{i}^{M} c_{j,i}\chi_i^*(r)\sum_{k}^{M} c_{j,k}\chi_k(r)\mathrm{d}^3r \tag{8.23}$$

where we have M functions in the basis set and $c_{j,i}$ is the coefficient for the expansion of the i^{th} basis function in the j^{th} molecular orbital. Therefore the density is actually built up from products of basis functions known as overlap functions. In a localized basis set it is easy to assign basis functions to atoms, since each is based on an atomic orbital belonging to a particular center. The basis functions belonging to a particular atom, A, will appear in Equation 8.23 in some terms that involve only functions centered on A and in some giving overlap with other centers. The first set of terms are usually assigned as belonging wholly to A, but to assign a particular portion of the density to atom A we must also take some component of the overlap with other atoms. Mulliken [40] proposed that these overlaps between different atomic centers be divided equally between the atoms involved, and this estimate of the atomic charge is widely reported in the output of periodic electronic structure codes. When a plane-wave basis set is used in the calculation the assign-

ment of basis functions to particular atoms is not so straightforward. A way around this is to use the plane-wave basis to do the calculation and then fit a local basis representation to the resulting density and use the Mulliken analysis on that. The fitting process is often referred to as the projection of the plane-wave calculated density onto the localized basis set.

Mulliken analysis is a quick and relatively simple way to break down the charge density into atomic contributions but it is dependent on the basis set used. In particular, if the number of basis functions is unevenly distributed between atoms, those with rich basis sets will tend to have too much charge assigned through the Mulliken procedure. To attempt to rectify this, methods based on the charge density alone have also been developed. For example, Bader analysis uses the minima in the density to define a region around each atom over which the density can be integrated numerically [41].

8.2.3.3 **Pseudopotentials**

To describe the bonding between atoms, it is convenient to split the electrons for each atom into valence and core states. In general, the core states are those not directly involved in bonding interactions and the valence states are the outermost atomic orbitals that can mix or otherwise interact strongly with neighboring atoms. It is usual to replace the influence of the core electrons of an atom on the valence states by the use of pseudopotentials, that is, a function which represents the true full electron potential in the valence region but varies more smoothly in the core region of the atoms. In the valence region, the wave functions from calculations using pseudopotentials and those with all electrons included should match closely. In the core region, the smooth variation of the pseudopotential leads to a more smoothly varying wavefunction. In essence, the radial nodes in the core region are eliminated. To be resolved correctly, rapid spatial variation of core state nodes would require a large number of plane-waves in the basis set; hence the use of pseudopotentials reduces the number of plane-waves that have to be used in a calculation while maintaining a good representation of the chemically important valence states. An additional benefit for heavy elements is that relativistic effects are more pronounced in the core region but their effect on the electrons in the valence region can be reproduced by calibrating the pseudopotential against full relativistic calculations on atoms. The valence electronic structure is then free to use non-relativistic DFT.

Each pseudopotential is defined within a cut-off radius from the atom center. At the cut-off, the potential and wavefunctions of the core region must join smoothly to the all-electron-like valence states. Early functional forms for pseudopotentials also enforced the norm-conserving condition so that the integral of the charge density below the cut-off equals that of the all-electron calculation [42, 43]. However, smoother, and so computationally cheaper, functions can be defined if this condition is relaxed. This idea leads to the so called soft and ultra-soft pseudopotentials defined by Vanderbilt [44] and others. The link between the pseudo and real potentials was formalized more clearly by Blöchl [45] and the resulting

projector augmented-wave pseudopotentials have also been implemented in plane-wave basis set codes [46].

In oxides, the division between core and valence states should be carried out with care. For example, in strongly ionic materials the cation may have lost all valence electrons to the anion and so the cation/anion interaction involves orbitals on the cation that are atomic "core" states. In this situation, explicit inclusion of the outermost cation orbitals would be required for accurate results. Even so, the replacement of the core region with a smoother potential can reduce the calculation time even for H atoms, and so pseudopotentials are available even in this case.

For consistency, pseudopotentials should be based on the same functionals as used for the valence states. This point has been illustrated by Gale and coworkers in their study of aluminum trihydroxides [47]. Table 8.3 compares their results of cell optimizations using various mixtures of psuedopotential and valence state functionals with the experimental structure of gibbsite [48]. LDA pseudopotentials in an LDA optimization of the cell gives underestimated cell parameters, consistent with the usual expectation that LDA gives over-binding in chemical bonds. This is partially corrected by switching just the valence states to the GGA functional PBE, which is a fortuitous consequence of over-binding in LDA being compensated for by under-binding in the GGA. If PBE is used for both pseudopotential and valence states, the ***a*** and ***b*** lattice vectors are over-estimated and the best estimate for the ***c*** parameter is obtained. This structure is layered and held together in the ***c*** direction by hydrogen bonding (see Figure 8.4). Using LDA/LDA or LDA/PBE these hydrogen bonds are foreshortened, leading to underestimation of the lattice vector. In the mixed case this means that a calculation using a GGA in the valence states still performs like the LDA calculation because of the influence of the pseudopotential. The use of mixed functionals has also been found to lead to large errors in the calculated binding energies of molecules to metal surfaces which are corrected by employing a pseudopotential consistent with the GGA used for the valence states [49].

Table 8.3 Optimized structural parameters for $Al(OH)_3$ (gibbsite) using various functionals for the pseudopotential/valence states.

parameter	LDA/LDA	LDA/PBE	PBE/PBE	Expt.[a)]
a (Å)	8.504	8.623	8.798	8.684
b (Å)	4.867	5.017	5.110	5.078
c (Å)	9.224	9.598	9.674	9.736
β (°)	93.06	92.76	92.54	94.54
Cell vol. ($Å^3$)	381.2	414.7	434.4	428.0

Data taken from ref. [47].
a Ref. [48].

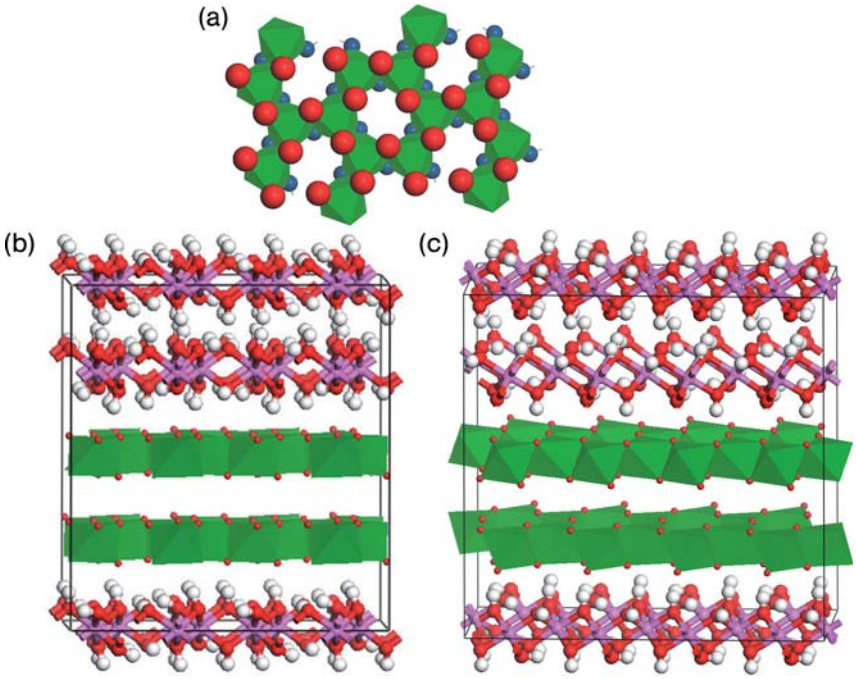

Figure 8.4 The structure of $Al(OH)_3$ aluminum hydroxides: (a) a layer of edge-sharing octahedra taken from the bayerite structure, oxygen atoms on top of this bi-layer shown as large red spheres while those on the underside are shown as small blue spheres. (b) The structure of bayerite: two bi-layers are shown in the polyhedra representation of (a) with H atoms omitted for clarity, the remainder of the structure is shown with Al in pink, O in red and H in white. (c) The structure of gibbsite using the same representations as (b).

8.2.3.4 **Density of States**

Within a band of states, the fact that ***k*** is virtually continuous means that the separation between individual energy levels is vanishingly small. It makes no sense, then, to try and draw a conventional energy level diagram of the type used in molecular orbital calculations. The idea of a density of states (DOS) plot is to show the number of states in a small energy interval as a function of state energy. The number of states in a band per unit energy depends on the band width and the number of cell-based functions that contribute to the band. The localized metal cation d orbitals, for example, tend to give narrow bands with correspondingly high density of states.

Figure 8.5 shows example calculated DOS plots for MgO and TiO_2 (rutile). In both cases the zero of energy is taken as the highest occupied state which occurs at the top of the upper valence band (UVB). The small tail on the UVB that indicates some states with positive energy is an artefact of the smoothing process used to construct the DOS plot from a calculation using finite number of ***k***-points. In addition to the total density of states, a decomposition into states associated with

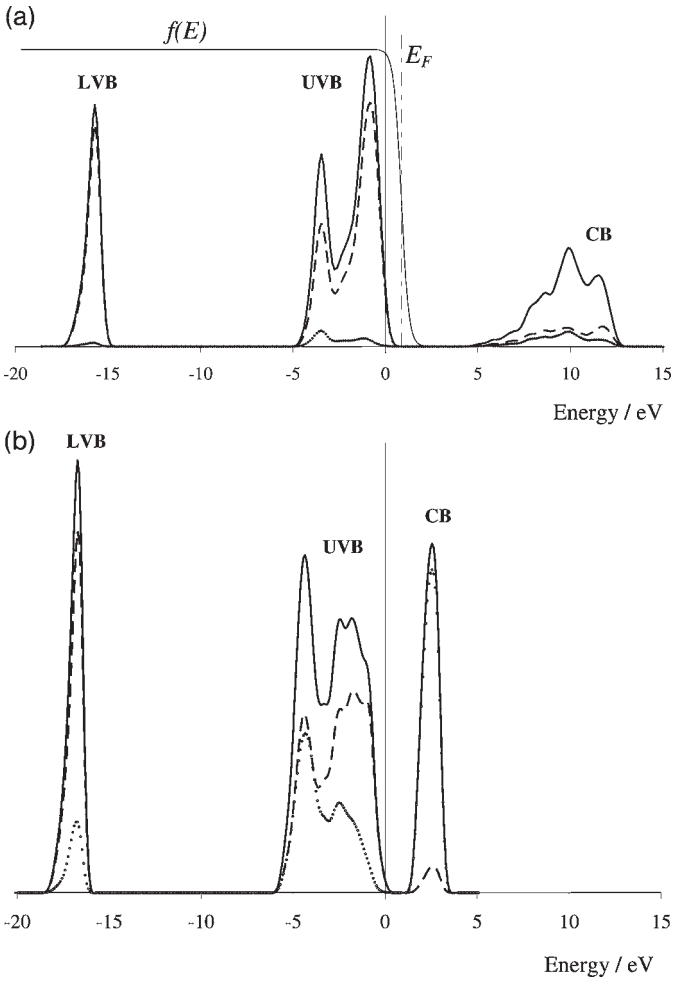

Figure 8.5 (a) The DOS for MgO and the smearing function ($f(E)$) used for calculating the state occupancy. (This has a maximum value of 1.) (b) The DOS of TiO_2 (rutile). Both calculations used the VASP code with PAW pseudopotentials and the PW91 functional; a Gaussian smearing of 0.2 eV has been used for each calculated point in the DOS. Total DOS shown as a solid line, partial DOS for O dashed line and for the metal ions dotted line, arbitrary units are used for the DOS magnitude. LVB, lower valence band; UVB, upper valence band; CB, conduction band.

the oxygen and states associated with the metal atoms has been carried out. This involves a projection of the density calculated using the plane-wave basis set onto an atom localized basis of s, p and d functions. There is some arbitrariness in the choice of this basis and so the absolute values of the partial density of states will vary according to the choice made. In this case, we have relied on the PAW pseudopotential functions used in the VASP code to define the localized basis set into

which the projection takes place. These technicalities aside the relative contribution of metal and oxygen orbitals in each band do give some qualitative information on the character of bonding in the materials.

The plot for MgO (Figure 8.5a) is typical of a main group metal oxide which fits with the classical ionic bonding model of oxide structures. The lower valence band (LVB) consists almost exclusively of O(2s) states and the UVB of O(2p) states. In the conduction band (CB) both Mg and O basis functions contribute to the crystal orbitals. The valence bands are completely filled and, since they have mainly O character, this corresponds to complete transfer of valence electrons from Mg to O to give the ionic species Mg^{2+} and O^{2-}.

In the TiO_2 calculated DOS (Figure 8.5b) the LVB is also mainly constructed from of O(2s) orbitals but in the UVB the lowest energy states (between −6 and −4 eV) are around 50 : 50 O and Ti in character with O(2p) orbitals being the major constituent for higher energy states. In the conduction band the Ti orbitals make up the larger part of the available states. The mixing of Ti and O states in the UVB is consistent with a more covalent bonding model since electrons in these states are shared between metal and oxygen atoms.

The width of the band formed is an indication of the degree of delocalization of the band states and a comparison of Figure 8.5a and b shows the biggest difference in the UVB region. In the ionic model of MgO, the localization of electron density on the O^{2-} ions leads to a relatively narrow UVB, while the covalent bonding in TiO_2 gives rise to more delocalized states and so to a broader UVB.

This effect is also found for the bandwidth of the O(2p) bands for the alkaline earth metal oxides which, at the LDA level of theory, decrease down the group from a calculated value of 4.44 eV (MgO) to 1.83 eV (BaO). This is partly due to the increase in lattice parameter, which spaces the O^{2-} ions more widely in BaO than in MgO. However, in addition, it is found that the outermost valence electrons for the metal ions interact more strongly with the O(2p) states in BaO than in MgO, giving more localization of the electron density at O^{2-} and so a smaller anion in BaO [50].

Converging the self-consistent procedure in periodic calculations can be a difficult task, particularly if there are free states within any band. Movement of electrons between almost identical states has little effect on the energy of the system and so the search for the optimal distribution of electrons is hampered by many trivial alterations to the occupation numbers. To make the process more efficient, partial occupancies can be used for states near the highest filled level by introducing a smoothing function which defines the occupancy as a function of state energy, E_k. The smoothing function used in the MgO calculation was:

$$f(E_k) = \frac{1}{\exp\left(\frac{E_k - E_F}{\sigma}\right) + 1} \tag{8.24}$$

This expression is based on the statistical mechanics of electrons which have an energy distribution given by Fermi–Dirac statistics [51]. The partial occupancy

$f(E_k)$ of a state of energy E_k is controlled by the "Fermi energy" E_F and a smearing parameter σ which was set to 0.2 eV in Figure 8.5a. We have placed the term "Fermi energy" in quotes because it is usually defined as the chemical potential of the electronic system at some temperature. However, DFT calculations are used to identify the ground state electron density at 0 K and the application of Equation 8.24 is simply a tool to speed up convergence. Indeed, other functions which can smear out the occupation of the highest filled states can also be used. In the MgO calculation, occupations of 2 electrons per state are obtained for the LVB and UVB with 0 occupation numbers for all CB states. Figure 8.5a shows that this is achieved by placing E_F just sufficiently above the top of the valence band to give $f(E_k) = 1$ for all UVB states. The exact position of E_F depends on the smearing parameter and so it is effectively a variable in the SCF procedure.

In the literature, the value of the Fermi energy is often reported as the highest occupied state at 0 K (the "HOMO" state). In metals this is correct because the boundary between filled and empty states corresponds to the energy of the highest occupied state at zero Kelvin. More generally, E_F is defined from the Fermi–Dirac distribution (as Equation 8.24 with $\sigma = k_B T$) as the energy at which the probability of occupancy falls to 1/2. In insulators and semiconductors, the position of the Fermi energy is set by the detailed balance between states occupied by electrons thermally excited to the CB and the empty states left behind in the UVB. This difference between the value of E_F used in the smearing function and the true Fermi energy becomes important when trying to align the energies of states of two calculations, say a surface calculation and that on an isolated adsorbate. The Fermi energy gives the chemical potential of the individual systems, which will equalize if they are bought together. The use of E_F from a calculation for aligning the energies of electronic states between different calculations is not a reliable way to do this. In a calculation, the electronic energy is set by the potentials used in the Kohn–Sham equations and should reflect the binding energy of an electron with respect to the vacuum. This means that the energy scales between different calculations should be directly comparable.

The band gaps between the UVB and empty CB states in Figure 8.5 are calculated as 5.1 eV for MgO (Figure 8.5a) and 2.0 eV for TiO_2 (Figure 8.5b). The presence of a band gap is indicative of an electrical insulator or semiconducting material and we would expect MgO to have the larger band gap of the two materials. However, it has been found that the band gap obtained in a calculation is strongly dependent on the method used. Bredow and Gerson employed MgO as one example in their systematic study of the effect of electron exchange and correlation on the bulk properties of rock-salt structured oxides [52]. Their results are included along with others in Table 8.4. Using RHF, the band gap between the UVB and CB states is substantially overestimated at 16.5 eV compared with experimental values which range from 7.8 [53] to 8.7 eV [54]. In RHF calculations, exchange is included explicitly but correlation is ignored. At the other extreme, the results of Gillan and coworkers [55] using an LDA approach underestimated the band gap by around 3 eV and the lattice constant is also smaller than found experimentally. The various pure GGA-DFT results shown in Table 8.4 (BLYP,

Table 8.4 Comparison of calculations on bulk MgO by various methods.

Method	Basis[a)]	a (Å)	E_g (eV)	Reference
RHF	O:8-411/1G Mg:8-511/1G	4.20	16.5	
RHF + LYP	O:8-411/1G Mg:8-511/1G	4.09	17.5	
BLYP	O:8-411/1G Mg:8-511/1G	4.28	5.3	
PBE	O:8-411/1G Mg:8-511/1G	4.25	5.3	
PW91	O:8-411/1G Mg:8-511/1G	4.25	5.2	
B3LYP	O:8-411/1G Mg:8-511/1G	4.25	7.6	
LDA	600 eV (pw, NC)	4.16	4.8	[55]
PBE	400 eV (pw, PAW)	4.25	5.1	this chapter
Expt		4.212	7.8	[53]
			8.7	[54]

a Basis set notation such as 8-411/1G indicates an atomic orbital basis set using Gaussian radial functions. This example would be referred to as a triple-ζ basis since the valence region is represented by three basis functions, the first of which is a contraction based on 4 Gaussians (411). There is also one polarization function (*d*-type function for O) indicated by /1. For plane-wave basis sets (pw) the value of E_{cut} is given along with an indication of the type of pseudopotential employed: NC = Norm conserving, PAW = Projected Augmented Wave.

PBE and PW91) improve on this slightly, but still significantly underestimate the band gap and overestimate the lattice constant. This trend, for HF to overestimate and DFT to underestimate E_g, has been noted for a wide range of oxide materials. In the HF case, the omission of correlation energy is the likely cause. The correlation energy will most strongly influence the gap between bands of different occupation. Therefore the energy difference between the LVB and UVB will not be in as great an error as UVB to CB.

In the example of MgO, inclusion of GGA-DFT style correlation using the LYP functional for the RHF method actually increases the band gap by a further 1 eV. In addition the lattice constant optimized in this calculation is significantly smaller than the experimental reference structure [56], so it appears that adding in correlation to a HF wavefunction model is not an answer. For GGA-DFT, the self-interaction problem is thought to be the main reason for underestimation of the band gap, and addition of HF exchange to correct the calculated band gap has been more successful. In Table 8.4, the choice made in B3LYP is seen to give a band gap in quite close agreement with experiment. The use of hybrid functionals, such as B3LYP, to give a good compromise between the over-estimation of the band gap in oxides by HF and its under-estimation by DFT appears to be quite general. For example in work by Muscat and coworkers [57], the band gaps of a wide range of materials including MgO, Al_2O_3 and TiO_2 are calculated using B3LYP, giving 7.3, 8.5 and 3.4 eV respectively and these compare favorably with experimental estimates of 7.8, 9.0 and 3.0 eV [58]. Zhang and coworkers [59] have shown that for TiO_2 the calculated band gap increases in proportion to the amount of exact

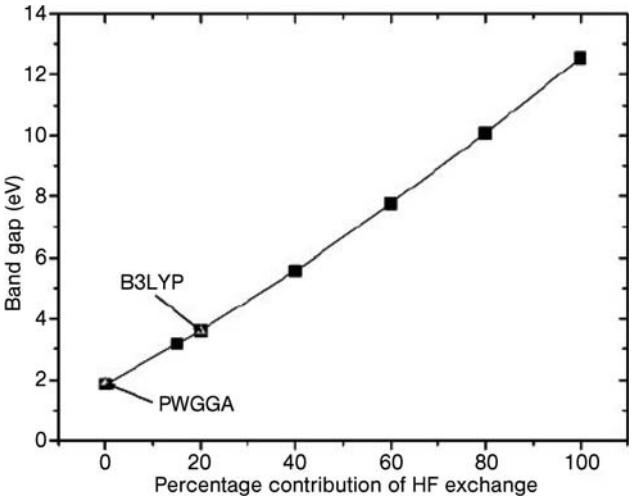

Figure 8.6 Calculated band gap in TiO_2 as a function of percentage HF exchange. From ref. [59].

exchange included in the functional, as shown in Figure 8.6. The optimal choice of 13% exact exchange gives a perfect match to the band gap energy. The choice made in B3LYP is slightly larger at 20% but the well documented performance of this functional for molecular bond energies makes it a good compromise for giving reliable properties of the solid and adsorbates when modeling catalytic reactions. Further tailoring of the amount of HF exchange to use according to the solid state property of interest has been discussed by Cora and coworkers, who also show that the introduction of HF exchange increases electronic localization [60].

Despite this failure to correctly represent the relative energies of the occupied and unoccupied states correctly, HF and DFT methods have been widely applied in the simulation of the electronic structure of oxides. Examples in the remainder of this chapter will include comments on the reliability of these results along with further examples of the use of hybrid functionals.

8.3 Bulk Structure: Alumina

Alumina provides a good example of a main group metal oxide that has been studied using a variety of simulation techniques. Alumina has several phases, which occur during its synthesis, by heating, from aluminum hydroxides such as gibbsite, $Al(OH)_3$, or boehmite, AlO(OH). The most stable form is the dense oxide α-Al_2O_3 which has the corundum structure but this is obtained from the hydroxides via a series of transition aluminas following the pathways shown in Figure 8.7.

In all of these structures the oxygen sub-lattice can be thought of in terms of the stacking of hexagonal layers, familiar from close packed solids. For example,

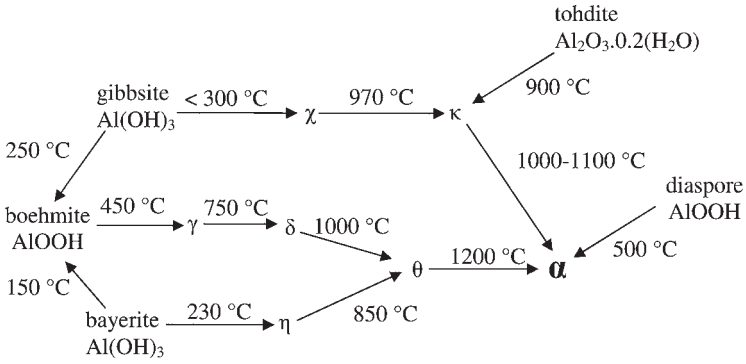

Figure 8.7 The aluminum oxides and hydroxides and their temperatures of interconversion. Hydroxide materials are named along with their chemical formulae; oxides all have the composition Al_2O_3 and so are indicated by the Greek letter associated with the phase. The α-phase is indicated in large font and bold as it is the thermodynamically most stable oxide. Adapted from reference [61].

the minerals gibbsite and bayerite are aluminum hydroxides of general formula $Al(OH)_3$. In both structures, Al is octahedrally coordinated by O atoms forming layers of edge-sharing octahedra, one of which is shown in Figure 8.4a. The oxygen sub-lattice is controlled by the resulting bi-layers with the triangular faces of the octahedra giving a roughly hexagonal arrangement. In the extended structures these bi-layers are stacked perpendicular to the crystallographic **c** direction. The two oxygen layers of the bi-layer can be assigned as A and B layers in the stacking sequence for the oxygen sub-lattice. In bayerite, the bi-layers are stacked directly over one another giving an ..AB.AB.AB.. sequence (Figure 8.4b), while the structure of gibbsite has alternate bi-layers set as reflections of one another leading to an ..AB.BA.AB.. structure (Figure 8.4c). The bi-layers are held together by hydrogen bonding via the H atoms that can be seen in the interlayer space of the atomic representation regions of Figure 8.4b and c. In addition, there are hydrogen bonds between OH groups and the O ions in the same layer. The hydrogen bonding network in these materials appears to be well ordered since the H atom positions have been obtained in neutron (bayerite [62]) and X-ray diffraction (gibbsite [48]) experiments. Gale and coworkers have studied these hydroxides using a combination of plane-wave (CASTEP) and localized basis set (SIESTA) methods with the PBE functional [47]. Despite the similarity between the two structures, gibbsite is the more commonly observed form in nature. The plane-wave and localized orbital calculations both gave total energies that indicate gibbsite to be more stable than bayerite, by 7.7 and 6.3 kJ mol^{-1}, respectively. This is consistent with calorimetric measurement of the heats of formation, which suggest that gibbsite is the more stable by around 5 kJ mol^{-1}. In the simulation study, calculations of the vibrational frequencies of the O—H stretching modes also showed that the interlayer hydrogen bonding is stronger than the intralayer interactions.

The trihydroxides gibbsite and bayerite were included in the work of Sautet and coworkers along with the monohydroxides boehmite and diaspore [61]. They also used a localized basis set within the SIESTA code and PBE functionals, but refined the basis set radial functions based on reference calculations of α-Al_2O_3. Diaspore has an oxygen sub-lattice with an hcp-type, ..ABAB.., stacking sequence and, as indicated in Figure 8.7, dehydrates directly to the low surface area oxide α-Al_2O_3 on heating above 500 °C. As we will see later, α-Al_2O_3 also has a hexagonal structure, resulting in this simple relationship between diaspore and the thermodynamically most stable alumina. Both gibbsite and bayerite dehydrate to boehmite which is also the major component of many bauxite minerals. Its oxygen sub-lattice has an fcc-type ..ABCABC.. packing and it is this monohydroxide that is the precursor to the technologically important γ-, δ- and θ-aluminas.

Boehmite is a layered hydroxide with the structure shown in Figure 8.8. For the AlO(OH) hydroxide, the intralayer hydrogen bonds of the trihydroxides have been lost and only interlayer interactions remain. The positions of the hydrogens in this structure are not well known experimentally and Sautet considered two possible structures. The hydroxyls form in rows which run into the page in the view illustrated in Figure 8.8 and are shown here with the hydroxyls in the interlayer region pointing to the right. There is an equivalent structure in which all hydroxyls point left, and in real materials mixtures of these hydroxyl orientations could occur. In a simulation we are limited by the repeating unit used, but by doubling the unit cell in the hydroxyl row direction Sautet was able to compare structures with all hydroxyls in a row pointing in the same direction and the case in which the hydroxyls alternate left/right down the row direction. These structures differed by only 0.2 kJ mol^{-1}, suggesting that the uncertainty in the experimental determination of H-positions is a result of disorder in the H-bonding network. Molecular

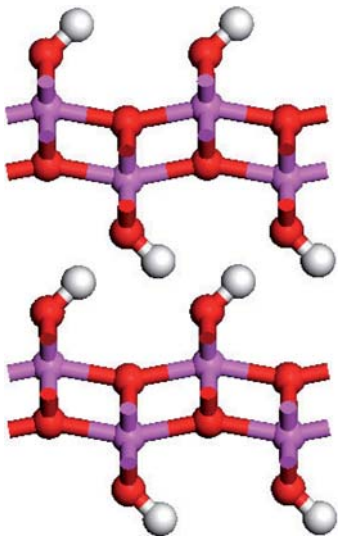

Figure 8.8 The structure of boehmite (AlO(OH)). Aluminum, pink; oxygen, red; hydrogen, white.

dynamics calculations, in which Newton's laws are used to follow the motion of the system based on DFT calculated forces, also show that the interchange of hydrogens between oxygen atoms in the interlayer region is rapid, even at low temperatures (350–600 K) [63].

Sautet also used the calculated energies for the trihydroxides, monohydroxides and α-Al_2O_3 structures to estimate the relative stability of these materials based on the dehydration sequence:

$$2Al(OH)_3 = 2AlO(OH) + 2H_2O = Al_2O_3 + 3H_2O \tag{8.25}$$

Here the DFT-calculated energy differences for the oxide and hydroxide materials were used in the place of free energies and for the internal energy of H_2O. Standard thermodynamic data for the enthalpy of vaporization and entropy of water were then used to plot the relative stabilities as a function of temperature. This plot is reproduced in Figure 8.9. Although the temperatures of transition do not agree closely with experiment, the sequence of stability is correct. Trihydroxides are preferred up to around 560 K, at which point dehydration to monohydroxide should take place. The calculated energies actually place diaspore marginally below boehmite; however, the layered structure of boehmite is much closer to the trihydroxide lattices and so it is kinetically preferred. The monohydroxides are unstable with respect to the dense oxide above 730 K. Figure 8.9 also contains the result for HAl_5O_8, a spinel structure containing H atoms in the bulk, which was proposed as a candidate new composition for γ-Al_2O_3 based on DFT calculations [64]. However, at all temperatures this candidate structure is considerably thermodynamically less stable than one of the alternatives. It is more

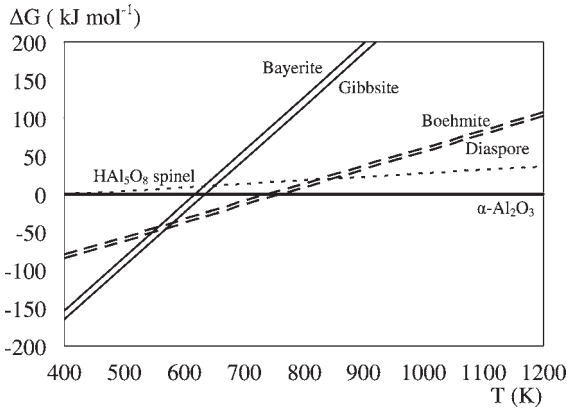

Figure 8.9 Calculated free energies of trihydroxides (solid lines) and monohydroxides (dashed lines) relative to α-Al_2O_3. The dotted line represents the calculated free energy for a hypothetical hydrogen spinel structure postulated for γ-Al_2O_3. Adapted from reference [61].

likely that the apparent hydrogen content of γ-Al_2O_3 is due to surface hydroxylation on these high surface area materials, rather than the inclusion of H in the bulk structure.

The first oxide material produced in the series from boehmite, γ-alumina, is important in catalysis as a widely used support material for precious metal catalysts. For example, Pt/Al_2O_3 used in steam reforming catalysts takes advantage of the high surface area of γ-alumina along with a significant metal-support interaction which maintains Pt dispersion [65]. The surface areas of the other transition aluminas δ-, θ- and η-Al_2O_3 tend to be lower and so, in this application, they are of less direct use. However, they may appear as minor phases in γ-alumina samples, particularly after prolonged use at high temperatures, and so their structure and properties need to be considered. In addition, aluminas have useful Lewis acid properties that have been used in reactions such as methyl chloride synthesis and these are known to vary according to the phase of the material [66].

The bulk structures of the transition oxides γ-, δ-, θ- and η-alumina are all based on an fcc (...ABCABC..) array of oxygen ions, whereas χ-, and α-Al_2O_3 have hcp (...ABABAB..) oxygen sub-lattices. α-Alumina has the corundum structure, with cations well ordered and exclusively in octahedral co-ordination sites. For this reason, the α-polymorph has been widely studied using both atomistic potential and periodic quantum chemical approaches and we will discuss calculations of its surface structure in the next section. The oxygen lattice of κ-Al_2O_3 is intermediate with a complex ...ABACABAC... stacking sequence. Its structure was solved with the aid of periodic DFT calculations based on the PW91 functional by Yourdshahyan and coworkers [67]. While κ-Al_2O_3 can be prepared by heat treatment methods, it is more often obtained by chemical vapor deposition (CVD) and so is more widely used for wear resistant coatings, for example on cemented-carbide cutting tools, than in catalysis [68].

Transition aluminas are metastable with respect to the α-phase and so this is usually used as a reference point for comparing the energies of other phases. Wolverton and Hass have used the PW91 functional to estimate δE(θ–α) and δE(κ–α) obtaining 0.04 and 0.08 eV per formula unit, respectively. They point out that these energies are within the upper bounds set experimentally, whereas LDA calculations by the same authors are not. These positive energy differences confirm that the need for high temperatures to obtain α-Al_2O_3 in the schemes shown in Figure 8.7 is due to a kinetic barrier between phases.

The best ordered of the fcc-type materials is θ which has the same structure as β-Ga_2O_3. In turn, δ-alumina appears more ordered that the γ-phase since it is observed in diffraction experiments by the appearance of superstructure not present in γ-Al_2O_3. Analysis of the diffraction data for transition aluminas gives cation site occupancies of less than 1, that is, it is the cation sub-lattice that is disordered. This has led to suggestions that the transition series $\gamma \rightarrow \delta \rightarrow \theta$ should be thought of as a process of ordering the cations on the interstices of the fcc oxygen lattice [69]. From a simulation point of view, the repeat unit in a calculation cannot have partial occupancy of cation sites and so a choice must be made to give

a representative structure. The structure of γ-alumina is the most challenging from this perspective as it contains the highest degree of disorder. It has been considered for some time to have a lattice based on a disordered cubic spinel, a suggestion that was first made based on X-ray diffraction data [70], although later work found the cell to have a tetragonal distortion [71]. However, since this is a small effect, the spinel model has been retained by most workers. The classic spinel $MgAl_2O_4$ has an oxygen sub-lattice forming an fcc-type array with Mg^{2+} in tetrahedral, T_d, and Al in octahedral, O_h, interstitial sites. The general formula for γ-Al_2O_3 in this system is $Al_{21\frac{1}{3}}\square_{2\frac{2}{3}}O_{32}$, where the symbol □ is used to indicate a vacancy in a standard spinel cation site. This structure falls into the space group $Fd\bar{3}m$ and a simulation cell containing of 96 oxygen atoms appears necessary to give the required Al_2O_3 stoichiometry with eight cation vacancy sites. There is disagreement in the experimental literature on how to apportion the Al cations in γ-alumina between the two spinel sites. In 1991, X-ray and neutron diffraction were combined to give lattice parameters for the cubic cell [72]. The line widths of specific reflections were used to suggest that the Al tetrahedral sub-lattice is extremely disordered and that the distribution of Al between tetrahedral and octahedral sites is roughly 50 : 50. This assignment of the occupancy ratio was difficult as no reflections from the octahedral sub-lattice alone are present in the diffraction pattern. More recently ^{27}Al MAS NMR has been used to show that 70 ± 2% of Al ions occupy octahedral sites [73, 74], which, in the spinel structure, suggests that the octahedral sub-lattice is less disordered than the tetrahedral. Even if a simulation is restricted by assuming that only disorder on the tetrahedral sites need be considered, the number of cation arrangements in the simplest stoichiometric cubic cell runs into hundreds of thousands [75]. This means that a complete survey with first principles methods is impracticable. To simplify the problem, Gutiérrez and coworkers [76] used a smaller simulation cell based on the primitive rhombohedral unit corresponding to the $Fd\bar{3}m$ spinel. They began with the spinel cubic cell of stoichiometry $Mg_8Al_{16}O_{32}$, and replaced the Mg atoms by Al to give a cell with a surplus of cations ($Al_{24}O_{32}$). The corresponding primitive rhombohedral cell is one quarter the volume and so would be Al_6O_8. Taking three of these primitive cells as a simulation cell and creating two vacancies gives a cell containing $Al_{16}O_{24}$. The distribution of two vacancies, required to correct the stoichiometry, gives only 14 inequivalent arrangements and so LDA calculations on the entire set become feasible. They found an energetic preference for vacancy formation on the octahedral Al sub-lattice with the lowest energy structure after geometry relaxation having both vacancies at octahedral sites. The lowest energy structure in which one vacancy was at an octahedral and one at a tetrahedral site was 0.16 eV/Al_2O_3 higher in energy. Wolverton and Hass also identified a preference for Al to occupy tetrahedral sites by constructing a hypothetical rock salt structured simulation cell of formula Al_3O_3 and then removing one Al^{3+} ion. Here the oxygen sub-lattice is fcc and all Al are initially in O_h positions but they were able to demonstrate an energy lowering of around 1.2 eV per formula unit on relocating one of the Al ions to a T_d site.

Another approach to obtaining the structure of γ-Al_2O_3 is to start from the parent boehmite hydroxide and study the mechanism of dehydration. Boehmite contains only octahedrally coordinated Al species and so in addition to the removal of H_2O the migration of Al must be studied. Raybaud and coworkers [63] have used the PW91 functional and a plane-wave basis set (VASP code) to study a possible mechanism in which dehydration is followed by Al migration. After dehydration, the remaining oxygen atoms in the interlayer region of boehmite (see Figure 8.8) bridge between the layers. It is proposed that Al ions then migrate into tetrahedral voids in this interlayer region. Using thermodynamic free energy estimates they discuss the relative stability of the model oxides in terms of the population of these tetrahedral sites. As the first few Al ions are moved, the free energy increases, passing through a maximum when 6–9% of the Al ions have been migrated, then a minimum is identified around 30% T_d occupation, close to the experimental solid-state NMR estimates.

Although a spinel lattice has been used by most simulations to date, there is some evidence that cations may also occupy interstitial sites of the fcc oxygen sublattice that are not used in the spinel structure. A structure with 40% cations in non-spinel sites has been put forward by Paglia and coworkers [77]. Their work combined atomic potentials calculations to survey thousands of possible cation arrangements in both spinel and non-spinel locations. Then PW91 optimizations were carried out for selected structures with the localized basis set code SIESTA. This sub-set of structures was used to simulate the neutron diffraction pattern for comparison with experimental data. The tetragonal unit cell was also supported by transmission electron microscopy and solid-state NMR [74]. The idea of cations taking up non-spinel sites had also earlier been commented on by Wolverton and Hass for δ-Al_2O_3 since its cell dimensions are often quoted as non-integer multiples of the γ-phase. However, the debate is still on-going, with a recent comparison of XRD data with periodic DFT results rejecting the new structure in favor of the conventional disordered spinel [78].

8.4 Calculation of Surface Structure

8.4.1 Slab Models

XRD and neutron diffraction methods provide highly accurate information on the three-dimensional structure of crystalline materials. These methods depend on the regular array of atoms that form the bulk lattice in well ordered phases. However, the structure of the surface of oxides is much more difficult to probe experimentally, since the surface layers make up a minute fraction of the total sample. For some catalytically important materials for which large crystalline samples can be grown, such as α-Al_2O_3 and TiO_2, grazing angle XRD [79] does show surface sensitivity. Low energy electron diffraction (LEED) can also give data

on surface structure both in plane and perpendicular to the surface if the intensity of spots as a function of electron acceleration voltage, and so energy, is considered: the LEED-IV approach [80]. However, the resolution of surface structure is still quite low compared to bulk techniques and care must be taken with surface preparation. Here computer simulation can provide insight into the restructuring that occurs at the interface between a solid and its environment. Since the surface region is where most of the important processes in heterogeneous catalysis take place, the use of theoretical methods to consider surface structure has been an area of intense interest.

There are two main approaches to describing a surface in a periodic computer simulation model. A truly two-dimensional model requires dedicated programming to allow periodicity in the surface vector directions but not perpendicular to the surface. Some programs do include this [31], but most are written with periodic boundary conditions in all three dimensions and surface calculations require cells that isolate the surface as a repeating set of slabs. This can be done by introducing a vacuum gap in one of the lattice vector directions. All that is required is a simulation cell orientated so that the desired surface is perpendicular to, say, the ***c***-vector direction and then a repeating set of slabs is created by extending the ***c***-vector without altering the atom co-ordinates in the cell. The simulation remains three dimensional but a gap is opened in the direction perpendicular to the Miller plane of interest at the required cut to create two surfaces. This is best done by choosing a unit cell in which the ***a***, ***b*** face is the required surface, as shown in Figure 8.10. In this example, the MgO(110) plane is to be studied but this is not perpendicular to any crystallographic cell vector. However if we choose alternative vectors which are in the plane ($\boldsymbol{a}' = \boldsymbol{a} + \boldsymbol{b}$ and $\boldsymbol{b}' = \boldsymbol{c}$ in this case) the new cell will be orientated with the $\boldsymbol{a}'$, $\boldsymbol{b}'$ plane perpendicular to $\boldsymbol{c}'$, as shown in Figure 8.10b. The length of the new $\boldsymbol{c}'$ lattice vector is simply the interplane spacing, d_{110}. The vacuum gap is then introduced by simply extending the $\boldsymbol{c}'$-vector.

The creation of a surface requires energy and so the energy of the slab will be higher than that of the solid formed by closing the gap again. This means that once the slab is generated, volume optimization can no longer be undertaken because such a calculation should lower the energy by removing the vacuum gap.

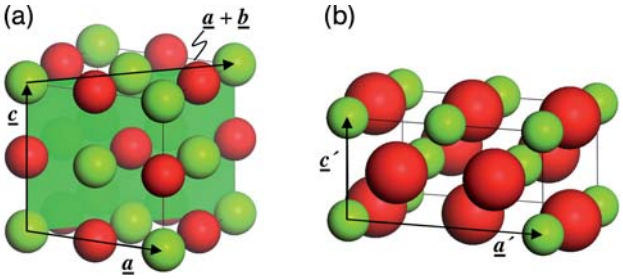

Figure 8.10 (a) The MgO(110) Miller plane and (b) a cell orientated to make the $\boldsymbol{c}'$-vector perpendicular to this surface.

It is normal to set the cell vector lengths based on the bulk optimized structure at the level of theory to be used in the slab calculations. This choice gives lattice parameters with zero strain in the bulk which is a likely constraint on the surface repeat unit.

The surface energy is given by the equation:

$$E_s = \frac{E_{slab} - E_{bulk}}{2A} \tag{8.26}$$

where E_{slab} and E_{bulk} are the energies for the slab model and that for an equivalent amount of the bulk structure and A is the surface area of one side of the slab. Care must be taken to obtain these energies at the same level of theory including basis set quality and k-point sampling. A refinement of Equation 8.26 to obtain surface energies based only on slab calculations is also discussed below.

The whole point of the slab model is to reproduce an isolated surface so that overlap of electron density between the slab and its periodic images must be vanishingly small. This means that k-point sampling used to describe interactions between unit cells in the direction perpendicular to the surface can be achieved with a single k-point. In the directions parallel to the surface, however, k-point sampling comparable to the reference bulk calculation must be maintained.

8.4.1.1 Electrostatic Stability of Surfaces

Early on in the simulation of the surfaces of ionic materials Tasker [81] pointed out that surface structure and stability depend not only on the Miller index of the plane exposed but also the point at which the "cut" of the bulk is made [82]. This can be illustrated by considering the examples shown in Figure 8.11. Figure 8.11a shows the rock salt structure of MgO with the ion sizes set using the values from Shannon's tabulation [83]. The {001} planes are the faces of the cubic unit cell. Looking at the stacking of ions perpendicular to any of these surfaces it is clear that layers are stoichiometric and so charge neutral. Moving from the surface into the bulk we pass through identical neutral layers which are simply offset from one another by half a lattice vector in a direction parallel to the surface. In this case any cut of the unit cell to create a surface will expose the same square two-dimensional repeat unit, (Figure 8.11b).

On electrostatic grounds, Tasker argued that surfaces made up of neutral layers should be expected to be stable and referred to examples in which atomic layers are neutral in this way as type I. Indeed the crystal habit of MgO is usually cubic with {001} faces dominant.

In more complex structures, cuts at different points in a unit cell will lead to very different surface terminations. For example, the corundum structure shown in Figure 8.11c and typified by α-Al_2O_3, has a hexagonal unit cell. The atom layering perpendicular to the (0001) surface follows an Al-O-Al-Al-O-Al-Al . . . sequence. In this case, cutting between two Al layers results in a stacking in which three

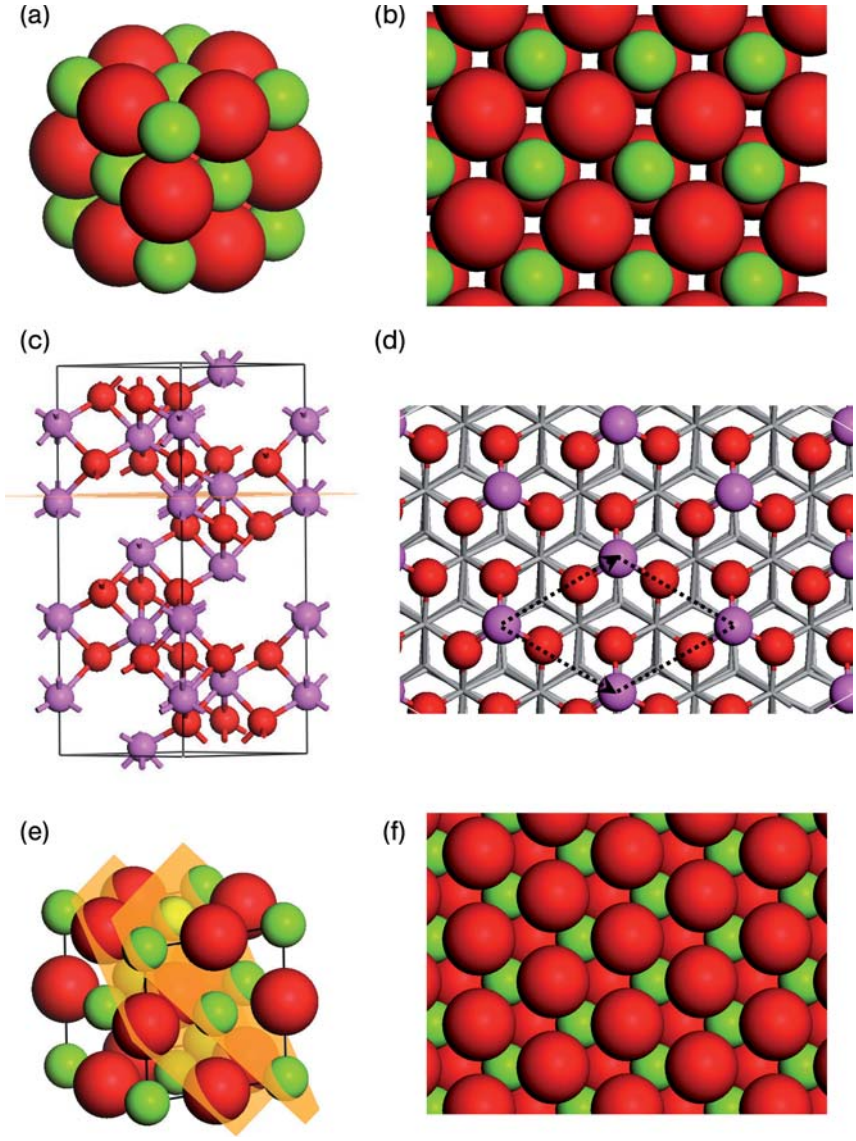

Figure 8.11 Examples of the effect of surface cuts on the character of an oxide surface. (a) The rock salt unit cell of MgO with ions drawn in proportion to ionic radius (Mg^{2+} 0.72 Å, O^{2-} 1.40 Å) From ref. [83] (b) Plan view of the MgO(001) surface, generated by taking the face of the cubic unit cell. (c) The hexagonal unit cell of the corundum structure typified by α-Al_2O_3. A non-polar (001) surface can only be generated by cutting between Al^{3+} layers such as the cut indicated by the plane. (d) Plan view of the surface termination for the non-polar α-Al_2O_3(0001) surface, dotted lines indicate the surface 2-D unit cell which shares the ***a*** and ***b*** lattice vectors (arrows) with the bulk structure. (e) The two possible (111) cuts for rock salt structures such as MgO. Either one will lead to a polar surface. (f) The O terminated (111) surface of MgO. Magnesium, green; oxygen, red; aluminum, pink.

layers (Al-O-Al) form a stoichiometric set of ions which is charge neutral and non-dipolar with the surface structure shown in Figure 8.11d. However, a different choice of cut, say between Al and O layers to expose an oxygen only surface, would result in a stacking sequence running (O-Al-Al-)-(O-Al-Al-)-(O-Al-Al-), with brackets indicating stoichiometric sets of layers. Clearly this choice of cut results in a dipolar repeating unit into the bulk and so the electrostatic energy in a purely ionic model will be divergent. This type of Miller plane, for which the choice of cut determines stability, is referred to as a type II surface.

Finally, in cases such as the (111) surface of MgO, alternating layers of anions and cations are obtained in the stacking sequence, Figure 8.11e. Here there are two choices of cut, one of which exposes a purely O^{2-} surface (Figure 8.11f) and one exposing purely Mg^{2+}. Either will produce a dipolar slab. This is an example of a type III surface which, on a purely electrostatic basis, is unstable and so should not be observed experimentally unless stabilized by adsorbates or reconstruction. Indeed LEED analysis has been used to show that the apparent occurrence of the MgO(111) surface under vacuum conditions can be explained by microfacets of {001} [84].

8.4.1.2 The Effect of Slab Dimensions

It is important to test the validity of the slab model to reproduce the surface properties of isolated surfaces. The two main parameters are clearly the vacuum gap introduced and the thickness of the slab employed. Both of these are system dependent but Figure 8.12 shows the effect of the vacuum gap on the calculated surface energy for the unrelaxed surface of α-Al_2O_3 taken from localized basis set GGA-DFT calculations using the DSOLID code. At small gap distances the surface energy is underestimated, since in the limit of a zero vacuum gap Equation 8.26 would give $E_s = 0$. The surface energy in this case is clearly converged above a

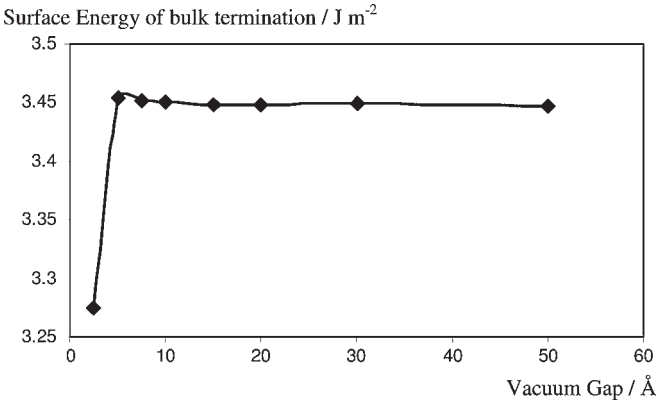

Figure 8.12 The variation of calculated surface energy for the bulk termination of α-Al_2O_3 (0001) with the vacuum gap used in the slab geometry calculation. Adapted from ref. [30].

vacuum gap distance of 10 Å. In plane-wave basis sets the vacuum gap is particularly important as the number of plane-waves required for a given accuracy increases with the simulation cell size and so a larger gap will require more computational time.

The convergence of the surface energy with slab thickness for α-Al_2O_3 has been studied by Ruberto and coworkers [85]. They point out that early work on the use of slabs to calculate the surface energy of simple metals showed that if a single cell bulk reference energy is used in Equation 8.26 the surface energy diverges with slab thickness [86]. The argument starts by considering a series of slab calculations in which the number of stacking layers perpendicular to the surface is increased systematically. Then we may expect the calculated surface energy to vary according to number of layers, n, so that Equation 8.26 becomes

$$E_s(n) = \frac{1}{2A}(E_{slab}(n) - nE_{bulk}) \tag{8.27}$$

where the reference bulk calculation is for the equivalent amount of material used for a single layer slab. At sufficiently large values of n the surface energy should converge so that:

$$E_s(n) = E_s(n-1) \tag{8.28}$$

which implies,

$$(E_{slab}(n) - nE_{bulk}) - (E_{slab}(n-1) - (n-1)E_{bulk}) = 0 \tag{8.29}$$

so that an alternative way to estimate E_{bulk} is to rearrange Equation 8.29 to read

$$E_{bulk} = E_{slab}(n) - E_{slab}(n-1) \tag{8.30}$$

Since this expression must be consistent with the slab calculations in terms of basis set, number of k-points and so on it provides a more reliable value than does a separate calculation of the bulk cell, which must have at least a different cell volume. The results obtained by Ruberto and coworkers [85] using the PW91 functional and a plane-wave basis set within the DACAPO code are plotted in Figure 8.13. For this type II surface the stacking layer is a single Al-O-Al unit, and in this plot we compare the surface energy calculated using E_{bulk} estimated from Equation 8.30 and the result of taking $E_{slab}(10) - E_{slab}(9)$ and using that value for E_{bulk} in Equation 8.26 for all slabs. In the latter case the result appears to have less variation than the recipe outlined above. However, the trend is for this method to diverge gradually away from the average, whereas the second method oscillates around it. These oscillations are ascribed to quantum-size effects by Ruberto and coworkers [85].

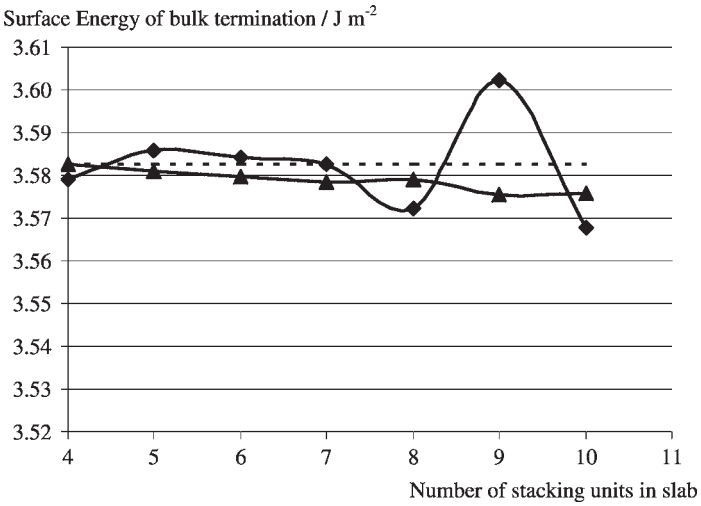

Figure 8.13 The surface energy for the unrelaxed (0001) surface of α-Al_2O_3 using the method of Ruberto and coworkers [85] (diamonds) and with a constant estimate of E_{bulk} (triangles). The average of the first method is included as a dotted line.

8.4.2
Surface Calculations on MgO, Al_2O_3 and TiO_2

There are few experimental estimates of surface energies and so most comparisons between simulation results and laboratory data are confined to surface structure. One exception is MgO{100}, which is formed from stoichiometric layers and was used as an example of a type I surface (Figure 11a and b). The MgO{100} planes are flat and charge neutral and so are easy cleavage planes for single crystal samples. This allows estimates for the surface energy to be made from the measured work required to cleave a sample [87]. This data has the advantage that it is free of errors arising from surface contamination. However, it does require large, perfect crystals and so there is only data available for favorable cases, such as MgO{100}. Estimates have also been made by comparing the heat capacities of powder samples with those of large crystallites [88]. This approach depends on the crystal habit of MgO, which is cubic, exposing only {100} surfaces.

Another possible reference is high-level correlated electronic structure methods such as quantum Monte Carlo (QMC) simulations [89]. Alfe and Gillan have used this approach to estimate the difference between DFT calculated surface energies and QMC values for the slab energies of MgO(100) [90]. The QMC value obtained for the surface energy lies in the range quoted from experimental cleavage values (Table 8.5). They find that LDA gives much closer agreement with this limiting value than do GGA calculations. For example the PBE functional underestimates

Table 8.5 Examples of type I, MgO(100), and type II, α-Al_2O_3(0001), surface energies and relaxations.

Surface	Method	Layers[a]	E_s (J m^{-2}) unrel.[b]	E_s (J m^{-2}) rel.[c]	ΔZ[d] (%)	Reference
MgO (100)	LDA	5	–	1.24	–	[90]
	PBE	5	–	0.87	–	[90]
	QMC	5	–	1.19	–	[90]
	LDA	3	1.39	1.38	2.2	[92]
	LDA	7	1.16	1.14	2.27	[50]
	PW91	7	0.92	0.90	2.27	[50]
	Expt.[e]			1.04–1.20		[87]
	Expt.[f]			1.09–1.36		[88]
α-Al_2O_3(0001)	LDA	3	3.77	1.76		[93]
	LDA	6	–	1.95	–77	[94]
	LDA			1.98	–85	[95]
	LDA	10	3.97	1.94	–86	[85]
	PW91	10	3.58	1.60	–86	[85]
	PW91	6	–	1.98	–84	[96]
	PBE	6	–	1.72	–92	This work
	Expt.[g]				–51	[79]
	Expt.[h]				–63	[97]
	Expt.[i]				–50	[98]

a Number of non-polar stacking units used in slab. For MgO(100) this is an atomic layer while for α-Al_2O_3(0001) it is an Al–O–Al tri-layer. Many papers study the convergence with number of layers; the largest value used is quoted here.
b Value for unrelaxed bulk termination at a non-polar cut.
c Value after geometry optimization.
d For MgO(100) the rumpling of the surface given by Equation 8.31; for α-Al_2O_3(0001) the displacement perpendicular to the surface of the outermost Al ion with respect to the first O layer on relaxation of the bulk terminated structure.
e Estimated from work required to cleave crystal.
f Calorimetric measurements on powders extrapolated to 0 K.
g Grazing incidence X-ray diffraction.
h TOF-SARS.
i LEED-IV (Low Energy Electron Diffraction, Intensity/Voltage analysis).

the surface energy by around 30%, which is consistent with the difference between LDA and GGA found for TiO_2 and SnO_2 by the same group [91]. QMC is a highly accurate method for obtaining the electronic structure of materials, but is also very expensive in terms of computer time. For this reference calculation, relaxation of the surface structure was carried out at the LDA level and the resulting co-ordinates used in a one-off calculation of the system energy using QMC. Since the relaxation of the MgO(100) surface is extremely small this leads to only small errors for this case. For example, Table 8.5 gives the surface energy from Alfonso and coworkers [92] and Skorodumova and coworkers [50] who report values calcu-

lated from both unrelaxed and relaxed slab calculations with LDA and PW91 functionals. The effect on the energy of optimizing the surface structure is only 0.01–00.02 J m^{-2}, which is, at most, around 2%.

For the relaxed surface, the interlayer spacing is hardly changed from the {100} bulk values. However, small surface rumpling does occur on slab optimization in which, for MgO at least, O^{2-} ions move to positions further from the slab center than the Mg^{2+} ions. This can be quantified by calculating the dimensionless quantity:

$$\Delta Z_{\text{rum}} = \frac{Z_{\text{O}} - Z_{\text{Mg}}}{\Delta Z_{\text{L}}} \tag{8.31}$$

in which Z_{O} and Z_{Mg} are the Z co-ordinates (assuming Z is perpendicular to the surface) of the O^{2-} and Mg^{2+} ions at the surface of the relaxed slab and ΔZ_{L} is the interlayer spacing in the bulk structure. The values given in Table 8.5 are in the range 2.2–2.3% and so the effect is quite small. Interestingly, CaO(100) shows a negative ΔZ_{rum}, of around the same magnitude, indicating that the metal ions move away from the bulk termination into the vacuum gap while the anions move toward the bulk in this case. Skorodumova and coworkers suggest that this is due to the greater repulsion between the semi-core electrons of the cation and the O(2p) states for the larger cation [50].

We saw from the bulk studies that α-Al_2O_3 is the most crystalline form of alumina and so many calculations have focused on this form for surface calculations. The most stable surface in the hexagonal setting is (0001) which was illustrated as a type II surface in Figure 8.11. Manassidis and Gillan [93] have considered this surface using the LDA, finding a surface energy of 1.76 J m^{-2} (Table 8.5). This is lower than found in later calculations at the LDA level by Ruberto and coworkers [85], Finnis and coworkers [94] and Di Felice and Northrup [95], who all find surface energies around 0.2 J m^{-2} higher. This may be due to the rather thin slab that was used by Manassidis and Gillan, with only three non-polar stacking units compared to 6–10 in the later calculations. Owing to the computational restrictions of the computers available at the time, Manassidis and Gillan could only test convergence for the unrelaxed slab with the ions at their bulk positions. In contrast to the MgO(100) example, relaxation of the α-Al_2O_3(0001) slab geometry causes a dramatic lowering of the surface energy by around 2 J m^{-2}, that is, over 50%. It is clear that in this case the slab thickness will become important. Indeed in the study by Ruberto and coworkers it was found that the center of the slab showed negligible relaxations only for the thickest slabs used, which contained 9 or 10 tri-layers.

Marmier and Parker [96] using PW91 within the VASP program found a surface energy which is close to the converged LDA results using a six tri-layer slab. This would be unexpected from the observations made earlier suggesting that GGA surface energies tend to be lower than LDA. Comparing values calculated by different research groups is always difficult; however, the consistent set of calculations on thicker slabs by Ruberto and coworkers do give a GGA surface energy around

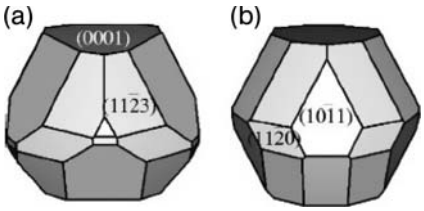

Figure 8.14 Comparison of the (a) calculated (from ref. [96]) and (b) observed (from ref. [97]) crystal habit of α-Al_2O_3.

20% lower than their LDA result. Our own PBE calculation on a six tri-layer slab also gives a lower surface energy than the LDA results reported in Table 8.5. Marmier and Parker also calculated the surface energy of six additional non-polar surfaces, confirming that the (0001) is the lowest energy. The other surfaces in order of calculated surface energies were $(01\bar{1}2)$, $(11\bar{2}3)$, $(11\bar{2}0)$, $(10\bar{1}0)$, $(10\bar{1}1)$ and $(22\bar{4}3)$ with values of 2.04, 2.25, 2.34, 2.56, 2.57 and 2.77 J m^{-2} respectively.

Based on these relative energies it is possible to predict crystal morphology by creating a Wulff plot in which low-energy surfaces are assumed to form the dominant crystal facets. The predicted morphology from Marimier and Parker's calculations is compared with that from optical microscopy [99] in Figure 8.14. There is agreement on the importance of the (0001) surface. However the calculations appear to overestimate the surface energy of the $(10\bar{1}1)$ surface as this is a major facet in the experimental structure but is relatively minor according to the GGA calculations. They suggest that this could be due to microfaceting, where the crystallite surface of this energetically unfavorable facet is actually made up of many tiny steps expressing lower energy Miller planes. The same group successfully showed this to be the correct explanation for experimental observations of the MgO(111) "polar" surface.

As already mentioned, the relaxation of the α-Al_2O_3(0001) surface results in much more dramatic atomic displacements than are seen for MgO(001). For the non-polar bulk termination, the outermost Al ion has three O neighbors (Figure 8.15a) compared to the six found for the bulk site. On relaxation this Al atom moves downward, becoming almost co-planar with the first oxygen layer as shown in Figure 8.15b. This example calculation was carried out using the SIESTA code with the PBE functional. The calculated lattice parameters for the hexagonal unit cell of the bulk are slightly longer than the experimental reference structure ($a = b = 4.801$ Å, $c = 13.078$ Å compared to $a = b = 4.759$ Å, $c = 12.991$ Å) [23]. The difference in the Z-co-ordinates (direction perpendicular to the surface) between the surface Al and O layers decreases by 92%, from 0.836 Å to 0.063 Å. This is accompanied by an expansion of the equilateral triangle formed by the three nearest neighbor oxygen atoms to the outermost Al atoms. As a result the Al—O bond distances on the surface change to a lesser extent, with Al—O in the bulk termination being only 0.17 Å longer than in the relaxed surface (1.70 Å versus 1.87 Å). This type of relaxation has been observed in many earlier calculations,

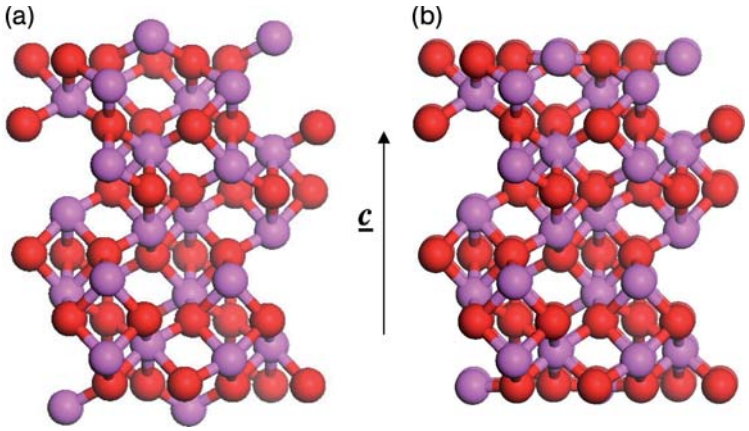

Figure 8.15 A slab simulation of the $Al_2O_3(0001)$ surface consisting of six tri-layer units, viewed with surface running into the page. A 10Å vacuum gap in the *c* direction was used to isolate periodic images. (a) Bulk non-polar termination. (b) After relaxation of atom co-ordinates. Aluminum, pink; oxygen, red.

some of which are also listed in Table 8.5. Our own calculation is on the high end of the reported data, but for this illustrative example we used a relatively thin slab and did not optimize the SIESTA basis set. Even so our value is in reasonable agreement withthat of Ruberto and coworkers, who used the thickest slabs and carefully considered the convergence of surface energy with simulation parameters. HF and B3LYP methods have also been shown to give an inward relaxation of around 80% in a systematic study of this surface by Gomes and coworkers using the localized basis set code CRYSTAL with 15 layer two-dimensional periodic simulations. They also show that using surface lattice vectors obtained from an optimization of the structure at each level of theory is preferable to using the experimental crystal structure parameters.

Experimentally, surface relaxation has been studied using time of flight scattering and recoil spectroscopy (TOF-SARS) [97], glancing angle X-ray diffraction [79] and LEED-IV [98]. All three techniques show the same inward relaxation, but the percentage difference between the bulk termination and observed separation of the outermost Al and O layers is only between 50 and 63%. This discrepancy may be partly due to the difficulty of eliminating H from the experimental surfaces. The presence of H in hydroxyl groups changes the character of the outer layer by increasing the effective co-ordination of the outermost Al atoms and reducing the degree of relaxation considerably.

The electronic structure of the α-$Al_2O_3(0001)$ surface also shows features that differ from the bulk material [30]. Figure 8.16 compares the calculated DOS for the dense phase with that of a slab calculation. In the DOS for the slab (Figure 8.16b) a state just below the bottom of the conduction band can be seen which

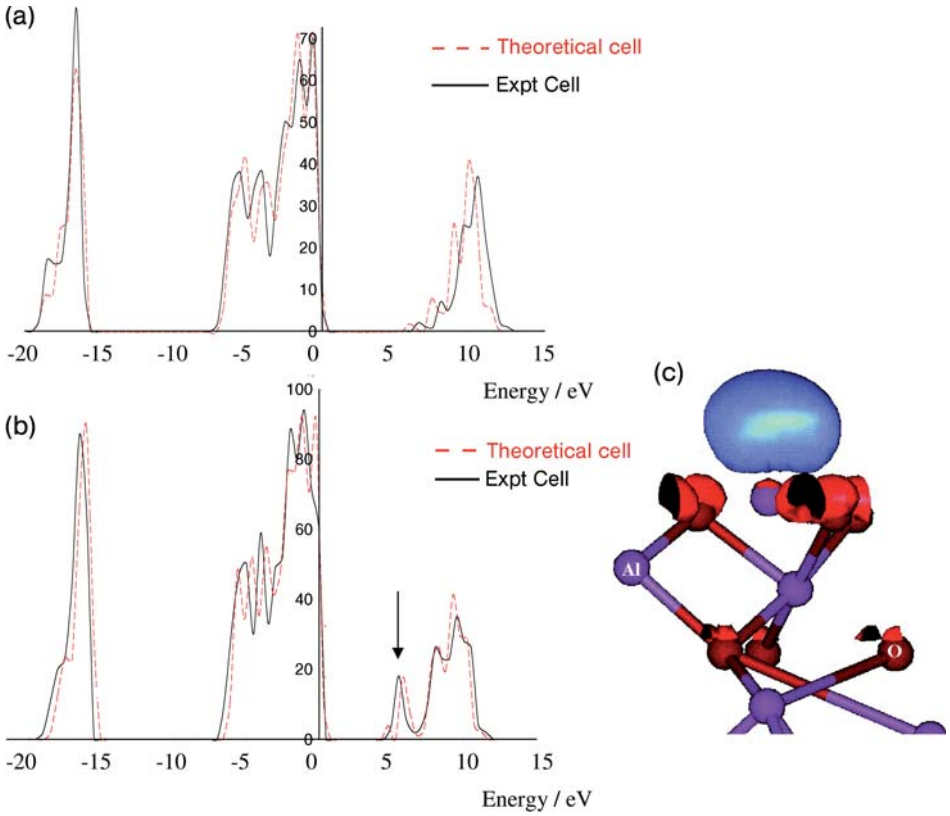

Figure 8.16 Density of states calculated for (a) the bulk and (b) the (0001) surface of α-Al_2O_3, using the localized basis set code DSOLID with the PW91 functional, from ref. [30]. In each case the solid line is calculated at the experimental geometry while the dotted line is for the optimized cell. (c) The lowest unoccupied state indicated by the arrow in (b).

is not present in the bulk calculation (Figure 8.16a). This is the lowest unoccupied state in the system and the plot of the corresponding real space orbital in Figure 8.16c shows that it is localized at the surface and contains mainly Al s and p orbitals combined to give a lobe perpendicular to the surface. This orbital will be accessible to adsorbates and, since it is empty, will be involved in charge transfer from surface species. This gives rise to Lewis acidity on the surface of α-Al_2O_3.

One example that demonstrates the role of this type of Lewis acid site in surface chemistry is a study of the mechanism of water dissociation over the clean α-Al_2O_3(0001) surface by Hass and coworkers [100]. They used the BLYP functional in the CPMD code to allow the free energy of dissociation to be estimated using constrained dynamics [101]. The initial adsorption mode involves the coordination

of the water O atom (O_w) with a low coordination Al ion through a dative bond in which charge is donated from the adsorbate into the Lewis acid center. This leads to a calculated binding energy of 97 kJ mol^{-1} which increases by a further 30–40 kJ mol^{-1} on heterolytic dissociation of an O—H bond to form two surface hydroxyl groups. The range of energies stems from the choices possible for the surface oxygen that receives the H^+ in the final state.

The free energy of dissociation based on constrained dynamics also showed that the calculated barrier depends on the geometry of the final state. If an O neighbor of the Al^{3+} to which molecular oxygen was adsorbed is used to receive H^+, the transition state is a strained four-membered ring and a barrier of 28 kJ mol^{-1} is obtained. This reduces to only 9 kJ mol^{-1} when the pathway to place H^+ on a second neighbor oxygen is used. The second neighbor has the advantage that the transition state formed is a six-membered ring and so the O_w—H—$O_{surf.}$ angle is nearer to linear at 166°, compared to 135° in the case of the nearest neighbor.

The geometry of the transition state has also been found to be important for the dissociation of HF on α-Al_2O_3(0001) and the subsequent halogen exchange with CH_2Cl_2 based on DSOLID calculations [102].

One of the easiest cleavage planes on rutile-structured TiO_2 corresponds to the (110) surface. In the bulk structure [103] all Ti atoms are six coordinate with four equivalent equatorial Ti—O bonds (1.97 Å (PBE)) slightly shorter than the two axial (2.00 Å (PBE)). The preferred termination of the (110) surface is shown in Figure 8.17a and contains a mixture of sixfold (Ti_{6c}) ions joined by surface bridging oxygen atoms (O_{2c}) and fivefold (Ti_{5c}) coordinate surface cations. Compared to bulk centers the Ti_{5c} atoms have lost one axial Ti—O bond. The line of bridging oxygen atoms on the bulk termination is mirrored below the surface plane and so a neutral stacking unit consists of an atomic tri-layer. For the simulation of this surface the choice of the number of these tri-layers in the slab is important. Figures 8.17b and c show the result of relaxations using the SIESTA code with three and four tri-layer slabs respectively. In both cases the Ti_{5c} atoms move down into the surface toward their remaining axial oxygen atom, but this is a small effect compared with the surface ion movement seen for α-Al_2O_3(0001). In addition, the four tri-layer slab is deformed and the surface appears to optimize to a rumpled structure. In the thinner three tri-layer slab the surface is less distorted from the bulk termination. Pacchioni and coworkers [104] have pointed out that slabs with an odd number of tri-layers have a symmetry plane in the middle of the slab that is absent for even numbers of stacking units. To investigate this difference they used the PW91 functional, and compared results from the localized basis set code CRYSTAL and plane-wave basis set code VASP. The calculated bulk band gap from the plane-wave approach is around 0.2 eV lower than with the localized basis set and this is ascribed to the use of ultra-soft pseudopotentials in the VASP calculations. The different behavior for odd and even numbers of tri-layers also results in oscillations in the band gap with slab thickness, which are mainly due to changes in the calculated position of the bottom of the conduction band. These states are associated with the coordinatively unsaturated Ti_{5c} surface atoms and are composed largely of the d orbitals with lobes perpendicular to the surface.

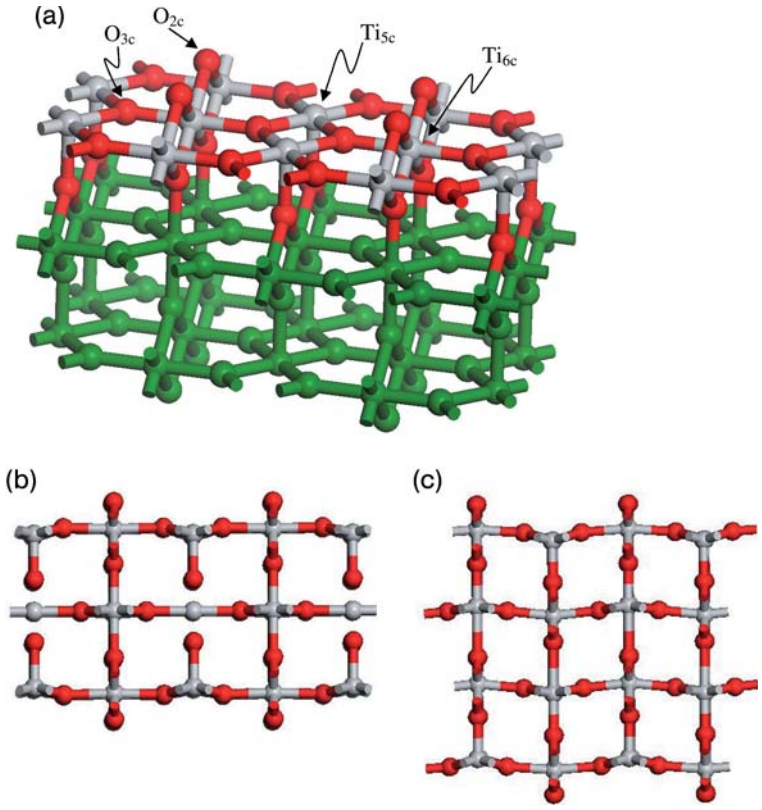

Figure 8.17 (a) The TiO_2(110) surface with surface Ti_{6c} and Ti_{5c} atoms. Titanium, silver; oxygen, red; other atoms in the slab, green. (b) The relaxed structure of the three tri-layer slab viewed in cross-section. (c) The relaxed structure of the four tri-layer slab. Atom colors for the surface layer of (a) are used throughout (b) and (c).

However, unlike the α-Al_2O_3(0001) example, these are not separate gap states at the surface but simply the lowest lying states of a band that also contains mixed Ti—O crystal orbitals.

In Pacchioni's calculations it was found that the occupied bonding Ti—O hybridized orbitals tend to form bonds that are stronger between the surface tri-layer and the first sub-surface one than are found between tri-layers in the bulk. For the even slabs this leads to a tendency to form a set of paired tri-layers, which give rise to the observed rumpling, whereas for odd slabs a more regular spacing of the tri-layers in the slab center is achieved.

The (110) surface of TiO_2 has also been subjected to LEED-IV experiments, giving direct information on the surface structure [80]. Thompson and Lewis have used the odd-numbered tri-layer slabs recommended by Pacchioni to consider the

Table 8.6 The displacement of surface atoms from their bulk positions in TiO_2(110).

	Expt [79]	Method (Number of tri-layers in slab)					
		PW91 (5) [105]	PW91 (7) [105]	PW91 (9) [105]	PW91 (11) [105]	LDA (7) [106]	HF (7) [106]
Ti_{6c}	0.25 ± 0.03	0.29	0.33	0.42	0.43	0.22	0.25
Ti_{5c}	−0.19 ± 0.03	−0.10	−0.07	−0.03	−0.03	−0.17	−0.17
O_{2c}	0.25 ± 0.03	0.09	0.13	0.23	0.23	0.01	−0.01
O_{3c}	0.27 ± 0.08	0.24	0.27	0.32	0.32	0.13	0.11

accuracy of the surface geometry from calculations compared to this data [105]. They employed the plane-wave basis set code VASP with the PW91 functional. Their results, for the surface layer atoms, are reproduced in Table 8.6 and shows that the surface relaxations are converged for slabs of nine tri-layers. This table also includes results of earlier calculations by Gale and Harrison, who compared LDA and HF methods for the same surface and who employed seven tri-layer slabs [106]. Gale and Harrison found that the bridging O_{2c} atoms remain at their positions in the simple bulk termination whereas the experimental data and the more recent calculations indicate a significant outward movement. However the metal ion positions are better reproduced in the earlier work.

8.4.3
Influence of Environment on Surface Structure

It is clear from experiments that the character of an oxide surface is dependent on its environment. For example, surfaces may be prone to hydroxylation and many catalytic processes require reduction/oxidation cycles that must create/replenish oxygen ion defect sites at the surface. If the surface composition of an oxide is different to the bulk, the surface energy can no longer be defined as simply the difference between the bulk and slab calculations per unit surface area. However, the equilibrium surface energy can still be obtained from calculated energies if we turn to the idea of the chemical potential [94]. The surface of an oxide should be in equilibrium with both the oxide bulk and the atmosphere above the oxide and so the chemical potential of all species must be constant in the three regions, bulk, surface and atmosphere. The simplest case to consider is the effect of oxygen partial pressure on the surface stoichiometry. For an oxide of formula A_mO_n the formation of a non-stoichiometric surface in a slab simulation can be thought of as the chemical reaction

$$\frac{N_A}{m}A_mO_n + N_{eO}O \rightarrow A_{N_A}O_{\frac{n}{m}N_A + N_{eO}} \tag{8.32}$$

where the formula on the right hand side is that of a simulation slab and the additional term on the left, required to balance the equation, can be thought of as coming from gas-phase oxygen. The term N_{eO} defines the oxygen excess in the slab and can be negative.

The surface free energy, γ, is just the free energy for the reaction of Equation 8.32 per unit surface area of the slab. If a slab simulation geometry gives two surfaces of area S:

$$\gamma = \frac{1}{2S}\left(G_{\text{slab}} - \frac{N_{\text{A}}}{m} g_{\text{AO}} - N_{\text{eO}}\mu_{\text{O}}\right) \tag{8.33}$$

where G_{slab} is the free energy of the slab representation of the surface and g_{AO} is the free energy per stoichiometric unit of the bulk material. The chemical potential, μ_{O}, is used to obtain the free energy of the excess O species. It is useful to define the oxygen excess per unit surface area, Γ_{O}, when Equation 8.33 becomes:

$$\gamma = \frac{1}{2S}\left(G_{\text{slab}} - \frac{N_{\text{A}}}{m} g_{\text{AO}}\right) - \Gamma_{\text{O}}\mu_{\text{O}} \tag{8.34}$$

To link this definition of surface energy to calculations on relaxed slabs we now make the assumption that the entropy in the slab and bulk oxide free energy terms can be neglected. Then the surface energy based on calculated quantities gives

$$\gamma = \frac{1}{2S}\left(E_{\text{slab}} - \frac{N_{\text{A}}}{m} e_{\text{AO}}\right) - \Gamma_{\text{O}}\mu_{\text{O}} \tag{8.35}$$

in which E_{slab} is the energy of the geometry optimized slab defined by the right hand side of Equation 8.32 and e_{AO} is the energy per formula unit of a relaxation of the bulk. Although Equation 8.35 defines the surface energy, it still requires the chemical potentials for the excess oxygen to be set. The oxygen chemical potential under any given conditions of temperature T and partial pressure P_{O_2} can be estimated using:

$$\mu_{\text{O}} = \mu_{\text{O}}^{0} + \frac{1}{2} RT \ln\left(\frac{P_{\text{O}_2}}{P^{0}}\right) \tag{8.36}$$

where the superscript 0 is used to indicate standard conditions and R is the molar gas constant. Usually the zero of chemical potential would be taken as the value for dioxygen gas under such standard conditions. However, using calculated data the energy is referenced to a state in which all atom cores and valence electrons are isolated and so an estimate of the energy of the dioxygen molecule is required to continue the calculation. The assumptions used by DFT and other first principles methods that can be applied to the solid state mean that

the accuracy of the calculation of such absolute values of molecular energy is not great. It is better to estimate the standard state chemical potential using a cycle which gives μ_O^0 as the difference between more reliable quantities such as lattice energies.

For example the standard energy of formation of the oxide is the energy for the reaction:

$$mA(s) + \frac{n}{2}O_2(g) \rightarrow A_mO_n(s) \tag{8.37}$$

for which,

$$\Delta G_f^0(A_mO_n) = g_{AO}^0 - m\mu_A^0 - n\mu_O^0 \tag{8.38}$$

Since the metal will usually have a standard state which is solid the values g_{AO}^0 and μ_A^0 can be obtained from extrapolation of DFT optimization calculations. Accurate values of $\Delta G_f^0(A_mO_n)$ are tabulated for the common oxides [56], for example the value for Al_2O_3 is $-1576\,kJ\,mol^{-1}$ and so Equation 8.38 provides a route to μ_A^0 without explicit calculations on O_2.

Equation 8.38 also sets the lower limit of the range of values accessible for μ_O since reduction of the oxide will occur spontaneously into the pure metal and dioxygen gas if the free energy for Equation 8.37 is positive. This means for a stable oxide:

$$\mu_O > \frac{g_{A_mO_n} - mg_A}{n} \tag{8.39}$$

An upper bound for μ_O can be estimated from the point at which $O_2(g)$ begins to condense on the surface. The thermodynamically stable composition of the surface can now be predicted over the range of accessible partial pressures of O_2 by using the pressure dependence of the chemical potential from Equation 8.36 in Equation 8.35.

This approach was first applied to α-$Al_2O_3(0001)$ by Finnis and coworkers [107] who demonstrated that the Al termination which forms the type II non-polar surface is stable under normal conditions. Elevated oxygen partial pressures (several tens of atmospheres) would be required to make an oxygen-terminated surface the preferred form. Reduction of the surface will not be favorable until the lower limit of oxygen partial pressure is met, at which point bulk reduction is favorable anyhow.

These thermodynamic arguments can also consider the hydroxylation of surfaces by including the chemical potential of hydrogen and/or water [108]. This type of analysis shows that Al_2O_3 surfaces of the α-phase are either Al or OH terminated under all accessible conditions. However, the influence of the environment is different for each Miller index owing to variation in the calculated surface energies.

Phase diagrams specific to each experimentally observed face have been derived, which show that conditions should exist for which the (0001) surface is dehydroxylated, to give an Al termination, while other surfaces remain fully hydroxylated.

For transition metal oxides the surface composition can be altered more readily by the partial pressure of oxygen. For example, RuO_2(110) has been shown to move from an over-oxidized state for high O chemical potential to a reduced form at the lower end of its accessible range [109]. In such cases the electrostatic arguments against "polar" surfaces have to be adapted in the light of surface cation reduction. It should also be remembered that these calculations give the thermodynamic stability of a given surface composition and do not take account of any kinetic barriers to the required changes.

8.4.4
Transition Metal Oxides with Partially Filled d Bands

The band picture of electronic states in solids works well when there is strong overlap between neighbors in the lattice. This leads to broad bands and delocalized electronic states. The early successes of band theory were in the description of the physical properties of metals such as electrical and thermal conductivity [110]. However, in transition metal oxides band structure alone is often not sufficient. Consider a d^8 system such as Ni^{2+} in NiO. The usual picture would be to draw localized orbitals at each Ni site which are split into three t_{2g} and two e_g energy levels by the crystal field. The eight d electrons per ion would then fill the energy levels as shown on the right in Figure 8.18. This is a highly localized picture of the electronic structure since the sets of d electrons are associated strongly with particular nuclei. If movement of electrons occurs between centers we have to remove an electron from one of the d^8 centers, leaving a d^7, and shift it to a neighbor which becomes d^9. The electron–electron repulsion between the d electrons will be proportional to the number of pairs of electrons present at each center. With two d^8 ions we have 56 electron pairs, while the $d^7 + d^9$ in isolation have a total of 57 electron pairs. So the movement of electrons between centers requires energy, effectively creating an energy gap. This type of argument was developed by Mott and Hubbard to explain the insulating properties of transition metal oxides with partially filled d shells. They introduced a parameter, U, which is used to represent the Coulomb term as a function of d-orbital occupation so that the relative energies of alternative arrangements can be estimated.

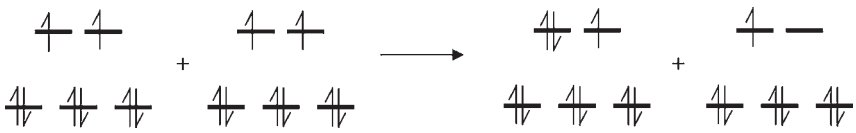

Figure 8.18 The localized electron populations of the t_{2g} and E_g states for two Ni^{2+} d^8 ions in NiO. The average configuration is d^8 but transport of electrons through the material would produce d^7 and d^9 centers.

A purely band structure-based treatment of this problem results in very narrow bands for the d orbitals because of the weak overlap between neighboring Ni^{2+} centers. However the band would be partially filled and so it would be concluded that the system is metallic. This is the result generated by a simple LSDA approach, as shown early on by Terakura and coworkers [111]. In the Mott–Hubbard analysis, the localized picture becomes important when U is greater than the band width predicted by band theory. In addition the electron configuration affects the exchange energy. For example, the two electrons in the triplet d^8 configuration will also have an exchange interaction and this is lost if one spin is reversed to produce a singlet. This means that the e_g energy levels appear lower in the triplet state than the singlet so that an "exchange gap" can be introduced.

For transition metal oxides such as NiO the Mott–Hubbard model gives much better agreement with experiment; localization of the electrons in this way explains the anti-ferromagnetic ordering observed in NiO and its electrical insulator properties [112]. The terms required to calculate the electron–electron interaction energy on a site, E_{MH}^{UHF}, can be written in terms of the d-electron occupations, using a UHF approach:

$$E_{MH}^{UHF} = \frac{U}{2}\sum_{\omega,m,m'} n_{m,\omega}n_{m',-\omega} + \frac{(U-J)}{2}\sum_{\omega,m\neq m'} n_{m,\omega}n_{m',\omega} \tag{8.40}$$

where the sum over ω is over the spin states α and β, with −ω signifying the opposite spin state to ω. The sum over m and m' considers each of the d states at the site. In this way the first term takes into account the Coulomb interaction between electrons of opposite spin while the second term is for Coulomb interactions between electrons of the same spin, with a correction for the exchange interaction (rather confusingly given the symbol J).

Of course some of these interaction terms are already present in an LSDA calculation and so to incorporate this into a general DFT scheme requires these duplicate contributions to be removed. One way to do this has been proposed by Dudarev and coworkers [113]. They have derived a functional incorporating the U and J parameters of the Mott–Hubbard model which is written:

$$E_{LSDA+U} = E_{LSDA+U} + \frac{(U-J)}{2}\sum_{\omega,m}\left(n_{m,\omega} - n_{m,\omega}^2\right) \tag{8.41}$$

The advantage of this expression is that U and J appear only as their difference $(U-J)$ and so it requires only a single parameter to be determined for any particular transition metal oxide under consideration. The J parameter shows little system-to-system variability and is taken to be around 1 eV in most cases. Based on a comparison of the calculated DOS and experimental electron energy loss spectra (EELS) the U parameter for NiO was set at 6.2 eV. This gave a ground state in which the Ni spins are aligned within (111) planes and neighboring planes have

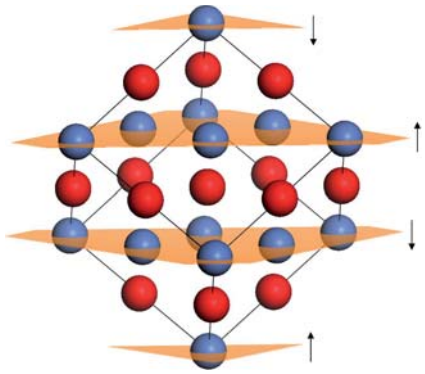

Figure 8.19 The antiferromagnetic AF_2 state of NiO. The (111) planes through Ni^{2+} centers are shown with arrows indicating the orientation of the majority spin for each plane. Note that the atoms at the top and bottom corners of the cell are crystallographically, but not magnetically, equivalent. Nickel, blue; oxygen, red.

opposite spin as shown in Figure 8.19. This anti-ferromagnetic ordering and the calculated site magnetization are in good agreement with experimental data. On a practical level, the ordering of spins in this way means that the crystallographic fcc unit cell cannot be used for the simulation as it contains an odd number of (111) planes, and a supercell has to be employed which is commensurate with the spin system. The calculated density difference between the LSDA + U and LSDA calculations is plotted in Figure 8.20. This shows that the inclusion of the Hubbard model leads to a reduction of density in the interatomic region between Ni^{2+} and O^{2-} ions and increased localization of charges at the metal centers. The LSDA calculation therefore overemphasizes the importance of covalent bonding between the ions compared to the LSDA + U results.

More recently Rohrbach and coworkers have used NiO as an example to test the implementation of the Hubbard model in the VASP code [114]. Their work allows the combination of the PW91 gradient corrected functional with the on-site Coulomb and exchange corrections given in Equation 8.41. To set the U parameter Rohrbach and coworkers plotted the bulk lattice parameter, metal center magnetic moment and band gap over the range $U = 1$ to 9 eV. The best compromise for accurate agreement with experiment on these three properties was $U = 6.3$ eV, practically the same value as used in the earlier calculations of Dudarev and coworkers [113]. The effect of the U term can be quantified by comparing results of calculations based on PW91 alone with those at this optimal value of U. Figures 8.21a and b show an overlay of the DOS from unrestricted calculations for the majority and minority spin states, respectively. At the PW91 level the band gap is underestimated at 0.5 eV compared to the experimental values of between 4.0 and 4.3 eV. The calculations also indicate a simple Mott–Hubbard band gap with the top of the valence band consisting of metal majority spin states of e_g symmetry

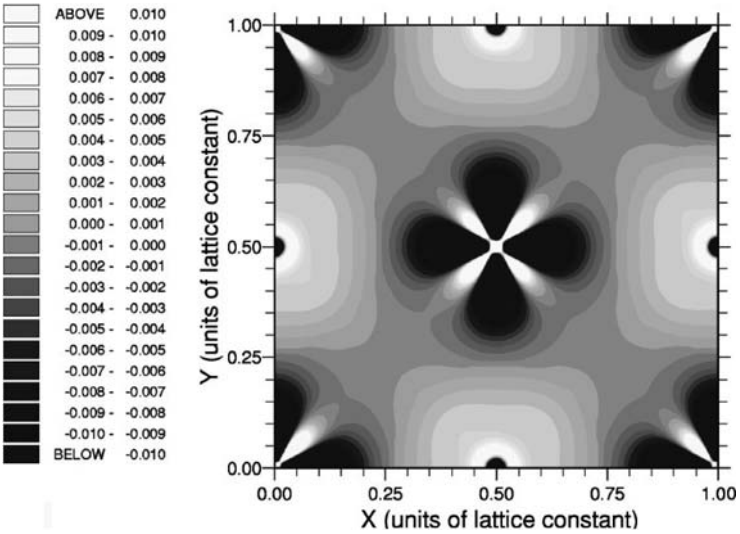

Figure 8.20 Charge density difference [LSDA + U] − LSDA (U = 6.2 eV) for bulk NiO taken through a (100) plane of the rock salt cubic unit cell, centered on a Ni^{2+} ion. Taken from ref [113].

along with minority t_{2g} states and the bottom of the conduction band being just minority spin e_g states. The O(2p) contribution at these energies is relatively minor. This means that the energy gap is created by the difference in energy levels for different spin states. The majority degenerate e_g states are occupied by two electrons and so have an exchange contribution to their energy whereas the minority e_g states are empty. Thus it is an "exchange splitting" of the e_g states that creates the gap, which is the classic Mott–Hubbard argument for insulating behavior in this type of oxide. In the PW91 + U this exchange splitting of the metal d orbitals is increased to around 9.5 eV, because the electron localization increases the stabilizing effect of the exchange interaction on the occupied majority e_g states. Now the top of the valence band has a largely O(2p) character, with contributions from both majority and minority Ni t_{2g} states. The lowest lying conduction band states are mainly from the minority spin e_g states, suggesting that the band gap is now of mixed charge-transfer and Mott–Hubbard type. The band gap has also widened to 3.2 eV, in much closer agreement with the experimental measurements.

Rohrbach and coworkers went on to consider the NiO(100) surface. Since NiO is isostructural with MgO, this is a non-polar flat surface corresponding to one of the faces of the cubic unit cell. Reference to Figure 8.19 shows that the surface will also have an anti-ferromagnetic structure with rows of surface cations having parallel spins along the lines in which the (111) planes intersect the surface. Relaxation with PW91 + U shows a very small (1%) inward movement of the surface layer, but no buckling of the type observed for MgO(100) is reported. Buckling only occurs at the LSDA level and has not been observed experimentally.

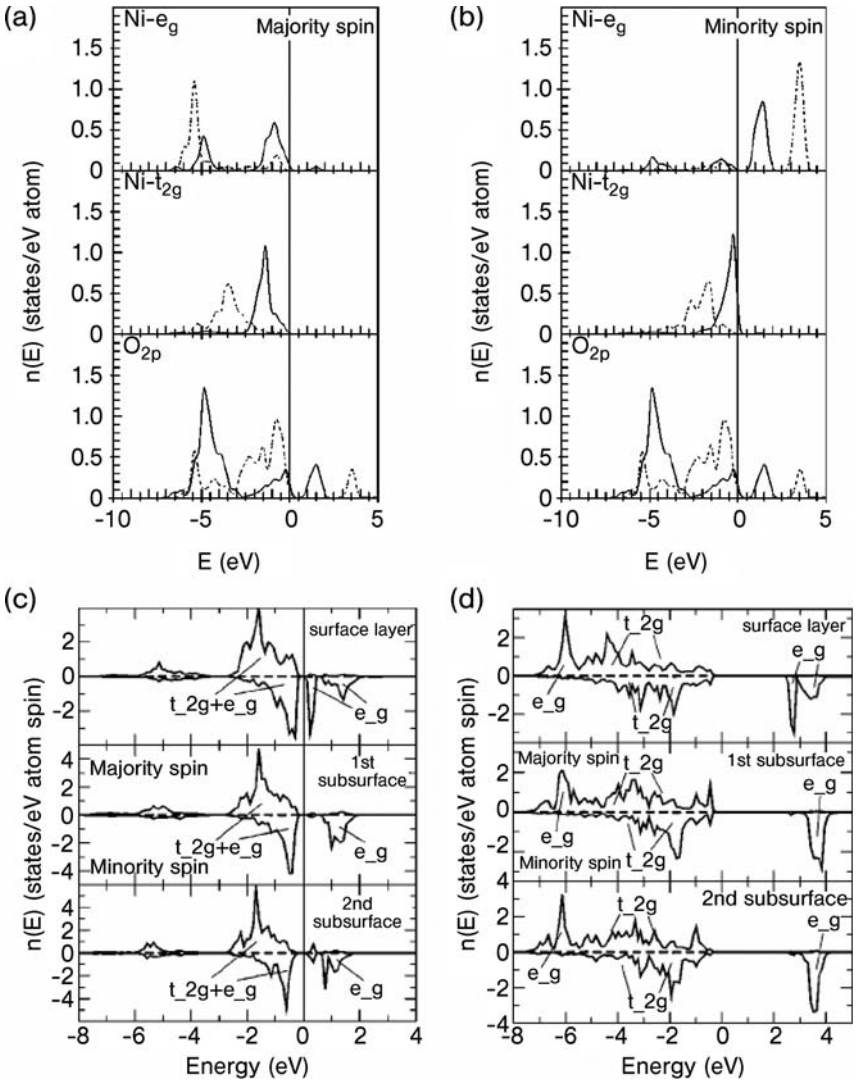

Figure 8.21 Calculated densities of states for NiO, (a) bulk structure at PW91 (solid lines) and PW91 + *U* (dashed lines) for the majority spin, (b) as (a) for the minority spin. (c) Breakdown of contributions to DOS by atomic layer for the PW91 calculation and (d) breakdown by layer for PW91 + *U*. In each case energies are referenced to the top of the valence band. Taken from ref. [114].

Figure 8.21c and d shows the density of states decomposed by layer for the first three surface planes. At the surface the octahedral environment of the bulk Ni^{2+} ions is lost and so the e_g orbitals are no longer degenerate. This is seen as a splitting of the minority spin states at the bottom of the conduction band in the PW91 calculation with the d_{z^2} orbital (z perpendicular to the surface) moving to lower energies, giving a further reduction in the estimated e_g to just 0.1 eV. A similar effect is seen for the PW91 + U model, which gives a surface layer band gap of 2.9 eV. By the second sub-surface layer the symmetry of the cation sites appears to be O_h as the splitting is removed.

The adsorption of both CO and NO on the NiO(100) surface has been investigated using photoelectron diffraction [115] giving a tilted geometry with Ni—C and Ni—N distances significantly longer than predicted using gradient-corrected DFT. Rohrbach and coworkers showed that the PW91 + U approach is able to give much better agreement with the experimental data for CO and NO. [116]. The observed tilted geometries are unexpected from comparable metal complex chemistry, for which π back-donation from metal to ligand would favor a linear geometry. However, in the metal oxide surface we have seen how exchange splitting shifts the occupied metal d orbital bands to lower energies and so their mixing with adsorbate orbitals becomes less efficient in a PW91 + U model. Molecular tilting allows σ donation of charge from the diatomic to the surface d_{z^2} from both the 5σ and occupied π orbitals, which would be symmetry forbidden in an upright adsorption mode. For the NO case, the partially occupied $2\pi^*$ orbital is hybridized with the d_{z^2} and the 5σ contribution is almost negligible. Similar geometries for NO adsorption on MgO, where there is no option for back-donation, have been found in the PW91 calculations of Schneider and coworkers [117].

The use of HF-like terms in Equation 8.40 suggests that just using HF itself for these types of material may be preferable. Indeed Towler and coworkers have shown that UHF correctly predicts the anti-ferromagnetic state to be lower in energy than either the ferromagnetic state or a solution with spins paired on a site-by-site basis. However, their estimated band gap of around 13.6 eV is a significant overestimate of the experimental value of 3.8 eV [58]. A much better agreement between calculated and experimental band gaps can be obtained with the hybrid B3LYP function, which gives 3.9 eV in this case [57].

Indeed, in these problems involving electron localization, hybrid functionals provide an alternative approach that has the advantage that exchange is applied uniformly to the electron density and not just to the transition metal centers. In the next section we look at examples using either DFT + U or hybrid functionals to examine defect states on oxide surfaces.

8.4.5
Defects on the Surfaces of Transition Metal Oxides

Anion defects on oxide surfaces are important centers for adsorption and activation of molecules in catalysis. For example, oxidation reactions following a Mars–van Krevelen mechanism require oxygen transfer from a surface to an

adsorbate, a process that creates an anion defect. Reduction of a metal oxide in its simplest form can be thought of as the liberation of oxygen:

$$M_mO_n = M_mO_{n-1} + 2e + \frac{1}{2}O_2(g) \tag{8.42}$$

In a calculation, m and n define the stoichiometry of the simulation cell, and the two electrons that remain after a surface O^{2-} ion has formed part of the neutral $O_2(g)$ molecule have been written explicitly. Using a periodic approach it should be remembered that the defect will be repeated in neighboring cells. To obtain results relevant to isolated defect sites requires cell sizes large enough to allow interactions between the defect and its own images to be neglected.

In alkaline earth oxides such as MgO, the two electrons of Equation 8.42 are known to be localized at the defect site by the Madelung potential of the solid [55]. However, in reducible oxides such as TiO_2 there is the alternative of localizing the electrons at metal sites to give two Ti^{3+} centers as shown schematically in Figure 8.22. Reduction of a stoichiometric oxide in this way is a local event giving an electronic structure in which the reduced metal centers are mixed in with fully oxidized ions. As we have seen, the correct modeling of charge and spin states in such a system requires a balanced treatment of exchange and correlation energies and is currently best achieved using either hybrid functionals or a DFT + U scheme.

Figure 8.22 also shows how heterolytic cleavage of water at such a defect site appears to repair the structure of the surface but leaves the two metal sites reduced. For the resulting hydroxylated surface it is possible to push electrons around to re-oxidize one center, creating an alternative description of the surface with a hydroxy radical. EELS experiments show little difference between the defective and hydroxylated surfaces [118] suggesting that water adsorption does not oxidize the defective surface. However, ultraviolet photoemission spectroscopy (UPS) does distinguish between them, suggesting that changes in the electronic energy levels at the vacancy do occur [119]. Surface hydroxyls are known to be important in the photocatalytic applications of TiO_2, so Valentin and Pacchioni set out to investigate the electronic

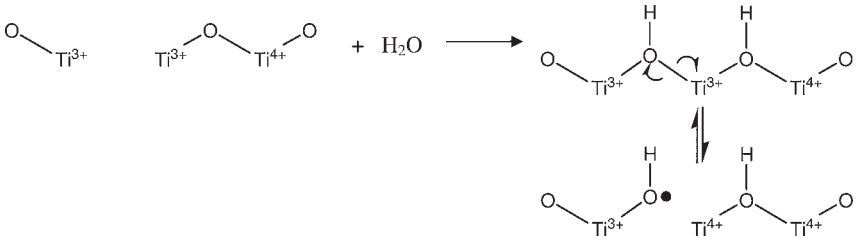

Figure 8.22 Reaction scheme for the adsorption of water at an O_{2c} vacancy on TiO_2(110). After adsorption there is the possibility of electron reorganization to give OH radical species.

nature of the surface hydroxyls and oxygen defect structures to attempt to clarify their electronic structure [120]. Their work compares the gradient-corrected DFT functional PBE and the hybrid B3LYP methods using the CRYSTAL localized basis set code. In the calculations the full electronic structure, including core states, is optimized self-consistently, avoiding the use of pseudopotentials.

Figure 8.23 compares the calculated band structures from PBE optimized geometries with B3LYP results both at the PBE geometry and after re-optimization of the atomic co-ordinates using the hybrid functional. In the PBE/PBE result the bands due to the hydroxylated Ti atom orbitals are contained within the conduction band states, much as the surface states of the perfect surface. Density and spin plots also show that the two electrons associated with the Ti^{3+} centers in Figure 8.22 are spread over the Ti ions of the entire slab. The geometries obtained from singlet and triplet electronic states are also identical and show only minor changes of bond lengths around the defect site. The Fermi level in this PBE calculation lies in the conduction band and so the pure functional is unable to reproduce the electronic structure even qualitatively. Fixing the PBE calculated geometry and carrying out a B3LYP calculation (PBE/B3LYP) does move the defect states out of the conduction band but the separation is small. The B3LYP geometry optimization gives different geometric structures for the singlet and triplet states, with the triplet 0.6 eV lower in energy. This B3LYP/B3LYP calculation gives a larger band gap than PBE as expected from the work of Zhang and coworkers on the dependence of E_G on the amount of exact exchange presented in Figure 8.6. The calculated adsorption energy for water at the vacancy site following the scheme in Figure 8.22 is 1.8 eV, which is in reasonable agreement with the experimental heat of adsorption of H_2O to this surface estimated using temperature programmed desorption (1.4 eV). The band structure from the B3LYP optimization shows two bands around 1 eV below the bottom of the conduction band. These bands are

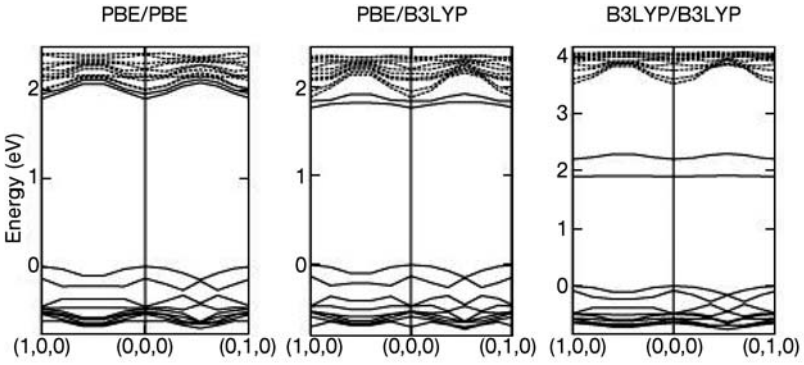

Figure 8.23 The calculated band structure for the O_{2c} defective TiO_2(110) surface with the geometry optimized using PBE and bands calculated at the PBE (PBE/PBE) or B3LYP (PBE/B3LYP) levels and with the geometry and bands calculated using B3LYP (B3LYP/B3LYP). From ref. [120].

narrow, indicating electron localization, and closely associated with two particular Ti surface ions. The first is the Ti_{6c} between the two hydroxyl groups, while the second is a nearby Ti_{5c}. The d orbitals involved are shown along with the calculated density of states plot of Figure 8.24. The lower of the two bands is for the Ti^{3+}_{6c} ion (Figure 8.24a) while the singly occupied d orbital of the under coordinated Ti^{3+}_{5c} ion gives a gap state nearer the conduction band (Figure 8.24b). The geometry relaxation of the surface leads to elongation of the Ti^{3+}—O bonds by up to 0.1 Å owing to the charge localization at these metal centers.

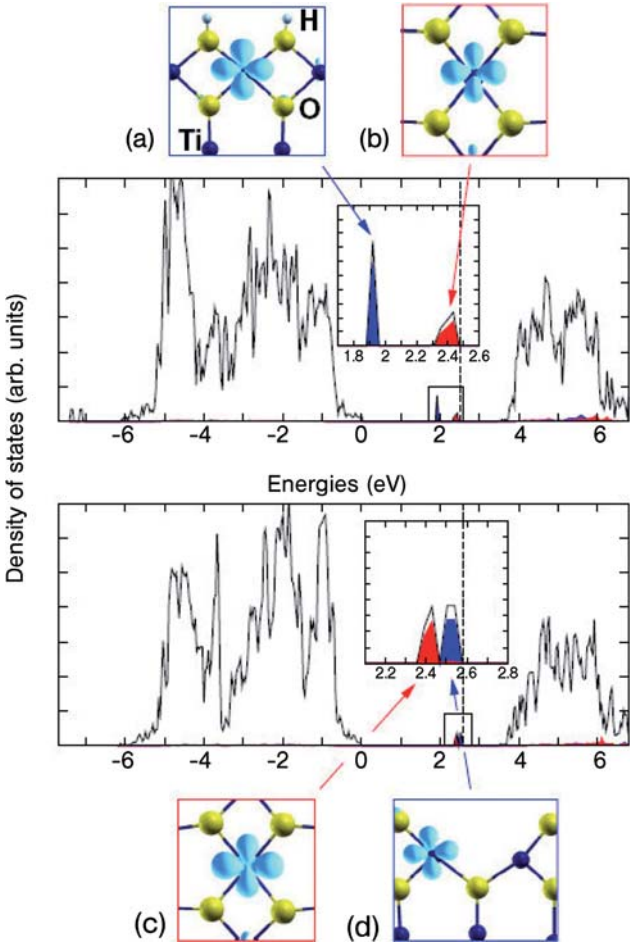

Figure 8.24 Calculated density of states for the O_{2c} defective TiO_2(110) surface (lower plot) and the same surface after hydroxylation (upper plot). Only the majority spin DOS is shown in each case. The metal orbitals responsible for the gap states are picked out in images (a)–(d). From ref. [120].

Calculations at the B3LYP level on the defective surface also show two localized d orbital states in the band gap. These are associated with the Ti_{5c}^{3+} site formed by removal of the O_{2c} atom (Figure 8.24d) and a nearby Ti_{5c} ion (Figure 8.24c) with the former higher in energy than the latter. This arrangement gives a smaller repulsion between the two electrons left by the vacancy formation than would placing them either side of the defect site as suggested in Figure 8.22. Comparing the calculated density of states in Figure 8.24 for the defective and hydroxylated surface confirms that there is a shift in the occupied energy levels, with the level associated with the Ti coordinated by O_{2c} oxygen atoms shifting down in energy by around 0.6 eV on adsorption of water. However, both structures indicate that the electrons left at the defect site by Equation 8.42 reside at metal centers, so that water does not act as a oxidizing agent in this case.

As an example application of the DFT + U method to the study of anion vacancies we turn to molybdenum oxide, MoO_3. Oxides of molybdenum have been known for some time to show activity for oxidation catalysis in which the oxide surface itself acts as the oxygen donor in Mars–van Krevelen-based mechanisms [121–123]. The structure of molybdenum trioxide is shown in Figure 8.25 and consists of bi-layers formed from edge-sharing MoO_6 octahedra, although there is considerable distortion away from O_h symmetry at Mo. There are three structurally distinct oxygen atoms: asymmetric, symmetric and terminal. The asymmetric bridging oxygen atoms are twofold coordinate, forming one long (2.25 Å) and one short (1.73 Å) bond with two Mo atoms in the same layer. The symmetric bridging oxygen atoms are threefold coordinate, with two equal bonds (1.95 Å) to Mo atoms in the same layer and one much longer interaction (2.33 Å) with a Mo atom of the

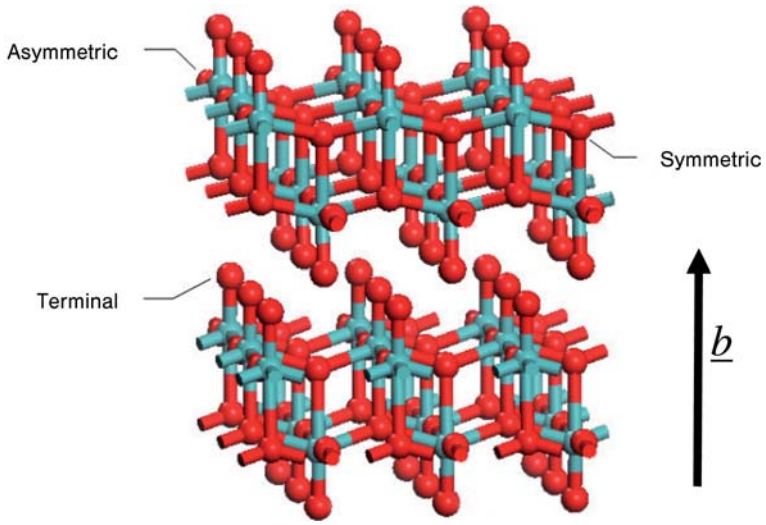

Figure 8.25 Two bilayers of bulk α-MoO_3. The three different types of O atoms are indicated (terminal, symmetric and asymmetric). Oxygen, red; molybdenum, blue.

other sub-layer. Finally, the terminal oxygen is bonded to only one Mo atom, forming the shortest Mo—O bond in the system (1.67 Å). The crystal unit cell is orthorhombic, with parameters $a = 3.9628$, $b = 13.855$ and $c = 3.6964$ Å for a unit cell containing Mo_4O_{12} [124]. The bi-layers are formed parallel to the (010) plane with no chemical bonds between them, making this the easiest surface to cleave.

MoO_3 is actually the fully oxidized end-member of a series of materials with stoichiometries from MoO_2 to MoO_3. For example, Wang and coworkers [125] identified two molybdenum sub-oxides $Mo_{18}O_{52}$ and Mo_8O_{23} by means of electron diffraction and high-resolution transmission electron microscopy (HRTEM) in combination with image simulation. These are derived from MoO_3 by crystallographic shearing to accommodate the large number of oxygen vacancies. However, the materials are related to the basic structure of MoO_3 with the $Mo_{18}O_{52}$(100) surface built up of MoO_3(010) terraces with MoO_3(100) edges and MoO_3(001) kinks [126]. Since the unit cells of these types of materials are complex, modeling studies have concentrated on the perfect MoO_3(010) and its point defects as representative of the terrace regions in the sub-stoichiometric material.

Different theoretical approaches have been used to study MoO_3 surfaces. Two major *ab initio* periodic HF studies were published almost at the same time by Papakondylis and Sautet [127] in 1996 and Corà and coworkers [128] in 1997. Papakondylis and Sautet used the CRYSTAL program to carry out HF-level calculations, with correlation energy estimates added using the PW91 functional with the HF density. They showed how the structure can thought of as built up from an MoO_3 molecule to the three-dimensional structure via a chain polymer and ribbon based on the components of the crystallographic bi-layers. The evolution of the band structure from the MoO_3 molecular orbitals could be followed through this sequence. The (100) surface of MoO_3 contains penta-coordinated Mo atoms, which are accessible Lewis acid centers. At the time automated geometry optimization was not possible, but the interaction of adsorbed H_2O with the fixed surface were optimized "by hand" based on the position and orientation of the molecule over the surface. This showed that the adsorption of H_2O molecules on these sites is favorable but the electron transfer between the surface and adsorbate was actually quite small.

Corà and coworkers also used HF and the localized basis set approach of CRYSTAL with *a posteriori* correlation corrections from PW91 [127]. They optimized the bulk structure by systematically varying each degree of freedom independently, starting with the weakest interaction first. This is the interlayer spacing for which they found a minimum, both at the correlated and the HF level. The GGA method gave an underestimated interlayer spacing while HF gave an overestimate, consistent with the expected under-binding in GGA approaches. The fact that minima are found at all indicates the presence of a weak attractive Coulombic force between bi-layers since the long-range correlation responsible for van der Waals interactions are absent in both approaches. They then analyzed the ground-state electronic properties of MoO_3, giving the electron density map shown in Figure 8.26a. Here the difference between the calculated density and that of a set

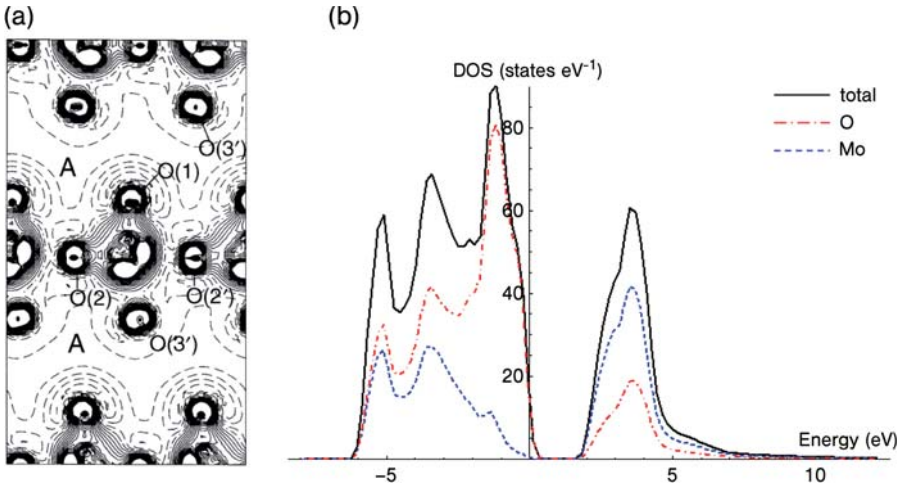

Figure 8.26 (a) Difference electronic charge density map (calculated bulk minus isolated Mo^{6+} O^{2-} ion densities), displayed in the crystallographic plane containing the central Mo and the vertices O(1)O(2′)O(3′)O(2) of one isolated MoO_6 octahedron. Continuous, dashed and dot-dashed lines correspond to positive, negative and zero difference respectively. The interval between the isodensity lines is 0.005 a.u. (electrons a_0^{-3}). The map extends beyond the central octahedron and includes part of the interlayer space, denoted by A. Taken from ref. [128]. (b) Total DOS curve (black solid) with decomposition into molybdenum (dashed) and oxygen (dot-dashed) contributions, for the MoO_3 bulk system. The energy origin is chosen as the highest occupied state and a Gaussian smearing width of 0.2 eV is applied.

of non-interacting ions placed at the lattice positions is plotted to show where charge has shifted to because of bonds formed between the ions. There is a net loss of charge from the interlayer region and a particularly notable increase in charge density between the Mo at the center of the figure and the associated terminal O atom. This, along with a Mulliken charge analysis, shows that the nature of the Mo—O interaction changes considerably according to the oxygen type, from strongly covalent for the shortest bond (terminal oxygen) to a predominantly ionic interaction for the longest bonds (interlayer Mo—O(symmetric)). The oxygen atoms denoted O(2) and O(2′) in Figure 8.26a are asymmetric, and this is clearly reflected in the asymmetry of the accumulation of charge density between the central Mo and O(2) or O(2′). The DOS plot from our own work [129] using PW91 functionals in the VASP code is shown in Figure 8.26b. The calculated valence band region has a width of 5.8 eV. The computed band gap is 2.1 eV and, as expected for a GGA method, this is an underestimate of the experimental value. MoO_3 is an n-type semiconductor with an indirect band gap between 2.9 eV and 3.15 eV [130]. The DOS shows that the valence band contains both metal and oxygen contributions, confirming that there is a considerable covalent character to the Mo—O bonds. Even so, the top of the valence band is largely O(2p) in

character and the bottom of the conduction band consists largely of Mo orbitals so the band gap is of a charge-transfer type.

Equation 8.42 indicates that the removal of a surface oxygen ion leaves two electrons to be accommodated by the surface. For the terminal oxygen vacancy on the MoO_3(010) surface we have compared PBE and PBE + U calculations using the VASP code [129]. In the PBE calculations the two electrons move into states in the conduction band and are spread evenly between the Mo centers of the simulation slab. In these calculations the surface structure is changed considerably, with one of the asymmetric oxygen atoms neighboring the defect moving to replace the lost terminal oxygen atom (Figure 8.27a). In the PBE + U case the two electrons are localized, reducing the single Mo ion from Mo^{6+} to Mo^{4+} and giving a triplet ground state. This is confirmed by a plot of the spin density difference ($\rho^{\alpha}(r) - \rho^{\beta}(r)$) which shows the two electron spins localized at the metal center where the terminal oxygen atom was removed (Figure 8.27c). The corresponding surface relaxation is considerably reduced, with the bridging symmetric and asymmetric oxygen atoms staying in plane (Figure 8.27b). As far as the rest of the lattice is concerned, the electronic structure of the Mo^{4+} center must closely resemble the original Mo^{6+}=O species. The value of U in these calculations was set to a value of 6.3 eV by comparing the calculated spin density with a reference cluster calculation at the B3LYP hybrid functional level.

Testing the accuracy of calculations on defects is more difficult, since experimentally the defects are a minority and randomly distributed species. However, we have been to make comparisons with surface spectroscopy results. Queeney and Friend have synthesized oxidized Mo(110) surfaces with specific types of oxygen coordination and characterize them using infrared and electron energy loss techniques [131, 132]. During the oxidizing process, two distinct vibrational frequencies υ(Mo=O) peaks were resolved at 992 and 1016 cm^{-1} using infrared spectroscopy. These are higher in frequency than any other surface vibrations owing to the high bond order between Mo and terminal oxygen atoms. When total oxidation was achieved by maintaining a flow of O_2 following high-temperature oxidation, all terminal (Mo=O) sites were populated, and a single υ(Mo=O) at 996 cm^{-1} was observed. Using the numerical second derivative approach the vibrational frequencies of $M{=}O_{term}$ were calculated for our perfect surface and for the terminal oxygen groups neighboring the defect site. This gave values of 1023 cm^{-1} and 995 cm^{-1} suggesting that the high-frequency peak seen experimentally is in areas that are relatively defect free while the lower frequency may be assigned to terminal oxygen atoms near to defects in the partially oxidized film.

Our final example is a study using DFT + U of the oxidation of CO over ceria. This concerns the reduction of surface sites with the simultaneous oxidation of an adsorbate. According to PW91 calculations [108] the most stable surfaces of fully oxidized CeO_2 are (111), (110) and (100), with calculated surface energies of 0.68, 1.01 and 1.41 $J\,m^{-2}$ respectively. Nolan and Watson [133] have carried out calculations on CO adsorption over these preferred surfaces using PW91 coupled with the Hubbard model using a value of U = 5 eV based on studies of the defective CeO_2 surface [134]. The adsorption of CO on the (111) surface is found

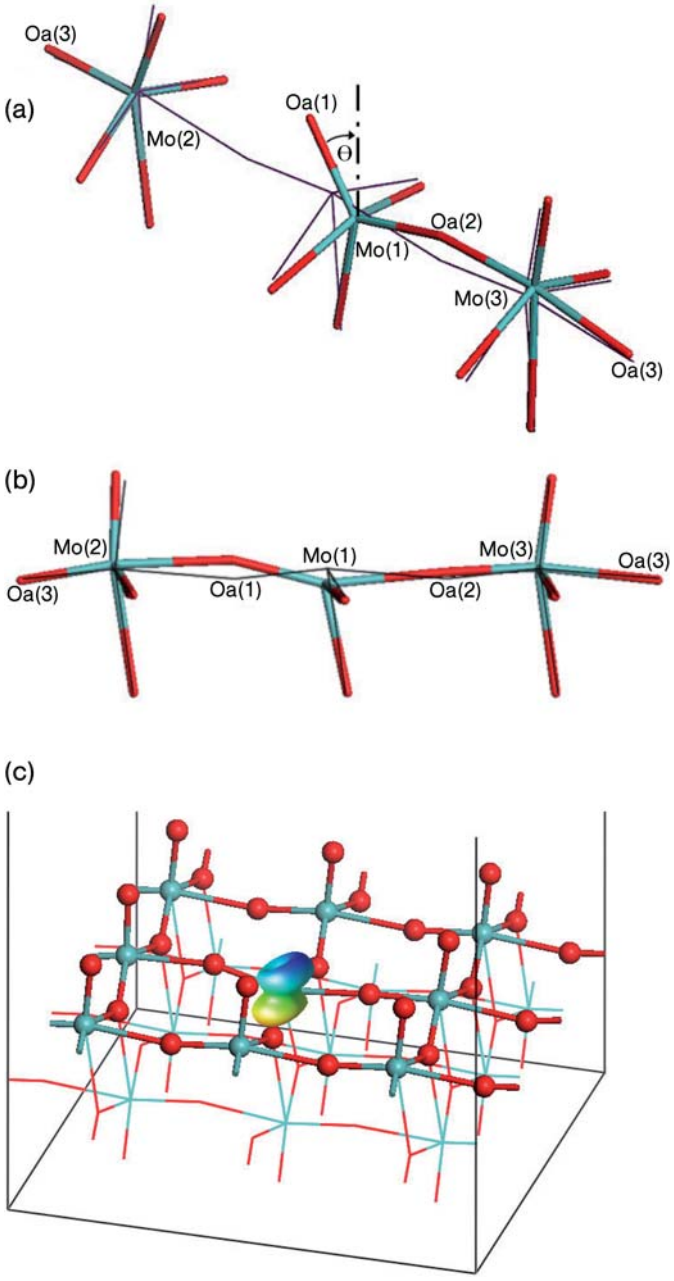

Figure 8.27 (a) Chain of sites along the asymmetric oxygen direction taken from the PBE relaxed MoO_3(010) surface with a terminal oxygen atom vacancy; the structure of the perfect surface is overlaid as a line drawing. (b) As (a) for the PBE + *U* optimization. (c) The calculated spin density for the PBE + *U* calculation showing the full simulation cell for parts (a) and (b).

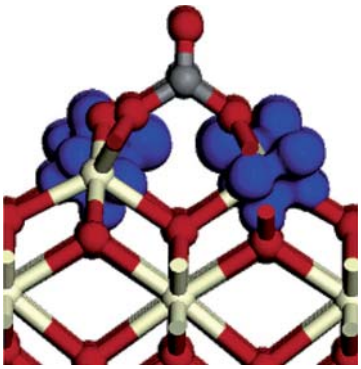

Figure 8.28 The spin density (blue) for CO chemisorption on the (100) surface of ceria. Taken from ref. [133]. Oxygen, red; Carbon, grey; Cerium, light yellow.

to be typical of physisorption, with an interaction energy of only $-25\,\mathrm{kJ\,mol^{-1}}$ and no structural alteration of either CO or the surface. Over the other two planes, initial placement of the CO molecule in a surface site bridging two oxygen ions resulted in the spontaneous formation of a carbonate CO_3^{2-} species. This involves removal of two O atoms and two electrons from the surface and so two Ce centers are reduced from Ce^{4+} to Ce^{3+} at the same time. In the calculated spin densities, Figure 8.28, the two reduced Ce centers are clearly seen with the additional electrons entering f states.

8.5 Conclusions

We have tried to highlight in this chapter the differences between the major computational methods for the simulation of the electronic structure of materials based on periodic boundary conditions. HF theory has a well defined theoretical framework but ignores correlation energy from the outset. This is introduced via the density in LSDA and GGA methods but at the expense of a less well defined treatment of exchange. Even so the surface structure of stoichiometric main group oxides is well described by either approach. The electronic states are less satisfactory, with HF tending to severely overestimate and DFT to underestimate band gaps. For catalysis, the empty states in the conduction band or in gap states are responsible for Lewis acidity and so an accurate description of the energies of these states is desirable. We have seen how hybrid functionals can correct for the underestimation of the band gap in DFT by including some proportion of exact exchange.

For transition metal oxides with partially filled d states, the balance between Coulomb and exchange interactions is even more critical. DFT strongly underestimates the exchange gap present in materials with magnetic order such as NiO, while it is again overestimated in HF. This can be corrected either through hybrid functionals or with the DFT + U approach.

In defects on transition metal oxides DFT again fails, giving structures that show unlikely relaxations and tending to delocalize electrons associated with the defect into conduction band states. Hybrid functionals and DFT + U have also been used to correct the models in these cases, giving a localized picture of surface reduction. These methods are now able to give useful descriptions of reactions at these defect sites, including the transfer of electrons between surface and adsorbate required in redox chemistry.

The DFT + U method is a pragmatic correction for the on-site Coulomb and exchange interactions at metal centers. Its parameterized nature does not sit well with "first principles" approaches, as the value of U must be set empirically. However hybrid DFT also involves parameterization, with the amount of exact exchange to add tailored to some physical property (such as the band gap or spin density). It does have the advantage that it is applied even-handedly to the electron density, whereas DFT + U is only applied to high angular momentum states (d and f functions). As more examples come to the fore the advantages and disadvantages of these two methods will become clearer.

All the examples used in this chapter have involved either surface properties alone or strong adsorbate/surface interactions. The weak adsorption of molecules to surfaces depends on van der Waals interactions. At the electronic structure level these require long-range correlation effects to be accounted for and so neither HF, DFT or the admixtures discussed so far give a good description. A brief mention of MP2 was given in the introduction and this extension of HF is able to treat the weak interactions of alkanes with zeolite frameworks [8]. However, this is likely to remain a computationally expensive option in the solid state. New functionals are appearing in this area specifically aimed at the long-range correlation problem and promise to advance the field further [135].

Acknowledgments

The projects from which our own illustrative calculations were drawn for this chapter made use of the Mott2 and HPCx facilities through the Materials Consortium. We are also indebted to Prof Graeme Watson and Dr Mark Bankhead for use of some of their data and for useful discussions on all the topics presented.

References

1 Sauer, J., Ugliengo, P., Garrone, E. and Saunders, V.R. (1994) *Chemical Reviews*, **94**, 2095.

2 Haber, J. and Witko, M. (2003) *Journal of Catalysis*, **216**, 416.

3 Bromley, S.T., French, S.A., Sokol, A.A., Catlow, C.R.A. and Sherwood, P. (2003) *Journal of Physical Chemistry B*, **107**, 7045.

4 See for example Jensen, F. (2007) *Introduction to Computational Chemistry*, 2nd edn, John Wiley & Sons, Inc.

5 See for example Cramer, C.J. (2004) *Essentials of Computational Chemistry*, John Wiley & Sons, Inc.

6 For an introduction to MP2 methods see: Atkins, P. and Friedman, R. (1997)

Molecular Quantum Mechanic, Oxford University Press.
7 For a detailed discussion of CI approaches see: Szabo, A. and Ostlund, N.S. (1989) *Modern Quantum Chemistry, Introduction to Advanced Electronic Structure Theory*, McGraw-Hill.
8 Tuma, C. and Sauer, J. (2006) *Physical Chemistry Chemical Physics*, **8**, 3955.
9 Hohenberg, P. and Kohn, W. (1964) *Physical Review*, **136**, B864.
10 Kohn, W. and Sham, L.J. (1965) *Physical Review*, **140**, A1133–A1138.
11 Ceperley, D.M. and Alder, B.J. (1980) *Physical Review Letters*, **45**, 566.
12 Vosko, S.H., Wilk, L. and Nusair, M. (1980) *Canadian Journal of Physics*, **58**, 1200.
13 Perdew, J.P. and Wang, Y. (1992) *Physical Review B*, **45**, 13244.
14 Perdew, J.P., Chevary, J.A., Vosko, S.H., Jackson, K.A., Pederson, M.R., Singh, D.J. and Fiolhais, C. (1992) *Physical Review B*, **46**, 6671.
15 Juan, Y.-M. and Kaxiras, E. (1993) *Physical Review B*, **48**, 14944.
16 Perdew, J.P., Burke, K. and Ernzerhof, M. (1996) *Physical Review Letters*, **77**, 3865–8.
17 Hammer, B., Hansen, L.B. and Nørskov, J.K. (1999) *Physical Review B*, **59**, 741.
18 Perdew, J.P. (1991) in *Electronic Structure of Solids* (eds P. Ziesche and H. Eschrig), Akademie Verlag, Berlin, p. 11.
19 Perdew, J.P., Chevary, J.A., Vosko, S.H., Jackson, K.A., Pederson, M.R., Singh, D.J. and Fiolhais, C. (1992) *Physical Review B*, **46**, 6671.
20 Becke, A.D. (1988) *Physical Review A*, **38**, 309.
21 Lee, C., Yang, W. and Parr, R.G. (1988) *Physical Review B*, **37**, 78.
22 Becke, A.D. (1993) *Journal of Chemical Physics*, **98**, 5648.
23 A thematic volume of Chemical Reviews covers this area: (2000) *Chemical Reviews*, **100**.
24 For a recent review see: Santoro, F., Barone, V., Benzi, C. and Improta, R. (2007) *Theoretical Chemistry Accounts*, **117**, 1073.
25 Payne, M.C., Teter, M.P., Allan, D.C., Arias, T.A. and Joannopoulos, J.D. (1992) *Reviews of Modern Physics*, **64**, 1045.
26 Hill, J-R, Subramanian L. and Maiti, A. (2005) *Molecular Modeling Techniques in Material Sciences*, CRC Press.
27 Jaffe, J.E., Pandey, R. and Kunz, A.B. (1991) *Physical Review B*, **43**, 14030.
28 Monkhorst, H.J. and Pack, J.D. (1976) *Physical Review B*, **13**, 518.
29 Kihlborg, L. (1963) *Arkiv for Kemi*, **21**, 357.
30 Bankhead, M. (1999) Theoretical Investigation of Alumina Based Fluorination Catalysts, PhD thesis, University of Liverpool.
31 *Details of the CRYSTAL code are given in*: Dovesi, R., Saunders, V.R., Roetti, C., Orlando, R., Zicovich-Wilson, C.M., Pascale, F., Civalleri, B., Doll, K., Harrison, N.M., Bush, I.J., D'Arco Ph. and Llunell, M. (2006) *CRYSTAL06 User's Manual*, University Of Torino, Torino. available from www.crystal.unito.it (accessed date: 13/06/08).
32 Orlando, R., Dovesi, R., Ugliengo, P., Roetti, C. and Saunders, V.R. (1999) *International Journal of Inorganic Materials*, **1**, 147.
33 Soler, J.M., Artacho, E., Gale, J.D., Garcia, A., Junquera, J., Ordejon P. and Sanchez-Portal, D. (2002) *Journal of Physics–Condensed Matter*, **14**, 2745.
34 *DMOL3* is commercial software available from Accelrys Software Inc. see: www.accelrys.com (accessed date: 13/06/08).
35 Towler, M.D., Allan, N.L., Harrison, N.M., Saunders, V.R., Mackrodt, W.C. and Aprà, E. (1994) *Physical Review B*, **50**, 504.
36 (a) Kresse, G. and Hafner, J. (1993) *Physical Review B*, **47**, 558. (b) Kresse, G. and Hafner, J. (1994) *Physical Review B*, **49**, 14251. (c) see also http://cms.mpi.univie.ac.at/vasp (accessed date: 13/06/08).
37 For information on the *DACAPO* code see http://www.fysik.dtu.dk/campos (accessed date: 13/06/08).
38 Clark, S.J., Segall, M.D., Pickard, C.J., Hasnip, P.J., Probert, M.J., Refson, K. and Payne, M.C. (2005) *Zeitschrift Fur Kristallographie*, **220**, 567. (b) Segall, M.D., Lindan, P.J.D., Probert, M.J., Pickard,

C.J., Hasnip, P.J., Clark, S.J. and Payne, M.C. (2002) *Journal of Physics–Condensed Matter*, **14**, 2717. (c) CASTEP is currently administered by UKCP see: http://www.cse.scitech.ac.uk/cmg/NETWORKS/UKCP (accessed date: 13/06/08).

39 Car, R. and Parrinello, M. (1985) *Physical Review Letters*, **55**, 247, see also: www.cpmd.org (accessed date: 13/06/08).

40 Mulliken, R.S. (1955) *Journal of Chemical Physics*, **23**, 1833.

41 Bader, R. (1994) *Atoms in Molecules, a Quantum Theory*. International Series of Monographs on Chemistry 22. Clarendon Press.

42 Hamman, D.R., Schlüter, M. and Chiang, C. (1979) *Physical Review Letters*, **43**, 1494.

43 (a) Zunger, A. and Cohen, M.L. (1978) *Physical Review B*, **18**, 5449. (b) Zunger, A. and Cohen, M.L. (1979) *Physical Review B*, **20**, 4082.

44 Vanderbilt, D. (1990) *Physical Review B*, **41**, 7892.

45 Blöchl, P.E. (1994) *Physical Review B*, **50**, 17953.

46 Kresse, G. and Joubert, D. (1999) *Physical Review B*, **59**, 1758.

47 Gale, J.D., Rohl, A.L., Milman, V. and Warren, M.C. (2001) *Journal of Physical Chemistry B*, **105**, 10236.

48 Saalfeld, H. and Wedde, M. (1974) *Zeitschrift Fur Kristallographie*, **139**, 129.

49 Mann, R., Hutchings, G.J., van Rensburg, W. and Willock, D.J. (2003) Catalysis in application, in *Proceedings of the International Symposium on Applied Catalysis, Glasgow 2003* (eds S.D. Jackson, J.S.J. Hargreaves and D. Lennon), Royal Society of Chemistry Publications, p. 247.

50 Skorodumova, N.V., Hermansson, K. and Johansson, B. (2005) *Physical Review B*, **72**, 125414.

51 See for example, Ashcroft, N.W. and Mermin, N.D. (1976) *Solid State Physics*, Saunders College Publishing.

52 Bredow, T. and Gerson, A.R. (2000) *Physical Review B*, **61**, 5194.

53 Roessler, D.M. and Walker, W.C. (1967) *Physical Review*, **159**, 733.

54 Garrone, E., Zecchina, A. and Stone, F.S. (1980) *Philosophical Magazine Part B*, **42**, 683.

55 Kantorovich, L.N., Holender, J.M. and Gillan, M.J. (1995) *Surface Science*, **343**, 221.

56 Lide, D.R. (ed.) (2007) *C.R.C. Handbook of Chemistry and Physics*, 88th edn, CRC Press.

57 Muscat, J., Wander, A. and Harrison, N.M. (2001) *Chemical Physics Letters*, **342**, 397.

58 Cox, P.A. (1995) *Transition Metal Oxides: An Introduction to their Electronic Structure and Properties*, Clarendon Press, Oxford.

59 Zhang, Y.-F., Lin, W. and Li, Y., Ding, K.-N. and Li, J.-Q. (2005) *Journal of Physical Chemistry B*, **109**, 19270.

60 Cora, F., Alfredsson, M., Mallia, G., Middlemiss, D.S., Mackrodt, W.C., Dovesi, R. and Orlando, R. (2004) *Principles and Applications of Density Functional Theory in Inorganic Chemistry II: Structure and Bonding*, Vol. 113, Springer-Verlag, Berlin, p. 171.

61 Digne, M., Sautet, P., Raybaud, P., Toulhoat, H. and Artacho, E. (2002) *Journal of Physical Chemistry B*, **106**, 5155.

62 Zigan, F., Joswig, W. and Burger, N. (1978) *Zeitschrift Fur Kristallographie*, **148**, 255.

63 Krokidis, X., Raybaud, P., Gobichon, A-E, Rebours, B., Euzen, P. and Toulhoat, H. (2001) *Journal of Physical Chemistry B*, **105**, 5121.

64 Sohlberg, K., Pennycook, S.J. and Pantelides, S.T. (1999) *Journal of the American Chemical Society*, **121**, 7493.

65 Gates, B.C. (1991) *Catalytic Chemistry*, John Wiley & Sons, Inc.

66 McInroy, A.R., Lundie, D.T., Winfield, J.M., Dudman, C.C., Jones, P. and Lennon, D. (2007) *Applied Catalysis B–Environmental*, **70**, 606.

67 Yourdshahyan, Y., Ruberto, C., Halvarsson, M., Bengtsson, L., Langer, V. and Lundqvist, B.I. (1999) *Journal of the American Ceramic Society*, **82**, 1365.

68 Chatfield, C., Lindström, J.N. and Sjöstrand, M.E. (1989) *Journal de Physique Colloques*, **C5**, 377.

69 Levin, I. and Brandon, D. (1998) *Journal of the American Ceramic Society*, **81**, 1995.

70 Verwey, E.J.W. (1935) *Zeitschrift Fur Kristallographie*, **91**, 317.

71 Lippens, B.C. and DeBoer, J.H. (1964) *Acta Crystallographica*, **17**, 1312.

72 Zhou, R.-S. and Snyder, R.L. (1991) *Acta Crystallographica*, **B47**, 617.

73 Lee, M.-H., Cheng, C.-F., Heine, V. and Klinoski, J. (1997) *Chemical Physics Letters*, **265**, 673.

74 Paglia, G., Buckley, C.E., Rohl, A.L., Hunter, B.A., Hart, R.D., Hanna, J.V. and Byrne, L.T. (2003) *Physical Review B*, **68**, 144110.

75 Watson, G.W. and Willock, D.J. (2001) *Chemical Communications*, 1076.

76 Gutiérrez, G., Taga, A. and Johansson, B. (2001) *Physical Review B*, **65**, 012101.

77 Paglia, G., Rohl, A.L., Buckley, C.E. and Gale, J.D. (2005) *Physical Review B*, **71**, 224115.

78 Sun, M., Nelson, A.E. and Adjaye, J. (2006) *Journal of Physical Chemistry B*, **110**, 2310.

79 Guenard, P., Renaud, G., Barbier, A. and Gautier-Soyer, M. (1998) *Surface Review and Letters*, **5**, 321.

80 Lindsay, R., Wander, A., Ernst, A., Montanari, B., Thornton, G. and Harrison, N.M. (2005) *Physical Review Letters*, **94**, 246102.

81 Tasker, P.W. (1979) *Journal of Physics C–Solid State Physics*, **12**, 4977.

82 Noguera, C. (2000) *Journal of Physics–Condensed Matter*, **12**, R367.

83 Shannon, R.D. (1976) *Acta Crystallographica*, **A32**, 751.

84 Onishi, H., Egawa, C., Aruga, T. and Iwasawa, Y. (1987) *Surface Science*, **191**, 479.

85 Ruberto, C., Yourdshahyan, Y. and Lundqvist, B.I. (2003) *Physical Review B*, **67**, 195412.

86 Boetteger, J.C. (1994) *Physical Review B*, **49**, 16798.

87 Tosi, M.P. (1964) in *Solid State Physics*, Vol. 16 (eds F. Seitz and D. Turnbull), Academic, New York, p. 1.

88 (a) Jura, G. and Garland, C.W. (1953) *Journal of the American Chemical Society*, **74**, 6033. (b) Jura, G. and Garland, C.W. (1953) *Journal of the American Chemical Society*, **75**, 1006.

89 Foulkes, W.M.C., Mitaš, L., Needs, R.J. and Rajagopal, G. (2001) *Reviews of Modern Physics*, **73**, 33.

90 Alfè, D. and Gillan, M.J. (2006) *Journal of Physics–Condensed Matter*, **18**, L435.

91 Goniakowski, J., Holender, J.M., Kantorovich, L.N. and Gillan, M.J. (1996) *Physical Review B*, **53**, 957.

92 Alfonso, D.R., Snyder, J.A., Jaffe, J.E., Hess, A.C. and Gutowski, M. (2000) *Physical Review B*, **62**, 8318.

93 Manassidis, I. and Gillan, M.J. (1994) *Journal of the American Ceramic Society*, **77**, 335.

94 Batyrev, I.G., Alavi, A. and Finnis, M.W. (2000) *Physical Review B*, **62**, 4698.

95 Di Elice, R. and Northrup, J.E. (1999) *Physical Review B*, **60**, R16287.

96 Marmier, A. and Parker, S.C. (2004) *Physical Review B*, **69**, 115409.

97 Ahn, J. and Rabalais, J.W. (1997) *Surface Science*, **388**, 121.

98 Soares, E.A., Van Hove, M.A., Walters, C.F. and McCarthy, K.F. (2002) *Physical Review B*, **65**, 195405.

99 Choi, J.H., Kim, D.Y., Hockey, B.J., Wiederhorn, S.M., Handwerker, C.A., Blendell, J.E., Carter, W.C. and Roosen, A.R. (1997) *Journal of the American Ceramic Society*, **80**, 62.

100 Hass, K.C., Schneider, W.F., Curioni, A. and Andreoni, W. (2000) *Journal of Physical Chemistry B*, **104**, 5527.

101 The background theory for estimating free energy barriers using constrained dynamics is covered in more detail in a similar study of dimethyl ether formation from methanol in zeolites: Hytha, M., Štich, I., Gale, J.D., Terakura, K. and Payne, M.C. (2001) *Chemistry–A European Journal*, **7**, 2521.

102 Bankhead, M., Watson, G.W., Hutchings, G.J., Scott, J. and Willock, D.J. (2000) *Applied Catalysis A, General*, **200**, 263.

103 Abrahams, S.C. and Bernstien, J.L. (1971) *Journal of Chemical Physics*, **55**, 3206.

104 Bredow, T., Giordano, L., Cinquini, F. and Pacchioni, G. (2004) *Physical Review B*, **70**, 35419.

105 Thompson, S.J. and Lewis, S.P. (2006) *Physical Review B*, **73**, 073403.

106 Swamy, V., Muscat, J., Gale, J.D. and Harrison, N.M. (2002) *Surface Science*, **504**, 115.

107 Batyrev, I., Alavi, A. and Finnis, M.W. (1999) *Faraday Discussions*, **114**, 33.

108 Parker, S.C., Kerisit, S., Marmier, A., Grigoleit, S. and Watson, G.W. (2003) *Faraday Discussions*, **124**, 155.

109 Reuter, K. and Scheffler, M. (2001) *Physical Review B*, **65**, 035406.

110 See for example: Kittel, C. (2004) *Introduction to Solid State Physics*, 8th edn, John Wiley & Sons, Inc.

111 (a) Terakura, K., Oguchi, T., Williams, A.R. and Kübler, J. (1984) *Physical Review Letters*, **52**, 1830. (b) Terakura, K., Oguchi, T., Williams, A.R. and Kübler, J. (1984) *Physical Review B*, **30**, 4734.

112 Anisimov, V.I., Zaanen, J. and Andersen, O.K. (1991) *Physical Review B*, **44**, 943.

113 Dudarev, S.L., Botton, G.A., Savrasov, S.Y., Humphreys, C.J. and Sutton, A.P. (1998) *Physical Review B*, **57**, 150.

114 Rohrbach, A., Hafner, J. and Kresse, G. (2004) *Physical Review B*, **69**, 075413.

115 Hoeft, J.T., Kittel, M., Polcik, M., Bao, S., Toomes, R.L., Kang, J.H., Woodruff, D.P., Pascal, M. and Lamont, C.L.A. (2001) *Physical Review Letters*, **87**, 086101.

116 Rohrbach, A. and Hafner, J. (2005) *Physical Review B*, **71**, 045405.

117 Schneider, W.F., Hass, K.C., Miletic, M. and Gland, J.L. (2002) *Journal of Physical Chemistry B*, **106**, 7405.

118 Henderson, M.A., Epling, W.S., Peden, C.H.F. and Perkins, C.L. (2003) *Journal of Physical Chemistry B*, **107**, 534.

119 Kurtz, R.K. (1989) *Surface Science*, **218**, 178.

120 Valentin, C.D. and Pacchioni, G. (2006) *Physical Review Letters*, **97**, 166803.

121 Lui, H.F., Lui, R.S., Liew, K.Y., Johnson, R.E. and Lunsford, J.H. (1984) *Journal of the American Chemical Society*, **106**, 4117.

122 Smith, M.R. and Ozkan, U.S. (1993) *Journal of Catalysis*, **142**, 226.

123 Taylor, S.H., Hargreaves, J.S.J., Hutchings, G.J., Joyner, R.W. and Lembacher, C.W. (1998) *Catalysis Today*, **42**, 217.

124 Kihlborg, L. (1963) *Arkiv for Kemi*, **21**, 357.

125 Wang, D., Dangsheng, S. and Schlögl, R. (2003) *Crystal Research and Technology*, **38**, 153.

126 Floquet, N. and Bertrand, O. (1988) *Surface Science*, **198**, 449.

127 Papakondylis, A. and Sautet, P. (1996) *Journal of Physical Chemistry*, **100**, 10681.

128 Corà, F., Patel, A., Harrison, N.M., Roetti, C. and Catlow, C.R.A. (1997) *Journal of Materials Chemistry*, **7**, 959.

129 Coquet, R. and Willock, D.J. (2005) *Physical Chemistry Chemical Physics*, **7**, 3819.

130 Krylov, O. (1980) *Catalysis by Non-Metals*, Academic Press, New York.

131 Queeney, K.T. and Friend, C.M. (1998) *Journal of Physical Chemistry B*, **102**, 5178.

132 Queeney, K.T. and Friend, C.M. (2000) *Journal of Physical Chemistry B*, **104**, 409.

133 Nolan, M. and Watson, G.W. (2006) *Journal of Physical Chemistry B*, **110**, 16600.

134 Nolan, M., Parker, S.C. and Watson, G.W. (2005) *Surface Science*, **595**, 223.

135 Chakarova-Käck, D.S., Borck, Ø., Schröder, E. and Lundqvist, B.I. (2006) *Physical Review B*, **74**, 155402.

9
Thermal Analysis and Calorimetric Methods

Simona Bennici and Aline Auroux

9.1
Introduction

Thermal analysis is a group of techniques that study the changes in the properties of a sample occurring while the sample is subjected to a controlled temperature program. Calorimetric methods measure heat changes that occur during a process. Important changes on a molecular level occur in a material as it is heated, and their study may enable the analyst to draw valuable conclusions about the sample, its previous history, preparation, chemical nature and the likely behavior during its proposed use. The temperature at which a particular event takes place, or the temperature range over which a reaction happens, is often characteristic of the nature and history of a sample [1]. Calorimetry encompasses a very large variety of techniques, including titration, flow, reaction or sorption calorimetry. The most frequently used thermal analysis techniques in catalysis and the properties they measure are shown in Table 9.1, together with the names most usually employed for them.

During investigation of a new material it is unlikely that any single thermal analysis technique will provide all the information required to understand its behavior. Complementary information is usually needed, which may be from another simultaneous thermal technique such as thermogravimetric–differential scanning calorimetric–mass spectrometry (TG-DSC-MS), gas chromatography (TG-GC, or DSC-GC), or spectroscopic methods such as IR spectroscopy or X-ray photoelectron spectroscopy (XPS).

All these techniques, whether used by themselves or coupled to other techniques, are fully described in extended reviews [1–3].

Static or flow adsorption microcalorimetry, less extensively used, is a very powerful method for describing surface reactions and merits a more detailed overview.

In heterogeneous gas–solid systems, a catalytic reaction proceeds according to the following stages: adsorption of the reactant on the surface of the catalyst, reaction on the surface, desorption of the products from the surface. All these steps

Metal Oxide Catalysis. Edited by S. David Jackson and Justin S. J. Hargreaves

ISBN: 978-3-527-31815-5

Table 9.1 Thermal analysis techniques in catalysis.

Technique	Abbreviation	Property	Uses
Thermogravimetry or Thermogravimetric analysis	TG TGA	mass mass	decomposition, oxidation, reduction
Differential thermogravimetry	DTG	dm/dt	
Differential thermal analysis	DTA	temperature difference	reactions, phase changes
Differential scanning calorimetry	DSC	power difference or heat flow rate	heat capacity, reaction, adsorption, desorption
Heat flow calorimetry		heat flow	

involve the surface active sites, whose redox or acid–base properties are important factors which determine their industrial application.

Many industrial processes are based on acid–base- or redox-catalyzed reactions. The majority of these processes use heterogeneous catalysts, particularly mixed or supported oxides possessing both hydroxyl groups (Brønsted acid or basic sites) and coordinatively unsaturated metallic cations (Lewis acid sites) and anions (Lewis basic sites such as O^{2-} ions). A good description and knowledge of the surface active sites is essential for improved understanding of the relationships between their physico-chemical properties and their catalytic behavior (activity, selectivity, stability, etc.) The heterogeneity of oxides in terms of composition (particularly between the bulk and the surface), nature (Brønsted, Lewis), strength, concentration and distribution of sites renders the characterization more complex. Moreover, the hydrophilic or hydrophobic character of the surface is an important parameter that should be known.

The main purpose of this chapter is to review the applications of thermal analysis and calorimetric techniques to the study of catalysts such as oxides, heteropolyanions, hydrotalcites, layered silicates and microporous or mesoporous molecular sieves. A brief summary of studies that made use of calorimetry to characterize crystalline or amorphous oxides and related materials is also presented.

From the literature it is apparent that microcalorimetry is very useful in providing information on the strength and distribution of acidic and basic sites of catalysts. The technique for determining the acid site distribution is quite well developed, especially if ammonia is used as the basic probe molecule. Moreover, the energetics of surface reactions, including oxidation and reduction of metal oxides, oxidation of adsorbed hydrocarbons or hydrogen and decomposition reactions can be determined directly by calorimetry [4].

9.2
Techniques and Procedures

9.2.1
Experimental Techniques

The thermal techniques most commonly used to investigate the acid–base or redox character of solid surfaces are differential thermal analysis (DTA), thermogravimetric (TG) and differential thermogravimetric (DTG) methods, differential scanning calorimetry (DSC) and calorimetry. These techniques can be used either by themselves, or in conjunction with other techniques (for instance, TG-DSC, calorimetry-volumetry, DSC-chromatography, etc.) [5, 6].

Techniques such as DTA, TG or DSC study the thermal behavior of a catalyst as it undergoes heating at a constant rate. For example, DTA relies on the measurement, as function of time, of the difference between the temperature of the sample (T_s) and that of a reference material (T_r), upon heating both materials in a furnace. $\Delta T = T_s - T_r$ is related to the heat evolved (or absorbed) by the sample at a time when the sample undergoes an endothermic or exothermic reaction. In the TG and DTG methods, the variation with time of the sample mass (dm or dm/dt) is measured as a function of temperature while the sample is heated at a constant rate [7].

Finally, in the case of DSC, the measured quantity is the heat flow evolved per unit time by the sample as it is being heated at a constant rate [8]. For the determination of the heat of a given process using DSC, it is necessary not only to measure the DSC curve, but also to construct carefully the baseline [9]. These techniques are preferentially used for studying the redox character of catalyst surfaces. In contrast, in the adsorption microcalorimetry technique, the sample is kept at a constant temperature while a probe molecule adsorbs onto its surface, and a heat flow detector emits a signal proportional to the amount of heat transferred per unit time. Adsorption microcalorimetry is a very powerful tool for the energetic characterization of solid surfaces, as well as for the thermodynamic description of solid–gas interface phenomena. Several review articles describing this technique in detail and the operating conditions are available [2, 4, 8, 10–17].

The definition of the various heats of adsorption/desorption and their relationship with thermodynamic quantities directly obtainable by calorimetry are given in Table 9.2 [2].

Adsorption calorimetry consists of the coupling of a heat flow calorimeter with a system able to monitor the adsorption of a probe molecule by determining the amount of probe gas that has reacted with the solid under study. It is probably the most direct method for describing in detail both the quantitative and energetic features of surface sites. The adsorption of a probe molecule is an exothermic phenomenon ($\Delta H_{ads} < 0$), while desorption processes are associated with endothermic peaks ($\Delta H_{des} > 0$). Heats of reduction are generally associated with an

Table 9.2 Definition of the various heats of adsorption/desorption.

Name	Symbol	Unit	Definition
Integral heat of adsorption	Q_{int}	J	Quantity of heat evolved when n_a moles are adsorbed at constant temperature on an adsorbent initially *in vacuo*, without a change in the volume of the cell: $Q_{int} = n_a(U_a - U_g)$
Molar integral heat	$-Q_{int} = Q_{int}/n_a$	J mol^{-1}	Integral heat per mole adsorbed
Differential heat of adsorption or adsorption enthalpy	$Q_{diff} = -\Delta H_{ads}$	J mol^{-1}	Defined from integral heat by: $Q_{diff} = (\partial Q_{int}/\partial n_a)_{T,A}$
Isosteric heat	Q_{st}	J mol^{-1}	Heat of adsorption calculated from isotherms of adsorption: $Q_{st} = (RT^2(\partial \ln P/\partial T)_{na}$ (Clapeyron)
Desorption energy	$E_d = \Delta H_{des}$	J mol^{-1}	Heat of adsorption derived from TPD: $E_d = k_B T_{max}[\ln(\nu T_{max}/\beta) -$ const] (Redhead equation)

a, the adsorbed phase; A, surface area of the adsorbent; T, temperature of the gaseous phase; n, number of moles; U, internal energy; P, pressure; k_B, Boltzmann constant; T_{max}, temperature of the maximum desorption rate; ν, pre-exponential frequency factor; β, heating rate dT/dt.

endothermic peak and a weight loss, while heats of oxidation are associated with an exothermic peak and a weight gain.

9.2.1.1 A Static Method: Coupling Calorimetry and Volumetry

The simultaneous assessment of the adsorbed quantity of a suitable probe molecule and the heats evolved at increasing coverage makes it possible to picture the heterogeneity of the surface (structural and/or chemical) by processing the overall set of combined volumetric and calorimetric data.

A system that links microcalorimetry to the volumetric measurement of quantities of adsorbed reactants makes it possible to study gas–solid interactions and catalytic reactions. This system works under static vacuum. The admission of gases into the calorimeter can be performed either in a discontinuous way (by successive doses) by means of a valve, or in a continuous manner by means of a capillary. The classical technique of adsorption calorimetry by doses is the most appropriate way to measure the energy of interaction between the adsorbed species and the catalyst. If the surface can be *a priori* considered as heterogeneous, the heat of adsorption, the amount adsorbed and the kinetics of adsorption must be measured for very small successive doses of the adsorbate so as to obtain accu-

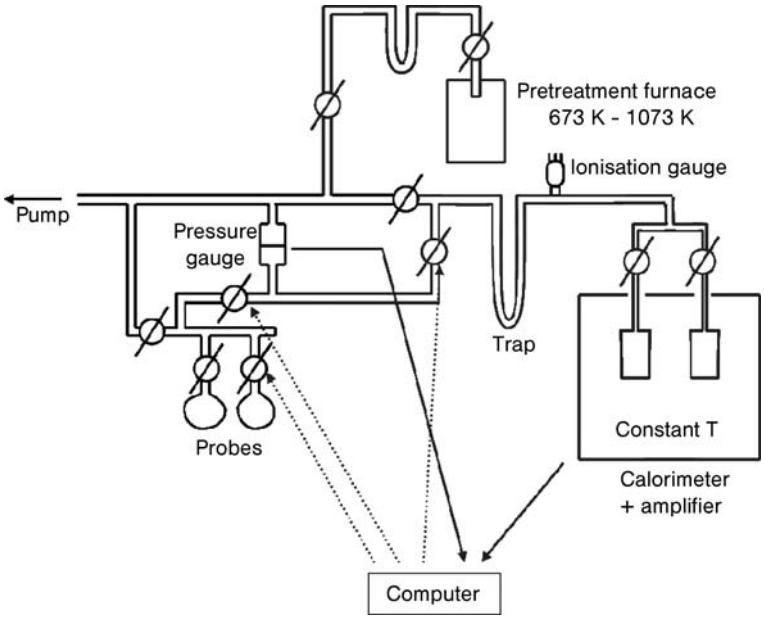

Figure 9.1 Schematic diagram of the volumetric-calorimetric line.

rate information on the variation of these quantities as a function of the coverage.

The volumetric determination of the adsorbed amount of gas is performed in a constant-volume vessel linked to a vacuum pump. The apparatus consists of two parts (Figure 9.1): the measuring element equipped with a capacitance manometer and the cell section, which includes the cells placed in the calorimeter (a sample cell in which the adsorbent solid is placed, and an empty reference cell). The volume of this vessel is determined by the expansion of a known quantity of gas, contained in the measuring part of the assembly, into the previously evacuated cell section.

This calibration must be made with the same gas and at the same temperature as the proposed study. The experiment consists of sending successive doses of the reactant gas onto the initially out-gassed catalyst and waiting for thermal equilibrium after each increment. The heat flow signal and the concomitant pressure change are continuously recorded. The aim is to minimize the volume of each dose in order to be able to observe any change as a function of the coverage as closely as possible. The adsorption is considered complete when, for a significant increase in pressure, there is no detectable heat evolution or gas adsorption. The adsorption temperature is maintained at a constant value (usually of the order of 353–423 K, in order to ensure that there are no diffusional restrictions and to ensure that adsorption is almost exclusively chemisorption). The irreversibly chemisorbed amount (V_{irr}) can be evaluated from the difference between the primary adsorption isotherm (adsorbed volume as a function of equilibrium pressure over

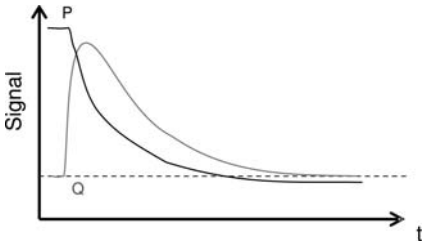

Figure 9.2 Recorded data (pressure and heat flow signals) for each dose of probe molecule as a function of time.

the sample) and a secondary isotherm obtained after desorption under vacuum and re-adsorption of the gaseous probe at the same temperature. This difference can be roughly interpreted as the amount of strong sites (often associated with adsorption heats of the order of at least 100–120 kJ mol^{-1}, depending on the probe molecule and the experimental conditions).

For each dose or expansion, the equilibrium data such as the pressure P_i and the integral evolved heat $\Delta Q_{\text{int},i}$, are measured. Kinetic results for each dose are also measured, such as the heat flow and the evolution of the gas pressure as a function of time. (Figure 9.2).

From these results we can also obtain the equilibrium pressure P, the adsorbed amount up to the dose i ($\Sigma \Delta n_{\text{a},i} = n_{\text{a}}$), and the corresponding evolved heat ($\Sigma \Delta Q_{\text{int},i} = Q_{\text{int}}$). These data can be expressed in five ways, as illustrated in Figure 9.3.

1. The volumetric isotherms (n_{a}, P) for a cycle consisting of adsorption I, desorption, and re-adsorption II (Figure 9.3a)

2. The corresponding calorimetric isotherms (Q_{int}, P) (Figure 9.3b).
   From these two types of isotherm (calorimetric and volumetric) the internal energy and the molar entropy of adsorption $\overline{S}_a = S_g + \frac{Q_{\text{int}}}{Tn_a} + \frac{R}{n_a}\int_0^{n_a} n_a d\ln P$ can be evaluated as functions of the degree of coverage, using the pairs of values (n_{a}, Q_{int}) measured at the same equilibrium pressure.

   When there are several possible adsorption mechanisms (e.g. reversible and irreversible adsorption), these isotherms can be used to evaluate the sequence and the importance (number of active sites and bond energy) of the different processes.

3. Another representation of calorimetric data is that of integral heats as a function of the adsorbed quantities ($Q_{\text{int}} = \text{f}(n_{\text{a}})$) (Figure 9.3c). This representation leads to the detection of coverage ranges with constant heat of adsorption, for which the evolved heat is a linear function of the coverage.

4. Complementary information is given by the variation of the differential heats Q_{diff} as a function of n_{a} (Figure 9.3d).

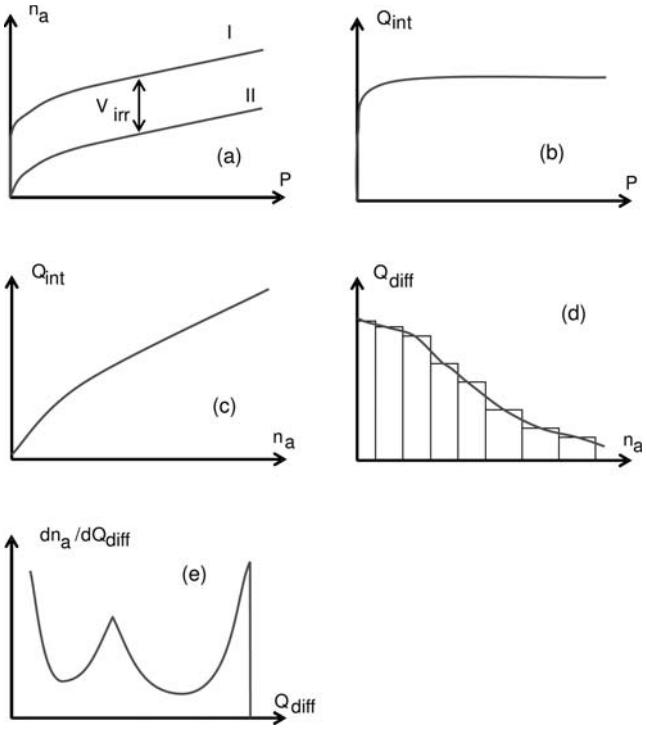

Figure 9.3 Data obtained from volumetric–calorimetric adsorption experiments.

The variation of the differential heat of adsorption ($Q_{diff} = \Delta Q_{int,i}/\Delta n_{a,i}$) as a function of coverage is an indication of the homogeneity or heterogeneity of the adsorption sites.

The ratio of the amount of heat evolved for each increment to the number of moles adsorbed is equal to the average value of the differential enthalpy of adsorption for the adsorbed quantity considered. The curve showing the differential heat variation as a function of the adsorbed amount is traditionally represented by histograms. However, for simplification, the histogram steps are often replaced by a continuous curve connecting the midpoints of the histograms.

A decrease in the differential heat values as a function of coverage is generally attributed to heterogeneity of the adsorption sites on the surface of the solids.

A classical calorimetric curve of differential heat of adsorption against probe uptake is presented in Figure 9.4.

This curve can present:

(a) An initial region of high adsorption heat, mainly ascribed to adsorption on Lewis sites, which falls abruptly.

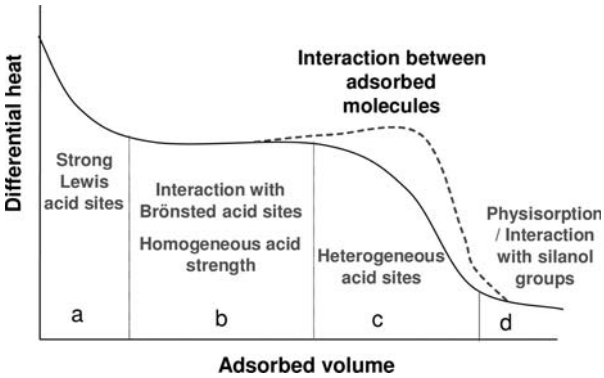

Figure 9.4 Regions in a typical curve of differential heats of adsorption versus adsorbed amount. All regions (a, b, c, d) can be observed for zeolite samples presenting both Lewis and Brønsted acid sites, as probed by ammonia adsorption. For oxides presenting only Lewis acid sites, the regions a, c and d are observed.

(b) One or more plateaux of intermediate strength sites with a nearly constant heat, attributed preferentially to homogeneous Brønsted sites.

(c) A region where heats decrease more or less steeply depending on the heterogeneity of the sites (probably Lewis sites).
A bump in the curve can also be observed sometimes, indicating interactions between adsorbed molecules.

(d) A reversible adsorption domain, characteristic of physisorption of the probe, or hydrogen bonding between the probe and the sample, or very weak Lewis acidity. The curve reaches a value close to that of the heat of condensation of the adsorbate in the liquid phase [14].

Such a heat (enthalpy) diagram can be used to assess the uniformity–non-uniformity of the surface of the adsorbent with respect to energy, the energy of the lateral (adsorbate–adsorbate) interactions, and the structural or textural changes that the adsorbent often undergoes as a result of interaction with the adsorbate [17].

5. It is possible to obtain a distribution of the energies of the adsorption sites by plotting dn_a/dQ_{diff} as a function of Q_{diff}. The area under the curve is representative of the number of molecules that are adsorbed with a given evolved heat and thus the number of sites corresponding to a given strength (Figure 9.3e). However, this type of representation is somewhat less accurate than the previous one.

Finally, the systematic determination of the time constants (or thermokinetic parameters) of the calorimetric signal peaks gives information on the diffusion

rate of the probe molecule on the solid framework. The change of gas pressure is related to the kinetics of the adsorption process; however, concerning the calorimetric curve, the kinetic data necessary to detect reaction mechanisms can sometimes be distorted by the inertia of the calorimeter. The limitations and advantages of the technique are fully described in Ref. [15].

Micro-calorimetric adsorption measurements require a proper *in situ* vacuum activation at a higher temperature than the adsorption process. A first pre-treatment under oxygen is performed in the calorimetric cell in order to eliminate the impurities present on the sample (essentially carbonates, nitrates, carbonaceous residues and water present from the preparation, calcination and exposure to atmosphere) and to avoid the partial reduction of the surface of an oxide that is easily reduced under vacuum.

9.2.1.2 Gas Flow Methods

An alternative method is flow adsorption microcalorimetry, which involves the use of a carrier gas passing continuously through the adsorption cell. The catalyst is placed on a glass frit in a gas circulation cell in the calorimeter. In order to determine the amounts of gas adsorbed, flow calorimetry must be used in combination with another technique, most frequently TG, MS or GC [8, 18].

When the system is used in pulse mode, it allows the measurement of heats of adsorption of a gaseous reactant on a solid or interaction heats between a gaseous reactant and pre-adsorbed species. When used as a flow reactor, it allows the kinetic study of catalytic reactions as well as the study of the activation or the aging of the catalyst. This is also a suitable system to perform calorimetric temperature programmed reduction (TPR), temperature programmed oxidation (TPO) or temperature programmed desorption (TPD) experiments. In addition to calorimetry, temperature programmed desorption (TPD) of adsorbed probe molecules can in principle also be used to estimate heats of adsorption [19].

A comparison between pulsed flow and conventional pulsed static calorimetry techniques for characterizing surface acidity using base probe molecule adsorption has been performed by Brown and coworkers [20, 21]. In a flow experiment, both reversible and irreversible probe adsorption occurring for each dose can be measured, and the composition of the gas flow gas can be easily modified. The ΔH_{ads} versus coverage profiles obtained from the two techniques were found to be comparable. The results were interpreted in terms of the extent to which NH_3 adsorption on the catalyst surface is under thermodynamic control in the two methods.

Thermal desorption techniques have gained great popularity owing to their comparatively easy operation. Various different mathematical analyses of the thermodesorption profiles have been proposed by different authors to provide kinetic information about the distribution of the surface acid strength [22]. A simple approach is based on the analysis of thermodesorption curves collected at different heating rates (β). The shift of the temperature of the maximum rate of desorption (T_{max}) as a function of β can be exploited to derive activation parameters (i.e. E_a)

of the desorption reaction by means of different model equations. When heterogeneous solids are concerned, in order to derive the activation energy distribution of the solid surface, the shift of T_{max} with β has to be considered separately for each peak. However, for this approach to provide a reliable determination of the activation parameters, the thermodesorption curves have to be well resolved, with clearly detectable T_{max} values [23]. It has been shown that the results obtained by this method are in good agreement with those derived from ammonia adsorption calorimetry when the comparison is confined to the strong fraction of acid sites. In general, when the experiments are carefully conducted and the samples are pre-treated identically, similar values of numbers of acid sites and heats of adsorption can be obtained from both calorimetric and TPD measurements when using NH_3 as probe. However, the results for pyridine adsorption can be quite different for the two techniques [24]. The difference has been attributed to the fact that desorption of pyridine can be severely limited by restricted diffusion, for example within zeolite crystallites. The limitations and advantages of the TPD techniques are fully described in Ref. [19].

9.2.1.3 **Calorimetry in Liquid Phase**

Finally, it should be noted that calorimetric measurements can also be used to monitor adsorption phenomena at the solid–liquid interface (in a solvent). This method has been used to measure the adsorption heats evolved upon injection of dilute solutions of pyridine in alkanes (*n*-hexane, cyclohexane) onto an acidic solid itself in a slurry with *n*-hexane. The amount of free base in solution is measured separately with a UV-Vis spectrometer, leading to an adsorption isotherm that is measured over the range of base addition used in the calorimetric titrations. The combined data from the calorimetric titration and adsorption measurements are analyzed simultaneously to determine equilibrium constants, quantities of sites per gram and acid site strengths for different acid sites on the solid.

The measurements are performed in a non-interacting hydrocarbon solvent (e.g. cyclohexane) whose molecular mass is close to that of the donor (e.g. pyridine) in order to cancel out contributions from a dispersion component to the measured enthalpy [25]. As an example, the acid strength of tungsten oxide supported on a silica gel has been determined by this method [26].

A similar technique has been used to determine the acidic character of niobium oxide and niobyl phosphate catalysts in different solvents (decane, cyclohexane, toluene, methanol and isopropanol) using aniline and 2-phenyl-ethylamine as probe molecules [27, 28]. The heat evolved from the adsorption reaction derives from two different contributions: the exothermic enthalpy of adsorption and the endothermic enthalpy of displacement of the solvent, while the enthalpy effects describing dilution and mixing phenomena can be neglected owing to the differential design and pre-heating of the probe solution.

The titration of acid sites in liquids of different polarities and proticities (decane, cyclohexane, toluene, methanol and isopropanol) makes it possible to discriminate the acid site strength distribution more accurately than from the more conventional gas–solid phase titration with ammonia.

9.2.2
Temperature Dependence of Adsorption–Desorption Heats

In adsorption microcalorimetry, surface equilibration depends not only on the chosen probe molecule but also on the adsorption temperature. It is worth mentioning that the literature contains some controversial articles on this subject [29].

Heats of adsorption of probe molecules have frequently been measured at room temperature [8]; however, the results obtained from such measurements can sometimes be of questionable accuracy as a result of non-equilibrium conditions and non-specific adsorption.

In fact, the adsorption temperature should not be too low, in order to allow the detection of differences among the sites; otherwise under certain circumstances the measured evolved heat can be just an average value. Another important issue is that one must ensure that chemisorption predominates over physisorption.

Cardona-Martinez and Dumesic [30] have analyzed the problem of surface mobility of the adsorbates for the particular case of adsorption of basic probe molecules on acid sites of oxides. Without equilibration of adsorbate with surface sites, the measured differential heat would only be an average value of the sites that the molecules adsorb on, and differences among sites would not be detected. Thus, ideally, measurements should be made at as a high a temperature as feasible without desorbing or decomposing the adsorbate.

In addition to isothermal measurements, temperature programmed calorimetry experiments can also be performed using DSC. For such measurements, the sample is equilibrated with the adsorbate at low temperatures. The temperature is then increased in a controlled manner, and the heat absorbed (or evolved) by the sample over a certain temperature region is related to the heat of the event occurring at that point.

The data obtained from the temperature programmed method must be interpreted with care in order to properly determine the distribution of surface sites of different heats of adsorption. If adsorption is carried out at room or slightly elevated temperatures at the beginning of the experiment, sufficient time must be provided to ensure coverage of all the sites. Otherwise non-discriminating adsorption would occur. It has been shown that, for porous samples, re-adsorption along the pore as a desorbed molecule diffuses out of a pore is practically unavoidable. Therefore, although a temperature programmed experiment might appear to be simpler to perform, there are more potential artifacts that complicate quantitative interpretation of the results than in the case of isothermal experiments [4, 19].

9.2.3
Probe Molecules

Appropriate probe molecules to be selected for adsorption microcalorimetry should be stable with time and with temperature. Furthermore, in the case of

zeolites and other microporous materials, they should be small enough to readily penetrate into the intra-crystalline space. The adsorbed probe at a given temperature should also have sufficient mobility to equilibrate with active sites. As calorimetry gives the total number of adsorption sites, and possibly catalytically active centers, the values obtained depend on the nature and size of the probe molecule [14].

9.2.3.1 Probing Surface Basicity

The number of acidic probes able to cover a wide range of strength is rather small. The ideal probe molecule should be specific to basic sites and should not be amphoteric. For example CO_2 ($pK_a = 6.37$) is commonly chosen to characterize the basicity of solids, but it may be either adsorbed on cations or physisorbed, or may react with hydroxyls and oxide ions to form carbonated species.

CO_2 is a poor donor but a good electron acceptor. Owing to its acidic character, it is frequently used to probe the basic properties of solid surfaces. IR evidence concerning the formation of carbonate-like species of different configurations has been reported for metal oxides [31], which accounts for the heterogeneity of the surface revealed by micro-calorimetric measurements. The possibility that CO_2 could behave as a base and interact with Lewis acid sites should also be considered. However, these sites would have to be very strong Lewis acid sites and this particular adsorption mode of the CO_2 molecule should be very weak and can usually be neglected [32].

The same problems may arise when using SO_2 as an acidic probe, despite the fact that SO_2 ($pK_a = 1.89$) is more acidic than CO_2 and, thus, more likely to probe the total basicity of the surface.

9.2.3.2 Probing Surface Acidity

Ammonia ($pK_a = 9.24$, proton affinity in gas phase = 857.7 kJ mol^{-1}) and pyridine ($pK_a = 5.19$, proton affinity in gas phase = 922.2 kJ mol^{-1}) are the favored molecules for probing the overall solid acidity, since both Lewis and Brønsted acid sites retain these molecules. However the use of IR spectroscopy or XPS is necessary to distinguish qualitatively and unambiguously between these two types of sites. In addition to NH_3 and pyridine, trimethylamine and triethylamine have also been used to probe the acidity of supported oxides. However, it has been mentioned [33] that these two molecules might not be able to equilibrate completely with the surface under typical experimental conditions. The use of substituted pyridines (2,6-dimethylpyridine) has also been considered in order to probe specifically the Brønsted sites [34].

Ammonia is among the smallest strongly basic molecules, and its diffusion is hardly affected by a porous structure. In the light of the different possible modes of interaction of this molecule with the oxide surface, it has been found that NH_3 mostly coordinates to Lewis sites, but in a few cases the results were interpreted by considering the simultaneous occurrence (to a low extent) of dissociative adsorption leading to NH_2^- and OH^- surface species. Dissociative

adsorption of ammonia is related to the presence of very strong Lewis-type acid sites.

Reviews by Gorte and coworkers [35, 36] deal with the adsorption complexes formed by strong and weak bases with acid sites in zeolites. They examine the adsorption enthalpies of a series of strongly basic molecules such as alkylamines, pyridines and imines. These workers also performed studies of the adsorption properties of weak bases, including water, alcohols, thiols, olefins, aldehydes, ketones and nitriles. They report a poor correlation between the differential heats of adsorption on H-MFI zeolites and the enthalpies of protonation in aqueous solutions, but a much better correlation with gas-phase proton affinities [37].

Acetonitrile is also an interesting molecule for probing acid sites in catalysts. It is a weak base, so no protons are abstracted and actual hydroxyl groups can be observed. It also allows the investigation of both Lewis and Brønsted acidities [15].

NO and CO can also be employed as probes to identify Lewis acid sites and characterize their density and strength [38].

9.2.3.3 **Probing Redox Properties**

The heats of reduction of oxide samples can be determined by studying the adsorption of hydrogen, CO and various hydrocarbons on the fully oxidized catalysts. The extent of reduction of the catalyst surface can be evaluated in particular using H_2. The measurement of hydrocarbon (e.g. propene, propane, acrolein, etc.) adsorption heats is complicated by the subsequent reaction of the adsorbed species or by incomplete desorption of the products.

In the case of CO reduction, the catalyst–oxygen bond energy has to be calculated by subtracting the heat of formation of CO_2.

However, it is known that, in the absence of processes other than plain surface coordination, CO acts as a weak Lewis base and can interact with the strongest surface Lewis acid sites. NO can also be employed either as a probe to identify Lewis acid sites (as mentioned in Section 9.2.3.2) or as a reducing agent. However, NO may disproportionate into N_2O and oxygen and it is also very likely to form nitrosyl complexes in the presence of transition metal ions.

The heats of oxidation of the reduced oxides can be further measured using O_2 adsorption. Large variations of the re-oxidation heat can be sometimes observed when any further oxidation is limited by the diffusion of oxygen into the reduced portion of the particle.

9.3
Surface Properties of Oxides

On one hand, both acidity and basicity of catalysts are known to be important factors for partial oxidation reactions. Moreover, strong acidity can reduce the selectivity by carbon–carbon bond breaking and by promoting the production of

CO_2. Acid sites are cations that exhibit either a high oxidation state or an unsaturated coordination. On the other hand, redox properties are also known to play an important role and to be related to $M^{n+} \rightarrow M^{(n-1)+}$ equilibrium constant and to lattice O^{2-} ion lability.

Since various supported and unsupported metal oxides are oxidation catalysts for hydrocarbons, there has been interest in determining the relationship between the reduction/re-oxidation properties of the oxides and their catalytic properties. A common oxidation mechanism involves a redox cycle in which lattice oxygen is removed in the reaction and then replenished by oxygen from the gas phase. Thus there are studies to determine the energetics of removal of oxygen from the catalysts and replenishment by various routes. These energetics have been determined as a function of catalyst formulation or modification, and as a function of the oxidation state of the catalyst [4].

In order to try to clarify the different types of mechanism involving either redox cycles and/or acid–base properties, a study of the surface chemistry of single, doped and mixed oxides is of much interest. The calorimetric technique, by allowing heat transfer measurements, can provide very informative data on the thermodynamics of solid–gas interactions and for the study of the surface and reactivity of these metal oxides.

9.3.1 Bulk Oxide Catalysts

The surface acid–base properties of bulk oxides can be conveniently investigated by studying the adsorption of suitably chosen basic–acidic probe molecules on the solid. Acidic and basic sites are often present simultaneously on solid surfaces. The two centers may work independently or in a concerted way, and the occurrence of bifunctional reaction pathways requiring a cooperative action of acidic and basic centers has also received considerable attention [39]. The acid–base properties of numerous amorphous metal oxides investigated by microcalorimetry have been summarized in an extensive review by Cardona-Martinez and Dumesic [11].

The influence of the pre-treatment temperature on the acidic properties is a very important factor. For Brønsted sites, the differential heat is the difference between the enthalpy of dissociation of the acidic hydroxyl and the enthalpy of protonation of the probe molecule. For Lewis sites, the differential heat of adsorption represents the energy associated with the transfer of electron density towards an electron-deficient, coordinatively unsaturated site, and probably an energy term related to the relaxation of the strained surface [40].

Increasing the pre-treatment temperature modifies the surface acidity of the solids. For γ-alumina, there are numerous surface models, and various acid sites having different strengths are formed on the surface during dehydration. The influence of the pre-treatment temperature, between 573 and 1073 K, on the surface acidity of a transition alumina has been studied by ammonia adsorption microcalorimetry. The number and strength of the strong sites, which should be

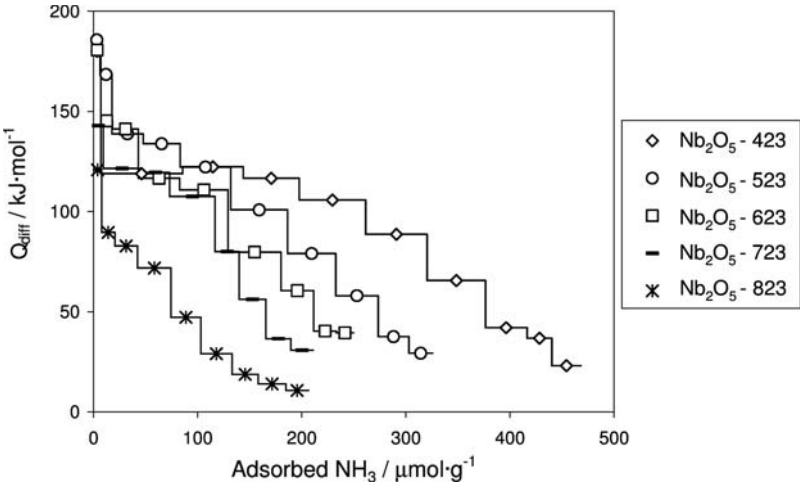

Figure 9.5 Variation with the activation temperature of the differential heats of adsorption versus ammonia coverage.

mainly Lewis sites, have been found to increase when the temperature increases. Moreover the pre-treatment temperature affects the whole spectrum of adsorption heats at various coverages, and not only the initial heat [13].

Niobium oxide surfaces are also very dependent on the dehydration temperature. An illustration is given in Figure 9.5, which represents the differential heats of NH_3 adsorption versus ammonia coverage for a niobium oxide from CBMM pre-treated at 423, 523, 623, 723 and 823 K [41].

As can be seen, a regular decrease in the adsorption heats occurs when the evacuation temperature increases from 423 to 823 K. The number of strong sites is less affected by dehydroxylation of the surface than that of weak sites, and tends to a limit.

Figure 9.6 represents the differential heats of NH_3 and SO_2 adsorption as a function of coverage for silica, magnesia and γ-alumina samples [15].

Silica presents low heats of adsorption for both basic and acidic molecules, indicating that the surface sites on silica are either weakly acidic or weakly basic. The adsorption is mainly due to hydrogen bonding and van der Waals interaction. The differential heats of adsorption of ammonia on silica show a decrease as the adsorption temperature increases [12]. The differential heats of adsorption of ammonia and sulfur dioxide on the surface of alumina show the presence of strong acid and strong basic sites, respectively. The heats of adsorption for alumina are typical of a strong acidic surface, but also indicate the amphotericity of the surface. The initial heat increases and the adsorption capacity decreases with increasing pre-treatment temperature [13]. By contrast, magnesia displays only basic sites adsorbing SO_2 molecules preferentially, and very few acidic sites.

The differential heats of adsorption of NH_3 and CO_2 over 18 bulk oxides have been determined [42, 43]. These oxides were classified, according to their

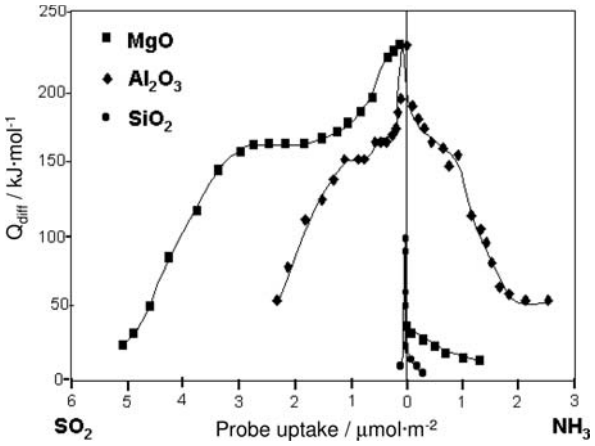

Figure 9.6 Differential heats of adsorption of ammonia and sulfur dioxide on SiO_2, γ-Al_2O_3 and MgO.

properties, as acidic oxides: Cr_2O_3, WO_3, Nb_2O_5, V_2O_5 and MoO_3; amphoteric oxides: BeO, TiO_2, Al_2O_3, ZrO_2 and ZnO; and basic oxides: ThO_2, Nd_2O_3, MgO, CaO and La_2O_3. It was found that many oxides in the amphoteric group adsorbed more NH_3 and with higher heats (>200 kJ mol^{-1}) than some of those in the acidic group. Also the ZrO_2 sample adsorbed NH_3 with a heat of 150 kJ mol^{-1}, comparable to Nb_2O_5 and WO_3. The group of basic oxides adsorbed NH_3 very weakly (<20 kJ mol^{-1}) and essentially by physisorption. The oxides of La, Nd and Th adsorbed CO_2 in larger abundance and with higher heats, for instance 200 kJ mol^{-1} for Nd_2O_3, than other oxides. It is worth noting that, on the alkaline earth oxides, the heats of adsorption of CO_2 were only 120–160 kJ mol^{-1}, perhaps because of bidentate adsorption of CO_2. Some of the oxides of the amphoteric group such as TiO_2, ZrO_2 and Al_2O_3 also adsorbed CO_2 with heats higher than 100 kJ mol^{-1}, but with an amount adsorbed smaller than on the basic oxides. Except for the adsorption of NH_3 on Cr_2O_3 and ZnO, and CO_2 on the alkaline earth oxides, the other data all indicate heterogeneous site distributions. A fair correlation was found between the average adsorption heats and the percentage of ionic character of the oxides.

The surface acid–base properties of polycrystalline MgO surfaces have been assessed by means of thermogravimetry and DSC of desorption of pyridine and CO_2 in the room temperature to 400 °C temperature range [44]. The endotherms and corresponding ΔH of desorption were discussed in relation with results determined previously using differential adsorption calorimetry and taking into account the structure, surface area and defects of the studied surfaces.

Differential and integral heats of chemisorption of H_2O on nanocrystalline α-Al_2O_3 and γ-Al_2O_3 as a function of hydroxyl coverage have been reported by McHale and coworkers [45]. A greater number of high-energy sites was evidenced on α-Al_2O_3 per unit surface area.

Another study examined the NH_3 and CO_2 adsorption heats on several zirconia catalysts, differing in their preparation procedure and/or in the addition of dopants [46]. The differential heats of NH_3 and CO_2 adsorption show a wide range of variability, displaying either a plateau of constant heat or a continuous decrease indicative of adsorption heterogeneity [12]. The ratio between the number of the basic and acidic sites, n_B/n_A, was calculated for each catalyst from the microcalorimetry results, by dividing the amount of adsorbed CO_2 by the amount of adsorbed NH_3. These catalysts were used to produce alk-1-ene from 4-methylpentan-2-ol. Alk-1-ene selectivity was found to first increase with the n_B/n_A ratio, reach a maximum and then decrease, whereas ketone formation continuously increased, being negligible for low n_B/n_A values.

Calorimetric measurements of adsorption of CO_2 at 303 K on different titania samples have provided evidence of their surface heterogeneity, as expected for oxides, with heats of adsorption ranging from ~100 to 30 kJ mol^{-1}. Acidity measurements by ammonia adsorption microcalorimetry on the same samples gave rise to adsorption heats ranging between 150 and 60 kJ mol^{-1} [47].

Information on the acid–base properties of lanthanum and cerium oxides has been obtained by adsorption microcalorimetry of ammonia and carbon dioxide at 353 K. The initial heats of NH_3 adsorption ranged from 125 to 95 kJ mol^{-1} and the differential heats smoothly decreased with increasing coverage. The results for CO_2 adsorption showed high initial heats (180–225 kJ mol^{-1}, depending on the samples). A plateau can be seen around 145–160 kJ mol^{-1}, followed by a continuous decrease of the differential heat. The interaction of CO_2 is more pronounced for La_2O_3 than for CeO_2, in terms of both number and strength of the adsorbing sites [32].

The acidity and basicity of bulk Ga_2O_3 and SnO_2 were determined by microcalorimetry of NH_3 and SO_2 adsorptions performed at 353 K. Both are amphoteric, with initial heats of NH_3 adsorption of 110 and 180 kJ mol^{-1} and initial heats of SO_2 adsorption of 195 and 180 kJ mol^{-1} for Ga_2O_3 and SO_2 respectively [48]. The Lewis acidity of a phase-pure γ-Ga_2O_3 was also studied by the adsorption of CO at ambient temperature. The Q_{diff} values at low coverage are in the range 40–45 kJ mol^{-1} and rather heterogeneous, and are followed by a weak and reversible adsorption process in the 25–30 kJ mol^{-1} range [49].

The interactions of ammonia, methanol, water and dimethyl ether with amorphous Nb_2O_5 and $NbOPO_4$ samples have been investigated by means of adsorption microcalorimetry in order to determine the number and strength of the active sites for dimethyl ether (DME) synthesis by dehydration of methanol [50]. $NbOPO_4$ is more acidic than Nb_2O_5, and both present Brønsted and Lewis sites on their surface. They both strongly chemisorb a small amount of water, while most of the adsorbed water corresponds to reversible physical adsorption. The results of microcalorimetry experiments associated with IR spectroscopy suggest that methanol was, for the most part, strongly dissociatively adsorbed on Nb_2O_5 and $NbOPO_4$ to form methoxy species, and that DME was mainly molecularly chemically adsorbed. The four probe molecules used in this work were adsorbed more strongly on $NbOPO_4$ than on Nb_2O_5 because of the stronger acidity of $NbOPO_4$.

9.3.2
Doped and Modified Oxides

Doped metal oxide catalysts are widely used in various catalytic processes. In many cases, the catalytic activity and selectivity of these catalysts may be related to their acidity or basicity.

Microcalorimetry of ammonia and sulfur dioxide adsorption and the catalytic reaction of 2-propanol conversion have been used to study the effects on the acid–base properties of adding small amounts of various ions (Ca^{2+}, Li^{2+}, Nd^{3+}, Ni^{2+}, Zn^{4+}, SO_4^{2-}) to γ-alumina, silica or magnesia surfaces [51].

It was found that the modification of γ-Al_2O_3 surface properties with small amounts of the above ions changed its amphoteric properties only moderately. More substantial changes, consisting of the formation of centers of moderate and weak basic strength, were observed on magnesia. The number of acid–base centers on silica was strongly affected by the introduction of doping ions. The acidity of the catalysts correlated with the charge/radius ratio and with the electronegativity of the doping ions. The basicity correlated with the partial oxygen charge of the corresponding oxides.

The effect of Ca loading on the acid–base and redox properties of chromia catalysts supported on alumina has been investigated by microcalorimetry of NH_3 adsorption and TPR. This alkaline promoter strongly decreases the acidity of the chromia catalyst, particularly suppressing the medium and strong acid sites. No clear correlations were found between the surface acidic properties and the catalytic behavior of the investigated samples in the oxidative dehydrogenation of isobutene, while clear trends were observed between reducibility and catalytic activity [52].

Sulfated zirconias and sulfated titanias are interesting solids that were first reported to be superacids. The acidity of such samples has been determined by NH_3 adsorption calorimetry [47, 53–56]. Depending on the preparation method, the quantity of sulfate ions, calcination temperature and hydroxylation degree, the initial heats of adsorption of NH_3 observed can vary from ~120 up to 200 kJ mol^{-1}, but most of these materials display heats of adsorption close to those of H-ZSM-5 zeolite.

The very low initial enthalpy of adsorption observed by calorimetry on sulfated titanias suggests the occurrence of an endothermic process (the dissociation of NH_3) counterbalancing the exothermic process of adsorption. A plateau of heats around 150 kJ mol^{-1} is then observed, followed by a regular decrease of the heats.

9.3.3
Supported Metal Oxide or Metal Catalysts

The even spreading of an oxide over another oxide as support has been widely investigated. Depending on the coverage, different types of species are deposited,

for instance monomeric, polymeric or bulk-type species. These three main types of species often exhibit different catalytic and acidic properties.

Gervasini and coworkers [57] have studied the modifications of the acid–base properties of materials obtained by depositing variable amounts (from 1 up to 50% of the support surface coverage) of Li^+, Ni^{2+} or SO_4^{2-} on supports such as alumina, magnesia and silica, using NH_3 and SO_2 adsorption microcalorimetry experiments to probe the surfaces. It has been demonstrated that the addition of lithium, nickel or sulfate ions to γ-Al_2O_3, SiO_2 or MgO results in non-linear changes in the number and character of acid–base sites. However the effects of modification are more pronounced on silica owing to its very weak acidity. The observed acid–base site strengths and numbers have been correlated with an ion-specific effect and the charge difference between the host and guest oxides.

Supported boria catalysts have been prepared using two different methods, a classical impregnation method and chemical vapor deposition (CVD) on porous and non-porous γ-aluminas, and studied using ammonia adsorption microcalorimetry [58]. The acid sites, at least for the weaker sites of the samples, have been shown to increase in number but not in strength with boron oxide content. A large number of weak acid sites were created on the catalyst surface when the boria amount was greater than the theoretical monolayer. However the number of acid sites determined when using pyridine as probe molecule was lower than when using ammonia. Ammonia was shown to cover all types of sites from strong to weak acid sites, while pyridine only titrated the stronger sites of the samples, perhaps because of steric hindrance.

At low loadings, new acid sites of medium strength were generated by coverage of the strong acid sites of alumina. At high boron oxide loadings, weak acid sites were generated by formation of oxide agglomerates. The basicity of the system, measured by sulfur dioxide adsorption, decreased progressively with the increase in boron oxide content. It was also shown that the basic sites of the amphoteric alumina support are neutralized by 10 wt% of boron oxide on a non-porous alumina support and 20 wt% of B_2O_3 on a porous alumina. Moreover, the catalytic activity for partial oxidation of ethane increased with acidity and reached a maximum constant value for the monolayer [58].

The atomic layer deposition (ALD) method based on surface-saturating gas–solid reactions was applied to obtain highly dispersed titania species on a silica support [59]. The surface-controlled gas-phase deposition of titania on silica progressed at a growth rate of $1\,\text{atom}\,\text{nm}_{\text{support}}^{-2}$ per ALD cycle. The acidic properties of the catalysts and pure TiO_2 (DT51 Rhône-Poulenc anatase) were probed by NH_3 adsorption microcalorimetry at 353 K. The acid site strength distributions of the support and ALD samples are represented in Figure 9.7 [60].

The deposition of sub-monolayer and super-monolayer (monolayer = 4 Ti atoms $\text{nm}_{\text{supp}}^{-2}$) amounts of titania by ALD greatly changed the neutral character of the silica support. Even at the low titania coverage of $3.2\ \text{Ti atoms}\ \text{nm}_{\text{supp}}^{-2}$ (3 TiSi), the highly dispersed titania species on silica contributed to the creation of strong surface acid sites by the formation of strong Ti–O–Si bonds. Those sites exhibited

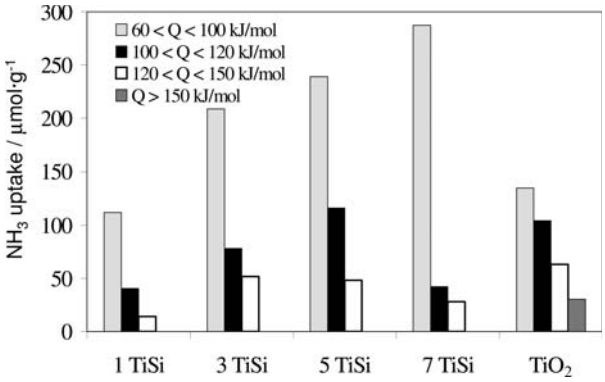

Figure 9.7 Acid site distributions of ALD silica-supported TiO_2 determined by ammonia adsorption at 353 K. The labels 1, 3, 5, 7 represent the precursor-oxygen cycle number for titania growth (number of Ti atom $nm^{-2}_{support}$).

differential heat values from 120 to 150 kJ mol^{-1}. A further increase of the titania content to above monolayer level 7.1 Ti atoms nm^{-2}_{supp} in the 7 TiSi sample mainly produced additional weak and medium strength acid sites at Q_{diff} values from 60 to 120 kJ mol^{-1}.

Alumina-supported tin and gallium oxides with varying amounts of tin and gallium were prepared by wet impregnation, and characterized by NH_3, SO_2, NO_2 and NO adsorption microcalorimetry [48]. NO showed only physisorption properties whatever the amount of tin or gallium oxide. On varying the concentration of tin dioxide deposited on Al_2O_3, the amount of chemisorbed ammonia passed through a maximum around monolayer coverage, while the amount of SO_2 adsorbed was found to decrease. The authors concluded that either tin oxide is preferentially bonded to the basic sites of the amphoteric alumina, or that SnO_2 creates new acid sites and weakens existing basic sites. NO_2 appeared to behave as an acidic probe, showing the same behavior as SO_2 on the tin dioxide samples.

The number of sites titrated by SO_2 on the supported gallium oxide samples increased with increasing amounts of Ga_2O_3. This behavior suggested that gallium oxide is bonded more to the acid sites than to the basic sites of alumina, creating a loss of acid sites in alumina, although it may also reflect the presence of new basic sites provided by Ga_2O_3.

Among various other properties, the hydrophilic/hydrophobic character of gallia supported on zirconia, titania or alumina has been studied using calorimetry [61].

Figure 9.8 represents the differential heats of water adsorption versus coverage at 353 K on pure zirconia, pure gallia and a sample with 12.7 wt% of Ga_2O_3 (close to monolayer coverage) on zirconia. The deposition of Ga_2O_3 on zirconia decreased considerably the strength of water interaction with the surface and confirmed the higher hydrophobicity of the gallia surface [62].

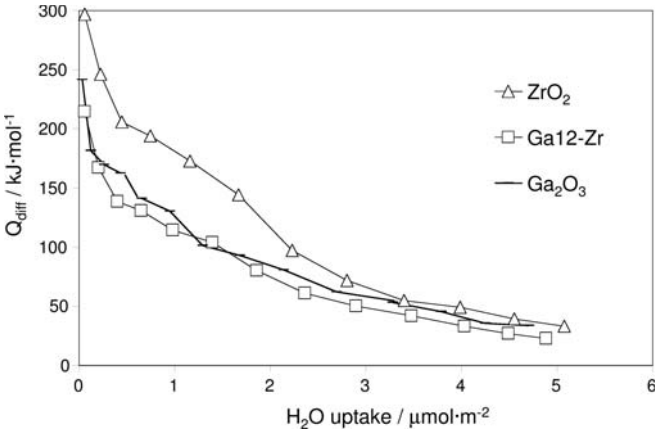

Figure 9.8 Differential heats of water adsorption versus coverage for bulk zirconia and gallia, and zirconia-supported gallia.

The differential heats as a function of adsorbate coverage for the adsorption of NH_3 and CO_2 at 423 K on γ-Al_2O_3 and SnO_2/ γ-Al_2O_3 pre-treated at 753 K have been reported by Shen and coworkers [63]. The initial heat of ammonia adsorption on γ-Al_2O_3 was close to 160 kJ mol^{-1}, while the addition of SnO_2 decreased the initial heat of NH_3 adsorption to ~145 kJ mol^{-1}. Moreover, the authors observed that the addition of SnO_2 decreased the strength of stronger acid sites and increased the strength of intermediate and weak acid sites. Similarly they observed that the addition of SnO_2 decreased the heat of CO_2 adsorption on essentially all the basic sites and decreased the saturation CO_2 coverage. These data are in accordance with those of Ref. [48].

Samples with various amounts of tin oxide were prepared by impregnation of γ-Al_2O_3, TiO_2, SiO_2, ZrO_2 and MgO with tin tetrachloride solutions and studied by ammonia adsorption microcalorimetry [64, 65]. The influence of the adsorption temperature, evacuation temperature, amount of SnO_2 deposited and nature of the support on the adsorption properties were studied. The properties of the resulting samples were strongly determined by the support. Supporting SnO_2 on TiO_2 or ZrO_2 did not result in an appreciable change in the acidity, whereas remarkable increases were observed for SiO_2 and MgO, and alumina was mainly modified in the medium acid strength domain. The amount of deposited tin dioxide had less influence; an increase from 3 to 20 wt% Sn did not reinforce significantly the acidity, except for the magnesia-supported samples. For the 20 wt% Sn series, based on the temperature at the maximum of the reduction peak observed by DSC under a flow of mixed H_2 and He, the reducibility scale for Sn^{IV} to Sn^{II} was found to be in the order SnSi > SnTi > SnAl > SnZr.

The influence of the oxide support (i.e. Al_2O_3, Nb_2O_5, SiO_2 and TiO_2) on the surface properties, reduction and oxidation properties and acid–base properties of supported indium oxide catalysts has been investigated by temperature pro-

grammed reduction/oxidation using thermogravimetry coupled to DSC, and ammonia and sulfur dioxide adsorption calorimetry [66].

Two series of In_2O_3-containing catalysts with low (~3 wt%) and theoretical geometric monolayer (from 20 to 40 wt%) In_2O_3 contents were prepared, and their surface properties were compared with those of bulk In_2O_3 material. Moreover, in the case of the γ-alumina support, the influence of the In_2O_3 loading was studied in detail [67].

As general rule, indium oxide can be considered as more basic than acidic: the overall acidity was slightly decreased and the basicity significantly increased upon deposition of indium oxide on the support. The irreversible amounts of SO_2 adsorbed were greater than the irreversible amounts of NH_3 adsorbed, suggesting the presence of stronger basic sites on the indium-loaded samples.

Indium oxide is easily reduced, at a temperature related to particle size, whereas oxidation is more strongly influenced by the nature of the support. The oxidation of indium oxide takes place at a lower temperature than the reduction, but the measured oxidation heats are higher than the reduction heats.

The redox properties of some alumina-supported indium oxide samples, as well as bulk indium oxide, have been studied by TG-DSC (Figure 9.9). Only one endothermic peak is observed, at a reduction temperature that increases with increasing indium oxide loading. Moreover, the measured heat increases with the amount of indium oxide deposited, varying from 48.5 up to 171.4 kJ mol^{-1} 171.4 kJ $mol^{-1}_{In_2O_3}$ for InAl with 13 wt% In_2O_3 and bulk In_2O_3, respectively. As the measured reduction heats are given per mole of indium oxide, a constant value could be expected *a priori*. This variation of the measured heat with the loading is attributed to varying interactions with the support. At low loadings, strong interactions with the support lower the reduction heats.

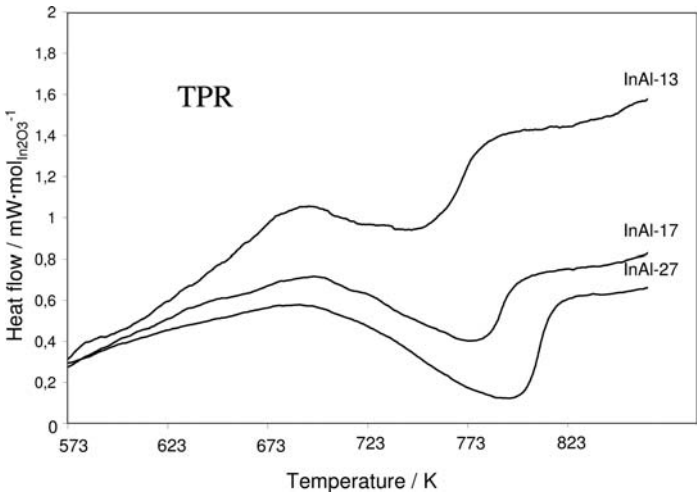

Figure 9.9 DSC TPR profiles of alumina-supported india samples.

Niobium oxide has been extensively studied as a potential catalyst. However, it has seldom been used as a support for metallic or oxide catalysts. With the aim to involve Mo as an active cation for partial oxidation of olefins or for oxidative dehydrogenation of alkanes or oxygenated compounds, Jin and coworkers [68] studied the deposition of molybdenum oxide species on niobium oxide. The impregnation of molybdenum oxide on Nb_2O_5 calcined at 773 K led to a material exhibiting a few more strong acid sites of Lewis type and hydroxyl groups of lower acidity than the corresponding support, as confirmed by NH_3 adsorption calorimetry and FTIR specroscopy. In fact, the samples constituted poor catalysts for the partial oxidation of propene.

The acid–base properties of a series of oxides of group III metals (Al_2O_3, Ga_2O_3, In_2O_3) supported on niobia, prepared by incipient impregnation and with a loading close to the theoretical monolayer, were studied by adsorption microcalorimetry using NH_3 and SO_2 as probe molecules at 353 K. The acid site densities were found to vary in the following order: $Ga_2O_3/Nb_2O_5 < In_2O_3/Nb_2O_5 < Al_2O_3/Nb_2O_5$. This means that gallium and indium oxides neutralize part of the acid sites of niobia and present a more basic than acidic character. Since no basicity could be observed for Nb_2O_5, the basicity observed for the three supported samples should be attributed to the supported oxides only. The order of basic strength as determined by SO_2 adsorption was: $Al_2O_3/Nb_2O_5 >> Ga_2O_3/Nb_2O_5 \approx In_2O_3/Nb_2O_5$. Since it is commonly accepted that indium oxide is the most basic of the three amphoteric group III oxides, the low basicity observed for this sample has been attributed to a very poor dispersion [69].

Cobalt, copper and nickel metal ions were deposited by two different methods, ionic exchange and impregnation, on an amorphous silica–alumina and a ZSM-5 zeolite. The adsorption properties towards NH_3 and NO were determined at 353 and 313 K, respectively, by coupled calorimetric–volumetric measurements. The average acid strength of the catalysts supported on silica–alumina was stronger than that of the parent support, while the zeolite-based catalysts had (with the exception of the nickel sample) weaker acid sites than the parent ZSM-5. The oxide materials used as supports adsorbed NO in very small amounts only, and the presence of metal cations improved the NO adsorption [70].

Oxidation of ethene on silver catalysts to yield ethene oxide is a good example of an industrial catalytic process with a high selectivity. In order to confirm a possible correlation between the catalysts' affinity towards oxygen and their activity in ethene epoxidation, a heat-flow microcalorimeter equipped with a pulse flow reactor has been used to study the reaction of oxygen at 473 K with a series of silica-supported silver catalysts [71]. At 473 K, adsorption of oxygen at the surface of silver is a fast process; incorporation of oxygen into deeper metal layers, though present, is a slow process.

The differential heats of interaction were found to decrease with the amount of oxygen consumed, but always exceeded the heat of formation of bulk silver oxides. The average heat of formation of an oxygen monolayer varied from sample to sample and correlated linearly with the intrinsic activity of the catalysts for ethene

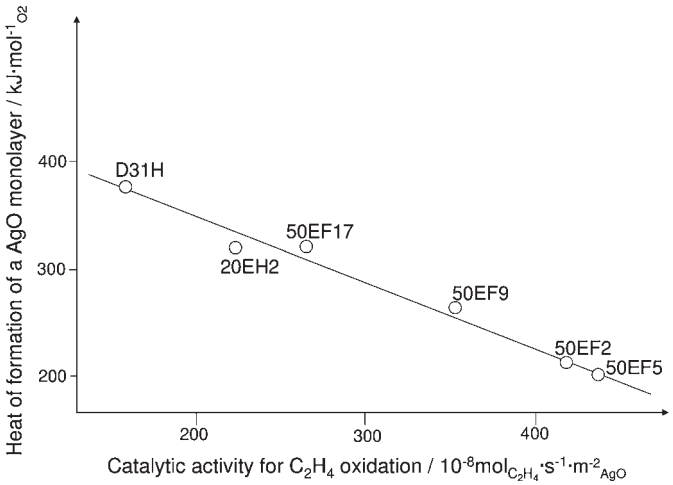

Figure 9.10 Average heat of formation of an AgO monolayer at 473 K for a series of silica-supported silver catalysts, as a function of their intrinsic activity for the oxidation of ethene at the same temperature.

oxidation (Figure 9.10); surface oxygen species are apparently more catalytically active when they are less energetically bonded to the silver surface.

Ag/Al_2O_3 catalysts with various contents have been characterized using TG, DTA, TPD and NH_3 and CO_2 adsorption calorimetry [72]. The results were discussed in terms of silver loading and interactions with the alumina surface. An increase of the total amount of basic sites was globally observed.

Supported Pd catalysts have been found to be the most active and promising catalysts for methane combustion, and therefore they have been extensively studied by adsorption calorimetry, in particular using CO as probe molecule, which can give useful information about the surface state and active sites of the catalyst [11, 73]. Moreover, three-way catalysts(TWCs), which are widely used for elimination of pollutants in automobile exhausts, are also composed of precious metals (Pt and Rh) dispersed on different supports (SiO_2, Al_2O_3, etc.) to increase the exposed metal surface. In these catalysts, other additives such as cerium oxide have important roles as promoters, enhancing the metal dispersion, avoiding metal sintering and enhancing the oxygen storage capacity of the catalyst.

The adsorption of CO on Pd catalysts supported on Al_2O_3, ZrO_2, ZrO_2-SiO_2 and ZrO_2-La_2O_3 has been studied by Guerrero-Ruiz and coworkers [74] using both calorimetry and IR spectroscopy. They found that CO was adsorbed on Pd catalysts in three different modes, with differential adsorption heats lying in high (210–170 kJ mol^{-1}), medium (140–120 kJ mol^{-1}) and low (95–60 kJ mol^{-1}) value ranges, respectively. The nature of the support, the reduction temperature and the pretreatment conditions affected the surface fraction of sites adsorbing CO with specific heats of adsorption.

Supported palladium oxide catalysts present the best performance for methane combustion in lean conditions. Consequently, the interactions between methane and palladium oxide or metallic palladium supported on Al_2O_3, ZrO_2 and BN at 673 K have been studied by microcalorimetry. At this temperature, methane reduced the palladium oxide, and the heat of reduction of palladium oxide was shown to depend on the dispersion and the support. The lowest heats of reduction corresponded to the highest rates of methane combustion [75].

Oxygen, hydrogen and CO adsorption heats were measured on 2% Pt/Al_2O_3 calcined at different temperatures, and so presenting various metal particle sizes. It was shown that hydrogen adsorption sites have a broad site energy distribution (attributed to the higher surface mobility of hydrogen), with an initial heat of about 120 kJ mol^{-1}. Intermediate and weak adsorption sites were not observed for carbon monoxide and oxygen, which gave rise to uniform site energy distributions not influenced by the metal particle size. The initial heats were close to 180–190 kJ mol^{-1} for both of them [76].

H_2 adsorption on high surface area Rh/CeO_2 catalysts has been studied by calorimetry [77]. As the reduction progresses, the mean heat of adsorption and the amount of hydrogen adsorbed on the metal, as determined by volumetry and calorimetry, decrease considerably. The initial heats were around 37 kJ mol^{-1}.

The oxidation of alumina-supported rhodium by oxygen in a temperature range between 280 and 870 K has been studied using calorimetry. The heat of dioxygen adsorption was found to vary only slightly with the dispersion of rhodium, with a value of 294 ± 6 kJ mol^{-1} $294 \pm 6\,\mathrm{kJ\,mol}_{O_2}^{-1}$ [78].

9.3.4
Binary Mixed Metal Oxides to Quaternary Metal Oxides

No general rules for predicting the basic character of mixed oxides have been proposed up to now. On the contrary, qualitative models have been developed concerning the generation of new acidic features upon mixing different oxides. The models most frequently cited are those developed by Tanabe [79] and Kung [80].

The acid–base properties of mixed metal oxides have been found to change with the nature of the constituents, with their relative concentrations and with the preparation and pre-treatment procedures [81]. Accordingly, mixed oxides can be used to obtain catalysts with the desired acid–base characteristics by appropriately choosing the above-mentioned variables.

Regarding preparation procedures, the grafting of metal alkoxides on surface hydroxy groups, the co-precipitation procedure and sol–gel synthesis can lead to systems where the mixed oxides can be either close to a classical supported impregnated oxide (for sub-monolayer coverages) or close to solid solutions or multi-layered supported oxides. So the frontier between supported oxides and mixed oxides cannot be well defined.

The acid–base properties of ceria–zirconia solid solutions [82] and ceria–lanthana co-precipitated mixed oxides have been investigated by Cutrufello and

coworkers using calorimetry [39]. Such systems have been studied in an attempt to enhance the redox properties of ceria by incorporating foreign cations in its lattice. Besides the redox properties, the acid–base features could be expected to change as well, since it is well known that the acid–base properties of a metal oxide can be significantly modified by chemical mixing with another oxide.

It has been shown that the total concentration of the acid sites is the lowest for pure ceria, and markedly increases upon addition of 20 mol% of zirconia, then decreases as the ZrO_2 content is further increased up to 80 mol% and finally attains the highest value on pure zirconia. The heat evolved upon NH_3 adsorption increases with increasing ZrO_2 content in the mixed oxides, while the basic properties are attenuated as the zirconia content is increased up to 80 mol% and then grow again for pure zirconia. Hence the inclusion of increasingly high contents of zirconium into the ceria lattice has a complex influence on both the acidity and basicity of the pure parent oxide.

The co-precipitated ceria–lanthana samples were found to present initial Q_{diff} values for ammonia adsorption ranging from 105 to 130 kJ mol^{-1}, the highest value corresponding to CeO_2 and the lowest one to the La_2O_3 sample. For all the samples, an increase in the ammonia uptake is accompanied by a rapid decrease on the differential heat to a low value (≈35 kJ mol^{-1}). Concerning basicity, the heterogeneity revealed by the Q_{diff} versus uptake profiles cannot be ascribed to sites of different chemical nature (virtually the only basic sites on the ceria surface are coordinatively unsaturated O^{2-} ions). The formation of bicarbonates either very strongly or very weakly held could explain the occurrence of some very high and very low CO_2 adsorption heats.

One-step partial oxidation of propane to acrylic acid (an essential chemical widely used for the production of esters, polyesters, amides, anilides, etc.) has been investigated so far on three types of catalysts, namely, vanadium phosphorus oxides, heteropolycompounds and, more successfully, on mixed metal oxides. The active catalysts generally consist of Mo and V elements, which are also found in catalysts used for the oxidation of propene to acrolein and that of acrolein to acrylic acid.

Mo–V–Te and Mo–V–Te–Nb mixed-metal oxide catalysts have been characterized by means of C_3H_8-TPR and NH_3 adsorption calorimetry. All samples were strongly heterogeneous, with initial adsorption heats of ≈ 100–80 kJ mol^{-1} for the Mo–V–Te samples. Introducing an Nb component into the catalysts slightly decreased the initial adsorption heats to ≈ 60 kJ mol^{-1} but drastically increased the surface density of weak acid sites (<30 kJ mol^{-1}) [83].

The oxidative dehydrogenation (ODH) of lower alkanes is an attractive process for the formation of alkenes. The ODH of propane to produce propene has been particularly studied, given its high demand for the production of polypropene, acrylonitrile and propene oxide. There is a combined influence of the redox and acid–base properties of the surface of the oxides used for propane ODH. Intermediate reducibility, weak Lewis acid centers and oxygen mobility represent the essential requirements for selective ODH, as they are consistent with the trends in ODH rates observed in VO_x, MoO_x and WO_x based catalysts.

DSC has been used to determine the heat effects associated with propene adsorption [84] on Mo/Si:Ti catalysts with different K:Mo molar ratios. The heats associated with reversible $(-3.193\times10^{-4}\,\mathrm{mJ\,m^{-2}_{sample}})$ and irreversible $(-0.126\times10^{-4}\,\mathrm{mJ\,m^{-2}_{sample}})$ adsorption of propene were found to decrease with the addition of potassium.

Thermal analysis studies provide insight into the stability of the catalyst and its chemical evolution. DSC studies can be used to determine not only the temperature of the transformation if any, but also the corresponding heat evolved. For example, El Jamal and coworkers [85] studied the stability of the β-phase of bismuth molybdate ($Bi_2Mo_2O_9$) by DSC in order to check whether this phase is stable at the high temperatures required for propene oxidation. It was shown that the β-phase is metastable at room temperature but stable enough to be used in catalytic tests. It was also confirmed that the β-phase is different from an equimolar mixture of the α- and γ- phases of bismuth molybdate ($Bi_2Mo_3O_{12}$ and Bi_2MoO_6 respectively). The enthalpy of transformation of the α+γ mixture to β at 833 K was found to be 6330 J mol^{-1}. The endothermic nature of the observed peak confirms the evolution of the system to a more organized one, according to the reaction

$$Bi_2Mo_3O_{12} + Bi_2MoO_6 \rightarrow 2Bi_2Mo_2O_9$$

Numerous examples of applications of DSC to the study of the stability of binary, ternary and quaternary metal oxides can be found in the literature, and we will not focus on this type of systematic characterization. Fewer studies have been performed to determine the acid–base character of mixed oxides using adsorption calorimetry of probe molecules.

Depending on the preparation method, on the SiO_2/Al_2O_3 ratio and on the micro- or mesoporous structure, very different acidic properties have been observed for silica–alumina mixtures. Some samples contain both Brønsted and Lewis sites, while for others only acidity of the Lewis type was observed [86, 87].

Thermogravimetric analysis (TGA) has been used to collect thermodesorption curves of 2-phenylethylamine (PEA) from acid surfaces of mixed oxides prepared by the sol–gel method, with the aim of determining the amount and distribution of the acid sites of the samples [23]. Thermodesorption curves from silica–alumina, silica–zirconia and silica–titania samples (≈87 wt% SiO_2) were collected at different heating rates ($5 \le \beta\ (\mathrm{K\,min^{-1}}) \le 30$) in an inert atmosphere. The activation energies of PEA desorption from the acid sites were calculated from the dependence upon the heating rate β of the displacements of the observed desorption peaks (T_{max}) as determined from the derivative of the TGA profiles. The numbers of acid sites, as well as the activation energies, determined by this method were in the order SiO_2–TiO_2 < SiO_2–ZrO_2 < SiO_2–Al_2O_3.

However, this order is strongly dependent on the preparation method and respective amounts of the two oxides. This fact is illustrated in Figure 9.11, which shows strengths and numbers of acid sites varying in a different order as determined by ammonia adsorption calorimetry for sol–gel-prepared silica–alumina,

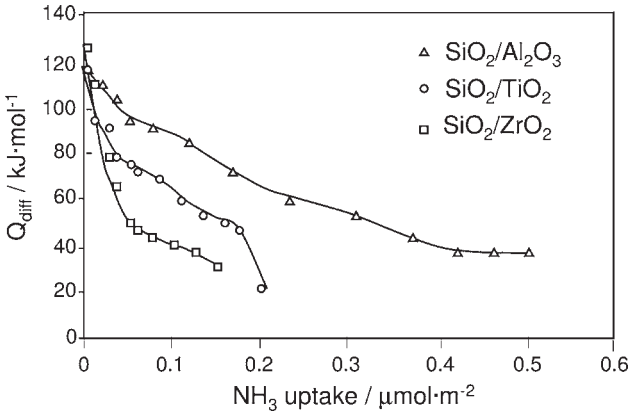

Figure 9.11 Differential heats of ammonia adsorption versus coverage for various mixed oxides.

silica–titania and silica–zirconia with SiO_2/Al_2O_3, SiO_2/TiO_2 and SiO_2/ZrO_2 ratios of 31, 26 and 26 respectively.

Binary and ternary systems containing copper, zinc oxide and aluminum are widely used for industrial methanol synthesis. The adsorption of CO on a fully reduced and clean Cu surface is fully reversible at room temperature, with heats of adsorption ranging between 70 kJ mol^{-1} at low coverage and 45 kJ mol^{-1} at high coverage [88].

Silica–alumina has been used as support for dispersing CuO, Ga_2O_3 and SnO_2 oxide phases, and the corresponding $CuO–Ga_2O_3$ and $CuO–SnO_2$ binary systems [89] have been used in NO_x reduction or methane combustion reactions. The uptakes and interaction energies of CO adsorbed on the different samples were determined by adsorption calorimetry at 303 K (Figure 9.12). As complementarily shown by IR CO adsorption measurements, only the copper phase was able to adsorb CO, so the scale of CO uptake was related to the amounts of dispersed copper species (Cu^+ and $Cu^{\delta+}$) available at the surface. The rather high values of the initial heats (around 105–115 kJ mol^{-1}) confirmed the abundant presence of Cu^+ species, strongly interacting with the support.

Calorimetric and spectroscopic studies of NH_3 adsorption have been performed on the same samples to study the surface acidities of the bare silica–alumina support and of the $CuO–Ga_2O_3/SiO_2–Al_2O_3$ and $CuO–SnO_2/SiO_2–Al_2O_3$ catalysts (Figure 9.13) from the qualitative (nature of acid sites) and quantitative (number, strength and strength distribution of acid sites) points of view [90]. The CuO species increased the capacity to adsorb NH_3 (in particular on medium and weak acid sites, 100 kJ mol^{-1} < Q_{diff} < 150 kJ mol^{-1}), while the strongest fraction of acid sites (Q_{diff} > 150 kJ mol^{-1}) was enhanced by the addition of Ga_2O_3 and SnO_2. In these papers [89, 90] the authors demonstrated, by means of microcalorimetry measurements, that it is possible to modulate the acid strength of metal oxide surfaces by suitable addition of a second oxide component.

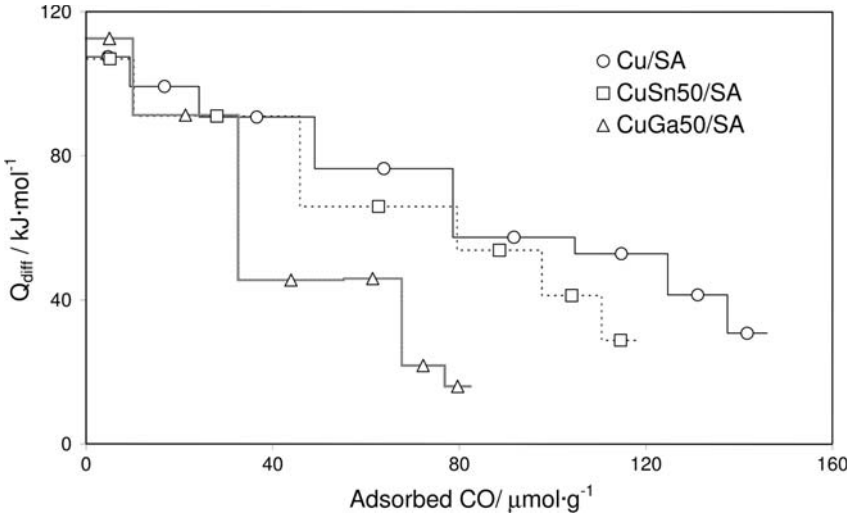

Figure 9.12 Differential heats of carbon monoxide adsorption versus coverage.

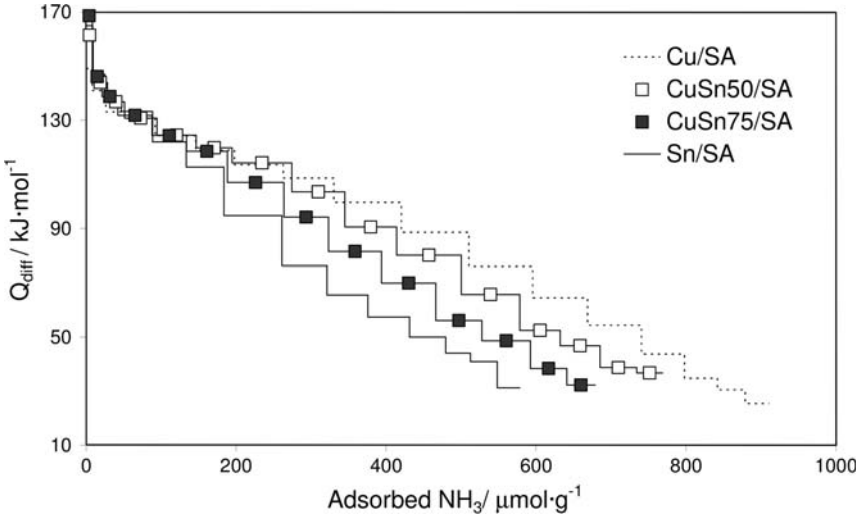

Figure 9.13 Differential heats of ammonia adsorption versus coverage.

Ceria-based catalysts are intensively used because of their high chemical and physical stability, high oxygen mobility and high oxygen vacancy concentrations, which are characteristic of fluorite-type oxides. The possibility of cycling easily between reduced and oxidized states ($Ce^{3+} \leftrightarrow Ce^{4+}$) permits the reversible addition and removal of O_2 from CeO_2. All these features explain the applicability of these materials as catalysts or catalytic supports in many oxidation reactions or as three-way catalysts.

The combination of ceria with another oxide from a group III metal (boria, alumina, gallia and india) using either a co-precipitation method or a sol–gel route has led to mixed oxide samples with specific acid–base and redox features, as evidenced by thermal techniques [91].

The calorimetric study of the adsorption of NH_3 and SO_2 has shown that, among all the investigated co-precipitated samples, only those containing boria had significantly enhanced acidity, whereas the basicity has been found to depend on the nature and amount of group III metal. The amphoteric character of ceria, already known from the literature, has been confirmed. The Me_2O_3–CeO_2 mixed oxides have also shown amphoteric behavior, in a manner dependent on the character of the group III metal. Among the investigated systems, Al_2O_3–CeO_2 and In_2O_3–CeO_2 express somewhat more pronounced basic than acidic characters. Importantly, B_2O_3–CeO_2 samples present an acidic character that becomes more evident with an increase in the boron content.

In the case of sol–gel solids [92], even if the boria–ceria sample had a higher amount of boria compared to co-precipitated samples, it expressed only insignificant acidity. The sol–gel method produces an unfavorable distribution of the guest oxide particles in the mixed oxide, and the acid–base features of the investigated mixed oxides are quite different from those of the samples obtained by co-precipitation.

Ammonia adsorption microcalorimetry experiments have been conducted on various acidic tungsten/zirconia catalysts prepared by different techniques [93]. The results show that the co-precipitation method produced a tungsten/zirconia catalyst with a greater number of acidic sites than impregnation of tungsten on hydrous zirconia, and that the addition of small amounts of iron to the tungsten/zirconia catalyst increased the acid site strength. The acid site strength of the tungsten/zirconia materials was similar to or slightly higher than that found in zeolites or sulfated zirconia, with initial heats ranging from 120 to 170 kJ mol^{-1} depending on the samples.

9.3.5 Hydrotalcites

Hydrotalcites are layered double hydroxides with general formula $\left(M^{2+}_{1-x}M^{3+}_{x}(OH)_2\right)^{x+}\left(A^{m-}_{x/m}\right)\cdot nH_2O$, where the divalent ion may be Mg^{2+}, Ca^{2+}, Zn^{2+} or Ni^{2+}, the trivalent ion, Al^{3+}, Fe^{3+}, Cr^{3+}, and so on, and the charge compensating anions, OH^-, Cl^-, NO_3^-, CO_3^{2-} or SO_4^{2-}. The value of x can be between 0.25 and 0.33.

Thermal treatments induce dehydration, dehydroxylation and loss of the charge-compensating anions, resulting in mixed oxides with the MgO-type structure. Hydrotalcites are consequently a class of precursors useful for the preparation of catalytically active oxides showing basic properties [94]. The acid–base properties of Mg–Al mixed oxides are governed by the Mg : Al molar ratio, calcination temperature and preparation conditions. The study of the influence of the acid–base properties and chemical composition on the catalytic performance of calcined hydrotalcites is thus of interest.

Layered double hydroxides with the hydrotalcite structure were synthesized with varying Mg : Al atomic ratios and with different contents of exchangeable Cl^- and CO_3^{2-} anions. The CO_2 adsorption isotherms showed an increase of the uptake and consequently of the basicity with initial CO_3^{2-} content and calcination temperature up to 800 K. Increasing the Mg : Al ratio of the hydrotalcites from 2.33 to 3 resulted in an increase of the total number of basic sites [94].

In another study, Mg–Al hydrotalcite catalysts with different Mg : Al molar ratios (0.6, 1.4, 2.2, 3.0) were characterized by microcalorimetry using CO_2 in the gas phase and benzoic acid in toluene [95]. The calcined Al-rich sample (Mg : Al molar ratio of 0.6) possesses Lewis acid sites similar in strength to those found on Al_2O_3, but stronger than those found on the Mg-rich hydrotalcites. The liquid-phase basicity microcalorimetry measurements with benzoic acid in toluene correlated very well with the catalytic activity for Michael additions.

The strength and accessibility of the basic sites of hydrotalcites with an Mg : Al ratio of 2, prepared via co-precipitation of the respective nitrates using carbonate or oxalate as the compensating anions, were assessed by calorimetry of CO_2 adsorption. Two different methods were used to activate the Mg–Al hydrotalcites and impart Brønsted basicity. The initial enthalpies of CO_2 adsorption at 303 K on the activated hydrotalcites presented very similar values of $\approx 108\,kJ\,mol^{-1}$ [96].

The acid–base properties of CuMgAl and NiCuMgAl mixed oxides with hydrotalcite-like structures containing different proportions of Ni^{2+}, Cu^{2+}, Mg^{2+} and Al^{3+} cations have been investigated using adsorption microcalorimetry and XPS with SO_2 (for basicity) and NH_3 (for acidity) as probe molecules [97, 98]. For the CuMgAl mixed oxides, the adsorption data indicated an optimum of the concentration and strength of acid sites for the material with Cu : Mg : Al = 1 : 1 : 1, and suggested that the basicity (number and strength) is the most important for Mg-rich samples.

The basicity of the NiCuMgAl materials depends principally on the Ni/Cu ratio and increases with the proportion of Ni. The basic sites are strong and particularly homogeneous (plateau around 150–170 $kJ\,mol^{-1}$ depending on the samples), and they are of both Brønsted and Lewis types (the former being predominant) as confirmed by XPS. Meanwhile, the acidity (of Lewis type only) is rather weak, heterogeneous and dependent on the Ni : Cu ratio (as is basicity). The observed heterogeneity of these acidic sites can be related to the heterogeneity of the interaction between the nickel atoms and the other elements. The acidity

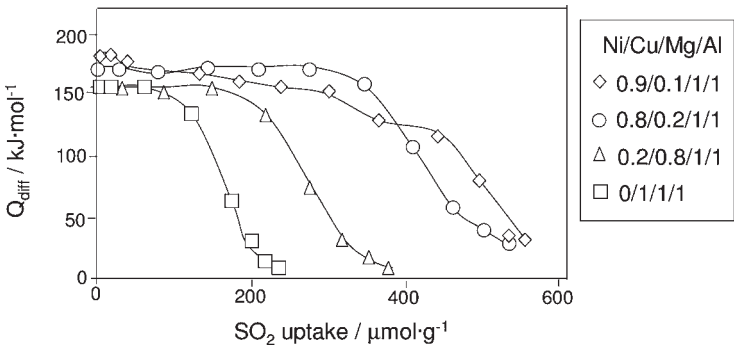

Figure 9.14 Differential heats of sulfur dioxide adsorption versus coverage on NiCuMgAl mixed oxides.

and the basicity both increase with the Ni:Cu ratio, as shown in Figure 9.14, whereas the basicity decreases with increasing Mg:Al ratio [98, 99].

The decarbonation of carbonated layered double hydroxides containing Mg with either Al, Fe or Cr trivalent cations or Al with Mg, Ni, Cu or Zn divalent cations has been studied by thermal analysis. The enthalpy of adsorption of CO_2 on the resulting calcined mixed oxides was measured by calorimetry, with initial heats of adsorption close to those reported for MgO (about 100 kJ mol^{-1}) and a relatively homogeneous strength distribution [100].

9.3.6
Bulk and Supported Heteropolyacids

Keggin-type heteropoly compounds have attractive and important characteristics in terms of catalysis. They consist of heteropolyanions and counter-cations such as H^+, Cs^+ or NH_4^+. When the counter-cations are protons, they are called heteropolyacids (HPA). An important characteristic of HPAs, such as 12-tungstophosphoric acid ($H_3PW_{12}O_{40}$), is the presence of very strong Brønsted acid sites. But the characteristics of HPAs strongly depend on temperature and relative humidity. When they are used in heterogeneous catalysis, it is often necessary to support them on high-surface-area oxides or activated carbons, in order to increase the surface contact with the reactants.

These materials are used industrially mainly in the reaction of hydration of alkanes (acid catalysis) and in the synthesis of methacrolein or isobutyric acid (redox catalysis). Because of the considerable number of available polyanion structures, it is possible to vary their acidic and redox properties according to the needs of a specific application.

The number and strength of the acid centers of tungstic heteropolyacids have been determined by ammonia adsorption calorimetry. Ammonia is irreversibly absorbed, with the formation of the corresponding ammonium salts. An increase in the number of protons in Keggin heteropolyanions decreases the acidic strength.

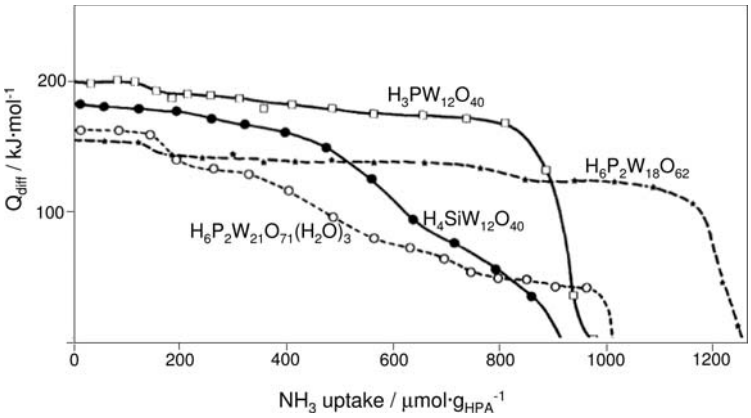

Figure 9.15 Differential heat of ammonia adsorption versus ammonia uptake for various HPA samples.

The acidity varies between compounds, but always presents a plateau of sites of the same strength. The initial heats vary in the order $H_3PW_{12}O_{40} > H_4SiW_{12}O_{40} > H_6P_2W_{21}O_{71} > H_6P_2W_{18}O_{62}$. Diffusion phenomena can be important for some of the compounds, such as $H_6P_2W_{21}O_{71}$, depending on the structure [101], as can be observed in Figure 9.15.

It is worth noting that differences in acid strength between anhydrous Keggin heteropolyacids ($H_3PW_{12}O_{40} > H_4SiW_{12}O_{40} > H_3PMo_{12}O_{40} > H_4SiMo_{12}O_{40}$) measured by ammonia adsorption calorimetry did not correlate simply with the catalytic activity in the reaction of rapeseed oil transesterification with methanol and ethanol [102].

A study of the acidity of carbon-supported and unsupported heteropolyacid catalysts by ammonia sorption calorimetry has been performed at 423 K [103]. The acidity of the supported Keggin-type heteropolyacids is slightly reduced compared to that of the corresponding bulk samples, while that of $H_{21}B_3W_{39}O_{132}$ is enhanced when supported on carbon. Heterogeneity in acid strength is greatly enhanced when the HPAs are grafted on the carbon support.

The acidic properties of the alkaline earth salts of 12-tungstophosphoric acid have been investigated using ammonia adsorption microcalorimetry [104]. As a result of the substitution of two protons with one alkaline earth cation, decreases were observed in both the total number of acid sites and the number of the strongest acid sites (characterized by differential heats higher than 150 kJ mol^{-1}), compared to the values found for 12-tungstophosphoric acid. In the case of Sr salts, some steric effects were observed. The acidity of the investigated systems, even if strong, is uniform only in the case of the parent tungstophosphoric acid. On the contrary, energetic heterogeneity is evident for the other investigated solids, both from differential heat versus ammonia uptake profiles and from the results of TPD of ammonia performed in a TG-DSC-MS experiment.

Changes in the acidic properties of $Cs_{2.5}H_{0.5}PW_{12}O_{40}$ upon heat treatment in water have been investigated by Nakato and coworkers [105]. Ammonia adsorption calorimetry showed that the water treatment reduced the acid site number, whereas the acid strength was little changed, indicating that the decrease observed in catalytic activity was due to that in the number of acid sites. The plateau of heat of adsorption observed was only slightly affected by the water treatment: 165 kJ mol^{-1} before water treatment and 160 kJ mol^{-1} after treatment.

The acidity of a series of $Cs_xH_{3-x}PW_{12}O_{40}$ samples has been studied by NH_3 flow calorimetry linked to mass spectrometry [18]. The incorporation of Cs lowers the number of titratable acid sites, in quantitative agreement with the theoretical degree of H^+ exchange. The average heat of NH_3 adsorption falls only slightly with Cs doping up to $x = 2.3$, suggesting that the residual acid strength of the Cs-doped HPW materials is not strongly perturbed during proton exchange. In contrast, however, the acidity of the heavily substituted ($x > 2.4$) samples is significantly lower.

Ru–HPA metal–acid bifunctional catalysts on various supports (silica, graphite, KL zeolite) have also been characterized by NH_3 adsorption calorimetry, which revealed heterogeneous acid site strength distributions varying in the order HPA-SiO_2 > HPA-graphite > HPA-KL [106].

9.3.7
Pillared Clays and Layered Silicates

Pillared clays (PILC) have been reported to show catalytic properties comparable to zeolites in several reactions, and therefore to have comparable acidities [107].

The preparation and properties of smectites pillared with Al hydroxy oligomers have been extensively investigated. Most of the work has been performed on montmorillonite and hectorite, which have been intercalated with a great variety of pillaring agents and oligocations.

Intercalation of hydroxy silicoaluminum compounds increases the thermal stability and the acidity of the pillared clays.

The distributions of acid strengths of various pillared clays obtained by calorimetry of NH_3 adsorption showed that Al-PILC displays high acidity, with a small number of sites as strong as those measured on zeolites. Acidity should be directly related to the environment of the Al ions in the pillars, which could be modified by the preparation. The adsorption of NH_3 on pillared beidellite showed the presence of many strong acid sites (160 kJ mol^{-1}) [108].

A natural clay has been pillared with mixed solutions containing both Al and Fe, Ti or Cr. The intercalation-generated solids' distribution of acid strengths measured by calorimetric adsorption of ammonia is comparable to that of zeolites. The surfaces appear as heterogeneous and show initial adsorption heats close to 150–160 kJ mol^{-1} if one excludes the first point of the differential heat versus coverage curves, which is much higher (≈190 kJ mol^{-1}) [109].

The acidity of mesoporous expanded clay catalysts has been studied using ammonia adsorption microcalorimetry [110]. The inclusion of SiO_2–TiO_2 clusters

drastically increased the total (Brønsted + Lewis) acidity of the clay, in terms of both the strength and the density of acid sites.

The acidity of pillared clays has been characterized by both microcalorimetric measurements of the adsorption of aromatic molecules and pyridine and the catalytic ethylbenzene test reaction [111]. The aromatic probe molecules used were a reactant and a product of the catalytic reaction: ethylbenzene and *m*-diethylbenzene, respectively. In this way, only the strongest of the accessible acid sites were titrated. The heats of adsorption of these molecules indicate that a zirconium oxide pillared clay had stronger acidity than an aluminum oxide pillared clay, whereas the pyridine results were equal for both samples.

9.3.8 Zeolites

Aluminosilicates can be divided into two categories, amorphous silica–aluminas (described in Section 9.3.4) and crystalline zeolites or molecular sieves.

In crystalline aluminosilicates, all aluminum and silicon atoms form tetrahedra which are linked by shared oxygen atoms. These tetrahedra join to form secondary building units, which can be interconnected to give numerous distinctive zeolite structures. Each has a regular and well defined pore structure together with inner cavities. The precise control of pore size is one of the greatest distinctions between zeolites and amorphous silica–aluminas. The morphology, free volume, pore geometry and electric field gradients determine their acidity and selectivity.

Numerous reviews dealing with the adsorption capacities and acid–base properties of zeolites have been published [4, 8, 10–14, 17] so we will not give a detailed description of these systems. Only some case studies will be given in order to assess the possibilities of thermal techniques for characterizing such materials. In general the total number of acid sites is greater in zeolites than in amorphous silica–aluminas for a similar Si : Al ratio.

The acidity of high-silica zeolites produced either by direct synthesis or by chemical dealumination of parent zeolites (either by steaming and acid leaching or by $SiCl_4$ vapor treatment), which makes it possible in principle to extract the aluminum from the network without the structure collapsing, was extensively studied in the 1990s.

Together with ZSM-5 zeolites, dealuminated HY (ultra-stable Y or USY) zeolites are the most widely used in petrochemistry (fluid catalytic cracking processes) [112]. The active centers are Brønsted acid sites carried by the zeolite framework. USY is derived from synthetic Y faujasites dealuminated by chemical or, more commonly, hydrothermal treatments. These treatments partially remove aluminum atoms from the crystal framework, improving the thermal stability, as well as decreasing the number of Brønsted sites, which is a function of the concentration of Al atoms, but generating extra-framework aluminum (EFAL) species and framework defects, which are generally associated with Lewis acidity. The Lewis sites may have their own catalytic activity and also may interact with Brønsted sites, increasing their strength [62].

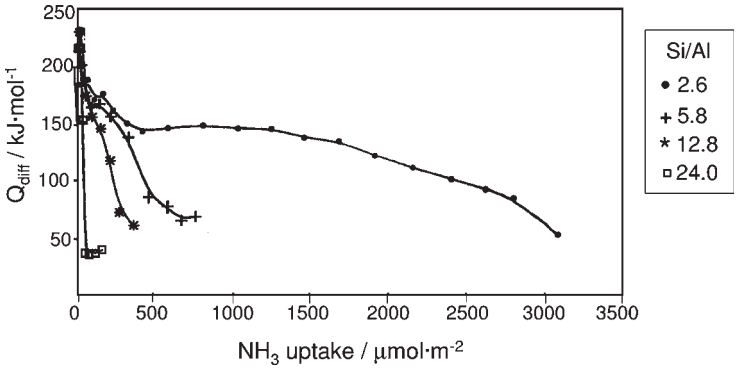

Figure 9.16 Differential heats of ammonia adsorption versus coverage for dealuminated HY zeolites.

The effect of dealumination can be observed in a series of commercial Y-faujasites with Si:Al ratios of 2.6, 5.8, 12.8 and 24. The modification of the acidity resulting from the dealumination is illustrated by the curves of differential heats of ammonia adsorption (Figure 9.16).

The initial heats, in the 180–230 kJ mol^{-1} range, correspond to particularly strong Lewis sites. With the exception of the most dealuminated zeolite, the curves present a quasi plateau of heats around 140 kJ mol^{-1} (attributed to Brønsted sites), then decrease to about 70 kJ mol^{-1}, a value often considered as the chemisorption–physisorption limit for ammonia. These curves indicate the existence of three populations of sites: strong sites (Q above 150 kJ mol^{-1}), medium sites ($120 < Q < 150$ kJ mol^{-1}) and weak acid sites ($70 < Q < 120$ kJ mol^{-1}). In terms of relative site populations, the two most dealuminated zeolites present a higher number of very strong sites, owing to the presence of EFAL species.

Flow adsorption microcalorimetry has been used to measure the heats of adsorption of ammonia in a nitrogen carrier on the H^+ and Na^+ forms of a Y zeolite [21]. The calorimeter was linked to a thermal conductivity detector in which the rates of adsorption and desorption and the associated rates of heat evolution or absorption were measured simultaneously at atmospheric pressure. The authors found that, as surface coverage increased, the sites covered first were not necessarily those with the highest molar heats of adsorption.

Calorimetric investigations of the adsorption of water, ammonia, methanol and other small polar molecules on the Na forms of synthetic zeolites A, X and Y have demonstrated the heterogeneous nature of the Q_{diff} versus n_a relation, which can be explained by the successive interactions of the exchange cations at the various crystallographic positions [14].

The energy of interaction with ammonia and therefore the acid strength of mordenite at low coverages are higher than the corresponding data for HY molecular sieves. The overall initial acid strengths of the H-forms of mordenite, ZSM-5 and faujasite may be arranged in the following order: HM (≈170 kJ mol^{-1}) > H-ZSM-5 (≈155 kJ mol^{-1}) > H-Y (≈140 kJ mol^{-1}).

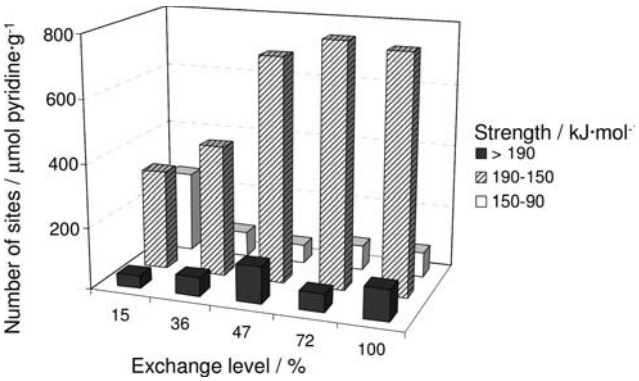

Figure 9.17 Acid site strength distribution of Na,H-mordenites as a function of the exchange level. Pyridine adsorption at 573 K, activation at 773 K.

When using pyridine as a probe molecule, the heats evolved are higher than with ammonia [36]. However, unlike ammonia, pyridine, which is a larger molecule, can titrate only OH groups located in large channels. Heats of adsorption of pyridine were measured at 573 K on a series of Na-exchanged mordenites [113]. The curves of differential heats of adsorption versus pyridine coverage were analyzed, and Figure 9.17 shows the number of sites of a given strength as a function of the exchange level. Three populations of sites, above 190 kJ mol^{-1}, within 190–150 kJ mol^{-1} and within 150–90 kJ mol^{-1}, are apparent (Figure 9.17). A moderate increase of the population of very strong sites (heat above 190 kJ mol^{-1}) is apparent in this figure, whereas the number of sites with Q_{diff} values lying between 190 and 150 kJ mol^{-1} increases considerably with the exchange degree up to 47% exchange and then remained constant above this value. These results suggest that, as long as new hydroxyls are formed in large channels, their average acidic strength increases. Above 47% exchange, the acidic strength of hydroxyls in the large channels remains constant, which indicates that the formation of hydroxyls taking place in side pockets (above 50% of cation exchange) does not influence the properties of hydroxyls in large channels [14]. Concomitantly, the number of sites that display a moderate strength (between 150 and 90 kJ mol^{-1}) decreases and then remains constant.

Adsorption enthalpies of N_2, CO, CH_3CN and NH_3 on H-BEA and H-MFI zeolites have been measured calorimetrically at 303 K in order to assess the energetic features of the various interactions occurring within the zeolite nanocavities, namely: (i) specific adsorption on Lewis and Brønsted acid sites; (ii) H-bonding interaction with hydroxyl nests; (iii) confinement effects. Whereas CO and N_2 single out contributions from Lewis and Brønsted acid sites, CH_3CN and NH_3 are not preferentially adsorbed on Lewis sites, suggesting that adsorption on Brønsted sites is competitive with that on Lewis sites. For CO adsorbed on a Lewis-rich H-β zeolite, the initial Q_{diff} value is ≈ 70 kJ mol^{-1}, compared with 60 kJ mol^{-1} for H-ZSM-5 [114].

Alkali-exchanged zeolites are basic solids and are recognized as effective catalysts for a wide range of organic transformations, such as aldol condensation, alkylation and etherification. The basic strength and catalytic activity of alkali-exchanged zeolites can be increased by the occlusion of alkali metal oxide clusters via impregnation and decomposition of alkali metal compounds such as acetates or hydroxides. Oxides of cesium and potassium have been synthesized in the supercages of zeolite X and the alkali-loaded zeolites have been characterized by both CO_2 adsorption microcalorimetry and stepwise TPD (STPD) of CO_2 [115]. For a loading of about two alkali metal atoms per zeolite supercage, the majority of CO_2 adsorption sites at 373 K were characterized by a ΔH_{ads} of about 80–100 kJ mol^{-1}. The CO_2 adsorption capacity of CsO_x/CsX increased linearly with the number of excess cesium atoms, but the strength of most adsorption sites seemed to be unaffected by the amount of excess cesium species. The basic strengths were found to vary in the order CsO_x/CsX > CsO_x/KX > KO_x/KX. However the differential heats at low CO_2 coverage were about the same for all samples. The values of CO_2 adsorption capacities from STPD were slightly higher than those from adsorption microcalorimetry [115].

Silicalite can be regarded as a new polymorph of silica, presenting adsorption characteristics close to those of a ZSM-5 zeolite with an extremely high Si : Al ratio. The heats of adsorption of both quadrupole (N_2 and CO_2) and non-polar (Ar, O_2, CH_4, C_2H_6 and SF_6) gases were determined on a silicalite in order to study the effect of adsorbate size and polarity on the energetics of adsorption in zeolites [116]. Silicalite was classified as a relatively homogeneous adsorbent compared to X-type zeolite. The accuracy of the calculated isosteric heats of adsorption was estimated to be ±2% for heats larger than 20 kJ mol^{-1} and ±5% for heats smaller than 20 kJ mol^{-1}. Examples of calorimetrically measured heats for adsorption of pure SF_6 and CO_2 on a silicalite sample bonded with alumina have also been reported and compared with calculated isosteric heats [117].

ETS-10 is a titanosilicate with a three-dimensional 12-ring pore system and a very high ion-exchange capacity. The integral heats of adsorption of monoalkylamines on ETS-10 have been measured by isothermal calorimetry as a function of the *n*-alkylamine concentration [118]. The heats vary in the order methyl < ethyl < propyl < butyl amine.

Copper-exchanged ETS-10 catalysts with low and high degrees of exchange have been prepared and studied using calorimetry of adsorption of NO, CO, C_2H_4 and NH_3 probe molecules [119]. Moreover, DSC curves of reduction by hydrogen as a function of temperature yielded useful information concerning the identification of supported species and the determination of the intermediate oxidation states of copper during reduction (Figure 9.18).

The low-temperature shoulder for the under-exchanged Cu-ETS-04 and Cu-ETS-1 samples can be assigned to the reduction of Cu^{2+} to Cu^{+} and the main peak to the reduction of Cu(I) to Cu(0), which confirms that Cu(I) species are predominant in these samples, while in the over-exchanged sample Cu-ETS-5, most of the Cu^{2+} species are in close contact and not inserted in the support.

A fairly large number of papers have been published on the use of calorimetry to study the acidity of mesoporous materials [14].

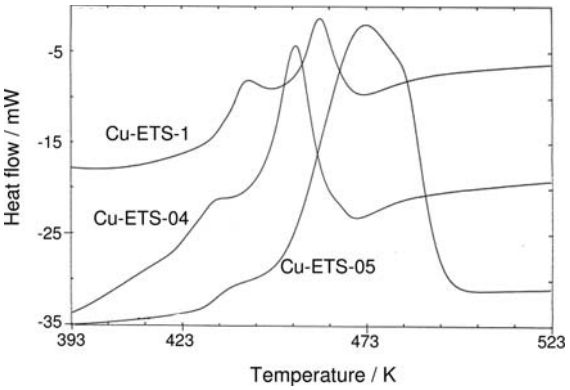

Figure 9.18 Heat flow profiles for reduction under H_2 flow as a function of temperature for various Cu-ETS samples.

Mesoporous molecular sieves are close to microporous zeolites in their methods of preparation and principal regions of application. These materials are usually synthesized by using supermolecular templates and, in particular, the micelles of cationic surfactants [17].

According to the data from calorimetric investigations of the adsorption of ammonia, unlike silica gel, the pure-silica mesoporous sieve MCM-41 possesses specific although weak acidity. The introduction of titanium or zirconium, and particularly aluminum, ions into the structure of this sieve substantially increases the acid strength of the sorbent [120, 121].

Using ammonia as probe, the strength of the acid centers of the investigated samples can be arranged in the following order: silica gel < Si-MCM-41 < Si,Zr-MCM-41 < Si,Ti-MCM-41 < Si,Al-MCM-41. The heats of NH_3 adsorption on the latter sample with molar ratio $SiO_2 : Al_2O_3 = 32:8$ are 130–150 kJ mol^{-1}, which is close to the heats of interaction of ammonia with a ZSM-5 zeolite.

Spectroscopic and calorimetric investigations of the adsorption of acetonitrile [122] have shown that the sorbent Si,Al-MCM-41 has strong Lewis (aprotic) acidity and poorly defined Brønsted (protic) acidity [17]. The presence of strong Lewis centers on Si,Al-MCM-41 was confirmed by flow microcalorimetry for the adsorption of 1-butanol from a solution of *n*-hexane [123, 124]. Depending on the aluminum content of the structure, the number of strong Lewis centers on the surface of this sample was found to vary in the range of 43 to 70% of the total number of active centers.

9.4
A Case Study: Vanadia Catalysts

It is known that catalytic activity in selective oxidation of hydrocarbons can be related to the co-operative action of an oxidizing function and an acidic function. From this perspective, the determination of both the redox and the acidic

properties of the catalytic centers, as carried out in the present study using pulsed adsorption and flow calorimetry, becomes a topic of renewed importance.

Vanadium oxide is known to catalyze oxidation of hydrocarbons, and the selective ODH of ethane over V_2O_5 catalysts has been extensively studied. The acid–base and redox characters of vanadium pentoxide, V_2O_5/SiO_2, $V_2O_5/\gamma\text{-}Al_2O_3$, V_2O_5/TiO_2, $V_2O_5/TiO_2/SiO_2$, V_2O_5/CeO_2, V_2O_5/Nb_2O_5 and V_2O_5/MgO catalysts have been investigated by adsorption microcalorimetry of probe molecules and/or TPR/TPO calorimetric experiments respectively.

NH_3 adsorption calorimetry experiments performed on bulk V_2O_5 indicated a weak acidity, with an initial heat of adsorption of 70 kJ mol^{-1} and a large heterogeneity [125].

TPR/TPO experiments were performed in a TG-DSC apparatus on a bulk V_2O_5 [125] using a gas flow of C_2H_6, C_2H_4 or H_2 (diluted in helium) as the reducing agents, at a heating rate of 5 K min^{-1}. The reduction temperatures and heat flows depended greatly on the reducing agent, with reduction heats increasing in the order $C_2H_6 < C_2H_4 < H_2$. According to the weight loss, a similar reduction extent occurred whether hydrogen, ethane or ethene was used as reducing agent, corresponding to the formation of V_2O_3 in all cases. In the case of ethene, various intermediate suboxides could be deduced by examining the derivative of the thermogravimetric curve. Following each reduction, re-oxidation studies were performed under oxygen flow in the same equipment, clearly showing different steps in the re-xidation process.

Regular pulses of pure ethane on bulk V_2O_5 maintained at 823 K in a microcalorimeter linked to a gas chromatograph provided kinetic data of theoretical significance, as well as an insight into the mechanism of the reduction process. The results of this work carried out using mainly calorimetric techniques led to the conclusion that diffusion of oxygen from the bulk is predominant in the selective oxidation of ethane and that the redox process plays a more important role than the acidic sites in the case of unsupported vanadium pentoxide.

V_2O_5/SiO_2 catalysts prepared by grafting or wet impregnation methods have also been studied in the ethane ODH reaction. The surface characteristics and the reactivity of these catalysts have been investigated using microcalorimetry linked to other techniques such as volumetric studies and thermogravimetry. The vanadia amounts ranged from 1 to 20 wt%. The numbers of acid sites of the supported catalysts were found to increase with vanadium loading, leading to materials with a moderately acidic character [126, 127].

Compared to bulk vanadia, higher values of the initial heats of NH_3 adsorption have been measured for the V_2O_5/SiO_2 catalysts (78 to 124 kJ mol^{-1}). Considering the overall value of chemisorbed ammonia versus the vanadium content, the population of titrated acid sites was slightly higher for the grafted V_2O_5/SiO_2 catalysts than for the samples prepared by wet aqueous impregnation for similar V_2O_5 loadings. A linear relation was also observed between the integral enthalpy of ammonia adsorption and the vanadium content of the catalysts.

Interaction with the support was enhanced after catalytic reaction, as indicated by the detection of new strong Lewis acid sites by DRIFT spectroscopy measure-

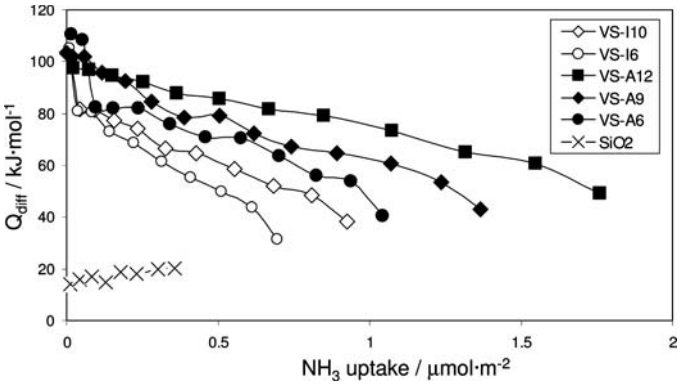

Figure 9.19 Differential heats of ammonia adsorption over a silica support and silica-supported vanadia catalysts prepared by ALD (filled symbols) and impregnation (open symbols). VS-A6 and VS-I6 on one hand, and VS-A12 and VS-I10 on the other hand, have comparable vanadia contents.

ments and higher heats of ammonia adsorption [128]. The catalytic activity increased with the vanadium content and the ammonia uptake of the V_2O_5/SiO_2 catalysts, that is with their acidity. However, selectivity to ethane appeared to be more closely related to the coordination of the vanadium atoms than to the acidic character of the surface of the V_2O_5/SiO_2 catalysts. The activity and selectivity to ethane were enhanced on V_2O_5/SiO_2 especially for very low vanadium contents, presumably corresponding to isolated vanadium cations, which are more easily reduced in ethene as shown by DSC. As stated above, both the number and the strength of the acid sites of the silica-supported catalysts increased as the vanadia loading increased, independently of the preparation method. Comparing catalysts at similar V_2O_5 loadings prepared by impregnation and by atomic layer deposition (ALD) it appears that the ALD preparation yields a V_2O_5 phase characterized by a higher number of acid sites and a stronger surface acidity than the preparation by impregnation (Figure 9.19) [129]. ALD is a gas-phase layer-by-layer processing method based on surface-saturating precursor adsorption on the support, thus allowing a high dispersion of the deposited species.

The acid–base properties of $V_2O_5/\gamma\text{-}Al_2O_3$ catalysts prepared by the impregnation method have been characterized by ammonia, pyridine and sulfur dioxide adsorption microcalorimetry. Sulfur dioxide adsorption made it possible to differentiate a vanadate layer from free alumina.

Ammonia and sulfur dioxide adsorption experiments also showed that, at low vanadium coverage, a large part of the vanadate layer is bound to acid–base pairs of alumina. At low vanadium coverage (<3 wt% V_2O_5), the acidic character of the $V_2O_5/\gamma\text{-}Al_2O_3$ catalyst can be ascribed to vanadium-free alumina, whereas at higher vanadium coverage it is largely attributed to vanadate compounds [130].

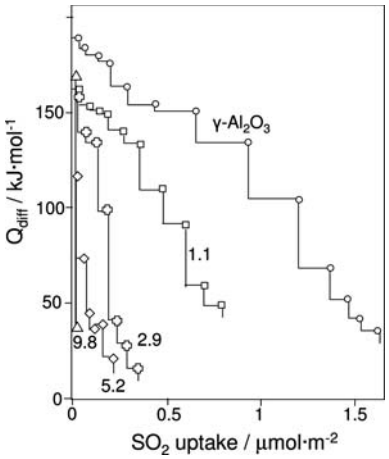

Figure 9.20 Differential heat of sulfur dioxide adsorption at 353 K as a function of the probe uptake on V_2O_5/γ-Al_2O_3 catalysts with different wt% of V_2O_5 as indicated in the figure.

Figure 9.20 displays the differential enthalpy of SO_2 adsorption at 353 K as a function of the probe uptake on samples with various vanadium contents and on pure γ-Al_2O_3.

The adsorption of sulfur dioxide of the catalysts rapidly decreased with the vanadium content of the samples. As sulfur dioxide is not chemisorbed on bulk vanadium pentoxide and also appears not to chemisorb on vanadate species, on V_2O_5/γ-Al_2O_3 catalysts this probe can be considered to be selective for the titration of the basic sites of vanadium-free alumina. Thus, by selectively probing uncovered alumina, SO_2 further allows the distinction between the acid–base features of the vanadium oxide layer and those of uncovered alumina.

The acid–base properties of a 5.2 wt% V_2O_5/γ-Al_2O_3 catalyst have also been studied after performing measurements of catalytic activity for ethane conversion to ethene by microcalorimetry of adsorption of NH_3 and SO_2 at 353 K. Figure 9.21 displays the acidic and basic features of this catalyst before and after the catalytic run. The acid–base features of γ-Al_2O_3 are also reported for reference. This figure confirms that V_2O_5 is preferentially anchored on the basic sites of the alumina, resulting in a large decrease in basicity. It was also observed that some additional acid sites (0.1 µmol m^{-2}) have appeared after the catalytic run. This amount corresponds to 5% of the overall acidic sites of the catalyst. It is interesting to note the same increase in basic sites. These features are consistent with the restoration of some acid–base pairs of γ-Al_2O_3 and show the overall stability of the acid–base character of the vanadium oxide layer [131].

A 20 wt% V_2O_5/γ-Al_2O_3 catalyst has been subjected to a TPR in ethane and reoxidation in air using TG-DSC equipment, and compared to bulk vanadium pentoxide. Reduction in ethane occurs at a lower temperature on the V_2O_5/γ-Al_2O_3 catalyst (717 compared with 794 K for bulk vanadium pentoxide). The exothermic

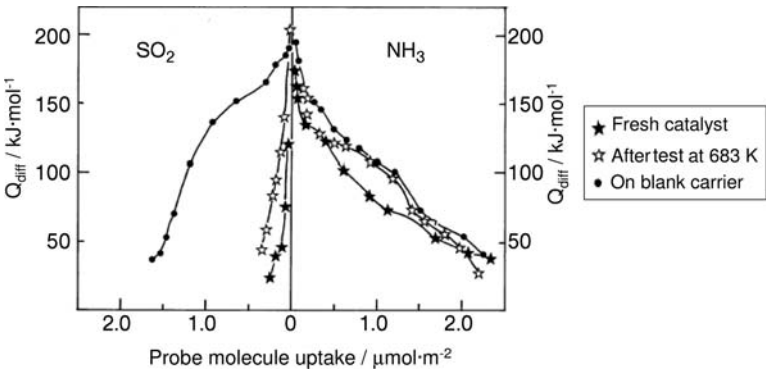

Figure 9.21 Differential enthalpies of adsorption of ammonia and sulfur dioxide at 353 K on 5.2 wt% $V_2O_5/\gamma\text{-}Al_2O_3$.

enthalpy evolved in the reduction is much higher on the alumina-supported catalyst. A reduction step by itself is an endothermic process. The observed exothermic enthalpies involve two terms: an enthalpy of reaction (exothermic) and an enthalpy due to lattice oxygen migration (endothermic). It was deduced from the calorimetric data that lattice oxygen migration to react with ethane requires less energy on the $V_2O_5/\gamma\text{-}Al_2O_3$ catalyst, that is lattice oxygen mobility is improved on that catalyst.

Nano-sized V_2O_5/SiO_2, V_2O_5/Al_2O_3, V_2O_5/TiO_2 and $V_2O_5/TiO_2/SiO_2$ can be prepared by ALD. Compared to liquid-phase preparations, the technique gives greater benefits in terms of species dispersion and uniformity.

Alumina-, silica- and titania-supported vanadium oxide systems with V_2O_5 loadings ranging from 3 to 12 wt%, corresponding to 0.02 to 0.09 V/(Al, Si, Ti) atomic ratios, were prepared by ALD and compared with the corresponding impregnated catalysts [129]. The surface acidic properties of the supports and catalysts were investigated using ammonia adsorption microcalorimetry to determine the number and strength of the surface acid sites. Deposition of V_2O_5 on alumina and titania supports gave rise to catalysts with lower numbers of acid sites than the respective supports, while for the samples prepared on silica, an increase of the number of acid sites was observed after V_2O_5 deposition, thus confirming the study performed by Le Bars and coworkers [131]. As a common trend, the surface acid strength was greater for the ALD catalysts than for the impregnated ones, suggesting a stronger interaction of the VO species with the support centers, which act as electron attractor centers creating Lewis-like vanadium species.

Synergistic interactions of highly dispersed vanadia and titania species on silica have been shown to control the acidity, reducibility and thus the overall activity of the $V_2O_5/TiO_2/SiO_2$ catalysts in the selective oxidation reaction of *o*-xylene to phthalic anhydride [132]. Using ammonia adsorption calorimetry and pyridine adsorption IR spectroscopy it was shown in this study that the strong Lewis acidity of a pure titania support was masked by the deposition of vanadia, the decrease in the number of acid sites being especially pronounced in the case of the highly

dispersed ALD samples. On $V_2O_5/TiO_2/SiO_2$ samples, the better dispersion of active species in the ALD samples was verified by the acidity measurements. The number of strong, mainly Lewis, acid sites increased in the ALD catalysts with sub-monolayer titania coverage. In the catalysts with high titania content, the ALD vanadia species masked the acidity better than the species prepared by impregnation. It was also shown using ammonia and *o*-xylene adsorption microcalorimetry that the presence of strong surface acidic and *o*-xylene adsorption sites decreased the activity of the catalysts in the test reaction of *o*-xylene oxidation. Medium-strength and strong *o*-xylene adsorption sites, with evolved heats between 120 and 150 kJ mol^{-1}, seemed to be the most detrimental for the catalytic activity.

In another study [133], microcalorimetric adsorption of reactants and products on supported vanadia catalysts for the selective oxidation of propene to acetone was used to provide information about the surface bonding strengths that may be used for the microkinetic analysis of the corresponding surface reactions. The initial heat for water adsorption on the studied V_2O_5/TiO_2 catalyst is lower than 90 kJ mol^{-1}, indicating that water is reversibly adsorbed at temperatures higher than 360 K. The heat of adsorption of acetone on the reduced V_2O_5/TiO_2 catalyst is about 100 kJ mol^{-1}, which can be used to estimate the activation energy for desorption of acetone from the catalyst [133].

The acid–base properties of V_2O_5/CeO_2 catalysts prepared by the wetness impregnation technique have been determined by NH_3 and CO_2 adsorption calorimetry at 423 K [134]. Variations in V_2O_5 loading and calcination temperature brought about changes in the surface structure of the dispersed vanadium species, and hence in the surface acidic and redox properties. CeO_2 possessed fairly strong surface acidity and basicity. Addition of V_2O_5 enhanced the surface acidity as well as the redox properties, but decreased the surface basicity. Calcination of the 10 wt% V_2O_5/CeO_2 catalyst at 873 K resulted mainly in the formation of $CeVO_4$ on the surface, which showed low surface acidity and redox ability.

Microcalorimetry was also used to measure the heats of adsorption of ethanol and 2,2,2-trifluoroethanol as a function of coverage at 300 K for a 6 wt% V_2O_5/CeO_2 sample. The calorimetric data showed a constant heat of adsorption of 65 kJ mol^{-1} [135].

V_2O_5 catalysts supported on niobyl phosphate ($NbOPO_4$) with V_2O_5 loadings from 5 to 25 wt% were prepared by incipient wetness impregnation, and the surface acidity was determined by microcalorimetry using NH_3 as a probe molecule. The results suggested that the loaded V_2O_5 weakened the surface acidity of $NbOPO_4$ while increasing the proportion of weak acid sites (Figure 9.22). The surface of $NbOPO_4$ presented a purely acidic character and weakened the redox properties of supported V_2O_5 [136].

Magnesium vanadates, also known as VMgO catalysts, are known to be efficient catalysts for the ODH of light alkanes. Corma and coworkers [137] suggested that the incorporation of small amounts of V on a MgO surface notably modified not only the redox properties of the system but also the acid–base character of the oxygen species present on the catalyst surface. These acid–base properties were related to the nucleophilic character of the lattice oxygen anions.

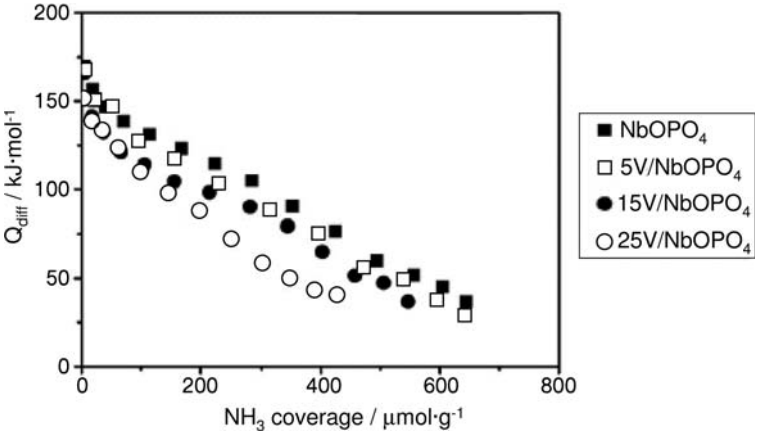

Figure 9.22 Differential heats of ammonia adsorption versus coverage for various niobyl phosphate supported vanadia samples.

A series of VMgO catalysts with various compositions and surface areas were characterized at 353 K, using adsorption calorimetry of NH_3 and SO_2 to probe their acid–base properties. The acid strength of the VMgO samples increased up to 14 wt% of V loading. For higher loadings, the strong acidity decreased, while weaker acid sites developed above 25 wt%. The basicity of the VMgO samples remained nearly unchanged for loadings up to 25 wt% V. At higher loadings, the basicity decreased, and vanished for the 45 wt% V loading sample [138].

All these studies have demonstrated the usefulness of calorimetry for studying the surface characteristics of vanadia-based catalysts. Among the surface properties of vanadia catalysts of relevance to their catalytic activity in selective oxidation reactions, acidity is one of the most significant.

Protonic acidity of the support is not desirable as it leads to side-reactions such as polymerization or cracking of organic molecules at high temperatures and coking. Complete coverage of the support by a V_2O_5 phase might give rise to Lewis-like vanadium centers, which are characterized by a lower acid strength than the acid centers of the oxide supports.

For vanadia catalysts supported on alumina, titania or niobyl phosphate, the main trend evidenced by ammonia adsorption microcalorimetry is a remarkable decrease of the number of acid sites, together with a decrease of the total acid strength compared with the acidic properties of the bare support. By contrast, owing to the neutral behavior of the silica surface, the acidity of V_2O_5 phases deposited on silica becomes much more apparent. A similar trend was observed on the basic magnesia and amphoteric ceria. A decrease in basicity was observed on all amphoteric supports (γ-Al_2O_3,TiO_2,TiO_2/SiO_2, CeO_2), allowing the distinction between acid–base features of the vanadium oxide layer and those of the uncovered support.

9.5 Conclusion

We hope that the impression left by this chapter will be that of a field with exciting prospects for the future, as the sophisticated use of powerful tools such as microcalorimetry linked to other techniques begins to make connections with computational approaches to the chemistry of solid surfaces.

Adsorption microcalorimetry is probably the most direct method for describing in detail both the quantitative and the energetic features of surface sites. The ability of the microcalorimetric technique to readily reveal subtle differences among samples is worth stressing. Even though one has to be cautious about the nature of the acidic and basic sites, calorimetric information on the concentration and strength of the sites can be used with confidence for interpreting the catalytic behavior.

Metal oxides are largely used as catalysts in the chemical industry, and many organic reactions such as cracking, isomeration, alkylation and partial oxidation are performed over such catalysts. Hence, a deep knowledge of the surface properties is of great importance for the development of catalysts with suitable and tailored acid–base characteristics.

Because no single technique can provide an exhaustive comprehension of the acid–base picture of oxide surfaces, the joint use of calorimetric and spectroscopic techniques (FTIR, XPS) is necessary for full characterization.

XPS displays great analytical power in the detection of surface species in providing their oxidation state. Moreover, the N_{1s} or S_{2p} XP spectra of chemisorbed N-probes (NH_3, pyridine) or S-probes (SO_2) on surface acid–base sites make it possible to distinguish between Brønsted and Lewis sites and to evaluate their relative concentrations. Vibrational spectroscopy (FTIR) is also a powerful technique for evaluating the qualitative nature of the surface sites. Nevertheless, we have demonstrated in this chapter that calorimetry, although a time-consuming technique, has great power in determining in a single experiment the number, strength and strength distribution of the active sites of oxides. Moreover, flow calorimetry methods (DSC) have also demonstrated the possibility of characterizing the redox properties of solid surfaces from an energetic point of view, even if they compete in this area with more classical systems such as TPR-TPO reactors equipped with thermal conductivity detectors.

References

1 Haines, P.J. (ed.) (2002) *Principles of Thermal Analysis and Calorimetry*. Royal Society of Chemistry, Cambridge, 1–220.

2 Auroux, A. (1994), in *Catalyst Characterization, Physical Techniques for Solid Materials* (eds B. Imelik and J.C. Védrine), Plenum Press, New York, pp. 611–50.

3 Gravelle, P.C. (1972) *Advances in Catalysis*, **22**, 191–263.

4 Andersen, P.J. and Kung, H.H. (1994) *Catalysis*, **11**, 441–66, Royal Society of Chemistry.

5 Gervasini, A. and Auroux, A. (1993) *Journal of Physical Chemistry*, **97**, 2628–39.

6 Lohse, U., Parlitz, B. and Patzelova, V. (1989) *Journal of Physical Chemistry*, **93**, 3677–83.

7 Klyachko, A.L., Brueva, T.R. and Kapustin, G.I. (1986) in *Recent Advances in Catalysis and Catalytic Engineering* (ed. K. Rao), Hyderabad, pp. 607–12.

8 Auroux, A. (2002) *Topics in Catalysis*, **19**, 205–13.

9 Sigrist, K. and Stach, H. (1996) *Thermochimica Acta*, **278**, 145–56.

10 Farneth, W.E. and Gorte, R.J. (1995) *Chemical Reviews*, **95**, 615–34.

11 Cardona-Martinez, N. and Dumesic, J.A. (1992) *Advances in Catalysis*, **38**, 149–244.

12 Solinas, V. and Ferino, I. (1998) *Catalysis Today*, **41**, 179–89.

13 Auroux, A. (1997) *Topics in Catalysis*, **4**, 71–89.

14 Auroux, A. (2008) in *Molecular Sieves – Science and Technology: Acidity and Basicity, Determination by Adsorption Microcalorimetry*, Vol. 6, Springer Verlag, pp. 45–152.

15 Damjanovic, L. and Auroux, A. (2008) Handbook of thermal analysis and calorimetry, in *Recent Advances Techniques and Applications*, Vol. 5 (eds M.E. Brown and P.K. Gallagher), Elsevier, pp. 387–438.

16 Fubini, B. (1988) *Thermochimica Acta*, **135**, 19–29.

17 Tarasevich, Y.I. (2001) *Theoretical and Experimental Chemistry*, **37**, 197–214.

18 Narasimharao, K., Brown, D.R., Lee, A.F., Newman, A.D., Siril, P.F., Taverner, S.J. and Wilson, K. (2007) *Journal of Catalysis*, **248**, 226–34.

19 Damjanovic, L. and Auroux, A. (2008) in *Zeolite Chemistry and Catalysis: an Integrated Approach and Tutorial* (eds A. Chester and E. Derouane), Springer Verlag (to be published).

20 Felix, S.P., Savill-Jowitt, C. and Brown, D.R. (2005) *Thermochimica Acta*, **433**, 59–65.

21 Brown, D.R. and Groszek, A.J. (2000) *Langmuir*, **16**, 4207–12.

22 Karge, H.G. and Dondur, V. (1990) *Journal of Physical Chemistry*, **94**, 765–72.

23 Gervasini, A., Carniti, P. and Auroux, A. (2005) *Thermochimica Acta*, **434**, 42–9.

24 Sharma, S.B., Meyers, B.L., Chen, D.T., Miller, J. and Dumesic, J.A. (1993) *Applied Catalysis A: General*, **102**, 253–65.

25 Drago, R.S., Dias, S.C., McGilvray, J.M. and Mateus, A.L.M.L. (1998) *Journal of Physical Chemistry B*, **102**, 1508–14.

26 Kob, N., Drago, R.S. and Young, V. (1997) *Inorganic Chemistry*, **36**, 5127–31.

27 Carniti, P., Gervasini, A., Biella, S. and Auroux, A. (2005) *Chemistry of Materials*, **17**, 6128–36.

28 Carniti, P., Gervasini, A., Biella, S. and Auroux, A. (2006) *Catalysis Today*, **118**, 373–8.

29 Babitz, S.M., Williams, B.A., Kuehne, M.A., Kung, H.H. and Miller, J.T. (1998) *Thermochimica Acta*, **312**, 17–25.

30 Cardona-Martinez, N. and Dumesic, J.A. (1990) *Journal of Catalysis*, **125**, 427–44.

31 Busca, G. and Lorenzelli, V. (1982) *Materials Chemistry*, **7**, 89–126.

32 Auroux, A., Artizzu, P., Ferino, L., Monaci, R., Rombi, E., Solinas, V. and Petrini, G. (1996) *Journal of the Chemical Society – Faraday Transactions*, **92**, 2619–24.

33 Cardona-Martinez, N. and Dumesic, J.A. (1991) *Journal of Catalysis*, **128**, 23–33.

34 Boreave, A., Auroux, A. and Guimon, C. (1997) *Microporous Materials*, **11**, 275–91.

35 Gorte, R.J. and White, D. (1997) *Topics in Catalysis*, **4**, 57–69.

36 Gorte, R.J. (1999) *Catalysis Letters*, **62**, 1–13.

37 Parillo, D.J. and Gorte, R.G. (1993) *Journal of Physical Chemistry*, **97**, 8786–92.

38 Itadani, A., Sugiyama, H., Tanaka, M., Mori, T., Nagao, N. and Kuroda, Y. (2007) *Journal of Physical Chemistry C*, **111**, 16701–5.

39 Cutrufello, M.G., Ferino, I., Monaci, R., Rombi, E. and Solinas, V. (2002) *Topics in Catalysis*, **19**, 225–40.

40 Auroux, A., Muscas, M., Coster, D.J. and Fripiat, J.J. (1994) *Catalysis Letters*, **28**, 179–86.

41 Oliveira de Souza, A., Rangel-Santos-Varela, M., Bennici, S. and Auroux A. (2008) *Thermochimica Acta* (to be published).

42 Auroux, A. and Gervasini, A. (1990) *Journal of Physical Chemistry*, **94**, 6371–9.

43 Gervasini, A. and Auroux, A. (1991) *Journal of Thermal Analysis*, **37**, 1737–44.

44 Mekhemer, G.A.H., Halawy, S.A., Mohamed, M.A., and Zaki, M.I. (2004) *Journal of Physical Chemistry B*, **108**, 13379–86.

45 Mc Hale, J.M., Auroux, A., Perrotta, A.J. and Navrotsky, A. (1997) *Science*, **277**, 788–91.

46 Auroux, A., Artizzu, P., Ferrino, I., Solinas, V., Leofanti, G., Padovan, M., Messina, G. and Mansani, R. (1995) *Journal of the Chemical Society–Faraday Transactions*, **91**, 3263–7.

47 Desmartin-Chomel, A., Flores, J.L., Bourane, A., Clacens, J.M., Figueras, F., Delahay, G., Giroir-Fendler, A. and Lehaut-Burnouf, C. (2006) *Journal of Physical Chemistry B*, **110**, 858–63.

48 Gergely, B. and Auroux, A. (1999) *Research on Chemical Intermediates*, **25**, 13–24.

49 Rodriguez Delgado, M., Morterra, C., Cerrato, G., Magnacca, Q. and Otero Arean, C. (2002) *Langmuir*, **18**, 10255–60.

50 Sun, Q., Fu, Y., Yang, H., Auroux, A. and Shen, J. (2007) *Journal of Molecular Catalysis A: Chemical*, **275**, 183–93.

51 Gervasini, A., Bellussi, G., Fenyvesi, J. and Auroux, A. (1995) *Journal of Physical Chemistry*, **99**, 5117–25.

52 Neri, G., Pistone, A., De Rossi, S., Rombi, E., Milone, C. and Galvagno, S. (2004) *Applied Catalysis A: General*, **260**, 75–86.

53 Marcus, R.L., Gonzalez, R.D., Kugler, E.L. and Auroux, A. (2003) *Chemical Engineering Communications*, **190**, 1601–19.

54 Kim, S.Y., Goodwin, J.G., Hammache, S., Auroux, A. and Galloway, D. (2001) *Journal of Catalysis*, **201**, 1–12.

55 Deutsch, D., Quaschning, V., Kemnitz, E., Auroux, A., Ehwald, H. and Lieske, H. (2000) *Topics in Catalysis*, **13**, 281–5.

56 Occelli, M., Schiraldi, D.A., Auroux, A., Keogh, K.A. and Davis, B.H. (2001) *Applied Catalysis A: General*, **209**, 165–77.

57 Gervasini, A., Fenyvesi, J. and Auroux, A. (1996) *Langmuir*, **12**, 5356–64.

58 Colorio, G., Védrine, J.C., Auroux, A. and Bonnetot, B. (1996) *Applied Catalysis A: General*, **137**, 55–68.

59 Keränen, J., Iiskola, E., Guimon, C., Auroux, A. and Niinistö, L. (2002) *Studies in Surface Science and Catalysis*, vol. 143 (eds E. Gaigneaux et al.), Elsevier, pp. 777–85.

60 Keränen, J., Guimon, C., Auroux, A., Iiskola, E. and Niinistö, L. (2003) *Physical Chemistry Chemical Physics*, **5**, 5333–42.

61 Petre, A.L., Auroux, A., Gervasini, A., Caldararu, M., Ionescu, N.I. (2001) *Journal of Thermal Analysis and Calorimetry*, **64**, 253–60.

62 Keränen, J., Guimon, C. and Auroux, A. (2006) *Proceedings of the 8th International Conference on Fundamental and Applied Aspects of Physical Chemistry, Belgrade*, Vol. 1, pp. 123–31.

63 Shen, J., Cortright, R.D., Chen, Y. and Dumesic, J.A. (1994) *Catalysis Letters*, **26**, 247–57.

64 Sprinceana, D., Caldararu, M., Ionescu, N.I. and Auroux, A. (1999) *Journal of Thermal Analysis and Calorimetry*, **56**, 109–15.

65 Auroux, A., Sprinceana, D. and Gervasini, A. (2000) *Journal of Catalysis*, **195**, 140–50.

66 Gervasini, A., Perdigon-Melon, J.A., Guimon, C. and Auroux, A. (2006) *Journal of Physical Chemistry B*, **110**, 240–9.

67 Perdigon-Melon, J.A., Gervasini, A. and Auroux, A. (2005) *Journal of Catalysis*, **234**, 421–30.

68 Jin, Y.S., Ouqour, A., Auroux, A. and Védrine, J.C. (1989) in *Structure and Reactivity of Surfaces* (eds C. Morterra, A. Zecchina and G. Costa), Elsevier, Amsterdam, pp. 525–4.

69 Petre, A.L., Perdigon-Melon, J.A., Gervasini, A. and Auroux, A. (2003) *Catalysis Today*, **78**, 377–86.

70 Gervasini, A., Ragaini, V. and Auroux, A. (1995) in *Environmental Catalysis* (eds G. Centi et al.), SCI, Rome, pp. 279–82.

71 Auroux, A. and Gravelle, P.C. (1981) *Thermochimica Acta*, **47**, 333–41.

72 Wang, Z.M., Yamaguchi, M., Goto, I. and Kumagai, M. (2000) *Physical Chemistry Chemical Physics*, **2**, 3007–15.

73 Dropsch, H. and Baerns, M. (1997) *Applied Catalysis A: General*, **158**, 163–83.

74 Gerrero-Ruiz, A., Yang, S., Xin, Q., Maroto-Valiente, A., Benito-Gonzalez, M. and Rodriguez-Ramos, I. (2000) *Langmuir*, **16**, 8100–6.

75 Perdigon-Melon, J.A., Auroux, A. and Bonnetot, B. (2003) *Journal of Thermal Analysis and Calorimetry*, **72**, 443–51.

76 Uner, D. and Uner, M. (2005) *Thermochimica Acta*, **434**, 107–12.

77 Belzunegui, J.P., Sanz, J. and Guil, J.M. (2005) *Journal of Physical Chemistry B*, **109**, 19390–6.

78 Wang, C.B. and Yeh, C.T. (1997) *Journal of Molecular Catalysis A – Chemical*, **120**, 179–84.

79 Tanabe, K., Sumiyoshi, T., Shibata, K., Kiyoura, T. and Kitagawa, J. (1974) *Bulletin of the Chemical Society of Japan*, **47**, 1064–6.

80 Kung, H.H. (1984) *Journal of Solid State Chemistry*, **52**, 191–6.

81 Tanabe, K. (1981) in *Catalysis Science and Technology*, Vol. 2 (eds J.R. Anderson and M. Boudart), Springer, New York, pp. 231–73.

82 Cutrufello, M.G., Ferino, I., Solinas, V., Primavera, A., Trovarelli, A., Auroux, A. and Picciau, C. (1999) *Physical Chemistry Chemical Physics*, **1**, 3369–75.

83 Feng, R-M., Yang, X-J., Ji, W-J., Zhu, H-Y., Gu, H-D, Chen, Y., Han, S. and Hibst, H. (2007) *Journal of Molecular Catalysis A–Chemical*, **267**, 245–54.

84 Watson, R.B. and Ozkan, U.S. (2003) *Journal of Molecular Catalysis A – Chemical*, **194**, 115–35.

85 El Jamal, M.M., Forissier, M. and Auroux, A. (1988) *Journal of the Chemical Society–Faraday Transactions I*, **84**, 3169–74.

86 Occelli, M.L., Biz, S., Auroux, A. and Iyer, P.S. (1999) *Applied Catalysis A: General*, **179**, 117–29.

87 Dragoi, B., Gervasini, A., Dumitriu, E. and Auroux, A. (2004) *Thermochimica Acta*, **420**, 127–34.

88 Naumann d'Alnoncourt, R., Bergmann, M., Strunk, J., Löffler, E., Hinrichsen, O. and Muhler, M. (2005) *Thermochimica Acta*, **434**, 132–9.

89 Bennici, S., Auroux, A., Guimon, C. and Gervasini, A. (2006) *Chemistry of Materials*, **18**, 3641–50.

90 Gervasini, A., Bennici, S., Auroux, A. and Guimon, C. (2007) *Applied Catalysis A: General*, **331**, 129–37.

91 Yuzhakova, T., Rakic, V., Guimon, C. and Auroux, A. (2007) *Chemistry of Materials*, **19**, 2970–81.

92 Bonnetot, B., Rakic, V., Yuzhakova, T., Guimon, C. and Auroux, A. (2008) *Chemistry of Materials*, **20**, 1585–96.

93 Vartuli, J.C., Santiesteban, J.G., Traverso, P., Cardona-Martinez, N., Chang, C.D. and Stevenson, S.A. (1999) *Journal of Catalysis*, **187**, 131–8.

94 Tichit, D., Lhouty, M.H., Guida, A., Chiche, B.H., Figueras, F., Auroux, A., Bartolani, D. and Garrone, E. (1995) *Journal of Catalysis*, **151**, 50–9.

95 Prescott, H.A., Li, Z.J., Kemnitz, E., Trunschke, A., Deutsch, J., Lieske, H., Auroux, A. (2005) *Journal of Catalysis*, **234**, 119–30.

96 Winter, F., Xia, X., Hereijgers, B.P.C., Bitter, J.H., Jos van Dillen, A., Muhler, M. and de Jong, K.P. (2006) *Journal of Physical Chemistry B*, **110**, 9211–18.

97 Casenave, S., Martinez, H., Guimon, C., Auroux, A., Hulea, V. and Dumitriu, E. (2003) *Journal of Thermal Analysis and Calorimetry*, **72**, 191–8.

98 Dussault, L., Dupin, J.C., Dumitriu, E., Auroux, A. and Guimon, C. (2005) *Thermochimica Acta*, **434**, 93–9.

99 Dussault, L., Dupin, J.C., Martinez, H., Dumitriu, E., Auroux, A. and Guimon, C. (2006) *Surface and Interface Analysis*, **38**, 234–7.

100 Sanchez Valente, J., Figueras, F., Gravelle, M., Kumbhar, P., Lopez, J. and Besse, J-P. (2000) *Journal of Catalysis*, **189**, 370–81.

101 Lefebvre, F., Liu-Cai, F.X. and Auroux, A. (1994) *Journal of Materials Chemistry*, **4**, 125–31.

102 Morin, P., Hamad, B., Sapaly, G., Corneiro Rocha, M.G., Pries de Oliveira, P.G., Gonzalez, W.A., Andrada Sales, E.

and Essayem, N. (2007) *Applied Catalysis A: General*, **330**, 69–76.
103 Liu-Cai, F.X., Sahut, B., Faydi, E., Auroux, A. and Hervé, G. (1999) *Applied Catalysis A: General*, **185**, 75–83.
104 Damjanovic, L., Rakic, V., Mioc, U.B. and Auroux, A. (2005) *Thermochimica Acta*, **434**, 81–7.
105 Nakato, T., Kimura, M., Nakata, S. and Okuhara, T. (1998) *Langmuir*, 319–25.
106 Bachiller-Boeza, B., Alvarez-Rodriguez, J., Guerrero-Ruiz, A. and Rodriguez-Ramos, I. (2007) *Applied Catalysis A: General*, **333**, 281–9.
107 Occelli, M.L. (1988) *Catalysis Today*, **2**, 339–55.
108 Figueras, F., Klapyta, Z., Massiani, P., Mountassir, Z., Tichit, D., Fajula, F., Guegen, C., Bousquet, J. and Auroux, A. (1990) *Clays and Clay Minerals*, **38**, 257–64.
109 Belkhadem, F., Clacens, J.M., Bengueddoch, A. and Figueras, F. (2006) *Applied Catalysis A: General* **298**, 188–93.
110 Occelli, M.L., Olivier, J.P., Perdigon, J.A. and Auroux, A. (2002) *Langmuir*, **18**, 9816–23.
111 Jeronimo, D., Guil, J.M., Corbella, B.M., Vasques, H., Miranda, A., Silva, J.M., Lobato, A., Pires, J. and Corvalho, A.P. (2007) *Applied Catalysis A: General*, **330**, 89–95.
112 Shen, J. and Auroux, A. (2004) in *Fluid Catalytic Cracking IV: Preparation and Characterization of Catalysts* (ed. M.L. Occelli), Studies in Surface Science and Catalysis, vol. 149, Elsevier, Amsterdam, pp. 35–70.
113 Auroux, A. and Datka, J. (1997) *Applied Catalysis A: General*, **165**, 473–9.
114 Busco, C., Barbaglia, A., Broyer, M., Bolis, V., Foddanu, G.M. and Ugliengo, P. (2004) *Thermochimica Acta*, **418**, 3–9.
115 Li, J. and Davis, R.J. (2003) *Applied Catalysis A: General*, **239**, 59–70.
116 Dunne, J.A., Mariwala, R., Rao, M., Sircar, S., Gorte, R.J. and Myers, A.L. (1996) *Langmuir*, **12**, 5288–895.
117 Sircar, S. (2005) *Applied Surface Science*, **252**, 647–53.
118 Ruiz, J.A-C., Ruiz, V.S.O., Airoldi, C. and Pastore, H.O. (2004) *Applied Catalysis A: General*, **261**, 87–90.
119 Gervasini, A., Picciau, C. and Auroux, A. (2000) *Microporous and Mesoporous Materials*, **35–36**, 457–69.
120 Occelli, M.L., Biz, S. and Auroux, A. (1999) *Applied Catalysis A: General*, **183**, 231–9.
121 Occelli, M.L., Biz, S. and Auroux, A. (1998) *Microporous and Mesoporous Materials*, **26**, 193–213.
122 Janchen, J., Stach, H., Busio, M. and Van Wolput, J.H. (1998) *Thermochimica Acta*, **312**, 33–45.
123 Meziani, M.J., Zajac, J., Jones, D.J., Partyka, S., Roziere, J. and Auroux, A. (2000) *Langmuir*, **16**, 2262–8.
124 Meziani, M.J., Zajac, J., Jones, D.J., Roziere, J. and Partyka, S. (1997) *Langmuir*, **13**, 5409–17.
125 Le Bars, J., Vedrine, J.C., Auroux, A., Pommier, B. and Pajonk, G.M. (1992) *Journal of Physical Chemistry*, **96**, 2217–21.
126 Le Bars, J., Vedrine, J.C., Auroux, A., Trautmann, S. and Baerns, M. (1992) *Applied Catalysis A: General*, **88**, 179–95.
127 Le Bars, J. and Auroux, A. (1993) *Journal of Thermal Analysis*, **40**, 1277–84.
128 Le Bars, J., Auroux, A., Védrine, J.C. and Baerns, M. (1992) *Studies in Surface Science and Catalysis*, **72**, 181–9.
129 Gervasini, A., Carniti, P., Keränen, J., Niinistö, L. and Auroux, A. (2004) *Catalysis Today*, **96**, 187–94.
130 Le Bars, J., Védrine, J.C., Auroux, A., Trautmann, S. and Baerns, M. (1994) *Applied Catalysis A: General*, **119**, 341–54.
131 Le Bars, J., Auroux, A., Forissier, M. and Védrine, J.C. (1996) *Journal of Catalysis*, **162**, 250–9.
132 Keränen, J., Carniti, P., Gervasini, A., Iiskola, E., Auroux, A. and Niinistö, L. (2004) *Catalysis Today*, **91–92**, 67–71.
133 Li, M. and Shen, J. (2002) *Journal of Catalysis*, **205**, 248–58.
134 Gu, X., Ge, J., Zhang, H., Auroux, A. and Shen, J. (2006) *Thermochimica Acta*, **451**, 84–93.

135 Feng, I. and Vohs, J.M. (2004) *Journal of Physical Chemistry*, **108**, 5647–52.

136 Sun, Q., Fang, D., Wang, S., Shen, J. and Auroux, A. (2007) *Applied Catalysis*, **327**, 218–25.

137 Corma, A., Lopez-Nieto, J.M. and Paredes, N. (1993) *Journal of Catalysis*, **144**, 425–38.

138 Pantazidis, A., Auroux, A., Herrmann, J.M. and Mirodatos, C. (1996) *Catalysis Today*, **32**, 81–8.

10
Transmission Electron Microscopy

Wuzong Zhou

10.1
Introduction

The identification of the electron by J.J. Thomson in 1897 [1] was one of the most important scientific discoveries of all time, and changed human life completely. In 1924, the theory of the wave motion of the electron was established by Louis de Broglie [2]. From the wave motion of the electron comes one of the most fascinating and powerful applications of the electron, namely the electron microscope. The first electron diffraction experiments were performed by G.P. Thomson in 1927 [3], proving Louis de Broglie's theory. The first electron microscope was constructed by Ruska and Knoll in 1931.

In the 1940s, it was realized that interaction between electrons and atoms might change the phase of an electron wave and make possible the observation of single atoms using phase contrast. This is the theoretical foundation of high-resolution transmission electron microscopy (HRTEM). It was also established by O. Scherzer [4] that using under-focus conditions could overcome the effect of lens defects and therefore increase resolution. This is the practical foundation of HRTEM. In the early 1970s, the resolution of HRTEM was improved to 0.3 nm as demonstrated by the observation of lattice fringes in the images of $Ti_2Nb_{10}O_{29}$ crystals [5]. Thus transmission electron microscopy (TEM) has a history going back over 70 years and HRTEM one of about 40 years.

HRTEM investigation of solid oxides is one of the most active research fields in solid-state and materials science. The structures of metals are relatively simple; for example, many metals have one of two common structures – cubic close packing (ccp) and hexagonal close packing (hcp). When a metal is oxidized forming oxides, the different oxidation states of metal cations and various types of metal–oxygen–metal bonding states result in a large number of new structures and many possible structural modifications, including the formation of superstructures and defects. HRTEM has proved to be essential in studying the structures of solid oxides, and its importance in materials science and nanoscience today is obvious.

Although the theory of electron optics was established many years ago, technical developments of TEM continue. It is well known that a crystal structure can be

Metal Oxide Catalysis. Edited by S. David Jackson and Justin S. J. Hargreaves

ISBN: 978-3-527-31815-5

accurately determined by X-ray diffraction (XRD) or neutron diffraction methods. However, these diffraction techniques collect structural information from a large number of unit cells (typically 10^{15}). In other words, the structure determined by these techniques is an average structure. Diffraction methods can only give indirect structural information. On the other hand, HRTEM is unique for directly imaging three-dimensional microstructures of solids. Many local structures on the nanometer scale can be observed. For nano-scale materials, such as nanoparticle catalysts, nanowires and nanotubes of metal oxides, HRTEM is particularly useful, since the dimensions of the nanomaterials are very small and information from conventional diffraction methods is limited.

10.2 HRTEM and Related Techniques

10.2.1 Ray Diagram of TEM

The principles of TEM and HRTEM have been discussed in several textbooks [6, 7]. A TEM column can be described using a ray diagram as shown in Figure 10.1, which is very similar to that for an optical microscope. The most important components in an electron microscope are the electron source (normally called the electron gun) and a group of electromagnetic lenses.

Electrons are emitted from the electron gun and accelerated by a potential difference (a typical value for HRTEM is 200 to 300 kV). These electrons are focused by the condenser lenses to form a parallel beam. The electron beam strikes a

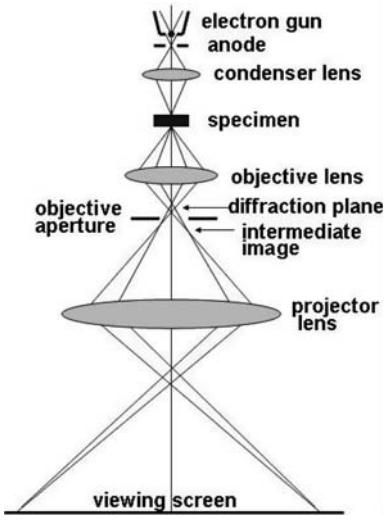

Figure 10.1 Ray diagram of TEM set-up.

specimen, creating different forms of energy. The transmitted and scattered electrons are then recombined and focused by the objective lens to form a diffraction pattern and an intermediate image at different stages. The beams then diverge and are focused by the projective lenses to form the final image. Magnification of an image in a modern HRTEM can be ca 800 000 × to 1 500 000 × at maximum.

10.2.2
Electron Wavelength

In comparison with X-rays, an electron beam can have a very short wavelength, which can be calculated according to the equation below when the relativistic correction is considered:

$$\lambda = \frac{h}{\sqrt{2m_o eV_o\left(1+\frac{eV_o}{2m_o C^2}\right)}}$$

where h is Planck's constant, m_o the electron rest mass, e the charge on the electron, V_o the accelerating voltage and C the speed of light. Thus, an electron beam accelerated by a voltage of 200 kV has a wavelength $\lambda = 0.002\,51$ nm, which is much shorter than the wavelength of X-rays used in conventional diffraction experiments (e.g. Cu K_α is 0.154 nm). This results in electron beams being very powerful in detecting microstructures of solids.

10.2.3
Interaction between Electrons and Solids

Another characteristic of the high-energy electron beam is its very strong interaction with specimens. At least ten different forms of energy can be expected from such interaction as show in Figure 10.2. The most useful energy forms for scanning electron microscopy (SEM) are backscattered electrons and secondary electrons. X-rays are used in energy dispersive X-ray spectroscopy (EDX or EDS). Electron diffraction patterns and TEM images are formed by transmitted electrons and scattered electrons.

It is also important to know that the interaction volume of electrons with a solid specimen is much larger than the beam size. According to a Monte Carlo simulation, in which the detailed history of an electron trajectory is calculated in a stepwise manner, the interaction volume is a function of the accelerating voltage and properties of the target specimen.

10.2.4
Formation of Image Contrast

There are three main formation mechanisms of TEM image contrast: mass–thickness contrast, diffraction contrast and phase contrast. When electrons pass

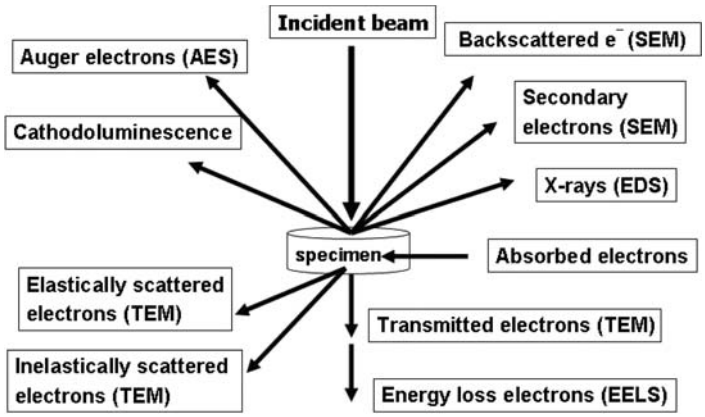

Figure 10.2 Schematic drawing showing different forms of energy created from an interaction between electron beam and solid.

through a particle, some are reflected and some are absorbed by the specimen. Only some of the electrons can pass through the objective aperture, making a contribution to the image contrast. If the electrons are scattered with a large angle, they may not pass through the objective aperture and therefore will not contribute to the image formation as shown in the inset of Figure 10.3a. Thus, the region with higher scattering power (heavier constituent elements or greater specimen thickness) appears darker in contrast. For example, the edge of the particle in Figure 10.3a shows a lighter contrast in comparison with the central area. The mass–thickness contrast can be enhanced by using a smaller objective aperture or a lower accelerating voltage. TEM image contrast at low magnifications is normally dominated by the mass–thickness contrast.

Crystals with different structures, the same crystals with different crystal orientations with respect to the incident electron beam, and crystals with dislocations or various grain boundaries will create different patterns of Bragg reflections. This difference causes image contrast. Diffraction contrast is widely used to study dislocations and defects in crystals, because the regions around the defects have Bragg angles differing from the perfect crystalline matrices and thus produce contrast that can be observed. Figure 10.3b is a HRTEM image obtained from a high Tc superconducting $RuSr_2GdCu_2O_8$ [8]. The dark lines do not mean a mass–thickness difference, but indicate antiphase grain boundaries.

Electron radiation is a wave, which can be characterized by two physical terms: amplitude (A) and phase (θ): $Ae^{i\theta}$. Since electron radiation is coherent, when two waves meet, the resulting wave is a sum of the two waves, $Ae^{i\theta} = A_1e^{i\theta} + A_2e^{i\theta}$, and the resultant intensity is not necessarily bigger than any individual wave intensity but depends on the phase difference of the two waves. A phase-object refers to a specimen so thin that when a coherent plane wave passes through it, only the phase of the wave changes but the amplitude keeps its original value. Thus, there

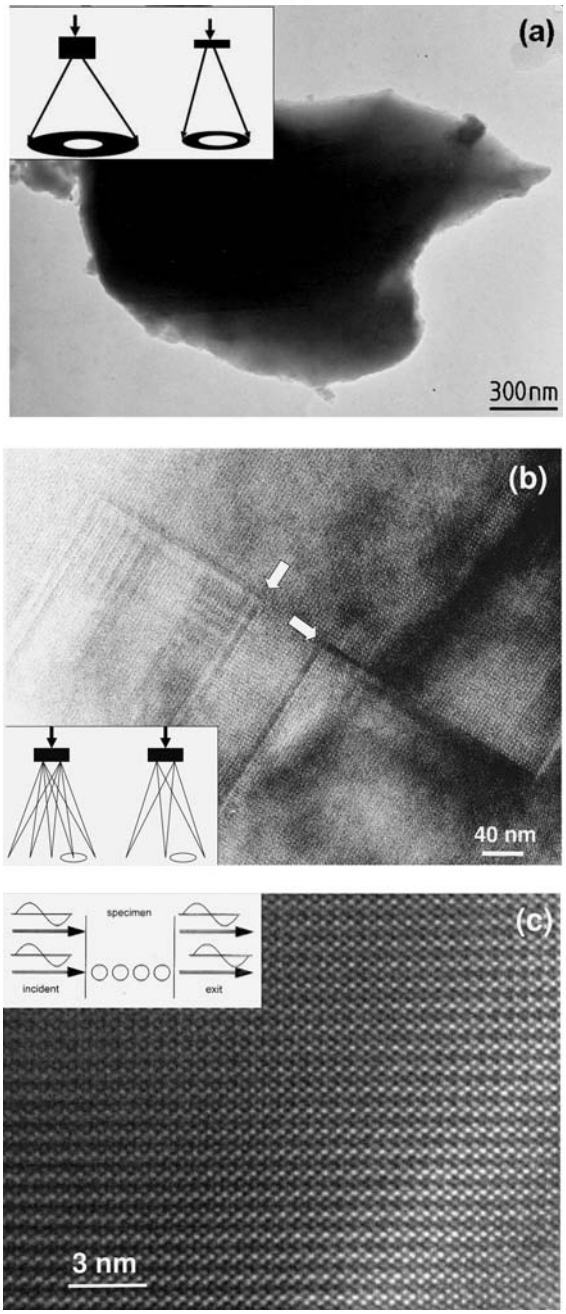

Figure 10.3 Three examples of electron microscopic images showing different formation mechanisms of image contrast, (a) mass–thickness contrast; (b) diffraction contrast and (c) phase contrast. The insets are schematic pictures showing the principles of the contrast formation.

is no intensity ($I = A^2$) variation in the exit wave, and a minimum contrast image is observed when the exit wave is properly imaged at the in-focus condition. The image contrast due to the phase change is called phase contrast, which can be increased by defocusing.

Unlike optical microscopy or electron microscopy at low magnification, where mass–thickness contrast (absorption/amplitude contrast) plays an important role, HRTEM image interpretation uses phase contrast and needs a full understanding of the beam–specimen interaction and the effects of lens errors. Figure 10.3c is a HRTEM image of $YSrCo_2O_5$ [9]. The black spots correspond to atomic columns. This can be altered by changing the phase of the electron wave using a change in the lens focus value. Therefore, the black spots can be changed into white spots or vice versa. The phase-contrast image has three important differences from the amplitude-contrast image. (1) An amplitude-contrast image is focused on the ideal image plane, the so-called Gaussian image plane. For a phase-object image at the Gaussian image plane, if there is no lens error, the image wave function is a copy of the exit wave, so that the image intensity is uniformly unity. In order to obtain phase contrast, HRTEM images must be taken at a plane away from the Gaussian image plane. (2) The nature of phase contrast is the interfering effect of waves scattered by individual atoms. Therefore, the incident electron wave must be coherent. (3) The least distinguishable distance criterion is no longer valid in phase-contrast images.

10.2.5 Resolution of TEM

The overall resolution in HRTEM is governed partly by the electron wavelength and partly by the optical characteristics of the objective lens. The most important effect of the latter arises from spherical aberration. This aberration introduces a phase difference into the individual diffracted beams and when the real image is synthesized by the lens from these diffracted beams this can give rise to considerable confusion in the image contrast.

Figure 10.4 shows two rays emanating from the point Q, one along the optic axis and another at a scattering angle α (generally of the order of 10 milliradians). If the lens is perfect, these two rays should intersect at a point P. If spherical aberration is present, the non-axial ray would reach the Gaussian image plane at the point P′ with an amount Δr from the optic axis, where Δr is the radius of the disk of least confusion. The total phase shift introduced from the spherical aberration is:

$$W_S(\alpha) = \left(\frac{2\pi}{\lambda}\right)\frac{1}{4}C_S\alpha^4$$

where C_s is coefficient of spherical aberration.

Increasing the focal length by an amount ΔF causes a non-axial ray to be brought to the optic axis further from the specimen. The phase difference between axial and non-axial rays is:

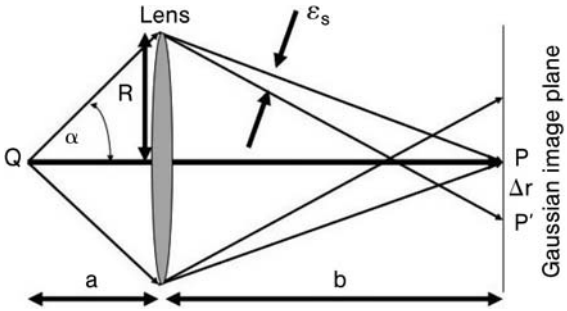

Figure 10.4 Schematic diagram showing the effect of spherical aberration on a ray with a scattering angle.

$$W_f(\alpha) = \left(\frac{2\pi}{\lambda}\right)\frac{1}{2}\Delta F\alpha^2$$

The phase shifts from spherical aberration and defocus have opposite signs. Consequently, owing to the imperfection of the lens and an introduced defocus value, electrons scattered through a scattering angle α have their phase altered by a factor exp(iχ), where χ is defined by:

$$\chi(\alpha) = \frac{2\pi}{\lambda}\left(\frac{1}{2}\Delta F\alpha^2 - \frac{1}{4}C_s\alpha^4\right)$$

which is Scherzer's equation, derived in 1949 [4].

By differentiating the Scherzer equation, an interpretable resolution limit can be derived, $r = AC_s^{\frac{1}{4}}\lambda^{\frac{3}{4}}$ at the Scherzer focus $\Delta F = -B\lambda^{\frac{1}{2}}C_s^{\frac{1}{2}}$, where A and B are positive constants [10]. Therefore, reducing either C_s or λ may lead to an increase of the resolution of TEM. For example, for a microscope operating at 200 kV (λ = 0.002 51 nm) with C_s = 0.41 mm and Scherzer focus ΔF = −380 nm, the resolution limit, r, is 0.18 nm. When the accelerating voltage is increased to 800 kV and 1300 kV, the resolution limit may be improved to 0.14 nm and 0.104 nm respectively [11].

The most exciting recent development of HRTEM is the so-called C_s-corrected HRTEM. This type of HRTEM, based on the design of Rose [12], functions through two electromagnetic hexapoles and some additional lenses. It allows the value of C_s to be tuned from positive to zero and even to negative numbers. In 2003, Urban and coworkers demonstrated that, using C_s-corrected TEM, the resolution was improved from 0.24 nm to 0.13 nm [13]. Oxygen atoms in $SrTiO_3$ were directly imaged. The most recent achievement of high resolution in HRTEM is the unique microscope at the Department of Energy's National Center for Electron Microscopy at the Lawrence Berkeley National Laboratory in collaboration with several National Laboratories and FEI, which is one of the largest companies producing electron microscopes. This microscope has a further improved resolution of 0.5 Å

and therefore was named TEAM0.5 (TEAM stands for Transmission Electron Aberration-corrected Microscope).

In addition to its power of directly imaging atomic structures of crystals, HRTEM is often equipped with several other powerful devices for characterization of solids, such as electron diffraction (ED), EDX, electron energy loss spectroscopy (EELS), scanning transmission electron microscopy (STEM) and so on. In this chapter, only the most commonly used supporting techniques for HRTEM, ED and EDX, are discussed in detail.

10.2.6 Electron Diffraction

Like other diffraction techniques, ED obeys Bragg's law, that is, $2d\sin\theta = n\lambda$, where d is the d-spacing of the crystal planes defined by $(h\ k\ l)$, n the order of reflection, θ the angle of incidence (Bragg angle) and λ the wavelength of the electron beam. If $d\ (h\ k\ l) = 0.5$ nm, $n = 1$, $\lambda = 0.0251$ nm, the Bragg angle, θ, is then 0.14°, which is significantly smaller than that in conventional X-ray diffraction.

One of the advantages of electron microscopy is that a very small specimen area can be examined. An aperture, inserted into the intermediate image plane (Figure 10.1), enables us to collect beams scattered from only a small area in a specimen. This operation is called selected area electron diffraction (SAED). Therefore, SAED patterns can be obtained from very small particles and even from a single nanoscale domain in a particle.

Powder XRD shows one-dimensional patterns created from three-dimensional structures, while SAED patterns are two-dimensional pictures reflecting two-dimensional structural information. The disadvantage of SAED is that the structural information along the projected direction is lost, unless a special technique is used, for example high-order Laue zone (HOLZ) diffraction [14, 15]. The advantage of SAED is that the relation between any two diffraction spots in a pattern, i.e. an interplane angle, can be easily revealed. This helps greatly in determination of a unit cell.

Since the Ewald sphere (diffraction sphere) is large, with a radius of $1/\lambda$, the set of diffraction spots obtained along a principal zone axis is an almost undistorted picture of the zero level of the reciprocal lattice. Calculation of d-spacings from SAED patterns is relatively simple. Derived from Bragg's law, a reciprocal d-spacing (d^*) can be calculated according to the following equation (Figure 10.5):

$$d^* = \frac{2\sin\theta}{\lambda} = \frac{D^*}{L\lambda}$$

where λ is the wavelength of the electron beam, L the camera length and D^* the distance directly measured from the recorded SAED pattern corresponding to 2θ.

Reciprocal interplane angles can be directly measured from SAED patterns. If several SAED patterns are recorded from a crystal through tilting, a 3D reciprocal

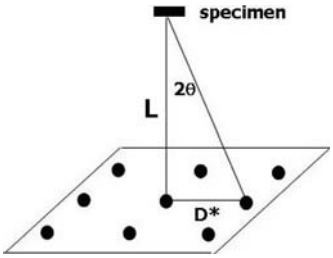

Figure 10.5 Schematic illustration showing the relation between camera length and recorded reciprocal space corresponding to a scattering angle.

unit cell can be determined with the parameters of a^*, b^*, c^*, α^*, β^*, γ^*. Real space unit cell parameters can then be calculated according to the group of equations below:

$$a = \frac{b^*c^*\sin\alpha^*}{V^*},\ \alpha = \cos^{-1}\left[\frac{\cos\beta^*\cos\gamma^* - \cos\alpha^*}{\sin\beta^*\sin\gamma^*}\right]$$

$$b = \frac{c^*a^*\sin\beta^*}{V^*},\ \beta = \cos^{-1}\left[\frac{\cos\alpha^*\cos\gamma^* - \cos\beta^*}{\sin\alpha^*\sin\gamma^*}\right]$$

$$c = \frac{a^*b^*\sin\gamma^*}{V^*},\ \gamma = \cos^{-1}\left[\frac{\cos\beta^*\cos\alpha^* - \cos\gamma^*}{\sin\beta^*\sin\alpha^*}\right]$$

where V and V^* are unit cell volumes in real space and reciprocal space, respectively.

The positions of the diffraction spots give us the unit cell information. The intensities of these spots are dependent on the positions of atoms, i.e. the crystal structure. Electrons are scattered by the electrical potential in a specimen, $\phi(r)$ and the scattering factor, f_B, may be written as:

$$f_B = 8\pi^2\lambda^2\frac{me^2}{h^2}\frac{[Z - f_x]}{\sin^2\theta}$$

where f_x is the X-ray scattering factor, m and e are the electron mass and charge, Z is the atomic number, λ is the wavelength of electron beam, h is Planck's constant, and θ is the scattering angle. If f_B is evaluated, it is found that its value varies from atom to atom in a manner which is very roughly proportional to $Z^{1/3}$. This means that scattering is less sensitive to the atomic numbers. Consequently, electron diffraction is a far better method of detecting light atoms than X-ray diffraction, for example being more sensitive to oxygen in metal oxides.

Another characteristic of electron diffraction in comparison with other diffraction methods is multiple scattering. The interaction between the electron beam

and matter is so strong that the electrons may be scattered several times by different atomic planes before leaving a specimen. This makes the intensities of the scattered electron beams hard to predict, because they depend not only on the specimen structure but also on the specimen thickness. Unlike single scattering, after multiple scattering the intensities of some beams increase and some decrease. Some diffraction peaks, which should be systematically absent, may appear in SAED patterns, so that extracting space group information from SAED patterns is normally difficult. Fortunately, determination of unit cell dimensions is not complicated by multiple scattering. In fact, the appearance due to multiple scattering of systematically absent diffraction spots may help to reveal unit cell dimensions, because SAED patterns may show a correct unit cell with a lower symmetry.

To identify an extra diffraction spot caused by multiple scattering of the electron beam, we may try to record several SAED patterns from one crystallite with a change of specimen thickness to observe the relative intensity of the spot. Alternatively, we may tilt the specimen around the axis including the spot to see a change of its relative intensity. The relative intensity of a diffraction peak due to multiple scattering may reduce significantly or the peak may even disappear completely with a reduction of specimen thickness or with a small angle tilt. A more reliable method for detecting the space group of a crystal structure is convergent beam electron diffraction (CBED) [16, 17].

10.2.7
Energy Dispersive X-ray Spectroscopy

The electrons in atoms are located in different shells, each of them having a definite energy within a particular type of atom. Starting with the shell closest to the nucleus, the shells are termed K, L, M, N and so on with a certain number of electrons in each shell, that is, the K shell holds a maximum of two electrons, the L shell eight, the M shell eighteen, and the N shell thirty-two electrons.

If one electron in the K shell is ejected from an atom by an incident electron, one electron in the L shell may drop down to the vacancy in the K shell. According to energy conservation laws a quantum of radiation will be emitted with a discrete energy corresponding to the difference in energy between the K level and the L level, $h\nu = E_K - E_L$. The vacancy in the K shell may also be filled by an electron directly from the M shell, resulting in a quantum of radiation with another energy, $h\nu = E_K - E_M$. The vacancy in the L shell will also be re-occupied by an electron from a shell with a higher energy level, such as the M shell, and so on. A series of characteristic X-rays are emitted from the solid with the energies being completely dependent upon the atomic numbers of the elements present. The radiation corresponding to the transition between the L and K levels is designated K_α radiation. The radiation corresponding to the M to K transition is designated K_β. L_α, L_β, and so on denote the radiations corresponding to the electron transitions from the M shell to the L shell, and so on.

An X-ray photon carrying a certain energy is collected by the EDX detector. The Si detector is a semiconductor with a band gap of 3.8 eV. Therefore, to excite an electron to form a charge pair, 3.8 eV is required. For example, a Ca K_α X-ray photon has an energy value of 3.7 KeV and it can generate about 1000 charge pairs in the detector. The charge deposited in the detector is collected in 30 to 40 microseconds and appears at the output as a voltage step (pulse).

There are two different situations concerning pulses: (1) The pulses are separated from each other. The detector collects these pulses and transfers the signals to an EDX spectrum. (2) Two pulses overlap and the corresponding current generated gives incorrect information. In this case, the detection system will reject them (by identifying the shapes of the pulses). While such rejection is taking place, the system is unable to respond to other incoming pulses, and this produces a counter "dead time." It is for this reason that using the highest intensity electron beam on a sample, and consequently generating very large amounts of X-rays, does not always produce better EDX spectra, as most pulses are rejected. Therefore, the dead time is normally kept to below 30%.

In EDX experiments on thick samples, for example in SEM, almost all the energy of the incident electron beam is consumed to produce X-rays and the number of atoms in a sample can be calculated from the X-ray intensities in the EDX spectra, by carrying out the ZAF calibration (Z = the atomic number effect; A = the absorption effect and F = the fluorescence effect) [18]. However, HRTEM specimens are usually thin, 200 nm or less. In this case, most electrons in the incident beam will pass through the specimen and the ZAF calibration cannot be done. In practice, we use some standard specimens (whose compositions are known) as references to obtain a relative composition of a target sample. A good approximation is that, for a very thin sample (<100 nm) the concentration ratio of two types of atoms, x and y, can be written:

$$\frac{C_x}{C_y} = K_{xy}\frac{I_x}{I_y}$$

where I_x and I_y are the intensities of the selected X-ray emission lines from elements x and y and K_{xy} is a constant related to these X-ray emission lines, which can be obtained by using standard specimens containing the elements x and y.

Quantitative analysis of the chemical composition of the specimen by EDX relies on obtaining good EDX spectra with the intensities of all the emission lines being almost purely proportional to the concentration of the atoms in the sample. However, there are several technical problems that could affect the quality of an EDX spectrum. The most important one is the absorption problem. Absorption of X-rays can occur in various situations. For example, the X-rays may be absorbed by the specimen itself, by the sample near the examined area, by the specimen grid bars and so on. Therefore isolated particles and thin areas of the particles are always selected to collect the EDX spectra so that the absorption can be reduced to its lowest level. Even when the experimental conditions are well controlled, the

accuracy of the EDX results may still be low, normally > ±5% on an elemental ratio. Therefore, it is necessary to analyze many particles (e.g. 20 to 30) and take an average value of the results. The absorption rate is a function of the energy of the X-rays. At the low energy range, the absorption increases very quickly. This is why it is always difficult to obtain a quantitative composition of oxygen in oxides.

In the following sections, some typical cases of TEM investigations of metal oxides are reviewed, with most examples being taken from the author's own research since the mid-1980s.

10.3
Basic Structures of Oxide Crystals

As mentioned above, the unit cell of a crystalline specimen can be determined by SAED. However, the accuracy of the unit cell dimensions obtained is largely dependent upon the calibration of camera length, which is a function of specimen position and the conditions of the microscope. The procedure is complicated, and in most cases the unit cell parameters determined by SAED are less accurate than those obtained from XRD or neutron diffraction. Owing to the multiple scattering problem, determination of space group by SAED is less reliable. Consequently, HRTEM is not an ideal technique for final determination of crystal structure.

On the other hand, since HRTEM gives direct atomic images, atomic arrangement in a complicated structure can be revealed. Figure 10.6 shows a HRTEM

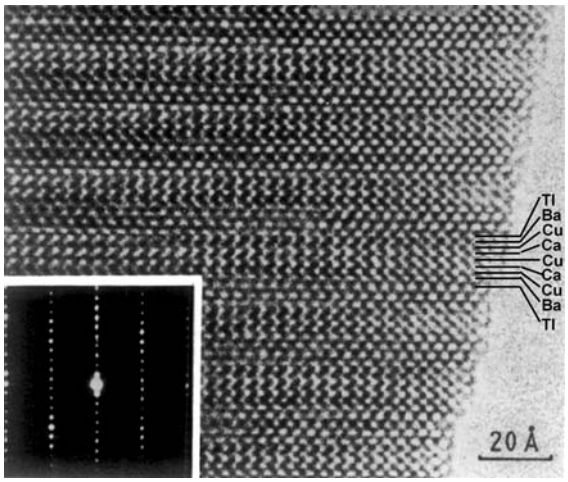

Figure 10.6 HRTEM image and the corresponding SAED pattern (inset) of a crystal of $Tl_2Ba_2Ca_2Cu_3O_{10}$ viewed down the [110] zone axis of a tetragonal unit cell with a = 0.545 and c = 3.661 nm.

image of superconducting oxide $Tl_2Ba_2Ca_2Cu_3O_{10}$ [19]. The atomic layers can be recognized from the image contrast and their relative spaces in the unit cell. This information helps to elucidate the structure. However, accurate atomic positions in the structure can only be determined by XRD and neutron diffraction methods. A combination of powder diffraction and HRTEM thus becomes a very powerful tool in the determination of crystal structures.

HRTEM examines individual crystallites or small areas of a crystallite. It is very useful in identifying different structures, especially the minor phases in multiphasic specimens. In the first decade of high Tc superconductivity research, many new phases were discovered from HRTEM evidence together with compositional information from EDX, including $YBa_2Cu_4O_8$ [20], $Y_2Ba_4Cu_7O_{15}$ [21], $Bi_2Sr_2Ca_2Cu_3O_{10}$ [22], $TlBa_2Ca_{n-1}Cu_nO_{2n+3}$ [23], $Pb_2SrLaCu_2O_6$ [24] and so on.

Although HRTEM has atomic resolution, most images of oxides show only metal atoms, as oxygen's contribution to the image contrast is not significant. As a result of the development of Cs-corrected TEM, it has become possible to "see" directly oxygen atoms [13]. Even then, determination of the positions and occupation factors of oxygen in oxides still has to be rely on diffraction methods.

The most important role of HRTEM in the structural investigation of oxides is the detection of microstructures derived from their basic structures, such as superstructures, various defects and also nano-scale materials, where XRD and neutron diffraction are less powerful since their intensities are very low.

10.4 Superstructures

Superstructures refer to secondary ordering derived from the basic unit cells of oxide crystals. The formation of superstructures in oxides can be due to cation ordering, oxygen ordering or both.

10.4.1 Superstructures Based on Cation Ordering

Secondary cation ordering often occurs when one type of cation in a metal oxide is partially substituted by another. Mixed oxides are good examples. Many oxide catalysts fall within this category.

General speaking, when a solid solution of mixed oxides is identified, its XRD pattern does not change significantly when the composition varies in the solid-solution range. It is generally assumed that the location of the guest cation in the host oxide crystal is random. However, this is not always the case. In many mixed oxides, cation ordering often leads to the occurrence of superstructures, for example superstructures in Bi_2O_3-based solid solutions [25–32]. The high temperature δ-phase of Bi_2O_3, has a defect fluorite structure, which is face centered cubic with $a = 0.56$ nm. The unit cell contains four Bi^{3+} cations occupying the corner and face-centered positions. When a small proportion of Bi is replaced by Nb, a 2×2

× 2 superstructure (type I) forms. The guest cations selectively replace Bi at the body-centered positions of this superunit cell. The ideal unit cell formula is therefore $Bi_{30}Nb_2O_{50}$ [25], which was confirmed by experimental data. The superstructure was clearly revealed by the SAED patterns and also seen from the HRTEM image contrast patterns, although both the diffraction intensities in SAED and the image contrast corresponding to the superstructure were very weak. Similar superstructures were also found in other Bi_2O_3-based solid solutions, such as the Bi_2O_3–V_2O_5 [27] and Bi_2O_3–WO_3 [31] systems. The type I superunit cell dimensions in the latter systems were $3 \times 3 \times 3$ instead of $2 \times 2 \times 2$ in the Bi_2O_3–Nb_2O_5 system. Other types of superstructure, such as type II or type III, in these systems also occur owing to cation ordering.

$TlBa_2Ca_2Cu_3O_9$ (Tl-1223) is a high Tc superconductor with low thermal stability. Partial substitution of Tl by Bi can stabilize the structure. The Tl-1223 phase has a perovskite-related tetragonal unit cell with $a = 0.382$ and $c = 1.53$ nm. When the substitution was performed, it was found that the amount of Tl replaced by Bi was limited to 25%, as indicated by the change of unit cell dimensions (Figure 10.7a). SAED patterns from the compound with 25% substitution seem to be very complicated (Figure 10.7b). The smallest possible superunit cell is $4 \times 4 \times 4$ based on the basic cell. The positions of Bi in the Tl layers were proposed by consideration of the appearance of the diffraction spots, and were confirmed by computer simulation of the SAED patterns. In the final model, it was found that Bi replaces Tl in the Tl layers only at the corners and the center of $2a \times 4b$ or $4a \times 2b$ 2D superlattices (Figure 10.7c) [33]. When all these sites are occupied by Bi, the ratio of Bi : Tl is exactly 1 : 3, i.e. there is 25% substitution. The local distortion resulting from this substitution prevented any further substitution beyond the 25% limit.

The computer simulation indicated that the two types of 2D supercells with dimensions of $2a \times 4b$ and $4a \times 2b$ can give identical SAED patterns along the [001] projection by a 90° rotation around the [001] axis, as shown at the bottom of Figure 10.7. The combination of these two patterns resulted in a SAED pattern similar to the experimental one in Figure 10.7b. In this case, for an approximate measure, a complicated SAED pattern can be divided into two or more simpler patterns, which may aid structure solution.

Because the cations in the host and guest oxides in the above solid solutions have different oxygen coordination, cation ordering is usually accompanied by anion ordering. Bearing in mind that, in most metal oxides, metal atoms are much heavier than oxygen atoms and therefore can scatter electrons more strongly, cation ordering dominates in the contribution to the diffraction intensities of SAED and the image contrast patterns in HRTEM corresponding to the superstructures.

In some layered compounds, electric charge separation between the layers may destabilize the structures: Aurivillius phases $[Bi_2O_2]^{2+}[B_{n-1}M_nO_{3n+1}]^{2-}$ are examples. If oxygen vacancies are introduced into an Aurivillius phase, a stepped superstructure may form to release the charge separation and, probably, reduce the number of oxygen vacancies. For example, Bi_2WO_6 is a well known $n = 1$ member of the family of Aurivillius phases. The unit cell consists of fluorite-like $[Bi_2O_2]$ and

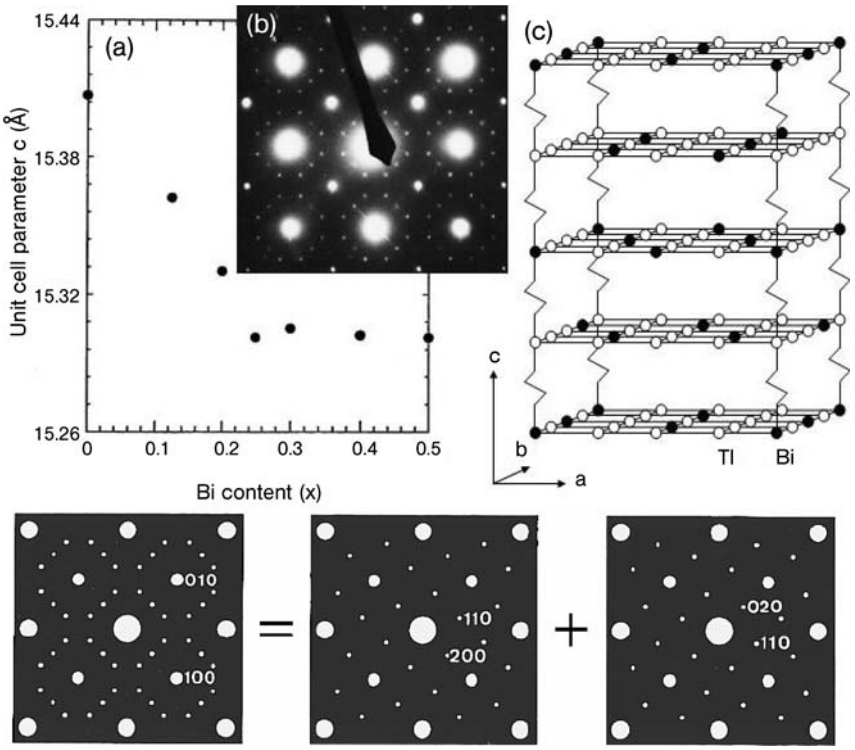

Figure 10.7 (a) The basic unit cell parameter *c* via the nominal content of Bi in solid solution $Tl_{1-x}Bi_xSr_{1.6}Ba_{0.4}Ca_2Cu_3O_9$. (b) SAED pattern of the solid solution specimen with $x = 0.3$, viewed down the [001] zone axis. (c) A $4a \times 4b \times 4c$ superstructural model for (Tl, Bi)-1223 with the ratio Tl: Bi of 3 : 1. Only the (Tl,Bi)–O layers are shown. The bottom schematic drawing shows the division of the SAED pattern in (b) into two simpler patterns corresponding to $4a \times 2b$ and $2a \times 4b$ supercells in the (*ab*) planes.

perovskite-like $[WO_4]$ layers and no superstructure forms. When half the W^{6+} cations are substituted by Nb^{5+} in this compound, the composition becomes $Bi_2W_{0.5}Nb_{0.5}O_{5.75}$, with the two layered components being $[Bi_2O_2]^{2+}$ and $[W_{0.5}Nb_{0.5}O_{3.75}]^{2-}$. The oxygen vacancies seem to enhance formation of a stepped superstructure, which can release the charge separation [34, 35] (Figure 10.8). Unfortunately, the oxygen positions cannot be determined by conventional HRTEM, although those at the junctions of the steps are very important in understanding the nature of the connection of the $[Bi_2O_2]^{2+}$ and $[W_{0.5}Nb_{0.5}O_{3.75}]^{2-}$ components in the (*ab*) planes.

Many Aurivillius phases have such stepped superstructures, which can only be revealed by direct HRTEM imaging. $Bi_5Nb_3O_{15}$ has a structure with an intergrowth of $n = 1$ and $n = 2$ Aurivillius members, $[Bi_2O_2]^{2+}[NbO_4]^{3-}[Bi_2O_2]^{2+}[BiNb_2O_7]^{-}$. Owing to a greater charge separation, this compound forms a stepped superstructure even without oxygen vacancies [36].

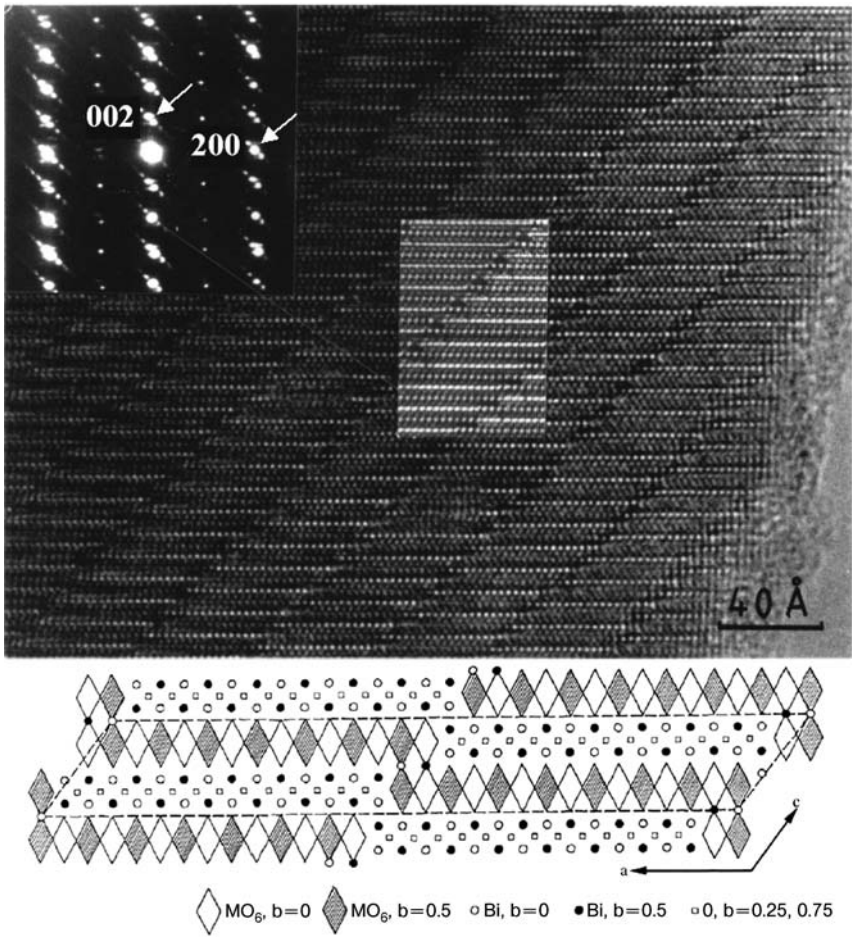

Figure 10.8 HRTEM image of $Bi_8W_2Nb_2O_{23}$ viewed down the [010] zone axis of a Bi_2WO_6-like sub-cell. The insets show a corresponding SAED pattern (top) and a simulated image from a proposed model (bottom) with 8 nm specimen thickness and 60 nm lens defocus. In the model, the *M* sites are shared by W and Nb.

Charge separation can occur with the same type of cations. A well known example is $BaBiO_3$, which has a perovskite structure. The ideal basic unit cell is cubic with $a = 0.43$ nm when all Bi cations are in a 4+ oxidation state. A charge separation of Bi^{5+} and Bi^{3+} (believed to be the real oxidation states in $BaBiO_3$) leads to a $\sqrt{2} \times \sqrt{2} \times 2$ monoclinic distorted superstructure with the supercell parameters, $a = 0.618\,14$, $b = 0.613\,60$, $c = 0.866\,97$ nm, and $\beta = 90.173°$ [37]. This superstructure was originally detected by XRD and can easily be confirmed by SAED.

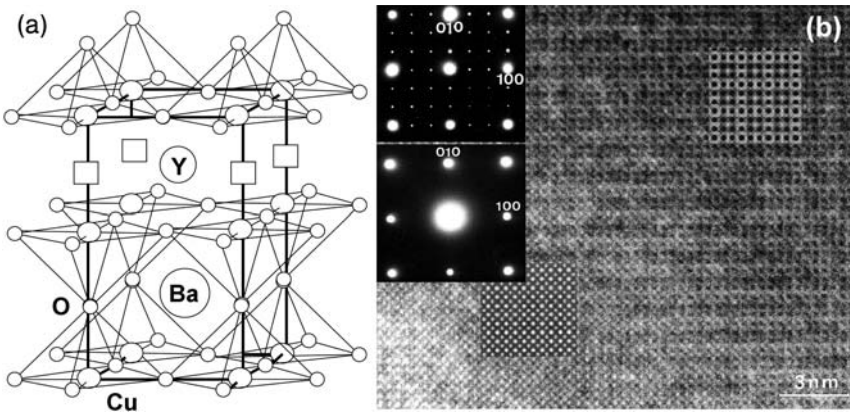

Figure 10.9 (a) Structural model of $YBaCo_2O_{5+x}$, $x = 0$. Oxygen vacancies in the Y layer are marked by squares. (b) HRTEM image of the compound with $x = 0.444$, viewed down the [001] direction. The top inset is the corresponding SAED pattern. The SAED pattern below was recorded after electron beam irradiation with the screen brightness of 150 PA cm^{-2}. Both patterns are indexed to the basic unit cell shown in (a). Computer simulated images were created with the conditions of specimen thicknesses 0.76 (left) and 3.8 nm (right); and lens defocuses −40 (left) and −70 nm (right).

10.4.2
Superstructures Based on Oxygen Ordering

In some oxides, formation of superstructures is merely due to oxygen ordering. A good example was demonstrated by Reller and coworkers in 1984, by showing many distinct superstructures in perovskite-type oxides $CaMnO_{3-x}$ with oxygen contents of 2.5, 2.556, 2.667, 2.75 and 2.80 [38].

Another good example of oxygen ordering was found in $YBaCo_2O_5$. This compound has a double-perovskite structure as shown in Figure 10.9a, and contains one Co^{2+} and one Co^{3+} per formula unit when the oxygen sites in the Y layer are not occupied. Upon annealing the sample in pure oxygen, these sites will be partially occupied by oxide anions, forming a $3 \times 3 \times 1$ superstructure [39], which can be clearly shown by the SAED pattern along the [001] zone axis. An ideal model has a unit cell composition of $Y_9Ba_9Co_{18}O_{49}$, in which the oxidation state of all Co is close to 3+. Under electron beam irradiation, the extra oxygen in the Y layer was removed and the diffraction spots corresponding to the superstructure in the SAED patterns disappeared [40].

In one study, Sr was introduced into $YBaCo_2O_5$ to substitute Ba in order to tune the space of the oxygen vacancies [9]. When the content of Sr in $YBa_{1-x}Sr_xCo_2O_{5+\delta}$ was increased, the ordering of extra oxygen reduced gradually as indicated by SAED patterns, where the diffraction spots from the superstructure diffused before completely disappearing. The high mobility of excess oxygen in $YBaCo_2O_{5+x}$ implies that this material may be developed into a good oxide ion conductor or an oxide catalyst. The conductivity of some selected compositions of this solid

solution was measured with a maximum in conductivity in the range 180–320 °C indicating a form of metal-to-insulator transition at this temperature that is unlikely to be related to a major change in oxygen content.

The perovskite-type structure is one of the most extensively investigated oxide structures. Its ideal composition is ABO_3. A is the large cation and B is the small cation. In $YBa_{1-x}Sr_xCo_2O_5$, A = Y, Ba, Sr (12 coordinated by oxygen) and B = Co (octahedrally coordinated by oxygen). In addition to having a charge balance, the formation of the perovskite structure should meet the requirement of the lattice tolerance factor, t = 0.8 to 1.0, which is calculated from

$$t = \frac{R_a + R_o}{\sqrt{2}(R_b + R_o)}$$

where R_a is the radius of the large cation, R_b is the radius of the small cation and R_o is the radius of the oxygen anion (O^{2-} = 0.132 nm). When t is small, a very common $\sqrt{2} \times \sqrt{2} \times 2$ superstructure is developed due to lattice distortion (or rotation of the MO_6 octahedra). For example, for $CaMnO_3$ the lattice tolerance factor is about 0.85. The real structure is $\sqrt{2} \times \sqrt{2} \times 2$ derived from the perovskite unit cell [38]. The postulated perovskite unit, $Ba^{2+}Co^{3+}O_3$ in the $YBa_{1-x}Sr_xCo_2O_5$ solid solution, has a tolerance factor of 0.965. No $\sqrt{2} \times \sqrt{2} \times 2$ superstructure was observed. On the other hand, the postulated perovskite units, $Sr^{2+}Co^{2+}O_3$ and $Sr^{2+}Co^{3+}O_3$ have tolerance factors of 0.846 and 0.885, respectively. A SAED study showed that a $\sqrt{2} \times \sqrt{2} \times 2$ superstructure was gradually developed when the content of Sr increased in the $YBa_{1-x}Sr_xCo_2O_5$ solid solution [9]. This is the most commonly observed superstructure due to oxygen ordering in perovskite-type oxides, even though there are no oxygen vacancies. The diffraction intensities from such a superstructure are normally very weak and may not be observed in XRD patterns. However, SAED can detect this type of superstructure easily. Some example compounds are the perovskite-related $Bi_3Pb_2Nb_2O_{11}Cl$ [41] and $RuSr_2GdCu_2O_8$ [8], as well as some ruthenocuprates such as $Pb_2RuSr_2Cu_2O_8Cl$ and $(Ru,M)Sr_2GdCu_2O_8$(M = Sn, Nb) [42].

10.4.3
Incommensurate Superstructures

An incommensurate superstructure is a superstructure derived from a basic structure without a proportional relation of dimensions to the basic unit cell. This type of superstructure is often found in mixed oxides. A good example is Bi_2O_3-based solid solutions.

When a small percentage of guest oxide, for example Nb_2O_5, is mixed with Bi_2O_3, the high-temperature phase of δ-Bi_2O_3 can be stabilized and several superstructures will be developed depending on the Nb_2O_5 concentration [25]. Type I is a $2 \times 2 \times 2$ commensurate superstructure with an ideal composition of $Bi_{30}Nb_2O_{50}$, which has been already mentioned previously in Section 10.4.1. Further increasing

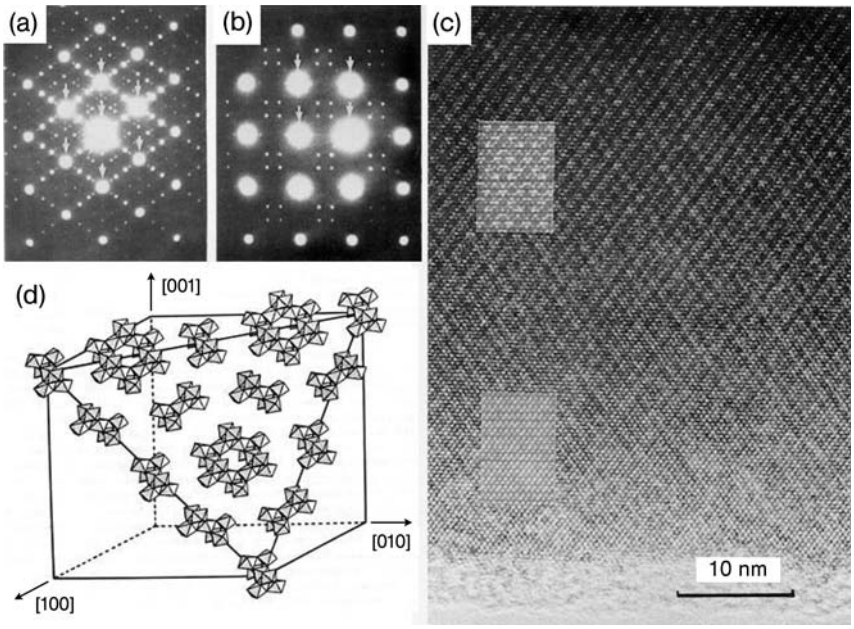

Figure 10.10 SAED patterns of $Bi_8Nb_2O_{17}$ solid solution along the (a) [110] and (b) [100] zone axes. Maxima corresponding to the δ-Bi_2O_3 fluorite sub-cell are shown by arrows. (c) HRTEM image corresponding to (a). The insets are computer simulated images using the proposed commensurate $8 \times 8 \times 8$ superstructural model shown in (d) with conditions of specimen thickness of 4 nm and defocus of 120 nm (nearer to the edge of the crystal) and thickness of 8 nm and defocus of 140 nm (thick area). (d) Pyrochlore-type Nb-O clusters in a (111) plane of the fluorite-type Bi_2O_3 matrix.

the Nb_2O_5 content results in a type II incommensurate superstructure as shown in Figure 10.10.

A cursory look at the SAED patterns (Figure 10.10a and b) may give the impression that the dimensions of the superstructure are $3 \times 3 \times 3$. However, careful measurement of the positions of the superstructural diffraction spots can reveal that the reciprocal spacing corresponding to these spots is disproportional to the dimensions of the reciprocal basic unit cell [25, 32]. The HRTEM image in Figure 10.10c shows a superstructural image contrast pattern. In fact, it is difficult to draw a superunit cell for the whole crystal. In other words, the superstructure has no long-range ordering. The reason for forming such a structure is that Nb_2O_5 forms some pyrochlore-like clusters in the δ-Bi_2O_3 matrix as shown in Figure 10.10d and these clusters are not perfectly ordered in a large area. These structural properties cannot easily be determined by powder XRD, but are clearly shown in SAED patterns and HRTEM images. To confirm the proposed model for this type II superstructure, a commensurate model must be used. It was found that the closest commensurate superunit cell with an operable dimension is $8 \times 8 \times 8$. The model

was successfully confirmed by computer simulation of the HRTEM images and SAED patterns [25, 32]. This type of incommensurate superstructure is also found in the Bi_2O_3–Ta_2O_5 system [30].

Some incommensurate superstructures are developed from lattice distortion instead of partial ordering of cations. One example is the superconducting oxide $Bi_{2+x}Sr_2Ca_{1-x}Cu_2O_{8+\delta}$ [43, 44].

10.5 Surface Profile Imaging

The surface structures of oxide catalysts are important in the understanding of their catalytic properties. HRTEM has been used to investigate the surface structures of oxides for many years, the method of HRTEM surface profile imaging having been introduced in the 1980s [45]. Unlike scanning tunneling microscopy (STM), which is also a direct imaging technique, HRTEM is not mentioned in most surface science text books. Nevertheless, HRTEM is an important supplementary technique in surface science. STM looks down a surface, giving 2D images, while HRTEM reveals the surface of solids in profile (Figure 10.11a). The disadvantage of HRTEM is that only one-dimensional information of a surface can be obtained. On the other hand, HRTEM surface profile imaging provides surface

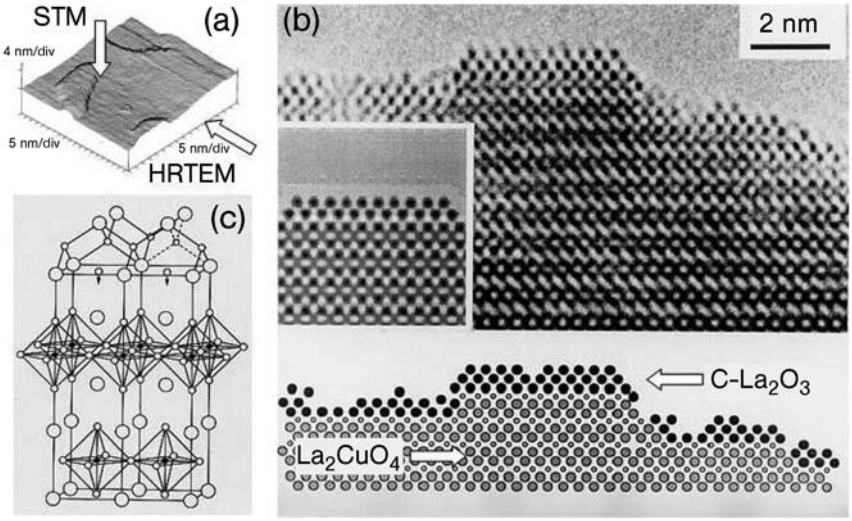

Figure 10.11 (a) Schematic drawing of the viewing directions of STM and HRTEM for a solid surface; (b) HRTEM surface profile image of the (001) surface of La_2CuO_4 showing a different image contrast pattern at surface in comparison with that in the bulk. The inset is a computer simulated image using a model shown in (c).

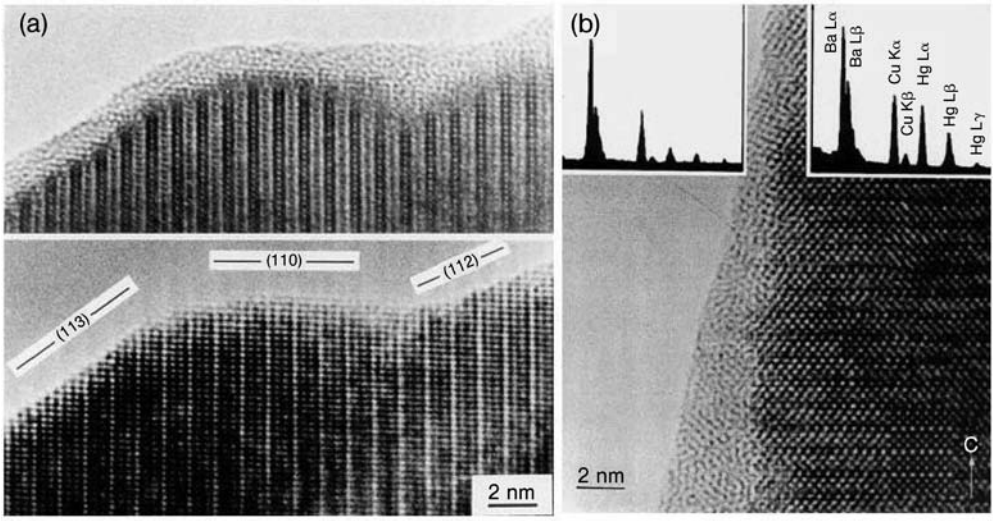

Figure 10.12 (a) HRTEM images of $YBa_2Cu_3O_{7-\delta}$, viewed down the [110] direction. The initial image showing a thin layer of disordered coating, and the image recorded from the same area after electron beam irradiation for 3 h. The disordered layer recrystallized into a clean crystalline surface. The (113), (110) and (112) crystal planes on the surface are indicated. (b) HRTEM image of $HgBa_2CuO_{4+\delta}$ viewed down the [010] direction, showing a disordered coating on the (100) surface. The insets are EDS spectra from the surface area (top left) and the interior area (top right).

structural information as well as subterranean structures of solids. The surface-related properties of materials can therefore be better understood [46]. There are several other advantages of surface investigation by HRTEM. For example, specimen preparation is simple. Normally, small particles with any size and any morphology can be directly used. Multiple scattering can normally be ignored, since the surface areas are often very thin and can legitimately be treated as "weak phase" objects, where the image intensity indicates the projected electrostatic potential.

Figure 10.11b shows a typical HRTEM surface profile image of La_2CuO_4. It was found that the image contrast pattern in the top surface layers is different from that in the bulk area. Image simulation revealed that the (001) surface of La_2CuO_4 crystals was frequently coated by several atomic layers of C-La_2O_3 [47, 48].

HRTEM profile imaging can reveal many surface microstructures. For example, many high Tc superconducting crystals suffer from surface decomposition and an amorphous coating layer can be observed. If this surface coating layer has the same composition as the parent compound, the coating can recrystallize under electron beam irradiation. Figure 10.12a shows a $YBa_2Cu_3O_7$ crystal with surface decomposition into an amorphous layer of about 2 nm thickness, and an image of the same specimen area after recrystallization of the coating layer under the electron beam irradiation [49, 50]. Similar phenomena were also observed from other

high Tc superconducting oxides [51–54]. To make sure that recrystallization only takes place at the interface of the crystal and the amorphous layer, the beam brightness should be carefully controlled to allow a lengthy process. Otherwise, individual nanocrystallites of metal oxides, for example copper oxide and barium oxide, may be created in the amorphous layer. On the other hand, if the composition of the decomposed surface coating layer changes, the amorphous layer cannot be repaired. For example, the surface of $HgBa_2CuO_{4+\delta}$ crystals is often decomposed by loss of Hg as detected by a narrow electron beam EDX analysis (Figure 10.12b) [55]. This amorphous layer cannot recrystallize into the parent crystal, although formation of barium copper oxide microcrystallites is still possible. The surface crystallinity of these high Tc superconducting materials certainly affects the physical properties of the materials [56].

It is worth mentioning that a very small electron beam, for example about 2 nm in the case in Figure 10.12b for $HgBa_2CuO_{4+\delta}$, should be used in EDX. The collection time for the EDX spectrum shown in the left inset was several hours, while the EDX spectrum in the right inset was obtained in only a few minutes. During such a long collection time, the operator must make sure that the beam location is always at the surface amorphous region. Narrow beam diffraction patterns may help in this respect. When the beam is very small, different diffraction patterns from different areas can be observed. From the crystalline region, a single crystal pattern with individual diffraction disks is shown. The pattern from the disordered region shows one or more diffraction rings. When the beam shifts away from the particle, no diffraction signals can be observed. Exposing the specimen area to an electron beam for a long time may result in heavy carbon contamination. The beam location at the amorphous layer should therefore be moved many times along the surface.

When a clean surface of a crystallite is observed without any coating layer, it is possible to determine the terminal atomic planes on various crystal surfaces. For example, three distinct surface terminal planes are marked in Figure 10.12a. HRTEM studies of the [001] surface of $YBa_2Cu_4O_8$ by examination of profile images indicated that the surface usually terminated with the CuO_2 plane corresponding to a sequence of bulk–Y–CuO_{2-x}, while the [001] surface of $YBa_2Cu_3O_7$ prefers to terminate with the BaO atomic plane [57]. Zandbergen investigated a CuO terminal plane on the [001] surface of $GdBa_2Cu_3O_7$ and found that the terminal atomic plane often had a different image contrast indicating lattice distortion including surface relaxation [58], especially when oxygen in the termination plane was partially lost.

By exposing a clean crystal surface to the electron beam, a series of HRTEM surface profile images can be recorded and a movement of surface atoms from a high-energy site to a low-energy site may be observed [47].

Observation of various surface defects is an important topic in HRTEM surface profile imaging. In Figure 10.11b, it can be seen that over a large area the coating layer of C-La_2O_3 is not continuous. Instead, the coating layer is broken into some small islands. This is because the lattices of C-La_2O_3 and La_2CuO_4 as shown in Figure 10.11c do not match each other perfectly. Very interesting surface profile

images of CeO_2 observed by Jacobson and coworkers showed sharp microfaceting on the surface of the CeO_2 film, indicating that nominally designated crystallographic surfaces might not coincide with the as-grown surfaces [59].

When HRTEM is used for examining nanoparticles of oxides, in which the proportion of surface area greatly increases, most structural information concerns the surface. For example, HRTEM images of core–shell quantum dots can show the shell structure and its thickness directly. HRTEM images of metal oxide nanotubes can also be regarded as surface profile images. The application of TEM in nanomaterials will be further discussed below.

10.6 Defects in Oxides

General speaking, a crystal defect is a type of microstructure in which the parent crystal structure is locally disturbed. Such a microstructure cannot be described by a superstructure, even by an incommensurate superstructure. Since the defect areas are usually very small, they may not be detected by XRD and neutron diffraction methods. HRTEM is the most powerful technique to detect them and to investigate their relation with the parent crystals. The defects can greatly change the properties of an oxide. Some examples of the common defects in oxides are given in the following sub-sections.

10.6.1 Layered Defects

Layered defects often form in layered oxides when several different, but closely related, phases intergrow together in a disordered manner. In the high Tc superconducting oxide series $Tl_2Ba_2Ca_{n-1}Cu_nO_{2n+4}$, n can vary from 1 to 4. The half unit cells of all these members contain a $[Tl_2Ba_2O_4]$ layer and a $[Ca_{n-1}Cu_nO_{2n}]$ perovskite-like block. Therefore, they have a tetragonal structure with similar a dimensions (~0.385 nm) and different c dimensions, 2.323 nm (n = 1), 2.931 nm (n = 2), 3.588 nm (n = 3) and 4.160 nm (n = 4). It is easy to form disordered intergrowth along the c axis as shown in Figure 10.13 [19].

The corresponding SAED pattern in Figure 10.13 shows diffused diffraction spots along the c axis. As described above, a superunit cell can be drawn from a superstructure. SAED patterns of incommensurate superstructures also show sharp diffraction spots. Therefore, an approximate unit cell can be suggested for image simulation and for studying its structural principle. However, it is impossible to figure out a unit cell from the SAED and the image in Figure 10.13. We have to analyze individual layered components if we are to understand the whole structure.

Another well known layered defect is the so-called stacking fault, often forming in close-packed structures of metals. This is because ccp and hcp have a very small energy difference. They can intergrow along the [111] axis (ABCABC stacking) of

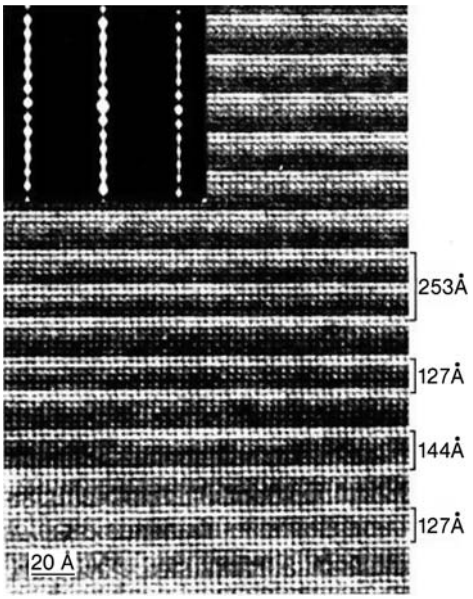

Figure 10.13 HRTEM image of a specimen in $Tl_2Ba_2Ca_{n-1}Cu_nO_{2n+4}$ with a nominal composition with $n = 2$, viewed down the [100] direction. A disordered intergrowth of different members is shown. The inset is the corresponding SAED pattern

the cubic phase and the [001] axis of the hexagonal phase (ABAB stacking) to share identical planes. Such a defect is uncommon in metal oxides, although it has been detected in some zeolites. Recently, stacking fault defects have been observed in face centered cubic or hexagonal mesoporous silica, in which the pore arrangements can be regarded as close-packed structures [60].

10.6.2 Twin Defects

$YBa_2Cu_3O_7$ is orthorhombic, with unit cell parameters $a = 0.381$, $b = 0.388$ and $c = 1.163$ nm. The reason for the difference between a and b is that there is a Cu–O chain along the b axis and, in the same layer, oxygen vacancies are located between Cu atoms along the a axis. But the oxygen can easily move from the b axis to the a axis, equivalent to a rotation of the unit cell around the c axis by 90°, as shown by a model in the inset of Figure 10.14a. The thick line indicates the twin plane. Domains on the two sides of this plane have mirror symmetry. When the domains are large, low magnification TEM images may show a strong contrast pattern (Figure 10.14a), mainly attributed to diffraction contrast [61]. Figure 10.14b shows a HRTEM image of $YBa_2Cu_3O_7$ with microtwin defects, where the domain sizes are very small.

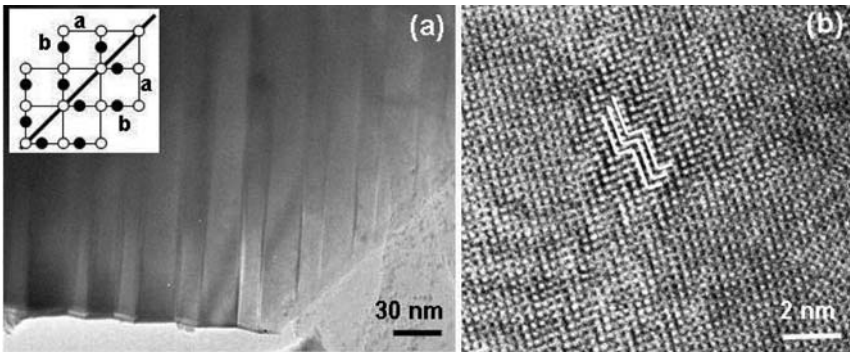

Figure 10.14 (a) TEM and (b) HRTEM images of $YBa_2Cu_3O_7$ on the [001] projection, showing twin defects. The inset of (a) is a schematic model of twin defects. In (b), the *a* axis across the twin planes is marked by the white lines.

In a crystal containing twin defects, the crystal lattices continue across the twin boundaries without a break. Another similar defect, the antiphase defect, is formed by a shift of the crystal by half a unit cell along the antiphase boundary. This defect can also contribute to strong image contrast as shown in Figure 10.3b.

10.6.3 Point Defects

Point defects occur where an atom is missing, or is replaced by an impurity atom or is in an irregular place in the structural lattice. Point defects include self-interstitial atoms and interstitial impurity atoms in a random arrangement.

Since the defects are very small and disordered, the corresponding diffraction intensities in SAED and image contrast in HRTEM are normally too low to be visible. On the other hand, some point defects can cause a local lattice distortion and the real defect areas are much larger than a single atom. For example, a vacancy may induce relocation of the atoms towards it or an interstitial atom may push the surrounding atoms away from their ideal positions. Even a substitutional atom at an ideal lattice position can cause a local distortion owing to its different property (size, charge, etc) from those of the atoms in a bulk oxide. In these cases, it is possible to see the image contrast created by these defects.

An example of such expanded point defects was demonstrated in the perovskite-based $La_4Sr_{n-4}Ti_nO_{3n+2}$ series [62, 63]. When the n value is small, the amount of excess oxygen per perovskite unit x_p in the compound is large. For example, x_p = 0.5 in $La_2Ti_2O_7$ (n = 4), x_p = 0.4 in $La_4SrTi_5O_{17}$ (n = 5), x_p = 0.333 in $La_4Sr_2Ti_6O_{20}$ and so on. To accommodate these excess oxygen anions, the perovskite structures are broken into blocks so that excess oxygen can be accommodated in between the blocks. When the n value increases, the dimensions of the blocks increase and the overall structure approaches that of a perovskite phase. When n is 12, a cubic phase

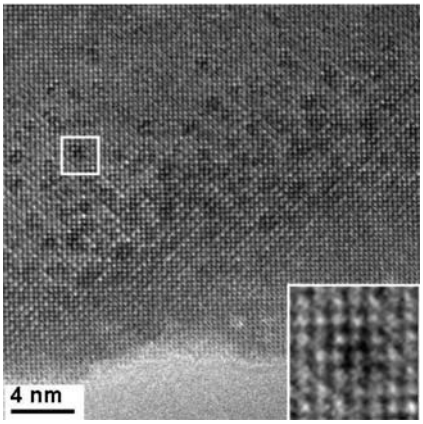

Figure 10.15 HRTEM image of n = 12 member in the $La_4Sr_{n-4}Ti_nO_{3n+2}$ series. Randomly distributed local defects are visible as dark spots. The inset is an enlarged image of a single defect.

is synthesized. However, in this compound, the average value of excess oxygen is still significant, $x_p = 0.1667$ per perovskite unit. These oxygen atoms occupy interstitial sites in the perovskite structure. Since oxygen anions are too large to stay in any spare space in the perovskite matrix, local distortion must be induced. This distortion gave us an opportunity to see directly the disordered nature of these oxygen anions in the compound (Figure 10.15). The evidence is crucial in understanding the properties of materials developed for application in solid-state fuel cells [63].

10.7 Porous Materials

10.7.1 Microporous Zeolites

Microporous zeolites with pore diameters normally smaller than 1 nm (mainly aluminum silicates) are important industrial materials for catalysis, gas absorption and so on. Most known crystal structures of zeolites containing corner-sharing SiO_4 and AlO_4 tetrahedra, were determined by XRD. The principal role of HRTEM in studying these materials in the last 30 years was to directly image the open framework structures and therefore to discover the local microstructures. However, for some new zeolites with very complicated, low symmetry structures, the pore arrangements revealed by HRTEM are indeed essential to the final solution of the structures [64, 65]. One example is the determination of a TNU complex zeolite structure by combining powder diffraction and electron microscopy [66].

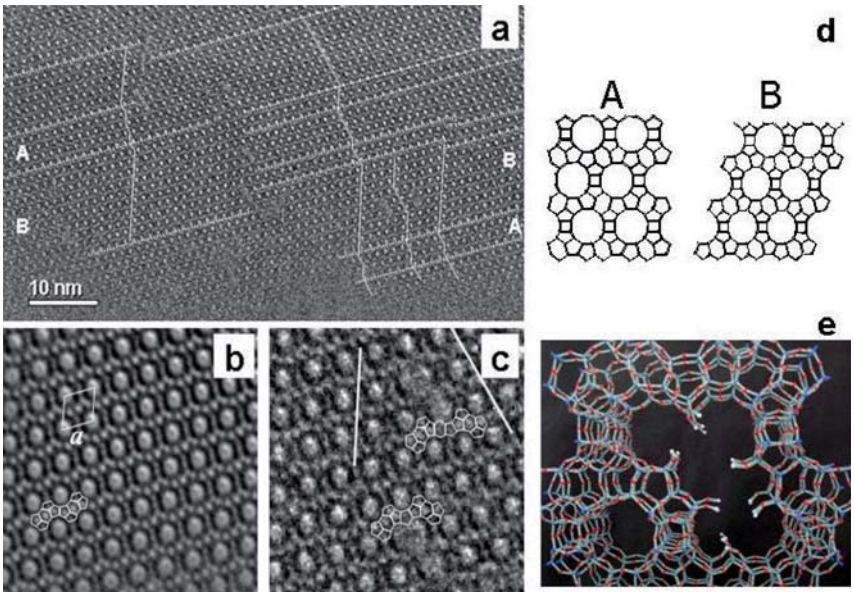

Figure 10.16 (a) HRTEM of an edge of a zeolite β crystallite, annotated to show the stacking directions in different parts. Nanodomains related to polytypes A and B are indicated. Defects are visible in the center of the image, where domains with different stacking directions meet; (b) Fourier-averaged image of a domain of type B, with structural units outlined; (c) Image of two double pore defects, showing different stacking directions and outlining secondary structural details on either side of the defects; (d) Models of the polytypes A (tetragonal) and B (monoclinic); (e) Model of the observed defects, obtained by stacking in the two ways onto a single layer and continuing to the third similar layer.

Zeolite-β, as an excellent catalyst, is one of the most useful high-silica zeolites. The crystal structure of zeolite-β has been comprehensively determined. However, the previously elucidated structures contain no open bonds and cannot explain why a large number of silanol groups are present in zeolite-β.

A HRTEM investigation of zeolite-β gave a reasonable explanation [67]. Figure 10.16a is a HRTEM image of zeolite-β. The basic pore structure contains large pores, each surrounded by a group of small pores (Figure 10.16b). There are two polytypes, A and B, with different modes of stacking (Figure 10.16d). These two polytypes can intergrow together, forming many layered defects in a disordered manner. It was found that the two stacking variants can grow in the same layer from different sites and are unable to connect each other at the boundary, leading to the formation of larger pore defects as shown in Figure 10.16c and e. In the defective large pores, open bonds are created, which serve as the sites for accommodating silanol groups [67]. The observation of these defects by HRTEM also shed light on the crystallization mechanism of zeolite-β.

Zeolites are crystalline oxides. However, HRTEM imaging of these materials usually suffers from some difficulties. Although unit cells of zeolites are large, the

separations of atomic planes in zeolites are very small (see Figure 10.16d). It is impossible to observe the atomic fringes that we often see from normal non-porous metal oxide crystals. The image contrast patterns of zeolites only show the pore networks. The second difficulty is that many zeolites, especially those containing Al, are beam sensitive. The specimen should be dried before being inserted into the microscope column. The application of charge-coupled devices (CCD) allows significant reduction in the exposure time to the electron beam, thus reducing specimen damage, since CCDs are much more sensitive to electrons than photographic detectors [68]. The third difficulty is low image contrast because the elements in zeolite frameworks are normally Al, Si and O, without any heavy metals. Using a small objective aperture may increase the contrast. When a zeolite contains heavy metal cations, image contrast can be significantly improved [69].

10.7.2 Mesoporous Silica

Since Mobil scientists reported their synthesis of the M41S series materials in 1992 [70], tremendous progress has been made in the synthesis of new mesoporous phases and in potential applications of these materials. Unlike crystalline zeolites, the frameworks of these materials are amorphous. The so-called ordered mesoporous silicas normally refer only the ordering of the mesopores. Strictly speaking, they are not "crystals," which must have short-range ordering, although the term "crystal" is still used for these materials in many relevant papers because no better term is available. The unit cell dimensions of the mesoporous silicas are much larger than those of the microporous zeolites, and the X-ray powder diffraction method often gives insufficient reflection peaks. TEM therefore becomes the most powerful technique for structural characterization of these materials [65, 71–74], although a complete solution of the structures relies on a combination of various techniques such as XRD, TEM, NMR, gas adsorption–desorption and so on.

TEM images of mesoporous silica can only show the pore arrangement on a nanometer scale. Therefore, a low magnification is sufficient and the multiple scattering problem in HRTEM at high magnifications becomes insignificant. When the pores are large enough, the mass–thickness contrast dominates in the formation of TEM images and the explanation of the images is relatively easy, especially when the shapes of pores are simple, for example cylindrical pores in MCM-41 [75] and SBA-15 [76, 77] and spherical pores in SBA-2 [60, 78], SBA-12 [76], SBA-16 [77], FDU-12 [79, 80] and so on. Figure 10.17 shows TEM images of FDU-12 with a pore diameter of about 20 nm. The face centered cubic structure of the pores can be determined. The pore size can be directly estimated from the image of an edge of a particle (Figure 10.17c).

From other techniques (e.g. gas adsorption/desorption), it is known that the spherical pores in these mesoporous silicas are connected by some small channels. A similar property has been found in SBA-15 in which the straight cylindrical pores are connected by randomly located small channels. TEM cannot show these

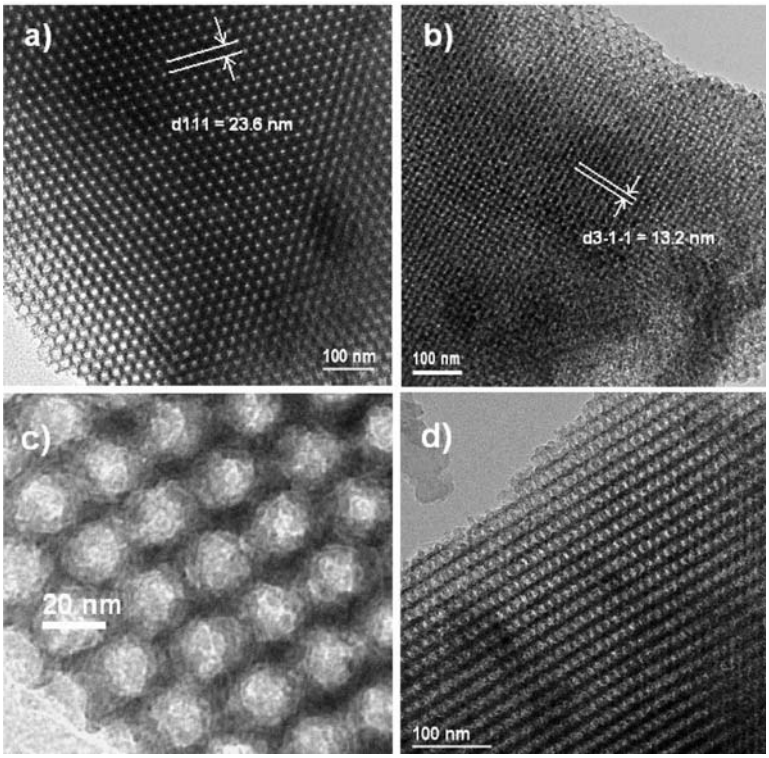

Figure 10.17 TEM images of mesoporous silica FDU-12 viewed down the (a) [110] and (b) [233] directions. (c) Enlarged TEM image of an edge area of (a). (d) TEM image of FDU-12 viewed down the [112] direction.

channels directly owing to their extremely low contrast. One possible way to reveal these channels is to fill the pores with a heavy metal. The morphology of the as-produced metal nanoparticles is the negative replica of the pores in mesoporous silica [79]. TEM images of the metal nanoparticles show that some of these nanoparticles are connected by small bridges, which reflect the small channels in the original mesoporous silica.

Another group of mesoporous silicas, such as MCM-48 and KIT-6, have much more complicated pore structures. The elucidation of these pore structures is not straightforward. MCM-48 is one of the first reported mesoporous phases [70]. Its structure can be described using a gyroid minimal surface model, first suggested in 1993 [81], and confirmed a few years later using HRTEM [82, 83] and by newly developed electron crystallography [71]. This minimal surface divides space into two identical but separate compartments, forming a cubic unit cell containing bicontinous pores with space group *Ia-3d*. This is probably the best example to demonstrate the successful application of HRTEM in the field of structural chemistry of mesoporous silicas.

Unlike zeolites, pure silica materials have no acidic sites and are of limited use for catalysis and other applications. In order to produce acidic mesostructured materials, aluminum has been successfully introduced into the framework of the mesoporous MCM-41 and can be detected by EDX. However, TEM indicated that the degree of order of the mesopores in MCM-41 was significantly reduced by incorporation of even a small percentage of Al into the wall [84].

Incorporation of many other cations into MCM-41 to form porous mixed oxides has been investigated extensively. The guest elements include Ti [85], V [86], Ga [87], Mn [88], Fe [89] and Sn [90]. The doped materials often have a lower degree of ordering compared with the undoped parent MCM-41 silica.

Another method for creating active sites in MCM-41 is introducing catalytically active metal clusters on the inner surface of the pores. If the metal particles are very small, for example in the form of individual atoms, and are evenly distributed in the pores, HRTEM may not give enough image contrast. But the presence of the metal can be confirmed by EDX elemental mapping. When larger clusters (>1 nm) form, they can be detected by HRTEM. It has been shown that direct images can easily differentiate between clusters inside the pores and on the outer surface of the mesoporous MCM-41 [91]. In the case of Ag_3Ru_{10} anchored on the inner surface of the pores, the clusters can be imaged as some dark dots even though they are not ordered [92]. Ordered or partially ordered metal clusters inside the mesopores result in a formation of the so-called rosary pattern of image contrast [93, 94]. In this case, an average distance of the cluster separation can be estimated. The incorporation of metals inside the MCM-41 pores usually has no significant effect on the original silica framework. Recently, the clusters inside the mesoporous materials have been better elucidated by electron tomography, a very powerful 3D technique developed by Midgley and coworkers [95, 96].

10.7.3 Porous Oxides

Mesoporous silicas are synthesized using some surfactants as soft templates. If mesoporous silicas are used as hard templates and crystal growth of metal oxides is allowed inside the pores, the pore system can be regarded as a nanoreactor. By removal of the silica template, many porous single crystals of metal oxides have been fabricated. The first such single crystal oxide, Cr_2O_3 templated by SBA-15, was reported in 2003 [97]. Figure 10.18a is a low-magnification TEM image from this specimen. The morphology and size of the particle seems to be the same as those of the SBA-15 template. Two sets of SAED patterns can be obtained simultaneously from the same particle, showing the single crystal nature of rhombohedral Cr_2O_3 (left inset of Figure 10.18a) as well as the ordering of the mesostructure (right inset, Figure 10.18a). With higher magnification, TEM images reveal that the particles consist of an array of hexagonally arranged nanorods (Figure 10.18b). Further increasing magnification allows us to view some small bridges connecting the nanorods (Figure 10.18c). The diameter of the nanorods is ca 8 nm and the hollow space between the nanorods is visible as white fringes. HRTEM images

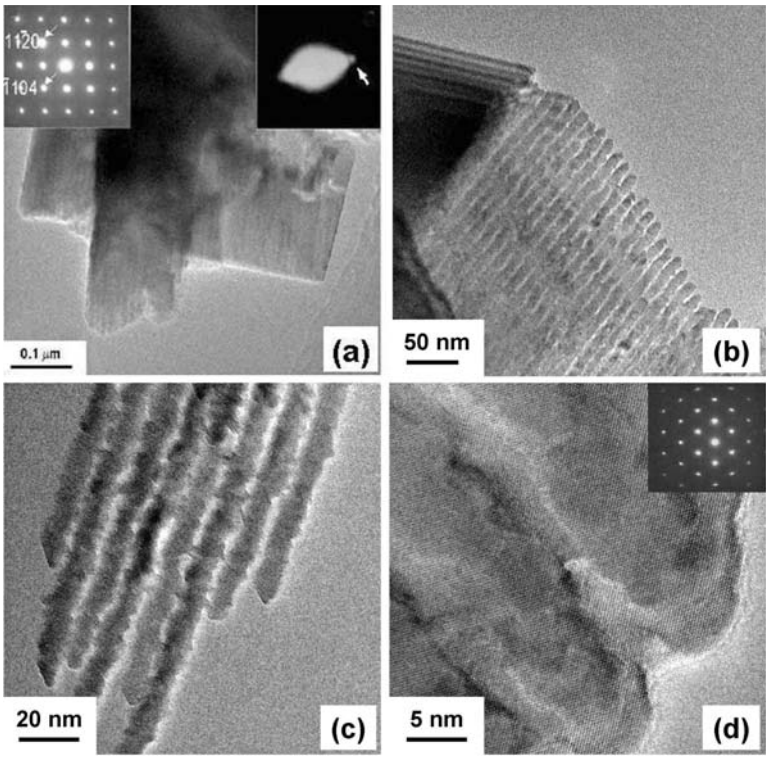

Figure 10.18 TEM and HRTEM images of porous crystals of Cr_2O_3 templated by SBA-15. (a) Low magnification image showing particle morphology. The insets are SAED patterns corresponding to the crystal structure of Cr_2O_3 (left) and the one-dimensional ordered porous structure (right); (b) TEM image at a higher magnification showing a group of parallel nanorods; (c) TEM image with further increasing magnification showing small bridges between the nanorods; (d) HRTEM image showing perfectly oriented crystal structure in the nanorods. The inset is the corresponding SAED pattern from multi-nanorods.

further corroborate the single crystal property of the specimen as shown in Figure 10.18d. Any nanorod in a particle is part of the same crystal even when the nanorods are separated by a nanoscale space. It is assumed that the whole original mesopore structure in SBA-15 has been replicated by Cr_2O_3 crystals.

Several synthetic methods have been developed and various transition metal oxides, such as Cr_2O_3 [97, 98], WO_3 [99], Co_3O_4 [100], Fe_2O_3 [101], In_2O_3 [102] and others, have been produced as porous single crystals. Most of them are known to be catalysts. The general route for producing porous crystals of oxides using mesoporous silica as template is by introducing a metal-containing precursor into the silica pores and allowing the precursor to decompose, followed by crystal growth of metal oxides inside the pores during a thermal treatment. Therefore, a crucial step in the above process is the impregnation of the precursor. Five methods of

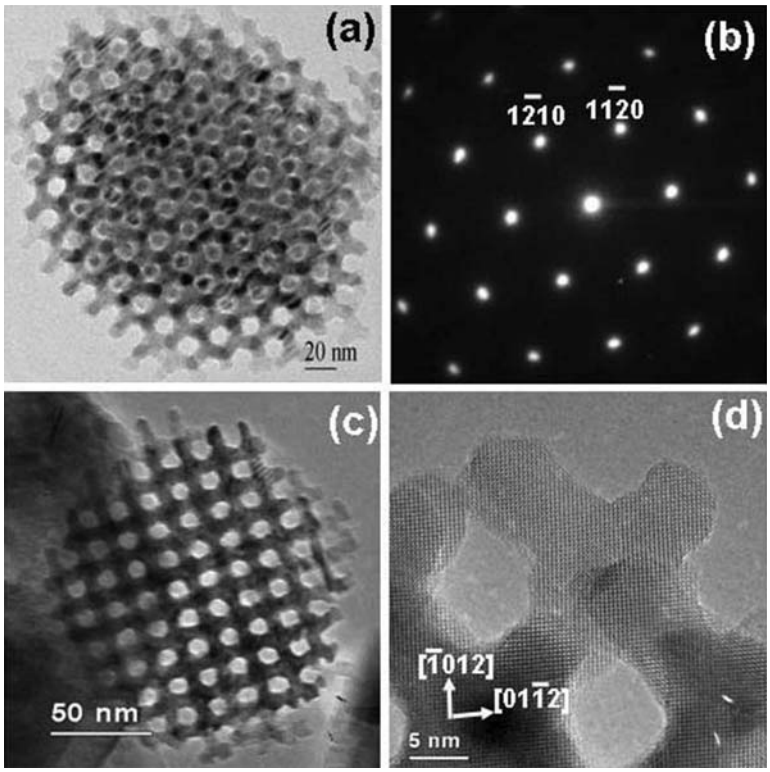

Figure 10.19 TEM examination of porous single-crystal of KIT-6 templated Cr_2O_3 viewed down two principal zone axes. (a) TEM image showing mesopore structure along the [111] direction of the KIT-6 related cubic unit cell and (b) the corresponding SAED pattern indexed to the rhombohedral unit cell of crystalline Cr_2O_3. (c) TEM image showing the mesopore structure along the [100] zone axis of the KIT-6 related unit cell and (d) the corresponding HRTEM image on the $[2\bar{2}1]$ zone axis of Cr_2O_3 unit cell.

impregnation have been previously developed: the so-called surface functionalization method [97, 99], the dual solvent method [98, 103], the evaporation method [100, 104, 105], the one-step nanocasting method [102] and the most recently reported solid–liquid method [106–108], respectively. The most popular templates used are SBA-15, KIT-6 and FDU-12.

When KIT-6 is used as a template, the typical morphology of the porous crystals is spherical as shown in Figure 10.19a and c and the particle size (~300 nm) is much smaller than the size of KIT-6 particles (from several microns to tens of microns). The reason for this phenomenon is a relatively low loading level of chromium nitrate and a large shrink effect of the phase transformation of the Cr-containing compounds [98].

The most unusual feature of Figure 10.19 is that the crystal orientation has a very close relation with the mesopore structure. For example, when one looks

down the [111] zone axis of the KIT-6 templated mesopore structure (Figure 10.19a), seeing a hexagonal pattern of the pores, a hexagonal pattern of SAED corresponding to the [001] zone axis of the rhombohedral Cr_2O_3 can be obtained without specimen tilting (Figure 10.19b). Consequently, the [111] axis of the KIT-6-like cubic mesoporous unit cell and the [001] axis of Cr_2O_3 are perfectly parallel. When a particle is imaged on the [100] projection of the cubic mesoporous system (Figure 10.19c), a perfect square pattern of the mesopores can be seen. Figure 10.19d is the corresponding HRTEM image recorded from a corner of the particle in Figure 10.19c. The image viewed down the $[2\bar{2}1]$ axis of Cr_2O_3 shows a contrast pattern which is the closest to a square pattern from the Cr_2O_3 crystal structure. From this sample, many particles have these peculiar orientations, which seem to have a close relation with the structural symmetry of KIT-6. This unique phenomenon has not been observed with other samples of porous oxides. At present, the reason for the formation of such coherence between crystal structure and the symmetry of the nanopore system is not understood.

If we compare the image contrast pattern in Figure 10.19c with the corresponding one from KIT-6, we can conclude that Cr_2O_3 only replicated one of two interlaced pores in KIT-6. Figure 10.19a is a rare example showing replication of both pores in the central area. On the other hand, TEM images from KIT-6-templated Co_3O_4 showed that two interlaced pores were replicated in all the particles [100]. Pore size and pore volume measurements by N_2 adsorption/desorption of these two specimens confirmed the above conclusion. This implies that there are some small channels connecting the two interlaced pores in KIT-6.

Crystal growth of metal oxides has also been performed in the pore systems of some cage-containing mesoporous silicas, such as FDU-12 [79, 80] and SBA-16 [77]. SBA-16 has a body centered cubic structure (space group $Im\bar{3}m$) and FDU-12 is face centered cubic (space group $Fm\bar{3}m$). Accordingly, each spherical nanocage is 8 coordinated by the neighboring nanocages in SBA-16, but 12 coordinated in FDU-12. When crystals of oxides form in these two silica phases, it can be expected that the structures of the products are 3D arrangements of solid nanospheres connected to each other by some very short nanorods [107, 109]. The HRTEM technique has been used to examine the yields and the single crystal properties of these porous oxides. The small bridges are barely revealed in the TEM images. However, it is possible to see a bridge at an edge of a particle where two adjacent nanospheres can be identified. Another difficulty in imaging the porous crystals templated by these mesoporous silicas is that, since the crystal orientation has no relation to the mesostructure, it is difficult to find a view direction parallel with principal axes of both the crystal structure and the mesopore structure.

It seems to be possible that most transition metal oxides can be made in porous crystals with different morphologies using various mesoporous silicas as templates. It is expected that these materials have potential in applications such as catalysis, fuel cell, gas sensors and Li-batteries. Their physical properties would fall in between nanoparticles and bulk specimens, although our knowledge about these properties is still very limited.

10.8 Low-Dimensional Oxide Crystals

It has been well known that HRTEM is a powerful tool to investigate structures of low-dimensional oxides, such as nanoparticles, nanowires, nanorods and nanotubes, while the information from powder diffraction of these low-dimensional materials is normally very limited merely because their small crystallite sizes. For the nanoscale oxides, HRTEM can give useful information on particle size, crystal structure, particle morphology, structural defects and possible inter-particle connections.

10.8.1 Nanoparticles

An important type of nanoscale oxide is the so-called quantum dot (QD) which has size-dependent photoemission properties. Fu and coworkers have reported an aqueous dispersion of ZnO QDs with strong blue emission (quantum yield of 76%). HRTEM images directly show the particle size of about 5 nm or below and quite narrow size distributions [110].

Nanoscale core–shell structures are also of great interest. When Zn/ZnO core–shell nanoparticles are imaged by TEM at a low magnification, the image contrasts from the core and the shell may be significantly different due to a difference of the mass–thickness (or density of Zn cations) between these two components [111]. The structures of the core and shell are also different, leading to a large diffraction contrast as well. Consequently, the thickness of the ZnO shells can be measured directly from the images. The information helps in the refinement of the synthetic conditions and allows the dimensions of nanoparticles to be controllable. HRTEM images can further reveal the crystal structures of ZnO in the shell. As observed by Zeng and coworkers, the ZnO shells are polycrystalline [111].

The overall properties of nanoparticle materials depend not only on their structures but also on their size. It is therefore crucial to have a narrow particle size distribution for some applications. Since TEM often shows individual particles, it is necessary to examine a large number of particles for a reasonably good estimation of particle size distribution. A good example was shown by Park and coworkers, who observed almost uniform sizes of spherical nanocrystals of MnO, CoO, Fe_3O_4 (magnetite) and Fe_2O_3 (maghemite) from large areas of the specimens [112]. Fe/Fe_3O_4 core–shell nanotubes were imaged by HRTEM by Shavel and coworkers [113]. The crystal structures of the iron core and the Fe_3O_4 shell can be clearly identified.

Magnetic nano-γ-Fe_2O_3 is a useful material in nanodevices as it allows separation of nanomaterials in a magnetic field. For example, Pang and coworkers simultaneously embedded fluorescent CdSe/ZnS QDs and magnetic nano-γ-Fe_2O_3 into hydrazinized styrene/acrylamide (H_2N-St-AAm) copolymer nanospheres to produce cell-targeting multifunctional nanospheres [114]. Figure 10.20 shows a typical spherical polymer particle of the specimen with QDs and Fe_2O_3 nanoparti-

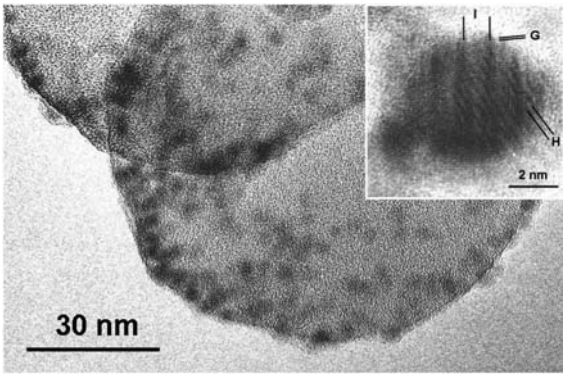

Figure 10.20 TEM image of polymer nanspheres embedded with both CdSe/ZnS QDs and nano-γ-Fe_2O_3. The inset is HRTEM of a Fe_2O_3 nanoparticle showing the (222) fringes (G) with $d = 0.24$ nm and two d-spacings related to superstructures, $d = 0.76$ nm (H) and $d = 2.71$ nm (I).

cles embedded. To ensure these nanoparticles are inside the polymer spheres instead of on the surface of the spheres, the specimen should be rotated and be examined by TEM from different angles. HRTEM images of individual nanoparticles can be obtained as shown in the inset of Figure 10.20. In these nanocrystallites, twin defect superstructures are often observed.

Nanoparticles often aggregate to form large clusters. An interesting phenomenon is oriented aggregation, in which all the nanoparticles connect to each other with exactly the same crystal orientation. When the early stage crystal growth of zeolite analcime was investigated, it was found that the crystals grew from the seeds up to some nanoplatelets with a size of about 20 nm in diameter. The growth orientation of the nanoplatelets with the short axis along the [111] zone axis was observed by SAED. These [111]-oriented nanoplatelets stack to form aligned discus-shaped aggregates via an oriented aggregation mechanism [115]. In the aggregates, boundaries of the nanoplatelets can be seen clearly with light contrast lines and each discus may contain at least a few hundreds nanoplatelets as shown in Figure 10.21. The corresponding SAED pattern shows a single crystal-like structure, which can be further confirmed from HRTEM images [115].

10.8.2
Nanorods, Nanowires and Nanobelts of Oxides

When nanocrystals grow with a preferential crystal orientation, nanorods may be produced. Umar and coworkers demonstrated the synthesis of ZnO nanonails [116]. For this type of nanocrystallite, HRTEM was used to determine the crystal structure, the single crystal state for individual nanonails, the particle morphology and also the long axis, that is, growth along the [0001] direction of the wurtzite hexagonal-phase of ZnO. This material is of interest as a hydrazine

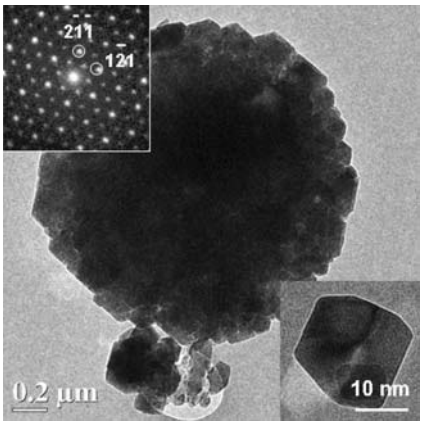

Figure 10.21 TEM image of oriented aggregation of nanoplatelets of zeolite analcime. The inset (top) is the corresponding SAED pattern. Another inset (bottom) is TEM image of a single nanoplatelet.

electrochemical sensor. It is not surprising to see the direction of growth of a hexagonal phase along its [0001] zone axis. Zeolite analcime crystals have a perfectly icositetrahedral morphology arising from their cubic structure. The discovery of a nanorod intermediate phase during the early stage of crystal growth was very surprising [115]. All the nanorods grew along the [111] direction but the reason for this has yet to be investigated. It is obvious that the final morphology of the nanorods is affected by the synthetic conditions. Even for ZnO nanorods, Yang and Wang reported a transverse growth, forming interpenetrative nanorods. The ends of the ZnO nanorods were bullet shaped [117].

Using a thermal vapor deposition method, WO_{3-x} nanorods were produced [118]. These nanorods grew along the [001] axis and were believe to contain a large number of stacking faults in the (200) planes as shown by HRTEM images.

Nanorods of oxide can also be made using a template. In this case, the morphology of the nanorods would depend on the shape of the template. For example, WO_3 can grow in mesoporous silica MCM-41 which consists of an array of cylindrical pores without interconnections [119]. The growing orientation of the nanorods is variable.

When nanorods grow to further increase their length, nanowires are produced. The surface-to-volume ratio increases greatly. The materials are very useful in semiconducting nanodevices and catalysis. In_2O_3 nanowires were prepared as a gas-sensing material by Vomiero and coworkers [120]. The growing direction, the [100] direction of its cubic structure, was determined by SAED and HRTEM imaging. At low magnification, TEM images of nanowires often show some dark contrast features owing to bending of the nanowires. These dark features can move along the wire when the specimen is tilted with a small angle. The HRTEM images of In_2O_3 presented by Vomiero [120] showed uniform fringe contrast, indicating

a constant specimen thickness across the nanowires on the projecting direction. This property reflected a regular (non-cylindrical) cross-section of the nanowires and allowed the scientists to carry out convergent beam electron diffraction, from which the structural symmetry of In_2O_3 can be determined.

Many oxide nanowires have been characterized by HRTEM, such as very long single crystalline β-Ga_2O_3 nanowires with a zigzag surface termination [121], a large-scale fabrication of single crystalline Cu_2O nanowires [122], Er-doped polycrystalline SnO_2 nanowires [123], and anodized aluminum oxide-templated single crystalline TiO_2 nanowires [124].

Nano-scale ZnO is one of the most popular nanomaterials investigated in the last few years. It is partly because ZnO can form many different forms of nanostructure, such as nanoparticles, nanonails, nanocombs, nanorings, nanosprings, nanobows, nanobelts, nanocages and nanowires, and partly because of its interesting physical properties [125]. The most attractive and beautiful example of HRTEM investigation of nano-scale ZnO is the study of ZnO nanobelts, first demonstrated by Wang and coworkers [126]. ZnO has a wurtzite structure, which is hexagonal (space group C_{6mc}) with unit cell dimensions $a = 0.3296$ and $c = 0.52065$ nm. Owing to its polar surfaces, containing positively charged Zn-(0001) and negatively charged O-$(000\,\overline{1})$ surfaces, a ZnO nanobelt can form nanorings when the shortest dimension is along the [0001] axis as shown in Figure 10.22a–c [127, 128]. A very detailed formation mechanism of this peculiar morphology has been reported. A core–shell structure in ZnO nanobelts has also been observed and investigated using HRTEM (Figure 10.22d and e) [127, 129].

10.8.3 Oxide Nanotubes

Many metal oxides have been made in the form of nanotubes, but most of them have an amorphous wall. SEM is normally used to characterize these materials. For some crystalline oxide nanotubes, HRTEM is the only technique to determine their structures. Titania-related nanotubular material is a good example.

Any crystalline TiO_2 treated in a high-concentration NaOH aqueous solution at 130°C for a few days can undergo a phase transformation to nanotubes [130, 131]. However, a later HRTEM study revealed that the structure is derived from $H_2Ti_3O_7$ instead of TiO_2 [132]. Figure 10.23a is a HRTEM image of a nanotube viewed down a profile direction. In addition to the single crystalline wall, it was found that the numbers of the layers on two sides are different, three on the top side and four on the bottom side. The cross-section image in Figure 10.23b reveals that, unlike carbon nanotubes, the nanotubes form from scrolling up a single sheet of titanium oxide. Further studies with computer image simulations indicated that the structure is derived from H-form titanium oxide, $H_2Ti_3O_7$, which consist of $[Ti_3O_7]^{2-}$ sheets separated by some protons. The formation mechanism of the nanotubes from scrolling up $[Ti_3O_7]^{2-}$ layer by layer on the [001] surface of $H_2Ti_3O_7$ have been confirmed by HRTEM examination of several specimens with different reaction times and extensive *ab initio* calculations of the surface tension, elastic strain

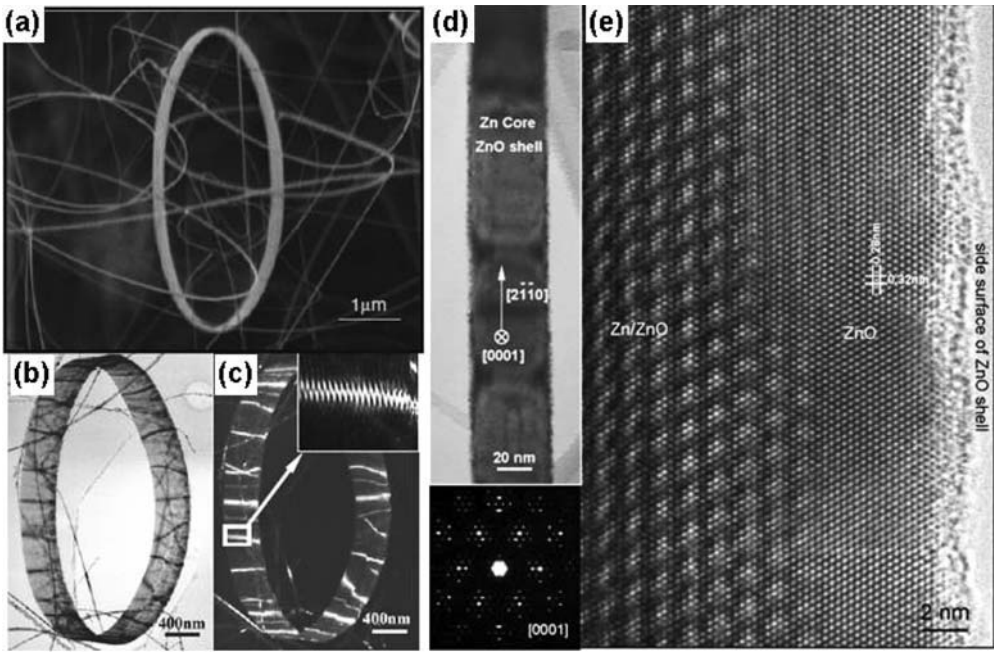

Figure 10.22 (a) Seamless single-crystal nanorings of ZnO; (b) Bright-field and (c) dark-field TEM images of a nanoring. The inset in (c) is an enlargement of a local region, displaying the contrast produced by the uni-radius, loop-by-loop, self-coiling nanobelt. (d) A low magnification TEM image of a Zn–ZnO core–shell heteronanobelt. (e) A [0001] high resolution TEM image recorded near the right-hand edge of a nanobelt, showing the Zn–ZnO overlap region and the ZnO wall. The corresponding electron diffraction pattern is given below (d) [127].

energy, interlayer coupling energy and Coulomb force [133]. Because HRTEM is unable to detect protons in the structures, the presence of protons in the above-mentioned nanotubes was proved by solid-state NMR spectroscopy and measurement of proton conductivity [134].

It is proposed that the principal of exfoliating layered compounds into nanotubes can be used for many layered oxides. Potassium hexaniobate ($K_4Nb_6O_{17}$) is one such compound, consisting of $[Nb_6O_{17}]^{4-}$ layers separated by K^+ cations. Using the intercalating and exfoliating methods, the $[Nb_6O_{17}]^{4-}$ layers can be peeled off from the crystal layer by layer to form nanotubes. The interlayer distance in the wall of the nanotubes is variable from 0.83 to 3.6 nm when different intercalating molecules such as tetra-*n*-butylammonium hydroxide (TBA^+OH^-) and alkylamines ($C_nH_{2n+1}NH_2$) with different lengths of alkyl chain. The HRTEM observations indicated that the organic molecules stayed in the interlayer space. HRTEM also indicated that the number of layers in the wall was in the range of 3 to 8 and the rolling direction was around the [100] zone axis of $K_4Nb_6O_{17}$, while a helical angle larger than 10° was observed for some nanotubes [135, 136].

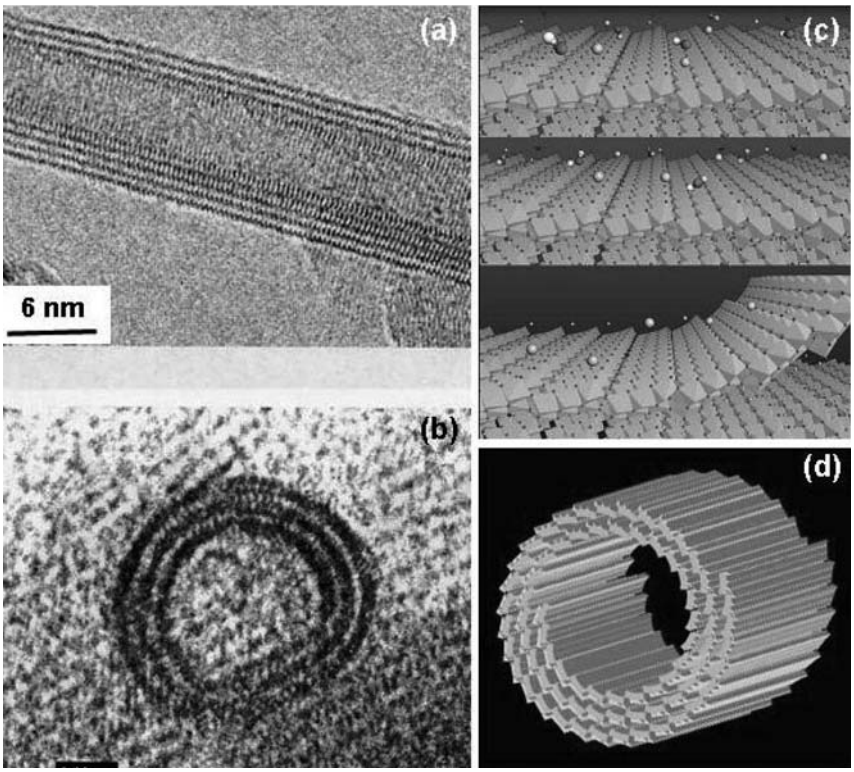

Figure 10.23 (a) HRTEM image of a $H_2Ti_3O_7$ nanotube showing three layers on one side and four on another side. (b) HRTEM image of the cross-section of a nanotube. (c) Schematic model showing the effect of the alkaline environment and cleavage of the surface layer due to hydrogen deficiency on the surface. (d) Three-dimensional model of the $H_2Ti_3O_7$ nanotubes.

10.9 Summary

In summary, as demonstrated within this chapter, HRTEM and associated techniques are very powerful in the study of the microstructures of oxides and oxide catalysts. The detailed characterization of superstructures, surface structures and defects enriches our knowledge of the structures of oxides and their structure-dependent physico-chemical properties. For characterizing nano-scale oxides, HRTEM plays a particularly important and unique role. Further exciting developments resulting from this fascinating area can be anticipated.

References

1 Thomson, J.J. (1897) *Philosophical Magazine*, **44**, 293.
2 de Broglie, L. (1924) Researches on the quantum theory, Thesis, Paris.
3 Thomson, G.P. (1939) *Theory and Practice of Electron Diffraction*, Macmillan & Co, London.
4 Scherzer, O. (1949) *Journal of Applied Physics*, **20**, 20.
5 Iijima, S. (1971) *Journal of Applied Physics*, **42**, 5891.
6 Spence, J.C.H. (1981) *Experimental High-resolution Electron Microscopy*, Clarendon Press, Oxford.
7 Hirsch, P.B. (1977) *Electron Microscopy of Thin Crystals*, Krieger Publishing Company.
8 McLaughlin, A.C., Zhou, W.Z., Attfield, J.P., Fitch, A.N. and Tallon, J.L. (1999) *Physical Review B*, **60**, 7512.
9 McKinlay, A., Connor, P., Irvine, J.S.T. and Zhou, W.Z. (2007) *The Journal of Physical Chemistry C*, **111**, 19120.
10 Thomas, J.M. and Zhou, W.Z. (2003) *Chemphyschem*, **4**, 927.
11 Horiuchi, S. (1993) *Materials Science Forum*, **129**, 31.
12 Rose, H. (1990) *Optik*, **85**, 19.
13 Jia, C.L., Lentzen, M. and Urban, K. (2003) *Science*, **299**, 870.
14 Williams, D.B. and Carter, C.B. (1996) *Transmission Electron Microscopy*, Plenum, New York.
15 Che, R., Peng, L.M. and Zhou, W.Z. (2005) *Applied Physics Letters*, **87**, 173122.
16 Liu, Y. (2001) in *Progress in Transmission Electron Microscopy 1: Concepts and Techniques*, Springer, London, p. 273.
17 Liu, Y., Eades, J.A. and Mazumder, J. (1994) *Ultramicroscopy*, **56**, 253.
18 Stobiecki, F., Stobiecki, T., Kellner, F., Thoma, K., Roll, K. and Gartner, H. (1991) *Fresenius' Journal of Analytical Chemistry*, **341**, 365.
19 Zhou, W.Z., Porch, A., van Damme, I.B.M., Jefferson, D.A., Liang, W.Y. and Edwards, P.P. (1990) *Journal of Solid State Chemistry*, **88**, 193.
20 Marsh, P., Fleming, R.M., Mandich, M.L., DeSantolo, A.M., Kwo, J., Hong, M. and Martinez-Miranda, L.J. (1988) *Nature*, **334**, 141.
21 Bordet, P., Chaillout, C., Chenavas, J., Hodeau, J.L., Marezio, M., Karpinski, J. and Kaldis, E. (1988) *Nature*, **334**, 596.
22 Maeda, H., Tanaka, Y., Fukutomim, M. and Asano, T. (1988) *Japanese Journal of Applied Physics*, **27**, L209.
23 Parkin, S.S.P., Lee, V.Y., Nazzal, A.I., Savoy, R., Beyers, R. and Laplaca, S.J. (1988) *Physical Review Letters*, **61**, 750.
24 Zandbergen, H.W., Fu, W.T., Vanruitenbeek, J.M., Dejongh, L.J., Vantendeloo, G. and Amelinckx, S. (1989) *Physica C*, **159**, 81.
25 Zhou, W.Z., Jefferson, D.A. and Thomas, J.M. (1986) *Proceedings of the Royal Society of London B*, **A406**, 173.
26 Zhou, W.Z., Jefferson, D.A., and Thomas, J.M. (1987) *Journal of Solid State Chemistry*, **70**, 129.
27 Zhou, W.Z. (1988) *Journal of Solid State Chemistry*, **76**, 290.
28 Zhou, W.Z. (1990) *Journal of Solid State Chemistry*, **87**, 44.
29 Zhou, W.Z. (1990) *Advanced Materials*, **2**, 414.
30 Zhou, W.Z. (1992) *Journal of Solid State Chemistry*, **101**, 1.
31 Zhou, W.Z. (1994) *Journal of Solid State Chemistry*, **108**, 381.
32 Tang, D. and Zhou, W.Z. (1995) *Journal of Solid State Chemistry*, **119**, 311.
33 Lee, E., Wu, S., Zhou, W.Z. and Liang, W.Y. (1996) *Journal of Applied Physics*, **80**, 326.
34 Zhou, W.Z. (1990) *Advanced Materials*, **2**, 94.
35 Zhou, W.Z. (2002) *Journal of Solid State Chemistry*, **163**, 479.
36 Zhou, W.Z., Jefferson, D.A. and Thomas, J.M. (1989) *Geophys. Monograph 45: Perovskite: A Structure of Greut Interest to Geophysics and Material Science*, American Geophysical Union, Washington DC, 113.
37 Cox, D.E. and Sleight, A.W. (1979) *Acta Crystallographica. Section B, Structural Science*, **35**, 1.
38 Reller, A., Thomas, J.M., Jefferson, D.A. and Uppal, M.K. (1984) *Proceedings of the Royal Society*, **A394**, 223.

39 Zhou, W.Z., Lin, C.T. and Liang, W.Y. (1993) *Advanced Materials*, **5**, 735.

40 Zhou, W.Z. (1994) *Chemistry of Materials*, **6**, 441.

41 Kusainova, A.M., Lightfoot, P., Zhou, W.Z., Yu Stefannovich, S., Mosunov, A.O. and Dolgikh, V.A. (2001) *Chemistry of Materials*, **13**, 4731.

42 Mclaughlin, A.C., Attfield, J.P., Liu, R.S., Jang, L.Y. and Zhou, W.Z. (2004) *Journal of Solid State Chemistry*, **177**, 834.

43 Zhou, W.Z., Kirkland, A.I., Porch, A., Mackay, K.D., Armstrong, A.R., Harrison, M.R., Jefferson, D.A., Edwards, P.P. and Liang, W.Y. (1989) *Angewandte Chemie (International Edition in English)*, **28**, 810.

44 Zandbergen, H.W., Groen, W.A., Mijlhoff, F.C., van Tendeloo, G. and Amelinckx, S. (1988) *Physica C*, **156**, 325.

45 Marks, L.D. and Smith, D.J. (1983) *Nature*, **303**, 316.

46 Zhou, W.Z. and Thomas, J.M. (2001) *Current Opinion in Solid State and Materials Science*, **5**, 75.

47 Zhou, W.Z., Jefferson, D.A. and Liang, W.Y. (1989) *Surface Science*, **209**, 444.

48 Zhou, W.Z., Jefferson, D.A. and Liang, W.Y. (1994) *Surface Science*, **310**, 52.

49 Zhou, W.Z., Jefferson, D.A. and Liang, W.Y. (1992) *Journal of Solid State Chemistry*, **98**, 437.

50 Zhou, W.Z., Jefferson, D.A. and Liang, W.Y. (1993) *Superconductor Science and Technology*, **6**, 81.

51 Zhou, W.Z., Jefferson, D.A., Liang, W.Y., Soeta, A., Kamo, T. and Matsuda, S.P. (1992) *Physica C*, **202**, 335.

52 Zhou, W.Z., Jefferson, D.A. and Liang, W.Y. (1993) *Materials Science Forum*, **129**, 65.

53 Zhou, W.Z. (1996) *Journal of Superconductivity*, **9**, 311.

54 Zhou, W.Z., Xin, Y. and Jefferson, D.A. (2000) *Journal of Solid State Chemistry*, **149**, 327.

55 Zhou, W.Z., Asab, A., Gameson, I., Jefferson, D.A. and Edwards, P.P. (1995) *Physica C*, **248**, 1.

56 Panagopoulos, C., Zhou, W.Z., Athanassopoulou, N. and Cooper, J.R. (1996) *Physica C*, **269**, 157.

57 Xin, Y., Zhou, W.Z. and Humphreys, C.J. (1995) *Physica C*, **249**, 319.

58 Zandbergen, H.W. (1992) *Physica C*, **194**, 287.

59 Jacobson, S.N., Helmersson, U., Erlandsson, R., Skarman, B. and Wallenberg, L.R. (1999) *Surface Science*, **429**, 22.

60 Zhou, W.Z., Hunter, H.M.A., Wright, P.A., Ge, Q. and Thomas, J.M. (1998) *Journal of Physical Chemistry B*, **102**, 6933.

61 Lin, C.T., Zhou, W.Z., Liang, W.Y., Schonherr, E. and Bender, H. (1992) *Physica C*, **195**, 291.

62 Canales-Vazquez, J., Smith, M.J., Irvine, J.T.S. and Zhou, W.Z. (2005) *Advanced Functional Materials*, **15**, 1000.

63 Ruiz-Morales, J.C., Canales-Vázquez, J., Savaniu, C., Marrero-López, D., Zhou, W.Z. and Irvine, J.T.S. (2006) *Nature*, **439**, 568.

64 Bursill, L.A., Lodge, E.A. and Thomas, J.M. (1980) *Nature*, **286**, 111.

65 Thomas, J.M., Terasaki, O., Gai-Boyes, P.L., Zhou, W.Z. and Gonzalez-Calbet, J. (2001) *Accounts of Chemical Research*, **34**, 583.

66 Gramm, F., Baerlocher, C., McCusker, L.B., Warrender, S.J., Wright, P.A., Han, B., Hong, S.B., Liu, Z., Ohsuna, T. and Terasaki, O. (2006) *Nature*, **444**, 79.

67 Wright, P.A., Zhou, W.Z., Perez-Pariente, J. and Arranz, M. (2005) *Journal of the American Chemical Society*, **127**, 494.

68 Ohnishi, N. and Hiraga, K. (1996) *Journal of Electron Microscopy*, **45**, 85.

69 Readman, J.E., Barker, P.D., Gameson, I., Hriljac, J.A., Zhou, W.Z., Edwards, P.P. and Anderson, P.A. (2004) *Chemical Communications*, 736.

70 Kresge, C.T., Leonowicz, M.E., Roth, W.J., Vartulli, J.C. and Beck, J.S. (1992) *Nature*, **359**, 710.

71 Carlsson, A., Kaneda, M., Sakamoto, Y., Terasaki, O., Ryoo, R. and Joo, S.H. (1999) *Journal of Electron Microscopy*, **48**, 795.

72 Sakamoto, Y., Kaneda, M., Terasaki, O., Zhao, D., Kim, J.M., Stucky, G.D., Shin, H.J. and Ryoo, R. (2000) *Nature*, **408**, 449.

73 Sakamoto, Y., Diaz, I., Terasaki, O., Zhao, D., Perez-Pariente, J., Kim, J.M. and Stucky, G.D. (2002) *Journal of Physical Chemistry B*, **106**, 3118.

74 Kaneda, M., Tsubakiyama, T., Carlsson, A., Sakamoto, Y., Ohsuna, T., Terasaki, O., Joo, S.H. and Ryoo, R. (2002) *Journal of Physical Chemistry B*, **106**, 1256.

75 Beck, J.S., Vartulli, J.C., Roth, W.J., Leonowicz, M.E., Kresge, C.T., Schmitt, K.D., Chu, C.T.-W., Olson, D.H., Sheppard, E.W., McCullen, S.B., Higgins, J.B. and Schlenker, J.L. (1992) *Journal of the American Chemical Society*, **114**, 10834.

76 Zhao, D., Feng, J., Huo, Q., Melosh, N., Fredrickson, G.H., Chmelka, B.F. and Stucky, G.D. (1998) *Science*, **279**, 548.

77 Zhao, D., Huo, Q., Feng, J., Chmelka, B.F. and Stucky, G.D. (1998) *Journal of the American Chemical Society*, **120**, 6024.

78 Huo, Q., Leon, R., Petroff, P.M. and Stucky, G.D. (1995) *Science*, **268**, 1324.

79 Fan, J., Yu, C., Gao, F., Lei, J., Tian, B., Wang, L., Luo, Q., Tu, B., Zhou, W.Z. and Zhao, D. (2003) *Angewandte Chemie (International Edition in English)*, **42**, 3146.

80 Fan, J., Yu, C.Z., Lei, J., Tu, B. Zhang, Q., Zhou, W.Z. and Zhao, D.Y. (2005) *Journal of the American Chemical Society*, **127**, 10794.

81 Monnier, A., Schuth, F., Huo, Q., Margolese, D., Maxwell, R.S., Stucky, G.D., Krishamurty, M., Petroff, P., Firouzi, A., Janicke, M. and Chmelka, B.F. (1993) *Science*, **261**, 1299.

82 Alfredsson, V. and Anderson, M.W. (1996) *Chemistry of Materials*, **8**, 1141.

83 Alfredsson, V., Anderson, M.W., Ohsuna, T., Terasaki, O., Jacob, M. and Bojrup, M. (1997) *Chemistry of Materials*, **9**, 2066.

84 Luan, Z., He, H. Zhou, W.Z., Cheng, C. and Klinowski, J. (1995) *Journal of the Chemical Society, Faraday Transactions*, **91**, 2955.

85 Corma, A., Navarro, M.T. and Perez-Pariente, J. (1994) *Chemical Communications*, 147.

86 Reddy, K.M., Mondrakovski, I. and Sayari, A. (1994) *Chemical Communications*, 1059.

87 Cheng, C.F., He, H., Zhou, W., Klinowski, J., Gonclaves, J.A. and Gladden, L.F. (1996) *Journal of Physical Chemistry*, **100**, 390.

88 Zhao, D. and Goldfarb, D. (1995) *Chemical Communications*, 875.

89 Yuan, Z.Y., Zhou, W., Zhang, Z.L., Chen, Q., Su, B.-L. and Peng, L.M. (2002) *Studies in Surface Science and Catalysis*, **141**, 403.

90 Corma, A., Navarro, M.T., Nemeth, L. and Renz, M. (2001) *Chemical Communications*, 2190.

91 Shephard, D.S., Zhou, W.Z., Maschmeyer, T., Matters, J.M., Roper, C.L., Parsons, S., Johnson, B.F.G. and Duer, M. (1998) *Angewandte Chemie (International Edition in English)*, **37**, 2719.

92 Shephard, D.S., Maschmeyer, T., Johnson, B.F.G., Thomas, J.M., Sankar, G., Ozkaya, D., Zhou, W.Z., Oldroyd, R.D. and Bell, R.G. (1997) *Angewandte Chemie (International Edition in English)*, **36**, 2242.

93 Zhou, W.Z., Thomas, J.M., Shephard, D.S., Johnson, B.F.G., Ozkaya, D., Maschmeyer, T., Bell, R.G. and Ge, Q. (1998) *Science*, **280**, 705.

94 Ozkaya, D., Zhou, W.Z., Thomas, J.M., Midgley, P., Keast, V.J. and Hermans, S. (1999) *Catalysis Letters*, **60**, 113.

95 Midgley, P.A. and Weyland, M. (2003) *Ultramicroscopy*, **96**, 413.

96 Arslan, I., Yates, T.J.V., Browning, N.D. and Midgley, P.A. (2005) *Science*, **309**, 2195.

97 Zhu, K.K., Yue, B., Zhou, W.Z. and He, H.Y. (2003) *Chemical Communications*, 98.

98 Jiao, K., Zhang, B., Yue, B., Ren, Y., Liu, X.Y., Yan, S.R., Dickinson, C., Zhou, W.Z. and He, H.Y. (2005) *Chemical Communications*, 5618.

99 Yue, B., Tang, H., Kong, Z., Zhu, K., Dickinson, C., Zhou, W.Z. and He, H. (2005) *Chemical Physics Letters*, **407**, 83.

100 Dickinson, C., Zhou, W.Z., Hodgkins, R.P., Shi, Y.F., Zhao, D.Y. and He, H.Y. (2006) *Chemistry of Materials*, **18**, 3088.

101 Jiao, F., Harrison, A., Jumas, J.C., Chadwick, A.V., Kockelmann, W. and Bruce, P.G. (2006) *Journal of the American Chemical Society*, **128**, 5468.

102 Yang, H.F., Sui, Q.H., Tian, B.Z., Liu, Q.Y., Gao, F., Xie, S.H., Fan, J., Yu, C.Z., Tu, B. and Zhao, D.Y. (2003) *Journal of the American Chemical Society*, **125**, 4724.

103 Imperor-Clerc, M., Bazin, D., Appay, M., Beaunier, P. and Davidson, A. (2004) *Chemistry of Materials*, **16**, 1813.

104 Tian, B.Z., Liu, X.Y., Yang, H.F., Xie, S.H., Yu, C.Z., Tu, B. and Zhao, D.Y. (2003) *Advanced Materials*, **15**, 1370.

105 Tian, B.Z., Liu, X.Y., Solovyov, L.A., Liu, Z., Yang, H.F., Zhang, Z.D., Xie, S.H., Zhang, F.Q., Tu, B. Yu, C.Z., Terasaki, O. and Zhao, D.Y. (2004) *Journal of the American Chemical Society*, **126**, 865.

106 Wang, Y.M., Wu, Z.Y., Wang, H.J. and Zhu, J.H. (2006) *Advanced Functional Materials*, **16**, 2374.

107 Yue, W.B., Hill, A.H., Harrison, A. and Zhou, W.Z. (2007) *Chemical Communications*, 2518.

108 Yue, W.B. and Zhou, W.Z. (2007) *Chemistry of Materials*, **19**, 2359.

109 Yue, W.B. and Zhou, W.Z. (2007) *Journal of Materials Chemistry*, **17**, 4947.

110 Fu, Y.-S., Du, X.-W., Kulinich, S.A., Qiu, J.-S., Qin, W.-J., Li, R., Sun, J. and Liu, J. (2007) *Journal of the American Chemical Society*, **129**, 16029.

111 Zeng, H., Li, Z., Cai, W., Cao, B., Liu, P. and Yang, S. (2007) *Journal of Physical Chemistry B*, **111**, 14311.

112 Park, J., An, K., Hwang, Y., Park, J.-G., Noh, H.-J., Kim, J.-Y., Park, J.-H., Hwang, N.-M. and Hyeon ,T. (2004) *Nature Materials*, **3**, 891.

113 Shavel, A., Rodriguez-Gonzalez, B., Spasova, M., Farle, M. and Liz-Marzan, L.M. (2007) *Advanced Functional Materials*, **17**, 3870.

114 Xie, H., Zuo, C., Liu, Y., Zhang, Z., Pang, D., Li, X., Gong, J., Dickinson, C. and Zhou, W.Z. (2005) *Small*, **1**, 506.

115 Chen, X.Y., Qiao, M.H., Xie, S.H., Fan, K.N., Zhou, W.Z. and He, H.Y. (2007) *Journal of the American Chemical Society*, **129**, 13305.

116 Umar, A., Rahman, M.M., Kim, S.H. and Hahn, Y.B. (2008) *Chemical Communications*, 166.

117 Yang, R.S. and Wang, Z.L. (2005) *Solid State Communications*, **134**, 741.

118 Cheong, F.C., Varghese, B., Zhu, Y., Tan, E.P.S., Dai, L., Tan, V.B.C., Lim, C.T. and Sow, C.H. (2007) *Journal of Physical Chemistry C*, **111**, 17193.

119 Zhu, K., He, H., Xie, S., Zhang, X., Zhou, W.Z., Jin, S. and Yue, B. (2003) *Chemical Physics Letters*, **377**, 317.

120 Vomiero, A., Bianchi, S., Comini, E., Faglia, E.G., Ferroni, M. and Sberveglieri, G. (2007) *Crystal Growth and Design*, **7**, 2500.

121 Wang, Y., Hou, L., Qin, X., Ma, S., Zhang, B., Gou, H. and Gao, F. (2007) *Journal of Physical Chemistry C*, **111**, 17506.

122 Tan, Y., Xue, X., Peng, Q., Zhao, H., Wang, T. and Li, Y. (2007) *Nano Letters*, **7**, 3723.

123 Wu, J. and Coffer, J.L. (2007) *Journal of Physical Chemistry C*, **111**, 16088.

124 Miao, Z., Xu, D., Ouyang, J., Guo, G., Zhao, X. and Tang, Y. (2002) *Nano Letters*, **2**, 717.

125 Wang, Z.L. (2004) *MaterialsToday*, **7**(6), 26.

126 Pan, Z.W., Dai, Z.R. and Wang, Z.L. (2001) *Science*, **291**, 1947.

127 Wang, Z.L. (2004) *Journal of Physics – Condensed Matter*, **16**, R829.

128 Kong, X.Y., Ding, Y., Yang, R.S. and Wang, Z.L. (2004) *Science*, **303**, 1348.

129 Kong, X.Y., Ding, Y., Yang, R.S. and Wang, Z.L. (2004) *Journal of Physical Chemistry B*, **108**, 570.

130 Kasuga, T., Hiramatsu, M. and Hoson, A. (1998) *Langmuir*, **14**, 3160.

131 Kasuga, T., Hiramatsu, M., Hoson, A., Sekino, T. and Nihara, K. (1999) *Advanced Materials*, **11**, 1307.

132 Chen, Q., Zhou, W.Z., Du, G. and Peng, L.M. (2002) *Advanced Materials*, **14**, 1208.

133 Zhang, S., Peng, L.-M., Chen, Q., Du, G.H., Dawson, G. and Zhou, W.Z. (2003) *Physical Review Letters*, **91**, Art. No. 256103.

134 Thorne, A., Kruth, A., Tunstall, D., Irvine, J.T.S. and Zhou, W.Z. (2005) *Journal of Physical Chemistry B*, **109**, 5439.

135 Du, G.H., Chen, Q., Yu, Y., Zhang, S., Zhou, W.Z. and Peng, L.M. (2004) *Journal of Materials Chemistry*, **14**, 1437.

136 Du, G.H., Peng, L.-M., Chen, Q., Zhang, S. and Zhou, W.Z. (2003) *Applied Physics Letters*, **83**, 1638.

11
Oxidation Reactions over Supported Metal Oxide Catalysts: Molecular/Electronic Structure–Activity/Selectivity Relationships

Israel E. Wachs and Taejin Kim

11.1
Overview

Supported vanadium oxide catalysts find wide application as oxidation catalysts and are the focus of this chapter. The highly dispersed nature of the surface vanadium oxide phases on oxide supports allows their detailed characterization and the establishment of molecular/electronic structure–activity/selectivity relationships. The surface vanadium oxide species exist on oxide supports under dehydrated conditions as isolated and polymeric surface VO_4 species with one terminal V=O bond and three bridging V–O–M bonds, in which M represents either an adjacent V or an oxide support cation. Fundamental oxidation studies with the CH_3OH chemical probe molecule over the well defined supported vanadium oxide catalysts show that the bridging V–O–V and terminal V=O bonds do not play a critical role in this redox reaction. However, kinetic studies reveal that the bridging V–O–Support bond dominates the overall reaction by controlling the number of chemisorbed methanol molecules present on the catalyst surface during steady-state reaction conditions. The number of chemisorbed methanol molecules is determined by the electron density on the oxygen atom in the bridging V–O–Support bond, which increases with decreasing electronegativity of the support cation. This general trend is also observed for other oxidation reactions involving one surface VO_4 site. For oxidation reactions involving multiple redox or redox–acidic sites, both the specific oxide support, via the bridging V–O–Support bond, and the surface density of catalytic active sites control the surface intermediate coverage during steady-state reaction. These observations are outlined in more detail in this chapter.

11.2
Introduction

Supported metal oxide catalysts consist of dispersed surface metal oxide species, the catalytic active sites, which are supported on high-surface-area oxides [1–3]. The

Metal Oxide Catalysis. Edited by S. David Jackson and Justin S. J. Hargreaves

ISBN: 978-3-527-31815-5

surface coverage of the supported metal oxide phase can vary from below to above monolayer coverage. Below monolayer surface coverage, isolated and polymerized surface metal oxide species are generally present on the support. Above monolayer surface coverage, crystalline nanoparticles (NPs) are also present and reside on top of the surface metal oxide monolayer. Although this class of catalysts has been referred to as "monolayer oxide catalysts," it should be recognized that the surface coverage of the supported metal oxide phase can vary widely over all coverage (sub-monolayer, monolayer and above monolayer). Monolayer surface coverage is a critical parameter for supported metal oxide catalysts, since different molecular structures of the catalytically active supported metal oxide phase are present below and above monolayer coverage (surface species and crystalline NPs, respectively).

Supported metal oxide catalysts have been extensively investigated since the 1950s. They are employed in numerous large-volume industrial catalytic applications [4–6]: olefin metathesis over supported Re_2O_7/Al_2O_3 and WO_3/SiO_2 [7, 8], ethylene polymerization over supported CrO_3/SiO_2 [9, 10], *o*-xylene oxidation to phthalic anhydride over supported V_2O_5/TiO_2 [11, 12], oxidation/ammoxidation of alkyl pyridines for production of pharmaceuticals over supported V_2O_5/TiO_2 and V_2O_5/Al_2O_3 catalysts [13], selective catalytic reduction (SCR) of NO_x with ammonia or other reducing agents to N_2 over supported V_2O_5-WO_3/TiO_2 and V_2O_5-MoO_3/TiO_2 catalysts [14–20], H_2S oxidation to elemental sulfur over supported Fe_2O_3/SiO_2 and MnO_x/SiO_2 catalysts [21], combustion of automotive exhaust over supported PtO_x/CeO_2 and NO_x storage over supported $PtO_x/BaO_x/Al_2O_3$ [22, 23]. Supported metal oxide catalysts represent model well defined catalysts for fundamental studies since the surface coverage of the catalytic active sites can be varied in the sub-monolayer region and their molecular and electronic structures readily characterized by many available spectroscopic techniques, even under reaction conditions [3]. Furthermore, combination of the molecular and electronic structural information with corresponding catalytic performance data allows the establishment of molecular/electronic structure–activity/selectivity relationships that facilitate the design of advanced catalytic materials.

The focus of this chapter will be on supported vanadia catalysts since they represent the most examined and applied supported metal oxide catalyst systems. The characterization and catalysis data will emphasize the work of the Wachs group and collaborators since both characterization and examination of their catalytic performance has been conducted on the same samples. For the development of structure–activity relationships it is critical that the characterization and catalytic performance data be performed on the same catalyst samples so that any discrepancies are minimized.

11.3
Monolayer Surface Coverage

As indicated in the introduction, it is critical to determine the surface coverage corresponding to monolayer coverage because of the different metal oxide species present above and below monolayer coverage. Many methods have been developed

to determine monolayer surface coverage of supported metal oxide catalytic materials and all methods essentially give the same results, as should be the case if the methodologies employed are correct. The discussion below assumes that the supported metal oxide catalysts were well prepared in the sub-monolayer region so that crystalline NPs are not present. Monolayer surface coverage can be determined with (i) X-ray Photoelectron Spectroscopy (XPS) by plotting the intensity ratio of surface MO_x/support signals as a function of MO_x content and establishing where there is a break or "knee" in the curve when crystalline NPs are present [1, 24], (ii) by plotting the Low Energy Ion Scattering Spectroscopy (LEISS) intensity ratio of surface MO_x/support signals as a function of MO_x content and establishing where there is a break in the curve [25], (iii) by plotting the Raman intensity ratio of surface MO_x/support signals as a function of MO_x content and establishing where there is a break in the curve (in this method, the support Raman band must be employed as an internal reference) [24, 26], (iv) determining the appearance of crystalline MO_x NPs as a function of MO_x content [1, 25, 27], (v) monitoring the consumption of surface hydroxyls vs MO_x content with IR spectroscopy since the surface metal oxides anchor to the support by titrating the surface hydroxyls [1, 24], (vi) CO_2 chemisorption on the unreacted surface hydroxyls, but care must be taken if there is selective titration of surface hydroxyls by the supported MO_x [1, 24], and (vi) CH_3OH-Temperature Programmed Surface Reaction (TPSR) spectroscopy which monitors the number of exposed surface MO_x sites, since this parameter decreases above monolayer coverage as crystalline metal oxide NPs are introduced into the catalyst [26]. The catalytic activity (moles $(g\,s)^{-1}$) generally also levels off above monolayer coverage because of the reduced number of exposed MO_x sites above monolayer coverage, but this approach only works if the catalytic reaction being employed is not sensitive to the presence of the crystalline metal oxide NPs [11–13]. Consequently, it is risky to rely solely on the catalytic reaction to determine monolayer coverage, and independent spectroscopic determination of monolayer coverage is the proper method for monolayer determination. As already mentioned, the monolayer surface coverage usually has the same value independent of the method of determination.

The Raman spectra of a series of supported V_2O_5/Al_2O_3 catalysts as a function of vanadium oxide loading are presented in Figure 11.1. Monolayer surface coverage is readily determinable from this series of Raman spectra since below monolayer coverage only the broad Raman band of dehydrated surface VO_x species are present at 1008–1031 cm^{-1} and the sharp crystalline V_2O_5 NPs Raman band at 995 cm^{-1} as well as accompanying broader bands at 690 and 525 cm^{-1} appear above monolayer surface coverage. Thus, monolayer surface coverage of vanadium oxide on Al_2O_3 corresponds to 7.9 V atoms/nm^2. For supported vanadium oxide catalysts, monolayer surface coverage has been determined to be ~8 V atoms/nm^2 [25] on all oxide supports (Al_2O_3, TiO_2, ZrO_2, Nb_2O_5, CeO_2, etc.) with the exception of SiO_2. The lower reactivity of the silica surface hydroxyls results in a maximum surface vanadium oxide dispersion of ~3 V atoms/nm^2 on SiO_2 [27]. The bulk V_2O_5 phase has a surface vanadium oxide density of ~10 V atoms/nm^2 on the V_2O_5 (010) basal plane, which shows that surface density of bulk metal oxides is not always quantitatively representative of surface metal oxide phases on oxide supports.

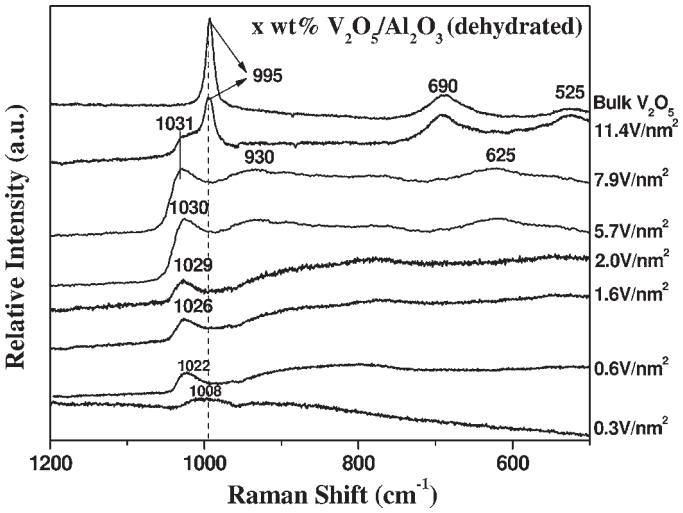

Figure 11.1 Raman spectra of supported V_2O_5/Al_2O_3 catalysts under dehydrated conditions as a function of vanadium oxide loading.

11.4 Molecular and Electronic Structures

The molecular structures of the surface vanadium oxide species have been determined in recent years with the application of numerous *in situ* spectroscopic techniques. *In situ* solid-state ^{51}V NMR, X-ray Absorption Near-Edge Spectroscopy (XANES) and Extended X-ray Absorption Fine Structure (EXAFS) characterization studies have demonstrated that the surface vanadium oxide species possess VO_4 coordination under dehydrated conditions [28, 29]. Furthermore, both isolated and polymerized surface VO_4 species are present on oxide supports. The extent of polymerization of the surface VO_4 species has recently been estimated with *in situ* UV-Vis Diffuse Reflectance Spectroscopy (DRS) from the optical edge energy, E_g, which reflects the extent of polymerization (E_g decreases monotonically with increasing extent of polymerization and is related to the electron mobility). The extent of polymerization of the surface VO_4 species as a function of surface vanadium oxide density in the sub-monolayer region is presented in Figure 11.2 from UV-Vis DRS measurements [30]. Below ~15% of monolayer coverage, the surface VO_4 species are isolated and possess one terminal V=O bond (Raman bands at 1008–1031 cm^{-1} in Figure 11.1) and three bridging V–O–Support bonds (weak and broad Raman band at ~900 cm^{-1} in Figure 11.1). At intermediate surface coverage, both isolated and polymeric surface VO_4 species coexist on the Al_2O_3 support and the extent of polymerization increases monotonically with surface coverage. At monolayer surface coverage, essentially all the surface VO_4 species are polymerized and possess one terminal V=O bond (1031 cm^{-1}) together with bridging

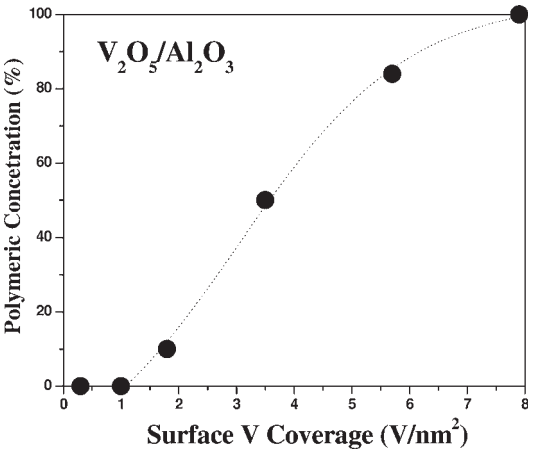

Figure 11.2 Concentration of polymeric surface VO_4 species for dehydrated supported V_2O_5/Al_2O_3 catalysts in the sub-monolayer region as a function of surface vanadium oxide density.

V—O–Support (930 cm^{-1}) and V—O—V (625 cm^{-1}) bonds. Similar distributions of monomeric and polymeric surface VO_4 species are found on other oxide supports with the exception of SiO_2 [30]. For the supported V_2O_5/SiO_2 catalyst system, only isolated surface VO_4 species are present below the maximum dispersion limit (<3 V atoms/nm^2). For all supported vanadium oxide catalysts, crystalline V_2O_5 NPs are also present above the monolayer surface coverage or maximum dispersion limit [31].

11.5
Number of Exposed Catalytic Active Sites (N_s)

Below monolayer surface coverage, the number of exposed catalytic active sites is just the number of surface VO_4 species present on the support, and increases linearly with surface vanadium oxide coverage until monolayer. Above monolayer surface coverage, both exposed surface VO_4 and crystalline V_2O_5 NP sites are present and the contribution of each component must be considered. The number of exposed vanadium oxide catalytic active sites can be determined with CH_3OH-TPSR spectroscopy, since a monolayer of surface $CH_3O^{\cdot}$ is formed during CH_3OH chemisorption at ~100 °C [32, 33]. The redox vanadium oxide sites yield HCHO as the reaction product and the exposed acidic Al_2O_3 sites form dimethyl ether. The area under the HCHO TPSR curves reflects the number of redox sites. The number of redox sites for the supported V_2O_5/Al_2O_3 catalyst system as a function of vanadium oxide loading is shown in Figure 11.3. In the sub-monolayer region, the number of catalytic redox sites increases linearly with the vanadium oxide

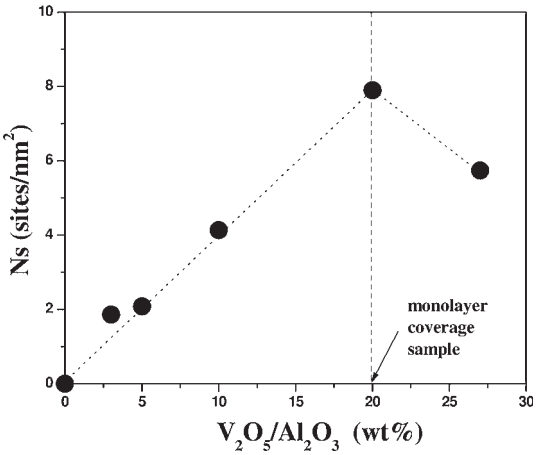

Figure 11.3 Number of exposed redox catalytic active sites for supported V_2O_5/Al_2O_3 catalysts as a function of vanadium oxide loading. Monolayer coverage corresponds to the 20% V_2O_5/Al_2O_3 (~7.9 V atoms/nm^2) catalyst sample.

loading and then decreases with increasing vanadium oxide loading above 20% V_2O_5/Al_2O_3 (7.9 V atoms/nm^2) when crystalline V_2O_5 NPs are also present. Note that the maximum number of catalytic active redox sites corresponds to monolayer surface VO_4 coverage. This suggests that the crystalline V_2O_5 NPs are covering up more surface VO_4 sites than their contribution to the number of catalytic active sites. The low number of exposed redox catalytic sites for the supported V_2O_5 NPs is a consequence of their platelet morphology, which results in an inactive (001) basal plane that terminates with the V=O functionality and only the minor edge sites terminating with V–O–V and V-OH sites are able to chemisorb CH_3OH [34, 35].

11.6 Surface Reactivity

The surface reactivity of the isolated and polymeric surface VO_4 species present in supported V_2O_5/Al_2O_3 catalysts was also determined from CH_3OH-TPSR experiments. As mentioned above, CH_3OH chemisorbs as surface $CH_3O^{\bullet}$ on supported vanadium oxide catalysts and the rate determining step involves breaking the surface methoxy C–H bond to form the HCHO redox product. The CH_3OH-TPSR spectra revealed that the peak temperature for breaking the C–H bond of the surface methoxy intermediate was ~190 °C (corresponding to a first-order rate constant of ~0.2 HCHO molecules/(site sec) at 230 °C) and is independent of surface vanadium oxide coverage in the sub-monolayer region. The constant surface kinetics with coverage indicates that there is no difference in the reactivity

between monomeric and polymeric surface VO_4 species on Al_2O_3. Furthermore, this also suggests that the bridging V—O—V bonds in the polymeric surface VO_4 species are not critical in the surface $CH_3O^{\cdot}$ dehydrogenation to HCHO reaction step. The TPSR peak temperature was also not affected by the presence of crystalline V_2O_5 NPs since they contributed too few sites and the peak temperature value for bulk crystalline V_2O_5 corresponds to ~188 °C, which is not very different.

Similar findings were also observed for other supported vanadium oxide catalysts as a function of surface vanadium oxide coverage. Furthermore, with the exception of the supported V_2O_5/SiO_2 catalyst, the CH_3OH-TPSR peak temperature of all the supported vanadium oxide catalysts were not very different and varied within the narrow temperature range 182–192 °C, which corresponds to a factor of ~2 in k_{rds}. Thus, the surface methoxy C—H breaking kinetics are relatively constant for all the supported vanadium oxide catalysts and not significantly affected by the oxide support.

11.7
Steady-State Reactivity (TOF)

The methanol oxidation Turnover Frequency, (TOF) (the number of HCHO molecules/(site sec)), for the supported V_2O_5/Al_2O_3 catalysts were determined from steady-state methanol oxidation studies at 230 °C and knowledge of N_s (see Figure 11.3 above). The TOF for methanol oxidation over the supported V_2O_5/Al_2O_3 was found to be essentially constant at ~7×10^{-3} HCHO molecules/(site sec) for all vanadium oxide loading. The constant TOF demonstrates that the TOF is the same for surface VO_4 monomers and polymers, and that the bridging V—O—V bonds in the polymeric surface VO_4 species are not critical for methanol oxidation to formaldehyde. It is not easy to determine the TOF for the crystalline V_2O_5 NPs above monolayer coverage since their contribution to the overall TOF was minor.

Changing the specific oxide support, however, dramatically affected the steady-state TOF values by orders of magnitude: V_2O_5/CeO_2 (~1.0 HCHO molecules/(site sec)) > V_2O_5/ZrO_2 (~0.22 HCHO molecule/(site sec)) > V_2O_5/TiO_2 (~0.17 HCHO molecules/(site sec)) > V_2O_5/Al_2O_3 (~0.007 HCHO molecules/(site sec)). To fully understand the origin of this significant variation in TOF, it is necessary to examine the overall kinetics for methanol oxidation. The steady-state kinetics is expressed by [36]

$$\mathrm{TOF} = K_{ads} \times k_{rds} \times P_{CH3OH} \tag{11.1}$$

in which k_{rds} represents the rate determining step of methanol oxidation to HCHO (the surface methoxy C—H bond-breaking step), K_{ads} is the CH_3OH equilibrium adsorption (the CH_3OH O—H bond breaking step) and P_{CH3OH} is the methanol partial pressure. The methanol oxidation reaction is zero order in O_2 partial pressure because the surface VO_4 sites are fully oxidized under the methanol oxidation reaction conditions in excess oxygen [37]. The CH_3OH-TPSR findings demonstrate

that k_{rds} is relatively constant as the oxide support is changed, which means that changes in K_{ads} are responsible for the dramatic TOF variations since the methanol partial pressure is constant in all the studies. Increases in K_{ads} result in higher surface $CH_3O^{\bullet}$ concentrations under reaction conditions. This means that the dramatic changes in TOF with the specific oxide support is related to the number of surface methoxy intermediates on the catalyst surface during methanol oxidation and not variations in the rate-determining-step first-order k_{rds}.

Recent density functional theory calculations for CH_3OH chemisorption found that the most energetically favorable chemisorption site on supported VO_4 species is the bridging V—O–Support bond [38–40]. The density functional theory methanol oxidation calculation over supported V_2O_5/SiO_2 also concluded that the changes in reactivity for the different supports must be in the chemisorption step since the first-order energetics and kinetics for breaking the C—H bond of the surface $CH_3O^{\bullet}$ intermediate is very similar for the gas phase $O{=}V{-}(OCH_3)_3$ molecular complex and the surface methoxy intermediate on the model V_2O_5/SiO_2 cluster [39].

11.8
Number of Participating Catalytic Active Sites in Oxidation Reactions

Below monolayer coverage, the redox VO_4 catalytic active sites are 100% dispersed on the oxide supports and their surface coverage can be systematically varied (see Figure 11.3). Thus, the kinetic Equation 11.1 can be rewritten as

$$\text{Rate} = K_{ads} \times k_{rds} \times P_{CH3OH} \times N_s^n \tag{11.2}$$

in which n represents the number of participating catalytic active sites. Furthermore, for constant temperature and methanol partial pressure the log of Equation (11.2) results in

$$\log \text{Rate} = \log(K_{ads} \times k_{rds} \times P_{CH3OH}) + n \log N_s \tag{11.3}$$

and a plot of log Rate vs log N_s yields a line with slope n, the number of participating redox surface VO_4 catalytic active sites in the reaction, and the constant intercept of log ($K_{ads} \times k_{rds} \times P_{CH3OH}$). The value of n for CH_3OH oxidation is 1 since the TOF is constant with coverage in the sub-monolayer region. Equation 11.3 can also be generalized to other oxidation reactions over supported vanadium oxide catalysts where the reaction is zero order in oxygen partial pressure, which corresponds to excess oxygen, as

$$\log \text{Rate} = \log(K_{ads} \times k_{rds} \times P_{Reactant}) + n \log N_s \tag{11.4}$$

The values of n have been determined for a number of oxidation reactions over supported vanadium oxide catalysts and are given in Table 11.1.

Table 11.1 Number of participating catalytic active sites for different oxidation reactions. Determined by application of Equation (11.4).

Catalytic oxidation reaction	Number of participating sites	Ref.
$CH_3OH \rightarrow HCHO$ (formaldehyde)	1	[41]
$SO_2 \rightarrow SO_3$ (sulfur trioxide)	1	[42]
$C_2H_6 \rightarrow C_2H_4$ (ethylene)	1	[43]
$C_3H_8 \rightarrow C_3H_6$ (propylene)	1	[30, 44, 45]
$C_3H_6 \rightarrow C_3H_4O$ (acrolein)	2	[46]
$n\text{-}C_4H_{10} \rightarrow C_4H_2O_3$ (maleic anhydride)	multiple[a)]	[47]
$NO_x/NH_3 \rightarrow N_2$ (molecular N_2)	multiple[a)]	[15]

a Exact values of *n* have not been determined, but TOF increases with surface coverage, reflecting the participation of multiple catalytic active sites.

All the reactions involving the participation of one surface VO_4 site are 2 e^- reactions that require only one O atom. All the reactions involving multiple surface VO_4 sites are 4 to 8 e^- reactions requiring the involvement of multiple O atoms. Note that each surface VO_4 species can only be reduced from V^{+5} to V^{+3}, which corresponds to the release of one O atom. Similar to the CH_3OH oxidation to HCHO, varying the oxide support changes the TOF values by a couple of orders of magnitude for all the oxidation reactions listed in Table 11.1, which again demonstrates the pronounced effect of the bridging V—O–Support bond on all oxidation reactions.

11.9 Role of Surface Acid Sites on Oxidation Reactions

The concentration of surface Brønsted acids increases monotonically with surface VO_4 coverage and qualitatively follows the presence of polymeric surface VO_4 species [43, 48]. The presence of the surface Brønsted acid sites, however, has no effect on the TOF values for oxidation reactions involving only one surface VO_4 site. Surface Brønsted acid sites, however, can facilitate oxidation reactions requiring both surface redox and acid sites. For example, (i) the oxidation of *n*-butane to maleic anhydride does require the presence of acid sites and is probably related to the ring-closure step [47, 49], (ii) the presence of surface acid sites, Brønsted as well as Lewis, enhances the NO_x SCR reaction because the acid sites facilitate the chemisorption of basic NH_3 [14, 20] and (iii) the presence of surface acid sites enhances the chemisorption of propane via a precursor state [50]. Thus, surface Brønsted acid sites do not facilitate oxidation reactions involving one redox surface VO_4 site, but may facilitate oxidation reactions involving multiple redox surface VO_4 sites, especially if the oxidation reaction requires the participation of dual redox–acid sites.

11.10
Other Supported MO_x Redox Active and Acidic Systems

Although this chapter focuses on oxidation reactions involving redox supported vanadium oxide catalysts, similar trends with surface coverage and specific oxide support also apply for other redox supported transition metal oxide catalysts, such as supported MoO_3 [51], CrO_3 [52] and Re_2O_7 [53]. The redox supported vanadium oxide catalytic system was chosen for this review because of the extensive studies that these catalysts have received in recent years as well as their widespread industrial applications.

Supported Nb_2O_5 [54], Ta_2O_5 [55] and WO_3 [26] catalysts typically possess almost no redox potential and exclusively behave as surface acid sites. Other than their acidic properties, these supported metal oxides possess similar molecular and electronic structural characteristics as the redox surface sites discussed above.

11.11
Conclusions

Supported metal oxide catalysts are a new class of catalytic materials that are excellent oxidation catalysts when redox surface sites are present. They are ideal catalysts for investigating catalytic molecular/electronic structure–activity selectivity relationships for oxidation reactions because (i) the number of catalytic active sites can be systematically controlled, which allows the determination of the number of participating catalytic active sites in the reaction, (ii) the TOF values for oxidation studies can be quantitatively determined since the number of exposed catalytic active sites can be easily determined, (iii) the oxide support can be varied to examine the effect of different types of ligand on the reaction kinetics, (iii) the molecular and electronic structures of the surface MO_x species can be spectroscopically determined under all environmental conditions for structure–activity determination and (iv) the redox surface sites can be combined with surface acid sites to examine the effect of surface Brønsted or Lewis acid sites. Such fundamental structure–activity information can provide insights and also guide the molecular engineering of advanced hydrocarbon oxidation metal oxide catalysts such as supported metal oxides, polyoxo metallates, metal oxide supported zeolites and molecular sieves, bulk mixed metal oxides and metal oxide supported clays.

Acknowledgments

The support of the United States Department of Energy–Basic Energy Sciences grant DEFG02–93ER14 350 during the writing of this manuscript is gratefully acknowledged.

References

1 Wachs, I.E. (1996) *Catalysis Today*, **27**, 437.
2 Wachs, I.E. (2005) *Catalysis Today*, **100**, 79.
3 Weckhuysen, B.M. and Wachs, I.E. (2001) Catalysis by supported metal oxides, in *Handbook of Surfaces and Interfaces of Materials* (ed. H.S. Nalwa), Academic Press, New York, p. 63.
4 Thomas, C.L. (1970) *Catalytic Processes and Proven Catalysts*, Academic Press, New York.
5 Weissermel, K. and Arpe, H.-J. (1978) *Industrial Organic Chemistry*, Verlag Chemie, Weinheim.
6 Wachs, I.E. (ed.) (1999) Special issue on *Supported Metal Oxide Catalysts. Catalysis Today*, **51**(2), 271.
7 Xiaoding, X., Boelhouwer, C., Vonk, D., Benecke, J.I. and Mol, J.C. (1986) *Journal of Molecular Catalysis*, **36**, 47.
8 Banks, R.L. (1984) Olefin metathesis: technology and application, in *Applied Industrial Catalysi* (ed. B.E. Leach), Academic Press, New York, p. 215.
9 McDaniel, M.P. (1986) *Advanced Catalysis*, **33**, 4.
10 Weckhuysen, B.M., Wachs, I.E. and Schoonheydt, R.A. (1996) *Chemical Reviews*, **96**, 3327.
11 Wachs, I.E., Saleh, R.Y., Chan, S.S. and Chersich, C.C. (1985) *Applied Catalysis*, **15**, 339.
12 Grabowski, R., Grzybowska, B., Haber, J. and Sloczynski, J. (1975) *Reaction Kinetics and Catalysis Letters*, **2**, 81.
13 Heinz, D., Hoelderich, W.F., Krill, S., Boeck, W. and Huthmacher, K. (2000) *Journal of Catalysis*, **192**, 1.
14 Bosch, H. and Janssen, F. (1988) *Catalysis Today*, **2**, 369.
15 Wachs, I.E., Deo, G., Weckhuysen, B.M., Andreini, A., Vuurman, M.A., de Boer, M. and Amiridis, M.D. (1996) *Journal of Catalysis*, **161**, 211.
16 Amiridis, M.D., Wachs, I.E., Deo, G., Jehng, J.-M. and Kim, D.S. (1996) *Journal of Catalysis*, **161**, 247.
17 Ramis, G., Busca, G., Lorenzelli, V. and Forzatti, P. (1990) *Applied Catalysis*, **64**, 243.
18 Lietti, L., Svachula, J., Forzatti, P., Busca, G., Ramis, G. and Bregani, F. (1993) *Catalysis Today*, **17**, 131.
19 Topse, N.-Y., Dumesic, J. and Topsoe, H. (1995) *Journal of Catalysis*, **151**, 241.
20 Amiridis, M.D., Duevel, R.V. and Wachs, I.E. (1999) *Applied Catalysis B Environmental*, **20**, 111.
21 Visser, R.J.A.M., Terörde, P.J., van den Brink, L.M., van Dillen, A.J. and Geus, J.W. (1993) *Catalysis Today*, **17**, 217.
22 Weber, W.H. (2000) Raman applications in catalysts for exhaust-gas treatment, in *Raman Scattering in Materials Science* (eds W.H. Weber and R. Merlin), Springer, New York, p. 233.
23 Takahashi, N., Shinjoh, H., Iijima, T., Suzuki, T., Yamazaki, K., Yokota, K., Suzuki, H., Miyoshi, N., Matsumoto, S., Tanizawa, T., Tanaka, T., Tateishi, S. and Kasahara, K. (1996) *Catalysis Today*, **27**, 63.
24 Wachs, I.E. and Segawa, K. (1992) Supported metal oxides, in *Characterization of Catalytic Materials*, Butterworth-Heinemann, Stoneham, MA, p. 69.
25 Briand, L.E., Tkachenko, O.P., Gurya, M., Gao, X., Wachs, I.E. and Gruenert, W. (2004) *Journal of Physical Chemistry B*, **108**, 4823.
26 Kim, T.J., Burrows, A., Kiely, C.J. and Wachs, I.E. (2007) *Journal of Catalysis*, **246**, 370.
27 Gao, X., Bare, S.R., Weckhuysen, B.M. and Wachs, I.E. (1998) *Journal of Physical Chemistry B*, **102**, 10842.
28 Eckert, H. and Wachs, I.E. (1989) *Journal of Physical Chemistry*, **93**, 6796.
29 Yoshida, S., Tanaka, T., Nishimura, Y., Mizutani, H. and Funabiki, T. (1998) *Proc. 9th Intern. Congress Catal., Calgary, Canada*, Vol. 3 (eds M.J. Phillips and M. Ternan), p. 1473.
30 Tian, H., Ross, E.I. and Wachs, I.E. (2006) *Journal of Physical Chemistry B*, **110**, 9593.
31 Vuurman, M.A., Hirt, A.M. and Wachs, I.E. (1991) *Journal of Physical Chemistry*, **95**, 9928.
32 Briand, L.E., Farneth, W.E. and Wachs, I.E. (2000) *Catalysis Today*, **62**, 219.

33 Burcham, L.J., Briand, L.E. and Wachs, I.E. (2001) *Langmuir*, **17**, 6164.
34 Briand, L.E., Jehng, J.-M., Cornaqglia, L., Hirt, A.M. and Wachs, I.E. (2003) *Catalysis Today*, **78**, 257.
35 Badlani, M. and Wachs, I.E. (2001) *Catalysis Letters*, **75**, 137.
36 Holstein, W. and Machiels, C. (1996) *Journal of Catalysis*, **162**, 118.
37 Burcham, L.J., Deo, G., Gao, X. and Wachs, I.E. (2000) *Topics in Catalysis*, **11/12**, 85.
38 Khaliullin, R.Z. and Bell, A.T. (2002) *Journal of Physical Chemistry B*, **106**, 7832.
39 Doebler, J., Pritzsche, M. and Sauer, J. (2005) *Journal of the American Chemical Society*, **127**, 10861.
40 Calatayud, M. and Minot, C. (2004) *Journal of Physical Chemistry B*, **108**, 15679.
41 Deo, G. and Wachs, I.E. (1994) *Journal of Catalysis*, **146**, 323.
42 Dunn, J.P., Koppula, P.R., Stenger, H.G. and Wachs, I.E. (1998) *Applied Catalysis B Environmental* **19**, 103.
43 Martinez-Huerta, M.V., Gao, X., Tian, H., Wachs, I.E., Fierro, J.L.G. and Banares, M.A. (2006) *Catalysis Today*, **118**, 279.
44 Gao, X., Jehng, J.-M. and Wachs, I.E. (2002) *Journal of Catalysis*, **209**, 43.
45 Zhao, Z., Gao, X. and Wachs, I.E. (2001) *Journal of Physical Chemistry B*, **107**, 6333.
46 Zhao, C. and Wachs, I.E. (2006) *Catalysis Today*, **118**, 332.
47 Wachs, I.E., Deo, G., Jehng, J.-M., Weckhuysen, B.M., Guliants, V.V., Benziger, J.B. and Sundaresan, S. (1997) *Journal of Catalysis*, **170**, 75.
48 Turek, A.M., Wachs, I.E. and DeCanio, E. (1992) *Journal of Physical Chemistry*, **96**, 5000.
49 Deo, G. and Wachs, I.E. (1994) *Journal of Catalysis*, **146**, 335.
50 Mitra, B., Wachs, I.E. and Deo, G. (2006) *Journal of Catalysis*, **240**, 151.
51 Hu, H. and Wachs, I.E. (1995) *Journal of Physical Chemistry*, **99**, 10911.
52 Kim, D.S. and Wachs, I.E. (1993) *Journal of Catalysis*, **142**, 166.
53 Kim, D.S. and Wachs, I.E. (1993) *Journal of Catalysis*, **141**, 419.
54 Jehng, J.-M. and Wachs, I.E. (1990) *Catalysis Today*, **8**, 37.
55 Chen, Y., Fierro, J.L.G., Tanaka, T. and Wachs, I.E. (2003) *Journal of Physical Chemistry B*, **107**, 5243.

12
Vanadium Phosphate Catalysts

Jonathan K. Bartley, Nicholas F. Dummer, and Graham J. Hutchings

12.1
Introduction

Vanadium phosphates have been of considerable interest since the mid-1960s, when Bergman and Frisch [1] found them to be effective catalysts for the oxidation of *n*-butane to maleic anhydride (Equation 12.1).

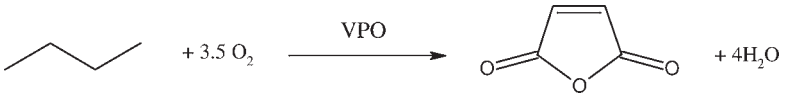

(12.1)

Prior to this, maleic anhydride had been industrially manufactured by the oxidation of benzene over supported V_2O_5-MoO_3 catalysts. In the late 1970s, when pollution laws that restricted benzene emissions came into effect, industry began to use the *n*-butane route. The reaction is of great importance as it is the only industrial large-scale selective oxidation of alkanes currently in operation. It also involves the functionalization of an alkane, providing a use for this rather unreactive oil fraction.

Maleic anhydride is used as a chemical intermediate in the synthesis of fumaric and tartaric acids, certain agricultural chemicals, resins in numerous products, dye intermediates and pharmaceuticals [2]. It is primarily used as a co-monomer for unsaturated polyester resins, which are used in the production of bonding agents for plywood manufacture and when mixed with glass fibres for reinforced plastics. Annual production of maleic anhydride is estimated to be over one million tonnes [3].

The selective oxidation of C_4 hydrocarbons leads to various commercially desirable products, which encouraged the development of the route involving the oxidation of *n*-butane to maleic anhydride. This new route was also less expensive owing to the lower cost of butane compared with benzene.

The *n*-butane oxidation process is interesting as it is an extensive oxidation, with the cleaving of eight C—H bonds and the introduction of three oxygen atoms, yet

Metal Oxide Catalysis. Edited by S. David Jackson and Justin S. J. Hargreaves

ISBN: 978-3-527-31815-5

it still manages to occur selectively. The process is a fourteen-electron oxidation, in comparison to other selective oxidation processes, which only require a maximum of four electrons.

Many well characterized, crystalline vanadium phosphate phases have been identified, whose structure and catalytic properties have been well documented. Some of the most widely studied are the V^{5+} vanadyl orthophosphates (α-, β-, γ-, δ-, ε- and ω-$VOPO_4$, and $VOPO_4 \cdot 2H_2O$), and the V^{4+} vanadyl hydrogen phosphates ($VOHPO_4 \cdot 4H_2O$, $VOHPO_4 \cdot ½H_2O$, $VO(H_2PO_4)_2$), vanadyl pyrophosphate ($(VO)_2P_2O_7$) and vanadyl metaphosphate ($VO(PO_3)_2$). Of these compounds, $VOHPO_4 \cdot ½H_2O$ (vanadyl hydrogen phosphate hemihydrate) is of particular interest as a catalyst precursor, which after activation gives a catalyst mainly composed of $(VO)_2P_2O_7$ (vanadyl pyrophosphate, hereafter VPP).

In this chapter we will discuss how the behavior of the catalyst is influenced by a number of factors including: the method of preparation of the precursor, the oxidation state of the catalyst, the phosphorus/vanadium ratio of the catalyst and the activation conditions. A variety of techniques have been used to characterize the morphology and nature of the active sites of the catalysts and gain insight into the mechanism. Furthermore, the effect of these preparatory techniques will be discussed, with emphasis on the partial oxidation of *n*-butane. We will pay particular attention to industrially relevant examples where possible and attempt to describe the current state of the art.

Although there is a great deal of debate about certain aspects of vanadium phosphate catalysts, Hodnett [4] has laid out a set of statements that most researchers generally agree upon:

- The most active and selective catalysts comprise mainly $(VO)_2P_2O_7$.
- During testing in *n*-butane lean conditions, the oxidation state of the catalyst is close to +4.
- The surface has some phosphorus enrichment. Only the surface layers are directly involved in catalysis.
- The rate determining step is butane activation by hydrogen abstraction

12.2 The Active Catalyst

The structure of vanadium phosphate catalysts is dependent on a number of factors. The P/V stoichiometry, thermal treatment time, activation temperature and gas phase composition can all affect catalyst composition. By varying these factors a variety of crystalline phases can be identified (by high-resolution transmission electron microscopy (HRTEM) [5] Figure 12.1a and X-ray diffraction Figure 12.1b) in the freshly activated catalyst [6]. It is widely accepted that VPP plays an important role in the oxidation of butane to maleic anhydride and most hypotheses are based on the (100) face (Figure 12.2). Additionally, this phase has been reported to be an efficient catalyst for the oxyfunctionalization of light paraf-

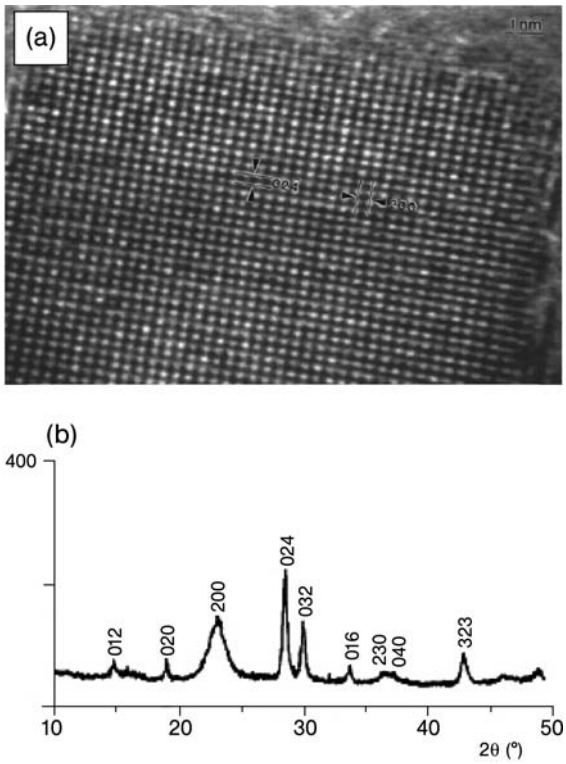

Figure 12.1 (a) An axial HREM image from the (021) projection of $(VO)_2P_2O_7$, (b) XRD pattern of an activated $(VO)_2P_2O_7$ catalyst. (Reproduced with permission).

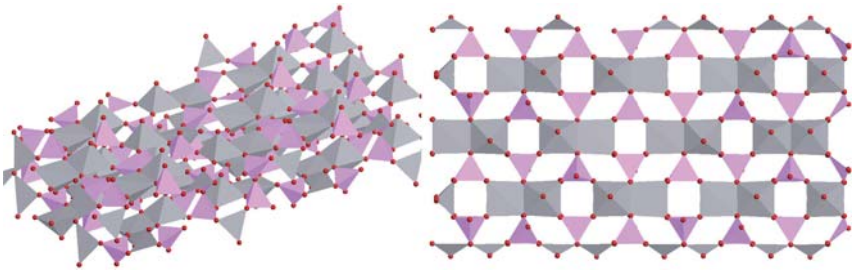

Figure 12.2 The (100) plane of $(VO)_2P_2O_7$. Grey = V octahedra, Purple = P tetrahedra, Red = O.

fins: (a) for the oxidation of ethane to acetic acid [6, 7], (b) for the oxidation and ammoxidation of propane to acrylic acid [8] and acrylonitrile [9, 10], respectively, and (c) for the oxidation of *n*-pentane to maleic and phthalic anhydrides [10–19].

The catalytic behavior of the different crystal faces has been investigated by Inumaru and coworkers by exposing individual planes [20]. VPP was deactivated by the surface deposition of SiO_2. The crystallites were then fractured to expose

the side faces, for example the (021) and (001) faces. The side faces were found to be non-selective, with maleic anhydride formed only on the (100) face. There is debate as to whether VPP is indeed the active catalyst, or if a combination of phases are responsible for the reaction.

Transient studies by Ballarini and coworkers showed that the active surface of equilibrated catalysts is different depending on the reaction conditions and the P/V ratio of the catalyst [21]. At low temperature (320 °C) an active surface forms that is selective and probably is more like $VOPO_4$ than VPP. However, as the temperature is increased to 380 °C this material becomes less selective. The active phase formed at $T > 380$ °C was found to be less active than the low-temperature phase ($T < 380$ °C) but has increased selectivity at this temperature. At these temperatures the active site is found to hydrolyze and oxidize and Ballarini and coworkers propose that the active surface is a VO_x/polyphosphoric acid mixture. The authors speculate that the different phase evolutions at different temperatures, which are also dependent on very minor changes in the P/V ratio, could be the cause for the very differing surfaces observed by both *in situ* and *ex situ* studies of the active catalyst.

12.2.1 The Oxidation State of the Catalyst

The final oxidation state of the activated catalysts varies between +4.00 and +4.40, depending on the amount of V^{5+} present in the catalyst. There is extensive discussion as to whether V^{5+} and V^{3+} phases are important in the reaction mechanism.

Ebner and Thompson have postulated that the V^{5+} phases that are formed during the activation period, are unimportant and do not contribute to the oxidation mechanism [22]. They have found that after several hundred hours on stream, the V^{5+} orthophosphate phases are reduced to pyrophosphate, giving an active catalyst with a final oxidation state of +4.00 to +4.04. The concentration of oxygen and butane in the reactant feedstock determines the time needed to equilibrate the catalyst. Based on this study, they suggest that other researchers (who find V^{5+} phases in the active catalyst) have not performed the activation process fully, or have an unfavorable redox potential in the gas stream.

A series of vanadium phosphate catalysts prepared by different routes and containing different phases were examined by Guliants and coworkers [23]. From this study it was concluded that the catalytically active phase is an active surface layer on VPP. Their experimental results showed $VOPO_4$ phases to be detrimental to the performance of the catalyst. This was confirmed by Cavani and Trifirò, who suggested that V^{5+} sites are responsible for the over-oxidation of maleic anhydride to carbon oxides [24].

A number of groups dispute this one-phase hypothesis. They suggest that V^{5+} phases are important in the active catalyst and are formed as the result of a redox mechanism (Figure 12.3) [25–27]. Bordes cites the apparent need for two contradictory conditions during the oxidation of butane as evidence for a multi-phase active catalyst [19]. It was stated that oxygen associated with V^{4+} activates butane

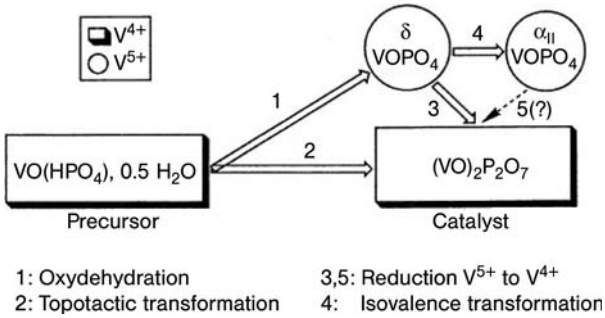

Figure 12.3 Scheme of the proposed evolution of the VPO catalyst with time [32].

while the oxygen associated with V^{5+} is incorporated later. V^{4+} gives a very active catalyst that has poor selectivity, while V^{5+} gives a very selective catalyst that has a low activity. This mechanism has been supported by the X-ray Photoelectron Spectroscopy (XPS) studies of Coulston and coworkers [28] and Temporal Analysis of Products (TAP) studies by Rodemerck and coworkers [29, 30] and Lorences and coworkers [31]. These studies report that in the absence of V^{5+} sites no maleic anhydride was observed and the main reaction product was furan. When V^{5+} sites were present maleic anhydride was produced.

Experimental results on pure vanadium phosphate phases and active catalysts suggest that the active catalyst is VPP with domains of V^{5+} on the (100) face [33] The lack of selectivity of side faces found by Inumaru and coworkers [34, 35] is attributed to the difficulty of the re-oxidation to V^{5+} of these planes. Hutchings and coworkers propose a V^{4+}/V^{5+} couple, which can be present on the surface of a range of vanadium phosphate phases, as the active site [36]. The active phase is suggested to comprise a well dispersed micro-crystalline $VOPO_4$ on a VPP matrix. Centi and coworkers proposed that the reaction proceeds via a series of redox couples [37], the activation of butane requiring a V^{4+}–V^{3+} couple, while the subsequent conversion to maleic anhydride requires a V^{5+}–V^{4+} couple.

There has been speculation about the source of the V^{5+} in these two-phase systems. α_{II}-$VOPO_4$, γ-$VOPO_4$ and δ-$VOPO_4$ are commonly found in $(VO)_2P_2O_7$-based catalysts [38, 39]. More recently, ω'-$VOPO_4$ has been identified as a surface species [40–42] in the final active catalysts, especially those activated in slightly reducing conditions. Koyano and coworkers [43, 44] propose the X_1 phase as the V^{5+} source, although they admit this phase may be δ-$VOPO_4$. It should also be noted that a recent *in situ* X-ray Diffraction (XRD) study by Conte and coworkers [45] showed that metastable $VOPO_4$ phases can exist at the elevated temperatures of the catalytic process but that these can be undetectable in the final catalyst as they disorder into an amorphous material at room temperature.

Agaskar and coworkers [46] proposed that the catalyst surface contains clusters of four active dimeric sites that can each exist in one of four states. These states differ in the number of oxygen atoms associated with them and in the oxidation state of the vanadium ions present (Scheme 12.1). The V^{3+} site [$\mathbf{S_0}$] acts as an

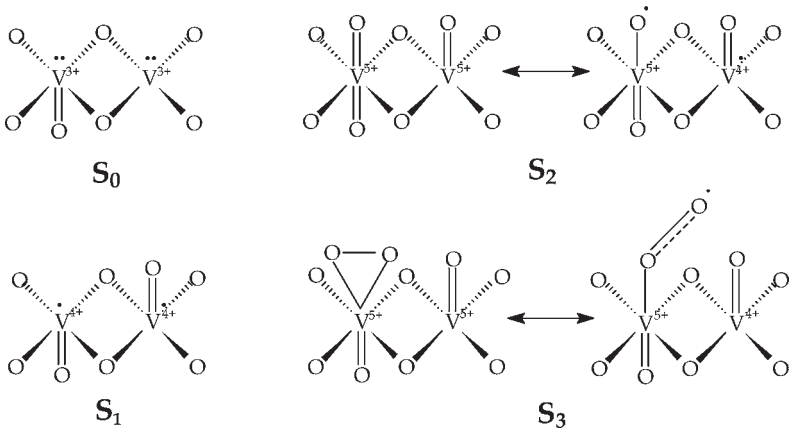

Scheme 12.1

oxygen acceptor. It can either react with gaseous oxygen to give [$\mathbf{S}_2$], or accept an oxygen atom from [$\mathbf{S}_2$] to give [$\mathbf{S}_1$]. The active site for the butane adsorption and reaction is thought to be one associated with two vanadyl groups ([$\mathbf{S}_2$] or [$\mathbf{S}_3$]). Rodemerck and coworkers [29] have investigated the importance of V^{3+} using TAP experiments. They propose that only V^{4+} and V^{5+} sites are important, and demonstrate that maleic anhydride was not formed on catalysts with an oxidation state below +3.96 [29]. However, this is the bulk oxidation state and so does not discount the possibility of isolated V^{3+} sites being present at the catalyst surface.

12.2.2
The Phosphorus-to-Vanadium Ratio of the Catalyst

Trifirò has proposed that the active catalyst is pure VPP and found that the catalyst had a slight increase in oxidation state after the equilibrium period [47]. The small increase from +4.00 to +4.03 was reproducible and attributed to isolated V^{5+} surface sites being formed. The P/V ratio is proposed to be a key factor in the stabilization of V^{4+} within the catalyst, as $VOPO_4$ formation becomes very difficult at P/V ratios above 2.0. Trifirò had stated that a very high surface P/V ratio is required for an active and selective catalyst, and experimentally has found surface P/V ratios of 10 : 1.

The P/V ratio was proposed by Ruiz and coworkers to be an important factor in determining the activity and selectivity of the catalyst [48]. They acknowledge that the majority of industrial catalysts have two or more different phases present, and suggest that the active catalyst is a mixture of two phases with different P/V ratios. By mixing a low P/V ratio catalyst and a high P/V ratio catalyst, they found a 5.7-fold increase in yield and a 3.8-fold increase in selectivity, compared to the sum of the individual phases. Ruiz suggests different roles for the two phases. The high P/V ratio phase acts as an oxygen acceptor, whereas the low P/V ratio phase acts as an oxygen donor. Experiments with Sb_2O_4 and $BiPO_4$, which are

known to be good oxygen donors, support this assignment of roles for the different phases. Ruiz found mechanical mixtures of a high P/V ratio catalyst with Sb_2O_4 and $BiPO_4$ gave a 6.0-fold increase in yield and a 5.4-fold increase in selectivity, over the standard $(VO)_2P_2O_7$ catalyst.

Garbassi and coworkers [49] observed that a P/V ratio of 1.05–1.1 is necessary for a high catalytic performance.

This slight excess of phosphorus is proposed to stabilize the V^{4+} phase, as V^{5+} is only detected in catalysts with a bulk P/V ratio less than 1.0. The findings of Garbassi and coworkers were confirmed by Hodnett and coworkers [50, 51] who suggested that a surface enrichment of phosphorus (P/V = 2.4) is the important factor for a selective catalyst. They propose that the excess surface phosphorus is responsible for the selectivity of the catalyst by isolating the V^{4+} active site on the surface.

Morishige and coworkers [52–54] found that although the industrial catalyst had a bulk P/V ratio of approximately 1.0, the surface had a high phosphorus concentration. Their studies showed that the surface P/V ratio was 1.6–1.8, when the bulk P/V ratio was 0.95–1.2. They suggested that a phosphorus-rich layer, supported on the surface of $(VO)_2P_2O_7$, is responsible for the oxidation of butane to maleic anhydride. For catalysts with a P/V ratio of between 1.0 and 2.0, Satsuma and coworkers also found catalytic improvements [55]. They proposed that at P/V ratios less than 1.0 a number of vanadium sites remain inactive but at higher P/V ratios all surface sites are active.

However, it should be noted that Coulston and coworkers [28] reported contradictory findings. In summary, they found that the surface P/V of a number of pure vanadium phosphate phases and activated catalysts are all closer to that of the bulk than has been previously reported, leading to the claim that phosphorus enrichment reported by other groups was based on incorrect calibration of XPS instrumentation.

12.2.3
The Role of Amorphous Material

There is considerable discussion in the literature as to whether amorphous material, commonly found in vanadium phosphate catalysts, plays a role in the catalysis of *n*-butane to maleic anhydride. Industrial catalysts undergo a lengthy activation process (often >1000 h) before they are equilibrated. During the activation, the crystallinity of the catalysts increases, leading some researchers to suggest that the more crystalline the catalyst, the better the performance [25]. Guliants and coworkers observed that although an amorphous surface layer was found to be present on fresh catalysts this disappeared on-line, leading to an increase in catalytic activity [56]. Most researchers consider that the (100) plane of crystalline VPP is the catalytically active plane, and the mechanisms that have been proposed use this as their active site [46, 57–69]. However, other researchers consider that an amorphous material supported on a $(VO)_2P_2O_7$ matrix plays an important role in catalysis.

As catalysts commonly contain both amorphous and crystalline material, it cannot be stated with any certainty whether or not the amorphous phase is catalytically active. However, experimental observations have added weight to the theory that amorphous material is the catalytically active phase in vanadium phosphate catalysts.

Research by Ruiz and coworkers [48] into high and low P/V ratio catalysts, led to the hypothesis that the active catalyst is made up of VPP in conjunction with an amorphous phase with a high oxidation state near +5.

Morishige and coworkers also suggested that the active catalyst is an amorphous phase with excess phosphorus on the surface of $(VO)_2P_2O_7$ [52]. Evidence was found by extracting the amorphous phase from the bulk. Catalytic testing yielded the same activity and selectivity as $(VO)_2P_2O_7$, suggesting that the amorphous phase is catalytically active. It has been proposed that the amorphous phase is phosphorus rich, accounting for the high surface P/V ratio that is commonly observed experimentally [28, 48, 50–52, 70].

In situ Raman spectroscopy has been carried out on precursors prepared in aqueous solution (referred to as VPA materials see Section 12.3.1), as they were converted to the active catalyst [38]. They found that during the activation, there is a structural disordering at 370 °C, which corresponds to the appearance of maleic anhydride. The disordering was found to occur at a lower temperature (300 °C), when maleic anhydride was added to the butane/air reaction mixture. This demonstrates that the presence of the products is important in controlling the structural transformations, and that a highly disordered structure can be important in selective butane oxidation.

Further evidence for the catalytic importance of amorphous material comes from experiments using cobalt-doped catalysts. Hutchings and coworkers found that doping the catalysts with cobalt improved their performance [36]. Additionally, Sajip and coworkers [71] found that the cobalt-promoted catalysts are far more disordered than the undoped catalysts. In the doped catalysts, the promoter is dispersed in the amorphous phase and cobalt is not found in the VPP crystals. It is thought that one of the properties of the cobalt promoter is the stabilization of the disordered phase and V^{5+} phases in the final catalysts, which leads to improved performance. This implies that the disordered material is the catalytically active vanadium phosphate phase.

Hutchings and coworkers [72–74] have prepared vanadium phosphate catalysts using supercritical precipitation methods. These materials were found to be amorphous by XRD and electron diffraction, but showed activity comparable to standard vanadium phosphate catalysts. This demonstrates that an amorphous surface layer can be the active phase in these catalysts and that the crystalline VPP that has been so well studied may be nothing more than an elaborate support.

However, Schimoda and coworkers [75] and others [6, 76] have dismissed the V^{4+} amorphous phases prepared from the precursor $VO(H_2PO_4)_2$ as less selective than the crystalline $(VO)_2P_2O_7$ catalyst.

12.2.4
The Disordered Plane

The selective oxidation of *n*-butane and 1-butene on vanadium phosphate catalysts prepared via different routes was investigated by Cavani and coworkers [77] Precursors prepared in aqueous medium were found to have greater crystallinity than those prepared in organic solvents (the activity and selectivity of which was the same for 1-butene oxidation). However, for butane activation, the crystalline catalyst was considerably less active than the organically prepared catalyst, which had an XRD pattern showing some disorder in the (100) plane.

It has been suggested that organic compounds occluded between the vanadium phosphate layers cause this disorder [78]. The disorder may be derived from a number of structural modifications: a missing oxygen atom, an inversion from a *trans*- to a *cis*- vanadyl position, or from the modification of the V—O bond strength. It is proposed that these defects can all cause the creation of new active centers for butane activation. Furthermore, Cornaglia and coworkers [79] also report an increase in selectivity to maleic anhydride as the disorder in the (100) plane decreases.

The opposite effect has been reported for a series of organically prepared catalysts [25]. The catalytic performance to maleic anhydride was found to improve with the increase of crystallinity of VPP. A number of studies on catalysts that have been on-line for several hundred hours have provided supporting evidence that crystalline compounds are the most active and selective [79, 80].

12.2.5
Acid–Base Properties

Some research groups consider the acidity of the catalysts to be an important aspect in controlling the catalyst performance. An infrared study of the acid sites using NH_3, pyridine and acetonitrile as probe molecules showed the existence of Lewis and Brønsted acid sites [24, 65, 79, 81–83]. A correlation was observed between the selectivity to maleic anhydride and the number of strong Lewis acid sites. It has been suggested that hydrogen abstraction occurs on Lewis acid sites (V^{4+}), and that butane C—H bond cleavage results from interactions between Lewis acid sites and Brønsted acid sites (P—OH) [83].

Centi and coworkers [84] have suggested that, in addition to Lewis acidity, Brønsted acidity plays an important role in the selective oxidation of butane to maleic anhydride. The surface phosphorus enrichment means that a number of P—OH groups are present on the catalyst surface. Centi offers three hypotheses for the role of Brønsted acidity: the stabilization of reaction intermediates, the stabilization of an adsorbed oxygen species, or the generation of an organic surface species that is involved in oxygen activation or transport.

Ai measured the acid site concentration by the adsorption of ammonia [85]. No correlation was found between the P/V ratio, the acidity and the catalytic activity.

This has been attributed to the use of ammonia as a probe molecule, since this cannot distinguish between Lewis and Brønsted acidity. Cornaglia and coworkers [79] measured the acid sites using pyridine and acetonitrile. However, the pyridine results showed no correlation between the activity and selectivity to maleic anhydride and either the Lewis-to-Brønsted acid sites ratio (L/B acidity ratio) or the Lewis acid site concentration.

Adsorption of acetonitrile enabled the strength of the Lewis sites to be measured and a greater number of strong Lewis sites were found to be present in organically made catalysts than in those prepared in an aqueous medium. Thus, the greater the concentration of strong Lewis acid sites in the catalyst, the higher the maleic anhydride yield. Cornaglia and coworkers suggest that the strong Lewis sites are responsible for butane dehydrogenation.

12.3 Preparation of VPP Precursors

Vanadium phosphate catalysts are obtained by activating the catalyst precursor in the reaction feedstock. After pre-treatment, the catalyst is equilibrated and catalytic activity remains consistent throughout the lifetime of the catalyst. The activated catalysts are formed topotactically from the precursors [86]. For this reason, a great deal of research is based around the preparation of catalyst precursors with well defined, favorable morphologies.

$VOHPO_4 \cdot ½H_2O$ (Figure 12.4) is the catalytic precursor for $(VO)_2P_2O_7$. A number of preparation methods are commonly used to prepare $VOHPO_4 \cdot ½H_2O$. These usually involve reacting V_2O_5 and H_3PO_4 in the presence of a reducing agent.

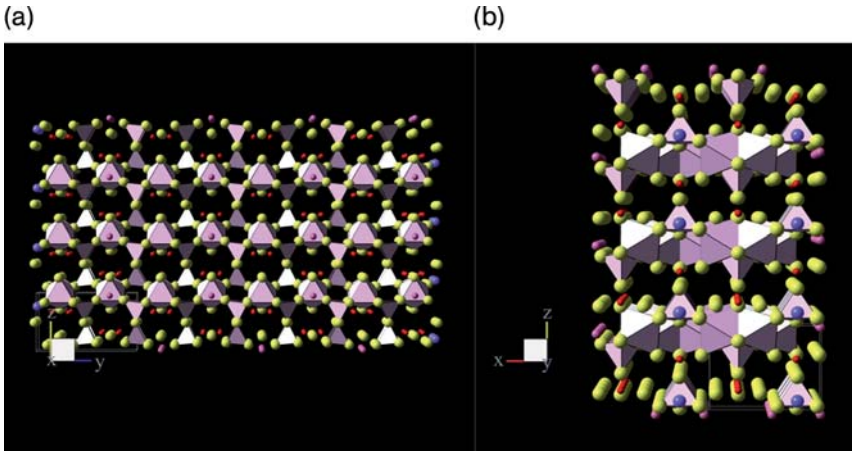

Figure 12.4 Schematic diagram showing the layered structure of hemihydrate precursors in the (a) (100) and (b) (010) directions (both orthogonal to the (001) layer normal direction) [87].

Originally, catalyst precursors were prepared in aqueous media, most commonly using hydrochloric acid as the reducing agent [80, 88–91]. This is commonly referred to as the VPA route:

$$V_2O_5 + HCl \xrightarrow[2.\ H_3PO_4]{1.\ \Delta,\ 2h} VOHPO_4{\cdot}\tfrac{1}{2}H_2O \qquad (12.2)$$

Alternative aqueous routes have been used by a number of groups to prepare $VOHPO_4 \cdot \frac{1}{2}H_2O$. Oxalic acid [88, 92], lactic acid [93], phosphorous acid [93] and $NH_2OH.HCl$ [75] have all been investigated as reducing agents in place of hydrochloric acid.

There has also been investigation into alternative vanadium sources. Poli and coworkers [88, 92] used NH_4VO_3 as the vanadium source in conjunction with H_3PO_4 and oxalic acid, and Harouch Batis and coworkers [91] used a VCl_3/V_2O_5 mixture instead of vanadium pentoxide. Mizuno and coworkers [95] reported a

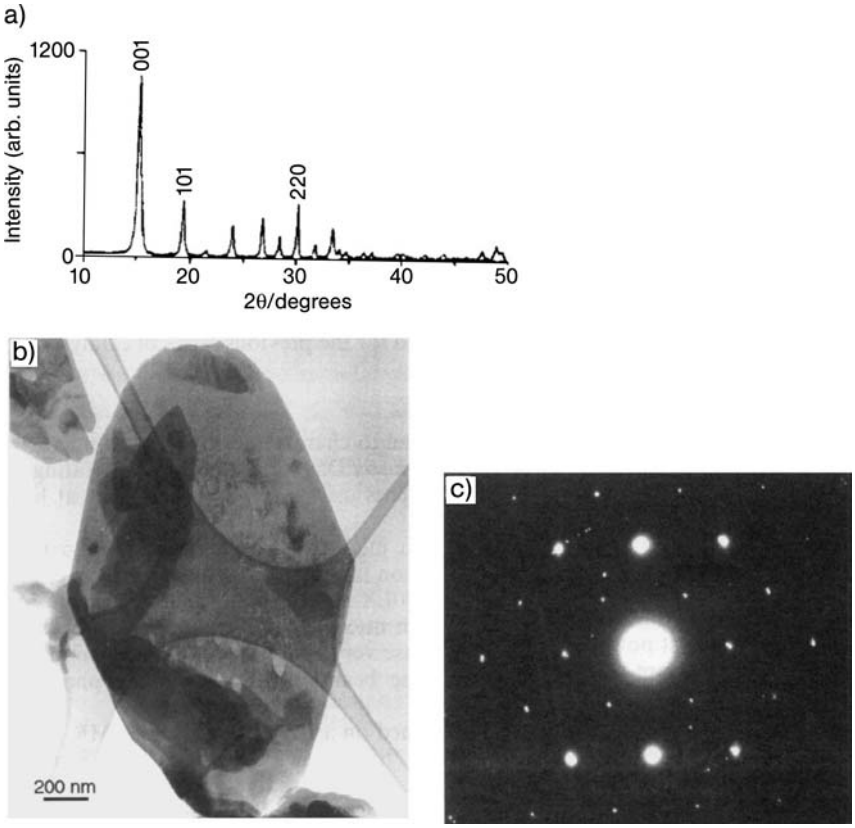

Figure 12.5 (a) XRD pattern, (b) bright-field image and (c) selected area diffraction pattern from the hemihydrate precursor material [94]. (Reproduced with permission).

preparative route using vanadium metal to reduce vanadium pentoxide. They heated a mixture of phosphoric acid, cetyltrimethylammonium chloride, vanadium and vanadium pentoxide in an autoclave, at 200 °C for 48 h. Schimoda and coworkers [75] have also reported the direct reaction of V_2O_4 and H_3PO_4.

In the 1970s, catalyst precursors prepared in organic media became increasingly popular. The most common route (the VPO route, Figure 12.5), is a one-pot method using alcohol as both the solvent and the reducing agent:

$$V_2O_5 + H_3PO_4 + \text{alcohol} \xrightarrow{\Delta,\ 16h} VOHPO_4{\cdot}\tfrac{1}{2}H_2O \qquad (12.3)$$

A number of alcohols have been used in this preparation, isobutanol being the most common [96]. Another common organic route uses a mixture of isobutanol and benzyl alcohol. V_2O_5 is refluxed in the alcohol for an hour before H_3PO_4 is added, and the mixture refluxed for a further hour [96, 97].

Johnson and coworkers [86] described a method for the preparation of $VOHPO_4 \cdot \frac{1}{2}H_2O$ by reduction of $VOPO_4 \cdot 2H_2O$ with alcohol. This is known as the VPD route. This route was investigated more fully by Horowitz and coworkers [98] for short-chain alcohols, and Ellison and coworkers [99, 100] for longer chain alcohols. $VOPO_4 \cdot 2H_2O$ is prepared by heating an aqueous solution of V_2O_5 and H_3PO_4 under reflux conditions for 16 h. This is then reduced with alcohol to yield $VOHPO_4 \cdot \frac{1}{2}H_2O$:

$$V_2O_5 + H_3PO_4 \xrightarrow[\Delta,\ 16h]{H_2O} VOPO_4{\cdot}2H_2O \xrightarrow[\Delta,\ 16h]{\text{alcohol}} VOHPO_4{\cdot}\tfrac{1}{2}H_2O \qquad (12.4)$$

Alternative vanadium sources have been investigated using organic solvents. Doi and Miyake [101, 102] used V_4O_9 as the vanadium source. V_2O_5 was initially reduced to V_4O_9 by isobutanol. The V_4O_9 was then reacted with H_3PO_4 with a range of alcohols as the solvent. As with their aqueous preparations Harouch Batis and coworkers [91] used a VCl_3/V_2O_5 mixture instead of vanadium pentoxide.

Guilhaume and coworkers [103] investigated the effect of the reactant V_2O_5 morphology on the morphology of the final catalysts. They found a correlation between the size of the V_2O_5 grains and the preferentially exposed planes of $(VO)_2P_2O_7$. This study was only carried out on a few V_2O_5 samples, and further research on this aspect of the preparation is needed.

Investigations comparing organically and aqueously prepared $VOHPO_4 \cdot \frac{1}{2}H_2O$, found that the final catalysts had very similar specific activities [89, 91] However, the organic preparation routes tend to give precursors with a higher surface area than those prepared in aqueous solution. As the morphology of the precursor is retained in the active catalyst, the organically prepared catalysts show the better catalytic performance (Figure 12.6).

Hutchings and coworkers [89] investigated VPA, VPO and VPD catalysts, prepared with a range of alcohols (Figure 12.7). VPA catalysts were found to have a cubic morphology and a low surface area and VPO catalysts were found to have a platelet morphology. However, VPD catalysts prepared with primary alcohols gave a high surface area catalyst with a rosette structure, characterized by an X-ray dif-

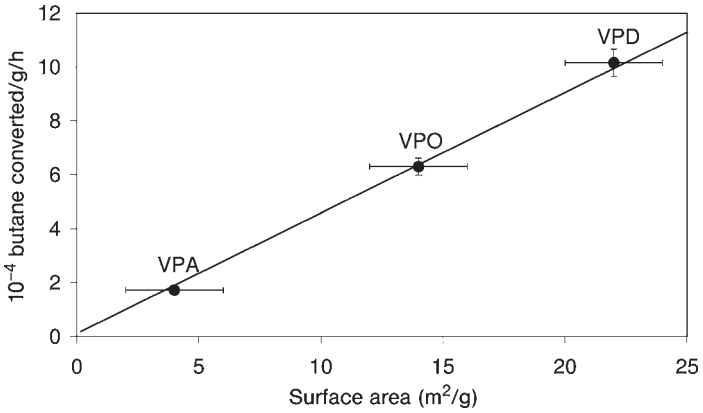

Figure 12.6 Relationship between catalyst activity and surface area for standard vanadium phosphate catalysts for the oxidation of *n*-butane [89]. (Reproduced with permission).

fraction pattern with only one peak corresponding to the (220) reflection. VPD catalysts prepared with secondary alcohols had a similar morphology and surface area to VPO catalysts and have a characteristic X-ray diffraction pattern containing many peaks, with the (001) reflection as the dominant feature. The catalysts with rosette morphology were found to have a considerably higher activity than the platelets. This is probably due to the increased surface area, as all the $VOHPO_4 \cdot ½H_2O$ catalysts are reported to have similar specific activities (the activity to maleic anhydride per unit area).

Horowitz and coworkers [98] investigated a range of preparations in organic solvents. They reported the rosette structure for catalysts prepared by a VPD method with isobutanol and straight-chain alcohols, as well as a VPO type preparation using a 1 : 10 mixture of benzyl alcohol and isobutanol or 1-butanol. This study found that the platelet catalysts were more selective than the rosettes. They suggest this is due to the rosette structure obscuring the active plane. The greater selectivity of thick platelets has been confirmed by other researchers [26].

Okuhara and coworkers [104–110] have modified the preparations using intercalated and exfoliated $VOPO_4 \cdot 2H_2O$. Using this technique, intercalating compounds such as amines, amides, alcohols or carboxylic acids can replace the water between the vanadium phosphate layers. These materials can then be delaminated in a polar organic solvent and the exfoliated $VOPO_4$ reduced to give V^{4+} vanadium phosphates with unusual morphologies. It is thought that this process can occur in an alcohol, which leads to the formation of the rosette structures found by reduction of $VOPO_4 \cdot 2H_2O$ with a primary alcohol [106].

The crystallization of $VOHPO_4 \cdot ½H_2O$ from V_2O_5 and H_3PO_4 has been studied in detail by O'Mahony and coworkers [111, 112] using time-resolved X-ray diffraction. They found that an intermediate phase was formed initially but this then disappeared as $VOHPO_4 \cdot ½H_2O$ was detected. Concurrent focused ion beam

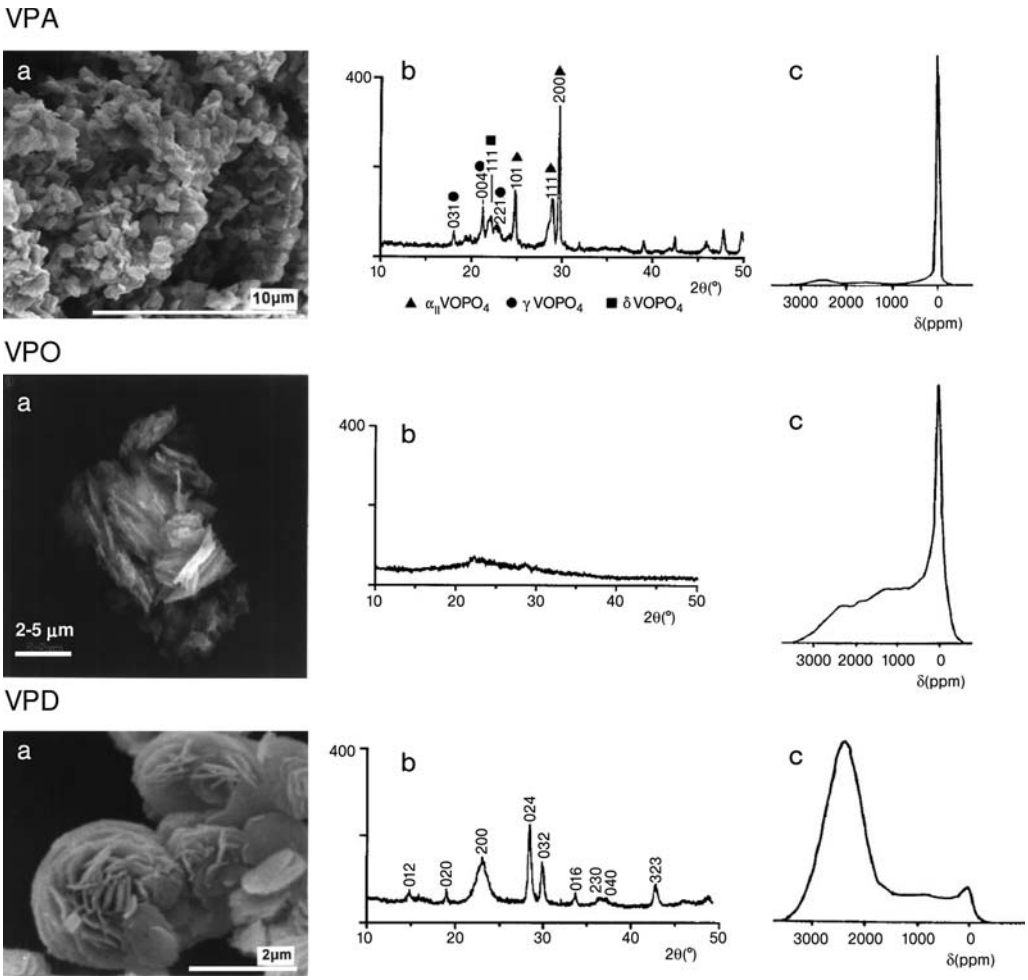

Figure 12.7 (a) An SEM micrograph, (b) an XRD pattern, (c) ^{31}P NMR spin echo mapping spectrum from: activated VPA, activated VPO, and activated VPD [5]. (Reproduced with permission).

microscopy showed rosette structures forming from delaminated plates as the reaction proceeded (Figure 12.8).

A number of groups have also studied $VO(H_2PO_4)_2$ as a catalyst precursor [113–118]. Mount and Raffleson [119] prepared $VO(H_2PO_4)_2$ by heating V_2O_5 and H_3PO_4 with H_3PO_3 in an autoclave at 150 °C. They found this material decomposed at 360 °C to yield $VO(PO_3)_2$. Hannour and coworkers [120–122] prepared $VO(H_2PO_4)_2$ by heating an aqueous solution of V_2O_5, H_3PO_4 and oxalic acid. This was calcined in air to give β-$VO(PO_3)_2$. They also prepared α-$VO(PO_3)_2$ by heating V_2O_5 in a large excess of H_3PO_4. Both of these catalysts were poorly selective to maleic anhydride, with carbon oxides being the major products.

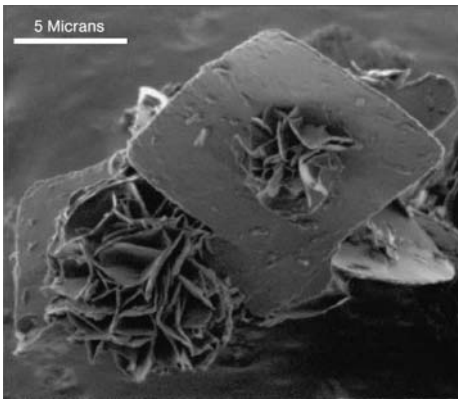

Figure 12.8 A focused ion beam image of the samples recovered 2 min after reaction of V_2O_5 and H_3PO_4 in alcohol. Rosette-shaped hemihydrate particles appear to grow out from the basal plane of the platelets [112]. (Reproduced with permission).

This is consistent with previous studies that have shown $VO(PO_3)_2$ is not as catalytically active as $(VO)_2P_2O_7$. Hutchings and Higgins [123] found beneficial results by removing $VO(H_2PO_4)_2$ by solvent extraction, from the $VOHPO_4 \cdot ½H_2O$. This yielded a higher surface area precursor and a more active catalyst after activation. Most $VOHPO_4 \cdot ½H_2O$ preparations include boiling in water as a final step to remove water soluble impurities.

12.3.1
The Preparation of Novel Vanadium Phosphates

Bordes and Courtine [124] prepared a number of precursors that required calcination in air, oxygen or nitrogen to give the final catalyst. $NH_4(VO_2)_2PO_4$, $(NH_4)_2[(VO_2)_2C_2O_4(HPO_4)_2] \cdot 5H_2O$ and NH_4HVPO_6 gave final catalysts mainly comprising $(VO)_2P_2O_7$, $VO(PO_3)_2$ or $V(PO_3)_3$, depending on the activation conditions.

The synthesis of new vanadium phosphate precursors as reported by Benziger and coworkers [125] consisted of intercalated *n*-alkyl amine pillars inserted between the layers of $VOHPO_4 \cdot ½H_2O$. The $(VO)_2P_2O_7$ catalysts derived from these precursors show an increase in selectivity which is attributed to stacking faults created by the pillars. Vanadyl phosphonates with the formula $VOC_nH_{2n+1}PO_3 \cdot xH_2O$, ($n = 0$ to 4, $x = 1$ or 5) were also synthesized. These could be converted into $(VO)_2P_2O_7$ at considerably lower temperatures than $VOHPO_4 \cdot ½H_2O$ and produced catalysts with higher surface areas and increased yields of maleic anhydride.

The gas-phase synthesis of $VOPO_4 \cdot 2H_2O$ has been reported [126]. A gas stream of $VOCl_3$, $POCl_3$ and H_2O with N_2 as carrier, was passed through a furnace where the powdered $VOPO_4 \cdot 2H_2O$ was collected. This was converted to α- and β-$VOPO_4$ by calcination in nitrogen, before *in situ* activation gave the $(VO)_2P_2O_7$ catalyst.

Michalakos and coworkers [127] prepared vanadium phosphate catalysts using an aerosol process. The aerosol was created with aqueous solutions of NH_4VO_3 and H_3PO_4 (with air as the carrier) and sprayed into a furnace. The solid was collected at the reactor exit on a cooled filter. The compound was found to be $VOPO_4 \cdot nH_2O$ which was converted to α_I-$VOPO_4$ with a small amount of $VO(H_2PO_4)_2$ by calcining. The catalyst was found to be more active than VPA catalysts, despite having a lower surface area.

A number of groups have prepared vanadium phosphate catalysts using hydrothermal synthesis [92, 93, 128–130]. Using standard reaction mixtures, Dong and coworkers [128] showed that at elevated temperatures and pressures different materials are synthesized from those obtained under reflux conditions. Pressure did not seem to affect the product formed, but as the temperature increased to >200 °C further reductions occurred and V^{3+} products formed. However, these materials were not found to have enhanced catalytic activity compared to traditionally prepared materials. At lower temperatures, hydrothermal syntheses have produced catalysts with comparable activity to those prepared under standard conditions [92, 93, 129, 130]. Taufiq-Yap and coworkers [129] found an enhancement in activity for hydrothermally prepared catalysts and suggested this was due to a modification in the redox behavior of the catalysts evidenced by TPO/TPR experiments.

Hydrothermal syntheses have also been used to prepare new porous materials. Doi and Miyake [131] obtained a mesoporous vanadium phosphate compound by intercalating a surfactant (*n*-tetradecyltrimethyl ammonium chloride) between the layers of $VOHPO_4 \cdot ½H_2O$. Furthermore, Bu and coworkers [132] have also reported a new mesoporous vanadium phosphate compound synthesized with an organic template molecule. $NaVO_3$, V, H_3PO_4, H_2O and the template piperazine were mixed in a molar ratio of 1.0 : 0.5 : 5.17 : 476 : 0.71. A dark blue gel was formed after 15 minutes stirring, and the mixture was then heated at 170 °C for seven days in an autoclave. Light blue, needle-like crystals were observed and then recovered by filtration. The catalytic activity of these mesoporous vanadium phosphates have not been reported.

12.4 Activation of the Catalyst Precursors

Research into the activation of precursors falls into two categories: the study of structural and morphological changes during the activation period, and the effect of different activation methods on the final catalytic behavior.

12.4.1 Activation Procedures

The catalyst precursor $VOHPO_4 \cdot ½H_2O$ must be activated to the $(VO)_2P_2O_7$ catalyst. This is usually done *in situ* with the reaction feedstock of 1.5% butane in air.

Table 12.1 Influence of activation conditions on unpromoted V—P—O catalysts [135].

Entry	Activation atmosphere	Temp (°C)	Time (h)	MA_{selc} @400 °C (%)	Conv @400 °C (%)	Ref.
1	1% Bu/Air	380	100	50	20	[133]
2	1% Bu/Air	380	1000	80	20	[133]
3	O_2[a)]	500	1	84	ca. 12	[134]
4	30% O_2 in N_2	400	3	62.3	98.2	[135]

a Sample heated in N2 (750 °C, 72 h) then heated in O_2.

A number of pre-treatments have been claimed to speed up the activation process. These can involve heating the catalyst in an inert atmosphere, a reducing environment or an oxidizing environment (Table 12.1).

The effects of standard activation procedures (adopted by industry) and fast activation procedures (often reported in the literature) have been investigated by Lombardo and coworkers [80]. In the standard activation procedure, the catalyst was heated in air up to reaction temperature, followed by introduction of the butane in three steps, up to 1.5%. The gas hourly space velocity (GHSV) was increased in four steps to 2500 h^{-1}. This procedure could take up to 380 hours.

In the fast activation procedure the catalyst was heated under 1.0% butane in air up to reaction temperature, at a GHSV of 900 h^{-1}. This was held for 3 h before the butane concentration was increased to 1.5% and the GHSV to 2500 h^{-1}. Lombardo and coworkers found that the standard activation procedure gave final catalysts that were more crystalline, had less V^{5+} phases present and were far more active than the fast activated catalysts.

Albonetti and coworkers [133] have compared equilibrated and non-equilibrated catalysts. Non-equilibrated catalysts, which had only been on-line for 100 hours, were found to be poorly crystalline, with an oxidation state of +4.36 and a surface area of 11 $m^2 g^{-1}$. The equilibrated catalysts that had been on-line for 1000 hours were more crystalline, had an increased surface area (23 $m^2 g^{-1}$), and an oxidation state of +4.00. The equilibrated catalyst was found to be considerably more active and selective than the non-equilibrated catalyst.

The effect of oxidation pre-treatments on the catalyst have been investigated by Aït-Lachgar and coworkers [134]. Pure VPP catalysts were obtained by heating $VOHPO_4 \cdot ½H_2O$ in a flow of N_2 at 750 °C for 72 h. This was then oxidized in a flow of O_2 for between 0.5 and 24 h. The catalyst oxidized for 1 h showed the highest selectivity to maleic anhydride, although all the pre-treated catalysts were more selective than pure $(VO)_2P_2O_7$. This is thought to be due to the introduction of V^{5+} phases. Previous studies have found V^{5+} to be detrimental to catalysts, many researchers suggesting they may be responsible for the total oxidation of butane [22–24, 80, 133].

Cheng and Wang [135] have studied the effect of calcining catalysts in air, N_2 and CO_2. $VOHPO_4 \cdot ½H_2O$ could be converted into an amorphous V^{5+} phase,

crystalline $VOPO_4$ or $(VO)_2P_2O_7$ with varying crystallinity, depending on the calcining temperature and atmosphere. The calcining environment that resulted in the best catalyst was different for promoted and unpromoted catalysts, depending on how easily they were oxidized. It was found that for unpromoted $VOHPO_4 \cdot ½H_2O$ the best environment was 30% O_2 in N_2. This gave a catalyst that was composed of dispersed V^{5+} species on a $(VO)_2P_2O_7$ matrix.

The addition of water to the reaction feed was investigated [136]. This led to two significant effects being noted. The selectivity to maleic anhydride increased (with increased yields of acetic and acrylic acids). There was also an increase in the surface area of the catalysts activated with the *n*-butane/water/air feed compared to the dry activated catalyst. Arnold and Sundaresan excluded the possibility of the water vapor acting as a diluent by performing experiments with an *n*-butane/N_2/air feed. Instead they proposed that water is adsorbed onto the surface, blocking sites that are responsible for over-oxidation of the products.

Contractor and coworkers [137] confirmed the effects of water vapor in the gas feed, using a riser reactor. They proposed that the water and oxygen are in direct competition for catalytic sites. Adsorbed water decreases the amount of activated oxygen available, which decreases the activity, but prevents over-oxidation, which in turn increases the selectivity. It is suggested that lattice oxygen is responsible for the selective oxygen, while adsorbed or gaseous oxygen (which is inhibited by the steam) forms the total oxidation products. Furthermore, Vedrine and coworkers [138] proposed that water plays an important role in maintaining a hydrated catalyst surface, which allows a redox mechanism to occur easily.

Centi and Perathoner [139] have discussed the benefits of small amounts of sulfur dioxide in the reaction feed. The SO_2 is thought to adsorb on the surface to form stable $VOSO_4$, blocking the redox activity of surface V^{5+} sites (considered to be responsible for over-oxidation). This results in an increase in selectivity to maleic anhydride, particularly at high conversions.

Recently a very detailed study of activation conditions was carried out by Patience and coworkers [140]. A number of parameters were investigated including temperature, pressure, time and gas-phase composition with respect to O_2 and H_2O. They found that standard conditions (390 °C and atmospheric pressure) gave the best performance although the activation time could be shortened by increasing the pressure. Water had a deleterious effect on the catalyst even at low concentrations and this was proposed to be due to an increase in the V^{5+} observed.

Mechanochemistry has been proposed as an activation method [141–146]. This involves milling the catalyst precursor in a solvent, usually ethanol, prior to its conversion to the active catalyst. Experiments have shown that this procedure promotes the exposure of the (100) plane in the catalyst, which is considered to be the active crystal face [141–143, 146], and can reduce the particle size thus increasing the surface area [141, 144–146]. Experiments with promoters show that this procedure gives more active and selective catalysts than those prepared by either chemical means or mechanical mixing [93, 141, 146].

12.4.2
Structural Transformations during Activation

The importance of precursor morphology in determining catalyst performance was reported by Johnson and coworkers [86]. This is due to the topotactic transformation (Figure 12.3), so the $(VO)_2P_2O_7$ catalyst retains the morphology of the $VOHPO_4 \cdot ½H_2O$ precursor. Insight into how the transformation occurs can help in the design of pre-treatments and activation procedures that will produce catalysts with improved properties.

Kiely and coworkers [94] investigated the differences in activated catalysts which were obtained from $VOHPO_4 \cdot ½H_2O$ precursors prepared via VPA, VPO and VPD routes. The VPA catalyst XRD pattern shows a mixture of $VOPO_4$ phases, with $(VO)_2P_2O_7$ present as a minority phase, and there is a weak V^{4+} peak seen in the ^{31}P NMR spin echo mapping spectrum. TEM revealed α_{II}-$VOPO_4$, δ-$VOPO_4$, $(VO)_2P_2O_7$ and some amorphous material (Figure 12.9). The $(VO)_2P_2O_7$ widely considered to be the active phase constituted only 10% of the catalyst.

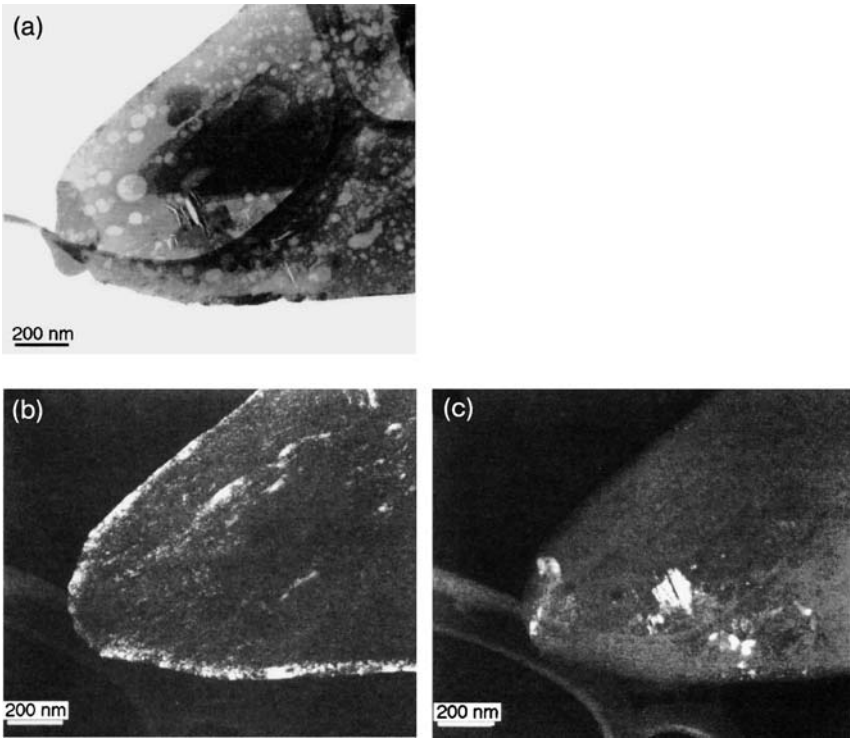

Figure 12.9 Bright-field image showing a typical platelet from the VPO-0.1 sample. Corresponding dark-field micrographs taken in (b) the $\boldsymbol{g}^{pyro}$ = (024) reflection of $(VO)_2P_2O_7$ and (c) the $\boldsymbol{g}^{delta}$ = (022) reflection of δ-$VOPO_4$ ($\boldsymbol{g}$ = diffraction vector) [94]. (Reproduced with permission).

No crystalline phases were detected in the VPO catalyst using XRD. The ^{31}P NMR spin echo mapping spectrum showed two peaks that were assigned to disorganized and crystalline $(VO)_2P_2O_7$. TEM showed large plates, proposed to be amorphous material with small rectangular crystals of $(VO)_2P_2O_7$, preferentially exposing the (100), (021) and (012) planes. About 20% of the sample was composed of δ-$VOPO_4$ plates containing cracks, which may be formed by the initial loss of water from $VOHPO_4 \cdot ½H_2O$.

The VPD catalyst appears more crystalline than the VPO catalyst. XRD and ^{31}P NMR both show crystalline $(VO)_2P_2O_7$, with a small amount of $VOPO_4$ and disorganized $(VO)_2P_2O_7$ also visible in the spin echo mapping spectrum. The TEM study shows the characteristic rosettes make up 95% of the catalyst, with a few flat platelets. Diffraction patterns showed the rosettes to be made up of $(VO)_2P_2O_7$ (100) planes, while the flat plates can be indexed to α_{II}-$VOPO_4$.

It is clear that the method of preparation, as well as the activation procedure, can have an effect on the structure of the active catalyst. This must be taken into account when comparing activation procedures carried out on catalyst precursors prepared by different means.

Research has been carried out to investigate the changes observed during the activation process. This takes the form of heating a catalyst precursor up to the reaction temperature in an *n*-butane/air feedstock, and leaving it on-line for varying times (the standard times that have been adopted are 0.1 hour, 8 hours, 84 hours and 132 hours). The samples are then taken off-line and characterized as fully as possible.

Abon and coworkers [32] report that during the activation period the catalyst goes through a number of changes. Initially, $VOHPO_4 \cdot ½H_2O$ is transformed into poorly crystalline $(VO)_2P_2O_7$ and δ-$VOPO_4$. The initial δ-$VOPO_4$ is transformed into α_{II}-$VOPO_4$ and $(VO)_2P_2O_7$, which become more crystalline with time on-line. The increase in crystallinity and surface area are proposed to be responsible for the increase in activity observed. A decrease in V^{5+} phases (responsible for total oxidation) is observed with activation time, which accounts for the increase in selectivity to maleic anhydride.

Additionally, a similar study was conducted by Kiely and coworkers [94] on VPO catalysts. Prior to activation, rhomboidal plates of the precursor $VOHPO_4 \cdot ½H_2O$ were observed by TEM. As the sample is heated in the reaction feedstock, cracks are formed in the plates, due to the loss of water of crystallization (0.1 hour) (Figure 12.10a). Even after a short time on-line $(VO)_2P_2O_7$ and δ-$VOPO_4$ are seen in the diffraction pattern. The δ-$VOPO_4$ and $VOHPO_4 \cdot ½H_2O$ phases gradually diminish with time, until they can no longer be observed in the 132 hour sample (Figure 12.10d).

As the activation proceeds, a crystalline rim starts to form around the edge of the plate, while in the center of the plate a more disordered phase is formed, with dispersed crystals of δ-$VOPO_4$ (8 hours) (Figure 12.10b). After 84 hours the rim (made up of small oblong crystallites of $(VO)_2P_2O_7$) has thickened and large holes start to appear in the center of the plates (Figure 12.10c). After 132 hours the inside of the platelet has also become more crystalline $(VO)_2P_2O_7$ (Figure 12.10d).

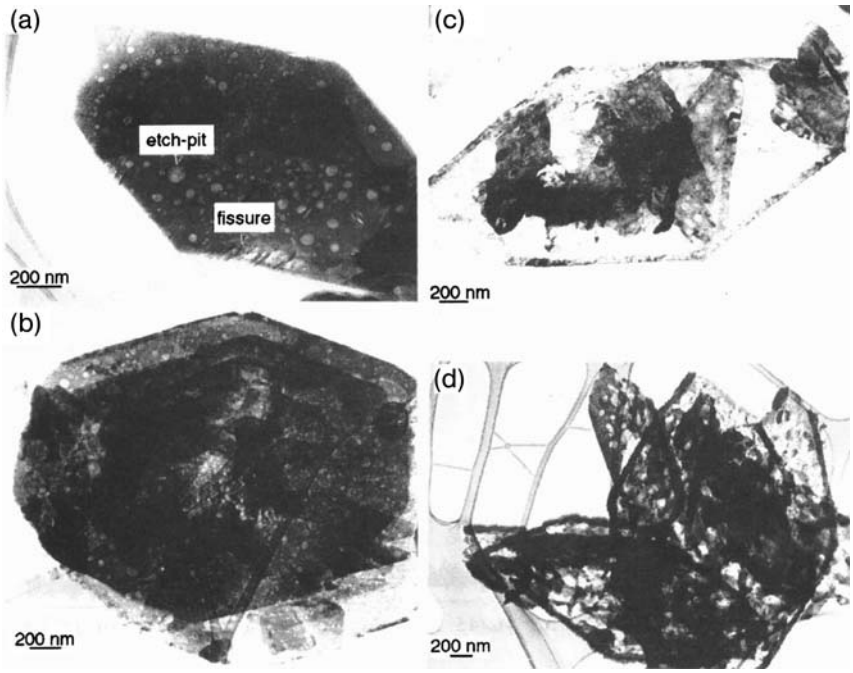

Figure 12.10 Bright-field transmission electron micrographs of platelet morphologies in (a) VPO-0.1, (b) VPO-8, (c) VPO-84 and (d) VPO-132 activated catalysts [94]. (Reproduced with permission).

12.5
Promoted Catalysts

Industrial catalysts for oxidation reactions rarely use a single bulk phase. A number of promoter elements are added that can act purely as textural promoters, or enhance the activity and selectivity of the bulk catalyst. The role of promoters on vanadium phosphate catalysts has been addressed mainly in the patent literature and Hutchings [147] has provided an extensive review of these patents.

A number of groups have tested a wide range of promoter elements and compounds. Hutchings and Higgins [148] found that chromium, niobium, palladium, antimony, ruthenium, thorium, zinc and zirconium had very little effect on the specific activity of $(VO)_2P_2O_7$. A significant increase in surface area was observed with zirconium, zinc and chromium, which could be of use as structural promoters. Iron-, cesium- and silver-doped catalysts showed a decrease in the specific activity, while cobalt and molybdenum were the only promoters found to increase the specific activity.

The selectivity decreased for catalysts doped with cesium, palladium, ruthenium, zinc and zirconium. This was thought to be due to these metals promoting the over-oxidation of maleic anhydride to carbon oxides. However, molybdenum

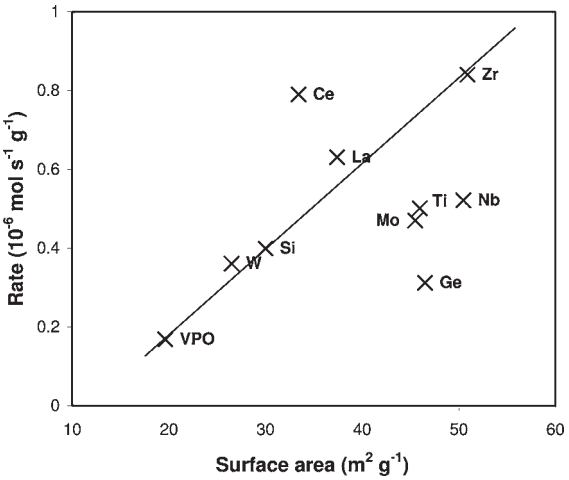

Figure 12.11 Plot of the activity against surface area for a number of promoted catalysts [155]. (Reproduced with permission).

was found to poison the over-oxidation reaction. From this work Hutchings and Higgins concluded that only cobalt and molybdenum act as promoters. Other elements reported as promoters are only responsible for an increase in surface area of $(VO)_2P_2O_7$.

Ye and coworkers [149–154] tested a large number of promoter elements and found the activity to maleic anhydride changes in the order:

$$Zr > Ce > La > Fe > Co > Cu > Nb > Ti > Mo > Ca > Si > W > Ni > Ge > K$$

However, the activity reported by Ye and coworkers is not the specific activity, and the surface areas of the promoted catalysts show a large variation (26.3 to 50.8 $m^2 g^{-1}$). Hutchings [155] has plotted (Figure 12.11) the activity against the surface area for a number of promoted catalysts and deduced that most of the catalysts conform to a linear correlation. The only enhancement of the specific activity was given by the Ce-promoted catalyst. This shows that care must be taken in the interpretation of results, particularly when catalysts prepared by different methods are compared. A review of the promoter literature revealed that Ce, Co, Cr, Cu, Fe, Hf, La, Mo, Nb, Ni, Ti and Zr are commonly reported to enhance the activity [155]. These cations are suggested to form solid solutions, $[(VO)_xM_{1-x}]_2P_2O_7$ (where M is a promoter cation). The inclusion of cations of different size or charge in the VPP lattice is likely to cause defects, which could then function as active sites for butane oxidation. In this section we shall discuss the common promoter elements that have been shown to give an increase in activity compared to undoped catalysts.

A number of other groups have also found that zirconium enhances the activity of vanadium phosphate catalysts [11, 56, 146, 148, 150, 154, 156–163]. Zeyss and coworkers [158] investigated catalysts doped with 5 to 15% zirconium. Unlike the

observations of Hutchings and Higgins [148], the zirconium was not incorporated into the $(VO)_2P_2O_7$ lattice, but was found in an amorphous phase, which is proposed to be the catalytically active phase. This is probably the reason that zirconium was not found to increase the surface area as Ye and coworkers [153] observed. Zeyss suggested that the zirconium influences the amount of $VOPO_4$ phases formed during the activation of the catalyst and that these are the cause of the increased activity. The positive or negative effect of $VOPO_4$ in the active catalyst is the subject of considerable discussion (see Section 12.2), so this explanation of the promotional effect of zirconium is quite controversial. Sant and Varma [164] also studied the role of zirconium as a promoter. They found that low concentrations of zirconium lowered the temperature required to reach the maximum yield. Various reasons for this observation have been put forward. The increase in surface area and the increase in oxygen transport rates can be sufficiently altered by the zirconium to result in high yields of maleic anhydride at lower temperatures. The roles of zirconium, zinc and titanium have been studied as catalytic and structural promoters [156]. The results showed that all these promoters had a significant effect, if added in the correct proportion. Confirming previous findings, 1.5% zirconium had the most beneficial effect on the activity; good catalytic performance could be achieved at lower temperatures.

It is proposed that zirconium and titanium both create acidic surface sites on the vanadium phosphate surface. This prevents the desorption of reaction intermediates (butene, butadiene and furan), while facilitating the desorption of the acidic maleic anhydride. A large amount of zinc promoter resulted in a loss of surface acidity, leading to over-oxidation of strongly adsorbed maleic anhydride. However, a small addition of 0.6% zinc enhanced the catalyst performance by creating basic sites, which increase the rate of butane activation. At low zinc concentrations the slight loss in surface acidity does not have a great effect. Takita and coworkers [157, 165] studied the effects of zinc oxide on the catalyst. They found an increase in catalytic performance that was ascribed to the increased rate of re-oxidation of catalyst. Additionally, a range of transition metals and transition metal oxides were tested to determine if they could act as promoters. It was found that the conversion is significantly increased over catalysts containing manganese, cobalt and zirconium, but decreased over the catalysts containing TiO_2 and MoO_2. Also the selectivity to maleic anhydride showed an increase of 8 to 10% for catalysts containing TiO_2, copper and zinc.

The conclusions of their study related the specific activity to maleic anhydride to the electronegativity of the promoter elements added. They found that the V=O stretching mode has a larger wavenumber as the electronegativity of the promoter increases, and that the larger the wavenumber of the V=O stretching mode, the smaller the specific activity becomes. The stronger the V=O bond is, the higher the frequency of the V=O stretching mode will be, hence the larger the wavenumber will be. So the more electronegative the promoter, the stronger the V=O bond, and the lower the specific activity.

Bej and Rao [166–170] conducted a detailed study of molybdenum- and cerium-promoted vanadium phosphate catalysts. They found an increase in the selectivity

of these catalysts, compared to the unpromoted catalyst, albeit with a slight decrease in activity. They attribute this finding to the promoters preventing over-oxidation of the maleic anhydride to carbon oxides. They also found that the promoted catalyst could withstand more severe reaction conditions, which was again attributed to less carbon oxides being formed, which can poison the catalyst.

In common with Hutchings and Higgins [148], Bej and Rao suggest that the molybdenum prevents the reduction of the V^{4+} ions to V^{3+}, a species that is considered to be responsible for the formation of total oxidation products. Cerium is proposed to increase the conversion of butane.

The promotional effects of cobalt [71, 74, 150, 152, 154, 157, 162, 171–184] and iron [71, 110, 148, 151, 152, 160–163, 173, 175, 176, 182, 185–189] have been widely studied. Ben Abdelouahab and coworkers [173] looked at the effect of various promoters on the structure of organically prepared catalysts. Both cobalt and iron promoters were found to increase the selectivity to maleic anhydride, but butane conversion was found to decrease with cobalt promoters and increase with iron promoters.

As with the zirconium study by Zeyss and coworkers, cobalt and iron were found to promote the formation of $VOPO_4$ phases during activation of the precursor to the active catalyst. The difference in activity is considered to be due to the redox potentials of the promoters. As the V^{4+}/V^{5+} ratio decreases the butane conversion is stabilized by iron (as the Fe^{3+}/Fe^{2+} redox potential is lower than the V^{5+}/V^{4+} redox potential). As the Co^{3+}/Co^{2+} redox potential is higher than the V^{4+}/V^{5+} redox potential, the conversion of butane decreases when the V^{4+}/V^{5+} ratio decreases.

A similar promotional effect was observed for catalysts prepared using an aqueous route [174]. The iron- and cobalt-promoted catalysts are associated with an increase in selectivity. The iron-doped catalyst showed an increase in activity while the cobalt-doped catalyst activity decreased. The decrease in activity of the cobalt-promoted catalyst is attributed to the formation of $VOPO_4 \cdot 2H_2O$ in the final catalyst. The $VOPO_4 \cdot 2H_2O$ is formed by the oxidation of $VOHPO_4 \cdot ½H_2O$ during the introduction of the promoters using the incipient wetness technique.

The method of preparation of the catalyst was found to alter the effect of the promoter [177]. With standard organically prepared VPO, the effect of cobalt and iron was found to be the same as previously described [133, 173–176, 183]. The increase in catalytic performance is proposed to be due to the stabilization of V^{4+}—V^{5+} dimers; the proposed active site. However, with catalysts prepared from $VOPO_4 \cdot 2H_2O$ in organic solvents, iron has no promotional effect. This is proposed to be due to the loss of crystallinity and surface area of the rosette crystals formed by this preparative route. Similarly the increase in activity due to cobalt is thought to be a structural effect, influencing the development of the (100) plane of $(VO)_2P_2O_7$.

Zazhigalov and coworkers [143] investigated cobalt-doped VPO catalysts prepared by co-precipitation and impregnation methods. The performance of catalysts prepared by both methods was increased, compared to the unpromoted catalyst. The cobalt is thought to be present as cobalt phosphate, which is considered to stabilize excess phosphorus at the surface, which has previously been found to be an important feature of active catalysts (Section 12.2).

Oxygen donors (Sb_2O_4 and $BiPO_4$) were used by Ruiz and coworkers [48], and it was found these increased the activity and selectivity when used to promote a high P/V ratio catalyst. Tamaki and coworkers [190] tested the promotional affects of magnesium, manganese, lanthanum and bismuth. They found bismuth to be the most effective promoter, increasing the selectivity at conversions up to 90 mol%, compared with unpromoted VPP. In line with studies on the active catalyst by Morishige and coworkers [52], there is speculation that the bismuth is incorporated into a phosphorus-rich amorphous surface species. Again, the additive is thought to reduce the over-oxidation of products and the total combustion of butane to carbon oxides.

The promotional effects of alkali and alkali earth metals, were investigated by Zazhigalov and coworkers [143]. The promoters can easily donate electrons to the $(VO)_2P_2O_7$. This was reported to lead to an increased negative charge on the oxygen atoms and an increase in the basic properties of the catalyst. The activation of butane by dehydrogenation occurs more readily on a basic catalyst and so the rate is increased. Acid sites are also proposed to be important to enable desorption of products to prevent over-oxidation. It has been suggested that surface species must be tuned by the promoters, to have a mix of acid and base sites in appropriate amounts for butane activation to be enhanced while allowing the selectivity to maleic anhydride to remain undiminished.

Centi and coworkers [84] have examined the effect of potassium doping, which was found to inhibit the P—OH Brønsted acid sites. The lack of Brønsted sites was thought to have two unfavorable effects on the catalyst. Firstly; the formation of lactones and maleic anhydride from furan was inhibited and, secondly, carbon-containing residues were strongly adsorbed onto the surface, deactivating the catalyst.

An increased performance has been reported with catalysts doped with indium and tetraethylorthosilicate (TEOS) [185]. The increase in catalytic performance is only observed with both promoters in the catalyst. It is proposed that the promoters work by facilitating the oxidation of the catalyst during activation, giving rise to $VOPO_4$ phases, and drastically decreasing the thickness and size of the $(VO)_2P_2O_7$ crystallites leading to a higher surface area.

Harouch Batis and coworkers [91] investigated the effect of chromium, which Hutchings and Higgins [148] observed had no effect on specific activity or selectivity. In this study, a surface enrichment of chromium was found to give a decreased maleic anhydride yield, while at high conversion, the catalyst was deactivated by surface coking. It is thought that the active site is different on the doped catalyst and the undoped vanadium phosphate. This leads to the formation of butene and furan at low conversions, which cannot usually desorb from vanadium phosphate catalysts, and at high conversions to over-oxidation to carbon oxides. Matsuura and coworkers [191] report that using niobium phosphate as promoter leads to an increase in activity of vanadium phosphate catalysts. It is thought that an increase in Lewis acid sites is responsible for the enhanced performance.

Zazhigalov and coworkers [142, 143] have reported the incorporation of bismuth compounds into vanadium phosphate catalysts using mechanochemistry. This involves milling the catalyst precursor and the promoter in ethanol. The

mechanochemistry preparation yields catalysts with a higher activity and greater selectivity to maleic anhydride than those prepared by chemical means, or mechanical mixtures.

As illustrated by the work by Sananes-Schulz and coworkers [177] the preparation method of the catalyst can alter the effect of the promoter, as can the method of doping. Hutchings and Higgins have warned against misinterpretation of promotional effects for catalysts prepared by incipient wetness and co-precipitation using acid solutions. Acidic solutions can cause the formation of $VOPO_4 \cdot 2H_2O$, which has a detrimental effect on the catalytic performance that can be mistakenly attributed to the promoter. They recommend that these methods of introducing promoters must be used with care, and in particular that the acidity of the impregnation solution should be carefully monitored. Further confusion is caused by different groups reporting contrasting results for the same promoters.

The effect of promoters on VPO performance has been summarized by Ballarini and coworkers (Table 12.2) [192].

12.6 Mechanism of *n*-Butane Partial Oxidation

The oxidation of *n*-butane to maleic anhydride is a 14-electron oxidation. It involves the abstraction of eight hydrogen atoms, the insertion of three oxygen atoms, and a multi-step polyfunctional reaction mechanism that occurs entirely on the adsorbed phase. No intermediates have been observed under standard continuous flow conditions, although mechanisms for this process have been proposed based on a variety of experimental and theoretical findings. The description of the active site is linked to the mechanism and is the subject of considerable debate in the literature. The mechanisms are linked to the researchers' hypotheses of the active site, which will be discussed in a separate section in this chapter. It is widely accepted that the (100) plane of vanadyl pyrophosphate, $(VO)_2P_2O_7$, (referred to as the (020) plane by certain authors) plays an important role in the selective oxidation of butane.

The structure has been determined by XRD and consists of edge-sharing VO_5 units linked by pyrophosphate tetrahedra (Figure 12.2). This is viewed as the active surface for most of the proposed mechanisms. Here we will discuss several of the mechanisms thought to account for the production of maleic anhydride, which have been debated in the literature.

12.6.1 Consecutive Alkenyl Mechanism

A consecutive alkenyl mechanism has the widest support in the literature [58–64, 83, 200]. Once butane has adsorbed onto the vanadium phosphate surface, it is transformed via adsorbed alkenyl intermediates into maleic anhydride. A summary of the mechanism is shown in Scheme 12.2.

Table 12.2 Summary of recent achievements on the effect of promoters on VPO performance [192].

Dopant, optimal amount (% w.r.t. V)	Promotional effect[a)]	Reasons for promotion	Ref.
Co, 0.77	C 15–25%, S 0–11%, under hydrocarbon-rich conditions	Control of the optimal V^{5+}/V^{4+} surface ratio; stabilization of an amorphous Co/V/P/O compound	[71, 193, 194]
Co, 13%	C 55–79%, S 43–35%, at 653K	Optimal surface Lewis acidity	[179, 183, 195, 196]
Ce + Fe	C 44–60%, S63–66% in the absence of O_2	Improvement of redox properties	[182]
Fe, 8%	Increase of catalytic activity	Fe replaces V^{4+} in VPP. The re-oxidation rate is increased	[105, 197]
Ga, 10%	C 22–73%, S 55–51%	Increase of surface area + increase of intrinsic activity (electronic effect)	[198]
Nb	C 20–17%, S 35–53%	Increase of surface acidity promotes desorption of MA	[159]
Nb, 1%	C 58–75%, S 70–70%	Nb concentrates at the surface, where defects are generated. Nb acts as an *n*-type dopant; development of a more oxidized surface	[199]

a C = conversion; S = selectivity for the undoped compared with the doped catalyst, under fixed reaction conditions.

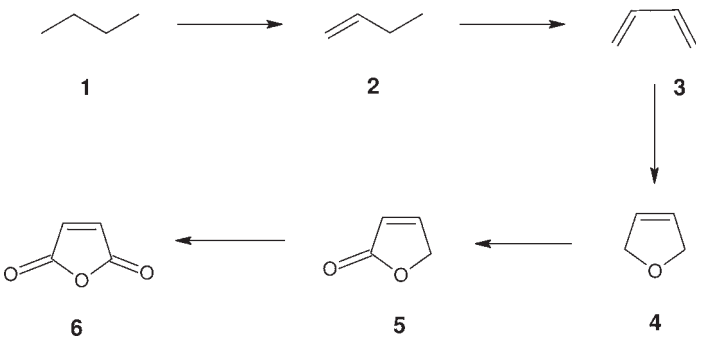

Scheme 12.2

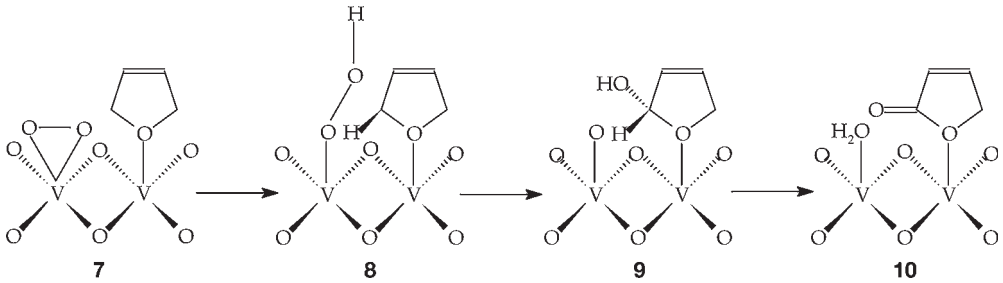

Scheme 12.3

The initial step is thought to be hydrogen abstraction from *n*-butane (**1**), giving 1-butene (**2**), followed by a further hydrogen abstraction to form 1, 3-butadiene (**3**). A 1, 4 insertion of an electrophilic surface oxygen atom occurs, producing dihydrofuran (**4**). Dihydrofuran is then oxidized to the asymmetric lactone (**5**) from which maleic anhydride (**6**) is formed by a final oxidation of the remaining CH_2 group.

There are different ways in which gaseous oxygen can adsorb onto the surface of the catalyst. In their theoretical study, Schiøtt and Jørgensen [58, 59] suggest that the gaseous oxygen is adsorbed in an η^2-peroxo coordination mode (Scheme 12.3) as this leads to a favorable overlap of the ϕ_{C-H} and ϕ^*_{O-O} orbitals. Furan is formed by oxygen insertion into adsorbed 1, 3-butadiene (**7**). The ϕ_{C-H} orbital donates electron density into the ϕ^*_{O-O} orbital, weakening the C—H bond and forming an O—H bond (**8**). Then there is a favorable carbon–oxygen interaction to give intermediate (**9**). The asymmetric lactone intermediate (**10**) is finally formed by the loss of water. This process is repeated on the reverse side of the lactone to give maleic anhydride.

A consecutive reaction mechanism was also proposed by Gleaves and Centi [61]. This was based on experimental work to back up the theoretical calculations of Schiøtt and Jørgensen. Although the proposed intermediates are not detected under reaction conditions they have been seen with fuel-rich gas feeds and under temporal conditions. Using a TAP reactor, the products are detected in the order: butane → butene → butadiene → furan. However, these conditions differ significantly from standard continuous flow reaction conditions. Taufiq-Yap and coworkers [64] surmised the same mechanism from temperature programmed reaction (TPR) and temperature programmed desorption (TPD) experiments on *n*-butane, 1-butene and 1, 3-butadiene. Temperature programmed oxidation (TPO) experiments suggest that the active oxygen species for selective oxidation is lattice oxygen, and that the replenishment of the surface oxygen from the bulk is the rate determining step.

The active oxygen species was investigated by Abon and coworkers [57], using isotopic labeling experiments. Initially, they found the products contained only lattice ^{16}O. As the reaction proceeded, more ^{18}O atoms were incorporated into the products. They also concluded that lattice oxygen was the active oxygen species,

and that it was replenished by the gas-phase oxygen. This is widely accepted to be the case and has been confirmed by numerous studies [31].

Although Misono and coworkers [63] agreed with the consecutive mechanism, they suggested a different rate determining step to Taufiq-Yap and coworkers [64]. By determining kinetic data for the reaction of *n*-butane, 1-butene and 1, 3-butadiene over VPP, they concluded that the initial dehydrogenation of butane was rate determining. The mechanism for this H abstraction has been studied in more detail by Millet [201].

Other research [65, 67, 202] has shown that butene oxidation can produce many selective products (furan, acetaldehyde and methyl vinyl ketone) which are not detected during butane oxidation. It cannot be assumed that the oxidation of butane and the unsaturated reactants proceed along the same pathway. The kinetic data must be viewed with this in mind, although butane activation is widely accepted to be the rate determining step. The intermediates are capable of desorbing from the surface, (as seen in the TAP studies) but do not do so, indicating that the further reactions occur more readily than desorption.

12.6.2
Consecutive Alkoxide Mechanism

A consecutive mechanism was proposed by Zhang-Lin and coworkers [68, 69]. The mechanism was based on kinetic data calculated for the oxidation of butane, 1-butene, 1, 3-butadiene and furan over $(VO)_2P_2O_7$ and $VOPO_4$ phases. Unlike TAP studies, the kinetic data suggested that furan is not an intermediate for butane oxidation, but is an intermediate for butadiene oxidation. The differences observed in the oxidation of butane and the unsaturated hydrocarbons questions the validity of applying butene and butadiene oxidation results to the butane system.

The consecutive alkenyl mechanism (Scheme 12.4) was put forward by Zhang-Lin and coworkers [68, 69] as the route for oxidation of unsaturated reactants such as 1-butene. The weakly adsorbed intermediates are in equilibrium with the gas phase, which enables furan to be seen as a product for butene oxidation [65–67].

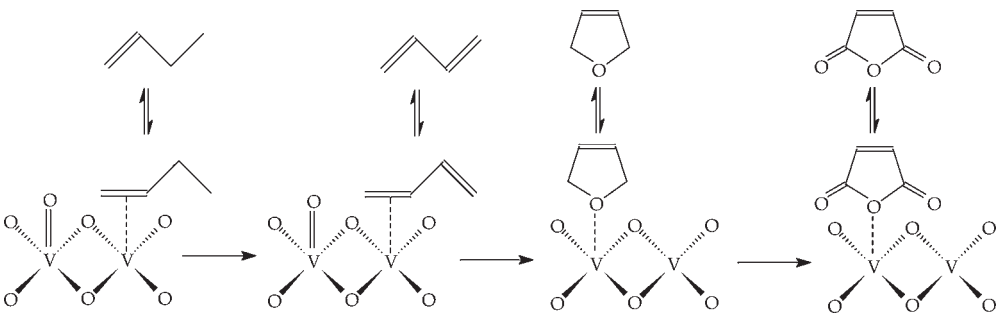

Scheme 12.4

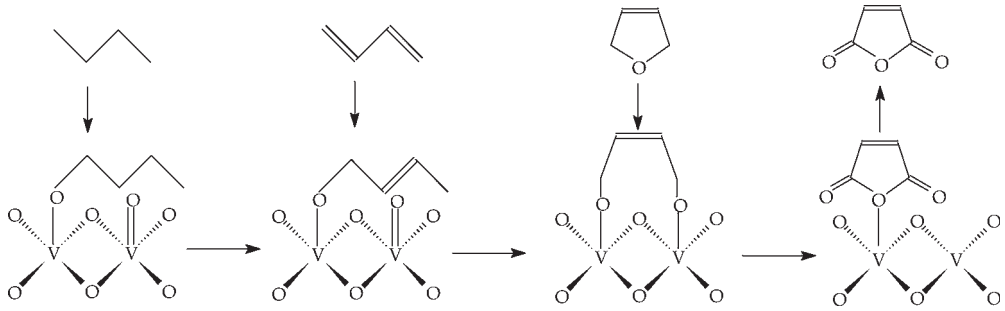

Scheme 12.5

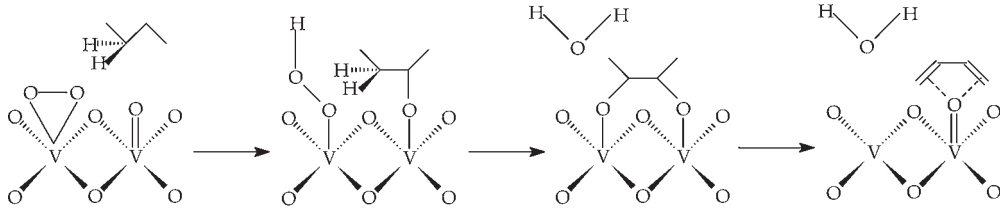

11 12 13 14

Scheme 12.6

Unlike the previous work, this study examined the fact that none of the alkene intermediates desorb from the surface. Zhang-Lin and coworkers proposed that the reaction proceeded via more strongly adsorbed alkoxide intermediates that would remain on the surface for the whole oxidation scheme (Scheme 12.5).

Agaskar and coworkers [46] have proposed a different consecutive alkoxide mechanism, based on theoretical and experimental results. Unlike other proposals, they suggest that adsorbed oxygen is the active oxygen species.

Theoretical calculations imply that gaseous oxygen is adsorbed onto the surface as a η^2-peroxo species. However, it is thought that a η^1-superoxo species may be the dominant form, if the oxide species is stabilized by interactions with neighboring metal-oxo atoms (**11**) (Scheme 12.6).

Gaseous butane is activated by hydrogen abstraction by the adsorbed superoxo species, to give a surface-bound hydroperoxy group (**12**). Simultaneously, the butene is adsorbed onto a surface vanadyl group. This is followed by a further hydrogen abstraction by the hydroperoxy group, to give a water molecule and a bridging alkoxide surface species (**13**). The next step involves a Brønsted acid site, where the alkoxide undergoes an acid-catalyzed reaction, to give 1,3-butadiene and another water molecule (**14**). The final steps to maleic anhydride then proceed as described by Schiøtt and Jørgensen [58, 59] (Scheme 12.3).

12.6.3
Concerted Mechanism

The concerted mechanism proposed by Ziółkowski and coworkers [203, 204] is based on theoretical calculations on the (100) plane of $(VO)_2P_2O_7$. The butane is adsorbed via hydrogen bonds to the active site. The active site has the following properties:

The site has three routes of relatively easy movement of hydrogen along the surface. Abstraction of the first two hydrogen atoms (from carbons $\mathbf{C_1}$ and $\mathbf{C_4}$) forms very strong bonds between the molecule and the catalyst **(C_1—V_C, C_4—V_D).** These bonds enable the molecule to be anchored to the surface long enough for the reaction to occur (Figure 12.12).

The molecule must have contact with five active oxygen atoms: **P_A—O_A, P_B—O_B, V_E—O_E,** and weakly adsorbed oxygen atoms $\mathbf{O_D}$ and $\mathbf{O_C}$. $\mathbf{O_E}$, $\mathbf{O_A}$ and $\mathbf{O_B}$ make bridges from which hydrogen atoms from all four carbons may move away. The oxygen atoms $\mathbf{O_E}$ and $\mathbf{O_C}$ are responsible for anchoring the terminal carbons, and **P_A—O_A, V_E—O_E** and **V_C—O_C** are in convenient positions to be incorporated into the molecule to form maleic anhydride (Scheme 12.7).

The adsorbed butane is activated (by hydrogen abstraction) to give butadiene before the concerted step to form maleic anhydride. The formation of maleic anhydride creates seven oxygen vacancies on the surface. The re-oxidation of the surface is proposed to be the rate determining step.

However, there is no experimental evidence for this mechanism. It is based on the deduction that the idealized surface structure has the right configuration for

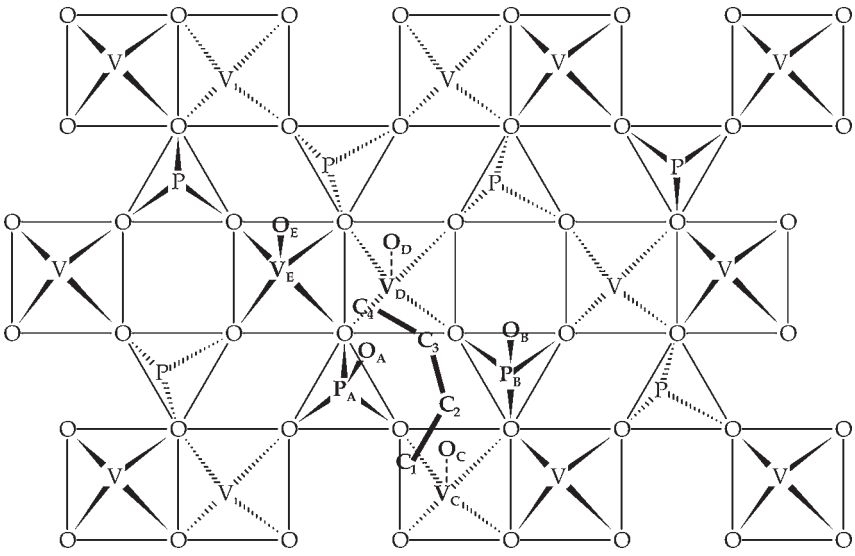

Figure 12.12 The active site for the concerted mechanism proposed by Ziółkowski and coworkers [203, 204]. (Reproduced with permission).

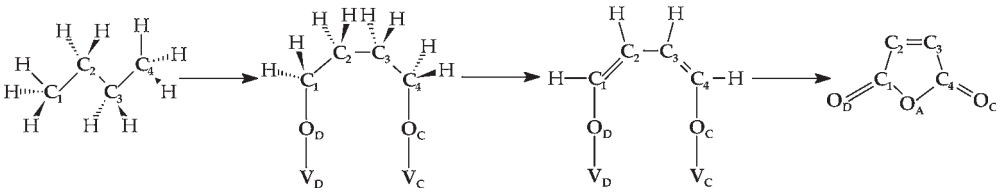

Scheme 12.7

the reaction to occur in this way. It is proposed that the reaction occurs in one step after the adsorption of butane on the active site.

12.6.4
Redox Couple Mechanism

Centi and coworkers [37] have proposed that the reaction proceeds via a series of redox couples. The mechanism is based on experimental data obtained at high butane concentrations and total oxygen conversions. Under these conditions the catalyst undergoes a partial reduction and many V^{3+} sites are formed. The activation of butane requires a V^{4+}—V^{3+} couple, while the subsequent conversion to maleic anhydride needs a V^{5+}—V^{4+} couple. The alkenes from butane dehydrogenation can desorb if no oxidizing sites are available. When the oxidizing sites are available, the alkenes are adsorbed and react very quickly to give maleic anhydride.

Under normal reaction conditions with lower concentrations of butane, there will be fewer V^{3+} sites. Following butane activation there will be numerous oxidizing sites available and so desorbed alkenes are not detected. Apart from the distribution and availability of the different sites, the authors consider that the mechanism at low and high butane concentrations is the same.

12.7
Concluding Comments

Vanadium phosphates have been applied to a number of selective oxidation and ammoxidation reactions, although the partial oxidation of *n*-butane to maleic anhydride remains the most widely studied reaction for these catalysts. Even though the first patent for this reaction was filed over 40 years ago, there are still a large number of papers published on this system every year.

This may, in part, be due to this reaction being the only industrial large scale functionalization of an alkane currently in operation, and knowledge gleaned from vanadium phosphate systems can provide valuable information that can be applied to different alkane activation reactions. To this end a number of the publications have focused and continue to focus on a fundamental understanding of the catalyst active surface and the active site. In recent years, transient techniques such as the use of TAP reactors and *in situ* characterization studies have advanced the under-

standing of the system, although this has led to considerable debate as to the exact nature of the active surface and the active site. Despite the fact that model studies and mechanistic proposals have been postulated using crystalline VPP as the active surface, increasingly this is being disputed, with evidence pointing to the importance of V^{5+} and/or amorphous phases in the catalyst.

It is no surprise that a large number of publications and patents describing the addition of promoter elements, as these can be easily introduced into the industrial catalyst formulation. It is perhaps more surprising that a number of publications are focused on new preparation methods for a catalyst that is used industrially with high selectivity and activity. These investigations may be driven by engineering requirements, with the advances in new technology such as riser reactors or membrane reactors requiring catalysts with different characteristics to those used in fixed-bed reactors.

It is clear that vanadium phosphate catalysts are still widely studied although not widely understood. Advances in research methodology, particularly the number of complementary *in situ* characterization techniques now available, may be able to further the understanding of alkane activation and selective oxidation. This fundamental understanding will be beneficial in the design of new catalyst systems for alkane functionalization and provide new uses for this relatively unreactive, under-utilized feedstock.

References

1 Bergman, R.I. and Frisch, N.W. (1966) US patent 3 293 268.

2 Trivedi, B.C. and Culbertson, B.M. (1982) *Maleic Anhydride*, Plenum, New York.

3 Varma, R.L. and Saraf, D.N. (1979) *Industrial & Engineering Chemistry Product Research and Development*, **18**, 7.

4 Hodnett, B.K. (1993) *Catalysis Today*, **16**, 131.

5 Kiely, C.J., Burrows, A., Sajip, S., Hutchings, G.J., Sananes, M.T., Tuel, A. and Volta, J.-C. (1996) *Journal of Catalysis*, **162**, 31.

6 Bordes, E. (1987) *Catalysis Today*, **1**, 499.

7 Ai, M. (1986) *Journal of Catalysis*, **101**, 389.

8 Centi, G., Tosarelli, T. and Trifiro, F. (1993) *Journal of Catalysis*, **142**, 70.

9 Centi, G., Pesheva, D. and Trifiro, F. (1987) *Applied Catalysis*, **33**, 343.

10 Centi, G. and Trifiro, F. (1990) *Chemical Engineering Science*, **45**, 2589.

11 Chen, S., Lao, L. and Shao, H. (2006) *Petroleum Science*, **3**, 65.

12 Sobalik, Z., Carrazan, S.G., Ruiz, P. and Delmon, B. (1999) *Journal of Catalysis*, **185**, 272.

13 Zanthoff, H.W., Kubias, B. and Hutchings, G.J. (1997) *DGMK Tagungsbericht*, **9705**, 307.

14 Lopez Granados, M., Fierro, J.L.G., Cavani, F., Colombo, A., Giuntoli, F. and Trifiro, F. (1998) *Catalysis Today*, **40**, 251.

15 Sobalik, Z., Gonzalez, S., Ruiz, P. and Delmon, B. (1997) *Studies in Surface Science and Catalysis*, **110**, 1213.

16 Sobalik, Z., Ruiz, P. and Delmon, B. (1997) *Studies in Surface Science and Catalysis*, **110**, 481.

17 Sobalik, Z., Gonzalez, S. and Ruiz, P. (1995) *Studies in Surface Science and Catalysis*, **91**, 727.

18 Centi, G., Lopez-Nieto, J., Pinelli, D. and Trifiro, F. (1989) *Industrial & Engineering Chemistry Research*, **28**, 400.

19 Bordes, E. (1993) *Catalysis Today*, **16**, 27.

20 Inumaru, K., Misono, M. and Okuhara, T. (1997) *Applied Catalysis, A: General*, **149**, 133.

21 Ballarini, N., Cavani, F., Cortelli, C., Ricotta, M., Rodeghiero, F., Trifiro, F., Fumagalli, C. and Mazzoni, G. (2006) *Catalysis Today*, **117**, 174.

22 Ebner, J.R. and Thompson, M.R. (1993) *Catalysis Today*, **16**, 51.

23 Guliants, V.V., Benziger, J.B., Sundaresan, S., Wachs, I.E., Jehng, J.M. and Roberts, J.E. (1996) *Catalysis Today*, **28**, 275.

24 Cavani, F. and Trifiro, F. (1997) *Applied Catalysis, A: General*, **157**, 195.

25 Volta, J.-C. (1996) *Catalysis Today*, **32**, 29.

26 Okuhara, T. and Misono, M. (1993) *Catalysis Today*, **16**, 61.

27 Schuurman, Y. and Gleaves, J.T. (1994) *Industrial & Engineering Chemistry Research*, **33**, 2935.

28 Coulston, G.W., Thompson, E.A. and Herron, N. (1996) *Journal of Catalysis*, **163**, 122.

29 Rodemerck, U., Kubias, B., Zanthoff, H.W., Wolf, G.U. and Baerns, M. (1997) *Applied Catalysis, A: General*, **153**, 217.

30 Rodemerck, U., Kubias, B., Zanthoff, H.W. and Baerns, M. (1997) *Applied Catalysis, A: General*, **153**, 203.

31 Lorences, M.J., Patience, G.S., Cenni, R., Diez, F. and Coca, J. (2006) *Catalysis Today*, **112**, 45.

32 Abon, M., Bere, K.E., Tuel, A. and Delichere, P. (1995) *Journal of Catalysis*, **156**, 28.

33 Zhang, Y., Sneeden, R.P.A. and Volta, J.C. (1993) *Catalysis Today*, **16**, 39.

34 Okuhara, T., Inumaru, K. and Misono, M. (1993) *Catalytic Selective Oxidation* (eds J. Hightower and T. Oyama), ACS Symposium Series, **523**, ACS: Washingon, DC, p. 156.

35 Inumaru, K., Okuhara, T. and Misono, M. (1992) *Chemistry Letters*, 1955.

36 Hutchings, G.J., Kiely, C.J., Sananes-Schulz, M.T., Burrows, A. and Volta, J.C. (1998) *Catalysis Today*, **40**, 273.

37 Centi, G., Fornasari, G. and Trifiro, F. (1984) *Journal of Catalysis*, **89**, 44.

38 Hutchings, G.J., Desmartin-Chomel, A., Oller, R. and Volta, J.C. (1994) *Nature (London)*, **368**, 41.

39 Abdelouahab, F.B., Olier, R., Guilhaume, N., Lefebvre, F. and Volta, J.C. (1992) *Journal of Catalysis*, **134**, 151.

40 Amoros, P., Marcos, M.D., Roca, M., Alamo, J., Beltran-Porter, A. and Beltran-Porter, D. (2001) *Journal of Physics and Chemistry of Solids*, **1393**, 62.

41 Kubias, B., Wolf, H., Wolf, G.-U., Duvauchelle N. and Bordes E. (2000) *Chemie-Ingenieur-Technik*, **72**, 249.

42 Amoros, P., Marcos, M.D., Alamo, J., Beltran, A. and Beltran, D. (1994) *Materials Research Society Symposium Proceedings*, **346**, 391.

43 Koyano, G., Okuhara, T. and Misono, M. (1995) *Catalysis Letters*, **32**, 205.

44 Koyano, G., Okuhara, T. and Misono, M. (1998) *Journal of the American Chemical Society*, **120**, 767.

45 Conte, M., Budroni, G., Bartley, J.K., Taylor, S.H., Carley, A.F., Schmidt, A., Murphy, D.M., Girgsdies, F., Ressler, T., Schloegl, R. and Hutchings, G.J. (2006) *Science (Washington, DC)*, **313**, 1270.

46 Agaskar, P. A., DeCaul, L. and Grasselli, R.K. (1994) *Catalysis Letters*, **23**, 339.

47 Trifiro, F. (1993) *Catalysis Today*, **16**, 91.

48 Ruiz, P., Bastians, P., Caussin, L., Reuse, R., Daza, L., Acosta, D. and Delmon, B. (1993) *Catalysis Today*, **16**, 99.

49 Garbassi, F., Bart, J.C.J., Montino, F. and Petrini, G. (1985) *Applied Catalysis*, **16**, 271.

50 Hodnett, B.K. and Delmon, B. (1984) *Journal of Catalysis*, **88**, 43.

51 Hodnett, B.K., Permanne, P. and Delmon, B. (1983) *Applied Catalysis*, **6**, 231.

52 Morishige, H., Tamaki, J., Miura, N. and Yamazoe, N. (1990) *Chemistry Letters*, 1513.

53 Yamazoe, N., Morishige, H. and Teraoka, Y. (1989) *Studies in Surface Science and Catalysis*, **15**, 44.

54 Morishige, H., Teraoka Y. and Yamazoe N. (1988) *Shokubai*, **30**, 480.

55 Satsuma, A., Hattori, A., Mizutani, K., Furuta, A., Miyamoto, A., Hattori, T. and Murakami, Y. (1989) *Journal of Physical Chemistry*, **93**, 1484.

56 Guliants, V.V., Benziger, J.B., Sundaresan, S., Wachs, I.E. and Hirt, A.M. (1999) *Catalysis Letters*, **62**, 87.

57 Abon, M., Bere, K.E. and Delichere, P. (1997) *Catalysis Today*, **33**, 15.
58 Schiott, B. and Jorgensen, K.A. (1993) *Catalysis Today*, **16**, 79.
59 Schiott, B., Jorgensen, K.A. and Hoffmann, R. (1991) *Journal of Physical Chemistry*, **95**, 2297.
60 Gleaves, J.T., Ebner, J.R. and Kuechler, T.C. (1988) *Catalysis Reviews–Science and Engineering*, **30**, 49.
61 Gleaves, J.T. and Centi, G. (1993) *Catalysis Today*, **16**, 69.
62 Gleaves, J.T., Yablonskii, G.S., Phanawadee, P. and Schuurman, Y. (1997) *Applied Catalysis, A: General*, **160**, 55.
63 Miyamoto, K., Nitadori, T., Mizuno, N., Okuhara, T. and Misono, M. (1988) *Chemistry Letters*, 303.
64 Taufiq-Yap, Y.H., Sakakini, B.H. and Waugh, K.C. (1997) *Catalysis Letters*, **48**, 105.
65 Busca, G., Ramis, G. and Lorenzelli, V. (1989) *Journal of Molecular Catalysis*, **50**, 231.
66 Cavani, F., Centi, G., Manenti, I., Riva, A. and Trifiro, F. (1983) *Industrial & Engineering Chemistry Product Research and Development*, **22**, 565.
67 Lischke, G., Hanke, W., Jerschkewitz, H.G. and Oehlmann, G. (1985) *Journal of Catalysis*, **91**, 54.
68 Zhang-Lin, Y., Forissier, M., Sneeden, R.P., Vedrine, J.C. and Volta, J.C. (1994) *Journal of Catalysis*, **145**, 256.
69 Zhang-Lin, Y., Forissier, M., Vedrine, J.C. and Volta, J.C. (1994) *Journal of Catalysis*, **145**, 267.
70 Garbassi, F., Bart, J.C.J., Tassinari, R., Vlaic, G. and Lagarde, P. (1986) *Journal of Catalysis*, **98**, 317.
71 Sajip, S., Bartley, J.K., Burrows, A., Sananes-Schulz, M.-T., Tuel, A., Claude Volta, J., Kiely, C.J. and Hutchings, G.J. (2001) *New Journal of Chemistry*, **25**, 125.
72 Hutchings, G.J., Bartley, J.K., Webster, J.M., Lopez-Sanchez, J.A., Gilbert, D.J., Kiely, C.J., Carley, A.F., Howdle, S.M., Sajip, S., Caldarelli, S., Rhodes, C., Volta, J.C. and Poliakoff, M. (2001) *Journal of Catalysis*, **197**, 232.
73 Hutchings, G.J., Lopez-Sanchez, J.A., Bartley, J.K., Webster, J.M., Burrows, A., Kiely, C.J., Carley, A.F., Rhodes, C., Haevecker, M., Knop-Gericke, A., Mayer, R.W., Schloegl, R., Volta, J.C. and Poliakoff, M. (2002) *Journal of Catalysis*, **208**, 197.
74 Lopez-Sanchez, J.A., Bartley, J.K., Burrows, A., Kiely, C.J., Haevecker, M., Schloegl, R., Volta, J.C., Poliakoff, M. and Hutchings, G.J. (2002) *New Journal of Chemistry*, **26**, 1811.
75 Shimoda, T., Okuhara, T. and Misono, M. (1985) *Bulletin of the Chemical Society of Japan*, **58**, 2163.
76 Guliants, V.V., Benziger, J.B., Sundaresan, S., Yao, N. and Wachs, I.E. (1995) *Catalysis Letters*, **32**, 379.
77 Cavani, F., Centi, G. and Trifiro, F. (1985) *Journal of the Chemical Society, Chemical Communications*, 492.
78 Busca, G., Cavani, F., Centi, G. and Trifiro, F. (1986) *Journal of Catalysis*, **99**, 400.
79 Cornaglia, L.M., Lombardo, E.A., Anderson, J.A. and Garcia Fierro, J.L. (1993) *Applied Catalysis, A: General*, **100**, 37.
80 Lombardo, E.A., Sanchez, C.A. and Cornaglia, L.M. (1992) *Catalysis Today*, **15**, 407.
81 Cornaglia, L.M. and Lombardo, E.A. (1994) *Studies in Surface Science and Catalysis*, **90**, 429.
82 Ben Abdelmalek, S., Batis, H. and Ghorbel, A. (1993) *Journal de la Societe Algerienne de Chimie*, **3S**, 265.
83 Abon, M. and Volta, J.-C. (1997) *Applied Catalysis, A: General*, **157**, 173.
84 Centi, G., Golinelli, G. and Busca, G. (1990) *Journal of Physical Chemistry*, **94**, 6813.
85 Ai, M. (1986) *Journal of Catalysis*, **100**, 336.
86 Johnson, J.W., Johnston, D.C., Jacobson, A.J. and Brody, J.F. (1984) *Journal of the American Chemical Society*, **106**, 8123.
87 Sartoni, L., Delimitis, A., Bartley, J.K., Burrows, A., Roussel, H., Herrmann, J.-M., Volta, J.-C., Kiely, C.J. and Hutchings, G.J. (2006) *Journal of Materials Chemistry*, **16**, 4348.
88 Poli, G., Resta, I., Ruggeri, O. and Trifiro, F. (1981) *Applied Catalysis*, **1**, 395.
89 Hutchings, G.J., Sananes, M.T., Sajip, S., Kiely, C.J., Burrows, A., Ellison, I.J. and

Volta, J.C. (1997) *Catalysis Today*, **33**, 161.
90 Cornaglia, L.M., Sanchez, C.A. and Lombardo, E.A. (1993) *Applied Catalysis, A: General*, **95**, 117.
91 Batis, N.H., Batis, H., Ghorbel, A., Vedrine, J.C. and Volta, J.C. (1991) *Journal of Catalysis*, **128**, 248.
92 Meisel, M., Wolf, G.-U., Worzala, H., Eichele, K. and Grimmer, A.-R. (2000) *Phosphorus Research Bulletin*, **11**, 81.
93 Hutchings, G.J. and Higgins, R. (1997) *Applied Catalysis, A: General*, **154**, 103.
94 Kiely, C.J., Burrows, A., Hutchings, G.J., Bere, K.E., Volta, J.-C., Tuel, A. and Abon, M. (1997) *Faraday Discussions*, **105**, 103.
95 Mizuno, N., Hatayama, H. and Misono, M. (1997) *Chemistry of Materials*, **9**, 2697.
96 O'Connor, M., Dason, F. and Hodnett, B.K. (1990) *Applied Catalysis*, **64**, 161.
97 Cavani, F., Centi, G. and Trifiro, F. (1984) *Applied Catalysis*, **9**, 191.
98 Horowitz, H.S., Blackstone, C.M., Sleight, A.W. and Teufer, G. (1988) *Applied Catalysis*, **38**, 193.
99 Ellison, I.J., Hutchings, G.J., Sananes, M.T. and Volta, J.C. (1994) *Journal of the Chemical Society, Chemical Communications*, 1093.
100 Sananes, M.T., Ellison, I.J., Sajip, S., Burrows, A., Kiely, C.J., Volta, J.C. and Hutchings, G.J. (1996) *Journal of the Chemical Society–Faraday Transactions*, **92**, 137.
101 Doi, T. and Miyake, T. (1997) *Applied Catalysis, A: General*, **164**, 141.
102 Miyake, T. and Doi, T. (1995) *Applied Catalysis, A: General*, **131**, 43.
103 Guilhaume, N., Roullet, M., Pajonk, G., Grzybowska, B. and Volta, J.C. (1992) *Studies in Surface Science and Catalysis*, **72**, 255.
104 Hiyoshi, N., Yamamoto, N., Ryumon, N., Kamiya, Y. and Okuhara, T. (2004) *Journal of Catalysis*, **221**, 225.
105 Kamiya, Y., Ueki, S., Hiyoshi, N., Yamamoto, N. and Okuhara, T. (2003) *Catalysis Today*, **78**, 281.
106 Yamamoto, N., Hiyoshi, N. and Okuhara, T. (2002) *Chemistry of Materials*, **14**, 3882.
107 Yamamoto, N., Okuhara, T. and Nakato, T. (2001) *Journal of Materials Chemistry*, **11**, 1858.
108 Hiyoshi, N., Yamamoto, N. and Okuhara, T. (2001) *Chemistry Letters*, 484.
109 Nakato, T., Furumi, Y., Terao, N. and Okuhara, T. (2000) *Journal of Materials Chemistry*, **10**, 737.
110 Nakato, T., Furumi, Y. and Okuhara, T. (1998) *Chemistry Letters*, 611.
111 O'Mahony, L., Curtin, T., Zemlyanov, D., Mihov, M. and Hodnett, B.K. (2004) *Journal of Catalysis*, **227**, 270.
112 O'Mahony, L., Henry, J., Sutton, D., Curtin, T. and Hodnett, B.K. (2003) *Catalysis Letters*, **90**, 171.
113 Bartley, J.K., Wells, R.P.K. and Hutchings, G.J. (2000) *Journal of Catalysis*, **195**, 423.
114 Hannour, F.K., Martin, A., Bruckner, A., Wolf, G.U. and Lucke, B. (1998) *Reaction Kinetics and Catalysis Letters*, **63**, 225.
115 Bethke, G.K., Wang, D., Bueno, J.M.C., Kung, M.C. and Kung, H.H. (1997) *3rd World Congress on Oxidation Catalysis*.
116 Sananes, M.T., Ellison, I.J., Sajip, S., Burrows, A., Kiely, C.J., Volta, J.C. and Hutchings, G.J. (1996) *Journal of the Chemical Society-Faraday Transactions*, **92**, 137.
117 Sananes, M.T., Hutchings, G.J. and Volta, J.C. (1995) *Journal of Catalysis*, **154**, 253.
118 Sananes, M.T., Hutchings, G.J. and Volta, J.C. (1995) *Journal of the Chemical Society-Chemical Communications*, 243.
119 Mount, R.A., Raffelsonand, H. and Robinson, W.D. (1978) Monsanto Co., USA, US Patent 4116868.
120 Martin, A., Hannour, F.K., Bruckner, A. and Lucke, B. (1998) *Reaction Kinetics and Catalysis Letters*, **63**, 245.
121 Hannour, F.K., Martin, A., Kubias, B., Lucke, B., Bordes, E. and Courtine, P. (1998) *Catalysis Today*, **40**, 263.
122 Martin, A., Steinike, U., Rabe, S., Lucke, B. and Hannour, F.K. (1997) *Journal of the Chemical Society–Faraday Transactions*, **93**, 3855.
123 Higgins, R. and Hutchings, G.J. (1980) Imperial Chemical Industries Ltd., UK. Application: US Patent 4222945.
124 Bordes, E. and Courtine, P. (1979) *Journal of Catalysis*, **57**, 236.
125 Benziger, J.B., Guliants, V. and Sundaresan, S. (1997) *Catalysis Today*, **33**, 49.

126 Takita, Y., Hashiguchi, T. and Matsunosako, H. (1988) *Bulletin of the Chemical Society of Japan*, **61**, 3737.

127 Michalakos, P.M., Bellis, H.E., Brusky, P., Kung, H.H., Li, H.Q., Moser, W.R., Partenheimer, W. and Satek, L.C. (1995) *Industrial & Engineering Chemistry Research*, **34**, 1994.

128 Dong, W.-S., Bartley, J.K., Dummer, N.F., Girgsdies, F., Su, D., Schloegl, R., Volta, J.-C. and Hutchings, G.J. (2005) *Journal of Materials Chemistry*, **15**, 3214.

129 Taufiq-Yap, Y.H., Hasbi, A.R.M., Hussein, M.Z., Hutchings, G.J., Bartley, J. and Dummer, N. (2006) *Catalysis Letters*, **106**, 177.

130 Griesel, L., Bartley, J.K., Wells, R.P.K. and Hutchings, G.J. (2005) *Catalysis Today*, **99**, 131.

131 Doi, T. and Miyake, T. (1996) *Chemical Communications (Cambridge)*, 1635.

132 Bu, X., Feng, P. and Stucky, G.D. (1995) *Journal of the Chemical Society, Chemical Communications*, 1337.

133 Albonetti, S., Cavani, F., Trifiro, F., Venturoli, P., Calestani, G., Granados, M.L. and Fierro, J.L.G. (1996) *Journal of Catalysis*, **160**, 52.

134 Aït-Lachgar, K., Abon, M. and Volta, J.C. (1997) *Journal of Catalysis*, **171**, 383.

135 Cheng, W.-H. and Wang, W. (1997) *Applied Catalysis, A: General*, **156**, 57.

136 Arnold, E.W. III and Sundaresan, S. (1988) *Applied Catalysis*, **41**, 225.

137 Contractor, R.M., Horowitz, H.S., Sisler, G.M. and Bordes, E. (1997) *Catalysis Today*, **37**, 51.

138 Vedrine, J.C., Millet, J.M.M. and Volta, J.-C. (1996) *Catalysis Today*, **32**, 115.

139 Centi, G. and Perathoner, S. (1998) *Catalysis Today*, **41**, 457.

140 Patience, G.S., Bockrath, R.E., Sullivan, J.D. and Horowitz, H.S. (2007) *Industrial & Engineering Chemistry Research*, **46**, 4374.

141 Taufiq-Yap, Y.H. and Goh, C.K. (2005) *Eurasian Chemico-Technological Journal*, **7**, 73.

142 Haber, J., Zazhigalov, V.A., Stoch, J., Bogutskaya, L.V. and Batcherikova, I.V. (1997) *Catalysis Today*, **33**, 39.

143 Zazhigalov, V.A., Haber, J., Stoch, J., Bogutskaya, L.V. and Bacherikova, I.V. (1996) *Applied Catalysis, A: General*, **135**, 155.

144 Taufiq-Yap, Y.H., Goh, C.K., Hutchings, G.J., Dummer, N. and Bartley, J.K. (2006) *Journal of Molecular Catalysis A: Chemical*, **260**, 24.

145 Wang, X., Xu, L., Chen, X., Ji, W., Yan, Q. and Chen, Y. (2003) *Journal of Molecular Catalysis A: Chemical*, **206**, 261.

146 Ji, W., Xu, L., Wang, X., Hu, Z., Yan, Q. and Chen, Y. (2002) *Catalysis Today*, **74**, 101.

147 Hutchings, G.J. (1991) *Applied Catalysis*, **72**, 1.

148 Hutchings, G.J. and Higgins, R. (1996) *Journal of Catalysis*, **162**, 153.

149 Ye, D., Satsuma, A., Hattori, T. and Murakami, Y. (1991) *Applied Catalysis*, **69**, L1.

150 Ye, D., Satsuma, A., Hattori, T. and Murakami, Y. (1990) *Journal of the Chemical Society, Chemical Communications*, 1337.

151 Ye, D., Fu, M., Cheng, S. and Liang, H. (2003) *Abstracts of papers*, 226th ACS National Meeting. New York, NY, September 7–11, 2003, COLL.

152 Ye, D., Fu, M., Tian, L., Liang, H., Rong, T., Cheng, S. and Pang, X. (2003) *Research on Chemical Intermediates*, **29**, 271.

153 Ye, D., Satsuma, A., Hattori, A., Hattori, T. and Murakami, Y. (1993) *Catalysis Today*, **16**, 113.

154 Ye, D., Fu, M., Hong, L., Cheng, S., Rong, T. and Pang, X. (2004) *Huanan Ligong Daxue Xuebao Ziran Kexueban*, **32**, 49.

155 Hutchings, G.J. (1993) *Catalysis Today*, **16**, 139.

156 Sananes, M.T., Petunchi, J.O. and Lombardo, E.A. (1992) *Catalysis Today*, **15**, 527.

157 Takita, Y., Tanaka, K., Ichimaru, S., Mizihara, Y., Abe, Y. and Ishihara, T. (1993) *Applied Catalysis, A: General*, **103**, 281.

158 Zeyss, S., Wendt, G., Hallmeier, K.-H., Szargan, R. and Lippold, G. (1996) *Journal of the Chemical Society – Faraday Transactions*, **92**, 3273.

159 Guliants, V.V., Benziger, J.B., Sundaresan, S. and Wachs, I.E. (2000) *Studies in Surface Science and Catalysis*, **130B**, 1721.

160 Kourtakis, K. and Gai, P.L. (2005) US Patent 6903047.

161 Xu, L., Chen, X., Ji, W. and Yan, Q. (2002) *Reaction Kinetics and Catalysis Letters*, **76**, 335.

162 Liang, H. and Ye, D. (2005) *Journal of Natural Gas Chemistry*, **14**, 177.

163 Liang, H., Ye, D. and Lin, W. (2006) *Yunnan Daxue Xuebao, Ziran Kexueban*, **28**, 68.

164 Sant, R. and Varma, A. (1993) *Journal of Catalysis*, **143**, 215.

165 Takita, Y., Tanaka, K., Ichimaru, S., Ishihara, T., Inoue, T. and Arai, H. (1991) *Journal of Catalysis*, **130**, 347.

166 Bej, S.K. and Rao, M.S. (1992) *Industrial & Engineering Chemistry Research*, **31**, 2075.

167 Bej, S.K. and Rao, M.S. (1992) *Applied Catalysis, A: General*, **83**, 149.

168 Bej, S.K. and Rao, M.S. (1991) *Industrial & Engineering Chemistry Research*, **30**, 1819.

169 Bej, S.K. and Rao, M.S. (1991) *Industrial & Engineering Chemistry Research*, **30**, 1824.

170 Bej, S.K. and Rao, M.S. (1991) *Industrial & Engineering Chemistry Research*, **30**, 1829.

171 Hodnett, B.K. and Delmon, B. (1983) *Applied Catalysis*, **6**, 245.

172 Abdelouahab, F.B., Herrmann, J.-M., Volta, J.-C. and Ziyad, M. (1995) *Journal of the Chemical Society–Faraday Transactions*, **91**, 3231.

173 Abdelouahab, F.B., Olier, R., Ziyad, M. and Volta, J.C. (1995) *Journal of Catalysis*, **157**, 687.

174 Hutchings, G.J., Ellison, I.J., Sananes, M.T. and Volta, J.C. (1996) *Catalysis Letters*, **38**, 231.

175 Sananes-Schulz, M.T., Abdelouahad, F.B., Hutchings, G.J. and Volta, J.C. (1996) *Journal of Catalysis*, **163**, 346.

176 Cavani, F., Colombo, A., Trifiro, F., Sananes Schulz, M. T., Volta, J.C. and Hutchings, G.J. (1997) *Catalysis Letters*, **43**, 241.

177 Sananes-Schulz, M.T., Tuel, A., Hutchings, G.J. and Volta, J.C. (1997) *Journal of Catalysis*, **166**, 388.

178 Cornaglia, L.M., Carrara, C.R., Petunchi, J.O. and Lombardo, E.A. (1999) *Applied Catalysis, A: General*, **183**, 177.

179 Cornaglia, L., Carrara, C., Petunchi, J. and Lombardo, E. (2000) *Studies in Surface Science and Catalysis*, **130B**, 1727.

180 Carrara, C., Irusta, S., Lombardo, E. and Cornaglia, L. (2001) *Applied Catalysis, A: General*, **217**, 275.

181 Sajip, S., Bartley, J.K., Burrows, A., Rhodes, C., Claude Volta, J., Kiely, C.J. and Hutchings, G.J. (2001) *Physical Chemistry Chemical Physics*, **3**, 2143.

182 Shen, S., Zhou, J., Zhang, F., Zhou, L. and Li, R. (2002) *Catalysis Today*, **74**, 37.

183 Cornaglia, L., Irusta, S., Lombardo, E.A., Durupty, M.C. and Volta, J.C. (2003) *Catalysis Today*, **78**, 291.

184 Taufiq-Yap, Y.H. (2006) *Journal of Natural Gas Chemistry*, **15**, 144.

185 Cheng, W.-H. (1996) *Applied Catalysis, A: General*, **147**, 55.

186 McCormick, R.L., Alptekin, G.O., Herring, A.M., Ohno, T.R. and Dec, S.F. (1997) *Journal of Catalysis*, 172 (1), 160.

187 Boudin, S., Guesdon, A., Leclaire, A. and Borel, M.M. (2000) *International Journal of Inorganic Materials*, **2**, 561.

188 Taufiq-Yap, Y., Goh, C.K., Waugh, K.C. and Kamiya, Y. (2005) *Reaction Kinetics and Catalysis Letters*, **84**, 271.

189 Dobner, C., Duda, M., Raichle, A., Wilmer, H., Rosowski, F. and Hoelzle, M. (2007) BASF Aktiengesellschaft, Germany. Application: WO 2007012620.

190 Tamaki, J., Morishita, T., Morishige, H., Miura, N. and Yamazoe, N. (1992) *Chemistry Letters*, 13.

191 Matsuura, I., Ishimura, T. and Kimura, N. (1995) *Chemistry Letters*, 769.

192 Ballarini, N., Cavani, F., Cortelli, C., Ligi, S., Pierelli, F., Trifiro, F., Fumagalli, C., Mazzoni, G. and Monti, T. (2006) *Topics in Catalysis*, **38**, 147.

193 Mota, S., Volta, J.C., Vorbeck, G. and Dalmon, J.A. (2000) *Journal of Catalysis*, **193**, 319.

194 Abon, M., Herrmann, J.M. and Volta, J.C. (2001) *Catalysis Today*, **71**, 121.

195 Cornaglia, L.M., Carrara, C.R., Petunchi, J.O. and Lombardo, E.A. (2000) *Catalysis Today*, **57**, 313.

196 Pries de Oliveira, P.G., Eon, J.G., Chavant, M., Riche, A.S., Martin, V., Caldarelli, S. and Volta, J.C. (2000) *Catalysis Today*, **57**, 177.
197 Satsuma, A., Kijima, Y., Kamiya, S.-I., Komai, Y., Nishikawa, E. and Hatttori, T. (2001) *Catalysis Today*, **71**, 161.
198 Sartoni, L., Bartley, J.K., Wells, R.P.K., Kiely, C.J., Volta, J.C. and Hutchings, G.J. (2004) *Journal of Molecular Catalysis, A: Chemical*, **220**, 85.
199 Duarte de Farias, A.M., Gonzalez, W.D.A., Pries de Oliveira, P.G., Eon, J.-G., Herrmann, J.-M., Aouine, M., Loridant, S. and Volta, J.-C. (2002) *Journal of Catalysis*, **208**, 238.
200 Busca, G. and Centi, G. (1989) *Journal of the American Chemical Society*, **111**, 46.
201 Millet, J.-M.M. (2006) *Topics in Catalysis*, **38**, 83.
202 Cavani, F., Centi, G. and Trifiro, F. (1983) *Industrial & Engineering Chemistry Product Research and Development*, **22**, 570.
203 Ziółkowski, J., Bordes, E. and Courtine, P. (1993) *Journal of Molecular Catalysis*, **84**, 307.
204 Ziółkowski, J., Bordes, E. and Courtine, P. (1990) *Journal of Catalysis*, **122**, 126.

13
Heterogeneous Catalysis by Uranium Oxides

Stuart H. Taylor

13.1
Introduction

The element uranium has been used, in the form of its natural oxide, since ancient times. It was used as an orange-yellow coloring agent for ceramics dating from at least 79 AD. The element was identified by Martin Heinrich Klaproth in 1789 when it was discovered in natural minerals. The element was named in honor of the recently discovered new planet Uranus. In 1841 Peligot showed that Klaproth's *substance*, previously believed to be the metal, was in fact the oxide UO_2. Shortly thereafter Peligot showed that it was possible to produce the metal by reduction of uranium tetrachloride by the metals sodium and potassium. The construction of the periodic table by Mendeléev in 1872 focused attention on uranium as it was then the heaviest of the known elements. This stimulated much research on the element but it was not until 1896 that Antoine Becquerel recognized the radioactive properties of uranium. A research program starting in 1934 and led by Enrico Fermi resulted in the fissile properties of uranium being used for power generation and production of nuclear weapons. The isotope ^{235}U is still of primary importance and is used for power generation in both metallic and oxide forms. It is the only naturally occurring nuclide that undergoes nuclear fission with thermal neutrons.

The average concentration of uranium in the earth's crust is somewhere in the range 2–4 ppm, which is very similar to elements such as molybdenum and approximately 40 times greater than silver. Estimates of uranium reserves suggest that there are 4.7 million tons of easily accessible uranium minerals, and a further 35 million tons that could be recovered with further investment. In addition, a further 4.6 billion tons is present in sea water. Uranium is obtained mainly from the mineral uraninite, also called pitchblende, which consists largely of UO_2. Uranium-rich mineral resources are mined by a combination of open-cast and underground extraction methods, whilst poorer grade deposits are often recovered by leaching with acid or alkali.

Heterogeneous catalysis by compounds of uranium, and in particular the oxides of uranium, is well established and has a long history. The versatility of uranium

Metal Oxide Catalysis. Edited by S. David Jackson and Justin S. J. Hargreaves

ISBN: 978-3-527-31815-5

oxide based catalysts is related to the rich and diverse properties of the wide variety of phases and mixed phases that can be synthesized. The aim of this chapter is to introduce the reader to the chemistry of uranium compounds and highlight their uses as heterogeneous catalysts.

13.2
Structure of Uranium Oxides

Before examining the efficacy of uranium oxides as catalysts it is beneficial to consider the structures of the oxides. The three main oxides of uranium are UO_2 (brown-black), UO_3 (orange-yellow) and U_3O_8 (green-black). In addition to these three compounds, a considerable number of oxides exist within the stoichiometric range UO_2—UO_3. The range of stoichiometries and structures that are possible for the uranium–oxygen system make it the most complex of the Actinide elements, and one of the most complicated of all the elements. Changing the oxidation state of a given uranium ion is often accompanied by a modification of the structure. For example, within a limited temperature range, the uranium oxide structure and the uranium oxidation state can be influenced by the atmosphere to which it is exposed [1]. The complexity of the uranium–oxygen system is illustrated in Figure 13.1.

Allen and Holmes [2] have investigated the mechanism of transformation of UO_2 to UO_3 and they have also summarized the intermediate phases that have been identified (Table 13.1).

UO_2 has the fluorite structure; it is a face centered cubic based structure with each uranium ion coordinated to eight oxygen ions (Figure 13.2). The fact that there are vacant coordination positions in the lattice is critical for the catalytic, and other, properties of the oxide. This is because ion exchange is more efficient by

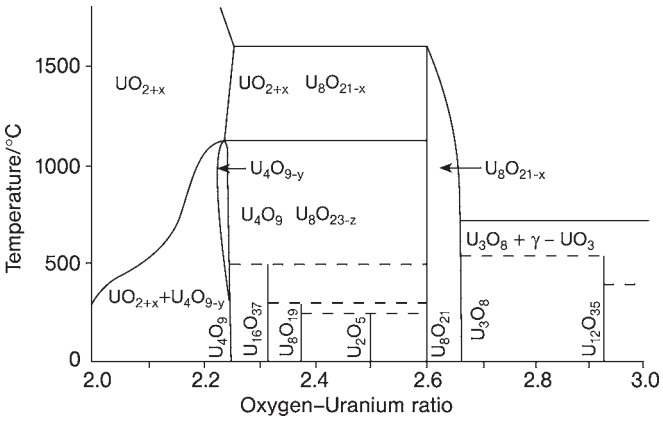

Figure 13.1 Phase diagram of uranium oxides. (*Journal of the Chemical Society, Dalton Transactions* (1982), 2169; reproduced by permission of The Royal Society of Chemistry).

Table 13.1 Crystallographic data for the known uranium oxides [2].

Phase	O:U ratio	Structure	Crystal class	Unit cell dimensions (Å)	Ref.
UO_2	2.00	fluorite	cubic	$a = 5.470$	[3]
UO_{2+x}	2.00–2.25	fluorite	cubic	$a = 5.470$–5.445	[4]
α-U_4O_9	2.45–2.25	fluorite	rhombohedral	$a = 4 \times (5.441$–$5.444)$; $\alpha = 90.078°$ ($T = 20\,°C$)	[5]
β-U_4O_9	2.25	fluorite	cubic	$a = 4 \times 5.438$ ($T = 65\,°C$)	[6]
γ-U_4O_9	2.25	fluorite	cubic	$a = 4 \times (5.47$–$5.50)$ ($T > 600\,°C$)	[6]
α-U_3O_7	2.27–2.33	fluorite	tetragonal	$a = 5.472$; $c = 5.397$	[7]
β-U_3O_7	2.33	fluorite	tetragonal	$a = 5.363$; $c = 5.531$	[7]
$U_{16}O_{37}$ (γ-U_3O_7)	2.31	fluorite	tetragonal	$a = 5.407$; $c = 5.497$	[8]
U_8O_{19} (δ-U_3O_7)	2.375	fluorite	monoclinic	$a = 5.378$; $b = 5.559$; $c = 5.378$; $\beta = 90.29\,°C$	[9]
γ-U_2O_5	2.50	fluorite	monoclinic	$a = 5.410$; $b = 5.481$; $c = 5.410$; $\beta = 90.49°$	[8]
α-U_2O_5	2.50	layered	hexagonal	$a = 3.885$; $c = 4.082$	[8]
β-U_2O_5	2.50	layered	hexagonal	$a = 3.813$; $c = 13.18$	[8]
U_2O_5	2.50	layered	orthorhombic	$a = 8.29$; $b = 31.71$; $c = 6.73$	[10]
α-U_3O_8	2.660–2.667	layered	orthorhombic	$a = 6.715$; $b = 11.96$; $c = 4.146$	[11, 12]
β-U_3O_8	2.67	layered	orthorhombic	$a = 7.07$; $b = 11.45$; $c = 8.30$	[13]
$U_{12}O_{35}$	2.92	layered	orthorhombic	$a = 6.91$; $b = 3.92$; $c = 4.12$	[14]
α—UO_3	3.00	layered	orthorhombic	$a = 6.84$; $b = 43.45$; $c = 4.12$	[15]
β-UO_3	3.00	layered	monoclinic	$a = 10.34$; $b = 14.33$; $c = 3.91$; $\beta = 99.03$	[16]
γ-UO_3	3.00		tetragonal	$a = 6.013$; $c = 19.975$	[17]
δ-UO_3	3.00	ReO_3-type	cubic	$a = 4.16$	[18]
ε-UO_3	3.00	layered	triclinic	$a = 4.002$l; $\alpha = 98.10°$; $b = 3.841$; $\beta = 90.20°$; $c = 4.165$; $\gamma = 120.17$	[19]
η-UO_3	3.00		orthorhombic	$a = 7.511$; $b = 5.466$; $c = 5.224$	[20]

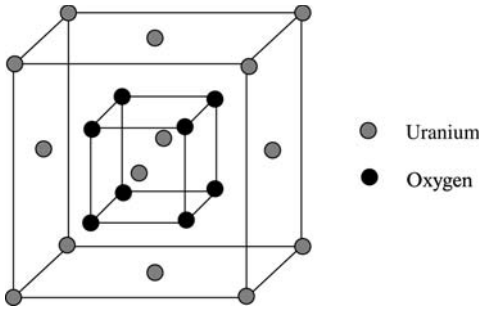

Figure 13.2 Fluorite structure of UO_2.

exchange through lattice vacancies. Another important factor is that the UO_2 fluorite structure is readily able to accommodate up to 10% additional oxygen in the lattice without any change of the structure [21].The study of the oxidation of uranium oxides can be divided into two distinct regions: the oxidation of stoichiometric cubic UO_2 to orthorhombic U_3O_8 and the subsequent oxidation of this phase to UO_3 [22].

In the first region the initial stage is the oxidation step of UO_2 to $UO_{2.25}$, where gradual addition of oxygen leads to displacement of the ideal lattice positions until the structure of U_4O_9 ($UO_{2.25}$) is reached. The addition of this oxygen has no effect on the uranium sub-lattice as the oxygen is incorporated in interstitial sites. Increasing the stoichiometry to $UO_{2.12}$, the oxygen is distributed randomly in the interstitial sites; however, as the O/U ratio increases further towards $UO_{2.25}$, the formation of clusters in the lattice takes place. The clusters develop to form ordered cluster chains. The clusters are known as 2 : 2 : 2 clusters and contain two interstitial oxygen atoms in the (110) direction, two vacancies in the oxygen sublattice and two interstitial oxygen atoms in the (111) direction [23, 24].

For the stoichiometry $UO_{2.25}$, the structure can be simplified to an arrangement of 4 : 3 : 2 clusters [25].These clusters are composed of four interstitial oxygen atoms in the (110) direction with three oxygen vacancies and two interstitial oxygen atoms in the (111) direction. The addition of this oxygen causes the expansion of the cubic structure so that the cell dimension for U_4O_9 is approximately four times that of UO_2 [6], although the cubic structure is retained.

Increasing the O/U ratio further from the stoichiometry U_4O_9 to U_3O_7, the structure of the oxide changes from the cubic crystal system to a variety of tetragonal structures [7, 8]. Further oxidation from U_3O_7 to U_2O_5 results in a further change of structure from the fluorite structure to a layered structure that is close to that observed for U_3O_8 [8, 10]. The U_2O_5 phase was first shown conclusively to exist by Rundle and coworkers in 1948 [10]. This work showed that the structure was orthorhombic like U_3O_8, but the actual cell dimensions were larger [11–13]. It is interesting that U_2O_5 phases have been reported with a monoclinic fluorite structure [8], with a hexagonal layered structure [8] and with an orthorhombic layered structure similar to that for U_3O_8 [10]. Allen and Holmes [2] suggest that the β-U_2O_5 could represent an intermediate bridging structure, since it shows neither fluorite-type nor U_3O_8-type structure.

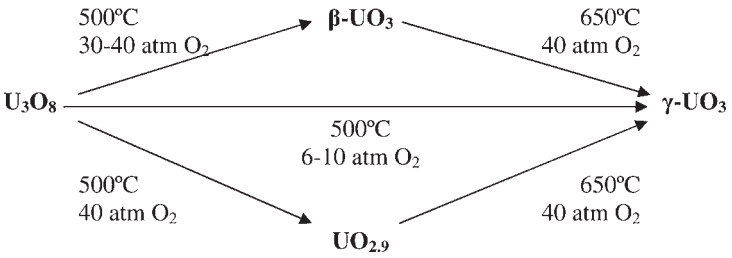

Figure 13.3 Summary of preparation of γ-UO_3 from U_3O_8. (Adapted from [14]).

The second region of oxidation covers the addition of oxygen from U_3O_8 to UO_3. Numerous phases have been identified for UO_3, with the majority showing layered structures similar to U_3O_8 [14–19]. UO_3 can be prepared from U_3O_8 by heating between 400 and 700 °C; however, it must be prepared under pressures of up to 40 atmospheres [13]. The transformation of U_3O_8 to UO_3 phases is summarized in Figure 13.3.

In UO_3 phases the uranium atom may be coordinated to six, seven or eight oxygen atoms, leading to at least five known modifications. For example the γ-UO_3 phase has two independent uranium atoms U (1) and U (2) in the structure [17]. The coordination polyhedron around U (2) is a slightly distorted octahedron, whereas U (1) is surrounded by eight oxygen atoms forming a somewhat distorted dodecahedron. This chapter is not intended to provide a detailed understanding of the multiple and complex phases of the uranium oxides, but it is clear even from a brief survey that the structures and chemistry are diverse.

13.3
Historical Uses of Uranium Oxides as Catalysts

Uranium compounds have historically been used as catalysts for many years, dating back to the initial development of catalysis as a recognized scientific discipline. In 1922, James published a paper detailing the vapor-phase low-temperature catalytic oxidation of fuel oil and other crude petroleum fractions [26]. It was concluded that to obtain satisfactorily high yields of sufficient quality for industrial use a catalyst must be employed. An apparatus was developed to test catalysts on a pilot-plant scale and it was found that the most effective configuration consisted of three catalyst layers, called catalyst screens. The most effective catalyst system for the reaction was an initial bed composed of uranium oxide and two subsequent beds containing molybdenum oxide. The uranium oxide was the best catalyst for the oxidation to aldehyde-type compounds and was particularly favored when acids were the desired products, as the higher yields of aldehyde were converted to acids over the molybdenum oxide screens. Typically the catalyst was supported on asbestos, although it is unclear whether the asbestos was a support in the way conventionally associated with a catalyst or merely acted as gauze to hold the

catalyst bed in place. Air was used as oxidant and this was fed independently before each catalyst bed, which ensured that the oxygen concentration laterally through the catalyst screens was relatively low and probably helped to reduce over-oxidation. The production of acids was typically carried out at 280 °C, whilst increasing the reaction temperature to ca. 400 °C resulted in the production of hydrocarbons and lower molecular weight oxygenates, which were suitable for use as fuels. The data presented are relatively scant; however, the publication is one of the first to indicate that uranium oxide is a potentially important oxidation catalyst.

Early work has also demonstrated that uranium oxide catalysts show promising activity for the oxidation of hydrocarbons in the liquid phase. A patent granted to the Dow Chemical Company describes a process for the manufacture of phenol from the partial oxidation of benzene [27]. The Dow Chemical patent claims that oxides of vanadium, molybdenum, tungsten and uranium were all effective catalysts for the oxidation of benzene to phenol in the presence of aqueous sodium hydroxide. The process was operated at approximately 200 atm under air in the temperature range 320–400 °C with an alkali solution of 20–25%. Sodium benzoate was formed in the aqueous phase and the unreacted benzene remained as an immiscible organic phase. Phenol was liberated by acidification of the aqueous phase. The process was 100% selective to the mono phenol product, and the unreacted benzene was easily recycled. It is stated that the uranium oxide catalyst gave the best results, although these results are not specified. Furthermore, the nature of the uranium oxide catalyst is not clear, but the patent acknowledges the existence of several different oxides and it is implied that all have been investigated and there is no differentiation in their activity.

The vapor phase oxidation of aromatic hydrocarbons using uranium oxide catalysts is also discussed in a patent filed shortly after the liquid-phase process and was assigned to the Barrett Corporation of New Jersey [28]. Studies concentrated mainly on the oxidation of toluene, and a large range of metal oxides were investigated. Air was used as the oxidant and it was pre-mixed with toluene before passing over the catalyst maintained at standard test conditions. The conditions are not specifically stated although it is thought that they are similar to 14/1 air/toluene by weight, pressure slightly elevated above atmospheric and a temperature of 500 °C. The reactivity was classed into four groups, these are described below and the oxides contained in them are also listed:

Group 1: Relatively high benzaldehyde production and relatively low combustion oxides of tantalum, tungsten, zirconium and molybdenum.

Group 2: Relatively high benzaldehyde production and relatively high combustion oxides of manganese, chromium, copper, nickel, thorium and uranium.

Group 3: Relatively low benzaldehyde production and relatively high combustion oxides of cobalt and cerium.

Group 4: Relatively low benzaldehyde production and relatively low combustion oxides of titanium, bismuth and tin.

Table 13.2 Catalytic data for toluene oxidation using uranium oxide based catalysts [6].

Catalyst	GHSV (h^{-1})	Toluene : air	Temp (°C)	O_2 consumed in total oxidation (%)	O_2 consumed in partial oxidation (%)
UO_2WO_4	1455	0.72	445	7.8	4.8
			480	23.8	14.2
			545	50.5	26.2
$UO_2WO_4 + Al_2O_3$	1455	0.72	405	30.9	21.4
			545	62.8	28.8
UO_2MoO_4 (no support)	414	0.63	406	6.7	8.6
			430	15.2	12.4
			524	74.3	23.8
$U(MoO_4)_2$	500	0.28	385	7.1	7.1
			415	27.6	16.2
			450	68.6	29.5
$U(MoO_4)_2$			510	73.3	24.7
	492	0.16	390	15.2	8.6
			420	36.1	12.4
			470	75.3	16.2

GHSV, gas hourly space velocity.

The activity demonstrated by uranium and molybdenum was significantly better than the other catalysts in the respective groups, whilst vanadium oxide was not classified in any of the groups as it produced quantities of maleic acid and benzoic acid in addition to benzaldehyde and carbon oxides. The catalyst performance was considerably enhanced by synthesizing catalysts containing mixtures of the oxides. The catalysts were prepared by a type of impregnation technique which involved placing a support, usually pumice or asbestos, in a solution of the metal salts before evaporating the solution to dryness.

Parks and Katz [29] also carried out early studies into the oxidation of toluene to benzaldehyde and benzoic acid over a range of catalysts, concentrating on uranium, tungsten and molybdenum oxides. Reactions used an air/toluene mixture with a gas hourly space velocity ranging from ca 400–1500 $hour^{-1}$ and reaction temperatures 350–520 °C. Catalytic activity was expressed in terms of oxygen consumption to total and partial oxidation products. Selected data are presented in Table 13.2. A considerable range of catalysts were tested, and although specific yields of products are not available it is clear that the catalysts are active for oxidation. Appreciable yields of selective oxidation products were obtained when uranium oxide was used in combination with other oxides that are recognized as selective oxidation components.

In another patent also granted to the Barrett Corporation of New Jersey [30], the partial oxidation of ethanol to acetaldehyde by oxide catalysts was investigated. The patent details a process for reducing combustion by controlling the reaction temperature by means of efficient heat removal from the functioning catalyst. This was achieved by packing the catalyst in a series of tubular reactors, and is the precursor to the multi-tubular design that is used so effectively by the modern chemical industry. The majority of results are concerned with vanadium oxide as the catalyst, which at 300 °C and 0.39 sec contact time produced 70 parts acetaldehyde per 100 parts of ethanol. Acetic acid (10 parts) was also produced and only approximately 3% of the ethanol feed was combusted to carbon dioxide. No specific data were presented but it was acknowledged that many oxides, including those of uranium, were active. Cobalt, tin, cerium and titanium oxides only showed low acetaldehyde yields; all the other oxides showed reasonable yields although they were all lower than vanadium oxides. It was also highlighted that oxides of uranium, chromium, manganese and copper showed higher levels of combustion. The study was extended to include mixed oxide catalysts: one such system consisted of 93% uranium oxide and 7% molybdenum oxide, which yielded almost exclusively acetaldehyde with virtually no carbon dioxide and only a small amount of acetic acid products.

In 1932 Wietzel and Pfaundler [31] described the use of a uranium oxide based catalyst to produce *valuable hydrocarbons of low boiling point* from various sources including coal, tar and mineral oils. One example describes the use of uranium oxide in a process in which a fraction of mineral oil (BPt > 270 °C) was passed with excess hydrogen over the catalyst at 450 °C and 200 at. The actual catalytic material was fine aluminum granules activated with 1–2% of uranyl nitrate. The catalyst produced aromatics of boiling point less than 200 °C in a yield of over 80%. Uranium oxide was also cited for an example to convert bituminous coal tar (BPt 300–420 °C). The pressure was the same as in the experiments described above, with the temperature raised to 480 °C. The catalyst in this example was formed by heating aluminum gauze in ammonium vanadate and uranyl nitrate in hydrochloric acid. The resulting uranium–vanadium–aluminum catalyst was able to convert the coal tar to 70% oil.

Thus, historically, uranium oxides have been used as catalysts, and more often they have been used as catalyst components in combination with other metal oxides. Often it is difficult to identify the catalysts unambiguously: there is little characterization data in the studies, and it is most likely that the specific stoichiometries of uranium oxides quoted as catalysts are not correct. There are many other examples of the use of uranium oxides for heterogeneous catalysis and the few examples presented in this section are typical of some of the earliest uses. It is interesting to note that, although some of the work highlighted was carried out over 80 years ago, some of the aims, such as selective hydrocarbon oxidation, are still major research aims for heterogeneous catalysis today.

13.4
Catalysis by Uranium Oxides

13.4.1
Total Oxidation

One of the earlier studies investigating the total oxidation of uranium oxides concentrated on the oxidation of carbon monoxide [32]. The oxide U_3O_8 was the most active catalyst probed for the formation of carbon dioxide by oxidation by molecular oxygen. Comparison was made with V_2O_5, MoO_3 and WO_3; although these oxides are not recognized as high-activity catalysts for carbon monoxide oxidation the results indicated that U_3O_8 was a potential catalyst for total oxidation.

The oxidative destruction of volatile organic compounds (VOCs) over uranium oxides has been studied by Hutchings, Taylor and coworkers [33, 34]. Studies have shown that U_3O_8 is a highly active catalyst for the destruction of a wide range of chemically diverse VOCs. In the case of benzene oxidation over U_3O_8 a conversion of 100% at 400 °C was reached, with selectivities of 27% and 73% for CO and CO_2 respectively. Comparing these results with the total oxidation activity of Co_3O_4, a well known active combustion catalyst, it was found that even at 450 °C the conversion of benzene over Co_3O_4 was only 90%. The uranium oxide U_3O_8 was particularly active for the total oxidation of chlorinated VOCs [33]. For example, investigating the oxidation of chlorobenzene, 99.7% conversion was reached at only 350 °C with selectivity to CO_x of 100%. Furthermore, oxidation of chlorobutane at 350 °C led to 100% selectivity to CO_x with a conversion higher than 99.5%. No catalyst deactivation was observed for the oxidation of the VOCs, even for prolonged oxidation of chlorinated compounds [35].

Short-chain linear alkanes are amongst the most difficult of VOCs to destroy. A study has investigated the catalytic activity of uranium oxide catalysts for the destruction of alkanes in the C_1—C_4 range [36]. Uranium oxide, U_3O_8, showed relatively low activity for the combustion of methane and ethane and moderate activity for propane and *n*-butane. Catalyst activity was improved by supporting the uranium oxide on silica and further improvements were achieved by the addition of chromium. X-ray Diffraction (XRD), X-ray Photoelectron Spectroscopy (XPS) and Temperature-Programmed Reaction (TPR) characterization data indicated that supporting the U_3O_8 phase and adding chromium modified the structure and chemistry of the oxide. This modification may culminate in an increase of the detect structure of the oxide, resulting in the increased oxidation activity.

The effect of water addition on the complete oxidation of benzene and propane VOCs by uranium oxide catalysts has been investigated [37]. Benzene oxidation was studied using a silica-supported U_3O_8 catalyst. Complete oxidation was promoted by the addition of 2.6% water compared with the reactivity when no water was added to the reactant feed. Increasing the water concentration to 12.1% resulted in a suppression of oxidation activity. Investigation of propane oxidation using U_3O_8 showed a dramatic promotion of activity. Propane conversion was ca 50% at 600 °C without added water, whilst it increased to 100% at 400 °C with the

addition of 2.6% water. Comparison of total oxidation activity with Mn_2O_3 showed that any level of water addition suppressed conversion, and this was in clear contrast to the U_3O_8 catalyst. *In situ* powder XRD studies showed that the bulk U_3O_8 structure was stable under all the reaction conditions. The origin of the increased activity is not clear but it may be due to modification of the catalyst surface, possibly aiding the activation of the VOCs by increased hydroxylation.

A Temporal Analysis of Products (TAP) reactor has been used to investigate the mechanism of oxidation by uranium oxide catalysts [35, 38]. A combination of TAP pulse experiments with oxygen present and absent in the gas phase indicated that the lattice oxygen from the catalyst was responsible for the total oxidation activity. It was proposed that the catalyst operates by a redox mechanism using lattice oxygen and the high activity shown by U_3O_8 was due to the facile uranium redox couple and the non-stoichiometry of the oxide. Isotopically labeled oxygen studies of carbon monoxide oxidation confirmed that lattice oxygen was the active oxidant.

In a much earlier patent, the removal of organics from exhaust gases by oxidation over a supported uranium oxide catalyst was reported by Hofer and Anderson [39]. The catalyst was 4% U_3O_8 supported on alumina spheres. The authors used the incipient wetness technique to impregnate alumina with uranyl nitrate solution. In this case the catalyst precursors were calcined at 700 °C for 3 h to decompose the uranium salt. The use of other uranium compounds as starting materials was mentioned and these included uranyl acetate, uranium ammonium carbonate and uranyl chloride. The alumina-supported catalyst had a surface area of ca $400\,m^2\,g^{-1}$ and further added components, such as copper, chromium and iron, were highlighted as efficient additives to increase activity.

The catalysts were evaluated by exposure to a simulated automobile exhaust gas stream composed of 0.2% isopentane, 2% carbon monoxide, 4% oxygen and a balance of nitrogen. The temperature required to oxidize the isopentane and carbon monoxide was used to compare catalyst performance. The chromium-promoted catalyst oxidized isopentane at the lowest temperature, and a mixed chromium/copper-promoted catalyst proved the most efficient for oxidizing carbon monoxide and isopentane. It is interesting to note that the test rig used a stationary engine with 21 pounds of catalyst. Although the catalyst was very effective it is difficult to envisage uranium oxide catalysts employed for emission control of mobile sources.

13.4.2 Selective Oxidation

Uranium oxides have been investigated as catalysts and catalyst components for selective oxidation. They are more commonly used as catalyst components, but there are also reports of uranium oxide alone as a selective oxidation catalyst. The oxidation of ethylene over UO_3 has been studied by Idriss and Madhavaram [40] using the technique of temperature programmed desorption (TPD). Table 13.3 shows the desorption products formed during TPD after ethylene adsorption at room temperature on UO_3. The production of acetaldehyde from ethylene indicates

Table 13.3 Products from TPD of ethylene adsorbed on UO_3 [33].

Product	Desorption temperature (°C)	Carbon yield (%)	Carbon selectivity (%)
Ethylene	127–427	85.7	–
Acetaldehyde	207	8.3	58
Furan	277	6.0	42
CO_2	above 527	not calculated	–

the ability of UO_3 to oxidize olefins in a relatively facile manner owing to the lability of lattice oxygen. However, in this case it must be taken into account that during TPD there is no regeneration of surface reduced sites in contrast to steady-state oxidation with oxygen present in the gas phase. On the other hand, the identification of furan among the products shows that uranium oxides are active for carbon–carbon bond formation in addition to carbon–oxygen selective bond formation.

Idriss and Madhavaram [41] have also studied the partial oxidation of ethanol to furan over UO_3. The oxides U_3O_8 and UO_2 were also studied; UO_2 was inactive whilst U_3O_8 only exhibited very low activity. Using UO_3, the maximum selectivity to furan was 23% at 150 °C with a conversion of 81%, with acetaldehyde being the other major product. Comparing the reactions of ethylene and ethanol, the authors highlight two points. Firstly, no ethylene was formed during the reaction of ethanol. Secondly, acetaldehyde was formed from both ethylene and ethanol, and ethanol was formed as a trace product from ethylene oxidation. These facts were used to propose a mechanism in which the formation of furan was via an ethoxide intermediate [41].

More commonly, uranium has been used as a catalyst component for mixed-metal oxide catalysts for selective oxidation. Probably the most well known of these mixed oxide catalysts are those based on uranium and antimony. The uranium–antimony catalysts are exceptionally active and selective and they have been applied industrially. An interpretation of the catalyst structure and reaction mechanism has been reported by Grasselli and coworkers [42, 43] who discovered the catalyst. The USb_3O_{10} mixed oxide has been extensively used for the oxidation/ammoxidation reaction of propylene to acrolein and acrylonitrile. The selective ammoxidation of propylene was investigated by Grasselli and coworkers [44], and it has been demonstrated that at 460 °C a 62.0% selectivity to acrolein with a conversion of 65.2% can be achieved. Furthermore, Delobel and coworkers [45] studied the selective oxidation of propylene over USb_3O_{10}, which at 340 °C gave a selectivity to acrolein of 96.7%.

The structure of USb_3O_{10} is complex and it is crucial for selective oxidation activity. USb_3O_{10} contains one type of uranium, two types of antimony and four different types of oxygen. The unit cell is composed of eight formula weight units ($Z = 8$). The structure is composed of layers that contain heavy atoms and oxygen alternating with layers of oxygen only. Five layers of planes containing heavy metal atoms are required to completely describe the unit cell of USb_3O_{10}. It was found that there are two types of lattice oxygen in the structure, one giving high selectivity

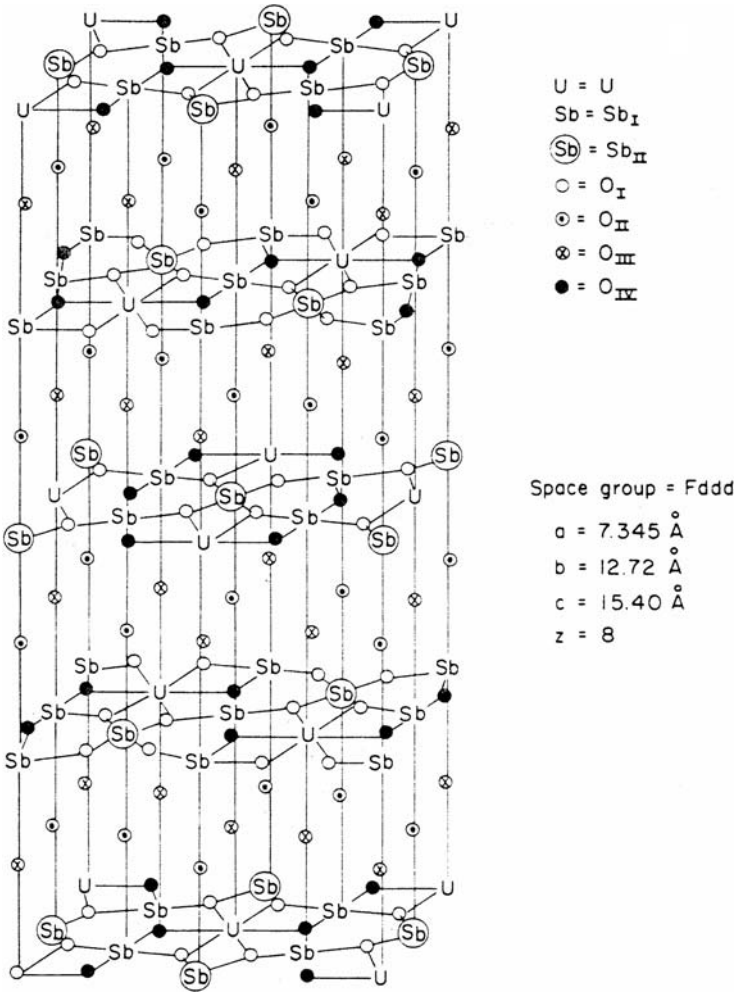

Figure 13.4 USb_3O_{10} structure. (*Journal of Catalysis*, 25 (1972), 273; reproduced by permission of Academic Press).

for partial oxidation, and the other, which was less active and tended to be less selective, producing carbon oxides. Grasselli and coworkers [43] suggested that the active oxygen was O(IV) and the less active one was O(I), as shown in Figure 13.4. The $USbO_5$ structure is very similar to that of USb_3O_{10}. $USbO_5$ has the heavy atoms at positions close to those of USb_3O_{10}, but with a slight distortion of all atoms, leading to a lower symmetry sub-group.

The $USbO_5$ phase was proposed as a precursor to the USb_3O_{10} phase, which at high temperature decomposes to give $USbO_5$. The decomposition of UO_2 $(NO_3)_2$ and oxidation of the Sb_2O_3, from which the catalyst was prepared, led to the formation of UO_3 and Sb_2O_4 respectively. On thermal treatment the antimony oxide

penetrates the lattice of UO_3 and forms the $USbO_5$ phase, according to the reactions

$$2UO_3 + Sb_2O_4 \rightarrow [2UO_3 \cdot Sb_2O_4] \rightarrow 2USbO_5$$

$$2U_3O_8 + 3Sb_2O_4 + O_2 \rightarrow [6UO_3 \cdot 3Sb_2O_4] \rightarrow 6USbO_5$$

The Sb_2O_5 phase is stabilized by the presence of the $USbO_5$ phase and further reaction proceeds to form the desired USb_3O_{10} catalytically active phase.

$$USbO_5 + Sb_2O_5 \rightarrow [USbO_5 \cdot Sb_2O_5] \rightarrow USb_3O_{10}$$

$$USbO_5 + Sb_2O_4 + \frac{1}{2}O_2 \rightarrow [USbO_5 \cdot Sb_2O_5] \rightarrow USb_3O_{10}$$

Powder X-ray diffraction studies of $USbO_5$, USb_3O_{10} and Sb_2O_4 as a function of calcination time and temperature allowed investigation of the mechanism of formation of the phases, $USbO_5$ and USb_3O_{10}. Accordingly, $USbO_5$, which was formed at about 675 °C, was considered to be the precursor of the USb_3O_{10} phase [43]. At this temperature Sb_2O_5 was also initially present and since it was not stable it reacted with $USbO_5$ to produce USb_3O_{10}. The USb_3O_{10} phase increased in concentration as the temperature was increased. At 980 °C the USb_3O_{10} phase was decomposed to re-form $USbO_5$.

The uranium–antimony oxide system remains as a basis of interest for catalysts. The preparation of a new uranyl antimonate has been described and it was prepared by hydrothermal synthesis from UO_3, Sb_2O_3 and KCl [46]. A detailed structural analysis was reported, but more importantly the $UO_2Sb_2O_4$ was selective for the oxidation of propylene to acrolein.

Some further mixed-metal oxides containing uranium, such as bismuth uranates, are known to be effective catalysts in certain selective oxidation reactions, for instance toluene partial oxidation. The oxidative demethylation of toluene using bismuth uranate as oxidant has been studied by Van deer Baan and coworkers [47] in a non-steady-state reactor. The reaction conditions were: temperature, 480 °C; pulse volume, 0.534 cm^3; mole fraction of toluene, 0.023; gas flow, 25 $cm^3 min^{-1}$ and catalysts used were samples with different Bi to U atomic ratios. Results indicated that at the reaction temperature the most active catalyst was Bi_2UO_6 with a selectivity of 70% to benzene in the absence of gas-phase oxygen. The experiments carried out showed that bismuth uranate is a very active but unselective oxidant in the very early stages of the toluene oxidation reaction. However, as soon as the catalyst starts to become depleted of oxygen the activity decreased and the selectivity increased. The reduced uranate was easily reoxidized by molecular oxygen in a second step. The mechanism proposed for this reaction was a redox mechanism, which occurred via a benzoate-like intermediate. It was stated that the oxidation of toluene gave two main products: benzaldehyde, which dissociated to benzene and carbon monoxide and benzoic acid, which also dissociated to produce benzene and carbon dioxide.

In a more detailed study of bismuth uranate reduction by toluene using pulsed flow and steady-state flow, further insight into the mechanism of oxidation was obtained [48]. In the temperature range 455–527 °C, Bi_2UO_6 was reduced by toluene to metallic bismuth and UO_2. The reaction rate was related to the surface reaction rate and the rate of diffusion of oxygen through the lattice. It was apparent that Bi_2UO_6 contained two types of reactive lattice oxygen. The first was a nonselective species that was ca. 2% of the total lattice oxygen and it showed activation for diffusion of ca. 107 kJ mol^{-1}. The second type was a species responsible for selective oxidation and had a diffusion energy of ca. 261 kJ mol^{-1} at 470 °C. Evidence for the formation of shear planes in the Bi_2UO_6 structure was presented and the relatively small concentration of nonselective oxygen was thought to be from positions in the shear planes.

The oxidation of carbon monoxide to carbon dioxide using similar bismuth uranate catalysts has been reported by Derouane and coworkers [49]. The work on carbon monoxide oxidation confirmed that the bismuth uranate catalyst operated by a redox mechanism. These studies on bismuth uranates highlight the important role played by oxygen transfer via the lattice, and reinforce the importance of the ability of uranium to exhibit relatively facile redox behavior.

The selective oxidation of toluene has been studied over a number of catalysts based on metal oxides, with the U/Mo oxide system being one of the most active and selective[50, 51]. The main products in the oxidation of toluene, excluding the non-oxidative coupling products, were benzaldehyde, benzoic acid, maleic anhydride, benzene, benzoquinone, CO and CO_2. Under the same reaction conditions toluene may also yield coupling products such as phthalic anhydride, methyldiphenylmethane, benzophenone, diphenylethanone and anthraquinone, as shown by Zhu and coworkers [51]. A range of different uranium-based oxides were tested [51] and the results obtained are shown in Table 13.4.

Table 13.4 Conversion and selectivity data for toluene oxidation using U-based mixed oxides at 500 °C [51].

Catalyst (atomic ratio)	Contact time (s)	Conversion (%)	Benzaldehyde selectivity (%)	Benzaldehyde yield (mol%)
U alone	0.065	21.4	90	19.3
	0.200	47.6	69	32.1
	0.320	66.0	49	32.0
	0.400	77.4	47	35.8
U:P (8:2)	0.032	37.8	47	17.6
	0.065	54.2	38	15.4
U:W (9:1)	0.032	38.4	69	26.4
U:V (9:1)	0.032	48.4	54	26.4
U:Sb (1:4)	1.3	11.0	50	5.6

Under the reaction conditions used, a U_3O_8 catalyst demonstrated appreciable selective oxidation activity. The best results, in terms of both activity and selectivity to benzaldehyde, were obtained with the mixed oxides with U : Mo atomic ratios in the range 8 : 2 to 9 : 1. The maximum yield of benzaldehyde was 40 mol%. On the other hand, antimony-based uranium oxides were not found to be effective as catalyst for this reaction. U—Mo and Bi—Mo mixtures also exhibited promising activity and selectivity to benzaldehyde. Bi—Mo and Bi—Mo—P—Si catalysts were also tested. Qualitatively there was little difference between the product distributions from the two catalysts. The major products formed were benzaldehyde, benzene and carbon oxides, as well as traces of anthraquinone and benzoic acid.

Perhaps one of the most demanding selective oxidation reactions is the oxidation of methane to the oxygenates formaldehyde and methanol. Although the use of uranium as a catalyst component for selective methane partial oxidation is relatively rare, there is one notable attempt. Dowden and Walker reported the activity of a range of two-component catalysts, one component of which was molybdenum [52]. They developed these catalysts based on the principles outlined by the proposal of a virtual mechanism [53]. Results were reported for MoO_3/ZnO, $(MoO_3)_4/Fe_2O_3$, MoO_3/VO_2 and MoO_3/UO_2 supported on 1 : 3 $Al_2O_3 : SiO_2$ with a low area of ca. $0.1\,m^2\,g^{-1}$, containing ca. 5% active oxide. Experimental conditions were 30 bar pressure with a $CH_4 : O_2$ ratio of 97 : 3 in the temperature range 430–500 °C. In order to maintain high selectivity to CH_3OH the reactor effluent was cooled to below 200 °C within 0.03 s of leaving the heated catalyst bed, by the injection of cooling water. Although the most successful catalyst was the mixed oxide of molybdenum and iron, which gave yields of 869 g (kg cat)$^{-1}$ h^{-1} and 100 g (kg cat)$^{-1}$ h^{-1} of CH_3OH and HCHO respectively, these were only marginally greater than the yields from the molybdenum–uranium oxide catalyst.

A study has been undertaken to compare the effectiveness of molybdenum and uranium oxide and iron sodalite catalysts with the homogeneous gas-phase oxidation of methane [54]. Catalyst performance was evaluated in a high-pressure annular reactor and data were compared to the reactivity of the empty reactor. It was concluded that none of the catalysts gave any advantage over the homogeneous reaction. Indeed, using a catalyst only reduced the selectivity to the desired partial oxidation products. Similar conclusions have been reached for many catalysts used for the partial oxidation of methane, and therefore it is perhaps not surprising that uranium oxide catalysts are no different.

Catalysts using molybdenum and uranium oxides have also been used for selective oxidation of other alkanes. The partial oxidation of isobutane over MoO_3—UO_3—SiO_2 was studied by Corma and coworkers [55], and led to the formation of a range of oxygenated hydrocarbons. The primary products formed in this reaction were methallyl alcohol, methacrolein, acetone and biacetyl. In addition, a large number of secondary products were obtained, such as acetic acid, ethanal, formic acid, methanal, and methacrylic acid. Total oxidation to carbon oxides was also determined. The best performance of the silica-supported MoO_3/UO_3 catalyst was obtained at 380 °C, with an oxygen : isobutene ratio of 12 : 1, to produce a 45% selectivity to methacrolein and 10% to acetone.

Taylor and coworkers demonstrated that catalysts of iron and uranium oxide were effective for the selective oxidation of propane and propene to formaldehyde [56]. Catalysts were prepared by co-precipitation and were most effective when prepared with Fe : U ratios of 0.5 : 3 and 1 : 3. It was possible to achieve 44% selectivity towards formaldehyde at 450 °C with a 42% conversion. The balance of the products was carbon oxides. Characterization of the catalysts showed that they were composed of iron oxide highly dispersed on UO_3, and it was a combination of the highly dispersed iron oxide and the UO_3 that was responsible for the selective oxidation. The mechanism of formaldehyde production is not clear, but there are other studies in the literature reporting similar observations. Oxidation of propane over highly dispersed iron oxide supported on SiO_2 showed the formation of formaldehyde [57]. Lee and coworkers have also shown that formaldehyde is produced during the oxidation of isobutene using a urania–titania catalyst [58]. Supporting the uranium oxide on titania modified the redox behavior of the uranium component and this modification was responsible for the enhanced selective oxidation function.

In recent years, interest in the use of gold-based catalysts has expanded considerably. In particular, the potential of gold catalysts for selective oxidation now receives significant attention. Gold-based catalysts supported on a wide range of materials have been prepared and tested for a wide range of reactions. Choudhary and coworkers have used nanoparticles of gold supported on U_3O_8 for the selective oxidation of benzyl alcohol to benzaldehyde by molecular oxygen in solvent-free conditions [59]. Variations of catalyst preparation conditions and reaction conditions were studied. The best catalysts were those with high gold loadings and small gold particles. Increasing the reaction temperature or time increased benzyl alcohol conversion, whilst benzaldehyde selectivity decreased and benzyl benzoate selectivity increased. The addition of a range of solvents was deleterious for catalyst performance.

13.4.3 Reduction

The versatility of uranium oxides in functioning as catalysts for a range of reactions is demonstrated by their ability to catalyze a range of reduction reactions, although primarily they have been used for oxidation. The reduction of acetaldehyde on UO_2, prepared by reduction of UO_3 with hydrogen, has been studied by Idriss and coworkers [40] using TPD. The formation of C_4 olefins indicated the ability of UO_2 surfaces to abstract large amounts of oxygen from carbonyl species bound to the surface. This functionality was due to the ability of the fluorite structure of UO_2 to readily abstract and accommodate a considerable quantity of oxygen in vacant sites in the oxide lattice. As discussed in Section 13.2, this behavior is well known and is a specific feature of the structure of UO_2.

More recently, Madhavaram and Idriss studied the reactions of acetaldehyde over the oxides UO_2, α-U_3O_8 and β-UO_3 [60]. The products were strongly dependent on the U : O ratio of the oxide. In agreement with earlier work, UO_2 showed activity for reductive coupling to produce C_4 olefins, whilst U_3O_8 produced predominantly crotonaldehyde by aldol condensation. It was possible to produce both

furan and crotonaldehyde over UO_3, and stoichiometric reactions using TPD demonstrated that the type of product was related to the surface coverage. At low surface coverage of acetaldehyde, furan was predominant and the product distribution shifted to furan and crotonaldehyde as the surface coverage increased. The mode of acetaldehyde adsorption was studied by FTIR, and distinctly different modes were identified depending on the uranium oxide catalyst. The differences in products over the oxides have been explained in terms of the possible adsorption modes and the variation in the semiconductor properties of the different oxides.

Two further reduction reactions of interest are the TPD of acetone over U_3O_8, the principal product being isobutene, and over UO_2 forming mainly propylene [61]. Again a significant difference between the two uranium oxides used for these reactions resides in the fact that, in the first case, U_3O_8 reacted leading to C—C bond formation to give a C_4 olefin. However, over UO_2 the main product was propylene, once again showing the ability of UO_2 to accommodate excess oxygen in its fluorite structure.

The dehydrogenation of ethylbenzene is an important process used for styrene manufacture, and uranium oxide catalysts have been investigated for this reaction. A catalyst of uranium dioxide supported on alumina showed high selectivity to styrene of 96% at high conversion [62, 63]. The catalyst was synthesized as a higher oxide of uranium and initially it was not UO_2. Consequently, over the initial on-stream period only carbon dioxide and water were observed, as the catalyst produced total oxidation products. However, as the reaction preceeded the uranium oxide was reduced *in situ* by the ethylbenzene and hydrogen to form the active UO_2 phase. It was only when the uranium oxide was fully reduced to UO_2 that styrene was produced with high selectivity.

Nickel catalysts supported on uranium oxides have been reported for the hydrogenation of carbon dioxide to methane [64, 65]. The catalysts were selective below 500 °C, as CO was the major product at higher temperatures. The nickel was deposited on the catalysts by evaporation and the reduction characteristics of the catalysts were complex, depending on the calcination conditions and the metal content. The uranium oxide support had a crucial role in maintaining the high dispersion of the active nickel by preventing sintering. The most active catalysts were those with the highest stable nickel surface areas.

Uranium oxide catalysts have largely been employed for the reduction of organic species but, in a series of interesting studies, a uranium oxide catalyst has also been used for the reduction of NO_x and simultaneous oxidation of CO [66]. Studies showed that NO_x was converted to N_2 with 100% selectivity under favorable reaction conditions. Using a mixture of 4%NO, 4%CO with a balance of He, different uranium oxides were tested in a fixed bed micro-reactor. The results obtained are shown in Table 13.5, and compared with a conventional supported Pt catalyst.

At lower temperatures, reduction of NO produced N_2O as the major product, whereas an increase of reaction temperature not only enhanced NO conversion but generally improved selectivity, as the only product obtained was N_2.

More-detailed studies of uranium-based catalysts for NO_x reduction and CO oxidation have been published and concentrate on catalyst characterization [67]

Table 13.5 NO conversion and selectivity to N_2 over uranium oxide catalysts [66].

Catalyst	Conversion (%)	Selectivity (%)	Temperature (°C)
U_3O_8	100	100	800
$U_3O_8/\gamma\text{-}Al_2O_3$ 800 °C[a)]	100	100	400
$U_3O_8/\gamma\text{-}Al_2O_3$ 450 °C[a)]	100	100	400
$Pt/\gamma\text{-}Al_2O_3$	10	100	250
	100	35	400

a Calcination temperature.

and catalyst performance [68]. Catalysts were prepared from the precursors uranyl nitrate and uranium(IV) chloride, which were supported on $\gamma\text{-}Al_2O_3$, SiO_2 and mesoporous SiO_2. Both the support and the uranium oxide precursor were found to influence the nature of the catalyst. Calcination of the mesoporous SiO_2 supported material at 800 °C resulted in significant extrusion of the uranium from the support, resulting in the formation of large orthorhombic domains of U_3O_8. The formation of a U_3O_8 phase was promoted on the mesoporous support and by the presence of chloride. On the silica and alumina supports hexagonal U_3O_8 was formed, with the presence of chloride inhibiting the growth of larger uranium oxide domains on all the catalysts.

Calcination of the uranium oxide mesoporous SiO_2 supported catalyst resulted in sintering of the active uranium oxide phase into larger particles and this was detrimental to catalytic activity. However, preparing the mesoporous supported catalysts from uranyl nitrate using thermal treatment in dilute CO/O_2 or CO/NO resulted in the best catalysts with high activity comparable to a Pt/Al_2O_3 catalyst. The rate expression for the best catalyst was zero order with respect to NO and showed an order of 1.4 with respect to CO. This was in clear contrast to the reaction over bulk U_3O_8, which was dependent solely on the NO concentration. For the majority of catalysts the presence of residual chloride resulted in lower activity. The exception was the $\gamma\text{-}Al_2O_3$ supported catalyst prepared from the chloride precursor and thermally treated at 600 °C in dilute CO/O_2. It was possible to correlate the catalytic activity with the residual chloride content and the average crystallite size of the supported uranium oxide.

13.4.4 Steam Reforming

Nicklin, with others, filed several early patents describing the use of uranium oxides as steam reforming catalysts [69]. U_3O_8 was used along with nickel oxide as the basis of a steam reforming catalyst, and it was modified with potassium species (potassium hydroxide, potassium oxide and/or potassium carbonate), all supported on either alumina or a mix of alumina and magnesium oxide. The uranium and nickel catalysts proved to be extremely efficient for steam reforming.

In later work Nicklin describes a reduction–oxidation cycle that was used to treat the catalysts prior to use [70]. Four to six cycles were performed, with the oxidation

taking place at 600–650 °C and the reduction at temperatures no higher than 600 °C (preferably not above 550 °C). The gases used for these processes were hydrogen and oxygen for the reduction and oxidation steps respectively. The catalyst studied in this patent differed from the previous work, as additional UO_3 was present in the catalyst. The reduction–oxidation step was added to enhance catalyst activity compared to the earlier work. The authors observed that during the oxidation part of the process cycle the amount of oxygen used must be reduced with each successive oxidation to prevent the catalyst becoming highly pyrophoric.

A later patent presents more details of catalyst performance and specific details of the preparation and composition of the catalyst [71]. The supported catalyst used was composed of nickel (23.20%), uranium (11.45%) and potassium (0.23%). A naphtha stream was used to determine catalyst activity. A steam : naphtha ratio of 3.8 : 1 was employed at a pressure of ca. 11 bar and a gas hourly space velocity of 2058 h^{-1}. The temperature of the inlet gas was 465 °C, whilst the temperature of the outlet gas was 756 °C. The outlet of the reactor contained methane, carbon monoxide, carbon dioxide and hydrogen in the proportions $CH_4 : CO : CO_2 : H_2 = 6.7 : 12.5 : 14.6 : 66.0$.

Results of experiments varying the ratio of uranium to nickel showed that the ratios giving the largest surface area and catalyst volume were in the range 0.45–0.76 (U : Ni). These two characteristics were the most important for activity for these reactions. The catalysts were in a reduced state, which could explain the addition of the reduction–oxidation step in the previous patent. A further reason for using catalysts in the 0.45–0.74 U : Ni range was that the catalyst demonstrated greatest resistance to coke deposition at a ratio of 0.71 : 1.

Gavin [72] has studied similar catalysts to Nicklin and coworkers for steam reforming. It has been suggested that the nickel and uranium combine to form a nickel uranate phase ($NiO \cdot 3UO_3$). Once the catalysts were reduced, the active components were nickel from excess nickel oxide, nickel from the nickel uranate and tetra-uranium oxide (U_4O_9). Gavin described how the composition of the catalyst affected the amount of $NiO \cdot 3UO_3$. The relationship between the catalyst composition and activity for steam reforming is shown in Table 13.6.

Table 13.6 Activity of nickel–uranium oxide catalysts for steam reforming of naphtha [72].

Catalyst composition (%)				Relative amount of $NiO \cdot 3UO_3$	Conversion (%)
Ni	U	Ba	K		
11.0	7.0	0	0	9.1	100.0
11.7	7.6	1.5	0	4.6	100.0
11.7	7.7	1.6	0	5.2	99.0
11.3	7.4	2.11	0	5.0	98.5
10.9	6.7	2.12	0	3.6	95.6
10.6	7.2	0	0.59	3.6	93.0
12.0	7.9	1.72	0.50	2.0	90.0

The presence of the alkaline components is essential and they are converted into carbonates by heating in carbon dioxide during the catalyst preparation. It is argued that as the concentration of the alkaline component increased there was increased likelihood that the nickel uranate phase would react to produce barium uranate (BaU_2O_7) and NiO. The barium and potassium were also thought to reduce the tendency of coking on the catalyst surface, and their concentration is a balance between their efficacy for producing the most active phases and reducing coke formation.

Despite the earlier patent reports of the suitability of nickel-based catalysts incorporating uranium oxide for steam reforming, uranium did not become a component of commercial steam reforming catalysts. Nevertheless, interest has continued in assessing the efficacy of uranium oxide as a steam reforming catalyst component. Gordeva and coworkers prepared relatively porous oxides of UO_2 and U_3O_8 as supports for nickel and ruthenium as catalysts for methane steam reforming [73].The catalysts were designed so that they could be used for conversion of nuclear energy to chemical energy by the production of hydrogen. High production rates of hydrogen were observed at 1 bar pressure and temperatures of 600–700 °C. Under operating conditions in a nuclear reactor, fissile products would be expected to contaminate the syngas. In order to try and limit contamination, studies also investigated containing the uranium oxide within a thin coating of MgO/Al_2O_3. The influence of the coating on catalyst activity is not clear and catalysts to be used for such advanced processes would clearly need further development. However, uranium oxide based catalysts are ideal for applications of this type, owing to their fissile properties and the knowledge base that is already in place because of the use of uranium oxides by the nuclear industry.

13.5 Conclusions

Uranium oxides have been used as catalysts and catalyst components for a relatively wide range of reactions. The oxides of uranium are numerous, with the main oxides being UO_2, U_3O_8 and UO_3. The structures of the oxides can be complex, as can the relationship between the phases. However, the oxides have many properties that make them versatile catalysts and catalyst components. Uranium oxides have been most widely applied as catalysts for oxidation reactions, and these include total oxidation and partial oxidation. Uranium oxide based catalysts have demonstrated excellent performance for selective oxidation and have been used commercially, although this is no longer the case. Uranium oxides have also been employed as catalysts for a range of reduction reactions and for steam reforming. The use of uranium oxides as catalysts may be a controversial issue; however, depleted uranium oxide is relatively widely available. The main concern in using uranium as a catalyst component is associated with its toxicity, which is comparable with that of lead, and it must be handled accordingly.

Acknowledgments

The author would like to thank Dr Maria-Luisa Palacios and Dr Richard Harris.

References

1 Allen, G.C. and Tempest, P.A. (1982) *Journal of the Chemical Society, Dalton Transactions*, 2169.
2 Allen, G.C. and Holmes, N.R. (1995) *Journal of Nuclear Materials*, **223**, 231.
3 Cordfunke, E.H.P. (1969) *The Chemistry of Uranium*, Elsevier, New York.
4 Lynds, L., Young, W.A., Mohl, J.S. and Liebowitz, G.G. (1962) *Nonstoichiometric compounds*, ACS Advances in Chemistry Series (ed. R.F. Gould), American Chemical Society, vol. 39, p. 58.
5 Vanlierde, W., Pelsmaekers, J. and Lecocq-Robert, A. (1970) *Journal of Nuclear Materials*, **37**, 276.
6 Belbeoch, B., Boivineau, J.C. and Perio, P. (1967) *Journal of Physics and Chemistry of Solids*, **28**, 1267.
7 Westrum, E.F. and Gronvold, F. (1962) *Journal of Physics and Chemistry of Solids*, **23**, 39.
8 Hoekstra, T.H.R., Siegel, S. and Gallagher, F.X. (1970) *Journal of Inorganic and Nuclear Chemistry*, **32**, 3237.
9 Hoekstra, H.R., Siegel, S. and Charpin, P. (1968) *Journal of Inorganic and Nuclear Chemistry*, **30**, 519.
10 Rundle, R.E., Baeziger, N.C., Wilson, A.S. and MacDonald, R.A. (1948) *Journal of the American Chemical Society*, **70**, 99.
11 Loopstra, B.O. (1964) *Acta Crystallographia*, **17**, 651.
12 Ball, R.G.J. and Dickens, P.G. (1991) *Journal of Materials Chemistry*, **1**, 105.
13 Loopstra, B.O. (1970) *Acta Crystallographia*, **B26**, 656.
14 Hoekstra, H.R. and Siegel, S. (1961) *Journal of Inorganic and Nuclear Chemistry*, **18**, 154.
15 Greaves, C. and Fender, B.E.F. (1972) *Acta Crystallographia*, **28**, 3609.
16 Debets, P.C. (1966) *Acta Crystallographia*, **21**, 589.
17 Loopstra, B.O., Taylor, J.C. and Waugh, A.B. (1977) *Journal of Solid State Chemistry*, **20**, 9.
18 Wait, E. (1955) *Journal of Inorganic and Nuclear Chemistry*, **1**, 309.
19 Kovba, L.M., Viadavskii, L.M. and Labut, E.L. (1963) *Zhurnal Strukturnoi Khimii*, **4**, 627.
20 Siegel, S., Hoekstra, H.R. and Sherry, E. (1966) *Acta Crystallographia*, **20**, 292.
21 Allen, G.C. and Tempest, P.A. (1983) *Journal of the Chemical Society, Dalton Transactions*, **267**, 7.
22 Colmenares, C.A. (1984) *Progress in Solid State Chemistry*, **12**, 257.
23 Willis, B.T.M. (1964) *Proceedings of the British Ceramic Society*, **1**, 9.
24 Willis, B.T.M. (1978) *Acta Crystallographia*, **A34**, 88.
25 Catlow, C.R.A. (1977) *Proceedings of the Royal Society of London*, **A353**, 533.
26 James, J.H. (1922) *Chemical and Metallurgical Engineering*, **26**, 209.
27 Hall, W.J. (1926) US Patent 1,595,299, August 10, 1926.
28 Craver, A.E. (1927) US Patent 1,636,954, July 26, 1927.
29 Parks, W.G. and Katz, J. (1933) *Industrial and Engineering Chemistry*, **28**, 3193.
30 Craver, A.E. (1927) US Patent 1,636,952, July 26, 1927.
31 Wietzel, R. and Pfaundler, C. (1932) US Patent 1,844,998, February 16, 1932.
32 Nozaki, F. and Ohki, K. (1972) *Bulletin of the Chemical Society of Japan*, **45**, 3473.
33 Hutchings, G.J., Heneghan, C.S., Hudson, I.D. and Taylor, S.H. (1996) *Nature*, **384**, 341.
34 Hutchings, G.J., Heneghan, C.S., Hudson, I.D. and Taylor, S.H. (1996) *Heterogeneous Hydrocarbon Oxidation* (eds B.K. Warren and S.T. Oyama), ACS Symposium Series, ACS, Washington, DC, vol. 638, p. 58.

35 Taylor, S.H., Heneghan, C.S., Hutchings, G.J. and Hudson, I.D. (2000) *Catalysis Today*, **59**, 249.

36 Taylor, S.H. and O'Leary, S.R. (2000) *Applied Catalysis B*, **25**, 137.

37 Harris, R., Hutchings, G.J., Boyd, V.J. and Taylor, S.H. (2002) *Catalysis Letters*, **78**, 369.

38 Heneghan, C.S., Hutchings, G.J., O'Leary, S.R., Taylor, S.H., Boyd, V.J. and Hudson, I.D. (1999) *Catalysis Today*, **54**, 3.

39 Hofer, L.J.E. and Anderson, R.B. (1964) US Patent 3,140,148, July 7, 1964.

40 Madhavaram, H. and Idriss, H. (1997) *Studies in Surface Science and Catalysis*, **110**, 265.

41 Madhavaram, H. and Idriss, H. (1999) *Journal of Catalysis*, **184**, 553.

42 Grasselli, R.K., Suresh, D.D. and Knox, K. (1970) *Journal of Catalysis*, **18**, 356.

43 Grasselli, R.K. and Suresh, D.D. (1972) *Journal of Catalysis*, **25**, 273.

44 Grasselli, R.K. and Callahan, J.L. (1969) *Journal of Catalysis*, **14**, 93.

45 Delobel, R., Baussart, H., Le Bras, M., Le Maguer, D. and Leroy, J.M. (1982) *Journal of the Chemical Society, Faraday Transactions*, **78**, 485.

46 Sykora, R.E., King, J.E., Illies, A.J. and Albrecht-Schmitt, T.E. (2004) *Journal of Solid State Chemistry*, **177**, 17170.

47 Van der Baan, H.S., Steenhof, J.G., De Jong, J.G. and Guffens, C.H.E. (1972) *Journal of Catalysis*, **26**, 401.

48 Steenhof, J.G., Guffens, C.H.E. and Van der Baan, H.S. (1973) *Journal of Catalysis*, **32**, 149.

49 Collette, H., Derouane, E.G., Verbist, J.J., Deremince-Mathieu, V. and Nagy, J.B. (1987) *Journal of the Chemical Society, Faraday Transactions*, **83**, 1263.

50 Ai, M. (1991) *Heterogeneous Catalysis and Fine Chemicals II*, Elsevier Science Publishers B.V, Amsterdam, pp. 423–30.

51 Zhu, J. and Anderson, S.L.T. (1989) *Journal of the Chemical Society, Faraday Transactions*, **85**, 3629.

52 Dowden, D.A. and Walker, G.T. (1971) UK Patent 1,244,001, August, 1971.

53 Dowden, D.A., Schnell, C.R. and Walker, G.T. (1968) *Proceedings of the 4th International Congress on Catalysis, Moscow*, Paper 62, pp. 201–15.

54 Walker, G.S., Lapszewicz, J.A. and Foulds, G.A. (1994) *Catalysis Today*, **21**, 519.

55 Corma, A., Corberán, V.C. and Kremeric, G. (1984) *Industrial & Engineering Chemistry Product Research and Development*, **23**, 546.

56 Taylor, S.H., Hutchings, G.J., Palacios, M. and Lee, D.F. (2003) *Catalysis Today*, **81**, 171.

57 Teng, Y. and Kobayashi, T. (1998) *Catalysis Letters*, **55**, 33.

58 Lee, A.F., Sears, P.J., Pollington, S.D., Overton, T.L., Wells, P.B. and Lee, D.F. (2000) *Catalysis Letters*, **70**, 183.

59 Choudhary, V.R., Jha, R. and Jana, P. (2007) *Green Chemistry*, **9**, 267.

60 Madhavaram, H. and Idriss, H. (2004) *Journal of Catalysis*, **224**, 3589.

61 Madhavaram, H., Buchanan, P. and Idriss, H. (1997) *Journal of Vacuum Science and Technology A*, **15**, 1685.

62 Heynen, H.W.G. and Van der Baan, H.S. (1974) *Journal of Catalysis*, **34**, 167.

63 Heynen, H.W.G., Van der Baan, H.S. and Camp-van Berkel, C.G.M.M. (1977) *Journal of Catalysis*, **48**, 386.

64 Berry, F.J., Murray, A. and Parkyns, N.D. (1993) *Applied Catalysis A*, **100**, 131.

65 Berry, F.J., Murray, A. and Steel, A.T. (1998) *Journal of the Chemical Society, Faraday Transactions*, **84**, 2783.

66 Pollington, S.D., Lee, A.D., Overton, T.L., Sears, P.J., Wells, P.B., Hawley, S.E., Hudson, I.D., Lee, D.F. and Ruddock, V.J. (1999) *Journal of the Chemical Society, Chemical Communications*, 725.

67 Campbell, T., Newton, M.A., Boyd, V., Lee, D.F. and Evans, J. (2005) *Journal of Physical Chemistry B*, **109**, 2085.

68 Campbell, T., Newton, M.A., Boyd, V., Lee, D.F. and Evans, J. (2006) *Journal of Molecular Catalysis A*, **245**, 62.

69 Nicklin, T. and Burgess, K.H. (1970) GB Patent 1,198,991, July 15, 1970.

70 Nicklin, T., Clack, J. and Burges, K.H. (1971) US Patent 3,630,967, January 1, 1971.

71 Nicklin, T. and Farrington, F. (1974) US Patent 3,847,836, November 12, 1974.

72 Gavin, D.G. (1974) US Patent 3,974,098, 1974.

73 Gordeva, L.G., Moroz, Y.I. Aristov, E.M., Rudina, N.A., Zaikovskii, V.I., Tanashev, Y.Y. and Parmon, V.M. (1995) *Journal of Nuclear Materials*, **218**, 202.

14
Heteropolyoxometallate Catalysts for Partial Oxidation

Jacques C. Védrine and Jean-Marc M. Millet

14.1
Introduction

Polyoxometallates (POMs) are a large class of nanosized transition metal–oxygen clusters [1]. Their structures, sizes and properties correspond to compounds intermediate between molecules and oxides. They are composed of anions having metal–oxygen octahedra as the basic structural unit. The octahedra are linked together to yield a stable and compact skeleton of polymeric oxoanions formed by the condensation of mononuclear oxoanions (isopolyanions) or of more than two different mononuclear oxoanions (heteropolyanions) in acidic media as shown in the equation:

$$p[XO_r]^{x-2r} + q[MO_n]^{m-2n} + zH^+ \rightarrow X_pM_qO_s^{(p\cdot x+m\cdot q-z\cdot s)} + (z/2)H_2O$$

with M = metal (designated as addenda atom), X = heteroatom, x = the valency of the heteroatom, m = the valency of the addenda atom and $s + (z/2) = n\cdot q + r\cdot p$ (oxygen balance). The elements M that can act as addenda atoms in heteropoly or isopolyanions are limited to those with both a favorable combination of ionic radius and charge and the ability to form dπ–pπ M—O bonds. However, there are no such restrictions for the heteroatom X. The most common addenda atoms are molybdenum or tungsten and, less frequently, tantalum, vanadium and niobium, or mixtures of these elements in their highest oxidation state (d^0) [2]. In principle all the elements of the periodic table could act as heteroatoms, though the most usual are P^V, As^V, Si^{IV}, Ge^{IV}, Ce^{IV}, Th^{IV}, B^{3+}, Co^{3+}, Al^{3+}, Cr^{3+}, and so on. The counter ions, required to charge balance the anions, may be protons, alkali metals or other metal cations.

More than twenty types of structure, incorporating from four to forty metal atoms and from one to nine heteroatoms are known. There are five general types of POM, namely (i) the "Lindqvist" structure (O_h symmetry of six MoO_6 edge-shared octahedra) $[M_6O_{19}]^{n-}$; (ii) the "Keggin" structure, α-$[(XO_4)M_{12}O_{36}]^{n-}$ (T_d symmetry of four M_3O_{13} groups of three MO_6 octahedra), (iii) the "Dawson" structure

Metal Oxide Catalysis. Edited by S. David Jackson and Justin S. J. Hargreaves

ISBN: 978-3-527-31815-5

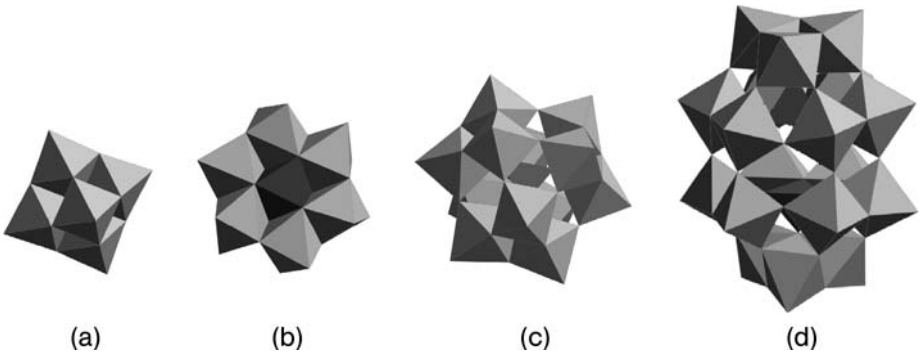

Figure 14.1 Types of polyoxometallates formed by different arrangements of MO_6 octahedra. (a) Lindqvist, (b) Anderson, (c) Keggin, (d) Dawson.

α-$[(XO_4)_2M_{12}O_{54}]^{n-}$ (D_{3h} symmetry of two "Keggin" fragments α-XM_9O_{34}), (iv) the "Anderson" structure $[H_x(XO_6)M_6O_{18}]^{n-}$ (D_{3h} symmetry planar arrangement of seven edge-shared MO_6 octahedra), (v) the $[(XO_{12})M_{12}O_{30}]$ structure (I_h symmetry with an XO_{12} icosahedron surrounded by six equivalent M_2O_9 groups of face-shared MO_6 octahedra, linked together by corner-sharing tetravalent cations). A schematic drawing of the first four types is presented in Figure 14.1.

The most common compounds, particularly for catalytic application, belong to the 12 series (M/X = 12) and are Keggin-type heteropolyacids (HPA), as they are the most stable, are more easily available and have been studied in more detail. The well defined Keggin structure comprises a central XO_4 tetrahedron surrounded by twelve edge- and corner-sharing metal–oxygen octahedra (MO_6) units as shown in Figure 14.2. They contain heterododecametallate anions with the formula

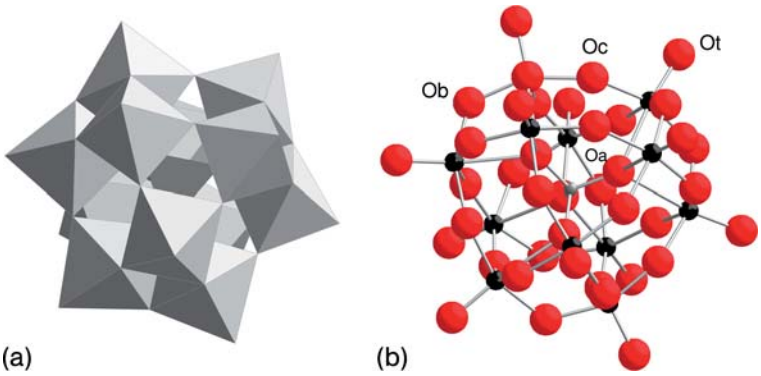

Figure 14.2 Schematic representations of the Keggin anion showing the four distinct oxygen sites. (a) Polyhedral, (b) ball and stick.

$[XM_{12}O_4]^{x-8}$ where x is the oxidation degree of the central heteroatom X. The addenda atoms, M (Mo^{VI}, W^{VI}), can be partly replaced by other metals, in particular by Ta^{V}, V^{V} and Nb^{V}, resulting in a change of the anionic charge (one per substituted metal atom) and thus also in the number of counter-cations. These compounds are nearly always negatively charged and their negative charge density is variable depending on their elemental composition and molecular structure.

Solid POMs have a hierarchical structure and can be divided into three sub-structures [3], namely: primary, secondary and tertiary, as shown in Figure 14.3. These structures are important for understanding their heterogeneous catalytic properties. The primary structure is the structure of the heteropolyanion itself, that is the metal oxide cluster. The secondary structure is the three-dimensional arrangement consisting of polyanions, counter-cations and additional molecules (in particular organic molecules or water clusters such as $H_5O_2^+$, hydrated species, or dimethyl sulfoxide (DMSO) in $H_4SiW_{12}O_{40} \cdot 9DMSO$ and pyridine in $PW_{12}O_{40} \cdot [(C_5H_5N)_2H]_3$). The tertiary structure is the arrangement by which the secondary structure assembles into solid particles, and this relates to properties

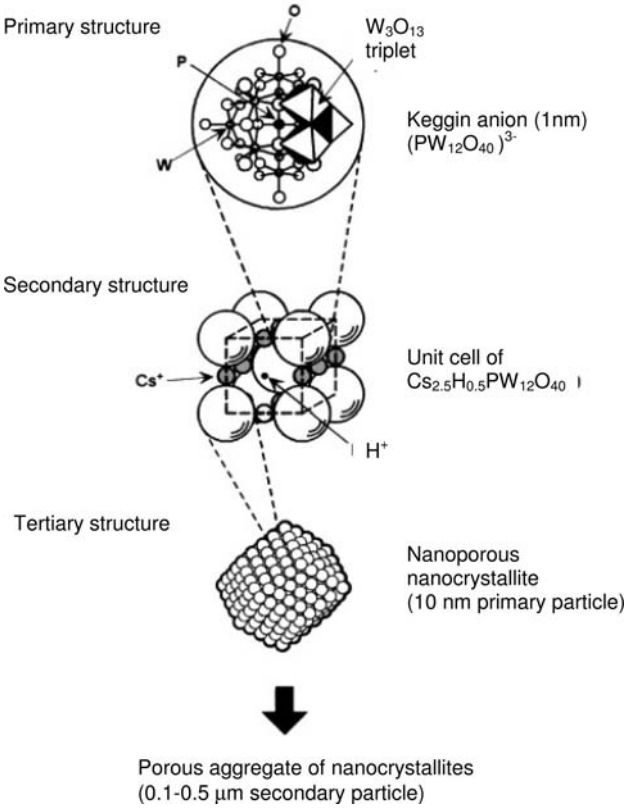

Figure 14.3 Primary, secondary and tertiary structures. (Taken from figure 14.2 in Ref. [3]).

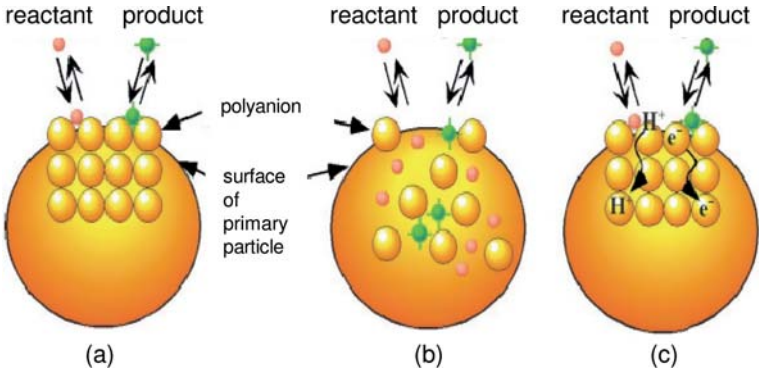

Figure 14.4 Types of catalysis in solid heteropoly compounds. (a) Surface, (b), pseudo-liquid bulk type (I), (c) bulk-type (II). (Taken from Ref. [3]).

such as particle size, surface area and porosity. Based on this hierarchical structure, it was demonstrated that there are three different modes of catalysis: surface-type catalysis, pseudo-liquid bulk-type catalysis and bulk-type catalysis, as represented in Figure 14.4. Surface-type catalysis corresponds to ordinary heterogeneous catalysis, which takes place on the outer surface of the solid. The other two types of catalysis are bulk-type and occur when the diffusion of reactant molecules in the solid (diffusion into the lattice rather than into the pores) is faster than the reaction. The solid bulk forms a pseudo-liquid phase in which catalytic reaction can proceed. Thus the catalyst appears solid but behaves like a liquid (solvent). As the active sites in the bulk, for example protons or transition metals, take part in catalysis, very high catalytic activity is observed. Owing to the flexible nature of the solid structure of some POMs (variable secondary structure), reactants having polarity or basicity are readily absorbed into the solid lattice, between the polyanions in the lattice, sometimes causing expansion of the lattice, and reaction occurs therein. In other words, the reaction becomes three-dimensional as in a solution. Owing to this behavior, POM catalysts often exhibit high catalytic activities and unique selectivity.

Heteropolyacids generally have a small surface area ($10\,m^2\,g^{-1}$) and no porosity. However, microporosity has been observed in the presence of alkali metal countercations, especially in cases involving large cations such as K^+ and Cs^+ as well as with NH_4^+, and so on. A full chapter detailing the microporosity of POMs can be found in Ref. [4]. For instance, the pore size of acidic Cs^+ salts ($Cs_xH_{3-x}PW_{12}0_{40}$) has been shown to be controlled by the Cs^+ content, for example $Cs_{2.2}H_{0.8}PW_{12}0_{40}$ has micropores in the range 0.62–0.72 nm diameter compared to less than 0.59 nm for $Cs_{2.1}H_{0.9}PW_{12}O_{40}$ and >0.85 nm for $Cs_{2.5}H_{0.5}PW_{12}O_{40}$. Correspondingly, there is a great difference in surface area values, for example ~$10\,m^2\,g^{-1}$ for $H_3PW_{12}O_{40}$ and $130\,m^2\,g^{-1}$ for its $Cs_{2.5}$ salt. The microporosity of NH_4^+ and Cs^+ salts of H_3PW_{12}, H_3PMo_{12} and H_4SiW_{12} Keggin-type heteropolyacids (HPA) has been investigated

[5] by ^{129}Xe NMR. It has been observed that ammonium salts had a pore size of 0.9 nm regardless of the anion, while for Cs^+ salts pore size varies between 0.7 and 1.0 nm depending upon the nature of the anion. However, this porosity has frequently been observed to be lost upon catalytic application.

Control of the shape and size of pores (micro- and meso-pores) in polyoxometallates is an important objective for the future. Pioneering studies have shown that such control may be applied to the primary structure with generation of pores between the anionic species [6] or to the tertiary structure with generation of pores between self-assembled $(NH_4)_3PW_{12}O_{40}$ micro-crystallites [7]. However, attempts to control the pore size in primary structures with the use of organic templates have failed so far, mainly because of the difficulties encountered in the template removal step, during which the structure collapses. Success has been reported in the control of pore size in tertiary structures for applications at low temperatures; however, for applications at high temperature, procedures need to be improved, as the aggregates are thermally unstable. Alkali and alkaline earth substituted Keggin-type phosphomolybdic or phosphotungstic acids have been shown to form nano-crystallites composed of alkaline salt particles (10–20 nm) thickly covered by the acid after precipitation [8]. Upon heat treatment, these particles are converted to particles having a size similar to those before heat treatment with a more or less uniform composition. These particles are connected epitaxially to each other to form aggregates that can develop an important internal porosity when the ratio of alkaline earth cations to protons is greater than or equal to 2.5 [8]. The complete homogeneity of the composition of this type of polyoxometallate after heat treatment is rather difficult to prove, since the acid phase coating the salt particles is not detectable by X-ray diffraction and can only be observed by X-ray photoelectron spectroscopy or Raman spectroscopy [9].

14.2 History of Polyoxometallates

POMs have been known for about two centuries. The discovery of the first ammonium salt of the dodecamolybdophosphate $(NH_4)_3PMo_{12}O_{40}$ (12 : 1 composition) was reported by Berzelius [10] in 1826 and its tungsto counterpart by Galissard de Marignac [11] in 1864. However, the field remained undeveloped. The first attempts to understand the composition of heteropolyanions were based on Werner's coordination theory [12]. Structure determination for heteropoly compounds was not possible until the advent of X-ray diffraction techniques. A hypothesis proposed in 1908 by Miolati and Pizzighelli [13], based upon sharing metal–oxygen polyhedra, was adopted and developed by Rosenheim [14] and Pauling [15], during the following 25–30 years. Rosenheim was probably the most productive and influential researcher in the field of polyanion chemistry. According to the Miolati–Rosenheim theory, heteropoly acids are based on six-coordinate heteroatoms bound with MO_4. It was Keggin [16] who solved the structure of the most important 12 : 1 heteropoly compound $H_3PW_{12}O_{40} \cdot 5H_2O$ by X–ray diffraction. Evans [17]

determined the structure of the Anderson compound (6 : 1 series for $Te^{6+}[Mo_6O_{24}]^{6-}$) and Dawson [18] determined that of the 18 : 2 heteropoly compound $[P_2W_{18}O_{62}]^{6-}$.

Souchay and his group brought clarity in the field and have provided a major contribution to polyoxometallate chemistry [1a, 19]. Since the early 1990s, polyoxometallate chemistry has expanded tremendously, following fundamental discoveries by Müller and his group at Bielefeld University [20]. These scientists have shown that aqueous solutions of molybdates result in a huge variety of linkable units and a large variety of clusters, among them amazing wheels and spheres such as the giant anions $[La_{16}As_{12}W_{148}O_{524}]^{76-}$ (mass ~4000, diameter 4 nm) or $\{Mo_{132}\}$, an inorganic superfullerene built up from 12 pentagonal $(Mo)Mo_5$ units (one pentagonal MoO_7 unit sharing edges with five MoO_6 octahedra) and 30 different Mo_2^V linkers or $\left[Mo_{72}^{VI}Mo_{60}^{V}O_{372}(CH_3COO)_{30}(H_2O)_{72}\right]^{42-}$ or $\left[Mo_{126}^{VI}Mo_{28}^{V}O_{462}H_{14}(H_2O)_{70}\right]^{14-}$, and so on. These wheels can be considered as nanostructures mimicking oxide surfaces and allowing reactions to occur on well defined sites. The history of polyoxometallate chemistry and its applications for nano-chemistry has been published [21]. Today, POMs still represent an exciting area of research and technology, and new compounds are discovered every month. For instance, the development of functionalized polyoxometallate [22] and polyoxometallate-based polymers [23] with creation of giant two-dimensional networks has appeared recently and constitute new perspectives in the field of organic–inorganic frameworks.

14.3 Properties and Applications of Polyoxometallates

There are more commercial applications of polyoxometallates than of any other class of cluster compound and there is also much potential for additional applications in areas ranging from catalysis and medicine to proton conductors, materials and micro-device technology [24]. These applications stem from the wide range of molecular architectures, surface charge density and chemical and electronic properties exhibited by POMs, as described above. Varying in size from one to a few nanometers, they are used as electrode functionalization agents [25], anti-retroviral agents [26] and for detection, separation and quantification. The latter uses are based on properties such as their high molecular weight (>2000), their solubility in water or organic solvents (depending on the size of the counter-ion size–solubility decreases with size), the fact that a wide variety of elements can be incorporated into the polyanion framework changing the properties, their electrochemical activity and their reducibility to form colored species depending on the substitution element and extent (e.g. from yellow to orange when Mo is substituted by V, while reduction leads to the famous "heteropoly blues"). A vast range of applications has been described in fields as different as synthesis of organic and organometallic derivatives of POMs, absorbents (ion-exchange materials and alcohol or carboxylic acid radical detectors), electron-transfer reactions, photo- and electro-chromism, flame retardants and smoke suppressants, together with appli-

cations in metallurgy (corrosion inhibitors and coatings on steel and aluminum), medicine and catalysis. Nevertheless, catalysis is by far the most important field of application (representing > 80% in terms of patent applications). Most of the pioneering work was performed in Japan (Izumi, Misono, Mizuno, Ono, Otake, Yoneda and coworkers), in Russia (Matveev, Kozhevnikov, Kholdeeva and coworkers) and in France (Souchay, Hervé and coworkers).

POMs can display very strong Brønsted acidity and are efficient oxidants, exhibiting fast and reversible multi-electron redox transformations under mild conditions. This acidity is very strong, as the negative charge is delocalized over much larger anions than for mineral acids or solids such as zeolites. Consequently, the electrostatic interaction between protons and the anion is much less for POMs. The general trend in acidity among the most common HPAs is a function of the hetero atom [27] with Co < B < Si, Ge < P, falling into the following order [28] determined in an ammonia desorption study:

$$H_3PW_{12}O_{40} > H_4SiW_{12}O_{40} \sim H_4GeW_{12}O_{40} > H_3PMo_{12}O_{40} > H_4SiMo_{12}O_{40} \sim H_4GeMo_{12}O_{40}$$

with NH_3 desorption maxima being at 865, 805, 736 and 696 K, respectively. Recent studies report a decrease in the quantity of acid sites, but not in their strength, when dispersing POMs on silica-type supports [29–31] such as HMS, MCM41 and Kenyaite.

The acid–base and redox properties can be controlled across a broad spectrum by varying the chemical composition, the extent of hydration, the type of support for supported samples, the thermal treatment, and so on. For instance, the substitution of M^{VI} by M^{n+} of close valence (n = 5, 4, 3 or 2) has been studied and leads to additional negative charges on the HPA and thus to additional protons (from one to four respectively) for charge balance, thus generating a higher acid density. An example is $H_{3+x}PV_x^VM_{12-x}^{VI}O_{40}$, which can be synthesized with x = between 1 and 3. Other metal elements can also be substituted. The problem is that during synthesis one could have either framework substitution of the M element or cationic exchange between protons and the added metal cation, as is well known for zeolite materials. It follows that the number of protons could be less than $3 + x$ in the above formula, so that the balance between redox and acid properties of such materials is difficult to control during synthesis, since they depend on temperature, pH conditions, and so on.

POMs are promising catalysts for acid, redox and bifunctional catalysis. In many structures, the transition metal addenda atoms such as Mo or W exist in two oxidation states, which results in different redox properties as determined by polarography. The exceptional ability of heteropolyanions to act as electron reservoirs has been demonstrated by the preparation and characterization of numerous reduced derivatives [32]. They also exhibit high solubility in polar solvents, which means that they can be used in homogeneous catalysis. The wide range of applications of heteropoly compounds are based on their unique properties which include size, mass, electron and proton transfer (and hence storage) abilities, thermal stability,

lability of "lattice oxygen" and the high Brønsted acid strength of the corresponding acids. An added advantage is that the HPAs can be separated and can be extracted into organic solvents.

Transition metal substituted polyoxometallates (TMSP) are synthesized using transition metals as addenda ions. Most commonly, first row transition metals are incorporated into the framework. The transition metal element fits into the lacunary vacancy created in the Keggin structural unit by the loss of an MO_6 octahedron, which is equivalent to the stoichiometric loss of an MO^{n+} unit, resulting in the formation of the $[XM_{11}O_{39}]^{n-}$ anion. This involves the partial degradation of the Keggin unit by lowering the pH of the solution upon the addition of a suitable buffer. The solubilities of the TMSP complexes can be controlled by selecting an appropriate counter-cation. Usually alkali metals and tetra-alkyl ammonium groups are the counter-cations of choice. There are two methods for the synthesis of a TMSP. The first method involves the addition of a transition metal salt to the already prepared isolated lacunary salt under appropriate synthetic conditions, while the second method corresponds to the generation of *in situ* lacunary vacancies followed by the addition of the transition metal salt.

Applications of POMs to catalysis have been periodically reviewed [33–40]. Several industrial processes were developed and commercialized, mainly in Japan. Examples include liquid-phase hydration of propene to isopropanol in 1972, vapor-phase oxidation of methacrolein to methacrylic acid in 1982, liquid-phase hydration of isobutene for its separation from butane–butene fractions in 1984, biphasic polymerization of THF to polymeric diol in 1985 and hydration of *n*-butene to 2-butanol in 1989. In 1997 direct oxidation of ethylene to acetic acid was industrialized by Showa Denko and in 2001 production of ethyl acetate by BP Amoco.

Since the application of POMs is so widespread across areas such as homogeneous and heterogeneous catalysis, as well as acid and redox catalysis, it is not possible to exhaustively review all the applications. Thus the rest of this chapter focuses only on the catalytic properties of the polyoxometallates in heterogeneous gas- or liquid-phase oxidation reactions, and reviews the most recent progress in the knowledge of their properties and working process, underlining both their potential and their limitations.

14.4
Catalytic Applications in Partial Oxidation Reactions

It is known [41] that partial oxidation reactions in heterogeneous catalysis involves redox properties of the solid catalysts, allowing the well known Mars–van Krevelen mechanism [42] to occur, or at least to be facilitated. Acid–base properties are also an important feature, as they play a determining role in the activation of the reactants and in the desorption of the intermediate compounds. For instance, an acid surface will favor desorption of acid products, thus avoiding further over-oxidation, while a basic surface will favor desorption of basic products as olefins. It follows that heteropolyoxometallate compounds, in particular TMSP, appear as potential

catalysts for partial oxidation reactions [43]. Oxidation catalysis by polyoxometallates, especially of the Keggin type, is a rapidly expanding area owing to their unusual versatility and compatibility with environmentally friendly conditions (employing oxidants such as O_2 and H_2O_2) and reactions. Research in the area of oxidation using these compounds has been intense since the 1990s, as existing catalytic processes leave ample margin for improvement with scope to develop new catalysts working under more stringent reaction conditions. A general overview of applications of POMs in oxidation reactions has been presented by Centi and coworkers [44]. Extensive applications have been found in areas ranging from fine chemical synthesis and alkane up-grading, to the degradation of toxic materials.

As described above, substitution of the addenda atoms by either transition metals (TMSP) or other addenda atoms modifies the redox features of the heteropolyoxometallates. The synthesis of TMSP associated with metalloporphyrins was studied thoroughly by Hill and his group [45]. These systems behave as oxidation catalysts by transferring oxygen from a typical donor to the organic substrate and exhibit the attractive features of metalloporphyrins, namely ability for dioxygen binding, formation of high valence species with stoichiometric oxygen transfer, reaction with oxidants such as iodosobenzene, sodium periodate and *tert*-butyl hydroperoxide. The strong binding of the metalloporphyrin with the d electrons of the transition metal ions permits it to be retained within the structure during the catalytic cycle, although changes in oxidation state of the metal occur, which influence its mobility. If during the oxidation process structural degradation of the catalyst takes place, the transition metal species is lost and precipitates as metal oxide. On their own, metalloporphyrins are organic molecules that are thermodynamically unstable in the presence of strong oxidizing agents and hence can undergo oxidative degradation during reaction. However, the TMSP complexes are more thermally robust than the uncomplexed metalloporphyrin and are not susceptible to oxidative degradation. Consequently, they are able to catalyze oxidation reactions for longer periods than metalloporphyrins alone.

Mixed addenda complexes are those in which one or more of the addenda atoms in the framework are substituted by other addenda-type atoms. The attractiveness of this class of compounds as catalysts for oxidation is their high oxidation potential, low cost, thermal stability and oxidative robustness, ease of preparation and solubility in media ranging from water to hydrocarbons. The redox potential of a POM depends on the negative charge density and on the elemental composition. Both factors can be controlled to a great extent during the synthesis process. The relationship between redox potential and elemental composition is dictated by the presence or absence of highly oxidizing addenda metal atoms. The decreasing order of redox potentials is $V^{V} > Mo^{VI} > W^{VI}$. Hence, the molybdovanadophosphate system has been the most extensively studied for oxidation reactions. All the types of Keggin compounds mentioned above have been found to be compatible in operation with environmentally friendly oxidants, such as oxygen and hydrogen peroxide, and also with oxidants like *tert*-butyl hydroperoxide, iodosobenzene, sodium periodate and potassium persulfate. Many examples are given below so that the readers can appreciate the breadth of the field of application of POMs for

catalytic oxidation reactions using either oxygen (air) or hydrogen peroxide (H_2O_2) as oxidizing agents.

14.4.1 Oxidation with Molecular Oxygen

For TMSP materials, the efficacy of oxidation using molecular oxygen is influenced by their oxidation potential. They act as catalysts by oxygen transfer from a typical donor to a typical TMSP followed by transfer of this activated form of oxygen to an organic substrate. TMSPs are potential catalysts for the epoxidation of olefins in the presence of aldehydes and molecular oxygen or air. Mizuno and coworkers [46] have demonstrated the significant catalytic activity of $[PW_{11}CoO_{39}]^{5-}$ for the epoxidation of alkenes such as cyclohexene, 1-decene and styrene by molecular oxygen at 303 K in the presence of aldehydes such as isobutyraldehyde and pivaldehyde. They proposed that this reaction involves peracids as intermediates, and the formation of per-isobutyric acid has been confirmed by ^1H NMR [47].

Alkene epoxidation by dioxygen in the presence of isobutyraldehyde and of the tetrabutylammonium salts of transition metal substituted heteropolyanions $[PW_{11}MO_{39}]^{n-}$ ($M = Co^{2+}$, Mn^{2+}, Cu^{2+}, Pd^{2+}, Ti^{IV}, Ru^{3+}, V^{V}) has been studied by Kholdeeva and coworkers [48]. In this work, *trans*-stilbene was used as the model substrate in an acetonitrile medium. Selectivity of epoxidation reached 95% at complete alkene conversion. The reaction was inhibited by 2,6-di-*tert*-butyl-4-methylphenol indicating a chain radical mechanism, and the acyl peroxy radical was the active species for epoxidation. Oxidation of olefins and ketones by molecular oxygen/aldehyde on a V heteropolyoxometallate system has been studied by Hamamoto and coworkers [49]. Olefins were epoxidized with dioxygen in the presence of two equivalents of 2-methyl propanal under the influence of $(NH_4)_6[PMo_6V_6O_{40}]$ to give the corresponding epoxides in moderate to good yields. This system was also extended to allylic and homo allylic alcohols. Baeyer–Villiger oxidation of cyclic ketones was achieved using benzaldehyde instead of 2-methylpropanal.

Kuznetsova and coworkers have shown that $[PW_{11}Fe(H_2O)O_{39}]$ in the pH range 3.5–5 at 293 K is an active catalyst for the oxidation of H_2S with O_2 to produce elemental sulfur [50]. Harrup and coworkers have found that polyoxometallate catalysts such as $K_5[ZnPW_{11}O_{39}]$, α-$K_8[SiW_{11}O_{39}]$, α-$K_6[ZnSiW_{11}O_{39}]$ and $K_4[NaP_5W_{30}O_{110}]$ are active for the oxidation of H_2S to elemental sulfur at 60 °C under 1.1 atmospheres pressure of O_2 [51]. Khenkin and Hill have observed that Cr^{3+} heteropolytungstate and its corresponding oxo-form Cr^{V} are efficient catalysts for the oxidation of alkenes, alkanes, alcohols and triphenylphosphines by a variety of oxidants such as ClO, H_2O_2 or PhIO [52]. Kuznetsova and coworkers have studied complexes of Pd^{2+} and Pt^{2+} with $[PW_{11}O_{39}]^{7-}$ and have found that they are active for the oxidation of benzene to phenol in a mixture of O_2 and H_2 gases in a two-phase water–benzene system at a temperature of 283–313 K [50]. Iron heteropolyacid has also been found by Seo and coworkers to be active for phenol synthesis by liquid phase oxidation of benzene with molecular oxygen [53].

The vanadium-substituted heteropolyanions have a fairly high oxidation potential (0.7 V relative to the normal hydrogen electrode) and are capable of oxidizing substrates ranging from organic to inorganic compounds. They act as reversible oxidants, that is, their reduced forms can be reoxidized to the original form by oxygen under mild conditions. The $V^{IV} \leftrightarrow V^{V}$ transformation is actually responsible for the redox activity. Neumann and coworkers have successfully carried out the oxidative dehydrogenation of α-terpinene to *p*-cymene by mixed addenda compounds of the type $H_5[PMo_{10}V_2O_{40}]$ [54]. The reaction mechanism involves the formation of a stable substrate complex in the catalyst reduction (substrate oxidation state) stage and the formation of a μ-peroxo intermediate in the catalyst reoxidation stage. Oxidation of trialkyl-substituted phenols such as 2,3,6-trimethyl phenol in the presence of phosphomolybdovanadium heteropolyacids has been reported by Kholdeeva and coworkers [55]. The product obtained was the 2,3,5-trimethyl-1,4-benzoquinone, an intermediate in Vitamin E synthesis, with 86% yield at 100% conversion, with 2,2′-3,3′-6,6′-hexamethyl-4,4′-biphenol being isolated as an intermediate. The divanadium-substituted phosphomolybdates have been found to catalyze the oxidation of dialkylphenols to diphenoquinones. The rate is highly dependent on the oxidation potential of the substrate, and the reaction proceeds by electron transfer from the substrate to the heteropolyanion catalyst. The divanadium-substituted heteropolyanion has been found by Lissel and coworkers to catalyze aerobic oxidation of dialkyl phenols to diphenoquinones and the oxidation of 2,3,5-trimethylphenol to 2,3,5-trimethyl-1,4-benzoquinone [56]. The reaction rate has been found to be dependent on the oxidation potential of the substrate and to proceed by electron transfer from the substrate to the heteropolyanion catalyst. These catalysts are equally efficient for oxybromination in organic media. For instance, oxybromination of phenol, anisole, *o*-cresol, *p*-cresol, 1-naphthol, *N,N*-diethylaniline, toluene, cumene, acetone, cyclohexanone and 1-octene to the corresponding bromides has been achieved under ambient conditions by Neumann and coworkers [57]. The oxidation of 2-methylcyclohexanone and cyclohexanone by O_2 to 6-oxo-heptanoic acid and adipic acid respectively has been observed on molybdovanadophosphoric acids [58].

The oxidation of benzylic derivatives with oxygen has been studied using $(NH_4)_6[PMo_6V_6O_{40}]$ as catalyst [59], as well as the oxidative dehydrogenation of benzylic amines to the corresponding Schiff base amines with oxygen in toluene solution at 373 K and the oxidation of isochroman and indan to 3,4-dihydroisocoumarin and 1-indanone with high selectivity. Similarly, oxidative cleavage of ketones, such as substituted cycloalkanones, 1-phenylalkanones and open-chain ketones to the corresponding acids was observed [60]. For instance, substrates such as 2,4-dimethyl cyclopentanone were oxidized to 5-oxo-3-methyl hexanoic acid and 1-phenylpropan-1-one, and open-chain ketones such as pentan-3-one was oxidized to the corresponding carboxylic acid.

The oxyfunctionalization of low molecular weight alkanes has attracted much attention because of their low cost and chemical stability as feedstock. Their oxidation over POM catalysts has been widely studied by controlling redox properties upon substituting M addenda by transition metal elements [61–63]. For example,

TMSP catalysts have been studied for the oxidation of propane with M = Co^{2+}, Fe^{3+}, Ga^{3+}, Ni^{2+}, Sb^{3+} and Zn^{2+} incorporated into $Cs_{2.5}H_{1.5}(M)PV_1Mo_{11}O_{40}$ in an M : V = 1 : 1 atomic ratio [36a]. Propene was the main product with about 80% selectivity at 5% propane conversion with Ni > Co > Fe > Zn at T_{react} = 595, 618, 646 and 673 K respectively, carbon oxides being the other main products. About 60% selectivity has been obtained for Ga- and Sb-substituted POMs at 613 and 628 K respectively and 26% at 578 K for the starting $Cs_{2.5}H_{1.5}$ material, which also led to CO_x (46%), acetic acid (24%) and acrylic acid (4%). It has been shown that the acidity of all samples was different (about 1.6 H^+/KU (Keggin unit) for the starting $Cs_{2.5}H_{1.5}$ sample and 2.4, 2.3, 1.9, 1.4, 2.1 and 3.0 H^+/KU for M = Ni, Co, Fe, Zn, Ga and Sb respectively). It was then clear that the balance between the redox and acid properties of the POMs are important features in determining their catalytic properties. For Ga samples, by changing the relative amount of Ga [43d], oxygenates, propene and CO_x have been found to be formed with a maximum for 0.16 Ga/KU (about 45% acrolein, acetic and acrylic acids against about 33% CO_x and 22% propene at 573 K), while the number of protons has been found to be similar (3.0–3.3 per KU). Substituting W for Mo in a $Cs_{2.5}H_{1.5}PV_1Mo_{11}O_{40}$ led to stronger acidity of the sample and more CO_x and acetic acid in propane oxidation reaction at the expense of propene [64].

Substituting Mo by V (x = 1, 2 and 3 per KU) in $PMo_{12-x}V_xO_{40}$, Centi and coworkers have shown that pentane is oxidized mainly to maleic anhydride while the VPO catalyst gives both maleic and phthalic anhydrides [65]. Such V-substituted $PMo_{12-x}V_xO_{40}$ POMs are the best known catalysts for the oxidation of isobutane to methacrolein and methacrylic acid [66]. Insertion of Ni into the $Cs_{2.5}$ of $Cs_{2.5}Ni_{0.08}H_{1.34}PVMo_{11}O_{40}$ has been demonstrated to improve the oxidation of isobutane to methacrolein and methacrylic acid with molecular oxygen [67, 68]. At 613 K the yield of methacrylic acid reached 9.0%. The optimal content of Cs and V was found to be equal to 2.5 and 1, respectively, and the addition of Ni enhanced the yield of methacrylic acid. In agreement with the statements above, it has been clearly shown that for $Cs_xH_{3-x}PMo_{12}O_{40}$ catalysts the factors that control the catalytic activity are the oxidizing ability and the protonic acidity of the catalysts [69].

Iron and copper have been the most widely studied addenda elements. It has been suggested in a study of $Cs_{2.5}M_{0.08}H_{1.5-0.08n}PVMo_{11}O_{40}$ (M = Cu^{2+}, Fe^{3+}, Ni^{2+}, Mn^{2+}, Co^{2+}) that iron addition promotes the reduction of the catalyst under oxygen-rich conditions while iron and copper promote the re-oxidation, under oxygen-poor conditions [70]. $Cs_{2.5}M^{n+}_{0.08}H_{1.5-0.08n}PVMo_{11}O_{40}$ (M = Ni^{2+}, Fe^{3+}) has also been found to catalyze the oxidation of propane and ethane [71, 72]. The state and role of V is quite important [73]. Light alkanes (C_1—C_3) have been observed to be transformed at reasonable yield to the corresponding carboxylic acid over $H_{3+x}PV_xMo_{11-x}O_{40}$ with x = 1–3 in presence of CO and in the $K_2S_2O_8/CF_3COOH$ system [74].

The role of transition metals as counter-cations in polyoxometallates used as oxidation catalysts has been reviewed [75]. Transition metals have important and complex effects on textural, acid–base and redox properties of the heteropolyanions, as described in a number of studies. The interaction of the molybdophosphoric Keggin heteropolyanion with the iron counter-ion has been studied and

Figure 14.5 Schematic representation of the $FeO(H_2O)_5^{3+}$ counter-cation in interaction with the Keggin anion leading to a charge transfer between iron and molybdenum. Iron, yellow; molybdenum, black; oxygen, red.

the influence of the latter on the reducibility of iron-doped acid has been explained by an electron transfer between the heteropolyanion to the iron counter-ion as clearly demonstrated [76] and illustrated in Figure 14.5. Quantum-chemical calculations have further confirmed the existence of this transfer and explained why it was possible only under hydration of the solid [77]. The microscopic mechanism of this transfer is due to the modification of the relative position of the counter-ion, which enters into strong interaction with terminal oxygens of the heteropolyanion.

The effect of copper has also been studied in detail. Reduction experiments have shown that copper has a positive effect on the rate of reduction. Characterization of the samples after reduction by different techniques has clearly shown that Cu participates in the reduction of the heteropolycompound and that the reduction rate increases linearly with Cu content, with approximately $7\,e^-/Cu$ [78]. This is shown in Figure 14.6 and Table 14.1.

Considering that one electron corresponds to the reduction of Cu^{2+} to Cu^+, the reduction of six Mo^{VI} species to six Mo^V can be attributed to one copper ion. The reduction proceeds in the vicinity of the copper cations via a concerted mechanism between the copper and one molybdenum cation of each of the six surrounding Keggin anions, the Cu^{2+} cations thus "catalyzing" the reduction of molybdenum cations:

$$Cu^{2+} + 2\,Mo^{6+} + O^{2-} + H_2 \rightarrow Cu^+ + Mo^{5+} + Mo^{6+} + H_2O$$

$$Cu^+ + Mo^{5+} + Mo^{6+} \rightarrow Cu^{2+} + 2\,Mo^{5+}$$

It is interesting to note that reduced heteropoly compounds show higher selectivity towards methacrylic acid than the non-reduced ones in the oxidation of isobutane. Mizuno and coworkers have also reported the oxidation of isobutane under oxygen-deficient conditions [67]. Ueda and coworkers have studied reduced 12-molybdophosphoric acid for the oxidation of propane [79]. This highly reduced

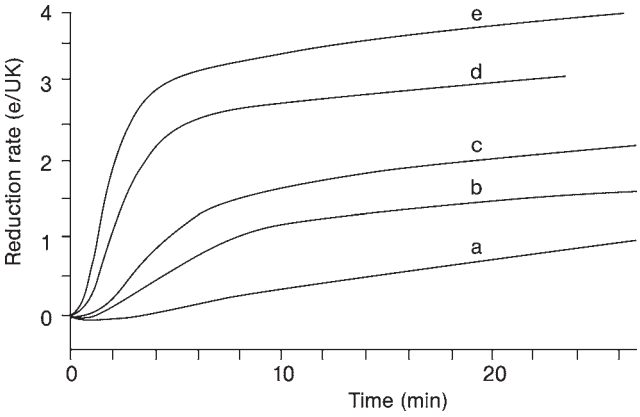

Figure 14.6 Extent of reduction at 613 K as a function of time for Cs_2Cu_x compounds. (a) Cs_2H_1, (b) $Cs_2Cu_{0.05}$, (c) $Cs_2Cu_{0.1}$, (d) $Cs_2Cu_{0.2}$ and (e) $Cs_2Cu_{0.3}$. (Taken from Ref. [77]).

Table 14.1 Extent and rate of the first rapid reduction period of the compounds Cs_2Cu_x by hydrogen at 613 K, calculated in electrons per KU and per copper ion. (Taken from Ref. [78]).

Compound	Reduction extent		Reduction rate	
	$(e^- KU^{-1})$	$(e^- Cu^{-1})$	$(e^- (KU\,min)^{-1})$	$(e^- (Cu\,min)^{-1})$
Cs_2	1.2	–	0.05	–
$Cs_2Cu_{0.05}$	1.5	6.5	0.19	3
$Cs_2Cu_{0.10}$	1.9	7.0	0.35	3.1
$Cs_2Cu_{0.20}$	2.7	7.5	0.81	3.8
$Cs_2Cu_{0.30}$	3.2	6.7	1.21	3.9

12-molybdophosphoric acid, formed by the heat treatment of the pyridinium or quinolinium salts, showed 50% selectivity to acrylic acid at 12% conversion.

Oxidative dehydrogenation at low temperatures and high pressures can result in the complete conversion of alkanes in comparison with simple dehydrogenation. Cavani and coworkers [80] have shown that Dawson-type mono-iron-substituted heteropolytungstates and Keggin-type heteropolymolybdates are active in the oxidative dehydrogenation of isobutane [80] and ethane [81], respectively. The rate per specific surface area of $K_7P_2W_{17}FeO_{61}$ for the oxidative dehydrogenation of isobutane was higher than those of active catalysts such as $Mg_3V_3O_8/MgO$ and Y_2O_3/CeF_3.

In a study employing negative differential resistance (NDR) features of $H_3PMo_{12}O_{40}$ HPA substituted with V, Barteau and coworkers have shown there is a relationship between their values and the redox potentials of the samples, and

consequently with catalytic properties in partial oxidation reactions [82, 83]. For instance, this holds true for the oxidation of alkanes (propane, *n*-butane, isobutane) to the corresponding acids or alkenes, of acetaldehyde to acetic acid, of isobutyric acid to methacrylic acid [84]. The following order has been found: propane > butane, isobutane, isobutyric acid > acetaldehyde, corresponding to the weakest C—H bonds order. NDR values have been measured by scanning tunneling spectroscopy in a scanning tunneling microscope under a given atmosphere. This has been extended by the substitution of Mo with other elements such as Ag^{+}, Cu^{2+} and Pd^{2+}. A volcano curve of selectivity vs NDR or catalytic activity has been observed for the propane to acrylic acid reaction, with the optimum being at NDR ~0.8 V.

Interesting properties may also be obtained when using a mixed addenda system in the presence of a co-catalyst. The best known system [34d] is the V-substituted phosphomolybdate in conjunction with Pd^{2+} for the oxidation of olefins to carbonyl compounds. This is analogous to the Wacker oxidation process based on $CuCl_2$ and Pd^{2+}. Unlike the Wacker process, the HPA system works at very low chloride concentration, or even in its absence. In addition the HPA is more active and selective and less corrosive. Other examples of such two-component catalytic systems include Tl^{3+}/Tl^{+}, Pt^{4+}/Pt^{2+}, Ru^{4+}/Ru^{3+}, Ir^{4+}/Ir^{3+}, Br^{2-}/Br^{-} and I^{-}/I_2.

Although synergetic effects have been shown to be very important in heterogeneous catalysis, very few examples have been reported with polyoxometallates. Synergism is the overall improvement of performance obtained for a mixture of phases when it is greater than the sum of the performances of each individual phase. Such effects may have different origins. Synergy has been reported between polyoxometallate-based catalysts used for the partial oxidation of isobutane to methacrylic acid. These synergetic effects have led to the most efficient catalysts for that reaction. The first report on such synergies was based on the combination of the strong acid component corresponding to a sulfated tantalum oxide with a P—Mo—V Keggin-type phosphomolybdic acid. The strong acid site on the hydrated tantalum oxide treated with sulfuric acid would abstract an H^{-} ion from isobutane to form $i\text{-}C_4H_9^{+}$. It has been postulated that the $i\text{-}C_4H_9^{+}$ migrates to the polyoxometallate acid where it is oxidized to methacrolein and methacrylic acid [85]. The second report relates the combination of a lanthanum molybdate $La_2Mo_2O_9$ with a Keggin-type molybdophosphoric heteropolyacid with protons partially substituted by tellurium, vanadium and cesium cations, with the composition $Cs_2Te_{0.2}V_{0.1}H_{0.4}PMo_{12}O_{40}$. The synergy results primarily from a support effect, the lanthanum molybdate stabilizing the phosphomolybdic salt and preventing its sintering and degradation. The origin of this support effect has been related to the crystallographic fit between the two cubic structures of the phases [86].

14.4.2
Oxidation by Hydrogen Peroxide

Hydrogen peroxide is an important and widely used oxidant for organic substrates as it is cheap, easily available and yields water as a side-product, which is environmentally friendly, although H_2O_2 synthesis in not so eco-friendly. A wide range of

oxidation processes such as epoxidation and hydroxylation have employed POMs with H_2O_2 as oxidant. Since POMs are generally insoluble in organic substrates they are rendered soluble by using alkylammonium groups as the counter-cations. W and Mo containing POMs have been shown to catalyze the oxidation of a wide range of organic substrates in either homogeneous or two-phase systems, with peroxo-type POMs being assumed to be the active intermediates. The most significant developments in this field have been reported by the groups of Venturello and Ishii. Venturello and coworkers observed that the tungstophosphate POM catalyzes the epoxidation of different alkenes with dilute H_2O_2 solution (15%) as oxidant [87]. Ishii and coworkers reported that $H_3PW_{12}O_{40}$ and cetylpyridinium chloride mixture catalyzes epoxidation of alkenes with commercially available H_2O_2 solution (35%) as oxidant [88]. More recently, the epoxidation mechanism on these catalysts was investigated by several groups [89–93]. It was demonstrated that $\{PO_4[WO(O_2)_2]_4\}^{3-}$ is the active species in the olefin epoxidation in the Venturello–Ishii system. Heteropolyacids with the Keggin structure, for example $H_3PW_{12}O_{40}$, are degraded in the presence of excess H_2O_2 to form peroxo species, for example $\{PO_4[WO(O_2)_2]_4\}^{3-}$ and $[W_2O_3(O_2)_4(H_2O)_2]^{2-}$, which are the true catalytic active intermediates.

Cyclohexene epoxidation by anhydrous urea–hydrogen peroxide adduct (UHP) has been studied over a series of Keggin-type heteropoly compounds using acetonitrile as an alternative solvent [94]. Among a series of Keggin-type POMs, tris(cetylpyridinium)12-tungstophosphate ($(CPB)_3[PW_{12}O_{40}]$) gave 80% conversion of cyclohexene and 97% selectivity for cyclohexene oxide in the UHP/CH_3CN system. Epoxidation of 1-octene was achieved in a biphasic system [90a]. The oxidation of trimethoxybenzene to dimethoxy-*p*-benzoquinone in an acetic or formic acid medium was obtained at 303 K [95] over a mixture of molybdophosphoric, molybdosilicic and tungstophosphoric acids. Aromatic amines were oxidized with H_2O_2 catalyzed by cetylpyridinium salts of heteropolyoxometallates [96]. For instance, substituted anilines were oxidized to nitrosobenzenes at room temperature or nitrobenzene at elevated temperature under two-phase conditions in chloroform solvent and in azoxybenzene in aqueous medium. The oxidation of sulfides to sulfoxides and sulfones was observed in two-phase reaction conditions in chloroform solvent with 93–99% conversion [97]. Ballistreri and coworkers [98] were able to oxidize both internal and terminal alkynes by H_2O_2 in the presence of $(cetylpyridinium)_3(PMo_{12}O_{40})$, with an activity better than that for Na_2MO_4 ($M = Mo^{VI}$ or W^{VI}). 1,2-Hexanediol and 1,2-octanediol were oxidized by H_2O_2 to 1-hydroxy-2-hexanone and 1-hydroxy-2-octanone respectively with yields above 90% on peroxotungstophosphates at reflux temperatures in chloroform [99]. Tris(cetylpyridinium)-12-tungstophosphate has been used to prepare epoxy acids from α,β-unsaturated acids, such as crotonic acid [100]. The epoxidation of allylic alcohols such as geraniol, 3-hydroxy-endotricyclo-deca-3,8-diene with H_2O_2 was performed over 12-molybdophosphoric acid and cetylpyridinium chloride at refluxing temperature in chloroform under two-phase conditions [101]. Epoxidation of cyclopentene was found to be more efficiently catalyzed by $H_3PMo_{12-n}W_nO_{40}$ with $n = 1$–11 than with $H_3PMo_{12}O_{40}$ and $H_3PW_{12}O_{40}$, when combined with cetylpyri-

dinium bromide (CPB) as a phase transfer reagent with 50 equiv. H_2O_2 (30% solution) in acetonitrile [102]. It was then shown by UV-Vis, FTIR and ^{31}P NMR spectroscopies that these mixed Mo/W POMs are degraded during reaction into peroxo-type complexes $[(PO_4)(Mo_{4-x}W_xO_{20})]^{3-}$ with $x = 1–4$. These were not obtained from $H_3PW_{12}O_{40}$ although it was degraded during reaction. This explains the increased catalytic activity of the mixed Mo/W POMs. In the case of alcohol oxidation over mono-substituted $PM_{12}O_{40}$ (M = Mo or W) Keggin POMs, it was observed that they were degraded under reaction conditions into peroxo-phosphometallates $\left(PO_4[M(O_2)_2]_4^{3-}\right)$, which are in fact the active catalysts.

Efficient H_2O_2-based oxidation has been observed with three types of polyoxometallate [103], $[\gamma\text{-}SiW_{10}O_{34}(H_2O)_2]^{4-}$, $[\gamma\text{-}1,2\text{-}H_2SiV_2W_{10}O_{40}]^{4-}$ and $[W_2O_3(O_2)_4(H_2O)_2]^{2-}$. The first POM catalyzed epoxidation of various olefins including non-activated terminal olefins such as propene and 1-octene with 99% selectivity to epoxide and 99% efficiency of H_2O_2 utilization. The second POM showed unique stereospecificity, regioselectivity and diastereoselectivity for the epoxidation of cis/trans olefins, non-conjugated dienes and 3-substituted cyclohexenes, respectively. The epoxidation of various allylic alcohols with only one equivalent H_2O_2 in water was catalyzed by the third POM and gave high yields of the corresponding epoxy alcohols.

The activation of the relatively inert C–H bonds as found in alkanes, alkenes and aromatic compounds via oxygen insertion was observed to be catalyzed by transition metal substituted heteropolyanions using H_2O_2. Di-iron substituted polyoxometallates were found to be highly efficient for the selective oxygenation of cyclohexane with H_2O_2. Other alkanes such as *n*-hexane, *n*-pentane and adamantane were oxidized employing such POMs. The efficiency and activity for the use of H_2O_2 greatly depends on the iron centers and the di-iron substituted complexes showed the highest efficiency for H_2O_2 conversion [104]. The catalytic properties of the transition metal substituted polyoxometallates $[PMW_{11}O_{39}]$ with ($M = Fe^{3+}$, Cr^{3+}, Ru^{4+}, Ti^{IV} and V^{IV}) were studied for substrates such as cyclohexene, benzene, alcohols and aldehydes with H_2O_2 and other oxidants [105]. Ti-substituted polyoxotungstate with the composition $[PTi_xW_{12-x}O_{40}]^{(3+2x)-}$ (where $x = 1, 2$) and peroxo titanium complexes were found to be efficient catalysts for alkene epoxidation reactions with H_2O_2 [106]. The epoxidation results from the synergistic interaction between a tungsten-peroxo site with an adjacent Ti-peroxo (μ) site which acts as an electrophilic centre for the alkene on the catalyst, involving OH radicals.

Catalytic properties of heteropoly complexes containing Fe^{3+} ions and the heteropolyanion $[PW_{11}O_{39}]^{7-}$, isolated from aqueous solution as tetrabutylammonium salts were studied for the oxidation of benzene by H_2O_2 in acetonitrile medium at 343 K [107]. The mechanism of H_2O_2 activation by one of the complexes, $[PW_{11}O_{39}Fe(OH)]^{5-}$, most likely involves the initial formation of a peroxo complex, which was observed spectroscopically. Chromium-containing derivatives of $[PW_{11}O_{39}]^{7-}$ were synthesized and used as catalysts for the oxidation of unsaturated hydrocarbons, such as benzene and cyclohexene, with H_2O_2. The surface location of Cr^{3+} was assumed to favor oxygen transfer from H_2O_2 to hydrocarbon. The

resulting oxidized species $PW_{11}Cr[O]$ are active oxidants in the reaction with unsaturated hydrocarbons [108]. The oxidation of cyclohexane by H_2O_2 was studied in acetonitrile medium, using tetrabutylammonium salts of Keggin-type polyoxotungstates. The polyanions $[PW_{11}O_{39}]^{7-}$ and $[PW_{11}Fe(H_2O)O_{39}]^{4-}$ showed higher catalytic activity and different selectivity for oxidation than the corresponding Cu, Co, Mn and Ni substituted complexes [109]. Oxidation of alkenes such as cyclooctene, 2-octene, 1-octene, cyclohexene, styrene and *trans*-stilbene was found to be affected by catalytic amounts of di-iron-substituted silicotungstate with high and efficient utilization of $W_{11}O_{39}$ [110]. The catalytic activity of di-iron-substituted silicotungstate was observed to be approximately 100 times higher than for non-, mono- and tri-iron-substituted silicotungstates [111].

Characteristic features of vanadium-containing heteropoly catalysts for the selective oxidation of hydrocarbons by H_2O_2 were described by Misono and coworkers [112] Conversion was 93% for oxidation of benzene to phenol with 100% selectivity. Over selectively V^{5+}-substituted Keggin heteropolytungstates, the catalytic activities for the hydroxylation of benzene in the presence of H_2O_2 was studied in a two-liquid aqueous and organic phase [113]. The activities and stabilities of catalysts were compared with those of V^V-substituted Dawson POMs, V^V-containing isopolyanions, Milas reagent and the picolinato–vanadium(V) oxo peroxo complex. It was observed that Keggin-type mixed addenda heteropolyanions containing vanadium such as $[PMo_{10}V_2O_{40}]^{5-}$ are effective as catalysts for the oxidation of alkyl aromatics to their respective acetates or alcohols and aldehydes or ketones using 30% H_2O_2 as oxidant in acetic acid [114]. The catalyst was not degraded during the catalytic cycle. The reaction proceeds by homolytic cleavage of the $[PMo_{10}V_2O_{40}]^{5-}$–peroxo intermediate, resulting in hydroperoxy and hydroxy radicals, which initiate the formation of benzyl radicals, and then to the products.

14.5 Characterization: Redox and Acid–Base Properties

Since the early 1970s, UV-Vis, infrared, Raman, MAS-NMR and inelastic neutron scattering spectroscopies and other techniques such as thermal desorption and thermogravimetry have been extensively used for identifying POM structure/type and chemical properties such as redox and acid–base behavior. MAS-NMR spectroscopy has been widely used, in particular for ^{31}P in the $PM_{12}O_{40}$ Keggin-type structure and in lacunary compounds, for structure determination and, in the case of ^1H, to characterize Brønsted acidic features. Such acidity has been shown to be high and to be rather difficult to characterize. The protons are in fact quite mobile and can move around the big POM anions, leading to strong acidity. It follows that hydroxyl groups do not exist on the IR timescale and IR bands are quite broad, which is a difference compared to other solid acid catalysts such as zeolites. Protonic sites have been identified in $H_3PW_{12}O_{40}$ and its Cs salts $Cs_xH_{3-x}PW_{12}O_{40}$, by *in situ* IR spectroscopy as a function of dehydration extent [115]. Similarly, protonic sites have been identified for $H_3PW_{12}O_{40}$ and $Cs_{1.9}H_{1.1}PW_{12}O_{40}$ by ^1H, ^2H, ^{31}P MAS-

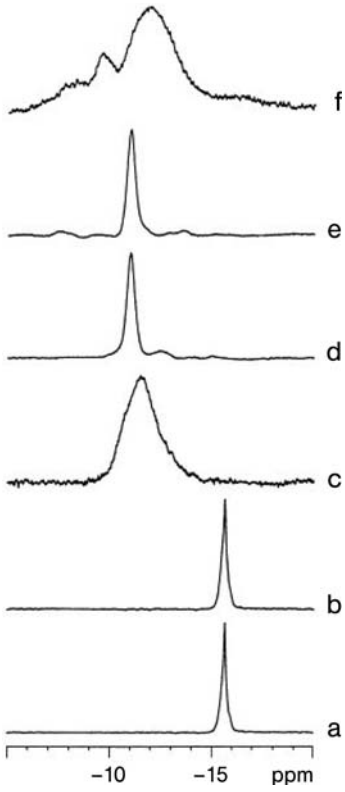

Figure 14.7 Room temperature MAS-NMR spectra of $H_3PW_{12}O_{40} \cdot nH_2O$ as a function of dehydration under dry N_2 flow for 2 h at: (a) 323 K, (b) 373 K, (c) 473 K, (d) 573 K, (e) 673 K, (f) 873 K. (Taken from Ref. [116]).

NMR spectroscopies, thermal analysis and inelastic neutron scattering as a function of the hydration state of the samples, as illustrated in Figure 14.7 and described in Section 14.5.4 [116].

An alternative way to determine acidity was to outgas the samples at increasing temperatures and to follow the weight losses by thermogravimetric analysis (TGA). Physisorbed water desorbs initially followed by water release from acid OH groups, according to the equations

$$H_3PW_{12}O_{40} \cdot n\ H_2O \rightarrow H_3PW_{12}O_{40} + n\ H_2O$$

followed by

$$H_3PW_{12}O_{40} \rightarrow PW_{12}O_{38.5} + 1.5\ H_2O$$

Another way to characterize acidity is to study the differential heat of adsorption of a basic probe compound, such as ammonia or pyridine, by microcalorimetry as a function of uptake. This technique yields the distribution of acid strength relative to coverage, but unfortunately does not differentiate between Brønsted and Lewis

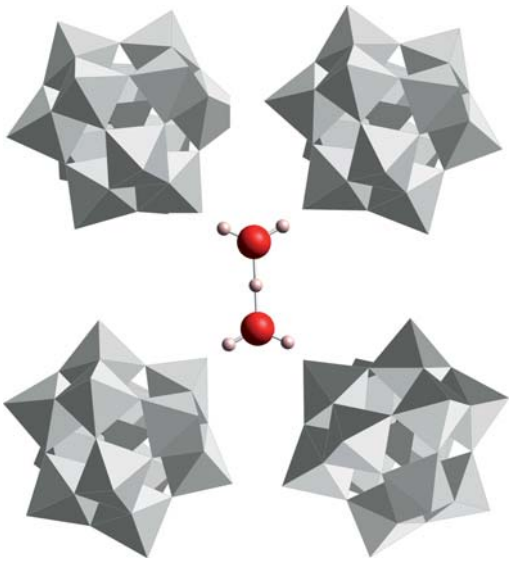

Figure 14.8 $H_5O_2^+$ species located between Keggin anions.

acid sites. It should thus be coupled with IR spectroscopic study of adsorption of the same basic probe molecule (Section 14.5.1).

X-ray and neutron diffraction and MAS-NMR techniques were successfully applied to identify the structure of hydrated and/or partially dehydrated HPAs [117–119]. The structure of 12-tungstophosphoric acid hexahydrate was solved using X-ray and neutron diffraction. The proton was shown to be coordinated to two water molecules in $H_5O_2^+$ species hydrogen bonded to four terminal W=O_t oxide ions as shown in Figure 14.8. The occupancy factor of the water O site was found to be equal to 0.5, supporting the suggestion of formation of $H_5O_2^+$, in the inter-Keggin anion space.

^{17}O NMR has been applied to differentiate the types of oxide ions in the Keggin anion [120], except for the PO_4 tetrahedron, which did not give rise to O exchange. The up-field NMR shift of the O_t resonance, upon dehydration of polycrystalline $H_3PW_{12}O_{40} \cdot xH_2O$ was interpreted as an indication that protonation sites in the anhydrous form of $H_3PW_{12}O_{40}$ are the terminal oxide ions. However, based on IR spectroscopy data, the identification of protonation sites in anhydrous POMs with the Keggin structure resulted in a different interpretation. Both terminal oxygens (M=O_t) and/or bridged oxygens (M–O–M) were proposed [121, 122]. Additionally, IR and Raman spectroscopies were used extensively to monitor the structural variations against the nature of the heteroatom (X) and/or of the transition metal element (M). Valuable information has been collected regarding both the assignment of the absorption frequency of the M=O, M–O–M and X–O vibrations [123] and the sensitivity of these vibrations to structural changes and/or hydration state or partial replacement of protons by alkaline cations.

14.5.1 IR Spectroscopy

The IR spectra of polyoxometallates have already been comprehensively discussed in the literature. The IR bands have been assigned previously [124–127]. The four distinct oxygen sites in a Keggin unit are represented in Figure 14.2(b) and correspond to the following description:

- Four O_a belong to the central tetrahedra PO_4.
- Twelve O are terminal oxygens, to a lone addendum M atom.
- Twelve O_b are involved in M—O_b—M bridges, between two different M_3O_{13} groups.
- Twelve O_c are involved in M—O_c—M bridge, in the same M_3O_{13} groups.

The most relevant assignments are as follows: ν_{as}(P—O_a), (1080–1060 cm^{-1}), ν_{as}(M—O_t) (990–960 cm^{-1}), ν_{as}(M—O_b—M) (900–870 cm^{-1}) and ν_{as}(M—O_c—M) (810–760 cm^{-1}). Some differences have been observed for lacunary Keggin-related compounds α-$[XM_{11}O_{39}]^{n-}$, which have a defect structure in which one metal atom and its terminal oxygen atoms are missing. These anions have a hole surrounded by five oxygen atoms and behave as pentadentate ligands. A general splitting of P—O stretching frequencies was observed and interpreted as a weakening of anion cohesion. In particular, the decrease in frequency of asymmetric bridge stretching is consistent with the lowering of M—Oc—M angles. The P—O stretching band for $[PM_{11}O_{39}]^{7-}$ is split into 1085 and 1040 cm^{-1}. This splitting is due to change of symmetry from T_d (XM_{12}) to C_s (XM_{11}) and may cause broadening of the band.

The protons were suggested to be localized on the most highly negatively charged O atoms, namely the O_b atoms. The ν_{as}(M—O_b—M) mode is thus expected to be sensitive to the degree of hydration owing to hydrogen bonding, which decreases the M—O bond strength, thus increasing the bond length and decreasing the vibration frequency. Consequently, it is also sensitive to the nature of the cations exchanging protons. An increase in the ν_{as}(M—O_b—M) frequency is thus expected upon dehydration as clearly shown in an *in situ* study of $Cs_{2.5}H_{1.5}W_{12}O_{40}$. Moreover, when the M—O bond strength increases, the bond becomes more covalent, its vibration frequency increases and the protons more free and thus more acidic. Thus an increase in ν_{as}(M—O_b—M) frequency may correspond to an increase in Brønsted acidity strength and/or to a dehydrated state.

The acidic properties can also be estimated by NH_3 thermal desorption, although NH_3 can also act as a reductant at high temperature [128] and does not differentiate between Brønsted and Lewis acid sites. The acid subjected to evacuation at room temperature for 30 min showed a strong ν_{OH} absorption at 3209 cm^{-1} with a prominent shoulder at 3355 cm^{-1}. In addition, the δ_{H2O} absorption band appeared at 1708 cm^{-1} as previously reported [129–134]. TGA performed under the same conditions, vacuum at ambient temperature for 30 min, showed that the HPA sample corresponded to $H_3PW_{12}O_{40} \cdot 5H_2O$, a state close to the stable hexahydrate form. The former absorption, at 1708 cm^{-1}, is typical of the presence of the protonated water clusters, probably the di-aqua-hydrogen ion $H_5O_2^+$, as demonstrated to be present

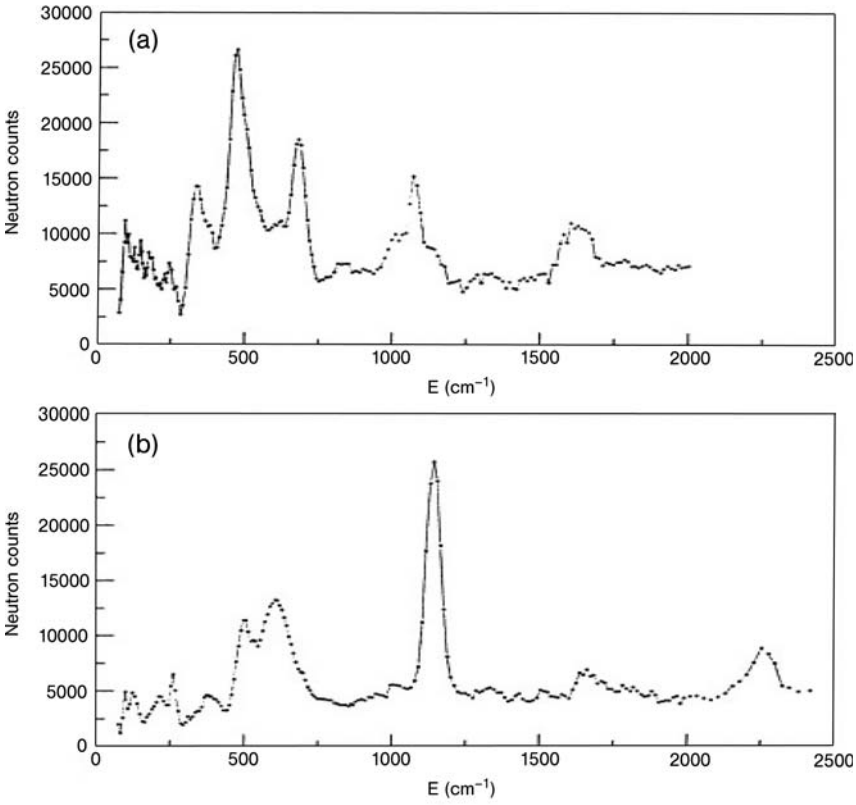

Figure 14.9 4 K INS spectra of $H_3PW_{12}O_{40} \cdot nH_2O$ as a function of dehydration under dry N_2 flow for 2 h at: (a) 473 K (H_3O^+ species) and (b) 573 K (lone protons). (Taken from Ref. [116]).

in $H_3PW_{12}O_{40} \cdot 6H_2O$ by X-ray and neutron diffraction studies [135], and/or hydroxonium ion which has been recently identified by inelastic neutron scattering (INS) in partially dehydrated 12-tungstophosphoric acid [116, 136]. INS data as a function of hydration state of $H_3PW_{12}O_{40}$ are illustrated in Figure 14.9. At 4K $H_5O_2^+$, H_3O^+ and H^+ (lone protons) were identified. $Cs_{1.9}H_{1.1}PW_{12}O_{40}$ was also characterized in the same way by INS.

14.5.2
Photoacoustic Spectroscopy

This technique is complementary to IR spectroscopy and well suited for dark colored samples. As for IR, it has been employed for structural determination

using five or six bands below 1100 cm^{-1} that are characteristic of POMs and for water species such as H_3O^+ (~1710 cm^{-1}) and water (broad bands at ~3200 cm^{-1}, at ~2240 cm^{-1} due to H-bonded crystal water) [137].

14.5.3
UV-Visible Spectroscopy

Electronic spectroscopy of Keggin-type heteropoly compounds has been used for structural and quantitative analyses. POMs mainly absorb in the 180–270 nm region. The incorporation of a transition metal in the framework gives rise to additional bands in the UV-Vis region, depending on its nature and oxidation state. Postulation of reaction mechanisms, especially for oxidation reactions by performing *in situ* studies of the reaction mixture, has been based upon application of the technique. The changes observed in the spectra can be correlated to the formation of active intermediates formed due to the interaction between the active center in the catalyst and the oxidant, and the change in oxidation state of the transition metal elements.

14.5.4
Nuclear Magnetic Resonance Spectroscopy

NMR spectroscopy is a valuable tool in the study of the electron density distribution which results in large chemical shifts induced by both paramagnetic atoms and electron transfer between atoms in diamagnetic HPAs. Some paramagnetic contributions may exist depending on the presence of paramagnetic elements, such as V^{IV}, Mo^{V}, $Cr^{3+/V}$, Fe^{3+}, Ni^{2+}, Co^{2+}, and so on (d^n ions, $n \neq 0$ or 10) and leads to variations of the observed chemical shift. Several important elements can be studied easily. The most widely investigated nuclei include ^{31}P, ^{183}W, ^{51}V, ^{1}H, ^{13}C and ^{17}O. Studies of the electron density distribution in both diamagnetic and paramagnetic species are important for understanding the nature of chemical bonding in POMs and their role in chemical reactions.

^{17}O NMR spectroscopy provides information about the bonding nature of the oxygen atoms. There is a correlation between the downfield shift and the decreasing number of metal atoms to which the oxygen atom is bonded. Unfortunately, ^{17}O NMR spectroscopy is not often used, owing to the low natural abundance of ^{17}O. In contrast, ^{1}H NMR is an important and widely used tool for the detection of the different types of protons present in the heteropoly compound, especially because there is a change in the spectra with the number of hydration water molecules. ^{31}P NMR is widely used for structure description, especially in mixed addenda heteropoly compounds owing to the presence of a number of structural isomers, which become more numerous as the number of addenda atoms increases. It is greatly dependent on the degree of hydration in 12-phosphotungstic acid, containing $n\,H_2O$, values being −15.1 to −15.6 ppm for $n = 6$ and −11.1 to −10.5 ppm for $n = 0$ as shown in Figure 14.7. The difference

is explained as follows: the former band is assigned to protonated water, $H(H_2O)_2^+$, connected with the heteropolyanion by hydrogen bonding at terminal oxygen and the latter band is assigned to the protons directly attached to the oxygen atoms of the polyanion. ^1H MAS-NMR spectra of $H_3PW_{12}O_{40}$ have been recorded at room temperature as a function of dehydration state [116] as for ^{31}P spectra in Figure 14.7. Samples a to c showed a single peak at about 7 ppm, samples d and e showed a broad peak at 7.5 ppm while sample f showed a peak at 6.6 ppm. The assignment of the different peaks was as follows: the peak at 10.5 ppm for bare protons, at 9.7 ppm for H_3O^+, at 7.5 ppm for $H_5O_2^+$ and at 7 ppm for $H(H_2O)_n^+$. A similar study of ^{31}P and ^1H on a $Cs_{1.9}H_{1.1}PW_{12}O_{40} \cdot nH_2O$ sample showed that the dehydration state was reached at a temperature about 100 K lower [116].

^{51}V NMR has also been widely used for structural elucidation of vanadium-containing mixed addenda heteropoly compounds, owing to the large natural abundance of ^{51}V nuclei. The number of structural isomers increases with the increase in the number of addenda atoms and their position in the Keggin structure is confirmed by ^{51}V NMR spectroscopy [138].

14.5.5
Electron Spin Resonance (ESR) Spectroscopy

Electron Spin Resonance (ESR) spectroscopy is well suited to the study of electron delocalization problems and spin density distribution, but it is limited to systems containing unpaired electrons. It gives information about the site symmetry and electronic structure of paramagnetic metal ions. ESR spectra may give information about mixed valence structure of reduced heteropoly compounds. The presence of unpaired spin in reduced HPA species gives rise to an ESR spectrum whose pattern depends on the number of atoms acquiring the unpaired electrons and also the temperature. For axial MO_6 complexes, to which the reduced form of HPA containing V^{IV}, Mo^V or W^V belong, an anisotropic ESR spectrum is observed [139]. The spectrum can become symmetrical at high temperature owing to molecular tumbling and electron delocalization over several atoms. The presence of a non-degenerate d_{xy} orbital for each octahedron allows these HPAs to be reversibly reduced by one or more electrons with retention of the original structure. Reduction of the anion results in the blue color arising from the intervalence band. The one-electron-reduced species gives rise to ESR spectra that have been interpreted to show complete delocalization of the unpaired spin over the twelve metal atoms. The ESR spectra at different temperatures have shown that one electron is trapped at quite low temperatures with only a partial delocalization, whereas it is completely delocalized at higher temperatures. This suggests that the spin is partially localized in the ground state but is involved in rapid thermal hopping from one site to another at elevated temperatures. This unpaired electron resides on a more easily reduced metallic atom. The degree of electron delocalization in the ground state is determined by the extent of interaction in the bridges [138].

14.5.6
Electrochemistry of Keggin Heteropoly Compounds

Heteropoly compounds can act as redox active materials when changing the heteroatom transition metal, without affecting the basic Keggin structure. The vast chemistry of heteropolyanion involves oxidation/reduction of addenda or the active transition metal. The electrochemical analysis of such species forms the basis of identification of redox active species. Thus electrochemical techniques such as cyclic voltammetry are means to understand the reactivity and mechanistic behavior of heteropolyanions as redox agents and redox catalysts in the liquid phase. The wide range of counter-cations assists in the study of the redox behavior of these anions, inducing solubility in a variety of solvents from water to a wide range of organic solvents. The heteropolyanions undergo rapid one- and two-electron reversible reduction to produce the heteropolyblues and further irreversible reduction can lead to their concomitant decomposition. Reduction is accompanied by an increase in the charge density and basicity. Reduction can also be accompanied by protonation depending on the pK_a of the produced oxometallate. The reduction potentials of the Keggin-type heteropoly tungstates and heteropoly molybdates are controlled by factors such as the nature of isomers. The reducibility increases in the sequence α-, β-, γ-. The reduction potential of one-electron waves is found to decrease linearly with a decrease in the valence of the central metal or an increase in the negative charge of the heteropolyanion. Transition metals incorporated into heteropolyanions reside in an octahedral environment, with one coordination site occupied by a solvent molecule, most commonly water. They can be oxidized to the corresponding oxometal, hydroxometal or peroxometal derivative depending on the nature of the metal and the oxidant. These species play an important role in oxidation catalysis.

The formal redox potential depends on a number of factors such as the nature of the heteroatom and addenda atom. The redox potential of the metal increases with increasing formal charge on the central atom. For a given oxidation state, the redox potential increases with the size and decreasing electronegativity of the central metal atom. The electrolytic conditions such as pH, counter-cation and the nature of the solvent also play an important role in determining the formal redox potential. By varying the addenda atom, the electrochemical character of the polyoxometallates can be changed. The addenda atoms can be arranged in decreasing oxidizing ability in the following order $V^{V} > Mo^{VI} > W^{VI}$. In case of one-electron-reduced mixed addenda heteropolyanions, the added electron is localized on the more reducible atom at room temperature [140]. For HPA-n = $H_{3+n}PMo_{12-n}V_nO_{40}$, $E_{Red} < E_{HPA\text{-}n} < E_{O2}$, where Red indicates reduced The reduction potential $E_{HPA\text{-}n}$ equals about 0.7 V versus standard hydrogen electrode (SHE) for HPA-n with n = 1–4 at pH = 1 and the standard reduction potential of oxygen E_{O2} equals 1.23 V at 298 K.

14.5.7
Thermal Analysis

TGA, Differential Thermal Analysis (DTA) and Differential Thermogravimetric Analysis (DTG) measurements have been employed to determine the number and nature of water molecules present in the POMs. The results of TGA show the presence of two types of water in POM compounds, namely "water of crystallization" and "constitutional water molecules." The loss of the former usually occurs at temperatures below 443–473 K [141]. At temperatures exceeding 543 K for $H_3PMo_{12}O_{40}$ and 623 K for $H_3PW_{12}O_{40,}$ the constitutional water molecules (the acidic protons bound to the oxygens of the polyanion) are lost, according to the literature and for the acid forms [140]. For example the thermolysis of $H_3PMo_{12}O_{40}$ proceeds in two steps as schematized below:

$$H_3PMo_{12}O_{40} \cdot n\ H_2O \rightarrow H_3PMo_{12}O_{40} + n\ H_2O \text{ below } 543\,K$$

$$H_3PMo_{12}O_{40} \rightarrow H_{3-x}PMo_{12}O_{40-x/2} + (x/2)\ H_2O \text{ above } 623\,K$$

When protons are exchanged with metal cations, some water molecules physisorbed on these cations may be released at temperatures higher than 623 K, which unfortunately makes the assignment of water release above 270 °C to constitutional water, and therefore to protonic sites, questionable [142].

Thermal desorption of basic molecules such as ammonia and pyridine has been used to characterize acidic properties. For instance, ammonia has been observed to desorb at about 573 K on SiO_2—Al_2O_3 against >773 K on acid zeolites and >873 K on $H_3PW_{12}O_{40}$ and its $(NH_4)_xH_{1-x}$ and $Cs_{2.5}$ salts. Moreover it has also been shown that decomposition of ammonia to N_2, H_2, H_2O, as detected by MS analysis on line, has occurred during desorption at high temperature, which precludes the assignment to acid strength.

14.5.8
Microcalorimetry of Acid or Basic Probe Adsorption

The technique has been fruitfully used to characterize acid and basic sites in many catalysts, in particular for zeolites and metal oxides [143]. It has also been applied for POMs [144]. It consists of measuring the differential heats of adsorption when adsorbing successive increments of a basic probe molecule such as ammonia or pyridine for acidity characterization or of an acid probe molecule such as CO_2 or SO_2 to characterize basicity. The technique produces a histogram of the acid–base strength as a function of coverage, in particular when heterogeneity in strength exists. The data should then be compared with ammonia or pyridine desorption data from IR and thermal desorption experiments (see above).

14.6
Conclusions and Perspectives in Polyoxometallate Application in Heterogeneous Oxidation Catalysis

Owing to their multifunctional properties and easy preparation methods, wheel- or ball-shaped nanostructured POMs appear promising for applications in many fields, especially in heterogeneous catalysis for acid- and oxidation-type reactions. Industrial applications have already been established as mentioned at the end of Section 14.3. The problem of relatively weak stability under catalytic conditions has been partly circumvented by using alkali metal salts such as those of Cs^+. However, further progress is required and the stabilization of POMs in reaction conditions for long periods of time remains a key issue in their industrial development, and a real challenge for the future. The tertiary structure is modified under oxidation reaction conditions with a systematic decrease of the surface area, but more crippling is the observed change in the primary and consequently the secondary structures. For example, it was shown using Raman spectroscopy that the Keggin anion structure of $H_4PVMo_{11}O_{40}$ was relatively unstable upon heat treatment [145]. Vanadyl and molybdenyl species are expelled from the anions of the first layers of the compounds during oxidation reactions and defective Keggin structures are formed. These defective structures further disintegrate, presumably to form Mo_3O_{13} triads. In time, these fragments oligomerize to molybdenum oxygen clusters comparable to hepta- or octamolybdates, and finally to MoO_3-type oxides. The presence of water in the gas feeds, thought to be positive for the stabilization of the proton-containing phases, turned out to promote degradation of the anion. As stated above, only the presence of alkali metal cations, such as cesium, as counter-cations led to a partial stabilization of the structure. It has been shown that pure molybdophosphoric Keggin anions with Te or V cations capping these anions, as schematized in Figure 14.10, were very stable in the reaction conditions for isobutane partial oxidation up to 633 K and no degradation species could be detected [146]. Similar cappings have been observed with vanadium [147].

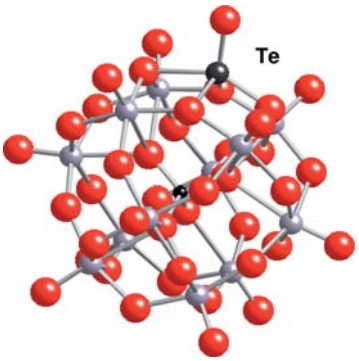

Figure 14.10 Example of Te capping a Keggin unit and helping to stabilize the anion. The Te cation is five coordinated, involving four oxygens from the same Keggin unit. (Taken from Ref. [146]).

In this chapter, we have reviewed the acid and redox properties of such materials which can be controlled and tuned by changing the chemical composition, whatever the addenda elements or the counter-cations, and the structure of the POMs.

The porosity of such materials has also been shown to vary depending on their chemical composition, and some examples have been given above based on "shape selectivity" properties. Moreover new POMs have been discovered (e.g. Figure 14.10) for instance the giant wheel- and ball-shaped anions, able to model metal oxide surfaces or to trap large entities such as metal oxide nanoparticles, metalloporphyrins, proteins, enzymes and so on, which opens up tremendous possibilities in many fields of application. Spherical clusters such as $\{Mo_{132}\}$ have pores about 0.5 nm in diameter which is comparable to zeolitic materials such as MFI or mordenite-type zeolites. However, unlike Si/Al zeolites, the POMs have acid and redox ($M^{VI/V}$) centers and are electron-rich, which are key parameters to promote catalytic reactions. The development of functionalized polyoxometallate [148] and polyoxometallate-based polymers [149] with creation of giant two-dimensional networks has been reported and provides new perspectives in the field of organic–inorganic frameworks.

The $\{Mo_{154}\}$ clusters are linked to form layered frameworks with nanosized channels [150] and could be considered as a model for bulk layered materials. The problem is how to remove cations between the layers, which prevent reactant access to the sites. These giant clusters can be considered as models for bulk layered metal oxides, including defects [151], as observed on large surfaces. The effect of such defects on catalytic properties, mainly for oxidation reactions, is quite important although still only partly known. For instance, local defects such as anionic or cationic vacancies leading to different coordination spheres of the surface O^{2-} anion in MgO have been characterized by DFT calculation, photoluminescence, IR and ^1H NMR [152] and have been shown to influence their basic properties as illustrated by the 2-methyl-but-3-yn-2-ol (MBOH) decomposition reaction, Such a reaction has been shown [153] to give 3-methyl-but-3-en-1-yne (Mbyne) and 3-methyl-but-2-enal (Prenal) on acid sites, 3-hydroxy-3-methyl-butanone (HMB) and 3-methyl-but-3ene-2-one (MIPK) on amphoteric sites and acetone and acetylene on basic sites. In a study of alkaline earth oxides involving Mg, Ca and Sr, insertion of Nd^{3+} cations and the use of different preparation and activation procedures (sol–gel against co-precipitation) have been shown in both cases by detailed XRD analysis to lead to local defects, which have been demonstrated to be of major importance for the propane oxidation reaction mechanism (radical-type) and selectivity to propene and ethene [154].

Great effort is now devoted to the design of functionalized POM catalysts to aid the development of green catalytic processes. Many examples have been presented in this chapter using either oxygen (air) or hydrogen peroxide as green oxidants for the up-grading of many organic chemicals to valuable compounds.

References

1 (a) Souchay, P. (1963) *Polyanions et Polycations*, Gauthier-Villars, Paris.
(b) Souchay, P. (1969) *Ions Minéraux Condensés*, Masson, Paris.
(c) Pope, M.T. (1983) *Heteropoly and Isopoly Oxometalates*, Springer, New York.
(d) Pope, M.T. and Müller, A. (1991) *Angewandte Chemie–International Edition*, **30**, 34.

2 (a) Tsigdinos, G.A. (1978) *Topics in Current Chemistry*, **1**, 76.
(b) Tsigdinos, G.A. and Hallada, C.J. (1968) *Inorganic Chemistry*, **7**, 437.

3 Misono, M. (2001) *Chemical Communications*, 1141.

4 Moffat, J.B. (2001) *Metal-oxygen Clusters. The Surface and Catalytic properties of Heteropoly Oxometallates*, Kluwer, New York, pp. 97–142.

5 Bonardet, J.L., Fraissard, J., Mc Garvey, G.B. and Moffat, J.B. (1995) *Journal of Catalysis*, **151**, 147.

6 Höchler, M., Englert, U., Zibrowius, B. and Hölderich, W.F. (1994) *Angewandte Chemie–International Edition*, **33**, 2991.

7 Inumaru, K., Nakajima, H., Itoh, T. and Misono, M. (1996) *Chemistry Letters*, 559.

8 Na, K., Lizaki, T., Okuhara, T. and Misono, M. (1995) *Chemistry Letters*, 155.

9 Langpape, M., Millet, J.-M.M., Ozkan, U.S. and Boudeulle, M. (1999) *Journal of Catalysis*, **181**, 80.

10 Berzelius, J.J. (1826) *Poggend. Ann. Phys. Chem.*, **6**, 369.

11 Galissard de Marignac, J.-C. (1864) *Ann. Chim. & Phys., 4è série*, **3**, 1.

12 Werner, A. (1907) *Berichte der Deutschen Chemischen Gesellschaft*, **40**, 40.

13 Miolati, A. and Pizzighelli, R. (1908) *Journal für Praktische Chemie*, **77**, 417;

14 Rosenheim, A. (1921) *Handbuch Der Anorganischen Chemie* (eds E. Abegg and F. Auerbach), Vol. 4, Part 1, ii, Hizel Verlag, Leipzig, pp. 997–1064.

15 Pauling, L. (1929) *Journal of the American Chemical Society*, **51**, 2868.

16 Keggin, J.F. (1934) *Proceedings of the Royal Society of London*, **A144**, 75.

17 Evans, H.T. (1948) *Journal of the American Chemical Society*, **70**, 1291.

18 Dawson, B. (1953) *Acta Crystallographica*, **6**, 113.

19 (a) Souchay, P. (1943) *Annales de Chimie France*, **19**, 102.
(b) Souchay, P. (1945) *Contribution à l'étude des Hétéropolyacides Tungstiques*, Masson, Paris.
(c) Souchay, P. (1965) *Talanta*, **12**, 1187.
(d) Souchay, P., Massart, R. and Hervé, G. (1967) *Review of Polarography*, **14**, 270.
(e) Jolivet, J.-P. (1994) *De la Solution à l'oxyde. Condensation des Cations en Solution Aqueuse. Chimie de Surface des Oxides*, EDP Sciences, Paris, CNRS Editions.

20 (a) Müller, A., Plass, W., Krickemeyer, E., Dillinger, S., Bögge, H., Armatage, A., Proust, A. and Beugholt, C. (1994) *Angewandte Chemie–International Edition*, **33**, 349.
(b) Delgado, O., Dress, A. and Müller, A. (2001) *Polyoxometallate Chemistry from Topology via Self-Assembly to Applications* (eds M.T. Pope and A. Müller), Kluwer, Dordrecht, p. 69.

21 (a) Baker, L.C.W. and Glick, D.D. (1998) *Chemical Reviews*, **98**, 3.
(b) Gouzerh, P. and Che, M. (2006) *Actualité en Chimie*, **298**, 9.

22 (a) Mialane, P., Dolbecq, A. and Secheresse, F. (2006) *Chemical Communications*, **33**, 3477.
(b) Dolbecq, A., Mellot-Draznieks, C., Mialane, P., Marrot, J., Ferey, G. and Secheresse, F. (2005) *European Journal of Inorganic Chemistry*, **15**, 3009.

23 Kong, X.J., Ren, Y.P., Zheng, P.Q., Long, Y.X., Long, L.S., Huang, R.B. and Zheng, L.S. (2006) *Inorganic Chemistry*, **45**, 10702.

24 Mioc, U.B., Todorovic, M.R., Davidovic, M., Colomban, P. and Holclajtner-Antunovic, I. (2005) *Solid State Ionics*, **176**, 3005.

25 Keita, B. and Nadjo, L. (1990) *Journal of Electroanalytical Chemistry*, **287**, 149.

26 Rhule, J.T., Hill, C.L. and Judd, D.A. (1998) *Chemical Reviews*, **98**, 327.

27 (a) Okuhara, T., Mizuno, N. and Misono, M. (1996) *Advanced Catalysis*, **41**, 113.
(b) Okuhara, T., Mizuno, N. and Misono, M. (2001) *Applied Catalysis A: General*, **222**, 63.

28 Kozhevnikov, I.V. (1998) *Chemical Reviews*, **98**, 171.

29 Chu, W., Yang, X., Shan, Y., Ye, X. and Wu, Y. (1996) *Catalysis Letters*, **42**, 201.

30 Kozhevnikov, I.V., Kloetstra, K.R., Sinnema, A., Zandbergen, H.W. and van Bekkum, H. (1996) *Journal of Molecular Catalysis A–Chemical*, **114**, 287.

31 Marme, F., Coudurier, G. and Védrine, J.C. (1998) *Microporous and Mesoporous Materials*, **22**, 151.

32 (a) Massart, R. (1969) *Annales de Chimie France*, **4**, 365 and 431.
(b) Souchay, P. and Hervé, G. (1965) *Comptes rendus de l'Académie des Sciences, Paris*, **261**, 2486.
(c) Hervé, G. (1966) *Comptes rendus de l'Académie des Sciences, Paris*, **263**, 1297.
(d) Hervé, G. (1967) *Comptes rendus de l'Académie des Sciences, Paris*, **265**, 805.
(e) Hervé, G. (1971) *Annales de Chimie France*, **6**, 219.
(f) Tézé, A. and Hervé, G. (1977) *Journal of Inorganic and Nuclear Chemistry.*, **39**, 999.

33 Otake, M. and Onoda, T. (1976) *Shokubai*, **18**, 169.

34 (a) Matveev, K. (1977) *Kinetika i Kataliz*, **18**, 862.
(b) Matveev, K.I. and Kozhevnikov, I.V. (1980) *Kinetika i Kataliz*, **21**, 1189.
(c) Kozhevnikov, I.V. (1995) *Catalysis Reviews–Science and Engineering*, **37**, 311.
(d) Kozhevnikov, I.V. (1998) *Chemical Reviews*, **98**, 171.
(e) Kozhevnikov, I. (2002) *Catalysis for Fine Chemical Synthesis. Catalysis by Polyoxometalates*, John Wiley & Sons, Ltd, Chichester, UK.
(f) Kozhevnikov, I.V. (2007) *Journal of Molecular Catalysis A–Chemical*, **262**, 86.

35 (a) Misono, M. (1987) *Catalysis Reviews–Science and Engineering*, **29**, 268.
(b) Misono, M. (1988) *Catalysis Reviews–Science and Engineering*, **30**, 339.
(c) Okuhara, T., Mizuno, N. and Misono, M. (1996) *Advanced Catalysis*, **41**, 113.
(d) Okuhara, T., Mizuno, N. and Misono, M. (2001) *Applied Catalysis A: General*, **222**, 63.
(e) Mizuno, N. and Misono, M. (1998) *Chemical Reviews*, **98**, 199.
(f) Misono, M. and Acad, C.R. (2000) *Comptes rendus de l'Académie des Sciences, Paris, Sér IIc Chimie/Chemistry*, **3**, 471.
(g) Min, J.S. and Mizuno, N. (2001) *Catalysis Today*, **71**, 89.
(h) Mizuno, N., Hikichi, S., Yamaguchi, K., Uchida, S., Nakagawa, Y., Uehara, K. and Kamata, K. (2006) *Catalysis Today*, **117**, 32.

36 (a) Moffat, J.B. (1987) *Reviews of Chemical Intermediates*, **8**, 1.
(b) Moffat, J.B. (1989) *Journal of Molecular Catalysis*, **52**, 169.
(c) Moffat, J.B. (2001) *Metal-oxygen clusters. The Surface and Catalytic properties of Heteropoly Oxometallates*, Kluwer, New York.

37 Corma, A. (1995) *Chemical Reviews*, **95**, 559.

38 Hill, C.L. (1998) *Chemical Reviews*, **98**, 1.

39 Alekar, N. (2000) PhD thesis, Pune, India.

40 Guo, Y. and Hu, C. (2007) *Journal of Molecular Catalysis A–Chemical*, **262**, 136.

41 (a) Védrine, J.C. (2002) *Topics in Catalysis*, **21**, 97.
(b) Novakova, E.K. and Védrine, J.C. (2006) *Metal Oxides. Chemistry and Applications* (ed. J.L.G. Fierro), CRC Taylor & Francis, Boca Raton, Fl., pp. 413–61.

42 Mars, P. and van Krevelen, D.W. (1953) *Chemical Engineering Science*, **3**, 41.

43 (a) Dimitratos, N. and Védrine, J.C. (2003) *Catalysis Today*, **81**, 561.
(b) Dimitratos, N. and Védrine, J.C. (2003) *Catalysis in Application* (eds S.D. Jackson, J.S.J. Hargreaves and D. Lennon), Royal Society of Chemistry, Cambridge, pp. 145–52.
(c) Dimitratos, N. and Védrine, J.C. (2003) *Applied Catalysis A: General*, **256**, 251–63.
(d) Dimitratos, N. and Védrine, J.C. (2006) *Journal of Molecular Catalysis A–Chemical*, **255**, 184–92.

44 Centi, G., Cavani, F. and Trifiro, F. (2001) *Selective Oxidation by Heterogeneous Catalysis*, Kluwer, New York.

45 Hill, C.L. and Proster-McCartha, C.M. (1995) *Coordination Chemistry Reviews*, **143**, 407.

46 Mizuno, N., Hirose, T., Tateishi, M. and Iwamoto, M. (1993) *Chemistry Letters*, 1839.

47 Mizuno, N., Hirose, T. and Iwamoto, M. (1994) *Studies in Surface Science and Catalysis*, **82**, 593.

48 Kholdeeva, O.A., Grigoriev, V.A., Maksimov, G.M., Fedotov, M.A., Golovin, A.V. and Zamaraev, K.I. (1990) *Journal of Molecular Catalysis*, **114**, 123.

49 Hamamoto, M., Nakayama, K., Nishitama, Y. and Ishii, Y. (1993) *Journal of Organic Chemistry*, **58**, 6421.

50 Kuznetova, N.I. and Yurchenko, E.N. (1989) *Reaction Kinetics and Catalysis Letters*, **39**, 399.

51 Harrup, M.K. and Hill, C.L. (1994) *Inorganic Chemistry*, **331**, 5448.

52 Khenkin, A.M. and Hill, C.L. (1993) *Journal of the American Chemical Society*, **115**, 8178.

53 Seo, Y.-J., Makai, Y., Taganawa, T. and Goto, S. (1997) *Journal of Molecular Catalysis*, **120**, 149.

54 Neumann, R. and Levin, M. (1992) *Journal of the American Chemical Society*, **114**, 7278.

55 Kholdeeva, O.A., Golovin, A.V. and Kozhevnikov, I.V. (1992) *Reaction Kinetics and Catalysis Letters*, **46**, 107

56 Lissel, M., In de Val, H.J. and Neumann, R. (1992) *Tetrahedron Letters*, **33**, 1795.

57 Neumann, R. and Assael, I. (1998) *Journal of the Chemical Society D–Chemical Communications*, 1285.

58 Atlamsani, A., Brégeault, J.-M. and Ziyad, M. (1993) *Journal of Organic Chemistry*, **58**, 5663.

59 Nakayama, K., Hamamoto, M., Nishiyama, Y. and Ishii, Y. (1993) *Chemistry Letters*, 1699.

60 Ali, B.E., Brégeault, J.-M., Mercier, J., Martin, J., Martin, C. and Convert, O. (1989) *Journal of the Chemical Society D–Chemical Communications*, 825.

61 Ai, M. (1982) *Applied Catalysis*, **4**, 245.

62 Akimoto, M., Tsuchida, Y., Sato, K. and Echigoya, E. (1981) *Journal of Catalysis*, **72**, 83.

63 Eguchi, K., Aso, I., Yamazoe, N. and Seiyama, T. (1979) *Chemistry Letters*, 1345.

64 Dimitratos, N. and Védrine, J.C. (2006) *Catalysis Communications*, **7**, 811.

65 Centi, G., Lopez Nieto, J.M. and Iapalucci, C. (1989) *Applied Catalysis*, **46**, 197.

66 (a) Cavani, F., Trifiro, F. and C. (1994) *Catalysis Today*, **11**, 247.
(b) Cavani, F., Mezzogori, R., Pigamo, A. and Trifirò, F. (2001) *Catalysis Today*, **71**, 97.

67 (a) Mizuno, N., Tateishi, M. and Iwamoto, M. (1994) *Journal of the Chemical Society D–Chemical Communications*, 1411.
(b) Mizuno, N., Tateishi, M. and Iwamoto, M. (1994) *Applied Catalysis A: General*, **118**, L1.
(c) Mizuno, N., Han, W., Kudo, T. and Iwamoto, M. (1996) *Studies in Surface Science and Catalysis*, **101**, 1001.
(d) Mizuno, N., Tateishi, M. and Iwamoto, M. (1997) *Journal of Catalysis*, **163**, 87.

68 Cavani, F., Etienne, E., Favaro, M., Gall, A., Trifiro, F. and Hecquet, G. (1995) *Catalysis Letters*, **32**, 215.

69 Cavani, F., Mezzogori, R., Pigamo, A. and Paris, F. Trifirò (2000) *Comptes rendus de l'Académie des Sciences,Paris, Série IIc, Chimie/Chemistry*, **3**, 523.

70 Min, J.-S. and Mizuno, N. (2001) *Catalysis Today*, **71**, 89.

71 Mizuno, N., Tateishi, M. and Iwamoto, M. (1995) *Applied Catalysis A: General*, **128**, L165.

72 Mizuno, N., Suh, D.J., Han, W. and Kudo, T. (1996) *Journal of Molecular Catalysis A–Chemical*, **114**, 309.

73 Bayer, R., Marchal, C., Liu, F.X., Tézé, A. and Hervé, G. (1996) *Journal of Molecular Catalysis A–Chemical*, **110**, 65.

74 Kirillova, M.V., da Silva, J.A.L., Fraústo da Silva, J.R. and Plombeiro, A.J.L. (2007) *Applied Catalysis A: General*, **332**, 159.

75 Marchal-Roch, C. and Millet, J.-M.M. (2001) *Comptes rendus de l'Académie des*

Sciences,Paris, Sér. IIc, Chimie/ Chemistry, **4**, 321.

76 (a) Langpape, M. and Millet, J.M.M. (2000) *Applied Catalysis A: General*, **200**, 89.(b) Huynh, Q. and Millet, J.M.M. (2005) *Journal of Physics and Chemistry of Solids*, **66**, 887.

77 Borshch, S.A., Duclusaud, H. and Millet, J.M.M. (2000) *Applied Catalysis A: General*, **200**, 103.

78 (a) Langpape, M., Millet, J.M.M., Ozkan, U.S. and Delichere, P. (1999) *Journal of Catalysis*, **182**, 148.
(b) Langpape, M., Millet, J.M.M., Ozkan, U.S. and Boudeulle, M. (1999) *Journal of Catalysis*, **181**, 80.

79 (a) Ueda, W., Suzuki, Y., Lee, W. and Imanoka, S. (1996) *Studies in Surface Science and Catalysis*, **101**, 1065.
(b) Ueda, W. and Suzuki, Y. (1995) *Chemistry Letters*, 541.

80 (a) Cavani, F., Comuzzi, C., Dolcetti, G., Etienne, E., Finke, R.G., Selleri, G., Trifirò, F. and Trovarelli, A. (1996) *Journal of Catalysis*, **160**, 317.
(b) Comuzzi, C., Dolcetti, G., Trovarelli, A., Cavani, F., Trifirò, F., Llorca, J. and Finke, R.G. (1996) *Catalysis Letters*, **36**, 75.

81 Albonetti, S., Cavani, F., Trifirò, F. and Koutyrev, M. (1995) *Catalysis Letters*, **30**, 253.

82 Barteau, M.A., Lyons, J.E. and Song, I.K. (2003) *Journal of Catalysis*, **216**, 236.

83 Song, I.K. and Barteau, M.A. (2002) *Journal of Molecular Catalysis A–Chemical*, **185**, 182–3.

84 Ballarini, N., Candiracci, F., Cavani, F., Degrand, H., Dubois, J.-L., Lucarelli, G., Margotti, M., Patinet, A., Pigamo, A. and Trifirò, F. (2007) *Applied Catalysis A: General*, **325**, 263.

85 Ushikubo, T. (2003) *Catalysis Today*, **78**, 79.

86 Huynh, Q., Selmi, A., Lacorre, L. P. and Millet, J.-M.M. *Applied Catalysis A: General* (in press).

87 (a) Venturello, C., Alneri, E. and Ricci, M. (1983) *Journal of Organic Chemistry*, **48**, 3831.
(b) Venturello, C., Aloisio, R.D., Bart, J.C.J. and Ricci, M. (1985) *Journal of Molecular Catalysis*, **32**, 107.
(c) Venturello, C. and Aloisio, R.D. (1988) *Journal of Organic Chemistry*, **53**, 1553.

88 Ishii, Y., Yamawaki, K., Ura, T., Yamada, H., Yoshida, T. and Ogawa, M. (1988) *Journal of Organic Chemistry*, **53**, 3587.

89 Csanyi, L.J. and Jaky, K. (1990) *Journal of Molecular Catalysis*, **61**, 75.

90 (a) Aubry, C., Chottard, G., Platzer, N., Brégeault, J.-M., Thouvenot, R., Chauveau, F., Huet, C. and Ledon, H. (1991) *Inorganic Chemistry*, **30**, 4409;
(b) Salle, L., Aubry, C., Thouvenot, R., Robert, F., Doremieux-Morin, C., Chottard, G., Ledon, H., Jeanin, Y. and Brégeault, J.-M. (1994) *Inorganic Chemistry*, **33**, 871.
(c) Salle, L., Piquemal, J.Y., Thouvenot, R., Minot, C. and Brégeault, J.-M. (1997) *Journal of Molecular Catalysis A–Chemical*, **117**, 375.

91 Gresley, N.M., Griffith, W.P., Laemmel, A.C., Nogueira, H.I.C. and Parkin, B.C. (1997) *Journal of Molecular Catalysis A–Chemical*, **117**, 185.

92 Duncan, D.C., Chambers, R.C., Hecht, E. and Hill, C.L. (1995) *Journal of the American Chemical Society*, **117**, 681.

93 Gao, J., Chen, Y., Han, B., Feng, Z., Zhou, N., Li, C., Gao, S. and Xi, Z. (2004) *Journal of Molecular Catalysis A–Chemical*, **210**, 197.

94 (a) Ding, Y., Gao, Q., Li, G., Zhang, H., Wang, J., Yan, L. and Suo, J. (2004) *Journal of Molecular Catalysis A–Chemical*, **218**, 161.
(b) Gao, Q., Ding, Y., Liu, H. and Suo, J. (2005) *Journal of Chemical Research*, 716.

95 Orita, H., Shimizu, H., Hayakawa, T. and Takehiro, K. (1991) *Reaction Kinetics and Catalysis Letters*, **44**, 3633.

96 Sakaue, S., Tsubakino, T., Nishiyama, Y. and Ishii, Y. (1993) *Journal of Organic Chemistry*, **58**, 3633.

97 Ishii, Y., Tanaka, H. and Nishiyama, Y. (1994) *Chemistry Letters*, 1.

98 Ballistreri, F.P., Failla, S., Spina, E. and Tomaselli, G.A. (1989) *Journal of Organic Chemistry*, **54**, 947.

99 Sakata, Y. and Ishii, Y. (1991) *Journal of Organic Chemistry*, **56**, 6233.

100 Oguchi, T., Sakata, Y., Takeuchi, N., Kaneda, K., Ishii, Y. and Ogawa, M. (1989) *Chemistry Letters*, 865.

101 Matoba, Y., Inoue, H., Akagi, J., Okabayashi, T., Ishii, Y. and Ogawa, M. (1984) *Synthetic Communications*, **14**, 865.

102 Li, G., Ding, Y., Wang, J., Wang, X. and Suo, J. (2007) *Journal of Molecular Catalysis A–Chemical*, **262**, 67.

103 Mizuno, N., Hikichi, S., Yamaguchi, K., Uchida, S., Nakagawa, Y., Uchara, K. and Kamata, K. (2006) *Catalysis Today*, **117**, 32.

104 Mizuno, N. (1998) *Journal of the American Chemical Society*, **120**, 9267.

105 Kuznetsova, L.I., Detusheva, L.G., Kuzenesova, N.I., Fedotov, M.A. and Likholobov, V.A (1997) *Journal of Molecular Catalysis*, **117**, 389.

106 Toshihiro, Y., Eri, I., Yasushi, A. and Kanai, S. (1996) *Journal of Molecular Catalysis*, **114**, 237.

107 Kuznetsova, N.I., Detusheva, L.G., Fedotov, M.A. and Likholobov, V.A. (1996) *Journal of Molecular Catalysis*, **111**, 81.

108 Kuznetsova, N.I., Kuznetsova, N.L.I. and Likholobov, V.A. (1996) *Journal of Molecular Catalysis*, **108**, 135.

109 Simoes, M.M.Q., Conceicao, C.M.M., Gamelas, J.A.F., Domingues, P.M.D.N., Cavaleiro, A.M.V., Ferre-Correia, A.J.V. and Johnstone, R.A.W. (1999) *Journal of Molecular Catalysis*, **144**, 461.

110 Mizuno, N., Nozaki, C., Kiyoto, I. and Misono, M. (1999) *Journal of Catalysis*, **182**, 285.

111 Mizuno, N., Kiyoto, I., Nozaki, C. and Misono, M. (1999) *Journal of Catalysis*, **181**, 171.

112 Misono, M., Mizuno, N., Inumaru, K., Koyano, G. and Lu, X.-H. (1997) *Studies in Surface Science and Catalysis*, **110**, 35.

113 Nomiya, K., Yanagibayashi, H., Nozaki, C., Kondoh, K., Hiramatsu, E. and Shimizu, Y. (1996) *Journal of Molecular Catalysis*, **114**, 181.

114 Neumann, R. and Delavega, M. (1993) *Journal of Molecular Catalysis*, **84**, 93.

115 Essayem, N., Holmqvist, A., Gayraud, P.-Y., Védrine, J.C. and Ben Taârit, Y. (2001) *Journal of Catalysis*, **197**, 273.

116 Essayem, N., Yong, Y.Y., Jobic, H. and Védrine, J.C. (2000) *Applied Catalysis A: General*, **194–195**, 109.

117 Brown, G.M., Noe-Spirlet, M.-R., Busing, W.R. and Levy, H.A. (1977) *Acta Crystallographica*, **B33**, 1038.

118 Fournier, M., Feumi-Jantou, C., Rabia, C., Hervé, G. and Launay, S. (1992) *Journal of Materials Chemistry*, **2**, 971.

119 Massart, R., Constant, R., Fruchart, J.-M., Ciabrini, J.-P. and Fournier, M. (1977) *Inorganic Chemistry*, **16**, 2916.

120 Kozhevnikov, I.V., Sinnema, A., Jansen, R.J.J. and van Bekkum, H. (1994) *Catalysis Letters*, **27**, 187.

121 Lee, K.Y., Mizuno, N., Okuhara, T. and Misono, M. (1989) *Bulletin of the Chemical Society of Japan*, **62**, 1731.

122 Bielanski, A., Maleka, A. and Kubelkova, L. (1989) *Journal of the Chemical Society–Faraday Transactions I*, **85**, 2847.

123 Rocchiccioli-Deltcheff, C.R., Thouvenot, R. and Franck, R. (1976) *Spectrochimica Acta*, **A32**, 587.

124 Okuhara, T., Mizuno, N. and Misono, M. (1996) *Advanced Catalysis*, **41**, 113.

125 Orita, H., Hayakawa, T., Shimizu, M. and Takehira, K. (1991) *Applied Catalysis*, **77**, 133.

126 Rocchiccioli-Deltcheff, C.R., Fournier, M., Franck, R. and Thouvenot, R. (1983) *Inorganic Chemistry*, **22**, 207.

127 Rocchiccioli-Deltcheff, C.R. and Fournier, M. (1991) *Journal of the Chemical Society–Faraday Transactions*, **87**, 3913.

128 Essayem, N., Fréty, R., Coudurier, G. and Védrine, J.C. (1997) *Journal of the Chemical Society–Faraday Transactions*, **93**, 3243.

129 Mizuno, N., Katamura, K., Yoneda, K. and Misono, M. (1983) *Journal of Catalysis*, **83**, 384.

130 Highfield, J.G. and Moffat, J.B. (1984) *Journal of Catalysis*, **88**, 177.

131 Bielanski, A., Maleka, A. and Kubelkova, L. (1989) *Journal of the Chemical Society–Faraday Transactions I*, **85**, 2847.

132 Bielanski, A., Datka, J., Gil, B. and Malecka-Lubanska, A. (1999) *Catalysis Letters*, **57**, 61.

133 Essayem, N., Kieger, S., Coudurier, G. and Védrine, J.C. (1996) *Studies in Surface Science and Catalysis*, **101**, 591.

134 Essayem, N., Coudurier, G., Védrine, J.C., Habermacher, D. and Sommer, J. (1999) *Journal of Catalysis*, **183**, 292.

135 Brown, G.M., Noe-Spirlet, M.-R., Busing, W.R. and Levy, H.A. (1977) *Acta Crystallographica*, **B33**, 1038.

136 Moic, U.B., Colomban, P., Davidovic, M. and Tomkinson, T. (1994) *Journal of Molecular Structure*, **326**, 99.

137 (a) Highfield, J.G. and Moffat, J.B. (1984) *Journal of Catalysis*, **88**, 177.
(b) Highfield, J.G. and Moffat, J.B. (1984) *Journal of Catalysis*, **89**, 185.
(c) Highfield, J.G. and Moffat, J.B. 1985) *Journal of Catalysis*, **95**, 108.

138 Kazansky, L.P. and Mc Garvey, B.R. (1999) *Coordination Chemistry Reviews*, **188**, 157.

139 (a) Che, M., Védrine, J. and Naccache, C. (1969) *Journal de Chimie Physique*, **65**, 579.
(b) Che, M., Védrine, J. and Naccache, C. (1970) *Bulletin de la Société chimique de France*, 3307.
(c) Derouane, E.G. and Védrine, J.C. (1973) *Industrie Chimique Belge-Belgische Chemische Industrie*, **38**, 375.

140 Sadakane, M. and Steckhan, E. (1998) *Chemical Reviews*, **98**, 219.

141 Bielanski, A., Malecka, A. and Pozniczek, J. (1989) *Journal of Thermal Analysis*, **35**, 1699.

142 Dimitratos, N. and Védrine, J.C. (2003) *Catalysis in Application* (eds S.D. Jackson, J.S.J. Hargreaves and D. Lennon), Royal Society of Chemistry, Cambridge, p. 145.

143 (a) Gravelle, P.C. (1972) *Advanced Catalysis*, **22**, 191.
(b) Gravelle, P.C. (1985) *Thermochimica Acta*, **96**, 365.
(c) Gravelle, P.C. (1977) *Catalysis Reviews–Science and Engineering*, **16**, 37.
(d) Auroux, A. (1994) *Catalyst Characterization: Physical Techniques for Solid Materials* (eds B. Imelik and J.C. Védrine), Plenum Press, New York, p. 611.
(e) Auroux, A. (1997) *Topics in Catalysis*, **4**, 71.
(f) Damjanovic, L. and Auroux, A. (2007) *Handbook of Thermal Analysis and Calorimetry*, Chapter 12 (in press).

144 (a) Lefebvre, F., Dupont, P. and Auroux, A. (1995) *Reaction Kinetics and Catalysis Letters*, **3**, 55.
(b) Liu-Cai, F.X., Sahut, B., Faydi, E., Auroux, A. and Hervé, G. (1999) *Applied Catalysis A: General*, **185**, 75.

145 Mestl, G., Ilkenhans, T., Spielbauer, D., Dieterle, M., Timpe, O., Kröhnert, J., Jentoft, F., Knözinger, H. and Schlögl, R. (2001) *Applied Catalysis A: General*, **210**, 13.

146 Huynh, Q. (2005) PhD thesis, University of Lyon, No. 168.

147 Rodriguez-Fortea, A., de Graaf, C. and Poblet, J.M. (2006) *Chemical Physics Letters*, **428**, 88.

148 (a) Mialane, P., Dolbecq, A. and Secheresse, F. (2006) *Chemical Communications*, **33**, 3477.
(b) Dolbecq, A., Mellot-Draznieks, C., Mialane, P., Marrot, J., Ferey, G. and Secheresse, F. (2005) *European Journal of Inorganic Chemistry*, **15**, 3009.

149 Kong, X.J., Ren, Y.P., Zheng, P.Q., Long, Y.X., Long, L.S., Huang, R.B. and Zheng, L.S. (2006) *Inorganic Chemistry*, **45**, 10702.

150 (a) Müller, A., Krickemeyer, E., Schmidtmann, H., Bögge, M., Beugholt, C., Das, S.K. and Peters, F. (1999) *Chemistry–A European Journal*, **5**, 1496.(b) Müller, A., Das, S.K., Bögge, H., Beugholt, C. and Schmidtmann, M. (1999) *Chemical Communications*, 1935.

151 Müller, A., Rabindranath, M., Schmidtmann, M., Bögge, H., Das, S.K. and Zhang, W. (2001) *Chemical Communications*, 2126.

152 (a) Chizallet, C., Costentin, G., Lauron-Pernot, H., Krafft, J.-M., Che, M., Saussey, J., Delbecq, F. and Sautet, P. (2006) *Journal of Physical Chemistry B*, **110**, 15878.
(b) Chizallet, C., Bailly, M.L., Costentin, G., Lauron-Pernot, H., Krafft, J.-M., Bazin, P., Saussey, J. and Che, M. (2006) *Catalysis Today*, **116**, 196.

153 Lauron-Pernot, H. (2006) *Catalysis Reviews–Science and Engineering*, **48**, 315.

154 Savova, B., Filkova, D., Petrov, L., Crisan, D., Crisan, M., Răileanu, M., Drăgan, N., Galtayries, A. and Védrine, J.C. (to be submitted).

15
Alkane Dehydrogenation over Vanadium and Chromium Oxides

S. David Jackson, Peter C. Stair, Lynn F. Gladden, and James McGregor

15.1
Introduction

The dehydrogenation of light alkanes over chromia systems has been known as a catalytic process since the early 1930s [1]. A comprehensive review of the pre-1954 literature can be found in Emmett's book on catalysis [2]. The dehydrogenation of light alkanes is highly endothermic (for example, propane to propene, $C_3H_8 \Leftrightarrow C_3H_6 + H_2$, $\Delta H^{o}_{298} = +110\,\mathrm{kJ\,mol^{-1}}$) and is equilibrium limited at temperatures below 1000 K. Commercial processes based on chromia catalysts have been operational for over 60 years. During the Second World War chromia/alumina catalysts were used for the dehydrogenation of butane to give butenes, which were then dimerized and hydrogenated to produce high-octane aviation fuel. As was so often the case in the early years of the twentieth century, the dehydrogenation process using a chromia/alumina catalyst was first developed and commercialized in Germany at Leuna. There was also independent development by UOP (then Universal Oil Products) in the United States, together with ICI (Imperial Chemical Industries) in the UK. The first UOP-designed plant came on stream in Billingham, in the North-East of England, in 1940 [3]. Houdry made a significant process development by using a less than atmospheric pressure system, a highly innovative move in an industry where high pressure is the norm. In this way it was possible to achieve a higher per-pass conversion and, indeed, typical operating conditions for current commercial reactors are 0.3–0.5 atm and 823–923 K [4]. A very good review concerning the process chemistry is that of Bhasin [5]. In this chapter we will examine both chromia and vanadia, which although not used commercially, has been thoroughly examined for these reactions. The oxide surfaces have been subject to analysis by a wide range of techniques pre-, during and post-reaction.

Metal Oxide Catalysis. Edited by S. David Jackson and Justin S. J. Hargreaves

ISBN: 978-3-527-31815-5

15.2
Commercial LPG Dehydrogenation Process

The deactivation of chromia catalysts during the dehydrogenation of light alkanes, due to the deposition of carbonaceous species onto the catalyst surface, is well known. Regeneration of the catalyst is periodic and by oxidation. The designs of commercial reactors for this process take different approaches both to managing the deactivation and to the regeneration. Of specific interest in the present context is the following system that uses a chromium oxide catalyst.

15.3
Lummus/Houdry CATOFIN® Process [6]

The CATOFIN process technology is currently owned by Süd-Chemie and is offered for license by ABB Lummus. The CATOFIN process converts propane to propene over a fixed-bed chromia–alumina catalyst [7]. The process takes place in a series of fixed-bed reactors that operate on a cyclic basis. In one complete cycle, hydrocarbon is dehydrogenated and the reactor is purged with steam then subjected to air to reheat the catalyst and burn off coke, which is deposited during the reaction cycle. These steps are followed by an evacuation and reduction and then another cycle is begun. The cycle time is typically 15–25 minutes. In the classic process, the regenerating (heating) gas is fed in the same direction as the process gas, which leads initially to a higher temperature at the feed than the exit. With time on stream, a temperature front will move through the bed as the front of the bed is cooled by the endothermic reaction. Operation is generally at 823–873 K and ~0.3 atm. CATOFIN is also used commercially for isobutane to isobutene. The reaction conditions are usually 923 K and 0.5 atm. The overall operation is similar to that described for propane to propene, with conversion in region of ~50% per pass and selectivity for isobutane to isobutene of greater than 90%; the selectivity of propane to propene is >86% [8]. A catalyst formulation taken from a recent patent [9] has the following make-up, ~20% Cr, ~1% Zr as ZrO_2, ~0.75% Mg as MgO, supported on alumina with an alkali metal oxide promoter such as Na_2O at ~0.75%.

15.4
Chromia

A wide range of techniques has been used on both fresh and used catalysts to characterize the nature of the oxide surface, for example X-ray powder diffraction (XRD) [10–12], UV-Visible diffuse reflectance spectroscopy (UV-Vis DRS) [11, 12], Raman spectroscopy [10, 11, 14–17], X-ray photoelectron spectroscopy (XPS) [11, 12, 18], electron paramagnetic resonance (EPR) [12, 19], infrared spectroscopy [10, 20] and temperature programmed reduction (TPR) [16, 21]. Given the number of

publications we will not review them all but will summarize the main conclusions from this body of work.

Chromium can exist in the (II), (III), (V) and (VI) oxidation states; however, in an as-prepared catalyst the (III) and (VI) oxidation states are the predominant species. At low loadings the +6 state is favored on alumina. On zirconia however Cr(V) was found to be ~50% of the chromium present [22]. As loading increases the surface species change from monochromate to polychromate to α-Cr_2O_3. Typically catalysts are prepared by impregnation of alumina, although zirconia is also used, from a variety of chromium-containing solutions such as ammonium dichromate, chromic acid and chromium nitrate. After calcination in air at 823 K, UV-visible analysis of a 6% w/w chrome oxide/γ-alumina revealed the presence of Cr(III) with bands at 280 nm ($^4A_{2g} \rightarrow {}^4T_{1g}[P]$), 354 nm ($^4A_{2g} \rightarrow {}^4T_{1g}[F]$), 454 nm ($^4A_{2g} \rightarrow {}^2T_{2g}$), 590 nm ($^4A_{2g} \rightarrow {}^4T_{2g}$) and 706 nm ($^4A_{2g} \rightarrow {}^2E_g$, $^2T_{1g}$). XPS analysis indicated that the predominant chromium species was Cr(III) with a small amount of Cr(VI) also detected. This was confirmed by wet chemical analysis of a typical chromium oxide supported on alumina catalyst which gave <10% Cr(VI) [23]. XRD analysis revealed that the only detectable chromium species was Cr_2O_3. Usually no XRD detectable phase is present until the loading is greater than monolayer coverage, typically ~7 wt% for alumina supported catalysts. Raman spectroscopic analysis [13], however, reveals the complexity of the chromia species on the surface (Figure 15.1). Analysis of the spectra gave approximate values for the various components as 14% monomer/dimer, 50% polymer, 7% crystalline, with the balance found in mixed bands.

To obtain the active catalyst the chromia can be reduced with hydrogen, alkane or carbon monoxide [12, 24, 25]; as reported above the commercial process uses a hydrogen reduction. TPR analyses reveal that reduction starts at 543–553 K (T_{int}) increases up to 693 K (T_{max}) and then decreases, with the reduction finishing by

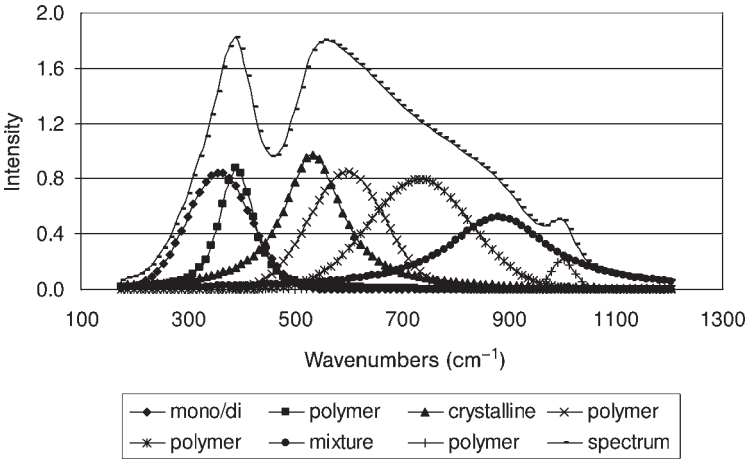

Figure 15.1 Raman spectrum obtained from a 6% CrO_x/alumina catalyst.

723–743 K (T_{fin}) [9, 26]. Burwell and coworkers [27] studied the exchange reaction between alkanes and deuterium over chromia and found that no activity was present if the catalyst had not been activated above 573 K, and maximum activity was observed with samples that had been activated at 743 K, confirming the need for reduction to activate chromia samples.

The active species was initially suggested to be Cr(II) by Sachtler and coworkers [28]. In more recent studies, Cr(III) as the active species has gained prominence [12, 24, 25, 29]. However, it has not been possible to definitively state that Cr(III) is the active site. Other groups have suggested a Cr(II)/Cr(III) pair [18]. In general spectroscopic analyses favor Cr(III), but quantification of the reduction and re-adsorption/absorption of oxygen suggests that hydrogen reduction reduces Cr_2O_3 to CrO [26].

The presence of residual hydrogen retained by a chromia catalyst after reduction was shown by pulsing aliquots of deutero-propane (C_3D_8 or $[^2H]C_3H_8$) over a hydrogen-reduced catalyst and aliquots of propane over a deuterium-reduced ($^2H_2$ or D_2) catalyst. In both cases isotope exchange occurred such that deuterium incorporation was observed in the propane for a deuterium-reduced catalyst and hydrogen incorporation was observed in the deutero-propane for a hydrogen-reduced catalyst [30].

The rate determining step for propane dehydrogenation over chromia was found to be the loss of the second hydrogen:

$$C_3H_7\,(ads) \rightarrow C_3H_6\,(ads) + H\,(ads)$$

with an activation energy for propene formation of $72 \pm 7\,kJ\,mol^{-1}$.

At 823 K and 16,800 GHSV (gas hourly space velocity) a chromia/alumina catalyst gives the following product distribution for propane dehydrogenation; 1% methane, 1% ethane, 1% ethene, 39% propene and 54% unreacted propane (S.D. Jackson, unpublished results), showing nearly equilibrium conversion and high selectivity. For butane dehydrogenation at 873 K and 14,500 GHSV the product distribution is 70% unreacted butane, 5% trans-2-butene, 6% 1-butene, 4% *cis*-2-butene, 1.5% butadiene and ~1% C_1—C_3. For butane dehydrogenation, 1-butene is the primary product [31].

Both systems deposit carbon, and when run for extended cycles under propane dehydrogenation polynuclear aromatics form. A Raman spectrum from a 1% chromia/alumina coked catalyst is shown in Figure 15.2. The main peak appears at $1592\,cm^{-1}$ with a shoulder at $1550\,cm^{-1}$, also broad features are observable at $1170\,cm^{-1}$ and $1380\,cm^{-1}$. With the exception of the shoulder at $1550\,cm^{-1}$ the Raman spectrum is characteristic of polynuclear, aromatic carbon. Espinat and coworkers [32] characterized a wide variety of carbon compounds including coke on a series of mono- and bi-metallic catalysts and assigned the Raman bands found from 1300 to $1700\,cm^{-1}$. The D ($1350\,cm^{-1}$) and G ($1600\,cm^{-1}$) bands can be used to identify the type of coke deposited on the catalyst. For the spectrum shown in Figure 15.2, the D band is half the intensity of the G band. This ratio indicates pre-graphitic coke, which is composed of graphite with crystal defects

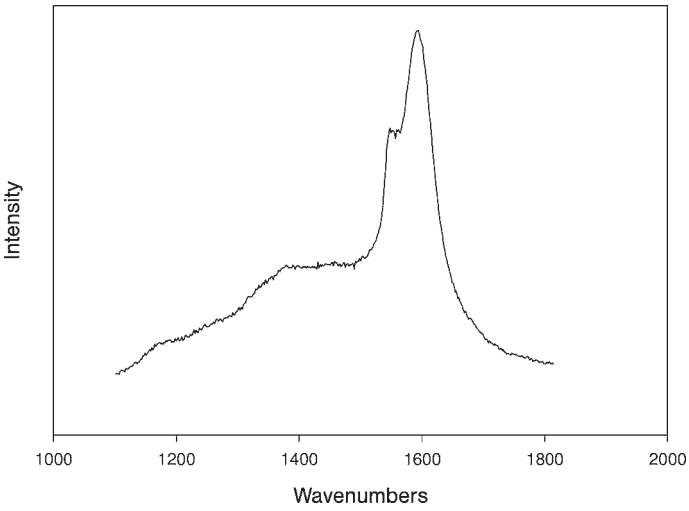

Figure 15.2 UV Raman spectrum of coke deposited on 1% Cr/Al_2O_3 catalyst used for propane dehydrogenation.

or pre-graphitic paracrystals [32] The shoulder at 1550 cm^{-1} is characteristic of conjugated olefins or polyenes.

Confirmation of this interpretation of the Raman spectrum came from analysis of yellow oil produced during extended use of a catalyst. The analysis revealed the presence of pyrene ($C_{16}H_{10}$), fluoranthene ($C_{16}H_{10}$), benzanthracene ($C_{18}H_{12}$) and perylene ($C_{20}H_{12}$) among other compounds. The alumina support principally produced perylene in the absence of chromia but with chromia a wider range of polynuclear aromatics were detected [26].

Studies using isotopically labeled propane [30] have shown that the route to the coke deposits during propane dehydrogenation goes through a C_1 species, probably CH(a). However, before these species convert to coke there is a period when they are labile and can be hydrogenated off the surface as methane [26, 30]. This was shown using isotopically labeled propane [26] and by using a mixed continuous/pulse reaction system where a chromia/alumina catalyst was reduced and subjected to a continuous flow of propane for 10 min at 873 K followed by two pulses of propane in helium [20]. With both pulses the H : C ratio was ~3.3 much higher than the inlet 2.7; also the mass balance was >100%. However the propene : propane ratio was what would have been expected from a continuous flow experiment after 10 min. Clearly carbonaceous material retained by the catalyst was being desorbed into the pulse as methane. Therefore under continuous flow conditions there is a reservoir of C_1 fragments on the surface of the catalyst that is continually in flux between removal as methane and consolidation on the surface to generate higher molecular weight species. A study by Krause and coworkers [33] showed that if the chromia is not pre-reduced the reduction of chromates by propane may proceed through the formation of isopropoxide species, which react

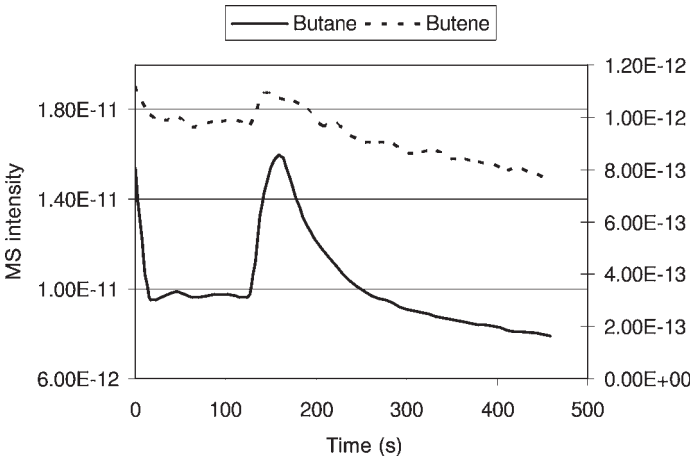

Figure 15.3 Desorption of butane and butene at room temperature in a flow of 2% O_2/Ar from a 6% chromia/alumina catalyst after butane dehydrogenation at 873 K.

further first to adsorbed acetone and then to formates and acetates. They also found that dehydrogenation of propane resulted in sequential formation of aliphatic, unsaturated/aromatic and graphite-like hydrocarbon deposits, which deactivated the catalyst.

The situation with butane is similar but with significant differences. The formation of coke on the surface is very similar to that found with propane; however, Edussuriya and coworkers (unpublished results) found that although the majority of the catalyst deactivation was due to polynuclear aromatics or other forms of coke strongly adsorbed reaction intermediates were also detected. These species can be desorbed at room temperature by treating with a low concentration O_2 in Ar mix. Figure 15.3 shows the desorption of butane. The catalyst had been catalyzing the dehydrogenation reaction for 2 h at 873 K when the gas stream was switched from butane to argon. Online mass spectrometry indicated that all hydrocarbon components were rapidly swept out of the reactor at 873 K and no other gases apart from the argon carrier were detected during the cool-down period. However, when 2% O_2/Ar was passed over the sample at room temperature, butane, butenes and butadiene were evolved. This desorption process can be viewed as an oxidative displacement, resulting in recombination of reaction intermediates (hydrogen and alkyl, alkenyl and alkadienyl) from the surface of reduced CrO_x species. Removal of these species did not regenerate the catalyst. The polynuclear aromatics were only removed when the catalyst was subjected to a full regeneration involving high-temperature oxidation. Only after this treatment did the catalyst regain its activity.

15.5 Vanadia

Although vanadia catalysts have not been used commercially there is a significant literature concerning the dehydrogenation reaction over supported vanadia systems. The structure of supported vanadia catalysts under redox reaction conditions is directly related to the catalytic performance. Vanadia catalysts are usually reduced to some extent during redox reactions, and the reduced vanadia species have been proposed as the active sites [20, 34, 35]. Therefore, information on the valence state and molecular structure of the reduced vanadia catalysts is of great interest. A number of techniques have been applied to investigate the reduction of supported vanadia catalysts, such as TPR [36–38], X-ray photoelectron spectroscopy (XPS) [35], electron spin resonance (ESR) [39], UV-Vis DRS [40–45], X-ray absorption fine structure spectroscopy (XAFS) [46] and Raman spectroscopy [37, 47–50]. Most of these techniques give information only on the oxidation state of vanadia species. Although Raman spectroscopy is a powerful tool for characterization of the molecular structure of supported vanadia [34, 42, 51], it has been very difficult to detect reduced supported vanadia species with conventional (visible) Raman measurements [37, 47–52]. A widely accepted explanation for this phenomenon is that the Raman cross-section of reduced vanadium oxide species is very small or near zero [53]. Thus, it remains challenging to use Raman spectroscopy for obtaining information on the molecular state of reduced vanadia species.

It is notable that most Raman studies of supported VO_x catalysts were carried out using a single excitation wavelength in the visible region (488, 514 or 532 nm) [34, 46, 47, 54]. However, several recent investigations on supported transition metal oxides [55–58], including vanadium oxides [55, 56] under ambient conditions, using both UV and visible wavelength Raman excitations suggest that more complete and sometimes new structural information of supported metal oxides can be achieved by using multiple excitation wavelengths. The reason lies in the strong electronic absorptions in the UV and visible wavelength regions exhibited by most transition metal oxides, which make it possible to measure resonance-enhanced Raman spectra. Under circumstances where supported VO_x species are present in a distribution of cluster sizes or coordination geometries, it is likely that these species also possess a corresponding distribution of electronic absorption wavelengths. Excitation of Raman spectra within the absorption region will produce resonance-enhanced spectra from the subset of VO_x species with absorptions at the excitation wavelength. By measuring the Raman spectra at several wavelengths, more information can be obtained about the various VO_x species in the distribution. Moreover, when UV excitation is employed, even Raman spectra from supported VO_x at low loadings (<1 wt%) on oxides having strong fluorescence are possible because of the avoidance of fluorescence and enhanced sensitivity [59, 60]. In addition, the decreased self-absorption effects in the UV region indicated by *in situ* UV-Vis DRS studies of reduced VO_x and CrO_x [40–44, 61, 62] suggests

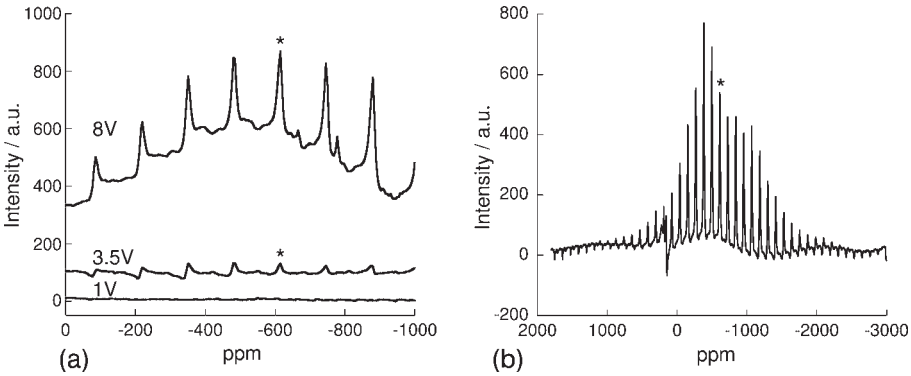

Figure 15.4 51-V MAS NMR spectra. (a) As-prepared catalysts, from top 8, 3.5 and 1 V; (b) 8 V after regeneration at 873 K. * indicates an isotropic resonance. In spectrum (b) the peaks to negative intensity correspond to Al atoms in the support.

that UV Raman spectroscopy may be capable of detecting reduced supported metal oxides.

Studies on alumina supported catalysts with a range of vanadia weight loadings revealed [63, 64] that isolated VO_x species dominated at surface densities below 1 V/nm^2; polyvanadates coexisted with monovanadates at surface densities between 1.2–4.4 V/nm^2; and V_2O_5 formed at a surface density higher than 4.4 V/nm^2. The vanadia densities of the catalysts were 1.1 V/nm^2 for the sample with the 1% loading, 3.7 V/nm^2 for the 3.5% loading and 10.4 V/nm^2 for the 8% loading. Only the XRD pattern for the catalyst with the 8% loading exhibited additional characteristic peaks of crystalline V_2O_5 at 2θ values 26.3 and 34.6 [65, 66]. However, analysis by ^{51}V NMR revealed V_2O_5 on the 3.5% vanadium as well as on the 8% (Gladden and McGregor, unpublished results).

Figure 15.4a shows simple pulse-acquire ^{51}V MAS NMR spectra for catalysts with vanadium loadings of 1, 3.5 and 8 wt%. This simple 1-D spectroscopy identifies a ^{51}V resonance only in the 3.5 and 8 wt% catalysts. The spectra are dominated by spinning sidebands, with the isotropic chemical shift (denoted by *) at –612 ppm being indicative of V^{5+} in a V_2O_5 environment. The broad background upon which these peaks are superimposed in the case of the 8 wt% sample is characteristic of V^{5+} in more amorphous environments. The spectra clearly suggest that the population of V_2O_5-like species in the 8 wt% catalyst is larger than in the 3.5 wt% catalyst, consistent with the Raman data. Alongside characterizing the ^{51}V environment, NMR spectroscopy of the ^{27}Al species is also of interest. Figure 15.5a shows a simple pulse-acquire ^{27}Al spectrum of an as-prepared 8 wt% catalyst. Two broad resonances are observed; the peak at ~6 ppm is characteristic of sixfold, octahedrally coordinated Al, while Al in four-fold and five-fold coordinated sites contribute to the broader resonance in the range 25–70 ppm. Interpretation of the broader

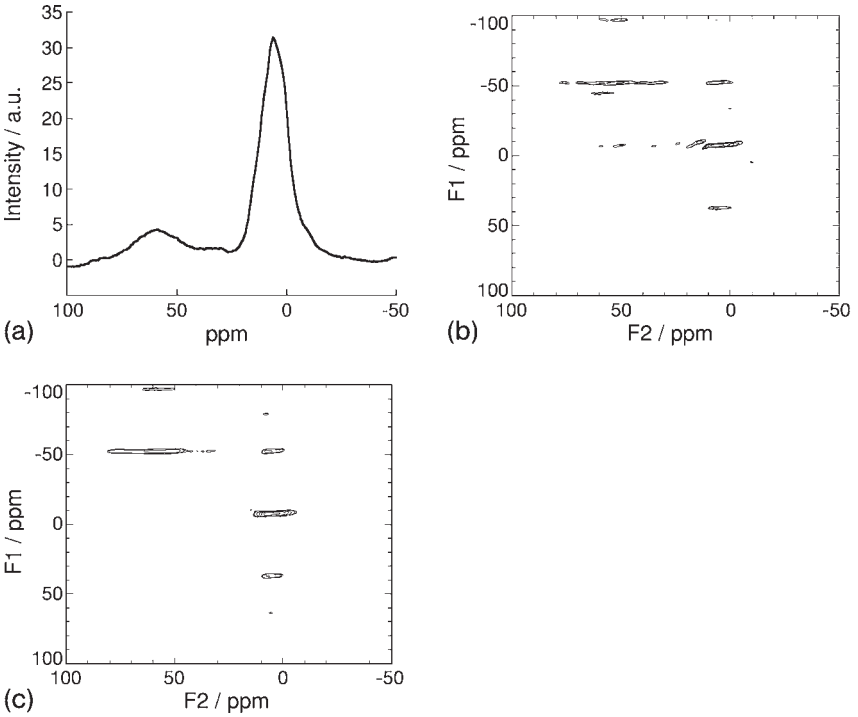

Figure 15.5 ^{27}Al NMR spectra. (a) ^{27}Al MAS NMR spectrum of as-prepared 8%V/alumina catalyst; (b) ^{27}Al 3Q MAS NMR spectrum of as-prepared 8%V/alumina; (c) ^{27}Al 3Q-MAS NMR spectrum of 8%V/alumina after regeneration at 873 K.

resonance is made significantly easier – although the NMR technique itself is more challenging – by using multiple quantum NMR spectroscopy. A triple-quantum spectrum from the 8 wt% catalyst is shown in Figure 15.5b. The projection of such spectra in the F1 dimension yields the isotropic peaks, while the anisotropic lineshapes (corresponding to a standard MAS spectrum) are displayed by the projection in the F2 dimension. The resolution of the isotropic resonance provided by the triple-quantum MAS experiment unambiguously confirms the presence of three distinct ^{27}Al environments, assigned to 4-, 5- and 6-coordinate Al.

Studies reveal that reduction takes place over a broad range of temperatures and the onset of reduction follows the weight loading with 8% < 3.5% < 1% but reduction is complete for each sample by ~873 K. This difference in onset of reduction may be attributed to different reducibilities of vanadia species, monovanadates, polyvanadates and V_2O_5 coexisting on the catalyst's surface. The weight loss at the reduction step increases with vanadia loading: when these weights are translated into oxygen loss we see that there is a 1 : 1 relationship between vanadium atoms and oxygen atom loss (Table 15.1). The same trend in mass loss is observed during

Table 15.1 Extent of oxygen removal during reduction of vanadia/alumina catalysts.

Catalyst (V/nm^2)	V atoms in 1 g of catalyst (×10^{20})	O atoms removed from 1 g of catalyst (×10^{20})	V:O ratio
1.1	1.18	1.13	1.0:1
3.7	4.13	4.14	1.0:1
10.4	9.45	7.90	1.2:1

Tapered Element Oscillating Microbalance (TEOM) studies of catalyst reduction (Gladden and McGregor, unpublished results). These studies also yield an average 1:1 relationship between vanadium atoms and oxygen atom loss.

This would suggest a change of 2 in the vanadium oxidation state, so if the vanadium were in a +5 oxidation state before reduction it would be converted to +3 after reduction. This was confirmed by *in situ* UV-Vis DRS. Before reduction the catalysts were in a V^{5+} oxidation state with typical charge transfer bands at 267 nm for a 1% loading, 290 nm for a 3.5% loading and 357 nm for an 8% loading. This change in position of the charge transfer band is indicative of the increasing polymeric nature of the vanadia [67]. Over the course of the reduction the spectrum changes to give spectra typical for a V^{3+} state with d–d transitions around 575 nm and 625 nm for 3.5 %V and 8 %V. However, the spectrum of the 1% sample is more indicative of V^{4+}, with a single band at 585 nm [31]. ^{51}V NMR spectroscopy revealed a total loss in signal after reduction, indicating the presence of V(III) or V(IV) species (Gladden and McGregor, unpublished results).

Using oxygen chemisorption at 293 K and 873 K the average oxidation state of the 1% VO_x/alumina was calculated as 3.8, whereas the average oxidation state for the 3.5% VO_x/alumina was calculated as 2.6 [31]. Both of these figures are in excellent agreement with the conclusions from the UV-Vis DRS.

Bulk re-oxidation data in conjunction with thermogravimetric analysis (TGA) and TEOM results indicated that the ease of replacing oxygen that had been removed during reduction was 8% > 3.5% > 1% [31], (Gladden and McGregor, unpublished results). This difference was also seen in the UV-Vis DRS and in TEOM data. TEOM data provide information on the quantity of oxygen taken up by the catalysts and on their rate of re-oxidation. The rate of catalyst re-oxidation was seen to be greater for the 8 wt% catalyst than for materials of lower vanadium loading (Gladden and McGregor, unpublished results). Once reduced, the 3.5 %V sample did not regain its original state even after high temperature oxidation; however, the reduced 8 %V sample did convert to a species that was similar to the original oxidation state.

Supported VO_x catalysts show good catalytic performance in both oxidation and reduction reactions; for example, they are among the most active and selective simple metal oxides for dehydrogenation and oxidative dehydrogenation of alkanes. The possibility of using oxide systems other than chromia is being

explored in an effort to make the alkane–alkene conversion process more selective and stable. Supported VO_x catalysts have been extensively studied for the oxidative dehydrogenation of light alkanes [40, 54, 68–72]. They have also been explored in the dehydrogenation of light alkanes including propane and butane [35, 39, 73, 74] and have shown promise to be both active and selective for the dehydrogenation reactions. However deactivation of VO_x catalysts by coke species is also observed with time-on-stream in butane dehydrogenation reactions. Owing to the limited number of studies of supported VO_x for alkane dehydrogenation, the mechanism of deactivation/coke deposition and also the structure of supported VO_x species under dehydrogenation conditions are unclear. Conventional visible Raman spectroscopy usually cannot provide meaningful spectra for a catalytic system that produces carbonaceous deposits because of strong fluorescence interference. These two issues were addressed in an investigation of butane dehydrogenation reaction on $V/\theta\text{-}Al_2O_3$ catalysts with various surface VO_x densities (0.03–14.2 V/nm^2) via *in situ* UV Raman spectroscopy [75].

$V/\theta\text{-}Al_2O_3$ catalysts with surface VO_x density from 0.03 to 14.2 V/nm^2 were tested for butane dehydrogenation under low partial pressures of butane at 873 K, and the activity and selectivity data on these different catalysts were compared [75]. In essence, the initial dehydrogenation activity increases as a function of surface VO_x density. However, the activity decreases significantly with prolonged reaction time for samples with VO_x density higher than 1.2 V/nm^2, apparently due to the formation of surface coke deposits and blocking of surface sites during the reaction. Interestingly, the dehydrogenation activity remains nearly unchanged on the catalysts with surface VO_x density no higher than 1.2 V/nm^2. However, at higher butane pressures, although the behavior of the 1.2 V/nm^2 sample is unchanged, catalysts with higher V/nm^2 densities show enhanced activity (Table 15.2).

In the *in situ* UV Raman study [75], $V/\theta\text{-}Al_2O_3$ samples (0.03 V, 1.2 V, 4.4 V and 14.2 V) that contain surface VO_x species with different structures were treated in dilute butane flow at different temperatures and examined by Raman spectra measurements at each temperature. Taking the 1.2 V sample as an example, the Raman spectra collected during butane dehydrogenation at different temperatures are shown in Figure 15.6.

Table 15.2 Activities and turnover frequencies for butane dehydrogenation at 1 bar pressure and 873 K with time-on-stream.

Time-on-stream (min)	Rate ($\mu mole\,g^{-1}\,s^{-1}$)			Turnover frequency (s^{-1})		
	1.1 V/nm^2	3.7 V/nm^2	10.4 V/nm^2	1.1 V/nm^2	3.7 V/nm^2	10.4 V/nm^2
15	1.1	20.3	5.8	0.051	0.269	0.037
30	1.0	5.8	3.7	0.047	0.077	0.023
45	1.0	4.7	2.9	0.044	0.063	0.018
60	1.0	4.2	2.5	0.044	0.056	0.016
105	0.9	3.5		0.041	0.046	–

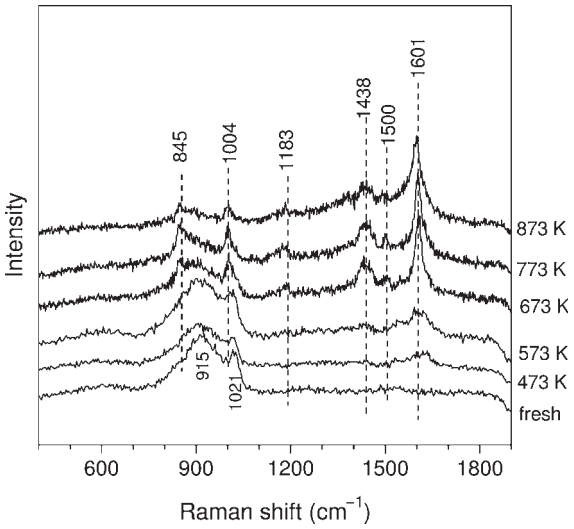

Figure 15.6 UV Raman spectra of butane dehydrogenation over oxidized 1.2 V at different temperatures.

At temperatures below 673 K, a weak Raman band at 1620 cm^{-1}, assigned to C=C stretching in polyalkenes, is observed together with the two bands at 1021 and 915 cm^{-1} due to the V=O and V—O—Al modes of surface VO_x species, respectively. After butane dehydrogenation at 673 and 773 K, an intense band at 1601 cm^{-1} due to polyaromatic hydrocarbons develops. Simultaneously, bands at 1500, 1438, 1183, 1004 and 845 cm^{-1} are also observed. Meanwhile, Raman bands at 1021 and 915 cm^{-1} from surface VO_x species are no longer observable, owing to a combination of the reduction of VO_x species [43, 45, 47, 65, 71] and strong optical absorption by surface coke species. The band at 1500 cm^{-1} is usually assigned to conjugated polyalkenes or cyclopentadienyl species [76, 77]. The band at 1438 cm^{-1} is due to the bending mode of CH_3/CH_2 or C—H in aromatic rings. C—H bending in aromatics usually appears near 1180 cm^{-1}. The two sharp bands at 1004 and 845 cm^{-1} are rarely reported for coke species, and thus one might ascribe them to surface VO_x species. However, the absence of an isotope shift on an ^{18}O-exchanged V/θ-Al_2O_3 sample confirms that these bands are due to surface coke deposits. As the dehydrogenation temperature is increased to 873 K, the intensity of the Raman bands below 1500 cm^{-1} decreases significantly. Raman spectra obtained after the reaction of butane with pre-reduced 1.2 %V (not shown) are very similar to those on pre-oxidized 1.2 %V. This suggests that the initial valence state of surface VO_x does not affect the nature of coke species and most likely the VO_x species is at least partially reduced under butane dehydrogenation conditions. This conclusion can also be inferred from the similar activity/selectivity results from butane dehydrogenation tests on either oxidized or pre-reduced 1.2 %V and also the similar UV-Visible spectra from V/θ-Al_2O_3 treated in either hydrogen or butane.

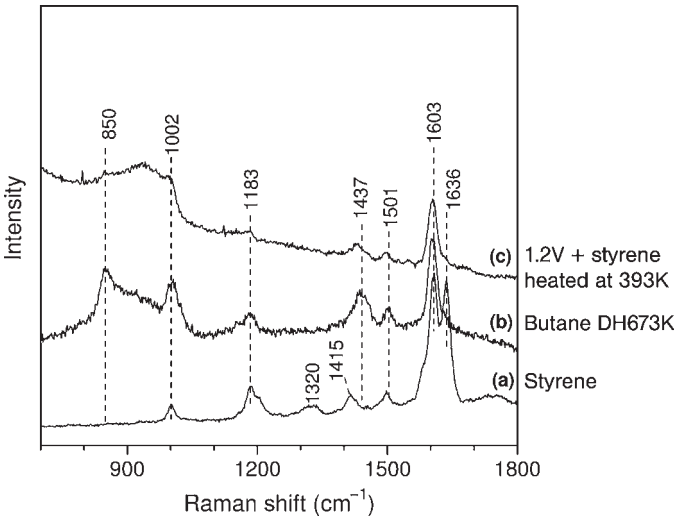

Figure 15.7 Comparison of Raman spectra from (a) styrene, (b) butane dehydrogenation over 1.2 V at 673 K and (c) a mixture of 1.2 V and styrene heated at 393 K.

The set of Raman bands near 850, 1002, 1183, 1437, 1501 and 1603 cm^{-1} is also observed to grow simultaneously on all other V/θ-Al_2O_3 samples when treated in butane at high temperatures. To aid the assignment of these bands, the adsorption and reaction of different C_4 olefins were studied on the V/θ-Al_2O_3 samples via Raman spectroscopy. It turned out that they all form similar coke species, indicating that they are precursors to coke species in butane dehydrogenation on V/θ-Al_2O_3 catalysts. It is interesting to find out that 1,3-butadiene adsorption at room temperature results in similar spectra to that from butane dehydrogenation on 1.2 V at 673 K. Considering the low temperature (298 K), a possible chemical change for 1,3-butadiene is its cyclization to form styrene on the surface. A comparison of the spectrum from styrene with that after butane dehydrogenation at 673 K on 1.2 %V (Figure 15.7) reveals a very similar set of bands. Also included is the spectrum from a mixture of 1.2 %V with styrene heated at 393 K (Figure 15.7c).

Styrene is known to polymerize easily upon heating. Comparison of spectrum c to that reported for polystyrene [78] confirms the identity of spectrum c: the set of Raman bands near 850, 1002, 1183, 1437, 1501 and 1603 cm^{-1} is due to polystyrene. Thus, it appears that polystyrene is a key intermediate in the coke formation process during butane dehydrogenation on the 1.2 V catalyst. Further Raman spectroscopy study of styrene on V/θ-Al_2O_3 samples heated to 873 K showed that the characteristic Raman bands of polystyrene disappear, owing to its decomposition. This is consistent with catalytic studies of polystyrene degradation over solid acid catalysts [79]. An interesting new observation is that although the Raman

spectrum seems to indicate that the catalyst surface is free of coke species after polystyrene decomposition, the follow-up TPO (Temperature Programmed Oxidation) shows the evolution of a considerable amount of CO_2. This suggests that the absence of typical Raman bands (1000–1650 cm^{-1} range) due to coke species does not necessarily mean the catalyst is coke free. Investigation of the catalytic surface with multi-wavelength Raman spectroscopy should be helpful in determining the chemical nature of this surface carbon. Microanalysis of a used 1.2 V catalyst for carbon and hydrogen gave a C : H value of 0.9 as per polystyrene monomer in agreement with the Raman spectra [31].

One important general characteristic of coke is its topology, which can be assessed by the intensity ratio of the band at around 1600 cm^{-1} (G band) to the band at around 1400 cm^{-1} (D band) [76, 80]. UV Raman spectra from a series of polyaromatic compounds [76, 81] show that the intensity in the spectral range 1600–1650 cm^{-1} is significantly higher than that in the region 1300 to 1450 cm^{-1} for coke species with a 2-D, sheet-like topology. By contrast, the intensity is more nearly equal in these two spectral regions for coke species with chain-like topologies. The topology of coke species formed from butane dehydrogenation on the various $V/\theta\text{-}Al_2O_3$ catalysts at 873 K is compared by plotting the intensity ratio of I_G to I_D as a function of surface VO_x density. It is shown that the coke species are more 2-D, sheet-like from butane dehydrogenation on $V/\theta\text{-}Al_2O_3$ with high surface VO_x density (>1.2 V/nm^2) while more 1-D-like on $V/\theta\text{-}Al_2O_3$ with lower surface VO_x density (≤1.2 V/nm^2). The 2-D coke species can, presumably, reorganize into pre-graphitic entities that have been thought to be the kind of coke that causes the deactivation of dehydrogenation catalysts [33, 82, 83]. A study of coke deposited on a 1 wt% V/Al_2O_3 catalyst, in which the deactivation was studied as a function of time-on-stream (TOS) using ^{13}C CP MAS (cross-polarization magic angle spinning) NMR reveals a significant increase in the aromatic peak at 130 ppm up to 3 h, then a gradual decrease in this peak [84]. The initial increase in the peak intensity was explained by an initial coke build-up, whereas the decrease in intensity was due to formation of very slowly relaxing, NMR "invisible", highly polyaromatic coke, which formed under prolonged exposure to the reaction conditions. This interpretation is consistent with the constant decrease in T_2 of adsorbed pentane observed, which also suggests an increasing aromaticity of coke with increasing TOS. Further, a monotonic decrease in pentane self-diffusion coefficient as a function of TOS was observed; these data are consistent with restriction in molecular motion resulting from pore blockage due to coke deposition as deactivation proceeds. However, in another study it was found that the majority of the catalyst deactivation in the early stages of reaction was not due to polynuclear aromatics or other forms of coke but to strongly adsorbed reaction intermediates [31]. These species can be desorbed at room temperature by treating with a low concentration O_2 in Ar mix. Figure 15.8 shows desorption of butane from a series of VO_x/alumina catalysts.

The catalyst had been running under butane for 2 h at 873 K when the gas stream was switched from butane to argon. Online mass spectrometry indicated that all hydrocarbon components were rapidly swept out of the reactor at 873 K and no

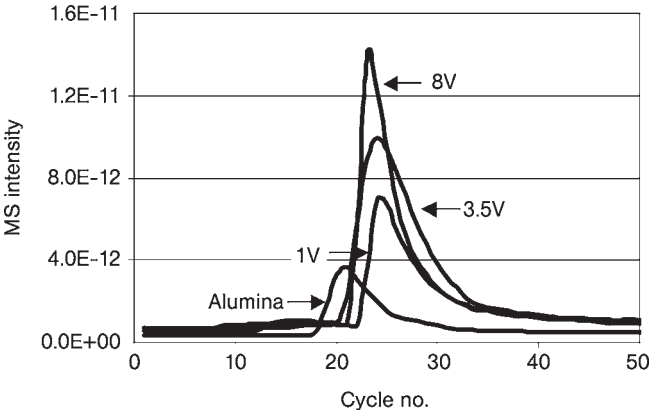

Figure 15.8 Desorption of butane at room temperature in a flow of 2% O_2/Ar from vanadia/alumina catalysts after butane dehydrogenation at 873 K and 1 bar.

other gases apart from the argon carrier were detected during the cool-down period. However when 2% O_2/Ar was passed over the sample at room temperature butane, butenes and butadiene were evolved. This desorption process can be viewed as an oxidative displacement, resulting in recombination of reaction intermediates (hydrogen and alkyl, alkenyl and alkadienyl) from the surface of reduced VO_x species. The polynuclear aromatics were only removed when the catalyst was subjected to a full regeneration involving high temperature oxidation [31].

The regeneration of samples of V/θ-Al_2O_3 coked from low partial pressure butane dehydrogenation via oxidation was also followed by UV Raman spectroscopy as well as gas chromatography (GC). The Raman spectroscopy indicates that the structure of the VO_x species can be restored by oxidation of the coke deposits up to 873 K. UV-Vis DRS, however, suggests that only high loaded samples are fully restored. ^{51}V MAS NMR confirms the re-oxidation of reduced vanadium species and, as such, spectra of the regenerated catalyst can be acquired (Gladden and McGregor, unpublished results). Figure 15.4b shows the spectrum of the 8 wt% catalyst after reaction at 973 K and regeneration at 873 K (note the peaks to negative intensity correspond to Al atoms in the support). By comparison with Figure 15.4a it can be seen that the spectrum of the regenerated catalysts indicates the presence of a greater quantity of ordered V_2O_5-like species than were present in the as-prepared catalyst. However, one must take care as each technique has its "blind spots" and it is possible that it is the inability of each of the techniques to "see" all of the vanadia species that leads to apparent differences. At low butane partial pressure, TPO quantification results showed that the amount of coke formed in butane dehydrogenation follows the sequence: polymeric VO_x > monomeric VO_x > V_2O_5, Al_2O_3. However, at 1 bar butane pressure the order is changed slightly with V_2O_5 > polymeric VO_x > monomeric VO_x > Al_2O_3. After regeneration the surface area of an 8%V catalyst was reduced by 50%, a

change assigned to transformations in the nature of the support. A similar effect was observed after propane dehydrogenation over a vanadia/alumina catalyst [73], where a conversion of the γ-alumina support to α-alumina was confirmed by XRD. ^{27}Al triple-quantum (3Q) MAS NMR studies have also demonstrated that the nature of the support undergoes a transformation. Figure 15.5c shows the ^{27}Al 3Q MAS NMR spectrum of 8V after reaction and regeneration. Comparison with Figure 15.5b shows the loss of an isotropic resonance; this resonance was assigned to 5-coordinate Al and the loss of this species suggests a transformation towards a more crystalline state in agreement with the reduced surface area.

It is rare for a structure–function relationship to be shown unambiguously in heterogeneous catalysis. However, a structure–coke relationship has been established in the dehydrogenation of butane on VO_x/θ-Al_2O_3 catalysts by combined reactivity, UV-Vis DRS, NMR, TEOM and UV Raman investigations. In this case, both the nature and amount of coke show a dependence on the structure of the VO_x/θ-Al_2O_3 catalysts.

15.6 Conclusions

In this chapter we have reviewed the use of chromia and vanadia in alkane dehydrogenation. In both systems there is a rich and complex chemistry that is still not yet fully understood, although considerable advances have been made over the last few years. Both patent and academic literature are active and it can be expected to be so for many years to come.

References

1 Frey, F.E. and Huppke, W.F. (1933) *Industrial and Engineering Chemistry*, **25**, 54.
2 Kearby, K.K. (1955) *Catalysis*, Vol. **3** (ed. P.H. Emmet), Reinhold, New York, p. 453.
3 Hornaday, G.F., Ferrell, F.M. and Mills, G.A. (1961) *Advances in Petroleum Chemistry and Refining*, Vol. 4, Interscience, Paris, p. 451.
4 Waddams, A.L. (1978) *Chemicals From Petroleum*, 4th edn, Gulf Publishing Company, Houston, p. 1980.
5 Bhasin, M.M., McCain, J.H., Vora, B.V., Imai, T. and Pujado, P.R. (2001) *Applied Catalysis A: General*, **221**, 397.
6 http://www.sud-chemie.com/scmcms/web/page_en_4504.htm (May 2008)
7 http://www.sud-chemie.com/scmcms/web/page_en_4506.htm (May 2008)
8 http://www.cbi.com/lummus/process-technology/pdfs/catofindehydrogenation.pdf (May 2008)
9 Fridman, V. and Rokicki, A. (2005) WO2,005,040,075, assigned to Sud Chemie.
10 Zaki, M.I., Fouad, N.E., Leyrer, J. and Knozinger, H. (1986) *Applied Catalysis*, **21**, 359.
11 Cavani, F., Koutyrev, M., Trifirò, F., Bartolini, A., Ghisletti, D., Iezzi, R., Santucci, A. and Del Piero, G. (1996) *Journal of Catalysis*, **158**, 236.
12 Puurunen, R.L. and Weckhuysen, B.M. (2002) *Journal of Catalysis*, **210**, 418.
13 Jackson, S.D., Matheson, I.M., Naeye, M.-L., Stair, P.C., Sullivan, V.S., Watson, S.R. and Webb, G. (2000) *Studies in Surface Science and Catalysis*, Vol. 130 (eds A. Corma, F.V. Melo, S. Mendioroz, J.L.G. Fierro), Elsevier, Amsterdam, p. 2213.

14 Mentasty, L.R., Gorriz, O.F. and Cadùs, L.E. (2001) *Industrial and Engineering Chemistry Research*, **40**, 136.

15 Vuurman, M.A., Wachs, I.E., Stufkens, D.J. and Oskam, A. (1993) *Journal of Molecular Catalysis*, **80**, 209.

16 Grzybowska, B., Sloczyñski, J., Grabowski, R., Wcislo, K., Kozlowska, A., Stoch, J. and Zieliñski, J. (1998) *Journal of Catalysis*, **178**, 687.

17 Sullivan, V.S., Jackson, S.D. and Stair, P.C. (2005) *Journal of Physical Chemistry B*, **109**, 352.

18 Rahman, A., Mohamed, M.H., Ahmed, M. and Aitani, A.M. (1995) *Applied Catalysis A: General*, **121**, 203.

19 Ashmawy, F.M. and McAuliffe, C.A. (1984) *Journal of the Chemical Society–Faraday Transactions I*, **80**, 1985.

20 De Rossi, S., Ferraris, G., Fremiotti, S., Garrone, E., Ghiotti, G., Campa, M.C. and Indovina, V. (1994) *Journal of Catalysis*, **148**, 36.

21 Kanervo, J.M. and Krause, A.O.I. (2002) *Journal of Catalysis*, **207**, 57.

22 De Rossi, S., Casaletto, M.P., Ferraris, G., Cimino, A. and Minelli, G. (1998) *Applied Catalysis A: General*, **167**, 257.

23 Cutrufello, M.G., De Rossi, S., Ferino, I., Monaci, R., Rombia, E. and Solinas, V. (2005) *Thermochimica Acta*, **434**, 62.

24 Weckhuysen, B.M. and Schoonheydt, R.A. (1999) *Catalysis Today*, **51**, 223.

25 Hakuli, A., Kytokivi, A. and Krause, A.O.I. (2000) *Applied Catalysis A: General*, **190**, 219.

26 Jackson, S.D. and Stitt, E.H. (2003) *Current Topics in Catalysis*, **3**, 245.

27 Pass, G., Littlewood, A.B. and Burwell, R.L., Jr (1960) *Journal of the American Chemical Society*, **82**, 6281.

28 van Reijin, L.L., Sachtler, W.M.H., Cossee, P. and Brouwer, D.M. (1965) *Proceedings of the 3rd International Congress on Catalysis*, Vol. 2 (eds W.M.H. Sachtler, G.C.A. Schuit and P. Zwietering), North Holland, Amsterdam, p. 829.

29 Weckhuysen, B.M., Wachs, I.E. and Schoonheydt, R.A. (1996) *Chemical Reviews*, **96**, 3327.

30 Jackson, S.D., Grenfell, J., Matheson, I.M. and Webb, G. (1999) *Reaction Kinetics and the Development of Catalytic Processes*, Studies in Surface Science and Catalysis, **122** (eds G.F. Froment and K.C. Waugh), Elsevier, Amsterdam, pp. 149–55.

31 Jackson, S.D. and Rugmini, S. (2007) *Journal of Catalysis*, **251**, 59.

32 Espinat, D., Dexpert, H., Freund, E., Martino, G., Couzi, M., Lespade, P. and Cruege, F. (1985) *Applied Catalysis*, **16**, 343

33 Airaksinen, S.M.K., Bañares, M.A. and Krause, A.O.I. (2005) *Journal of Catalysis*, **230**, 507.

34 Wachs, I.E. and Weckhuysen, B.M. (1997) *Applied Catalysis A: General*, **157**, 67.

35 Harlin, M.E., Niemi, V.M. and Krause, A.O.I. (2000) *Journal of Catalysis*, **195**, 67.

36 Gao, X., Banares, M.A. and Wachs, I.E. (1999) *Journal of Catalysis*, **188**, 325.

37 Ruitenbeek, M., Van Dillen, A.J., de Groot, F.M.F., Wachs, I.E., Geus, J.W. and Koningsberger, D.C. (2000) *Topics in Catalysis*, **10**, 241.

38 Wachs, I.E. and Chan, S.S. (1984) *Applied Surface Science*, **20**, 181.

39 Harlin, M.E., Niemi, V.M., Krause, A.O.I. and Weckhuysen, B.M. (2001) *Journal of Catalysis*, **203**, 242.

40 Wachs, I.E., Jehng, J.-M., Deo, G., Weckhuysen, B.M., Guliants, V.V., Benziger, J.B. and Sundaresan, S. (1997) *Journal of Catalysis*, **170**, 75.

41 Wachs, I.E., Jehng, J.-M., Deo, G., Weckhuysen, B.M., Guliants, V.V. and Benziger, J.B. (1995) Proceedings of the 5th European workshop meeting on selective oxidation by heterogeneous catalysis. *Catalysis Today*, **32**, 47.

42 Sun, Q., Jehng, J.-M., Hu, H., Herman, R.G., Wachs, I.E. and Klier, K. (1997) *Journal of Catalysis*, **165**, 91.

43 Mul, G., Banares, M.A., Garcia Cortez, G., van der Linden, B., Khatib, S.J. and Moulijn, J.A. (2003) *Physical Chemistry Chemical Physics*, **5**, 4378.

44 Banares, M.A., Cardoso, J.H., Agullo-Rueda, F., Correa-Bueno, J.M. and Fierro, J.L.G. (2000) *Catalysis Letters*, **64**, 191.

45 Christodoulakis, A., Machli, M., Lemonidou, A.A. and Boghosian, S. (2004) *Journal of Catalysis*, **222**, 293.

46 Olthof, B., Khodakov, A., Bell, A.T. and Iglesia, E. (2000) *Journal of Physical Chemistry B*, **104**, 1516.

47 Banares, M.A. and Wachs, I.E. (2002) *Journal of Raman Spectroscopy*, **33**, 359.

48 Li, C. (2003) *Journal of Catalysis*, **216**, 203.

49 Gao, X. and Wachs, I.E. (2000) *Journal of Physical Chemistry B*, **104**, 1261.

50 Xie, S., Iglesia, E. and Bell, A.T. (2000) *Langmuir*, **16**, 7162.

51 Xie, S., Iglesia, E. and Bell, A.T. (2001) *Journal of Physical Chemistry B*, **105**, 5144.

52 Argyle, M.D., Chen, K.D., Iglesia, E. and Bell, A.T. (2005) *Journal of Physical Chemistry B*, **109**, 2414.

53 Dupuis, A.C., Abu Haija, M., Richter, B., Kuhlenbeck, H. and Freund, H.J. (2003) *Surface Science*, **539**, 99.

54 Argyle, M.D., Chen, K.D., Bell, A.T. and Iglesia, E. (2002) *Journal of Catalysis*, **208**, 139.

55 Xiong, G., Li, C., Li, H.Y., Xin, Q. and Feng, Z.C. (2000) *Chemical Communications*, 677.

56 Chua, Y.T., Stair, P.C. and Wachs, I.E. (2001) *Journal of Physical Chemistry B*, **105**, 8600.

57 Xiong, G., Li, C., Feng, Z.C., Ying, P.L., Xin, Q. and Liu, J.K. (1999) *Journal of Catalysis*, **186**, 234.

58 Xiong, G., Feng, Z., Li, J., Yang, Q., Ying, P., Xin, Q. and Li, C. (2000) *Journal of Physical Chemistry B*, **104**, 3581.

59 Li, C. and Stair, P.C. (1996) *11th International Congress on Catalysis–40th Anniversary*, Studies in Surface Science and Catalysis, 101 (Pt. B) (eds J.W. Hightower, W.N. Delgass, E. Iglesia and A.T. Bell), Elsevier, Amsterdam, p. 881.

60 Stair, P.C. and Li, C. (1997) *Journal of Vacuum Science & Technology. A, Vacuum, Surfaces, and Films*, **15**, 1679.

61 Tian, H., Ross, E.I. and Wachs, I.E. (2006) *Journal of Physical Chemistry B*, **110**, 9593.

62 Catana, G., Rao, R.R., Weckhuysen, B.M., Van Der Voort, P., Vansant, E. and Schoonheydt, R.A. (1998) *Journal of Physical Chemistry B*, **102**, 8005.

63 Wu, Z., Kim, H.S., Stair, P.C., Rugmini, S. and Jackson, S.D. (2005) *Journal of Physical Chemistry B*, **109**, 2793.

64 Jackson, S.D., Rugmini, S., Stair, P.C. and Wu, Z. (2006) *Chemistry-Engineering Journal*, **120**, 127.

65 Kanervo, J.M., Harlin, M.E., Krause, A.O.I. and Banares, M.A. (2003) *Catalysis Today*, **78**, 171.

66 Khodakov, A., Olthof, B., Bell, A.T. and Iglesia, E. (1999) *Journal of Catalysis*, **181**, 205.

67 Arena, F., Frusteri, F., Martra, G., Coluccia, S. and Parmaliana, A. (1997) *Journal of the Chemical Society–Faraday Transactions*, **93**, 3849.

68 Albonetti, S., Cavani, F. and Trifiro, F. (1996) *Catalysis Reviews–Science and Engineering*, **38**, 413.

69 Mamedov, E.A. and Corberan Cortes, V. (1995) *Applied Catalysis, A: General*, **127**, 1.

70 Blasco, T. and Lopez Nieto, J.M. (1997) *Applied Catalysis, A: General*, **157**, 117.

71 Cavani, F. and Trifiro, F. (1995) *Catalysis Today*, **24**, 307.

72 Madeira, L.M. and Portela, M.F. (2002) *Catalysis Reviews–Science and Engineering*, **44**, 247.

73 Jackson, S.D., Lennon, D., Webb, G. and Willis, J. (2001) *Catalyst Deactivation*, Studies in Surface Science and Catalysis, 139, Elsevier, Amsterdam, p. 271.

74 Volpe, M., Tonetto, G. and de Lasa, H., (2004) *Applied Catalysis, A: General*, **272**, 69.

75 Wu, Z. and Stair, P.C. (2006) *Journal of Catalysis*, **237**, 220.

76 Chua, Y.T. and Stair, P.C. (2003) *Journal of Catalysis*, **213**, 39.

77 Baruya, A., Gerrard, D.L. and Maddams, W.F. (1983) *Macromolecules*, **16**, 578

78 Noda, L.K. and Sala, O., (2000) *Spectrochimica Acta Part A–Molecular and Biomolecular Spectroscopy*, **56**, 145.

79 Ukei, H., Hirose, T., Horikawa, S., Takai, Y., Taka, M., Azuma, N. and Ueno, A. (2000) *Catalysis Today*, **62**, 67.

80 Kuba, S. and Knozinger, H. (2002) *Journal of Raman Spectroscopy*, **33**, 325.

81 Asher, S.A. (1993) *Analytical Chemistry*, **65**, 201A.

82 Davis, S.M., Zaera, F. and Somorjai, G.A. (1982) *Journal of Catalysis*, **77**, 439.

83 Tinnemans, S.J., Kox, M.H.F., Nijhuis, T.A., Visser, T. and Weckhuysen, B.M. (2005) *Physical Chemistry Chemical Physics*, **7**, 211.

84 Huang, Z., McGregor, J., Steiner, P., Gladden, L.F., Rugmini, S. and Jackson, S. D. (2007) *Magnetic Resonance Imaging*, **25**, 562.

16
Properties, Synthesis and Applications of Highly Dispersed Metal Oxide Catalysts

Juncheng Hu, Lifang Chen, and Ryan Richards

16.1
Introduction

Metal oxides can be found in the form of single crystals (pure or defective), powder (with large numbers of crystals), polycrystalline samples (crystals with various orientations) or thin films and constitute an important class of materials covering the entire range from metals to insulators. The insulating oxides are made up of the metals from the far left and right sides of the periodic table. Typical examples of insulating oxides include MgO, CaO, Al_2O_3 and SiO_2. The oxides of the metals in the middle of the periodic table (Sc to Zn) make up semiconducting and metallic oxides. Typical examples include ZnO, TiO_2, NiO, Fe_2O_3 and Cr_2O_3. Additionally, transition metal oxides, which include the oxides of Ru, Mo, W, Pt, V and so forth, exhibit a wide-ranging array of properties and phenomena. The diverse structures adopted by metal oxides demonstrate the relationship between structure and properties. Correlation of structure and physical properties of transition metal oxides requires an understanding of the valence electrons that bind the atoms in the solid state [1]. Band theory and ligand field theory have been invoked to explain the electronic properties of transition metal oxides. The important properties of metal oxides that are of interest are magnetic, electrical, dielectric, optical, Lewis acid–base and redox behaviour. The transition metal oxides are of particular interest for applications in catalysis, sensor materials and other potential applications. Indeed, metal oxides are the key components for a variety of catalytic reactions, functioning directly as reactive components or as supports for dispersed active metal species, or as additives or promoters to enhance the rate of catalytic reactions. The importance of metal oxides in the field of catalysis is thus profound. Hitherto, the main interest in heterogeneous catalysis had centered on the kinetics of the reactions rather than on their mechanisms; now it is the catalyst itself and, in particular, its surface, that has become the focus of attention. In considering the action of a catalyst and its surface, two particular factors have been explored. One is the geometrical factor, for which experiments with chemisorption and catalysis on the various faces of single crystals have helped to define the role. The second factor is the role

Metal Oxide Catalysis. Edited by S. David Jackson and Justin S. J. Hargreaves

ISBN: 978-3-527-31815-5

of electrons in the catalytic process, and the surface science of metal oxides has received tremendous attention during recent years. The advent of several advanced techniques to probe surfaces has led to a new understanding of their surface properties and structures. This has helped catalyst scientists tailor the properties of the oxide materials for appropriate applications.

This chapter presents an overview of structures, properties, synthetic methods and applications in catalysis for highly dispersed metal oxides, with special attention given to recent developments in nano-scale metal oxides.

16.2 Properties

In the case of nano-scale materials one of the most influential factors towards their properties is the large number of atoms at the surface. For example, spherical nanoparticles with a diameter of 3 nm have nearly 50% of the atoms or ions on the surface, allowing the possibility of manipulation of bulk properties by surface effects and allowing near-stoichiometric chemical reaction [2]. Delocalization can vary with size when strong chemical bonding is present, and can lead to different chemical and physical properties [3]. The formation of ultra-small particles is facilitated by the refractory nature of most of the metal oxides [2]. For some materials, especially MgO, Al_2O_3, ZrO_2 and TiO_2, their highly ionic nature allows the formation of many stable defect sites, including edges, corners and anion/cation vacancies. MgO and CaO were found to be attractive materials to study because they are highly ionic and have high melting points and it would be expected that samples of very small particle size might be stable and isolable. Furthermore, reactive surface sites on these oxides have been extensively studied for macroscopic and conventionally prepared samples.

Metal oxides prepared via aerogel methods have found various applications, including as detectors for radiation, super insulators, solar concentrators, coatings, glass precursors, catalysts, insecticides and destructive adsorbents. Nanoparticles of crystalline substances have been found to possess about 10^{19} interfaces cm^{-3} and surface areas up to $800\,m^2g^{-1}$. Upon compaction, but without growing the nanocrystals, solids with multitudinous grain boundaries are formed. It has been proposed that further work in the area of consolidated nano-phase materials may lead to ceramics with increased flexibility, less brittleness and perhaps greater strength [2]. It may also be possible to form materials with a large fraction of atoms at grain boundaries, perhaps in unique arrangements.

16.2.1 Structure and Bonding

Characterization of the exact nature of structure and bonding in nanomaterials is particularly difficult because they generally consist of very small crystallites or are

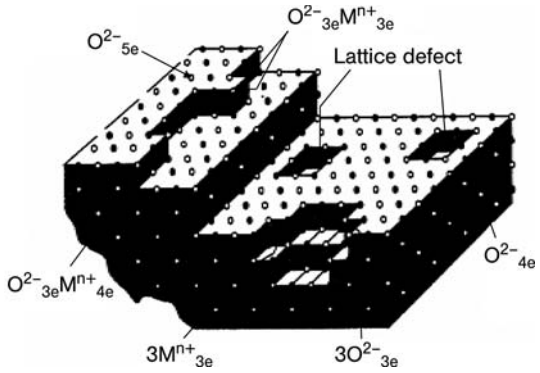

Figure 16.1 A representation of the various defects present on metal oxides (from [4]).

amorphous. Advances in crystallography for powders and crystals employing X-ray, electron and neutron diffraction have provided insight into the structures of metal oxides. Metal oxides crystallize in a variety of structures and the bonding in these materials can range from ionic (MgO, $Fe_{1-x}O$) to metallic (TiO, ReO_3) [1].

An understanding of both crystal structure and bonding, as well as the local microstructures that are due to defects, is necessary to understand the structure of complex transition metal oxides. Of course, on the nanometer scale the number of defects due to edges, corners, "F" centers and other surface imperfections is greatly enhanced by the large surface area (Figure 16.1) [4]. The pursuit of an understanding of the structure/property relationships at an atomic or molecular level is integral to the understanding of the unique properties observed on the nano-scale.

Five types of crystals found in bulk structures can be defined based on bonding considerations: covalent, ionic, metallic, molecular (van der Waals) and hydrogen bonded. These are also present on the nano-scale. However, the number of atoms at the surface must also be considered when examining the structure of nano-scale materials. When highly electronegative and highly electropositive elements are combined in a lattice, ionic crystals are formed. It has been found that the ionic model is a poor approximation for crystals containing large anions and small cations (e.g. oxides and sulfides) where the covalent contribution to bonding becomes significant [5]. Van der Waals interactions play a crucial role in many transition metal oxides, especially those with layered structures. In many oxide hydrates or hydroxy oxides, hydrogen bonding also contributes to the cohesive energy. In most transition metal oxides the bonding is only partly ionic; in other words, there is a considerable overlap between the orbitals of the cations and anions. However, there are several examples of metal oxides that are primarily ionic, such as MgO and CaO. Many transition metal oxides also exhibit metallic properties. Inorganic compounds of the formula AB can have the rock salt (B1),

CsCl (B2), zinc blende (B3), Wurtzite (B4), or NiAs (B8) structure [6]. Alkaline earth metal oxides such as MgO and monoxides of 3d transition metals as well as of lanthanides and actinides such as TiO, NiO, EuO and NpO, exhibit the rock salt structure with 6:6 octahedral coordination.

16.2.2 Defects

The physical and chemical properties of metal oxides are dominated by defects. Thermodynamic considerations imply that all crystals must contain a certain number of defects at temperatures above absolute zero. Structural defects can arise from a variety of causes: they may be thermally generated or they may arise in the course of fabrication of the solid, incorporated either unintentionally or deliberately. Defects are important because they are much more abundant at surfaces than in bulk, and in oxides they are usually responsible for many of the catalytic and chemical properties. Because of the number of atoms at the surface and the limited number of atoms within the lattice, the chemistry and bonding of oxide nanoparticles is greatly affected by the defect sites present. Point defects in crystals, such as vacancies and interstitials described by Schottky and Frenkel, account for the transport properties of ionic solids [6]. However, it appears that the point defect model is valid only when the defect concentration (or the deviation from stoichiometry) is extremely small. The defects that occur in ionic solids are grouped into the following classes: point, linear, planar and volumetric defects. Point defects are a result of the absence of one of the constituent atoms (or ions) on the lattice sites, or their presence in interstitial positions. Foreign atoms or ions present in the lattice represent another type of point defect. Point defects cause displacements on neighboring atoms or ions because of polarization in the surrounding region. A cationic vacancy in an ionic solid will have an electronegative charge, causing displacements of neighboring anions [7]. The energy of formation of a point defect depends primarily on the atomic arrangement in the immediate environment of the corresponding rows of atoms that do not possess the proper coordination. Boundaries between small crystallites (grain boundaries), stacking faults, crystallographic shear planes, twin boundaries and anti-phase boundaries are planar defects. Three-dimensional volumetric defects are a result of segregating point defects. The common point defects in ionic solids are Schottky pairs (pairs of cation and anion vacancies) and Frenkel defects (cation or anion interstitial plus a vacancy) [8]. When there is a large concentration of Schottky pairs, the measured pyknometric density of the solid is considerably lower than the density calculated from the X-ray unit cell dimensions (e.g. VO_x) [5]. Creation of defects is generally an endothermic process with the formation energies of vacancies in ionic solids generally 2 eV or more. Therefore, the intrinsic defect concentration in these solids is extremely low even at high temperatures [7]. The surface of a crystal constitutes a planar, 2-D defect. The environment of atoms or ions on the surface of a crystal is considerably different from that in the bulk. In polycrystalline materials, there are grain boundaries

between the particles. The interface between two solid phases is an important factor in determining the course of reactions, crystal growth, and so on. An interface may be coherent, incoherent or semicoherent. It is coherent when the interface matches perfectly between the contact planes of two solid planes. Epitaxial growth occurs even when there is considerable mismatch (semicoherent interface). In close packed solids, one also often encounters stacking faults. For example, in a solid with cubic close packing, ABC ABC ABC, there can be a fault such as ABC AB ABC. Other types of planar defects include tilt boundary (array of periodically spaced edge dislocations), twist boundary (array of screw dislocations), twin boundary (a layer with mirror plane symmetry with respect to the rotation of one part of the crystal, on a specific plane, with respect to another) and antiphase boundary (boundary across which the sublattice occupation becomes interchanged).

The radius of the oxide anion (1.44 Å) given by Shannon and Prewitt is larger than most cations. However, in crystals, the anions are subjected to a positive Madelung potential, which gives rise to a contraction of the charge cloud, while cations are subjected to negative potential causing an opposite effect [7]. Generally, phase purity is hard to achieve, especially for phases containing more than one cation [9]. Often, phase segregation occurs and so the particles are a mixture of other possible phases derivable form the precursors.

The high surface areas of nano-scale particles yield a number of defect sites. There have been numerous studies of their surfaces in an attempt to clarify the type of defect sites that can exist [10–13]. The most common defects are coordinatively unsaturated ions arising from planes, edges, corners, anion/cation vacancies and electron excess centers. Such sites are often attributed as the active sites for many useful and interesting reactions, including methane activation [14], D_2-CH exchange [15], methanol oxidation [16, 17], CO oligomerization [18], oxygen exchange in CO_2 [7] and H_2O [8].

16.2.3
Acid–Base Properties of Metal Oxides

Metal oxides are often hard acids or bases and thus possess sites capable of catalyzing acid–base chemistry. Acidic metal oxides include Al_2O_3, TiO_2, CeO_2, V_2O_5, WO_3, etc. Basic metal oxides include MgO, CaO, SrO, BaO, Li_2O, etc. The interactions of the oxide surfaces with gases or liquids, which are relevant in the fields of adsorption and catalysis, are mainly governed by acid–base interactions. Acidic properties of metal oxides sometimes play an important role in the catalytic oxidations of hydrocarbons, where reactions, especially the selectivities to the target products, are strongly affected by the functions of acidic sites.

Acid–base characterizations of metal oxide surfaces are often used to explain their catalytic behavior. Extensive studies have been performed on the interaction of acid–base probe molecules with powders or supported metal oxides. The adsorption of NH_3 at cation sites has been used to characterize the Lewis acidity of metal oxides. The systematic use of CO adsorption at room temperature as a probe for

(strong) Lewis acidity at the surface of a number of metal oxides (TiO_2, ZrO_2, HfO_2 and Al_2O_3) of interest in catalysis was also illustrated. The adsorption of CO_2, a standard acidic probe molecule, has also been used to characterize the Lewis basicity of the oxygen anions on metal oxides.

Several insulating oxides and oxide composites were found to be potential catalysts for a variety of important reactions as a result of their surface basicity or acidity [14, 19–22]. Some selected reactions typical to metal oxides include dehydration of alcohols, cracking of hydrocarbons, isomerization of olefins and paraffins, dehydrohalogenation, alkylation and esterification. Several metal oxides, such as MgO, CaO and SrO, exhibit surface basic behavior while others, such as Al_2O_3 and WO_3, are considered to be acidic solids that possess more and stronger acidic sites on their surfaces. Acid–base behavior and the presence of several types of deficiencies in the lattice and on the surface are two major driving forces for surface reactivity of metal oxides. When metal oxides are prepared on the nanoscale, the percentage of coordinatively unsaturated ions, especially on edges and corners, increases significantly. Consequently, surface chemistry effects, which are barely noticeable in macroscopic systems, become prevalent in nanoparticle systems. These effects are demonstrated by enhanced surface reactivities and catalytic potentials possessed by many nanoparticle systems of metal oxides [23–27]. As indicated earlier, two of the most intensively studied nanoparticulate systems of the metal oxides are MgO and CaO. In particular, two types of nanocrystalline oxides have been prepared and thoroughly studied: a "conventional preparation" (CP) and an "aerogel preparation" (AP). Nanocrystalline MgO prepared by a modified AP yields a fine, white powder of 400–500 $m^2 g^{-1}$ and 4 nm average crystallite size. High-resolution transmission electron microscope (TEM) imaging of a single crystallite indicated a polyhedral structure suggesting the presence of high surface concentrations of edge/corner sites and various exposed crystal planes (such as (002), (001), (111)) [28]. Conversely, CP yields particles with surface areas of 150–200 $m^2 g^{-1}$ and 8 nm average crystallites. If intrinsic surface chemistry differences due to size are to be uncovered, it is important to consider that in bulk MgO the effective ionic charges are close to +2, whereas the MgO molecule is much more covalent with effective charges close to +1. Lower coordination surface ions such as Mg^{2+}_{3c}, Mg^{2+}_{4c}, O^{2-}_{3c} and O^{2-}_{4c} are expected to have effective charges between +1 and +2. Surface sites on crystalline and powdered MgO have been probed by theoretical as well as experimental efforts. *Ab initio* calculations with H_2 have been used to probe perfect crystal surfaces and various defect sites. On the perfect (100) MgO surface, H_2 has a small adsorption energy and does not dissociate. However, temperature programmed desorption methods have shown that polycrystalline samples do dissociate H_2, probably on O_{3c}–Mg_{3c} sites. These sites are apparently very active for heterolytic H_2 dissociation. The microfaceted (111) surface of MgO is particularly reactive, and steps, kinks and point defects (ion vacancies and substitutions) are also important. Indeed, the unique catalytic properties of defective MgO surfaces also depend on a plethora of unusual coordination sites.

16.2.4
Redox Property of Metal Oxides

In some catalytic reactions, metal oxides often undergo reduction and re-oxidation simultaneously by loss and gain of surface lattice oxygen to and from the gas phase. This phenomenon is called redox catalysis. The redox property as well as the acidic and basic nature are the most important properties of metal oxide catalysis. It is well known that some simple metal oxides such as V_2O_5, CoO_2, NiO, MnO_2, CeO_2, MgO and some mixed metal oxides have redox properties. Mars and van Krevelen first proposed a redox mechanism to describe oxidation of compounds over oxide catalysts [29]. The Mars–van Krevelen mechanism (MvK) is now commonly accepted. When an adsorbate is oxidized at the surface, the oxidant is often a surface lattice oxygen atom, thus creating a surface oxygen vacancy. Surface oxygen vacancies are proposed to participate in many chemical reactions catalyzed by metal oxides. Vacancies also bind adsorbates more strongly than normal oxide sites and assist in their dissociation. The redox property of a metal oxide catalyst can be characterized by using the techniques of temperature-programmed reduction/temperature-programmed oxidation (TPR/TPO).

16.3
Synthesis

The development of synthetic methods is one of the fundamental aspects to the understanding and development of nano-scale materials. The novel properties and numerous applications of nano-scale materials have encouraged many researchers to invent and explore preparation methods that allow control over such parameters as particle size, shape, size distributions and composition. While considerable progress has taken place, one of the major challenges is the development of a "synthetic toolbox" which would afford access to size and shape control of structures on the nano-scale and conversely allow scientists to study the effects these parameters impart to the chemical and physical properties of the nanoparticles.

The two principal approaches to the preparation of nano-scale materials are "bottom-up" and "top-down". While "top-down" preparations involve approaching the nano-scale by breaking down larger starting materials, the "bottom-up" preparation methods are of primary interest to chemists and materials scientists because the fundamental building blocks are atoms or molecules, and these methods will be the focus of this chapter. Among the most sought after goals of synthetic chemists is gaining control over the way these fundamental building blocks come together and form particles. Interest in "bottom-up" approaches to nano-scale oxides and other materials is clearly indicated by the number of reports and reviews on this subject [30–46]. There are, of course, numerous "bottom-up" approaches to the preparation of nano-scale materials, and metal oxides are no exception. Gas–solid (wet chemical) and liquid–solid (physical) transformations

are two different approaches to synthesizing nanomaterials by "bottom-up" preparation methods. Several physical aerosol methods have been reported for the synthesis of nano-size particles of oxide materials including gas condensation techniques [47–53], spray pyrolysis [51, 54–60], thermochemical decomposition of metal–organic precursors in flame reactors [53, 61–63] and other aerosol processes named after the energy sources applied to provide the high temperatures during gas–particle conversion. The sol–gel process is by far the most common and widely used "bottom-up" wet chemical method for the preparation of nano-scale oxides. Other wet chemistry methods including novel micro-emulsion techniques, oxidation of metal colloids and precipitation from solutions have also been used.

The methods of sample preparation are critical as they determine the morphology of the resulting material [64]. For example, burning Mg in O_2 (MgO smoke) yields 40–80 nm cubes and hexagonal plates, while thermal decomposition of $Mg(OH)_2$, $MgCO_3$ and especially $Mg(NO_3)_2$ yields irregular shapes often exhibiting hexagonal platelets. Surface areas can range from $10\,m^2g^{-1}$ (MgO smoke) to $250\,m^2g^{-1}$ for $Mg(OH)_2$ thermal decomposition, but surface areas of about $150\,m^2g^{-1}$ are typical. In the case of calcium oxide, surface areas can range from 1 to $100\,m^2g^{-1}$ when prepared by analogous methods, but about $50\,m^2g^{-1}$ is typical. In the following discussion, the most common methods for the synthesis of metal oxides will be the focus.

16.3.1 Sol–Gel Technique

Sol–gel processing describes a type of solid materials synthesis procedure, performed in a liquid and at low temperature (typically $T < 100\,°C$). The development of sol–gel techniques has long been known for preparations of metal oxides and has been described many times [30–38, 40–46, 65]. The process is typically used to prepare metal oxides via the hydrolysis of reactive precursors, usually alkoxides in an alcoholic solution, resulting in the corresponding hydroxide. It is usually easy to maintain such hydroxide in a dispersed state in the solvent. Condensation of the hydroxide molecules with loss of water leads to the formation of a network. When hydroxide species undergo polymerization by condensation of the hydroxy

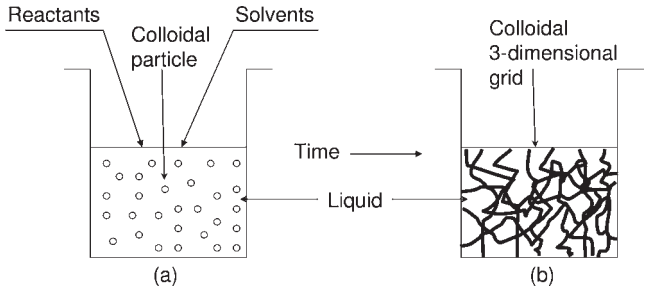

Figure 16.2 The sol–gel process: (a) sol, (b) gel.

network, gelation is achieved and a dense porous gel is obtained. The gel is a polymer with a three-dimensional skeleton surrounding interconnected pores, and the gels that are obtained are termed colloidal gels (Figure 16.2b). Removal of the solvents and appropriate drying of the gel are important steps that result in an ultra-fine powder of the metal hydroxide. Heat treatment of the hydroxide is a final step that leads to the corresponding ultra-fine powder of the metal oxide. Depending upon the heat treatment procedure, the final product may be in the form of a nano-scale powder, bulk material or oxygen-deficient metal oxide. A flow chart of typical sol–gel processing of nano-scale metal oxides is shown in Figure 16.3.

The chemical and physical properties of the final product are primarily determined by the hydrolysis and drying steps.

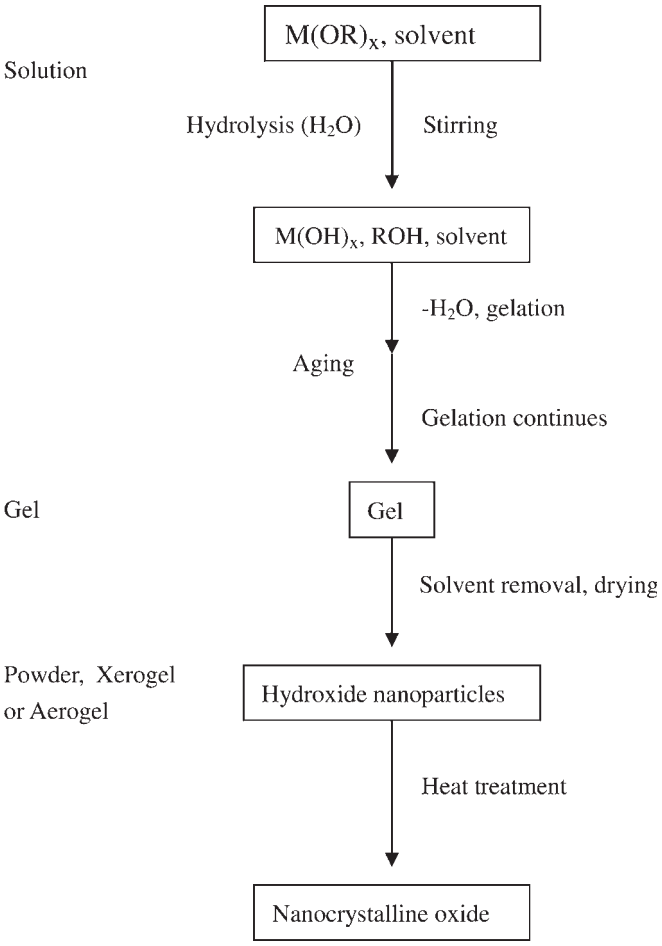

Figure 16.3 A flow chart of a typical sol–gel process for preparing nano-scale metal oxide powder.

16.3.1.1 Hydrolysis and Condensation of Metal Alkoxides

The initial species used in sol–gel processing are metal alkoxides ($M(OR)_y$). Hydrolysis of metal alkoxides involves nucleophilic reactions with water as follows:

$$M(OR)_y + xH_2O \leftrightarrow M(OR)_{y-x}(OH) + xROH$$

The mechanism of this reaction involves the addition of a negatively charged $HO^{\delta-}$ group to the positively charged metal center ($M^{\delta+}$). The positively charged proton is then transferred to an alkoxy group followed by the removal of ROH.

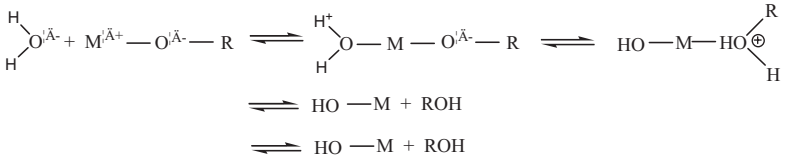

Condensation occurs when the hydroxide molecules bind together as they release water molecules and a gel/network of the hydroxide is obtained as shown below:

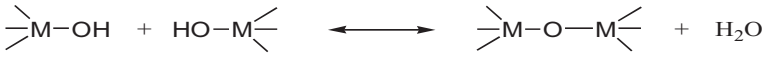

The rates at which hydrolysis and condensation take place are important parameters that affect the properties of the final product, as slower and more controlled hydrolysis typically leads to smaller particle sizes and more unique properties. Hydrolysis and condensation rates have been found to depend on the electronegativity of the metal atom, the alkoxy group, the solvent system and the molecular structure of the metal alkoxide. Those metals with higher electronegativities undergo hydrolysis more slowly than those with lower electronegativities. For example, the hydrolysis rate of $Ti(OEt)_4$ is about five orders of magnitude greater than that of $Si(OEt)_4$. Hence, the gelation times of silicon alkoxides are much longer (on the order of days) than those of titanium alkoxides (few seconds or minutes) [55]. The sensitivity of metal alkoxides toward hydrolysis decreases as the OR group size increases, with smaller OR groups leading to higher reactivity of the corresponding alkoxide toward water, in some cases resulting in uncontrolled precipitation of the hydroxide.

The choice of solvents in sol–gel processes is very important because alcohol interchange reactions are possible. As an example, when silica gel was prepared from $Si(OMe)_4$ and heated to 600 °C the surface area was $300\,m^2\,g^{-1}$ with a mean pore diameter of 29 Å when ethanol was used as a solvent. However, when methanol was used, the surface area dropped to $170\,m^2\,g^{-1}$ and the mean pore diameter increased to 36 Å [32]. The rate of hydrolysis also becomes slower as the coordination number around the metal center in the alkoxide increases. Therefore, alkoxides that tend to form oligomers usually show slower rates of hydrolysis and,

hence, are easier to control and handle. *n*-Butoxide (O-*n*-Bu) is often preferred as a precursor to different oxides including TiO_2 and Al_2O_3, because it is the largest alkoxy group that does not prevent oligomerization [33].

Because most metal alkoxides are highly reactive toward water, careful handling in dry atmospheres is required to avoid rapid hydrolysis and uncontrolled precipitation. For alkoxides that have low rates of hydrolysis, acid or base catalysts can be used to enhance the process. The relatively negative alkoxides are protonated by acids, creating a better leaving group and eliminating the need for proton transfer in the transition state. Alternatively, bases provide better nucleophiles (OH^-) for hydrolysis; however, deprotonation of metal hydroxide groups enhances their condensation rates. In the case of highly reactive compounds, controlling the hydrolysis ratio may necessitate the use of non-aqueous solvents, where hydrolysis is controlled by strict control of water in the system rather than by acids or bases. Klabunde and coworkers have demonstrated the effectiveness of this approach in the preparation of gels from $Mg(OEt)_2$ in methanol and methanol–toluene solvents [66].

16.3.1.2 **Solvent Removal and Drying**

Developments in the areas of solvent removal and drying have further facilitated the production of nano-scale metal oxides with novel properties. When drying is achieved by solvent evaporation at ambient pressure with moderate shrinkage, the gel network shrinks as a result of capillary pressure, and the hydroxide product obtained is referred to as xerogel. However, if supercritical drying is applied using a high-pressure autoclave reactor at temperatures higher than the critical temperatures of solvents, less shrinkage of the gel network occurs, as there is no capillary pressure and no liquid–vapor interface, which allows the pore structure to remain largely intact by avoiding the pore collapse phenomenon. In practice, supercritical drying consists of heating the wet gel in a closed container, so that the pressure and temperature exceeds the critical temperature, T_c, and critical pressure, P_c, of the liquid entrapped in the pores inside the gel. The critical conditions are very different depending on the fluid which impregnates the wet gel. A few values are given in Table 16.1 [67]. The hydroxide product obtained in this manner, which is the traditional drying technique, is referred to as an aerogel and is the origin of the label "aerogel". Aerogel powders usually demonstrate higher porosities and larger surface areas than analogous xerogel powders. Aerogel processing has been very useful in producing highly divided powders of different metal oxides [28, 68, 69] (Figures 16.4–16.6).

Sol–gel processes have several advantages over other techniques for the synthesis of nano-scale metal oxides. Because the process begins with a relatively homogeneous mixture, the resulting product is generally a uniform ultra-fine porous powder. Sol–gel processing also has the advantage that it can be scaled up to accommodate industrial-scale production.

Numerous metal oxide nanoparticles have been produced by making some modifications to the traditional AP method. One modification involved the addition of large amounts of aromatic hydrocarbons to the alcohol–methoxide

Table 16.1 Critical point parameters of common fluids.

Fluid	Formula	T_c (°C)	P_c (MPa)
water	H_2O	374.1	22.04
carbon dioxide	CO_2	31.0	7.37
Freon 116	$(CF_3)_2$	19.7	2.97
acetone	$(CH_3)_2O$	235.0	4.66
nitrous oxide	N_2O	36.4	7.24
methanol	CH_3OH	239.4	8.09
ethanol	C_2H_5OH	243.0	6.3

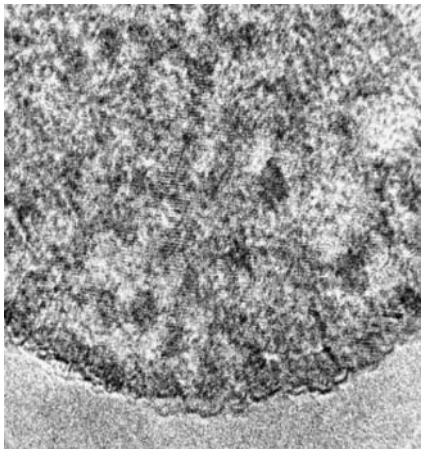

Figure 16.4 TEM micrograph of the nanostructure of CP-MgO. Note the absence of porosity and that all of the nanocrystals have agglomerated (from [68]).

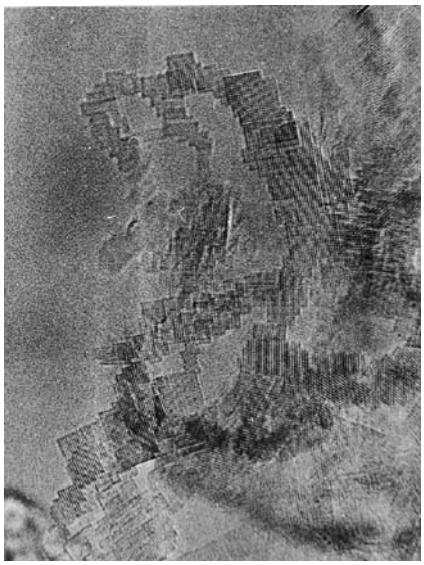

Figure 16.5 TEM micrograph of the nanostructure of AP-MgO (supercritical solvent removal). Porosity is formed by the interconnected cubic nanocrystals of MgO (from [28]).

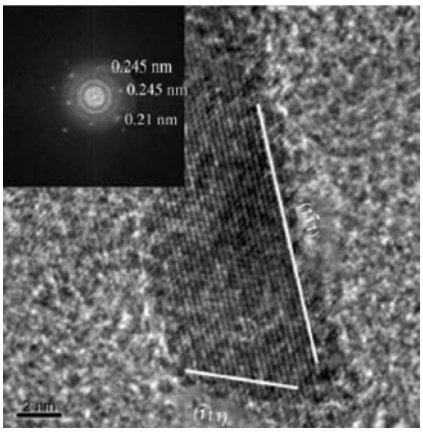

Figure 16.6 TEM micrograph of MgO(111) (supercritical solvent removal). Here the MgO nanoplates possess the (111) surface on the edges (from [69]).

solutions before hydrolysis and alcogel formation. This was done in order to further reduce the surface tension of the solvent mix and to facilitate solvent removal during the alcogel–aerogel transformation [30, 64, 70]. The resulting nanoparticles exhibited higher surface areas, smaller crystallite sizes and more porosity for samples of MgO, CaO, TiO_2 and ZrO_2 [71, 72].

Nano-structured MgO and CaO have been reported to be extremely effective for the destructive adsorption of numerous environmental toxins and several chemical warfare agents. Figure 16.7 outlines briefly how nano-crystalline and micro-crystalline MgO and CaO were prepared. For nano-crystalline MgO (AP-MgO) surface areas ranged from 250 to 500 $m^2 g^{-1}$ and for AP-CaO 100–160 $m^2 g^{-1}$. For CP micro-crystalline MgO and CaO, the surface areas are 130–250 and 50–100 $m^2 g^{-1}$, respectively, whereas commercially available MgO and CaO had the lowest surface areas. Richards and coworkers have reported a simple method for preparing a sheet-like MgO with a thickness of less than 10 nm and, more interestingly, exhibiting the highly ionic (111) facet as the major surface of the "nanosheet". In this system, a mixture of water and methanol was added slowly to hydrolyze a magnesium methoxide/benzyl alcohol solution to produce the nanosheets. Theoretical studies suggest that water plays an important role as chemisorption of water forms a hydroxyl surface which stabilizes the otherwise unstable (111) surface of MgO [69].

Mesoporous and spherical TiO_2 materials are interesting candidates for applications in catalysis, biomaterials, microelectronics, optoelectronics and photonics. Zhang and coworkers have put forward a new method to synthesize mesoporous TiO_2 as well as hollow spheres, using titanium butoxide, ethanol, citric acid, water and ammonia [73]. The mesoporous solid and hollow spheres were formed with the same reactants but adding them in a different order. The TiO_2 possessed a mesoporous structure with the particle diameters of 200–300 nm for solid spheres and 200–500 nm for hollow spheres. The average pore sizes and BET surface areas of the mesoporous TiO_2 solid and hollow spheres are 6.8 and 7.0 nm and 162

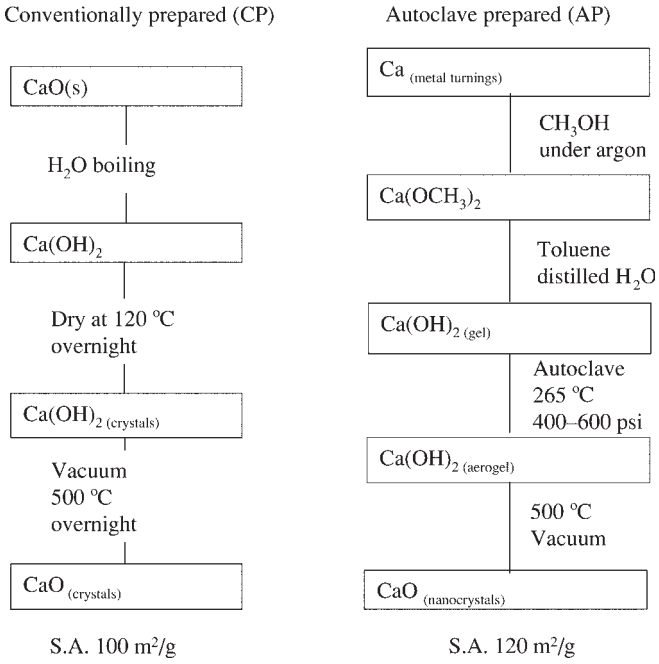

Figure 16.7 Schematic of the preparative scheme for nanocrystalline MgO (CaO) labeled AP-MgO (CaO) and microcrystalline MgO (CaO) labeled CP-MgO (CaO).

and 90 $m^2 g^{-1}$, respectively. Optical adsorption studies showed that the TiO_2 solid and hollow spheres possess a direct band gap structure with the optical band gap of 3.68 and 3.75 eV, respectively. The advantage of this route is that it does not use surfactants or templates, as is more usual for synthesizing mesoporous materials. In the proposed preparation mechanism (Figure 16.8), ammonium citrate forms and plays a key role in the formation of the mesoporous solid [73]. The formation of solid mesoporous TiO_2 or of hollow spheres was highly dependent on the extent of TiO_2 condensation at the onset of ammonium citrate crystal growth. That is, mesoporous solid spheres form when the TiO_2 condensation process takes place simultaneously with the formation of ammonium citrate crystals; mesoporous hollow spheres are produced when the nucleation and growth of ammonium citrate crystals occurs before the TiO_2 condensation process.

The chemistry of transition metals differs from those systems previously discussed, and only a few transition metals exhibit metal–alkoxide chemistry amenable to sol–gel synthesis. Cerda and coworkers prepared $BaSnO_3$ [74] by calcining a gel formed between $Ba(OH)_2$ and K_2SnO_3 at pH ≈ 11. The material possessed a particle size of 200–500 nm and contained $BaCO_3$ as an impurity, which can be eliminated by high temperature calcination. O'Brien and coworkers [75] synthe-

Figure 16.8 Schematic illustration of the formation mechanisms for mesoporous TiO_2 hollow and solid spheres (from [73]).

sized samples of monodisperse nanoparticles of barium titanate with diameters ranging from 6 to 12 nm by the sol–gel method. The technique was extended by Meron and coworkers [76] to the synthesis of colloidal cobalt ferrite nanocrystals. This synthesis involved the single-stage high-temperature hydrolysis of metal–alkoxide precursors to obtain crystalline, uniform, organically coated nanoparticles, which were well dispersed in an organic solvent. They were also able to form Langmuir–Blodgett films consisting of a close packed nanocrystal monolayer. The structural and magnetic properties of these nanocrystals were similar to those of bulk Fe_3O_4 with a very high coercivity at low temperatures. Other aerogel oxides, such as V_2O_5 [77, 78] MoO_3 [78] and MnO_2 [79, 80], have also been prepared. Nanocomposites of RuO_2–TiO_2 [81] are of particular interest because of their supercapacitor properties.

16.3.2
Co-precipitation Methods

One of the conventional syntheses to prepare nanoparticles is the precipitation of sparingly soluble products from aqueous solutions, followed by thermal decomposition of those products to oxides [82–84]. This process involves dissolving a salt precursor, usually a chloride, oxychloride or nitrate, such as $AlCl_3$ to make Al_2O_3, $Y(NO_3)_3$ to make Y_2O_3 and $ZrOCl_2$ to make ZrO_2. The corresponding metal hydroxides are usually formed and precipitated in water by the addition of a basic solution such as sodium hydroxide or ammonia solution. The resulting chloride or nitrate salts, such as NaCl or NH_4Cl, are then washed away and the hydroxide is calcined after filtration and washing to obtain the final oxide powder. This method is useful in preparing composites of different oxides by co-precipitation of the corresponding

hydroxides in the same solution. One of the disadvantages of this method is the difficulty in controlling the particle sizes and size distribution. Very often, fast (uncontrolled) precipitation takes place, resulting in large particles. In order to overcome this shortcoming, some new co-precipitation methods have developed, such as sonochemical co-precipitation and microwave-assisted co-precipitation.

16.3.2.1 Co-precipitation from Aqueous Solution at Low Temperature

The products of co-precipitation reactions are usually amorphous at or near room temperature. It is difficult to determine experimentally whether the as-prepared precursor is a single-phase solid solution or a multi-phase, nearly homogeneous mixture of the constituent metal hydroxides, carbonates and oxides that react to form a single phase mixed metal oxide when heated.

Many nano-particulate metal oxides are prepared by calcining hydroxide co-precipitation products. As an example, the zirconia system is highlighted here because of its interesting properties and applications. Zirconia has very interesting properties as an acid–base catalyst, as a promoter for other catalysts and as an inert support material [85, 86]. Sulfated ZrO_2 is of great interest on account of its high activity as a solid acid catalyst in alkylation, while ZrO_2 has also been found to act as a photocatalyst, owing to its n-type semiconductor nature.

The typical preparation consists of the calcination of a hydroxylated gel prepared by hydrolysis of zirconium salts in various media [72, 87–94]. Amorphous zirconia undergoes crystallization at around 450 °C and hence its surface area decreases dramatically at that temperature. At room temperature the stable crystalline phase of zirconia is monoclinic while the tetragonal phase forms upon heating to 1100–1200 °C For several applications, it is desirable to have the tetragonal phase with a high surface area. However, preparation protocols are needed to obtain the tetragonal phase at lower temperatures. Many researchers have tried to maintain the high surface area (HSA) of zirconia by several means. Usually the ZrO_2 is mixed with CaO, MgO, Y_2O_3, Cr_2O_3, or La_2O_3 for stabilization of the tetragonal phase at low temperature [95]. Bedilo and Klabunde [92, 93] have prepared HSA sulfated zirconia by a supercritical drying technique and found that the resulting material was active towards alkane isomerization reactions [92, 94]. Recently, Chane-Ching and coworkers [96] reported a general method to prepare HSA materials through the self-assembly of functionalized nanoparticles. This process involves functionalizing the oxide nanoparticles with bifunctional organic anchors such as aminocaproic acid and taurine. After the addition of a copolymer surfactant, the functionalized nanoparticles will slowly self-assemble on the copolymer chain through a second anchor site. Using this approach the authors prepared several metal oxides, including CeO_2, ZrO_2 and CeO_2–$Al(OH)_3$ composites. The method yielded ZrO_2 of surface area 180 $m^2 g^{-1}$ after calcining at 500 °C, 125 $m^2 g^{-1}$ for CeO_2 and 180 $m^2 g^{-1}$ for CeO_2–$Al(OH)_3$ composites.

Table 16.2 [97–100] shows the literature data for zirconia obtained by different processes and the resulting surface area obtained at different calcination temperatures. Richards and coworkers [101] obtained stable ZrO_2 by the cetyltrimethylammonium chloride stabilization route and the data indicate that digesting the

Table 16.2 Survey from the literature of ZrO_2 prepared using precipitation methods.

Starting material	Ppt agent	Surfactant[a)]	Conditions	Surface area ($m^2 g^{-1}$)	Ref.
$ZrOC1_2$	NH_3 (aq)	none	calcined 450 °C	247	[97]
$ZrOC1_2$	NH_3 (aq)	$C_{12}TACl$	calcined 450 °C	274	[97]
$ZrOC1_2$	NH_3 (aq)	$C_{14}TACl$	calcined 450 °C	300	[97]
$ZrOC1_2$	NH_3 (aq)	$C_{16}TACl$	calcined 450 °C	312	[97]
$ZrOC1_2$	NH_3 (aq)	$C_{18}TACl$	calcined 450 °C	313	[97]
$ZrOC1_2$	NaOH	P_{123}	calcined 450 °C	103	[98]
$ZrOC1_2$	NaOH	P_{123}	calcined 600 °C	51	[98]
$Zr(NO_3)_4$	TEA	CTAB	calcined 500 °C	–	[99]
$ZrOC1_2$	NH_3 (aq)	CTAB	calcined 600 °C	168	[100]
$ZrOC1_2$	NH_3 (aq)	CTAB	calcined 800 °C	105	[100]

a $C_{12}TACl$, dodecyltrimethylammonium chloride; P_{123}, poly(ethylene oxide)-b-poly(propylene oxide)-b-poly(ethylene oxide) triblock copolymer; CTAB, cetyltrimethylammonium bromide.

material in the presence of cetyltrimethylammonium chloride and ammonia provided higher surface areas. Moreover, surface area and thermal stability were found to depend on digestion time. In their study, digestion at 110 °C for 100 hours provided high thermal stability and the highest surface area of 370 $m^2 g^{-1}$; the same sample when calcined at 700 °C possessed a surface area of 160 $m^2 g^{-1}$, which was the best value obtained to date. Zirconia samples that were digested more than 100 hours had high thermal stability but no increases in surface area were observed. The same samples that were dried by applying supercritical techniques did not yield better results.

As previously stated, a common method for producing crystalline nanoparticle oxides is the co-precipitation of metal cations as carbonates, dicarbonates or oxalates, followed by their subsequent calcination and decomposition. Unfortunately, the calcination invariably leads to agglomeration or, at high temperatures, aggregation and sintering. As an example, CeO_2 nanopowders have been prepared by calcining the product of the precipitation between $Ce(NO_3)_3$ and $(NH_4)_2CO_3$, resulting in crystalline 6 nm particles of CeO_2 at calcination temperatures as low as 300 °C [106]. NiO with 10–15 nm particles has been similarly prepared by precipitating aqueous Ni^{2+} solutions with $(NH_4)_2CO_3$ and calcining the products at 400 °C [107]. In some rare instances, crystalline oxides can be precipitated from aqueous solution, eliminating the need for a calcination step and greatly reducing the risk of agglomeration. For example, TiO_2 can be prepared by precipitation using aqueous $TiCl_3$ with NH_3(aq) under ambient conditions. The products were 50–60 nm aggregates and stabilized with poly(methyl methacrylate) [108].

The direct co-precipitation of complex ternary oxides is somewhat uncommon, but is nonetheless possible, particularly when the product assumes a very thermodynamically favorable structure such as spinel. In such cases, the precipitation reactions are normally carried out at elevated temperatures (50–100 °C). Condensation of the two hydroxide intermediates into oxides and the induction of co-

precipitation were carried out in the same reaction vessel. For instance, Pr^{3+}-doped ceria has been precipitated to yield monodispersed 13 nm particles by aging aqueous solutions of $Ce(NO_3)_3$ and $PrCl_3$ at 100 °C in the presence of a hexamethylenetetramine stabilizer [109]. In such a case, the stabilizer indirectly serves as the precipitating agent by raising the pH sufficiently to induce precipitation of the metal hydroxides. Likewise, $MnFe_2O_4$ was prepared from aqueous Mn^{2+} and Fe^{2+} at temperatures up to 100 °C to yield 5–25 nm particles [110].

Chinnasamy and coworkers have reported an extensive series of experiments for the preparation of spinel-structured $CoFe_2O_4$ [111]. The sizes of the products were determined by the influence of reaction temperature, reactant concentration and reactant addition rate. In each case, aqueous solutions of Fe^{3+} and Co^{2+} were precipitated with dilute NaOH. The results were predominantly in line with expectations based on the considerations outlined in reaction temperature, reactant concentration and reactant addition rate. Increasing the temperature from 70 °C to 98 °C increased the average particle size from 14 to 18 nm. Increasing the NaOH concentration from 0.73 to 1.13 *M* increased particle size from 16 to 19 nm. NaOH concentrations of 1.5 *M* or greater resulted in the formation of a secondary FeOOH phase and slowing the NaOH addition rate appeared to broaden the particle size distribution. Li and coworkers also prepared 12 nm $CoFe_2O_4$ by a similar route but stabilized the product by acidification with dilute nitric acid [112].

A summary of oxides precipitated from aqueous solutions, including the relevant reaction conditions, is given in Table 16.3 [113–119].

16.3.2.2 **Sonochemical Co-precipitation**

The principle of sonochemistry is breaking the chemical bond with the application of high-power ultrasound waves, usually between 10 and 20 MHz. The physical

Table 16.3 Summary of reactions for the precipitation of oxides from aqueous solution.

Oxide	Starting material	Ppt agent	Stabilizer	Conditions	Product size (nm)	Ref.
Fe_2O_3	$FeCl_2$	NH_3 (aq)	H^+	calcined 550 °C	53.5	[113]
TiO_2	$Ti(SO_4)_2$	NH_3 (aq)	H^+	calcined 550 °C	9.2	[113]
Al_2O_3	$Al(NO_3)_3$	NH_3 (aq)	H^+	calcined 550 °C	13.2	[113]
CeO_2	$Ce(NO_3)_3$	NH_3 (aq)	none	calcined 650 °C	12–15	[114]
TiO_2	$TiCl_3$	Na_2O_2	NaCl	calcined 700 °C	30	[115]
VO_2	NH_4VO_3	$N_2H_4 \cdot H_2O$	none	calcined 300 °C	35	[116]
Cr_2O_3	$K_2Cr_2O_7$	$N_2H_4 \cdot H_2O$	none	calcined 500 °C	30	[116]
γ-Mn_2O_3	$KMnO_4$	$N_2H_4 \cdot H_2O$	none	–	8	[116]
Fe_3O_4	$FeCl_2$	NH_3 (aq)	H^+	N_2 atm	8–50	[117]
NiO	$NiCl_2$	NH_3 (aq)	CTAB	annealed 500 °C	22–28	[118]
ZnO	$ZnCl_2$	NH_3 (aq)	CTAB	annealed 500 °C	40–60	[118]
SnO_2	$SnCl_4$	NH_3 (aq)	CTAB	annealed 500 °C	11–18	[118]
Sb_2O_3	$SbCl_3$	NaOH	PVA	annealed 350 °C	10–80	[119]

phenomenon responsible for the sonochemical process is acoustic cavitation. According to published theories for the formation of nanoparticles by sonochemistry, the main events that occur during the preparation are creation, growth and collapse of the solvent bubbles that are formed in the liquid. These bubbles are in the nanometer size range. Solute vapors diffuse into the solvent bubble and when the bubble reaches a certain size, its collapse takes place. During the collapse very high temperatures of 5000–25 000 K [127] are obtained, which is enough to break chemical bonds in the solute. The collapse of the bubble takes place in less than a nanosecond [128, 129] hence a high cooling rate (1011 $K s^{-1}$) is also obtained. This high cooling rate hinders the organization and crystallization of the products. Since the breaking of bonds in the precursor occurs in the gas phase, amorphous nanoparticles are obtained. Though the reason for the formation of amorphous products is well understood, the formation of nanostructures is not. One possible explanation is that in each collapsing bubble a few nucleation centers are formed and while the fast kinetics does not stop the growth of nuclei that growth is limited by the collapse. Another possibility is that the precursor is a non-volatile compound and the reaction occurs in a 200 nm ring surrounding the collapsing bubble [130]. In the latter case, the sonochemical reaction occurs in a liquid phase and the products could be either amorphous or crystalline depending on the temperature in the ring region of the bubble. Suslick has estimated the temperature of the ring region as 1900 °C. The sonochemical method has been found useful in many areas of material science, from the preparation of amorphous products [131, 132] through the insertion of nanomaterials into mesoporous materials [102, 103] to the deposition of nanoparticles on ceramic and polymeric surfaces [104, 105].

Sonochemical methods for the preparation of nanoparticles were pioneered by Suslick in 1991 [127]. If a reaction is carried out in the presence of oxygen by similar methods, the product formed will be an oxide. $NiFe_2O_4$ has been synthesized by sonicating the mixture of $Fe(CO)_5$ and $Ni(CO)_4$ in decalin under 1–1.5 atm pressure of oxygen [133]. ZrO_2 was synthesized using $Zr(NO)_3$ and NH_3(aq) in aqueous phase under ultrasonic irradiation, followed by calcination at 300–1200 °C to improve the crystallinity or, for temperatures of 800 °C and above, to induce the tetragonal to monoclinic phase transformation [100, 134]. Nanocrystalline $La_{1-x}Sr_xMnO_3$ was prepared in a similar manner [135]. The method has also been successfully applied to synthesize $Ni(OH)_2$ and $Co(OH)_2$ nanoparticles [136] and iron(III) oxide [137]. Polycrystalline CeO_2 nanorods 5–10 nm in diameter and 50–150 nm in length were synthesized via ultrasonication using polyethylene glycol (PEG) as a structure-directing agent at room temperature. The content of PEG, the molecular weight of PEG and the sonication time were confirmed to be the crucial factors determining the formation of one-dimensional CeO_2 nanorods. A possible ultrasonic formation mechanism is suggested in Figure 16.9 [138].

16.3.2.3 **Microwave-Assisted Co-precipitation**

The microwave processing of nanoparticles results in rapid heating of the reaction mixtures, particularly those containing water. As a consequence, the precipitation

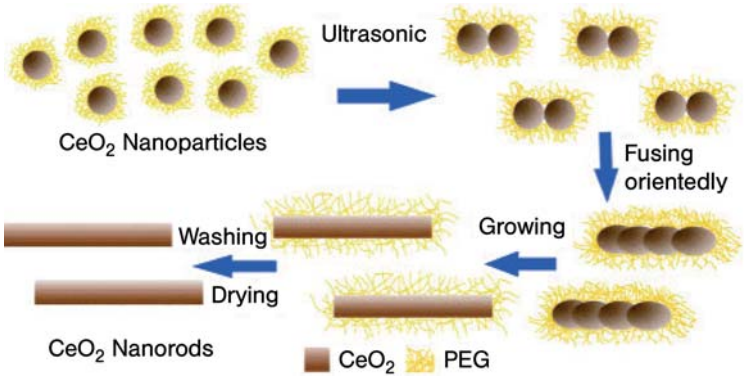

Figure 16.9 Possible formation mechanism of CeO_2 nanorods (from [139]).

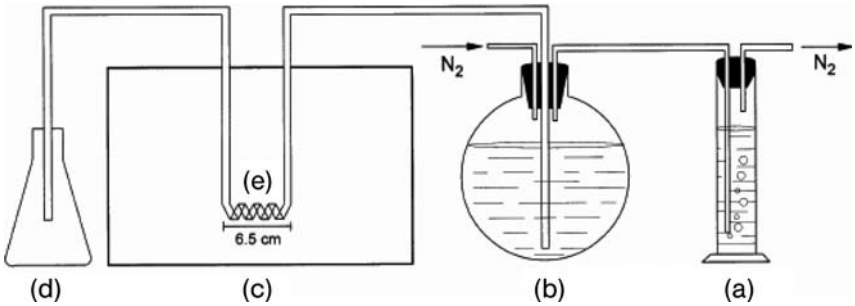

Figure 16.10 Schematic of a continuous-flow microwave reactor consisting of (a) a liquid column as a pressure regulator, (b) a metal salt solution container, (c) a microwave oven cavity, (d) a metal cluster dispersion receiver and (e) a spiral tube reactor (from [139]).

of particles from such solutions tends to be rapid and nearly instantaneous, leading to very small particle sizes and narrow size distributions within the products. The method offers the additional benefit of requiring very short reaction times and has similarly been used for the synthesis of Ag and Au nanoparticles and transition metal oxides. Tu and coworkers [139] adapted a continuous flow reactor which is depicted in Figure 16.10. For example, two nano-structured cerium(IV) oxide powders were synthesized by different synthetic routes: two samples were obtained by precipitation from a basic solution of cerium nitrate and treated at 523 and 923 K, respectively. A broad particle size distribution is observed for CeO_2 obtained by precipitation (8.0–15.0 nm). Smaller particles (sizes around 3.3–4.0 nm) with a narrow particle size distribution characterize the ceria obtained by microwave irradiation. Uniform α-Fe_2O_3 nanoparticles were prepared by forced hydrolysis of ferric salts under microwave irradiation. Gedanken's group has also published extensively on various oxides and chalcogenides prepared by microwave-assisted irradiation [120–122, 140].

16.3.3
Solvothermal Technique

Hydrothermal processes [123–126] involve using water at elevated temperatures and pressures in a closed system, often in the vicinity of its critical point. A more general term, "solvothermal," refers to a similar reaction in which a non-aqueous solvent (organic or inorganic) is used. Under solvo(hydro)thermal conditions, certain properties of the solvent, such as density, viscosity and diffusion coefficient, change dramatically and the solvent behaves much differently from what is expected under ambient conditions [126]. Consequently, the solubility, the diffusion process and the chemical reactivity of the reactants (usually solids) are greatly increased or enhanced, enabling the reaction to take place at a much lower temperature than normal. The method has been widely applied and adopted for crystal growth of many inorganic materials, such as zeolites, quartz, metal carbonates, phosphates and other oxides and halides [141–148].

Solvothermal techniques have been extensively developed for the synthesis of metal oxides [149–152]. Unlike many other synthetic techniques, solvothermal synthesis concerns a much milder and softer chemistry conducted at low temperatures. The mild and soft conditions make it possible to leave polychalcogen building-blocks intact while they reorganize themselves to form various new structures, many of which might be promising for applications in catalysis, electronic, magnetic, optical and thermoelectronic devices [153–155]. They also allow the formation and isolation of phases that may not be accessible at higher temperatures because of their metastable nature [156, 157].

Although some solvothermal processes involve supercritical solvents, most simply take advantage of the increased solubility and reactivity of metal salts and complexes at elevated temperatures and pressures without bringing the solvent to its critical point. The metal complexes are decomposed thermally either by boiling the contents in an inert atmosphere or by using an autoclave. A suitable capping agent or stabilizer such as a long-chain amine, thiol, trioctylphosphine oxide (TOPO), etc. is added to the reaction contents at a suitable point to hinder the growth of the particles and hence stabilize them against agglomeration. The stabilizers also help in dissolution of the particles in different solvents. Unlike the cases of co-precipitation and sol–gel methods, solvothermal processes also allow substantially reduced reaction temperatures, and the products of solvothermal reactions are usually crystalline and do not require post-annealing treatments.

The synthesis of nanocrystalline TiO_2, which is an important photocatalyst for the decomposition of toxic chemicals, is one of the more thoroughly investigated solvothermal/hydrothermal reactions. Approaches to this preparation have involved the decomposition of metal alkoxides, [158] a TOPO-capped autoclave synthesis of TiO_2 by metathetic reaction [159] and decomposition of a metal *N*-nitroso-*N*-phenyl hydroxylamine complex [160, 161]. In 1988, Oguri and coworkers reported the preparation of anatase by hydrothermally processing hydrous titania prepared by the controlled hydrolysis of $Ti(OEt)_4$ in ethanol [162]. The reaction conditions leading to monodispersed anatase nanoparticles by this approach

were elucidated by others [163]. Extension of the method to the preparation of lanthanide-doped titania particles has also been reported [164]. Cheng and coworkers developed a method for preparing nano-scale TiO_2 by hydrothermal synthesis using an aqueous $TiCl_4$ solution [165]. They found that acidic conditions favored rutile while basic conditions favored anatase. It was also found that higher temperature favored the highly dispersed product and that grain size could be controlled by the addition of minerals such as $SnCl_4$ or NaCl, although the presence of NH_4Cl led to agglomeration of particles. The approach was extended, and revealed that phase purity of the products depends primarily on concentration, with higher concentrations of $TiCl_4$ favoring the rutile phase, while particle size depends primarily on reaction time [166]. Yin and coworkers produced 2–10 nm crystallites of monodispersed, phase-pure anatase by using citric acid to stabilize the TiO_2 nanoparticles and treating the precursors hydrothermally in the presence of KCl or NaCl mineralizers [167].

Niederberger and coworkers [150] reported a widely applicable solvothermal route to nanocrystalline iron, indium, gallium and zinc oxides based on the reaction between the corresponding metal acetylacetonate as metal oxide precursor and benzylamine as solvent. They proved that with the exception of the iron oxide system, in which a mixture of the two phases magnetite and maghemite is formed, only phase-pure materials are obtained, γ-Ga_2O_3, zincite ZnO and cubic In_2O_3. The particle sizes lie in the ranges 15–20 nm for the iron, 10–15 nm for the indium, 2.5–3.5 nm for the gallium and around 20 nm for the zinc oxide (Figure 16.11). Moreover, the same group developed mixed nanocrystalline $BaTiO_3$, $SrTiO_3$ and (Ba,Sr)-TiO_3. $BaTiO_3$ nanoparticles are nearly spherical in shape, with diameters ranging from 4 to 5 nm, while $SrTiO_3$ particles display less-uniform particle shapes, the size vaying between 5 and 10 nm [168].

Masui and coworkers [169] reported the hydrothermal synthesis of nanocrystalline, monodispersed CeO_2 with a very narrow size distribution. They combined $CeCl_3 \cdot 6H_2O$ and aqueous ammonia with a citric acid stabilizer and heated the solution in a sealed Teflon container at 80 °C. The CeO_2 nanoparticles exhibited a 3.1 nm average diameter. The ceria particles were subsequently coated with turbostratic boron nitride by combining them with a mixture of boric acid and 2,2′-iminodiethanol, evaporating the solvent and heating at 800 °C under flowing ammonia. Inoue and coworkers were able to reduce the particle size of hydrothermally prepared colloidal CeO_2 to 2 nm using a similar approach by autoclaving a mixture of cerium metal and 2-methoxyethanol at 250 °C [170]. In this case, the autoclave was purged with nitrogen prior to heating and the colloidal particles were coagulated after heating with methanol and ammonia. The higher reaction temperatures resulted in increased particle size.

In many cases, anhydrous metal oxides have been prepared by solvothermal treatments of sol–gel or micro-emulsion-based precursors. Wu and coworkers prepared anatase and rutile TiO_2 by a micro-emulsion-mediated method, in which the micro-emulsion medium was further treated by hydrothermal reaction [171]. This micro-emulsion-mediated hydrothermal (MMH) method could lead to the formation of crystalline titania powders under much milder reaction conditions.

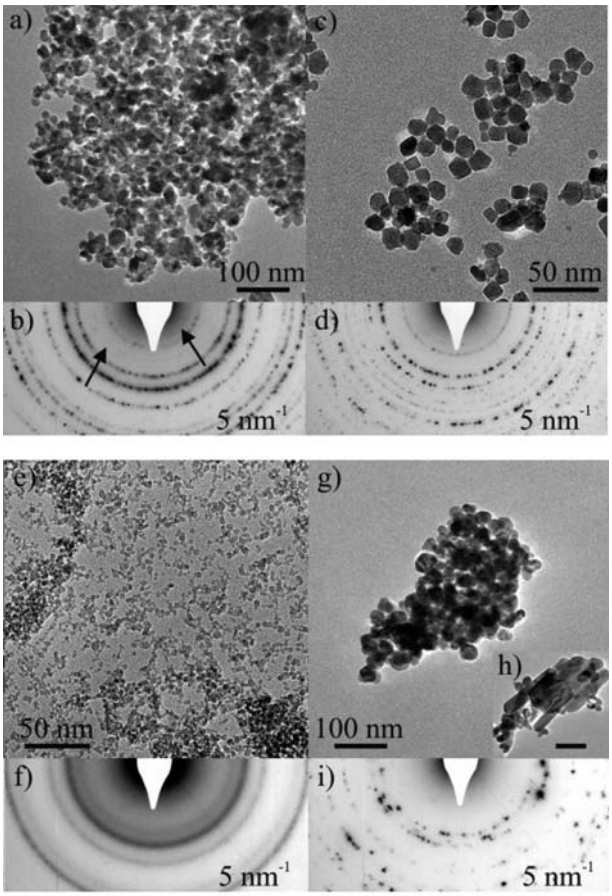

Figure 16.11 TEM overview images of (a) iron oxide, (c) indium oxide, (e) gallium oxide and (g) and (h) zinc oxide nanoparticles (scale bar 100 nm) and their respective selected-area electron diffraction patterns (b, d, f and i); (i) corresponds to (g) (from [150]).

The micro-emulsion medium was heated to 120–200 °C in a stainless steel autoclave. Micro-emulsions acidified with HNO_3 produced monodispersed anatase nanoparticles while those acidified with HCl produced rutile nanorods. Titanium dioxide (TiO_2) nanoparticles prepared this way have been shown to be active toward the photocatalytic oxidation of phenol [172].

Metal oxides can also be synthesized by the decomposition of metal–cupferron complexes, M^xCup_x (Cup = $C_6H_5N(NO)O^-$) [160]. Seshadri and coworkers were able to replace amine-based solvents with toluene, and prepared ≈10 nm diameter γ-Fe_2O_3 and ≈7 nm $CoFe_2O_4$ by hydrothermal processes [161]. They synthesized maghemite γ-Fe_2O_3 nanoparticles from a Fe^{III}–cupferron complex and spinel $CoFe_2O_4$ nanoparticles starting from Co^{II}–cupferron complex and Fe^{III}–cupferron

complex. However, the authors found that the presence of at least trace quantities of a strongly coordinating amine was necessary to act as a capping agent and prevent aggregation. They were also able to synthesize nanoparticulate $ZnFe_2O_4$ by a similar approach [173].

16.3.4
Micro-Emulsion Technique

Micro-emulsions or micelles (including reverse micelles) represent an approach based on the formation of micro/nano reaction vessels for the preparation of nanoparticles, and has received considerable interest in recent years [174–180]. A literature survey indicates that ultra-fine nanoparticles in the size range 2–50 nm can be easily prepared by this method. This technique uses an inorganic phase in water-in-oil micro-emulsions, which are isotropic liquid media with nano-sized water droplets dispersed in a continuous oil phase. In general, micro-emulsions consist of, at least, a ternary mixture of water, a surfactant (or a mixture of surface-active agents) and oil. The dispersion of the aqueous phase is shown in Figure 16.12 [68]. The classical examples of emulsifiers are sodium dodecyl sulfate (SDC) and aerosol bis(2-ethylhexyl) sulfosuccinate (AOT). The surfactant (emulsifier) molecule stabilizes the water droplet because they have polar head groups and non-polar organic tails. The organic (hydrophobic) portion faces towards the oil phase and the polar (hydrophilic) group towards water. In diluted water (or oil) solutions, the emulsifier dissolves and exists as a monomer, but when its concentration exceeds a certain limit called the critical micelle concentration (CMC), the molecules of emulsifier associate spontaneously to form aggregates called micelles. These micro-water droplets then form nano-reactors for the formation of nanoparticles. The nanoparticles formed usually have monodisperse properties. One method of formation consists of mixing two micro-emulsions or macro-emulsions and aqueous solutions carrying the appropriate reactants in order to obtain the

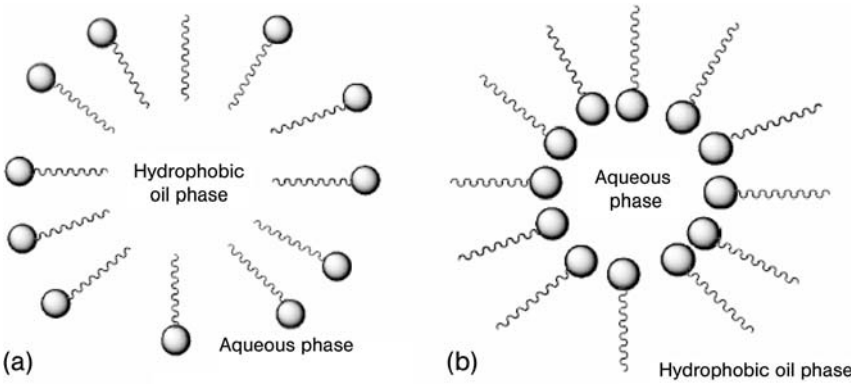

Figure 16.12 Schematic representation of (a) a micelle and (b) an inverse micelle (from [68]).

desired particles. The interchange of the reactants takes place during the collision of the water droplets in the micro-emulsions. The interchange of the reactant is very fast so that, for the most commonly used micro-emulsions, it occurs simply during the mixing process. The reduction, nucleation and growth occur inside the droplets, which controls the final particle size. The chemical reaction within the droplet is very fast, so the rate determining step will be the initial communication step of the micro-droplets with different droplets. The rate of communication has been defined by a second-order communication-controlled rate constant and represents the fastest possible rate constant for the system. The reactant concentration has a major influence on the reaction rate. The rate of both nucleation and growth are determined by the probabilities of the collisions between several atoms, between one atom and a nucleus and between two or more nuclei. Once a nucleus forms with the minimum number of atoms, the growth process starts. For the formation of monodisperse particles, all of the nuclei must form at the same time and grow simultaneously and with the same rate.

The preparation of metal oxide nanoparticles within micelles involves forming two micro-emulsions, one with the metal salt of interest and the other with the reducing or oxide-containing agent and mixing them together. When the two different reactants mix, the interchange of the reactants takes place through the collision of water micro-droplets. The reaction (reduction, nucleation and growth) takes place inside the droplet, which controls the final size of the particles. The interchange of nuclei between two micro-droplets does not take place owing to the special restrictions from the emulsifier. Once the particle inside the droplets attains its full size, the surfactant molecules attach to the metal surface, thus stabilizing and preventing further growth.

Reverse micelles are used to prepare nanoparticles by using an aqueous solution of reactive precursors that can be converted to insoluble nanoparticles. Nanoparticle synthesis inside the micelles can be achieved by a variety of methods, including hydrolysis of reactive precursors, such as alkoxides, and precipitation reactions of metal salts [181, 182]. Solvent removal and subsequent calcination leads to the final product. A variety of surfactants can be used in these processes such as pentadecaoxyethylene nonylphenylether (TNP-35) [182], decaoxyethylene nonylphenyl ether (TNT-10) [182], poly(oxyethylene)$_5$ nonylphenylether (NP5) [183] and many others that are commercially available. Several parameters, such as the concentration of the reactive precursor in the micelle and the weight percentage of the aqueous phase in the micro-emulsion, affect the properties, including particle size, particle size distribution, agglomerate size and phases of the final oxide powders. There are several advantages to using this method, including the preparation of very small particles and the ability to control the particle size. Disadvantages include low production yields and the need to use large amounts of solvents and surfactants.

This method has been successfully applied for the synthesis of metals, metal oxides, alloys and core–shell nanoparticles. The synthesis of metal oxides from reverse micelles is similar in most aspects to their synthesis in aqueous phase by a precipitation process. For example, precipitation of hydroxides is obtained by addition of a base such as NH_3(aq) or NaOH to a reverse micelle solution

containing aqueous metal ions at the micellar cores. This method has been also used to synthesize mixed metal iron oxides [162],

$$M^{2+} + 2Fe^{2+} + OH^- \text{ (excess)} \xrightarrow{\Delta, O_2} MFe_2O_4 + xH_2O \uparrow$$

where M = Fe, Mn or Co. The resultant particles obtained are of the order of 10–20 nm in diameter. The cation distribution in the case of spinels depends on the temperature used in the reaction [184]. If the transition metal cation is unstable or insoluble in aqueous media, nanoparticles of those metals can be prepared by hydrolysis of suitable precursors; for example, TiO_2 has been prepared from tetraisopropyl titanate [185] in the absence of water. The hydrolysis occurs when a second water-containing solution of reverse micelles is added to the solution of the first micelle containing the metal precursor. Adjusting the concentration of reactants can change the final crystal form, that is between amorphous and crystalline. The reaction can be described as follows,

$$Ti(O^iPr)_4 + 2H_2O \rightarrow TiO_2 + 4(^iPr\text{-}OH)$$

Micro-emulsions have been also employed to prepare precursors that decompose during calcination, resulting in desired mixed metal oxides. A series of mixed-metal ferrites have been prepared by precipitating the metal precursor in a H_2O-AOT-isooctane system and calcining the products at 300–600 °C [186]. A superconductor material $YBa_2Cu_3O_{7-\delta}$ with 10 nm particles have been prepared by combining a micellar solution of Y^{3+}, Ba^{2+} and Cu^{2+} prepared in an Igepal CO-430–cyclohexene system with a second micellar solution containing oxalic acid in the aqueous cores (Note: Igepal CO-430 is a surfactant with chemical name "Nonyl phenol 4 mole ethoxylate"). The precipitate was subsequently calcined to 800 °C to remove oxalic precursors [187]. Other metals and metal oxides that are prepared by a similar method include tungsten and tungsten oxide nanoparticles [188] and high-surface-area Al_2O_3 [189].

16.3.5 Combustion Methods

The combustion synthesis technique consists of bringing a saturated aqueous solution of the desired metal salts and a suitable organic fuel to the boil, until the mixture ignites a self-sustaining and rather fast combustion reaction, resulting in a dry, usually crystalline, fine oxide powder. By simple calcination, the metal nitrates can, of course, be decomposed into melt oxides upon heating to or above the phase transformation temperature.

Flame processes have been widely used to synthesize nanosize powders of oxide materials. Chemical precursors are vaporized and then oxidized in a combustion process using a fuel/oxidant mixture such as propane/oxygen or methane/air [190]. They combine the rapid thermal decomposition of a precursor/carrier gas stream in a reduced pressure environment with thermophoretically driven deposi-

tion of the rapidly condensed product particles on a cold substrate [63]. The flame usually provides a high temperature (1200–3000 K), which promotes rapid gas-phase chemical reactions [191]. Several types of flame reactors have been used in research settings and have produced numerous types of nano-scale metal oxides [63, 190–196].

Chromium oxides have been synthesized by Lima and coworkers using solution combustion [197]. The results suggest that glycine is a better complexing/combustible agent for ammonium dichromate than urea. The addition of extra ammonium nitrate to stoichiometric compositions improved the specific surface area and reduced the crystallite size. The smallest crystallite size (≈20 nm) of Cr_2O_3 was obtained with glycine as fuel/complexant agent in fuel-lean mixtures. The highest specific surface area ($63\,m^2g^{-1}$) was observed with urea in fuel-rich mixtures, forming amorphous CrO_3. Pratsinis and coworkers synthesized well structured nanocrystals of ceria–zirconia mixed oxides with high temperature stability and surface area. They sprayed cerium and zirconium precursors dissolved in carboxylic acid into a methane–oxygen flame [198]. The mixed products had surface areas from $60–90\,m^2g^{-1}$. ZrO_2 powder was prepared by the gel combustion technique using citric acid as a fuel and nitrate as an oxidant. Calcination at 600 °C of the dried powder, obtained after sluggish combustion of the citrate–nitrate gel, produced spherical nanocrystalline ZrO_2 with diameter about 10 nm [199]. Nanocrystalline $LiMn_2O_4$ with cubic spinel structure has been prepared by combustion of reaction mixtures containing Li(I) and Mn(II) nitrates that operate as oxidizers and sucrose that acts as fuel [200]. Annealing at 700 °C led to single-phase cubic spinels. In these phases, the smallest average particle size (ca. 30 nm) corresponded to the sample obtained with a hyperstoichiometric amount of fuel.

16.3.6 Others

There are numerous approaches to the synthesis of highly dispersed metal oxides in addition to those discussed. These include some methods that have been less commonly used to prepare metal oxides, such as vapor condensation methods, spray pyrolysis and templated techniques.

16.3.6.1 Vapor Condensation Methods

Among the earliest methods for producing nanoparticles were gas condensation techniques, which produce nanoparticles directly from a supersaturated vapor of metals. These methods generally involve two steps: first, a metallic nano-phase powder is condensed under inert convection gas after a supersaturated vapor of the metal is obtained inside a chamber. A high pressure of inert gas is usually needed to achieve supersaturation, then the powder is oxidized by allowing oxygen into the chamber. This post-oxidation is a critical step and it is very often necessary for the process to be performed slowly. Because of the highly exothermic reaction, particles heat up for short times (usually less than one second) to temperatures as high as 1000 °C, resulting in their agglomeration into large particles by rapid

diffusion processes. A subsequent annealing process at higher temperature is often required to complete the oxidation.

Gas condensation methods to prepare nanoparticles directly from supersaturated vapor have many advantages over other techniques including versatility, the ease of performance and analysis and the high purity of the products. These methods can also be employed to produce films and coatings. However, in spite of their success, there are drawbacks in the high production cost because of low yields and the difficulty in scaling-up. Heating techniques have other disadvantages, which include the possibility of reactions between the metal vapors and the heating source materials. Furthermore, the operating temperature is limited by the choice of the source material and, because of that, they cannot be used to make a wide variety of materials.

16.3.6.2 **Spray Pyrolysis**

Another useful method for the synthesis of high-purity homogeneous oxide powders is spray pyrolysis [201–206]. This technique has been known by several other names, including solution aerosol thermolysis [203], evaporative decomposition of solutions [204], plasma vaporization of solutions [205] and aerosol decomposition [206]. The starting materials in this process are chemical precursors, usually appropriate salts, in solution, sol or suspension form. The process involves the generation of aerosol droplets by nebulizing or atomizing the starting solution, sol or suspension. The generated droplets undergo evaporation and solute condensation within the droplet, drying, thermolysis of the precipitate particle at higher temperature to form microporous particles and, finally, sintering to form dense particles.

Aqueous solutions are usually used because of their low cost, safety and the availability of a wide range of water-soluble salts. Metal chloride and nitrate salts are commonly used as precursors because of their high solubility. Precursors that have low solubility or those that may induce impurities, such as acetates that lead to carbon in the products, are less suitable [202, 204]. During the transformation of the aerosol droplets into particles, different processes are involved, including solvent evaporation, precipitation of dissolved precursor and thermolysis of precipitated particles. One advantage to this process is that all of these processes take place in one step. Other advantages include the production of high-purity nanosize particles, the homogeneity of the particles as a result of the homogeneity of the original solution, the fact that each droplet/particle undergoes the same reaction conditions and that no subsequent milling is necessary. Disadvantages of spray pyrolysis include the large amounts of solvents necessary and the difficulty of scaling-up the production. The use of large amounts of non-aqueous solvents increases production expenses because of the high cost of pure solvents and the need for proper disposal.

16.3.6.3 **Templated/Surface Derivatized Nanoparticles**

In recent years, varieties of porous materials have been obtained by templated techniques. Generally two types of templates have been reported in the literature,

soft templates (surfactants [207]) and hard templates (porous solids such as carbon or silica). In the case of hard templates, the formation of porous material takes place in a confined space formed by the porosity of the template. Two types of hard templates have been employed in template synthesis, active carbon [208] and mesoporous silica materials [209–212]. Commercial active carbons were used as templates to prepare different types of HSMO [213] and monodisperse and porous spheres of oxides and phosphates [214]. However, the use of active carbons as templates has certain limitations since, at the high treatment temperature employed during the synthesis, infiltrated salts and the carbon may react with each other, destroying the intended material. Moreover, if the heat treatment is performed in air, the carbon may be rapidly oxidized (ignition) even at relatively low temperature owing to the catalytic effect of the infiltrated salts. On the other hand, some metallic salts may end up as metal instead of metal oxide as carbon is a good reducing agent at high temperature under inert atmosphere.

16.4 Applications in Catalysis

As discussed in a previous section, metal oxides represent an important class of materials exhibiting a broad range of properties from insulators to semiconductors and conductors and have found applications as diverse as electronics, cosmetics and catalysts. Metal oxides have been widely used in many valuable heterogeneous catalytic reactions. Typical metal oxide-catalyzed reactions, including alkane oxidation, biodiesel production, methanol adsorption and decomposition, destructive adsorption of chlorocarbons and warfare agents, olefin metathesis and the Claisen–Schmidt condensation will be briefly discussed as examples of metal oxide-catalyzed reactions.

16.4.1 Oxygenation of Alkanes

Oxidation remains one of the principal paradigms for the activation of alkanes, which are well known for their low reactivity, and is of interest both academically and commercially. Among hydrocarbons, the oxidation of *n*-alkanes has attracted much attention because they are abundant as feedstocks [215–218]. Catalytic oxidation of alkanes has been explored using several oxidants and, for economic and environmental reasons, oxidation processes used in bulk chemical industries predominantly involve the use of atmospheric oxygen as the primary oxidant. Their success depends largely on the use of metal catalysts to promote both the rate of reaction and the selectivity to partial oxidation products of organic substrates for successful commercial processes [219, 220]. There have been a number of publications concerning alkane oxidation with molecular oxygen under mild conditions, using transition metal oxide catalysts systems (summarized in Table 16.4) [221–232].

Table 16.4 Aerobic partial oxidation of alkanes by metal oxide catalysts.

Entry	Alkane	Catalyst	*T* (°C)	Oxidant/others	Conversion (%)	Selectivity (%)	Products	Ref.
1	ethane	Mo-V-Nb-O	400	O_2/He	22.7	47.8	ethene	[221]
2	propane	V_2O_5/SBA-15	400	O_2	8	84	acrylic acid	[222]
3	propane	Co3O4	100	O_2/Ar	0.8	100	propene	[223]
4	propane	V-P-O	400	air/H_2O	23.0	48.1	acrylic acid	[224]
5	propane	V-P-O/TiO_2-SiO_2	300	O_2/H_2O	21.8	61.2	acrylic acid	[225]
6	propane	V-P-O	300	O_2/H_2O	15	47.2	acrylic acid	[225]
7	propane	Mo-V-Sb-O	380	O_2	46	27	acrylic acid	[226]
8	propane	$MoV_{0.3}Te_{0.23}P_{0.15}O_n$	500	O_2	46.6	8.1	acrylic acid	[227]
9	*n*-butane	V_2O_5/MgO	500	O_2	9.9	66.6	butene	[228]
10	isobutane	Mo-V-O	300	O_2	34.9	54.7	ethanoic acid	[229]
11	*n*-pentane	Mo-V-O	300	O_2	41.4	70.8	maleic anhydride	[229]
12	cyclohexane	V-P-O	65	H_2O_2/acetonitrile	84	50/50	cyclohexanol/cyclohexanone	[230]
13	*n*-heptane	Co_3O_4	450	O_2/H_2	20.4	14.2	CO_2	[231]
14	*n*-hexane	Co_3O_4	450	O_2/H_2	66.5	46.2	CO_2	[231]
15	*n*-heptane	CeO_2	450	O_2/H_2	7.5	9.0	CO_2	[231]
16	*n*-hexane	CeO_2	450	O_2/H_2	24.4	29.2	CO_2	[231]
17	*n*-hexane	Ti-Si-O	50	H_2O_2	7.0 (TON)	56	alcohols	[232]
18	*n*-heptane	Ti-Si-O	50	H_2O_2	45 (TON)	80	alcohols	[232]

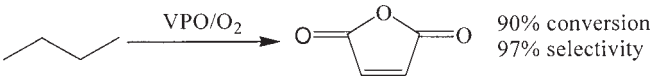

Scheme 16.1

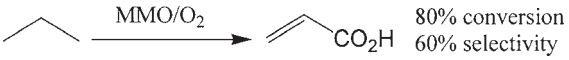

Scheme 16.2

The conversion of butane to maleic anhydride over a VPO catalyst remains the only selective alkane oxidation technology that has achieved commercial operation. The yields of maleic anhydride vary from 45 to 67%, with *n*-butane conversion at ~90% and selectivity to maleic anhydride ranging from 65% to as high as 97% (Scheme 16.1) [232, 245].

The success of VPO catalysts in *n*-butane oxidation has stimulated great interest in the selective oxidation of propane to acrylic acid [236, 237]. On the basis of the excellent performance of VPO for converting *n*-butane to maleic anhydride, it is reasonable to believe that they also have potential for converting propane to acrylic acid effectively. Many studies are focused on the supported vanadium-catalyzed partial oxidation of hydrocarbons and the supports can be SiO_2 [246, 247], TiO_2 [248, 249], Al_2O_3 [250] and CeO_2 [251]. Most supported vanadium catalysts and vanadium-based mixed-metal oxides MMO [252] were been studied for the oxidation of propane (Scheme 16.2). Although the history of the MMOs in propane to acrylic acid oxidation is relatively short, they have shown excellent conversion (80%) and selectivity (60%).

16.4.2 Biodiesel Production

The increasing concern over greenhouse gas emissions and the search for alternative renewable fuels has led to increased interest in fuels developed from renewable feedstocks. One such alternative fuel is biodiesel, which is recognized as a "green fuel" produced from vegetable oils (VO) and other feedstocks that primarily contain triglycerides (TG) and free fatty acids (FFA) [253]. Biodiesel as a non-petroleum-based fuel is normally synthesized through a chemical process called transesterification, whereby TGs react with a low molecular weight alcohol in the presence of a catalyst to produce a complex mixture of fatty acid alkyl esters (biodiesel) and glycerol. Transesterification of TGs with low molecular weight alcohols proceeds via three successive and reversible reactions. Figure 16.13 shows the consecutive chemical reactions involved in the transesterification of triacetin with methanol. There are different processes that can be applied to the synthesis of biodiesel: (1) base-catalyzed transesterification [254], (2) acid-catalyzed transesterification [255], (3) integrated acid-catalyzed pre-esterification of FFAs and base-catalyzed transesterification [256], (4) enzyme-catalyzed transesterification

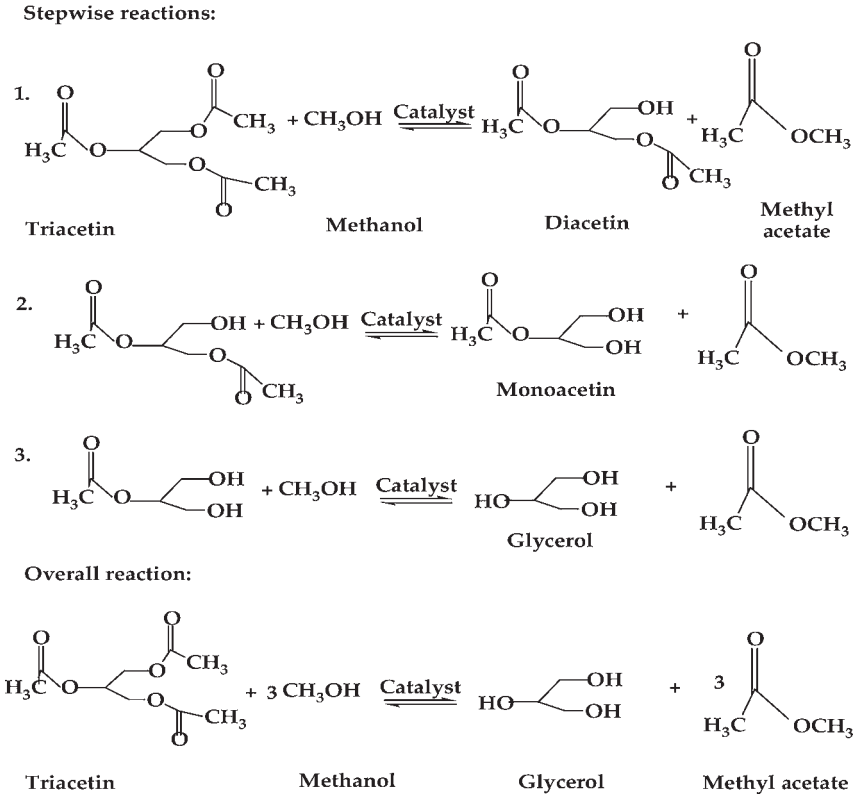

Figure 16.13 The transesterification reactions of triacetin and methanol.

[257], (5) hydrolysis and acid-catalyzed esterification, (6) pyrolysis [258] and (7) supercritical alcohol transesterification [259].

Industrially, homogeneous base catalysts (such as NaOH, KOH and $NaOCH_3$) are used. Base catalysis is preferred to the use of acid catalysts such as sulfuric or sulfonic acids, given the corrosivity and lower activity of the latter. However, the application of an alkaline catalyst in the transesterification of waste cooking oil is somewhat limited, because the FFA in waste cooking oil reacts with the alkaline catalyst (KOH, NaOH) and forms soap. The soap formed during the reaction prevents the glycerol separation, which drastically reduces the ester yield. The water in waste cooking oil also affects the methyl ester yield by favoring a saponification reaction. Further, removal of the base catalyst after reaction is problematic.

In order to circumvent these problems, the use of heterogeneous catalysts has been explored. This approach eliminates the need for an aqueous quench and largely eliminates the formation of metal salts, thereby simplifying downstream separation steps; consequently, biodiesel production can be more readily performed as a continuous process. Based on their ready availability, solid acid

catalysts such as zeolites, clays and ion exchange resins are attractive for this purpose. Supported tungsten oxide catalysts have also received much attention because of their acid properties and their ability to catalyze both esterification and transesterification reactions, which play major roles in biodiesel production. Furuta and coworkers [260] reported that soybean oil can be efficiently converted to methyl esters at a reaction temperature of 250 °C using tungstated zirconia alumina (WZA) calcined at 800 °C. However, reaction rates are generally found to be unacceptably low. Consequently, solid base catalysts have attracted attention. Catalysts of this type include simple metal oxides such as MgO and CaO in supported or unsupported form, Zn–Al mixed oxides, cesium-exchanged zeolite X, anion exchange resins, polymer-supported guanidines, $Na/NaOH/Al_2O_3$ and K- and Li-promoted oxides, prepared by impregnating the corresponding nitrate or halide salt onto an oxidic carrier such as Al_2O_3, ZnO or CaO. Nano-crystalline calcium oxide is an efficient catalyst for the production of environmentally compatible biodiesel fuel in high yields at room temperature using soybean oil (SBO) and poultry fat as raw materials. An SBO : MeOH ratio of 1 : 27 is suitable for obtaining high product yields: the conversion can reach 99%. Under the same conditions, laboratory-grade CaO gave only 2% conversion in the case of SBO and there was no observable reaction with poultry fat [261].

16.4.3
Methanol Adsorption and Decomposition

One possible way to extend the application of metal oxides as catalysts is to tailor their surface chemistry, as the catalytic process occurs only on solid surfaces and surface structure typically controls activity and selectivity kinetically. Therefore, it is desirable to obtain a high surface area of inexpensive metal oxides with a preferentially grown outer surface to provide catalytically active sites, which requires a combination of both surface science and catalysis. One case in point is the typical rock salt structure of MgO. The traditional method of preparing MgO is the thermal decomposition of either magnesium salts or magnesium hydroxides, which results in inhomogeneity of morphology and crystallite size, with low surface area. Many attempts were therefore made to tailor the texture and morphology of MgO [262–267]. Most catalytic reactions reported to date are related to the well known and conventional (100) surface [233, 268]; however, the (111) surface is more interesting as it is composed of alternating monolayers of anions and cations so that a strong electrostatic field perpendicular to the (111) surface is created [234]. Such a surface has provided a prototype for the study of surface structure and surface reactions, and has received great attention for theoretical and experimental studies [235, 236]. Figure 16.14 shows the relation between the exposed face and the coordination of MgO [237].

Identification of the active sites of the MgO surface is of crucial importance for the understanding of the reaction mechanisms and the properties of MgO(111) nanosheets. Methanol is a “smart” molecular probe that can provide fundamental information about the number and nature of active surface sites [238]. Methanol

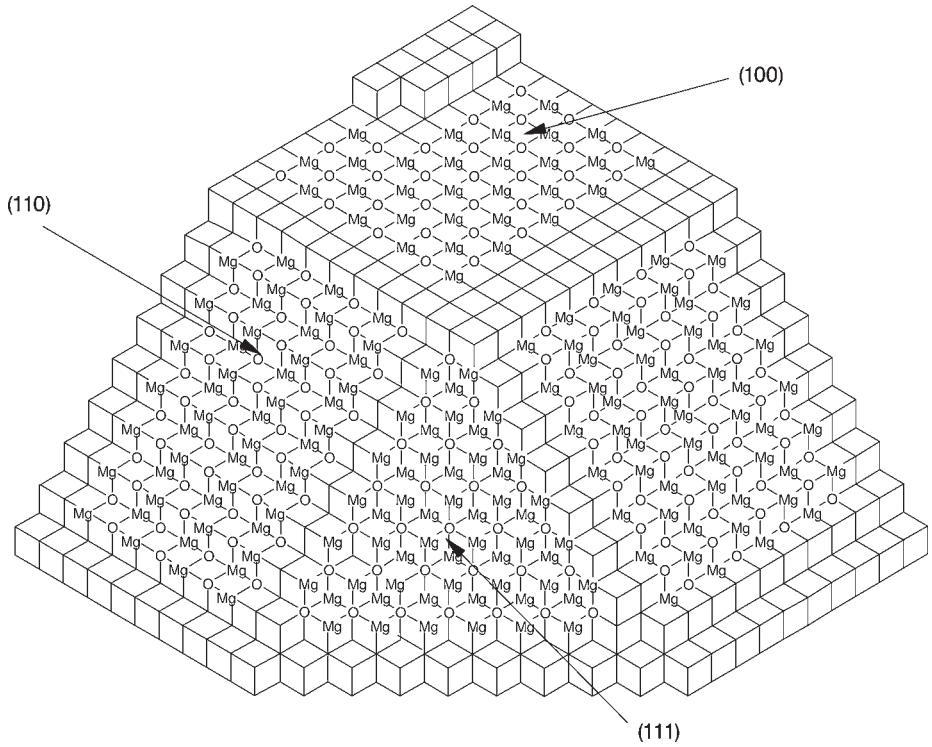

Figure 16.14 The disposal of MgO on (001), (110) and (111) facets (from [240]).

decomposition has been found to be structure-sensitive, in that the selectivity depends on the arrangement of the surface atoms. To satisfy ever-increasing energy needs, all feasible alternative energy sources to our available oil and gas resources must be considered. Methanol is an excellent fuel in its own right and it can also be blended with gasoline, although it has half the volumetric energy density relative to gasoline or diesel [239]. It is also used in the direct methanol fuel cell (DMFC). The performance of liquid-feed methanol fuel cells is already attractive for some applications and is approaching the levels required for electric vehicle propulsion [240]. In this electrochemical cell, methanol is directly oxidized with air to carbon dioxide and water to produce electricity, without the need to first generate hydrogen [241–244]. This greatly simplifies the fuel-cell technology and makes it accessible to a wide range of applications. For low-temperature fuel cells, restricted by the extreme sensitivity of fuel-cell catalysts to CO poisoning, it is very important to control the selectivity in this process [269]. Low-temperature fuel cells require an external processor to produce H_2 and remove CO, which not only reduces the efficiency of the system but also increases its complexity and cost [270]. The conventional Cu/ZnO-based methanol synthesis catalysts performed

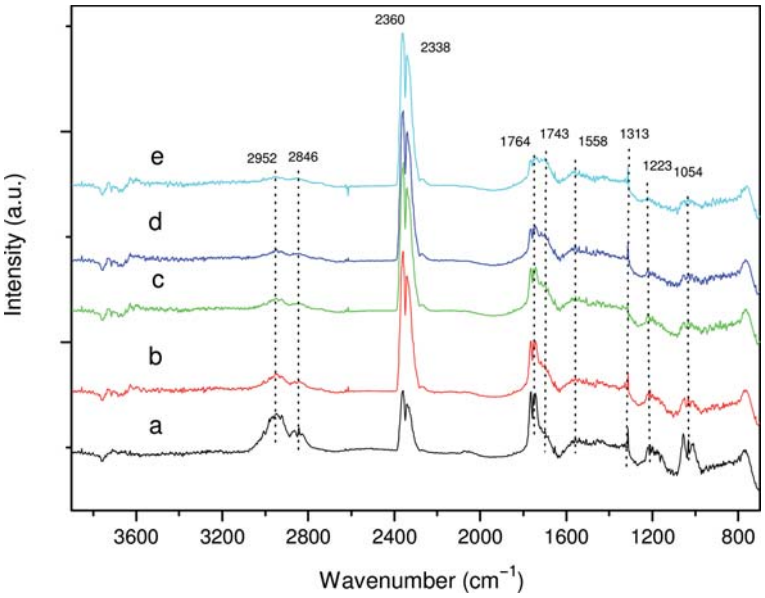

Figure 16.15 DRIFT spectra of methanol adsorption and reaction on MgO(111) nanosheets at 70 °C after different times: (a) 3 minutes, (b) 10 minutes, (c) 15 minutes, (d) 20 minutes, (e) 25 minutes (from [273]).

poorly for methanol decomposition and the catalysts suffered from rapid deactivation [271]. The activity and stability of the catalyst systems have been two major challenges in the decomposition of methanol. MgO(111) nanosheets can decompose methanol at low temperature and oxidize the surface C=O species formed during methanol decomposition. The preparation of MgO(111) nanosheets is simple and can be readily scaled-up. The large-scale application of MgO(111) nanosheet catalysts without the necessity for transition metals for low-temperature methanol decomposition may therefore be feasible.

The decomposition of methanol over MgO(111) nanosheets has been studied via *in situ* IR spectroscopy, and both undissociated and dissociated methanol were observed when MgO(111) nanosheets were exposed to methanol at 70 °C (Figure 16.15) [273]. A large amount of CO_2 formed upon exposure to methanol at 70 °C (peaks at 2360 and 2341 cm^{-1}) and increased with time. The bands centered at 1558, 1313 and 1223 cm^{-1} can be attributed to chemisorbed CO_2. A weak pair of peaks at 1764 and 1743 cm^{-1} can be attributed to the C=O asymmetric stretching of CO and formic acid [274, 275], free CO stretching (2036, 2014 cm^{-1}) peaks were also visible at 3 min. The intensity of the pair of peaks at 1764 and 1743 cm^{-1} decreased and the peaks at 2036 and 2014 cm^{-1} disappeared with time. This may indicate that the C=O species formed were oxidized by the oxygen anions on the surface of MgO(111) nanosheets. From the DRIFTS results we can see that methanol was oxidized and decomposed to near completion on the surface of MgO(111)

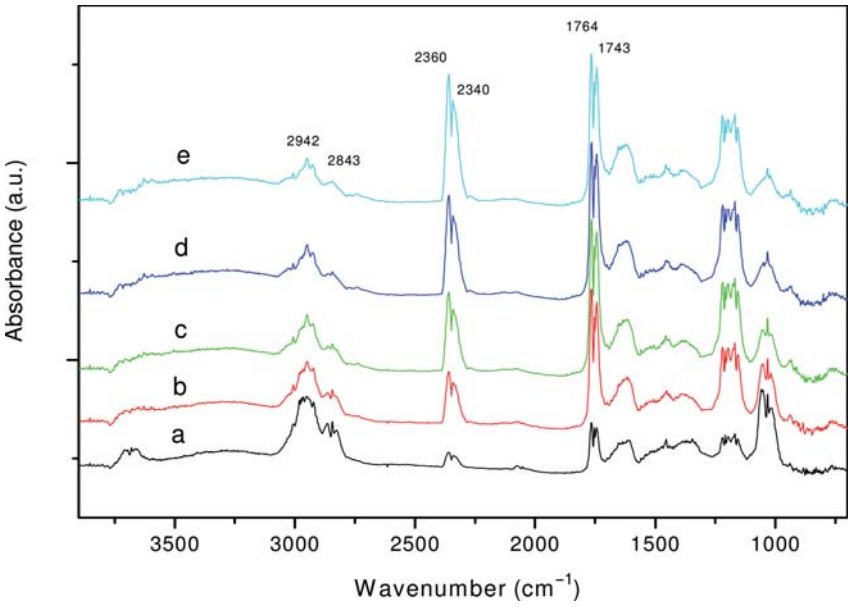

Figure 16.16 DRIFT spectra of methanol adsorption and reaction on CM-MgO at 70 °C after different times: (a) 3 minutes, (b) 10 minutes, (c) 15 minutes, (d) 20 minutes and (e) 25 minutes (from [273]).

nanosheets by 25 min, indicating that MgO(111) nanosheets are highly active for methanol decomposition. In comparison with the spectra at room temperature, the region of O—H stretching has no distinct change; indicating that methanol interacts primarily with surface oxygen anions and oxygen defects but not hydroxyl groups at 70 °C. This suggests that the main active sites for methanol decomposition are oxygen defects and oxygen anions. First, methanol interacts with oxygen defect sites to form methoxides, then the formed methoxides are oxidized by surface oxygen anions. In order to better understand the surface structure of MgO(111) nanosheets, methanol decomposition behavior and the relationship between them, methanol adsorption on the surface of Commerial MgO (CM–MgO) at 70 °C under high vacuum was studied for comparison. The spectra are shown in Figure 16.16. The bands of CO_2 at 2360 and 2341 cm^{-1} increase and the bands of C—H stretching between 2800 and 3100 cm^{-1} decrease in intensity with time, indicating that methanol decomposition continues over time. Compared to the spectra in Figure 16.15e, the intensity of the bands between 2800 and 3100 cm^{-1} in Figure 16.16e are much stronger. This suggests that the methanol conversion is significantly lower and the activity of CM-MgO is lower than that of MgO(111) nanosheets. Comparison of the peaks at 1764 and 1743 cm^{-1} in Figures 16.15 and 16.16, which have been attributed to surface C=O species, shows that the pair of peaks in Figure 16.15 are weak and decrease in intensity with time, indicating that the rate of formation of the surface C=O species is lower than the rate of further

oxidation; but in Figure 16.16 the pair of peaks are strong and increase in intensity with time, indicating that the rate of formation is higher than the further oxidation rate. This shows that the surface C=O species formed can be oxidized quickly by the high concentration of oxygen anions on the surface of MgO(111) nanosheets.

16.4.4 Destructive Adsorption of Chlorocarbons

The carcinogenic and toxic properties of chlorocarbons have encouraged scientists to find efficient ways to destroy them. The desired reaction is the complete oxidation of chlorocarbons to water, CO_2 and HCl, without the formation of any toxic by-products. High surface area and high surface reactivity are desired properties of such destructive adsorbents and nanoparticles fall into this category. Nanoparticles will react to a greater extent than normal metal oxides because there are more molecules of metal oxide available for reaction with chemicals adsorbed on the surface of the particles. Also, nanocrystals exhibit intrinsically higher chemical reactivities owing to the presence of a large number of defect sites such as edges/corners and high concentrations of coordinatively unsaturated ions. The mechanism to describe the oxidation of chlorocarbons has been developed and involves chemisorption followed by surface-to-adsorbate oxygen transfer and adsorbate-to-surface chlorine transfer, that is a chloride–oxide exchange [272].

CaO and MgO destroy chlorocarbons such as CCl_4, $CHCl_3$ and C_2Cl_4 at temperatures around 400 to 500 °C in the absence of an oxidant, stochiometrically yielding mainly CO_2 and the corresponding metal chlorides [276–278]. Nanoparticles of MgO and CaO react with CCl_4 to yield $MgCl_2$, $CaCl_2$, and CO_2. The reaction with $CHCl_3$ yields $CaCl_2$, CO and H_2O, while C_2Cl_4 yields $CaCl_2$, carbon and $CaCO_3$. All of these reactions are thermodynamically favorable; however, kinetic parameters demand that high-surface-area metal oxides are used. The mobility of oxygen and chlorine atoms in the bulk of the material becomes important and kinetic parameters involving the migration of these atoms are rate-limiting. The reaction efficiencies can be improved by the presence of small amounts of transition metal oxide as catalyst; for example, Fe_2O_3 on CaO. Morphological studies indicate that iron chloride intermediates help shuttle chloride and oxide anions in and out of the base metal oxide (CaO or MgO). Nano-crystalline MgO and CaO also allow the destruction of chlorinated benzenes (mono-, di- and trichlorobenzenes) at lower temperatures (700 to 900 °C) than incineration [279]. The presence of hydrogen as a carrier gas allows still lower temperatures to be used (e.g. 500 °C). MgO was found to be more reactive than CaO, as the latter induces the formation of more carbon.

In 1993, some environmental groups proposed the need for a chlorine-free economy. The cost of complete elimination of chlorinated compounds is quite staggering, with the latest estimate as high as $160 billion/year [280]. The most common method of destroying chlorocarbons is by high-temperature thermal oxidation (incineration). The toxic chlorinated compounds seem to be completely destroyed at high temperatures; however, there is concern about the formation of

toxic by-products such as dioxins and furans. The catalytic oxidation of chlorinated compounds over metal oxides yields mainly HCl and CO_2. Catalysts such as V_2O_3 and Cr_2O_3 have been used with some success [281, 282]. Nano-scale MgO and CaO prepared by a modified aerogel/hypercritical drying procedure (AP-MgO and AP-CaO) were found to be superior to conventionally prepared (CP) CP-CaO, CP-MgO and commercial CaO/MgO catalysts for the dehydrochlorination of several toxic chlorinated substances [283, 284]. The interaction of 1-chlorobutane with nano-crystalline MgO at 200 to 350 °C results in both stoichiometric and catalytic dehydrochlorination of 1-chlorobutane to isomers of butene and simultaneous topochemical conversion of MgO to $MgCl_2$ [285, 286]. The particle sizes in these nano-scale materials are of the order of nanometers (~4 nm). These oxides are efficient owing to the presence of a high concentration of low-coordinated sites, structural defects on their surfaces and high specific surface area.

16.4.5
Alkene Metathesis

Maximizing the value of the steam cracker- or refinery-based C_4 stream is a major objective for most petrochemical companies. One approach towards this objective, olefin metathesis, has become an important reaction for producing a wide variety of more valuable products from available olefin substrates [287]. Figure 16.17 shows the possible reaction pathways of 1-butene. Tungsten oxide supported on silica is a well known metathesis catalyst [288, 289]. The activity of 1-butene metathesis over WO_3/SiO_2 was dependent on the states of tungsten oxide species on the surface of the catalyst, and the tetrahedrally coordinated tungsten oxide species on the surface of silica were suggested to be the active sites of metathesis [290]. Owing to the weak interaction of silica and tungsten oxide, WO_3/SiO_2 catalysts prepared by the traditional impregnation method have low amounts of surface tetrahedrally coordinated tungsten oxide species.

SBA-15 is a mesoporous silica molecular sieve with high surface area, tunable uniform hexagonal channels ranging from 5 to 30 nm and thick framework walls (3–6 nm), which is therefore thermally and hydrothermally robust [291, 292]. The active sites in the molecular sieves are often from heteroatoms such as Al and Ti species and it is therefore greatly significant to introduce heteroatoms into the

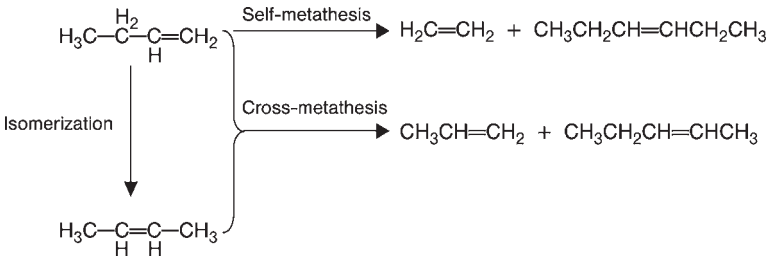

Figure 16.17 Possible reaction pathways of 1-butene (from [294]).

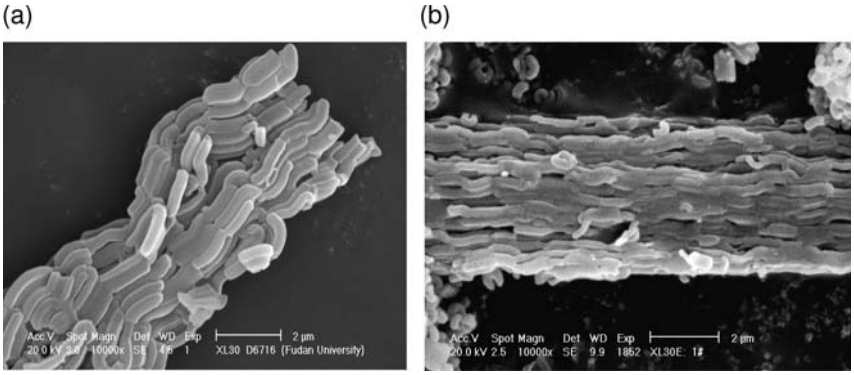

Figure 16.18 SEM images of (a) SBA-15 and (b) MWS (Si/W = 30) (from [294]).

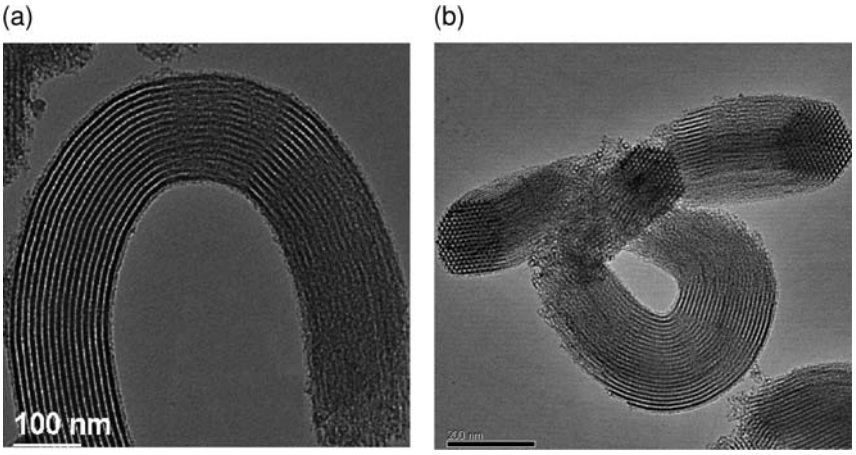

Figure 16.19 TEM images of (a) SBA-15 and (b) MWS (Si/W = 30) (from [294]).

framework of SBA-15 [293]. A one-step co-condensation sol–gel method improves dispersion of the tungsten species, alleviates aggregation of WO_3 and strengthens interactions between tungsten species and silica [294]. Figure 16.18 shows scanning electron microscopy (SEM) images of (a) SBA-15 and (b) MWS (Si/W = 30). The SEM image (Figure 16.18a) reveals that the SBA-15 sample consists of well defined wheat-like macrostructures aggregated together with rope-like domains with relatively uniform sizes of 1 µm. After tungsten oxide incorporation, a significant degradation in macroscopic structure can be observed; however, the rope-like domains with average sizes of 1 µm were still largely maintained (Figure 16.18b). Transmission electron microscopy (TEM) images (Figure 16.19) show the well ordered hexagonal arrays of one-dimensional mesoporous channels and confirm that the MWS samples have a two-dimensional P_{6mm} hexagonal structure, as does SBA-15, and unambiguously confirm that the hexagonal pore structure of

the SBA-15 is robust enough to survive the tungsten-incorporation process and thus offers a good matrix to support highly dispersed tungsten oxide. The distance between two consecutive centers of the hexagonal pores estimated from the TEM image is ca. 10 nm. The average thickness of the wall is ca. 3 nm, which is much larger than for MCM-41 and the pore diameter is around 7 nm, in agreement with N_2 adsorption measurements. TEM analysis also reveals that no obvious extra-framework phases of the WO_3 species are present outside the mesoporous structure. The resulting tungsten-substituted mesoporous SBA-15 materials exhibit the best catalytic performance at present for the metathesis of 1-butene using tungsten-based catalysts.

16.4.6 Claisen–Schmidt Condensation

MgO nanoparticles have proven to be very effective chemical reagents in the Claisen–Schmidt condensation, which is a very valuable C–C bond-formation reaction commonly employed in the pharmaceutical and fine chemical industries [295]. When MgO(111) nanosheets were employed for the Claisen–Schmidt condensation of benzaldehyde and acetophenone, they were found to exhibit activity superior to other systems, such as $AlCl_3$, BF_3, $POCl_3$, alumina and other reported nano-crystalline MgO samples [296]. This development is particularly noteworthy as it represents a potential heterogenization of the Claisen–Schmidt catalytic process, which offers numerous advantages including easier product recovery and catalyst recycling.

It has been established that for the base-catalyzed Claisen–Schmidt condensation reaction, shape and exposed crystal facets are crucial parameters for the utilization of magnesium oxide as a solid base catalyst. Polar anionic surfaces are of particular interest for the reaction, and we have therefore evaluated the catalytic activity of MgO(111) nanosheets. The catalytic activities for the Claisen–Schmidt condensation of benzaldehyde with acetophenone at 110 °C over different crystallites of magnesium oxide samples are shown in Figure 16.20. CM-MgO samples are generally large cubic crystals, the NA-MgO samples are thin hexagonal platelets about 150 nm in diameter and 10 nm thick having large exposed areas of the (100) crystal face while the NAP-MgO samples are very small, irregular stacks of square plates exhibiting numerous crystal faces, edges and corners. As shown in Figure 16.20, NAP-MgO displays higher activity than that of NA-MgO and CM-MgO, which has been attributed to the NAP-MgO possessing a single-crystallite polyhedral structure, which has high surface concentrations of edges/corners and various exposed crystal planes (such as (001) and (111)), hence leading to an inherently high surface reactivity per unit area. It is notable that the MgO(111) nanosheets display a much higher catalytic activity for the Claisen–Schmidt condensation than the best of the reported NAP-MgO catalysts. Previous studies indicate that the Claisen–Schmidt condensation is largely driven by Lewis basic O^{2-} sites while the Brønsted basic –OH surface groups are less important in the reaction. The pronounced activity for the Claisen–Schmidt condensation taken together

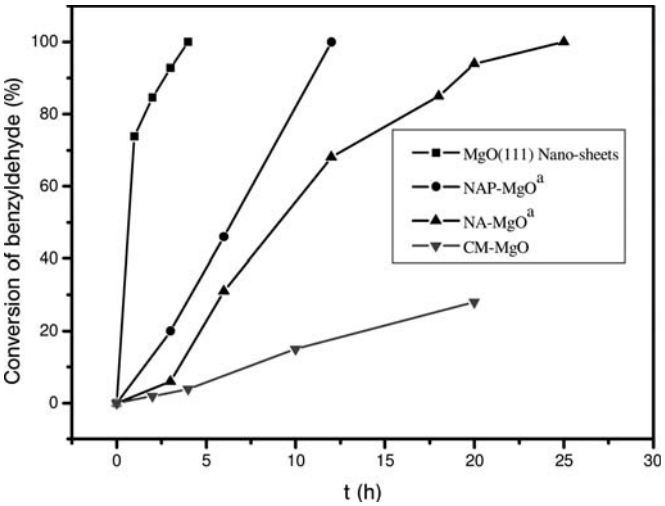

Figure 16.20 Claisen–Schmidt condensation of benzaldehyde with acetophenone using different crystallites of magnesium oxide at 110 °C. (NAP-MgO: aerogel prepared MgO, SA = 590 $m^2 g^{-1}$; NA-MgO: conventionally prepared MgO, SA = 250 $m^2 g^{-1}$; CM-MgO: commercial MgO, SA = 30 $m^2 g^{-1}$.) (from [69]).

with CO_2 temperature programmed desorption studies demonstrates clearly that the MgO(111) nanosheets are Lewis basic and the MgO(111) face which has O^{2-} anions on one surface is particularly important for the reaction. The high concentration of oxygen anions on the surface of MgO(111) thus provides a possible explanation for the excellent catalytic activity observed for the Claisen–Schmidt condensation.

16.5 Conclusions

Nano-scale metal oxides represent an important class of material, owing to their chemical and physical properties as well as their potential widespread applications. While a great deal of knowledge about these materials has developed during recent years, an atomic/molecular level understanding of the materials, their chemistry and their preparation will greatly impact their future. Ultimately, breakthroughs in the areas of synthesis, instrumentation and modeling will aid scientists in their quest to understand relationships between physical, electronic and chemical properties.

Metal oxides display a wide range of properties, from metallic to semiconductor to insulator. Owing to the compositional variability and their more localized electronic structures compared to metals, the presence of defects (such as corners,

kinks, steps and coordinatively unsaturated sites) play a very important role in oxide surface chemistry and hence in catalysis. As described, the catalytic reactions also depend on the surface crystallographic structure and the example of MgO(111) has been highlighted. The catalytic properties of the oxide surfaces can often be explained in terms of Lewis acidity and basicity. The electronegative oxygen atoms accumulate electrons and act as Lewis bases while the metal cations act as Lewis acids.

As is hopefully obvious from this chapter and the entire book, the science of metal oxides is vast and requires synergistic contributions from multiple disciplines if the potential of nano-scale metal oxides is to be reached. As the general field of nano-scale materials develops, metal oxides are likely to be at the forefront owing to their stability and the intensive studies that have already been reported for their bulk counterparts.

References

1 Rao, C.N.R. and Gopalakrishnan, J. (1986) *New Directions in Solid State Chemistry*, Cambridge University Press, Cambridge, UK.

2 Klabunde, K.J., Stark, J.V., Koper, O., Mohs, C., Park, D.G., Decker, S., Jiang, Y., Lagadic, I. and Zhang, D. (1996) *Journal of Physical Chemistry*, **100**, 12142–53.

3 Klabunde, K.J. and Mohs, C. (1998) Nanoparticles and nanostructural materials, in *Chemistry of Advanced Materials: An Overview* (eds L.V. Interrante and M.J. Hampden-Smith), Wiley-VCH Verlag GmbH, New York, p. 317.

4 Dyrek, K. and Che, M. (1997) *Chemical Reviews*, **97**, 305–31.

5 Rao, C.N.R. and Raveau, B. (eds) (1998) *Transition Metal Oxides, Structure, Properties and Synthesis of Ceramic Oxides*, 2nd edn, Wiley-VCH Verlag GmbH, New York.

6 Shriver, D.F., Atkins, P.W. and Langford, C.H. (1990) *Inorganic Chemistry*, W.H. Freeman and Co., New York.

7 Zhang, X.G. and Armentrout, P.B. (2003) *Journal of Physical Chemistry A*, **107**, 8915–22.

8 Li, Y.X. and Klabunde, K.J. (1992) *Chemistry of Materials*, **4**, 611–15.

9 Klabunde, K.J., Stark, J.V., Koper, O., Mohs, C., Khaleel, A., Glavee, G.N., Zhang, D., Sorensen, C.M. and Hadjipanayis, G.C. (1994) *Nanophase Materials, Synthesis, Properties and Applications* (eds G.C. Hadjipanayis and R.W. Siegel), Kluwer Academic Publishers, Dordrecht, The Netherlands, p. 73.

10 Liu, H., Feng, L., Zhang, X. and Xue, O. (1995) *Journal of Physical Chemistry*, **99**, 332–4.

11 Radha, A.V., Thomas, G.S., Kamath, P.V. and Shivakumara, C. (2007) *Journal of Physical Chemistry*, **111**, 3384–90.

12 Utiyama, M., Hattori, H. and Tanabe, K. (1978) *Journal of Catalysis*, **53**, 237–42.

13 Morris, R.M. and Klabunde, K.J. (1983) *Inorganic Chemistry*, **22**, 682–7.

14 Driscoll, D.J., Martin, W., Wang, J.X. and Lunsford, J.H. (1985) *Journal of the American Chemical Society*, **107**, 58–63.

15 Hoq, M.F. and Klabunde, K.J. (1986) *Journal of the American Chemical Society*, **108**, 2114–16.

16 Zhang, Z., Bondarchuk, O., White, J.M., Kay, B.D. and Dohnalek, Z. (2006) *Journal of the American Chemical Society*, **128**, 4198–9.

17 Sanchez de Armas, R., Oviedo, J., San Mihuel, M.A. and Sanz, J.F. (2007) *Journal of Physical Chemistry C*, **111**, 10023–8.

18 Wyrwas, R.B. and Jarrold, C.C. (2006) *Journal of the American Chemical Society*, **128**, 13688–9.

19 Philipp, R., Omata, K., Aoki, A. and Fujimoto, K. (1992) *Journal of Catalysis*, **134**, 422–33.

20 Ito, T., Wang, J.X., Liu, C.H. and Lunsford, J.H. (1985) *Journal of the American Chemical Society*, **107**, 5062–8.

21 Baily, M.L., Chizallet, C., Costentin, G., Krafft, J.M., Lauron-Pernot, H. and Che, M. (2005) *Journal of Catalysis*, **235**, 413–22.

22 Stakheev, A.Yu., Shapiro, E.S. and Apijok, J. (1993) *Journal of Physical Chemistry*, **97**, 5668–72.

23 Vishwanathan, B., Tanka, B. and Toyoshima, L. (1986) *Langmuir*, **2**, 113–16.

24 Chizallet, C., Bailly, M.L., Costentin, G., Lauron-Pernot, H., Krafft, J.M., Bazin, P., Saussey, J. and Che, M. (2006) *Catalysis Today*, **116**, 196–205.

25 Sun, N. and Klabunde, K.J. (1999) *Journal of the American Chemical Society*, **121**, 5587–8.

26 Stankic, S., Sterrer, M., Hofmann, P., Diwald, O. and Knoziger, E. (2005) *Nano Letterss*, **5**, 1889–93.

27 Napoli, F., Chiesa, M., Giamello, E., Finazzi, E., Di Valentin, C. and Pacchioni, G. (2007) *Journal of the American Chemical Society*, **129**, 10575–81.

28 Richards, R., Li, W., Decker, S., Davidson, C., Koper, O., Zaikovski, V., Volodin, A., Rieker, T. and Klabunde, K.J. (2000) *Journal of the American Chemical Society*, **122** (20), 4921–5.

29 Mars, P. and van Kravelen, D.W. (1954) *Chemical Engineering Science*, **3**, 41–59.

30 Itoh, H., Utamapanya, S., Stark, J.V., Klabunde, K.J. and Schlup, J.R. (1993) *Chemistry of Materials*, **5** (1), 71–7.

31 Palkar, V.R. (1999) *Nanostructured Materials*, **11** (3), 369–74.

32 Klabunde, K.J. and Mohs, C. (1998) *Chemistry of Advanced Materials: An Overview* (eds L.V. Interrante and M.J. Hampden-Smith), Wiley-VCH Verlag GmbH, New York, p. 317.

33 Feldmann, C., Matschulo, S. and Ahlert, S. (2007) *Journal of Materials Science*, **42**, 7076–80.

34 Gesser, H.D. and Goswami, P.C. (1989) *Chemical Reviews*, **89** (4), 765–88.

35 Agarwala, M.K., Bourell, D.L. and Persad, C. (1992) *Journal of the American Ceramic Society*, **75**, 1975–7.

36 Chatry, M., Henry, M. and Livage, J. (1994) *Materials Research Bulletin*, **29**, 517–22.

37 Kumazawa, H., Inoue, T. and Sada, E. (1994) *Chemical Engineering Journal*, **55**, 93–6.

38 Laberty-Robert, C., Long, J.W., Lucas, E.M., Pettigrew, K.A., Strous, R.M., Doescher, M.S. and Rolison, D.R. (2006) *Chemistry of Materials*, **18**, 50–8.

39 Hench, L.L. and West, J.K. (1990) *Chemical Reviews*, **90** (1), 33–72.

40 Malenfant, P.R.L., Wan, J.L., Taylor, S.T. and Manoharan, M. (2007) *Nature Nanotechnology*, **2**, 43–6.

41 Polarz, S., Roy, A., Lehmann, M., Driess, M., Kruis, F.E., Hoffmann, A. and Zimmer, P. (2007) *Advanced Functional Materials*, **17**, 1385–91.

42 Chandler, C.D., Roger, C. and Hampden-Smith, M.J. (1993) *Chemical Reviews*, **93** (3), 1205–41.

43 Brinker, C.J. and Scherer, G.W. (1990) *Sol–Gel Science*, Academic Press, San Diego, CA.

44 Segal, D. (1989) *Chemical Synthesis of Advanced Ceramic Materials* (eds A.R. West and E.H. Baxter), Cambridge University Press, Cambridge, UK, p. 58.

45 Hench, L.L. and Nogues, J.L. (1993) *Sol–Gel Optics: Processing and Applications* (ed. L.C. Klein), Kluwer Academic Publishers, Boston, MA, p. 39.

46 Narula, C.K. (1995) *Ceramic Precursor Technology and Its Applications*, Marcel Dekker, New York.

47 Siegel, R.W., Ramasamy, S., Hahn, H., Li, Z.Q., Lu, T. and Gronsky, R. (1988) *Journal of Materials Research*, **3** (6), 1367–72.

48 El-Shall, M.S., Slack, W., Vann, W., Kane, D. and Hanley, D. (1994) *Journal of Physical Chemistry*, **98** (12), 3067–70.

49 Epifani, M., Diaz, R., Arbiol, J., Comini, E., Sergent, N., Pagnier, T., Siciliano, P., Taglia, G. and Morante, J.R. (2006)

Advanced Functional Materials, **16**, 1488–98.
50 Skarman, B., Nakayama, T., Grandjean, D., Benfiels, R.E., Niihara, K. and Wallenberg, L.R. (2002) *Chemistry of Materials*, **14**, 3686–99.
51 Hadjipanayis, G.C. and Siegel, R.W. (eds) (1994) *Nanophase Materials: Synthesis, Properties and Application*, Kluwer Academic Publishers, Dordrecht, The Netherlands.
52 Xu, C.H., Shi, S.Q., Surya, C. and Woo, C.H. (2007) *Journal of Materials Science*, **42**, 9855–8.
53 Cow, G.M. and Gonsalves, K.E. (eds) (1996) *Nanotechnology, Molecularly Designed Materials*, American Chemical Society, Washington, DC.
54 Majumdar, D., Kodas, T.T. and Glicksman, H.D. (1996) *Advanced Materials*, **8** (12), 1020–2.
55 Janackovic, D., Jokanovic, V., Kostic-Gvozdenovic, L. and Uskokovic, D. (1998) *Nanostructured Materials*, **10** (3), 341–8.
56 Jossen, R., Pratsinis, S.E., Stark, W.J. and Masler, L. (2005) *Journal of the American Chemical Society*, **88**, 1388–93.
57 Parguay-Delgado, F., Antunez-Flores, W., Miki-Yoshida, M., Aguilar-Elguezaba, A., Santiago, P., Siaz, R. and Ascencio, J.A. (2005) *NanoTechnology*, **16**, 688–94.
58 Witanachchi, S., Dedigamuwa, G. and Mukherjee, P. (2007) *Journal of Materials Research*, **22**, 649–54.
59 Jayanthi, G.V., Zhang, S.C. and Messing, G.L. (1993) *Aerosol Science and Technology*, **19** (4), 478–90.
60 Kavitha, R., Meghani, S. and Jayaram, V. (2007) *Materials Science and Engineering B*, **2007** (139), 134–40.
61 Ulrich, G.D. and Riehl, J.W. (1982) *Journal of Colloid and Interface Science*, **87** (1), 257–65.
62 Lindackers, D., Janzen, C., Rellinghaus, B., Wassermann, E.F. and Roth, P. (1998) *Nanostructured Materials*, **10** (8), 1247–70.
63 Skandan, G., Chen, Y.-J., Glumac, N. and Kear, B.H. (1999) *Nanostructured Materials*, **11** (2), 149–58.
64 Klabunde, K.J., Stark, J.V., Koper, O., Mohs, C., Park, D.G., Decker, S., Jiang, Y., Lagadic, I. and Zhang, D.J. (1996) *Journal of Physical Chemistry*, **100** (30), 12142–53.
65 Klabunde, K.J. (ed.) (2001) *Nanoscale Materials in Chemistry*, Wiley Interscience, New York, pp. 85–114.
66 Diao, Y.L., Walawender, W.P., Sorensen, C.M., Klabunde, K.J. and Ricker, T. (2002) *Chemistry of Materials*, **14** (1), 362–8.
67 Matson, D.W. and Smith, R.D. (1989) *Journal of the American Ceramic Society*, **72** (6), 871–81.
68 Schwarz, J.A., Contescu, C. and Putyera, K. (eds) (2004) *Encyclopedia of Nanoscience and Nanotechnology*, Marcel Dekker, New York, pp. 1905–9.
69 Zhu, K.K., Hu, J.C., Kübel, C. and Richards, R. (2006) *Angewandte Chemie–International Edition*, **45** (43), 7277–81.
70 Utamapanya, S., Klabunde, K.J. and Schlup, J.R. (1991) *Chemistry of Materials*, **3** (1), 175–81.
71 Klabunde, K.J., Stark, J.V., Koper, O., Mohs, C., Khaleel, A., Glavee, G.N., Zhang, D., Sorensen, C.M. and Hadjipanayis, G.C. (1994) *Nanophase Materials, Synthesis, Properties and Applications* (eds G.C. Hadjipanayis and R.W. Siegel), Kluwer Academic Publishers, Dordrecht, The Netherlands, p. 71.
72 Bedilo, A.F. and Klabunde, K.J. (1997) *Nanostructured Materials*, **8** (2), 119–35.
73 Zhang, Y.X., Li, G.H., Wu, Y.C., Luo, Y.Y. and Zhang, L.D. (2005) *Journal of Physical Chemistry B*, **109** (12), 5478–81.
74 Cerda, J., Arbiol, J., Diaz, R., Dezanneau, G. and Morante, J.R. (2002) *Material Letters*, **56** (3), 131–6.
75 O'Brien, S., Brus, L. and Murray, C.B. (2001) *Journal of the American Chemical Society*, **123** (48), 12085–6.
76 Meron, T., Rosenberg, Y., Lereah, Y. and Markovich, G. (2005) *Journal of Magnetism and Magnetic Materials*, **292**, 11–16.
77 Harreld, J.H., Dong, W. and Dunn, B. (1998) *Materials Research Bulletin*, **33** (4), 561–7.
78 Dong, W., Rolison, D.R. and Dunn, B. (2000) *Electrochemical and Solid State Letters*, **3** (10), 457–9.

79 Long, J.W., Swider-Lyons, K.E., Stroud, R.M. and Rolison, D.R. (2000) *Electrochemical and Solid State Letters*, **3** (10), 453–6.

80 Long, J.W., Young, A.L. and Rolison, D.R. (2003) *Journal of the Electrochemical Society*, **150** (9), A1161–5.

81 Swider, K.E., Merzbacher, C.I., Hagans, P.L. and Rolison, D.R. (1997) *Chemistry of Materials*, **9** (5), 1248–51.

82 Gao, L., Wang, H.Z., Hong, J.S., Miyamoto, H., Miyamoto, K., Nishikawa, Y. and Torre, S.D.D.L. (1999) *Nanostructured Materials*, **11** (1), 43–9.

83 Qian, Z. and Shi, J.L. (1998) *Nanostructured Materials*, **10** (2), 235–44.

84 Rao, K.R.M., Rao, A.V.P. and Komarneni, S. (1996) *Materials Letters*, **28** (4–6), 463–7.

85 Corma, A. (1995) *Chemical Reviews*, **95**, 559–614.

86 Srinivasan, R., Watkins, T.R., Hubbard, C.R. and Davis, B.H. (1995) *Chemistry of Materials*, **7** (4), 725–30.

87 Pârvulescu, V., Coman, S., Grange, P. and Pârvulescu, V.I. (1999) *Applied Catalysis A*, **176** (1), 27–43.

88 Pârvulescu, V.I., Pârvulescu, V., Endruschat, U., Lehmann, C.W., Grange, P., Poncelet, G. and Bönnemann, H. (2001) *Microporous and Mesoporous Materials*, **44–45**, 221–6.

89 Pârvulescu, V.I., Bönnemann, H., Pârvulescu, V., Endruschat, U., Rufinska, A., Lehmann, C.W., Tesche, B. and Poncelet, G. (2001) *Applied Catalysis A*, **214** (2), 273–87.

90 Stichert, W. and Schüth, F. (1998) *Journal of Catalysis*, **174** (2), 242–5.

91 Chuah, G.K., Jaenicke, S. and Pong, B.K. (1998) *Journal of Catalysis*, **175** (1), 80–92.

92 Bedilo, A.F. and Klabunde, K.J. (1998) *Journal of Catalysis*, **176** (2), 448–58.

93 Bedilo, A.F. and Klabunde, K.J. (1997) *Nanostructured Materials*, **8** (2), 119–35.

94 Bedilo, A.F., Timoshok, A.V. and Volodin, A.M. (2000) *Catalysis Letters*, **68** (3–40), 209–24.

95 (a) Heuer, A.H. and Hobbs, L.W. (eds) (1981) *Science and Technology of Zirconia I*, American Ceramic Society, Westerville, OH.
(b) Claussen, N. Rühle, M. and Heuer, A.H. (eds) (1984) *Science and Technology of Zirconia II*, American Ceramic Society, Westerville, OH.
(c) Claussen, N., Rühle, M. and Heuer, A. H. (eds) (1988) *Science and Technology of Zirconia III*, American Ceramic Society, Westerville, OH.

96 Chane-Ching, J.Y., Cobo, F., Aubert, D., Harvey, H.G., Airiau, M. and Corma, A. (2005) *Chemistry – A European Journal*, **11** (3), 979–87.

97 Hudson, M.J. and Knowles, J.A. (1996) *Journal of Materials Chemistry*, **6** (1), 89–95.

98 Liu, X.M., Lu, G.Q. and Yan, Z.F. (2004) *Journal of Physical Chemistry B*, **108** (40), 15523–8.

99 Zhou, L.P., Xu, J., Li, X.Q. and Wang, F. (2006) *Materials Chemistry and Physics*, **97** (1), 137–42.

100 Rezaei, M., Alavi, S.M., Sahebdelfar, S., Yan, Z.F., Teunissen, H., Jacobsen, J.H. and Sehested, J. (2007) *Journal of Materials Science*, **42** (4), 1228–37.

101 D'Souza, L., Saleh-Subaie, J. and Richards, R. (2005) *Journal of Colloid and Interface Science*, **292**, 476–85.

102 Landau, M.V., Vradman, L., Herskowitz, M., Koltypin, Y. and Gedanken, A. (2001) *Journal of Catalysis*, **201** (1), 22–36.

103 Perkas, N., Wang, Y.Q., Koltypin, Y., Gedanken, A. and Chandrasekhar, S. (2001) *Chemical Communications*, 988–9.

104 Ramesh, S., Koltypin, Y., Prozorov, R. and Gedanken, A. (1997) *Chemistry of Materials*, **9** (2), 546–51.

105 Pol, V.G., Reisfeld, R. and Gedanken, A. (2002) *Chemistry of Materials*, **14**, 3920–4.

106 Li, J.G., Ikegami, T., Wang, Y.R. and Mori, T. (2002) *Journal of Solid State Chemistry*, **168** (1), 52–9.

107 Xiang, L., Deng, X.Y. and Jin, Y. (2002) *Scripta Materialia*, **47** (4), 219–24.

108 Borse, P.H., Kankate, L.S., Dassenoy, F., Vogel, W., Urban, J. and Kulkarni, S.K. (2002) *Journal of Materials Science, Materials in Electronics*, **13** (9), 553–9.

109 Rojas, T.C. and Ocana, M. (2002) *Scripta Materialia*, **46** (9), 655–60.

110 Tang, Z.X., Sorensen, C.M., Klabunde, K.J. and Hadjipanayis, G.C. (1991) *Journal of Colloid and Interface Science*, **146** (1), 38–52.

111 Jeyadevan, B., Chinnasamy, C.N., Perales-Perez, O., Iwasaki, Y., Hobo, A., Shinoda, K., Tohji, K. and Kasuya, A. (2002) *IEEE Transactions on Magnetics*, **38** (5), 2595–7.

112 Li, J., Dai, D.L., Zhao, B.G., Lin, Y.Q. and Liu, C.Y. (2002) *Journal of Nanoparticle Research*, **4** (3), 261–4.

113 Wang, M.L., Wang, C.H. and Wang, W. (2007) *Journal of Materials Chemistry*, **17** (20), 2133–8.

114 Natile, M.M., Boccaletti, G. and Glisenti, A. (2005) *Chemistry of Materials*, **17** (25), 6272–86.

115 Perera, S., Zelenski, N. and Gillan, E.G. (2006) *Chemistry of Materials*, **18** (9), 2381–8.

116 Gui, Z., Fan, R., Mo, W.Q., Chen, X.H., Yang, L. and Hu, Y. (2003) *Materials Research Bulletin*, **38** (1), 169–76.

117 Liu, Z.L., Liu, Y.J., Yao, K.L., Ding, Z.H., Tao, J. and Wang, X. (2002) *Journal of Materials Synthesis and Processing*, **10** (2), 83–7.

118 Sun, X.D., Ma, C.L., Wang, Y.D. and Li, H.D. (2002) *Inorganic Chemistry Communications*, **5** (10), 747–50.

119 Zhang, Z.L., Guo, L. and Wang, W.D. (2001) *Journal of Materials Research*, **169** (3), 803–5.

120 Palchik, O., Kerner, R., Gedanken, A., Weiss, A.M., Slifkin, M.A. and Palchik, V. (2001) *Journal of Materials Chemistry*, **11**, 874–8.

121 Grisaru, H., Palchik, O., Gedanken, A., Palchik, V., Slifkin, M.A. and Weiss, A.M. (2002) *Journal of Materials Chemistry*, **12**, 339–44.

122 Kerner, R., Palchik, O. and Gedanken, A. (2001) *Chemistry of Materials*, **13**, 1413–19.

123 Laudise, R.A. (1962) *Progress in Inorganic Chemistry*, Vol III (ed. F.A. Cotton), Interscience, New York, p. 1.

124 Barrer, R.M. (1982) *Hydrothermal Chemistry of Zeolites*, Academic Press, London.

125 Rabenau, A. (1985) *Angewandte Chemie–International Edition in English*, **24**, 1026–40.

126 Laudise, R.A. (1987) Hydrothermal synthesis of crystals, C&EN News, September 28, 30–43.

127 Suslick, K.S., Choe, S.B., Cichowlas, A.A. and Grinstaff, M.W. (1991) *Nature*, **353**, 414–16.

128 Hiller, R., Putterman, S.J. and Barber, B.P. (1992) *Physical Review Letters*, **69** (8), 1182–4.

129 Barber, B.P. and Putterman, S.J. (1991) *Nature*, **352**, 318–20.

130 Suslick, K.S., Hammerton, D.A. and Cline, R.E. (1986) *Journal of the American Chemical Society*, **108** (18), 5641–2.

131 Livage, J. (1981) *Journal of Physics*, **42** (NC4), 981–92.

132 Sugimoto, M. (1994) *Journal of Magnetism and Magnetic Materials*, **133** (1–3), 460–2.

133 Koltypin, K.V.P.M., Shafi, Y., Gedanken, A., Prozorov, R., Balogh, J., Lendavi, J. and Felner, I. (1997) *Journal of Physical Chemistry B*, **101** (33), 6409–14.

134 Liang, J.H., Jiang, X., Liu, G., Deng, Z.X., Zhuang, J., Li, F. and Li, Y.D. (2003) *Materials Research Bulletin*, **38** (1), 161–8.

135 Pang, G., Xu, X., Markovich, V., Avivi, S., Palchik, O., Koltypin, Y., Gorodetsky, G., Yeshurun, Y., Buchkremer, H.P. and Gedanken, A. (2003) *Materials Research Bulletin*, **38**, 11–16.

136 de Torresi, S.I.C., Vidotti, M., Ponzio, E.A. and Greco, C.V. (2006) *ElectroChemical Communications*, **8** (4), 554–60.

137 Fulton, J.L., Matson, D.W., Pecher, K.H., Amonette, J.E. and Linehan, J.C. (2006) *Journal of Nanoscience and Nanotechnology*, **6** (2), 562–7.

138 Zhang, D., Fu, H., Shi, L., Pan, C., Li, Q., Chu, Y. and Yu, W. (2007) *Inorganic Chemistry*, **46** (7), 2446–51.

139 Tu, W.X. and Liu, H.F. (2000) *Chemistry of Materials*, **12** (2), 564–7.

140 Palchik, O., Zhu, J.J. and Gedanken, A. (2000) *Journal of Materials Chemistry*, **10**, 1251–4.

141 Breck, D.W. (1974) *Zeolite Molecular Sieves, Structure, Chemistry and Use*, John Wiley & Sons, Inc., New York.

142 Corbett, J.D. (1985) *Chemical Reviews*, **85**, 383–97.

143 Lii, K.H. and Haushalter, R.C. (1987) *Journal of Solid State Chemistry*, **69**, 320.

144 Haushalter, R.C. and Lai, F.W. (1988) *Journal of Solid State Chemistry*, **76**, 218.

145 Haushalter, R.C., Strohmaier, K.G. and Lai, F.W. (1989) *Science*, **246**, 1289–91.

146 Mundi, L.A., Strohmaier, K.G., Goshorn, D.P. and Haushalter, R.C. (1990) *Journal of the American Chemical Society*, **112** (22), 8182–3.

147 Mundi, L.A. and Haushalter, R.C. (1990) *Inorganic Chemistry*, **29** (16), 2879–81.

148 Haushalter, R.C. and Mundi, L.A. (1992) *Chemistry of Materials*, **4** (1), 31–48.

149 Cao, Y., Hu, J., Hong, Z., Deng, J. and Fan, K. (2002) *Catalysis Letters*, **81** (1), 107–12.

150 Pinna, N., Garnweitner, G., Antonietti, M. and Niederberger, M. (2005) *Journal of the American Chemical Society*, **127** (15), 5608–12.

151 Niederberger, M., Pinna, N., Polleux, J. and Antonietti, A. (2004) *Angewandte Chemie – International Edition*, **43** (17), 2270–3.

152 Su, C.Y., Goforth, A.M., Smith, M.D., Pellechia, P.J. and zur Loye, H.C. (2004) *Journal of the American Chemical Society*, **126** (11), 3576–86.

153 Parise, J.B., Ko, Y.H., Rijssenbeck, J., Nellis, D.M., Tan, K.M. and Koch, S. (1994) *Journal of the Chemical Society – Chemical Communications*, 527.

154 Tan, K.M., Ko, Y.H., Parise, J.B. and Darovsky, A. (1996) *Chemistry of Materials*, **8** (2), 448–53.

155 Ramirez, A.P., Cava, R.J. and Krajewski, J. (1997) *Nature*, **386**, 156–9.

156 Stein, A., Keller, S.W. and Mallouk, T.E. (1993) *Science*, **259**, 1558–64.

157 Sheldrick, W.S. and Wachhold, M. (1997) *Angewandte Chemie – International Edition in English*, **36** (3), 207–24.

158 Chemseddine, A. and Moritz, T. (1999) *European Journal of Inorganic Chemistry*, 235–45.

159 Trentler, T.J., Denler, T.E., Bertone, J.F., Agrawal, A. and Colvin, V.L. (1999) *Journal of the American Chemical Society*, **121** (7), 1613–14.

160 Rockenberger, J., Scher, E.C. and Alivisatos, A.P. (1999) *Journal of the American Chemical Society*, **121** (49), 11595–6.

161 Thimmaiah, S., Rajamathi, M., Singh, N., Bera, P., Meldrum, F., Chandrasekhar, N. and Seshadri, R. (2001) *Journal of Materials Chemistry*, **11** (12), 3215–21.

162 Oguri, Y., Riman, R.E. and Bowen, H.K. (1988) *Journal of Materials Science*, **23**, 2897–904.

163 Kondo, M., Shinozaki, K., Ooki, R. and Mizutani, N. (1994) *Journal of the Ceramic Society of Japan*, **102** (2), 742–846.

164 Jeon, S. and Braun, P.V. (2003) *Chemistry of Materials*, **15** (6), 1256–63.

165 Cheng, H.M., Ma, J.M., Zhao, Z.G. and Qi, L.M. (1995) *Chemistry of Materials*, **7** (4), 663–71.

166 Zheng, Y.Q., Shi, E.R., Chen, Z.Z., Li, W.J. and Hu, X.F. (2001) *Journal of Materials Chemistry*, **11** (5), 1547–51.

167 Yin, H.B., Wada, Y., Kitamura, T., Kambe, S., Murasawa, S., Mori, H., Sakata, T. and Yanagida, S. (2001) *Journal of Materials Chemistry*, **11** (6), 1694–703.

168 Niederberger, M., Garnweitner, G., Pinna, N. and Antonietti, M. (2004) *Journal of the American Chemical Society*, **126** (29), 9120–6.

169 Masui, T., Hirai, H., Hamada, R., Imanaka, N., Adachi, G., Sakata, T. and Mori, H. (2003) *Journal of Materials Chemistry*, **13** (3), 622–7.

170 Inoue, M., Kimura, M. and Inui, T. (1999) *Chemical Communications*, 957–8.

171 Wu, M.M., Long, J.B., Huang, A.H. and Luo, Y.J. (1999) *Langmuir*, **15** (26), 8822–5.

172 Andersson, M., Österlund, L., Ljungström, S. and Palmqvist, A. (2002) *Journal of Physical Chemistry B*, **106**, 10674–10679.

173 Gautam, U.K., Ghosh, M., Rajamathi, M. and Seshadri, R. (2002) *Pure and Applied Chemistry*, **74** (9), 1643–9.

174 He, P., Shen, X.H. and Gao, H.C. (2005) *Journal of Colloid and Interface Science*, **284** (2), 510–15.

175 Wallin, M., Cruise, N., Klement, U., Palmqvist, A., Skoglundh, M. and Klement, U. (2004) *Colloids and Surfaces A*, **238** (1–3), 27–35.

176 Lu, C.H. and Wang, H.C. (2004) *Journal of the European Ceramic Society*, **24** (5), 717–23.

177 Koetz, J., Bahnemann, J., Lucas, G., Tiersch, B. and Kosmella, S. (2004) *Colloids and Surfaces A*, **250** (1–3), 423–30.

178 Chen, D.L. and Gao, L. (2004) *Journal of Colloid and Interface Science*, **279** (1), 137–42.

179 Zhang, X. and Chan, K.Y. (2003) *Chemistry of Materials*, **15** (2), 451–9.
180 Holzinger, D. and Kickelbick, G. (2003) *Chemistry of Materials*, **15** (26), 4944–8.
181 Bruch, C., Kruger, J.K., Unruh, H.G., Krauss, W., Zimmermeier, B., Beck, C. and Hempelmann, R. (1997) *Berichte Der Bunsen-Gesellschaft-Physical Chemistry Chemical Physics*, **101** (11), 1761–4.
182 Hartl, W., Beck, C., Roth, M., Meyer, F. and Hempelmann, R. (1997) *Berichte Der Bunsen-Gesellschaft-Physical Chemistry Chemical Physics*, **101** (11), 1714–17.
183 Fang, J.Y., Wang, J., Ng, S.C., Chew, C.H. and Gan, L.M. (1997) *Nanostructured Materials*, **8** (4), 499–505.
184 Zhang, Z.J., Wang, Z.L., Chakoumakos, B.C. and Yin, J.S. (1998) *Journal of the American Chemical Society*, **120** (8), 1800–4.
185 Moran, P.D., Bartlett, J.R., Bowmaker, G.A., Woolfrey, J.L. and Cooney, R.P. (1999) *Journal of Sol-Gel Science and Technology*, **15** (3), 251–62.
186 Yener, D.O. and Giesche, H. (1999) *Journal of the American Chemical Society*, **84** (9), 1987–95.
187 Kumar, P., Pillai, V., Bates, S.R. and Shah, D.O. (1993) *Materials Letters*, **16** (2–3), 68–74.
188 Xiong, L.F. and He, T. (2006) *Chemistry of Materials*, **18** (9), 2211–18.
189 Pang, Y.X. and Bao, X.J. (2002) *Journal of Materials Chemistry*, **12** (12), 3699–704.
190 Ulrich, G.D. and Riehl, J.W. (1982) *Journal of Colloid and Interface Science and Technology*, **87** (1), 257–65.
191 Cow, G.M. and Gonsalves, K.E. (eds) (1996) *Nanotechnology, Molecularly Designed Materials* American Chemical Society, Washington, DC, pp. 64–78, 79–99.
192 Singhal, A., Skandan, G., Wang, A., Glumac, N., Kear, B.H. and Hunt, R.D. (1999) *Nanostructured Materials*, **11** (4), 545–52.
193 Wu, M.K., Windeler, R.S., Steiner, C.K.R., Bors, T. and Friedlander, S.K. (1993) *Aerosol Science and Technology*, **19** (4), 527–48.
194 Lindackers, D., Strecker, M.G.D., Roth, P., Janzen, C. and Pratsinis, S.E. (1997) *Combustion Science and Technology*, **123** (1–6), 287–315.
195 Glumac, N.G., Chen, Y.J., Skandan, G. and Kear, B. (1998) *Materials Letters*, **34** (3–6), 148–53.
196 Zachariah, M.R., Chin, D., Semerjian, H.G. and Katz, J.L. (1989) *Combustion and Flame*, **78** (3–4), 287–98.
197 Lima, M.D., Bonadimann, R., de Andrade, M.J., Toniolo, J.C. and Bergmann, C.P. (2006) *Journal of the European Ceramic Society*, **26** (7), 1213–20.
198 Stark, W.J., Mädler, L., Maciejewski, M., Pratsinis, S.E. and Baiker, A. (2003) *Chemical Communications*, 588–9.
199 Purohit, R.D., Saha, S. and Tyagi, A.K. (2006) *Materials Science and Engineering B*, **130** (1–3), 57–60.
200 Kovacheva, D., Gadjov, H., Petrov, K., Mandal, S., Lazarraga, M.G., Pascual, L., Amarilla, J.M., Rojas, R.M., Herrero, P. and Rojo, J.M. (2002) *Journal of Materials Chemistry*, **12** (4), 1184–8.
201 Kodas, T.T. (1989) *Advanced Materials*, **6**, 180–92.
202 Janackovic, D., Jokanovic, V., Kostic-Gvozdenovic, L. and Uskokovic, D. (1998) *Nanostructured Materials*, **10** (3), 341–8.
203 Messing, G.L. and Gardner, T. (1984) *American Ceramic Society Bulletin*, **64**, 1498–501.
204 Pollinger, J.P. and Messing, G.L. (1993) *Journal of Aerosol Science and Technology*, **19** (4), 217–27.
205 Jayanthi, G.V., Zhang, S.C. and Messing, G.L. (1993) *Journal of Aerosol Science and Technology*, **19** (4), 478–90.
206 Kodas, T.T., Datye, A., Lee, V. and Engler, E. (1989) *Journal of Applied Physics*, **65**, 2149–51.
207 Zhang, H.F. and Cooper, A.I. (2005) *Soft Matter*, **1** (2), 107–13.
208 Li, W.-C., Lu, A.-H., Weidenthaler, C. and Schuth, F. (2004) *Chemistry of Materials*, **16** (26), 5676–81.
209 Tian, B.Z., Liu, X.Y., Yang, H.F., Xie, S.H., Yu, C.Z., Tu, B. and Zhao, D.Y. (2003) *Advanced Materials*, **15** (15), 1370–4.
210 Tian, B.Z., Liu, X.Y., Solovyov, L.A., Liu, Z., Yang, H.F., Zhang, Z.D., Xie, S.H., Zhang, F.Q., Tu, B., Yu, C.Z., Terasaki,

O. and Zhao, D.Y. (2004) *Journal of the American Chemical Society*, **126** (3), 865–75.
211 Fuertes, A.B. (2005) *Journal of Physics and Chemistry of Solids*, **66**, 741–7.
212 Laha, S.C. and Ryoo, R. (2003) *Chemical Communications*, 2138–9.
213 Schwickardi, M., Johann, T., Schmidt, W. and Schuth, F. (2002) *Chemistry of Materials*, **14**, 3913–19.
214 Dong, A.G., Ren, N., Tang, Y., Wang, Y.J., Zhang, Y.H., Hua, W.M. and Gao, Z. (2003) *Journal of the American Chemical Society*, **125** (17), 4976–7.
215 Shilov, A.E. and Shul'pin, G.B. (1997) *Chemical Reviews*, **97**, 2879–932.
216 Punniyamurthy, T., Velusamy, S. and Iqbal, J. (2005) *Chemical Reviews*, **105**, 2329–63.
217 Barton, D.H.R., Csuhai, E. and Ozbalik, N. (1990) *Tetrahedron*, **46**, 3743–52.
218 Collman, J.P., Tanaka, H., Hembre, R.T. and Brauman, J.I. (1990) *Journal of the American Chemical Society*, **112**, 3689–90.
219 Grasselli, R.K. (1999) *Catalysis Today*, **49**, 141–53.
220 Sigman, M.S. and Schultz, M.J. (2004) *Organic and Biomolecular Chemistry*, **2**, 2551–4.
221 Botalla, P., Nieto, J.M.L., Dejoz, A., Vazquez, M.I. and Martinez-Arias, A. (2003) *Catalysis Today*, **78**, 507–12.
222 Hess, C., Looi, M.H., Hamid, S.B.A. and Schlögl, R. (2006) *Chemical Communications*, 451–3.
223 Davies, T.E., García, T., Solsona, B. and Taylor, S.H. (2006) *Chemical Communications*, 3417–19.
224 Batis, N.H., Batis, H., Ghorbel, A., Vedrine, J.C. and Volta, J.C. (1991) *Journal of Catalysis*, **128**, 248–63.
225 Han, Y.-F., Wang, H.-M., Cheng, H. and Deng, J.-F. (1999) *Chemical Communications*, 521–2.
226 Ueda, W., Endo, Y. and Watanabe, N. (2006) *Topics in Catalysis*, **38** (4), 261–8.
227 Ushikubo, T., Nakamura, H., Koyasu, Y. and Wajiki, S. (1995) U.S. Patent 5,380,933.
228 Pillai, U.R. and Sahle-Demessie, E. (2002) *Chemical Communications*, 2142–3.
229 Pedrosa, A.M.G., Souza, M.J.B., Melo, D.M.A., Araujo, A.S., Zinner, L.B., Fernandes, J.D.G. and Martinelli, A.E. (2003) *Solid State Sciences*, **5**, 725–8.
230 Raja, R., Thomas, J.M., Xu, M., Harris, K.D.M., Greenhill-Hooper, M.L and Quill, K. (2006) *Chemical Communications*, 448–50.
231 Chen, C.X., Tang, J., Li, W.S., Au, C.T. and Zhou, X.P. (2006) *Catalysis Letters*, **111**, 103–9.
232 Tatsumi, T., Nakamura, M., Negishi, S. and Tominaga, H. (1990) *Journal of the Chemical Society–Chemical Communications*, 476–7.
233 Rudberg, J. and Foster, M. (2004) *Journal of Physical Chemistry B*, **108**, 18311–17.
234 Tasker, P.W. (1979) *Journal of Physics C: Solid State Physics*, **12**, 4977–84.
235 Zuo, J.M., O'Keeffe, M., Rez, P. and Spence, J.C.H. (1997) *Physical Review Letters*, **78**, 4777–80.
236 Plass, R., Egan, K., Collazo-Davila, C., Grozea, D., Landree, E., Marks, L.D. and Gajdardziska-Josifovska, M. (1998) *Physical Review Letters*, **81**, 4891–4.
237 Verziu, M., Cojocaru, B., Hu, J., Richards, R., Ciuculescu, C., Filip, P. and Parvulescu, V.I. (2007) *Green Chemistry*, **4**, 373–81.
238 Badlani, M. and Wachs, I.E. (2001) *Catalysis Letters*, **75**, 137–49.
239 Olah, G.A. (2005) *Angewandte Chemie–International Edition*, **44**, 2636–9.
240 Surampudi, S., Narayanan, S.R., Vamos, E., Frank, H., Halpert, G., LaConti, A., Kosek, J., Surya, G.K. and Olah, G.A. (1994) *Journal of Power Sources*, **47**, 377–85.
241 Surumpudi, S., Narayanan, S.R., Vamos, E., Frank, H., Halpert, G., Prakash, G.K.S. and Olah, G.A. (2001) US Patent 6,248,460.
242 Surumpudi, S., Narayanan, S.R., Vamos, E., Frank, H., Halpert, G., Laconti, A., Kosek, J., Prakash, G.K.S. and Olah, G.A. (1997) US Patent 5,599,638.
243 Surumpudi, S., Narayanan, S.R., Vamos, E., Frank, H., Halpert, G., Laconti, A., Kosek, J., Prakash, G.K.S. and Olah, G.A. (2002) US Patent 6,444,343.

244 Prakash, G.K.S., Smart, M.C., Wang, Q.J., Atti, A., Pleynet, V., Yang, B., McGrath, K., Olah, G.A., Narayanan, S.R., Chun, W., Valdez, T. and Surumpudi, S. (2004) *Journal of Fluorine Chemistry*, **125**, 1217–30.

245 Cavani, F. and Trifiro, F. (1992) *Applied Catalysis A: General*, **88**, 115–35.

246 Abon, M., Bere, K.E., Tuel, A. and Delichere, P. (1995) *Journal of Catalysis*, **156**, 28–36.

247 Zhao, Z., Yamada, Y., Teng, Y., Ueda, A., Sakurai, H. and Kobayashi, T. (2000) *Journal of Catalysis*, **190**, 215–27.

248 Zhao, Z., Yamada, Y., Ueda, A., Sakurai, H. and Kobayashi, T. (2004) *Catalysis Today*, **93–95**, 163–71.

249 Santacesaria, E., Cozzolino, M., Serio, M.D., Venezia, A.M. and Tesser, R. (2004) *Applied Catalysis A: General*, **270**, 177–92.

250 Jiménez-Jiménez, J., Mérida-Robles, J., Rodríguez-Castellón, E., Jiménez-López, A., Granados, M.L., del Val, S., Cabrera, I.M. and Fierro, J.L.G. (2005) *Catalysis Today*, **99**, 179–86.S.

251 Yang, S., Iglesia, E. and Bell, A.T. (2005) *Journal of Physical Chemistry B*, **109**, 8987–9000.

252 Daniell, W., Ponchel, A., Kuba, S., Anderla, F., Weingand, T., Gregory, D.H. and Knözinger, H. (2002) *Topics in Catalysis*, **20**, 65–74.

253 Lopez, D., Goodwin, J., Bruce, D. and Lotero, E. (2005) *Applied Catalysis*, **295**, 97–105.

254 Dorado, M.P., Ballesteros, E., Almeida, J.A., Schellert, C., Lohrlein, H.P. and Krause, R. (2002) *Transactions of the American Society of Agricultural Engineers*, **45**, 525.

255 Lotero, E., Liu, Y., Lopez, D.E., Suwannakarn, K., Bruce, D.A. and Goodwin, J.G., Jr (2005) *Industrial and Engineering Chemistry Research*, **44**, 5353–63.

256 Ramadhas, A.S., Jayaraj, S. and Muraleedharan, C. (2005) *Fuel*, **84**, 335–40.

257 Du, W., Xu, Y.Y., Liu, D.H. and Zeng, J. (2004) *Journal of Molecular Catalysis B Enzyme*, **30**, 125–9.

258 Demirbas, A. (2003) *Energy Conversion and Management*, **44**, 2093–109.

259 Saka, S. and Kusdiana, D. (2001) *Fuel*, **80**, 225–31.

260 Furuta, S., Matsuhashi, H. and Arata, K. (2004) *Catalysis Communications*, **5**, 721–3.

261 Venkat Reddy, C.R., Oshel, R. and Verkade, J.G. (2006) *Energy and Fuels*, **20**, 1310–14.

262 Ranjit, K.T. and Klabunde, K.J. (2005) *Chemistry of Materials*, **17**, 65–73.

263 Utamapanya, S., Klabunde, K.J. and Schlup, J.R. (1991) *Chemistry of Materials*, **3**, 175–81.

264 Diao, Y., Walawander, W.P., Sorensen, C.M., Klabunde, K.J. and Rieker, T. (2002) *Chemistry of Materials*, **14**, 362–8.

265 Li, W.C., Lu, A.H., Weidenthaler, C. and Schueth, F. (2004) *Chemistry of Materials*, **16**, 5676–81.

266 Roggenbuck, J. and Tiemann, M. (2005) *Journal of the American Chemical Society*, **127**, 1096–7.

267 Stankic, S., Mueller, M., Dewald, O., Sterrer, M., Knoezinger, E. and Bernardi, J. (2005) *Angewandte Chemie–International Edition*, **44**, 4917–20.

268 Jensen, M.B., Pettersson, L., Swang, O. and Olsbye, U. (2005) *Journal of Physical Chemistry B*, **109**, 16774–81.

269 Rozovskii, A.Y. and Lin, G.I. (2003) *Topics in Catalysis*, **22**, 137–43.

270 Steele, B.C.H. (1999) *Nature*, **400**, 619–21.

271 Cheng, W. (1999) *Accounts of Chemical Research*, **32**, 685–91.

272 Richards, R. (2006) *Surface and Nanomolecular Catalysis*, CRC Press, Taylor & Francis Group, Boca Raton, FL, p. 56.

273 Hu, J., Zhu, K., Chen, L., Kubel, C. and Richards, R. (2007) *Journal of Physical Chemistry C*, **111**, 12038–44.

274 Millikan, R.C. and Pitzer, K.S. (1958) *Journal of the American Chemical Society*, **80**, 3515–21.

275 Kustov, L.M., Ostgard, D. and Sachtler, W.M.H. (1991) *Catalysis Letters*, **9**, 121–6.

276 Koper, O., Li, Y.X. and Klabunde, K.J. (1993) *Chemistry of Materials*, **5**, 500–5.

277 Koper, O., Lagadic, I. and Klabunde, K.J. (1997) *Chemistry of Materials*, **9**, 838–48.

278 Jiang, Y., Decker, S., Mohs, C. and Klabunde, K.J. (1998) *Journal of Catalysis*, **180**, 24–35.

279 Li, Y.X., Li, H. and Klabunde, K.J. (1994) *Environmental Science and Technology*, **28**, 1248–53.
280 Amato, I. (1993) *Science*, **261**, 152–4.
281 Mochida, I. and Yoneda, Y. (1968) *Journal of Organic Chemistry*, **33**, 2163–5.
282 Pistarino, C., Brichese, F., Finocchio, E., Romezzano, G., Di Felice, R., Balde, M. and Busca, G. (2000) *Studies in Surface Science and Catalysis*, **130**, 1613–18.
283 Wagner, G.W., Koper, O., Lucas, E., Decker, S. and Klabunde, K.J. (2000) *Journal of Physical Chemistry B*, **104**, 5118–23.
284 Wagner, G.W., Bartram, P.W., Koper, O. and Klabunde, K.J. (1999) *Journal of Physical Chemistry B*, **103**, 3225–8.
285 Fenelonov, V.B., Mel'gunov, M.S., Mishakov, I.V., Richards, R.M., Chesnokov, V.V., Volodin, A.M. and Klabunde, K.J. (2001) *Journal of Physical Chemistry B*, **105**, 3937–41.
286 Mishakov, I.V., Bedilo, A.F., Richards, R.M., Chesnokov, V.V., Volodin, A.M., Zaikovskii, V.I., Buyanov, R.A. and Klabunde, K.J. (2002) *Journal of Catalysis*, **206**, 40–8.
287 Mol, J.C. (1999) *Catalysis Today*, **51**, 289–99.
288 Pennella, F. and Banks, R.L. (1973) *Journal of Catalysis*, **31**, 304–8.
289 Luckner, R.C., Mcconchie, G.E. and Wills, G.B. (1973) *Journal of Catalysis*, **28**, 63–8.
290 Wang, Y.D., Chen, Q.L., Yang, W.M., Xie, Z.X., Xu, W. and Huang, D.Y. (2003) *Applied Catalysis A: General*, **250**, 25–37.
291 Zhao, D.Y., Feng, J.L., Huo, Q.S., Melosh, N., Fredrickson, G.H., Chmelka, B.F. and Stucky, G.D. (1998) *Science*, **279**, 548–52.
292 Cao, Y., Hu, J.C., Yang, P., Dai, W.L. and Fan, K.N. (2003) *Chemical Communications*, 908–9.
293 Han, Y., Xiao, F.S., Wu, S., Sun, Y., Meng, X., Li, D., Lin, S., Deng, F. and Ai, X. (2001) *Journal of Physical Chemistry B*, **105**, 7963–6.
294 Hu, J., Wang, Y., Chen, L., Richards, R., Yang, W., Liu, Z. and Xu, W. (2006) *Microporous and Mesoporous Materials*, **93**, 158–63.
295 Liu, Z., Cortés-Concepción, J.A., Mustian, M. and Amiridis, M.D. (2006) *Applied Catalysis A: General*, **302**, 232–6.
296 Choudary, B.M., Kantam, M.L., Ranganath, K.V.S., Mahendar, K. and Sreedhar, B. (2004) *Journal of the American Chemical Society*, **126**, 3396–7.

17
Preparation of Superacidic Metal Oxides and Their Catalytic Action

Kazushi Arata

17.1
Introduction

When an acid solution is highly diluted in water, the pH acidity scale is used, which becomes problematic when the acid concentration increases, and more so, when non-aqueous media are employed. Considering the limited application of the pH scale, a quantitative scale was provided by Hammett and Deyrup to express the acidity of more concentrated or non-aqueous solutions: that is, Hammett acidity function, H_0 [1].

The equilibrium between an acid, BH^+, and its conjugate base, B, can be written

$$BH^+ \rightleftharpoons B + H^+ \tag{17.1}$$

The corresponding thermodynamic equilibrium constant is K_{BH^+}, which is expressed as

$$K_{BH^+} = \frac{a_{H^+} \cdot a_B}{a_{BH^+}} = \frac{a_{H^+} \cdot C_B}{C_{BH^+}} \cdot \frac{f_B}{f_{BH^+}} \tag{17.2}$$

in which a is the activity, C the concentration, and f the activity coefficient. This equation can be written in the more usual form:

$$H_0 = pK_{BH^+} + \log \frac{[B]}{[BH^+]} \tag{17.3}$$

H_0 is also expressed by

$$H_0 = -\log \frac{a_{H^+} \cdot f_B}{f_{BH^+}} = -\log \frac{[H^+] \cdot f_{H^+} \cdot f_B}{f_{BH^+}} \tag{17.4}$$

Metal Oxide Catalysis. Edited by S. David Jackson and Justin S. J. Hargreaves

ISBN: 978-3-527-31815-5

Table 17.1 Base indicators used for the measurement of superacid strength.

Indicator[a)]	pK_{BH^+}
p-Nitrotoluene	–11.35
m-Nitrotoluene	–11.99
p-Nitrofluorobenzene	–12.44
p-Nitrochlorobenzene	–12.70
m-Nitrochlorobenzene	–13.16
2,4-Dinitrotoluene	–13.75
2,4-Dinitrofluorobenzene	–14.52
1,3,5-Trinitrobenzene	–16.04
1,3,5-Trichlorobenzene	–16.12

a Color of base form, colorless: color of acid form, yellow.

In dilute aqueous solution, as the activity coefficients tend to unity, the Hammett acidity function, H_0, becomes identical to pH.

The Hammett acidity function relates to the ability of a solution to convert a neutral base (B) into its conjugate acid (BH^+). Use is made of this in an experimental procedure which requires the determination of the BH^+ concentration derived from a very small amount of B (a Hammett indicator) diluted in the solution. This concept allows quantitative determination of the acidity of concentrated and non-aqueous acidic solutions. Gillespie and co-workers determined the acid strength of 100% H_2SO_4 to be $H_0 = -11.93$ [2]. After 1 mg of *p*-nitrotoluene $(pK_{BH^+} = -11.35)$ (B) was dissolved in 1000 ml of H_2SO_4 and the equilibrium was attained, the concentration of *p*-nitrotoluene-H^+, BH^+, was measured at λ_{max}376 nm with a spectrophotometer. The value of log[B]/[BH^+] obtained was –0.67 which corresponded to an H_0 value of –12.02. Further measurements using other indicators such as *m*-nitrotoluene $(pK_{BH^+} = -11.99)$ and nitrobenzene (–12.14) gave the average H_0 value of 100% H_2SO_4 to be –11.93. Lower values of H_0 correspond to greater acid strength. Table 17.1 shows the Hammett indicators used for the measurement of solid-superacidic strength, which we have usually used. The indicators with higher pK_{BH^+} values are (2,4-dinitrofluorobenzene)H^+ $(pK_{BH^+} = -17.35)$, (1,3,5-trinitrobenzene)H^+ (–18.93), and (*p*-methoxybenzaldehyde)H^+ (–19.50), but we have not applied these yet.

Any acid is termed a *superacid* when its acidity is stronger than that of 100% H_2SO_4, that is, $H_0 \leq -11.93$ [3–5], and a rapid development of superacid chemistry was seen in the 1960s and 1970s. Superacids can be both Brønsted and Lewis type and their conjugate combinations. Table 17.2 shows several superacids, which are generally made up by mixing a fluorine-containing Brønsted acid (e.g. HF, FSO_3H, CF_3SO_3H, etc.) and a fluorinated Lewis acid (BF_3, SbF_5, TaF_5, etc.) [6–8]. The Hammett acidity function is a logarithmic scale on which 100% H_2SO_4 has an H_0 of ~–12 and FSO_3H-SbF_5 in the table has an H_0 of ~–19. Thus, the acid strength of the latter is estimated to be seven orders of magnitude stronger than 100% sulfuric acid. This combination is termed *magic acid* [9].

Table 17.2 Liquid superacids and their acid strength.

Superacid	H_0
$HClO_4$	–13.0
$ClSO_3H$	–13.8
CF_3SO_3H	–14.1
FSO_3H	–15.1
H_2SO_4-SO_3 (1 : 1)	–14.5
FSO_3H-TaF_5 (1 : 0.2)	–16.7
FSO_3H-SbF_5 (1 : 0.1)	–18.9

Solid acids have been extensively studied and used as catalysts or catalyst carriers in the chemical industry, and in particular in the petroleum field, for many years. Aluminosilicates such as zeolites and silica-aluminas, together with mixed metal oxides such as TiO_2-ZrO_2, are typical examples. Replacement of homogeneous liquid acids by heterogeneous solid acids as catalysts is anticipated to bring about ease of continuous operation. Furthermore, the use of heterogeneous solid catalysts can lead to additional advantages, for example fewer problems in terms of reactor corrosion and environmental benefits in terms of the disposal of the used catalyst. However, their acidity is generally below the superacidity range. They are inactive for alkane isomerization and cracking at temperatures below 100 °C.

Novel organic syntheses that are possible in usual acidic media can be accomplished in superacids, including syntheses of economically important hydrocarbons. The remarkable ability of superacids to bring about hydrocarbon transformations can open up new fields in chemistry. In consideration of the exceptionally high activity of liquid superacids, research was extended to prepare solid superacids. As for chemical applications of liquid superacids, efforts were made to attach them to solid materials, and the results are found in extensive patent literature [10–13].

Primary studies to obtain the acidic materials of superacids attached to solid supports included the individual components of BF_3, SbF_5, TaF_5, FSO_3H, CF_3SO_3H, and their mixtures, supported on metals, alloys, resins, polymers, graphites, and various metal oxides such as zeolites and TiO_2-ZrO_2 [14–17]. The next general effort made to immobilize liquid superacids was to intercalate them in the lattice of graphite. An very rapid expansion occurred in this area of research, since graphite-intercalated compounds are also useful materials with applications as electronic conductors and battery components [18]. Graphite possesses a layered structure and consists of sheets of sp^2 carbon atoms, whose sheets are held together by weak van der Waals forces. SbF_5 can be intercalated easily in the lattice simply by heating a mixture of SbF_5 and graphite [19]. In addition to SbF_5, other superacids, $AlCl_3$, $AlBr_3$, NbF_5, and HF-SbF_5 were also synthesized as graphite intercalates and used for various superacid-catalyzed reactions [20–25]. Mixtures of aluminum halides and metal salts such as $AlCl_3$-$CuSO_4$ and $AlCl_3$-$CuCl_2$ are

active for the isomerization of paraffins at room temperature, and the acidity of the former was estimated to be below $H_0 = -13.75$ [26–28].

Although much effort was devoted to the immobilization of superacids, the major drawback in these catalysts was their short lifetime and ease of deactivation. Although initial conversions were high, the catalysts totally deactivated after a long period on stream. The immobilized superacids were not stable enough for the catalytic process, and metal halides were leached out by the feed from the graphite layers; reduction of metals in the superacids was also easily brought about [23, 29].

Superacidic metal oxides prepared by calcination at a high temperature can be used at elevated temperatures and, thus, provide new trends for developing environmentally benign processes. Superacidity is generated on the oxides of Fe, Ti, Zr, Hf, Sn, Si, and Al by treatment with sulfate, tungstate, and molybdate. Sulfated and tungstated zirconias have attracted much attention as potential catalysts; the latter are thermally stable superacids and can be calcined at temperatures above 1000 °C.

Table 17.3 summarizes the solid superacids we have prepared, together with their acid strengths. The acid strengths were estimated by the color change of Hammett indicators, TPD of pyridine, TPR of furan, and catalytic activities for various reactions. The temperatures shown in parentheses are the calcination temperatures to generate the highest acidity or activity. Although the optimum calcination temperature used varies with the type of vessel employed, the data shown in Table 17.3 were obtained for the catalysts calcined in a Pyrex glass tube below 700 °C and the catalysts calcined in a ceramic crucible above 700 °C for 3 h. The optimum calcination may vary more than 50 °C depending on the type of cal-

Table 17.3 Solid superacids and their acid strength.

Catalyst (calcination temperature, °C)[a)]	Highest acid strength (H_0 value)
SO_4/SnO_2 (550)	−18.0
SO_4/ZrO_2 (650)	−16.1
SO_4/HfO_2 (700)	−16.0
SO_4/TiO_2 (525)	−14.6
SO_4/Al_2O_3 (650)	−14.6
SO_4/Fe_2O_3 (500)	−13.0
SO_4/SiO_2 (400)	−12.2
WO_3/ZrO_2 (800)	−14.6
MoO_3/ZrO_2 (800)	−13.3
WO_3/SnO_2 (1000)	−13.3
WO_3/TiO_2 (700)	−13.1
WO_3/Fe_2O_3 (700)	−12.5
B_2O_3/ZrO_2 (650)	−12.5

a Named sulfated stannia, zirconia, hafnia, titania, alumina, ferria, and silica; tungstated zirconia; molybdated zirconia; tungstated stannia, titania, ferria; borated zirconia, respectively.

cination vessel, time, and so on. The notation SO_4/MeO_x means a sulfated metal oxide, such as sulfated zirconia and sulfated alumina. The valence of S in the sulfated metal oxides is +6, and this expression is not correct in the strict sense, since the SO_4 component does not carry a neutral charge.

Among the superacids listed in Table 17.3, sulfated zirconia (SO_4/ZrO_2) has been most frequently investigated, modified, and applied to various reactions. This may be because the sulfated zirconia possesses strong acid sites, is relatively easy to prepare, and was found to be a superacid early in the history of solid superacid development. Sulfated zirconia is now commercially available and used as a catalyst for organic synthesis in industry.

17.2 Preparation

17.2.1 Sulfated Metal Oxides of Zr, Sn, Ti, Fe, Hf, Si, and Al

17.2.1.1 **Preparation of Zirconia Gel** [30]

A sample of $ZrOCl_2 \cdot 8H_2O$ (200 g) is dissolved in water (3 l), and aqueous ammonia (28%) is added dropwise into the solution with stirring until the solution has a pH value of 8. The effect of pH of the solution can be dramatic in terms of the final catalytic activity, with the maximum activity being observed at pH 8 [31]. The aqueous portion is decanted from the precipitates, and fresh water is added followed by stirring and again decanting the aqueous portion; washing of the precipitates by decantation is repeated until the total amount of water used is 60 l, with almost no chloride ion being detected in the washings. The precipitates are dried at 100 °C for 24 h.

The catalysts prepared using the 'heating method' show higher activity [31]. For the 'heating method' aqueous ammonia is added dropwise to $ZrOCl_2 \cdot 8H_2O$ (25 g) dissolved in hot distilled water (0.5 l; 60–70 °C); the precipitated solution is kept in a water bath warmed at 60–70 °C for 3 h followed by washing the precipitates twice with hot water (0.25 l each time) and drying at 100 °C.

The gel can also be prepared in the manner described above from $ZrO(NO_3)_2 \cdot 2H_2O$ as a starting material [32]. Since residual nitrate ions are thermally decomposed, thorough washing of the precipitates is not needed; a few times would be enough for the decantation washing; in this respect the preparation is easier.

17.2.1.2 **Preparation of Stannia Gel** [33, 34]

A sample of $SnCl_4 \cdot nH_2O$ (100 g) is dissolved in distilled water (3 l) followed by addition of a 28% NH_3 solution dropwise with stirring, and the final pH of the solution is adjusted to 8. The precipitated product is collected by filtration, suspended in a solution containing 2–4% CH_3COONH_4, and washed three to five times. The precipitates are filtered by suction, dried at 100 °C for 24 h, and finally ground.

The gel is obtained as fine particles when it is washed with distilled water, and a large part of the precipitate passes through a conventional filter paper, resulting in diminished yields. This difficulty can be avoided by washing the gel with aqueous ammonium acetate solution, which provides a quantitative yield.

17.2.1.3 **Preparation of H_4TiO_4** [30]

A volume of $Ti[OCH(CH_3)_2]_4$ (290 ml) is added to distilled water (2 l) with stirring, and the white precipitates formed are dissolved by gradually adding conc. HNO_3 (250 ml) with stirring. Ammonia solution (28%, ~300 ml), is added into the aqueous solution with stirring until pH 8 is attained. The solution is then allowed to stand for a day. Washing is then undertaken by decantation of a 5 l beaker of deionized water twice. Finally the resultant material is dried at 100 °C for 24 h.

Another method of preparing H_4TiO_4 is by hydrolysis of $TiCl_4$ as follows. A volume of $TiCl_4$ (80 ml) is gradually added to distilled water (2 l) in a 5 l beaker cooled by ice water, with large amounts of HCl gas being formed. Ammonia solution (28%) is added at room temperature until a pH of 8 is attained. The resultant precipitates are washed thoroughly by decantation using 60 l of water until no chloride ions are detected in the filtrate. The aqueous portion might become cloudy during washing, but the white washings can be decanted.

17.2.1.4 **Preparation of $Fe(OH)_3$** [30]

To a solution of $Fe(NO_3)_3 \cdot 9H_2O$ (500 g) dissolved in 2 l of water in a 5 l beaker, ammonia solution (28%, ~300 ml used, pH 8) is added with stirring to precipitate $Fe(OH)_3$. The aqueous portion is decanted from the precipitate after allowing the solution to stand. The precipitates are washed by decantation until the liquid portion becomes cloudy (7–8 times), and dried.

17.2.1.5 **Preparation of $Hf(OH)_4$** [35]

$HfCl_4$ is gradually dissolved in distilled water with care, and the hydroxide is prepared in the manner described above for $Zr(OH)_4$.

17.2.1.6 **Sulfation, Calcination, and Catalytic Action** [30]

The above prepared materials are powdered below 100 mesh and treated with sulfate ions by exposing 2 g of the hydroxides (gel) in 30 ml of aqueous sulfuric acid for 1 h, filtering, drying in a desiccator at room temperature, and finally calcining [36]. The iron materials are again powdered because of solidification after drying [36, 37]. The concentration of H_2SO_4 is 0.5 M for the hydroxides of Zr and Ti [38, 39], 3 M for Sn [40, 41], 0.25 M for Fe [37], and 1 M for Hf [35]. A recent study shows that the optimum concentration for Zr is 0.25 N [42].

After calcination of the sulfate-adsorbed materials in air, the substances are catalytically active for the skeletal isomerization of butane to isobutane at room temperature. The activities are dependent on the calcination temperature. The maximum activity is observed with calcination at 575–650 °C for the Zr catalyst [32], 500–550 °C for Sn [34, 41], 525 °C for Ti [43], 500 °C for Fe [36, 37], and 700 °C for Hf [35].

All the catalysts are calcined in Pyrex glass tubes in air for 3 h and sealed in ampoules while being hot, to minimize exposure to humidity until use.

17.2.1.7 **Preparation of Sulfated Silica** [44]

Silica gel is obtained by hydrolyzing $Si(OC_2H_5)_4$ (100 ml) with water (100 ml) and a few drops of HNO_3. The mixture is stirred until gel formation. The precipitates are obtained by evaporation of excess water and ethanol, formed by hydrolysis of $Si(OC_2H_5)_4$, followed by drying at 100 °C, and powdering. The silica (3 g) is exposed to SO_2Cl_2 for 1 h followed by evacuating HCl evolved by the reaction of surface OH group with SO_2Cl_2 and excess SO_2Cl_2 in vacuum, and calcining in air at 400 °C.

17.2.1.8 **Preparation of Sulfated Alumina**

In the case of the sulfate-treated superacids of Zr, Sn, Ti, Fe, Hf, and Si, superacid sites are not created by the treatment of sulfate ion on the crystallized oxides but rather on the amorphous forms, followed by calcination to crystallization. The superacid of Al_2O_3 is prepared from the crystallized oxide, γ-Al_2O_3 [45, 46].

A highly active catalyst is obtained by hydrolysis of aluminum isopropoxide [47]. Distilled water is added with stirring to a solution of $Al[OCH(CH_3)_2]_3$ (10 g) dissolved in isopropanol (300 ml) to precipitate $Al(OH)_3$, followed by washing the precipitates, drying, and calcining for crystallization at 500 °C for 3 h. The crystallized materials are then hydrated before sulfation. The sample (5 g) is suspended in water (5 l) at 80 °C for 3 h, filtered, and dried at 100 °C. SO_4/Al_2O_3 is obtained by treatment with 2.5 M H_2SO_4 and calcination at 600–650 °C for 3 h.

17.2.1.9 **Property and Characterization**

Properties of the sulfated materials thus prepared are summarized as follows [43, 48].

1. Superacidity is generally created by adsorbing sulfate ions onto amorphous metal oxides followed by calcination in air to convert to the crystalline forms. However in the case of Al_2O_3, a superacid is prepared from the crystallized oxide.

2. Specific surface areas of the catalysts are much larger than those of the oxides without the sulfate treatment except for the Al_2O_3. A particularly large increase in the area is observed on the highly active and acidic catalysts. The main reason for the increase in surface area is the retardation of crystallization by sulfate treatment. The areas of the Al_2O_3 catalysts are smaller than those of the oxides without the sulfate treatment.

3. By XRD analysis the degree of crystallization of the sulfated oxides is much lower than that of the oxides without the sulfate treatment. Temperatures of the crystallization or phase transformation for SO_4/ZrO_2 and SO_4/TiO_2 are circa 150 and 200 °C higher than those for pure ZrO_2 and TiO_2, respectively; the XRD pattern of SO_4/ZrO_2 (650 °C) and SO_4/TiO_2 (525 °C), whose superacidities are highest, are pure tetragonal and anatase forms, respectively.

4. The sulfate samples have IR spectra that are different from those of metal sulfates; the materials show absorption bands at 980–990, 1040, 1130–1150, and 1210–1230 cm^{-1}, which are assigned to the bidentate sulfate coordinated to metal ions.

5. XPS spectra of SO_4/ZrO_2 and SO_4/Fe_2O_3 show that the surface is not $Zr(SO_4)_2$ and $Fe_2(SO_4)_3$, but composed of ZrO_2 and Fe_2O_3 with SO_4^{2-}, respectively. On the other hand, the spectra of SO_4/TiO_2 and SO_4/Al_2O_3 are consistent with the presence of surface $Ti(SO_4)_2$ and $Al_2(SO_4)_3$, respectively.

6. The IR spectra of pyridine adsorbed on SO_4/ZrO_2 and SO_4/TiO_2 show the facile conversion of Lewis sites to Brønsted sites by water molecules. Lewis and Brønsted sites are easily interchangeable by adsorption or desorption of water molecules [49–55].

7. Upon dehydration in N_2 at 375 °C, a new IR peak centered at 1370 cm^{-1} appears; the band is assigned to an S=O stretching vibration and is observed for the catalytically active material [56, 57].

8. The sulfated materials also show oxidizing action at elevated temperatures. In particular the superacids of Fe_2O_3 and SnO_2 demonstrate strongly oxidizing potential at temperatures above 100 °C [58, 59].

9. Catalysts obtained by treatment with sulfuric acid are usually more active than those obtained with ammonium sulfate treatment. However, a recent study shows that the analogous activity is generated on SO_4/ZrO_2 by the kneading method with ammonium sulfate [60].

17.2.1.10 One-Step Method for Preparation of SO_4/ZrO_2 [61–65]

Ward and Ko investigated preparation of sulfate-zirconia aerogels in a one-step synthesis by the sol–gel method followed by supercritical drying [61]. Sulfuric acid is mixed with zirconium *n*-propoxide (16.2 ml of 70 wt% in propanol) in *n*-propanol (30 ml) and reacted with water (1.3 ml) and nitric acid (1.9 ml of 70% w/w) to form a zirconia-sulfate co-gel; supercritical drying with carbon dioxide removes the alcohol solvent forming a high surface area aerogel. The properties and catalytic activities are similar to those of the compounds we have prepared. A single-step sol–gel method has also been used for the preparation of SO_4/TiO_2 [66].

17.2.1.11 Commercial Gels for Preparation of SO_4/ZrO_2 and SO_4/SnO_2

Commercial zirconia-gels are now supplied by chemical companies such as MEL, Nakarai, and Daiichi Kigenso. For instance, XZO631 and 632 are the gels, and XZO682 is a sulfate-adsorbed gel from MEL. According to our experience, commercial gels have often led to catalysts superior to those prepared in the laboratory [67, 68]. Similar observations have been made with SO_4/SnO_2. A commercial gel prepared from *meta*-stannic acid gives satisfactory results for this type of catalysis [69]. SO_4/SnO_2 was prepared using *meta*-stannic acids ($SnO_2 \cdot H_2O$, commercial

grade) supplied by Kojundo Kagaku, Ltd. and Yamanaka & Co. Ltd. The activity for the acid-catalyzed conversion of methanol into dimethyl ether was higher than for catalysts obtained by hydrolysis of $SnCl_4$ and much higher for the isomerization of butane.

17.2.1.12 Effect of Drying and Calcination Temperatures on the Catalytic Activity of SO_4/ZrO_2 [68]

The catalytic activity of SO_4/ZrO_2 varies with the type of zirconia gel and the drying and calcination conditions. The calcination temperature showing the maximum activity and acidity often varies with the type of prepared gel. For instance, the maximum activity for the conversion of butane to isobutane is observed with calcination at 575 and 650 °C, respectively, for the materials prepared from $ZrO(NO_3)_2$ and $ZrOCl_2$ as starting reagent [32].

The activity also depends on the drying temperature of the gel before sulfation. For the gels obtained by hydrolysis of $ZrO(NO_3)_2$ followed by drying at 100 °C and 300 °C, the difference in the calcination temperature showing the maximum activity for the butane conversion was 50 °C, and the difference in maximum activity was a factor of two.

Several sulfated zirconias were prepared by changing the drying temperature of gel in the range 100–400 °C and the final calcination temperature in the range 475–700 °C. It was found that the drying temperatures exhibiting the highest activity for the butane conversion are not always fixed, for instance 200 °C for one and 300 °C for another.

Figure 17.1 summarizes the effect of the calcination temperature on the catalytic activity for butane isomerization over sulfated zirconias prepared from different zirconia gels dried at the optimum temperatures. The figure indicates that the maximum activities are approximately the same for different catalysts even though

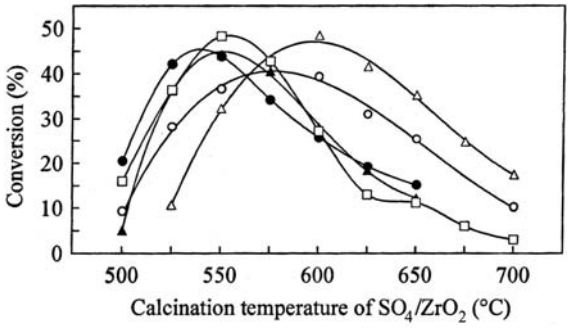

Figure 17.1 Activities for reaction of butane at 180 °C over the SO_4/ZrO_2 catalysts prepared from various Zr gels: MEL 631 dried at 300 °C (□), MEL 632 dried at 200 °C (▲), Nakarai dried at 300 °C (●), and the gels prepared by hydrolysis of $ZrO(NO_3)_2$ (△) and $ZrOCl_2$ (○) followed by drying at 300 and 200 °C, respectively.

the temperatures to give maximum activity are different. The calcination temperatures required to give maximum activity for different catalysts fall within a temperature range <50 °C. Residual species such as Cl^- and NO_3^- in the gel result in differences in the optimum drying and calcination temperatures owing to differences in the state of dehydration of the zirconia gel or to reactivity of the zirconia support with the sulfate species. However, selection of the optimum drying and calcination temperature generate the same ultimate catalytic activity. The present results point out that the optimum temperature for drying the Zr gel and the final calcination should be determined according to the type of zirconia gel.

17.2.2
Tungstated, Molybdated, and Borated Metal Oxides

17.2.2.1 Preparation of WO_3/ZrO_2 and MoO_3/ZrO_2 [30]

A sample of $Zr(OH)_4$ (10 g), obtained from $ZrOCl_2$, is heated at 300 °C, the gels are impregnated with aqueous ammonium metatungstate [$(NH_4)_6(H_2W_{12}O_{40}]\cdot nH_2O$, 50 wt% WO_3, 3.8 g] and water (15 ml) in a 100 ml beaker followed by evaporating water at room temperature, drying, and calcining in air at 800 °C for 3 h. The concentration is 15 wt% W based on the hydroxide, and 13 wt% W after calcination at 650–950 °C. The analogous material is also formed by the kneading method with tungstic acid (H_2WO_4) which is insoluble in water; a wet mixture of $Zr(OH)_4$ (10 g) and H_2WO_4 (2 g) with a little water is kneaded for 3 h [70, 71].

After heating $Zr(OH)_4$ (10 g) at 300 °C the sample is impregnated with molybdic acid (H_2MoO_4, 2.5 g) dissolved in ammonium hydroxide (28%, 2 ml) and water (15 ml) followed by evaporating water at room temperature, drying, and calcining at 800 °C in air for 3 h. The concentration is 5 wt% Mo metal based on the hydroxide [72].

17.2.2.2 Preparation of WO_3/SnO_2, WO_3/TiO_2, and WO_3/Fe_2O_3 [30]

After the hydroxides of Sn, Ti, and Fe, prepared by hydrolysis of $SnCl_4$, $TiCl_4$, and $Fe(NO_3)_3$, respectively, are dried at 300 °C, the gels are impregnated with aqueous ammonium metatungstates [$(NH_4)_6(H_2W_{12}O_{40})$] followed by evaporating water, drying, calcining in air for 3 h at 1000, 700, and 700 °C for the Sn, Ti, and Fe materials, respectively. The concentration is 15 wt% W based on the hydroxides (11–13 wt% W after calcination) [73, 74].

WO_3/SnO_2 is also prepared from a commercial gel, used after drying *meta*-stannic acid of Kojundo Kagaku, Ltd. at 100 °C [69]. Calcination at 1000 °C after impregnation of the tungstate generates the highest activity for acid-catalyzed reactions. High temperatures such as 1000 °C for calcination do not discriminate precursor stannia gels, though the calcination temperature giving the highest activity for SO_4/SnO_2 differs according to the gel.

17.2.2.3 Preparation of B_2O_3/ZrO_2 [75, 76]

Zirconium hydroxide is impregnated with aqueous boric acid followed by evaporating water and calcining in air at 650 °C (3 wt% B). The same catalyst is obtained

by suspending the hydroxide in 2-propanol solution of trimethyl borate followed by adding water to hydrolyze the borate.

17.2.2.4 **Property and Characterization**

Properties of the catalysts thus prepared are summarized as follows [43, 48].

1. Superacid sites are not created by impregnation on the crystallized oxides, but on the amorphous forms whose calcination then converts them to the crystalline forms. Recent work shows that a WO_3/ZrO_2 catalyst prepared by impregnation of the crystalline zirconia (65% tetragonal, 35% monoclinic) exhibits comparable behavior [77, 78].
2. WO_3/ZrO_2(800 °C) and MoO_3/ZrO_2(800 °C), whose activities are highest, are observed to be 100% tetragonal ZrO_2 by XRD, with the TiO_2 in WO_3/TiO_2(700 °C) being the anatase polymorph [74].
3. Specific surface areas of the WO_3 and MoO_3 catalysts are much larger than those of the oxides without tungsten and molybdenum oxides, pure metal oxides.
4. XPS spectra of the WO_3 and MoO_3 supported catalysts show their surface to be WO_3 or MoO_3 and ZrO_2, SnO_2, TiO_2 or Fe_2O_3 [73].

17.3 Determination of Acid Strength

Several methods have been used to determine the surface acidity of solid acids, but each method has its limitations. Common methods are titration with the Hammett indicators, temperature-programmed desorption (TPD) , adsorption microcalorimetry, catalytic test reactions, and IR and NMR spectroscopies. These techniques exhibit several advantages and disadvantages.

Titration with a variety of Hammett indicators is one of the most widely used techniques to determine the distribution of acid strengths on the solid surface [79]. However, many arguments have been raised in the past against the use of Hammett indicators for evaluation of solid acidity [80–83].

A commonly used technique is TPD of adsorbed bases such as ammonia and pyridine [84–86]. However, there are critical questions in this method [87–89]. The NH_3 molecule is well known to interact with both the acidic OH group and the basic oxygen [90]. Thus, NH_3 gives information on dual acid–base sites.

Instead of TPD, microcalorimetry of adsorption shows the heat evolved during the adsorption of probe molecules, usually ammonia, on acid sites [91–94]. This measurement can determine the distribution of adsorption enthalpies but cannot differentiate between adsorption on Lewis and Brønsted acid sites.

Catalytic activity can be used to rank solid acidity, and activity for the skeletal isomerization of butane is often used to indicate very strong acidity, in particular superacidic strength [95]. A comparative study using the isomerizations of butane

and pentane as test reactions gave good correlations between their rate constants and the Hammett acid strengths [96]. These test reactions do not differentiate between the acid strength and the number of acid sites. The mechanism of butane or pentane isomerization, however, has been shown to be bimolecular, so rates of alkane isomerization alone cannot be used to compare acidities [97–100]. One paper indicates that the isomerization of α-pinene enables solid acids to determine the Brønsted acid strength; superacidity promotes the formation of limonene over camphene [101].

A comparative study using IR spectroscopy can rank solid acidity by determining the frequency shift of the adsorption band of pyridine [102], the band shift of OH groups due to the adsorption of benzene or CD_3CN [103, 104], and the shift of the adsorbed CO on Lewis sites [105]. These IR techniques, however, are not widely used for evaluation of solid acidity.

Solid-state NMR spectroscopy enables site-specific characterization of solid acids such as protonated zeolites [106, 107]. Attempts have been made to relate the acid strength of solids to the ^1H chemical shift of surface OH groups, the shift brought by the adsorbed bases such as CD_3CN and CCl_3CN, and the ^{31}P shift of the adsorbed $^{31}P(CH_3)_3$ [108–113]. A disadvantage of NMR spectroscopy is the complicated chemical shift due to hydrogen bonding.

17.3.1 Hammett Indicators

The acid strength of a solid is defined as the ability of the surface to convert an adsorbed neutral base into its conjugate acid. The strength is expressed by the Hammett acidity function, H_0, as explained in the Introduction. The color of suitable indicators adsorbed on a surface can give a measure of acid strength. If the color is that of the acid form of the indicator, then the value of the H_0 function of the surface is equal to or lower than the pK_{BH^+} of the conjugate acid of the indicator. Lower values of H_0 correspond to greater acid strength.

The acid strengths shown in Table 17.3 were examined by the visual color change method using the Hammett indicators shown in Table 17.1 [43, 48]. The indicator dissolved in solvent was added to the sample in powder form in a nonpolar solvent, sulfuryl chloride [38] or cyclohexane [40]. The strength of colored materials such as SO_4/Fe_2O_3 and MoO_3/ZrO_2 was estimated from their catalytic activities in comparison with those of the catalysts determined by the Hammett-indicator method.

Determination of the acid strength of solid catalysts using Hammett indicators, however, has been criticized frequently because of the heterogeneity of the solid surface [81, 104, 110, 114–116]. The principle of the Hammett acidity function is based on the equilibrium equation in a homogeneous solution, and its application to the heterogeneous condition is subject to severe criticism. In addition, the color change of the adsorbed indicators on solids as determined by the naked eye is subjective. The effects of interactions between the solvent and the solid surface has also been raised [9].

Table 17.4 Acid-catalyzed reactions.

Dehydration of alcohol → MeOH, EtOH, i-PrOH
Decomposition of alkylbenzene → Ph-Me, Ph-Et, Ph-^{i}Pr
Friedel–Crafts acylation → acetylation, benzoylation, and so on
Isomerization of paraffin → open-chain C_1–C_7, cyclic C_6–C_{12}
Esterification → AcOH + MeOH, EtOH, and so on
C_8OH + phthalic acid, and so on
Cationic polymerization → Me, Et, ^{i}Bu vinyl ether
Oligomerization → β-pinene, 1-octene, 1-decene
Others → aldol condensation, and so on

17.3.2
Test Reactions

Owing to the heterogeneity of solid superacids, accurate acidity measurements are difficult to perform and interpret. The most simple and useful way to estimate the acidity of a solid catalyst is to test its catalytic activity in acid-catalyzed reactions. We usually compare activity with those of aluminosilicates such as silica-aluminas and zeolites. These materials have strong enough acidities to cause the Friedel–Crafts reactions, and their acidities are known to be in the range of superacidity [117]. The Hammett-indicator method indicates that the acid strength of the SiO_2-Al_2O_3 used is in the range of $-12.70 < H_0 \leq -11.35$, whose acidity is $H_0 = \sim\!-12$ and superacidic [37]. The acidity and catalytic activity of zeolites are generally higher than the silica-aluminas, with mordenites being highest among them ($H_0 = \sim\!-14$) (ZSM-5: $H_0 = \sim\!-13$) [67].

In order to confirm the acidity results measured using the indicators shown in Table 17.1, we have investigated as many acid-catalyzed reactions as possible. The reactions are summarized in Table 17.4 [43, 48, 118, 119]. Among them, the skeletal isomerization of light paraffins, in particular butane and pentane, has been the most widely applied. The isomerization of butane at room temperature was a well known test reaction for superacidity at the beginning of this work [43, 48, 118]. The activity for many of the reactions tested correspond to the acidities as determined by use of the Hammett indicators.

17.3.3
Temperature-Programmed Desorption (TPD)

TPD using base adsorbents such as ammonia and pyridine has been one of the common techniques to evaluate the amount and strength of acid sites on solid acids. However, the desorption temperature of ammonia and pyridine adsorbed on solid superacids is so high (500 °C and above) owing to the strong interaction that the adsorbed compounds are decomposed or oxidized before desorption. The surface structure can even be destroyed by reactions with probe molecules [120–122].

TPD using pyridine was attempted for estimating the acidity of superacidic materials, even though this method suffers a major drawback. An examination of the termination temperature of pyridine desorption was made using TG-DTA [123]. When the adsorbed compound is decomposed or oxidized to destruction before desorption, its temperature must be below that of the real desorption. The temperatures of pyridine desorption obtained were generally proportional to the H_0 values of the highest acid strength determined by the Hammett method or estimated by catalytic activity, except that of SO_4/SnO_2. All of the temperatures for the superacids were higher than those of Al_2O_3, ZrO_2-TiO_2, SiO_2-ZrO_2, and SiO_2-Al_2O_3, whose acidities are below superacidic, and whose oxidative action is quite weak. In the case of SO_4/SnO_2 whose temperature was unexpectedly low, oxidation of the adsorbed pyridine occurred on the catalyst surface at a temperature below that expected from the acid strength by the Hammett method.

17.3.4
Temperature-Programmed Reaction (TPRa)

Another method similar to TPD, is temperature-programmed reaction (TPRa) using furan as a probe molecule [118]. Furan is resinified on the surface of solid acids when heated at a temperature that depends on the acid strength. Solids with weak acidity give rise to the reaction at elevated temperatures, and the reaction temperature is dependent on the surface acidity. A relationship is observed between decrease of the temperature and increase of the acid strength. The resinification of furan adsorbed on the surface of catalyst is exothermic, and TPRa using DTA is a technique for estimating the acid strength of superacids.

The initial temperatures of resinification were compared with the H_0 values of superacids as determined by the Hammett method, and a linear relationship was observed. The TPRa results gave the H_0 value of SO_4/SnO_2 as −18; the value was not determined by the Hammett method because −16.12 relates to 1,3,5-trichlorobenzene indicator which has the lowest pK_{BH^+} value among the Hammett indicators used to date (Table 17.1).

17.3.5
Ar-TPD [124, 125]

A new method has involved the use of Ar as a probe atom. We tried Ar as a probe TPD and found that Ar-TPD could be applied to the evaluation of the acid strength of solid superacids.

Noble gases such as Ar and Xe interact only with the acidic sites, giving information on these sites. Hence these atoms are useful as probes of the intrinsic nature of the acidic sites. For noble gases, polarization and dispersion are dominant. Ar shows an acid–base-like interaction in a polarized state with acid sites at low temperature owing to its induced dipole.

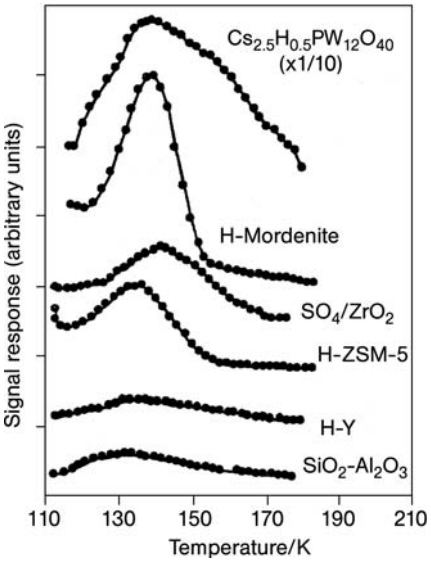

Figure 17.2 Ar-TPD profiles of solid acids; temperature programmed rate: 2 K min^{-1}.

The acid strength was first evaluated as an activation energy of Ar desorption. The activation energy was calculated by the following equation:

$$2\ln T_m - \ln b = E_d/RT_m + \text{const} \tag{17.5}$$

Here T_m is the peak temperature of desorption, b the rate of temperature increase, and E_d the activation energy. A linear plot is obtained between 2 ln T_m – ln b and $1/T_m$, and E_d is determined from the gradient.

The Ar-TPD experiments were performed in the temperature range 113–223 K at the programmed rate of 2–5 K min^{-1} using a cooling system with N_2 gas bubbled through liquid N_2 along with an electric heater regulated by a temperature controller. The profiles at the rate of 2 K min^{-1} are shown Figure 17.2. The activation energies of Ar desorption are calculated from the estimated values of T_m to be 5.5, 6.0, 6.6, 6.7, 7.6, and 9.3 kJ mol^{-1} for SiO_2-Al_2O_3, zeolites of H-Y, H-ZSM-5, and H-Mordenite, heteropoly acid ($Cs_{2.5}H_{0.5}PW_{12}O_{40}$), and SO_4/ZrO_2, respectively. The value for SO_4/SnO_2 is determined to be 10.6 kJ mol^{-1} [33, 34].

The heat of adsorption of ammonia correlates with the Hammett acidity function, H_0. Similarly, the activation-energies of SiO_2-Al_2O_3, three zeolites, and SO_4/ZrO_2 relate well with their H_0 values determined by the Hammett method and represented by their highest acid strengths, with a linear plot being obtained. By extrapolation of the linear plot to the activation energy 9.3 kJ mol^{-1} for SO_4/ZrO_2, the H_0 value is estimated to be –19 [68] , which agrees with that estimated from the heat of adsorption of ammonia [93]. The value of 10.6 kJ mol^{-1} found for SO_4/SnO_2 is estimated to correspond to $H_0 = -21$.

17.3.6
Ar-Adsorption [126, 127]

The heat of adsorption of Ar was also measured for acidity evaluation. In the case of Ar-TPD, an effect of the probe molecule diffusion in micropores is observed with some samples, such as zeolites, at high temperature-programmed rates. The adsorption method is not influenced by diffusion of the adsorbed molecule because the Ar isotherm is measured at static equilibrium. It is also advantageous that the usual BET apparatus can be used to obtain the adsorption isotherm. In addition, the adsorption behavior of Ar is of the Henry type at temperatures around room temperature.

Langmuir's adsorption equation can be converted into the following equation by the introduction of an approximation at low coverage:

$$\ln(V/P) = -(\Delta H/RT) + \ln b_0 + \ln V_m \tag{17.6}$$

where V is the volume adsorbed, P is the equilibrium pressure, ΔH is the heat of adsorption, R is the gas constant, T is the adsorption temperature, b_0 is a constant, and V_m is the volume corresponding to a monolayer. The heat of adsorption (ΔH) is calculated from the gradient of a plot of ln (V/P) vs $1/T$. This method of calculation is known as the H-method.

Experimental results by means of the volumetric method using a conventional BET system were observed to be Henry type in the temperature range 233–313 K and the pressure range $P = 5$–30 kPa, achieving the condition of small coverage. An example adsorption isotherm, for H-mordenite, is shown in Figure 17.3.

In addition to the above technique, the heat of adsorption can also be determined from Langmuir-type adsorption isotherms. Langmuir's adsorption equation pro-

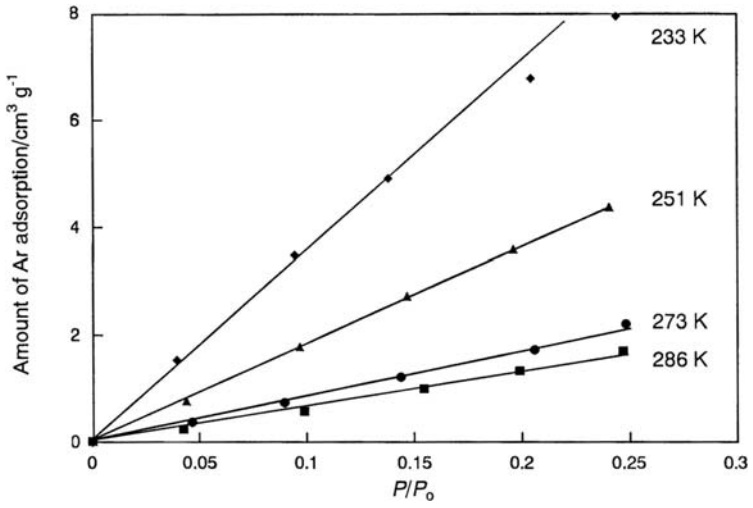

Figure 17.3 Adsorption isotherm of Ar on H-mordenite at various temperatures.

Table 17.5 Adsorption heats of Ar and acid amounts of various solid acids.

Sample	$-\Delta H_H$[a] (kJ mol^{-1})	$-\Delta H_L$[b] (kJ mol^{-1})	V_m[b] (mmol g^{-1})
SO_4/SnO_2	23.5	29.6	0.10
SO_4/ZrO_2	22.4	26.3	0.009
WO_3/ZrO_2	21.6		
SO_4/Fe_2O_3	18.9		
ZSM-5	17.3	17.9	0.39
Mordenite	17.3	17.7	1.44
Beta		17.1	0.10
HY	14.8	15.6	0.35
SiO_2-Al_2O_3	14.4	14.9	0.35
3 wt% Pt-SO_4/ZrO_2	22.8		
7.5 wt% Pt-SO_4/ZrO_2	24.6		

a Calculated by H-method.
b Calculated by L-method.

vides information regarding the saturated adsorption amount. It is expected that the number of adsorbed atoms translates into the number of acid sites on the solid surface. In this case, the heat of adsorption (ΔH) is related to the adsorption constant (b) as follows:

$$b = b_0 \exp(-\Delta H/RT) \tag{17.7}$$

and the adsorption heat is calculated from the gradient of a plot of ln b vs $1/T$. This method of calculation is known as the L-method.

On comparing the two methods of measurement, the advantage of the H-method is its ease of operation and its shorter experimental time. However, the adsorption isotherm must be measured with care, as the concentration of adsorbate is quite small in the low equilibrium pressure range.

The calculated heats of adsorption are summarized in Table 17.5 [125, 128]. The heats of adsorption presented are comparable with those obtained by applying the Henry and Langmuir equations. The relative order of SO_4/ZrO_2, mordenite, and ZSM-5 is consistent with that of the acid strength evaluated by the heat of ammonia adsorption [93]. The value of SO_4/SnO_2 is higher than that of SO_4/ZrO_2, indicating higher acidity for the former, the strongest acidity among the solid metal oxide-based superacids. For both materials, the heats of adsorption determined by the H-method are lower than those by the L-method. The heats of adsorption of Ar obtained from the L-method indicate the highest acid strength. On the other hand, the H-method provides an average value that includes the weak acid sites, owing to the wide pressure range used in the measurement. The saturated adsorption amount is the number of acid sites with high acidity. In general, ammonia cannot be used as a probe molecule for solid acids containing a component that actively decomposes ammonia, for example platinum. The table indicates that the present technique is applicable for metal-containing solid acids.

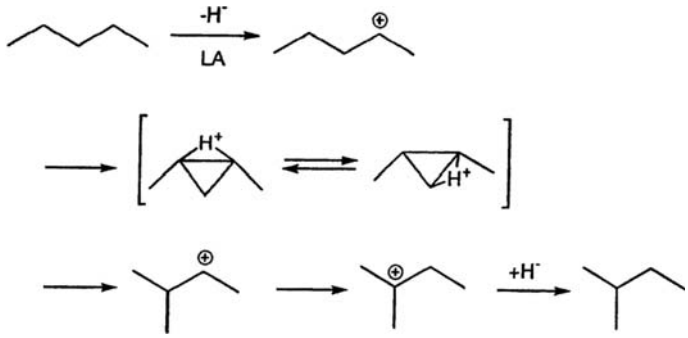

Scheme 17.1 Isomerization of pentane via monomolecular intermediate.

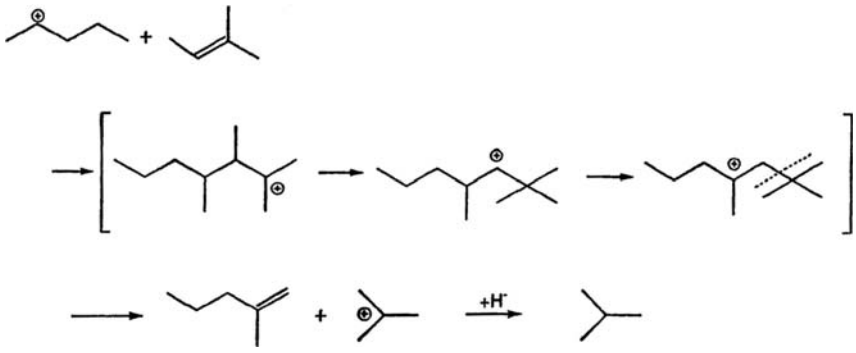

Scheme 17.2 Disproportionation of pentane via bimolecular intermediate.

17.4
Nature of Acid Sites

The skeletal isomerization of butane to isobutane is a typical reaction catalyzed by superacidity. Early in the history of this work, SO_4/Fe_2O_3, SO_4/TiO_2, and SO_4/ZrO_2, were termed superacids owing to their ability to isomerize butane at room temperature or below [32, 37, 39] The formation of isobutane from butane, however, does not necessarily require superacidic strength. A bimolecular reaction pathway based on the intermediacy of butane is energetically lower than a monomolecular mechanism [129–133]. The monomolecular and bimolecular mechanisms are shown in Schemes 17.1 and 17.2, respectively, using pentane as a model.

The processes are the monomolecular reaction through a protonated cyclopropane produced by the abstraction of H^- over Lewis acid sites and the bimolecular mechanism where an olefin takes part in the reaction. The olefin is produced over Brønsted acid sites. In the case of butane in the monomolecular mechanism, isobutane is formed through protonated methylcyclopropane with an activation energy of 8.4 kcal mol^{-1} followed by the formation of the primary isobutyl cation with high energy [134].

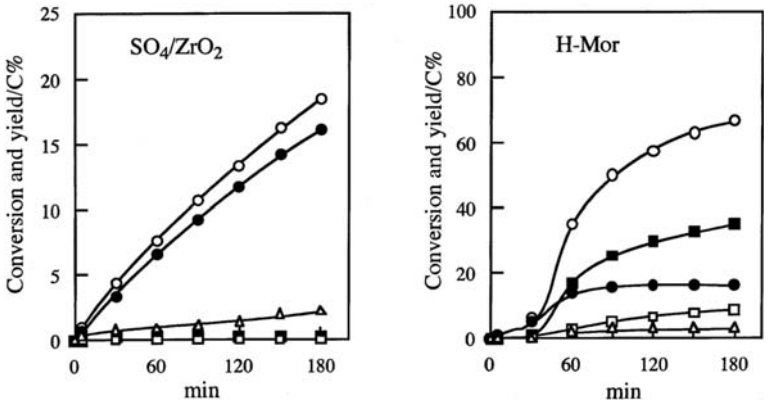

Figure 17.4 Isomerization and disproportionation of pentane on SO_4/ZrO_2 at 0 °C and H-mordenite at 200 °C; conversion (○), butane (□), isobutane (■), isopentane (●), hexanes (△).

On the Brønsted acid sites, H^+ is added to the C—H bond of the substrate, followed by elimination of H_2 and formation of the secondary butyl cation. The catalyst surface would be in a proton-deficient condition owing to the elimination of H^+ as H_2. As a result, the secondary butyl cation releases H^+ to convert into an alkene, which is an intermediate of the bimolecular reaction. The thermodynamic stability of the tertiary cation is higher than that of the secondary cation. The former cation is easily formed by methyl migration followed by a 1,2-hydrogen shift. The tertiary carbenium ion releases H^+ readily, converting into isopentene, and this would be the intermediate of the bimolecular reaction. The reaction proceeds via the bimolecular mechanism of oligomerization–cracking involving the formation of a C_{10} intermediate. This is formed from a C_5 alkene and C_5 cation followed by rearrangement and β-scission to yield isobutane as the final product, as shown in Scheme 17.2. Butane is also converted into isobutane in the same manner.

In order to compare the catalytic action of SO_4/ZrO_2 with that of H-mordenite (H-Mor), the reaction of pentane was performed in a closed recirculation system. The changes of product yields against reaction time are shown in Figure 17.4 [135]. The reaction rate with SO_4/ZrO_2 at 0 °C is almost constant during the reaction, and the main product is isopentane, with small amounts of isobutane and hexanes being detected.

In contrast, the reaction over H-Mor at 200 °C has different characteristics than that over SO_4/ZrO_2. H-Mor is inactive at 0 °C, and at 200 °C a short induction period is observed for the catalytic activity and product selectivity. Although the production of isopentane is predominant in the induction period, an increase in the activity is observed along with the formation of isobutane, butane, and hexanes. The main product is isobutane after the induction period, highlighting the effect of Brønsted acid sites. The surface alkenes for the bimolecular mechanism

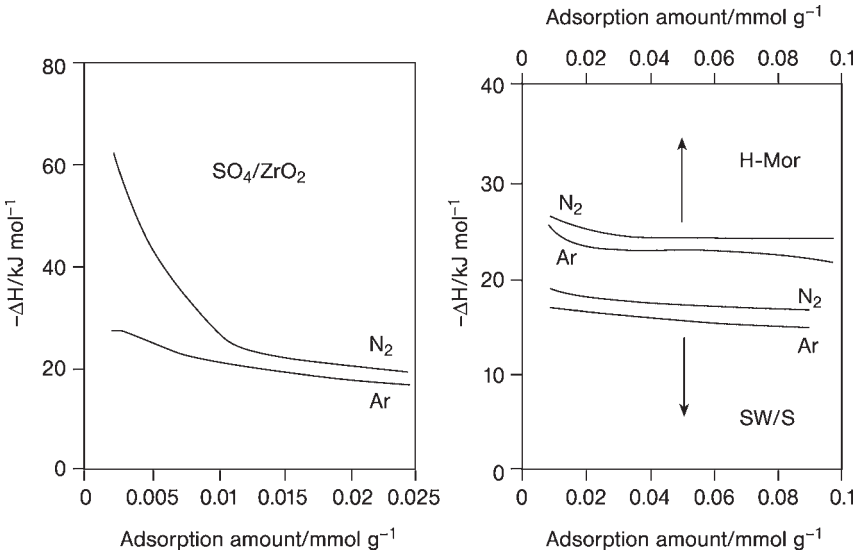

Figure 17.5 Heats of adsorption of Ar and N_2 on SO_4/ZrO_2, H-Mor, and SW/S.

are produced on the Brønsted acid sites, and alkenes accumulate on the surface during the induction period. The activity increases with increase in the amount of the accumulated alkenes. This leads to the conclusion that the monomolecular reaction proceeds on SO_4/ZrO_2 and the bimolecular mechanism proceeds on H-mordenite.

In order to examine the nature of acid sites on SO_4/ZrO_2, the heats of adsorption of N_2 and Ar were measured and compared with those of H-Mor and a heteropoly acid ($H_4SiW_{12}O_{40}$) supported on SiO_2 (SW/S). Both heats plotted against the quantity adsorbed are shown in Figure 17.5 [136]. The heat of adsorption of N_2 is larger than that of Ar, with the difference being 2–3 kJ mol^{-1} on H-Mor and SW/S. Both heats decrease gradually with increasing adsorption amounts, with an almost constant relationship. On the other hand, SO_4/ZrO_2 behaves differently. In particular, a very large heat of adsorption, more than 60 kJ mol^{-1}, is obtained for N_2 adsorption on SO_4/ZrO_2, which is much larger than that of H-Mor and the difference in the adsorption heats of the two gases is more than 30 kJ mol^{-1}.

The nitrogen molecule is strongly adsorbed on Lewis acid sites by interaction between the 5σ electron pair and the vacant molecular orbital of the Lewis site [137]. The stabilization of the N—N bond in addition to the stabilization by adsorption on the acid sites is responsible for the large heat of N_2 adsorption. The acid sites on SW/S are of Brønsted type [138], and the acidity on H-Mor is also regarded as Brønsted type, though a small number of Lewis sites are generated by treatment at high temperatures [139]. This is consistent with the formation of isobutane from pentane. Therefore it is concluded that the acidity of sulfated zirconia is of Lewis type.

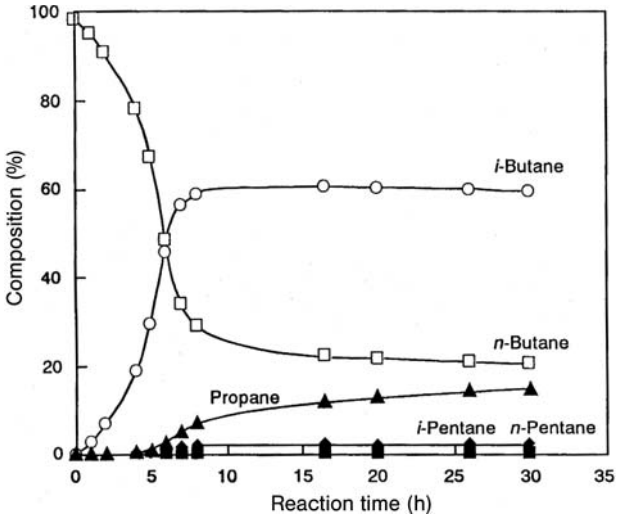

Figure 17.6 Reaction of butane over SO_4/ZrO_2 at 0 °C; the catalyst was pre-treated at 250 °C in vacuum for 3 h.

17.5
Isomerization of Butane Catalyzed by Sulfated Zirconia [140]

The skeletal isomerization of butane catalyzed by SO_4/ZrO_2 was carried out in a closed recirculation system under mild conditions, at 0 °C for a long reaction period; the results are shown Figure 17.6. A long induction period, ~4 h, is observed with the sole formation of isobutane. At longer times on stream, an increase in the activity is observed along with the formation of propane and pentanes. The ratio of butane to isobutane is close to the equilibrium value after 8 h. The apparent activation energy is 13.0 kcal mol^{-1} in the induction period and 8.8 kcal mol^{-1} after that period. The activation energy of the monomolecular mechanism is higher than that of the bimolecular mechanism. The isomerization of butane proceeds via a primary carbenium ion in the former mechanism and via a secondary carbenium ion in the latter. The monomolecular reaction is predominant on superacidic Lewis sites in the induction period, and the reaction changes to the bimolecular process on Brønsted sites by the formation of surface alkene intermediates, giving rise to the additional C_3 and C_5 products. The number of Brønsted sites over SO_4/ZrO_2 is reduced, and the proportion of Lewis sites is increased with increasing evacuation temperature. On the catalyst pre-treated in vacuum at 250 °C, some Brønsted acidity remains and causes the bimolecular reaction. However, the activity increase disappears and only isobutane is obtained on catalysts treated at 450 °C or higher, which is indicative of the monomolecular reaction.

17.6
Isomerization of Cycloalkanes [141]

Cyclohexane is known to be isomerized to methylcyclopentane when catalyzed by strong acids. In fact, the SO_4/ZrO_2 catalyst converts cyclohexane into methylcyclopentane and methylcyclopentane into cyclohexane [119, 142, 143]. The reactions proceed by the monomolecular mechanism via the intermediacy of secondary and tertiary carbenium ions followed by protonated cyclopropanes.

The isomerization of open-chain alkanes with more than six carbon atoms gives isobutane as the main product, together with disproportionated materials, even though the reaction proceeds by the monomolecular pathway [144]. On the other hand, for cyclic alkanes the monomolecular process with preservation of the cyclic structure seems to be the most probable, judging from the results for cyclohexane. The absence of isobutane in the products indicates that the reaction path does not involve open-chain intermediate species. Therefore, it is of interest to try cycloalkanes larger than cyclohexane for clarification of the reaction mechanism along with the catalytic action of SO_4/ZrO_2.

The skeletal isomerization of cycloalkanes with more than six carbon atoms, that is cycloheptane, cyclooctane, cyclodecane, and cyclododecane, was performed over SO_4/ZrO_2 in the liquid phase at 50 °C.

The results for cycloheptane after 30 min reaction time are shown in Table 17.6. Methylcyclohexane is the major product, with a selectivity of 97%, in addition to small amounts of four dimethylcyclopentanes and ethylcyclopentane. The reaction of methylcyclohexane under the same conditions also produced the latter five compounds, and the system reached its equilibrium state after 90 min of reaction.

The reaction results of cyclooctane are shown in Table 17.7. The major product is ethylcyclohexane with a selectivity of 93%. Small amounts of five dimethylcyclohexanes and methylcycloheptane were formed in addition. The comparable reaction of ethylcyclohexane produced dimtheylcyclohexanes and methylcycloheptane.

The reaction results of cycloheptane and cyclooctane indicate that the monomolecular pathway is followed, preserving the cyclic structure, without the formation

Table 17.6 Product distribution for the reaction of cycloheptane at 50 °C after 30 min reaction time over SO_4/ZrO_2.

Product	Yield (%)	Selectivity (%)
Methylcyclohexane	53	97
trans-1,2-Dimethylcyclopentane	0.7	1.3
trans-1,3-Dimethylcyclopentane	0.4	0.7
1,1-Dimethylcyclopentane	0.3	0.4
cis-1,3-Dimethylcyclopentane	0.2	0.3
Ethylcyclopentane	0.2	0.3

Table 17.7 Product distribution in the reaction of cyclooctane at 50 °C after 30 min reaction time over SO_4/ZrO_2.

Product	Yield (%)	Selectivity (%)
Ethylcyclohexane	57	93
trans-1,2-Dimethylcyclohexane	2.1	3.3
Methylcycloheptane	1.1	1.7
cis-1,3-Dimethylcyclohexane	1.0	1.3
trans-1,4-Dimethylcyclohexane	0.2	0.3
1,1-Dimethylcyclohexane	0.1	0.2
trans-1,3-Dimethylcyclohexane	0.1	0.2

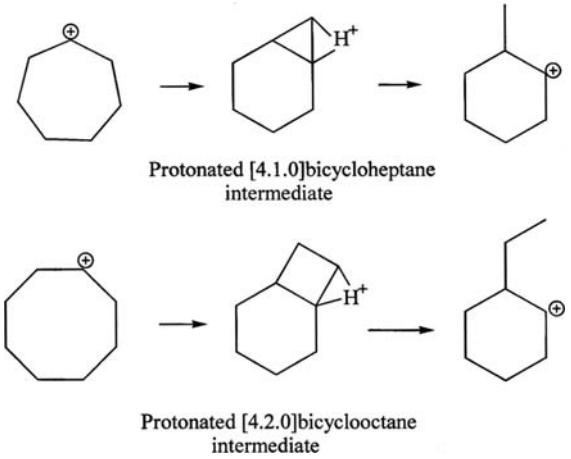

Scheme 17.3 Intermediates for the isomerizations of cycloheptane into methylcyclohexane and of cyclooctane into ethylcyclohexane.

of isobutane through protonated cyclopropane and cyclobutane intermediates, as shown in Scheme 17.3. The structure of the cyclic hydrocarbon has a large effect on reaction. No isomerization was observed with cyclodecane, with decalins being formed by dehydrogenation, and cyclododecane was converted into more than 30 product species by rearrangement, dehydrogenation, and cracking.

17.7 Structure of Sulfated Zirconia

In the very early stages of this work, we studied the catalytic surface using mainly XPS and IR spectroscopy [32], and proposed the surface structure to be SO_4 combined with two zirconium species in a bridging bidentate state (refer to Scheme 17.4). An analogous model was proposed by Segawa and coworkers [53], and Bolis and coworkers [145].

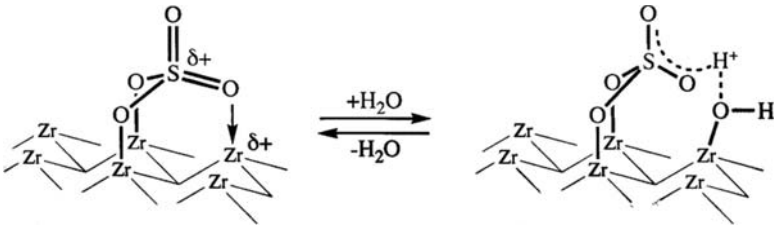

Scheme 17.4 A monosulfate structure.

Later, a number of studies attempted to determine the nature of acid sites in the catalyst. Also applying XPS and IR spectroscopy, Tanabe and others proposed a structure of chelating bidentate complexes, in which the sulfate species chelates to a single Zr atom [102, 146]. This model, a chelating bidentate species, was also proposed by Ward and Ko [61].

Morrow and coworkers proposed a structure, on the basis of ^{18}O exchange using $H_2{}^{18}O$ combined with IR analysis, in which three oxygens from the sulfate groups are bonded to Zr species in a tridentate form [147]. They also pointed out the possibility of the formation of a polysulfate structure at high sulfate loading [148]. This structure was supported by Morterra and coworkers using IR studies of adsorbed pyridine [149].

A monodentate structural model, which contains a bisulfate group, has been proposed by several workers [103, 104]. The bisulfate OH group is hydrogen-bonded to an oxygen on the surface of zirconia. A similar model has been proposed for the surface of sulfated alumina on the basis of NMR studies [150].

Another bisulfate structure was proposed by Riemer and coworkers using NMR and Raman spectroscopies, in which two sulfate oxygens are bonded to Zr atoms in a bridged bidentate state [106]. The same model was also proposed by Lunsford [151] and Clearfield [152].

Models in which SO_3 species are coordinated with zirconia have also been proposed. One of them, suggested by Vedrine and coworkers [52], is coordination of the SO_3 sulfur with lone pairs of the oxygen in ZrO_2 in addition to one of the SO_3 oxygens coordinating with a Zr. Another proposal by White and coworkers [153] is depicted in such a way that two of the SO_3 oxygens are coordinated with surface zirconium atoms, leaving a single S=O moiety. A thionyl tetraoxide species with four oxygens bonded to zirconia together with a single S=O has been proposed at low sulfate content [154].

Finally, sulfated zirconia was investigated by thermal analyses in addition to XPS in order to provide additional information on the surface. On the basis of the observations made, we have proposed possible surface structures of sulfated zirconia [155a]. The active species of sulfated zirconia are decomposed over a quite broad range of temperature, from 700 °C to >1000 °C. XPS data indicates that the S species comprise SO_4^{2-}. An example of the models is shown in Scheme 17.4, where two oxygens are bonded to Zr in addition to coordination of an S=O group with Zr, resulting in three grafting bonds in total. The addition of water causes the breakage

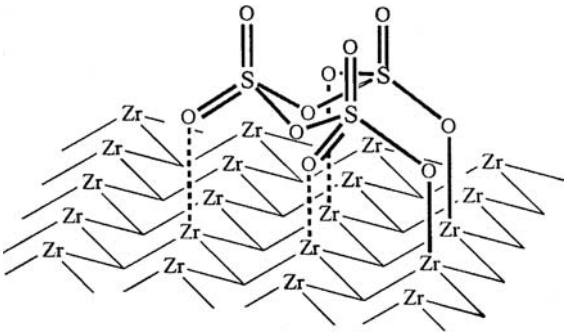

Scheme 17.5 A structural model of a trimer.

of this coordination, generating Brønsted acid sites. Another example, consisting of a cyclic trimer of SO_3, is shown in Scheme 17.5, where two terminal S=O anions are bonded to Zr cations including three coordinations of S=O with Zr. These coordination sites at Zr are also positions for water molecules giving Brønsted acid sites, as shown in Scheme 17.4 in the case of monosulfate species.

The surface is composed of a wide range of coordinated oligomeric species, predominantly species containing 3 or 4 S atoms, with two ionic bonds between S–O– and Zr being formed, which is identical to the models for monomer and trimer (Schemes 17.4 and 17.5). The active site is not on the metal species, but rather on the S atoms.

The addition of water causes the breakage of the coordination bonds to yield Brønsted acid sites strengthening Lewis acid sites, as shown in Scheme 17.4, for example. Many research groups report the simultaneous existence of Brønsted and Lewis acid sites or the reversible transformation between Brønsted and Lewis acidity upon hydration or dehydration [61, 106, 152]. Fraenkel suggests that in order to be an effective superacid, sulfated zirconia should contain a critical amount of moisture [155b]. Several workers propose that the strong acidity requires the presence of both Lewis and Brønsted sites.

17.8
Promoting Effect

17.8.1
Effect of Addition of Metals to Sulfated Zirconia on the Catalytic Activity

A large number of metal-promoted superacids, which are highly active for butane conversion, have been prepared by the addition of metal salts to SO_4/ZrO_2. Metal promoters include Fe-Mn [156–162]: Pt, Pd [163]: Pd [164]: Ga, In, Tl [165]: Pt-Ni [166]: Ni [167]: Mn [168]: Ce [169]: V, Cr, Mn, Fe, Co, Ni, Cu, Zn [170]: Pt, Pd, Ir [171]: Al, Ga [172]: Cu [173]: Al [174, 175a–175d]: Ni-Al [176]: Ga [177–181]: Pt, Nb

[182]: Pt, Cu, Zn, Cd [183]: Pt, Ni, Fe, Cr, Co, W [184]: Pt [185–194]. Among those metals, Fe, Pt, and Ga are promising additives and the simultaneous promotion with Fe and Mn has attracted much attention [195, 196], but their role is not clear. Catalysts containing small amounts of Pt were also developed and the role and state of Pt have been comprehensively summarized in a review by Song and Sayari [197].

A highly active catalyst for the conversion of butane is obtained by adding a large quantity (7–8 wt%) of Pt to SO_4/ZrO_2 [198], though an active component such as platinum is usually present in low quantity, 0.1–0.5%. The most active catalyst is prepared by impregnation of Zr gel with aqueous sulfuric acid followed by impregnation of the sulfated gel with a solution of H_2PtCl_6, followed by calcination [199]. The Pt-SO_4/ZrO_2 thus prepared gives the same butane conversion as SO_4/ZrO_2 but at much lower temperature, the temperature difference being 136 °C. The analogous enhancement of activity is also observed with other noble metals, Ir, Rh, Ru, Os, and Pd [198, 200].

The Pt-added SO_4/ZrO_2 catalyst is generally prepared by impregnation of the sulfated zirconia with $H_2[PtCl_6]$. The charge on the platinum compound has a large effect on the catalytic action [201]. Platinum particles in catalysts prepared using a cationic platinum compound, $[(NH_3)_4Pt]^{2+}$, showed much higher dispersion and more-even distribution than those in the catalysts prepared by an anionic precursor, $[PtCl_6]^{2-}$, because of strong interaction of the former with the support.

17.8.2
Effect of Mechanical Mixing of Pt-Added Zirconia on the Catalytic Activity

An active catalyst for the conversion of butane to isobutane was obtained by mechanically mixing WO_3/ZrO_2 and Pt/ZrO_2 (0.5 wt% Pt) as shown in Table 17.8. The activity of Pt-WO_3/ZrO_2 prepared by co-impregnation of zirconia with W and Pt materials was lower than that of the mechanical mixture of WO_3/ZrO_2 and Pt/ZrO_2 [202]. The reaction was carried out in a reactor in which two catalysts could

Table 17.8 The application of physical mixtures of WO_3/ZrO_2 and Pt/ZrO_2 for the reaction of butane into isobutane.

Catalyst	Products[a] (%)				
	$C_1 + C_2$	C_3	*i*-C_4[b]	*i*-C_4'[c]	C_5[d]
Pt-WO_3/ZrO_2	0	0.1	1.0	trace	0
WO_3/ZrO_2 + Pt/ZrO_2	0	2.9	7.8	0.6	0.2
$Pt/ZrO_2 \rightarrow WO_3/ZrO_2$	1.3	2.3	2.2	0.2	0
$WO_3/ZrO_2 \rightarrow Pt/ZrO_2$	1.4	2.6	1.5	1.2	0

a C_1: methane, C_2: ethane, C_3: propane.
b i-C_4: isobutene.
c *i*-C_4': isobutene.
d C_5: pentane.

Table 17.9 The reaction profile of butane over solid acids mixed with Pt/ZrO_2

Catalyst	Reaction temperature (°C)	Products (%)	
		C_3	*i*-C_4
SO_4/TiO_2	300	0.3	1
$SO_4/TiO_2 + Pt/ZrO_2$	200	6	13
SO_4/Al_2O_3	300	0	0.2
$SO_4/Al_2O_3 + Pt/ZrO_2$	200	4	19
$SO_4/Fe_2O_3 + Pt/ZrO_2$	220	3	7
Mordenite	300	1	2
Mordenite + Pt/ZrO_2	200	22	17
ZSM-5	300	0	0.1
ZSM-5 + Pt/ZrO_2	200	10	3
SiO_2-$Al_2O_3 + Pt/ZrO_2$	240	6	13

Table 17.10 Conversion of propane into butane.

Catalyst	Temperature (°C)	Conversion (%)	Products (%)			
			C_1	C_2	C_4	C_5
SO_4/ZrO_2	200	0.1			0.1	
Pt-SO_4/ZrO_2	200	0.2			0.2	
$SO_4/ZrO_2 + Pt/ZrO_2$	200	3.2	trace	0.2	3.0	trace
$SO_4/ZrO_2 + Pt/ZrO_2$	225	6.1	0.3	1.6	4.1	0.1

C_4: butanes.

be segregated and mixed. In the two arrangements where Pt/ZrO_2 was placed ahead of WO_3/ZrO_2 and WO_3/ZrO_2 was placed ahead of Pt/ZrO_2, the conversions of *n*-butane were less than that of the mechanical mixture, and methane and ethane were significant by-products.

The catalytic activities of several sulfated metal oxides, zeolites, and silica-aluminas were enhanced by addition of Pt/ZrO_2 as shown in Table 17.9. The order of activity of SO_4/MeO_x was $TiO_2 > Al_2O_3 > Fe_2O_3$ [203]. A mixture of SO_4/Al_2O_3 and Pt/ZrO_2 gave the highest selectivity for the skeletal isomerization. The mechanical mixtures of Pt/ZrO_2 with zeolites and silica-aluminas showed satisfactory conversions of butane, but their selectivities for isobutane were low.

Although mixing Pt/ZrO_2 with SO_4/ZrO_2 showed no appreciable enhancement of the activity of SO_4/ZrO_2, a positive effect was observed for the conversion of propane into butanes as shown in Table 17.10 [204]. The catalysts that are effective for butane conversion are not always efficient for propane conversion. As the acidic sites on SO_4/ZrO_2 are stronger than those on SO_4/TiO_2, SO_4/Al_2O_3, and SO_4/Fe_2O_3, it is suggested that a high superacidity is required for activity for propane conversion to butanes by mixing with Pt/ZrO_2.

The effect of mixing was specific to Pt/ZrO_2, because no efficacy was observed with Pt/other metal oxides such as Pt/TiO_2 and Pt/SiO_2. XPS analysis of Pt/ZrO_2 showed the binding energy of Pt 4f to be 72.6 eV, close to that of Pt^{2+}. On the other hand, the binding energies, 70.5–71.2 eV, for Pt-WO_3/ZrO_2, Pt/TiO_2, and Pt/SiO_2 were close to 71.7 eV, the binding energy for Pt^0. The results indicate that the affinity of Pt to ZrO_2 is quite specific.

Aubke and co-workers reported the existence of a molecular $[Pt(CO)_4]^{2+}$ cation from the following synthesis:

$$2\,Pt(SO_3F)_4 + 5\,CO \text{ in } HSO_3F \rightarrow [Pt(SO_3F)_6]\cdot[Pt(CO)_4] \tag{17.8}$$

where Pt^{2+} is a coordinating species [205]. Therefore, it is proposed that Pt^{2+} species on ZrO_2 act as coordinatiom sites for H^- formed during reaction or reservoirs for the coordination of H^-. A stable Pt^{2+} complex with a hydride ion is also known [206].

The catalytic activity of Fe- and Mn-added SO_4/ZrO_2 for butane is three orders of magnitude greater than that of SO_4/ZrO_2 around room temperature [196]. The promotional effect of Fe and Mn is explained in terms of the dehydrogenative action of Fe species giving butene and subsequent conversion via a bimolecular reaction pathway involving C_8 intermediates. Thermodynamically, the dehydrogenation step requires a high temperature. Similar to the case of mixing Pt/ZrO_2, the Fe species might act partly as the coodination sites, or reservoirs, for transfer of H^-.

17.9
Friedel–Crafts Acylation of Aromatics

The Friedel–Crafts reaction has been used as a test reaction since this work started [43, 48]; with the benzylation of toluene with benzyl chloride being achieved with heat-treated iron sulfates. Of the two main reactions, alkylation and acylation, the latter has been predominantly investigated, since it is more difficult than the former. In addition, the catalytic acylation of aromatics via the Friedel–Crafts reaction is attractive for organic synthesis and a prerequisite challenge to green technology. Traditional methods depend on the use of at least stoichiometric quantities of Lewis acids, such as aluminum trichloride and boron trifluoride, because the Lewis catalysts are consumed by coordination with the formed aromatic ketones [207, 208]. A large quantity of acids, and their waste matter after work-up procedures, cause serious environmental problems. There have been several efforts to conduct the reaction using catalytic amounts of acidic promoters. However, a high acidic strength is required on the surface to catalyze the acylation and hence a superacid is desired.

An important test reaction has been the benzoylation of toluene because of the ease of procedure operating in a batch mode at temperatures around 100 °C [209], an example on a comparative study is shown in Table 17.11 [67]. Both sulfated and

Table 17.11 Friedel–Crafts benzoylation of toluene with benzoyl chloride or benzoic anhydride at 100 °C.

Catalyst	Yield (%)	
	Ph-Cl	$(Ph\text{-}CO)_2O$
SO_4/ZrO_2	22	92
SO_4/SnO_2	52	48
WO_3/ZrO_2	19	55
WO_3/SnO_2	14	16

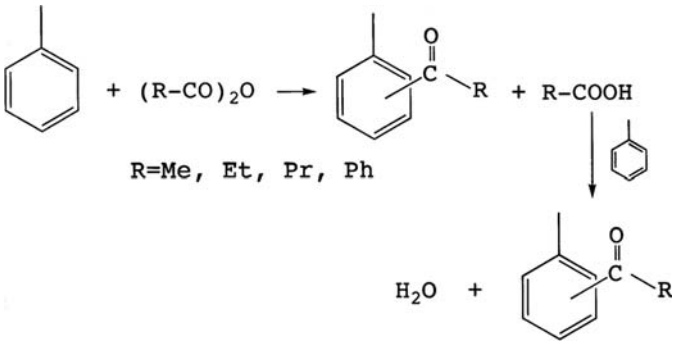

Scheme 17.6 Benzoylation of toluene with alkyl acid anhydride.

tungstated zirconias (Scheme 17.6) along with stannias show satisfactory activities. Yields in the reactions with benzoyl chloride are lower than those with the anhydride, though the reactivity with acylating reagents is generally PhCOCl > $(PhCO)_2O$, with strong acid sites being required for the formation of an acyl cation ($PhCO^+$) from the anhydride. However, the results are not consistent with the reactivity, in particular in the case of SO_4/ZrO_2. The reason is probably associated with strong interactions between oxygens of the anhydride and acid sites on the surface. Benzoylation by the benzoic acid produced does not occur when the reaction is performed with $(PhCO)_2O$; since the reaction occurs at temperatures above the reflux temperature of the mixture.

The catalysts were examined in the acetylation of toluene, one of the difficult acylations because of the difficulty in the formation of an intermediate acetyl cation ($MeCO^+$) from alkyl chain acid anhydrides and hydrides. The reactivities increase as the length of the hydrocarbon chain of the acylating agent is lengthened [210], which shows acetylation to be the most difficult acylation. The heterogeneous acetylation of toluene using solid acidic promoters has not been reported in detail. In fact, to complete acetylation with the anhydride is quite difficult under reflux conditions [211].

Acylations by more reactive acylating reagents with longer hydrocarbon chains, propionylation and butyrylation, have been examined [211]. The SO_4/ZrO_2 catalyst gave higher yields for propionylation and butyrylation than for acetylation, with buyrylation giving the highest yield. The reactivity with acylating reagents is $(PrCO)_2O > (EtCO)_2O > (MeCO)_2O$, which agrees with the stabilities of the intermediates $PrCO^+ > EtCO^+ > MeCO^+$.

The present catalyst was examined in a more reactive acetylation, the acetylation of anisole with acetic anhydride. A quantitative yield of methoxyacetophenone was obtained under the reaction conditions, showing how reactive anisole is in comparison with toluene – demonstrating the effect an oxygen has on reactivity. Several papers concerning the Friedel–Crafts reaction of anisole have been published [212–216], but studies of the reaction of toluene or even benzene are desired. The difference in reactivity between anisole and toluene is close to 100 °C in terms of the reaction temperature.

Although acid anhydride is predominantly used in place of the acid chloride for environmental considerations, the successive acylation with the carboxylic acid produced could be more advantageous, with the most efficient utilization of carbon. In this case, the reaction is equivalent to a dehydrated acylation, which requires strong acidity. In fact, the benzoylation of toluene with benzoic anhydride was carried out at 180 °C, a temperature above reflux, using an autoclave, and marked conversion with benzoic acid produced was observed, though the reaction with the anhydride took place even at 30 °C, as shown in Figure 17.7 [217]. In this point of view, a remarkable reaction is the acetylation of toluene, or benzene if possible, with acetic anhydride up to the consumption of acetic acid produced. A solid acid able to catalyze the reaction of benzene at temperatures below its boiling point, 80 °C, would be highly desirable, since the reactivity of benzene to toluene

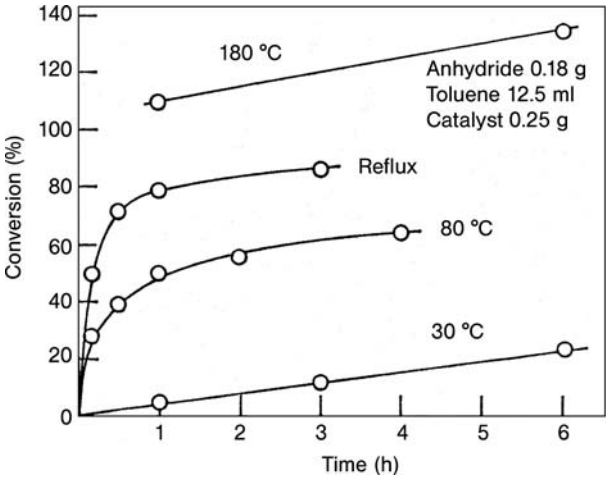

Figure 17.7 Benzoylation of toluene with benzoic anhydride catalyzed by SO_4/ZrO_2.

for acylation is 1/150. In addition, the ultimate catalyst would be one that facilitates the acetylation of deactivated aromatics, for instance nitrobenzene.

17.10
Ceramic Acid

A solid acid calcined at temperatures above 1000 °C is termed a "Ceramic Acid". Ceramics are made by calcination of inorganic materials at elevated temperatures and they possess favorable stability. Brick, usually produced by calcination at temperatures above 1000 °C, is a typical example of one of these materials. Solid acids are generally prepared by calcination at temperatures around 500 °C to generate the highest acidity on the surface, and it is known that the treatment with temperatures above 500 °C causes the surface acidity to reduce. A solid acid prepared by calcination at similar temperatures to a ceramic, would be highly desirable in terms of green chemistry, as a result of the corresponding stability of acid sites.

A pathway into this area arose in a study of the catalytic activity of molybdated zirconia (MO_3/ZrO_2) for the benzoylation of toluene with benzoic anhydride [72]. The catalysts were prepared by addition of different amounts of molybdic acid (H_2MoO_4) to zirconia gel and calcination at various temperatures. The activities are shown as a function of calcination temperature of the catalysts in Figure 17.8 [218]. The figure shows that the effect of modifying the proportion of Mo in the

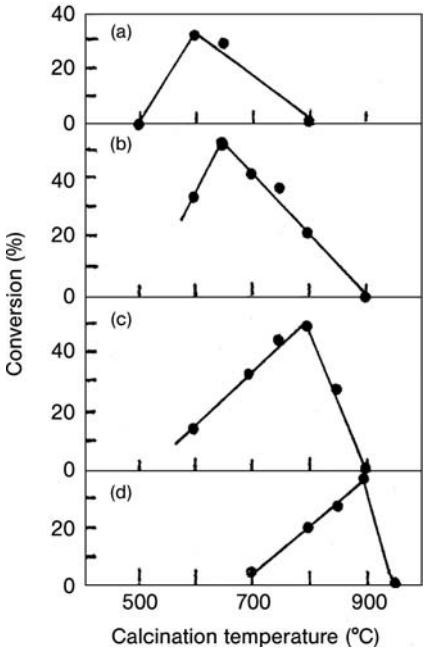

Figure 17.8 Catalytic activities of MoO_3/ZrO_2 for the benzoylation of toluene with benzoic anhydride. Quantity of molybdenum (wt% Mo): 20 (a), 10 (b), 5 (c), and 2 (d).

catalyst is very large. The maximum activity is a strong function of the Mo quantities and observed with 600, 650, 800, and 900 °C for 20%-, 10%-, 5%-, and 2%-Mo/ZrO_2 catalysts, respectively, indicating the lower the quantity, the higher the optimum calcination temperature. Analogous phenomena are also observed with tungstated zirconia [219]. The results indicate that the use of a small quantity of tungsten or molybdenum is desirable.

17.10.1
Tungstated Stannia [220]

A 13%W-added stannia generates remarkable acidity on the surface when calcined at 1000 °C (Table 17.3). The WO_3/SnO_2 catalysts were prepared by drying, at 100 °C, *meta*-stannic acid of Koujundo Kagaku, Ltd. (commercial grade, powdered below 100 mesh) followed by impregnation with aqueous ammonium metatungstate [$(NH_4)_6(H_2W_{12}O_{40})$, Nippon Inorganic Color & Chemical Co.], evaporating the water, drying, and calcining in air for 3 h. The concentrations were 2, 5, 10, 20, 40, and 80 wt% W based on the stannic acid.

The materials thus prepared were examined in the acid-catalyzed conversion of methanol into dimethyl ether. The conversions are shown as a function of calcination temperature of the catalysts in Figure 17.9. The highest activity for 40%- and 80%-WO_3/SnO_2 was observed at a calcination temperature of 800 °C, but materials with lower quantities of W required higher temperatures of calcination for optimum activity. This indicates the main tendency that the lower the quantity, the higher the temperature showing the optimum activity: namely, 900, 1000, 1100, and 1150 °C for the materials with 20, 10, 5, and 2% W, respectively.

The above results led to the synthesis of a ceramic acid, 5–10 wt% W-added SnO_2 materials calcined at 1000–1100 °C. The surface acidity determined by the heat

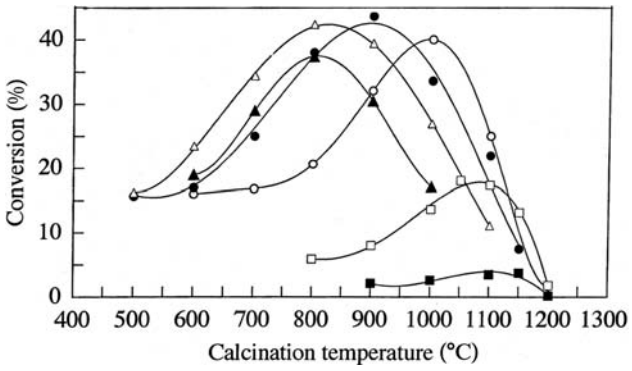

Figure 17.9 Catalytic activities of WO_3/SnO_2 with various concentrations of W for the dehydration of methanol to dimethyl ether at 210 °C. The concentration of W: 80% (▲), 40% (△), 20% (●), 10% (○), 5% (□), 2% (■).

of adsorption of Ar and the catalytic activity for decompositions of toluene and ethylbenzene were intermediate between the values for mordenite and for silica-alumina.

As stable materials, just like brick, ceramics have excellent durability against water. The ceramic catalysts were tested in the esterification of *n*-octanoic acid with methanol to methyl *n*-octanoate to determine their stability to the water liberated. The 5%- and 10%-WO_3/SnO_2 compounds heat-treated at 1100 °C showed activities much higher than mordenites and SiO_2-Al_2O_3 in the presence of water at a reaction temperature of 64 °C, though their activities for alkylbenzenes, together with their acidities, were lower than those of the mordenites.

17.10.2
Tungstated Alumina [221]

Tungstated aluminas (WO_3/Al_2O_3) were prepared by drying aluminum hydroxide [Koujundo Kagaku, Ltd., commercial grade (3N), powdered below 100 mesh] at 100 °C, followed by impregnation with the *meta*tungstate [$(NH_4)_6(H_2W_{12}O_{40})$], evaporation of the water, drying, and calcination in air for 3 h. The concentration applied was from 1 to 20 wt% W based on the alumina gel, denoted as 1%-WO_3/Al_2O_3 (1.18 wt% W after calcination at 1200 °C) and 5%-WO_3/Al_2O_3(4.43 wt% W after calcination at 1000 °C), for instance.

The materials thus prepared were examined in an acid-catalyzed reaction – the cracking of cumene into benzene and propylene. The conversions of cumene into benzene at 250 °C over the catalysts with 1, 3, 5, 10, and 20 wt% W for the impregnated concentration are shown in Figure 17.10. The highest activities for 5%-,

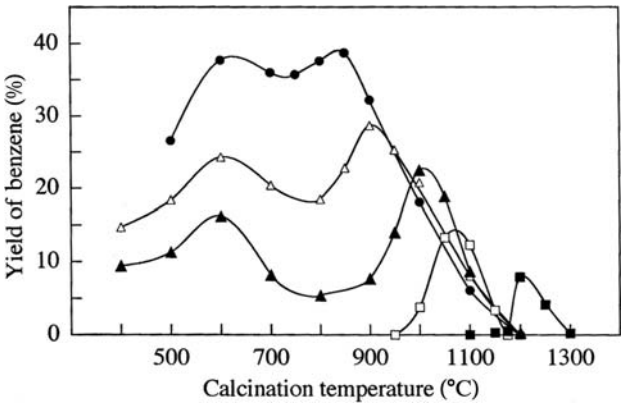

Figure 17.10 Catalytic activities of WO_3/Al_2O_3 with various concentrations of W for the cracking of cumene to benzene and propylene at 250 °C. The concentration of W: 20% (●), 10% (△), 5% (▲), 3% (□), 1% (■).

10%- and 20%-WO_3/Al_2O_3 were observed at two temperatures of calcination; the first temperature was identical among the three materials, 600 °C, and the second one was 850, 900, and 1000 °C for 20%-WO_3/Al_2O_3, 10%-WO_3/Al_2O_3, and 5%-WO_3/Al_2O_3, respectively. For the materials with 3 and 1% W the highest activity is produced by calcination at 1050 and 1200 °C, respectively, though their first peaks are not observed. The materials with lower quantities of W gave their second peaks in the higher temperature range of calcination, again illustrating the tendency: the lower the quantity, the higher the temperature.

The above studies resulted in novel ceramic acids, 1–5 wt%W-added aluminas calcined at 1000–1200 °C. The surface acidity determined by the heat of adsorption of Ar and the catalytic activity for decompositions of toluene, ethylbenzene, and cumene were higher than those of silica-alumina. The crystallographic phase was θ- or α-Al_2O_3.

17.11 Application to Sensors and Photocatalysis

Titanium and tin are important in terms of photocatalytic and sensor applications. There is insufficient space to continue this description here, but the literature on these topics can be found elsewhere [222–232]. Tungstated zirconia, for example, is a promising candidate for an ammonia exhaust gas sensor required to control a Urea-SCR (Selective Catalytic Reduction) system in diesel-engined cars [233, 234].

References

1 Hammett, L.P. and Deyrup, A.J. (1932) *Journal of the American Chemical Society*, **54**, 2721.
2 Gillespie, R.J., Peel, T.E. and Robinson, E.A. (1971) *Journal of the American Chemical Society*, **93**, 5083.
3 Hall, N.F. and Conant, J.B. (1927) *Journal of the American Chemical Society*, **49**, 3047.
4 Gillespie, R.J. (1968) *Accounts of Chemical Research*, **1**, 202.
5 Gillespie, R.J. and Peel, T.E. (1972) *Advances in Physical Organic Chemistry*, **9**, 1.
6 Gillespie, R.J. and Peel, T.E. (1973) *Journal of the American Chemical Society*, **95**, 5173.
7 Olah, G.A., Prakash, G.K.S. and Sommer, J. (1979) *Science*, **206**, 13.
8 Gillespie, R.J. and Liang, J. (1988) *Journal of the American Chemical Society*, **110**, 6053.
9 Olah, G.A., Prakash, G.K.S. and Sommer, J. (1985) *Superacids*, John Wiley & Sons, Inc., New York.
10 Oelderik, J.M., Mackor, E.L., Plattecuw, J.C. and van der Wiel, A. (1965) US Patent 3,201,494.
11 Oelderik, J.M. (1968) US Patent 3,394,202.
12 Olah, G.A. (1973) US Patents, 3,708,553 and 3,766,286.
13 Rodewald, P.G. (1976) US Patents, 3,962,133 and 3,984,352.
14 Dooley, K.M. and Gates, B.C. (1985) *Journal of Catalysis*, **96**, 347.
15 Tanabe, K. and Hattori, H. (1976) *Chemistry Letters*, 625.

16 Hattori, H., Takahashi, O., Takagi, M. and Tanabe, K. (1981) *Journal of Catalysis*, **68**, 132.

17 Namba, S., Ihara, K., Sakaguchi, Y. and Yashima, T. (1980) *Journal of the Japan Petroleum Institute*, **23**, 142.

18 Forsman, W.C., Dziemianowicz, T., Leong, K. and Carl, D. (1983) *Synthetic Metals*, **5**, 77.

19 Lalancette, J.M. and Lafontaine, J. (1973) *Journal of the Chemical Society, Chemical Communications*, 815.

20 Laali, K., Muller, M. and Sommer, J. (1980) *Journal of the Chemical Society, Chemical Communications*, 1088.

21 Laali, K. and Sommer, J. (1981) *Nouveau Journal de Chimie*, **5**, 469.

22 Lalancette, J.M., Fournier-Breault, M.J. and Thiffault, R. (1974) *Canadian Journal of Chemistry*, **52**, 589.

23 Olah, G.A., Kaspi, J. and Bukala, J. (1977) *Journal of Organic Chemistry*, **42**, 4187.

24 Olah, G.A. and Kaspi, J. (1977) *Journal of Organic Chemistry*, **42**, 3046.

25 Yoneda, N., Fukuhara, T., Abe, T., Suzuki, A. and Kudo, K. (1981) *Chemistry Letters*, 1485.

26 Ono, Y., Sakuma, S., Tanabe, T. and Kitajima, N. (1978) *Chemistry Letters*, 1061.

27 Ono, Y., Tanabe, T. and Kitajima, N. (1979) *Journal of Catalysis*, **56**, 47.

28 Ono, Y., Yamaguchi, K. and Kitajima, N. (1980) *Journal of Catalysis*, **64**, 13.

29 Heinermann, J.J.L. and Gaaf, J. (1981) *Journal of Molecular Catalysis*, **11**, 215.

30 Arata, K. (1996) *Journal of the Japan Petroleum Institute*, **39**, 185.

31 Tatsumi, T., Matsuhashi, H. and Arata, K. (1996) *Bulletin of the Chemical Society of Japan*, **69**, 1191.

32 Hino, M. and Arata, K. (1980) *Journal of the Chemical Society, Chemical Communications*, 851.

33 Matsuhashi, H., Miyazaki, H. and Arata, K. (2001) *Chemistry Letters*, 452.

34 Matsuhashi, H., Miyazaki, H., Kawamura, Y., Nakamura, H. and Arata, K. (2001) *Chemistry of Materials*, **13**, 3038.

35 Arata, K. and Hino, M. (1984) *Reaction Kinetics and Catalysis Letters*, **25**, 143.

36 Hino, M. and Arata, K. (1979) *Chemistry Letters*, 477.

37 Hino, M. and Arata, K. (1979) *Chemistry Letters*, 1259.

38 Hino, M., Kobayashi, S. and Arata, K. (1979) *Journal of the American Chemical Society*, **101**, 6439.

39 Hino, M. and Arata, K. (1979) *Journal of the Chemical Society, Chemical Communications*, 1148.

40 Matsuhashi, H., Hino, M. and Arata, K. (1988) *Chemical Communications*, 1027.

41 Matsuhashi, H., Hino, M. and Arata, K. (1990) *Applied Catalysis*, **59**, 205.

42 Cutrufello, M.G., Diebold, U. and Gonzalez, R.D. (2005) *Catalysis Letters*, **101**, 5.

43 Arata, K. (1991) *Trends in Physical Chemistry*, **2**, 1, and references cited therein.

44 Matsuhashi, H., Hino, M. and Arata, K. (1991) *Catalysis Letters*, **8**, 269.

45 Arata, K. and Hino, M. (1990) *Applied Catalysis*, **59**, 197.

46 Gawthrope, D.E., Lee, A.F. and Wilson, K. (2004) *Physical Chemistry Chemical Physics*, **6**, 3907.

47 Matsuhashi, H., Sato, D. and Arata, K. (2004) *Reaction Kinetics and Catalysis Letters*, **81**, 183.

48 Arata, K. and Hino, M. (1990) *Materials Chemistry and Physics*, **26**, 213, and references cited therein.

49 Ebitani, K., Konishi, J. and Hattori, H. (1991) *Journal of Catalysis*, **130**, 257.

50 Morterra, C., Cerrato, G., Emanuel, C. and Bolis, V. (1993) *Journal of Catalysis*, **142**, 349.

51 Zhang, C., Miranda, R. and Davis, B.H. (1994) *Catalysis Letters*, **29**, 349.

52 Babou, F., Coudurier, G. and Vedrine, J.C. (1995) *Journal of Catalysis*, **152**, 341.

53 Funamoto, T., Nakagawa, T. and Segawa, K. (2005) *Applied Catalysis A: General*, **286**, 79.

54 Stepanov, A.G., Luzgin, M.V., Arzumanov, S.S., Wang, W., Hunger, M. and Freude, D. (2005) *Catalysis Letters*, **101**, 181.

55 Ma, Z., Zou, Y., Hua, W., He, H. and Gao, Z. (2005) *Topics in Catalysis*, **35**, 141.

56 Li, B. and Gonzalez, R.D. (1998) *Applied Spectroscopy*, **52**, 1488.

57 Li, B. and Gonzalez, R.D. (1998) *Catalysis Today*, **46**, 55.

58 Hino, M., Kobayashi, S. and Arata, K. (1981) *Reaction Kinetics and Catalysis Letters*, **18**, 491.

59 Hino, M. and Arata, K. (1990) *Chemistry Letters*, 1737.

60 Matsuhashi, H. and Katada, N. (2006) *Catalysts and Catalysis*, **48**, 464.

61 (a) Ward, D.A. and Ko, E.I. (1994) *Journal of Catalysis*, **150**, 18.
(b) Ward, D.A. and Ko, E.I. (1995) *Journal of Catalysis*, **157**, 321.

62 Tichit, D., Coq, B., Armendariz, H. and Figueras, F. (1996) *Catalysis Letters*, **38**, 109.

63 Zhuang, Q. and Miller, J.M. (2001) *Canadian Journal of Chemistry*, **79**, 1220.

64 Melada, S., Signoretto, M., Ardizzone, S.A. and Bianchi, C.L. (2001) *Catalysis Letters*, **75**, 199.

65 Ardizzone, S., Bianchi, C.L., Cappelletti, G. and Porta, F. (2004) *Journal of Catalysis*, **227**, 470.

66 Noda, L.K., de Almeida, R.M., Probst, L.F.D. and Goncalves, N.S. (2005) *Journal of Molecular Catalysis A–Chemical*, **225**, 39.

67 Arata, K., Nakamura, H. and Shouji, M. (2000) *Applied Catalysis A: General*, **197**, 213.

68 Arata, K., Matsuhashi, H., Hino, M. and Nakamura, H. (2003) *Catalysis Today*, **81**, 17.

69 Hino, M., Takasaki, S., Furuta, S., Matsuhashi, H. and Arata, K. (2007) *Applied Catalysis A: General*, **321**, 147.

70 (a) Arata, K. and Hino, M. (1988) *Proceedings of the 9th International Congress on Catalysis, Calgary, Canada, 1988* (eds M.J. Phillips and M. Ternan), Vol. 4, 1727.

71 Hino, M. and Arata, K. (1988) *Journal of the Chemical Society, Chemical Communications*, 1259.

72 Hino, M. and Arata, K. (1989) *Chemistry Letters*, 971.

73 Arata, K. and Hino, M., (1993). *Proceedings of the 10th International Congress on Catalysis, Budapest, 1992* (eds L. Guczi, F. Solymosi and P. Tetenyi), Elsevier, Amsterdam, p. 2613.

74 Hino, M. and Arata, K. (1994) *Bulletin of the Chemical Society of Japan*, **67**, 1472.

75 Matsuhashi, H., Kato, K. and Arata, K., (1994) *Studies in Surface Science and Catalysis. Proceedings of the International Symposium on Acid-Base Catalysis II, Kodansha, Tokyo, 1994*, Vol. 90 (eds H. Hattori, M. Misono and Y. Ono), p. 251.

76 Hino, M. and Arata, K. (1992) 70th National Meeting Catal. Soc. Jpn, Niigata, Abstr. no. 4F409.

77 Gregorio, F.D. and Keller, V. (2004) *Journal of Catalysis*, **225**, 45.

78 Lebarbier, V., Clet, G. and Houalla, M. (2006) *Journal of Physical Chemistry B*, **110**, 13905.

79 Benesi, H.A. (1956) *Journal of the American Chemical Society*, **78**, 5490.

80 Cheung, T.K. and Gates, B.C. (1997) *Chemtech*, **27**, 28.

81 Deeba, M. and Hall, W.K. (1979) *Journal of Catalysis*, **60**, 417.

82 Umansky, B., Engelhardt, J. and Hall, W.K. (1991) *Journal of Catalysis*, **127**, 128.

83 Karge, H.G. (1991) *Studies in Surface Science and Catalysis*, **65**, 133.

84 Niwa, M., Iwamoto, M. and Segawa, K. (1983) *Bulletin of the Chemical Society of Japan*, **59**, 3735.

85 Karge, H.G. and Dondur, V. (1990) *Journal of Physical Chemistry*, **94**, 765.

86 Song, X. and Sayari, A. (1994) *Applied Catalysis A: General*, **110**, 121.

87 Katada, N., Igi, H., Kim, J. and Niwa, M. (1997) *Journal of Physical Chemistry B*, **101**, 5969

88 Corma, A., Fornes, V., Juan-Rajadell, M.I. and LopezNieto, J.M. (1994) *Applied Catalysis A: General*, **116**, 151.

89 Hunger, B., Heuchel, M., Clark, L.A. and Snurr, R.Q. (2002) *Journal of Physical Chemistry B*, **106**, 3882.

90 Teunissen, E.H., Jansen, A.P.J. and van Santen, R.A. (1995) *Journal of Physical Chemistry*, **99**, 1873.

91 Parrillo, D.J., Lee, C. and Gorte, R.J. (1994) *Applied Catalysis A: General*, **110**, 67.

92 Fogash, K.B., Yaluris, G., Gonzalez, M.R., Quraipryvan, P., Ward, D.A., Ko, E.I. and Dumesic, J.A. (1995) *Catalysis Letters*, **32**, 241.

93 (a) Katada, N., Endo, J., Notsu, K., Yasunobu, N., Naito, N. and Niwa, M. (2000) *Journal of Physical Chemistry B*, **104**, 10321.

(b) Katada, N., Endo, J., Notsu, K., Yasunobu, N., Naito, N. and Niwa, M. (2000) *Studies in Surface Science and Catalysis*, **130**, 3213.
94 Kim, S.Y., Goodwin, J.G., Jr, Hammache, S., Auroux, A. and Galloway, D. (2001) *Journal of Catalysis*, **201**, 1.
95 Tanabe, K., Misono, M., Ono, Y. and Hattori, H. (1989) *Studies in Surface Science and Catalysis*, **51**, 5.
96 Gao, Z., Chen, J., Hua, W. and Tang, Y. (1994) *Studies in Surface Science and Catalysis*, **90**, 507.
97 Adeeva, V., Lei, G.D. and Sachtler, W.M.H. (1995) *Catalysis Letters*, **33**, 135.
98 Wan, K.T., Khouw, C.B. and Davis, M.E. (1996) *Journal of Catalysis*, **158**, 311.
99 Tabora, J.E. and Davis, R.J. (1996) *Journal of the American Chemical Society*, **118**, 12240.
100 Bardin, B.B. and Davis, R.J. (1998) *Topics in Catalysis*, **6**, 77.
101 Ecormier, M.A., Wilson, K. and Lee, A.F. (2003) *Journal of Catalysis*, **215**, 57.
102 Jin, T., Yamaguchi, T. and Tanabe, K. (1986) *Journal of Physical Chemistry*, **90**, 4797.
103 Kustov, L.M., Kazansky, V.B., Figueras, F. and Tichit, D. (1994) *Journal of Catalysis*, **150**, 143.
104 Adeeva, V., de Haan, J.W., Janchen, J., Lei, G.D., Schunemann, G., van de Ven, L.J.M., Sachtler, W.M.H. and van Santen, R.A. (1995) *Journal of Catalysis*, **151**, 364.
105 Bolis, V., Broyer, M., Barbaglia, A., Busco, C., Foddanu, G.M. and Ugliengo, P. (2003) *Journal of Molecular Catalysis A–Chemical*, **204–5**, 561.
106 Riemer, T., Spielbauer, D., Hunger, M., Mekhemer, G.A.H. and Knozinger, H. (1994) *Journal of the Chemical Society, Chemical Communications*, 1181.
107 Haw, J.F. and Xu, T. (1998) *Advances in Catalysis*, **42**, 115.
108 Farcasiu, D., Ghenciu, A. and Miller, G. (1992) *Journal of Catalysis*, **134**, 118.
109 Biaglow, A.I., Gorte, R.J., Kokotailo, G.T. and White, D.J. (1994) *Journal of Catalysis*, **148**, 779.
110 Semmer, V., Batamack, P., Doremieux-Morin, C., Vincent, R. and Fraissard, J. (1996) *Journal of Catalysis*, **161**, 186.
111 Xu, T., Kob, N., Drago, R.S., Nicholas, J.B. and Haw, J.F. (1997) *Journal of the American Chemical Society*, **119**, 12231.
112 Haw, J.F., Zhang, J., Shimizu, K., Venkatraman, T.N., Luigi, D.P., Song, W., Barich, D.H. and Nicholas, J.B. (2000) *Journal of the American Chemical Society*, **122**, 12561.
113 Coster, D.J., Bendada, A., Chen, F.R. and Fripiat, J.J. (1993) *Journal of Catalysis*, **140**, 497.
114 Gonzalez, M.R., Kobe, J.M., Fogash, K.B. and Dumesic, J.A. (1996) *Journal of Catalysis*, **160**, 290.
115 Ghenciu, A. and Farcasiu, D. (1996) *Journal of Molecular Catalysis A–Chemical*, **109**, 273.
116 Figueras, F., Coq, B., Walter, C. and Carriat, J.-Y. (1997) *Journal of Catalysis*, **169**, 103.
117 Garin, F., Andriamasinoro, D., Abdulsamad, A. and Sommer, J. (1991) *Journal of Catalysis*, **131**, 199.
118 Arata, K. (1996) *Applied Catalysis A: General*, **146**, 3, and references cited therein.
119 Arata, K., Matsuhashi, H., Hino, M. and Nakamura, H. (2003) *Catalysis Today*, **81**, 17, and references cited therein.
120 Sikabwe, E.C., Coelho, M.A., Resasco, D.E. and White, R.L. (1995) *Catalysis Letters*, **34**, 23.
121 Srinivasan, R., Keogh, R.A., Ghenciu, A., Farcasiu, D. and Davis, B.H. (1996) *Journal of Catalysis*, **158**, 502.
122 Stevens, R.W., Jr, Chuang, S.S.C., Davis, B.H. (2003) *Applied Catalysis A: General*, **252**, 57.
123 Matsuhashi, H., Motoi, H. and Arata, K. (1994) *Catalysis Letters*, **26**, 325.
124 Matsuhashi, H. and Arata, K. (2000) *Chemical Communications*, 387.
125 Matsuhashi, H. and Arata, K. (2006) *Catalysis Surveys from Asia*, **10**, 1.
126 Matsuhashi, H., Tanaka, T. and Arata, K. (2001) *Journal of Physical Chemistry B*, **105**, 9669.
127 Matsuhashi, H. and Arata, K. (2004) *Physical Chemistry Chemical Physics*, **6**, 2529.
128 Matsuhashi, H. and Futamura, A. (2006) *Catalysis Today*, **111**, 338.
129 Knozinger, H. (1998) *Topics in Catalysis*, **6**, 107.

130 Adeeva, V., Liu, H.-Y., Xu, B.-Q. and Sachtler, W.M.H. (1998) *Topics in Catalysis*, **6**, 61.

131 Hong, Z., Fogash, K.B. and Dumesic, J.A. (1999) *Catalysis Today*, **51**, 269.

132 Kim, S.Y., Goodwin, J.G., Jr and Farcasiu, D. (2001) *Applied Catalysis A: General*, **207**, 281.

133 Ahmad, R., Melsheimer, J., Jentoft, F.C. and Schlogl, R. (2003) *Journal of Catalysis*, **218**, 365.

134 Boronat, M., Viruela, P. and Corma, A. (1996) *Journal of Physical Chemistry*, **100**, 633.

135 Wakayama, T. and Matsuhashi, H. (2005) *Journal of Molecular Catalysis A–Chemical*, **239**, 32.

136 Matsuhashi, H., Yamagata, K. and Arata, K. (2004) *Chemistry Letters*, **33**, 554.

137 Wakabayashi, F., Kondo, J.N., Domen, K. and Hirose, C. (1995) *Journal of Physical Chemistry*, **99**, 10573.

138 Misono, M., Ono, I., Koyano, G. and Aoshima, A. (2000) *Pure and Applied Chemistry*, **72**, 1305.

139 Wakabayashi, F., Kondo, J., Wada, A., Domen, K. and Hirose, C. (1993) *Journal of Physical Chemistry*, **97**, 10761.

140 Matsuhashi, H., Shibata, H., Nakamura, H. and Arata, K. (1999) *Applied Catalysis A: General*, **187**, 99.

141 (a) Satoh, D., Matsuhashi, H., Nakamura, H. and Arata, K. (2003) *Catalysis Letters*, **89**, 105.
(b) Satoh, D., Matsuhashi, H., Nakamura, H. and Arata, K. (2003) *Physical Chemistry Chemical Physics*, **5**, 4343.

142 Farcasiu, D. and Li, J.Q. (1998) *Applied Catalysis A: General*, **175**, 1.

143 Coman, S., Parvulescu, V., Grange, P. and Parvulescu, V.I. (1999) *Applied Catalysis A: General*, **176**, 45.

144 Sassi, A. and Sommer, J. (1999) *Applied Catalysis A: General*, **188**, 155.

145 Bolis, V., Magnacca, G., Cerrato, G. and Morterra, C. (1997) *Langmuir*, **13**, 888.

146 Tanabe, K., Hattori, H. and Yamaguchi, T. (1990) *Critical Reviews in Surface Chemistry*, **1**, 1.

147 Saur, O., Bensitel, M., Saad, A.B.M., Lavalley, J.C., Tripp, C.P. and Morrow, B.A. (1986) *Journal of Catalysis*, **99**, 104.

148 Bensitel, M., Saur, O., Lavalley, J.C. and Morrow, B.A. (1988) *Materials Chemistry and Physics*, **19**, 147.

149 Morterra, C., Cerrato, G., Pinna, F. and Signoretto, M. (1994) *Journal of Physical Chemistry*, **98**, 12373.

150 Yang, J., Zhang, M., Deng, F., Luo, Q., Yi, D. and Ye, C. (2003) *Chemical Communications*, 884.

151 Lunsford, J.H., Sang, H., Campbell, S.M., Liang, C.-H. and Anthony, R.G. (1994) *Catalysis Letters*, **27**, 305.

152 Clearfield, A., Serrette, G.P.D. and Khazi-Syed, A.H. (1994) *Catalysis Today*, **20**, 295.

153 White, R.L., Sikabwe, E.C., Coelho, M.A. and Resasco, D.E. (1995) *Journal of Catalysis*, **157**, 755.

154 Laizet, J.B., Soiland, A.K., Leglise, J. and Duchet, J.C. (2000) *Topics in Catalysis*, **10**, 89.

155 (a) Hino, M., Kurashige, M., Matsuhashi, H. and Arata, K. (2006) *Thermochimica Acta*, **441**, 35.
(b) Fraenkel, D. (1999) *Chemistry Letters*, 917.

156 Cheung, T.-K. and Gates, B.C. (1997) *Journal of Catalysis*, **168**, 522.

157 Rezgui, S., Jentoft, R.E. and Gates, B.C. (1998) *Catalysis Letters*, **51**, 229.

158 Scheithauer, M., Bossch, E., Schubert, U.A., Knozinger, H., Cheung, T.-K., Jentoft, F.C., Gates, B.C. and Tesche, B. (1998) *Journal of Catalysis*, **177**, 137.

159 Morterra, C., Cerrato, G. and Ciero, S.D. (1997) *Catalysis Letters*, **49**, 25.

160 Song, X., Reddy, K.R. and Sayari, A. (1996) *Journal of Catalysis*, **161**, 206.

161 Sayari, A., Yang, Y. and Song, X. (1997) *Journal of Catalysis*, **167**, 346.

162 Sayari, A. and Yang, Y. (1999) *Journal of Catalysis*, **187**, 186.

163 Grau, J.M. and Parera, J.M. (1997) *Applied Catalysis A: General*, **162**, 17.

164 Larsen, G., Lotero, E., Parra, R.D., Petkovic, L.M., Silva, H.S. and Raghavan, S. (1995) *Applied Catalysis A: General*, **130**, 213.

165 Parvulescu, V., Coman, S., Parvulescu, V.I., Grange, P. and Poncelet, G. (1998) *Journal of Catalysis*, **180**, 66.

166 Yori, J.C. and Parera, J.M. (1995) *Applied Catalysis A: General*, **129**, 83.

167 Perez-Luna, M., Toledo-Antonio, J.A., Montoya, A. and Rosa-Salas, R. (2004) *Catalysis Letters*, **97**, 59.

168 Jentoft, R.E., Hahn, A.H.P., Jentoft, F.C. and Ressler, T. (2005) *Physical Chemistry Chemical Physics*, **7**, 2830.

169 Sohn, J.R., Lim, J.S. and Lee, S.H. (2004) *Chemistry Letters*, **33**, 1490.

170 Lange, F.C., Cheung, T.-K. and Gates, B.C. (1996) *Catalysis Letters*, **41**, 95.

171 Demirci, U.B. and Garin, F. (2001) *Catalysis Letters*, **76**, 45.

172 Moreno, J.A. and Poncelet, G. (2001) *Journal of Catalysis*, **203**, 453.

173 Occelli, M.L., Schiraldi, D.A., Auroux, A., Keogh, R.A. and Davis, B.H. (2001) *Applied Catalysis A: General*, **209**, 165.

174 Hua, W., Goeppert, A. and Sommer, J. (2001) *Applied Catalysis A: General*, **219**, 201.

175 (a) Hino, M. and Arata, K. (2004) *Reaction Kinetics and Catalysis Letters*, **81**, 321.
(b) Wang, J.-H. and Mou, C.-Y. (2005) *Applied Catalysis A: General*, **286**, 128.
(c) Sun, Y., Walspurger, S., Louis, B. and Sommer, J. (2005) *Applied Catalysis A: General*, **292**, 200.
(d) Kim, S.Y., Lohitharn, N., Goodwin, J.G.Jr, , Olindo, R. Pinna, F. and Canton, P. (2006) *Catalysis Communications*, **7**, 209.

176 Perez-Luna, M., Toledo-Antonio, J.A., Hernandez-Beltran, F., Armendariz, H. and Borquez, A.G. (2002) *Catalysis Letters*, **83**, 201.

177 Chen, X.-R., Chen, C.-L., Xu, N.-P., Han, S. and Mou, C.-Y. (2003) *Catalysis Letters*, **85**, 177.

178 Cao, C.-J., Han, S., Chen, C.-L., Mou, N.-P. and Xu, C.-Y. (2003) *Catalysis Communications*, **4**, 511.

179 Cao, C.-J., Yu, X.-Z., Chen, C.-L., Xu, N.-P., Wang, Y.-R. and Mou, C.-Y. (2004) *Reaction Kinetics and Catalysis Letters*, **83**, 85.

180 Signoretto, M., Melada, S., Pinna, F., Polizzi, S., Cerrato, G. and Morterra, C. (2005) *Microporous and Mesoporous Materials*, **81**, 19.

181 Cerrato, G., Morterra, C., Delgado, M.R., Arean, C.O., Signoretto, M., Somma, F. and Pinna, F. (2006) *Microporous and Mesoporous Materials*, **94**, 40.

182 Serra, J.M., Chica, A. and Corma, A. (2003) *Applied Catalysis A: General*, **239**, 35.

183 Vera, C.R., Yori, J.C. and Parera, J.M. (1998) *Applied Catalysis A: General*, **167**, 75.

184 Yori, J.C. and Parera, J.M. (1996) *Applied Catalysis A: General*, **147**, 145.

185 Sparks, D.E., Keogh, R.A. and Davis, B.H. (1996) *Applied Catalysis A: General*, **144**, 205.

186 Bi, M., Pan, W.-P., Lloyd, W.G. and Davis, B.H. (1998) *Catalysis Letters*, **50**, 187.

187 Shishido, T. and Hattori, H. (1996) *Applied Catalysis A: General*, **146**, 157.

188 Shishido, Y., Tanaka, T. and Hattori, H. (1997) *Journal of Catalysis*, **172**, 24.

189 Manoli, J.-M., Potvin, C., Muhler, M., Wild, U., Resofszki, G., Buchholz, T. and Paal, Z. (1998) *Journal of Catalysis*, **178**, 338.

190 Comelli, R.A., Canavese, S.A., Vaudagna, S.R. and Figoli, N.S. (1996) *Applied Catalysis A: General*, **135**, 287.

191 Satoh, N., Hayashi, J. and Hattori, H. (2000) *Applied Catalysis A: General*, **202**, 207.

192 Vijay, S. and Wolf, E.E. (2004) *Applied Catalysis A: General*, **264**, 117.

193 Blekkan, E.A., Johnsen, K.A. and Loften, T. (2005) *Reaction Kinetics and Catalysis Letters*, **86**, 149.

194 Fottinger, K., Zorn, K. and Vinek, H. (2005) *Applied Catalysis A: General*, **284**, 69.

195 Lin, C.-H. and Hsu, C.-Y. (1992) *Journal of the Chemical Society, Chemical Communications*, 1479.

196 Hsu, C.-Y., Heimbuch, C.R., Armes, C.T. and Gates, B.C. (1992) *Journal of the Chemical Society, Chemical Communications*, 1645.

197 Song, X. and Sayari, A. (1996) *Catalysis Reviews–Science and Engineering*, **38**, 329.

198 Hino, M. and Arata, K. (1995) *Catalysis Letters*, **30**, 25.

199 Hino, M. and Arata, K. (1995) *Journal of the Chemical Society, Chemical Communications*, 789.

200 Hino, M. and Arata, K. (1999) *Reaction Kinetics and Catalysis Letters*, **66**, 331.

201 Furuta, S. (2003) *Applied Catalysis A: General*, **251**, 285.

202 Hino, M. and Arata, K. (1998) *Applied Catalysis A: General*, **169**, 151.

203 Hino, M. and Arata, K. (1998) *Applied Catalysis A: General*, **173**, 121.

204 Hino, M. and Arata, K. (1999) *Journal of the Chemical Society, Chemical Communications*, 53.

205 Hwang, G., Bodenbinder, M., Willner, H. and Aubke, F. (1993) *Inorganic Chemistry*, **32**, 4667.

206 Cotton, F.A. and Wilkinson, G. (1988) *Advanced Inorganic Chemistry*, 5th edn, John Wiley & Sons, Inc., New York, p. 922.

207 Olah, G.A. (1963–1964) *Friedel-Crafts and Related Reactions*, Wiley-Interscience, New York, Vol. **1–4**.

208 Olah, G.A. (1973) *Friedel-Crafts Chemistry*, Wiley-Interscience, New York.

209 Nakamura, H. and Arata, K. (2004) *Bulletin of the Chemical Society of Japan*, **77**, 1893.

210 Chiche, B., Finiels, A., Gauthier, C., Geneste, P., Graille, J. and Pioch, D. (1986) *Journal of Organic Chemistry*, **51**, 2128.

211 Nakamura, H., Kashiwara, Y. and Arata, K. (2003) *Bulletin of the Chemical Society of Japan*, **76**, 1071.

212 Quaschning, V., Deutsch, J., Druska, P., Niclas, H.-J. and Kemnitz, E. (1998) *Journal of Catalysis*, **177**, 164.

213 Parida, K., Quaschning, V., Lieske, E. and Kemnitz, E. (2001) *Journal of Materials Chemistry*, **11**, 1903.

214 Kawada, A., Mitamura, S., Matsuo, J., Tsuchiya, T. and Kobayashi, S. (2000) *Bulletin of the Chemical Society of Japan*, **73**, 2325.

215 Patil, P.T., Malshe, K.M., Kumar, P., Dongare, M.K. and Kemnitz, E. (2002) *Catalysis Communications*, **3**, 411.

216 Sakthivel, R., Prescott, H. and Kemnitz, E. (2004) *Journal of Molecular Catalysis A–Chemical*, **223**, 137.

217 Hino, M. and Arata, K. (1985) *Journal of the Chemical Society, Chemical Communications*, 112.

218 Hino, M. and Arata, K. (1996) *Hyoumen*, **34**, 51.

219 Barton, D.G., Soled, S.L. and Iglesia, E. (1998) *Topics in Catalysis*, **6**, 87.

220 (a) Hino, M., Takasaki, S., Furuta, S., Matsuhashi, H. and Arata, K. (2006) *Catalysis Communications*, **7**, 162. (b) Hino, M., Takasaki, S., Furuta, S., Matsuhashi, H. and Arata, K. (2007) *Applied Catalysis A: General*, **321**, 147.

221 Hino, M., Matsuhashi, H. and Arata, K. (2006) *Catalysis Letters*, **107**, 161, and unpublished data.

222 Muggli, D.S. and Ding, L. (2001) *Applied Catalysis B–Environmental Consulting*, **32**, 181.

223 Ohno, T., Mitsui, T. and Matsumura, M. (2003) *Chemistry Letters*, **32**, 364.

224 Muggli, D.S., Ding, L. and Odland, M.J. (2002) *Catalysis Letters*, **78**, 23.

225 Samantaray, S.K., Mohapatra, P. and Parida, K. (2003) *Journal of Molecular Catalysis A–Chemical*, **198**, 277.

226 Gerlich, M., Kornely, S., Fleischer, M., Meixner, H., Kassing, R. (2003) *Sensors and Actuators B*, **93**, 503.

227 Xie, C., Xu, Z., Yang, Q., Li, N., Zhao, D., Wang, D. and Du, Y. (2004) *Journal of Molecular Catalysis A–Chemical*, **217**, 193.

228 Wang, X., Yu, J.C., Hou, Y. and Fu, X. (2005) *Advanced Materials*, **17**, 99.

229 Nakajima, A., Obata, H., Kameshima, Y. and Okada, K. (2005) *Catalysis Communications*, **6**, 716.

230 Barraud, E., Bosc, F., Keller, N. and Keller, V. (2005) *Chemistry Letters*, **34**, 336.

231 Barraud, E., Bosc, F., Edwards, D., Keller, N. and Keller, V. (2005) *Journal of Catalysis*, **235**, 318.

232 Mohamed, M.M. and Al-Esaimi, M.M. (2006) *Journal of Molecular Catalysis A–Chemical*, **255**, 53.

233 Moos, R., Muller, R., Plog, C., Knezevic, A., Leye, H., Irion, E., Braun, T., Marquardt, K.-J., Binder, K. (2002) *Sensors and Actuators B*, **83**, 181.

234 Shimizu, K. and Satsuma, A. (2006) *Shokubai (Catalysts & Catalysis)*, **48**, 544.

18
Titanium Silicalite-1

Mario G. Clerici

Oxides of metals in Groups IV–VI of the periodic table are generally poor catalysts in oxidations using hydrogen peroxide [1]. Water and other protic solvents necessary to dissolve the oxidant compete for the active site, causing inhibition. Thus, activity and selectivity are low and the decomposition of hydrogen peroxide can be a major side-reaction. An exception is the epoxidation of α,β-unsaturated alcohols and acids, which are able to compete with water for the active site through their oxygenated functionalities. Ti, Mo, V and W compounds, on the other hand, are excellent catalysts in oxidations with organic hydroperoxides, since these allow the use of hydrocarbons and other non-coordinating solvents under water-free conditions.

The absence of co-products needing disposal or further processing makes hydrogen peroxide so attractive as an oxidant that physical and chemical means of avoiding the build-up of water in the oxidation medium were investigated. Early studies envisaged the use of an organic medium, maintained in nearly anhydrous conditions by the addition of dehydrating agents or by the continuous azeotropic distillation of water. This last option was specifically studied for the epoxidation of propene, although never applied industrially probably because of the potential hazards implicit in the method [2]. The alternative was indirect epoxidation carried out in a water-free organic solvent, physically separated from the aqueous hydrogen peroxide reservoir. The true oxidant species was a H_2O_2 carrier, cyclically consumed in the epoxidation medium and regenerated in the aqueous one, as in the epoxidation under phase-transfer conditions or with peracids [3]. In both cases, water was never allowed to come into contact with the epoxidation process.

More promising from an industrial perspective, however, is the separation of the oxidation zone from the aqueous one effected by the catalytic material itself, through the selective adsorption of the reagents. The introduction of Titanium Silicalite-1 (TS-1), in which the hydrophobic properties of the pores protect the active sites from the inhibition of the external aqueous medium, was a demonstration of the concept. The catalyst, the substrate and the aqueous solution of hydrogen peroxide can, in this case, be mixed together, with a great simplification of the process and also a reduction of the hazards. Three commercial processes,

Metal Oxide Catalysis. Edited by S. David Jackson and Justin S. J. Hargreaves

ISBN: 978-3-527-31815-5

superior to earlier ones in terms of both economic and environmental grounds, prove the viability of the method.

The number of studies on TS-1, and also on other Ti-zeolites, rose exponentially since the first one was published in 1986 and a vast literature now exists [4]. A few review articles deal with the synthesis, the characterization and, to a lesser extent, with the catalysis of such materials [5–9]. It is the aim of this chapter to focus on the last issue, providing a comprehensive picture of the variety of oxidations performed, a critical analysis of the problems and solutions envisaged in the use of hydrogen peroxide and an in-depth discussion of mechanistic aspects.

18.1 Synthesis and Characterization

Taramasso and others first prepared TS-1 at the end of the 1970s, using two different methods for the preparation of the crystallization gel [10]. In the most commonly used "mixed alkoxide method," this was obtained by the controlled hydrolysis of tetraethyltitanate and tetraethylsilicate in the presence of tetrapropylammonium hydroxide. Crystallization under hydrothermal conditions produced crystalline TS-1. In the preparation of the gel, it is crucial to prevent segregation of Ti phases by the correct choice of procedure and control of the conditions. The maximum Ti content, expressed as the atomic ratio Ti/(Ti+Si), was reported to be ca 0.025 [11]. Other information is available in Refs. [6–9] and references therein.

As indicated in the original patent, the absence of alkali metal ions in the synthesis mixture is critical for the incorporation of Ti in the lattice. Their presence as impurities in commercial samples of tetrapropylammonium hydroxide was not recognized in several studies, particularly in early ones, with the result that TS-1 was impure, containing TiO_2 particles and amorphous Ti-silicates. Sometimes, however, the presence of alkali and other impurities is the consequence of a deliberate decision, in an attempt to decrease the cost of production of the catalyst by the use of cheaper sources of Si, Ti and tetrapropylammonium hydroxide [12].

Titanium Silicalite-2 (TS-2), structurally similar to TS-1, could be prepared likewise using tetrabutylammonium hydroxide as the template [13, 14]. Titanium aluminum Beta (Ti,Al-β) was prepared by hydrothermal synthesis from amorphous silica, sodium aluminate, tetraethyltitanate and tetraethylammonium hydroxide [15]. The presence of Al was necessary for the crystallization of the product. Al-free Titanium Beta (Ti-β) could be obtained in the presence of particular templates, such as dibenzyldimethylammonium hydroxide [16]. Titanium Mordenite (Ti-MOR), conversely, was obtained by post-synthesis insertion of Ti to dealuminated Mordenite [17]. Ti-MWW (Ti-MCM-22) was obtained by the synthesis of the lamellar precursor of Ti,B-MCM-22 followed by acid treatment to remove most of the boron and extra-framework Ti and finally calcination to burn out the template and bring about the condensation of lamellae into the three-dimensional MWW structure [18]. Ti is present in a number of different environ-

Table 18.1 Structural properties and composition of some Ti-zeolites.[a)]

Name	Structure type	Pore dimensions (Å)	Pore structure	Metal
TS-1	MFI	5.6×5.3; 5.5×5.1	3 directional	Ti
TS-2	MEL	5.3×5.4	3 directional	Ti
Ti-Beta, Ti-β, Ti,Al-β	*BEA[c)]	6.4×7.6; 5.5×5.5	3 directional	Ti, (Al)
Ti-MOR[b)]	MOR	6.5×7.0; 2.6×5.7	1[b)] directional	Ti, (Al)
Ti-MWW, Ti-MCM-22	MWW	5.4×4.0	2 directional	Ti

a W.M. Meier and D.H. Olson, *Atlas of Zeolite Structure Types*, Butterworth-Heinemann, London, 1992.

b Residual Al can be present in the lattice. The size of the second channel system is too small for catalysis.

c * denotes a well-defined subunit for which pure end members have not been obtained.

ments, that is in the external pockets or cups (0.7×0.7 nm), in internal supercages ($0.7 \times 0.7 \times 1.7$ nm) and in medium-pore sinusoidal channels. Other Ti-zeolites are not mentioned here, because they are of little catalytic interest.

Ti-MCM-41 and Ti-MCM-48 are mesoporous molecular sieves with ordered porous systems. Owing to their amorphous nature, these cannot be classified as zeolites. Their inclusion, however, is useful in that it extends the range of pore sizes of Ti-molecular sieves to an upper limit of 2–4 nm [19].

Characterization is a crucial step preliminary to any catalytic study, since the selectivity of the catalyst is strictly related to the position of Ti, in atomic dispersion, within the crystal lattice. Extra-framework Ti species, such as TiO_2 particles and amorphous Ti-silicates, indeed, promote H_2O_2 decomposition and radical chain oxidations. Normally, a combination of different techniques is necessary for reliable characterization, for example, UV-Vis, IR and Raman spectroscopies, XRD, EXAFS, XANES, TEM and SEM [8, 20]. Table 18.1 illustrates the main structural features of TS-1 and other Ti-zeolites relevant to this review.

18.2 Hydroxylation of Alkanes

The oxidation of alkanes is a reaction known for the difficulties of its realization under mild conditions. Exceptions are enzymatic and a few organometallic systems, which are, however, unsuitable for industrial applications. The use of molecular oxygen as oxidant usually requires radical initiators or drastic conditions, leading to high selectivities only in a limited number of oxidations. The addition of a reducing agent (Equation 18.1) or the use of hydrogen peroxide and other monooxygen donors (Equation 18.2) allows the reaction to be performed under milder conditions, albeit with yields that are generally too low in relation to the cost of the oxidant. Mixed oxide materials are usually ineffective under the latter conditions. With this background, the efficacy of TS-1, discovered by three groups independently, represented a step-change [21–24].

$$R{-}H + O_2 + 2H^+ + 2e^- \longrightarrow R{-}OH + H_2O \quad (18.1)$$

$$R{-}H + H_2O_2 \longrightarrow R{-}OH + H_2O \quad (18.2)$$

18.2.1 Titanium Silicalite-1

TS-1 catalyzes the hydroxylation of alkanes with dilute solutions of hydrogen peroxide in water, in a biphasic system of alkane and aqueous H_2O_2, or in aqueous–organic solution. The rate of reaction decreases in the solvent order: *t*-butanol > *t*-butanol/water > methanol ≈ acetonitrile ≈ water [24, 25]. The temperature is generally lower than 55 °C in methanol, close to 100 °C in water and of intermediate values in other solvents. Hydroxylation occurs at secondary and tertiary C—H bonds, while primary ones are completely inert (Equations 18.3 and 18.4).

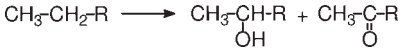

(18.3)

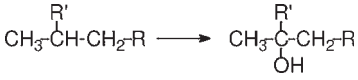

(18.4)

The main side reactions are the decomposition of hydrogen peroxide and, to a lesser extent, the oxidation of alcohol solvent. Their competition with C—H hydroxylation increases with increasing bulkiness of the paraffin, becoming predominant with those having a cross-section close to or larger than the size of the pores.

Linear alkanes yield a mixture of secondary alcohols and ketones (Table 18.2). In methanol, hydroxylation is reduced at more internal positions, while in water and in acetone it occurs randomly. The yield increases with the chain length up

Table 18.2 Hydroxylation of linear alkanes.[a)]

Alkane	$t_{1/2}$ (min)[b)]	Yield (% based on H_2O_2)[c)]	β/γ ratio	γ/δ ratio	Alcohol/ ketone ratio
C_3H_8	130	35	–	–	2.0
n-C_4H_{10}	62	69	–	–	1.2
n-C_5H_{12}	80	82	4.5	–	1.0
n-C_6H_{14}	30	86	2.6	–	1.4
n-C_7H_{16}	57	75	1.9	5.2	2.2
n-C_8H_{18}	57	63	2.6	1.9	1.7

a Adapted from Ref. [24]. Copyright 1991, with permission from Elsevier. Solvent, methanol 95%; alkane, 0.62 mol l^{-1}; TS-1, 15.7 g l^{-1}; *T*, 55 °C.

b Time required for 50% H_2O_2 conversion.

c Yields are referred to 98% H_2O_2 conversion.

to a maximum for C_5–C_7 *n*-alkanes. Values as high as 99% have recently been reported for the hydroxylation of *n*-hexane, by feeding the oxidant gradually to keep the H_2O_2/alkane ratio low [26]. The rather odd reactivity order, hexane > heptane ≈ octane > butane > pentane > propane, most likely results from the combined effects of electronic factors, diffusivity and adsorption strength. The increase of alkyl chain length actually affects adsorption heats and diffusivity in zeolites in opposite directions. Inductive effects, on the other hand, increase with chain length, gradually levelling off.

The hydroxylation of cyclohexane, of potential interest for the production of cyclohexanone, is exceedingly slow at near room temperature and has low selectivity at 100 °C [27, 28]. Tertiary C–H bonds yield tertiary alcohols, with little or no oxidation observed at the secondary carbons that may be present in the alkyl chain: *t*-C–H ≫ *sec*-C–H (Table 18.3). The steric constraints introduced by alkyl substitution strongly favor the competition of side reactions, at the expense of hydroxylation. On arylalkanes, oxidation occurs on both the aromatic ring and the alkyl chain, with a general preference for the latter. Consistently, the competitive hydroxylation of benzene and *n*-hexane or cyclohexane mainly occurs on the alkane. However, benzylic methyls, despite the relative weakness of their C–H

Table 18.3 Hydroxylation of branched and substituted alkanes.[a)]

Substrate	t (min)	Conversion (% based on H_2O_2)	Yield (% based on H_2O_2)	Products
cyclohexane	150	50	32	cyclohexanol, cyclohexanone
2-methylpropane	180	65	45	*t*-butanol
2-methylbutane	240	65	14	2-methyl-2-butanol
2-methylpentane	300	57	10	2-methyl-pentanol
1-chlorohexane[b)]	180	88	37	1-chloro-4-hexanol, 1-chloro-5-hexanol
				1-chloro-4-hexanone, 1-chloro-5-hexanone
methyl heptanoate	120	77	5	5-hydroxyheptanoate, 6-hydroxyheptanoate
				5-oxoheptanoate, 6-oxoheptanoate

a Adapted from Ref. [24]. Copyright 1991, with permission from Elsevier. Solvent, methanol, 95%; alkane, 0.62 mol l^{-1}; TS-1, 15.7 g l^{-1}; *T*, 55 °C.

b Solvent *t*-butanol.

bonds, are inert. The presence of electron-withdrawing groups in 1-chlorohexane and methyl heptanoate strongly decreases hydroxylation while orienting the attack on the remote methylene groups. Consistently, no dihydroxylation is observed under the conditions of Table 18.2, and it is negligible on C_8—C_{12} *n*-paraffins. Both the absence of consecutive hydroxylation and remote oxyfunctionalization reveal the electrophilic properties of the active species.

Evidence on the latter was obtained by the use of additives, substrate probes and labeled molecules. The addition of small amounts of protonic acids promoted hydroxylation. Alkali metal salts and basic compounds produced the opposite effect, with inhibition or complete deactivation of the catalyst, depending on the amount used. The subsequent addition of hydrochloric acid restored the initial activity, showing that inhibition and deactivation by salts and bases are completely reversible phenomena [24, 29]. On these grounds, the active species could be identified as a fairly acidic Ti hydroperoxide or an oxidant, still unknown, produced by its further transformation [24]. However, the involvement of Ti—OOH as the active species of a heterolytic mechanism is not consistent with the results of the competitive hydroxylation of aromatic and aliphatic C—H bonds, pointing instead to a homolytic pathway.

Two types of substrate probe, *cis*- and *trans*-1,3-dimethylcyclopentane and ethyl- and 2-propylcyclopropane, were used to shed light on mechanistic details of the hydroxylation step [30]. In the use of the first two probes, the participation of Ti—OOH species in a concerted mechanism would predict either the retention or the inversion of configuration at the chiral center, while the stereochemistry of a homolytic mechanism would be determined by the competition between the epimerization of the transient tertiary carbon radical and C—O formation (Scheme 18.1). In the hydroxylation of cyclopropyl probes, the cyclopropylcarbinyl radical clock can either rearrange to ring-opened 3-buten-1-yl radical before being trapped or rebound with the hydroxyl carrier to yield the alcohol product directly (Scheme 18.2). With TS-1, nearly equal amounts of *trans*- and *cis*-1,3-dimethylcyclopentanol were obtained from the first type of probe, while no rearranged products were obtained with the second ones. These results suggest that the putative radical intermediate is very short-lived, but not short enough to prevent the racemization of the tertiary carbon radical. Incidentally, it was estimated that epimerization and cyclopropyl rearrangement occurred with first order rate constants of 10^9 and ca $10^8\ s^{-1}$, respectively [30, 31].

The use of radical quenchers and the competitive oxidation of cyclohexane and cyclohexane-d_{12} led to identification of the active species as a Ti-centered radical

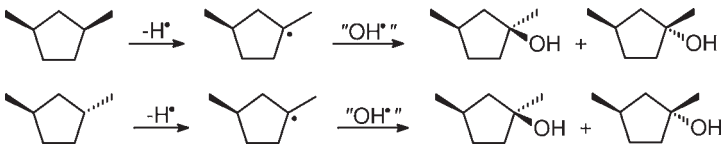

Scheme 18.1 Hydroxylation of sterically pure *cis*- and *trans*-1,3-dimethylcyclopentane.

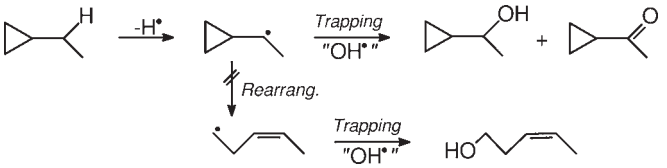

Scheme 18.2 Hydroxylation of ethylcyclopropane.

[24]. Actually, BHT (2,6-di-*tert*-butyl-4-methylphenol), carbon tetrachloride, chloroform and dichloromethane neither affected the hydroxylation rate nor produced chlorinated derivatives, thus excluding a free radical mechanism and the presence of long-lived alkyl radicals, both in the pores of the catalyst and in the external solution. The primary isotopic effect in methanol and *t*-butanol was 4.1 and 4.7, respectively. A k_H/k_D of this magnitude is not compatible with a radical chain oxidation initiated by hydroxyl radicals ($k_H/k_D = 1–2$), while it is fully consistent with substantial C—H bond cleavage in the transition state by a Ti-centered radical.

On the whole, it is conceivable to postulate an active species that is Ti centered, has a radical nature and originates from a Ti—OOH precursor, through some sort of reaction which the latter species may undergo. An early mechanistic proposal, based on a diradical peroxy species, does not match all these conditions (Scheme 18.3a). This requires that the adsorption of hydrogen peroxide on Ti leads to a side-on bonded peroxide and, more importantly, implies the splitting of one strong Ti—O bond instead of the weaker peroxidic O—O one. The unlikelihood of Ti—O cleavage is confirmed by the reaction of a Rh peroxide with carbon dioxide, occurring through the insertion of CO_2 into the O—O bond, to yield the corresponding peroxycarbonate [32].

Scheme 18.3b illustrates a recent mechanistic proposal. This bears similarities to the oxygen-rebound mechanism, proposed for the hydroxylation of alkanes by high-valent transition metal species in biomimetic and enzymatic systems [31, 33, 34]. The generation of the active species and other implications of the mechanism are discussed in detail in Section 18.11.3.

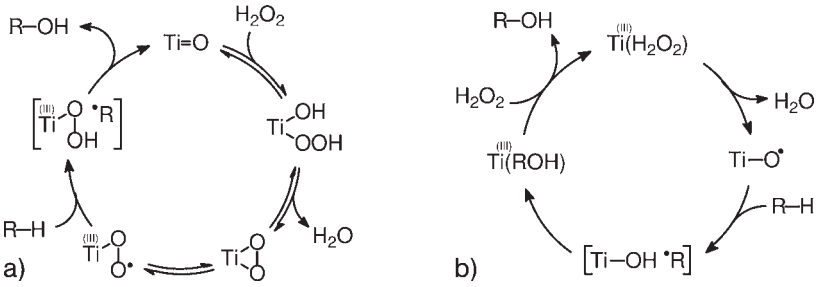

Scheme 18.3 (a) C—H hydroxylation by Ti(η^2—O_2);
(b) C—H hydroxylation by oxygen-rebound-like mechanism.

Table 18.4 Hydroxylation of alkanes on Ti,Al-β and comparison with TS-1 [35].

Alkane	Ti,Al-β		TS-1	
	TON (mol/mol$_{Ti}$)	Selectivity (% based on H_2O_2)	TON (mol/mol$_{Ti}$)	Selectivity (% based on H_2O_2)
n-hexane	0.5	32	48.5	100
cyclohexane	2.3	51	[a]	–
methylcyclohexane	5.2	88	[a]	–

a Products below detection limits.

18.2.2
Other Ti-Zeolites

Only TS-2 and Ti,Al-β, among other Ti-zeolites, catalyze the hydroxylation of alkanes. The close similarity of TS-2 with TS-1 suggests analogous catalytic properties. The somewhat poorer performances reported in the literature probably reflect the poor quality of early catalysts, containing extra-framework impurity Ti species. Ti,Al-β, on the other hand, is definitely inferior to TS-1, except in the hydroxylation of bulky alkanes (Table 18.4) [35]. Interestingly enough, Ti,Al-β catalyzes the hydroxylation of both *sec*-C—H and *t*-C—H in the same molecule, though the reactivity of the latter is significantly higher [36]. In 1,2- and 1,3-dimethylcyclohexanes, equatorial C—H bonds are more reactive than those at axial positions, probably because there is less hindrance in the approach to the active species. The direct link between the hydrophobicity of the sample used and catalytic performance is of mechanistic interest [37].

18.3
Hydroxylation of Aromatic Compounds

The synthesis of phenolic compounds, including the industrial production of a major commodity such as phenol, has historically been achieved by the transformation of pre-existing aromatic functional groups. The generally poor selectivity of direct hydroxylation routes is especially evident with molecular oxygen as the oxidant, though sometimes relatively high yields have been claimed. The use of hydrogen peroxide appears more promising, and is characterized by greater selectivity. Actually, in the early 1970s Brichima and Rhône-Poulenc commercialized two industrial processes for the hydroxylation of phenol with H_2O_2. The development of TS-1 and Fe-ZSM-5 opened new routes to selective hydroxylation processes with hydrogen peroxide (EniChem, hydroxylation of phenol) and nitrous oxide (Solutia, hydroxylation of benzene), respectively.

18.3.1 Hydroxylation of Phenol

18.3.1.1 Titanium Silicalite-1

Normally in a review the hydroxylation of benzene should come before that of phenol. The latter, however, has been the center of interest of most studies, particularly of early ones, whereas benzene has been considered often just for the completeness of the range of substrates. On these grounds, an exception for phenol is justified.

Hydroxylation is a consecutive reaction in which low conversion has to be maintained, to prevent the over-oxidation of catechol and hydroquinone to tars (Equation 18.5). This is normally achieved by operating with an excess of phenol over hydrogen peroxide. The greater the H_2O_2 : phenol ratio allowed in the feed, without penalty to the selectivity, the greater the effectiveness of the catalysts (Table 18.5) [5, 38, 39]. A stirred reactor is normally preferred, though the use of the fixed bed type has sometimes been reported [40–42].

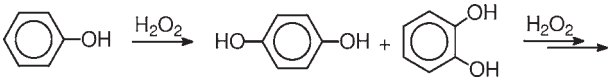

(18.5)

In aqueous acetone and methanol, TS-1 shows superior performance than in *t*-butanol or just water. The solvent has also a major effect on the catechol : hydroquinone ratio (see below). This varies in the range 0.5–1.3, which is some way from the value of 2 expected for a statistical attack at the *ortho* and *para* positions (Table 18.5, entries 1 and 2). Yet, under practical conditions, the main component of the reaction mixture could be phenol instead of the putative solvent and, under such conditions, the product ratio approaches unity.

The yields based on hydrogen peroxide are comparable to those obtained with acid catalysts, but at six-fold higher conversion (Table 18.4, entries 1 and 3). The most important parameters for the yield are the operating temperature and the purity, concentration and crystal size of the catalyst [5, 43]. Yields increased, at the expense of tar production, up to a maximum of ca 83% at 100 °C, and then

Table 18.5 Hydroxylation of phenol with hydrogen peroxide.

	Catalyst	Ortho/para	Phenol conversion (%)	Selectivity		Ref.
				(% based on H_2O_2)	(% based on C_6H_5OH)	
1	TS-1	0.5–1.3	30	82	92	[5]
2	Co^{+2}, Fe^{+2}	2–2.3	9	66	79	[39]
3	H^+	1.2–1.5	5	85–90	90	[38]

Table 18.6 Henry constants (K_P) for the adsorption of phenol in TS-1.[a)]

Solvent	K_P
Water	84.4
Methanol	0.7
Acetone	0.6

a Adapted from Ref. [47]. Copyright 2001, with permission of Elsevier.

decreased rapidly with further temperature rises. Extra-framework Ti phases promote non-productive side reactions, for example decomposition of the oxidant and radical chain oxidations. In general, this applies to any oxidation catalyzed by TS-1, but is crucial for aromatic hydroxylation that requires a relatively high temperature. The hydroxylation of phenol, indeed, was proposed as chemical test to assess the purity of TS-1 [5, 43, 44]. The concentration of TS-1 also affects the yields, owing to greater competition of secondary reactions in the presence of excess H_2O_2 and low catalyst contents. Van der Pool and others originally showed, and other authors confirmed, that the hydroxylation of phenol is diffusion limited for crystal sizes larger than 0.3 μm [45–47].

Experimental data fit well with kinetic expressions that are first order in both phenol and hydrogen peroxide [47]. Observed rate constants were significantly larger in water than in methanol and acetone. This was ascribed to the stronger adsorption of phenol from an aqueous solution in TS-1 (Table 18.6) [47, 48]. Surprisingly enough, in the presence of methanol or acetone the concentration of phenol in the pores was about the same as that in the external solution.

An issue of debate is the relative roles of internal and external sites in the catalytic process. The effects of shape selectivity, clearly present in product distribution, seem to indicate a predominance of intra-porous hydroxylation. However, the different catechol/hydroquinone ratio in methanol (0.5) and acetone (1.3), could indicate a significant contribution of sites located on the outer surface of the crystals, particularly for crystallite sizes <0.3 μm. Tuel and others, studying the time course of the reaction and the solubility of tarry deposits, went further and concluded that catechol and hydroquinone were produced on different sites, external and internal respectively [49]. The effect of acetone and methanol simply reflected their ability to maintain external sites clean from tar deposits, which are soluble in the former and insoluble in the latter. On the other hand, Wilkenhöner and others concluded, with the support of kinetic constants estimated independently for internal and external sites, that catechol was also produced in the pores over the entire reaction profile, albeit at a lower rate [47]. The contribution of the outer surface for crystal sizes close to 0.1 μm ranged from 46% in methanol to 69% in acetone.

Little is known of the active species and the hydroxylation mechanism. It is even unclear whether the mechanism is homolytic or heterolytic. Accordingly, mechanisms of both types have been proposed (Schemes 18.4 and 18.5).

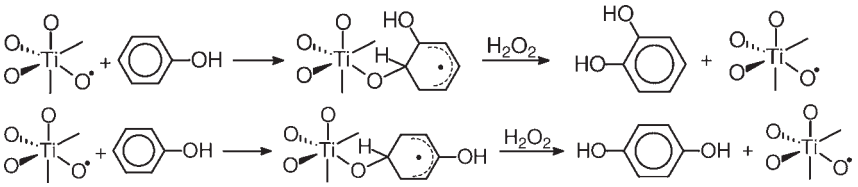

Scheme 18.4 Homolytic hydroxylation of phenol by Ti—O•species.

In the mechanism of Scheme 18.4, hydroxylation is carried out homolytically by the same species proposed for alkane hydroxylation [25]. The oxidation of the cyclohexadienyl intermediate by hydrogen peroxide produces the diphenol and regenerates the active species, closing the catalytic cycle. Scheme 18.5 illustrates the heterolytic routes proposed by Wilkenhöner and others for hydroquinone and catechol production, based on cationic peroxy intermediates [47]. Both types of mechanism, however, are little more than working hypotheses, needing validation by experimental evidence.

18.3.1.2 **Other Ti-Zeolites**

TS-2 was shown to be almost indistinguishable from TS-1, as predicted by similarity of structures and active sites [46]. Ti-Beta zeolites, with and without Al in the structure, were less effective than TS-1. The yields based on hydrogen peroxide, just above 60%, were typical of rather modest catalysts. Apparently, product selectivity was influenced by the Al content. The relatively hydrophilic Ti,Al-β produced catechol and hydroquinone in nearly equimolar amounts [50]. The Al-free Ti-β showed a higher catechol selectivity, with an *ortho*/*para* ratio of 2 [47]. In both cases, the greater spaciousness of pores favoured *ortho* hydroxylation. For a useful comparison, the *ortho*/*para* ratio on medium-pore TS-1 was 0.77 under analogous conditions.

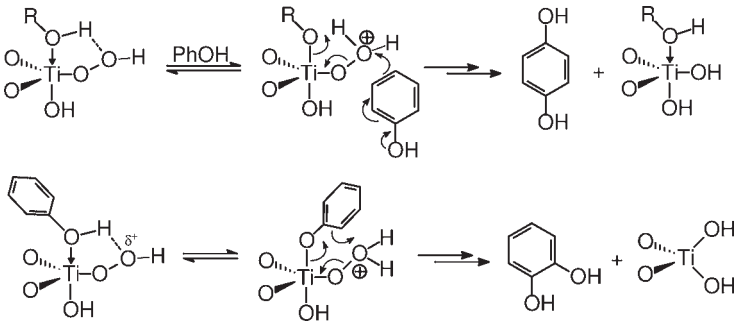

Scheme 18.5 Heterolytic hydroxylation of phenol by Ti—OOH species. (Adapted from Ref. [47]; Copyright 1991, with permission of Elsevier).

18.3.2
Hydroxylation of Benzene

The hydroxylation of benzene on TS-1 produces phenol as the primary product and, by consecutive oxidation, hydroquinone, catechol, benzoquinone and tarry products (Equation 18.6) [5, 30, 51]. The selectivity to phenol generally falls below 50% even at only 3–5% benzene conversion. Hydroxylation with a mixture of hydrogen and oxygen on Pd/TS-1 proved to be even less effective [52].

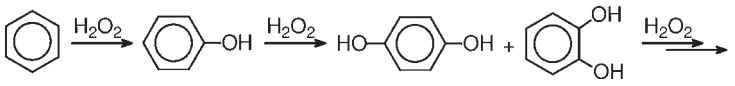

(18.6)

Recently, the use of sulfolane solvent allowed better kinetic control of the oxidation chain, with an increase of the selectivity to 80% or greater, at ca 8% benzene conversion. The by-products were catechol (7%), hydroquinone (4%), 1,4-benzoquinone (1%) and tar (5%) [53, 54]. According to these authors, a rather stable complex, formed by hydrogen bonding with sulfolane, promoted desorption and hindered the re-adsorption of phenol, protecting it from consecutive oxidation (Equation 18.7). Actually, the rate of oxidation of phenol in the presence of sulfolane was only 1.6 times that of benzene, while it was 10 times higher in the presence of acetone.

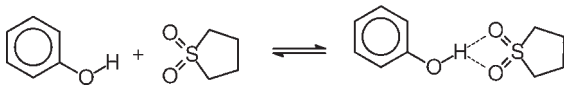

(18.7)

The pretreatment of TS-1 with a solution of ammonium fluoride and hydrogen peroxide further increased the conversion (ca 9%) and selectivity. The recovery of catechol and hydroquinone, by their hydrogenation back to phenol, was also considered [55]. It is worth noting that, at a threshold yield value of ca 9%, the hydroxylation of benzene could become competitive with the cumene process, considering that the overall per pass yield in the latter does not exceed 8–9%.

Far greater yields were reported for the hydroxylation of benzene under the so-called triphasic conditions, that is with the solid catalyst, aqueous hydrogen peroxide and an immiscible aromatic phase [56]. Others, however, could not reproduce these results [54].

Benzene hydroxylation on Ti,Al-MOR was studied by three different groups [57–59]. Despite the spaciousness of its pores, the activity of this catalyst was lower than that of TS-1, as expected for a more hydrophilic catalyst. Accordingly, increase in the Al content caused a decrease in the conversion, probably because of reduced adsorption of benzene.

18.3.3
Oxidation of Substituted Benzenes

Electron-withdrawing substituents decrease the rate of oxidation, revealing the electrophilic nature of the oxidant species. Accordingly, negligible or no yields were reported for the hydroxylation of chlorobenzene, nitrobenzene, benzonitrile, benzaldehyde and benzoic acid on TS-1 [5]. Alkyl groups produced contrasting effects: a rate enhancement by electron donation and a rate decrease by steric and transport restrictions. In this regard, the size of the methyl group in toluene virtually compensated for the increase of electron density [5]. For other alkylbenzenes, the nuclear reactivity trend was in the order: toluene > *p*-xylene ≥ ethylbenzene > *p*-methylethylbenzene, showing again the predominance of steric hindrance [5, 30, 59]. Bulkier substituents suppressed hydroxylation, for example in 2-propylbenzene [24].

The oxidation of alkylbenzenes also produced *sec*-alcohols and ketones, with no reaction at tertiary and primary carbons. At variance with the rule that double bonds are preferentially oxidized over other functionalities, side-chain epoxidation had to compete with aromatic hydroxylation in the oxidation of α-methylstyrene, 1-phenyl-2-butene and 4-phenyl-1-butene [60].

Ti-MOR promoted the ring hydroxylation of toluene, ethylbenzene and xylenes with negligible oxidation of the ethyl side chain [59]. In the same study, however, and in contrast to earlier ones, a similar result was also reported for TS-1. No oxidation of benzylic methyls was observed. Cumene yielded mainly the decomposition products of cumyl hydroperoxide. The oxidation of *t*-butylbenzene was negligibly low. The reactivity order, toluene > benzene > ethylbenzene > cumene, reflects the reduced steric constraints in the large pores of mordenite. Accordingly, the rate of hydroxylation of xylene isomers increased in the order *para* < *ortho* < *meta*, in contrast to the sterically controlled one, *ortho* < *meta* ≪ *para*, shown on TS-1. It is worth mentioning that the least hindered *p*-xylene exhibited the same reactivity on either catalyst.

18.4
Oxidation of Olefinic Compounds

18.4.1
Epoxidation of Simple Olefins

The oxidation of olefins with aqueous hydrogen peroxide in methanol can produce several products, by different reaction paths: double bond epoxidation, allylic H-abstraction, epoxide solvolysis, alcohol and glycol oxidation (Scheme 18.6). Normally, oxide catalysts of Group IV–VI metals are poorly selective, because of their acidic properties, the inhibition they are subject to in aqueous media and homolytic side reactions with hydrogen peroxide. The only exception concerns the epoxidation of α,β-unsaturated alcohols and acids, which are able to bind on the

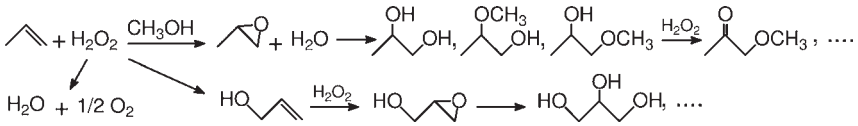

Scheme 18.6 Reaction pathways in the oxidation of propene with hydrogen peroxide.

Table 18.7 Epoxidation of linear olefins.[a)]

Olefin	T (°C)	t (min)	$t_{1/2}$ (min)[b)]	Conversion (%)	Selectivity (% based on H_2O_2)
1-butene	–5	60	–	96	96
1-pentene	25	60	5	94	91
1-hexene	25	70	8	88	90
cyclohexene	25	90	–	9	–
1-octene	45	45	5	81	91
allyl chloride	45	30	7	98	92
allyl alcohol	45[c)]	35	16	81	72

a Adapted from Ref. [62]. Copyright 1993, with permission from Elevier. Solvent, methanol; olefin, 0.90 mol l^{-1}; TS-1, 6.2 g l^{-1}.
b $t_{1/2}$ is the time necessary to 50% H_2O_2 conversion.
c TS-1 4.0 g/l

catalyst through the oxygenated functionality. However, TS-1, a mixed oxide of silica and titania similar in composition and Ti dispersion, but not structure, to the Ti/SiO_2 Shell catalyst, unexpectedly showed high activity and selectivity. Actually, a most remarkable feature of TS-1 is the smooth and preferential epoxidation of the double bond, over any other functionality that may be present in the molecule.

18.4.1.1 Titanium Silicalite-1

Epoxidation occurs in dilute solutions of aqueous hydrogen peroxide and at near room temperature [61, 62]. The rate is rapid even at H_2O_2 concentrations of 1% or lower and at temperatures as low as –5 °C. Electron-deficient olefins can also be oxidized at near room temperature (Table 18.7). Preferred solvents are alcohols and, in general, protic or polar media. The rate of epoxidation decreases in the solvent order: methanol > ethanol > *i*-propanol > acetone > acetonitrile > *t*-butanol, with a difference greater than one order of magnitude between the two extremes of the series [62, 63]. An exception could be the oxidation of cyclopentene, for which acetone and acetonitrile were reported to be less effective than *t*-butanol [64]. In the epoxidation of propene, the rates in water were possibly faster than in methanol, though the rapid decay of the catalyst did not allow unequivocal conclusions. As a matter of fact, water contents up to 50 wt% in methanol produced only a moderate reduction of the rate, probably because of the lower solubility of propene in aqueous media (TOF 1–2 s^{-1}, at 40 °C).

The epoxidation of unhindered olefins is nearly quantitative and the incidence of side reactions is negligible [62]. The epoxide selectivity can be higher than 90%. The by-products are merely those produced by the acid solvolysis of the oxirane ring, namely the corresponding glycol and methyl ethers. Basic compounds able to diffuse inside the pores of TS-1, such as sodium acetate, sodium hydroxide and ammonia, decrease the intra-porous acidity generated by Ti—OOH species and, sometimes, by lattice Al impurities. Their addition in parts per million quantities minimizes the cleavage of the epoxide, thus enhancing the selectivity up to 97–98%. Spontaneous hydrolysis, fairly slow but always present in protic media, prevents the achievement of quantitative yields [61]. Further increasing the concentration of the base gradually decreases the catalytic activity up to complete inhibition. Bulky tetrapropylammonium hydroxide, unable to diffuse into the pores of TS-1, does not affect the epoxidation process at any concentration.

The epoxidation rate is related to the electron density of the double bond, increasing with it. Thus, the epoxidation of propene is much faster than that of ethene. The formal substitution of one methyl, chloro or hydroxyl group at the allylic position of propene results into the reactivity order: 1-butene > allyl chloride > allyl alcohol. Methyl substitution on butenes also produces the expected ordering: 2-methyl-2-butene > 2-methyl-1-butene > 3-methyl-1-butene (Table 18.8).

However, since epoxidation occurs within pores of cross-section comparable to that of the olefin, steric restrictions generally prevail over inductive effects, leading to anomalous reactivity orders. They result from restrictions to diffusion in the pores (reactant shape selectivity) and to the approach of the double bond to the active species (transition state shape selectivity). The first is sufficient to explain

Table 18.8 Relative rates in the epoxidation of C_4 and C_5 olefins.[a)]

TS-1		TS-1		CH_3CO_3H
Olefin	r_1/r_n[b)]	Olefin	r_1/r_n[b)]	r_1/r_n
	1.0		1.0	1.0
	0.59		0.13	ca 1.0
	0.71		0.87[c]	20–24
	0.17[c)]		0.19	20–24
	2.7[c)]	–	–	20–24
–	–		0.79	240

a Data taken from Refs [62, 65].
b Averaged values from competition kinetics.
c Epoxidation occurred with complete retention of configuration.

the rate of epoxidation of cyclohexene, found to be slower than that of 1-hexene by almost two orders of magnitude at near room temperature [62]. The second is apparent in the epoxidation of freely diffusing olefins, for example of the methyl-substituted butenes mentioned above, in which the reactivity order is the expected one, but the relative rates are greatly different from those of a purely electrophilic oxidant (Table 18.8) [65]. Most striking is 2-methyl-2-butene compared to 1-pentene, with a rate somewhat slower on TS-1/H_2O_2 and 240 times faster on peracetic acid. Transition-state shape selectivity in these and other epoxidations is likely to result from steric repulsions exerted by the surface and by the species chemisorbed on Ti on alkyl substituents of the double bond.

The evidence provided so far, that is the quantitative yields (including glycols), the absence of allylic oxidation, the substituent effects and the role of shape selectivity, are consistent with a heterolytic mechanism, involving an electrophilic oxidant species subject to major steric constraints. The retention of configuration in the epoxidation of sterically pure *cis*- and *trans*-butenes is further and convincing support for this proposition. By analogy with many known transition metal peroxides, the active species may be identified among Ti(η^1—OOH), Ti(η^2—OOH) and Ti(η^2—O_2) peroxy species (Figure 18.1a–d). The detection of Ti superoxide radicals (Figure 18.1e), on addition of hydrogen peroxide to TS-1, and the homolytic nature of C—H abstraction do not weaken the idea of a heterolytic mechanism. Based on the author's and others' experience [66] (and in contrast to some other reports [9]), the superoxide species involve only a negligible fraction of Ti-sites.

The competition of one-electron pathways is sometimes detectable in the epoxidations catalyzed by transition metal catalysts [67]. However, in the epoxidation of unhindered olefins on TS-1, the typical radical products are below the detection limits. Their presence could no longer be neglected when the rate of epoxidation is so slow as to become comparable to that of homolytic side reactions, for example with bulky olefins (see also Section 18.11). It is possible that, within these limits only, the epoxide is produced in part through the addition of a radical peroxy intermediate to the double bond [68, 69]. Even so, a homolytic pathway has again been proposed as a generally valid epoxidation mechanism [7].

In early proposals based upon the mechanisms of Mo and V peroxides, Ti(η^2—O_2) was thought to be the active species [70, 71]. The epoxidation of the olefin occurred either by a coordinative mechanism, with the olefin adsorbing on Ti prior to the insertion into one Ti-peroxide bond, or by the attack of one peroxy oxygen directly on the double bond. However, the chemical inertness of known Ti(η^2—O_2) peroxides, the unlikelihood of olefin adsorption on oxophilic Ti in competition with the protic medium and other evidence led subsequently to the loss

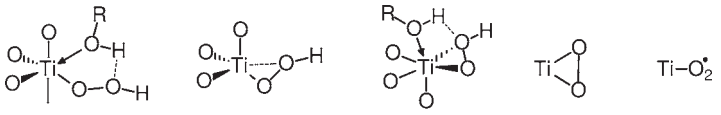

Figure 18.1 Active species proposed for epoxidations on TS-1.

of credibility for this proposal. Currently, a general consensus involving a central role of a Ti—OOH species seems to exist. There is less agreement on the details of its structure, particularly on the presence and the function of a co-adsorbed protic molecule (Figure 18.1a and c) and on the mono- (Figure 18.1a) or di-hapto (Figure 18.1b and c) coordination of the hydroperoxide group. In an early proposal, the latter was monodentate and was stabilized in a five-membered ring by a hydrogen-bonded protic molecule, typically methanol or water (Figure 18.1a) [24, 62]. This proposal was based on adsorption properties of Ti sites, on the reactivity behaviour of organic and inorganic peroxides and on the smooth formation of cyclic structures in hydroperoxides and other compounds. In the alternative species, based on quantum chemical studies, the hydroperoxide group was η^2 coordinated and did not require stabilization (Figure 18.1b) [72]. In another proposal, also based on DFT calculations, η^2 coordination and hydrogen bonding with a protic molecule coexist in the same structure (Figure 18.1c) [73, 74].

Scheme 18.7 illustrates a proposed early mechanism based on the intermediate of Figure 18.1a [62, 75]. The first steps in the catalytic cycle are reversible and envisage the adsorption of one molecule of H_2O_2, the formation of a Ti—OOH species and its hydrogen bonding with one alcohol or water molecule. In the irreversible epoxidation step, the attack on the double bond by the peroxy oxygen vicinal to Ti, leads to the formation of the epoxide, a Ti-alkoxide and a water molecule. Finally, the desorption of the epoxide and the reaction of Ti-alkoxide with water, to form again the initial Ti-site, complete the catalytic cycle. As an alternative to it, H_2O_2 could chemisorb directly on Ti-alkoxide to regenerate the Ti—OOH species. The desorption of the product is an important step for the activity, since the epoxide behaves as an inhibitor.

Scheme 18.8 illustrates the oxygen-transfer steps of species **b** and **c** in Figure 18.1 [72–74]. Both mechanisms are based on DFT studies and are similar to the epoxidations with organic hydroperoxides on Group IV–VI metal catalysts [1]. The

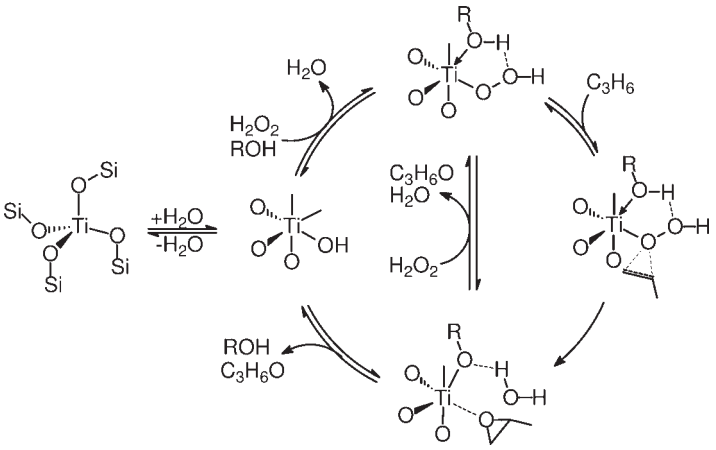

Scheme 18.7 Epoxidation mechanism of species (*a*) from Figure 18.1.

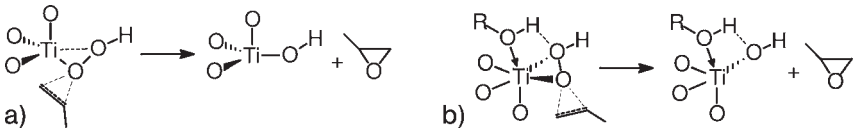

Scheme 18.8 (a) Epoxidation mechanism of species (*b*) from Figure 18.1; (b) Epoxidation mechanism of species (*c*) from Figure 18.1.

coordination of distal peroxy oxygen on Ti facilitates its removal as a titanol. A weakness of Scheme 18.8a is the absence of adsorbates other than hydrogen peroxide on Ti. The hypothesis could be correct for epoxidations with organic hydroperoxides carried out under anhydrous conditions, but not for the use of aqueous hydrogen peroxide. It is fully consistent, however, with epoxidations conducted under reduced pressure, in the conditions studied by Lin and Frei [76]. The same arguments for Scheme 18.7 could apply also to Scheme 18.8b.

18.4.1.2 **Other Ti-Zeolites**

The number of metal zeolites and their application to the epoxidation of olefins rose in parallel from the late 1980s. TS-2, Ti,Al-β, Ti-β, Ti-MWW and, rarely, Ti-MOR are catalysts that have been studied in some detail [7–9, 35, 77–84]. TS-2 behaves, according to the few studies published, similarly to TS-1. The greater spaciousness of pores in Ti-Beta zeolites and of external cups in Ti-MWW allows the epoxidation, under mild conditions, of olefins unable to diffuse in TS-1 and TS-2, such as methylcyclohexenes, cyclododecene, norbornene, camphene and methyl oleate [80–83]. Steric constraints still prevail over electronic factors, however, as in medium pore Ti-zeolites, even in the epoxidation of linear olefins (Table 18.9). It is generally believed that active sites and epoxidation mechanisms are not significantly different from those of TS-1.

There are major differences that distinguish Ti,Al-β, Ti-β and Ti-MWW. The first concerns the activity and selectivity, which, under optimum conditions for each catalyst, are considerably lower than for TS-1. The activity in methanol decreases in the order, TS-1 > Ti-β > Ti,Al-β ≥ Ti-MWW, in a parallel trend with the decrease of the hydrophobicity. Actually, the density of surface Si—OH species increases in the reverse order: TS-1 < Ti-β < Ti,Al-β ≤ Ti-MWW. The selectivity, in turn, drops owing to a greater incidence of solvolysis and hydrogen peroxide decomposition. Even in the absence of framework Al sites, as in Ti-β, the solvolysis can significantly reduce epoxide yields. Ion exchange with basic compounds or just their addition in the reaction medium is an effective tool to limit the losses of product [84].

A second difference compared to TS-1 concerns the solvent and its effects on kinetics and selectivity. The choice is again restricted to alcohols, ketones and acetonitrile, but the latter is now preferable to methanol for higher rates and lower solvolysis [77, 78]. As a general rule, methanol is the best solvent for oxidations catalyzed by TS-1, whereas acetonitrile is preferable for Ti-β, Ti,Al-β and Ti-MWW

Table 18.9 Epoxidation of olefins over Ti-β, Ti,Al-β, TS-1 and CH_3CO_3H. Relative rates.

Olefin	Ti,Al-β[a)]	Ti-β[b)]	TS-1[a)]	CH_3CO_3H[c)]
	1.0	1.0	1.0	1.0
	0.70	0.77	0.63	ca 1
	–	1.55	–	20–24
	1.1	–	2.2	20–24
	0.83	–	–	20–24
	1.6	1.2	–	27
	1.6	–	0.63	ca 240
	1.2	0.72	0	(≥240)

a Data from Ref. [83].
b Data from Ref. [81].
c Data from Ref. [65].

[81, 85, 86]. The enhanced activity is likely the result of the effects of different factors, while the greater selectivity has to be related to the reduction of acidity by the mildly basic medium. Interestingly enough, in various instances Ti-β, Ti,Al-β and Ti-MWW turn out to be more active catalysts than TS-1, when acetonitrile is a common solvent. In one study, however, trifluorethanol emerged as the best solvent for Ti,Al-β [84].

A third difference concerns Ti-MWW only. The siting of Ti in different porous environments, that is in external pockets, in internal supercages and in sinusoidal 10-MR channels, leads to active species associated with different diffusional and steric constraints [79]. Thus, the epoxidation of bulky olefins can occur exclusively in external pockets, whereas the linear ones are not subject to site limitations. Ti-MWW is also an unusual catalyst in the epoxidation of stereoisomers. At odds with TS-1 and Ti-Beta zeolites, *trans*-olefins are epoxidized faster than their *cis* analogues [85]. Though the mechanism is still unclear, a better fitting of the trans configuration to the tortuous nature of 10-MR channels could be an explanation.

Ti-Beta zeolites and, even more, mesoporous Ti-silicates can be somewhat unstable to aqueous hydrogen peroxide and to strongly chelating agents. A partial collapse of the lattice and the release of Ti, in the form of TiO_2 particles or soluble Ti peroxides, was sometimes observed under these conditions (see also Section 18.4.2). The structural instability grows in parallel with the hydrophilicity of the surface and the defectiveness of the silica matrix: Ti-β < Ti,Al-β ≪ Ti-MCM-41 [87–89]. For the same reason, the stability of the catalyst is indirectly related to the method of synthesis, as far as this is able to produce materials with a different content of connectivity defects.

Since water is detrimental to catalytic performance, and its presence is unavoidable with hydrogen peroxide as the oxidant, an alternative consists of the use of *t*-butyl hydroperoxide (TBHP), compatible with the pores of Ti-Beta zeolites and with external pockets of Ti-MWW. In the case of the former catalysts, rates are lower than with hydrogen peroxide while with Ti-MWW they are comparable [79, 83]. It should be considered, however, that in this use both large-pore Ti-zeolites and mesoporous Ti-silicates are in competition with the cheaper and easier to prepare Ti/SiO_2.

In summary, the poorer activity, the stronger acidity and sometimes the structural instability are major drawbacks that minimize the chances of application of large-pore Ti-zeolites. The reduced adsorption of alkanes, alkenes and other apolar reagents in favor of that of water, and the defectiveness of the surface, are the principal reasons for this (for a further treatment, the reader is referred to Section 18.11). In relation to these issues, synthetic methods for the production of materials with fewer defective sites and better connectivity, have been developed for both Ti-Beta zeolites and mesoporous Ti-silicates [7–9].

18.4.2 Epoxidation of Unsaturated Alcohols

In principle, the oxidation of allyl alcohols may concern the double bond or the alcohol group. In the absence of steric constraints, TS-1, TS-2, Ti,Al-β, Ti-β and Ti-MWW catalyze the epoxidation with generally high chemoselectivity [81, 88, 90–97]. Carbonyl compounds may form by competitive oxidation, to an extent that depends on steric constraints (Table 18.10). Normally, TS-1 is the most effective

Table 18.10 Oxidation of unsaturated alcohols over TS-1 and Ti-β.

Olefin	TS-1[a]		Ti-β[b]	
	Epoxide (%)	Aldehyde (%)	Epoxide (%)	Aldehyde (%)
	100	–	>90	–
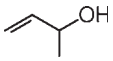	100	–	>90	–
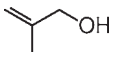	90	10	85	11
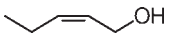	–	–	89	11
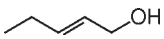	76	24	–	–
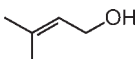	82	18	96	–
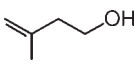	64	36	–	–

a Data from Ref. [90].
b Data from Ref. [81].

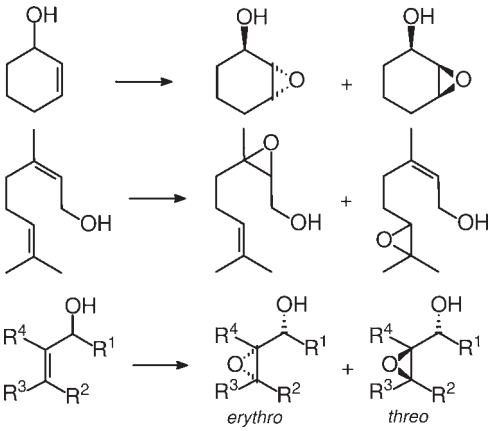

Scheme 18.9 Oxidation of allyl alcohols.

catalyst for unhindered substrates. However, Ti-MWW showed the best activity and selectivity for the synthesis of glycidol in acetonitrile and water: Ti-MWW > TS-1 > Ti-β [96]. Selective poisoning tests showed that the epoxidation occurred in the external pockets of crystallites.

Stereo-, diastereo- and regioselectivity can be very high (Scheme 18.9). This implies OH-assistance in the oxygen-transfer step, through the hydrogen bonding of the alcohol group with the oxidant species, as for vanadium catalysts and peracids. Thus, with TS-1, 3-cyclohexenol and 3-cyclopentenol yielded the *cis* epoxides with 90% selectivity [91]. Chiral allyl alcohols produced, with TS-1 and Ti,Al-β, a mixture of *threo* and *erythro* epoxy alcohols, in a ratio that was apparently independent of constraints produced by the pores [97]. The epoxidation of geraniol and nerol on TS-1 occurred on the vicinal double bond, while the remote and more nucleophilic one was reported to be inert [91]. However, Schofield and others observed epoxidation at either double bond, on TS-1 and Ti,Al-β, in the ratio of ca 2:1 in favor of the distant one [93]. Interestingly enough, the use of methanol completely inhibited epoxidation at the vicinal position, favoring the electron-rich distant one. This suggests that the competition of methanol for adsorption on Ti sites suppresses the coordinative interaction of the allyl alcohol with the active species.

The use of aqueous methanol, through the opening of oxirane rings, can have a detrimental effect on the stability of the catalyst. By-product triols coordinate strongly on Ti, facilitating its removal from the silica matrix, to the point that after an induction period the epoxidation of allyl alcohols on Ti,Al-β and Ti-β became an essentially homogeneous process [88]. In the epoxidation of crotyl alcohol, the trend of Ti leaching was: Ti,Al-β > Ti-β ≫ TS-1, the process being negligible on the latter. The use of acetonitrile and the adoption of anhydrous conditions protected the catalyst from structural degradation, by the reduction of solvolysis. Specific tests revealed that the simultaneous presence of triol and hydrogen peroxide was necessary for leaching to occur, while taken alone they did not produce any significant structural damage.

It is likely that the commercial value of glycidol is the unmentioned background of most studies. However, process parameters were specifically studied in only one case, in which TS-2 was the catalyst. The conversion of the olefin, under optimum conditions, was ca 88% with 100% selectivity [94]. Methallyl alcohol was the subject of a similar study [95].

18.4.3
Epoxidation of Allyl Chloride and other Substituted Olefins

Several patents and two papers deal with the epoxidation of allyl chloride [98, 99]. Actually, a process based on TS-1 would represent an environmentally cleaner alternative to current production of epichlorohydrin. In this regard, one study has addressed the cost of commercial hydrogen peroxide with the *in situ* production of the oxidant, by the use of molecular oxygen and anthrahydroquinone compounds [99]. In a mechanistic study, the kinetic data were interpreted on the basis of Eley–Rideal isotherms, with the rate of reaction being first order on TS-1 and between 0 and 1 on H_2O_2 and C_3H_5Cl (Equation 18.8) [98].

$$r = k_{app} \frac{[H_2O_2]\,[C_3H_5Cl]\,[TS\text{-}1]}{1 + K_1\,[H_2O_2] + K_2[C_3H_5Cl]} \tag{18.8}$$

Diallyl ether and diallyl carbonate produced monoglycidyl and diglycidyl ethers in a ratio that depended on the conversion. Allyl methacrylate yielded the corresponding glycidyl methacrylate [5]. Ti-MWW, in acetonitrile and acetone solvents, was again reported to be more active and selective than TS-1 [100].

The epoxidation of α,β-unsaturated ketones produced corresponding epoxides and minor amounts of glycols [101]. Methyl substitution on the double bond reduced, or even suppressed, the oxidation. α,β-Unsaturated aldehydes yielded the corresponding carboxylic acids and minor amounts of epoxides. α,β-Unsaturated acids were inert under analogous reaction conditions. In this regard, Ti-zeolites behave differently from homogeneous tungsten catalysts, in which epoxidation does occur through a coordinative mechanism [102]. Consistently, acrylic acid esters were inert to both kinds of catalyst.

18.4.4
Epoxidation with Solvolysis/Rearrangement of Intermediate Epoxide

The presence of acidity leads to a variety of end-products, depending on the catalyst, the olefinic substrate and the reaction conditions (e.g. the sort of solvent, the temperature and the use of acidity moderators). The acid properties of Ti,Al-β in this regard, and the use of basic additives to reduce their effects, have been illustrated [61, 84]. Ti-MOR is also acidic owing to residual Al in the framework [59]. TS-1, with Al, Ga, B or Fe inserted in the framework, behaves similarly [103]. Al-free Ti-β and Ti-MWW are less acidic catalysts than the former ones, but signifi-

cantly more acidic than TS-1. Most likely, the acid sites in the latter are the Ti—OOH species *a* of Figure 18.1 (see also Section 18.11.3).

In some instances, combined redox/acid catalysis might be desirable, as in the one-pot syntheses of β-phenylacetaldehyde by the oxidation of styrene. The primary product is generally believed to be 1,2-styrene oxide, which, in a second stage, undergoes acid-catalyzed rearrangement to the aldehyde. Acidic zeolites are known to behave as good catalysts in the latter reaction [104]. According to one study, however, 1,2-styrene oxide and β-phenyl acetaldehyde could be formed independently by two competing mechanisms [105].

Derouane and coworkers exploited the dual catalytic function and the spaciousness of pores of Ti,Al-β to prepare *trans*-2-alkoxycycloalkanols, of interest as pharmaceutical intermediates, by the oxidation of cyclohexene and cyclopentene [106]. The one-pot epoxidation/cyclization of unsaturated terpene alcohols, for example linalool and α-terpineol, to mono- and bicyclic derivatives also required the catalysis of large-pore Ti,Al-β (Scheme 18.10) [93, 107].

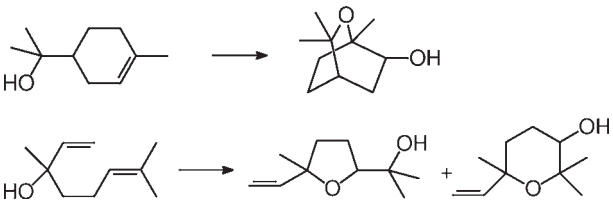

Scheme 18.10 Oxidation/cyclization of unsaturated alcohols on Ti,Al-β.

On TS-1, Ti-β, Ti,Al-β and Ti-MWW in water and, to a lesser extent, in acetonitrile, tetralkyl-substituted olefins yielded corresponding pinacols (tetralkyl-substituted glycols) [108]. In the oxidation of 3,4- and 4,5-unsaturated alcohols on TS-1, the intramolecular cyclization, by internal attack of the hydroxy group on the oxirane ring, competed successfully with hydrolysis by external attack of water (Scheme 18.11) [107]. Cyclization occurred regioselectively on the less remote carbon, with yields often higher than 85%. Oxidation of 5-hexen-1-ol, in which the five-membered ring cannot form, produced the tetrahydropyran derivative. Triol by-products increased with temperature and water content. Conversely, nearly anhydrous conditions and the control of acidity with basic additives turned the oxidation into epoxy alcohol production.

18.5
Oxidation of Alcohol and Other Oxygenated Compounds

The oxidation of primary and secondary alcohols using TS-1 and Ti,Al-β produces corresponding aldehydes and ketones [5, 77, 109–112]. While the latter are sufficiently stable under the reaction conditions, the former can undergo further oxidation to carboxylic acids. Acetals and esters are also produced when operating in

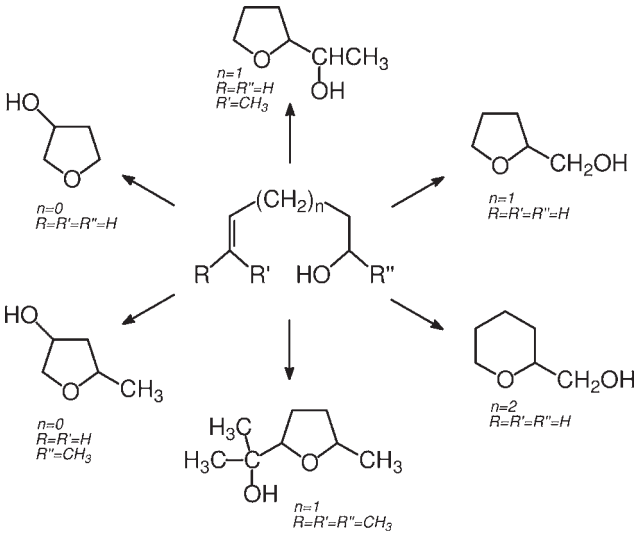

Scheme 18.11 Oxidation of 3,4-, 4,5- and 5,6-unsaturated alcohols on acidic Ti-zeolites.

neat alcohol or in methanol solvent (Equations 18.9 and 18.10). Tertiary alcohols yield corresponding hydroperoxides.

$$RCH_2OH \xrightarrow{H_2O_2} RCHO \xrightarrow{H_2O_2} RCO_2H \qquad (18.9)$$

$$RCHO \underset{}{\overset{R'OH}{\rightleftharpoons}} RCH(OR')_2 \xrightarrow{H_2O_2} RCO_2R' \qquad (18.10)$$

Primary alcohols react at a much slower rate than secondary ones, suggesting an electrophilic oxidation mechanism (Table 18.11). The relative inertness of methanol justifies its use as an oxidation solvent for TS-1. Within a homologous series, the rate increases with the chain length of the alcohol up to a maximum for octanol, then decreasing again [109]. It is likely that this trend involves the combined effects of electronic factors, deactivation of the catalyst and adsorption phenomena. A true kinetic ordering, only obtainable from initial rates, is substantially lacking for this as for other oxidations. Shape selectivity is apparent in the decrease of the rate of alcohols with the hydroxy group at more internal positions or with vicinal methyl groups, the decrease being larger with the increase of the number of methyl substituents [110, 111].

Two papers deal with the kinetics of the oxidation on TS-1 and Ti,Al-β [110, 111]. Equation 18.11 illustrates the general rate law valid for both catalysts, according to a Langmuir–Hinshelwood model. It is consistent with the competition of alcohol/solvent for Ti sites and the adsorption of the substrate and the oxidant on the same site. The inhibitory effect of water, implicit in the competitive adsorption of the solvent, was proved by oxidation tests performed in acetonitrile containing variable quantities of water [77, 111].

Table 18.11 Oxidation of alcohols catalyzed by TS-1.[a)]

Alcohol	$t_{1/2}$ (h)[b)]	H_2O_2 decomposition (%)[c)]
methanol	8.5	13
ethanol	0.7	2.5
1-propanol	1.0	5
1-butanol	1.3	6
1-octanol	3.0	–
2-methyl-1-propanol	3.4[d)]	–
2-propanol	0.01	<0.5
2-butanol	0.05	<0.5
2-pentanol	0.06	<0.5
3-pentanol	0.9	5
cyclohexanol	35	50

a Reprinted from Ref. [110]. Copyright 1994, with permission of Elsevier. Solvent, pure alcohol; *T*, 45 °C; TS-1, 5 wt%; H_2O_2, 0.5 mol l^{-1}.
b Time required for 50% conversion.
c Fraction of H_2O_2 decomposed at total conversion of alcohol.
d The product is *t*-butyl hydroperoxide.

$$r = \frac{k\,K_2\,K_4\,[Ti_0]\,[ROH]\,[H_2O_2]}{1 + K_1\,[solv] + K_2\,[ROH] + [H_2O_2]\,(K_3K_1\,[solv] + K_4K_2\,[ROH])} \qquad (18.11)$$

The oxidation mechanism, based on an early one proposed for a tungsten catalyst, entails a concerted step in which a C—H bond undergoes electrophilic attack by the distal peroxy oxygen of Ti—OOH (Scheme 18.12) [110, 111, 113].

The one-step synthesis of isoamyl butyrate from isoamyl alcohol and *n*-butyraldehyde, possibly through the formation and subsequent oxidation of an acetal intermediate, could represent a special case in TS-1 catalysis, since the oxidant was molecular oxygen [114]. The authors did not advance any mechanistic hypothesis. *n*-Butyl hydroperoxide, however, produced *in situ* by the autoxidation of *n*-butyraldehyde, could have been the true oxidant, by virtue of its dimensional compatibility with the narrow pores of TS-1.

The oxidation of glycols occurred preferentially at the secondary alcohol group. Thus, propene glycol and 2-phenyl-1,2-ethanediol afforded hydroxyacetone and β-hydroxyacetophenone, respectively, as the major product [115]. Ethene glycol

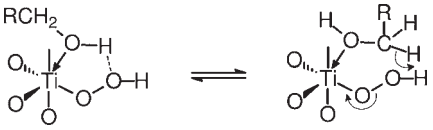

Scheme 18.12 Oxidation of alcohols on TS-1 and Ti,Al-β.

produced glycolic acid. Further oxidation yielded the α-dicarbonyl derivatives and, at prolonged contact time, C—C bond oxidative cleavage.

The oxidation of tetrahydrofuran, tetrahydropyran and dihydropyran produced γ-butyrolactone and δ-valerolactone in fairly good yields. Linear ethers, conversely, produced exclusively the corresponding acids, presumably through the *in situ* hydrolysis of intermediate esters [116].

The Baeyer–Villiger rearrangement of cyclohexanone and acetophenone with TS-1/H_2O_2 proved to be poorly selective [117]. Notably, Ti-β and Sn-β have different chemoselectivities in the oxidation of unsaturated ketones, leading selectively to corresponding epoxides and lactones, respectively [118]. The different oxidation pathways were attributed to the preferential adsorption of hydrogen peroxide on Ti-sites and of the carbonyl group on Sn-sites.

18.6 Ammoximation of Carbonyl Compounds

The word ammoximation defines the reaction of a carbonyl compound with ammonia, under oxidative conditions, to yield the corresponding oxime (Equation 18.12). Early homogeneous and heterogeneous catalysts, for example heteropoly compounds and amorphous Ti/SiO_2, had too poor selectivity to envisage any application. The prospects changed when Roffia and coworkers discovered that TS-1 was an excellent ammoximation catalyst with hydrogen peroxide as oxidant [119]. As Table 18.12 shows, TS-1 and amorphous Ti/SiO_2, albeit with similar Ti contents, lead to completely different results: to quantitative yields for the former and to a mixture of products, with only a minor amount of oxime, for the latter.

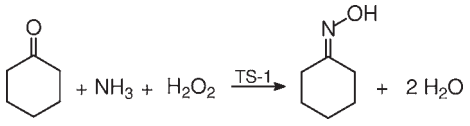

(18.12)

In contrast to the stability shown in other oxidations, TS-1 undergoes a slow but irreversible deactivation. The siliceous matrix of the catalyst, in fact, slowly dissolves in the basic medium, while Ti, released from the framework, aggregates to

Table 18.12 Ammoximation of cyclohexanone on different catalysts.[a)]

Cat.	Ti (wt%)	Conv. $C_6H_{10}O$ (%)	Sel. on $C_6H_{10}O$ (%)	Yield on H_2O_2 (%)
TS-1	1.5	99.9	98.2	93.2
Ti/SiO_2	1.5	49.3	9.3	4.4
S-1	–	59.4	0.5	0.3

a Solvent, *t*-butanol/water; *T*, 80 °C; molar ratios, cyclohexanone: NH_3: H_2O_2 1.0 : 2.0 : 1.1; t.o.s. 1.5 h.

form TiO_2 particles. Accordingly, the activity decreases with time on-stream, approaching that of conventional catalysts at prolonged times [120]. Major side reactions consist of the oxidation of ammonia to N_2, N_2O, nitrites and nitrates and in the decomposition of H_2O_2 to molecular O_2. Condensation reactions of cyclohexanone in the basic medium and consecutive oxidation of the oxime produce minor amounts of organic by-products. However, the losses of the oxidant are generally moderate, for example <7% under the conditions of Table 18.12, and the decay of the catalyst is not so fast as to preclude the development of an industrially viable process.

The reaction of ammoximation is generally applicable and provides an efficient route to many other oximes in addition to the industrially relevant cyclohexanone oxime. Acetone, butanone, acetophenone, C_5—C_8 cyclic ketones and methyl-substituted cyclohexanones produced the corresponding oximes with high conversion and selectivity. Even the ammoximation of cyclododecanone and 4-butylcyclohexanone, unable to diffuse in TS-1, occurred with high yields [121–123]. Other ammoximation catalysts are carbon-supported TS-1, TS-2, Ti-MOR and Ti-MWW, with conversions and selectivities close to those of TS-1 [124–128].

Two ammoximation mechanisms were initially proposed, one envisaging the formation of cyclohexanone imine (Equation 18.13) and the other that of hydroxylamine (Equation 18.14) as key intermediates.

$$R_2CO \xrightarrow{NH_3} R_2C{=}NH \xrightarrow[TS\text{-}1]{H_2O_2} R_2C{=}NOH \qquad (18.13)$$

$$NH_3 \xrightarrow[TS\text{-}1]{H_2O_2} NH_2OH \xrightarrow{R_2CO} R_2C{=}NOH \qquad (18.14)$$

The high yields obtained from ketones unable to diffuse inside the pores of TS-1, namely cyclododecanone and 4-butylcyclohexanone, strongly supports the second mechanism [121, 123]. The imine intermediate, if present, could only play a secondary role in the overall balance of the ammoximation process. In this regard, Mantegazza and others showed that TS-1, under the reaction conditions, catalyzes the oxidation of ammonia to hydroxylamine with yields greater than 60% [129]. The subsequent condensation with the carbonyl group is a fast reaction and does not require catalysis by TS-1. It occurs in the external medium with bulky ketones, while with smaller ones the intra-porous volume also could be involved. In the absence of a carbonyl group acceptor, hydroxylamine undergoes consecutive oxidation to N_2, N_2O, nitrites and nitrates. On these grounds, the overall ammoximation process could be better defined as an oximation reaction with *in situ* production of hydroxylamine. The relative rates of condensation and consecutive oxidation determine the selectivity of the overall process (Scheme 18.13).

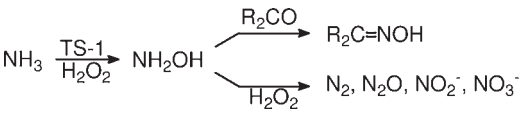

Scheme 18.13 Competing reactions of hydroxylamine with cyclohexanone and H_2O_2.

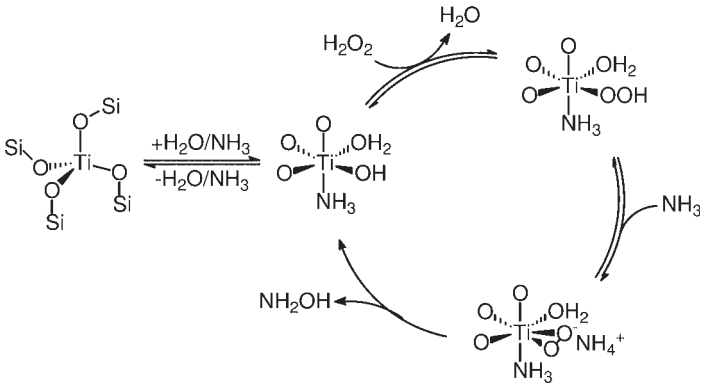

Scheme 18.14 Ammoximation mechanism on TS-1.
(Adapted from Ref. [130], with permission from Elsevier).

The nature of active species and the mode of generation of hydroxylamine are the subject of several studies by various spectroscopic techniques [20, 130]. According to Zecchina and coworkers, the chemisorption of hydrogen peroxide produces the familiar Ti—OOH species, which, however, in the basic medium evolves towards a side-on-bonded anionic peroxide Ti(η^2—O_2)$^-$ (Scheme 18.14). The adsorption of water and ammonia completes the coordination sphere of Ti, leading to various species in which either adsorbate can be present with one or two molecules at each time. In Scheme 18.14, the suggestion is made, somewhat arbitrarily, of the mixed adsorption species. A second issue that spectroscopic data do not help solve is whether hydroxylamine is formed by intramolecular reaction between chemisorbed species (in a Languimir–Hinshelwood-type mechanism) or by external attack of physisorbed ammonia on peroxy oxygen (in an Eley–Rideal-type mechanism). A recent kinetic study seems to favor the former pathway [131]. A third issue concerns a possible role of Ti—OOH species in the formation of hydroxylamine. The basic medium, indeed, shifts the acid–base equilibrium towards the formation of the anionic peroxy species, but the presence of Ti—OOH in small amounts cannot be ruled out completely. The greater electrophilicity of Ti—OOH could compensate for its lower concentration.

18.7
Oxidation of N-Compounds

Primary amines, with at least one α-C—H bond, undergo consecutive oxidation to yield unstable alkylnitroso intermediates. These can isomerize to corresponding oximes, dimerize to nitroso dimers and produce nitro derivatives by further oxidation (Scheme 18.15). The selectivity depends on the oxidant system and the reaction conditions. The size restrictions of TS-1 allow a greater selectivity to the

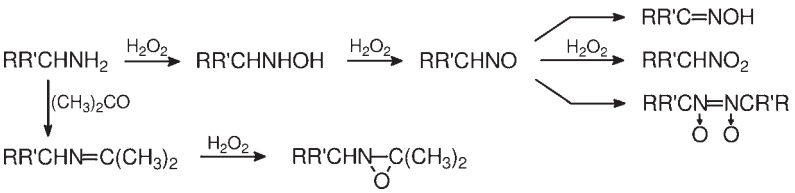

Scheme 18.15 Oxidation of primary amines.

desirable oxime than conventional catalysts, at the expense of the bulkier dimer. Methanol and *t*-butanol are suitable solvents, while acetone undergoes side reactions with the amine and the oxidant [132]. The oxidation was broadened to include several aliphatic and benzylic amines, owing to the versatility of alkyl oximes in organic synthesis [133].

The oxidation of secondary amines can produce the corresponding hydroxylamines and nitrones (Equation 18.15) [134, 135]. TS-1 and TS-2 catalyzed the production of the former, at H_2O_2/amine molar ratios below unity. The addition of alkali metal additives improved the selectivity up to 90% [136]. High yields of nitrones could be obtained at greater H_2O_2/amine ratios.

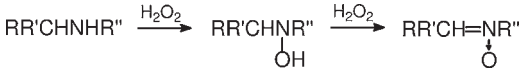

(18.15)

The oxidation of aniline and other arylamines yields a wide spectrum of products, among which azoxybenzenes are the most desirable (Scheme 18.16). TS-1, Ti-ZSM-5, TS-2, Ti,Al-β and Ti-MCM-41, were studied as catalysts, with hydrogen peroxide and *t*-butyl hydroperoxide as the oxidants [137–140]. The best yields, up to 95%, were reported for Ti,Al-β and mesoporous Ti-silicates, with high aniline/H_2O_2 molar ratios to minimize over-oxidation to nitrobenzene. Anilines, with either electron-donating or -withdrawing groups, and 1-naphthylamine behaved similarly. Owing to diffusional restrictions, TS-1 was less effective than large-pore and mesoporous catalysts.

The oxidation of aromatic and aliphatic oximes and of tosylhydrazones on TS-1 with excess H_2O_2 was reported to regenerate corresponding aldehydes [141, 142]. These were obtained also by the one-pot oxidation of primary amines under analogous conditions [143].

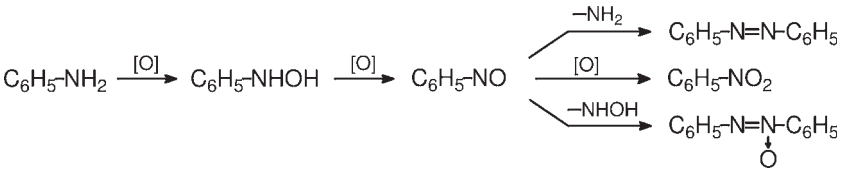

Scheme 18.16 Oxidation of aniline.

18.8
Oxidation of S-Compounds

The oxidation of thioethers on TS-1, Ti-β and Ti,Al-β produced corresponding sulfoxides and, more slowly, sulfones by consecutive oxidation [144–149]. Allyl methyl thioether was oxidized selectively on sulfur, with no reaction of the double bond [148]. The kinetic law was obtained for the oxidation of dibutylsulfoxide on Ti,Al-β [147].

The oxidation of thiophene sulfides combined with a selective separation process of oxidized products, for example by adsorption on inert materials, might offer an alternative to deep hydrotreating for desulfurization of oil fractions. On these grounds, the oxidation of disulfides has gained considerable interest [149]. Owing to the nature of sulfur impurities, large-pore and even more mesoporous Ti-silicates would be appropriate catalysts.

18.9
Industrial Processes Catalyzed by TS-1

Three oxidation processes are already commercial. Other processes could be developed in the future, for example for the production of epichlorohydrin and phenol, especially in the event that new production strategies reduced the cost of hydrogen peroxide (see below). It is unlikely, however, that Ti-zeolites other than TS-1 could find application in the foreseeable future.

18.9.1
Hydroxylation of Phenol to Catechol and Hydroquinone

In 1986 the EniChem process replaced the Brichima process, with significant materials and energy savings (Table 18.5, entries 1 and 2). It operates with excess phenol, fed with H_2O_2 into a slurry of TS-1 in aqueous acetone, at ca 100 °C [5]. While the conversion of the oxidant is driven to completeness, excess phenol is recovered by distillation and recycled. The catalyst is structurally stable under operating conditions, being deactivated only by pore plugging and active site fouling. The regeneration is conveniently carried out thermally under flowing air.

With an overall capacity of 10 000 $t\,a^{-1}$, it is a modest process when compared to recent applications of TS-1 in ammoximation and propene epoxidation. The introduction of digital photography, which no longer needs hydroquinone for the development of silver emulsions, risks the continuity of the process, unless the selectivity to catechol is greatly improved or new uses are developed for hydroquinone.

18.9.2
Salt-Free Production of Cyclohexanone Oxime

A demonstration plant, built by EniChem at the industrial site of Porto Marghera, near Venice, began operation in 1994 (12 000 $t\,a^{-1}$). The process was operated con-

tinuously in the liquid phase in a stirred reactor. Cyclohexanone, ammonia and hydrogen peroxide were fed, at 80–90 °C and slight over-pressure, into a slurry of TS-1 in aqueous *t*-butanol. The effluent was separated from the catalyst through a filter, and sent to a distillation column. Excess ammonia and the solvent, recovered overhead, were recycled in the reactor, while the aqueous solution of oxime, taken from the bottom, underwent further purification. Periodic purging and make-up operations of the catalyst were necessary to compensate for irreversible decay.

The first commercial application, made possible by an agreement between EniChem and Sumitomo, went on-stream in 2003 in Japan, within the context of an integrated process for the production of ε-caprolactam by a new salt-free technology (ca 60 000 t a^{-1}). Actually, besides the ammoximation step, no major by-product is produced even in the gas-phase rearrangement carried out on silicalite-1 as the catalyst. On the whole, the ammonium sulfate is no longer a burden and the gaseous emissions too are drastically reduced.

The truly innovative nature of the EniChem process over earlier ones is apparent. The preparation of hydroxylamine in the latter case necessitates multi-step operation, often ending with major co-production of inorganic salts, as in the Raschig process. The ammoximation of cyclohexanone, with its *in situ* generation of the intermediate, reduces significantly the investment and operation costs while improving the environmental compatibility. The new process represents a good example of how to combine profitability and environmental concern.

18.9.3
Propene Oxide Synthesis (HPPO)

The industrial process for propene oxide manufacture is commonly referred to as the HPPO (hydrogen peroxide propene oxide) process. EniChem set up a prototype plant in 2002 [150]. BASF/Dow Chemicals and Degussa, in turn, have the construction of commercial plants already in progress or at the planning stage [151].

In the EniChem process (6 t day^{-1}), a dilute solution of hydrogen peroxide and a gaseous stream of propene were fed into a stirred reactor containing TS-1 and aqueous methanol [150]. The process was operated continuously, at moderate pressure and temperature. The selectivity could be as high as 98%. Propene, the epoxide and methanol were recovered by distillation of the effluent, while glycol by-products accumulated in the aqueous solution at the bottom of the column. The latter, depending on the selectivity of epoxidation, was either processed to recover the glycols or sent directly to the biological plant, for final treatment before disposal. The stability of the catalyst to deactivation, achieved by the appropriate control of operating conditions, was very high and did not require frequent regeneration. According to Romano, the new process is characterized by lower environmental impact, simpler process design and relatively lower investment and operating costs than conventional ones [150].

Less is known of the processes developed by other companies. BASF/Dow Chemical, in a joint venture, started the construction of a 300 000 t a^{-1} plant at the BASF site in Antwerp (Belgium) at the end of 2006 [151]. Hydrogen peroxide will

be supplied by a 230 000 t a^{-1} plant based on Solvay's anthraquinone technology and located at the same site in Antwerp. The operative start-up is scheduled for early 2008. Both plants will be the world's largest single train ones in operation. HPPO technology is also under evaluation for other facilities in the USA and Asia.

Degussa, in turn, has recently announced the commercialization of a HPPO process, jointly developed with the engineering company Uhde. Parallel to this, Degussa with Headwaters is also working on the direct synthesis of H_2O_2, for which a demonstration plant was completed in 2006 [151]. According to the news release, hydrogen peroxide will be obtained in the new process as a dilute methanol solution to be used directly in the epoxidation of propene.

18.10
Problems in the Use of H_2O_2 and Possible Solutions

Hydrogen peroxide is currently produced by the anthraquinone autoxidation (AO) process. It is a relatively expensive chemical, used for bleaching in the pulp/paper (ca 57%) and textile industries (6%), for waste water and effluent treatment (5%) and for laundry products (ca 12%). Only a minor amount (ca 10%) is currently consumed for the production of fine chemicals (the figures refer to the early 2000s). The cost and the production technology, while compatible with its present uses, fit less well with petrochemical applications. For instance, the cost of commercial hydrogen peroxide (0.69 $/lb, 100% H_2O_2) is comparable, on a weight basis, to that of propene oxide (0.70 $/lb) [152]. The annual capacity of the plants, mainly comprising the ranges of 10 000–20 000 and 40 000–70 000 tons, with a very few slightly over 100 000 t a^{-1}, is undersized for average petrochemical production. The shipment of large amounts of hydrogen peroxide could represent a problem from the point of view of logistics and safety. In addition, the anthraquinone route involves complex technology, not easy to access (Figure 18.2). Thus, the applications of TS-1 in the petrochemical industry were, from the beginning, strong incentives for the investigation of potential alternatives for commercial hydrogen peroxide production. Direct synthesis from the elements,

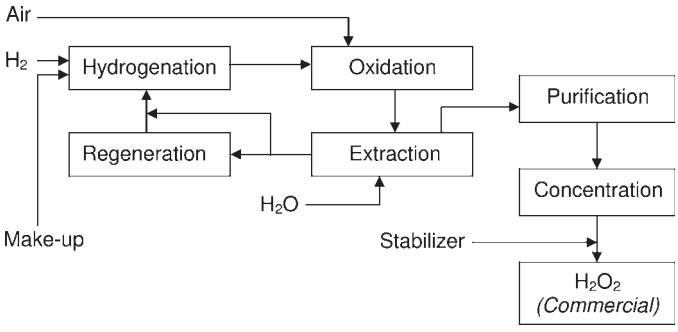

Figure 18.2 Simplified block diagram of anthrahydroquinone autoxidation (AO).

in situ production and process integration have been the most studied solutions. Unless otherwise specified, HPPO is the process of reference in the following discussion.

18.10.1
Direct Synthesis of Hydrogen Peroxide

The catalyzed reaction of the elements produces hydrogen peroxide directly, in competition with water (Equation 18.16). Most selective catalysts are based on supported Pd, often modified by other metals. Methanol is increasingly studied as a reaction medium, from the perspective of the direct use of the solution obtained in the HPPO process. For high selectivities, the reaction normally necessitates relatively low temperatures, often room temperature or lower, and the presence of mineral acids and other additives [153].

$$H_2 + O_2 \xrightarrow{Pd} H_2O_2 \tag{18.16}$$

The direct synthesis is in principle a one-step process, which is simpler and easier to scale-up for large capacity plants than the AO route. However, it also suffers from major drawbacks, for example continuing low yields and the hazards of mixing flammable gases. Various technical solutions are envisaged in the patent literature to minimize the risks of explosion and fire, such as the dilution of hydrogen and oxygen with an inert fluid.

18.10.2
In Situ Production of Hydrogen Peroxide

In situ generation removes dependence on external supplies. The availability of hydrogen at the chemical site is the only requisite for its feasibility. The approach generally envisaged in the literature is of two types [154–158]. The first requires that TS-1 is modified by a metal species, generally Pd, able to catalyze the direct synthesis. H_2, O_2 and propene are fed to the reactor to produce propene oxide and water directly (Equation 18.17). On a microscopic scale, hydrogen peroxide is formed on metal particles, then diffuses in TS-1 to react with propene on Ti sites. The high activity of TS-1 in very dilute solutions of hydrogen peroxide prevents the accumulation of the oxidant in contact with metal particles that would otherwise catalyze its decomposition. A major drawback of the method relates to the excellent hydrogenation properties of Pd, leading to significant losses of propene as propane.

$$H_2 + O_2 + C_3H_6 \xrightarrow{Pd/TS\text{-}1} C_3H_6O + H_2O \tag{18.17}$$

In early studies, carried out batch-wise on Pd-Pt/TS-1, the maximum yield was 11.7%, with 46% selectivity based on propene [156]. By operating in a continuous fixed-bed reactor, Jenzer and others showed that the selectivity could initially be

as high as 99% at 3.5% conversion. The catalyst, however, underwent rapid deactivation with a parallel decrease of the selectivity. Methyl formate from the oxidation of methanol, and acrolein, acetone and other compounds from that of propene became the main products after few hours on-stream [157]. The use of supercritical carbon dioxide, without the addition of methanol/water, allowed the reduction of side reactions [158]. Other studies envisage *in situ* generation by an electrochemical cell [159] and gas-phase epoxidation on Ag/TS-1 at 150 °C [160].

A second approach consists of the autoxidation of an organic carrier, in the presence of propene and TS-1 (Equations 18.18 and 18.19) [154, 155, 161, 162]. The solvent is a crucial aspect in the use of alkylanthrahydroquinone compounds [154]. It should be able to solubilize both the oxidized and the hydrogenated forms of the carrier and possess a molecular size larger than the pores of TS-1. On this basis, the various components of the working solution cannot interfere in the epoxidation mechanism or undergo oxidative degradation at the Ti sites. Normally, the conditions are met by the use of a mixture of two or more exotic solvents, to which methanol is also added to increase the rate of epoxidation. Specific tests proved the feasibility of the method, albeit with somewhat lower yields than when carried out with *ex situ* hydrogen peroxide [154]. A subsequent study, while confirming early results, provided useful information on the reactor and operative conditions [161]. The use of a gas-lift loop reactor, allowed the process to be carried out satisfactorily even in the presence of two liquid phases, one richer in methanol/water and the other in the working solution. The best yields were 82%, with 85% selectivity based on alkylanthrahydroquinone.

$$C_3H_6 + O_2 + QH_2 \xrightarrow{TS\text{-}1} C_3H_6O + H_2O + Q \qquad (18.18)$$

$$Q + H_2 \xrightarrow{Pd} QH_2 \qquad (18.19)$$

Major shortcomings also affect this *in situ* route to propene oxide. The most obvious one is the even greater complexity than for the AO process, owing to the modification required to accommodate the epoxidation of propene. This explains why patents have been filed on anthraquinone compounds and other organic carriers, soluble in aqueous methanol. The aim was a radical simplification of the working solution, trying to eventually use the simple methanol/water medium for the whole series of reactions. Examples of soluble carriers are anthraquinone compounds carrying hydrophilic alkyl ammonium or sulfonic substituent groups and secondary alcohols.

18.10.3 Process Integration

The integration of propene oxide and hydrogen peroxide processes appears, from a short-term perspective, a more realistic approach than *in situ* generation. It is also favored by the location of both facilities at the same chemical site. Basically, process integration envisages a simplification of H_2O_2 recovery that can even

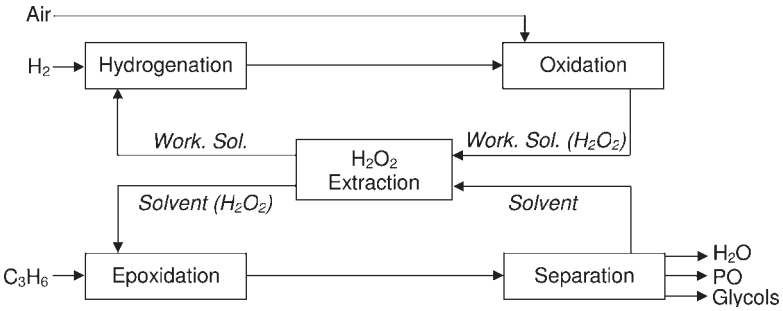

Figure 18.3 Integrated process scheme for the production of propene oxide.

result, at best, in the complete elimination of the purification, concentration and stabilization steps [154]. In this hypothesis, the aqueous H_2O_2 extract obtained is fed, without further processing, into the epoxidation reactor. Impurities from the working solution, which may have been extracted with the H_2O_2, are hindered from diffusing to Ti sites by their relatively large molecular size. Drawbacks could ensue, for example for the activity of the catalyst, from inorganic additives that may be required by the AO process [161]. Beside anthraquinone compounds, old and new carriers such as isopropanol, once used industrially for the production of hydrogen peroxide and 1-phenylethanol, have also been studied from the perspective of process integration [29, 163].

A variant envisages the use of aqueous methanol for both the extraction of hydrogen peroxide and the epoxidation of propene as shown, in a simplified form, by Figure 18.3. Thus, no extra water is added to the epoxidation reactor, which decreases separation and waste-treatment costs. On the laboratory scale, the quantity of methanol dissolving into the working solution is small and apparently does not interfere with the AO cycle of reactions [154, 161].

In principle, process integration applies even more to direct synthesis of hydrogen peroxide, further improving the advantages over the anthraquinone route. Methanol can be used to replace water as the solvent and the dilute methanol solution obtained fed into the epoxidation reactor. Minimal purification may be required, for example for the removal of hydrogen bromide and other additives that may have been needed to increase the selectivity.

18.10.4 Miscellanea

The relatively small capacity of the phenol hydroxylation process does not justify the development of alternatives to the use of commercial hydrogen peroxide. The direct synthesis of phenol, for which process integration might be crucial, would be a different matter.

The ammoximation process is not very compatible with *in situ* generation. From one side, the possible reaction of ammonia with the working solution and the complex recovery of cyclohexanone oxime rule out the use of organic carriers, and,

from the other, no catalyst of direct synthesis is known that is sufficiently active and selective in a basic medium. Process integration, however, is conceivable and is present in the patent literature. In an early patent, a mixture of cyclohexanone and hydrogen peroxide was produced by the autoxidation of cyclohexanol and fed directly into the ammoximation reactor [164]. Hydrogen peroxide from the autoxidation of anthrahydroquinones was extracted with aqueous methanol or *t*-butanol and used as obtained [165, 166].

18.11
Adsorption, Active Species and Oxidation Mechanisms

In previous sections, mechanistic proposals have been illustrated with a sometimes limited discussion of active species and of the relations existing between them. A deeper insight is also needed into adsorption phenomena and their role in the network of reactions catalyzed by TS-1. In this section, these issues will be examined more closely, with the aim of identifying the chemical and physical factors determining the direction of the oxidation pathway from the perspective of a general mechanistic scheme.

18.11.1
Adsorption and Catalytic Performances

It is clear from the first part of this chapter that the external medium has a major effect on the catalytic properties of TS-1 and other Ti-zeolites. Early rationalization suggested that the adsorption of a protic molecule, ROH, had a stabilizing effect for Ti—OOH species. In this view, water and alcohol solvents influenced the catalytic performance through the electronic and steric effects exerted in the oxidation step by the ROH molecule present in the active species (Section 18.4.1.1) [62].

Subsequently, Langhendries and others shed light on the key role the external medium has in the adsorption of olefins, alkanes and alcohols [167]. They showed that partition coefficients, defined as the ratio of intra-porous to extra-porous concentrations, decreased in the order of decreasing solvent polarity, $CH_3OH > C_2H_5OH > 1\text{-}C_3H_7OH$, $CH_3CN > CH_3COCH_3$, and for a given solvent with decreasing hydrophobicity of the molecular sieve, TS-1 > Ti,Al-β > Ti-MCM-41. Partition coefficients increased also with the chain length of the adsorbate. The reactivity orders in the epoxidation of a series of olefins were fully consistent with the trends. On these grounds, the authors concluded that the adsorption phenomena were sufficient to explain the effect of the solvent on kinetics, without the need to invoke other roles.

Actually, the study provides an experimental demonstration of the primary role the surface has in the catalytic performance of Ti-zeolites. TS-1 is superior to Ti,Al-β because its surface is more hydrophobic and, therefore, the intra-porous concentration of the olefins and other apolar reagents is greater, rather than because the activity of Ti-sites is substantially different. In this regard, the micro-

Table 18.13 Solvent effects in the oxidation of *n*-hexane on TS-1.[a)]

Solvent	K_s[b)]	$V_0 \cdot 10^{-4}$ ($m_{H_2O_2} \cdot s^{-1}$)[c)]
water	–	1.1 (two liquid phases)
methanol	16.5	1.2
acetonitrile	2.5	0.9
i-propanol	0.8	–
t-butanol/H_2O (27%)	–	2.4
t-butanol	–	4.3

a Reprinted from Ref. [169]. Copyright 2006, with permission of Thomas Vieth Publisher.
b Partition coefficients of *n*-hexane.
c Rates at 15–30% conversion.

porous nature of the catalyst has a major role in that it enhances both attractive and repulsive interactions between surface and adsorbate and, through them, the selective adsorption of some compounds over others. It is useful, in this regard, to recall the concept of zeolites as solid solvents [168]. Nonetheless, the partition coefficients alone are unable to account for the catalytic behavior of Ti-zeolites in all circumstances. So, the role of a protic adsorbate on Ti—OOH species is again of assistance [25]. Three pieces of evidence in the literature are interesting in this regard:

- If a correlation was apparent between adsorption and epoxidation rates within a homogeneous series of solvents, this no longer held when the solvents were considered all together and no distinction was made between protic and aprotic ones [25, 167].
- In a study by Corma and coworkers, the rate of epoxidation of 1-hexene on Ti,Al-β matched, for a homogeneous series of solvents, the trend of adsorption. However, it was twice as fast in acetonitrile than in methanol, in contrast to partition coefficients which are ordered in the reverse direction [77, 167]. The relationship for cyclohexanol oxidation was more complex, the rate increasing with the polarity of aprotic solvents and decreasing with polarity increase in protic ones [77].
- The hydroxylation of *n*-hexane on TS-1, in contrast to the epoxidation of propene, reached its maximum rate in the least polar solvent, *t*-butanol (Table 18.13). Acetonitrile behaved quite similarly to methanol and water [24, 25, 169]. On the assumption that *t*-butanol was comparable to *i*-propanol for the effects on adsorption, a clear relationship between rates and partition coefficients was lacking. Considering that hydroxylation and epoxidation involve different active species and mechanisms, a diverse role of the solvent in the two active species could contribute to the differences, whereas the partition coefficients alone could not.

In principle, the solvent can affect catalysis in a multiplicity of modes, for example through the adsorption of the reagents, the stabilization of Ti—OOH species or interaction with oxidation intermediates [25]. It is worth noting that the first two phenomena produce effects in the same direction, and their individual contributions are not easily distinguished. For instance, the rate of epoxidation in *t*-butanol may be slower than in methanol owing to smaller partition coefficients of the olefin, to more sterically hindered active species and to less electrophilic peroxidic oxygen.

18.11.2
The Structure of Ti—OOH Species

The structural and chemical properties of active species in TS-1 are strictly related to the tetrahedral configuration that Ti is forced to assume in the silicalite framework, to its preference for the octahedral one, which can be achieved by the adsorption of polar molecules, and to the reversible cleavage of one Ti—OSi bond by a protic molecule [8, 170, 171]. On this basis, Scheme 18.17 illustrates the formation of Ti—OH and Ti—OOH species, by the chemisorption of water and hydrogen peroxide, respectively. The use of an alcoholic solution leads to analogous results. Other Ti-species generally predicted by theoretical studies, for example, bearing an undissociated H_2O_2 molecule weakly adsorbed on Ti or consisting of Ti—O—O—Si peroxides, are not very compatible with the chemistry of TS-1 and are not considered further in this context.

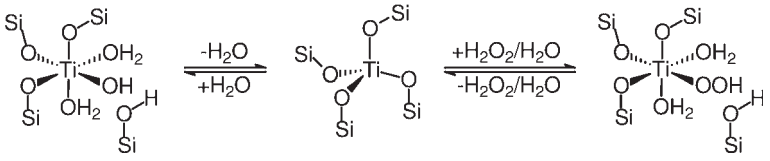

Scheme 18.17 Adsorption and reactions of Ti-sites.

The structures proposed for Ti—OOH have been illustrated in Section 18.4.1.1 and show η^1 (monodentate) or η^2 (bidentate) coordination (Figure 18.1a–c). Such a dualism in Ti—OOH binding parallels that in the role of a protic adsorbate. A spectator function for the latter and even its absence in the active species have generally been envisaged by theoretical calculations (Figure 18.1b) [20]. The opposite view, usually visualized as structure *a* in Figure 18.1, was originally based on the interpretation of early experimental results [24, 61, 62, 171]. Currently, the likelihood of structures *a* and *c* in Figure 18.1, entailing an active role for the protic adsorbate, can rely upon additional evidence in the literature.

- Freely diffusing olefins reveal large steric constraints in the approach to peroxidic oxygen, in the epoxidation on TS-1 and Ti-Beta zeolites (Tables 18.8 and 18.9) [62, 81, 83]. For the active species *b* in Figure 18.1, the repulsive effect exerted by the surface on the alkyl substituents is the only possible explanation. For species *a* and *c*, the R group would produce additional, and probably greater,

steric constraints. Whether the surface alone is sufficient to account for the magnitude of the effect is a matter of debate. However, the epoxidation of 2-butene compared to that of terminal olefins shows that the steric effects are large even for *cis*-isomers, in which both methyl groups can point away from the surface. Clearly, steric effects should be larger for *trans*-2-butene, as experimentally found, for the opposite reason.

- The addition of modest quantities of water to acetonitrile solvent increases the rate of oxidation of 1-hexene but decreases that of cyclohexanol [77]. The contrasting effects were attributed to the adsorption of water on Ti—OOH to form the cyclic structure of *a* (Figure 18.1). In the epoxidation mechanism (R=H), this was reputed to be the active species and, therefore, the addition of water promoted the rate through its formation. In the oxidation of the alcohol, a species with the same structure (R = cyclohexyl) was the oxidation intermediate and water, in competition with cyclohexanol for adsorption on Ti (R=H), could only decrease the rate. It should be added that the study was performed with Ti,Al-β as the catalyst, but, as mentioned in Section 18.4.1.2, the same active species is believed to apply generally [77–79].
- The diffusivity and adsorption capacity of aromatic molecules, in TS-1 and in Ti-MOR, were both reduced by the simultaneous presence of H_2O_2 and H_2O, in a linear relationship with the Ti content [172]. No such effects were produced by the use of H_2O alone under analogous conditions or by that of H_2O_2/H_2O mixtures with Ti-free zeolites. The underlying rationale, in the authors' view, is the formation of bulky peroxy species, with the structure *a* of Figure 18.1, protruding into the pores. Their presence hinders the movement of adsorbing reagents and reduces the free volume available for them in the pores. No such bulky species can be formed when water alone adsorbs on Ti-sites.

The evidence above and a number of other studies, of various strength, based upon IR and UV-Vis spectroscopy, together with XANES and EXAFS studies and the kinetic behavior of the oxidation of alcohols and allyl chloride (Equations 18.8 and 18.11), demonstrate the co-adsorption of H_2O_2 and, at least one further molecule of water or alcohol on Ti. In some cases, they also confirm the formation of cyclic structures like *a* and *c* in Figure 18.1, meaning that structure *b* is only possible under vacuum conditions. Their formation under the reaction conditions also favor, albeit not proving, their participation in the oxygen-transfer step to the double bond. Actually, the steric constraints in the epoxidation of linear olefins and the promoter or inhibitor effect of water, according to the type of substrate, point in this direction. The opposite view, based on theoretical models, is weakened by the variety of significantly different active species they lead to.

18.11.3
Reactive Intermediates and Oxidation Mechanisms

The heterolytic mechanism and the Ti—OOH nature of the active species in the epoxidation of olefins have the support of several chemical, spectroscopic and

theoretical studies. For the hydroxylation of alkanes, some indirect evidence favors homolytic H-abstraction by a Ti-centered radical, the nature of which, however, remains unknown. Scarce information exists on the oxidation mechanisms of arenes and alcohols, for which mechanistic proposals have been advanced by analogy with other oxidations. Even less is available for N- and S-compounds and for the decomposition of hydrogen peroxide. On the whole, the understanding of TS-1 catalysis is still limited, with epoxidation the only exception. Nonetheless, two deductions are possible from available information. Ti—OOH can directly perform the oxidation of certain substrates, for example, olefins and, maybe, O-, S- and N-compounds, or undergo a redox process, converting into a radical oxidant species. As a result, competitive heterolytic and homolytic pathways can co-exist in TS-1. Precedents in this regard can be found in the literature [67].

The epoxidation species received adequate attention in previous sections, with Figure 18.1 and Schemes 18.7, 18.8 and 18.17 illustrating the mode of generation, the possible structures and the mechanisms of oxygen transfer proposed in the literature. Conversely, the species responsible for the cleavage of saturated C—H bonds necessitates at this stage a deeper insight, particularly in the light of Scheme 18.3b, based on the atypical Ti—O$^{\bullet}$ radical. Actually, no precedent exists in the chemistry of Ti for such a species. Nonetheless, other conceivable mechanisms based on the participation of the species *a–d* of Figure 18.1, of Ti—$O_2^{\bullet}$ superoxide and of a Ti^{III}—OO$^{\bullet}$ diradical are even less credible. Actually, it is hard to reconcile C—H hydroxylation with Ti(η^2—O_2) and Ti—OOH species, considering that the reaction is homolytic whereas the oxidant is not. The implausibility of diradical Ti^{III}—OO$^{\bullet}$ has been discussed (Section 18.2.1). The fact that no major role is assigned to Ti—$O_2^{\bullet}$, is not only because this represents a negligible fraction of overall Ti content [66]. Actually, the reactivity of metal superoxides with alkanes was shown to be generally low or zero [1]. The generation of Ti—$O_2^{\bullet}$ requires the intervention of an OH$^{\bullet}$ radical, whose origin remains unknown. No evidence of its reactivity was detected in the oxidation of olefins, in which $TiO_2^{\bullet}$ is expected to add across the double bond (e.g. the stereo scrambling of cis and trans olefins by addition–elimination).

It is useful to note, at this stage, that TS-1 shows similarities in C—H hydroxylation with biomimetic catalysts and simple Fe^{II} ions dissolved in acetonitrile, for example the homolytic nature of the reaction, the electrophilic character of the active species, a significant primary H/D isotope effect, the competition between hydroxylation and H_2O_2 decomposition and, often, the stereoscrambling ability. Similarities exist also with enzymatic systems, notably with cytochrome P-450 and the methane monooxygenase (MMO) type of enzymes [31, 173]. On these grounds, it is tempting to extend further the analogy, proposing Ti—O$^{\bullet}$ as the active species related to the Fe^{IV}—O$^{\bullet}$ of biomimetic and enzymatic systems and Fe^{III}—O$^{\bullet}$ of Fe^{II}/H_2O_2/CH_3CN (Fe^{IV}—O$^{\bullet}$ and Fe^{III}—O$^{\bullet}$ are radical notations of Fe^{V}—O and Fe^{IV}—O, respectively). Indirect support for Ti—O$^{\bullet}$ comes from a study by Bonchio and others on the hydroxylation of benzene by the peroxide $VO(O_2)(H_2O)_2L$ (L = picolinic acid), in which evidence exists for the participation of a V^{V}—O$^{\bullet}$ species, instead of the diradical V^{IV}—OO$^{\bullet}$ previously suggested by others [174]. However, while the generation of high-valent iron oxo species from d^5 Fe^{III}—OOH

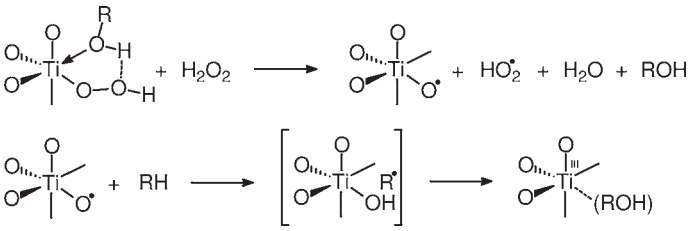

Scheme 18.18 Generation of Ti—O• active species and C—H hydroxylation.

and d^6 Fe^{II}—OOH hydroperoxides is straightforward, an external reducing agent would be required for that of Ti—O• from d^0 Ti^{IV}—OOH (Scheme 18.18). A redox process had been proposed also for V^V—O• formation from precursor $VO(O_2)(H_2O)_2L$.

The regeneration of the active species from Ti^{III} represents a second problem to solve. Actually, the one-electron oxidation of low-valent metal ions with H_2O_2 normally produces free hydroxyl radicals, which, however, are not detected with TS-1. A possible solution is suggested by the redox behavior of Fe^{II} perchlorate in acetonitrile solvent [33, 34]. At odds with aqueous media promoting Fenton-like reactions, acetonitrile favored the formation of an iron-bound oxidant, able to homolytically hydroxylate paraffinic C—H bonds. A parallel is apparent between the aprotic medium of Fe^{II} and the intra-porous volume of TS-1, in which surface Si—OH and protic adsorbates are negligible under the hydroxylation conditions. Thus, hydrogen peroxide could regenerate Ti—O• from Ti^{III}, as it does with Fe^{IV}=O from Fe^{II}, without being decomposed into free OH• radicals (Scheme 18.19). Whether this process passes through Ti^{III}—OOH, is of little interest at this stage. Scheme 18.19 only means that H_2O_2 regenerates the active species, by the oxidation of transient Ti^{III} intermediate, without decomposition into free hydroxyl radicals. The organophilic nature of the intra-porous volume of TS-1 promotes the process. It is remarkable, in this regard, that biomimetic catalysts are generally used in aprotic solvents and that the active species of MMO is thought to be located in a hydrophobic pocket of the enzyme.

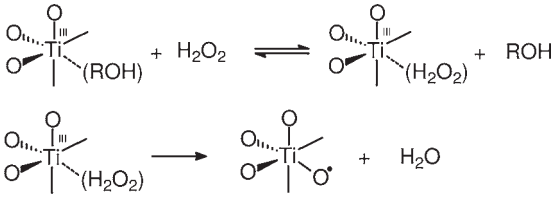

Scheme 18.19 Regeneration of Ti—O• species from Ti^{III} intermediate by hydrogen peroxide.

Ti—O• is also an excellent candidate as an initiator of H_2O_2 decomposition (Scheme 18.20). The subsequent decomposition of HO_2• species into molecular oxygen could follow, at least in part, known pathways [1]. The details of oxygen evolution, however, is an issue that goes beyond the scope of this chapter.

Scheme 18.20 Decomposition of hydrogen peroxide initiated by Ti—O• species.

The acidic character of Ti—OOH species is the final property to be addressed. An acid–base equilibrium is established under reaction conditions, with mildly basic compounds, including water and alcohols, adsorbed in the pores (Scheme 18.21) [24, 171, 175]. The addition of basic compounds in small amounts improves the selectivity of epoxidation through its effect on the equilibrium. On increasing the local basicity, this shifts completely to the right, with the formation of anionic η^2-peroxides [176]. Since $Ti(\eta^2—O_2)^-$ species are characterized by low electrophilicity, their formation has a profound effect on the reactivity of TS-1, with inhibition and eventually deactivation in most reactions (ammoximation is one exception). Protonic acids regenerate initial Ti—OOH species. Owing to the equilibrium nature of the reaction, any attempt to prepare anionic TS-1 peroxides in a pure state failed. Hydrogen peroxide and the base gradually leached into water washings, to be eventually completely removed with them [176].

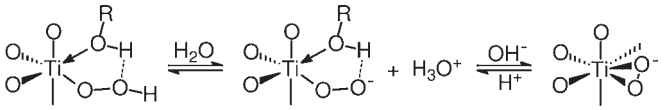

Scheme 18.21 Acid–base properties of Ti—OOH hydroperoxide.

18.11.4
Proposal for a General Mechanistic Scheme

In conclusion, different active species and different mechanisms are operative in TS-1, in a network of competing reactions. Scheme 18.22 is a tentative rationalization, in a simplified form, of information presented in previous sections on most studied reactions. Different factors determine the direction of the oxidation pathway, for example the temperature, the solvent, the nature of the surface and the substrate itself [169].

Scheme 18.22 pivots upon species **a** of Figure 18.1 (although the participation of **c** is equally conceivable). Each oxidation path is in competition with the others, becoming predominant under specific conditions. For instance, unhindered olefins in a methanol solution of hydrogen peroxide undergo fast epoxidation even at below room temperature (mechanism *A*). The oxidation of allylic C—H (mechanism *B*), the oxidation of CH_3OH (mechanism *C*) and the decomposition of H_2O_2 (reactions *D*), although equally possible, are too slow to be detectable to a significant extent. At the same time, the acid–base equilibrium can be controlled by the addition of parts per million quantities of basic compounds, to minimize the solvolysis of the product. On raising the temperature and contact time to assist the

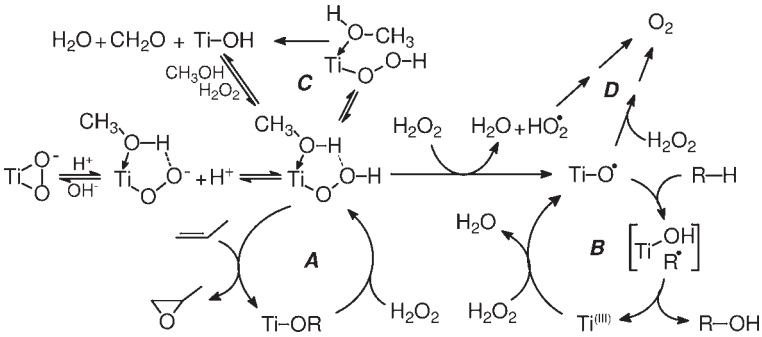

Scheme 18.22 Reactive intermediates and oxidation pathways in TS-1/H_2O_2. (Adapted from Ref. [169]; Copyright 2006, with permission of Thomas Vieth Publisher).

epoxidation of sterically hindered olefins, the reaction of Ti—OOH with H_2O_2, and therefore the homolytic pathways *B* and *D*, may compete significantly, to the point that with the least reactive olefins these can prevail over epoxidation *A*. The literature offers several examples in which epoxidation, allylic oxidation and H_2O_2 decomposition are all present, in different proportions, even in the oxidations with TS-1 and particularly in those with Ti-Beta catalysts.

The hydroxylation of alkanes is considerably slower than epoxidation and necessitates significantly higher temperatures to occur at a comparable rate. As a matter of fact, H_2O_2 decomposition *D* is never negligible in the hydroxylation of alkanes, its competition being significant even in the fastest one observed on TS-1, the hydroxylation of *n*-hexane (Table 18.2). It is also a side reaction in the generation of Ti—O$^\bullet$ species, but for the most part it should originate from the direct reaction of H_2O_2 (first reaction of Schemes 18.18 and 18.20). With the least activated hydrocarbons, for example with bulky alkanes, the decomposition of H_2O_2 becomes the main reaction. Analogous considerations hold also for the competition of the oxidation of methanol solvent, a side reaction that occurs to a significant extent with the least reactive substrates, together with decomposition of the oxidant. Table 18.11 shows, in this regard, why other alcohols are inappropriate for use as solvents.

The relative weight of different pathways in Scheme 18.22 is determined also by the combination of surface/solvent, through the control of the substrate-to-oxidant ratio in the pores. At a fixed composition of external medium, the H_2O_2-to-hydrocarbon and the H_2O-to-hydrocarbon ratios increase in the order TS-1 < Ti-β < Ti,Al-β ≪ Ti-MCM-41, owing to increasingly hydrophilic pores. Thus, the competition of H_2O_2 with the hydrocarbon for reaction with Ti—OOH increases in the same order and with it the generation of Ti—O$^\bullet$ radicals in the pores. Allylic oxidation (path *B*) and H_2O_2 decomposition (path *D*) increase accordingly, at the expense of epoxidation (path *A*). As a matter of fact, the epoxidation of olefins on large-pore catalysts is generally slower and less selective than on TS-1, becoming negligible on mesoporous Ti-silicates, owing to a lower adsorption of the substrate and a greater incidence of such side reactions.

Analogous considerations on the effect of the surface/solvent couple also apply to the oxidation of alkanes and aromatics. The lower reactivity of C—H bonds combines with decreasing alkane/H_2O_2 ratios in the order TS-1 > Ti-β > Ti,Al-β ≫ Ti-MCM-41, favoring the competition of hydrogen peroxide for Ti—O$^{\bullet}$ and, consequently, its decomposition over alkane hydroxylation in a similar trend. Actually, only a few alkanes are oxidized with relatively good yields on TS-1, while their hydroxylation on large-pore zeolites is normally an exception. With hydrophilic Ti-MCM-41, alcohols are likely produced by a free radical chain oxidation of the alkane occurring in the external medium. The hydroxylation of aromatics competes in a similar way with solvent oxidation and hydrogen peroxide decomposition. It is interesting to notice, in this regard, that oxygen evolution is significantly smaller in the hydroxylation of phenol than in that of alkanes, a possible indication of the quenching effect of phenolic species on the generation and the reactions of $HO_2^{\bullet}$ radicals.

18.12 Conclusions

Progress in the area of Ti-zeolites, since early papers published at the end of the 1980s, has been impressive. Synthesis, catalysis, characterization and modeling have been the subject of numerous studies. Most synthetic efforts concentrate on methods to obtain TS-1 by the use of cheaper template and silica sources. The lower grade TS-1 thus obtained is generally intended for the epoxidation of propene, in which the catalyst inventory is relatively high and a lower cost for it could compensate for moderate losses of selectivity. The search for large-pore Ti-zeolites is also the subject of many studies. Though their number in the patent literature is now of the order of several tens, only a few have been studied effectively and, moreover, these show little applicative potential. Currently, no new Ti-zeolite, sufficiently effective to at least supplement TS-1 in the oxidation of bulky substrates, is on the horizon. Combining the spaciousness of pores with a highly hydrophobic surface appears a task of maximum difficulty.

Characterization has confirmed, with plenty of data, the isomorphous substitution and tetrahedral structure of Ti, the reversible splitting of one Ti—OSi bond by water and methanol and the formation of Ti—OOH active species. Mechanistic proposals have been advanced on these and on chemical grounds, albeit limited for the most part to the epoxidation reaction. Modeling has in several cases provided valuable support in this regard. For further mechanistic insights, *in situ* studies might be helped by the recent availability of gaseous H_2O_2 in a pure state [175].

Catalytic studies have extended the applications of TS-1 from early aromatic hydroxylation to the oxidation of olefins, alkanes, alcohols, amines and thioethers, and to other minor reactions. A combination of three factors is the basis of its effectiveness: the high activity of Ti peroxy species, the organophilic properties of the surface and the size of the pores in the range of molecular dimensions. For

the role of propene oxide in the chemical industry, most of the research interest has focused on epoxidation, leading eventually to the development of a new process. On the whole, three oxidation processes are now commercial – HPPO, ammoximation and phenol hydroxylation – with prospects for other applications, particularly in the event that cheaper hydrogen peroxide becomes available in the future.

References

1 Sheldon, R.A. and Kochi, J.K. (1981) *Metal-Catalyzed Oxidations of Organic Compounds*, Academic Press, New York.

2 Schirmann, J.P. and Delavarenne, S.Y. (1979) *Hydrogen Peroxide in Organic Chemistry*, Edition et Documentation Industrielle, Paris.

3 Venturello, C., Alneri, E. and Ricci, M. (1983) *Journal of Organic Chemistry*, **48**, 3831.

4 Perego, G., Bellussi, G., Corno, C., Taramasso, M., Buonomo, F. and Esposito, A. (1986) *New Developments in Zeolite Science Technology* (eds Y. Murakami, A. Iijima and J.W. Ward), Kodansha, Tokyo, p. 129.

5 Romano, U., Esposito, A., Maspero, F., Neri, C. and Clerici, M.G. (1990) *La Chimica e l'Industria*, **72**, 610.

6 Bellussi, G. and Rigutto, M.S. (1994) *Advanced Zeolite Science and Applications* (eds J.C. Jansen, M. Stöcker, H.G. Karge and J. Weitkamp), Studies in Surface Science and Catalysis, Vol. **85**, Elsevier, Amsterdam, p. 177.

7 Notari, B. (1996) *Advances in Catalysis* (eds D.D. Eley, W.O. Haag and B. Gates), Academic Press, New York, Vol. **41**, p. 253.

8 Perego, G., Millini, R. and Bellussi, G. (1998) *Synthesis and Characterization of Molecular Sieves Containing Transition Metals in the Framework* (eds H.G. Karge and J. Weitkamp), Molecular Sieves Science and Technology, Vol. **1**, Springer Verlag, Heidelberg, p. 187.

9 Ratnasamy, P., Srinivas, D. and Knözinger, H. (2004) *Advances in Catalysis* (eds B. Gates and H. Knözinger), Academic Press, New York, Vol. **48**, p. 1.

10 Taramasso, M., Perego, G. and Notari, B. (1983) US 4,410,501, to Snamprogetti S.p.A.

11 Millini, R., Previde Massara, E., Perego, G. and Millini, R. (1992) *Journal of Catalysis*, **137**, 497.

12 Wang, X., Guo, X. and Li, G. (2002) *Catalysis Today*, **74**, 65.

13 Bellussi, G., Carati, A., Clerici, M.G., Esposito, A., Millini, R. and Buonomo, F. (1989) Belgian Patent 1,001,038.

14 Reddy, J.S., Kumar, R. and Ratnasamy, P. (1990) *Applied Catalysis*, **58**, L1.

15 Blasco, T., Camblor, M.A., Corma, A. and Pérez-Pariente, J. (1993) *Journal of the American Chemical Society*, **115**, 11806.

16 van der Waal, J.C., Rigutto, M.S. and van Bekkum, H. (1994) *Journal of the Chemical Society D – Chemical Communications*, 1241.

17 Wu, P., Komatsu, T. and Yashima, T. (1966) *Journal of Physical Chemistry*, **100**, 10316.

18 Wu, P., Tatsumi, T., Komatsu, T. and Yashima, T. (2001) *Journal of Physical Chemistry B*, **105**, 2897.

19 Ciesla, U. and Schüth, F. (1999) *Microporous and Mesoporous Materials*, **27**, 131.

20 Bordiga, S., Damin, A., Bonino, F. and Lamberti, C. (2005) *Surface and Interfacial Organometallic Chemistry and Catalysis* (eds V. Copéret and B. Chaudret), Topics in Organometallic Chemistry, Vol. 16, Springer-Verlag, Heidelberg, p. 37.

21 Clerici, M.G. and Bellussi, G. (1989) European Patents 315,247 and 315,248.

22 Tatsumi, T., Nakamura, M., Negishi, S. and Tominaga, H. (1990) *Chemical Communications*, 476.

23 Huybrechts, D.R.C., De Bruycker, L. and Jacobs, P.A. (1990) *Nature*, **345**, 240.

24 Clerici, M.G. (1991) *Applied Catalysis*, **68**, 249.

25 Clerici, M.G. (2001) *Topics in Catalysis*, **15**, 257.

26 Halasz, I., Agarwal, M., Senderov, E. and Marcus, B. (2003) *Applied Catalysis A: General*, **241**, 167.

27 Spinacé, E.V., Pastore, H.O. and Schuchardt, U. (1995) *Journal of Catalysis*, **157**, 631.

28 Tao, J., Tang, D., Li, Q., Yu, Z. and Min, E. (2001) *Journal of Natural Gas Chemistry*, **10**, 295.

29 Saxton, R.J. (1999) *Topics in Catalysis*, **9**, 43.

30 Khouw, C.B., Dartt, C.B., Labinger, J.A. and Davis, M.E. (1994) *Journal of Catalysis*, **149**, 195.

31 Costas, M., Chen, K. and Que, L. (2000) *Coordination Chemistry Reviews*, **200**-*2*, 517.

32 Aresta, M., Tommasi, I., Quaranta, E., Fragale, C., Mascetti, J., Tranquille, M., Galan, F. and Fouassier, M. (1996) *Inorganic Chemistry*, **35**, 4254.

33 Groves, J.T. and van der Puy, M. (1974) *Journal of the American Chemical Society*, **96**, 5274.

34 Groves, J.T. and McClusky, G.A. (1976) *Journal of the American Chemical Society*, **98**, 859.

35 Corma, A., Camblor, M.A., Esteve, P., Martínez, A. and Pérez-Pariente, J.P. (1994) *Journal of Catalysis*, **145**, 151.

36 Jappar, N., Xia, Q. and Tatsumi, T. (1998) *Journal of Catalysis*, **180**, 13.

37 Tatsumi, T. (2000) *Research on Chemical Intermediates*, **26**, 7.

38 Varagnat, J. (1976) *Industrial & Engineering Chemistry Product Research and Development*, **15**, 212.

39 Maggioni, P. and Minisci, F. (1977) *La Chimica e l'Industria*, **59**, 239.

40 Tendulkar, S.B., Tambe, S.S., Chandra, I., Rao, P.V., Naik, R.V. and Kulkarni, B.D. (1998) *Industrial and Engineering Chemistry Research*, **37**, 2081.

41 Liu, H., Lua, G., Guo, Y.L., Guo, Y. and Wang, J. (2004) *Catalysis Today*, **93**-*5*, 353.

42 Liu, H., Lua, G., Guo, Y.L., Guo, Y. and Wang, J. (2005) *Chemical Engineering Journal*, **108**, 187.

43 Martens, J.A., Buskens, P., Jacobs, P.A., van der Pol, A., van Hooff, J.H.C., Ferrini, C., Kouwenhoven, H.W., Kooyman, P.J. and van Bekkum, H. (1993) *Applied Catalysis A: General*, **99**, 71.

44 Kraushaar-Czarnetzki, B. and van Hooff, J.H.C. (1989) *Catalysis Letters*, **2**, 43.

45 van der Pol, A.J.H.P., Verduyn, A.J. and van Hooff, J.H.C. (1992) *Applied Catalysis A: General*, **92**, 113.

46 Tuel, A. and Ben Taarit, Y. (1993) *Applied Catalysis A: General*, **102**, 69.

47 Wilkenhöner, U., Langhendries, G., van Laar, F., Baron, G.V., Gammon, D.W., Jacobs, P.A. and van Steen, E. (2001) *Journal of Catalysis*, **203**, 201.

48 Wilkenhöner, U., Duncan, W.L., Möller, K.P. and van Steen, E. (2004) *Microporous and Mesoporous Materials*, **69**, 181.

49 Tuel, A., Moussa-Khouzami, S., Ben Taarit, Y. and Naccache, C. (1991) *Applied Catalysis A: General*, **68**, 45.

50 Camblor, M.A., Constantini, M., Corma, A., Esteve, P., Gilbert, L., Martinez, A. and Valencia, S. (1995) *Applied Catalysis A: General*, **133**, L185.

51 Thangaray, A., Kumar, R. and Ratnasamy, P. (1990) *Applied Catalysis*, **57**, L1.

52 Tatsumi, T., Yuasa, K. and Tominaga, H. (1992) *Journal of the Chemical Society D – Chemical Communications*, 1446.

53 Bianchi, D., Balducci, L., Bortolo, R., D'Aloisio, R., Ricci, M., Tassinari, R. and Ungarelli, R. (2003) *Angewandte Chemie – International Edition in English*, **42**, 4937.

54 Bianchi, D., Balducci, L., Bortolo, R., D'Aloisio, R., Ricci, M., Spanò, G., Tassinari, R., Tonini, C. and Ungarelli, R. (2007) *Advanced Synthesis Catalysis*, **349**, 979.

55 Bianchi, D., Bortolo, R., Buzzoni, R., Cesana, A., Dalloro, L. and D'Aloisio, R. (2002) European Patent 1,424,320.

56 Bhaumik, A., Mukherjee, P. and Kumar, R. (1998) *Journal of Catalysis*, **178**, 101.

57 Kim, G.J., Cho, B.R. and Kim, J.H. (1993) *Catalysis Letters*, **22**, 259.

58 Bhelhekar, A.A., Das, T.K., Chaudhari, K., Hegde, S.G. and Chandwadkar, A.J. (1998) *Recent Advances in Basic and Applied Catalysis* (eds T.S.R. Prasada Rao and G. Murali Dhar), Studies in Surface Science and Catalysis, Vol. **113**, Elsevier, Amsterdam, p. 195.

59 Wu, P., Komatsu, T. and Yashima, T. (1997) *Progress in Zeolites and Microporous Materials* (eds H. Chon, S.-Ihm and Y.S. Uh), Studies in Surface Science and Catalysis, vol. **105**, Elsevier, Amsterdam, p. 663.

60 Clerici, M.G. (2001) *Fine Chemicals through Heterogeneous Catalysis* (eds R.A. Sheldon and H. van Bekkum), Wiley-VCH, Weinheim, p. 538.

61 Clerici, M.G., Bellussi, G. and Romano, U. (1991) *Journal of Catalysis*, **129**, 159.

62 Clerici, M.G. and Ingallina, P. (1993) *Journal of Catalysis*, **140**, 71.

63 Liu, X., Wang, X., Guo, X. and Li, G. (2004) *Catalysis Today*, **93**, 505.

64 Hulea, V., Dumitriu, E., Patcas, F., Ropot, R., Graffin, P. and Moreau, P. (1998) *Applied Catalysis A: General*, **170**, 169.

65 Swern, D. (1947) *Journal of the American Chemical Society*, **69**, 1692.

66 Bonoldi, L., Busetto, C., Cangin, A., Marra, G., Ranghino, G., Salvalaggio, M., Spanò, G. and Giamello, E. (2002) *Spectrochimica Acta, Part A*, **58**, 1143.

67 Sheldon, R.A. and van Doorn, J.A. (1973) *Journal of Catalysis*, **31**, 427.

68 Koelewijn, P. (1972) *Recueil des Travaux Chimiques des Pays-Bas*, **91**, 759.

69 Sheldon, R.A. and van Doorn, J.A. (1973) *Recueil des Travaux Chimiques des Pays-Bas*, **92**, 253.

70 Huybrechts, D.R.C., Buskens, P.L. and Jacobs, P.A. (1992) *Journal of Molecular Catalysis*, **71**, 129.

71 Notari, B. (1993) *Catalysis Today*, **16**, 163.

72 Karlsen, E. and Schöffel, K. (1996) *Catalysis Today*, **32**, 107.

73 Sinclair, P.E. and Catlow, C.R.A. (1999) *The Journal of Physical Chemistry B*, **103**, 1084.

74 Barker, C.M., Kaltsoyannis, N. and Catlow, C.R.A. (2001) *Zeolites and Mesoporous Materials at the Dawn of the 21st Century* (eds A. Galarneau, F. Di Renzo, F. Fajula and J. Vedrine), Studies in Surface Science and Catalysis, Vol. **135**, Elsevier, Amsterdam, p. 260.

75 Neurock, M. and Manzer, L.E. (1996) *Chemical Communications*, 1133.

76 Lin, W. and Frei, H. (2002) *Journal of the American Chemical Society*, **124**, 9292.

77 Corma, A., Esteve, P. and Martínez, A. (1996) *Journal of Catalysis*, **161**, 11.

78 van der Waal, J.C. and van Bekkum, H. (1997) *Journal of Molecular Catalysis A–Chemical*, **124**, 137.

79 Wu, P., Tatsumi, T., Komatsu, T. and Yashima, T. (2001) *Journal of Catalysis*, **202**, 245.

80 Wu, P., Nuntasri, D., Ruan, J., Liu, Y., He, M., Fan, W., Terasaki, O. and Tatsumi, T. (2004) *Journal of Physical Chemistry B*, **108**, 19126.

81 van der Waal, J.C., Rigutto, M.S. and van Bekkum, H. (1998) *Applied Catalysis A: General*, **167**, 331.

82 Camblor, M.A., Corma, A., Esteve, P., Martínez, A. and Valencia, S. (1997) *Chemical Communications*, 795.

83 Corma, A., Esteve, P., Martínez, A. and Valencia, S. (1995) *Journal of Catalysis*, **152**, 18.

84 Sato, T., Dakka, J. and Sheldon, R.A. (1994) *Zeolites and Related Microporous Materials: State of the Art 1994* (eds J. Weitkamp, H.G. Karge, H. Pfeifer and W. Hölderich), Studies in Surface Science and Catalysis, Vol. **84**, Elsevier, Amsterdam, p. 1853.

85 Wu, P. and Tatsumi, T. (2002) *Journal of Physical Chemistry B*, **106**, 748.

86 Wu, P., Nuntasri, D., Liu, Y., Wu, H., Jiang, Y., Fan, W., He, M. and Tatsumi, T. (2006) *Catalysis Today*, **117**, 199.

87 Carati, A., Flego, C., Previde Massara, E., Millini, R., Carluccio, L., Parker, W.O. Jr and Bellussi, G. (1999) *Microporous and Mesoporous Materials*, **30**, 137.

88 Davies, L.J., McMorn, P., Bethell, D., Bulman Page, P.C., King, F., Hancock, F. E. and Hutchings, G.J. (2001) *Journal of Catalysis*, **198**, 319.

89 Chen, L.Y., Chuah, C.K. and Jaenicke, S. (1998) *Catalysis Letters*, **50**, 107.

90 Tatsumi, T., Yako, M., Nakamura, M. and Yuhara, Y. (1993) *Journal of Molecular Catalysis*, **78**, L41.

91 Kumar, R., Pais, G.C.G., Pandey, B. and Kumar, P. (1995) *Journal of the Chemical Society D–Chemical Communications*, 1315.

92 Hutchings, G.J. and Lee, D.F. (1994) *Journal of the Chemical Society D – Chemical Communications*, 1095.

93 Schofield, L.J., Kerton, O.J., McMora, P., Bethell, D., Ellwood, S. and Hutchings, G.J. (2002) *Journal of the Chemical Society–Perkin Transactions 2*, 1475.

94 Wróblewska, A. (2006) *Applied Catalysis A: General*, **309**, 192.

95 Wróblewska, A., Rzepkowska, M. and Milchert, E. (2005) *Applied Catalysis A: General*, **294**, 244.

96 Wu, P. and Tatsumi, T. (2003) *Journal of Catalysis*, **214**, 317.

97 Adam, W., Corma, A., Reddy, T.I. and Renz, M. (1997) *Journal of Organic Chemistry.*, **62**, 3631.

98 Gao, H., Lu, G., Suo, J. and Li, S. (1996) *Applied Catalysis A: General*, **138**, 27.

99 Wang, Q., Mi, Z., Wang, Y. and Wang, L. (2005) *Journal of Molecular Catalysis A*, **229**, 71.

100 Wu, P., Liu, Y., He, M. and Tatsumi, T. (2004) *Journal of Catalysis*, **228**, 183.

101 Sasidharan, M., Wu, P. and Tatsumi, T. (2002) *Journal of Catalysis*, **205**, 332.

102 Payne, G.B. and Williams, P.H. (1959) *Journal of Organic Chemistry*, **24**, 54.

103 Bellussi, G., Carati, A., Clerici, M.G. and Esposito, E. (1991) *Preparation of Catalysts V* (eds G. Poncelet, P.A. Jacobs, P. Grange and B. Delmon), Studies in Surface Science and Catalysis, Vol. **63**, Elsevier, Amsterdam, p. 421.

104 Smith, K. and Al-Shamali, M. (1999) *Proceedings of the 12th International Zeolite Conference, July 5–10, 1998, Baltimore* (eds E. Bei, M.M.J. Treacy, B. K. Marcus, M.E. Bisher and J.B. Higgins), Materials Research Society, Warrendale, PA, p. 1129.

105 Zhuang, J., Yang, G., Ma, D., Lan, X., Liu, X., Han, X., Bao, X. and Mueller, U. (2004) *Angewandte Chemie – International Edition in English*, **43**, 6377.

106 Derouane, E.G., Hutchings, G.J., Mbafor, W.F. and Roberts, S.M. (1998) *New Journal of Chemistry*, 797.

107 Bhaumik, A. and Tatsumi, T. (1999) *Journal of Catalysis*, **182**, 349.

108 Sasidharan, M., Wu, P. and Tatsumi, T. (2002) *Journal of Catalysis*, **209**, 260.

109 van der Pol, A.J.H. and van Hoof, J.H.C. (1993) *Applied Catalysis A: General*, **106**, 97.

110 Maspero, F. and Romano, U. (1994) *Journal of Catalysis*, **146**, 476.

111 Corma, A., Esteve, P. and Martínez, A. (1996) *Applied Catalysis A: General*, **143**, 87.

112 Hayashi, H., Kikawa, K., Murai, Y., Shigemoto, N., Sugiyama, S. and Kawashioro, K. (1996) *Catalysis Letters*, **36**, 99.

113 Jacobson, S.E., Muccigrosso, D.A. and Mares, F. (1979) *Journal of Organic Chemistry*, **44**, 921.

114 Zhao, R., Ding, Y., Peng, Z., Wang, X. and Suo, J. (1993) *Catalysis Letters*, **87**, 81.

115 Sheldon, R.A. and Dakka, J. (1993) *Erdöl Erdgas Kohle*, **109**, 520.

116 Sasidharan, M., Suresh, S. and Sudalai, A. (1995) *Tetrahedron Letters*, **36**, 9071.

117 Bhaumik, A., Kumar, P. and Kumar, R. (1996) *Catalysis Letters*, **40**, 47.

118 Corma, A., Nemeth, L.T., Renz, M. and Valencia, S. (2001) *Nature*, **412**, 423.

119 Roffia, P., Leofanti, G., Cesana, A., Mantegazza, M., Padovan, M., Petrini, G., Tonti, S. and Gervasutti, P. (1990) *New Developments in Selective Oxidations* (eds G. Centi and F. Trifirò), Studies in Surface Science and Catalysis, Vol. **55**, Elesevier, Amsterdam, p. 43.

120 Petrini, G., Cesana, A., De Alberti, G., Genoni, F., Leofanti, G., Padovan, M., Paparatto, G. and Roffia, P. (1991) *Catalysts Deactivation 1991* (eds C.H. Bartholomew and J.B. Butt), Studies in Surface Science and Catalysis, Vol. **68**, Elsevier, Amsterdam, p. 761.

121 Zecchina, A., Spoto, G., Bordiga, S., Geobaldo, F., Petrini, G., Leofanti, G., Padovan, M., Mantegazza, M. and Roffia, P. (1993) *New Frontiers in Catalysis* (eds L. Guczi, F. Solymosi and P. Tétényi), Studies in Surface Science and Catalysis, Vol. **75**, Elsevier, Amsterdam, p. 719.

122 Tatsumi, T. and Jappar, N. (1996) *Journal of Catalysis*, **161**, 560.

123 Zhang, Y., Wang, Y., Bu, Y., Wang, L., Mi, Z., Wu, W., Min, E., Fu, S. and Zhu, Z. (2006) *Reaction Kinetics and Catalysis Letters*, **87**, 25.

124 Sudhakar Reddy, J., Sivasanker, S. and Ratnasamy, P. (1991) *Journal of Molecular Catalysis*, **69**, 383.

125 Birke, P., Kraak, P., Pester, R., Schödel, R. and Vogt, F. (1994) *Zeolites and Microporous Crystals* (eds T. Hattori and T. Yashima), Studies in Surface Science and Catalysis, Vol. **83**, Elsevier, Amsterdam, p. 425.

126 Le Bars, J., Dakka, J. and Sheldon, R.A. (1996) *Applied Catalysis A: General*, **136**, 69.

127 Wu, P., Komatsu, T. and Yashima, T. (1997) *Journal of Catalysis*, **168**, 400.

128 Song, F., Liu, Y., Wu, H., He, M., Wu, P. and Tatsumi, T. (2006) *Journal of Catalysis*, **237**, 359.

129 Mantegazza, M., Leofanti, G., Petrini, G., Padovan, M., Zecchina, A. and Bordiga, S. (1994) *New Development in Selective Oxidation II* (eds V. Cortés-Corberán and S. Vic Bellon), Studies in Surface Science and Catalysis, Vol. **82**, Elsevier, Amsterdam, p. 541.

130 Zecchina, A., Bordiga, S., Lamberti, C., Ricchiardi, G., Scarano, D., Petrini, G., Leofanti, G. and Mantegazza, M. (1996) *Catalysis Today*, **32**, 97.

131 Kul'kova, N., Kotova, V.G., Kvyathovskaya, M.Yu. and Murzin, D.Yu. (1997) *Chemical Engineering and Technology*, **20**, 43.

132 Sudhakar Reddy, J. and Jacobs, P.A. (1993) *Journal of the Chemical Society – Perkin Transactions 1*, 2665.

133 Reni, J., Ravindranathan, T. and Sudalai, A. (1995) *Tetrahedron Letters*, **36**, 1903.

134 Reni, J., Sudalai, A. and Ravindranathan, T. (1995) *Synlett*, 1177.

135 Sudhakar Reddy, J. and Jacobs, P.A. (1996) *Catalysis Letters*, **37**, 213.

136 Jorda, E., Tuel, A., Teissier, R. and Kervenal, J. (1999) *Proceedings of the 12th International Zeolite Conference, July 5–10, 1998, Baltimore* (eds E. Bei, M.M.J. Treacy, B.K. Marcus, M.E. Bisher and J.B. Higgins), Materials Research Society, Warrendale, PA, p. 1269.

137 Sonawane, H.R., Pol, A.V., Moghe, P.P., Biswas, S.S. and Sudalai, A. (1994) *Journal of the Chemical Society D – Chemical Communications*, 1215.

138 Gontier, S. and Tuel, A. (1994) *Applied Catalysis A: General*, **118**, 173.

139 (a) Gontier, S. and Tuel, A. (1995) *Journal of Catalysis*, **157**, 124; (b) Gontier, S. and Tuel, A. (1995) *Catalysis Letters*, **31**, 103.

140 Selvam, T. and Ramaswamy, A.V. (1995) *Catalysis Letters*, **31**, 103.

141 Reni, J., Sudalai, A. and Ravindranathan, T. (1993) *Journal of the Chemical Society D–Chemical Communications*, 1553.

142 Reni, J., Sudalai, A. and Ravindranathan, T. (1994) *Tetrahedron Letters*, **35**, 5493.

143 Suresh, S., Joseph, R., Jayachandran, B., Pol, A.V., Vinod, M.P. and Sudalai, A. (1995) *Tetrahedron*, **41**, 11305.

144 Reddy, R.S., Sudhakar Reddy, J., Kumar, R. and Kumar, P. (1993) *Journal of the Chemical Society D – Chemical Communications*, 84.

145 Hulea, V., Moreau, P. and Di Renzo, F. (1996) *Journal of Molecular Catalysis A*, **111**, 325.

146 Hulea, V. and Moreau, P. (1996) *Journal of Molecular Catalysis A*, **113**, 499.

147 Moreau, P., Hulea, V., Gomez, S., Brunel, D. and Di Renzo, F. (1997) *Applied Catalysis A: General*, **155**, 253.

148 Robinson, D.J., Davies, L., McGuire, N., Lee, D.F., McMorn, P., Willock, D.J., Watson, G.W., Bulman Page, P.C., Bethell, D. and Hutchings, G.J. (2000) *Physical Chemistry Chemical Physics*, **2**, 1523.

149 Hulea, V., Fajula, F. and Bousquet, J. (2001) *Journal of Catalysis*, **198**, 179.

150 Romano, U. (2001) *La Chimica e l'Industria*, **83**, 30.

151 Tullo, A.H. and Short, P.L. (2006) *Chemical and Engineering News*, **84** (*41*), 22.

152 Chemical Market Reporter (2004) 20–27 December.

153 Campos Martin, J.M., Blanco Brieva, G. and Fierro, J.L.G. (2006) *Angewandte Chemie–International Edition in English*, **45**, 6962.

154 Clerici, M.G. and Ingallina, P. (1996) *Green Chemistry, Designing Chemistry for the Environment* (eds P.T. Anastas and T.C. Williamson), ACS Symposium

Series, Vol. **626**, American Chemical Society, Washington, DC, p. 58.
155 Clerici, M.G. and Ingallina, P. (1998) *Catalysis Today*, **41**, 351.
156 Meiers, R., Dingerdissen, U. and Hölderich, W.F. (1998) *Journal of Catalysis*, **176**, 376.
157 Jenzer, G., Mallat, T., Maciejewski, M., Eigenmann, F. and Baiker, A. (2001) *Applied Catalysis A: General*, **208**, 125.
158 Danciu, T., Beckman, E.J., Hancu, D., Cochran, R.N., Grey, R., Hajnik, D.M. and Jewson, J. (2003) *Angewandte Chemie – International Edition in English*, **42**, 1140.
159 Zimmer, A., Mönter, D. and Reschetilowski, W. (2003) *Journal of Applied Electrochemistry*, **33**, 933.
160 Wang, R., Guo, X., Wang, X., Hao, J., Li, G. and Xiu, J. (2004) *Applied Catalysis A: General*, **261**, 7.
161 Wang, C., Wang, B., Meng, X. and Mi, Z. (2002) *Catalysis Today*, **74**, 15.
162 Wang, Q., Mi, Z., Wang, Y. and Wang, L. (2005) *Journal of Molecular Catalysis A*, **229**, 71.
163 Liang, X., Mi, Z., Wu, Y., Wang, L. and Xing, E. (2003) *Reaction Kinetics and Catalysis Letters*, **80**, 207.
164 Roffia, P., Paparatto, G., Cesana, A. and Tauszik, G. (1990) US Patent 4,894,478.
165 Clerici, M.G. and Ingallina, P. (1993) US Patent 5,252,758.
166 Liu, T., Meng, X., Wang, Y., Liang, X., Mi, Z., Qi, X., Li, S., Wu, W., Min, E. and Fu, S. (2004) *Industrial and Engineering Chemistry Research*, **43**, 166.
167 Langhendries, G., De Vos, D.E., Baron, G.V. and Jacobs, P.A. (1999) *Journal of Catalysis*, **187**, 453.
168 Derouane, E.G. (1998) *Journal of Molecular Catalysis A*, **134**, 29.
169 Clerici, M.G. (2006) *Oil Gas European Magazine*, **32**, 77.
170 Boccuti, M.R., Rao, K.M., Zecchina, A., Leofanti, G. and Petrini, G. (1989) *Structures and Reactivity of Surfaces* (eds C. Morterra, A. Zecchina and G. Costa), Studies in Surface Science and Catalysis, Vol. **48**, Elsevier, Amsterdam, p. 133.
171 Bellussi, G., Carati, A., Clerici, M.G., Maddinelli, G. and Millini, R. (1992) *Journal of Catalysis*, **133**, 220.
172 Wu, P., Komatsu, T. and Yashima, T. (1998) *Journal of Physical Chemistry B*, **102**, 9297.
173 Merkx, M., Kopp, D.A., Sazinsky, M.H., Blazyk, J.L., Müller, J. and Lippard, S.J. (2001) *Angewandte Chemie – International Edition in English*, **40**, 2782.
174 Bonchio, M., Conte, V., Di Furia, F. and Modena, G. (1989) *Journal of Organic Chemistry*, **54**, 4368.
175 Prestipino, C., Bonino, F., Usseglio, S., Damin, A., Tasso, A., Clerici, M.G., Bordiga, S., D'Acapito, F., Zecchina, A. and Lamberti, C. (2004) *ChemPhysChem*, **5**, 1799.
176 Clerici, M.G., Ingallina, P. and Millini, R. (1993) *Proceedings of the 9th Zeolite Conference, Montreal 1992* (eds R. von Ballmoos, J.B. Higgins and M.M.J. Treacy), Butterworth-Heinemann, Boston, p. 363.

19
Oxide Materials in Photocatalytic Processes

Richard P.K. Wells

19.1
Introduction

In 1972, Fujishima and Honda reported the photocatalytic splitting of water using TiO_2 electrodes [1]. This event marked the beginning of a new era in the study of photocatalysis. Since then, considerable research effort has been invested in understanding the physicochemical processes occurring, and in the continued development of active heterogeneous photocatalysts based on metal oxide semiconductors such as TiO_2 [2]. The breadth of the subject, in terms of both the materials used and their applications, is immense, and it is not the aim of this chapter to deal with all aspects of the science; rather it is to present the basic principles of the process and to review progress in the modification of metal oxides in order to enhance their photoreactivity in the visible part of the spectrum. There are many excellent reviews in the literature dealing with the basic concepts of the photocatalytic process and the reader is referred in particular to those by Hoffmann and coworkers [3], Mills and coworkers [4], and Kamat [5]. By far the majority of research has focused on TiO_2 as the material of choice and much effort has gone into enhancing the ability of visible light to activate the material rather than merely the ultraviolet component of the spectrum [6, 7]. In terms of application, environmental remediation has been the target of most research, owing to the ability of TiO_2 to function as a slurry in aqueous media, the annual rate of publication in this area being of the order of four hundred reports [8, 9]. More recent uses include the abatement of contamination within gaseous environments, with particular emphasis on the removal of chlorinated and sulfurous compounds in air [10], and the incorporation of photocatalytically mediated steps in synthetic organic chemistry [11, 12].

Metal Oxide Catalysis. Edited by S. David Jackson and Justin S. J. Hargreaves

ISBN: 978-3-527-31815-5

19.2
Basic Principles of Heterogeneous Photocatalysis

Heterogeneous photocatalysis was defined by Palmisano and Sclafani [13] as "a catalytic process during which one or more reaction steps occur by means of electron–hole pairs photogenerated on the surface of semiconducting materials illuminated by light of a certain energy." The term photocatalysis in general, refers to any chemical process in which the external energy source is derived from radiation in the ultraviolet-visible range [14]. The basic mechanisms of heterogeneous photocatalysis have been investigated by many researchers [3, 9, 15–17] and can be represented schematically by the band gap model (Figure 19.1).

The band gap is characteristic of the electronic structure of the semiconductor and is defined as the energy difference (ΔE_g) between the valence and conduction bands; that is the highest energy band with all electronic levels occupied and the lowest energy band without electrons [18]. Table 19.1 shows some typical metal oxide and chalcogenide photocatalysts, together with their respective band gaps [9].

When energy greater than ΔE_g is applied to the semiconductor surface, valence band electrons are promoted to the conduction band, creating electron–hole pairs (**1**). Migration of the pairs to the semiconductor surface (**2**) allows the occurrence of redox reactions with adsorbates with suitable redox potentials (**3**). Thermodynamically, oxidation will occur if the redox potential of the valence band is more positive than that of the adsorbates. Similarly, conduction band electrons can reduce adsorbed species if their redox potential is more negative than that of the adsorbates. Clearly, the most likely outcome of the formation of electron–hole pairs is their simple recombination, with subsequent release of thermal energy and/or light (**4**). Recombination proceeding within the same timescale as the redox

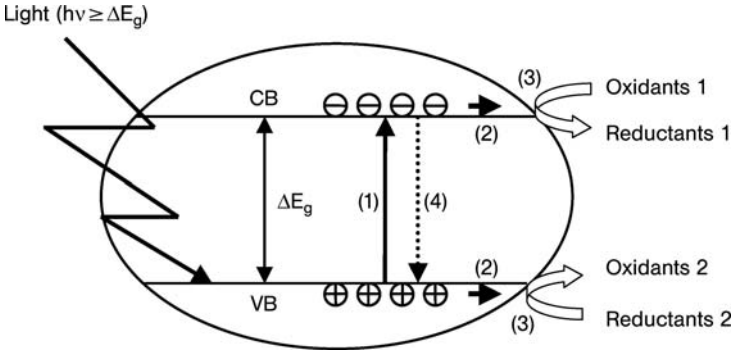

Figure 19.1 Schematic representation of the "band gap model". (1) Photoinduced electron–hole creation; (2) charge migration to the surface; (3) redox reactions; (4) recombination. VB and CB represent valence and conduction band respectively.

Table 19.1 Band gap energy of various photocatalysts.

Photocatalyst	Band gap energy (eV)	Photocatalyst	Band gap energy (eV)
Si	1.1	ZnO	3.2
TiO_2 (rutile)	3.0	TiO_2 (anatase)	3.2
WO_3	2.7	CdS	2.4
ZnS	3.7	$SrTiO_3$	3.4
SnO_2	3.5	WSe_2	1.2
Fe_2O_3	2.2	α-Fe_2O_3	3.1

processes being promoted reduces photocatalytic activity considerably. Therefore, for electron–hole pairs, whose lifetime can normally be considered to be of the order of femtoseconds, separation is a vital parameter when determining activity [19]. Before any reaction or recombination step can take place the charge carriers must be trapped, and defects play an important role in this process. Defects can be either intrinsic, for example oxygen vacancies in nanostructured reducible oxides, or extrinsic, such as dopants or impurities. Minimizing the likelihood of recombination has led to the preparation of nanostructured oxide materials [14] together with the development of materials capable of enhanced photocatalytic activity through spatial structuring [20] and encapsulation within host materials such as zeolites [21].

19.3 Traditional Photocatalysts

TiO_2 is by far the most widely investigated metal oxide, mainly because of its chemical stability, non-toxicity, and well-positioned valence and conduction bands. Two crystalline phases have been investigated, rutile and anatase. As shown in Figure 19.2, the valence band redox potential of both forms are more positive than that of the $\bullet OH/^{-}OH$ redox couple, resulting in the oxidation of adsorbed water and hydroxyl groups to highly reactive hydroxyl radicals on both irradiated forms of the oxide. This reaction is the basis behind the immense research effort into the oxidation of organic contaminants in aqueous waste streams [3, 9, 22–24]. Of the two phases of TiO_2, anatase is widely regarded as being the most photocatalytically active [25, 26]; this is due to a variety of factors, the main one being the more negative redox potential of the anatase conduction band, making it a more efficient reducing agent than rutile. For example, molecular oxygen can be reduced to superoxide radicals by illuminated anatase, but not by illuminated rutile. This also results in a greater amount of electron–hole recombination and hence lowers the efficiency in the latter material.

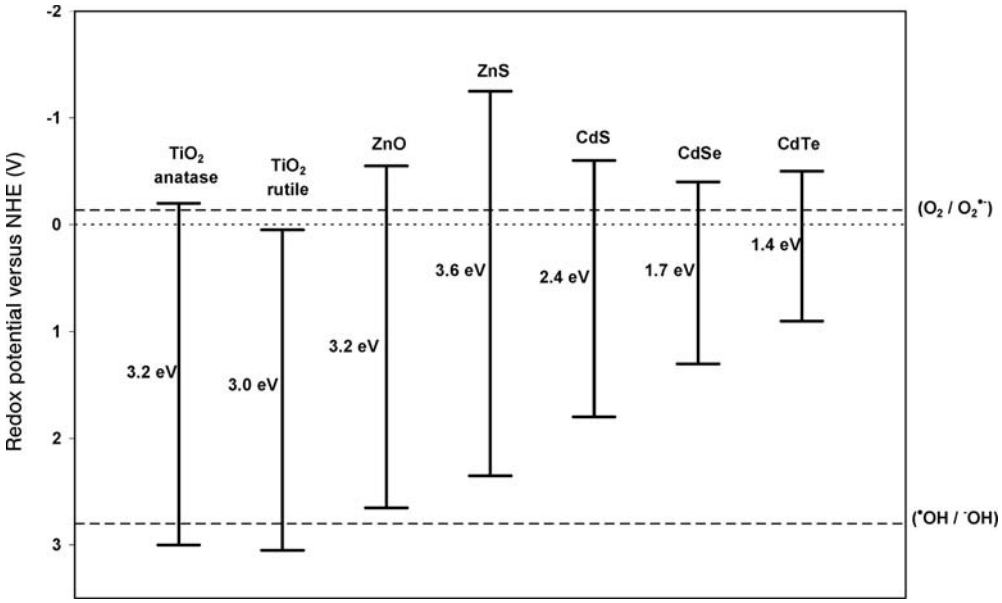

Figure 19.2 Band gaps, together with valence and conduction band edges of common semiconductors, placed alongside the standard redox potentials (versus normal hydrogen electrode (NHE)) of the $O_2/O_2^{\bullet-}$ and $\bullet OH/^{-}OH$ redox couple.

The origin of the differing band gaps between the various polymorphs of TiO_2 is in their structure. Anatase is the least thermodynamically stable, although from energy calculations this is the predominant phase when the particle size is small (<10 nm) [27]. The crystalline structure is made up of TiO_6 octahedral chains differing by the distortion of each octahedron and the assembly pattern of octahedral chains [14]. The Ti—Ti bond lengths in anatase are greater than those in rutile, whereas Ti—O distances are shorter [28]. These structural differences lead to differing mass densities and hence differing electronic structures of the bands. Anatase is 9% less dense than rutile, resulting in a greater degree of delocalization of the Ti 3d states, and therefore a narrower 3d band. Also the O 2p—Ti 3d hybridization of the two structures differs, with rutile exhibiting a greater degree of covalent mixing and hence anatase exhibiting a valence and conduction band with more pronounced O 2p—Ti 3d character [29]. These structural and electronic differences are responsible for the different reactivities of the materials.

Although anatase presents the highest photoactivities reported, a commercial material, Degussa P25, is commonly used as a reference catalyst. This product is a mixture of anatase and rutile in a ratio of 80 : 20 and displays an unexpectedly high photoactivity, the source of which is still a matter of some debate. Bickley and coworkers reported a model based upon there being a small amount of amorphous TiO_2 present in the mix [30]. The coexistence of the phases leads to a synergistic effect that improves the photoreactivity of the catalyst. A similar junction

effect has been reported for an anatase–brookite mixture, which presents a high activity for methanol photo-oxidation [31].

The principal use of TiO_2 as a photocatalyst has been in the degradation of organic material in either aqueous or gaseous waste streams. Two oxidation reactions can take place at the TiO_2 valence band. Firstly, adsorbed organic material (RH) can be directly oxidized by TiO_2 (h^+) producing cationic radicals $RH—^+$ (1). Secondly, the oxidation of water and/or hydroxyl groups can give rise to the formation of highly reactive hydroxyl radicals, •OH (2-3) that can subsequently initiate further compound oxidation.

$$TiO_2(h^+) + RH_{ads} \rightarrow TiO_2 + RH^{\bullet+}_{ads} \leftrightharpoons TiO_2 + R^{\bullet}_{ads} + H^+ \tag{19.1}$$

$$TiO_2(h^+) + H_2O_{ads} \rightarrow TiO_2 + H_2O^{\bullet+}_{ads} \leftrightharpoons TiO_2 + {}^{\bullet}OH_{ads} + H^+ \tag{19.2}$$

$$TiO_2(h^+) + {}^{-}OH_{ads} \rightarrow TiO_2 + {}^{\bullet}OH_{ads} \tag{19.3}$$

The main reaction occurring at the TiO_2 conduction band is the reduction of adsorbed molecular oxygen, resulting in the formation of superoxide radicals ($O^{\bullet-}_2$). Such superoxide radicals, can give rise to the formation of additional •OH radicals through a series of reactions (Equations 19.5 to 19.7).

$$TiO_2(e^-) + O_{2,ads} \rightarrow TiO_2 + O^{\bullet-}_{2\,ads} \tag{19.4}$$

$$O^{\bullet-}_{2\,ads} + H^+ \leftrightharpoons HO^{\bullet}_{2\,ads} \tag{19.5}$$

$$2\,HO^{\bullet}_{2\,ads} \leftrightharpoons H_2O_{2,ads} + O_{2,ads} \tag{19.6}$$

$$TiO_2(e^-) + H_2O_{2,ads} \rightarrow TiO_2 + OH_{ads} + {}^{-}OH_{ads} \tag{19.7}$$

However, photocatalytic reduction of organic compounds is generally less important than their oxidation because the reduction potential of a $TiO_2(e^-)$ is lower than the oxidation potential of a $TiO_2(h^+)$. Also, most of the reducible substrates cannot compete kinetically with oxygen as an electron scavenger [15].

Of the other potential photocatalysts listed in Table 19.1, ZnO has limited use as it is relatively unstable when illuminated in aqueous solution, particularly at low pH, tending to form Zn^{2+} (aq) after oxidation by the valence band positive holes. However, at higher pH it has been shown to be as active as TiO_2 for the degradation of phenol [32]. Also, for applications in the gas phase, such as the degradation of ethanal, ZnO thin films have been shown to be highly active [33]. WO_3, although active in a portion of the visible spectrum is considered in general to be less active than TiO_2 [34]. CeO_2 presents many of the characteristics of a suitable photocatalyst, having a band gap of 3.1 eV [35] and being relatively inexpensive and non-toxic; it is also highly absorbing in the UV spectrum and has been shown to have significant activity for the photocatalytic oxidation of water [36].

19.4
Improving Photocatalytic Activity

Because the band gap of TiO_2 is 3.2 eV it is defined as a "wide band gap semiconductor", with onset of the optical absorption band at about 350 nm [20]. Hence, only 5% of the solar energy can be absorbed by TiO_2. For this reason, considerable research effort has been invested into increasing the photocatalytic activity of TiO_2, particularly by enhancing its ability to be activated by visible light. In general, two approaches have been taken. One is to modify the band gap by addition of a secondary component, such as the adsorption of an organic dye or small amounts of another, usually metallic element. Alternatively, the basic concepts of physics can be used, and by changing the preparation methods producing photocatalytic particles of such dimensions that their band gaps are altered by quantum effects. Both methods have been shown to have a considerable effect on the reactivity, as outlined in the following section.

19.4.1
Visible Light Sensitization by Adsorption of Organic and Inorganic Dyes

Considerable research effort has been invested in the combination of photocatalysts with organic and inorganic dyes such as Erythrosin B [37] and *cis*-di(thiocyanato)-*N,N*-bis(2,2′-bipyridyl dicarboxylate)Ru(II) [38]. A huge number of potential dye-sensitizers have been reported in the literature, but the ones with optimum performance appear to be transition metal complexes derived from polypyridines [Ru(II)], porphyrins, or phthalocyanines [Zn(II), Mg(II) or Al(III)] as ligands [39, 40]. The principle behind these systems is that the dyes absorb the visible radiation and form excited states. From these states, electrons are injected into the conduction band of the semiconductor oxide, thereby inducing a visible response in the oxide. For effective function, the adsorbed dye needs to have an excited state located above the bottom of the semiconductor band [41] and to have a strong interaction with the oxide such that a fast and efficient electron junction is produced. Assuming these considerations are met the results of such sensitization are (i) an increased efficiency of the excitation process, and (ii) an expansion of the absorption spectrum of the semiconductor via excitation through the sensitizer. However, such dyes are complex molecules and are not a low-cost option. This, together with the fact that their thermal and/or photochemical stability is poor, can lead to poor lifetimes for photocatalysts prepared in this manner [42]. However, if oxygen is excluded from the system and the oxidation state of the dye is quenched with an appropriate electrolyte, such a strategy has been demonstrated to be successful [43].

19.4.2
Visible Light Sensitization by Anion Doping

More recently, visible light sensitization has been shown to be possible by doping with small quantities of C [44–47], N [48–50], F [51, 52], S [53, 54], and to a lesser

extent with B [55, 56], Cl and Br [57], P [58], and I [59]. The work by Asahi and coworkers [48] was the first to illustrate the effect that nitrogen doping has on the photocatalytic properties of TiO_2. Nitrogen-doped TiO_2 has since been shown to catalyze the visible-light-initiated oxidation of organic substrates, and extensive investigations have been conducted in order to characterize the photoelectrochemical properties of $TiO_{2-x}N_x$ with the goal of developing materials suitable for the promotion of the water splitting reaction. Photoelectrochemical characterization, together with theoretical calculations of the $TiO_{2-x}N_x$ materials indicate that the addition of anions introduces states above the valence band of TiO_2, owing to the mixing of the O 2p and N 2p states [60]. However, how much of the effect of anion doping is down to the narrowing of the band gap as predicted by Batzill and coworkers [60] is a matter of some debate. Such doping of TiO_2 not only changes the electronic properties of the oxide but also can induce the formation of oxygen defect sites [61]. These sites can then act as charge trapping centers, reducing the likelihood of electron–hole recombination. Irie and coworkers [62] suggested that the N 2p levels are separated from the valence band (formed from O 2p states), rather than mixed, thereby forming an isolated narrow band responsible for the enhanced light sensitivity of the nitrided oxides. Also, some researchers have suggested that the nitrogen exists as NO and that no direct Ti—N bonds are formed, in contrast to the assumption that the nitrogen substitutes for the oxygen in the lattice. Substantiation of this proposal has recently been published by Reyes-Garcia and coworkers, who have shown a range of nitrogen-containing species within TiO_2 by a combination of solid-state NMR and ESR spectroscopies, but observed no evidence for direct substitution of lattice oxygen [62]. However, the substitution of C for lattice O within TiO [2] has been suggested by density functional theory methods [63]. The resulting structure, being structurally the same as the parent oxides, has enhanced photoactivity in the visible spectrum owing to the resulting unoccupied impurity state occurring in the band gap. The degree of band gap narrowing is variable and depends upon the synthesis technique but values of 2.32 eV [44] and 2.0 eV [64] have been reported in materials prepared by simple thermal treatment of the carbon-modified sample in air. Some reports have suggested that optimum performance of modified TiO_2 materials can be obtained by treatment with a combination of dopants. Significant visible response has been reported using a combination of N, together with F [51] and C [65].

19.4.3
Visible Light Sensitization by Metal Ion Implantation Techniques

Another method for improving the efficiency of semiconductor oxides is the addition of transition metal cations within the photocatalyst structure [6]. Such modification of the structure has several effects, although the primary aim of such preparations is the expansion of the absorption into the visible spectrum. In certain cases, the metal dopants can act as electron/hole trappers, leading to an increase in the charge carrier lifetimes and by doing so reducing the likelihood of recombination processes [7, 66]. This occurs through the following processes:

$$M^{n+} + e^{-}_{cb} \rightarrow M^{(n-1)+} \quad \text{(electron trapping)} \tag{19.8}$$

$$M^{n+} + h^{+}_{vb} \rightarrow M^{(n+1)+} \quad \text{(hole trapping)} \tag{19.9}$$

If the $M^{n+}/M^{(n-1)+}$ pair is located below the conduction band edge and the energy level for $M^{n+}/M^{(n+1)+}$ above the valence edge then the trapping of electrons and holes would take place, affecting the lifetime of the charge carriers. The effect of the addition of metallic dopants is therefore a complex one and differentiating the individual effects is not simple. The efficiency of a metal ion dopant depends on whether it serves as a mediator of interfacial charge transfer or as a recombination center. Its efficiency as an electron/hole trap is related to several factors including the dopant concentration, its energy level within the semiconductor lattice, its electronic configuration, its distribution within the semiconductor, and the electron donor concentration. When metal ions are incorporated into the TiO_2 by conventional methods such as impregnation, a small absorption band is visible between 400 and 550 nm as a shoulder due to the formation of impurity levels in the band gap of the parent oxide [21] (Figure 19.3). However, in order to directly modify the band gap of the semiconductor, rather than simply insert an additional impurity energy level, a modified preparation technique can be used that applies transition metal ions at high acceleration energy (50–200 keV) [6, 42, 67, 68]. When the semiconductor is bombarded by such high-energy transition metal ions, the ions have been shown by a variety of spectroscopic techniques, including SIMS, EXAFS, and ESR, to be implanted into the lattice without destroying the underlying surface structure of the oxide. Rather than producing a small shoulder in the absorption band a much more significant and smooth shift is observed to higher wavelength, indicating that the resulting band gaps of the materials prepared in

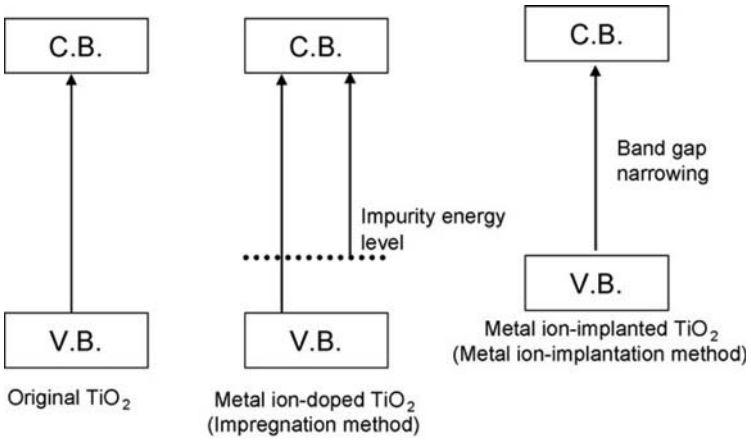

Figure 19.3 Schematic band structures of TiO_2, impregnated TiO_2, and ion implanted TiO_2.

this manner are significantly smaller than those of either the parent semiconductor or the parent oxide modified by conventional impregnation techniques.

Materials prepared by simple impregnation methods have been shown to exhibit a significantly lower photocatalytic activity than their parent oxides when illuminated solely with UV light. This has been accounted for by the dopants outside the structural framework acting as recombination centers for electron–hole pairs. Materials prepared by the ion implantation method showed no such decrease [21].

The techniques discussed above have all involved the preparation of powdered photocatalysts with enhanced visible light activity. A method recently developed for the preparation of thin-film photocatalysts with similar enhanced visible light activity is the deposition by radio-frequency magnetron sputtering, in which a TiO_2 plate is used as the source material and pure Ar as the sputtering gas [68–71]. It has been shown that the degree of absorption in the visible region is dependent upon both the temperature of preparation and the Ar pressure [72]. Similarly, nitrogen-doped materials have been prepared by the use of a mixed N_2/Ar sputtering gas mixture [73, 74]. With low concentrations of substituted nitrogen (<2%), a shoulder was observed in the UV-Vis absorption spectrum, but once concentrations above 2% were substituted a smooth shift in the absorption spectrum towards the visible region was observed. The band gaps of such materials were estimated to be between 2.25 and 2.58 eV. Such nitrided TiO_2 thin films showed good activity for the degradation of propan-2-ol diluted in water under visible irradiation [73].

19.4.4
Physical Methods to Enhance Photocatalytic Activity

Quantum physics dictates that by reducing particle size to the nanometer scale, a point is reached beyond which further decrease in the particle size will lead to variation in the position of the valence and conduction bands, and in the gap between the two [75, 76]. A variety of strategies have been suggested for controlling particle size and structure in order to produce particles in such a size regime and Table 19.2 includes some of them, together with the size range of the particles formed if such strategies are followed.

Table 19.2 Examples of preparation strategy together with the resulting particle scales.

Length scale	Examples
<1 nm	TiO_2 clusters encapsulated in zeolites
1–10 nm	TiO_2 nanoparticles forming periodic mesoporous powders
10 nm–10 μm	TiO_2 nanotubes
>200 μm	TiO_2 membranes/photonic crystals/photonic sponges

TiO_2 can be prepared on the nanometer scale [20], but the particles thus formed tend to agglomerate. One strategy to avoid aggregation of the particles has been to incorporate the TiO_2 clusters into the pores of a zeolite. Faujasite and zeolite β have been used extensively for this purpose [77]. Zeolites do not absorb in the UV-Vis region of the spectrum and hence it is possible to irradiate guest species anchored within the micropores of the host material. Two strategies have been explored for the incorporation of the TiO_2 into the zeolite, although both use molecular titanium sources with a single titanium atom that subsequently oligomerizes to form Ti—O—Ti structures. In the first approach, $TiCl_3$ or $TiCl_4$ vapors are absorbed into a partially or totally dehydrated zeolite structure, after which oligomerization is promoted by thermal treatment in the presence of moisture [78, 79]. The level of dehydration of the zeolite prior to the addition of the titanium source can give a degree of control as to where the TiO_2 structures locate. The greater the degree of dehydration the deeper into the microporous structure the $TiCl_3$ or $TiCl_4$ vapors can enter. The main problem with this technique is the explosive and pyrophoric nature of $TiCl_3$ and the highly corrosive HCl vapors formed upon hydrolysis which can cause subsequent damage to the zeolite framework [80]. The second approach is based upon the ion-exchange of the Na^+ counter-ions present in synthetic zeolites by $(Ti{=}O)^{2+}$ titanyl salts. This approach has the significant advantage that the titanium salts are non-corrosive and the ion-exchange process can be carried out in aqueous solution [81]. Hydrolysis and oligomerization can then be carried out by treatment of the titanyl salts at approximately 150 °C.

$$TiCl_4 + 2\,H_2O \rightarrow TiO_2 + 4\,HCl \tag{19.10}$$

$$TiO^{2+} + H_2O \rightarrow TiO_2 + 2\,H^+ \tag{19.11}$$

When low loadings of $TiCl_4$ were used, it was shown by UV-Vis spectroscopy that isolated titanium atoms are formed, bonded to the zeolite surface either mono, bi- or tripodally [82]. Increasing the loading led to the formation of aggregated moieties with Ti—O—Ti linkages present. The photoreactivity of materials produced was shown to be significantly higher than Degussa P25 TiO_2 for the partial oxidation of thianthrene [83].

Incorporation of titanium oxide species within the framework of mesoporous silicas has been shown to produce highly efficient photocatalytic materials. Extremely careful preparation conditions [84] leads to highly structured materials comprising anatase nanoparticles of dimension between 5 and 10 nm. The channeled structure, together with the hydrophobic/hydrophilic character, are also key features controlling their enhanced photoreactivity. The photocatalytic activity of such mesoporous catalysts has been studied for the degradation of phenol in aqueous solutions [85]. It was observed that for structured mesoporous materials with low Ti content, the turnover frequency was four times greater than that for standard P25.

A development in the use of structured TiO_2 has been the production of new one-dimensional materials such as nanotubes, nanofibers, and nanowires [86–

88]. TiO_2 nanotubes have a relatively high surface area compared with bulk titania powder but, most interestingly, time-resolved diffuse reflectance spectroscopy has shown that charge recombination is disfavored by the tubular morphology. Such nanotubes can be relatively easily prepared starting from conventional nanoparticles such as P25. Such particles are digested in strong base in an autoclave at 150 °C for several hours [89]. Annealing of the resulting material at 400 °C for 3 h results in nanotubes composed exclusively of anatase. Laser flash photolysis has shown that photogenerated holes on nanotubes have an average half-life approximately six times that of conventional TiO_2 of an equivalent BET area [89].

Only a small percentage of the solar flux can be absorbed by powdered metal oxide semiconductors. Hence considerable research effort has been invested in trying to modify the composition of such materials by chemical means, in order to enhance absorption in the visible region, and several examples of methods developed with this aim have been discussed earlier. In addition to such strategies, one physical approach is to increase the optimum light path, leading to entrapment of the light in the material. This methodology enhances light absorption by increasing the light path through the material in what are known as photonic crystals [90, 91]. Since the light is trapped within the crystal there is a significant enhancement in the likelihood of electron–hole pair formation, particularly at the onset of the absorption band where the specific absorption of the material is very low. The fundamental concept of a photonic crystal is the structuring of the space creating a periodic dielectric constant field in the scale of the visible light wavelength [92]. This spatial structuring produces coherent Bragg diffraction patterns that forbid light of the corresponding wavelength propagating through the material. At the Bragg diffraction frequencies, photons propagate with greatly reduced velocity and are known as "slow" photons. Crucially, if the slow photons exhibit energy which overlaps the absorption band of the material then the enhancement of the light absorption occurs as a consequence of the increase of the effective optical path length through the material. Ozin and coworkers prepared an inverse opal constituted of anatase nanocrystals ordered around monodisperse empty spheres of dimension between 280 and 500 nm. The system was investigated for the degradation of methylene blue. Using white light illumination, it was observed that the optimum void dimension was 300 nm, for which a photocatalytic activity enhancement of 2.3 was observed with respect to TiO_2 nanoparticles [93].

A further development of the opal structure was developed by Meseguer and coworkers, who expanded the concept to form a photonic sponge [94]. In this configuration, rather than having a monodispersion of spherical voids of a single dimension, the sponge has an appropriate distribution of differing size spheres, resulting in the trapping of an entire region of energy within a particular spectral region. Hence, with appropriate preparation, a sponge can be prepared that traps most of the visible spectrum. Such materials, when tested for the degradation of succinonitrile, have been reported to have their photocatalytic activity enhanced by an order of magnitude in comparison to TiO_2 nanoparticles [20].

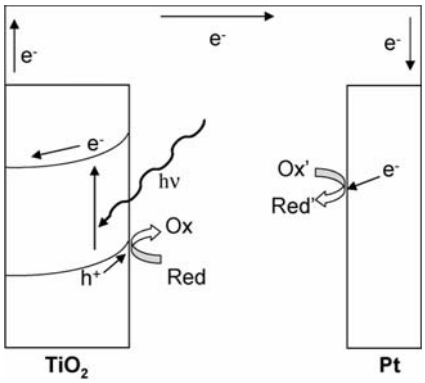

Figure 19.4 Schematic representation of a photoelectrocatalytic process.

19.4.5
Potential-Assisted Photocatalysis

Potential-assisted photocatalysis combines the advantages of photocatalysis with those of electrocatalysis. It is a combined technology that improves the efficiency of photocatalysis by the application of an external potential. This potential difference can either be simply a result of the resting potentials of the differing electrodes, or the application of an external electrically applied bias. This concept was first introduced by Honda and Fujishima, as they demonstrated the photoelectrocatalysis of water under the influence of an anodic bias [1].

Figure 19.4 shows a schematic representation of a photoelectrochemical cell. Photo-generated electrons are driven through the external circuit as a result of the potential difference across the cell. Hence, oxidation and reduction reactions occur at different electrodes of the device. Photoelectrochemically active semiconductor devices have been prepared from colloidal ZnO, TiO_2, SnO_2, and WO_3 [95]. In a photoelectrochemical cell the photocurrent observed provides a direct measurement of the reaction rate.

19.5
Conclusions

In a heterogeneous photocatalytic system, the efficiency for any chemical transformation depends upon the photoactivity of the adsorbate molecule and the catalyst substrate. In the case of a reactive semiconductor metal oxide, the catalyst can either provide energy levels to mediate electron transfer between adsorbate molecules (by temporarily accommodating an electron) or alternatively by acting as both an electron donor (derived from the photogenerated electron in the conduction band) and an electron acceptor (derived from the photogenerated hole in the valence band). Hence the band structure of the substrate plays a crucial role in

the reactivity of the oxide. A small change in the electronic structure of the material can lead to a significant change in the band structure. Such electronic modification can be achieved in a variety of ways, including the addition of dye sensitizers or cationic and anionic dopants, or alternatively the physical manipulation of the particles at a nanometer scale resulting in the alteration of the band structure as a result of quantum effects. Such methods, or a combination of methods, can be used to alter the absorption characteristics of the oxides resulting in their activity in the visible region of the spectrum, a vital characteristic for commercial viability. The ability to use fundamental design principles based upon modern experimental and theoretical techniques coupled with the ever-increasing cost of, and demand for energy, means semiconductor photocatalysis is a rich area for both scientific and technological development in the twenty-first century.

References

1 Fujishima, A. and Honda, K. (1972) *Nature*, **37**, 238.
2 Linsebigler, A.L., Lu, G. and Yates, J.T. (1995) *Chemical Reviews*, **95**, 735.
3 Hoffmann, M.R., Martin, S.T., Choi, W. and Bahnemann, D.W. (1995) *Chemical Reviews*, **95**, 69.
4 Mills, A., Davies, R.H. and Worsley, D. (1993) *Chemical Society Reviews*, **22**, 417.
5 Kamat, P.V. (1993) *Chemical Reviews*, **93**, 267.
6 Anpo, M. (1997) *Catalysis Survey from Japan*, **1**, 169.
7 Carlson, T. and Griffin, G.L. (1986) *Journal of Physical Chemistry*, **90**, 5896.
8 Blake, D.M. (2001) Bibliography of work on the heterogeneous photocatalytic removal of hazardous compounds from water and air (Update Number 4), Technical Report, National Renewable Energy Laboratory, Golden, CO.
9 Bhatkhande, D.S., Pangarkar, V.G. and Breenackers, A.A.C.M. (2001) *Journal of Chemical Technology and Biotechnology (Oxford, Oxfordshire: 1986)*, **77**, 102.
10 Demeestere, K., Dewulf, J. and Van Langenhove, H. (2007) *Critical Reviews in Environmental Science and Technology* , **37**, 489.
11 Fagnoni, M., Dondi, D., Ravelli, D. and Albini, A. (2007) *Chemical Reviews*, **107**, 2725.
12 Palmisano, G., Augugliari, V., Pagliaro, M. and Palmisano, L. (2007) *Chemical Communications*, 425.
13 Palmisano, L. and Sclafani, A. (1997) *Heterogeneous Photocatalysis*, John Wiley & Sons, Ltd, Chichester, p. 109.
14 Colón-Ibánez, G., Belver-Coldeira, C. and Fernández-García, M. (2007) *Synthesis, Properties and Applications of Oxide Nanomaterials*, John Wiley & Sons, Inc., Hoboken, NJ, p. 491.
15 Fox, M.A. and Dulay, M.T. (1993) *Chemical Reviews*, **93**, 341.
16 Zhao, J. and Yang, X. (2003) *Building and Environment*, **38**, 645.
17 Peral, J. and Ollis, D.F. (1997) *Journal of Molecular Catalysis A–Chemical*, **115**, 347.
18 Xu, Y. and Schoonen, M.A.A. (2000) *American Mineralogist*, **85**, 543.
19 Cao, L., Huang, A., Spiess, F. and Suib, S.L. (1999) *Journal of Catalysis*, **188**, 48.
20 Aprile, C., Corma, A. and Garcia, H. (2008) *Physical Chemistry Chemical Physics*, **10**, 769.
21 Kitano, M., Masaya, M., Ueshima, M. and Anpo, M. (2007) *Applied Catalysis A: General*, **325**, 1.
22 Mills, G. and Hoffmann, M.R. (1993) *Environmental Science and Technology*, **27**, 1681.
23 D'Oliveira, J.C. and Al-Sayyed, G. and Pcihat, P. (1990) *Environmental Science and Technology*, **24**, 990.

24 Janus, M. and Morawski, A.W. (2007) *Applied Catalysis B–Environmental*, **75**, 118.

25 Sclafini, A. and Herrmann, J.M. (1996) *Journal of Physical Chemistry*, **100**, 13655.

26 Carp, O., Huisman, C.L. and Rellr, A. (2004) *Progress in Solid State Chemistry*, **32**, 33.

27 Dietbold, U., Ruzycki, N., Herman, G.S. and Selloni, A. (2003) *Catalysis Today*, **85**, 93.

28 Burdett, J.K., Hughbands, T., Gordon, J.M., Richardson, J.W. and Smith, J. (1987) *Journal of the American Chemical Society*, **109**, 3639.

29 Asahi, R., Taga, Y., Mannstadt, W. and Freeman, A.J. (2002) *Physical Review B*, **65**, 224112.

30 Bickley, R.I., González-Correño, T., Lee, J.S., Palmisano, L. and Tilley, R.J.D. (1991) *Journal of Solid State Chemistry*, **92**, 178.

31 Ozawa, T., Iwasaki, M., Tada, H., Akita, T., Tanaka, K. and Ito, S. (2005) *Journal of Colloid and Interface Science*, **281**, 510.

32 Dindar, B. and Icli, S. (2001) *Journal of Photochemistry and Photobiology A: Chemistry*, **140**, 263.

33 Yamaguchi, Y., Yamazaki, M., Yoshihara, S. and Shirakashi, T. (1998) *Journal of Electroanalytical Chemistry*, **442**, 1.

34 Khalil, L.B., Mourad, W.E. and Rophael, M.W. (1998) *Applied Catalysis B–Environmental*, **17**, 267.

35 Bensalem, A., Shafeev, G. and Bozon-Verduraz, F. (1993) *Catalysis Letters*, **18**, 165.

36 Bamwenda, G.R., Uesigi, T., Abe, Y., Sayama, K. and Arakawa, H. (2001) *Applied Catalysis A: General*, **205**, 117.

37 Kamat, P.V. and Fox, M.A. (1983) *Chemical Physics Letters*, **102**, 379.

38 O'Regan, B. and Grätzel, M. (1991) *Nature*, **353**, 737.

39 Choi, Y.M., Choi, W.U., Lee, C.H., Hyeon, T. and Lee, H.I. (2001) *Environmental Science and Technology*, **35**, 966.

40 Cheung, S., Fung, A. and Lam, M. (1998) *Chemosphere*, **36**, 2461.

41 Zhang, J.Z. (2000) *Journal of Physical Chemistry B*, **104**, 7239.

42 Anpo, M. (2004) *Bulletin of the Chemical Society of Japans*, **77**, 1427.

43 Jin, Z., Zhang, X., Lu, G. and Li, S. (2006) *Journal of Molecular Catalysis A–Chemical*, **259**, 275.

44 Khan, S.U.M., Al-Shahry, M. and Ingler, W.B. (2002) *Science*, **297**, 2243.

45 Sakthivel, S. and Kisch, H. (2003) *Angewandte Chemie–International Edition*, **42**, 4908.

46 Tachikawa, T., Tojo, S., Kawai, K., Endo, M., Fujitsuka, M., Ohno, T., Nishijima, K., Miyamoto, Z. and Majima, T. (2004) *Journal of Physical Chemistry B*, **108**, 19299.

47 Li, Y., Hwang, D., Lee, N.H. and Kim, S.-J. (2005) *Chemical Physics Letters*, **404**, 25.

48 Ashai, R., Morikawa, T., Ohwaki, T., Aoki, K. and Taga, Y. (2001) *Science*, **293**, 269.

49 Sakthivel, S., Janczarek, M. and Kisch, H. (2004) *Journal of Physical Chemistry B*, **108**, 19384.

50 Di Valentin, C., Pacchioni, G., Selloni, A., Livaghi, S. and Giamello, E. (2005) *Journal of Physical Chemistry B*, **109**, 11414.

51 Li, D., Haneda, H., Hishita, S. and Ohashi, N. (2005) *Chemistry of Materials*, **17**, 2596.

52 Li, D., Haneda, H., Labhsetwar, N.K., Hishita, S. and Ohashi, N. (2005) *Chemical Physics Letters*, **401**, 579.

53 Umebayashi, T., Yamaki, T., Itoh, H. and Asai, K. (2002) *Applied Physics Letters*, **81**, 454.

54 Demeestere, K., Dewulf, J., Ohno, T., Salgado, P.H. and Langenhove, H.V. (2005) *Applied Catalysis B–Environmental*, **61**, 140.

55 Chu, S.Z., Inoue, S., Wada, K., Li, D. and Suzuki, J. (2005) *Langmuir*, **21**, 8035.

56 Zhao, W., Ma, W., Chen, C., Zhao, J. and Shuai, Z. (2004) *Journal of the American Chemical Society*, **126**, 4782.

57 Luo, H., Takata, T., Lee, Y., Zhao, J., Domen, K. and Yan, Y. (2004) *Chemistry of Materials*, **16**, 846.

58 Lin, L., Lin, W., Zhu, Y., Zhao, B. and Xie, Y. (2005) *Chemistry Letters*, **34**, 284.

59 Hong, X., Wang, Z., Cai, W., Lu, F., Zhang, J., Yang, Y., Ma, N. and Liu, Y. (2005) *Chemistry of Materials*, **17**, 1548.

60 Batzill, M., Morales, E.H. and Diebold, U. (2006) *Physical Review Letters*, **96**, 26103.

61 Ihara, T., Miyoshi, M., Iriyama, Y., Matsumoto, O. and Sugihara, S. (2003) *Applied Catalysis B–Environmental*, **42**, 403.

62 Reyes-Garcia, E.A., Sun, Y., Reyes-Gil, K. and Raftery, D. (2007) *Journal of Physical Chemistry*, **111**, 2738.

63 Irie, H., Watanabe, Y. and Hashimoto, K. (2003) *Journal of Physical Chemistry B*, **107**, 5483.

64 Barborini, E., Conti, A.M., Kholmanov, L., Piseri, P., Podestà, A., Milani, P., Cepek, C., Sakho, O., Macovez, R. and Sancrotti, M. (2005) *Advanced Materials*, **17**, 1842.

65 Noguchi, D., Kawamata, Y. and Nagatomo, T. (2005) *Journal of the Electrochemical Society*, **152**, D124.

66 Sclafani, A., Mozzanega, M.N. and Pichat, P.J. (1991) *Journal of Photochemistry and Photobiology A: Chemistry*, **59**, 181.

67 Anpo, M., Dohshi, S., Kitano, M., Hu, Y., Takeuchi, M. and Matsuoka, M. (2005) *Annual Review of Materials Research*, **35**, 1.

68 Anpo, M. and Takeuchi, M. (2003) *Journal of Catalysis*, **216**, 505.

69 Kitano, M., Takeuchi, M., Matsuoka, M., Thomas, J.M. and Anpo, M. (2005) *Chemistry Letters*, **34**, 616.

70 Matsuoka, M., Kitano, M., Takeuchi, M. and Thomas, J.M. (2005) *Topics in Catalysis*, **35**, 305.

71 Kikuchi, H., Kitano, M., Takeuchi, M., Matsuoaka, M., Anpo, M. and Kamat, P.V. (2006) *Journal of Physical Chemistry B*, **110**, 5537.

72 Kitano, M., Takeuchi, M., Matsuoka, M., Thomas, J.M. and Anpo, M. (2007) *Catalysis Today*, **122**, 51.

73 Kitano, M., Funatsu, K., Matsuoka, M., Ueshima, M. and Anpo, M. (2007) *Journal of Physical Chemistry B*, **110**, 25266.

74 Kitano, M., Kudo, T., Matsuoka, M., Ueshima, M. and Anpo, M. (2007) *Materials Science Forum*, **544–5**, 107.

75 Yamashita, H., Takeuchi, M. and Anpo, M. (2004) *Encyclopedia of Nanoscience and Nanotechnology*, Vol. 10 (ed. H.S. Nalwa), American Science Publishers, Los Angeles, CA, p. 639.

76 Anpo, M., Yamashita, H., Ichihashi, Y., Fujii, Y. and Honda, M. (1997) *Journal of Physical Chemistry B*, **101**, 2632.

77 Ikeue, K., Yamashita, H., Anpo, M. and Takewaki, T. (2001) *Journal of Physical Chemistry B*, **105**, 8350.

78 Grubert, G., Stockenhuber, M., Tkachenko, O.P. and Wark, M. (2002) *Chemistry of Materials*, **14**, 2458.

79 Bossmann, S.H., Turro, C., Schnabel, C., Pokhrel, M.R., Payawan, L.M., Baumeister, B. and Woerner, M. (2001) *Journal of Physical Chemistry B*, **105**, 5374.

80 Kaipas, T. and Griffiths, R.F. (2005) *Journal of Hazardous Materials*, **119**, 41.

81 Liu, X., Iu, K. and Thomas, J.K. (1993) *Journal of the Chemical Society–Faraday Transactions*, **89**, 1861.

82 Klaas, J., Schultz-Ekloff, G. and Jaeger, N.I. (1997) *Journal of Physical Chemistry B*, **101**, 1305.

83 Cosa, G., Galletero, M.S., Fernandez, L., Marquez, F., Garcia, H. and Scaiano, J.C. (2002) *New Journal of Chemistry*, **26**, 1448.

84 Bartl, M.H., Boettcher, S.W., Frindell, K.L. and Stucky, G.D. (2005) *Accounts of Chemical Research*, **38**, 263.

85 Alvaro, M., Aprile, C., Benitez, M., Carbonell, E. and Garcia, H. (2006) *Journal of Physical Chemistry B*, **110**, 6661.

86 McCann, J.T., Marquez, M. and Xia, Y. (2006) *Nano Letters*, **6**, 2868.

87 Zhong, Z., Ang, T.P., Luo, J., Gan, H.C. and Gedanken, A. (2005) *Chemistry of Materials*, **17**, 6814.

88 Xiong, C. and Balkus, K.J. (2005) *Chemistry of Materials*, **17**, 5136.

89 Tachikawa, T., Fujitsuka, M. and Majima, T. (2007) *Journal of Physical Chemistry C*, **111**, 5259.

90 Hall, N. (2003) *Chemical Communications*, 2639.

91 Baba, T. (2007) *National Photonics*, **1**, 11.

92 Ozin, G. and Yang, S.M. (2001) *Advanced Functional Materials*, **11**, 95.

93 Chen, J.I.L., von Freymann, G., Kitaev, V. and Ozin, G.A. (2006) *Advanced Materials*, **18**, 1915.

94 Ramiro-Manzano, F., Atienzar, P., Rodriguez, I., Meseguer, F., Garcia, H. and Corma, A. (2007) *Chemical Communications*, **242**.

95 Vinodgopal, K. and Kamat, P.K. (1995) *Solar Energy Materials and Solar Cells*, **38**, 401.

20
Catalytic Ammoxidation of Hydrocarbons on Mixed Oxides

Fabrizio Cavani, Gabriele Centi, and Philippe Marion

20.1
Introduction

Ammoxidation, sometimes also termed oxidative ammonolysis, describes the process of catalytic oxidation of hydrocarbons (particularly alkenes, alkanes, alkyl-aromatics and alkyl-pyridines) to organic nitriles in the presence of ammonia, typically using mixed oxide catalysts:

$$R{-}CH_3 + 1.5\,O_2 + NH_3 \rightarrow R{-}CN + 3\,H_2O \qquad (20.1)$$

The most important example of this process is the synthesis of acrylonitrile from propene. Acrylonitrile is a large-volume commodity chemical (within the top twenty). The world's production capacity for acrylonitrile was 6.14 million tons per annum in 2005 and the output reached 5.24 million tons, an increase of 0.5% over 2004. The operating rate of production units was more than 85%, lower than the operating rate of 90% in 2004. The drop in utilization of capacity has been higher than the growth rate of the new capacity in recent years, and is essentially related to the market situation and relatively old plant technology. There is a supply deficit of acrylonitrile in the world today, but profitability in the acrylonitrile sector is still low. The mean spread, that is the difference between the acrylonitrile price and the raw material cost, between 2002 and 2006 was about \$150/metric ton. Figure 20.1 reports the world acrylonitrile demand (by use) over the 1995–2006 period and projection up to 2010 [1, 2]. Figure 20.1 also shows that acrylonitrile is a chemical intermediate used mainly in acrylic fibres, ABS (acrylonitrile–butadiene–styrene), SAN (styrene–acrylonitrile) and NBR (nitrile–butadiene–rubber).

There is a mean annual increase in world demand of about 3%, driven mainly by ABS/SAN resin and other applications. Acrylonitrile is also used to produce adiponitrile (for manufacture of hexamethylenediamine used in Nylon-6,6 fibers and resins) and acrylamide for water-treatment polymers. Approximately 52% of the total EU production of acrylonitrile is used in production of fibres, 15% in production of ABS and SAN resins, 15% in the production of acrylamide and adiponitrile, and 18% for other uses [2].

Metal Oxide Catalysis. Edited by S. David Jackson and Justin S. J. Hargreaves

ISBN: 978-3-527-31815-5

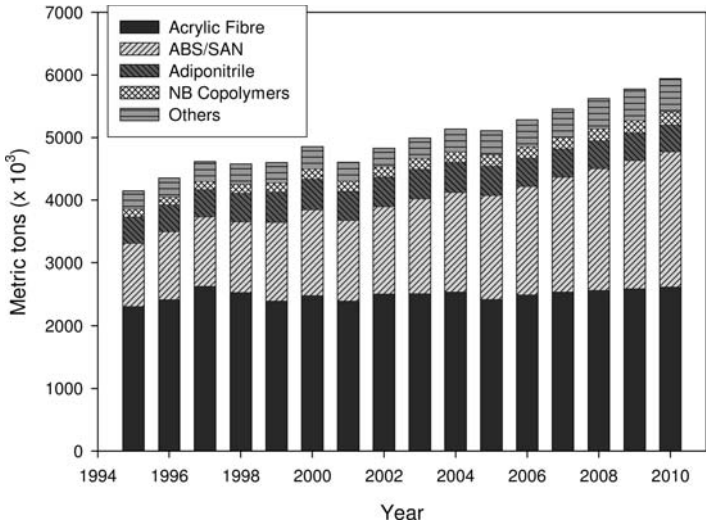

Figure 20.1 World acrylonitrile demand by derivative (data estimated from 2006 to year 2010). Data from PCI Acrylonitrile Ltd [1].

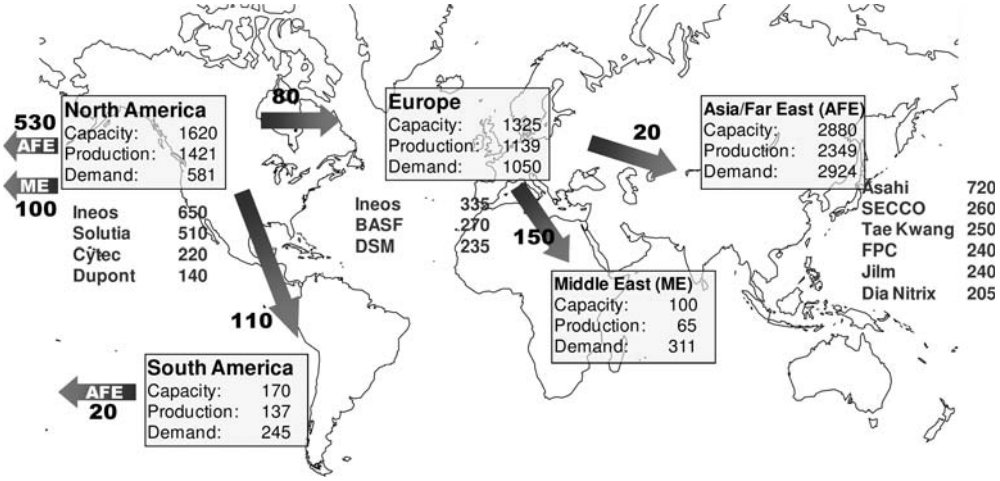

Figure 20.2 World acrylonitrile trade flow by year 2005 and major manufacturers' capacity. Data from PCI Acrylonitrile Ltd [1].

The global market for acrylonitrile is currently quite balanced. After a period of oversupply in 2001, brought about by the start-up of two large production units, many closures in Western countries offset capacity growth and brought the market into better balance. In general, a shift of capacity from Western to Asian countries has occurred between 2004 and 2008. Figure 20.2 shows the world acrylonitrile

Table 20.1 Propene demand by application (year 2005).

Application	Use (thousand metric tons)	%
Polypropene	39 289	60
Acrylonitrile	5 684	9
Propene oxide	4 780	7
Cumene	3 629	6
2-Ethylhexanol	2 424	4
Butanols	2 261	4
Isopropanol	1 350	2
Oligomers	1 327	2
Others	3 566	6

trade flow in 2005 [1] with an indication also of the major manufacturers' capacity. North America is still the largest acrylonitrile exporter and Asia is the major import area. However, recent and future expansion of production in Asia will result in a shrinking export market for North America. Costs of acrylonitrile production are highly dependent upon propene and ammonia prices. Since 2006, prices for acrylonitrile have increased substantially (by more than one-third), mainly because of rising feedstock costs. For this reason, and also because of weak demand, acrylonitrile margins remain poor.

The cost of propene is mainly driven from competing areas of application (Table 20.1). Acrylonitrile accounts for only about 9% of propene demand and, because of the expansion of the market for other applications, a further increase of propene cost is expected. Global propene demand grew from 16.4 million tons in 1980 to around 30 million tons in 1990 and about 52 million tons in 2000, with thus an average annual growth of about 6% per year, which is much higher than the average annual growth of demand for acrylonitrile. Expected demand for propene by 2010 will be 81 million tons with demand growing faster than supply. Propene supply/demand conditions and pricing are strongly dependent on refinery production and the supply/demand balance, operating rates and feedstock in the ethane industry. Globally, more than 25% of the new crackers currently planned are based on ethane, and therefore will produce little propene. Propene production by dehydrogenation of propane, although increasing, is still an expensive route. Therefore, higher prices for propene are forecast in the next decade.

Owing to the increasing cost of propene, interest in using alternative cheaper raw materials, particularly propane, is expanding rapidly. Asahi Kasei Chemicals Corporation (AKC) has begun commercial operation of the world's first propane process for acrylonitrile production, with the start-up and validation of a propane-process line at the Ulsan Plant of its Korean subsidiary Tongsuh Petrochemical Corporation. An existing 70 000 ton/year acrylonitrile line was modified to use the propane process. Propene, however, will still remain the main raw material to manufacture acrylonitrile for several years. The most used process is Innovene's (Ineos) acrylonitrile technology, known in the industry as the SOHIO acrylonitrile

process, which is used in the manufacture of over 90% of the world's acrylonitrile. In 1996, this process, which involves the oxidation of propene and ammonia to acrylonitrile in a fluid-bed reactor, was designated the eleventh National Historic Chemical Landmark by the American Chemical Society.

The SOHIO process involves the catalytic oxidative reaction of propene with ammonia in the vapor phase [3]. Approximately stoichiometric amounts of propene and ammonia, combined with air, are passed through the reactor in a single-pass operation with a residence time of just a few seconds.

$$H_2C{=}CHCH_3 + 3/2\,O_2 + NH_3 \rightarrow H_2C{=}CHCN + 3\,H_2O$$
$$\Delta H^\circ = -515\,\mathrm{kJ\,mol^{-1}} \qquad (20.2)$$

The reaction is highly exothermic and the heat of reaction is generally used to make high-pressure steam, utilized downstream in separation and purification operations. The main useful by-products from the process are HCN (about 0.1 kg per kg of acrylonitrile), which is used primarily in the manufacture of methyl methacrylate, and acetonitrile (about 0.03 kg per kg of acrylonitrile), a common industrial solvent. Smaller quantities of carbon oxides and nitrogen (from ammonia combustion) are also obtained. Unreacted ammonia in the reactor effluent is neutralized with sulfuric acid. The resulting ammonium sulfate can be recovered for use as a fertilizer.

Since the reactions generating by-products (carbon oxide formation and ammonia combustion) are themselves highly exothermic, the total exothermicity of the reaction is around 530–660 kJ mol^{-1}, making control of the reaction temperature critical.

Prior to 1960, acrylonitrile was produced commercially by processes based on either ethylene oxide and hydrogen cyanide or acetylene and hydrogen cyanide. In the late 1950s, Standard Oil (later Sohio and then BP) [4] and Distillers [5] developed a heterogeneous vapor-phase catalytic process for acrylonitrile by selective oxidation of propene and ammonia using a catalyst based on bismuth, tin and antimony salts of molybdic and phosphomolybdic acids and bismuth phosphotungstate. The $Bi_9PMo_{12}O_{52}/SiO_2$ system was first reported in 1955 for propene oxidation. The system works either in a cyclic oxidant process mode, or as a genuine redox catalyst. The first attempt to use it in a cyclic oxidant mode was abandoned after demonstration pilot operations, because about 200 kg of the solid catalyst had to be circulated to produce 1 kg of acrolein [6]. However, the same system operates successfully as a redox catalyst and was first commercialized for the production of acrolein from propene in 1957 (Degussa licensee), and subsequently commercialized internally in 1959 for the production of acrylonitrile from propene (licensed worldwide).

Around the same time, but slightly later, Edison (later Montedison) was also developing a similar process, but based on different catalysts (tellurium-cerium oxides) [7]. Although at that time the performance of these catalysts were equal or slightly superior to bismuth molybdenum oxides, the process was never commercialized.

As a consequence of the introduction of the new catalytic ammoxidation process, a steep rise in the production of acrylonitrile occurred starting from the year 1960 [6]. Further step changes were observed as a consequence of the introduction of each new generation of more effective catalysts (the acrylonitrile yield has been increased over the past 40 years from 50 to over 80%). The substitution of the inefficient and expensive process of IG Farben (HCN + acetylene) to produce acrylonitrile by the highly efficient and environmentally friendly SOHIO processs (propene + ammonia + air) can be considered as one of the first examples of 'green' sustainable chemistry. At the time of writing (2008), over 90% of the worldwide production of acrylonitrile is made using the Sohio ammoxidation process [8].

20.2 Propene Ammoxidation to Acrylonitrile

Commercial catalysts are made of multicomponent Bi-Fe-Ni-Co molybdates, also containing several additives: Cr, Mg, Rb, K, Cs, P, B, Ce, Sb and Mn are those more frequently mentioned in the several patents issued. The mixed oxide is dispersed in silica (50 wt%) for fluid-bed reactor applications. Owing to the high exothermicity of the reaction and by-product formation, most of the plants use a fluidized-bed technology. A typical empirical composition is $(K,Cs)_{0.1}(Ni,Mg,Mn)_{7.5}(Fe,Cr)_{2.3}Bi_{0.5}Mo_{12}O_x/SiO_2$ [9, 10]. The role of the various elements in the multi-component catalyst, in relation to the multi-step reaction mechanism, are discussed in detail by Grasselli [10]. Production improvements since 1980 have stemmed largely from the development of several generations of increasingly more efficient catalysts. In addition to mixed metal oxide catalysts based on multimetal molybdates (MMM), other types of commercially used catalysts were based on iron antimony oxide, uranium antimony oxide (in the past), and tellurium molybdenum oxide. MMM-based catalysts are the most commonly used nowadays.

Even though the literature on this topic has been mainly focussed on the structural and chemical-physical properties of Bi molybdates, and on the reactivity of its various polymorphs (the α, β and γ structures), the industrial catalyst consists of several divalent and trivalent metal molybdates. Indeed, Bi is present in minor amounts in catalyst formulations. The two classes of molybdate contribute differently to catalytic performance: (1) trivalent Bi/Fe/Cr molybdates, having the Scheelite-type structure, contain the catalytically active elements while (2) divalent Ni/Co/Fe/Mg molybdates, having the Wolframite-type structure, mainly enhance the catalyst re-oxidation rate.

The catalyst also contains excess Mo with respect to the stoichiometric requirement for the formation of the molybdates. The excess Mo is considered important for catalyst performance because:

- it provides a molecular bridge between the co-operating molybdates if their crystalline match is not perfect;

- it provides Mo to those phases partly depleted of it because of the redox cycle, especially under more reducing conditions (Mo is lost in the form of volatile $MoO(OH)_2$). For instance, owing to the reduction of Fe^{3+} to Fe^{2+}, part of the Mo is excluded from the molybdate, and is finally lost in volatile form.

Excess MoO_3, when present in the catalyst composition from the beginning, or when added during reaction, migrates along hydrated silica surfaces towards Mo-lean catalytically active phases. Often, Mo-enriched make-up MMM catalyst is preferentially added in place of MoO_3 during reactor operation. Fundamental understanding of these complex catalysts and the surface-reaction mechanism of propene ammoxidation has contributed substantially to the development of new catalyst generations (currently at the fourth generation). Detailed mechanisms for selective ammoxidation of propene over bismuth molybdate and antimonate catalysts have been proposed [11]. The rate-determining step is abstraction of an α-hydrogen of propene by an oxygen in the catalyst to form a π-allyl complex on the surface [11, 12]. Lattice oxygens from the catalyst participate in further hydrogen abstraction, followed by oxygen insertion to produce acrolein in the absence of ammonia, or nitrogen insertion to form acrylonitrile when ammonia is present [13]. The oxygen removed from the catalyst in these steps is replenished by gas-phase oxygen, which is incorporated into the catalyst structure at a surface site separate from the site of propene reaction. In the ammoxidation reaction, ammonia is activated by an exchange with oxygen ions to form isoelectronic NH^{2-} moieties, which are inserted into the allyl intermediate to produce acrylonitrile.

The active site on the surface of a selective propene ammoxidation catalyst contains three critical functionalities associated with the specific metal components of the catalyst [14]: an α-H abstraction component such as Bi^{3+}, Sb^{3+} or Te^{4+}; an olefin chemisorption and oxygen or nitrogen insertion component such as Mo^{6+} or Sb^{5+}; and a redox couple, such as Fe^{2+}/Fe^{3+} or Ce^{3+}/Ce^{4+}, to enhance transfer of lattice oxygen between the bulk and surface of the catalyst. Moreover, in general, it may be considered that the large improvement in the selectivity of these catalysts derives from the application of seven principles ('seven pillars') [6]: lattice oxygen, metal–oxygen bond strength, host structure, redox activity, multi-functionality of active sites, site isolation and phase co-operation.

The process schematic of propene ammoxidation is shown in Figure 20.3 [15, 16]. A single-pass configuration is possible, because over 95 wt% conversion can occur with selectivities to acrylonitrile which nowadays are well above 80%. Air, ammonia and propene are sent to a fluidized-bed reactor, which may contain up to 70–80 tons of catalyst in the form of fine spherical particles (<40 μm in diameter) highly resistant to mechanical attrition. The purity of reactants is very high (>90% for propene and >99.5% for ammonia). The ammonia to propene molar ratio is in the range 1.05 to 1.2 and the O_2/propene ratio in the range 1.9–2.1; typically, oxygen-enriched air is used in industrial operation. Reaction temperature is in the 420–450 °C interval, residence time is between 3 and 8 s, with a linear gas velocity from 0.2 and 0.5 m s^{-1} and pressure between 1.5 and 3 atm. Since the rate of acry-

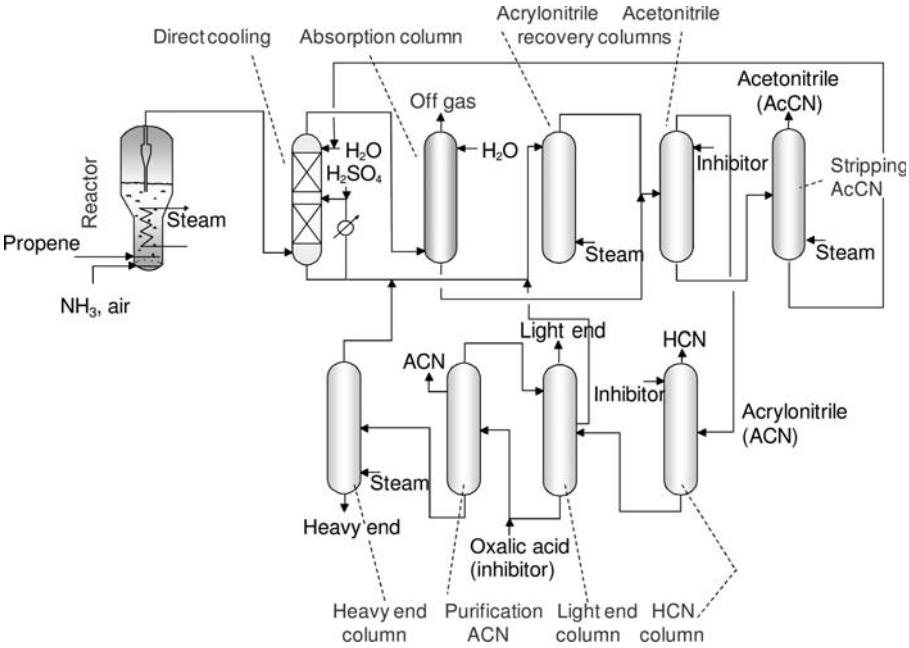

Figure 20.3 Schematic flow sheet of the SOHIO process of propene ammoxidation to acrylonitrile. Adapted from [11].

lonitrile synthesis is first order with respect to propene, with higher orders being shown towards the by-products, an increase in pressure has a negative effect on selectivity. However, positive pressure is necessary to maintain the correct fluidization characteristics in the reactor.

The feed enters the reactor through separate inlets, in order to minimize homogeneous reactions and prevent local flammable compositions developing, although owing to the effect of the solid in inhibiting radical propagation within the fluidized-bed reactor, it is possible to work inside the flammability region in the catalytic bed. The fluidized-bed reactor contains many steam coils to keep the reaction temperature constant, avoid bubble coalescence and reduce gas backmixing. By proper design of these coils a virtually plug-flow regime may be possible. An expansion area to homogenize the gas velocity profiles, and thus minimize the entrapment of solid particles, and cyclones, to recover the finest particles, are integrated into the fluidized-bed process.

The hot reactor effluent is sent to a water absorber where it is quenched countercurrently, while unreacted ammonia is neutralized with sulfuric acid. The resulting ammonium sulfate can be recovered and used as a fertilizer. The off-gases containing N_2, carbon oxides and unreacted hydrocarbon are sent to incineration. The solution of acetonitrile/acrylonitrile is a heteroazeotrope. After settling, an aqueous and an organic phase are obtained. The first is refluxed, while the latter, rich in acrylonitrile and HCN, is sent to the purification step. The aqueous aceto-

nitrile recovered at the bottom is further concentrated by azeotropic distillation. The crude acrylonitrile is first purified in two in-series columns to separate HCN and impurities (acetone, acetaldehyde, propionaldehyde, acrolein) and finally further purified under vacuum. Final polymer grade must have a purity higher than 99.4%. Disposal of the process impurities includes deep-well disposal (not sustainable), wet air oxidation, ammonium sulfate separation, biological treatment and incineration [17].

20.3
Propane Ammoxidation to Acrylonitrile

In the current process technology for the manufacture of acrylonitrile, the propene feedstock cost represents about 67% of the full (or fixed) cost of production [18]. The price differential between propene and propane depends on many factors, but can be estimated to be on average $360 per ton during 2007 [19], compared with around $320 per ton in 2004 [18]. This price differential makes propane ammoxidation competitive using the currently available catalysts. In fact some plants have already started to be revamped. For example, at Asahi Kasei Corporation an existing 70 000 ton/year acrylonitrile line was modified to use the propane process. Production began in January 2007 [20a]).

The reaction conditions claimed by the various companies are substantially different. As shown in Figure 20.4, sometimes propane-rich conditions have been claimed, as in earlier patents from Standard Oil, while in other cases propane-lean conditions are preferred. In the former case, the conversion of propane is low, and therefore recycling of the unconverted paraffin becomes necessary. Mitsubishi was the first to claim the use of hydrocarbon-lean conditions, that is conditions in which very high propane conversions can be reached. In more recent patents, BP has claimed the use of analogous conditions, using oxygen-rich feed, and propane as the limiting reactant. However, the lower activity of antimonates makes it necessary to use temperatures which are approximately 50 °C higher than those employed with the Mitsubishi catalyst.

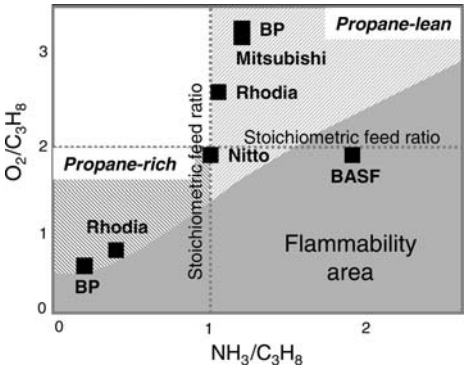

Figure 20.4 Feed composition in propane ammoxidation claimed by different companies.

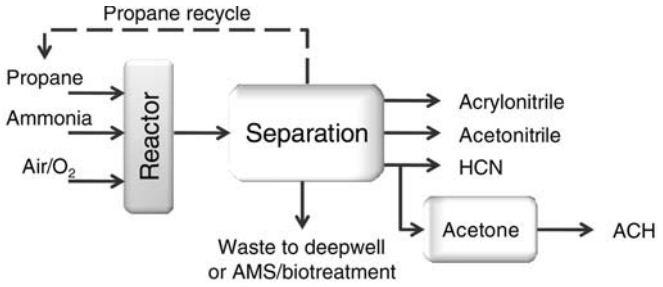

Process	Once-through	Recycle
Propane conv., %	90	28
Acrylonitrile yield, %	59	64
Catalyst	Mo/V/Nb/Te/O-SiO_2	
Reference	US 6,143,916 (2000)	JP 10-81,660 (1998)

Figure 20.5 Once-through and recycle processes for propane to acrylonitrile (ACH: acetone cyanohydrins). Adapted from [18a].

A once-through process is the preferred option [18a] (Figure 20.5). The catalyst and process conditions are tailored to achieve as near total feedstock conversion as possible. Products are separated and fresh feedstock is introduced into the reactor on a continuous basis. In addition to providing the lowest capital cost for a new-build plant, this also provides the best possibility for retrofitting existing plants by simply replacing catalyst and feedstock. This option is preferable to the combination of an alkane dehydrogenation unit with an existing propene-to-acrylonitrile process, owing to the significant capital cost involved. The significant improvement in selectivity at high conversion using V/Mo/Nb/Te oxide catalysts, compared to the earlier generation of catalysts based on V-Sb oxide, also makes the once-through option preferable to the recycle option (Figure 20.5) [18a]. Although selectivity is higher when operating at lower propane conversion, additional equipment is required for recovery and recycling of the unreacted feedstock. Nevertheless, if selectivities to acrylonitrile could exceed 80% at a propane conversion lower than about 30% using new generation catalysts, the recycle process could become an interesting option. The recycling of unconverted propane is also an option when high alkane conversion is reached, because this allows not only the complete recovery of propane but also propene recycling (one side-product of the reaction, which is a precursor of acrylonitrile), along with carbon dioxide, which may act as a ballast for the reaction. The Mitsubishi process makes use of the BOC-PSA technology for the removal of N_2 (both present in the feed and generated in the reactor by ammonia combustion), while the purge stream is incinerated [20b]. One Mitsubishi patent claims the staged feeding of ammonia along the catalytic bed [20c]; this is a necessary option if the catalyst is very active in ammonia

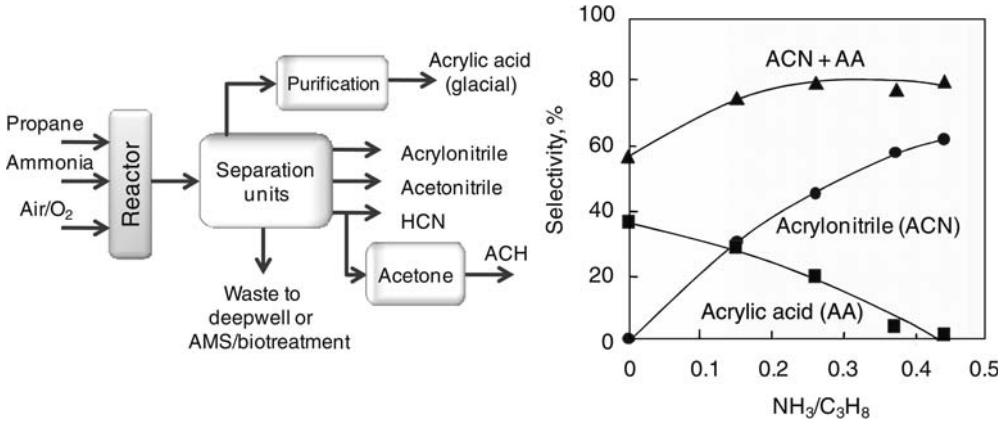

Figure 20.6 Multiple product option with propane feedstock (US Patent 6,166,241 (2000)). Adapted from [18a].

combustion to N_2, in order to avoid a lack of ammonia in the final part of the reactor, which would favor combustion of the hydrocarbons and the formation of propene.

More complex process concepts have also been proposed which attempt to optimize the processes. One option is the use of multiple reaction steps operating at different reaction conditions [18a]. Three sequential process steps are used, each operated with increasing conversion of propane. Product is separated after each step and the unreacted propane is sent to the next reactor with fresh ammonia and air/oxygen. An overall propane conversion of 95% with overall acrylonitrile yield of 63% is achieved in three steps. Another approach is to increase the process flexibility in synthesizing multiple products. By changing the ratio of propane/ammonia in the feed to the reactor, acrylonitrile and acrylic acid could be simultaneously produced with variable yields, depending on NH_3/C_3H_8 ratio (Figure 20.6). Even if the complexity of product purification and recovery sections increases the process costs, this option provides the opportunity to optimize the operation of the plant based on changes in feedstock and product price and demand.

A number of reviews have discussed the catalyst and catalytic reaction chemistry in propane ammoxidation [21–25]. So far, two main catalytic systems have been proposed in the literature. They are based on V-antimonates with rutile structure or multi-component molybdates (Mo/V/Nb/Te/O). Among the antimonates are compositions of the Al/Sb/V/W/O system which give the highest acrylonitrile yields reported (about 39%) [26]. The most promising catalyst discovered thus far is the Mo/V/Nb/Te/O system, which has been shown to be both active and selective, giving acrylonitrile yields up to 62% [6b, 27]. Mitsubishi Kasei [27] originally developed this catalyst composition which gives the highest yield of acrylonitrile to date, although the long-term stability is still unclear. The optimal catalyst composition is $MoV_{0.3}Te_{0.23}Nb_{0.12}O_x$, which gives a yield of acrylonitrile of about 50%; this can be further increased to nearly 60% by the addition of Sb, B or Ce. Key characteristics of the catalyst are not only its composition, but also the procedure

of synthesis and activation and the modality of doping. These catalysts are prepared by hydrothermal synthesis, which results in nucleation and growth of M1 and M2 phases with well defined crystal morphologies.

Several articles on synthesis and characterization of Mo/V/M/O (M = Te, Sb, Al) catalysts have been published recently [28]. The effects of metal oxide precursor sources, synthesis conditions and post-synthesis treatments are subjects of current studies. Asahi [29] has modified the composition of the Mitsubishi catalyst, by incorporation of Sb in place of Te in the M1 phase; this catalyst is more stable than the original one, and hence provides longer catalyst lifetime.

Standard Oil (later BP America, now Ineos) developed V–Sb-based catalysts which show a high selectivity to acrylonitrile especially when using high propane concentration [30, 31]. Single and dual catalyst compositions were patented, with the second catalyst having the function of converting the propene intermediate to acrylonitrile [30]. Claimed catalyst compositions are mixed oxides such as (i) $Cr_aMo_bTe_cM_d$, where M is Mg, Ti, Sb, Fe, V, W, Cu, La, P, Ce or Nb; (ii) VSb_aM_b, where M is one or more of Sn, Ti, Fe, Mn or Ga; (iii) $Bi_aFe_bMo_cA_dB_e$, where A is one or more alkali or alkaline metals, boron, W, Sn or La and B is one or more of the elements Cr, Sb, Pb, P, Cu, Ni, Co, Mn or Mg; and (iv) $Bi_aFeMo_{12}V_bD_cE_dF_eG_f$, where D is one or more of the alkali metals; E is one or more of Mn, Cr, Cu, Zn, Cd or La; F is one or more of P, As, Sb, F, Te, W, B, Sn, Pb or Se; and G is one or more of Co, Ni or an alkaline earth metal. The gas feed composition was usually propane/ammonia/oxygen/water in a 5/1/2/11 molar ratio, with excess alkane and water used as a diluent.

A third catalytic system, based on vanadium aluminum oxynitrides (VALON), has also been proposed [32]. Maximum acrylonitrile yield was about 30%, but with an acrylonitrile productivity four times higher than V-Sb-W-Al-O catalysts and one order of magnitude higher than Mo/V/Nb/Te/O catalysts [33].

Other companies have studied and developed proprietary formulations, but in general catalytic systems belong either to the antimonate family (Standard Oil, Rhodia, BASF, Nitto, Monsanto) [34–38] or to the molybdate family (Mitsubishi, Asahi).

All catalysts claimed are 'multi-functional' systems. Indeed, the formation of acrylonitrile from propane occurs mainly via the intermediate formation of propene, which is then transformed to acrylonitrile via the allylic intermediate. It follows that the catalyst possesses different kinds of active site: one site that is able to activate the paraffin and oxidehydrogenates it to the olefin, and one site that (amm)oxidizes the adsorbed olefinic intermediate. This second step must be very rapid to limit, as much as possible, the desorption of the olefin. In order to develop an effective cooperation between the two sites, it is necessary to have systems in which they are in close proximity. The multi-functionality is achieved either through the combination of two different compounds (phase-cooperation), or through the presence of different elements inside a single crystalline structure. In antimonate-based systems, the cooperation between the metal antimonate (having the rutile crystalline structure), responsible for propane oxidative dehydrogenation to propene and propene activation, and antimony oxide, active in allylic ammoxidation, is made more efficient through the dispersion of the latter compound over

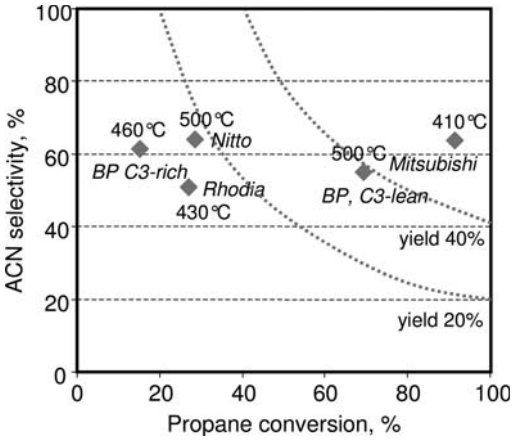

Figure 20.7 A summary of best performances in propane ammoxidation claimed by different companies.

the former one; in this case, an optimal ratio between the two compounds exists, which makes the cooperation more efficient. In metal molybdates (the Mitsubishi catalyst), one single crystalline structure contains the elements required for the activation and oxidative dehydrogenation of the hydrocarbon (vanadium), and those active for the transformation of the olefin and the allylic insertion of the NH^{2-} species (molybdenum and either tellurium or antimony). Niobium has the role of improving the structural stability of the compound.

The selectivity to acrylonitrile versus propane conversion is plotted in Figure 20.7 for the best performances reported in patents issued by different companies, and the temperature of reaction is also reported. In general, best per-pass yields obtained with propane-rich conditions are between 20 and 25%. The yield to acrylonitrile reported is close to 60% at 87–89% propane conversion, with a selectivity of 60–64% at 410 °C, under propane-lean conditions, reported in Mitsubishi patents with a catalyst made of mixed molybdate.

20.3.1 Mo/V/Te/Sb/(Nb)/O Catalysts

The elements constituting this catalyst are the basis for several crystalline structures, as illustrated in Figure 20.8, which summarizes the main mixed oxides that can be obtained by combination of V, Mo, Nb and Te(Sb). The figure shows the various bi-component systems in a triangular diagram of composition, as well as the areas which include tri- and multi-component systems, exhibiting superior performance in ethane oxidation, and in propane oxidation and ammoxidation. Many of the reported structures are related; for example orthorhombic $Mo_{5-x}(V,Nb)_xO_{14}$ solid solutions are isostructural with θ-Mo_5O_{14} and with several bi-component Sb/Mo, Nb/Mo and Te/Mo mixed oxides. The M1 phase is

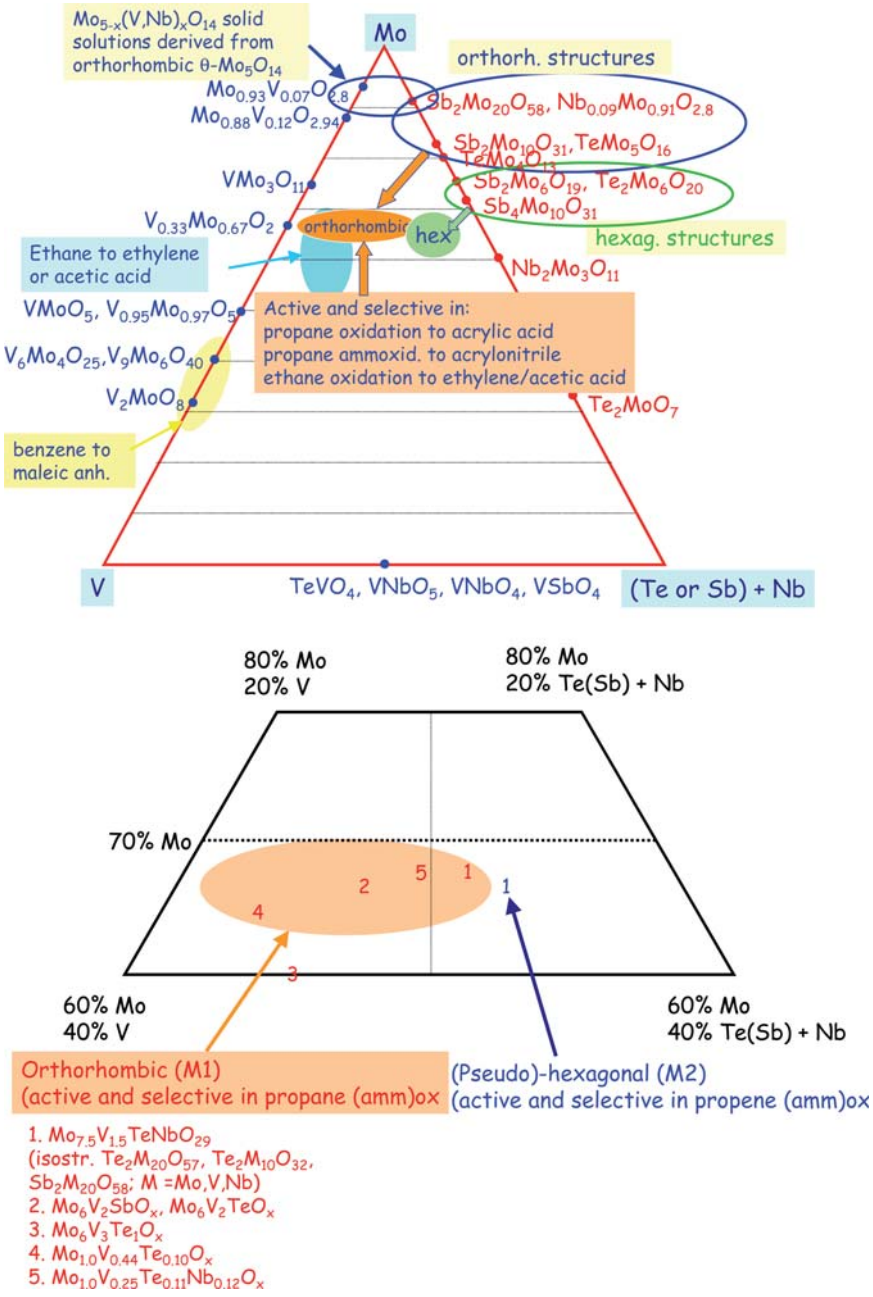

Figure 20.8 Top: Triangular diagram of composition for the Mo/V/Nb(+Te or Sb)/O system, indicating the stoichiometry of compounds which form, and the area of existence for systems active and selective in alkanes oxidation and ammoxidation. Bottom: detail of the top Figure.

structurally derived from the latter oxides, and the M2 phase is related to other Mo-leaner Te/Mo and Sb/Mo mixed oxides.

Two main preparation methods have been used to synthesize Mo/V/Te/(Nb)/O catalysts active in propane ammoxidation: (a) the dry-up and (b) the hydrothermal synthesis. The dry-up method involves mixing aqueous slurries of metal oxide precursors followed by a gradual evaporation of the combined aqueous slurry. Solvent evaporation leads to nucleation and growth of precursor metal oxide phases, which require further heat treatment to obtain active catalysts.

For the synthesis of Mo/V/Te/Nb/O catalysts, ammonium paramolybdate, vanadyl sulfate, ammonium niobium oxalate and tellurium oxide or telluric acid are mixed as aqueous solutions or slurries and dried at about 150 °C. These mixed slurries are then calcined at 500–650 °C in a N_2 stream [39]. In addition to the dominant M1 and M2 phases, impurity phases, for example MoO_3, $Mo_6V_9O_{40}$ and $Mo_3Nb_2O_{11}$, are also observed [28c]. It should be noted that Mo-V-Te-O catalysts cannot be obtained by the dry-up method.

The preferable method for catalyst preparation is the application of hydrothermal conditions [28a, 40], because they allow the syntheses of single-phase complex metal oxides, such as binary Mo/V/O, ternary Mo/V/Te/O and quaternary Mo/V/Te/Nb/O, which have various crystal structures [40g, 40h] and performance [41]. $Mo_{1.0}V_{0.44}Te_{0.1}O_x$ has an orthorhombic structure, $Mo_{1.0}V_{0.81}Te_{0.64}O_x$ a hexagonal structure and $Mo_{1.0}V_{0.25}O_x$ a tetragonal structure. All these basically have the same layered structure, in which networks of corner-shared MO_6 (M = Mo, V) octahedra form slabs and the octahedra between the slabs also share corner oxygen forming linear infinite chains of octahedra along the *c*-direction [41]. The structures differ in the arrangement of octahedra within the slabs. In the orthorhombic structure, the MO_6 (M = Mo, V) network in the slab is constructed with pentagonal and hexagonal rings of octahedra. The pentagonal bipyramidal sites may be occupied by Mo and V. Te, as the third constituent element, is exclusively located in hexagonal channels, whereas the heptagonal channels remain empty. The other structures do not possess the heptagonal rings and showed much worse performance, indicating that catalysts with the particular arrangement of MO_6 (M = Mo, V) octahedra forming slabs with pentagonal, hexagonal and heptagonal rings in the (001) plane of an orthorhombic structure is the active and selective phase in propane and ethane conversion [41]. Mo and V are indispensable elements for the structure formation. Te, located in the central position of the hexagonal ring, promoted the conversion of intermediate propene. Introduced Nb occupied the same structural position as V and the resulting catalyst clearly showed improved selectively.

Mo/V/Te/(Nb)/O catalysts owe their activity and selectivity towards propane conversion to the essential presence of so-called M1 (orthorhombic) and M2 (pseudo-hexagonal) phases [42]. The M1 phase alone is capable of selective transformation of propane [6b], and the presence of the M2 phase is claimed to improve the selectivity under more demanding conditions, such as high conversion [43]. Significantly improved acrylonitrile yields from propane above those obtained with pure M1 phase were observed using as catalyst a physical mixture with a composition of 50 wt% M1/50 wt% M2 and a surface area ratio of about 4/1. The two phases

must be thoroughly ground and brought into intimate contact with each other on a micro-/nano-scale for synergy to occur.

The orthorhombic and hexagonal structures of the M1 and M2 phases was first recognized by workers at CNRS and Elf Atochem [44] using electron microscopy. They were even able to propose schematic structures for these materials, but these models do not indicate which cation is found at a particular site and thus provide no knowledge of cation co-ordination or valence state.

The M1 and M2 compounds are not simple phases. They have large unit cells and do not form single crystals. Using combinatorial synthesis, it was possible to find ways to prepare the M1 and M2 phases separately [45] and subsequently perform structural analysis combining neutron and X-ray powder diffraction data. The result for the M1 phase shows that the material has a layer structure with two sets of channels, one approximately hexagonal, the other roughly heptagonal. The channels allow the accommodation of large metal cations. This is where the large Te^{4+} cation sits. The large channel provides access to the cation's lone pair electrons, which is likely quite important in the ammoxidation reaction (Figure 20.9).

The $MoVNbTeO_x$ system for propane ammoxidation comprises three crystalline phases: orthorhombic $Mo_{7.8}V_{1.2}NbTe_{0.94}O_{28.9}$ (**M1**) (*Pba2*: $a = 21.1337$ Å; $b = 26.6440$ Å; $c = 4.01415$ Å; $z = 4$), pseudo-hexagonal $Mo_{4.67}V_{1.33}Te_{1.82}O_{19.82}$ (**M2**) (*Pmm2*: $a = 12.6294$ Å; $b = 7.29156$ Å; $c = 4.02010$ Å; $z = 4$) and a trace of monoclinic $TeMo_5O_{16}$ (*P*21/*C*: $a = 10.0349$ Å; $b = 14.430$ Å; $c = 8.1599$ Å; $\beta = 90.781°$; $z = 1$) [45c]. The catalytically active and selective centers reside on the surface of the basal plane of the M1 phase and are composed of an assembly of five metal oxide octahedra ($2V^{5+}_{0.32}/Mo^{6+}_{0.68}$, $1V^{4+}_{0.62}/Mo^{5+}_{0.38}$, $1Mo^{6+}_{0.5}/Mo^{5+}_{0.5}$) and two tellurium–oxygen sites ($2Te^{4+}_{0.94}$), which are stabilized and structurally isolated from each other (site isolation) by four Nb^{5+} centers, each surrounded by five molybdenum–oxygen octahedra (Figure 20.8b). The V^{5+} surface sites, distinguished through their (V^{5+} = O↔V^{4+}—O) resonance structure, are the paraffin activating sites capable of methylene-H abstraction; the Te^{4+} sites (lone pair of electrons) are required for the α-H abstraction of the chemisorbed propene molecule, once formed; and the adjacent Mo^{6+} sites for NH insertion into the π-allylic surface intermediate. Within this structure are contained all key catalytic elements needed to transform propane directly to acrylonitrile, strategically arranged and within bonding distance of each other, generating the active center of the M1 phase [45c].

Under mild operating conditions, the M1 phase alone is enough to effectively convert propane directly to acrylonitrile. Under demanding conditions symbiosis between the M1 and M2 phases occurs, with the latter serving as a co-catalyst or mop-up phase to the former, transforming unconverted, desorbed propene to acrylonitrile. The M2 phase is incapable of propane activation, lacking V^{5+} sites, but is a good propene ammoxidation catalyst. A maximum acrylonitrile yield from propane of 61.8% (86% conversion, 72% selectivity at 420 °C) was achieved with a nominal catalyst composition of $Mo_{0.6}V_{0.187}Te_{0.14}Nb_{0.085}O_x$, identified by a combinatorial methodology, which is composed of 60% M1, 40% M2 and a trace of $TeMo_5O_{16}$ [45c]. The Te environment is consistent with that observed by Millet and coworkers using EXAFS in mixed-phase samples [46].

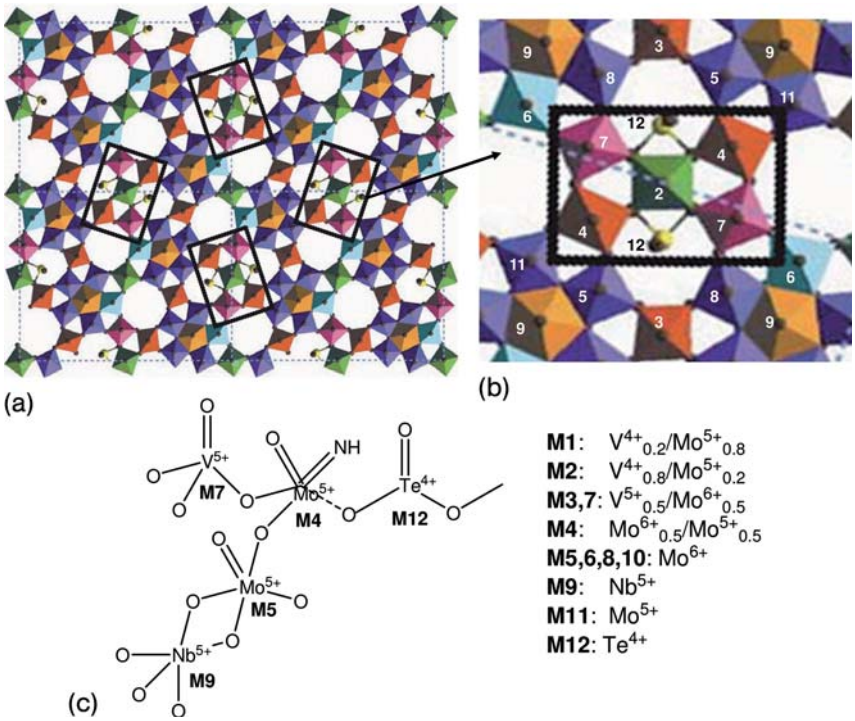

Figure 20.9 (a) Unit cell of the M1 (orthorhombic) phase along the *c* axis with the regions considered to be the active centers in propane ammoxidation shown in rectangular boxes. (b) Enlarged view of the proposed active center in M1 phase ($Mo_{7.5}V_{1.5}NbTeO_{39}$) in [001] projection with indication (numbers) of the different atoms summarized below in the scheme of the active site. (c) Elaborated from [6a, 45].

20.3.2
Rutile-Type Antimonate Catalysts

Several papers have been published dealing with the study of metal antimonates having the rutile structure. In particular, V/Sb/O and Fe/Sb/O systems have been the subject of many investigations, aimed at understanding the nature of these mixed oxides, and at the identification of the active species.

Indeed, the preparation of a truly stoichiometric metal antimonate, $MSbO_4$ (M = metal), is a difficult task. The method of preparation employed affects the nature of the catalysts prepared, but in general non-stoichiometry is a particular feature of these systems [47–50]. The most striking case is the V/Sb/O system, for which the composition $V_{0.92}Sb_{0.92}O_4$ (*quasi*-$VSbO_4$) has been reported for the catalyst with the V/Sb atomic ratio equal to 1/1 [49]. This cation-deficient structure, which has 0.04 cationic positions unoccupied per O^{2-} anion, contains Sb^{5+}, while

vanadium is present both as V^{4+} and as V^{3+}. Electroneutrality is preserved for the composition $V^{3+}_{0.28}V^{4+}_{0.64}Sb^{5+}_{0.92}O_4$ [51].

However, the ratio between V^{3+} and V^{4+} can vary depending on the method of preparation; of particular importance are the atmosphere and temperature of thermal treatment. The preparation procedure will affect the number of cationic vacancies (for V_{tot}/Sb ratio equal to 1.0) within the $V_{1-\gamma}Sb_{1-\gamma}O_4$ series, which is theoretically comprised between the two limiting compounds $V^{3+}_1V^{4+}_0Sb^{5+}_1O_4$ (the stoichiometric compound, with no cationic vacancies and only V^{3+}) and $V^{3+}_0V^{4+}_{0.89}Sb_{0.89}O_4$ (with only V^{4+}, and the maximum of 0.22 vacant cation positions), with γ varying between 0 and 0.11 [47, 48, 52]. This series of catalysts is preferentially formed by treatment in air. Therefore, the presence of cation vacancies is a consequence of V having an oxidation state higher than 3+ which explains why V/Sb/O systems give such large deviations from stoichiometry, at least under conditions that are not the most stable from the thermodynamic point of view.

Another possibility is to have a ratio between Sb^{5+} and V different from 1.0. The $V_{0.9+\gamma}Sb_{0.9}O_4$ non-stoichiometric series has been described, with γ theoretically ranging from 0 to 0.2, and correspondingly with a degree of vacant cation positions ranging from 0.2 (in $V_{0.9}Sb_{0.9}O_4$, with $V^{3+}_{0.1}V^{4+}_{0.8}$, where the ratio V_{tot}/Sb is 1.0) to 0 ($V_{1.1}Sb_{0.9}O_4$, with full occupancy of the cation sites, and with vanadium as $V^{3+}_{0.9}V^{4+}_{0.2}$) [53]. In practice, vacant positions in $V_{0.9}Sb_{0.9}O_4$ (0.2 per unit formula) are progressively occupied by V ions, with a corresponding increase of the V/Sb ratio and of the V^{3+}/V^{4+} ratio. The latter is mainly affected by the atmosphere of thermal treatment, and therefore this parameter finally affects the extent of cation site occupancy in the rutile structure.

Berry and coworkers [47] described a compound of composition $VSb_{1-\gamma}O_{4-2\gamma}$, where $\gamma \approx 0.1$, which does not formally contain cation vacancies, and which is obtained when the thermal treatment of the catalyst is carried out with oxygen-impure nitrogen. In practice, it is assumed that the ratio between V^{3+}/Sb^{5+} is equal to 1.0, and the solid solution is enriched with V^{4+} ions (and obviously with additional O^{2-} ions); which represents a solid solution between $VSbO_4$ and VO_2 (both rutile compounds). Only in the presence of oxygen-free nitrogen is it possible to obtain monophasic compounds belonging to the series $VSb_{1-\gamma}O_{4-1.5\gamma}$. For $\gamma = 0.1$ the compound $V_{1.039}Sb_{0.935}O_4$ is formed, with a small degree of cation site unoccupancy (0.026 vacancies per unit formula), a V/Sb ratio higher than 1.0 and again the presence of V^{4+}.

In most cases described in the literature, the rutile V/Sb/O system has been reported to possess either equimolar amounts of V and Sb, or an excess of V. Moreover, Sb is also present exclusively as Sb^{5+}. Excess Sb, if preparations are carried out with an Sb/V atomic ratio higher than 2 and calcination is performed in air, forms either α-Sb_2O_4 or β-Sb_2O_4 (the latter at calcination temperatures higher than 800 °C). Incorporation of small amounts of V in these Sb oxides is also likely, lowering the temperature of the α β transformation. Antimony oxide is also present in the form of amorphous oxide dispersed over the rutile, as suggested by IR spectroscopy, for Sb/V ratios between 1 and 2 [54].

The case of $FeSbO_4$ is different. It is known that the structure can host an excess of Sb. Berry and coworkers have demonstrated that on increasing the Sb/Fe ratio, an increase in cell volume of the tetragonal structure occurs [55]. Moreover, instead of a random distribution of iron and antimony in the cation sites, cation ordering has been found, with development of a tri-rutile-like structure. The change from the mono- to the tri-rutile-like ordering, from the $Fe^{3+}SbO_4$ stoichiometric compound to the $Fe^{2+}Sb_2O_6$ (with an Sb/Fe atomic ratio equal to 2) limiting compound occurs with the reduction of Fe^{3+} to Fe^{2+}. Therefore, it is possible that the formation of Sb-enriched solid solutions preferentially occurs with metal ions which can exist in stable 3+/2+ oxidation states. Indeed, the formation of very small amounts of crystalline $(VO)^{2+}Sb_2O_6$ has sometimes been observed [54a]. Fe/Sb/O systems also have been studied as catalysts for propane and propene ammoxidation [34b, 36, 56, 57].

The degree of structural defects can be checked by means of IR spectroscopy. Specifically, IR bands at 880 and 1015 cm^{-1} are attributed to the Sb—O—Sb and Sb—O—V^{4+} stretching vibrations involving co-ordinatively unsaturated O^{2-} ions adjacent to cationic vacancies [58]. Cationic vacancies play an important role in the catalytic performance of rutile-type mixed oxides [59–61]. For instance, it was found that an increased concentration of cationic vacancies and isolated V^{4+} species in V/Sb/(Fe)/O systems, due to the introduction of increasing amounts of Fe in the lattice, led to a proportionally higher activity [60c]. The formation of V^{4+} in Cr/V/Sb mixed oxides had the similar effect of increasing propane conversion considerably [62].

The IR band at around 820–840 cm^{-1}, also observed in all antimonates, is not typical of M—O stretching vibrations in rutile single oxides, and is also not observed in any antimony oxide [63]. This band has been attributed to the stretching vibration of Sb^{5+}—O—Sb^{3+} [50, 64], present on the surface of the rutile, and possibly constituting an active site for the reaction. Indeed, this vibration could be due to the presence of SbO_x-rich domains in the outer zones of non-stoichiometric rutile crystallites. Non-stoichiometric $FeSbO_4$ prepared by thermal treatment at 800 °C with excess antimony in the structure, is characterized by a tetragonal cell larger than that of stoichiometric $FeSbO_4$ and by the presence of the IR band at 820 cm^{-1}. Treatment of this compound at 1000 °C leads to (i) a decrease in the cell volume, which becomes similar to that of stoichiometric rutile and (ii) a strong decrease in the intensity of the mentioned IR absorption band [65]. Therefore, it is possible that the development to a well-crystallized, ordered rutile structure occurs as a consequence of a cation redistribution in the lattice at high temperature, with the disappearance of features related to Sb-enrichment.

The best performances among the variety of compositions which have been claimed for V/Sb/O-based systems are summarized in Table 20.2 [66]. It can be seen that Standard Oil (then BP and now Ineos) has claimed the same catalyst type for both propane-lean conditions, with high conversion of the paraffin, and propane-rich conditions, with low propane conversion.

In this system, the main catalyst component is the *quasi*-$VSbO_4$ rutile, which activates the paraffin and transforms it into the olefin-like adsorbed intermediate.

Table 20.2 Performance of some V/Sb/O-based catalysts described in the literature.

Catalyst formula	T (°C)	$C_3/NH_3/O_2/H_2O$/inert (mol%)	C_3H_8 conversion (%)	Selectivity to AN (%)	Ref.
$VSb_5W_{0.5}Te_{0.5}Sn_{0.5}O_x$–$SiO_2$	500	6.5/13/12.9/19.4/48.4	68.8	56.7	[31a]
$VSb_{1.4}Sn_{0.2}Ti_{0.2}O_x$	460	51/10.2/28.6/10.2/0	14.5	61.9	[29b]
$VSb_{1.4}Sn_{0.2}Ti_{0.1}O_x$	480	6.4/7.7/18.6/0/67.3	40.3	47.5	[31h]
$VSb_5Bi_{0.5}Fe_5O_x$–Al_2O_3	440	7.5/15/15/20/42.5	39	77	[34d]
$VSb_5Sn_5O_x$	450	8/8/20/0/64	30	49	[37b]

The intermediate may either desorb to yield propene, or be transformed to acrylonitrile over the SbO_x 'overlayers', the amount of which is a function of the excess Sb with respect to the rutile formula [22b].

In systems developed by Rhodia [34, 37] the main component is SnO_2 (cassiterite), which is inactive in propane ammoxidation, while it acts as the carrier for the V/Sb/O and SbO_x active components. Tin oxide is also able to disperse these components, through the dissolution of V and Sb ions, thus yielding a multi-functional catalyst where the two active compounds can effectively co-operate in the reaction.

Other antimonates have been studied as catalysts for this reaction [23, 67–70]. In the case of the Ga/Sb/O system [23, 67], a decrease in the Ga/Sb ratio (from $Ga_1Sb_1O_4$ to $Ga_1Sb_{49}O_{124}$) leads to a progressive decrease in activity and increase in selectivity to acrylonitrile. The best yield has been obtained at 550 °C with a catalyst having composition of $Ga_1Sb_{49}O_{124}$, with 28.3% propane conversion and 35.3% selectivity to acrylonitrile. The performance was improved by adding Ni, P and W as dopants. Recently, V^{5+}-doped $Al_{0.5}Ga_{0.5}PO_4$ was found to be active in propane ammoxidation, although its performance was not outstanding [71].

Rutile-type Cr antimonate, $CrSbO_4$, is fairly active and selective in propane ammoxidation [72] and adding V considerably improves the catalytic activity. The (Cr + V)/Sb atomic ratio is the main compositional parameter affecting the nature of these crystalline compounds [59a, 62, 73]. When almost equimolar ratios were used (e.g. in Cr/V/Sb 1/1/1), the corresponding XRD pattern showed the presence of a single, well-crystallized, rutile-type three-component $CrVSbO_6$ compound, which in practice corresponds to an equimolar solid solution between $CrSbO_4$ and VO_2 (both characterized by the rutile-type structure). In Cr/V/Sb/O samples with atomic ratios of Cr/V/Sb $1/x/1$, the general formula $Cr_1V_xSb_1O_{4+2x}$ was extrapolated, with compositions ranging from $CrSbO_4$ to $CrVSbO_6$. In these catalysts, V was present mainly as V^{4+}, and samples were extremely active in propane ammoxidation but poorly selective to acrylonitrile, leading to the predominant formation of propene and carbon oxides. When samples were instead prepared with an atomic ratio (Cr + V)/Sb < 1, V was present mainly in the rutile mixed oxide as a V^{3+} species. The main peculiarity of these Cr-based antimonates is their ability to

host excess Sb in the structure, thereby developing non-stoichiometric compounds, especially in samples with lower V content. The formation of cationic vacancies was evidenced by an intense Raman band at 880–920 cm^{-1}, especially in samples having very low (Cr + V)/Sb ratio (i.e. a large excess of Sb) and higher relative amounts of V (i.e. a Cr/V ratio close to 1).

Also with these systems, an excess of Sb with respect to the stoichiometric requirement for the rutile formation is necessary, in order to reach good selectivity to acrylonitrile and low selectivity to carbon oxides.

An important dopant for rutile-based mixed oxides is Nb oxide [59a]. The Nb/Sb/O system is active in the ammoxidation of ethane to acetonitrile [74], and the combination of Bi/Mo/O and alumina-supported Nb_2O_5 gives good performance in the ammoxidation of isobutane to methacrylonitrile [75]. Nb is one component of the V/Nb/Sb/O catalyst for propane ammoxidation developed by Nitto Chemical Industries [35]. When used as the support for V/Sb mixed oxide, Nb_2O_5 formed new phases by reaction with V and Sb under catalytic reaction conditions [76]. These phases, of unclear nature, affected catalytic performance in propane ammoxidation. When Nb was instead added as a promoter for the alumina-supported V/Sb/O system [77], the interaction between the active components V, Sb and Nb led to an improvement of catalytic performance with respect to undoped V/Sb/O. However, the Nb—Sb interaction may also lead to the development of $SbNbO_4$, which is not active for propane ammoxidation, and, in addition, removes Sb and Nb sites that would have been co-ordinated with V to form efficient V–Sb or V–Nb species. Nb also develops mixed (Cr)V/Nb/Sb oxides with the rutile structure, and hence modifies the properties of Sb cations in allylic ammoxidation [59a].

The incorporation of other elements, either trivalent or tetravalent, in the rutile lattice may substantially improve the performance of V antimonate [21]. This is the case for Al^{3+}, Ti^{4+} and W^{4+}. In the Al-Sb-V—O system, the active phase was identified as having the composition $Al_{1-x}SbV_xO_4$ with $0 < x < 0.5$ [78]. (Al,V)SbO_4 can be described as a solid solution between rutile-type $AlSbO_4$ and *quasi*-$VSbO_4$. A yield to acrylonitrile of almost 40% has been reported for an Al-Sb-V-W oxide catalyst, using feed ratios of propane, oxygen and ammonia that are stoichiometric with respect to the formation of acrylonitrile [26b]. A comprehensive study of the Al-Sb-V-W-O system has shown that the active phase in this system is $Sb_{0.9}V_{0.9-x}W_xO_4$, which is a solid solution between $V_{0.92}Sb_{0.92}O_4$ and rutile WO_2. Titanium substitution in rutile V/Sb/O produced an improved selectivity to acrylonitrile [79]; Ti^{4+} replaced for both V^{4+} and V^{3+}/Sb^{5+} pairs, forming solid solutions of continuous composition.

It was demonstrated that the better catalytic properties of (Al,V)SbO_4 and of *quasi*-Sb(V,W)O_4 compared with the pure rutile V/Sb/O phase could be rationalized in terms of the 'site-isolation' theory. According to this theory, which was originally formulated by Callahan and Grasselli [6c, 80], a catalyst that is selective for partial oxidation can be developed by creating structural isolation of the active site. Thus, the improvement of the selectivity to acrylonitrile by substitution of some of the V atoms with Al or W can be explained by the fact that substitution

creates isolation of the remaining vanadium atoms to a suitable degree, preventing combustion of the reactants and of the desired product.

Recently, an *operando* Raman technique was used to study the relationship between surface changes during reaction and catalytic performance using $VSbO_4$-based catalysts [81]. It was observed that the active rutile $VSbO_4$ phase forms during catalytic operation by reaction-induced interaction between surface vanadium and antimony oxide species.

20.4
Alkylaromatic Ammoxidation

Various aromatic nitriles such as benzonitrile, phthalonitrile, isophthalonitrile, terephthalonitrile and nicotinonitrile have applications as chemical intermediates. Nicotinonitrile can be hydrolyzed to nicotinoamide or nicotinic acid, which are used in the synthesis of vitamin B. Isophthalonitrile is used in the production of herbicides/fungicides. Phthalonitrile is an intermediate for phthalocyanine pigments. In addition, substituted aromatic nitriles have applications in the synthesis of several intermediates for applications as fine chemicals and in the life sciences.

20.4.1
Alkylbenzenes and Substituted Alkylbenzenes

Various catalysts have been reported to be active in this class of reaction (Scheme 20.1): (i) vanadium supported on TiO_2 (preferably in the anatase form) or ZrO_2 and modified by various dopants such as Cs, P, W; (ii) multi-component molybdate; (iii) doped vanadium antimonate; (iv) bulk V-P-O; (v) metal-containing (in particular Cu and Mo) zeolites; (vi) supported heteropolyacids ($PV_3Mo_{12}O_x$ on silica) and (vii) metal phosphates [82–91]. Other proposed catalysts are $AgAlBO_x$ and perovskite materials such as $YBaCu_3H_6$ and metal fluorides such as CeF_3, AlF_3 and MgF_2 [92]. However, the best catalysts belong to groups (i), (iii) and (iv), even though it should be noted that, depending on the specific substituents on the aromatic, a different ranking of these catalysts can be observed.

Various reviews have discussed in detail the characteristics and performance of these catalysts and the reaction mechanism in alkylaromatic ammoxidation [93–95]. Over V_2O_5/Al_2O_3 catalysts, the reaction mechanism proceeds via the

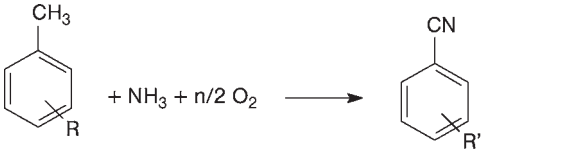

Scheme 20.1 Synthesis of aromatic nitriles by catalytic ammoxidation.

reaction of surface ammonium ions with benzoate ions, which are detected as surface species by IR spectroscopy [96]. Adsorbed benzylamine and benzaldehyde species were identified as reaction intermediates [97], while a kinetic study by Otamiri and Andersson [98] suggests that vanadium imido (V=NH) or hydroxylamino (V–NHOH) species may play a role as nitrogen insertion sites on the catalyst surface. On vanadium phosphate catalysts, in particular $(VO)_2P_2O_7$, the preferred role of a benzaldehyde-like species was also pointed out, whereas the reaction pathway via benzamide or benzylamine intermediates was suggested to be unlikely [99].

Adsorbed ammonia can exist in three different kinds of nitrogen-containing surface species such as a protonated cation (NH_4^+), and co-ordinately adsorbed NH_3 and $-NH_2$ groups. In addition, vanadium imido or hydroxylamino could be also present, especially upon interaction of ammonia with the catalyst at high temperature. All these species may potentially act as N-insertion species, and could be present and react on the catalyst surface during catalytic reaction. Therefore, unique mechanistic conclusions are difficult to obtain because multiple reaction pathways are clearly present, the relative reaction rates of which depend on the reaction conditions. However, in general terms it may be proposed that owing to the stronger chemisorption of the aromatic ring, the mechanism of reaction in alkylaromatic ammoxidation is different from that observed in propene and propane ammoxidation.

Besides selectivity to aromatic nitriles, the minimization of the direct ammonia oxidation to N_2 side-reaction is a critical factor, because otherwise runaway conditions may be possible. There is always competition between NH_3 oxidation and ammoxidation on the catalyst surface. Furthermore, contact between ammonia and the catalyst surface, particularly at high temperatures, causes a partial reduction of the oxide surface because of NH_3 oxidation to N_2. Therefore, control of the rate of unselective oxidation of ammonia to N_2 is an important factor in determining the selectivity of the nitrile product, because this side reaction limits the availability of the surface ammonia species that are necessary for nitrile synthesis.

Typical performance is a selectivity higher than 90% at a conversion in the 50–90% range, mainly depending on the type of substrate. Substituted pyridines yield better selectivities at high conversion than the equivalent alkylaromatics. The nature and position of the substituents in substituted alkylaromatics also play an important role in determining selectivity and activity. The commercial application of this technology is mainly hindered by the relatively small plant necessary for these products as compared to full-scale processes. The further implementation of the process of alkylaromatic catalytic ammoxidation would thus require the development of multi-purpose small-size continuous plants using small fluidized bed-reactors (to better control temperature and allow easier substitution of the catalyst).

Aromatic nitriles are relatively stable under oxidation conditions even at higher temperatures compared to the equivalent oxy products. Therefore these compounds are often used as intermediates for subsequent hydrogenation or reduction steps (Scheme 20.2).

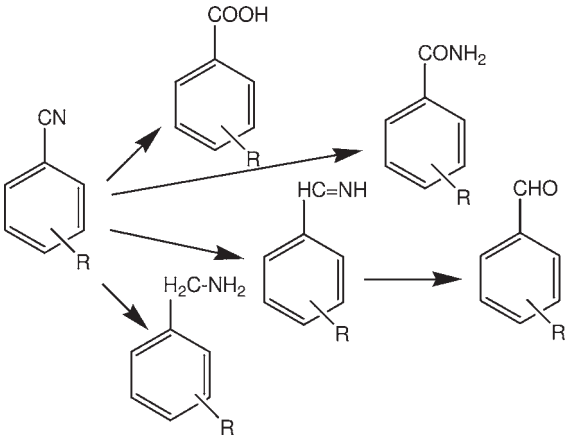

Scheme 20.2 Substituted aromatic nitriles as intermediates for aromatic acids, amides, imines, aldehydes and amines. Elaborated from [82a].

The reactivity of an alkylbenzene in the ammoxidation reaction increases with increasing size of the alkyl groups in the side chain. The rate of ammoxidation of alkylbenzenes mainly depends on the chemical nature, size and structure of substituent [92a]. The ammoxidation of substituted toluenes such as 1,2-,1,3- or 1,4-methyl-substituted toluenes can result in mono- or dinitriles [100]. There are a few reports on shape-selective ammoxidation, one such example being the ammoxidation of *m*- and *p*-xylenes over Cu-containing ZSM-5 zeolites to their corresponding mono- and dinitriles [87, 88]. Besides dialkyl-substitutions, higher methylated benzenes (e.g. mesitylene) can also be ammoxidized. However, with increase in the number of methyl groups the number of products will also increase. Furthermore, ammoxidations of substituted methylaromatics such as α-methylstyrene to atroponitrile [101a], and β-methylstyrene or allylbenzene to cinnamonitrile [101b] have also been reported in the literature. In these cases also, processes have never reached the commercial stage.

A commercially interesting area of application of alkylaromatic conversion is that of ammoxidation of halogen-substituted toluenes. The activity and the nitrile selectivity of the ammoxidations of substituted toluenes depend strongly on the position of the substituent, because it influences the accessibility of the methyl group and especially the strength of the chemisorption and the stabilization of reaction intermediates. Electron-withdrawing substituents enhance the nitrile yield, whereas electron-donating substituents cause an increased total oxidation. Therefore, halogen-substituted toluenes are easily converted into nitriles [102]. The conversion rate of *p*-halotoluenes was found to be nearly independent of the nature of the halogen substituent, but the selectivity decreases in the sequence *p*-Cl > *p*-Br >> *p*-I over V-P-O catalysts. The ammoxidation of the isomeric chlorotoluenes shows a dependence of the position of substitution in conversion ($p >> o > m$) and selectivity ($p > o > m$.)

The reaction of dichloro-substituted toluenes is much more influenced by the geometric position of the substituents. Closer proximity of the substituents to the methyl group results in lower conversions and nitrile selectivities (2,6-di-Cl < 2,5-di-Cl < 2,3-di-Cl < 2,4-di-Cl < 3,4-di-Cl) [102b, 103]. 2,6-Dichlorobenzonitrile is of particular industrial importance for the production of herbicides and pesticides, and for the preparation of special kinds of engineering plastics with high thermal resistance. Halogen-substituted xylenes can also be ammoxidized to their corresponding nitriles, for example 3,4,5,6-tetrachlorophthalodinitrile is formed from the corresponding chloro-substituted xylene in 45% yield [104]. Recently, especially in China, there has been renewed interest in these reactions.

The ammoxidation of toluenes substituted with electron-donating groups, for example hydroxy- and alkoxy-substituted toluenes is rather less selective. However, under carefully chosen conditions (choice of the catalyst, feed composition, reaction conditions) adequate yields of nitriles can be achieved. Stability of the catalyst performances is typically an issue.

Aromatic imides are another type of product which can be synthesized by catalytic ammoxidation. *o*-Xylene is converted over vanadium-titanium oxide catalysts to tolunitrile and then, depending on catalyst composition and reaction conditions, phthalimide or phthalonitrile can be selectively synthesized (Scheme 20.3) [94].

The product distribution between nitrile and imide depends upon the reaction conditions and the nature of the catalyst used [105]. The influence of various reaction parameters such as (i) reaction temperature; (ii) water vapor addition in the feed gas; (iii) NH_3/*o*-xylene mole ratio and (iv) space velocity, were studied [105]. The removal of water vapor from the feed gas has a highly pronounced promotional effect on the selectivity of phthalonitrile. The nitrile selectivity increased from 2.1 to 34% at the expense of phthalimide (which decreased from 53 to 9%) with the complete removal of water vapor in the reactant feed mixture. This observation gives an indication that phthalonitrile being formed in the reaction is further hydrolyzed to phthalimide via the amide intermediate in presence of water

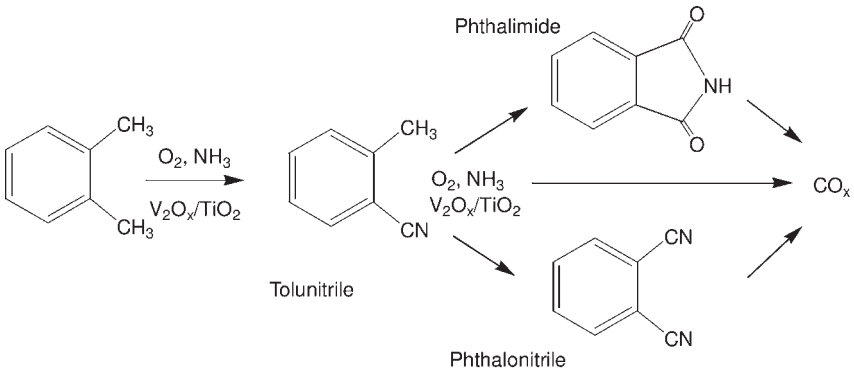

Scheme 20.3 Reaction network in *o*-xylene conversion to phthalimide and phthalonitrile. Adapted from [84].

vapor. Another interesting aspect is that titania-supported catalysts always gave significantly higher selectivities of phthalimide compared to phthalonitrile. Phthalimide yields of up to 80% were reached on a VPO/TiO_2 catalyst [105].

20.4.2
Alkylaromatics Containing Hetero-Groups

Another industrially relevant area of application of catalytic ammoxidation is the synthesis of cyano-pyridine. A relevant example is the new green process for producing nicotinic acid (niacin) developed by Lonza Ltd. Co-enzyme I (nicotinamide-adenine dinucleotide NAD) and co-enzyme II (nicotinamide-adenine dinucleotide phosphate NADP) are required by all living cells. They enable both the conversion of carbohydrates into energy and the metabolism of proteins and fats. Both nicotinamide and nicotinic acid are building blocks for these co-enzymes. Since the human body produces neither nicotinic acid nor the amide, it is dependent on intake via foodstuffs. Old methods to produce nicotinic acid cause large production of waste and use toxic reactants. For example, the classic method of preparing nicotinic acid was by oxidizing nicotine with potassium dichromate, which produces over 9 tons of waste per ton of nicotinic acid, and Cr^{VI} is carcinogenic and environmentally threatening.

A new route to prepare nicotinic acid starts from 2-methylglutaronitrile, a major side-product in the adiponitrile process and, as such, a readily available starting-material. It is easily hydrogenated to 2-methylpentanediamine, which is then condensed to methyl piperidine and dehydrogenated to 3-picoline. The gas-phase ammoxidation of the latter to cyanopyridine is followed by hydrolysis to either nicotinamide or nicotinic acid (Scheme 20.4). The cyanopyridine route for the production of nicotinic acid has the advantage of a significantly better selectivity with respect to the direct oxidation route from 3-picoline owing to the easy decar-

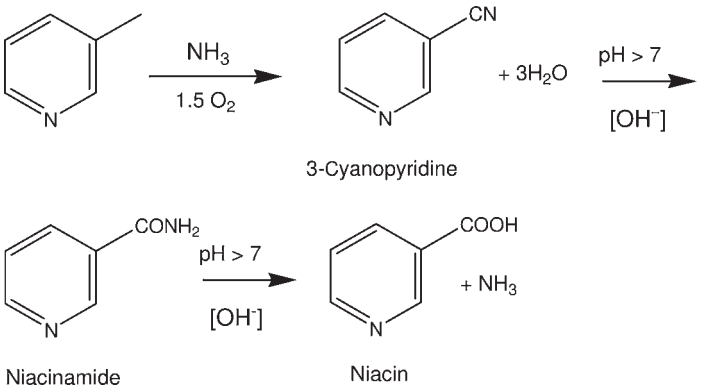

Scheme 20.4 Ammoxidation of 3-picoline and hydrolysis of cyanopyridine to niacinamide (nicotinamide) and niacin (nicotinic acid). Adapted from [106].

borboxylation and further oxidation of nicotinic acid during gas-phase oxidation. On the other hand, the cyanopyridine route involves more reaction steps and consumption of ammonia, even if it can be in part recycled.

In addition to ammoxidation of β-picoline (3-picoline), the conversion of γ-picoline (4-picoline) and α-picoline is also industrially relevant for the manufacture of various interesting intermediates starting from the corresponding cyanopyridines. Koei Chemical Company, for example, offers a range of cyanopyridine and cyanopyrazines produced by vapor-phase catalytic ammoxidation. The reaction and related catalysts have been known for a long time. In general, V antimonate-based catalysts active in propane ammoxidation also show quite good performance in methylpyridine and *m*-xylene ammoxidation to cyanopyridine and isophthalonitrile, respectively [107]. Vanadium on a variety of supports, such as TiO_2 [108], ceria [109] and CeF_3 [110] is active in the reaction, with yields up to about 80%. More recent proposed catalysts include (i) a vanadium-incorporated ammonium salt of 12-molybdophosphoric acid supported on titania or zirconia [111]; (ii) V_2O_5 supported on zirconium phosphate [112]; and (iii) metal phosphates (α- and β-$VOPO_4$) [113]. Despite the large research effort, no significant improvement in catalytic performance with respect to earlier investigated catalysts has been achieved.

The reaction mechanism on a vanadia-titania catalyst has been re-investigated using FTIR spectroscopy [114], although the conclusions were not markedly different from earlier proposals. The interaction of methylpyrazine with the catalyst surface involves a consecutive transformation of co-ordinatively bound methylpyrazine into oxygenated surface compounds, namely an aldehyde-like complex and an asymmetric carboxylate. The main reaction product, amidopyrazine, is formed through the interaction of the surface oxy-intermediates with adsorbed ammonia species.

In conclusion, research and industrial interest in the ammoxidation of methylpyridine and methylpyrazine is still active. This process could offer a greener alternative to current processes in the production of intermediates for a variety of specialty chemicals, especially in rapidly developing locations such as China where a growing interest in the reaction has been noted [115, 116].

20.4.3
Ammonolysis vs Ammoxidation

The ammoxidation of methylaromatic compounds has been shown to be a convenient route to produce many nitriles required for further syntheses of side-chain functionalized products. This method is versatile and can be carried out very easily because of the stability, and undamaged desorption, of the nitriles formed under severe gas-phase conditions. A series of interesting new patents on catalysts for the ammoxidation of alkylaromatics have been issued, indicating that there is still commercial interest in this reaction [117].

Another approach developed by Lummus Co is used commercially for isophthalonitrile production from *m*-xylene [118]. Oxidation is carried out in the absence of gaseous oxygen (ammonolysis) using lattice oxygen from the catalyst, which is regenerated in a separate vessel. The approach is analogous to the Dupont process

[119] for maleic anhydride production from *n*-butane. A fluidized catalyst is circulated continuously from a reaction zone to a regeneration zone where it is brought into contact with the aromatic + ammonia feed and air, respectively.

The reactor effluent contains the nitrile product, intermediates, unconverted feedstock for recycling, ammonia, water vapor, nitrogen, carbon oxides and traces of HCN. Separation is carried out by condensation to recover most of the organic components, which are separated (depending on the specific substrate converted) by distillation, extraction or crystallization. Off-gases are scrubbed with basic and then acidic solutions to eliminate CO_2 and NH_3, respectively, and then recycled.

The advantages of ammonolysis over ammoxidation are safer operation and higher selectivities, but fixed capital and running costs are higher and, furthermore, the process may be adapted only with difficulty to multi-purpose plants that require easy catalyst loading/unloading operations.

20.5
Ammoxidation of Unconventional Molecules

The literature on ammoxidation is very wide. The majority of papers and patents published in this field deal with propene and propane ammoxidation to acrylonitrile, of isobutane and isobutene ammoxidation to methacrylonitrile and methylaromatics and methylpyridines (picoline) ammoxidation to the corresponding cyano-containing compounds, as discussed in the previous sections. A small amount of literature deals with the ammoxidation of the following molecules:

- linear C_4 aliphatic hydrocarbons (*n*-butane, butenes, butadiene) to maleonitrile and fumaronitrile;
- cyclohexanol and cyclohexanone to adiponitrile;
- *n*-hexane and cyclohexane to adiponitrile;
- benzene to C_4 and C_6 unsaturated dinitriles.
- ethane ammoxidation to acetonitrile

Since these results are far less well known than those reported for C_3 and alkylaromatic ammoxidation, they are discussed in a more detail below.

20.5.1
The Ammoxidation of C_4 Hydrocarbons

Furuoya and coworkers [120] investigated the ammoxidation of butenes, *n*-butane and butadiene using different types of catalyst. The best results were obtained with a TiO_2-supported mixed active phase catalyst containing V, W, Cr and P, and using butadiene as the substrate. The approximate composition of the catalyst giving the best performance is (atomic ratios): $V_1W_{1.1}Cr_1P_{22}Si_{0.1}O_{x-87}TiO_2$. There is an equimolar amount of V, W and Cr, with a large excess of P. The formation of metal phosphates during the calcination treatment is highly likely.

The highest yield reported to a mixture of fumaronitrile (*trans*-1,4-dicyano-2-butene) and maleonitrile (*cis*-1,4-dicyano-2-butene) is 66.8% at 560 °C (conversion

Table 20.3 Summary of results for butadiene ammoxidation with the catalyst V/W/Cr/P/O-TiO_2[120]

Feed composition C_4/NH_3/air	T (°C)	τ (s)	Butadiene conversion (%)	Yield to MN + FN (%)
1/5/94	552	1.8	96.8	49.3
1/5/94	517	3.6	nr	49.1
0.5/2.5/97	560	1.2	nr (100%)	66.8
0.5/2.8/96.7	498	1.2	99.7	60.7

FN: fumaronitrile; MN: maleonitrile. The two compounds are reported to form with a ratio close to 1. τ = contact time, nr = not reproted.

is not reported, but extrapolation from the other results suggests it is likely total), with a contact time of 1.2 s, a dilute butadiene stream (0.5 mol%) and a butadiene/NH_3/O_2 feed ratio of 1/5/20. By-products were acetic acid, HCN, CO, CO_2 and traces of crotononitrile (these compounds were not detailed). The effects of important reaction parameters are summarized in Table 20.3.

The catalytic system appears to give interesting results. It is worth noting that in order to obtain a good performance, it is necessary to combine the properties of several elements. In fact, some of the corresponding bi-component systems (V/P, W/P, W/Cr) although active in butadiene conversion, were less selective to nitriles with the best yield being lower than 20%. However, from the data reported, it is very difficult to identify the role of each component in the reaction. In general, one might believe that V, W and Cr should play the same role of activation of the hydrocarbon, while P should play the role of an enhancer of surface acidity. The latter property is indeed very important, owing to the basic characteristics of both the reactant and the products. However, from the data reported it appears that the important step is not the activation of butadiene, but rather its transformation to the nitriles. This means that the adsorption properties of the catalyst and the insertion of N into the molecule are the key steps for the performance.

The considerations reported above suggest that the mechanism of reaction might not be the same as the well known allylic insertion of a nucleophilic NH^{2-} species onto the activated hydrocarbon, to generate the precursor of the cyano group. Indeed, none of the elements included in catalyst formulation is able to produce the M=NH species (which is generated by Mo and Sb in propene ammoxidation catalysts).

In view of this, the mechanism might consist of the following steps:

- Co-ordination of butadiene to the metal (V or W), with electron transfer from the diolefin to the metal ion, and intramolecular rearrangement of the residual double bond.
- Sequential attack of ammonia from the gas phase onto the activated hydrocarbon at the C1 and C4 atoms, with formation of amino groups and then nitriles (possibly via radical reactions).
- Desorption of the compound and re-oxidation of the reduced metal ion by O_2.

Therefore, the co-ordinating properties (intrinsic Lewis acidity) and the redox properties (electron transfer) of the metal ion are important for the first step, and for the transformation of the adsorbed hydrocarbon into the nitrile rather than to carbon oxides and HCN. It is also worth noting that when a conventional alkene ammoxidation catalyst is used, such as Bi/Mo/O, the performance is much worse (yield 4.5% at 450 °C).

An alternative mechanism might include the following steps: (i) transformation of butadiene to maleic anhydride (catalyzed by the V/P/O elements included in the catalyst); (ii) hydrolysis of the anhydride to the diacid (owing to the presence of water in the reaction environment, and catalyzed by the presence of P); (iii) transformation of the diacid to the diamide by reaction with ammonia and (iv) (oxy)dehydrogenation of the diamide to the dinitrile.

The best performance is obtained with very dilute hydrocarbon streams. This might be due to the fact that an excessive concentration of butadiene might lead to a high catalyst surface coverage and over-reduction, with a consequent modification of the adsorption–activation properties. The high selectivity achieved at high temperature indicates that the two cyan groups are very stable.

The catalyst based on V/W/Cr/P/O-TiO_2 also gives good performance with *n*-butene and *n*-butane reactants (Table 20.4).

The catalyst showed comparable selectivities from the various C_4 hydrocarbons. In the case of *n*-butane the yield was lower owing to the lower hydrocarbon conversion, but the selectivity remained close to 50% (46%). In this case, vanadium played the additional role of oxydehydrogenation of butane to butenes. The reactivity of butene was lower than that of butadiene (both were higher than that of *n*-butane) which indicates that the mechanism requires the oxy-dehydrogenation of butene to yield butadiene, which is the reactive intermediate that undergoes ammoxidation.

A recent patent by DSM [121] claims catalysts very similar to those reported by Furuoya [120]. Indeed, the catalyst preparation is the same as the one described by Furuoya [120b]. The only difference concerns the addition of silica in relevant amounts, in the form of silica sol. This is claimed to give better reproducibility in performance for catalysts prepared in the powder form (by spray-drying). The best performance reported is 95% conversion and 58% yield to nitriles (fumaronitrile + maleonitrile + succinonitrile, the saturated dinitrile). The authors report the use of a low O_2 concentration, with a feed composition of 0.50% butadiene, 2.50% ammonia and 4.4% oxygen (the balance being nitrogen).

Table 20.4 Ammoxidation of C_4 hydrocarbons with the V/W/Cr/P/O-TiO_2 system [120].

Feed composition C_4/NH_3/air	T (°C)	τ (s)	C_4 conversion (%)	Yield to MN + FN (%)
n-butene: 0.7/2.6/96.7	531	1.2	96.5	56.8
n-butane: 0.6/3.7/95.7	598	1.2	57.0	26.2

Table 20.5 Summary of performance of catalysts reported in [122] for butadiene ammoxidation.

Catalyst	T (°C), τ (s)	Butadiene conversion (%)	Selectivity to FN + MN (%)	Selectivity to crotonitrile (%)	Selectivity to CO_x (%)
V/Mo/O	450, 0.04	20	18	13	18
Sb/Fe/O	450, 0.04	16	9	11	ng
Bi/Mo/P/O	450, 0.04	9	51	11	18

Feed: butadiene/oxygen/ammonia/nitrogen/steam (molar ratios): 2/19/4/74/1.
FN: fumaronitrile; MN: maleonitrile.

Colleuille and coworkers [122] investigated catalysts for butadiene ammoxidation which are similar to those also studied in the ammoxidation of benzene (see below). Table 20.5 summarizes the results reported. The main products were fumaronitrile and maleonitrile, crotonitrile (the unsaturated mononitrile, 1-cyanopropene, with the two trans and cis isomers) and CO_x, with traces of acrylonitrile and furan. The residence time used was very low; in this case the best performance was obtained with a typical propene ammoxidation catalyst, made of Bi/Mo/P/O under conditions of low butadiene conversion.

Very interesting new types of catalyst, based on Re-Sb-O compounds ($SbRe_2O_6$, $SbOReO_4 \cdot 2H_2O$ and $Sb_4Re_2O_{13}$), were shown to be selective in the ammoxidation of isobutylene to methacrylonitrile [123]. The Re-based catalysts were active for methacrylonitrile synthesis with selectivities of 47.9–83.6% at 400 °C, depending on composition. Bulk Sb oxides (Sb_2O_3 and Sb_2O_4) showed no activity. Among these catalysts, $SbRe_2O_6$ was most active and selective (83.6%) for methacrylonitrile formation at 400 °C. No structural change in the bulk and surface of $SbRe_2O_6$ after *i*-C_4H_8 ammoxidation was evidenced by X-ray diffraction, X-ray photoelectron spectroscopy, scanning electron microscopy or confocal laser Raman microspectroscopy. The good performance of $SbRe_2O_6$ may be ascribed to its specific crystal structure composed of alternate octahedral $(Re_2O_6)^{3-}$ and $(SbO)^+$ layers. Pulse reaction studies suggested that adsorbed NH_3 species on the $SbRe_2O_6$ catalyst facilitated the adsorption and subsequent activation of isobutylene.

The same selective behavior in isobutane conversion to methacrylonitrile was reported, although at very low conversion (selectivity to methacrylonitrile at an isobutane conversion of 3 to 4% was about 45 to 50%), [123b].

20.5.2
The Ammoxidation of Cyclohexanol and Cyclohexanone

In one of the most controversial papers published in this field [124], a catalyst made of an alumina-supported V/P/Sb/O is reported to give very good performance in the ammoxidation of cyclohexanol and cyclohexanone to adiponitrile.

The elements claimed are the same as those reported in References [120, 121]. The preparation procedure employed is known to lead to the formation of $VOPO_4$, rather than $(VO)_2P_2O_7$. The presence of Sb, however, may lead to a modification of the structural features. Indeed, the authors claim the presence of vanadyl pyrophosphate as the major phase present in catalysts, with a minor amount of vanadium phosphate. The atomic ratio between the components of the γ-alumina-supported active phase was V/Sb/P 1/1.9/1.18. The reaction conditions were 425 °C (at which the best yields were reported), and a feed ratio of reactant/air/ammonia of 0.6–1.0/4.2/1.5. The following results were claimed under these conditions:

- from cyclohexanol, conversion 78%, selectivity to adiponitrile 75%, selectivity to hexanenitrile 18%. The by-products were CO, CO_2 and cracking products,
- from cyclohexanone, conversion 60%, selectivity to adiponitrile 48%, selectivity to hexanenitrile 30%. The by-products were CO, CO_2 and cracking products.

This performance is outstanding, but it has never been successfully reproduced by other teams active in this research field.

The reaction of cyclohexanol ammoxidation has been investigated by Chen and Lee, with a V_2O_5 catalyst [125]. The feed mixture comprised cyclohexanol/oxygen/ammonia in the ratio 1.2/9/15. A large excess of ammonia was thus used. Cyclohexanone, adiponitrile, adipic acid, benzene and CO_2 formed. The best yield to adiponitrile was 4%, with a conversion of approximately 52% (as inferred from the sum of the yields), at $W/F = 0.45\,g\,s\,cm^{-3}$ and 365 °C. At a higher W/F value, the maximum yield to cyclohexanone was reached (19%). All these products underwent consecutive reaction to benzene and CO_2. In a pulse reactor, the yield to adiponitrile was 6.3%, at 96% reactant conversion. Cyclohexanone was also used in the pulse reactor, but the predominant product was CO_2. The authors proposed that the reaction pathway includes the dehydrogenation of cyclohexanol to cyclohexanone, its oxidative cleavage to adipic acid and subsequent transformation to the dinitrile. The formation of benzene occurs via dehydration to cyclohexene, followed by dehydrogenation. The ammoxidation of cyclohexene exclusively yielded benzene.

The ammoxidation of cyclohexanol or cyclohexanone is also reported in one patent [126], using a cyclohexanone/air/ammonia/H_2O ratio of 1/10/2.5/10 (the presence of added steam is noteworthy), 450 °C, and a contact time of 1 s. Several catalysts were used, as reported in Table 20.6. The products obtained were aniline, phenol and adiponitrile.

The nature of the products formed is rather unusual. The formation of aniline implies a reaction between the ketone and ammonia to yield the cyclohexanoneimine. The latter then rearranges with aromatization, to yield aniline. Aromatization occurs with cyclohexanone, leading to the formation of phenol. Therefore, the formation of the aromatic ring is quicker than the opening of the aliphatic cycle. This is the key point of the reaction involving cyclic reactants: the competition between the parallel reactions of ring opening and aromatization controls the selectivity.

Table 20.6 A summary of catalyst performance reported in [126] for cyclohexanone ammoxidation.

Catalyst	Comment	Yield aniline (%)	Yield phenol (%)	Yield ADN (%)
K/Ni/Co/Fe/Bi/P/Mo/O-silica	Typical catalyst for propene ammoxidation	3.1	11.6	tr
V/W/Mo/O-silica	Typical catalyst for electrophilic oxidation	10.2	19.2	0.6
P/Mo/O-silica	Heteropolycompound	8.9	10.0	–
W/O-silica		5.4	7.8	–
Fe/V/Sb/O-silica	Catalyst for propane and propene ammoxidation	0.1	18.9	0.3
Sb/Mo/O	Catalyst for allylic (amm)oxidation	–	3.4	–

ADN: adiponitrile

20.5.3
The Ammoxidation of Cyclohexane and *n*-Hexane

Some papers and patents report on the ammoxidation of cyclohexane in the gas phase [124, 127–129] or in the liquid phase [130]. In Reference [124], which was discussed in the previous section, the ammoxidation of cyclohexane is reported to give 50% adiponitrile selectivity and 35% hexanenitrile selectivity for a conversion close to 70%, at 425 °C.

Osipova and coworkers [127] used a catalyst based on Ti/Sb mixed oxide, calcined at 750 °C. Under these conditions, titania is in the rutile form, and can host up to 7 mol% Sb_2O_5 in solid solution. Higher Sb content led to the development of also an equimolar Ti/Sb compound ($TiSbO_4$), while in systems with more than 50 mol% Sb_2O_5, the additional formation of α-Sb_2O_4 was found. A catalyst with the composition 70% Sb_2O_5–30%TiO_2 gave the best performance.

Catalytic tests were run in a pulse reactor, at 400 °C, with a cyclohexane/oxygen/ammonia feed composition in mol% of 3/6/4 (the balance being He). The main products obtained were adiponitrile (ADN) and benzene, with an overall selectivity of more than 90% (the cyclohexane conversion is not reported). The rates of benzene and ADN formation are plotted in Figure 20.10 as functions of the Sb_2O_5 content of catalysts. It is shown that the overall formation of benzene considerably decreased on increasing the amount of Sb in catalysts. The formation of ADN decreased, but the decrease was less pronounced than that of

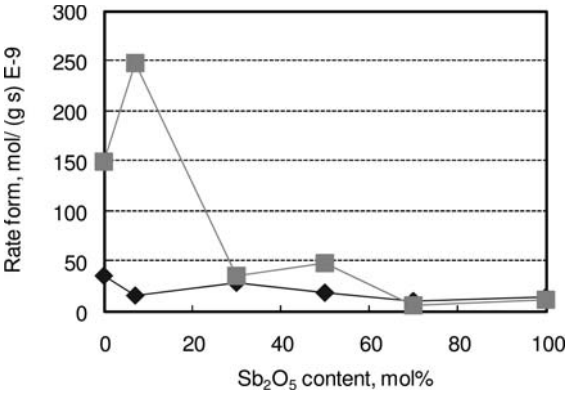

Figure 20.10 Rates of adiponitrile (ADN) (◆) and benzene (■) formation as functions of the content of Sb_2O_5 in catalysts for cyclohexane ammoxidation. Elaborated from [127a].

benzene. Moreover, the formation of benzene was much greater than that of ADN for low Sb contents, while the two rates became comparable for intermediate and large values of Sb content; therefore, the selectivity to ADN increased on increasing the Sb content in catalyst.

Osipova and coworkers [127] also found that under non-steady conditions (those utilized in the pulse reactor), a considerable fraction of ADN remained adsorbed on the catalyst. A rough estimation for the catalyst with 30% Sb_2O_5 led to the conclusion that the overall amount of ADN produced in the single pulse approximately corresponded to 1/3 of the reacted cyclohexane. In particular, ADN bound strongly to the catalyst surface and made heavy (polymeric compounds), at least at 300 °C and in the presence of ammonia. Adsorbed ammonia contributed to the polymerization of ADN at the catalyst surface.

Simon and Germain [128] investigated several catalytic systems and found that cyclohexane conversion is high (70%) even in the absence of catalyst at 460 °C (feed cyclohexane/oxygen/ammonia 1/3.6/1.5) yielding mainly cyclohexene, benzene and CO_x, with minor amounts of other compounds.

The presence of a catalyst led to the formation of C_4 dinitriles (maleonitrile, fumaronitrile, succinonitrile), C_5 dinitriles (glutaronitrile) and C_6 dinitriles (muconitrile, adiponitrile), but the yield of these compounds was very low. In the best case, with a V/Mo/O catalyst (atomic ratio V/Mo 4/1; phase: V_2O_5), the yield to maleonitrile was 1.9% and 0.8% to fumaronitrile, 17% to benzene, 23% to CO_x, with traces of muconitrile, at a conversion of 57% at 460 °C. With the same catalyst, the initial selectivity (extrapolated at zero conversion) to C_4 nitriles was approx 5% (negligible to other nitriles), while the predominant primary products were benzene and carbon oxides. For temperatures lower than 420 °C the predominant product was cyclohexene, while at higher temperatures benzene and CO_x prevailed (Figure 20.11).

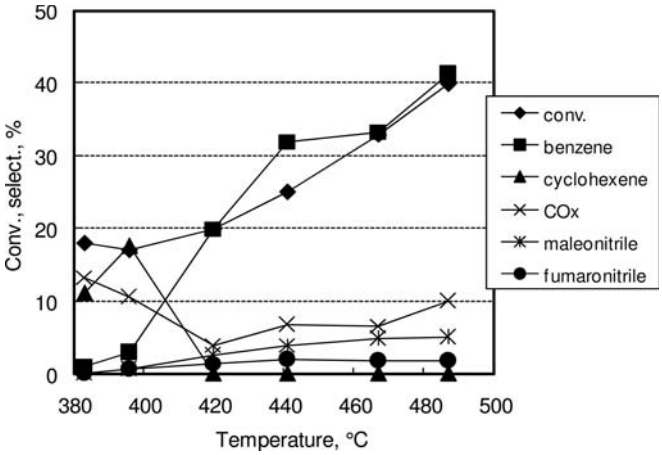

Figure 20.11 Effect of temperature on catalytic performance of V/Mo/O catalyst in cyclohexane ammoxidation [128].

The performance was very similar with a Ti/Mo/O catalyst (atomic ratio Ti/Mo 1.14/1; phases TiO_2 and MoO_3) and with a Bi/Mo/O catalyst (atomic ratio Bi/Mo 0.9/1.) Other catalysts (Sn/Mo/O, Sb/Mo/O, Sn/Sb/Fe/O) were more selective than V/Mo/O to either benzene or CO_x.

The mechanism of reaction included the rapid oxy-dehydrogenation of cyclohexane to cyclohexene and benzene. The latter was then transformed to successive products (see the section on benzene ammoxidation). The opening of the ring may occur either for cyclohexene or for benzene itself.

Table 20.7 summarizes the performance of catalysts described in a patent [129a] which reports the formation of saturated dinitriles (C_4, C_5 and C_6). All catalysts described contain Sb oxide as the main component. In References [129b, 129c], the same catalysts are described as those reported in Reference [129a], but with the addition of a halogenated compound in the feed stream.

The addition of halogenated compounds increased the conversion of cyclohexane, while the selectivities remained substantially unchanged. This indicates the presence of a radical-based mechanism for the activation of cyclohexane. In fact, it is known that the radical chain reaction is enhanced in the presence of halogens, owing to their tendency to give rise to X• species.

The only example reported in the literature concerning *n*-hexane ammoxidation is, once again, Reference [124]. In this paper, for a conversion of approx 12%, a selectivity to adiponitrile close to 40% and to hexanenitrile of approx 30% are reported, at 425 °C and with a molar feed ratio hexane/air/ammonia of 0.6–1.0/4.2/1.5. To our knowledge, these interesting results have never been confirmed.

Table 20.7 A summary of catalytic performance reported in [129a] for cyclohexane ammoxidation.

Catalyst	T (°C), τ (s), feed	Cyclohexane conversion (%)	Selectivity to ADN (%)	Selectivity to GN (%)	Selectivity to SN (%)
Sb/Sn/O 2/1	450, 1.95,[a)]	19.3	23.7	14.2	3.5
"	550, 1.95,[a)]	27.2	14.1	10.6	2.2
"	450, 3.9,[a)]	21.4	22.9	13.7	3.9
Sb/Sn/O 4/1	445, 2.0,[b)]	12.4	18.7	18.3	5.1
Sb/Sn/O 1/2	470, 2.0,[b)]	14.3	14.1	15.7	1.3
Sb/Sn/O 3/1	430, 1.5,[c)]	19.5	21.7	12.4	5.1
Sb/U/O 2/1	435, 2.0,[b)]	21.3	24.3	10.3	4.0
Sb/Ti/O 2/1	440, 2.0,[d)]	24.2	19.7	13.5	5.9

a feed composition (mol%) cyclohexane/oxygen/ammonia 5/10/6.6 (balance N_2).
b feed composition (mol%) cyclohexane/oxygen/ammonia 5/10/10 (balance N_2).
c feed composition (mol%) cyclohexane/oxygen/ammonia 8.4/10/14 (balance N_2).
d feed composition (mol%) cyclohexane/oxygen/ammonia 7/14.7/14 (balance N_2).
GN: glutaronitrile; SN: succinonitrile; ADN: adiponitrile.

20.5.4 The Ammoxidation of Benzene

The ammoxidation of benzene is described in some papers and patents [124, 128, 131, 132]. Whilst benzene has been reported to remain unconverted in the presence of ammonia and oxygen with a V_2O_5 catalyst [124], it was efficiently transformed to nitriles with catalysts based on mixed molybdates [128].

Figure 20.12 reports the performance of the best catalyst, based on V/Mo/O (V/Mo atomic ratio 4/1) at 465 °C, with a feed composition of benzene/oxygen/ammonia/nitrogen 1/4.4/1.6/17.6 (molar ratios). Among the various systems investigated, those giving the best performance were based on V/Mo/O and Ti/Mo/O which gave quite similar performance. Other systems were active but not selective to nitriles (i.e. Sn/Mo/O), or were neither active nor selective (i.e. Bi/Mo/O, Sb/Mo/O, Sn/Sb/Fe/O). The C_6 unsaturated dinitriles (muconontrile) included the three isomers: *cis-cis* dicyanobutadiene, *cis-trans* dicyanobutadiene and *trans-trans* dicyanobutadiene.

The data apparently indicate that the C_6 dinitrile was a primary product, and the overall selectivity at low benzene conversion (less than 7%) was around 20%; the selectivity to muconontriles (the three isomers) rapidly declined when the benzene conversion was increased above 7–8%, and finally became nil. The C_4 unsaturated dinitriles, maleonitrile and fumaronitrile, reached a maximum selectivity of around 20% and 10% respectively, at conversions lower than 10%. It is not clear whether they were primary or secondary products, because of the errors made in yield and selectivity calculation for low benzene conversions (and also errors made in data extrapolation from figures). It is worth noting that the C balance was much lower than 100%. Therefore, it is likely that some products were not detected.

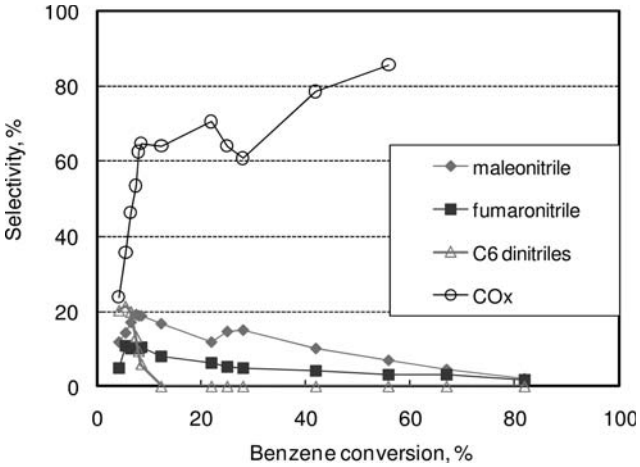

Figure 20.12 Catalytic performance of V/Mo/O catalyst in benzene ammoxidation [128].

The C_4 dinitriles were more stable than the C_6 dinitriles. Although their selectivity decreased with increasing benzene conversion, they were still present at high benzene conversion. CO_x formed mainly by decomposition of the nitriles, but a primary contribution (benzene combustion) cannot be excluded. The authors also mention a slight increase of the selectivity to C_6 dinitriles on increasing the reaction temperature (giving 5% more when raising from 440 to 500 °C).

The authors made a hypothesis about the mechanism. They assumed that benzene undergoes H• abstraction to generate a mono-radical which then reacts with an $\dot{N}H_2$ fragment to generate aniline (however, the latter is not found among the reaction products) and di-radicals. The *ortho* di-radical is transformed to *o*-quinone diimine, the *para* to *p*-quinone diimine. The opening of the ring in the former case generated the C_6 dinitriles, and in the latter case maleonitrile + $2CO_2$. The *meta* di-radical is supposed to give CO_x. In the case of benzene oxidation, the same authors reported that only *p*-quinone and maleic anhydride were found as the products (oxidation of the *para* di-radical), while *o*-quinone and muconic acid (oxidation of the *ortho* di-radical) were not found.

Unger [131] investigated several catalysts for the ammoxidation of benzene (Table 20.8). The report shows that the performance of catalysts was not much different from that reported in Reference [128]. However, in the only example where the conversion was reported, the selectivity to muconononitrile was 17% (for a yield of 7%), at 40% conversion. In this case, therefore, the compound can be saved from consecutive degradation. It is likely that one key factor in saving muconononitrile from consecutive degradation is the reactor configuration and catalytic bed arrangement. This is also clearly demonstrated in Reference [128].

Reference [132] also describes catalysts and methods for the ammoxidation of benzene to muconononitrile. The performance seems to be greatly affected by the type of reactor used and the reactor conditions.

Table 20.8 Summary of results reported in [131] for benzene ammoxidation.

Catalyst	Benzene conversion (%)	T (°C), τ (s), feed comp	Selectivity to muconononitrile (%)	Selectivity to maleic anhydride (%)	Selectivity to maleonitrile (%)
$Bi/Mo/P/O\text{-}BPO_4$	15–20	450, 1.4,[a)]	80[g)]	18	0
Co/Mo/O-SiC	ng	450, 1.4,[a)]	95[g)]	5	0
$Co/Mo/O\text{-}Al_2O_3$	ng	450, 1.5,[b)]	75[g)]	20	0
$V/P/O\text{-}Al_2O_3$	ng	450, 1.5,[c)]	70[g)] (mainly cis-cis)	30	0
$V/P/O\text{-}Al_2O_3$	ng	450, –,[d)]	78[g)]	12	10
$Bi/Mo/P/O\text{-}BPO_4$	ng	450, –,[e)]	99[g)]	0	0
$V/Mo/O\text{-}BPO_4$	40	450, –,[f)]	17[h)]	ng	ng

a Feed: benzene/oxygen/ammonia/nitrogen 30/120/70/200.
b Feed: benzene/oxygen/ammonia/nitrogen 30/60/60/250.
c Feed: benzene/oxygen/ammonia/nitrogen 30/70/70/200.
d Feed: benzene/oxygen/ammonia/nitrogen 15/90/110/425.
e Feed: benzene/oxygen/ammonia/nitrogen 17/60/80/450.
f Feed: benzene/oxygen/ammonia/nitrogen 15/50/50/200.
g the selectivity is expressed only in reference to the condensable (high-boiling) products.
h this is a true selectivity.
ng = not given.

Catalysts based on Fe/Sb/O, Sn/Sb/O and U/Sb/O were fairly active and selective to C_4 unsaturated dinitriles, but non-selective to muconononitrile. Catalysts made of Bi/Mo/P/O, alumina-supported Mo/O and alumina-supported W/O had low activities.

20.5.5 Ammoxidation of C_2 Hydrocarbons

Although industrial interest in the synthesis of acetonitrile directly from C_2 hydrocarbons is currently limited, with acetonitrile being mainly produced as a by-product in acrylonitrile production, there are a number of indications regarding the future need of direct production of acetonitrile by C_2 hydrocarbon (ethane, in particular) ammoxidation. In fact, acetonitrile is used as a solvent and also as an intermediate in the production of many chemicals, ranging from pesticides to perfumes. Production trends for acetonitrile generally follow those of acrylonitrile, but the growth rate for acetonitrile use is higher than that of acrylonitrile. The four

main producers of acetonitrile in the United States are: Ineos, DuPont, J.T. Baker Chemical and Sterling Chemicals.

Acetonitrile can be produced by catalytic ammoxidation of ethane and propane over Nb-Sb mixed oxides supported on alumina, with selectivities to acetonitrile of about 50–55% at alkane conversions of around 30% [133]. In both cases, CO forms in approximately a 1:1 molar ratio with acetonitrile, owing to a parallel reaction from a common intermediate. When feeding *n*-butane, the selectivity to acetonitrile halves. Bondareva and coworkers [134] also studied ethane ammoxidation over similar types of catalyst (V/Mo/Nb/O).

A different type of catalyst is constituted by Co ion-exchanged zeolites and mesoporous materials (MCM-49). Co-ZSM-5 was found to be selective in ethane ammoxidation [135]. A good correlation between the acidity and the catalytic activity was observed. The strength of ammonia bonding to the catalyst appears to have a crucial effect on the activity of Co-ZSM-5. Li and Armor [136] reported that dealuminated zeolite was active for the ammoxidation of ethane to acetonitrile. Pan and coworkers [137] instead studied ion-exchanged Co-Na-MCM-49 and Co-H-MCM-49 materials for the same reaction, reporting that the presence of ammonia in the feed considerably improved the selectivity and total yield of ethylene and acetonitrile.

It should be mentioned finally that acetonitrile could be also prepared by the catalytic ammoxidation of bioethanol over vanadium-alumino-phosphate (VAPO) catalysts [138], which is an alternative starting from biomass-derived raw materials.

20.5.6
Conclusions on the Ammoxidation of Unconventional Molecules

Analysis of the literature published in the field of catalytic, gas-phase ammoxidation of 'unconventional' molecules allows the following conclusions to be drawn:

1. The mechanism of catalytic ammoxidation generally accepted in literature for activated methyl groups (allylic position in olefins, or side position in alkylaromatics) includes the generation of a $-CH_2^{\cdot}$ radical as the first, rate-determining step. The data analyzed in the present report confirm that the generation of a radical species is also the key step for the ammoxidation of other molecules, such as butenes, cyclohexane, cyclohexanol and *n*-hexane. The first step is less evident in the case of butadiene or benzene (and also in the case of ethylene ammoxidation to acetonitrile). From benzene, the formation of the Ph· radical is hypothesized in literature. By analogy, the formation of a –C=CH· species can be postulated from butadiene. Catalysts able to perform this type of attack are a function of the type of molecule used, but in general V oxide is one key component of the catalysts.

2. Once the radical species has been generated, this is followed by π-allyl complex formation in the case of substrates in which the double bond is in the α-position with respect to the radical. Insertion of N into the substrate generally occurs

by insertion of the NH^{2-} species from an M=NH species (isoelectronic with the M=O species); M ions known to generate this moiety are Mo^{6+} and Sb^{5+}. However, it seems that the mechanism may indeed include the insertion of an $NH_2^{\bullet}$ species. The formation of the latter does not require the presence of metal ions able to generate the M=NH species. This may explain why with some molecules investigated, the performance of catalysts that do not include either Mo or Sb is at least comparable (and often better) than that of catalysts including these elements. So, the key-point is the generation of radical species that can either react to generate the nitrile precursors or react to yield the by-products. It is worth mentioning that the same hypothesis of a radical mechanism and reaction with $NH_2^{\bullet}$ has also been made for ammoxidation of alkylaromatics [97c].

3. An alternative mechanism may include first an O-insertion step, followed by the transformation of the oxidized compound into the cyano-containing compound. An example might be the oxidation of butadiene to maleic anhydride followed by hydrolysis to the acid, the formation of the diamide and the oxydehydrogenation to the dinitrile.

4. There are several contradictions in literature concerning the nature of the products obtained. Table 20.9 tries to summarize the literature information, with an indication of the best catalyst reported and of the best yield to nitriles. The main discrepancy concerns the nature of nitriles obtained. In general, it is possible to infer that starting from more reactive C_6 compounds (e.g. cyclohexane), which may also undergo a relevant number of transformations,

Table 20.9 A summary of literature data on 'unconventional' ammoxidation reactions.

Reactant	Major products	Best catalyst	Best yield (%)
Butadiene	maleonitrile + fumaronitrile (crotonitrile)	V/W/Cr/P/O-TiO_2	67
n-Butane	maleonitrile + fumaronitrile (crotonitrile)	V/W/Cr/P/O-TiO_2	26
Cyclohexanol	adiponitrile + hexanenitrile (aniline, phenol)	V/Sb/P/O-Al_2O_3	72[a)]
Cyclohexanone	adiponitrile + hexanenitrile(aniline, phenol)	V/Sb/P/O-Al_2O_3	47[a)]
Cyclohexane	adiponitrile + glutaronitrile + succinonitrile + maleonitrile + fumaronitrile (benzene, cyclohexene)	Ti/Sb/O	10
n-Hexane	adiponitrile + hexanenitrile	V/Sb/P/O-Al_2O_3	8[a)]
Benzene	muconononitrile + maleonitrile + fumaronitrile	V/Mo/O	9

a Reference [124] is very controversial.

the formation of both saturated and unsaturated nitriles (mono and di) with the number of C atoms ranging from 4 to 6 is possible. This is a further indication of the radical nature of the mechanism of the reaction. No author has reported the formation of C_1, C_2 or C_3 nitriles (cyanhydric acid, acetonitrile and acrylonitrile), but we believe that this is highly likely. When the reaction is instead carried out over benzene, the number of nitriles that can form is lower.

20.6
Use of Other Oxidants for Ammoxidation Reactions

There is very limited literature data on the possible use of other oxidants in ammoxidation reactions, because air (O_2) is the preferable source from an economic point of view. However, it may be interesting to cite direct propane ammoxidation with N_2O and O_2 over steam-activated Fe-silicalite zeolite [139]. Yields of acrylonitrile and acetonitrile below 5% were obtained using N_2O or O_2 as the oxidant. Co-feeding N_2O and O_2 boosts the performance of Fe-silicalite compared to the individual oxidants, leading to acetonitrile yields of 14% and acrylonitrile yields of 11% (propane conversions of 40% and product selectivities of 25–30%). The beneficial effect of O_2 on the propane ammoxidation with N_2O contrasts with other N_2O-mediated selective oxidations over iron-containing zeolites (e.g. hydroxylation of benzene and oxidative dehydrogenation of propane), where a small amount of O_2 in the feed dramatically reduces the selectivity to the desired product. It is shown that the productivity of acrylonitrile, and especially acetonitrile, expressed as mol(product) h^{-1} kg(cat)$^{-1}$, is significantly higher over Fe-silicalite than over active propane ammoxidation catalysts reported in the literature.

20.7
Conclusions

Catalytic vapor-phase ammoxidation on mixed oxides is an important class of industrial processes. Propene ammoxidation to acrylonitrile is a well established process for the synthesis of this widely used monomer and intermediate. Over the 40 years since its commercial introduction, the yield to acrylonitrile has nearly doubled to over 80% with the fourth generation of catalysts. This is due to the intensive research effort and understanding of the several factors underpinning catalytic activity. Commercial catalysts contain over 20 elements, the presence of all of which is necessary to optimize the catalytic behavior.

A new current challenge is the shift from propene to propane as feedstock. Since the early 1990s it has been necessary to develop new generations of multi-component catalysts to improve the performance. However, both technical and economic conditions (the price differential between propane and propene) now exist for the commercial introduction of direct propane to acrylonitrile processes. Initial exam-

ples already exist and rapid growth is expected in the near future, both in new plants and in retrofitted current ones.

The ammoxidation of (substituted) alkylaromatics, with or without heteroatoms, is also a well established reaction of interest for the production of fine and specialty chemicals. Although commercial, the number of processes is still limited. However, there is a growing interest in new market areas such as China, and new processes may be expected in the near future.

The ammoxidation process could be also used in the conversion of less-conventional molecules. Various examples are discussed in detail, and it can be remarked that owing to the relatively limited research effort, there is still a relatively large degree of possible improvement. The need for more reproducible results in some cases is also stressed. Nevertheless, this field could offer new interesting commercial opportunities.

Although still limited, there is also some interest in using biomass-derived raw materials (bio-ethanol, glycerine) in ammoxidation processes. These processes could be of value only in the context of valorization of side streams in bio-refinery plants. However, owing to the growing interest in the latter, it may be expected that some opportunities will arise for the ammoxidation of biomass-derived side-products in the near future.

This overview of the catalysts and catalytic processes of vapor-phase ammoxidation has briefly summarized the state of the art and some perspectives in the field, although it was not possible to present a comprehensive review owing to the very large volume of literature and patents that has appeared in recent years. In some cases, as for C_3 and akylaromatic ammoxidation, various reviews are available and these have been referenced.

In conclusion, this overview demonstrates that the ammoxidation field is still a quite attractive area from both fundamental and commercial points of view. It also stresses that the same concepts and catalysts used for more known areas (such as acrylonitrile synthesis) could also be successfully applied in the conversion of less-conventional molecules.

References

1 Garmston, S. (2005) Acrylonitrile and derivatives – World Supply/Demand Report 2005, PCI Acrylonitrile Ltd (http://www.pci-acrylo.com) (accessed Sept. 2007).

2 Association of petrochemical producers in Europe (2007) (http://www.petrochemistry.net) (accessed Sept. 2007).

3 Brazdil, J.F. (2001) Acrylonitrile, in *Kirk-Othmer Encyclopedia of Chemical Technology*, Vol. 1, John Wiley & Sons, Ltd, p. 397.

4 Idol, J.D. and Heights, S. (1959) US Patent 2,904,580, assigned to The Standard Oil Co. US.

5 (a) Barclay, J.L., Bream, J.B., Hadley, D.J. and Stewart, D.G. (1959) Brit. Patent 876,446.
(b) Barclay, J.L., Bream, J.B., Hadley, D.J. and Stewart, D.G. (1964) US Patent 3,152,170, assigned to Distillers Company Ltd, UK.

6 (a) Grasselli, R.K. (2002) *Topics in Catalysis*, **21**, 79.

(b) Grasselli, R.K., Burrington, J.D., Buttrey, D.J., DeSanto, P., Jr, Lugmair, C.G., Volpe, A.F. Jr, and Weingand, T. (2003) *Topics in Catalysis*, **23**, 5.
(c) Grasselli, R.K. (2001) *Topics in Catalysis*, **15**, 93.

7 Giordano, N., Caporali, G. and Ferlazzo, N. (1965, priority 1961) US Patent 3,226,421, assigned to Edison, Italy.

8 Callahan, J.L., Grasselli, R.K., Milberger, E.C. and Strecker, H.A. (1970) *Industrial Engineering Chemical Product: Research and Development*, **9**, 134,

9 Grasselli, R.K. and Burrington, J.D. (1981) *Advanced Synthesis Catalysis*, **30**, 133–63.

10 Grasselli, R.K. (1999) *Handbook of Heterogeneous Catalysis*, Vol. 5 (G. Ertl, H. Knözinger and J. Weitkamp), Wiley-VCH Verlag GmbH, pp. 2302–26.

11 Burrington, J.D., Kartisek, C.T. and Grasselli, R.K. (1984) *Journal of Catalysis*, **87**, 363.

12 (a) Adams, C.R. and Jennings, T.J. (1963) *Journal of Catalysis*, **2**, 63.
(b) Adams, C.R. and Jennings, T.J. (1964) *Journal of Catalysis*, **3**, 549.

13 (a) Keulks, G.W. (1970) *Journal of Catalysis*, **19**, 232.
(b) Brazdil, J.F., Suresh, D.D. and Grasselli, R.K. (1980) *Journal of Catalysis*, **66**, 347.

14 Grasselli, R.K. (1985) *Applied Catalysis*, **15**, 127.

15 Chauvel, A. and Lefebvre, G. (1989) *Petrochemical Processes*, Vol. 2, Editions Technip, Paris, pp. 219–32.

16 (a) Centi, G., Cavani, F. and Trifirò, F. (2001) *Selective Oxidation by Heterogeneous Catalysis. Recent Developments*, Series: Fundamental and Applied Catalysis (eds M.V. Twigg and M.S. Spencer), Plenum Publishing Corporation, New York & London.
(b) Arpentinier, P., Cavani, F. and Trifirò, F. (2001) *The Technology of Catalytic Oxidations*, Editions Technip, Paris.

17 *Chemical and Engineering News*, **67** (2), 23 (1989).

18 (a) Brazdil, J.F. (2006) *Topics in Catalysis*, **38**, 289.
(b) Morgan, M. (2002) *Hydrocarbon Engineering*, 14, October.

19 Cmaiglobal Monomers Market report (http://www.cmaiglobal.com/MarketReports/samples/mmr.pdf) (accessed Sept. 2007)

20 (a) Japan Corporate News (http://www.japancorp.net/Article.Asp?Art_ID=14097) (accessed Sept. 2007).
(b) Ramachandran, R. and Dao, L. (1994) Eur. Patent 646,558, assigned to the BOC Group.
(c) Ushikubo, T., Oshima, K., Ihara, T. and Amatsu, H. (1996) US Patent 5,534,650, assigned to Mitsubishi Chemical Co.

21 Andersson, A., Hansen, S. and Wickman, A. (2001) *Topics in Catalysis*, **15**, 103.

22 (a) Centi, G. and Perathoner, S. (1998) *CHEMTECH*, **28**, 13.
(b) Centi, G., Perathoner, S. and Trifiro, F. (1997) *Applied Catalysis A: General*, **157**, 143.
(c) Centi, G., Trifirò, F. and Grasselli, R. K. (1990) *La Chimica and L'Industria (Milan)*, **72**, 617.
(d) Catani, R., Centi, G., Trifirò, F. and Grasselli, R.K. (1992) *Industrial and Engineering Chemistry Research*, **31**, 107.
(e) Centi, G., Grasselli, R.K. and Trifirò, F. (1992) *Catalysis Today*, **13**, 661.
(f) Centi, G. and Mazzoli, P. (1996) *Catalysis Today*, **28**, 351.
(g) Centi, G., Mazzoli, P. and Perathoner, S. (1997) *Applied Catalysis*, **A**, 165–273.
(h) Cavani, F. and Trifirò, F. (2003) *Basic Principles in Applied Catalysis* (ed. M. Baerns), Series in Chemical Physics, 75, Springer, Berlin, p. 21.
(i) Ballarini, N., Cavani, F. and Trifirò, F. (2005), The Valorization of Alkanes by Oxidation: Still a Bridge between Scientific Challenges and Industrial Needs, Proceedings of the DGMK-Conference Oxidation and Functionalization: Classical and alternative routes and sources, Milan, 12–14 October 2005, ISBN 3-936418-39-X, 19–33.

23 Sokolovskii, V.D., Davydov, A.A. and Ovsitser, O.Yu. (1995) *Catalysis Reviews–Science and Engineering*, **37**, 425.

24 Moro-Oka, Y. and Ueda, W. (1994) *Catalysis*, **11**, 223.

25 Prada, S.R. and Grange, P. (2003) *Belg. Oil, Gas*, **29** (3), 145, Hamburg, Germany.

26 (a) Guttmann, A.T., Grasselli, R.K. and Brazdil, J.F. (1988) US Patent 4,746,641, assigned to Standard Oil Company, OH, USA.
(b) Nilsson, J., Landa-Cánovas, A.R., Hansen, S. and Andersson, A. (1999) *Journal of Catalysis*, **186**, 442.
27 (a) Ushikubo, T., Oshima, K., Kayo, A., Umezawa, T., Kiyono, K. and Sawaki, I. (1992) European Patent 529,853, assigned to Mitsubishi Chemical Corporation, Tokyo, Japan.
(b) Komada, S., Hinago, H., Kaneta, M. and Watanabe, M. (1998) European Patent 895,809, assigned to Asahi Kasei Kogyo Kabushiki Kaisha, Osaka, Japan.
28 (a) Ueda, W. and Oshihara, K. (2000) *Applied Catalysis A: General*, **200**, 135.
(b) Oshihara, K., Hisano, T. and Ueda, W. (2001) *Topics in Catalysis*, **15**, 153.
(c) Botella, P., Lopez Nieto, J.M. and Solsona, B. (2002) *Catalysis Letters*, **78**, 383.
29 Hamada, K. and Komada, S. (1999) US Patent 5,907,052, assigned to Asahi Kasei Kogyo Kabushiki Kaisha.
30 (a) Guttman, A.T., Grasselli, R.K. and Brazdil, J.F. (1988) US Patent 4,746,641, assigned to the Standard Oil Company, OH, USA.
(b) Lynch, C.S., Glaeser, L.C., Brazdil, J.F. and Toft, M.A. (1992) US Patent 5,094,989, assigned to the Standard Oil Company, OH, USA.
31 (a) Guttmann, A.T., Grasselli, R.K. and Brazdil, J.F. (1988) US Patent 4,788,317.
(b) Bartek, J.P. and Guttmann, A.T. (1989) US Patent 4,797,381.
(c) Glaeser, L.C., Brazdil, J.F. and Toft, M.A. (1989) US Patent 4,837,191.
(d) Seely, M.J., Friedrich, M.S. and Suresh, D.D. (1990) US Patent 4,978,764.
(e) Suresh, D.D., Seeley, M.J., Nappier, J.R. and Friedrich, M.S. (1992) US Patent 5,171,876.
(f) Brazdil, J.F., Glaeser, L.C. and Toft, M.A. (1992) US Patent 5,079,207.
(g) Bartek, J.P., Ebner, A.M. and Brazdil, J.R. (1993) US Patent 5,198,580.
(h) Brazdil, J.F. and Cavalcanti, F.A.P. (1996) US Patent 5,576,469.
(i) Brazdil, J.F. and Cavalcanti, F.A.P. (1996) US Patent 5,498,588. All patents assigned to Standard Oil Company (Cleveland, OH, US).
32 (a) Florea, M., Prada Silvy, R. and Grange, P. (2003) *Catalysis Letters*, **87**, 63.
(b) Prada Silvy, R., Florea, M., Blangenois, N. and Grange, P. (2003) *American Institute of Chemical Engineers*, **49**, 2228.
(c) Florea, M., Prada Silvy, R. and Grange, P. (2005) *Applied Catalysis A: General*, **286**, 1.
(d) Olea, M., Florea, M., Sack, I., Prada Silvy, R., Gaigneaux, E.M., Marin, G.B. and Grange, P. (2005) *Journal of Catalysis*, **232**, 152.
33 (a) Hatano, M. and Kayo, A. (1988) European Patent 318,295.
(b) Ushikubo, T., Oshima, K., Umezawa, T. and Kiyono, K. (1992) European Patent 512,846.
(c) Ushikubo, T., Oshima, K., Kayo, A., Umezawa, T., Kiyono, K. and Sawaki, I. (1992) European Patent 529,853. All patents assigned to Mitsubishi Chemical Co.
34 (a) Albonetti, S., Blanchard, G., Burattin, P., Cavani, F. and Trifirò, F. (1996) European Patent 723,934.
(b) Albonetti, S., Blanchard, G., Burattin, P., Cavani, F. and Trifirò, F. (1997) European Patent 932,662.
(c) Blanchard, G., Burattin, P., Cavani, F., Masetti, S. and Trifirò, F. (1997) WO Patent 97/23,287 A1.
(d) Blanchard, G. and Ferre, G. (1994) US Patent 5,336,804. All patents assigned to Rhodia.
35 Mimura, Y., Ohyachi, K. and Matsuura, I. (1999) *Science and Technology in Catalysis 1998*, Kodansha, Tokyo, p. 69.
36 Bowker, M., Kerwin, P. and Eichhorn, H.-D. (1997) UK Patent 2,302,291, assigned to BASF.
37 (a) Albonetti, S., Blanchard, G., Burattin, P., Cassidy, T.J., Masetti, S. and Trifirò, F. (1997) *Catalysis Letters*, **45**, 119.
(b) Albonetti, S., Blanchard, G., Burattin, P., Cavani, F., Masetti, S. and Trifirò, F. (1998) *Catalysis Today*, **42**, 283.
38 Shaikh, S., Bethke, K. and Mamedov, E. (2006) *Topics in Catalysis*, **38**, 241.
39 (a) Ushikubo, T., Nakamura, H., Koyasu, Y. and Wajki, S. (1995) US Patent 5,380,933 to Mitsubishi Chemical Corp.

(b) Lin, M. and Linsen, M.W. (2001) US Patent 6,180,825, to Rohm and Haas Company (USA).
(c) Ushikubo, T., Koyasu, Y., Nakamura, H. and Wajiki, S. (1998) JP 10,045,664, to Mitsubishi Chemical Corp.

40 (a) Oshihara, K., Hisano, T. and Ueda, W. (2001) *Topics in Catalysis*, **15**, 153.
(b) Ueda, W., Chen, N.F. and Oshihara, K. (1999) *Chemical Communications*, 517.
(c) Oshihara, K., Hisano, T., Kayashima, Y. and Ueda, W. (2001) *Studies in Surface Science and Catalysis*, **136**, 93.
(d) Oshihara, K., Nakamura, Y., Sakuma, M. and Ueda, W. (2001) *Catalysis Today*, **71**, 153.
(e) Ueda, W., Oshihara, K., Vitry, D., Hisano, T. and Kayashima, Y. (2002) *Catalysis Surveys from Japan*, **6**, 33.
(f) Vitry, D., Morikawa, Y., Dubois, J.-L. and Ueda, W. (2003) *Topics in Catalysis*, **23**, 47.
(g) Vitry, D., Morikawa, Y., Dubois, J.-L. and Ueda, W. (2003) *Applied Catalysis A: General*, **251**, 411.
(h) Katou, T., Vitry, D. and Ueda, W. (2003) *Chemistry Letters*, **32**, 1028.

41 (a) Vitry, D., Dubois, J.-L. and Ueda, W. (2004) *Journal of Molecular Catalysis A–Chemical*, **220**, 67.
(b) Watanabe, N. and Ueda, W. (2006) *Industrial & Engineering Chemistry Research*, **45**, 607.
(c) Merzouki, M., Taouk, B., Monceaux, L., Bordes, E. and Courtine, P. (1992) *Studies in Surface Science and Catalysis*, **72**, 165.
(d) Roussel, M., Bouchard, M., Bordes-Richard, E., Karim, K. and Al-Sayari, S. (2005) *Catalysis Today*, **99**, 77.

42 Ushikubo, T., Oshima, K., Kayou, A. and Hatano, M. (1997) *Studies in Surface Science and Catalysis*, **112**, 473.

43 (a) Holmberg, J., Grasselli, R.K. and Andersson, A. (2004) *Applied Catalysis A: General*, **270**, 121.
(b) Holmberg, J., Haeggblad, R. and Andersson, A. (2006) *Journal of Catalysis*, **243**, 350.

44 Aouine, M., Dubois, J.L. and Millet, J.M.M. (2001) *Chemical Communications*, **13**, 1180.

45 (a) DeSanto, P., Jr, Buttrey, D.J., Grasselli, R.K., Lugmair, C.G. and Volpe, A.F., Jr, Toby, B.H. and Vogt, T. (2003) *Topics in Catalysis*, **23**, 23.
(b) DeSanto, P., Jr, Buttrey, D.J., Grasselli, R.K., Lugmair, C.G. and Volpe, A.F., Jr, Toby, B.H. and Vogt, T. (2004) *Zeitschrift fuer Kristallographie*, **219**, 152.
(c) Grasselli, R.K., Buttrey, D.J., DeSanto, P., Jr, Burrington, J.D., Lugmair, C.G., Volpe, A.F., Jr, and Weingan, T. (2004) *Catalysis Today*, **91–2**, 251.

46 Millet, J.M.M., Roussel, H., Pigamo, A., Dubois, J.L. and Jumas, J.C. (2002) *Applied Catalysis A: General*, **1–2**, 23277.

47 Berry, F.J., Brett, M.E. and Patterson, W.R. (1983) *Journal of the Chemical Society–Dalton Transactions*, 9–13.

48 Teller, R.G., Antonio, M.R., Brazdil, J.F., Grasselli, R.K. (1986) *Journal of Solid State Chemistry*, **64**, 249.

49 Birchall, T. and Sleight, A.E. (1976) *Inorganic Chemistry*, **15**, 868.

50 Centi, G. and Trifirò, F. (1986) *Catalysis Reviews–Science and Engineering*, **28**, 165.

51 Hansen, S., Ståhl, K., Nilsson, R. and Andersson, A. (1993) *Journal of Solid State Chemistry*, **102**, 340.

52 Berry, F.J., Brett, M.E. and Patterson, W.R. (1982) *Journal of the Chemical Society D–Chemical Communications*, 695.

53 Landa-Canovas, A., Nilsson, J., Hansen, S., Ståhl, K. and Andersson, A. (1995) *Journal of Solid State Chemistry*, **116**, 369.

54 (a) Centi, G. and Perathoner, S. (1995) *Studies in Surface Science and Catalysis*, **91**, 59.
(b) Centi, G. and Mazzoli, P. (1996) *Catalysis Today*, **28**, 351.

55 (a) Berry, F.J., Brett, M.E., Marbrow, R.A. and Patterson, W.R. (1984) *Journal of the Chemical Society–Dalton Transactions Trans*, 985.
(b) Berry, F.J., Holden, J.G. and Loretto, M.H. (1987) *Journal of the Chemical Society–Faraday Transactions*, **I**, 83–615.
(c) Berry, F.J., Holden, J.G. and Loretto, M.H. (1986) *Solid State Communications*, **59**, 397.

56 (a) Allen, M.D. and Bowker, M. (1995) *Catalysis Letters*, **33**, 269.
(b) Bowker, M., Bricknell, C.R. and Kerwin, P. (1996) *Applied Catalysis A: General*, **136**, 205.

(c) Poulston, S., Price, N.J., Weeks, C., Allen, M.A., Parlett, P., Steinberg, M. and Bowker, M. (1998) *Journal of Catalysis*, **178**, 658.
57 Magagula, Z. and van Steen, E. (1999) *Catalysis Today*, **49**, 155.
58 Nilsson, R., Lindblad, T. and Andersson, A. (1994) *Journal of Catalysis*, **148**, 501.
59 (a) Ballarini, N., Cavani, F., Cimini, M., Trifirò, F., Millet, J.M.M., Cornaro, U. and Catani, R. (2006) *Journal of Catalysis*, **241**, 255.
(b) Cimini, M., Millet, J.M.M. and Cavani, F. (2004) *Journal of Solid State Chemistry*, **177**, 1045.
(c) Cimini, M., Millet, J.M.M., Ballarini, N., Cavani, F., Ciardelli, C. and Ferrari, C. (2004) *Catalysis Today*, **91**, 259.
60 (a) Roussel, H., Mehlomakulu, B., Belhadj, F., van Steen, E. and Millet, J.M.M. (2002) *Journal of Catalysis*, **205**, 97.
(b) Nguyen, D.L., Ben Taarit, Y. and Millet, J.M.M. (2003) *Catalysis Letters*, **90**, 65.
(c) Millet, J.M.M., Marcu, J.C. and Herrmann, J.M. (2005) *Journal of Molecular Catalysis A–Chemical*, **226**, 111.
61 Xiong, G., Sullivan, V.S., Stair, P.C., Zajac, G.W., Trail, S.S., Kaduk, J.A., Golab, J.T. and Brazdil, J.F. (2005) *Journal of Catalysis*, **230**, 317.
62 Ballarini, N., Cavani, F., Cimini, M., Trifirò, F., Catani, R., Cornaro, U. and Ghisletti, D. (2003) *Applied Catalysis A: General*, **251**, 49.
63 Cody, C.A., DiCarlo, L. and Darlington, R.K. (1979) *Inorganic Chemistry*, **18** (6), 1572.
64 Sala, F. and Trifirò, F. (1974) *Journal of Catalysis*, **34**, 68.
65 Carbucicchio, M., Centi, G. and Trifirò, F. (1985) *Journal of Catalysis*, **91**, 85.
66 Grasselli, R.K. (1999) *Catalysis Today*, **49**, 141.
67 Osipova, Z.G. and Sokolovskii, V.D. (1979) *Kinetics Catalysis*, **20**, 910.
68 Sasaki, Y., Sutsumi, H. and Miyaki, K. (1992) US Patent 5,139,988, assigned to Nitto Chem. Ind. Co.
69 Kahney, R.H. and McMinn, T.D. (1975) US Patent 4,000,178, assigned to Monsanto Co.
70 Albonetti, S., Blanchard, G., Burattin, P., Masetti, S. and Trifirò, F. (1997) *Studies in Surface Science and Catalysis*, **110**, 403.
71 Soria, M.A., Delsarte, S., Gaigneaux, E.M. and Ruiz, P. (2007) *Applied Catalysis A: General*, **325**, 296.
72 Ballarini, N., Cavani, F., Giunchi, C., Masetti, S., Trifirò, F., Ghisletti, D., Cornaro, U. and Catani, R. (2001) *Topics in Catalysis*, **15**, 111.
73 (a) Ballarini, N., Catani, R., Cavani, F., Cornaro, U., Ghisletti, D., Millini, R., Stocchi, B. and Trifirò, F. (2001) *Studies in Surface Science and Catalysis*, **136**, 135.
(b) Ballarini, N., Cavani, F., Ghisletti, D., Catani, R. and Cornaro, U. (2003) *Catalysis Today*, **78**, 237.
74 Catani, R. and Centi, G. (1991) *Journal of the Chemical Society D–Chemical Communications*, 1081.
75 Matsuura, I., Oda, H. and Oshida, K. (1993) *Catalysis Today*, **16**, 547.
76 (a) Guerrero-Perez, M.O., Fierro, J.L.G. and Bañares, M.A. (2006) *Topics in Catalysis*, **41**, 43.
(b) Guerrero-Perez, M.O., Fierro, J.L.G. and Bañares, M.A. (2003) *Catalysis Today*, **78**, 387.
(c) Guerrero-Perez, M.O., Fierro, J.L.G. and Bañares, M.A. (2003) *Physical Chemistry Chemical Physics*, **5**, 4032.
77 (a) Guerrero-Perez, M.O., Fierro, J.L.G. and Banares, M.A. (2006) *Catalysis Today*, **118**, 366.
(b) Guerrero-Perez, M.O., Martinez-Huerta, M.V., Fierro, J.L.G. and Banares, M.A. (2006) *Applied Catalysis A: General*, **298**, 1.
78 Nilsson, J., Landa-Canovas, A.R., Hansen, S. and Andersson, A. (1996) *Journal of Catalysis*, **160**, 244.
79 Wickman, A., Wallenberg, L.R. and Andersson, A. (2000) *Journal of Catalysis*, **194**, 153.
80 Callahan, J.L. and Grasselli, R.K. (1963) *American Institute of Chemical Engineers*, **9**, 755.
81 Guerrero-Perez, M.O. and Banares, M.A. (2007) *Journal of Physical Chemistry C*, **111**, 1315.
82 (a) Cavalli, P., Cavani, F., Manenti, I. and Trifiro, F. (1987) *Catalysis Today*, **1**, 245.

(b) Sanati, M. and Andersson, A. (1990) *Journal of Molecular Catalysis*, **59**, 233.
(c) Andersson, A., Andersson, S.L.T., Centi, G., Grasselli, R.K., Sanati, M. and Trifiro, F. (1994) *Applied Catalysis A: General*, 43.

83 (a) Narayana, K.V., Venugopal, A., Rama Rao, K.S., Venkat Rao, V., Masthan, S. Khaja and Kanta Rao, P. (1997) *Applied Catalysis A: General*, **150**, 269.
(b) Narayana, K.V., Venugopal, A., Rama Rao, K.S., Khaja Masthan, S., Venkat Rao, V. and Kanta Rao, P. (1997) *Applied Catalysis A: General*, **167**, 11.
(c) Kanta Rao, P., Rama Rao, K.S., Masthan, S.K., Narayana, K.V., Rajiah, T. and Rao, V.V. (1997) *Applied Catalysis*, **A**, 163–23.

84 Makedonski, L., Nikolov, V., Nikolov, N. and Blaskov, U. (1999) *Reaction Kinetics and Catalysis Letters*, **66**, 237.

85 Martin, A., Wolf, G.-U., Steinicke, U. and Luecke, B. (1998) *Journal of the Chemical Soceity–Faraday Transactions*, **94**, 2227.

86 Otamiri, J.C., Andersson, S.L.T. and Andersson, A. (1990) *Applied Catalysis*, **A**, 65–159.

87 Cavani, F., Trifiro, F., Jiru, P., Habersberger, K. and Tvaruzkova, Z. (1988) *Zeolites*, **8**, 12.

88 (a) Beschmann, K., Fuchs, S. and Hahn, T. (1998) *Chemie Ingenieur Technik*, **70**, 1436.
(b) Beschmann, K. and Riekert, L. (1993) *Chemie Ingenieur Technik*, **70**, 1251.

89 Kim, S.H. and Chon, H. (1992) *Applied Catalysis A: General*, **85**, 47.

90 Fu, J., Ferino, I., Monaci, R., Rombi, E., Salinas, V. and Forni, L. (1997) *Applied Catalysis A: General*, **154**, 241.

91 Srilakshmi, C., Lingaiah, N., Nagaraju, P., Sai Prasad, P.S., Narayana, K.V., Martin, A. and Luecke, B. (2006) *Applied Catalysis A: General*, **309**, 247.

92 (a) Luecke, B., Narayana, K.V., Martin, A. and Jaehnisch, K. (2004) *Advanced Synthesis & Catalysis*, **346**, 1407.
(b) Lucke, B. and Martin, A. (2001) *Fine Chemicals through Heterogeneous Catalysis* (eds R.A. Sheldon and H. Van Bekkum), Wiley-VCH Verlag GmbH, Weinheim, Germany, p. 527.
(c) Martin, A. and Lucke, B. (2000) *Catalysis Today*, **57**, 61.
(d) Lucke, B. and Martin, A. (1999) Recent Advances in the Oxidation and Ammoxidation of Aromatics, *Proceedings of the DGMK-Conference: The future role of aromatics in refining and petrochemistry, Erlangen, 13–15 October 1999*, p. 139.
(e) Martin, A. and Luecke, B. (1996) *Catalysis Today*, **32**, 279.

93 (a) Narayana, K.V., Khaja Masthan, S., Venkat Rao, V., Raju, David, B. and Kanta Rao, P. (2002) *Catalysis Communications*, **3**, 173.
(b) Narayana, K.V., Khaja Masthan, S., Venkat Rao, V., Raju, David, B. and Kanta Rao, P. (2002) *Catalysis Letters*, **48**, 27.

94 Centi, G. (1996) *Applied Catalysis A: General*, **147**, 267.

95 Rizaev, R.G., Mamedov, E.A., Vislovskii, V.P. and Sheinin, V.E. (1992) *Applied Catalysis A: General*, **83**, 103.

96 (a) Murakami, J.Y., Niwa, M., Hattori, T., Osawa, S., Igushi, S. and Ando, H. (1977) *Journal of Catalysis*, **49**, 83.
(b) Niwa, M., Ando, H. and Murakami, H. (1977) *Journal of Catalysis*, **49**, 92.

97 (a) Cavalli, P., Cavani, F., Manenti, F. and Trifiro, F. (1987) *Industrial and Engineering Chemistry Research*, **26**, 639.
(b) Centi, G., Marchi, F. and Perathoner, S. (1997) *Applied Catalysis A: General*, **149**, 225.
(c) Cavalli, P., Cavani, F., Manenti, I., Trifiro, F. and El-Sawi, M. (1987) *Industrial and Engineering Chemistry Research*, **26**, 804.
(d) Busca, G., Cavani, F. and Trifiro, F. (1987) *Journal of Catalysis*, **106**, 471.

98 Otamiri, J. and Andersson, A. (1988) *Catalysis Today*, **3**, 211–23.

99 Zhang, Y., Martin, A., Berndt, H., Luecke, B. and Meisel, M. (1997) *Journal of Molecular Catalysis A–Chemical*, **118**, 205.

100 (a) Rizayev, R.G., Mamedov, E.A., Vislovskii, V.P. and Sheimin, V.E. (1992) *Applied Catalysis A: General*, **83**, 103.
(b) Sze, M.C. and Gelbein, A.P. (1979) *Hydrocarbon Processing*, **55**, 103.

101 (a) Grasselli, R.K., Burrington, J.D., Suresh, D.D., Friedrich, M.S. and Hazle, M.A. (1981) *Journal of Catalysis*, **68**, 109.
(b) Grasselli, R.K., Burrington, J.D., Suresh, D.D., Friedrich, M.S. and Hazle, M.A. (1981) *Journal of Catalysis*, **41**, 317.

102 (a) Martin, A. and Luecke, B. (1996) *Catalysis Today*, **32**, 279.
(b) Martin, A., Luecke, B., Wolf, G.-U. and Meisel, M. (1994) *Chemie Ingenieur Technik*, **66** 948.

103 (a) Martin, A., Luecke, B., Wolf, G.-U. and Meisel, M. (1995) *Catalysis Letters* **33**, 349.
(b) Dropka, N., Kalevaru, V.N., Martin, A., Linke, D. and Luecke, B. (2006) *Journal of Catalysis*, 240–8.

104 Shapovalov, A.A. and Kh.Sembaev, D. (1996) *Izvestiya Ministerstva Nauki-Akademii Nauk Respubliki Kazakhstan, Seriya Khimicheskaya*, **2**, 89.

105 Narayana, K.V., Martin, A., Bentrup, U., Luecke, B. and Sans, J. (2004) *Applied Catalysis A: General*, **270**, 57.

106 Chuck, R. (2005) *Applied Catalysis A: General*, **280**, 75.

107 Brazdil, J.F. and Bartek, J.P., Jr (1998) US Patent 5,854,172, assigned to the Standard Oil Company, US.

108 (a) Narayana, K.V., Venugopal, A., Rama Rao, K.S., Khaja Masthan, S., Venkat Rao, V. and Kanta Rao, R. (1998) *Applied Catalysis A: General*, **167**, 11.
(b) Narayana, K.V., Venugopal, A., Rama Rao, K.S., Khaja Masthan, S., Venkat Rao, V. and Kanta Rao, R. (1997) *Applied Catalysis A: General*, **150**, 269.

109 Kanta Rao, P., Rama Rao, K.S., Khaja Masthan, S., Narayana, K.V., Rajiah, T. and Venkat Rao, V. (1997) *Applied Catalysis A: General*, **163**, 123.

110 Narayana, K.V., David Raju, B., Khaja Masthan, S., Venkat Rao, V., Kanta Rao, P. and Martin, A. (2004) *Journal of Molecular Catalysis A–Chemical*, **223**, 321.

111 (a) Reddy, K.M., Lingaiah, N., Rao, K.N., Rahman, N., Prasad, P.S.S. and Suryanarayana, I. (2005) *Applied Catalysis A: General*, **296**, 108.
(b) Srilakshmi, C., Lingaiah, N., Suryanarayana, I., Prasad, P.S.S., Ramesh, K., Anderson, B.G. and Niemantsverdriet, J.W. (2005) *Applied Catalysis A: General*, **296**, 54.
(c) Rao, K.N., Reddy, K.M., Lingaiah, N., Suryanarayana, I. and Prasad, P.S.S. (2006) *Applied Catalysis A: General*, **300**, 139.

112 Srilakshmi, C., Ramesh, K., Nagaraju, P., Lingaiah, N. and Prasad, P.S.S. (2006) *Catalysis Letters*, **106**, 115.

113 Srilakshmi, C., Lingaiah, N., Nagaraju, P., Prasad, P.S.S., Narayana, K.V., Martin, A. and Luecke, B. (2006) *Applied Catalysis A: General*, **309**, 247.

114 Bondareva, V.M., Andrushkevich, T.V., Paukshtis, E.A., Paukshtis, N.A., Budneva, A.A. and Parmon, V.N. (2007) *Journal of Molecular Catalysis A–Chemical*, **269**, 240.

115 Hong, C. and Li, Y. (2006) *Chinese Journal of Chemistry Engineering*, **14**, 670.

116 Ni, K., Chen, F., Fang, W. and Zhong, Y. (2007) *Ziran Kexueban*, **30**, 75.

117 (a) Huber, S., Petzoldt, J., Rosowski, F. and Hibst, H. (2007) Ger. Offen., DE 2005-102005033826.
(b) Huber, S., Hugo, R., Dahmen, K., Preiss, T. and Hibst, H. (2007) Hartmut PCT Int. Appl., WO 2007009921. Both patents assigned to Basf Aktiengesellschaft, Germany.

118 Sze, M.C. and Gelbein, A.P. (1976) *Hydrocarbon Processing*, **55**, 103.

119 Contractor, R.M. and Sleight, A.W. (1987) *Catalysis Today*, **1**, 587.

120 (a) Furuoya, I. (1999) *Studies in Surface Science and Catalysis*, **121**, 343.
(b) Furuoya, I. and Kitazawa, Y. (1984) US Patent 4,436,671, assigned to Takeda Chem Ind.

121 Peters, A. and Schevelier, P.A. (2006) WO Patent 2006/053786 A1, assigned to DSM IP Assets.

122 (a) Colleuille, Y. and Perron, R. (1972) UK Patent 1,394,207, assigned to Rhone-Poulenc.
(b) Colleuille, Y. and Perron, R. (1971) French Patent 2,151,704.

123 (a) Liu, H., Imoto, H., Shido, T., Iwasawa, Y. (2001) *Journal of Catalysis*, **200**, 69.

(b) Liu, H., Shido, T. and Iwasawa, Y. (2000) *Chemical Communications*, 1881.

124 Reddy, B.M. and Manohar, B. (1993) *Journal of the Chemical Society D–Chemical Communications*, 330.

125 Chen, W.-S. and Lee, M.-D. (1992) *Reaction Kinetics and Catalysis Letters*, **47**, 187.

126 Grasselli, R.K. and Suresh, D.D. (1981) US Patent 4,271,091, assigned to Standard Oil Co.

127 (a) Ovsitser, O.Yu., Osipova, Z.G. and Sokolovskii, V.D. (1989) *Reaction Kinetics and Catalysis Letters*, **38**, 91. (b) Ovsitser, O.Yu., Davydov, A.A., Osipova, Z.G. and Sokolovskii, V.D. (1989) *Reaction Kinetics and Catalysis Letters*, **38**, 125. (c) Ovsitser, O.Yu., Davydov, A.A., Osipova, Z.G. and Sokolovskii, V.D. (1989) *Reaction Kinetics and Catalysis Letters*, **40**, 307.

128 Simon, G. and Germain, J.-E. (1980) *Bulletin de la Societe Chimique de France*, **3**–4, 149.

129 (a) Burnett, C., Dewing, J. and Jubb, A.H. (1971) US Patent 3,627,817. (b) Burnett, C. and Dewing, J. (1974) US Patent 3,818,066. (c) Burnett, C. and Dewing, J. (1968) UK Patent 1,195,037, All patents assigned to ICI.

130 Mee, A. (1973) UK Patent 1,455,830, assigned to ICI.

131 Unger, M.O. (1971) US Patent 3,579,559, assigned to du Pont de Nemours.

132 Colleuille, Y. and Perron, R. (1971) UK Patent 1,338,952, assigned to Rhone Poulenc.

133 (a) Centi, G. and Perathoner, S. (1998) *Studies in Surface Science and Catalysis*, **119** (Natural Gas Conversion V), 569. (b) Catani, R. and Centi, G. (1991) *Journal of the Chemical Society D–Chemical Communications*, 1081.

134 Bondareva, V.M., Andrushkevich, T.V., Aleshina, G.I., Maksimovskaya, R.I., Plyasova, L.M., Dovlitova, L.S. and Burgina, E.B. (2006) *Reaction Kinetics and Catalysis Letters*, **88**, 183.

135 Boubaker, H. Ben, Fessi, S., Ghorbel, A., Marceau, E. and Che, M. (2004) *Studies in Surface Science and Catalysis*, **154C** (Recent Advances in the Science and Technology of Zeolites and Related Materials), 2655.

136 Li, Y. and Armor, J.N. (1999) *Applied Catalysis A: General*, **188**, 211.

137 Pan, W., Jia, M., Lian, H., Shang, Y., Wu, T. and Zhang, W. (2005) *Reaction Kinetics and Catalysis Letters*, **86**, 67.

138 Kulkarni, S.J., Rao, R.R., Subrahmanyam, M., Navis, S.F., Rao, P.K. and Rao, A.V.R. (2003) Indian Patent IN 191083 and IN 191169.

139 Perez-Ramirez, J., Blangenois, N. and Ruiz, P. (2005) *Catalysis Letters*, **104**, 163.

21
Base Catalysis with Metal Oxides

Khalaf AlGhamdi, Justin S. J. Hargreaves, and S. David Jackson

21.1
Introduction

With increasing recognition of the complimentarity of their behavior to that of acid catalysts, the study of base catalysts is becoming more widespread. Whilst, for example, both acid and base catalysts of appropriate strength can be applied to analogous processes, there are pronounced differences in the product distribution, which is a consequence of the fundamentally different pathways involved. An illustrative example of this behavior is the alkylaromatic side-chain alkylation reaction, where it is observed that in the presence of a basic catalyst the side chain of the alkyl group is alkylated rather than the aromatic ring, as would be expected with acid catalysis [1]. In a survey of industrial processes published in 1999, Tanabe and Holderich [2] identified 10 major base-catalyzed processes as compared to 103 acid-catalyzed processes and 14 solid acid–base-catalyzed processes. In this chapter we concentrate our attention on heterogeneous base catalysts, and the examples and discussion given are intended to be illustrative of the general field rather than providing an extensive bibliography. Additional reviews detailing this topic can be found elsewhere, for example References [3–8]. Within this chapter, we exclusively direct our attention to oxide, or oxide-based, catalytic systems.

Base catalysts are extremely sensitive to the atmosphere in which they have been stored and generally require some sort of activation procedure, usually heating, prior to application. For materials stored in air, the formation of surface carbonates via reaction with atmospheric carbon dioxide is problematic. Figure 21.1 illustrates the effect of pre-treatment upon base-catalyzed *n*-butene isomerization [9]. It can be seen that activity increases up to a maximum of circa 650 °C.

It is, of course, important to recognize that in general base catalysts exhibit bifunctional behavior and are therefore, strictly, amphoteric. The same general point can also be made concerning acid catalysts, and therefore the distinction between acidic and basic solid catalysts is made on the basis of dominant behavior, although in some cases, for example ZrO_2, there may be no single dominant behavior [10]. An illustrative example of this is the alkaline earth metal oxides, classical base catalysts, where oxide ions behave as bases and the metal cations

Metal Oxide Catalysis. Edited by S. David Jackson and Justin S. J. Hargreaves

ISBN: 978-3-527-31815-5

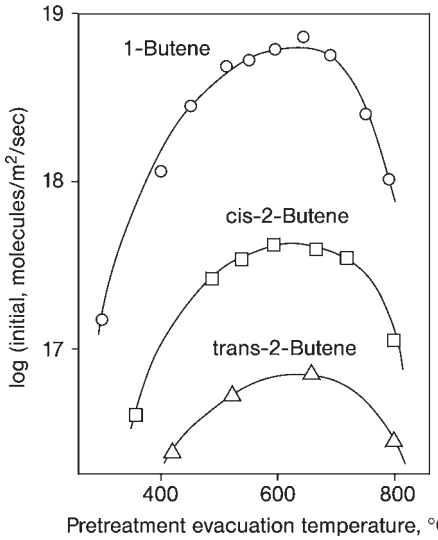

Figure 21.1 The development of base-catalyzed activity at 0 °C over La_2O_3 as a function of pre-treatment temperature. (Reproduced from [9] with permission).

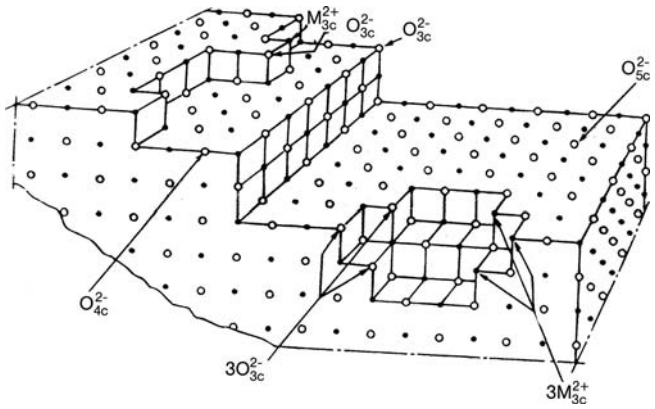

Figure 21.2 A schematic illustrating a variety of different co-ordination sites on the MgO (100) surface. (Reproduced from [12] with permission).

can function as Lewis acids. Given the distribution of different co-ordination sites present, as discussed elsewhere in this volume and shown schematically in Figure 21.2 [11, 12], it can be anticipated that a range of base strengths will be exhibited, and the stronger sites can be successively accessed by increasing severity of pre-treatment. Furthermore, such considerations are indicative that there would be a significant dependence of activity for a base-catalyzed reaction upon catalyst

morphology and/or particle size. This aspect has seldom been emphasized, although a study of structure sensitivity in a base-catalyzed reaction is given by Chizallet and coworkers [13]. In this work, a detailed study of the effect of surface morphology upon the conversion of 2-methylbut-3-yn-2-ol is presented and structure sensitivity is reported. $Mg_{3C}O_{4C}$ and $Mg_{4C}O_{3C}$ ion pairs, combining a strongly basic O^{2-} site with a Lewis acidic site able to stabilize the resultant anion, were shown to be active for the deprotonation of various probe molecules. High surface area forms of MgO have been applied to Michael addition of malonates to enones and a range of Michael addition and Knoevenagel condensation reactions by Kantam and coworkers [14] and Xu and coworkers [15] respectively.

In considering their application, it is, of course, crucial to be able to characterise a base catalyst both in terms of the strength of sites and their number. Unlike acids, the distinction between Brønsted and Lewis sites does not have to be made for bases. Historically, as for acid catalysts, base site strengths have been measured by application of indicator methods. This procedure relies upon the observation of color changes of indicators of known strength. Considering the general Brønsted acidic indicator A—H, and the base catalyst B, when the strength of the base is high enough the following process can occur:

$$A{-}H + B \rightarrow A^- + B{-}H^+$$

A Hammett base scale, H_-, can then be defined:

$$H_- = pK_a + \log([A^-]/[AH])$$

where pK_a refers to the acid strength of the indicator. Consequently, by applying a range of indicators of varying strength, the base site strength characteristics of a solid can be determined. A selection of indicators of different acid strength is given in Table 21.1. Indicators are generally applied as solutions in non-polar solvents such as benzene and isooctane. As for the case of acidity determination, the determination of base strengths by indicator methods is subject to severe limitations. Using the naked eye, color changes only become perceptible when circa 10%

Table 21.1 A selection of indicators used to probe base strength. (Adapted from [3]).

Indicators	Acid form color	Base form color	pK_a
Bromothymol blue	yellow	green	7.2
2,4,6-Trinitroaniline	yellow	reddish-orange	12.2
2,4-Dinitroaniline	yellow	violet	15.0
4-Chloro-2-nitroaniline	yellow	orange	17.2
4-Nitroaniline	yellow	orange	18.4
4-Chloroaniline	colorless	pink	26.5[a)]

a Estimated value.

Table 21.2 Base strength required to remove a proton from a $R_1—CH_2—R_2$ reactant molecule. (Adapted from [16]).

R_1	R_2	pK_a	Base required
CH_3	CH_3	42	Superbase
CH_3	$CH=CH_2$	35.5	Superbase
C_6H_5	H	35	Superbase
C_6H_5	C_6H_5	33	Superbase
CH_3	CN	25	Strong base
CH_3	COOR	24.5	Strong base
CH_3	$COCH_3$	20	Strong base
CH_3	COH	19.7	Strong base
COOR	COOR	11.5	Medium base
CN	CN	11.2	Medium base
CH_3	NO_2	10.6	Medium base
COR	COR	9	Medium base
COH	COH	5	Mild base
NO_2	NO_2	3.6	Mild base

of the adsorbed layer of indicator is adsorbed, giving a limiting accuracy, and hence UV-Visible spectroscopic methods would be preferred. Questions can also be raised concerning equilibration time effects, solvent effects, and color changes induced simply by adsorption. Consequently, although the application of indicator methods is still common in the literature, it is generally backed up by the use of additional methods, many of which also give site strength distributions, as described below.

Despite the fact that the additional methods do not generate H_0 values directly as such, base strength is most generally described and classified in terms of H_0 value. For example, "superbases" are defined as systems which contain sites with $H_0 \geq 26$. Recently, Kelly and King [16] have defined the minimum base strength requirements for different classes of reaction. The scale is reproduced in Table 21.2. It can be seen that the minimum site strength requirement for the base-catalyzed heterolytic activation of propane would have a pK_a of 42. To date, few solid bases have been identified as possessing such high strength, although $Na/NaOH/Al_2O_3$ is reported to be the strongest known superbase applied commercially, with a value of 37 [16]. Such materials would, of course, be extremely susceptible to poisoning.

If indicator methods are used, site distributions can be determined by UV-Visible spectroscopic procedures. Historically, a common way of determining distributions was via titration methods, although these are now less widespread.

Examination of the reaction pathways of probe molecules has also been applied to the characterization of basicity. In this method, a suitable probe molecule is selected with the intention that base sites will convert it uniquely to a given product. The conversion of isopropanol has been widely applied in this context,

for example Reference [17] and references therein, and it is generally considered that base sites will yield acetone via catalyzed dehydrogenation, whereas acid sites would yield propene via catalyzed dehydration. Whilst this type of test is normally used in a qualitative way – that is, the production of acetone demonstrating the presence of base sites – in principle careful determination of the kinetics *may* yield parameters that relate to base site strength (activation energies) and site density (pre-exponential factors.) Within the literature, a whole range of different probe molecules have been applied. Among the most popular has been methanol [18]. A potential pitfall with this method is the possible existence of alternative non-base-catalyzed pathways to yield the signature product, and consideration must also be given to the accessibility of surface sites to the probe molecule. In the former context, attention is drawn to the case of solid superacids, where suggestions of bimolecular and also one-electron oxidation pathways, as opposed to acid-catalyzed unimolecular isomerization pathways, have been raised, throwing into doubt the possibility that some solids are superacidic [19].

Providing the mode of adsorption is known, namely that it is truly an acid–base interaction, thermal methods are useful in quantifying the number and base strength of sites. Perhaps the simplest method is the thermal desorption of a probe molecule. Most commonly CO_2 has been used in this respect and a sample temperature-programmed desorption (TPD) profile is shown in Figure 21.3 [20]. Again, it may be possible to derive information concerning the number and strength of sites from this method, although appropriate caution must be applied. For example, in one study [21], it was shown that the CO_2 desorption temperature

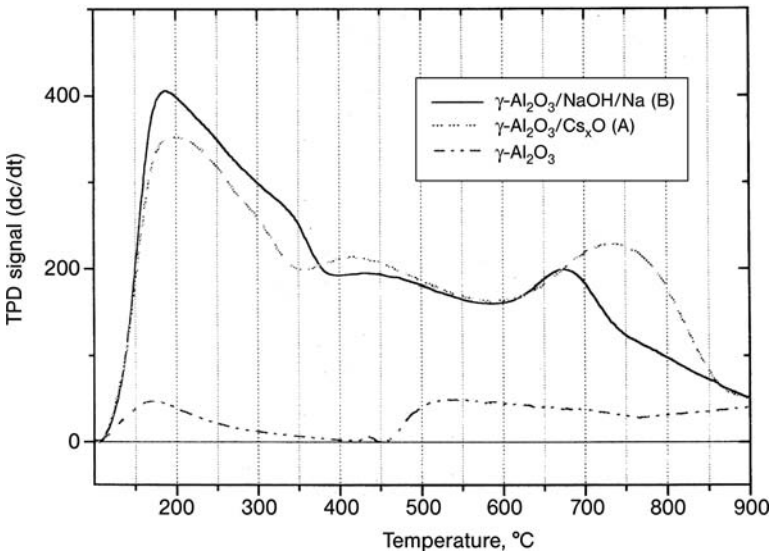

Figure 21.3 CO_2 TPD profiles on selected base catalysts. (Reproduced from [20] with permission).

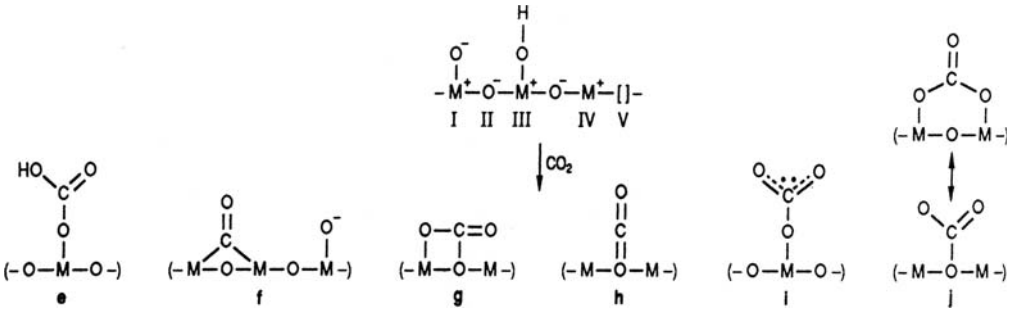

Figure 21.4 Different interactions of CO_2 with a metal oxide surface. (Reproduced from [22] with permission).

matched the decomposition temperature of the bulk metal hydrogencarbonate. The activation energy of desorption can be determined by investigation of the influence of temperature ramp rate on the temperature of the desorption maxima of profiles. In this method it is important that the adsorbate molecules do not modify the surface, and it is prudent to check that they desorb intact (i.e. that the true surface acid-based interaction is being probed and not a temperature-programmed reaction.) Again, in this respect, parallels can be drawn with the literature relating to the determination of acid site strength. Even with a molecule as simple as CO_2, a variety of different interactions could be envisaged as shown in Figure 21.4 [22].

For a selected range of heterogeneous bases, Martin and Duprez [23] have demonstrated that there is generally a good level of agreement between the determination of base strength via the cyclohexanol probe reaction and CO_2 chemisorption.

Although more complex experimentally, the application of microcalorimetry allows the determination of both base site strength and site distribution. In this method, the heat of adsorption of an acidic probe molecule, often CO_2, is measured directly as a function of surface coverage. An example of this type of measurement is given in Figure 21.5, which has been taken from the work of Auroux and Gervasini [22]. Again, it is prudent to verify the nature of the interaction via spectroscopic observation and, as for TPD, attention must be paid to aspects such as sample pre-treatment which can, for example, dramatically alter the degree of surface hydration and therefore the nature of interaction with the probe molecule. In general, the combination of thermal methods and spectroscopy, in particular Fourier-transform infrared FTIR spectroscopy, represents a very powerful tool for the characterization of surface acid-base characteristics.

Spectroscopic methods have been used in isolation for the determination of base characteristics. A number of studies, for example Reference [24], have correlated the O 1s binding energy measured by X-ray photoelectron spectroscopy (XPS) to the determination of base site strength. It has been proposed that decreasing binding energy relates to an increased ability for electron pair donation and hence

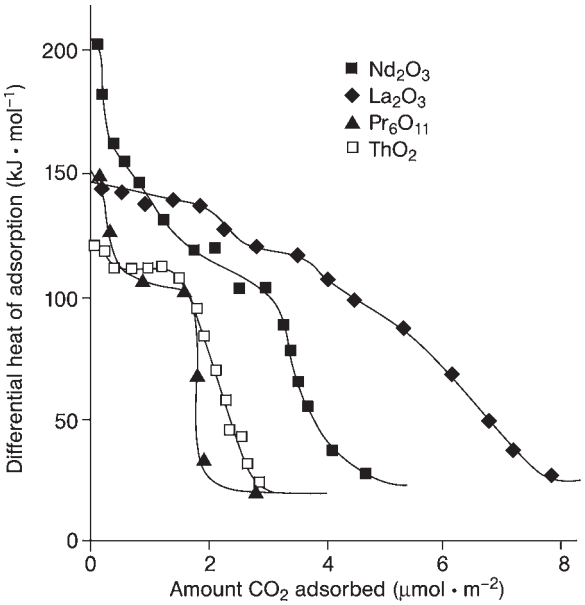

Figure 21.5 Differential heats of adsorption as a function of CO_2 coverage on various rare earth metal oxides. (Reproduced from [22] with permission).

stronger basicity. However, whilst such relationships have been established between materials of similar type, application to materials of different type must be treated with caution. In addition, it is generally the case that catalysts exhibit a range of differing site strengths and therefore spectral deconvolution is required. An example of the application of this type of method to solid "superbase" catalysts prepared from γ-Al_2O_3 is given in work by Tanaka and coworkers [25]. Table 21.3 presents the corresponding binding energies for the materials studied. N 1s XPS spectra of adsorbed pyrrole, a probe molecule, have also been applied to the measurement of basicity with a degree of success [2].

Pyrrole has also been applied as a probe molecule in FTIR specroscopic studies. Upon interaction with a base site, the N—H stretching vibration is found to shift to lower wavenumber and in alkali metal-exchanged zeolites this behavior has been found to correlate with both N 1s XPS data and the negative charge calculated from Sanderson electronegativities [4, 26].

21.2
Catalysts and Catalytic Processes

In this section, we briefly discuss some of the salient points concerning various different types of solid base catalyst. This section is not exhaustive and is designed

Table 21.3 Observed O 1s binding energies of a selection base catalysts. (Adapted from [25]).

Sample	O 1s (eV)
γ-Al_2O_3	531.1
NaOH/γ-Al_2O_3	530.3
Na/NaOH/γ-Al_2O_3	529.5
Na/NaOH/γ-Al_2O_3 exposed to air	531.5
α-Al_2O_3	530.1
NaOH/α-Al_2O_3	530.0
Na/NaOH/α-Al_2O_3	529.9
KOH/γ-Al_2O_3	530.4
K/KOH/γ-Al_2O_3	529.1
RbOH/γ-Al_2O_3	530.6
Rb/RbOH/γ-Al_2O_3	529.7
Rb/RbOH/α-Al_2O_3	530.2

to draw attention to some aspects of various classes of base, rather than providing detailed discussion of individual materials.

21.2.1 Alkali Metal Oxides

Alkali metal oxides have principally been studied in their supported form, most notably as catalyst modifiers. In these cases, the basic properties are often the key to the modifier action yet the potential for a direct base catalysis role is rarely considered. The literature concerning the use of alkali metal oxides as base catalysts is less extensive. The base strength increases down the group with $Li_2O < Na_2O < K_2O < Cs_2O$, hence many of the processes use cesium as the preferred base to optimize the basic strength of the catalyst. Production of supported alkali metal oxides usually involves impregnation with a simple alkali metal salt, typically the nitrate, followed by calcination at high temperatures, for example Reference [27]. It is rare for any characterization to be performed that confirms that it is indeed the oxide that is formed. In the presence of a hydroxylated support surface it is likely that more than a single species is formed, namely a combination of oxide and hydroxide. Indeed, from the study by Canning and coworkers [21], in which the alkali metal hydrogencarbonate was formed from carbon dioxide adsorption, one can postulate that a surface hydroxide was present. However, for this review we will consider that, unless there is specific evidence to the contrary, the material produced after high temperature calcination will be principally oxide and hence will fall within the scope of this discussion. This need for high temperature activation to produce the oxide, and the sensitivity of the oxide to poisons such as water and carbon dioxide, could potentially limit the industrial applicability of these materials. Nevertheless, supported alkali metal oxide catalysts are being actively

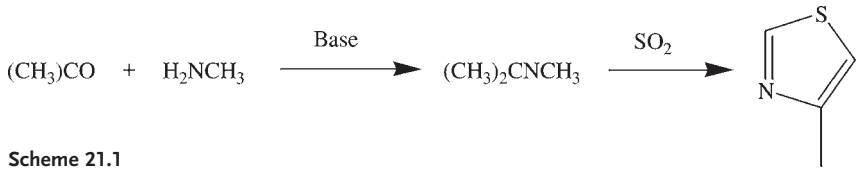

Scheme 21.1

researched by industry, as witnessed by reports in the patent literature. The synthesis of aziridine from *N*-methylethanolamine is reported in BASF [28] and Nippon Shokubai patents [29] using cesium and potassium oxides in conjunction with phosphoric acid supported on silica or glass fabric. Merck have patented a zeolite-supported cesium catalyst [30] for the production of 4-methylthiazole (Scheme 21.1).

4-Methylthiazole is a fungicide and a pharmaceutical intermediate. The catalyst gives a selectivity of >60% at a conversion of >85% but deactivates with time on stream such that half the activity is lost within two weeks.

The Lucite ALPHA process [31] for the production of methyl methacrylate via an aldol reaction between methyl propionate and formaldehyde, also uses a supported cesium oxide catalyst, which requires various additives to minimize catalyst deactivation. An issue that is rarely discussed in the academic literature, possibly because of the nature of catalyst testing in academia, is that of deactivation due to volatilization. Alkali metal oxides may exhibit appreciable volatility under reaction temperatures >400 °C and so there can be a loss of activity over time through volatilization. To overcome this deactivation mechanism, an AMOCO patent [32] describes adding an alkali metal compound into the process gas stream so that the alkali metal compound is deposited on the catalyst during operation to compensate for any loss. It was also noted in the Lucite patent [31] that alkali metal oxides under some reaction conditions (those where water is in the feedstream) might enhance the loss in surface area of the silica support. To counteract such effects the incorporation of modifiers, such as boron, aluminum, magnesium, zirconium or hafnium may be added to the catalysts to retard the rate of surface area decrease. In other studies [33], cesium oxide was thought to sinter under a water-containing feed but could re-distribute when the water was removed.

The use of alkali metal oxide catalysts for aldol condensation reactions has been examined for the production of 2-ethylhexenal from butanal [34]. When coupled to a hydrogenation catalyst the system can produce the plasticizer alcohol 2-ethylhexanol directly. When isobutyraldehyde was used as the feed to a silica-supported sodium oxide catalyst, no products were formed but a significant amount of carbon was deposited on the catalyst and in the reactor (Scheme 21.2).

These results indicated that an aldehyde with a methyl branch α- to the carbonyl group passed over a Na_2O/SiO_2 catalyst was unable to undergo an aldol reaction but did lay down carbon. This has implications for a combined $Pd/Na_2O/SiO_2$ system, as the 2-ethylhexanal that is formed as an intermediate has an ethyl branch α- to the carbonyl group and may lead to product poisoning of the base sites of the catalyst, in a manner similar to that found with isobutyraldehyde over a Na_2O/SiO_2 catalyst.

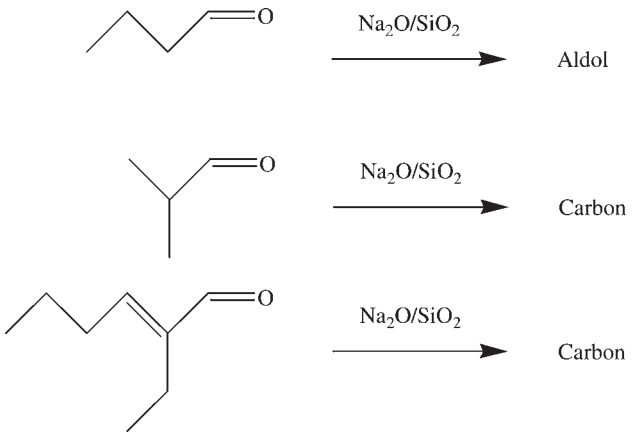

Scheme 21.2

The conversion of acetone to methyl isobutyl ketone (MIBK) also uses a combination of base catalysis with a hydrogenation catalyst [35]. The base component converts the acetone to diacetone alcohol (DAA) via an aldol reaction, which is then dehydrated by the silica to give mesityl oxide (MO). The final step is the hydrogenation of the MO to MIBK over the metal component. The action of the base catalyst in the absence of the hydrogenating metal has been studied [36]. As well as the aldol condensation reactions shown below, the cesium oxide also hydrogenated MO to MIBK, albeit at a low level (Scheme 21.3).

Deuterium studies showed that the hydrogenation was not affected by gas-phase deuterium but used protium left on the basic site from the exchange reaction of acetone and deuterium. Further studies [37] revealed that activation energies calculated for MO and MIBK showed a trend following the notional base strength, with the Na_2O/silica catalyst having the highest activation energy and the Cs_2O/silica catalyst having the lowest activation energy, as shown in Table 21.4.

The variation in the MO values, although following the same trend as MIBK, is, however, within the error limits of the measurement and so this variation is not statistically significant. The variation for the MIBK activation energies is significant. Also, these values are higher than those for MO formation and so can be related to the addition of hydrogen rather than the aldol condensation.

In Figure 21.6 it can be seen that there is a direct relationship between the activation energy and the ionization potential of the alkali metal. An outline mechanism for the hydrogenation of MO is shown in Scheme 21.4.

Table 21.4 Activation energies for MO and MIBK ($kJ\,mol^{-1}$).

	$NaOH/SiO_2$	KOH/SiO_2	$CsOH/SiO_2$
MO	33	25	23
MIBK	47	36	28

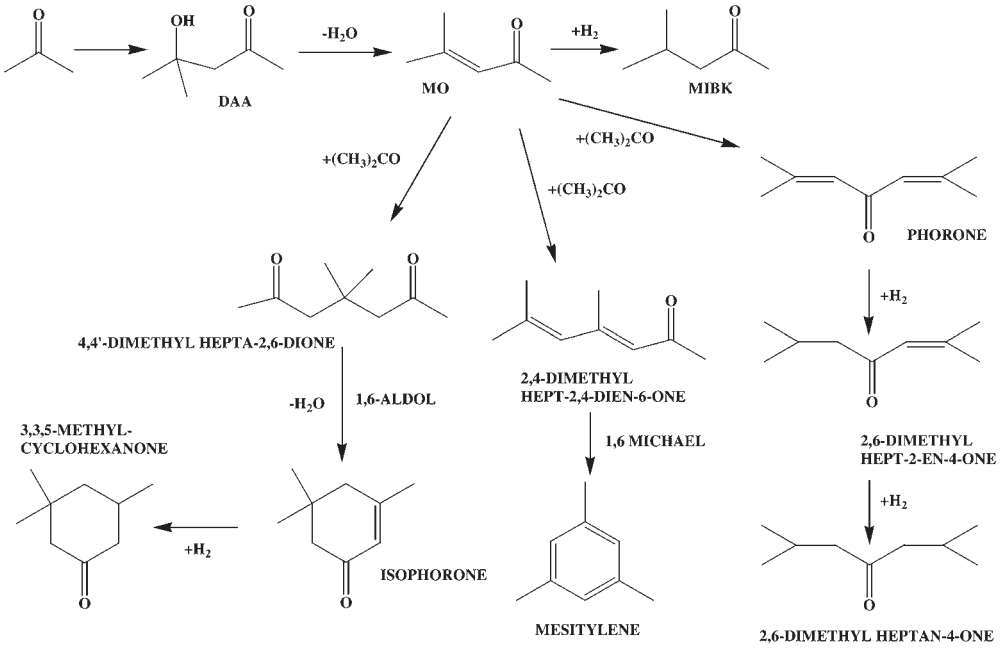

Scheme 21.3

Gorzawski and Holderich [38] examined the generation of a $Cs_xO/\gamma\text{-}Al_2O_3$ superbase from the decomposition of $CsOAc/\gamma\text{-}Al_2O_3$. After heating in vacuum to 700–750 °C the resulting material had an H_0 value ≥37. The catalyst was used for the transesterification of methyl benzoate and dimethyl terephthalate with ethylene glycol. A selectivity of 90% at a conversion of 87% was obtained for the methyl

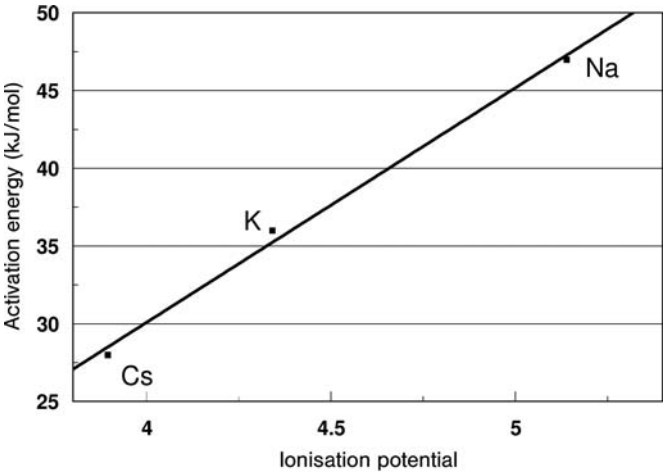

Figure 21.6 The relationship between ionization potential and hydrogenation activation energy.

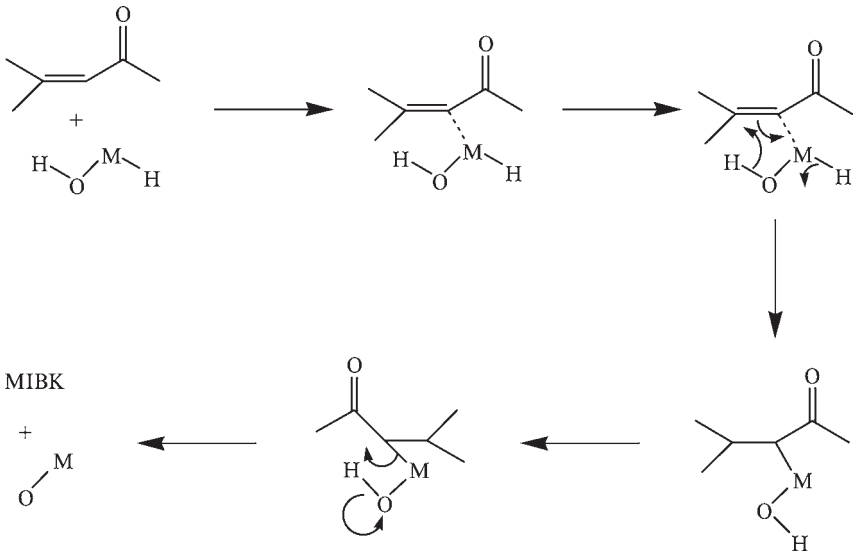

Scheme 21.4

benzoate reaction. In the transesterification of dimethyl terephthalate, a selectivity to bis(2-hydroxyethyl) terephthalate of 88% at a 100% conversion of dimethyl terephthalate was obtained. Once again the catalyst was not characterized to confirm the presence of Cs_2O, although the superbasic nature of the material suggests that the oxide was formed. Note that the support hydroxyl population will have been dramatically reduced and, as has been mentioned before, it is likely that the hydroxyl population will influence the strength and nature of the alkali metal basic site.

21.2.2
Alkaline Earth Metal Oxides

The alkaline earth metal oxides have been extensively studied in terms of their base behavior, for example Reference [39], with perhaps most attention centering upon MgO. In general, base strength increases down the group as anticipated, with the order being BaO > SrO > CaO > MgO, for example, in their surface-area-normalized reaction rates in the aldol condensation of acetone [40]. High-temperature pre-treatment is generally required in order to activate the oxides and they are particularly sensitive to rehydration and recarbonation. Figure 21.7, taken from Hattori's review [4], shows the equilibrium pressure for the decomposition of the carbonates where the increasing severity of necessary pre-treatment is evident, with decomposition equilibria being negligible at ambient temperature. Similar considerations apply to the metal hydroxides. Figure 21.8 shows the evolution of sites of varying strength as a function of the temperature applied in the thermal pre-treatment of $Mg(OH)_2$.

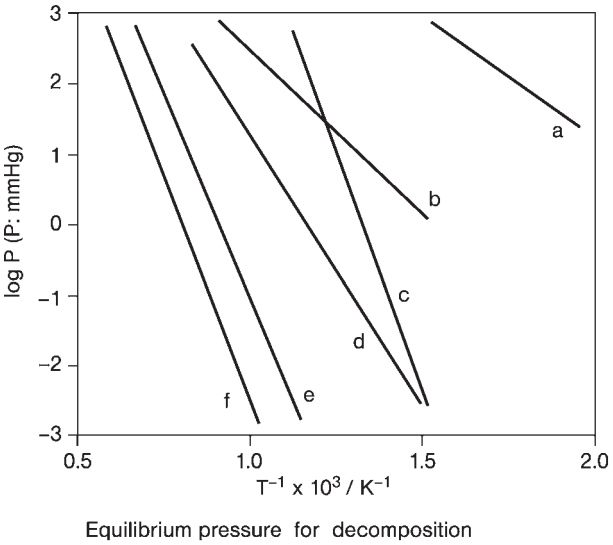

Figure 21.7 The decomposition characteristics of various alkaline earth metal oxide precursors as a function of temperature (a) SrO_2, (b) BaO_2, (c) $MgCO_3$, (d) $CaCO_3$, (e) $SrCO_3$ and (f) $BaCO_3$. (Reproduced from [5] with permission).

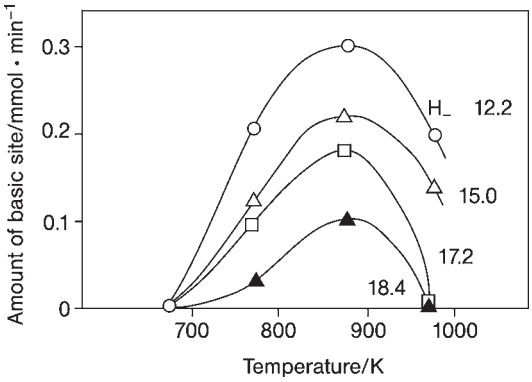

Figure 21.8 The evaluation of MgO base site strength as a function of $Mg(OH)_2$ decomposition temperature. (Reproduced from [5] with permission).

In alkaline earth metal oxides, the (100) surface termination plane, which exposes equal numbers of anions and cations, is prevalent and, as illustrated in Figure 21.2, it can be anticipated that an entire family of different co-ordination sites, of different basicity, can be exhibited. Furthermore, it would be expected that this would lead to a dependence upon crystallite morphology and/or particle size.

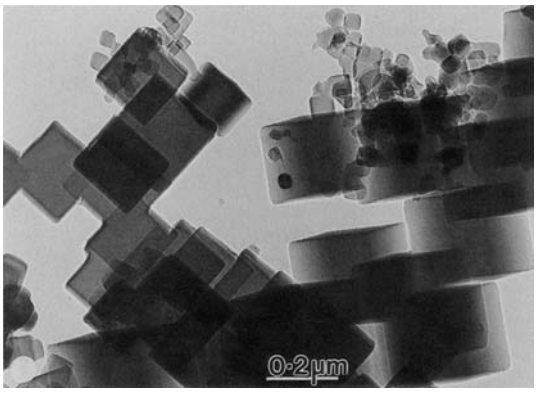

Figure 21.9 TEM of MgO prepared by burning magnesium in air and collecting the ribbon residue. (Reproduced from [41] with permission).

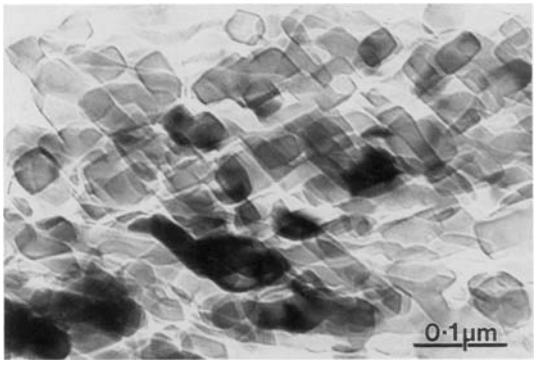

Figure 21.10 TEM of MgO prepared by thermal decomposition of $Mg(OH)_2$ at 800 °C. (Reproduced from [41] with permission).

The morphology of, for example, MgO is known to be a critical function of the preparative procedure adopted [41, 42]. Figures 21.9 to 21.11 are transmission electron microscopy (TEM) images of MgO samples prepared from a number of different routes [41].

Whilst all the samples display (100)-terminated crystallites, decomposition of the basic carbonate yields higher index mean planes generated by the aggregation of (100)-terminated microstructures as shown in Figure 21.12 [43]. The high-resolution TEM (HRTEM) image shown in Figure 21.13 displays terraced structures on a smoke sample recalcined after prolonged storage in air [44]. Further considerations to be made are that decomposition of $Mg(OH)_2$ at intermediate temperatures can lead to the generation of metastable (111)-terminated crystallites as shown in Figure 21.14 [45], which are believed to be stabilized by surface

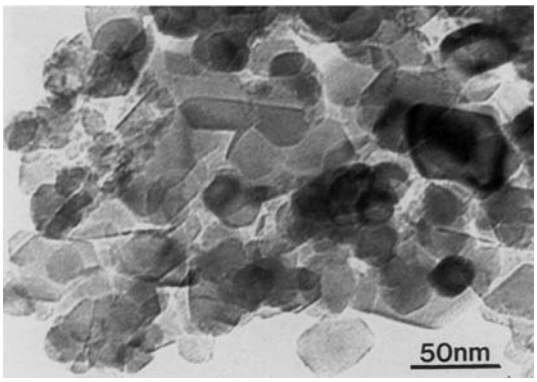

Figure 21.11 TEM of MgO prepared by thermal decomposition of magnesium hydroxycarbonate. (Reproduced from [41] with permission).

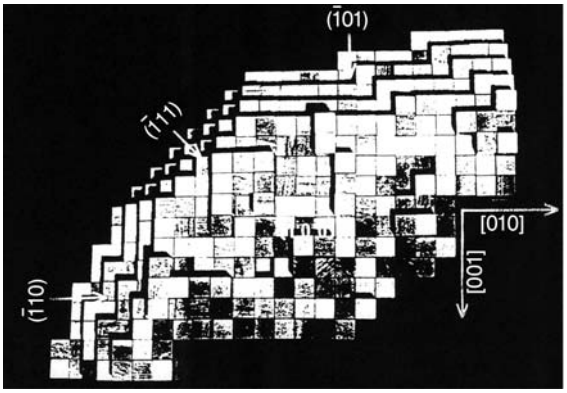

Figure 21.12 High index mean planes exhibited by MgO prepared by the decomposition of magnesium basic carbonate precursor. (Reproduced from [43] with permission).

hydroxyl groups. To our knowledge, the role of morphology and crystallite size on basicity has been little studied in relation to base catalysis and it would be anticipated that low co-ordination sites lead to higher base site strengths. However, caution in making such comparisons is necessary, since some precursors, in the case of MgO for example, can lead to high impurity levels in the resultant samples [41].

With the advent of synthetic procedures leading to the production of highly dispersed metal oxides [46, 47], access to a wide range of surface area is now possible (that is $<3\,m^2g^{-1}$ to $>300\,m^2g^{-1}$ for MgO) An alternative approach to the generation, and stabilization, of high surface area MgO samples is the use of a support, for example $MgO/\gamma\text{-}Al_2O_3$ [48].

Addition of alkali metal ions can also be used to modify base strength/defect structure as required, for example Reference [49], although this is not always

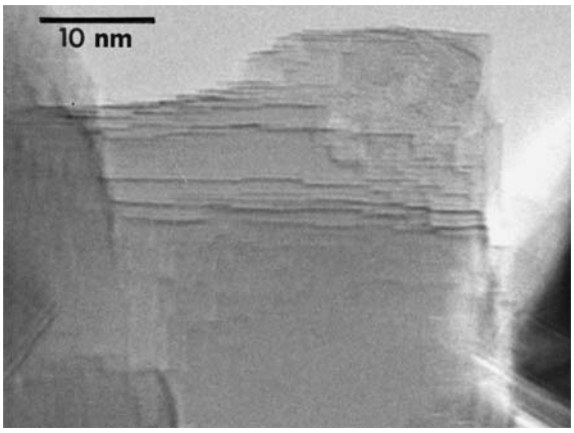

Figure 21.13 TEM of commercial MgO smoke following calcination after prolonged storage in air. (Reproduced from [44] with permission).

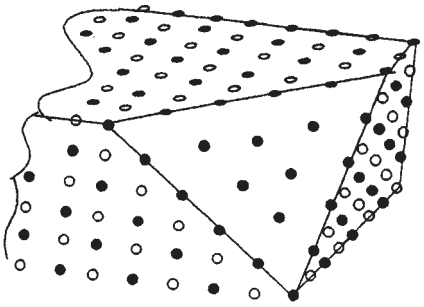

Figure 21.14 MgO (111) polar microfacet. (Reproduced from [45] with permission).

beneficial in terms of catalytic performance [50] and it can lead to substantial loss in surface area. The deposition of alkali metals themselves leads to the generation of "superbasicity", for example References [20, 51]. It has recently been reported that CaO can be made superbasic by appropriate treatment with ammonium carbonate [52].

The reaction of methanol and acetonitrile to form acrylonitrile has been studied over solid base catalysts derived from MgO [53]:

$$CH_3OH + CH_3CN \rightarrow CH_2{=}CHCN + H_2 + H_2O$$

Along with acrylonitrile (ACN), propionitrile (PPN) was also produced. Heating to 400 °C in nitrogen activated the catalysts. High surface area MgO produced the best yields of acrylonitrile and propionitrile but favored the hydrogenated nitrile. The low surface area MgO was considerably less effective at hydrogenation and

gave a high ACN : PPN ratio. The main role of the modifiers (Cr, Mn) was to inhibit hydrogenation of acrylonitrile to propionitrile; however, the Cr-promoted MgO showed slightly higher specific activity than MgO, suggesting a promotional effect.

Studies on the use of SrO as a base catalyst are much less common than those using MgO. However, Mohri and coworkers [54] investigated the use of SrO for the base-catalyzed isomerization of 1-butene. The isomerization of alkenes by base catalysts has been known for many years [55] and usually requires a strong base. Mohri and coworkers found that activity was only detected after heating SrO *in vacuo* to 650 °C and that a temperature treatment of 1000 °C was required to achieve maximum activity. Selective poisoning revealed that both the Sr^{2+} and the O^{2-} ions had discrete roles with the *trans*-2-butene yield associated with the Sr^{2+}, while the *cis*-2-butene yield was associated with the O^{2-}.

21.2.3
Hydrotalcites

Hydrotalcites, or layered double hydroxides (LDH), are a class of material related to the mineral hydrotalcite which has the formula $[Mg_6Al_2(OH)_{16}]CO_3 \cdot 4H_2O$. They are layered double hydroxides with the general formula $M^{2+}_x M^{3+}_{1-x} (OH)_{2x} A_m \cdot zH_2O$ which have the trivalent and divalent cations contained within the octahedral sites of positively charged hydroxide sheets, in a structure akin to that of brucite, $Mg(OH)_2$. The anions, A_m, and water are contained between the layers of sheets and their intercalation and removal can be monitored by the position of the (003) reflection in their powder diffraction patterns [56]. A schematic of the structure is shown in Figure 21.15 [56].

Hydrotalcites are of interest because of their ability to function as base catalysts, for example References [57–61]. In a very topical application, IFP have developed a biofuels process using Al, Zn and Ti mixed oxides [62]. The process is being commercialized by Axens. Figueras and coworkers [63]) have studied Mg-Al

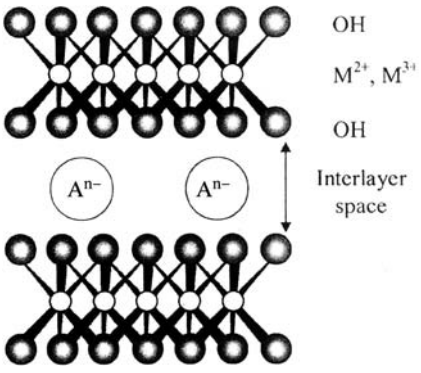

Figure 21.15 Schematic of the hydrotalcite structure. (Reproduced from [56] with permission).

hydrotalcites for the transesterification of methyl acetoacetate. The uncalcined material was as expected inactive; however, calcined and OH-exchanged materials were active with yields of 55 and 77% respectively. The best catalyst reported was a *tert*-BuO-exchanged hydrotalcite which gave 98% yield in a shorter reaction time and could be recycled. This Mg-Al-O^{t}Bu hydrotalcite was also used for a range of other reactions, which suggested a strong base although no measurement was made.

In addition, substitution of variable oxidation state metal ions such as Co^{2+}, Fe^{3+} and Cu^{2+} generates materials with redox catalytic properties, for example References [57, 64]. Hydrotalcites themselves have been used as basic supports for metals, leading to bifunctional catalysts. An example of this is provided in the study of de Jong and coworkers in which palladium–hydrotalcite combinations were reported to be active for single-stage synthesis of MIBK from acetone and hydrogen [65].

Although hydrotalcites are relatively stable (up to circa 500 °C), they are also of potential application as precursors of mixed metal oxide catalysts, for example Reference [66]. Dehydration–rehydration equilibria account for the switching between hydrotalcites and mixed/supported metal oxides, which is sometimes termed the "*memory effect*" [67–69]. Recent advances have seen attempts to prepare highly dispersed LDH systems, such as those dispersed within mesoporous carbon [70]. Owing to widespread interest in their application, hydrotalcite catalysts have been the subject of a number of reviews, for example References [71–75]. Other layered-based systems have also attracted attention for application in catalysis, for example Reference [76].

21.2.4 Rare Earth Oxides

Although comparisons are often drawn between the chemistry of alkaline earth and rare earth elements, rare earth oxides appear to have been less well studied than alkaline earth metal oxides as base catalysts. The activity of the rare earth oxides and preparation variables, with particular attention being paid to activity in catalytic pyrolysis, has been reviewed elsewhere [77]. Figure 21.5 shows the differential heats of CO_2 adsorption for some rare earth oxides. Rare earth oxides are generally tested as sesquioxides (M_2O_3), notable exceptions being CeO_2, PrO_2 and Tb_4O_7, and arguably most attention has centred upon La_2O_3. The bifunctional nature of these materials has been described in relation to Ho_2O_3 [78] where acid–base properties have been elucidated with a combination of temperature programmed isopropanol decomposition and FTIR spectroscopic studies of pyridine adsorption. Schuth and coworkers [79] have demonstrated that it is possible to disperse high loadings of yttria on SBA-15, which may open up new possibilities for the application of rare earth oxides. Furthermore, the inclusion of rare earth oxide components in other host matrices, such as yttria-stabilized zirconia, results in materials with catalytic activity, for example References [80, 81], although this has been ascribed to Lewis acidity. A comprehensive study [82]

detailing the influence of preparation route, calcination condition and atmosphere (often neglected) on the basicity and catalytic activity of single rare earth and alkaline earth oxides as well as mixed rare earth–alkaline earth oxides has been published recently.

21.2.5
Basic Zeolites

The occlusion of highly dispersed oxides of alkali metals leads to zeolites possessing pronounced base strengths. Whilst basicity can be generated by exchange of alkali metal ions, for example Reference [83], zeolites containing occluded highly dispersed alkali metal oxide clusters, which possess higher base strength, have attracted most attention, for example References [84–87]. The most widely studied systems have been based upon cesium, where loading is typically achieved by impregnation with cesium acetate followed by thermal decomposition to yield cesium oxide clusters. However, variation of the general procedure can modify the nature of the occluded species. For example, Doskocil and Mankidy [88] have reported that it is possible to obtain occluded sodium metal within NaX by thermal decomposition of loaded sodium azide. Sodium oxide clusters were produced via the oxidation of the sodium clusters or, alternatively, loaded sodium acetate. Zhu and coworkers [89] have reported that dispersion and decomposition of KNO_3 over KL zeolite leads to superbasicity. In addition to alkali metal modification, shape-selective base catalysts generated by the nitridation of zeolites and aluminophosphates have been reported by Ernst and coworkers [90].

21.2.6
Zirconia Superbases

Solid superbases, which have been defined as materials with base strengths, $H_- \geq 26$, represent a highly desirable class of solid materials. This is because they offer the possibility of activation of relatively unreactive species under mild reaction conditions.

Whilst the application of superbases is reasonably well established in organic synthesis, for example References [91–93], the field of heterogeneous catalytic superbases is less well developed. However, it is important to acknowledge that, as stated earlier, $Na/NaOH/Al_2O_3$, which is applied by Sumitomo on an industrial scale for the isomerization of 5-vinyl-2-norbornene to 5-ethylidene-2-norbornene, is reported to have a base strength of $H_- > 37$. Whilst a number of nitrides, have been claimed to be superbasic, for example Reference [94] we restrict our attention to oxide-based examples in this section. In the sections above, mention was made of the possibility of preparing superbases by alkali metal modification of alkaline earth oxides. The possibility of the generation of superbase sites via the controlled thermal decomposition of KNO_3/ZrO_2 has attracted some attention. Wang and coworkers [95, 96] reported that sites with a strength $H_- = 27$ could be generated in such systems providing attention was paid to the loadings and thermal

decomposition temperatures. Samples were prepared by grinding KNO_3 and ZrO_2 together followed by calcination. Furthermore, catalytic activity for the isomerization of *cis*-but-2-ene at 0 °C was reported and the samples were reported to be coke resistant in the high-temperature decomposition of isopropanol. It was argued that vacant sites in the structure of ZrO_2 were crucial to the development of such high base site strengths and this was used to explain the maximum activity observed at 14 wt% KNO_3/ZrO_2. In a study investigating the influence of zirconia and potassium precursor compounds upon the activity of potassium-doped zirconia for gas-phase and liquid-phase reactions by Kemnitz and coworkers [97], demonstrated that potassium leaching occurred for liquid-phase reactions. In addition, their studies indicated that employing hydrous zirconia precursors led to materials with a broader range of base sites with higher strength. Superbase sites have also been reported to be exhibited by KOH-modified ZrO_2 used to support Ru in ammonia decomposition catalysts for hydrogen generation [98]. Related systems, other than those employing ZrO_2, have also been identified as superbases, for example those derived from KNO_3 supported on MgO-modified SBA-15 [99]. Yamaguchi and coworkers [100] have reported that decomposition of carbonate and nitrate precursors, such as $CsCO_3$ and KNO_3, over alumina and zirconia supports can lead to the generation of catalysts with strong basicity. It was reported that both silica and titania were ineffective as supports and the generation of basicity was argued to be a consequence of the liberation of free oxygen species on thermal decomposition of the carbonate and nitrate salts (yielding CO_2 and O^{2-} and NO_2 and O^- respectively).

21.3 Outlook

The study of metal oxide-catalyzed base catalysis is becoming more widespread, although it still lags far behind acid catalysis. In this chapter, we have outlined some of the general considerations to be made in the characterization of base catalysts, have briefly described some of the common classes of base oxide materials applied as catalysts and have described a selection of the more commercially relevant reactions. Table 21.5, which is not intended to be exhaustive, summarizes some of the other base-catalyzed reactions that have been reported in the more recent literature. Attention has been restricted to oxides, although other basic materials such as oxynitrides, for example References [124, 125], may offer advantages, for example in terms of the ability to tune base site strength through control of the level of nitrogen incorporation. A survey of the literature demonstrates the vast scope of base-catalyzed reactions that have been studied with metal oxide catalysts. However, it is clear that in many cases fundamental studies, such as the elucidation of structure–activity relationships, are lacking. Ideally, the development of such understanding will lead to knowledge facilitating the tailored design of effective catalysts.

Table 21.5 Some examples of base-catalyzed reactions.

Reaction	Catalyst(s)	Ref.
Transesterification	CaO superbase	[52]
Transesterification of soybean oil	CaO	[101, 102]
Transesterification of rapeseed oil	Li/CaO, Na/CaO, K/CaO, Li/MgO	[103]
Transesterification of methyl benzoate and dimethyl terephthalate with ethylene glycol	Na/NaOH/γ-Al_2O_3 and Cs_xO/γ-Al_2O_3	[38]
Transesterification of glyceryl tributyrate with methanol	MgAl hydrotalcites	[56]
Transesterification of ethyl acetate with methanol	NaOH, KOH, LiOH supported on mesoporous smectites	[104]
Transesterification of soybean oil	ZrO_2, ZnO or γ-Al_2O_3 supported alkaline earth oxides	[105]
Synthesis of phytosterol esters	La_2O_3	[106]
Self-condensation of propanol	MgO	[50]
Dimerization of ethanol	MgO, CaO, BaO, Na/Al_2O_3, K/Al_2O_3, Cs/Al_2O_3, Mg/SiO_2	[107]
Isopropanol conversion to MIBK	CuMI(MII)O_x	[108]
Cyclohexanol conversion to cyclohexanone/cyclohexene	CaO/TiO_2, SrO/TiO_2, BaO/TiO_2	[109]
Cyanoethylation of methanol	BaO, MgO, KOH/Al_2O_3, KF/Al_2O_3	[110]
Cyanoethylation of alcohols	MgO, CaO, SrO, BaO, $Mg(OH)_2$, $Ca(OH)_2$, $Sr(OH)_2 \cdot 8H_2O$, $Ba(OH)_2 \cdot 8H_2O$, La_2O_3, KOH/Al_2O_3, KF/Al_2O_3	[111]
Synthesis of dimethyl carbonate from propylene carbonate and methanol	MgO, CaO	[112]
Synthesis of ethylene carbonate from urea and ethylene glycol	CaO, La_2O_3, MgO, ZnO, ZrO_2 and Al_2O_3	[113]
Synthesis of propylene carbonate from urea and propane-1,2-diol	CaO, MgO, ZnO, La_2O_3	[114] review

Table 21.5 Continued

Reaction	Catalyst(s)	Ref.
Synthesis of 1,3-dialkylureas from ethylene carbonate and amine	CaO, MgO, ZnO, ZrO_2, CH_3ONa	[115]
Synthesis of dimethyl carbonate from propylene oxide, carbon dioxide and methanol	NaOH, KOH, LiOH supported on mesoporous smectites	[104]
Propylene–ethylene conversion to pentenes and heptenes	MgO, K/MgO	[116]
Aldol condensation of citral with acetone	MgO, Li/MgO, Na/MgO, K/MgO, Cs/MgO	[117]
Self-condensation of acetone	MgO, Li/MgO, Na/MgO, K/MgO, Cs/MgO	[118]
Knoevenagel condensation of benzaldehyde with ethyl cyanoacetate	NaOH, KOH, LiOH supported on mesoporous smectites	[104]
Methylation of catchecol	Cs_2O/TiO_2, Cs_2O/Al_2O_3, Cs_2O/SiO_2	[119]
Benzaldehyde reduction	MgO, CaO, BaO, SrO	[120]
Ligand-free Heck reaction	Pd/MgO, Pd/CaO, Pd/SrO, Pd/BaO	[121]
Naphthenic acid decarboxylation	MgO	[122]
N-alkylation of aniline	Cs_2O	[123]

References

1 Pines, H. and Stalick, W.M. (1977) *Base-Catalyzed Reaction of Hydrocarbons and Related Compounds*, Academic Press, New York, pp. 240–308.

2 Tanabe, K. and Holderich, W.F. (1999) *Applied Catalysis A: General*, **181**, 399.

3 Tanabe, K. (1970) *Solid Acids and Bases*, Kodansha, Tokyo.

4 Hattori, H. (1995) *Chemical Reviews*, **95**, 537.

5 Hattori, H. (1988) *Materials Chemistry and Physics*, **18**, 533.

6 Ono, Y. and Baba, T. (1997) *Catalysis Today*, **38**, 321.

7 Pines, H. and Schaap, L.A. (1960) *Advanced Synthesis Catalysis*, **12**, 117.

8 Iglesia, E., Batron, D.G., Biscardi, J.A., Gines, M.J.L. and Soled, S.L. (1997) *Catalysis Today*, **38**, 339.

9 Rosynek, M.P., Fox, J.S. and Jensen, J.L. (1981) *Journal of Catalysis*, **71**, 64.

10 Angeles-Aramendia, M., Borav, V., Jiminez, C., Marinas, J.M., Marinas, A., Porras, A. and Urbano, F.J. (1999) *Journal of Catalysis*, **183**, 240.

11 Martra, G., Gianotti, E. and Coluccia, S. (2008) The application of UV-visible-NIR spectroscopy to oxides, in *Metal Oxide*

Catalysis, Vol. **1** (eds S.D. Jackson and J.S.J. Hargreaves), Wiley-VCH Verlag, Weinheim, pp. 51–94.
12 Coluccia, S. and Tench, A.J. (1981) *Proceedings of the 7th International Congress on Catalysis, Tokyo, 1980* (eds K. Tanabe and T. Sieyarna), Kodansha/Elsevier, Tokyo/Amsterdam, p. 1160.
13 Chizallet, C., Bailly, M.L., Costentin, G., Lauron-Pernot, H., Krafft, J.M., Bazin, P., Saussey, J. and Che, M. (2006) *Catalysis Today*, **116**, 196.
14 Kantam, M.L., Ranganathan, K.V.S., Mahendar, K., Chakrapani, L. and Choudary, B.M. (2007) *Tetrahedron Letters*, **48**, 7646.
15 Xu, C.L., Bartley, J.K., Enache, D.I., Knight, D.W. and Hutchings, G.J. (2005) *Synthesis–Stuttgart*, **19**, 3468.
16 King, F. and Kelly, G.J. (2002). *Catalysis Today*, **73**, 75.
17 Hathaway, P.E. and Davis, M.E. (1989) *Journal of Catalysis*, **116**, 263.
18 Tatibouet, J.M. (1997) *Applied Catalysis A: General*, **148**, 213.
19 Brown, A.S.C. and Hargreaves, J.S.J. (1999) *Green Chemistry*, **1**, 17.
20 Gorzawski, H. and Holderich, W.F. (1999) *Journal of Molecular Catalysis A–Chemical*, **144**, 181.
21 Canning, A.S., Jackson, S.D., McLeod, E. and Parker, G.M. (2007) *Science and Technology in Catalysis 2006*, Vol. **172** (eds K. Eguchi, M. Machida and I. Yamanaka), Studies in Surface Science and Catalysis, Elsevier, Tokyo, p. 401.
22 Auroux, A. and Gervasini, A. (1990) *Journal of Physical Chemistry*, **94**, 6371.
23 Martin, D. and Duprez, D. (1997) *Journal of Molecular Catalysis A–Chemical*, **118**, 113.
24 Vinek, H., Noller, H., Ebel, M. and Schwarz, K. (1977) *Journal of the Chemical Society–Faraday Transactions*, **1**, 73–743.
25 Tanaka, K., Yanashima, H., Minobe, M. and Suzukamo, G. (1997) *Applied Surface Science*, **121/122**, 461.
26 Huang, M., Adnot, A. and Kaliaguine, S. (1992) *Journal of Catalysis*, **137**, 322.
27 Shen, J., Tu, M., Hu, C. and Chen, Y. (1998) *Langmuir*, **14**, 2756.
28 Dingerdissen, U., Guenter, L. and Steuerle, U. (1996) DE Patent 19514146, assigned to BASF AG.
29 Tuneki, H., Yano, H., Shimasaki, Y. and Ariyoshi, K. (1993) US Patent 5231189, assigned to Nippon Catalytic Chem Ind.
30 Gortsema, F.P., Sharkey, J.J., Wildman, G.T. and Beshty, B.S. (1992) EP481674, assigned to Merck & Co. Inc.
31 Jackson, S.D., Johnson, D.W., Scott, J.D., Kelly, G.J. and Williams, B.P. (2001) European Patent EP1073517, assigned to INEOS Acrylics UK Ltd.
32 Hagen, G.P. and Montag, R.A. (1991) US Patent 4990662, assigned to Amoco Corp.
33 Tai, J. and Davis, R.J. (2007) *Catalysis Today*, **123**, 42.
34 Hamilton, C.A., Jackson, S.D. and Kelly, G.J. (2004) *Applied Catalysis A: General*, **263**, 63.
35 Canning, A.S., Gamman, J.J., Jackson, S.D. and Urquart, S. (2007) *Catalysis of Organic Reactions* (ed. S.R. Schmidt), Taylor & Francis, Boca Raton, FL, p. 67.
36 Canning, A.S., Jackson, S.D., McLeod, E. and Vass, E.M. (2005) *Applied Catalysis A: General*, **289**, 59.
37 Canning, A.S., Jackson, S.D., McLeod, E. and Parker, G.M. (2007) Studies in surface science and catalysis, in *Science and Technology in Catalysis 2006*, Vol. **172** (eds K. Eguchi, M. Machida and I. Yamanaka), Elsevier, Tokyo, p. 401.
38 Gorzawski, H. and Holderich, W.F. (1999) *Applied Catalysis A: General*, **179**, 131.
39 Wei, T., Wang, M.H., Wei, W., Sun, Y.H. and Zhang, B. (2003) *Fuel Processing Technology*, **83**, 175.
40 Zhang, G., Hattori, H. and Tanabe, K. (1988) *Applied Catalysis A: General*, **36**, 198.
41 Hargreaves, J.S.J., Hutchings, G.J., Joyner, R.W. and Kiely, C.J. (1992) *Journal of Catalysis*, **135**, 576.
42 Burrows, A., Coluccia, S., Hargreaves, J.S.J., Joyner, R.W., Kiely, C.J., Martra, G., Mellor, I.M. and Stockenhuber, M. (2005) *Journal of Catalysis*, **234**, 14.
43 Moodie, A.F. and Warble, C.E. (1971) *Journal of Crystal Growth*, **10**, 26.
44 Martra, G., Cacciatori, T., Marchese, L., Hargreaves, J.S.J., Mellor, I.M., Joyner, R.W. and Coluccia, S. (2001) *Catalysis Today*, **70**, 121.
45 Pantazidis, A., Burrows, A., Kiely, C.J. and Mirodatos, C. (1998) *Journal of Catalysis*, **177**, 325.

46 Knozinger, E., Diwald, O. and Sterrer, M. (2000) *Journal of Molecular Catalysis A–Chemical*, **162**, 83.

47 Utamapanya, S., Klabunde, K.J. and Schlup, J.R. (1991) *Chemistry of Materials*, **3**, 175.

48 Jiang, D., Zhao, B., Xie, Y., Pan, G., Ran, G. and Min, E. (2001) *Applied Catalysis A: General*, **219**, 69.

49 Wang, J.X. and Lunsford, J.H. (1986) *Journal of Physical Chemistry*, **90**, 5883.

50 Ndou, A.S. and Colville, N.J. (2004) *Applied Catalysis A: General*, **275**, 103.

51 Matsuhashi, H., Oikawa, M. and Arata, K. (2000) *Langmuir*, **16**, 8201.

52 Zhu, H., Wu, Z., Chen, Y., Zhang, P., Duan, S. and Liu, X. (2006) *Chinese Journal of Catalysis*, **27**, 391.

53 Jackson, S.D., Kelly, G.J., Hamilton, C.A. and Davies, L. (2003) *Reaction Kinetics and Catalysis Letters*, **79**, 213.

54 Mohri, M., Tanabe, K. and Hattori, H. (1974) *Journal of Catalysis*, **32**, 144.

55 Pines, H. and Haag, W. (1958) *Journal of Organic Chemistry*, **23**, 328.

56 Cantrell, D.G., Gillie, L.J., Lee, A.F. and Wilson, K. (2003) *Applied Catalysis A: General*, **287**, 183.

57 Palmores, A.E., Lopez-Nieto, J.M., Lazaro, F.J., Lopez, A. and Corma, A. (1999) *Applied Catalysis B–Environmental*, **20**, 257.

58 Corma, A., Fornes, V., Martin-Aranda, R.M. and Rey, F. (1998) *Journal of Catalysis*, **134**, 58.

59 Climent, M.J., Corma, A., Iborra, S. and Primo, J. (1995) *Journal of Catalysis*, **151**, 60.

60 Guida, A., Lhouty, M.H., Tichit, D., Figueras, F. and Gineste, P. (1997) *Applied Catalysis A: General*, **164**, 251.

61 Velu, S. and Swamy, C.S. (1996) *Applied Catalysis A: General*, **145**, 225.

62 Hillion, G., Delfort, B., Lendresse, C. and Le Pennec, D. (2005) French Patent 2,869,612, IFP.

63 Choudary, B.M., Lakshmi Kantam, M., Venkat Reddy, C., Aranganathan, S., Lakshmi Santhi, P. and Figueras, F. (2000) *Journal of Molecular Catalysis A–Chemical*, **159**, 411.

64 Lamonier, J.F., Boutoundou, A-B., Gernequin, C., Perez-Zurita, M.J., Siffert, S. and Aboukais, A. (2007) *Catalysis Letters*, **118**, 165.

65 Winter, F., Wothers, M., van Dillen, A.J. and de Jong, K.P. (2006) *Applied Catalysis A: General*, **307**, 231.

66 Liu, Y., Lotero, E., Goodwin, J.G., Jr and Mo, X. (2007) *Applied Catalysis A: General*, **331**, 138.

67 Cavani, F., Trifiro, F. and Vaccari, A. (1991) *Catalysis Today*, **11**, 173.

68 Rey, F., Fornes, V. and Rojo, J.M. (1992) *Journal of the Chemical Society–Faraday Transactions*, **88**, 2233.

69 Palomares, A.E., Prato, J.G. and Corma, A. (2004) *Journal of Catalysis*, **221**, 62.

70 Dubey, A. (2007) *Green Chemistry*, **9**, 424.

71 Kannan, S. (2006) *Catalysis Surveys from Asia*, **10**, 117.

72 Sels, B.F., de Vos, D.E. and Jacobs, P.A. (2001) *Catalysis Reviews–Science and Engineering*, **43**, 443.

73 Evans, D.G. and Duan, X. (2006) *Chemical Communications*, 485.

74 Tichit, D. and Coq, B. (2003) *CATTECH*, **7**, 206.

75 Figueras, F. (2004) *Topics in Catalysis*, **29**, 189.

76 Centi, G. and Perathoner, S. (2008) *Microporous and Mesoporous Materials*, **107**, 3.

77 Hussein, G.A.M. (1996) *Journal of Analytical and Applied Pyrolysis*, **37**, 111.

78 Mekhemer, G.A.H. (2004) *Applied Catalysis A: General*, **275**, 1

79 Schuth, F., Winger, A. and Sauer, J. (2001) *Microporous and Mesoporous Materials*, **44**, 465.

80 Kumar, P., Pandey, R.K., Bodas, M.S. and Dongare, M.K. (2001) *Synlett*, **2**, 206.

81 Pandey, R.K., Deshmukh, A.N. and Kumar, P. (2004) *Synthetic Communications*, **34**, 1117.

82 Ivanova, A.S. (2005) *Kinetics and Catalysis*, **46**, 620.

83 Walton, K.S., Abney, M.B. and LeVan, M.D. (2006) *Microporous and Mesoporous Materials*, **91**, 78.

84 Hathaway, P.E. and Davis, M.E. (1989) *Journal of Catalysis*, **116**, 279.

85 Barthomeuf, D. (1996) *Catalysis Reviews–Science and Engineering*, **38**, 521.

87 Rodriguez, I., Cambon, H., Brunel, D. and Lasperas, M. (1998) *Journal of Molecular Catalysis A–Chemical*, **130**, 195.

88 Doskocil, E.J. and Mankidy, P.J. (2003) *Applied Catalysis A: General*, **252**, 119.

89 Zhu, J.H., Chun, Y., Wang, Y. and Xu, Q.H. (1997) *Material Letters*, **33**, 207

90 Ernst, S., Hartmann, M., Sauerbeck, S. and Bongers, T. (2000) *Applied Catalysis A: General*, **200**, 117.

91 Pibre, G., Chaumant, P., Fleurzard, E. and Cassagnam, P. (2008) *Polymer*, **49**, 234.

92 Ozeryanskii, V.A., Milov, A.A., Minku, V.L. and Pozharskii, A.E. (2006) *Angewandte Chemie–International Edition in English*, **45**, 1453.

93 Mordini, A., Peruzzi, D., Russo, F., Valacchi, M., Reginato, G. and Brandi, A. (2005) *Tetrahedron*, **61**, 3349.

94 Kaskel, S. and Sclichke, K. (2001) *Journal of Catalysis*, **201**, 270.

95 Wang, Y., Huang, W.Y., Wu, Z., Chun, Y. and Zhu, J.H. (2000) *Material Letters*, **46**, 198.

96 Wang, Y., Huang, W.Y., Chun, Y., Xia, J.R. and Zhu, J.H. (2001) *Chemistry of Materials*, **13**, 670.

97 Li, Z.-J., Prescott, H.A., Deutsch, J., Trunschke, A., Lieske, H. and Kemnitz, E. (2006) *Catalysis Letters*, **92**, 175.

98 Yin, S.F., Xu, B.Q., Wang, S.J. and Au, C.T. (2006) *Applied Catalysis A: General*, **301**, 202.

99 Wu, Z.Y., Jiang, Q., Wang, Y.M., Wang, H.J., Sun, L.B., Shi, L.Y., Xu, J.H., Wang, Y., Chun, Y. and Zhu, J.H. (2006) *Chemistry of Materials*, **18**, 4600.

100 Yamaguchi, T., Komatsu, M. and Okawa, M. (2002) *Catalysis Surveys from Japan*, **5**, 81.

101 Liu, X.J., He, H.Y., Wang, Y.J., Zhu, S.L. and Piao, X.L. (2008) *Fuel*, **87**, 216.

102 Kouzu, M., Kasuno, T., Tajika, M., Yamanaka, S. and Hidaka, J. (2008) *Applied Catalysis A: General*, **334**, 357.

103 MacLeod, C.S., Harvey, A.P., Lee, A.F. and Wilson, K. (2008) *Chemical Engineering Journal*, **135**, 63.

104 Fujita, S.-I., Bhanage, B.M., Aoki, D., Ochiai, Y., Iwasa, N. and Arai, M. (2006) *Applied Catalysis A: General*, **313**, 151.

105 Zhenqiang, Y. and Wenlei, X. (2007) *Fuel Processing Technology*, **88**, 631.

106 Valange, S., Beauchard, A., Barrault, J., Gabelica, Z., Daturi, M. and Can, F. (2007) *Journal of Catalysis*, **251**, 113.

107 Ndou, A.S., Plint, N. and Coville, N.J. (2003) *Applied Catalysis A: General*, **251**, 337.

108 Di Cosimo, J.I., Torres, G. and Apesteguia, C.R. (2002) *Journal of Catalysis*, **208**, 114.

109 Reddy, B.M., Ratnam, K.J., Saika, P. and Thrimurthulu, G. (2007) *Journal of Molecular Catalysis A–Chemical*, **276**, 197.

110 Kabashima, H. and Hattori, H. (1997) *Applied Catalysis A: General*, **161**, L33.

111 Kabashima, H. and Hattori, H. (1998) *Catalysis Today*, **44**, 277.

112 Wei, T., Wang, M., Wei, W., Sun, Y. and Zhang, B. (2003) *Fuel Processing Technology*, **83**, 175.

113 Li, Q., Zhang, W., Zhao, N., Wei, W. and Sun, Y. (2006) *Catalysis Today*, **115**, 111.

114 Qibiao, L., Ning, Z., Wei, W. and Yuhan, S. (2007) *Journal of Molecular Catalysis A–Chemical*, **270**, 44.

115 Fujita, S., Bhanage, B.M., Kanamaru, H. and Arai, M. (2005) *Journal of Molecular Catalysis A–Chemical*, **230**, 43.

116 Sun, N. and Klabunde, K. (1999) *Journal of Catalysis*, **185**, 506.

117 Diez, V.K., Apesteguia, C.R. and Di Cosimo, J.I. (2006) *Journal of Catalysis*, **210**, 235.

118 Di, J.I. and Apesteguia, C.R. (1998) *Journal of Molecular Catalysis A–Chemical*, **130**, 177.

119 Vishwanathan, V., Ndou, A.S., Sikhwivhilu, L., Plint, N., Raghavan, K.V. and Coville, N.J. (2001) *Chemical Communications*, 893.

120 Saadi, A., Rassoul, Z. and Bettahar, M.M. (2006) *Journal of Molecular Catalysis A–Chemical*, **258**, 59.

121 Chen, F., Lin, I., Li, H., Gan, G.J., Toh, K. and Tham, L. (2007) *Catalysis Communications*, **8**, 2053.

122 Zhang, A., Ma, Q., Wang, K., Liu, X., Shuler, P. and Tang, Y. (2006) *Applied Catalysis A: General*, 303.

123 Sivasanker, S. (2003) *Science and technology in catalysis 2002*, Studies in Surface Science and Catalysis, Vol. **85**, Elsevier, p. 145.

124 Delsarte, S., Florea, M., Mauge, F. and Grange, P. (2006) *Catalysis Today*, **116**, 216.

125 Hasni, M., Prado, G., Rouchard, J., Grange, P., Devillers, M. and Delsarte, S. (2006) *Journal of Molecular Catalysis A–Chemical*, **247**, 116.

Index

Metal Oxide Catalysis. Edited by S. David Jackson and Justin S. J. Hargreaves

ISBN: 978-3-527-31815-5

d

f